IMAGE SCIENCE

COLLECTED PUBLICATIONS (VOL. 5)
CHRONOLOGICAL LISTING 2000—2015

TOPICS

OPTICS & IMAGES
FOURIER OPTICS
ELECTROMAGNETICS
COMPUTER SYSTEMS

NICHOLAS GEORGE
Pebble Beach, California
ngeorge59@ur.rochester.edu
585-329-1029
September 2022

ISBN 978-0-9914729-4-9

This series is dedicated to

Carol Joy Neufeld George

IMAGE SCIENCE

COLLECTED PUBLICATIONS (VOL. 5)

PREFACE

This syllabus is prepared to introduce an above average senior student or a first year graduate student to the field of **Image Science** and to encourage this student to continue studies forward to the PhD degree. This is not a textbook as such but simply a collection of about 49 or so current literature topics. We chose this collection so that a starting graduate student can readily gain a good understanding of the physics, engineering, and mathematics involved in the field of **Image Science**. Of course there are other topics depending on your interests, e.g., astronomy, medicine, business and so on. These areas were chosen since they are within the four topics listed on the cover and they will provide one with an overall feeling or understanding of the entire field. What is the purpose of the syllabus? It is to answer a frequent, typical question asked by an entering graduate student: How do I find an interesting topic that is all my own and that I can ultimately develop into a thesis?

First, please recognize that you are entering your studies at a wonderful time. Since the end of WWII, many useful aids have appeared such as the computer and the internet, vastly improved scientific instrumentation, and a technological network that never previously existed. These vast advancements and a very excellent range of dedicated faculty will guide you through the process. Funding for graduate students and summer jobs in related areas are also plentiful. So where to begin? In exploring this syllabus you will gain an overview of what is going on in these 4 fields within **Image Science**. In your early class work you will take 3 or 4 courses with different instructors and become acquainted with their special abilities and focus. This process is invaluable in helping you decide whom to choose to help guide you through your first year learning process.

There are a few things you can do as a senior without committing yourself to a formal decision. Here are a few suggestions. For example at the University of Rochester you have excellent libraries with many talented librarians who are experts at literature searches. Find them and let them help you with your searches. Likely there are useful collections they can show you how to access. Computer access is world-class too and the librarians are always helpful in suggesting programs like Google Scholar. A research-oriented librarian knows a great many fine points which they are happy to teach you. Connecting with a librarian is a critical resource and should not be missed. Tell them thanks!

As fine points about literature searching, see if there is any preference or difference between a Google search and a USPTO search. Also study a few patents.

So for an incoming graduate scholar, here are a few suggestions as to how to think about selecting a thesis topic. First do a literature study with only a few topics and make summary descriptions of each field. Here we present an example summary for the field of **Fourier Optics**:

Fourier Optics is the field of physics that encompasses the study of light at visible wavelengths but including infrared and ultraviolet portions of the electromagnetic spectrum as well. Based upon Maxwell's equations for the electromagnetic field and using modern transform mathematics, principally Fourier transform theory in the solutions, **Fourier Optics** is particularly well-suited to the study of cascades of lenses and phase masks as are widely used in optical instruments ranging from microscopes to telescopes, i.e., linear optical systems. Study the books by Professor Joseph Goodman and principally his recent booklet *Fourier Transforms Using Mathematica*. **Fourier Optics** also incorporates the advances in communication theory in the treatment of coherency topics to permit a rich full analysis of optical systems that use various sources of illumination ranging from incoherent or white light to modulated laser beams. For Physical Optics, systems study of the point-spread-function and the optical transfer function can be described in a rigorous fashion. General transmission functions for lenses can be formulated and optical-system design that is valid in the non-paraxial regime is now practical. **Fourier Optics** places the analyses of linear optical systems on a rigorous theoretical foundation enabling one to calculate resolution, imaging and other interference phenomena in a careful and accurate fashion.

Another interesting miracle with the modern computer is to make sample, short paper summaries using the ResearchGate.net website which is helpful in obtaining an overall view of a specific topic.

Science is fascinating! **Image Science** is fascinating and a field that offers you, the student, the chance to find intriguing topics that interest you and the chance to make important contributions to the field during your future career. Enjoy the new journey on which you are about to embark. May it bring you happiness, fulfillment and success.

solution analysis of a gradient-index rod and a gradient-index lens array

ticle

2008

Xi Chen · Nicholas George

physical optics analysis of a gradient-index (GRIN) rod and a GRIN lens array with aberrations is sented. We investigated the optical path length and aberration of a GRIN rod without definition of the stop ne. We also defined an effective aberration transmission function to include aberrations into physical optics lysis. Our theoretica...

w

nsor modulation transfer function measurement using band-limited laser speckle

ticle

2008

Xi Chen · Nicholas George · Gennadiy Agranov · [...] · Bob Gravelle

ew methodology for image sensor modulation transfer function measurement using band-limited laser *ckle is presented. We use a circular opal milk glass diffuser illuminated by a 5 mW He-Ne laser and a linear* arizer to generate band-limited speckle on the sensor. The power spectral density cut-off frequency of the ckle is chosen to be twi...

w

egrated Coded Aperture Imaging in Optical Region

nference Paper

2008

Wanli Chi · Nicholas George

ovel coded aperture imaging system working in optical spectrum region is described. Excellent simulation ults are presented. The camera is also shown to be capable of multi-wavelength imaging with a single nochromatic detector array.

w

+7

ended Depth of Field through Unbalanced OPD

nference Paper Full-text available

2006

Kaiqin Chu · Nicholas George · Wanli Chi

depth of field of a conventional camera is extended simply by inserting an annular glass ring in front of the s. The operating principle is explained and experimental results are shown.

w

ge Science Research for Speckle-based LADAR (Speckle Research for 3D Imaging LADAR)

ticle Full-text available

2008

Nicholas George

propose a basic study of image science topics related to a new class of speckle-based laser-ranging radars DAR). For this imaging radar we study two basic system configurations: a wavefront sensing configuration an imaging configuration. Three major research projects are (1) study of speckle patterns to establish 3D litative features f...

The page above is from the ResearchGate.net website. It illustrates one way to develop listings of current research programs.

"Fiat Lux," University of California, Berkeley

"The truth shall make you free," California Institute of Technology

"Meliora," University of Rochester

End of Preface

IMAGE SCIENCE

VOLUME V: PUBLICATIONS 2000-2014

Nicholas George
Wilson Professor of Electronic Imaging
The Institute of Optics

101 "Scanned-picture-beam holography for nonrigid objects," Appl. Opt. **43**, pp. 1703-1709, 2004, William W. Cook and Nicholas George.

108 "Fractional finite Fourier transform," J. Opt. Soc. Am. A **21**, pp. 1179-1185, 2004, K. Khare and Nicholas George.

115 "Integrated imaging with a centrally obscured logarithmic asphere," Opt. Comm. **245**, pp. 85-92, 2005, Wanli Chi and Nicholas George.

123 "Sampling theory approach to eigenwavefronts of imaging systems," J. Opt. Soc. Am. A **22**, p. 434, 2005, K. Khare and Nicholas George.

128 "Light-emitting diode illumination design with a condensing sphere," J. Opt. Soc. Am. A, **23**, No. 9, pp. 2295-2298, 2006, Wanli Chi and Nicholas George.

132 "Polarization coded aperture," Optics Express **14**, p. 6634, 2006, Wanli Chi, Kaiqin Chu, and Nicholas George.

141 "Electronic holography at terahertz and infrared frequencies," Proceedings of the International Conference on Display Holography, Wales, 2006, Nicholas George, Kedar Khare, and Wanli Chi.

148 "Electronic Holography at Terahertz and Infrared Frequencies," Invited Paper, OSA Annual Meeting, Rochester, NY, October 2006, Nicholas George, K. Khare and Wanli Chi.

161 "Correlation function for speckle size in the right-half-space," Opt. Commun. **276**, pp. 1-7, 2007, Kaiqin Chu and Nicholas George.

168 "Infrared holography using a microbolometer array," Appl. Opt. **47** No. 4, pp. A7 – A12, 2008, Nicholas George, Kedar Khare and Wanli Chi.

174 "Speckle in the 4F optical system," Appl. Opt. **47**, No.4, pp. A13 – A20, 2008, Nien-An Chang and Nicholas George.

182 "Resolution analysis of a gradient-index rod and a gradient-index lens array," Appl. Opt., November 2008, Xi Chen and Nicholas George.

194 "Optics Optimization in High-Resolution Imaging Module with Extended Depth of Field," Proceedings SPIE, **7061**, pp. 1-12, 2008, Xi Chen, Dmitry Bakin, Changmeng Lieu, Nicholas George.

206 "Extending the depth of field through unbalanced optical path difference," Appl. Opt. **47**, No. 36, pp. 6895-6903, 2008, Kaiqin Chu, Nicholas George and Wanli Chi.

215 "Sensor modulation transfer function measurement using band-limited laser speckle," Opt. Express, **16**, No. 24, 2008, Xi Chen, Nicholas George, Gennadiy Agranov, Changmeng Liu and Bob Gravelle.

228 "Phase-Coded aperture for optical Imaging," Opt. Comm. **282**, pp. 2110-2117, 2009, Wanli Chi and Nicholas George.

236 "Incoherently combining logarithmic aspheric lenses for extended depth of field," Appl. Opt. **48**, pp. 5371-5379, 2009, Kaiqin Chu, Nicholas George and Wanli Chi.

245 "Extended depth-of-field lenses and methods for their design, optimization and manufacturing, U.S. Patent Application Publication US 2010/0002310 Al, Jan. 7, 2010, Nicholas George and Xi Chen.

272 "Wavelength decorrelation of speckle in propagation through a thick diffuser," J. Opt. Soc. Am. A **28**, No. 2, Feb. 2011, Nien-an Chang, Nicholas George, and Wanli Chi.

282 "Optical imaging with phase-coded aperture," Optics Express **19**, Issue 5, 4294-4300, 2011, Wanli Chi and Nicholas George.

288 "Optical Element, Device, Method, and Applications," U.S. Patent Publication US 2011/0085051 A1, 2011, Wanli Chi and Nicholas George.

306 "Illustrative EDOF topics in Fourier optics," Invited Talk, SPIE Annual Meeting, Tribute to Joseph W. Goodman 75th Year, August 2011, Nicholas George, Xi Chen, and Wanli Chi.

321 "Remotely measuring a thin dielectric coating on a metallic cylinder," Opt. Express **19**, Issue 27, 26684-26695, December 2011, Nicholas George and Paul Zavattero.

333 "Digital Binary MEMS Wavefront Control," U.S. Patent No. 8,107,156 B2, 2012, Nicholas George and Kedar Khare.

355 "Fourier Optics," © 2012, published as a monograph written in an advanced style and presently posted as freeware on UR web. Further publishing on this and related topics is underway.

401 "Deductive derivation of the displacement term in Maxwell's equations," September 2013, unpublished manuscript with supplementary poster/talk, Songfeng Han and Nicholas George.

409 "Digital Binary MEMS Wavefront Control," U.S. Patent No. 8,634,126 B2, 2014, Nicholas George and Kedar Khare.

ISSN: 0003-6935

4

Applied Optics

Information Processing

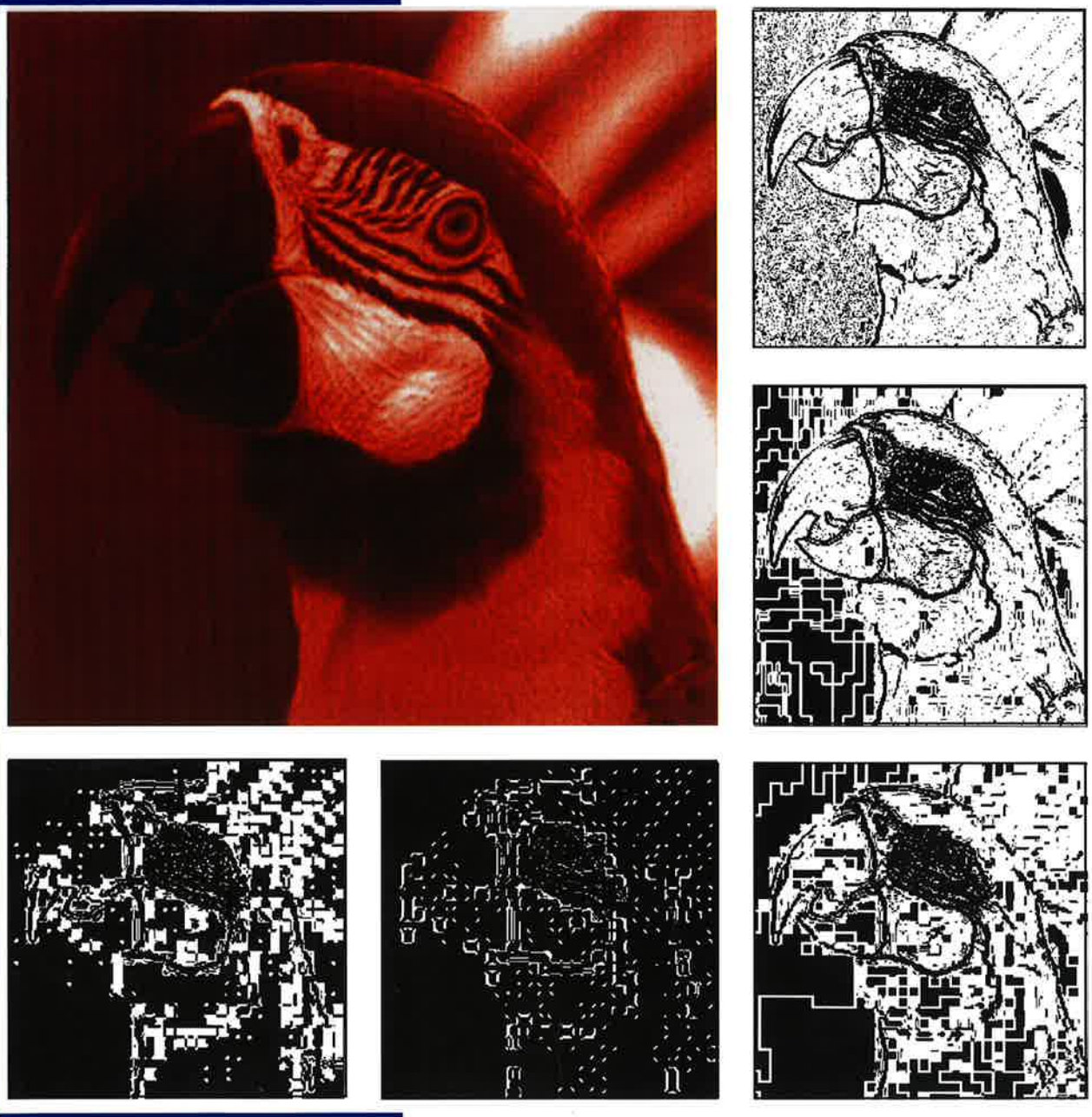

OSA
Optical Society of America

10 August 2000

All-digital ring–wedge detector applied to image quality assessment

David M. Berfanger and Nicholas George

In the automatic assessment of image quality we obtained a high accuracy in the classification of image degradations in a manner that is widely independent of scene content. Using an all-digital ring–wedge detector system combined with neural-network software, we conducted several experiments in which the end goal is to classify images according to numerical quality scales. Experiments are presented to stress the importance of both local and global image quality assessment. Two databases of degraded images were prepared. One uses five levels of Gaussian blur to simulate depth of field. The other was prepared with lossy compression and recovery with artifacts generated by a JPEG (Joint Photographic Experts Group) compression algorithm. In quantitative terms our best sorting of Gaussian blur without knowledge of the original scene was to an accuracy of 96%. For degradation using JPEG we obtained an accuracy of 95% without knowledge of the original and 98% when the original scene is available as a reference.

OCIS codes: 070.5010, 070.2590, 100.2000, 200.4260, 110.3000.

1. Introduction

The ever-increasing importance of electronic imaging has brought a new emphasis to the quality evaluation of digital imagery. In this paper we describe a system for the automatic assessment of image quality that is widely independent of scene content. A prevailing theme in the literature is that any definition of image quality is dependent on user requirements, which can vary greatly. For example, Eckert and Bradley are concerned with the visibility of distortions introduced into an image by lossy image-compression algorithms.[1] This definition is quite different from that used in studies both by Belaid *et al.*[2] and by Wen and Beaton,[3] who are concerned with the usefulness of an image in diagnosing a medical condition. An overview of several aspects of both the definition and the measurement of image quality is presented by Briggs.[4] For the purposes of this discussion we consider the quality of an image to be a lack of visible degradations from an ideal natural scene, and we restrict our consideration to digital images of real objects in real settings. Intended for visual inspection, these images are recorded by cameras or other sensors of the electromagnetic spectrum and are sampled and digitized for storage, retrieval, and eventual display.

Traditionally the assessment of image quality has been a labor-intensive task for highly trained photointerpreters or for psychovisual studies involving large numbers of human subjects. These human-perceptual methods of image quality assessment have a high correlation between observers and are widely considered to be the standard by which all other measures of image quality are compared. Examples of image quality evaluations involving photointerpreters are presented in studies by Coluccio *et al.*,[5] Latshaw *et al.*,[6] Snyder *et al.*,[7] and Burke and Snyder.[8] Examples of image quality evaluations involving large psychovisual studies are presented in studies by Chao *et al.*,[9] Westerink and Roufs,[10] Ohtsuka and Kosugi,[11] Hamberg and de Ridder,[12] and Kayargadde and Martens.[13] Comparative reviews of several methods by which humans make assessments of image quality are presented by Roufs[14] and by Roufs and Boschman.[15]

Early research in identifying objective measures of image quality described by Linfoot,[16,17] Schade,[18–22] Shaw,[23] and Wetherell[24] focused on characterizing specific degradations caused by imaging systems. In the 1970's there first appeared early reports of several experiments on the challenging task of auto-

The authors are with the Institute of Optics, Center for Electronic Imaging Systems, University of Rochester, Rochester, New York 14627. D. M. Berfanger's e-mail address is berfang@optics.rochester.edu. N. George's e-mail address is ngeorge@troi.cc.rochester.edu.

Received 16 August 1999; revised manuscript received 2 May 2000.

0003-6935/00/234080-18$15.00/0

mating the assessment of image quality, including studies by George,[25] George *et al.*,[26] Jensen,[27,28] Nill,[29] Tescher and Parsons,[30] Barnwell and Mersereau,[31] and Schindler.[32] More recent research in image quality has centered on the development of perceptually meaningful measures of image distortion, recognizing that more traditional and more tractable objective criteria do not correlate well to the visual appearance of individual scenes. Working primarily in the spatial-frequency domain, Barten introduced a metric incorporating the contrast sensitivity of the standard human observer,[33] and Nill and Bouzas presented an image quality measure based on the digital image power spectrum, which includes a model for the modulation transfer function (MTF) of the human visual system.[34] Similarly, using the discrete cosine transform, Saghri *et al.* presented a preliminary image quality measure that takes into account human sensitivities both to illumination level and to spatial-frequency content.[35] More involved models of the human perception derived from both psychophysical and neurophysiological studies were included in metrics by Grogan and Keene,[36] Davies *et al.*,[37] and Daly.[38] These multistage analysis algorithms include both image-domain and spatial-frequency-domain processing. Excellent practical summaries of several perceptually based image quality metrics are included in studies by Snyder,[39] Overington,[40] Jayant *et al.*,[41] and Abbey *et al.*[42]

Particularly important aspects of the studies cited above to the research described herein are the utility of using spatial-frequency information in the construction of image quality metrics and the importance of the Fourier domain in the modeling of the human visual system. This is especially evident in such multiresolutional approaches as the cortex transform described by Watson,[43,44] and the Gabor wavelet transform used by Taylor *et al.*[45] It is interesting to note that the calculations performed in these models are similar in many respects to the calculation of the all-digital ring–wedge data format.

In this paper we consider the application of the all-digital ring–wedge detector to the assessment of image quality. A principal objective is to establish limits on automatic, operator-independent, image quality assessment with the goal of establishing that computerized systems can perform at the level of a human observer even when assessing images widely varying in scene content. Our approach is to present several illustrative experiments, each with the end goal of classifying images according to numerical quality scales. For our experiments we devised two image quality bases with numerical quality scales. In the first, image quality of the original is degraded by use of a Gaussian blur function of increasing spread. In the second base set we use lossy JPEG (Joint Photographic Experts Group) compression to generate progressively poorer image quality in the recovered image. Our emphasis is on task-specific classifications in which an objective sorting is required.

In Section 2 we describe the recognition system platform that is used in our image quality assessment. In Appendix A we include an overview of two implementations of the all-digital ring–wedge detector format recently described in the literature: bin summing and mask summing.[46] Herein, we would like to emphasize that bin summing is conceptually straightforward and generally useful for larger-sized images. However, mask summing is more computationally expensive, but it is especially valuable when considering the evaluation of small areas of images.

In Section 3 we consider the problem of blur-level sorting. We report classification accuracies, using gray-scale images, each of which belongs to one of five established groupings relative to content: (a) animal, (b) architecture, (c) human face, (d) landscape, and (e) other. We report excellent experimental results in three stages. In the first stage we detail the results of a preliminary set of experiments intended to demonstrate the feasibility of our image quality rating system. In the second stage these preliminary experiments are extended to establish classification accuracy as a function of the size of the training set. In the third stage the testing data set is expanded to establish an overall classification accuracy of the system. Because it is important to characterize separately the value of ring data (power spectral density) and wedge data (edge-angle correlations) for making image quality assessments, sorting results from experiments with ring data only and wedge data only are also included. Additionally, given the importance of individual edges within a scene to the human assessment of image quality, we consider the use of ring–wedge data calculated from an edge profile of a scene. Briefly, for the task of blur-level sorting, wedge data either alone or in combination with ring data are found not to improve sorting accuracies over the use of ring data alone, although only limited preprocessing of these wedge data was tried in coupling to the neural network. However, the additional consideration of ring data from edge profiles of the imagery does improve system performance.

In Section 4 we continue our study by considering the sorting of images recovered from lossy compression. Using the standard JPEG image encoder,[47] we devised a novel database for the study of image quality. It consists of five image types and five degradation levels. Using both a gray-scale image and a corresponding edge profile in the assessment of each image, we report classification accuracies for ring-only, wedge-only, and ring–wedge experiments. Here we find that the ring–wedge sorting provides the best results, indicating that wedge data provide important features for quantifying the presence of localized artifacts introduced into an image by nonlinear degradations from the JPEG algorithm. Separately, since image fidelity is an important consideration in evaluating an image compression method, we demonstrate the ability of our system to perform the same sorting experiments using ring–wedge data calculated from the error image between

an original high-quality image and a corresponding degradation.

In Section 5 we conclude our discussion by considering the assessment of local image quality, using both ring–wedge and image-domain information. We stress the importance of this combination, because it offers a major improvement in performance over systems that use either image-domain or spatial-frequency-domain information alone. We present a series of experiments with the goal of estimating local image fidelity without explicit knowledge of the original image. We are again considering the standard JPEG compression algorithm. We report our best result, using a two-stage system. First, ring–wedge data from the entire image are used to sort the image into a summarized quality level, and then a segmented ring–wedge transform is used to estimate the local fidelity with one of five networks specially trained for the particular summarized quality level. This approach produced a 0.96 correlation between fidelity estimates made with the degraded image only and actual fidelity calculations made with the just-noticeable-distortion (JND) profile, which uses direct information from both the degraded image and a corresponding original.[48] We consider the JND approach of assessing image fidelity, since it was shown by Eude and Cherifi to predict well the visual fidelity of images degraded by the JPEG algorithm as assessed by human subjects.[49] We emphasize that our method uses information from the degraded image alone, without specific data from the original scene, thus verifying our initial goal.

2. All-Digital Ring–Wedge Detector System

For our studies of automatically assessing image quality we use a test setup shown in Fig. 1(b) that was adapted from an earlier analog system shown in Fig. 1(a). Since the early 1970's this optoelectronic hybrid based on the ring–wedge photodetector[26] has been used in a series of successful classifications and recognitions, such as cats versus dogs, hypodermic syringes, particulate sizing, handwriting, medical photomicrographs, and image quality. However, the advent of neural-network software has led to a remarkable improvement in user friendliness and a dramatic decrease of 400 to 1 in the time required to develop software.[46,50]

Also, the all-digital system in Fig. 1(b) has the advantage of affordability, and it permits one to use both spatial-frequency data and direct image data simultaneously. In a recent paper we describe extremely accurate recognition of thumbprints as well as the algorithm structure for obtaining the all-digital ring–wedge format.[46] Herein, in Appendix A, we provide an overview of these algorithms that is relevant to our present goal of establishing that it is possible to classify images by quality in a manner that is widely independent of scene content. Relations (A4)–(A6) provide the algorithm for the studies presented in this paper.

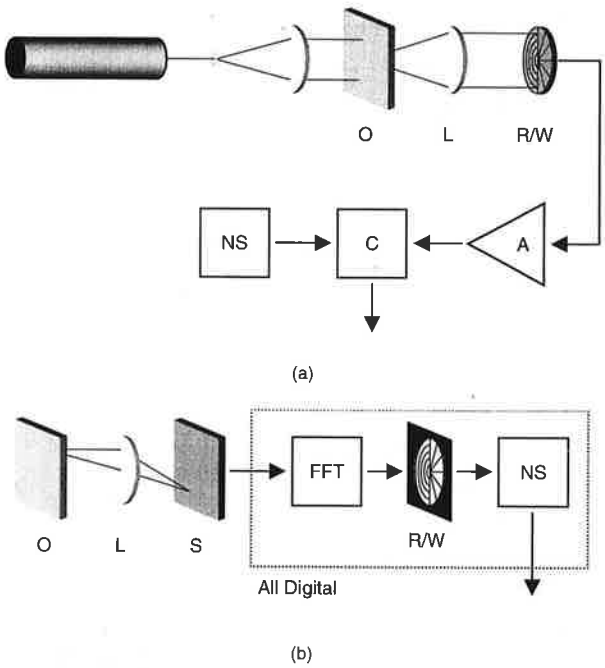

Fig. 1. (a) Coherent optoelectronic hybrid processor incorporating the analog ring–wedge detector array and neural-network software. (b) All-digital Fourier domain recognition system incorporating ring–wedge data format and neural-network software. O, input object; L, (a) optical transform lens, (b) imaging lens; S, sampling system; FFT, fast Fourier transform; R/W, digital ring–wedge detector; NS, neural-network software; C, digital computer; A, amplifier and interface.

3. Blur-Level Studies

In this section we consider the automatic estimation of blur-level involving images with widely varying scene content and using only data from degraded images without explicit knowledge of the original. Our method is to present several illustrative experiments with neural-network software to perform the sorting of images into established quality levels. We review the results in three stages: a preliminary set of image sortings to assess the feasibility of our approach, an expanded study to determine training requirements, and a final study to measure overall classification accuracy. In these studies we consider the relative importance of the ring data (power spectral density) and the wedge data (edge-angle correlations). Additionally, we consider the use of ring–wedge data calculated from an edge profile of the image being assessed.

Defocus and other types of image blurring are common image degradations. Other researchers have considered the role of image blur in image quality. Kusaka studied the psychological effects on perceived picture quality induced by image blur.[51] Burke and Snyder[8] and, later, Chao *et al.*,[9] considered the effects of blur along with noise as principal factors limiting human performance. Hamberg and de Ridder considered blur in studies measuring the human ability to estimate time-varying image quality,[12] and Kayargadde and Martens demonstrated that per-

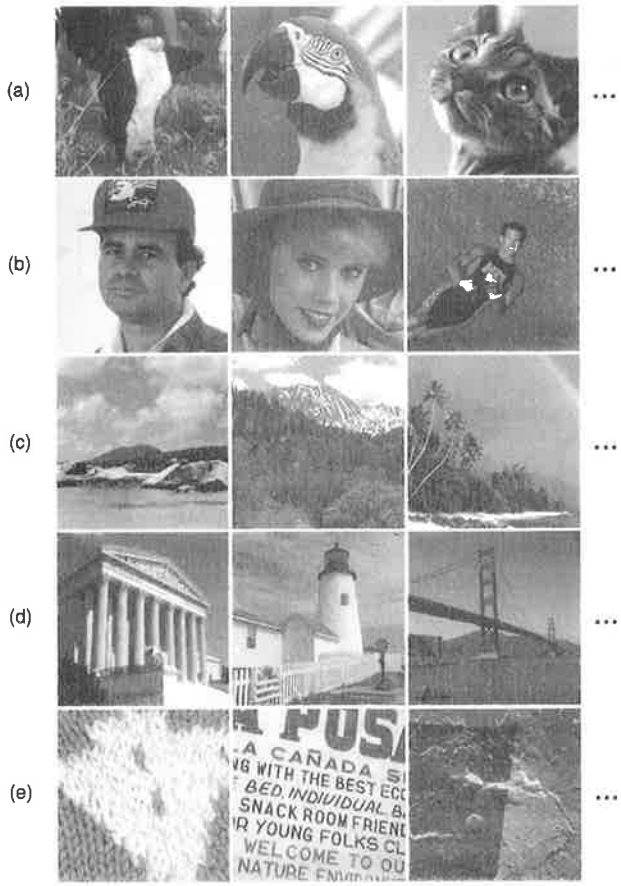

Fig. 2. Example gray-scale images used in blur-level and JPEG compression studies. Types of pictures include (a) animals, (b) human faces, (c) natural landscapes, (d) architecture, and (e) other.

ceived blur is an important factor in the construction of a multidimensional perceptual space for the characterization of overall image quality.[13,52] The automatic characterization of defocus using the laser-optical ring–wedge detector was first studied by Venable and George.[53] They devised object-related algorithms, which were tested on a limited number of widely varying scenes.

A. Preliminary Classifications of Image Quality

For the sorting of images based on blur level, high-quality images were acquired from digital stock photography representing five scene types: (a) animal, (b) human face, (c) landscape, (d) architecture, and (e) other. Images were 256×256 pixels at 8 bits/pixel. Some typical images for each image type in the data set are shown in Fig. 2.

As we have previously described, a preliminary set of experiments was conducted to test the feasibility of our approach.[54] For these experiments ten images were selected for our image database (two images per type). Four degrees of degradation for each of these images were generated by introduction of increasing amounts of computer-generated convolution-type blurring. A data set of 50 pictures was thus created with five visually distinct quality levels, which are described by the adjectives very good, good, fair, poor, and very poor. Details of the implementation of this type of image processing can be found in many standard image processing texts, such as that of Jain.[55] To generate the spatial masks used to obtain each blur level, we used the Gaussian impulse response with variance σ^2, described by the following equation:

$$h(x, y) = \frac{1}{2\pi\sigma^2} \exp\left(-\frac{x^2 + y^2}{2\sigma^2}\right), \tag{1}$$

where x and y are Cartesian spatial coordinates. Figure 3 shows the spatial masks used for each blur level, which were obtained with $\sigma = 1$, 2, 3, and 4 pixels. Representative examples for each of the quality levels are given in Fig. 4.

The images were subdivided into two disjoint sets: a learning set and a testing set. Ring–wedge data for both sets were calculated with the bin-summing method, and the resulting measurements were preprocessed as follows: The logarithm of the ring data was taken, and both the ring data and the wedge data were scaled to range between approximately -1 and 1 with maximum and minimum values for each network input as determined from the training set. It is interesting to consider the contrast between these rather straightforward preprocessing techniques to the complex algorithms used in much of the perceptual image quality research cited above.

In structuring the neural network, a fully connected, three-layer, feed-forward configuration was chosen with sigmoidal activation functions. There were 64 input neurons, 20 hidden neurons, and 5 output neurons corresponding to the five quality levels. This network was trained and tested with two different strategies. Tables 1–4 show the recognition results from these two experiments. The first strategy, detailed in Table 1, includes a representative from each scene type in both the learning and the testing sets. After training with this strategy, the neural network was able to recognize the blur level of the images in the testing set of 25 images with only three errors. The occurrences of these errors and their types for each blur level are presented in Table 2. The second strategy, detailed in Table 3, includes only three of the five scene types in the learning set and all five types in the testing set. Hence there are 15 images in the training set and 35 images in the learning set. After training with this strategy, the neural network was able to recognize the blur level of the images in the testing set with the exception of four errors. The occurrences of these errors are presented in Table 4. In summary, with this first series of experiments, we see that the neural network does provide a successful sorting of the images based on blur level.

B. Size of the Training Set

For a second phase of the blur-level classification the goals are (1) to determine classification accuracy as a function of the size of the training set used, (2) to ascertain the relative importance of ring data (power

$$\frac{1}{255}\begin{bmatrix} 1 & 3 & 6 & 3 & 1 \\ 3 & 15 & 25 & 15 & 3 \\ 6 & 25 & 43 & 25 & 6 \\ 3 & 15 & 25 & 15 & 3 \\ 1 & 3 & 6 & 3 & 1 \end{bmatrix}$$

(1)

$$\frac{1}{1020}\begin{bmatrix} 0 & 0 & 1 & 1 & 2 & 2 & 2 & 1 & 1 & 0 & 0 \\ 0 & 1 & 2 & 3 & 5 & 5 & 5 & 3 & 2 & 1 & 0 \\ 1 & 2 & 4 & 8 & 12 & 13 & 12 & 8 & 4 & 2 & 1 \\ 1 & 3 & 8 & 15 & 22 & 25 & 22 & 15 & 8 & 3 & 1 \\ 2 & 5 & 12 & 22 & 32 & 36 & 32 & 22 & 12 & 5 & 2 \\ 2 & 5 & 13 & 25 & 36 & 40 & 36 & 25 & 13 & 5 & 2 \\ 2 & 5 & 12 & 22 & 32 & 36 & 32 & 22 & 12 & 5 & 2 \\ 1 & 3 & 8 & 15 & 22 & 25 & 22 & 15 & 8 & 3 & 1 \\ 1 & 2 & 4 & 8 & 12 & 13 & 12 & 8 & 4 & 2 & 1 \\ 0 & 1 & 2 & 3 & 5 & 5 & 5 & 3 & 2 & 1 & 0 \\ 0 & 0 & 1 & 1 & 2 & 2 & 2 & 1 & 1 & 0 & 0 \end{bmatrix}$$

(2)

$$\frac{1}{2295}\begin{bmatrix} 0 & 0 & 0 & 0 & 0 & 1 & 1 & 1 & 1 & 1 & 1 & 1 & 0 & 0 & 0 & 0 & 0 \\ 0 & 0 & 0 & 1 & 1 & 2 & 2 & 3 & 3 & 3 & 2 & 2 & 1 & 1 & 0 & 0 & 0 \\ 0 & 0 & 1 & 1 & 2 & 3 & 4 & 5 & 6 & 5 & 4 & 3 & 2 & 1 & 1 & 0 & 0 \\ 0 & 1 & 1 & 3 & 4 & 6 & 8 & 10 & 10 & 10 & 8 & 6 & 4 & 3 & 1 & 1 & 0 \\ 0 & 1 & 2 & 4 & 7 & 10 & 14 & 16 & 16 & 16 & 14 & 10 & 7 & 4 & 2 & 1 & 0 \\ 1 & 2 & 3 & 6 & 10 & 15 & 20 & 24 & 25 & 24 & 20 & 15 & 10 & 6 & 3 & 2 & 1 \\ 1 & 2 & 4 & 8 & 14 & 20 & 27 & 31 & 33 & 31 & 27 & 20 & 14 & 8 & 4 & 2 & 1 \\ 1 & 3 & 5 & 10 & 16 & 24 & 31 & 37 & 39 & 37 & 31 & 24 & 16 & 10 & 5 & 3 & 1 \\ 1 & 3 & 6 & 10 & 16 & 25 & 33 & 39 & 43 & 39 & 33 & 25 & 16 & 10 & 6 & 3 & 1 \\ 1 & 3 & 5 & 10 & 16 & 24 & 31 & 37 & 39 & 37 & 31 & 24 & 16 & 10 & 5 & 3 & 1 \\ 1 & 2 & 4 & 8 & 14 & 20 & 27 & 31 & 33 & 31 & 27 & 20 & 14 & 8 & 4 & 2 & 1 \\ 1 & 2 & 3 & 6 & 10 & 15 & 20 & 24 & 25 & 24 & 20 & 15 & 10 & 6 & 3 & 2 & 1 \\ 0 & 1 & 2 & 4 & 7 & 10 & 14 & 16 & 16 & 16 & 14 & 10 & 7 & 4 & 2 & 1 & 0 \\ 0 & 1 & 1 & 3 & 4 & 6 & 8 & 10 & 10 & 10 & 8 & 6 & 4 & 3 & 1 & 1 & 0 \\ 0 & 0 & 1 & 1 & 2 & 3 & 4 & 5 & 6 & 5 & 4 & 3 & 2 & 1 & 1 & 0 & 0 \\ 0 & 0 & 0 & 1 & 1 & 2 & 2 & 3 & 3 & 3 & 2 & 2 & 1 & 1 & 0 & 0 & 0 \\ 0 & 0 & 0 & 0 & 0 & 1 & 1 & 1 & 1 & 1 & 1 & 1 & 0 & 0 & 0 & 0 & 0 \end{bmatrix}$$

(3)

$$\frac{1}{4080}\begin{bmatrix} 0 & 0 & 0 & 0 & 0 & 0 & 0 & 1 & 1 & 1 & 1 & 1 & 1 & 1 & 1 & 0 & 0 & 0 & 0 & 0 & 0 \\ 0 & 0 & 0 & 0 & 0 & 1 & 1 & 1 & 1 & 2 & 2 & 2 & 2 & 1 & 1 & 1 & 1 & 0 & 0 & 0 & 0 & 0 \\ 0 & 0 & 0 & 0 & 1 & 1 & 1 & 2 & 2 & 3 & 3 & 3 & 3 & 2 & 2 & 1 & 1 & 1 & 0 & 0 & 0 & 0 \\ 0 & 0 & 0 & 1 & 1 & 2 & 3 & 3 & 4 & 5 & 5 & 6 & 5 & 5 & 4 & 3 & 3 & 2 & 1 & 1 & 0 & 0 \\ 0 & 0 & 1 & 1 & 2 & 3 & 4 & 5 & 7 & 8 & 9 & 9 & 9 & 8 & 7 & 5 & 4 & 3 & 2 & 1 & 1 & 0 \\ 0 & 1 & 1 & 2 & 3 & 4 & 6 & 8 & 10 & 12 & 13 & 13 & 13 & 12 & 10 & 8 & 6 & 4 & 3 & 2 & 1 & 1 \\ 0 & 1 & 1 & 3 & 4 & 6 & 9 & 11 & 14 & 17 & 18 & 19 & 18 & 17 & 14 & 11 & 9 & 6 & 4 & 3 & 1 & 1 \\ 1 & 1 & 2 & 3 & 5 & 8 & 11 & 15 & 19 & 22 & 24 & 25 & 24 & 22 & 19 & 15 & 11 & 8 & 5 & 3 & 2 & 1 \\ 1 & 1 & 2 & 4 & 7 & 10 & 14 & 19 & 23 & 27 & 30 & 31 & 30 & 27 & 23 & 19 & 14 & 10 & 7 & 4 & 2 & 1 \\ 1 & 2 & 3 & 5 & 8 & 12 & 17 & 22 & 27 & 32 & 35 & 36 & 35 & 32 & 27 & 22 & 17 & 12 & 8 & 5 & 3 & 2 \\ 1 & 2 & 3 & 5 & 9 & 13 & 18 & 24 & 30 & 35 & 39 & 40 & 39 & 35 & 30 & 24 & 18 & 13 & 9 & 5 & 3 & 2 \\ 1 & 2 & 3 & 6 & 9 & 13 & 19 & 25 & 31 & 36 & 40 & 41 & 40 & 36 & 31 & 25 & 19 & 13 & 9 & 6 & 3 & 2 \\ 1 & 2 & 3 & 5 & 9 & 13 & 18 & 24 & 30 & 35 & 39 & 40 & 39 & 35 & 30 & 24 & 18 & 13 & 9 & 5 & 3 & 2 \\ 1 & 2 & 3 & 5 & 8 & 12 & 17 & 22 & 27 & 32 & 35 & 36 & 35 & 32 & 27 & 22 & 17 & 12 & 8 & 5 & 3 & 2 \\ 1 & 1 & 2 & 4 & 7 & 10 & 14 & 19 & 23 & 27 & 30 & 31 & 30 & 27 & 23 & 19 & 14 & 10 & 7 & 4 & 2 & 1 \\ 1 & 1 & 2 & 3 & 5 & 8 & 11 & 15 & 19 & 22 & 24 & 25 & 24 & 22 & 19 & 15 & 11 & 8 & 5 & 3 & 2 & 1 \\ 0 & 1 & 1 & 3 & 4 & 6 & 9 & 11 & 14 & 17 & 18 & 19 & 18 & 17 & 14 & 11 & 9 & 6 & 4 & 3 & 1 & 1 \\ 0 & 1 & 1 & 2 & 3 & 4 & 6 & 8 & 10 & 12 & 13 & 13 & 13 & 12 & 10 & 8 & 6 & 4 & 3 & 2 & 1 & 1 \\ 0 & 0 & 1 & 1 & 2 & 3 & 4 & 5 & 7 & 8 & 9 & 9 & 9 & 8 & 7 & 5 & 4 & 3 & 2 & 1 & 1 & 0 \\ 0 & 0 & 0 & 1 & 1 & 2 & 3 & 3 & 4 & 5 & 5 & 6 & 5 & 5 & 4 & 3 & 3 & 2 & 1 & 1 & 0 & 0 \\ 0 & 0 & 0 & 0 & 1 & 1 & 1 & 2 & 2 & 3 & 3 & 3 & 3 & 3 & 2 & 2 & 1 & 1 & 1 & 0 & 0 & 0 \\ 0 & 0 & 0 & 0 & 0 & 1 & 1 & 1 & 1 & 2 & 2 & 2 & 2 & 2 & 1 & 1 & 1 & 1 & 0 & 0 & 0 & 0 \\ 0 & 0 & 0 & 0 & 0 & 0 & 0 & 1 & 1 & 1 & 1 & 1 & 1 & 1 & 1 & 1 & 0 & 0 & 0 & 0 & 0 & 0 \end{bmatrix}$$

(4)

Fig. 3. Spatial masks used in the blurring of images in the blur-level study. No mask is shown for the original image (*o*). Quality descriptors for blurred images are (1) good, (2) fair, (3) poor, and (4) very poor.

spectral density) and wedge data (edge-angle correlation) in the assessment process, and (3) to study the utility of including ring–wedge data from edge profiles of the images being assessed. We include the study of edge profiles of a scene, since it has been shown that the edge content of a scene is particularly important to the human evaluation of image quality.[56] The edge profile at each pixel is determined by calculation of the weighted average of luminance changes around the pixel in four directions. The spatial masks used in this nonlinear filtering operation are shown in Fig. 5. At each pixel the maximum of the values calculated with each of these directional masks is used, and the resulting image is binarized by the following point operation: A global threshold is used, such that pixels with values above 2 and below 128 are set to 0, whereas all other pixels are set to 255. Figure 6 shows representative edge profiles calculated in this way for an architectural image at each of the various degradation levels.

We expanded our image database to include six original scenes per image type for a total of 150 images (30 originals at 5 degradation levels each). In structuring the neural networks we again chose fully connected three-layer configurations. Three cases are considered: data from gray-scale images only, data from edge profiles only, and data from both gray-scale images and edge profiles in combination. In the first and the second cases, 32 input neurons were used for both the ring-only and the wedge-only sort-

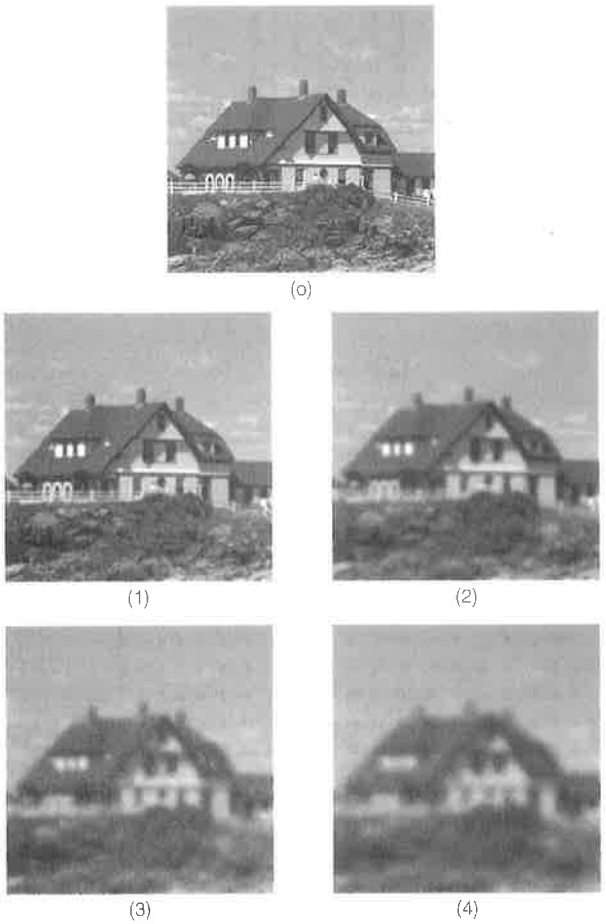

Fig. 4. Representative degradation levels for images used in the blur-level study. Quality descriptors for the images are (*o*) very good, (1) good, (2) fair, (3) poor, and (4) very poor.

ings, whereas 64 input neurons were used for the ring–wedge sortings. For experiments using data from both gray-scale images and edge profiles the input neuron counts were correspondingly doubled (see Fig. 7). In all cases the second (hidden) and the third (output) layers used 20 and 5 neurons, respectively.

Since the scene content varies greatly from image to image, even within a particular image type, it is interesting to score the classification as a function of the number of training images used. Hence in the training we used only a single image for each type with the remaining images used in testing. Then we repeated the training, using two images per type and so on. Table 5 shows the error in sorting the image degradation levels in columns that indicated the number of images used for each image type in the training. In all cases the training set was correctly identified, with the number of cycles showing the acceptable level of training. The error-rate fraction is defined as the number of errors over the number remaining in the test set. Of course, images used during the learning cycle are not included in the test set.

With this second series of experiments we see that

Table 1. Learning–Testing Strategy for a Preliminary Experiment Based on Blur-Level Classification Including a Single Representative Scene for Each of Five Types in Both the Learning and the Testing Sets

Image Type	Learn	Test
(a) Animal	A	B
(b) Human face	A	B
(c) Natural landscape	A	B
(d) Architecture	A	B
(e) Other	A	B

Table 2. Classification Results Detailing Error Occurrences for Each Degradation Level

	Maximum Valued Output Neuron				
Image Quality	1	2	3	4	5
(*o*) Very good	5				
(1) Good		5			
(2) Fair			4	(d)	
(3) Poor				4	(a)
(4) Very poor				(e)	4

the neural network does provide a successful sorting of image degradation level, across all five scene types. It is found to be important to train the system with a number of sample images for each image type so that the great variability in scene content can be properly accounted for by the network. In Table 5 when four or five of the six images are used in the training, we see that excellent classifications of image quality are obtained with rings only on images or images plus edge profiles. Moreover, excellent classifications also result with ring–wedge data, again, for images or images plus edge profiles. Interestingly, the wedge data alone do not contribute to the accuracy of the classification. Perhaps with some ingenuity in the

Table 3. Learning–Testing Strategy for a Preliminary Experiment Based on Blur-Level Recognition Including a Single Representative Scene for Only Three of the Five Types in the Learning Set and All Five Types in the Testing Set

Image Type	Learn	Test
(a) Animal	A	B
(b) Human face		A, B
(c) Natural landscape		A, B
(d) Architecture	A	B
(e) Other	A	B

Table 4. Recognition Results

	Maximum Valued Output Neuron				
Image Quality	1	2	3	4	5
(*o*) Very good	7				
(1) Good		7			
(2) Fair			6	(c)	
(3) Poor			(e)	5	(a)
(4) Very poor				(e)	6

$$\frac{1}{16}\begin{vmatrix} 0 & 0 & 0 & 0 & 0 \\ 1 & 3 & 8 & 3 & 1 \\ 0 & 0 & 0 & 0 & 0 \\ -1 & -3 & -8 & -3 & -1 \\ 0 & 0 & 0 & 0 & 0 \end{vmatrix} \quad G_1 \qquad \frac{1}{16}\begin{vmatrix} 0 & 0 & 1 & 0 & 0 \\ 0 & 8 & 3 & 0 & 0 \\ 1 & 3 & 0 & -3 & -1 \\ 0 & 0 & -3 & -8 & 0 \\ 0 & 0 & -1 & 0 & 0 \end{vmatrix} \quad G_2$$

$$\frac{1}{16}\begin{vmatrix} 0 & 0 & 1 & 0 & 0 \\ 0 & 0 & 3 & 8 & 0 \\ -1 & -3 & 0 & 3 & 1 \\ 0 & -8 & -3 & 0 & 0 \\ 0 & 0 & -1 & 0 & 0 \end{vmatrix} \quad G_3 \qquad \frac{1}{16}\begin{vmatrix} 0 & 1 & 0 & -1 & 0 \\ 0 & 3 & 0 & -3 & 0 \\ 0 & 8 & 0 & -8 & 0 \\ 0 & 3 & 0 & -3 & 0 \\ 0 & 1 & 0 & -1 & 0 \end{vmatrix} \quad G_4$$

Fig. 5. Spatial masks for calculating the weighted average of luminance changes in four directions.

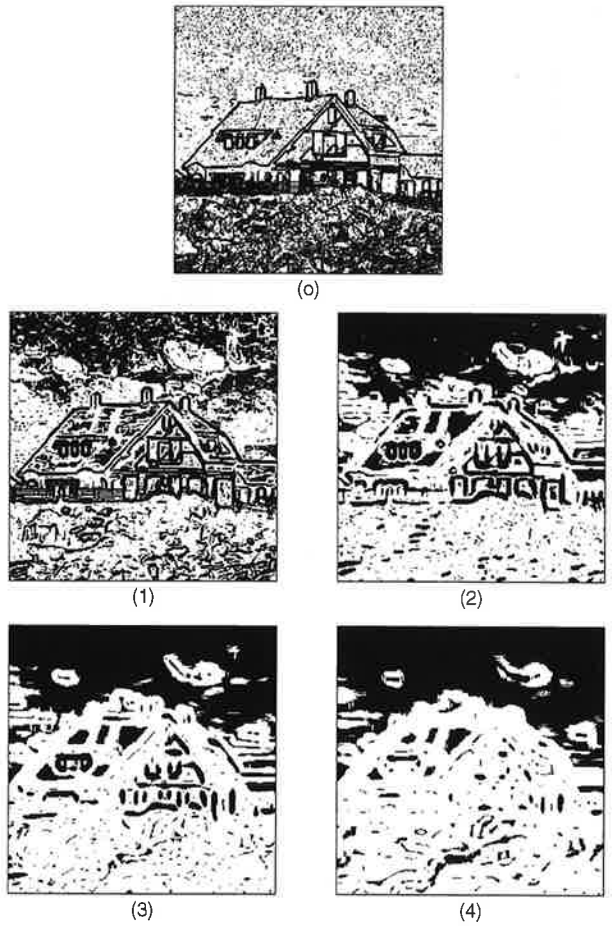

Fig. 6. Edge profiles of a representative image at the five degradation levels used in the blur-level study. Quality descriptors for the images are (*o*) very good, (1) good, (2) fair, (3) poor, and (4) very poor.

preprocessing, the effectiveness of the wedge data might be improved. Finally, it is interesting to point out that the activations of the second-largest neuron values were 0.4 and 0.2, respectively, for the ring-only error rate fractions of 1/25 (image) and 0/25 (image plus edge profile). From this we also recognize the importance of the edge-profile technique.

C. Accuracy of Sorting a Large Data Set

For a third phase of the blur-level classification we would like to establish a more accurate level of sorting accuracy than is possible with the smaller data sets used in Subsections 3.A or 3.B. Thus additional images were selected, increasing the database to include 15 original images for each of the 5 image types. The resulting database consists of 375 gray-scale images (75 high-quality originals with 4 additional degraded versions of each original).

Using the same neural-network configurations as described in Subsection 3.B (see Fig. 7) and five images per image type for training, we performed three separate experiments. First, using only ring data from both gray-scale images and edge profiles (64 input neurons), we found 10 errors out of 250. Second, using only wedge data (64 input neurons), we obtained 59 errors out of 250. Parenthetically, we remark that these two sortings are based on power spectral density and edge-angle correlations, respectively. In the third experiment, using both ring data and wedge data (128 input neurons), we found an error rate of 18 in 250. Detailed summaries of the errors from each of these experiments are presented in Tables 6, 7, and 8, respectively. We obtained the best classification accuracy of better than 95% with ring data only.

D. Algorithm Alternative for Image Quality Assessment

For comparative purposes it is instructive to consider an alternative method of automatic recognition to the all-digital ring–wedge data format. From the error-rate-fraction study above we can see that algorithms can be evaluated either singly or multiply with the neural network together with the image quality set. Hence we conducted the following experiment, using four traditional objective image quality metrics: correlation quantity,[17] relative structural content,[17] equivalent passband,[22] and power spectral moments,[29] as described in Eqs. (2), (3), (4), and (5), respectively. In these equations we use $\bar{F}(u, v)$ to denote the discrete Fourier transform of the intensity-based array image whose quality is being assessed and $\bar{F}_o(u, v)$ to denote the discrete Fourier transform of a corresponding ideal reference scene. u and v are discrete Cartesian spatial-frequency indices.

Linfoot's measures of image quality, which include correlation quantity Q and relative structural content T, were developed just ahead of the surge of digital computers. For digital images these metrics

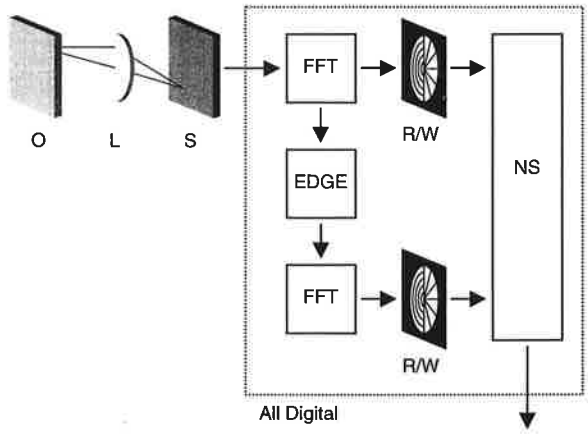

Fig. 7. All-digital Fourier domain image quality rating system incorporating ring–wedge data format and neural-network software: O, input object; L, imaging lens; S, sampling system; FFT, fast Fourier transform; EDGE, edge profile calculation; R/W, digital ring–wedge detector; NS, neural-network software.

can be described in the discrete frequency domain by the following equations:

$$Q = \frac{\sum_u \sum_v \tilde{F}(u, v)\tilde{F}_o^*(u, v)}{\sum_u \sum_v |\tilde{F}_o(u, v)|^2}, \tag{2}$$

$$T = \frac{\sum_u \sum_v |\tilde{F}(u, v)|^2}{\sum_u \sum_v |\tilde{F}_o(u, v)|^2}, \tag{3}$$

where the summations over u and v include all the pixels in the discrete transform and the symbol * denotes the complex conjugate. Q is the normalized cross correlation between $\tilde{F}(u, v)$ and $\tilde{F}_o(u, v)$ and is thus a figure of merit that quantifies the differential distortion within the image with respect to the reference. T, however, estimates the relative amount of detail retained between the image and the reference. We note that two other commonly used image fidelity metrics, mean-squared error and signal-to-noise ratio, can be inferred from these two metrics.

Equivalent passband, as described by Schade,[22] measures the quality of an imaging system in terms of its modulation transfer function by computing the passband of an ideal filter that passes the same power. To apply this concept to image fidelity analysis, we estimate the system modulation transfer function using the quotient of the discrete Fourier transforms of the image over the reference. The resulting metric calculation is given as follows:

$$N_e = \sum_u \sum_v \left| \frac{\tilde{F}(u, v)}{\tilde{F}_o(u, v)} \right|^2. \tag{4}$$

Power spectral moments, as described by Nill,[29] compress the Fourier power spectrum of the image down to a single-valued metric factor by summing together the pixel values after weighting to adjust for the typical drop-off of power with increasing spatial frequency, as follows:

$$M = \frac{\sum_u \sum_v (u^2 + v^2)^{3/2}|\tilde{F}(u, v)|^2}{\sum_u \sum_v (u^2 + v^2)^{1/2}|\tilde{F}_o(u, v)|^2}. \tag{5}$$

The resulting figure of merit places emphasis on midrange and high-frequency content of the image in the assessment of its quality.

Using the values of these four metrics for each of the degraded images as inputs, we constructed a neural network to perform the blur-level sorting. We obtained the best sorting results from a system that

Table 5. Error Rate Fraction for Blur-Level Classification Showing the Number of Cycles in the Training

	Number of Training Sets				
Error Rate Fractions	1	2	3	4	5
Ring-only cycles	10,000	20,000	30,000	40,000	50,000
Image	25/125	15/100	8/75	4/50	1/25
Edge profile	52/125	27/100	13/75	9/50	5/25
Image and edge profile	23/125	14/100	6/75	3/50	0/25
Wedge-only cycles	100,000	100,000	350,000	400,000	500,000
Image	100/125	70/100	50/75	20/50	10/25
Edge profile	99/125	72/100	55/75	23/50	11/25
Image and edge profile	98/125	70/100	52/75	22/50	11/25
Ring–wedge cycles	10,000	20,000	30,000	40,000	50,000
Image	30/125	16/100	10/75	3/50	1/25
Edge profile	50/125	23/100	10/75	6/50	3/25
Image and edge profile	26/125	15/100	8/75	4/50	1/25

Table 6. Blur-Level Classification Accuracy for Only Ring Data from Both Gray-Scale Imagery and Corresponding Edge Profiles for a Data Set of 250 Separate Images in the Testing Set with Ten Errors

	Maximum Valued Output Neuron				
Image Quality	1	2	3	4	5
(*o*) Very good	49	1			
(1) Good		49	1		
(2) Fair		2	48	1	
(3) Poor			2	46	2
(4) Very poor				2	48

Table 7. Blur-Level Classification Accuracy for Only Wedge Data from Both Gray-Scale Imagery and Corresponding Edge Profiles for a Data Set of 250 Separate Images in the Testing Set with 59 Errors

	Maximum Valued Output Neuron				
Image Quality	1	2	3	4	5
(*o*) Very good	49	1			
(1) Good		47	3		
(2) Fair		5	36	9	
(3) Poor			11	15	24
(4) Very poor			4	2	44

Table 8. Blur-Level Classification Accuracy for Both Ring and Wedge Data from Gray-Scale Imagery and Corresponding Edge Profiles for a Data Set of 250 Separate Images in the Testing Set with 18 Errors

	Maximum Valued Output Neuron				
Image Quality	1	2	3	4	5
(*o*) Very good	49	1			
(1) Good		49	1		
(2) Fair		1	47	2	
(3) Poor			3	42	5
(4) Very poor			3	2	45

Table 9. Blur-Level Classification Accuracy Using Four Common Image Objective Image Quality Measures from Gray-Scale Imagery for a Data Set of 250 Separate Images in the Testing Set with an Overall Accuracy of 53%

	Maximum Valued Output Neuron				
Image Quality	1	2	3	4	5
(*o*) Very good	50				
(1) Good		35	9	2	4
(2) Fair		17	15	4	14
(3) Poor		13	10	7	20
(4) Very poor		10	8	5	27

considered all four of the metrics in combination. The relatively poor results of this sorting are presented in Table 9. We note that, in each case that we tried, the ring–wedge system had superior performance to that of the system using the traditional image quality metrics as inputs. Thus this poor classification accuracy with *ad hoc* algorithms illustrates the difficulty of this sorting as well as the advantage inherent in grouping the Fourier domain data into the ring-wedge format.

Through the experiments presented in this section we have demonstrated an effective image quality rating system as shown in Fig. 7. This system incorporates data from both gray-scale images and corresponding edge profiles in the assessment process. Whereas for blur-level sorting wedge data did not improve system performance, we will continue to consider its use in future experiments, because it should be useful in detecting localized artifacts introduced into an image by other nonlinear degradations.

4. JPEG Compression Study

In Section 3 we showed that images can be sorted according to blur level or defocus in a manner that is widely independent of scene content. Although it is an interesting result, defocus is not the principal degradation of concern in electronic imaging. An important open question in image quality assessment is how to evaluate image degradations due to lossy compression and other noise artifacts introduced into imagery during processing. Equally important degradations to image quality are those due to atmospheric effects during acquisition and scanner or sensor noise. However, we do not explicitly consider these degradations herein.

In this section we present experiments with the goal of sorting images into degradation levels created with the standard JPEG image encoder.[47] We again consider the sorting of images with ring data only, wedge data only, and both ring and wedge data. Other researchers have considered the perceptibility of distortions introduced into an image by the JPEG algorithm, including Watson,[57] Fuhrman *et al.*,[58] and Eude and Cherifi.[49] These studies are concerned primarily with predicting perceptual image fidelity to improve the algorithm itself. Here, we continue our approach of making image quality sortings based on information from the degraded image alone; however, since image fidelity is an important consideration in the evaluation of image-compression techniques, we also report the results of a sorting experiment with ring–wedge data calculated from the image-domain error between the original and the degraded image. We believe our results will prove directly useful in the development of improved compression algorithms.

A. Quality Sorting

For the sorting of images based on degradations introduced by the standard JPEG image encoder, each of the 75 high-quality, original images used in the blur-level study were degraded into five visually distinct quality levels. We again describe these quality levels by the adjectives original, very good, good, fair, poor, and very poor. A representative example of these quality levels is presented in Fig. 8. Corresponding edge profiles for these images are presented in Fig. 9.

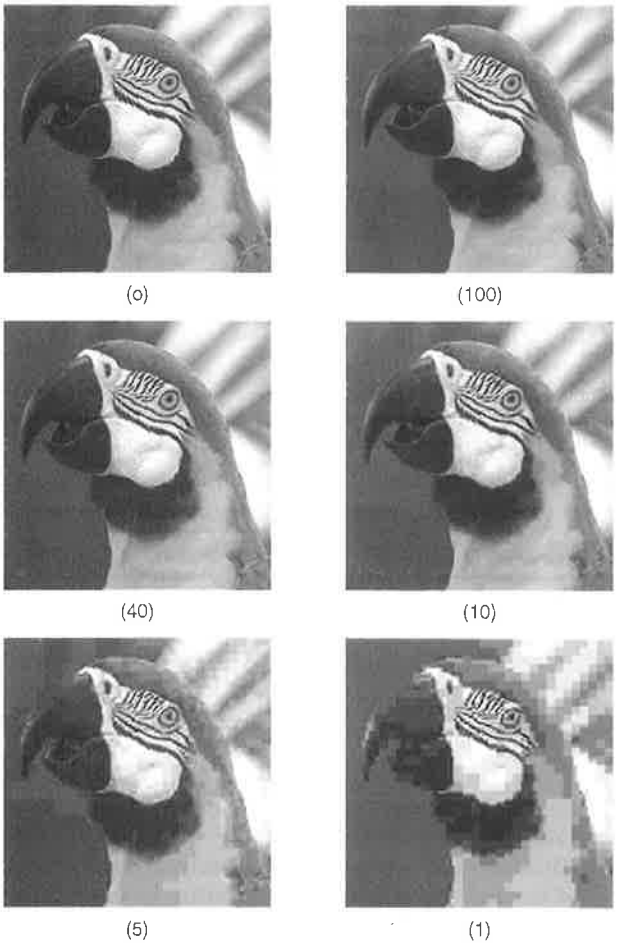

Fig. 8. Representative degradation levels for images used in the JPEG compression study. The original image is shown (*o*), and the *q* factors for each image are as shown.

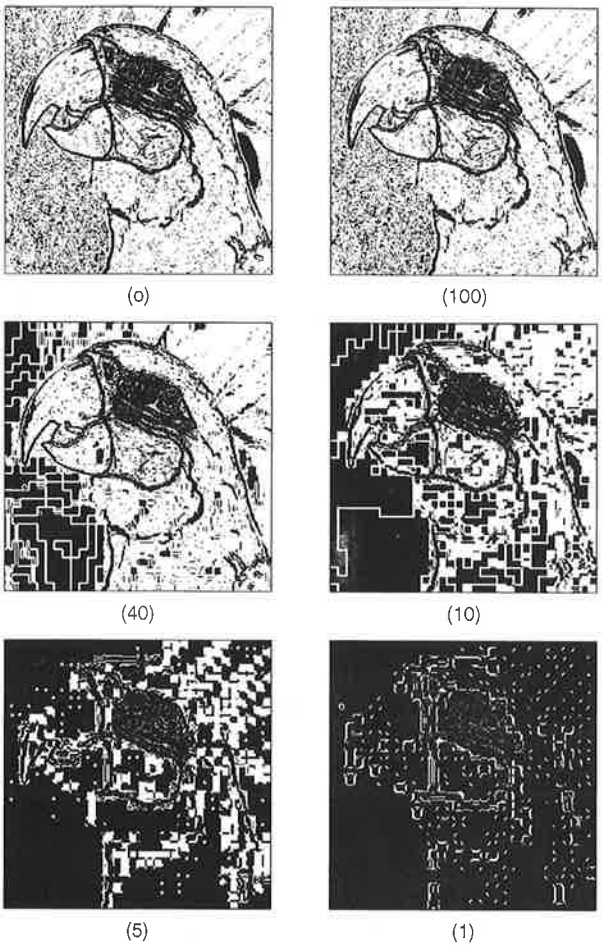

Fig. 9. Edge profiles for the representative images shown in Fig. 9 with *q* factors as labeled.

There are several excellent reviews of the JPEG algorithm in the literature, such as the one presented by Wallace.[59] A particularly important aspect of this algorithm to the present research is the role of the key parameter of the algorithm, known as the *q* factor. This is a parameter that is under the control of the user and that determines the bit rate and the loss of visual fidelity. More specifically, it determines the bin width used in the quantization of the transform coefficients. The higher the value of *q*, the larger the quantization bins, and hence the higher the compression rate and distortion introduced. Values used in the construction of our database were 100 for very good, 40 for good, 10 for fair, 5 for poor, and 1 for very poor.

Continuing with our standard methodology, we subdivided the images into a learning set and a testing set, and the ring-wedge data for each image in both sets were calculated and preprocessed with the system established in Subsection 3.B (see Fig. 7). We used data from both gray-level images and corresponding edge profiles, and we report on separate sortings, using ring data only, wedge data only, and both ring and wedge data in combination. The configurations of the neural networks used are unchanged with respect to the type and the number of inputs used. For the ring-only and the wedge-only experiments 64 input neurons were used, whereas for the ring-wedge experiment 128 input neurons were used. In all cases the second (hidden) and the third (output) layers used 20 and 5 neurons, respectively.

Using five images per image type for training, we obtained an accuracy of 92% for ring-only sorting, 73% for wedge-only sorting, and 95% for ring–wedge sorting. Tables 10, 11, and 12 detail the errors for each of these experiments, respectively. In contrast

Table 10. JPEG Quality Classification Accuracy for Only Ring Data from Both Gray-Scale Imagery and Corresponding Edge Profiles for a Data Set of 250 Separate Images in the Testing Set with 20 Errors

Image Quality (*q*)		Maximum Valued Output Neuron				
		1	2	3	4	5
(100)	Very good	49	1			
(40)	Good	1	45	3	1	
(10)	Fair	1	3	44	2	
(5)	Poor			3	44	3
(1)	Very poor				2	48

Table 11. JPEG Quality Classification Accuracy for Only Wedge Data from Both Gray-Scale Imagery and Corresponding Edge Profiles for a Data Set of 250 Separate Images in the Testing Set with 66 Errors

Image Quality (q)		Maximum Valued Output Neuron				
		1	2	3	4	5
(100)	Very good	45	4	1		
(40)	Good	9	37	2	2	
(10)	Fair	2	4	34	10	
(5)	Poor		5	6	28	11
(1)	Very poor		1	2	7	40

to the blur-level study, the best sorting results were obtained by the ring–wedge sorting experiment. This implies that the wedge data contain important features useful in characterizing the localized artifacts introduced into the images by the JPEG algorithm.

B. Fidelity Sorting

As a supplement to our JPEG study, we consider the fidelity sorting of images, using ring-wedge data from error images, each of which is calculated as the absolute difference between an original image and a corresponding degraded image. Representative examples of the error images of a particular image at each of the quality levels is presented in Fig. 10. With the same learning and testing strategy as in Subsection 4.A the ring–wedge data for each error image in both sets were calculated and preprocessed. We report the results from a sorting, using both ring and wedge data in combination. Using a neural network with 64 input neurons, 20 hidden neurons, and 5 output neurons, we obtained an accuracy of greater than 98%. Table 13 details the errors for this experiment. We find this approach to image fidelity assessment to be highly effective.

5. Localized Image Quality Evaluation

Researchers such as Ohtsuka and Kodugi have demonstrated that certain types of localized image degradation can be perceived as more severe than degradations that are persistent across a scene.[60] In this section an approach to characterizing local image quality is presented with the localized ring–wedge transform. This combination of ring–wedge data with image domain information is a major emphasis

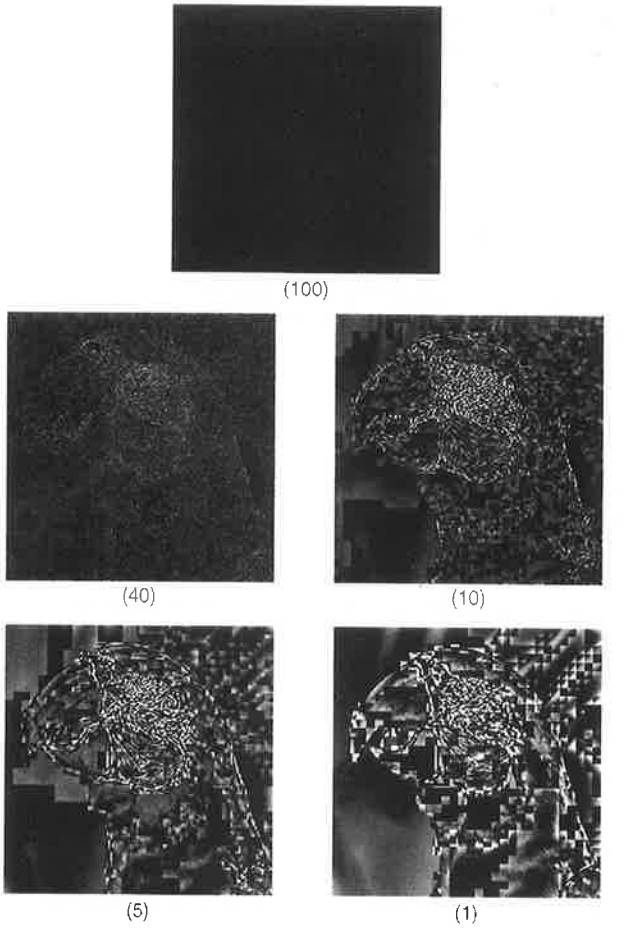

Fig. 10. Error images for a representative image at the five degradation levels used in the JPEG compression study with q factors as labeled.

of our research, offering potential improvement in classification accuracies over systems that use information from either domain separately.

The transform is calculated by means of sliding a window across an image and applying the all-digital ring–wedge detector to the resulting subimages. The result of this transform is localized information about the spatial-frequency content and edge-angle correlations of the image as a function of spatial position within the image. It is clear that these localized transform data are also useful for detecting

Table 12. JPEG Quality Classification Accuracy for Both Ring and Wedge Data from Gray-Scale Imagery and Corresponding Edge Profiles for a Data Set of 250 Separate Images in the Testing Set with 13 Errors

Image Quality (q)		Maximum Valued Output Neuron				
		1	2	3	4	5
(100)	Very good	50				
(40)	Good		50			
(10)	Fair		3	45	2	
(5)	Poor			2	45	3
(1)	Very poor				3	47

Table 13. JPEG Fidelity Classification Accuracy for Both Ring and Wedge Data from Error Images between Degraded Images and Corresponding High-Quality Originals for a Data Set of 250 Separate Images in the Testing Set with Five Errors

Image Quality (q)		Maximum Valued Output Neuron				
		1	2	3	4	5
(100)	Very good	50				
(40)	Good		50			
(10)	Fair		2	47	1	
(5)	Poor			1	48	1
(1)	Very poor					50

space-variant noise effects that may occur in the image acquisition. For the experiments presented in this section we consider a scanning window that is 32×32 pixels and tiled across and down the image in nonoverlapping 32-pixel increments. To calculate the ring–wedge data format, we use the mask-summing technique (see Appendix A).

A. Single-Stage Approach

As a first stage of our study of local image quality, we considered the localized ring–wedge transforms of the 375 images used in the previous JPEG study. Splitting the data into the same learning (125 images) and testing (250 images) sets as before, we obtained 8000 subimages for training and 16,000 subimages for testing. For each of these subimages we obtained ring–wedge data from both the gray-scale images and the edge profiles. Note that the ring–wedge data are calculated solely from the degraded images. Separately, for each of the subimages, we calculated the peak signal-to-perceptible-noise ratio (PSPNR) as described by Chou and Li (see Appendix B).[48] This image fidelity metric requires knowledge of the original image in its calculation.

We chose a four-layer, feed-forward network to perform the local quality evaluation. The network has 128 neurons in the input layer, 20 neurons in the first hidden layer, 101 neurons in the second hidden layer, and a single neuron in the output layer. The network was trained in two stages. In the first stage each neuron in the second hidden layer was trained to make a simple binary decision: Is the PSPNR greater than a given threshold value? In this training, neurons in the second hidden layer were assigned successively larger, equally spaced threshold values ranging between minimum and maximum values acquired from the training images. In the second stage of training, the weights between the first three layers were frozen and the single output neuron was trained to correlate to the actual PSPNR value. During testing, ring–wedge data from subimages were presented to this network and a corresponding prediction of the PSPNR was obtained. Figure 11 details the results of this first attempt at local quality evaluation. Our network obtained a correlation between its prediction and the actual PSPNR of 0.68.

B. Two-Stage Approach

To improve the performance of our local image quality rating system, we consider a two-stage approach. First, a network considering data from the entire image determines a summarized quality level for an image. Second, one of five specially trained networks corresponding to a particular quality level is used to assess local quality. For the first stage we used the network trained as set forth in Subsection 4.A. During training this network was used to presort the training set into predicted quality levels. For each of these levels a separate network was trained as described in Subsection 5.A. Figure 12 details the testing results for this two-stage system,

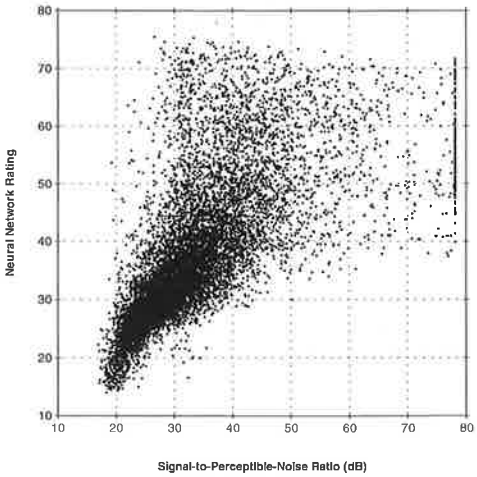

Fig. 11. Correlation diagram showing the neural network estimate (without knowledge of the original) versus the signal-to-perceptible-noise ratio (decibels). A single-stage system based on the localized ring–wedge transform is shown to yield a correlation coefficient of 0.68.

showing a correlation between predicted and actual PSPNR or 0.95.

As an illustrative example of our local quality assessment system we present the results of its application to a test image, which was not part of either the training or the testing sets used previously. The image was compressed with the standard JPEG algorithm and a q factor of 13. Subsequently, ring–wedge data were calculated for both the central 256×256-pixel region and each 32×32-pixel subimage tiled across the recovered image. The first-stage assessment placed the image in the fair category, and the results of the subsequent local image assessments as compared with the actual PSPNR are pre-

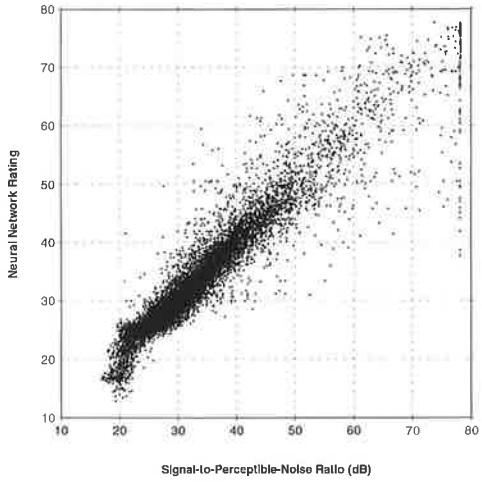

Fig. 12. Correlation diagram showing the neural-network estimate (without knowledge of the original) versus the signal-to-perceptible-noise ratio (decibels). A two-stage system incorporating both a global image quality assessment and subsequent localized assessments is shown to yield a correlation coefficient of 0.95.

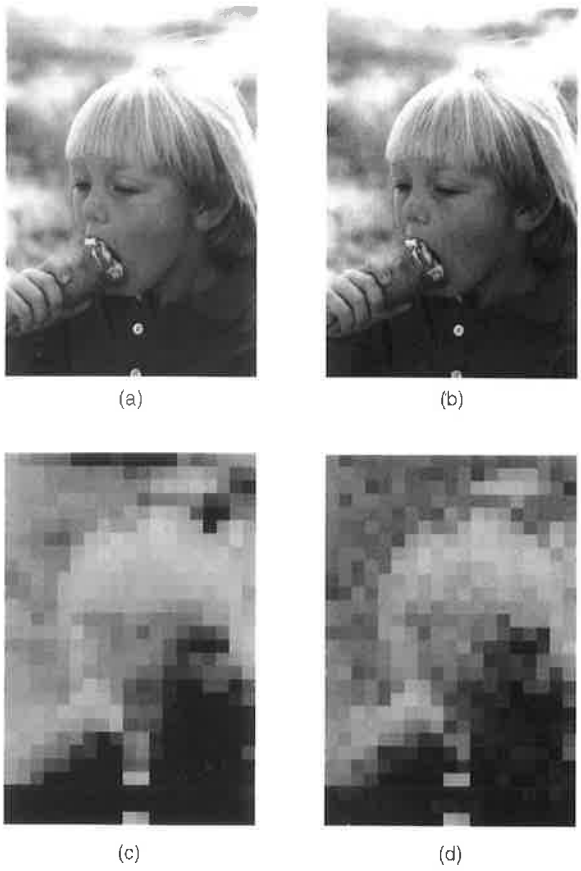

Fig. 13. Representative example of local image fidelity estimation showing a 0.93 correlation between estimates and calculated perceptual fidelity: (a) original image, (b) JPEG compressed image, (c) calculated local perceptual fidelity, and (d) estimated local fidelity.

sented in Fig. 13. Comparing Fig. 13(d), which is our estimate calculated with the degraded Fig. 13(b) and not the original, with the actual PSPNR in Fig. 13(c) shows the excellent correlation that we obtained in our local image quality assessment. For this test image we found a correlation of 0.93 between the predicted and the actual PSPNR.

6. Summary

In this research we have shown that it is possible to automate the sorting of pictorial images according to quality in a manner that is widely independent of scene content. The results are briefly summarized in Table 14. The recognition system is an all-digital ring–wedge detector with neural-network software. Two different image databases are used in these experiments. In the first we used a Gaussian blur function of varying radius to simulate depth-of-field blur. For the second database we used lossy JPEG compression with a succession of q factors to create a realistic set of degraded imagery for our classification experiments.

For images degraded by blur we found that the learning process is adequate with 5 sets of images (5 originals each in 5 categories and at 5 blur levels) containing a total of 125 images. In Table 5 with four or five sets in the training we see that the ring-only and the ring–wedge formats are both highly successful. Also, image data and edge-profile data are both important and useful inputs to the neural network.

In the image quality classification using the blur-ring function we enlarged this database to include 250 images in the testing set and a separate 125 images in the training, prepared from 50 and 25 high-quality originals, respectively. Table 7 shows poor classification results with wedge data only. Table 6 shows the best results of 96% accuracy with 10 errors in 250 classifications and no errors of two categories using ring-only data and both image and edge-profile input neurons. Importantly, this classification at 96% accuracy is obtained without knowledge of the original scene being input to the recognition system.

For the image database prepared by JPEG lossy compression we used a learning set of 125 images and a testing set of 250 images with (q) factors (100) very good, (40) good, (10) fair, (5) poor, and (1) very poor derived from 25 and 50 originals, respectively, as shown in Fig. 8. In Table 12, we see the impressive sorting at 95% accuracy with only 13 errors in 250 images. Both gray-scale imagery and the corresponding edge profiles are used for the input data. No knowledge of the original imagery is used in this classification.

In a separate experiment using the same JPEG database described above but also adding knowledge of the original, as is common in a photointerpreter's evaluation, we obtained an even higher accuracy. As shown in Table 13 for the image fidelity experiment, there are only 5 errors in 250 images for an accuracy of 98%. Here we use ring and wedge data from a hybrid image that is calculated as the absolute difference between the original and the degraded image (e.g., see error images in Fig. 10).

Finally, in Section 5, the localized ring–wedge transform was applied to the assessment of local image quality. Our final system worked in two stages: A first stage assessed global quality level for use in selecting one of five networks to be used in the second stage, in which the local image quality is assessed. Using this system, we are able accurately to match the ratings of a perceptual image fidelity metric without requiring direct information from the original scene. It now appears possible to automate any human visual recognition task.

Appendix A. All-Digital Ring–Wedge Sampling

Frequency-domain measures of image quality based on use of a ring–wedge geometry to sample the optical power spectrum of the amplitude transmittance of an input image have been used since the 1970's.[25–27] The solid-state detector array typically used to perform the sampling consists of semiannular ring sampling areas on one half and wedge-shaped sampling areas on the other, as in Fig. 14. The separate samplings over 180 deg are based on the assertion that the amplitude transmittance of the object function is

Table 14. Summary of Results for Automatic Image Quality Assessment Using the All-Digital Ring–Wedge Detector

Section/Subsection	Description	Results
3.A	Blur-level sorting Preliminary study	Good sorting results independent of scene content. Best to consider each image type in training.
3.B	Blur-level sorting System refinement	Ring data most important in making assessments. Improved sorting results by inclusion of data from edge profiles of individual images. Best to consider several image examples per image type in training.
3.C	Blur-level sorting System evaluation	Demonstrates excellent classification of a common linear degradation type: 96% accuracy (ring data only) 76% accuracy (wedge data only) 92% accuracy (ring and wedge data)
4.A	JPEG study Quality sorting	Demonstrates excellent classification of an important nonlinear degradation type. Wedge data useful for characterizing the severity of artifacts in the scene: 92% accuracy (ring data only) 73% accuracy (wedge data only) 95% accuracy (ring and wedge data)
4.B	JPEG study Fidelity sorting	Demonstrates a novel technique for evaluating image fidelity: 99% accuracy (ring and wedge data)
5	Localized ring–wedge transform	Effectively combines both image-domain and spatial-transform-domain information. Effectively estimates local fidelity with data from the degraded scene alone, without explicit information about the original image.

real valued. The radial sampling of the ring areas provides orientation-independent information about the distribution of spatial frequencies in the image, whereas the angular sampling of the wedge areas provides scale-independent information about the orientation of those spatial frequencies.[26] Figure 1(a) shows a schematic diagram of a coherent optoelectronic hybrid using the analog ring–wedge detector array for spatial spectral analysis.

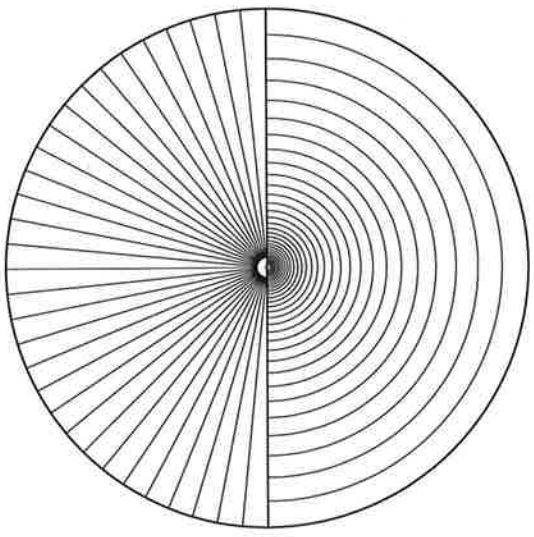

Fig. 14. Sampling geometry used by the all-digital ring–wedge detector incorporating 32 ring and 32 wedge sampling regions chosen to simulate the analog multielement array (figure reproduced from Ref. 26 with permission).

Allen and Schindler showed that digitally-derived power spectral estimates of image quality can be computed before an image is produced and used successfully to assess quality.[61] However, their studies were limited to aerial images. In this paper we emphasize the assessment of natural images widely varying in scene content. In Fig. 1(b) we show a block diagram of the all-digital processing algorithm. Here image processing and windowing have been incorporated along with a two-dimensional fast Fourier transform and a software ring–wedge detector, followed by data preparation and a neural network to perform the recognition.

We note that the digital system provides measurements of the spectrum from the intensity-based image rather than amplitude transmittance. The difference effects the interpretation of the resulting data, and its importance should not be minimized, since the relationship between the amplitude spectrum and the intensity spectrum is not, in general, a simple one. Also, we observe that the computer system can use both the phase and the amplitude of the Fourier transform, and it is relatively easy with the digital system to incorporate image processing stages into the system. These possibilities pro-

duce interesting variations on what one is able to do using the laser optical hybrid of Fig. 1(a). In the experiments described herein, we will limit ourselves to recognition with only the absolute value of the transform. Hence, for the all-digital system in Fig. 1(b), the ring–wedge data are described by the following equation,

$$m_j = \iint_{R_j} \mathrm{d}f_x \mathrm{d}f_y |F(f_x, f_y)|, \tag{A1}$$

where m_j is the jth measurement over the sampling area R_j defined by the sampling geometry. $F(f_x, f_y)$ is the Fourier transform of the intensity-based input image with f_x and f_y being Cartesian spatial-frequency coordinates. Parenthetically, we remark that the coherent optical processor uses power measurements of the Fourier transform of the image based on its amplitude transmittance.

There are several design trade-offs in choosing an appropriate sampling geometry. Since the original ring–wedge detector had 32 rings and 32 wedges based on automating recognition in high-resolution film, it was used as a basis for the all-digital ring–wedge detector (see Fig. 14). Separate investigators have shown that this sampling geometry represents a practical optimization for several applications.[26,27,62,63] The sampling regions for the ring-detector regions are described as follows:

$$R_j = [(f_x, f_y): \quad \rho_j \le (f_x^2 + f_y^2)^{1/2} < \rho_j + \Delta\rho_j, \quad \phi_{\min} \le \tan^{-1}(f_y/f_x) < \phi_{\min} + \pi], \tag{A2}$$

where ρ_j is the radial distance from the origin to the inner radius of the jth detector region and $\Delta\rho_j$ is its radial width. Note that the angular extent of all the ring detectors is assumed to be π rad, oriented as given by $\phi_{\min}$. The sampling regions for the wedge-detector regions are described as follows

$$R_j = [(f_x, f_y): \rho_{\min} \le (f_x^2 + f_y^2)^{1/2} < \rho_{\max}, \quad \phi_j \le \tan^{-1}(f_y/f_x) < \phi_j + \Delta\phi_j], \tag{A3}$$

where ϕ_j is the angular distance from the f_x axis to the leading edge of the jth detector region and $\Delta\phi_j$ is its angular width. Note that the radial extent of all the wedge detectors is assumed to be equal, as given by $\Delta\rho_{\min}$ and $\Delta\rho_{\max}$.

For the digital evaluation of Eq. (A1) the following discrete calculation is conducted,

$$m_j \approx \sum_{u=0}^{N-1} \sum_{v=0}^{M-1} |\tilde{F}(u, v)| \tilde{M}_j(u, v), \tag{A4}$$

where $\tilde{M}_j(u, v)$ is one of a set of discrete frequency-domain masks defined by the sampling geometry defined in Eqs. (A2) and (A3). $\tilde{F}(u, v)$ is the discrete Fourier transform of the intensity-based input array image with u and v being Cartesian spatial-frequency indices.

With relation (A4), ring–wedge data are calculated as a set of weighted summations for which the weighting masks $\tilde{M}_j(u, v)$ are calculated for each detector region as described recently by Berfanger and George.[46] For imagery larger than 256×256 pixels the individual weighting masks of this geometry are well approximated by binary, nonoverlapping regions described by the following equation,

$$\tilde{M}_j(u, v) = \begin{cases} 1 & (u\Delta f_x, v\Delta f_y) \in R_j \\ 0 & \text{otherwise} \end{cases}, \tag{A5}$$

where Δf_x and Δf_y are the spacing of the frequency-domain samples. Equation (A5) effectively defines a set of bins into which the values of member pixels are summed. This technique is known as bin summing. When we work with smaller images, the bin summing approximation produces unreliable results. In this case relation (A4) is implemented as written with mask values being calculated numerically by approximation of the contribution of each pixel to a particular detector region with the following equation,

$$\tilde{M}_j(u, v) = \iint_{R_j} \mathrm{d}f_x \mathrm{d}f_y I(f_x - u\Delta f_x, f_y - v\Delta f_y), \tag{A6}$$

where $I(f_x, f_y)$ is an appropriate interpolating function. There is a separate mask for each of the sampling regions in a given geometry. This is known as mask summing. With either implementation the masks are generated while taking into account the implicit periodicity of the discrete Fourier transform. In Sections 3 and 4 the all-digital ring–wedge detector is applied to full 256×256 pixel imagery, and bin-summed ring–wedge data are used. In Section 5 calculations involve smaller 32×32 pixel subimages, and mask summing is used to obtain the ring–wedge data format.

Appendix B. Peak Signal-to-Perceptible-Noise Ratio

The fidelity criterion termed the PSPNR is defined as follows,

$$\mathrm{PSPNR} = 20 \log_{10} \frac{255}{\{\langle [|f(n, m) - f_o(n, m)| - \mathrm{JND}(n, m)]^2 \delta(n, m) \rangle\}^{1/2}}, \tag{B1}$$

$$\delta(n, m) = \begin{cases} 1 & \text{if } |f(n, m) - f_o(n, m)| > \mathrm{JND}(n, m) \\ 0 & \text{otherwise} \end{cases}, \tag{B2}$$

where $f_o(n, m)$ denotes the original pixel and $f(n, m)$ denotes the reconstructed pixel at the discrete, Cartesian spatial index (n, m).[48] Here $\langle \cdot \rangle$ denotes the average value calculated over all of the pixels in the image. The PSPNR, as given above, is based on quantifying the amount of distortion that exceeds the threshold of noticeability as given by the JND profile, JND(n, m), recently introduced by Jayant *et al.*[41] The expressions for calculating this profile are given as follows:

$$\mathrm{JND}(n, m) = \max\{f_1[b(n, m), g(n, m)], \times f_2[b(n, m)]\}, \tag{B3}$$

$$f_1[b(n, m), g(n, m)] = g(n, m)\alpha[b(n, m)] + \beta[b(n, m)], \tag{B4}$$

$$f_2[b(n, m)] = \begin{cases} T_0\{1 - [b(n, m)/127]^{1/2} + 3\} \\ \gamma[b(n, m) - 127] + 3 \end{cases} \quad \begin{matrix} b(n, m) \le 127 \\ \text{otherwise} \end{matrix}, \tag{B5}$$

$$\alpha[b(n, m)] = 0.0001 \times b(n, m) + 0.115, \tag{B6}$$

$$\beta[b(n, m)] = \lambda - 0.01 \times b(n, m). \tag{B7}$$

In these equations empirical models for the human visual system are incorporated by the functions $f_1(\cdot)$ and $f_2(\cdot)$, which quantify, respectively, the spatial masking effect and the visibility threshold due to background luminance. The function $b(n, m)$ is the average background luminance and is calculated with the low-pass operator shown in Fig. 15. The function $g(n, m)$ is determined by calculation of the weighted average of luminance changes in four directions, as with the edge profile calculations introduced in Subsection 3.B. The spatial masks used in this nonlinear filtering operation are shown in Fig. 5. At each pixel the maximum of the values calculated with each of these directional masks is used. For this calculation no threshold operation is performed. The remaining parameters are dependent on viewing conditions and represent various aspects of the human visual response. For the experiments reported in this paper we use values for these parameters as established for experiments reported by Chou and Li: $T_0 = 17$, $\gamma = 3/128$, and $\lambda = 1/2$.[48]

$$\frac{1}{16}\begin{vmatrix} 1 & 1 & 1 & 1 & 1 \\ 1 & 2 & 2 & 2 & 1 \\ 1 & 2 & 0 & 2 & 1 \\ 1 & 2 & 2 & 2 & 1 \\ 1 & 1 & 1 & 1 & 1 \end{vmatrix}$$

Fig. 15. Low-pass operator for calculating the average background luminance.

The authors acknowledge discussions on image quality with Rulon Simmons and Bernie Brower of the Eastman-Kodak Company as well as financial support by the U.S. Army Research Office, the National Science Foundation, and the Rochester Center for Electronic Imaging Systems.

References

1. M. P. Eckert and A. P. Bradley, "Perceptual quality metrics applied to still image compression," Signal. Process. **70,** 177–200 (1998).
2. N. Belaid, J. Cespedes, J. M. Thijssen, and J. Ophir, "Lesion detection in simulated elastographic and echographic images: a psychophysical study," Ultrasound Med. Biol. **20,** 877–891 (1994).
3. C. Y. Wen and R. J. Beaton, "Subjective image quality evaluation of image compression techniques," in *Proceedings of the Human Factors and Ergonomics Society, 40th Annual Meeting 1996* (Human Factors and Ergonomics Society, Santa Monica, Calif., 1996), Vol. 2, pp. 1188–1192.
4. S. J. Briggs, "The definition and measurement of image quality," in *Advances in Image Transmission II*, A. G. Tescher, ed., Proc. SPIE **249,** 170–174 (1980).
5. T. L. Coluccio, S. MacLeod, and J. J. Maier, "Effect of image contrast and resolution on photointerpreter target detection and identification," J. Opt. Soc. Am. **59,** 1478–1481 (1969).
6. G. L. Latshaw, P. L. Zuzelo, and S. J. Briggs, "Tactical photointerpreter evaluations of hardcopy and softcopy imagery," in *Airborne Reconnaissance III: Collection and Exploitation of Reconnaissance Data*, J. H. Smith and T. C. Freitag, eds., Proc. SPIE **137,** 179–87 (1978).
7. H. L. Snyder, M. E. Maddox, D. I. Shedivy, J. A. Turpin, J. J. Burke, and R. N. Strickland, "Digital image quality and interpretability: database and hardcopy studies," Opt. Eng. **21,** 14–22 (1982).
8. J. J. Burke and H. L. Snyder, "Quality metrics of digitally derived imagery and their relation to interpreter performance," in *Image Quality*, P. S. Cheatham, ed., Proc. SPIE **310,** 16–23 (1981).
9. B. P. Chao, R. J. Beaton, and H. L. Snyder, "Human performance evaluations of digital image quality," in *Advances in Display Technology III*, E. Schlam, ed., Proc. SPIE **386,** 20–24 (1983).
10. J. H. D. M. Westerink and J. A. J. Roufs, "Subjective image quality as a function of viewing distance, resolution, and picture size," J. Soc. Motion Pict. Tel. Eng. **98,** 113–119 (1989).
11. S. Ohtsuka and M. Kosugi, "Quality evaluation of locally impaired pictures," J. Soc. Inf. Disp. **32,** 19–24 (1991).
12. R. Hamberg and H. de Ridder, "Continuous assessment of time-varying image quality," in *Human Vision and Electronic Imaging II*, B. E. Rogowitz and T. N. Pappas, eds., Proc. SPIE **3016,** 248–259 (1997).
13. V. Kayargadde and J.-B. Martens, "Perceptual characterization of images degraded by blur and noise: experiments," J. Opt. Soc. Am. A **13,** 1166–1177 (1996).
14. J. A. J. Roufs, "Perceptual image quality: concept and measurement," Philips J. Res. **47,** 35–62 (1992).
15. J. A. J. Roufs and M. C. Boschman, "Methods for evaluating the perceptual quality of VDUs," in *Human Vision and Electronic Imaging: Models, Methods, and Applications*, B. E. Rogowitz and J. P. Allebached, eds., Proc. SPIE **1249,** 2–11 (1990).
16. E. H. Linfoot, "Transmission factors and optical design," J. Opt. Soc. Am. **46,** 740–752 (1956).

17. E. H. Linfoot, *Fourier Methods in Optical Image Evaluation* (Focal Press, London, 1964).
18. O. H. Schade, "Image gradiation, graininess and sharpness in television and motion-picture systems. Part I. image structure and transfer characteristics," J. Soc. Motion Pict. Tel. Eng. **56,** 137–177 (1951).
19. O. H. Schade, "Image gradiation, graininess and sharpness in television and motion-picture systems. Part II. The trainstructure of motion picture images—an analysis of deviations and fluctuations of the sample number," J. Soc. Motion Pict. Tel. Eng. **58,** 181–222 (1952).
20. O. H. Schade, "Image gradiation, graininess and sharpness in television and motion-picture systems. Part III. The grain structure of television images," J. Soc. Motion Pict. Tel. Eng. **61,** 97–164 (1953).
21. O. H. Schade, "Image gradiation, graininess and sharpness in television and motion-picture systems. Part IV. Image analysis in photographic and television systems (definition and sharpness)," J. Soc. Motion Pict. Tel. Eng. **64,** 593–617 (1955).
22. O. H. Schade, "An evaluation of photographic image quality and resolving power," J. Soc. Motion Pict. Tel. Eng. **73,** 81–119 (1964).
23. R. Shaw, "Evaluating the efficient of imaging processes," Rep. Prog. Phys. **41,** 1103–1155 (1978).
24. W. B. Wetherell, "The calculation of image quality," in *Applied Optics and Optical Engineering*, R. Kingslake, ed. (Academic, New York, 1980), Vol. VIII, pp. 171–312.
25. N. George, "Image quality rating system," U.S. patent 3,788,749 (29 January 1974).
26. N. George, J. T. Thomasson, and A. Spindel, "Photodetector light pattern detector," U.S. patent 3,689,772 (5 September 1972).
27. N. Jensen, "High-speed image analysis techniques," Photograph. Eng. **39,** 1321–1328 (1973).
28. N. Jensen, *Optical and Photographic Reconnaissance Systems* (Wiley, New York, 1968), Chap. 8, pp. 102–115.
29. N. B. Nill, "Scene power spectra: the moment as an image quality merit factor," Appl. Opt. **15,** 2846–2854 (1976).
30. A. G. Tescher and J. R. Parsons, "Cross-spectrum error criterion as an image quality measure," Appl. Opt. **13,** 1460–1465 (1974).
31. T. P. Barnwell III and R. M. Mersereau, "A comparison of some subjective and objective measures for image quality," in *Proceedings of the Eleventh Annual Asilomar Conference on Circuits Systems and Computers* (Institute of Electrical and Electronics Engineers, New York, 1978), pp. 96–100.
32. R. A. Schindler, "Physical measures of image quality and their relationship to performance," in *Advances in Display Technology*, J. R. Parsons, ed., Proc. SPIE **199,** 117–125 (1979).
33. P. G. J. Barten, "Evaluation of subjective image quality with the square-root integral method," J. Opt. Soc. Am. A **7,** 2024–2031 (1990).
34. N. B. Nill and B. H. Bouzas, "Objective image quality measure derived from digital image power spectra," Opt. Eng. **31,** 813–825 (1992).
35. J. A. Saghri, P. S. Cheatham, and A. Habibi, "Image quality measure based on a human visual system model," Opt. Eng. **28,** 813–818 (1989).
36. T. A. Grogan and D. Keene, "Image quality evaluation with a contour-based perceptual model," in *Human Vision, Visual Processing, and Digital Display III*, B. E. Rogowitz, ed., Proc. SPIE **1666,** 188–197 (1992).
37. I. R. L. Davies, D. Rose, and R. J. Smith, "Automated image quality assessment," in *Human Vision, Visual Processing, and Digital Display IV*, J. P. Allebach and B. E. Rogowitz, eds., Proc. SPIE **1913,** 27–36 (1993).
38. S. Daly, "The visible differences predictor: an algorithm for the assessment of image fidelity," in *Human Vision, Visual Processing, and Digital Display III*, B. E. Rogowitz, ed., Proc. SPIE **1666,** 2–14 (1992).
39. H. L. Snyder, "Image quality: measures and visual performance," in *Flat Panel Displays and CRT's*, L. E. Tannas, Jr., ed. (Van Nostrand Reinhold, New York, 1980), pp 70–90.
40. I. Overington, "Image quality and observer performance," in *Image Quality*, P. S. Cheatham, ed., Proc. SPIE **310,** 2–9 (1981).
41. N. Jayant, J. Johnston, and R. Safranek, "Signal compression based on models of human perception," Proc. IEEE **81,** 1385–422 (1993).
42. C. K. Abbey, H. H. Barrett, and M. P. Eckstein, "Practical issues and methodology in assessment of image quality using model observers," in *Medical Imaging 1997. Physics of Medical Imaging*, R. L. Van Metter and J. Beutel, eds., Proc. SPIE **3032,** 182–194 (1997).
43. A. B. Watson, "The cortex transform: rapid computation of simulated neural images," Comput. Vision, Graph. Image Process. **39,** 311–27 (1987).
44. A. B. Watson, "Efficiency of a model human image code," J. Opt. Soc. Am. A **4,** 2401–2417 (1987).
45. C. C. Taylor, Z. Pizlo, J. P. Allebach, and C. A. Bouman, "Image quality assessment with a Gabor pyramid model of the human visual system," in *Human Vision and Electronic Imaging II*, B. E. Rogowitz and T. N. Pappas, eds., Proc. SPIE **3016,** 58–69 (1997).
46. D. Berfanger and N. George, "All-digital ring-wedge detector applied to fingerprint recognition," Appl. Opt. **38,** 357–369 (1999).
47. Joint Photographic Experts Group Compact Disc, "Information technology—digital compression and coding of continuous-tone still images," International Organization for Standardization/International Electrotechnical Commission Standard (available through American National Standards Institute web site, http://www.ansi.org). ISO/IEC 10918–1:1994.
48. C.-H. Chou and Y.-C. Li, "A perceptually tuned subband image coder based on the measure of just-noticeable-distortion profile," IEEE. Trans. Circuits Syst. V **5,** 467–476 (1995).
49. T. Eude and H. Cherifi, "Quality metrics for low bitrate coding," in *Human Vision and Electronic Imaging II*, B. E. Rogowitz and T. N. Pappas, eds., Proc. SPIE **3016,** 70–81 (1997).
50. N. George, S.-G. Wang, and D. L. Venable, "Pattern recognition using the ring-wedge photodetector and neural-network software," in *Optical Pattern Recognition II*, H. J. Caufield, ed., Proc. SPIE **1134,** 96–106 (1989).
51. H. Kusaka, "Consideration of vision and picture quality: psychological effects induced by picture sharpness," in *Human Vision, Visual Processing, and Digital Display*, B. E. Rogowitz, ed., Proc. SPIE **1077,** 50–55 (1989).
52. V. Kayargadde and J.-B. Martens, "Estimation of perceived image blur using edge features," Int. J. Imaging Syst. Technol. **7,** 102–109 (1996).
53. D. L. Venable, "Pattern classification using diffraction pattern sampling and the limitations due to film grain noise," Ph.D. dissertation (University of Rochester, Rochester, N.Y., 1989).
54. D. M. Berfanger and N. George, "Automatic image quality assessment," in *Proceedings of ICPS '94: The Physics and Chemistry of Imaging Systems, IS&T's 47th Annual Conference* (Society for Imaging Science and Technology, Springfield, Va., 1994), Vol 2, pp. 436–438.
55. A. K. Jain, *Fundamentals of Digital Image Processing* (Prentice Hall, Englewood Cliffs, N.J., 1989), pp. 244–255.

56. A. A. Webster, C. T. Jones, M. H. Pinson, S. D. Voran, and S. Wolf, "An objective video quality assessment system based on human perception," in *Human Vision, Visual Processing, and Digital Display IV*, J. P. Allebach and B. E. Rogowitz, eds., Proc. SPIE **1913,** 15–26 (1993).
57. A. B. Watson, "DCT quantization matrices visually optimized for individual images," in *Human Vision, Visual Processing, and Digital Display IV*, J. P. Allebach and B. E. Rogowitz, eds., Proc. SPIE **1913,** 202–216 (1993).
58. D. R. Fuhrmann, J. A. Baro, and J. R. Cox, Jr., "Experimental evaluation of psychophysical distortion metrics for JPEG-encoded images," J. Electron. Imaging **4,** 397–406 (1995).
59. G. K. Wallace, "The JPEG still picture compression standard," Commun. ACM **34,** 30–44 (1991).
60. S. Ohtsuka and M. Kosugi, "Quality evaluation of locally impaired pictures," J. Soc. Inf. Disp. **32,** 19–24 (1991).
61. C. Allen and R. Schindler, "Determining image quality from electronic or digital signal characteristics," in *Advances in Image Transmission II*, A. G. Tescher, ed., Proc. SPIE **249,** 179–184 (1980).
62. E. D. Hirleman, "Optimal scaling of the inverse Fraunhofer diffraction particle sizing problem: the linear system produced by quadrature," in *Optical Particle Sizing Theory and Practice*, G. Gouesbet and G. Grehan, eds. (Plenum, New York, 1988).
63. S. D. Coston and N. George, "Recovery of particle size distributions by inversion of the optical transform intensity," Opt. Lett. **16,** 1918–1920 (1991).

Electronic imaging using a logarithmic asphere

Wanli Chi and Nicholas George

Institute of Optics, University of Rochester, Rochester, New York 14627

Received December 19, 2000

Transmission functions are derived that are valid in the nonparaxial case for a class of lenses that will image a continuum of points along an optical axis to a single image point. This lens, which we call a logarithmic asphere, is then used in a digital camera. The resolution of the camera is limited by the pixel size of the CCD; i.e., it is not diffraction limited. Digital processing is used to recover the image, and image-plane processing is used for speed. We find a tenfold increase in the depth of field over that for the diffraction-limited case.

OCIS codes: 220.3620, 100.2000, 170.0110.

In electronic imaging, an integrated consideration of image acquisition and image processing is leading to important new optical systems. Illustrative of these new systems is the research to extend depth of field by means of computer processing of purposefully blurred images.[1–7] Related research on axilenses, which are optical elements that concentrate light energy along an optical axis, has also been done.[8–10] A fascinating application of multifocal lenses is the new intraocular implants that are designed with five annular refractive zones in a 4.7-mm diameter.[11]

The problem that we pose is to find a circularly symmetric lens with a focal length that varies continuously with radius. Hence, for a three-dimensional (3-D) object, there is always an annular portion of the lens that provides a sharp image. The remainder of the lens contributes to blurring, which we propose to reduce with digital processing. In the theory we use Fermat's principle to find the transmission function for a lens that will image an extended portion of the optical axis into a single image point. Below we present the theory for this lens and a discussion of its design and fabrication. This is followed by an experimental report on its use in a digital camera.

Consider the smart camera shown in Fig. 1, in which a 3-D staircase object is recorded by a CCD camera with a novel aspherical lens (L). The recorded blurred image is digitally processed and displayed. For the lens (L), we illustrate our imaging concept in Fig. 2. Object points ranging over distances s_1 through s_2 are all brought to focus at point P in plane II by means of a continuous radial variation in the focal length. Dividing the lens into annular rings of different focal lengths, one can verify that an equal area is obtained for each of N rings by choice of a radius r_n for the nth ring as follows:

$$r_n = (n/N)^{1/2} R\,, \tag{1}$$

where R is the outer radius of the lens in plane I.

Consider the imaging of point S at $x(r_n)$ by the rays through the annular ring, r_n. To provide uniform or natural illumination, we subdivide the interval from s_1 to s_2 into N segments, and we choose the $x(r_n)$ segment to be weighted as follows:

$$x(r_n) = s_1 + (s_2 - s_1)n/N\,. \tag{2}$$

Combining Eqs. (1) and (2) to eliminate the ratio n/N gives us the basic equation for the lens:

$$x(r) = s_1 + (s_2 - s_1)r^2/R^2. \tag{3}$$

As is well known in physical optics, the general transmission function, $t(r)$, for a lens can be written in the form

$$t(r) = \exp[-i\phi(r)], \tag{4}$$

in which $\phi(r)$ is the phase delay. The form of the phase delay $\phi(r)$ can be obtained by application of Fermat's principle.[12] First, we write an expression for the total optical length L for the ray through *SOP*:

$$L = \sqrt{r^2 + x^2} + \phi(r)\lambda_0/(2\pi) + \sqrt{r^2 + t^2}\,, \tag{5}$$

where t is the distance from lens plane I to plane II and λ_0 is the free-space wavelength.

From Fermat's principle and Eq. (5), setting $\partial L/\partial r = 0$ with x constant, and by use of Eq. (3), we find the following expression for the phase delay, $\phi(r)$:

$$\phi(r) = -\frac{2\pi}{\lambda_0}\int_0^r \left(\frac{r}{(r^2 + t^2)^{1/2}} + \frac{r}{\{r^2 + [s_1 + (s_2 - s_1)r^2/R^2]^2\}^{1/2}} \right) dr\,. \tag{6}$$

We can directly integrate this expression[13] to obtain the basic formula for the logarithmic asphere, expressed in two terms:

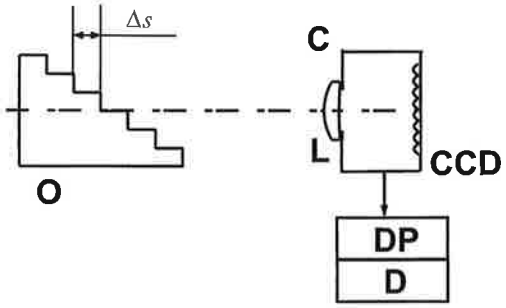

Fig. 1. Imaging setup: O, object; C, digital camera; DP, digital processor; D, display. See text for other definitions.

0146-9592/01/120875-03$15.00/0

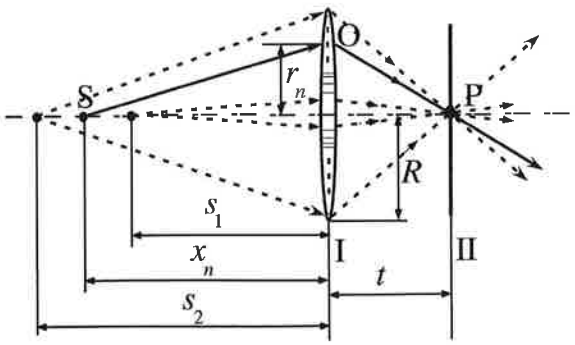

Fig. 2. Notation for lens theory. See text for definitions.

$$\phi(r) = -\left\{\frac{2\pi}{\lambda_0}[(r^2 + t^2)^{1/2} - t] + \frac{\pi}{\lambda_0}\frac{R^2}{s_2 - s_1}\right.$$

$$\times\left[\ln\left(2\frac{s_2 - s_1}{R^2}\left\{\left[r^2 + \left(s_1 + \frac{s_2 - s_1}{R^2}r^2\right)^2\right]^{1/2}\right.\right.\right.$$

$$\left.\left.\left. + \left(s_1 + \frac{s_2 - s_1}{R^2}r^2\right)\right\} + 1\right) - \ln\left(4\frac{s_2 - s_1}{R^2}s_1 + 1\right)\right]\Bigg\}. \quad (7)$$

The first term is an ideal lens for point-to-point imaging, and the second term introduces controlled blurring or aberration. In the interest of brevity, a more detailed examination of this result is omitted. However, as a first stage in lens design, it is useful to form a power-series expansion of Eq. (7), with $s_1 = 610$ mm, $s_2 = 6100$ mm, $R = 5$ mm, and $t = 25$ mm. We write the first and second members of Eq. (7) as

$$\phi(r) = -\frac{2\pi}{\lambda_0}\{[0.02r^2 - 8 \times 10^{-6}r^4 + 6.4 \times 10^{-9}r^6 - 6.4 \times 10^{-12}r^8 + 7 \times 10^{-15}r^{10}] + [7.435 \times 10^{-4}r^2 + -7.563 \times 10^{-5}r^4 + 5.1431 \times 10^{-6}r^6 + -1.803 \times 10^{-7}r^8 + 2.4614 \times 10^{-9}r^{10}]\}. \quad (8)$$

These expansions are accurate to $\pm 10^{-5}$ mm for the term in braces. The expansions are obtained with the NonlinearFit statistics package of Mathematica.[14]

A set of these logarithmic aspheres are being fabricated for t varying from 24 to 80 mm. Recent advances in optical fabrication methods make this type of logarithmic asphere practical commercially. In the facilities of the Center for Optics Manufacturing of the University of Rochester, two modern machines have been used: an OptiPro Model SX50 computer-controlled asphere grinding machine and a magneto-rheological finisher.[15] The lenses are fabricated in an optical grade of quartz to an overall accuracy of the order of one-tenth of a wavelength.

For the imaging and depth-of-field experiment, we used a 3-D object with 12 steps that are spaced axially by Δs of 50 mm, as shown in Fig. 1. The logarithmic asphere has a $t = 60$ mm, and the monochrome CCD array has a pixel size of 23 μm square, which limits the basic resolution of the system. A strip resolution chart that contains a series of letters of varying size along with a chirped series of vertical lines is placed on the riser of each step. We measured the point spread function for this camera and found excellent agreement with theory. This measured point spread function serves as the basis for digital recovery. For digital processing, we use an image-plane matrix for convolution filtering. This filter is obtained by an inversion of the Fourier plane Wiener–Helstrom inverse filter as described in the literature.[16,17] In our research both a 5×5 and a 3×3 matrix are used, with very similar results. A particularly interesting observation is the fact that the 3×3 matrix that we employ is very close to an edge-sharpening matrix. Hence, the filter is not strongly dependent on the point spread function. We plan further effort to optimize the digital processing.

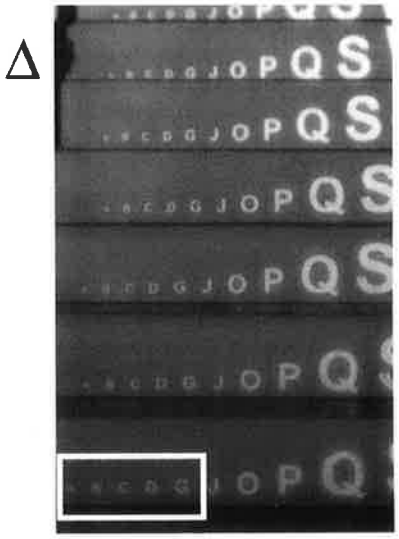

Fig. 3. Recovered image of a step chart from a 3-D object.

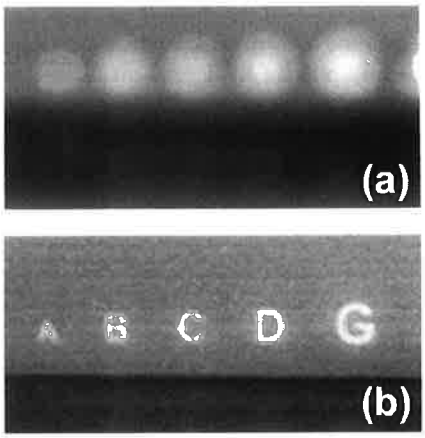

Fig. 4. Segments of images obtained with (a) a Nikon conventional camera and (b) a logarithmic asphere camera.

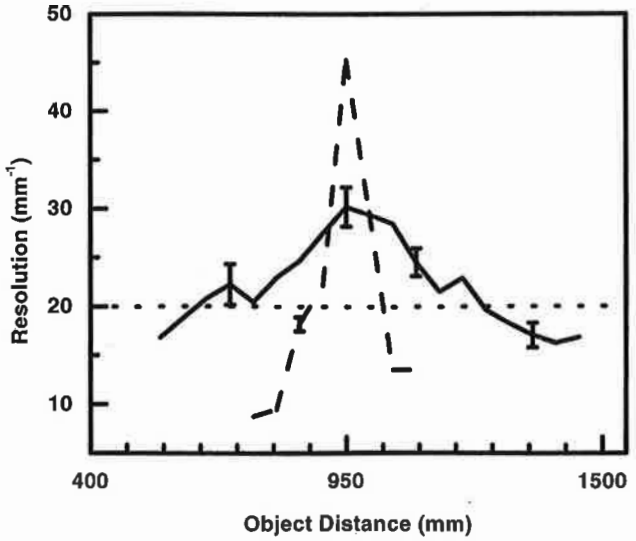

Fig. 5. Resolution versus object distance: dashed curve, Nikon camera; solid curve, logarithmic asphere; dotted line at 20 mm^{-1}.

For completeness, we include the matrices that gave good results:

$$\begin{bmatrix} 0 & 0 & -0.07 & 0 & 0 \\ 0 & 0.51 & -0.85 & 0.51 & 0 \\ -0.07 & -0.85 & 5 & -0.85 & -0.07 \\ 0 & 0.51 & -0.85 & 0.51 & 0 \\ 0 & 0 & -0.07 & 0 & 0 \end{bmatrix}, \quad \begin{bmatrix} 0 & -1 & 0 \\ -1 & 6 & -1 \\ 0 & -1 & 0 \end{bmatrix}. \tag{9}$$

Figure 3 shows a portion of the recovered (processed) 3-D step object, including six steps varying in object distance by 250 mm. The in-focus position (Δ in Fig. 3) is at $x = 950$ mm. Figure 4(b) shows an enlargement of the final processed image that is 250 mm (five steps) closer to the lens than the plane of best focus. For comparison, in Fig. 4(a) we show a blurred image obtained with a Nikon 60-mm lens with the same f/D. This image is obtained by use of the same object positioning as that described above. We observe a greatly extended depth of field for our logarithmic asphere.

In the second experiment we directly measure the resolution as a function of distance, as shown in Fig. 5. Data are taken at each step (50 mm), and the average value of five readings is plotted together with error bars. We use the same setup as described above, except that resolution is measured with a fine-line chirped chart. Also, the pixel size has in effect been reduced to 10 μm. The dotted line shows the resolution limit for a 25-μm pixel size. For comparison, we show the resolution obtained by the Nikon 60-mm lens under identical conditions. From these data, we can clearly see a greatly increased depth of field for the smart camera with the logarithmic asphere.

The authors acknowledge discussions with Harvey Pollicove, Director of the Center for Optics Manufacturing, University of Rochester, and David Skatrud as well as financial support by the U.S. Army Research Office. N. George's e-mail address is ngeorge@troi.cc.rochester.edu.

References

1. J. Ojeda-Castaneda, L. R. Berriel-Valdos, and E. Montes, Opt. Lett. **8,** 458 (1983).
2. T.-C. Poon and M. Motamedi, Appl. Opt. **26,** 4612 (1987).
3. J. Ojeda-Castaneda and L. R. Berriel-Valdos, Appl. Opt. **29,** 994 (1990).
4. E. R. Dowski and W. T. Cathey, Appl. Opt. **34,** 1859 (1995).
5. J. van der Gracht, E. R. Dowski, W. T. Cathy, and J. P. Bowen, Proc. SPIE **2537,** 279 (1995).
6. H. B. Wach, W. T. Cathey, and E. R. Dowski, Jr., Appl. Opt. **37,** 5359 (1998).
7. S. C. Tucker, E. R. Dowski, and W. T. Cathey, Opt. Express **4,** 467 (1999), http://www.opticsexpress.org.
8. L. M. Soroko, in *Progress in Optics*, E. Wolf, ed. (Elsevier, New York, 1989), pp. 109–160, and references therein.
9. J. Sochacki, S. Bara, Z. Jaroszewicz, and A. Kolodziejczyk, Opt. Lett. **17,** 7 (1992).
10. J. Sochacki, A. Kolodziejczyk, Z. Jaroszewicz, and S. Bara, Appl. Opt. **31,** 5326 (1992).
11. R. F. Steinert, C. T. Post, Jr., S. F. Brint, C. D. Fritch, D. L. Hall, L. W. Wilder, I. H. Fine, S. B. Lichtenstein, S. Masket, C. Casebeer, and H. Oksman, Opthalmology **99,** 853 (1983).
12. R. K. Luneburg, *Mathematical Theory of Optics* (University of California, Berkeley, 1964), p. 86.
13. See, for instance, H. B. Dwight, *Tables of Integrals and Other Mathematical Data* (Macmillan, New York, 1947), Eq. (380.001), p. 70.
14. S. Wolfram, *Mathematical Software 4.0* (Wolfram Reseach, Champaign, Ill., 2000), p. 859.
15. This type of magneto-theological finisher is available commercially from QED Technologies, Rochester, New York.
16. B. R. Hunt, IEEE Trans. Comput. **C-22,** 805 (1973).
17. R. C. Gonzalez and R. E. Woods, *Digital Image Processing* (Addison-Wesley, Reading, Mass., 1992), p. 218.

1 October 2002

ELSEVIER

Optics Communications 211 (2002) 85–94

OPTICS COMMUNICATIONS

www.elsevier.com/locate/optcom

Direct sampling and demodulation of carrier-frequency signals ☆

Kedar Khare, Nicholas George *

The Institute of Optics, University of Rochester, Rochester, NY 14627, USA

Received 26 February 2002; received in revised form 22 July 2002; accepted 7 August 2002

Abstract

We show that a generalized carrier-frequency signal can be directly and efficiently coarse-sampled based upon the notion of the space-bandwidth product. Using an envelope function form, we treat both amplitude-modulation and frequency-modulation cases simultaneously. We derive exact formulas for the sampled carrier-frequency signal and for the sampled envelope, showing that it is possible to recover the envelope from the coarsely sampled carrier without conventional mixing or heterodyning. This alternative to the conventional demodulation methods is illustrated with numerical examples including phase retrieval. Extension to the two-dimensional case is also included.

Keywords: Sampling; Space-bandwidth product; Envelope detection; Demodulation; Phase retrieval

1. Introduction

The Whittaker–Shannon sampling theorem [1,2] allows one to replace a continuous band-limited signal by a set of its discrete samples without any loss of information. The minimum sampling rate necessary for the exact reconstruction of the original signal is called the Nyquist rate. Several extensions of the sampling theorem exist in the literature [3–6]. Kohlenberg [7], Vaughan et al. [8], and Fritsch et al. [9] have treated the carrier-frequency case that is of interest to us as described in detail below.

Consider a carrier-frequency signal written in the following form as a real-valued function:

$$g(x) = a(x)\exp(\mathrm{i}2\pi f_0 x) + a^*(x)\exp(-\mathrm{i}2\pi f_0 x), \quad (1)$$

where $a(x)$ is the information carrying band-limited function and the carrier frequency f_0 is much larger than the bandwidth of $a(x)$. The asterisk, *, in the second term denotes a complex conjugation operation. We use functions of this form to represent both amplitude-modulated (AM) and frequency-modulated (FM) signals. The signal notation in (1) is consistent with the literature [10] and is suitable for treating the envelope and phase detection problems in a unified manner.

The function $a(x)$ is complex in general and we shall refer to it as the envelope function. The in-

☆ This research was supported in part by the US Army Research Office.

* Corresponding author. Fax: +1-716-244-6150.

E-mail addresses: kedar@optics.rochester.edu (K. Khare), ngeorge@troi.cc.rochester.edu (N. George).

0030-4018/02/$ - see front matter
PII: S0030-4018(02)01903-X

formation of interest is contained in this envelope function and hence demodulation or the retrieval of $a(x)$ from $g(x)$ is an important problem. Considering the Fourier transform of (1) with a band-limited envelope $a(x)$, it is well known from the notion of the space-bandwidth product that an efficient sampling process is likely related to the bandwidth of $a(x)$ and not to the carrier frequency f_0. This point is covered in illustrative exercises in Bracewell [11]. In particular, the demodulation of an AM signal involves recovery of the amplitude of $a(x)$. In practice this is commonly achieved by mixing, amplification, and a rectifier for envelope detection followed by an amplifier and output. An FM signal is also processed using mixing, except that the final stages involve some form of phase detection in the demodulation process followed by an amplifier and output. Once some mixing process is employed and the signal is reduced to a video signal starting at zero frequency, it is clear that the Nyquist sampling interval should be of the order of reciprocal of the bandwidth of $a(x)$. In fact, as kindly pointed out by a reviewer, there are complete demodulation chips such as Harris HSP50016 available for this purpose [12,13]. These chips invariably involve a mixing process with both sine/cosine local oscillators for phase retrieval. A further more detailed discussion of standard demodulation techniques may be found in the literature on communication systems [14–16].

In the study, herein, we would like to draw attention to the possibility of direct coarse sampling of carrier-frequency signals as in Fig. 1, without any local oscillator or mixing process. Based on an idealized comb-function like direct sampling, we show theoretically that it is possible to reconstruct the envelope function itself. With the widespread usage of digital processing and storage, it is reasonable to consider this alternative to mixing and demodulation as described earlier. In optics, important examples of two-dimensional sampling occur with images, e.g., in holography, synthetic radar, and phase retrieval as we illustrate in Section 7. In an early analysis of the exact interpolation of band-limited functions with a carrier frequency, Kohlenberg has treated a closely related problem, viz., reconstruction of the entire $g(x)$; and he has also obtained efficient sampling

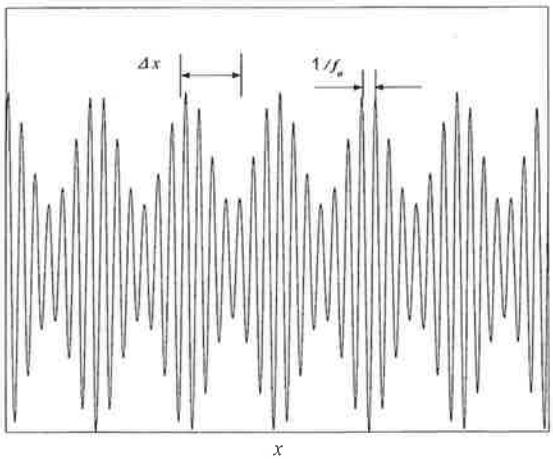

Fig. 1. Generalized carrier-frequency signal showing a coarse sampling interval Δx and carrier frequency f_0.

forms for this problem [7]. In the current literature approximate expressions are presented for a digital envelope detection filter for real-time operation [9]. In this paper, we show that it is possible to reconstruct the envelope function $a(x)$ from the discrete samples of $g(x)$ taken at a rate comparable to the reciprocal of the bandwidth of $a(x)$. To that effect, we introduce an exact sampling series representation for the envelope function $a(x)$.

The outline of this paper is as follows. In Section 2 we briefly describe the Whittaker–Shannon sampling theorem. In Section 3 the band-pass sampling theorem is discussed in some detail. The sampling series representation for the envelope function is introduced in Section 4. In Sections 5 and 6 we illustrate our result with numerical examples for the special cases of demodulation of AM and FM signals, respectively. The important problem of phase retrieval in optics is discussed in Section 7. Finally, in Section 8 we extend our sampling series to the case of two-dimensional signals.

2. Whittaker–Shannon sampling theorem

In this section we briefly review the Whittaker–Shannon sampling theorem and introduce our notation, which is fairly standard. Consider a band-limited function $a(x)$ that has a non-zero spectrum only in the interval $[-B, B]$ in the fre-

quency domain as shown by the magnitude of the Fourier transform $A(f_x)$ in Fig. 2. If $a(x)$ is sampled periodically at discrete values of x spaced Δx apart, an estimate of $a(x)$ may be obtained as [6]:

$$a_b(x) = b(x) * a(x)\ \mathrm{comb}(x/\Delta x), \tag{2}$$

in which the subscript 'b' indicates the estimate. Here $b(x)$ is a suitable interpolation function and * denotes a convolution operation. The sampling function comb(x) is defined as:

$$\mathrm{comb}(x) = \sum_{n=-\infty}^{\infty} \delta(x-n), \tag{3}$$

where $\delta(x)$ is the Dirac delta function.

Taking the Fourier transform of (2) gives:

$$A_b(f_x) = B(f_x) \sum_{n=-\infty}^{\infty} A(f_x - n/\Delta x). \tag{4}$$

Fig. 3(a) shows the function $|\sum_{n=-\infty}^{\infty} A(f_x - n/\Delta x)|$ for the special case of the Nyquist criterion, i.e., when

$$\Delta x = \frac{1}{2B}. \tag{5}$$

From Fig. 3(b) one sees the choice of a rect function for $B(f_x)$ which leads to the important result of the Whittaker–Shannon theorem [1,2]. Hence, choosing

$$B(f_x) = \mathrm{rect}\left(\frac{f_x}{2B}\right), \tag{6}$$

where

$$\mathrm{rect}(x) = \begin{cases} 1, & |x| < 1/2, \\ 0, & \text{otherwise}, \end{cases} \tag{7}$$

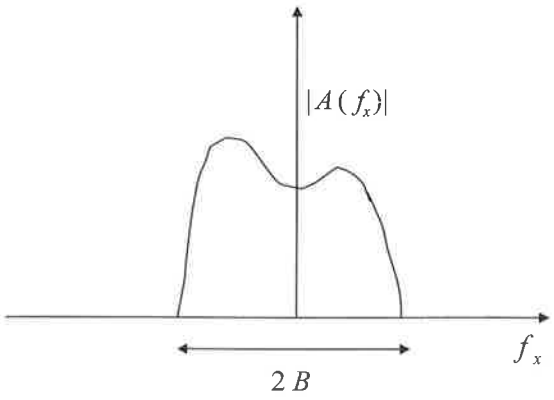

Fig. 2. Fourier transform of the band-limited function $a(x)$.

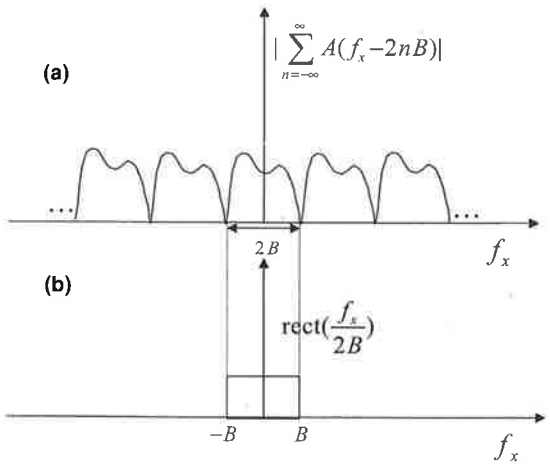

Fig. 3. (a) Fourier transform of the sampled function, (b) rect filter for recovery of $A(f_x)$.

one finds the ideal interpolation function:

$$b(x) = 2B\mathrm{sinc}(2Bx), \tag{8}$$

where

$$\mathrm{sinc}(x) = \frac{\sin \pi x}{\pi x}. \tag{9}$$

Moreover, since this choice of $B(f_x)$ assures that $A_b(f_x) = A(f_x)$, (2) can be rewritten in the Whittaker–Shannon form:

$$a(x) = \sum_{n=-\infty}^{\infty} a\left(\frac{n}{2B}\right)\mathrm{sinc}\left[2\mathrm{B}\left(x - \frac{n}{2B}\right)\right]. \tag{10}$$

3. Band-pass sampling

In order to explain band-pass sampling, we consider a band-limited function with carrier frequency as in (1) and Fig. 1:

$$g(x) = a(x)\exp(\mathrm{i}2\pi f_0 x) + a^*(x)\exp(-\mathrm{i}2\pi f_0 x). \tag{11}$$

The Fourier transform of $g(x)$ is given by:

$$G(f_x) = A(f_x - f_0) + A^*(-f_x - f_0). \tag{12}$$

The total spread of the function $G(f_x)$ is $2(f_0 + B)$, however, a sampling rate as high as $2(f_0 + B)$ is not necessary in order to reconstruct the function $g(x)$. To see this, let the sampling

interval Δx be much larger than $1/2(f_0 + B)$ and let $b_1(x)$ be the interpolation function used for estimating $g(x)$ from its samples. As before we obtain:

$$g_b(x) = b_1(x) * g(x)\mathrm{comb}(x/\Delta x). \tag{13}$$

The equivalent expression in the Fourier domain is:

$$G_b(f_x) = B_1(f_x) \sum_{n=-\infty}^{\infty} G(f_x - n/\Delta x). \tag{14}$$

The sampled Fourier transform in (14) is shown in Figs. 4(b) and (c). It is necessary to establish a criterion for non-overlap of various spectral terms. From Fig. 4 it is clear that an appropriate choice of Δx denoted by Δx_0 is given by:

$$\Delta x_0 = \frac{1}{4B_0}, \tag{15}$$

along with the condition that

$$\frac{f_0}{2B} \geqslant \frac{f_0}{2B_0} = N + \frac{1}{2}, \tag{16}$$

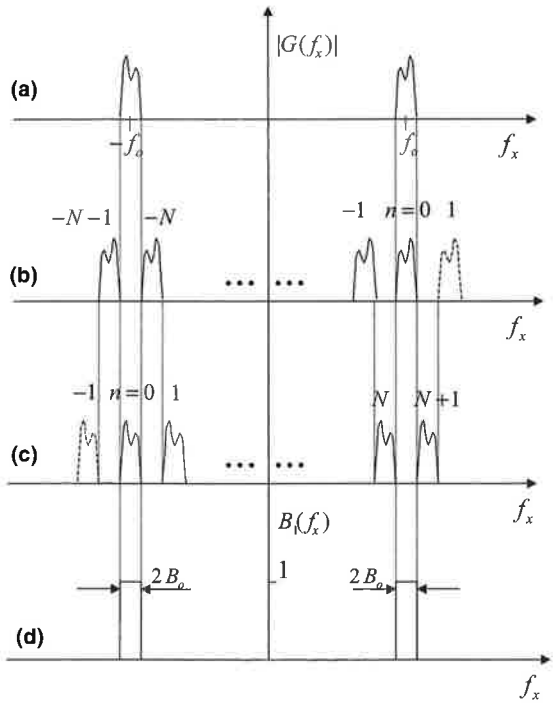

Fig. 4. (a) $G(f_x)$ in (12); (b) negative n and (c) positive n terms of transform in (14), (d) filter $B_1(f_x)$ for recovery.

where N is a positive integer. The choice of a sampling interval Δx_0 and a system of bandwidth $2B_0$ are sufficient for any signal having bandwidth $2B \leqslant 2B_0$. As shown in Fig. 4(d) we now choose:

$$B_1(f_x) = \left[\mathrm{rect}\left(\frac{f_x + f_0}{2B_0}\right) + \mathrm{rect}\left(\frac{f_x - f_0}{2B_0}\right)\right]. \tag{17}$$

This choice ensures that $G_b(f_x) = G(f_x)$. The interpolation function is the inverse transform of $B_1(f_x)$, viz.,

$$b_1(x) = 4B_0\mathrm{sinc}(2B_0x)\cos(2\pi f_0 x). \tag{18}$$

From (13) and (18) we see that the sampled carrier-frequency signal $g(x)$ can now be expressed in the following form:

$$g(x) = \sum_{n=-\infty}^{\infty} g\left(\frac{n}{4B_0}\right)\mathrm{sinc}\left[2B_0\left(x - \frac{n}{4B_0}\right)\right] \times \cos\left[2\pi f_0\left(x - \frac{n}{4B_0}\right)\right]. \tag{19}$$

Here the important distinction is that the sampling interval chosen according to (15) and (16) is related to the signal bandwidth $2B \leqslant 2B_0$ which is much smaller than the carrier f_0. Kohlenberg [7] also derived a result similar to (19) in a different form.

4. Recovery of the envelope function

With the result for the exact recovery of the carrier-frequency signal $g(x)$ established we simply replace the cosine term in (19) by a sum of two exponentials giving:

$$g(x) = \frac{1}{2}\exp(\mathrm{i}2\pi f_0 x) \sum_{n=-\infty}^{\infty} g\left(\frac{n}{4B_0}\right) \times \mathrm{sinc}\left[2B_0\left(x - \frac{n}{4B_0}\right)\right]\exp\left(-\mathrm{i}2\pi f_0 \frac{n}{4B_0}\right) + \frac{1}{2}\exp(-\mathrm{i}2\pi f_0 x) \sum_{n=-\infty}^{\infty} g\left(\frac{n}{4B_0}\right) \times \mathrm{sinc}\left[2B_0\left(x - \frac{n}{4B_0}\right)\right]\exp\left(\mathrm{i}2\pi f_0 \frac{n}{4B_0}\right). \tag{20}$$

The two terms in (20) have been written explicitly to facilitate comparison with (11).

The interesting central result is an exact reconstruction of the envelope function in terms of the samples $g(n/4B_0)$ given by:

$$a(x) = \frac{1}{2}\sum_{n=-\infty}^{\infty} g\left(\frac{n}{4B_0}\right)\operatorname{sinc}\left[2B_0\left(x-\frac{n}{4B_0}\right)\right] \times \exp\left(-\mathrm{i}2\pi f_0\frac{n}{4B_0}\right). \tag{21}$$

Note that according to (16) the exponential term in (21) is reduced to

$$\exp\left(-\mathrm{i}2\pi f_0\frac{n}{4B_0}\right) = (-1)^{nN}(-\mathrm{i})^n. \tag{22}$$

The alternate terms of the series (21) are thus purely real and purely imaginary, respectively. In other words, half of the samples in a finite interval reconstruct the real part of $a(x)$ while the remaining samples reconstruct the imaginary part. From our study of the literature, we do not find an explicit form for the envelope function as presented in (21). The significance of (21) is that the conventional analog methods for the demodulation of AM and FM signals may be replaced in principle by the alternative of direct sampling and interpolation.

5. Demodulation of an AM signal

Consider the application of the new sampling result (21) for an AM signal. In this case, the information is stored in the variation of the amplitude of the carrier. As an illustration, we choose the function:

$$g(x) = \operatorname{sinc}^2(2x)\cos(20\pi x - \pi/3), \tag{23}$$

in which the envelope is band-limited.

The phase shift in the cosine term is added intentionally to show that the real and imaginary parts of the envelope function can be reconstructed using our result. The envelope function is given by:

$$a(x) = \frac{1}{2}\exp(-\mathrm{i}\pi/3)\operatorname{sinc}^2(2x). \tag{24}$$

The Fourier transform of $a(x)$ is given by

$$A(f_x) = \frac{1}{4}\exp(-\mathrm{i}\pi/3)\Lambda(f_x/2), \tag{25}$$

where the triangle function $\Lambda(x)$ is defined as:

$$\Lambda(x) = \begin{cases} 1-|x|, & |x|\leqslant 1, \\ 0, & \text{otherwise.} \end{cases} \tag{26}$$

The spectrum of $a(x)$ is thus non-zero in the interval $[-2,2]$. The numerical values of $2B_0$ $(=4)$ and f_0 $(=10)$ have been chosen so as to satisfy the condition (16). Figs. 5(a) and (b) show the plot of the function $g(x)$ and its Fourier transform, respectively. The reconstruction of the envelope function is shown in Fig. 5(c). We have used 81 samples (shown by '*' marks in Fig. 5(a)) in the interval $[-5,5]$ and a sampling interval of $1/(4B_0) = 0.125$. This truncation is sufficient for the present purpose since the samples of $\operatorname{sinc}^2(2x)$ beyond this interval do not contribute significantly. Any desired accuracy may be achieved by increasing this interval.

6. Demodulation of an FM signal

In frequency modulation, the information is stored as a variation of the phase of the carrier, the amplitude of the carrier being kept constant. An FM signal may be expressed as [9]:

$$h(x) = \frac{1}{2}\exp[\mathrm{i}2\pi f_0 x + \mathrm{i}\beta\sin(2\pi\mu x)] + \text{c.c.}, \tag{27}$$

in which c.c. denotes the complex conjugate of the first term and the modulation function $m(x)$ can be expressed as the well-known expansion:

$$m(x) = \frac{1}{2}\sum_{n=-\infty}^{\infty} J_n(\beta)\exp(\mathrm{i}2\pi n\mu x), \tag{28}$$

where $J_n(x)$ is the Bessel function of nth order and of first kind [17]. From (27) and (28), one sees that the function $h(x)$ is not band-limited. In order to band-limit the envelope function $a_m(x)$, we truncate (28) to 10 sidebands. Hence our choice of the envelope function for the simulation is given by:

$$a_m(x) = \frac{1}{2}\sum_{n=-5}^{5} J_n(\beta)\exp(\mathrm{i}2\pi n\mu x). \tag{29}$$

The carrier-frequency signal is written as:

$$g_h(x) = a_m(x)\exp(\mathrm{i}2\pi f_0 x) + a_m^*(x) \times \exp(-\mathrm{i}2\pi f_0 x). \tag{30}$$

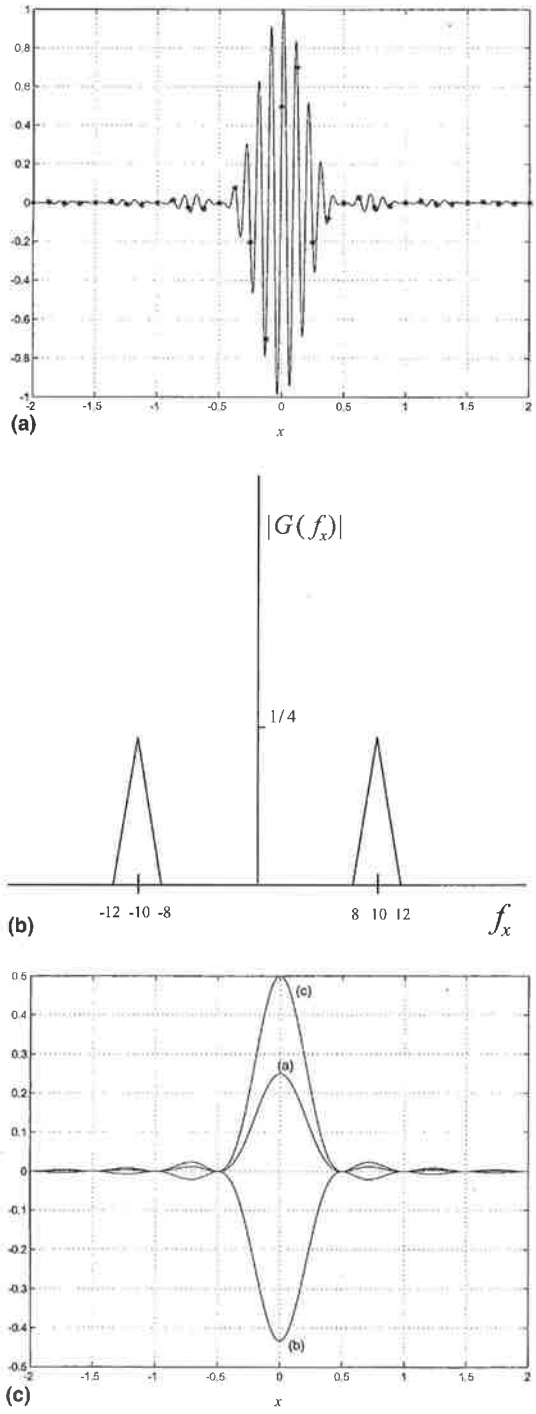

Fig. 5. (a) AM signal in (23), sampling interval $\Delta x_0 = 0.125$. (b) Magnitude of Fourier transform of the AM signal in (23). (c) Recovery of envelope function in (24): (a) real part, (b) imaginary part, (c) absolute value.

We choose the various parameters as follows: $f_0 = 10$, $\beta = 1.5$, $\mu = 0.35$. The function $g_h(x)$ and its transform are shown in Figs. 6(a) and (b), respectively. From the sampling choices shown in Fig. 6, it may be noted that the sample values are taken in an idealized comb-like manner at discrete points. It is seen clearly that there are five prominent sidebands on both sides of the carrier frequency. The spectrum of $a_m(x)$ is thus significant over a bandwidth $2B = 2 \times 5 \times 0.35 = 3.5$. A suitable value $2B_0 = 4$ satisfies the condition (16). The sampling interval is again $1/(4B_0) = 0.125$ and 161 samples (shown by '*' marks in Fig. 6(a)) in the interval $[-10, 10]$ are used for reconstruction. Fig. 6(c) shows the plot of $\arctan[\mathrm{Im}(a_m(x))/\mathrm{Re}(a_m(x))]$. The function $a_m(x)$ is determined from the identity (21). Several computations were made to verify that the recovery of $a_m(x)$ is insensitive to the modulation frequency μ and the parameter β as long as the bandwidth $2B \leqslant 2B_0$. Moreover, in separate calculations we have shown that in this method of direct sampling, the recovered signals are not sensitive to a phase offset in the timing of the clock. Also it is not essential that the clock rate be matched precisely to the frequency of the carrier. The computations were performed on a standard PC and the widely available software MATLAB version R12 was used.

7. Phase retrieval in holography

Measurement or recovery of the phase function from a recorded intensity pattern is an important problem in optics. Phase-stepping interferometric methods are commonly used for measuring the phase of an arbitrary wavefront [18]. Multiple interference patterns are recorded with a predetermined variation in the phase of the reference beam and combined linearly to detect the phase at every point in the interference pattern. We suggest an alternative to this method based on our sampling identity. A one-dimensional case is illustrated here for simplicity.

Consider a Twyman–Green interferometer setup for measuring surface profiles as shown in Fig. 7. A plane incident wave is split by the beamsplitter B. The mirror M in the reference arm is tilted to provide carrier frequency f_0. The fringe

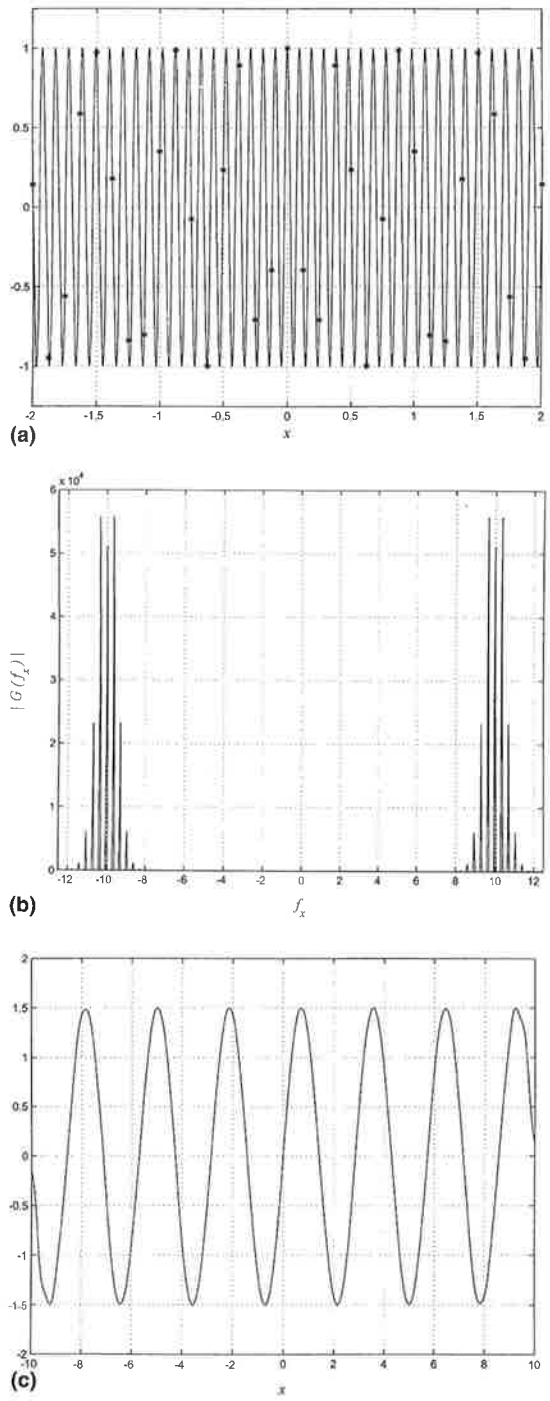

Fig. 6. (a) FM signal in (30), sampling interval $\Delta x_0 = 0.125$. (b) Fourier transform of the FM signal in (30), (Arbitrary units along y-axis). (c) Reconstruction of phase of $a_m(x)$ from $\arctan[\mathrm{Im}(a_m(x))/\mathrm{Re}(a_m(x))]$.

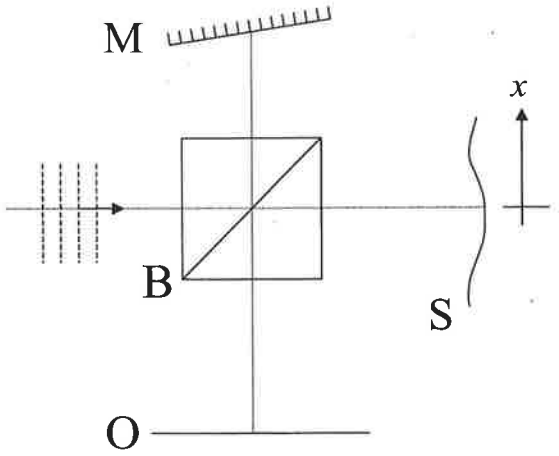

Fig. 7. Twyman–Green interferometer, M: reference mirror, B: beam-splitter, S: surface under test, O: observation plane.

pattern is observed in the plane O. If the optical path lengths in the interferometer are nominally matched, the interference pattern after subtracting the low-frequency intensity terms may be described as:

$$g(x) = \exp[\mathrm{i}2\pi f_0 x + \mathrm{i}\phi(x)] + \text{c.c.}, \tag{31}$$

where $\phi(x)$ is proportional to the profile function of the surface S. The envelope $\exp[\mathrm{i}\phi(x)]$ is not band-limited, however, when $\phi(x)$ is a smoothly varying function, the Fourier transform of $g(x)$ is predominant over a narrow band centered on the carrier frequency. As an example, we take $f_0 = 10$ and show the recovery of the phase $\phi(x)$ for two special cases, viz, $\phi(x) = \pm\Lambda(x/10)$, where $\Lambda(x)$ is the triangle function as defined in (26). The surface **S** in Fig. 7, for these two cases corresponds to a one-dimensional roof and an inverted peak, respectively. By direct application of (21), calculating the phase as described in the FM illustration, we find excellent phase recovery as shown in Fig. 8 without the appearance of significant aliasing errors. A total of 161 samples in the interval $[-10, 10]$ at a sampling rate $\Delta x = 0.125$ were used in each case. It is clear from these examples that only one interference pattern is sufficient for the purpose of distinguishing between peaks and valleys of the test wavefront. In other words, for a continuous wavefront the ambiguity in the sign of the phase function $\phi(x)$ is resolved. We also note that since the sampling rate is related to the

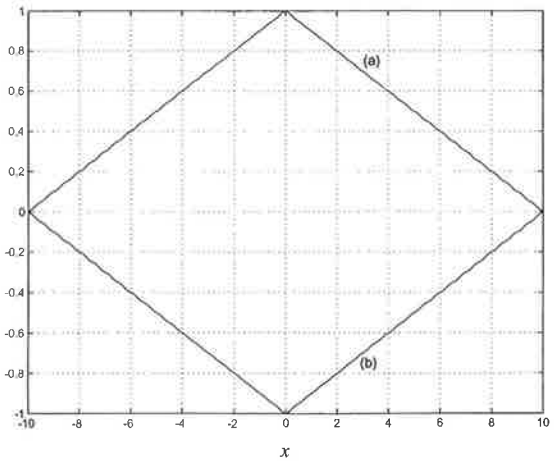

Fig. 8. Recovery of phase function: (a) $\phi(x) = \Lambda(x/10)$, (b) $\phi(x) = -\Lambda(x/10)$.

bandwidth of the envelope function, the amount of data required for phase reconstruction is reduced significantly.

8. Envelope recovery for two-dimensional carrier-frequency signals

In this section, we generalize (19) and (21) to two dimensions. Since we are considering, herein, the theoretical formulations of the sampling representations, we have not delved into the implementation aspects. However, it is interesting to consider the sampling problem for two cases of practical interest.

In the two-beam hologram of Leith and Upatneiks, the picture beam is approximately conical, with the angular spectrum of waves at the hologram plane subtending the object being centered about the normal. The reference beam is at a large angle and establishes the carrier frequency f_{0x} say along the x-axis. This case is shown in Fig. 9 and may be described by a real-valued carrier-frequency signal of the form:

$$g(x,y) = a(x,y)\exp(\mathrm{i}2\pi f_{0x}x) + a^*(x,y)\exp(-\mathrm{i}2\pi f_{0x}x). \tag{32}$$

Another case of interest is that of multiplexing in which several signals are stored in the same carrier-frequency signal. This case is shown in Fig. 10 and may be described as follows:

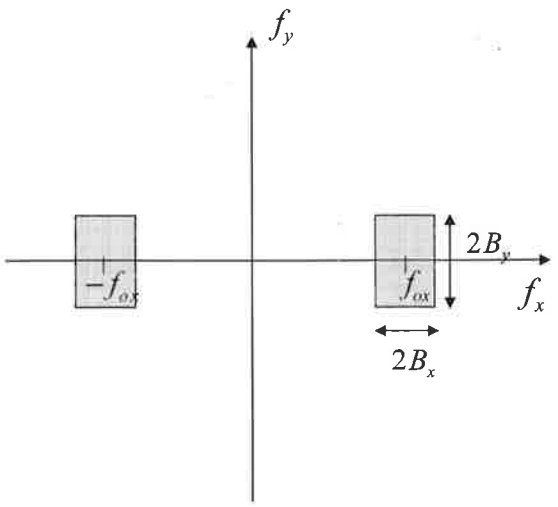

Fig. 9. Transform space with the non-zero regions shown shaded for the two-dimensional case (32).

$$\begin{aligned} g(x,y) = {} & a_1(x,y)\exp[\mathrm{i}2\pi(f_{0x}x + f_{0y}y)] \\ & + a_1^*(x,y)\exp[-\mathrm{i}2\pi(f_{0x}x + f_{0y}y)] \\ & + a_2(x,y)\exp[\mathrm{i}2\pi(f_{0x}x - f_{0y}y)] \\ & + a_2^*(x,y)\exp[-\mathrm{i}2\pi(f_{0x}x - f_{0y}y)]. \end{aligned} \tag{33}$$

The envelope functions $a(x,y)$, $a_1(x,y)$, and $a_2(x,y)$ in (32) and (33) are assumed to have a non-

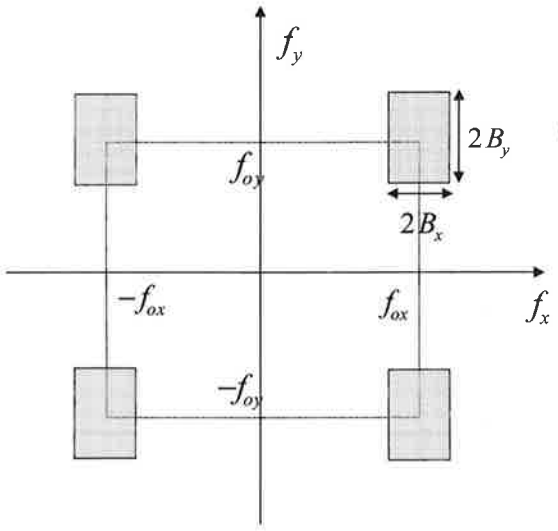

Fig. 10. Non-zero regions shown shaded for transform of two-dimensional signal in (33), multiplexing case.

zero spectrum only in the rectangular region of dimensions $2B_x \times 2B_y$ centered at the origin in the $f_x - f_y$ plane. Moreover, $2B_x$ and $2B_y$ are much less than the carrier frequencies f_{0x} and f_{0y}. The shaded areas in Figs. 9 and 10 show the regions of $f_x - f_y$-plane where the spectrum of $g(x,y)$ in (32) and (33) is non-zero, respectively. The generalization of (19) and (21) for the two-dimensional cases above is straightforward and the following results may be obtained by a derivation similar to the one-dimensional case.

From (32) we can write:

$$g(x,y) = \sum_{m=-\infty}^{\infty}\sum_{n=-\infty}^{\infty} g\left(\frac{m}{4B_x},\frac{n}{2B_y}\right) \times \operatorname{sinc}\left[2B_x\left(x-\frac{m}{4B_x}\right)\right] \times \operatorname{sinc}\left[2B_y\left(y-\frac{n}{2B_y}\right)\right] \times \cos\left[2\pi f_{0x}\left(x-\frac{m}{4B_x}\right)\right], \tag{34}$$

and

$$a(x,y) = \frac{1}{2}\sum_{m=-\infty}^{\infty}\sum_{n=-\infty}^{\infty} g\left(\frac{m}{4B_x},\frac{n}{2B_y}\right) \times \operatorname{sinc}\left[2B_x\left(x-\frac{m}{4B_x}\right)\right] \times \operatorname{sinc}\left[2B_y\left(y-\frac{n}{2B_y}\right)\right] \times \exp\left(-\mathrm{i}2\pi f_{0x}\frac{m}{4B_x}\right). \tag{35}$$

The sampling intervals in (34) and (35) are constrained by the following relation:

$$\frac{f_{0x}}{2B_x} = N_x + \frac{1}{2} \tag{36}$$

for positive integer N_x.

From (33) we get:

$$g(x,y) = \frac{1}{2}\sum_{m=-\infty}^{\infty}\sum_{n=-\infty}^{\infty} g\left(\frac{m}{4B_x},\frac{n}{4B_y}\right) \times \operatorname{sinc}\left[2B_x\left(x-\frac{m}{4B_x}\right)\right] \times \operatorname{sinc}\left[2B_y\left(y-\frac{n}{4B_y}\right)\right] \times \left\{\cos\left[2\pi f_{0x}\left(x-\frac{m}{4B_x}\right) + f_{0y}\left(y-\frac{n}{4B_y}\right)\right] + \cos\left[2\pi f_{0x}\left(x-\frac{m}{4B_x}\right) - f_{0y}\left(y-\frac{n}{4B_y}\right)\right]\right\}, \tag{37}$$

$$a_1(x,y) = \frac{1}{4}\sum_{m=-\infty}^{\infty}\sum_{n=-\infty}^{\infty} g\left(\frac{m}{4B_x},\frac{n}{4B_y}\right) \times \operatorname{sinc}\left[2B_x\left(x-\frac{m}{4B_x}\right)\right] \times \operatorname{sinc}\left[2B_y\left(y-\frac{n}{4B_y}\right)\right] \times \exp\left[-\mathrm{i}2\pi\left(f_{0x}\frac{m}{4B_x}+f_{0y}\frac{n}{4B_y}\right)\right], \tag{38}$$

and

$$a_2(x,y) = \frac{1}{4}\sum_{m=-\infty}^{\infty}\sum_{n=-\infty}^{\infty} g\left(\frac{m}{4B_x},\frac{n}{4B_y}\right) \times \operatorname{sinc}\left[2B_x\left(x-\frac{m}{4B_x}\right)\right] \times \operatorname{sinc}\left[2B_y\left(y-\frac{n}{4B_y}\right)\right] \times \exp\left[-\mathrm{i}2\pi\left(f_{0x}\frac{m}{4B_x}-f_{0y}\frac{n}{4B_y}\right)\right]. \tag{39}$$

The sampling intervals in (37)–(39) need to meet the following conditions:

$$\frac{f_{0x}}{2B_x} = N_x + \frac{1}{2}, \tag{40}$$

and

$$\frac{f_{0y}}{2B_y} = N_y + \frac{1}{2} \tag{41}$$

for positive integers N_x and N_y.

The above results establish sampling representations for the two-dimensional carrier-frequency signals (32) and (33). This is as one would anticipate from the assertion that the number of degrees of freedom (or the number of pixels) required is equivalent to the space-bandwidth product of the envelope functions $a(x,y)$, $a_1(x,y)$, and $a_2(x,y)$.

Throughout this paper we have assumed the carrier-frequency signal to be a real-valued function. However, this restriction is not necessary for the validity of the sampling expansions. For example, we may consider a carrier-frequency signal such as:

$$g_z(x) = z_1(x)\exp(\mathrm{i}2\pi f_0 x) + z_2(x)\exp(-\mathrm{i}2\pi f_0 x). \tag{42}$$

The subscript 'z' indicates that the function $g_z(x)$ is complex-valued. The functions $z_1(x)$ and $z_2(x)$ are also complex in general and have a non-zero Fourier transform only in the interval $[-B, B]$ in the frequency domain. If conditions (15) and (16) are obeyed, we may write $z_1(x)$ and $z_2(x)$ in the following form:

$$z_1(x) = \frac{1}{2}\sum_{n=-\infty}^{\infty} g_z\left(\frac{n}{4B_0}\right)\mathrm{sinc}\left[2B_0\left(x-\frac{n}{4B_0}\right)\right] \times \exp\left(-\mathrm{i}2\pi f_0\frac{n}{4B_0}\right), \tag{43}$$

$$z_2(x) = \frac{1}{2}\sum_{n=-\infty}^{\infty} g_z\left(\frac{n}{4B_0}\right)\mathrm{sinc}\left[2B_0\left(x-\frac{n}{4B_0}\right)\right] \times \exp\left(\mathrm{i}2\pi f_0\frac{n}{4B_0}\right). \tag{44}$$

The functions $z_1(x)$ and $z_2(x)$ are thus expressed in terms of the complex-valued samples $g_z(n/4B_0)$.

9. Conclusion

For a generalized carrier-frequency signal (1), we have established an efficient sampling method that is useful for digital representation as well as demodulation, i.e., exact recovery of envelope function $a(x)$. The important results in this paper are summarized below.

First, for (1), we derive the sampled forms for the function itself (19) and for the envelope function (21). Four computer simulations are presented to demonstrate the recoveries of envelope functions separately for AM signals, Figs. 4(a)–(c), FM signals, Figs. 5(a)–(c), and for phase recovery in holography, Fig. 8. In these cases, we show that the sampling interval can be chosen according to (15) and (16) without sensitivity to the signal bandwidth (assuming $2B \leqslant 2B_0$). However the choice of the sampling interval Δx_0 depends on the carrier frequency f_0. Finally, we describe sampling for the two-dimensional carrier-frequency case. The holography case, Fig. 9, and the multiplexing case, Fig. 10, are treated separately. In conclusion, exact sampling representations are presented for the envelope functions of one-dimensional, (21), (43), (44) and two-dimensional, (34)–(39), carrier-frequency signals. This research was supported in part by the US Army Research Office.

References

[1] E.T. Whittaker, Proc. Roy. Soc. Edinburgh 35 (1915) 181.
[2] C.E. Shannon, Proc. IRE 37 (1949) 10.
[3] D.A. Linden, Proc. IRE 47 (1959) 1219.
[4] A.J. Jerri, Proc. IEEE 65 (1977) 1565.
[5] M. Unser, Proc. IEEE 88 (2000) 569.
[6] A. Papoulis, Signal Analysis, McGraw-Hill, New York, 1977.
[7] A. Kohlenberg, J. Appl. Phys. 24 (1953) 1432.
[8] R.G. Vaughan, N.L. Scott, D.R. White, IEEE Trans. Signal Process. 39 (1991) 1973.
[9] C. Fritsch, A. Ibanez, M. Parrilla, IEEE Trans. Instrum. Meas. 48 (1999) 1287.
[10] S. Goldman, Frequency Analysis, Modulation and Noise, McGraw-Hill, New York, 1948.
[11] R.N. Bracewell, in: The Fourier Transform and its Applications, second ed., Mc-Graw Hill, New York, 1978, p. 217, problem 11,12.
[12] Digital Down Converter, Chip No. HSP50016, Data Sheet File No. 3288.7, Intersil Corporation, September 2000.
[13] W.R. Young, Digital Down Converter and Method, US Patent 5,757,794, 1998, Harris Corporation.
[14] A.B. Carlson, Communication Systems – An Introduction to Signals and Noise in Electrical Communication, third ed., McGraw-Hill, New York, 1986.
[15] D.J. Sakrison, Communication Theory: Transmission of Waveforms and Digital Information, Wiley, New York, 1968.
[16] J.B. Thomas, An Introduction to Statistical Communication Theory, Wiley, New York, 1969.
[17] G.N. Watson, Theory of Bessel Functions, Cambridge University Press, Cambridge, 1944.
[18] M. Servin, M. Kujawinska, Modern fringe pattern analysis in interferometry, in: D. Malacara, B.J. Thompson (Eds.), Handbook of Optical Engineering, Marcel Dekker, New York, 2001.

Holographic interference filters for infrared communications

Damon W. Diehl and Nicholas George

We demonstrate that high-quality interference filters for the wavelength range 1300–1600 nm can be holographically fabricated in DuPont HRF-800X001 photopolymer material by use of visible laser illumination. We also summarize a chain-matrix technique, which we call thin-film decomposition, that is useful for modeling multilayer films with an arbitrary index profile $n(z)$. We use the thin-film-decomposition technique to create design curves that allow one to choose the proper exposure angle and film thickness with which to fabricate a holographic interference filter with a desired transmission efficiency and bandwidth at a particular wavelength. These curves are of general utility and are not confined to any particular holographic recording medium. Excellent agreement between theory and experiment is found.

OCIS codes: 060.4510, 090.0090, 350.2460, 090.2890, 090.4220, 090.2900.

1. Introduction

Photopolymer materials offer attractive possibilities for use in the holographic fabrication of multilayer interference filters for infrared wavelengths; of particular interest are multitone filters with reflection bands at multiple wavelengths. Such filters are useful in optical communications applications. In this paper we demonstrate, through both theory and experiments, a technique for fabricating multitone interference filters for the wavelength range 1300–1600 nm, using visible wavelengths for the exposure.

It has long been known that one can produce highly efficient holographic mirrors by recording the interference of counterpropagating laser beams within a high-resolution photographic film. For early literature on this field, the reader is directed to a publication of collected reprints.[1] Of particular interest is the possibility of using a total internal reflection system to record infrared mirrors by using visible laser illumination.[2,3] Such mirrors have wavelength selection properties and bear a striking resemblence to rugate filters in which the index of refraction varies in a continuous, corrugated manner along the direction of propagation. A comprehensive history of the theory of inhomogeneous films has been compiled by Jacobsson.[4]

Photopolymer materials were first used for holography in 1969.[5] Since then, commercial classes of photopolymer have been introduced by Polaroid[6] and by DuPont.[7] Index modulation strengths as high as $\Delta n = 0.2$ have been reported for Polaroid's DMP-128 polymer, which has been used to develop high-quality infrared multilayers for eye-hazard protection at 1.06 μm.[3] Initially an important material for high-quality mirrors at 1.06 μm was dichromated gelatin. A comparison of the quality of holographic notch filters for visible wavelengths recorded in dichromated gelatin and in DuPont photopolymer has been made.[8] It is difficult to protect dichromated gelatin in an application environment in which humidity is a problem. Information relative to modulation profiles of gratings recorded in dichromated gelatin has been reported in the literature.[9] An important advance in photopolymer technology was DuPont's development of a material that is sensitized over the entire visible spectrum and thus is suitable for full-color holography.[10] Broadband multitone multilayer mirrors for visible wavelengths have been recorded in this material.[11] Furthermore, methods to characterize the index, shrinkage, and scattering of the DuPont photopolymer have been presented.[12,13] High reflectors fabricated from DuPont photopolymer are extremely efficient and are now found in enhanced reflective liquid-crystal displays.[14]

The authors are with The Institute of Optics, University of Rochester, Rochester, New York 14627-0186. D. W. Diehl's e-mail address is damon@optics.rochester.edu. N. George's e-mail address is ngeorge@troi.cc.rochester.edu.

Received 5 June 2002; revised manuscript received 11 October 2002.

0003-6935/03/071203-08$15.00/0

In Section 2 of this paper we describe the fabrication from DuPont HRF-800X001 photopolymer of holographic filters for operation in the wavelength range from 1300 to 1600 nm. The photopolymer requires exposure with visible wavelengths, which necessitates the use of the total internal reflection configuration mentioned above.[2,3] The holograms were measured with a conventional spectrophotometer. Using these data, we demonstrate that the DuPont HRF-800X001 photopolymer has low loss and low index dispersion in the near infrared. We also describe a scanning laser diode spectrophotometer that is useful for the characterization of infrared interference filters. It is calibrated by means of an acetylene absorption cell.[15]

In Section 3 we compile our experimental data into design curves that relate the exposure angle, hologram thickness, and index modulation required for fabrication of a holographic interference filter with a desired efficiency and bandwidth at a particular wavelength. To create these curves we use a computer-calculation technique, which we term thin-film decomposition. In thin-film decomposition, an inhomogeneous film is modeled as a stack of homogeneous layers, and each layer is characterized by a 2×2 matrix. The technique of thin-film decomposition has been used to model rugate filters[4] and more recently to model holographic multilayers.[16,17] The terminology "thin-film decomposition" is used in analogy to "thin grating decomposition," a similar technique in which a thick grating is treated as a cascade of thin gratings.[18–21]

2. Holographic Fabrication of Interference Filters

One fabricates a holographic multilayer mirror by recording the interference pattern created by two beams incident at equal angles from opposite sides of a film plate. For beams inclined from normal by an angle θ_f, the resulting index profile will vary only as a function of film depth, with a period Λ given by the equation

$$\Lambda = S \frac{\lambda_0}{2n_f(\lambda_0)\cos\,\theta_f}, \tag{1}$$

where S indicates the shrinkage of the film and $n_f(\lambda_0)$ is the average index of the film, before processing, at the exposure wavelength λ_0 as measured in free space. By varying either the exposure angle or the exposure wavelength, one may vary the period of the index modulation. A multilayer holographic mirror, with periods as described in Eq. (1), will have a reflection peak at the reconstruction wavelength (i.e., $\lambda = \lambda_p$) given by

$$\lambda_p = 2n_f'(\lambda_p)\Lambda\,\cos\,\theta_f', \tag{2}$$

where $n_f'(\lambda)$ is the average index of the postprocessed film at free-space wavelength λ and θ_f' is the angle of inclination of the reconstruction beam within the film.

A multitone filter is a holographic interference filter with two or more reflection peaks. We have explored two techniques for fabricating such a filter. The first technique involves making multiple exposures within a single layer of film, each with a different period. We term this an interleave filter. The second technique involves recording single holograms with different periods inside separate layers of film and then sandwiching the layers together. We term this a cascade filter.

For either type of hologram, one may control the period of the index modulation by adjusting the exposure wavelength or the exposure angle. Because the sensitivity of the DuPont photopolymer varies significantly with wavelength, it can be difficult to determine the optimal exposure time for multiple-wavelength exposures such that the final efficiencies of all the reflection tones will be equal. For this reason, in the experiments described in this paper we focus on varying the exposure angle.

Although the fabrication of multitone holograms is the final goal of this research, in this paper we describe the exposure techniques for fabricating single-tone holograms at a desired wavelength, with a desired bandwidth and efficiency. We intend to use these design curves in future research to fabricate multitone holographic interference filters.

Our objective for these experiments was to fabricate mirrors that reflect wavelengths in the range 1300–1600 nm when they are illuminated at normal incidence ($\theta_f' = 0$). Such a large period, Λ, requires that the recording beam angle, θ_f, be larger than the critical angle of the film–air interface. We therefore used a 45° roof prism to couple the TE-polarized beam into the film, as illustrated in Fig. 1. Total internal reflection at the film–air interface provides the second beam for our holographic exposures.[2,3] For the geometry shown, by using Snell's law we can write the following equations that relate the external angle of the beam, θ_i, to the angle within the film, θ_f:

$$\begin{aligned} n_p \sin\,\theta_1 &= n_0 \sin\,\theta_i, \\ \theta_2 &= 45° - \theta_1, \\ n_f \sin\,\theta_f &= n_p \sin\,\theta_2. \end{aligned} \tag{3}$$

The prism was made from Schott SF6 glass, which has an index of $n_p(590\text{ nm}) = 1.80518$. Such a high index ensured that light would couple into the film at an angle steep enough to create an index modulation of the desired large period. Were this system to be built anew, a suitable prism with an index more closely matched to the photopolymer could be used. However, in our experiments we did not experience undue reflections or parasitic gratings as a result of this index mismatch. The prism was mounted upon a Klinger rotation stage with a Heidenhain shaft encoder, allowing us to rotate the prism with a precision of 0.0001°. Our holograms were recorded with a Coherent Model 699-21 dye laser. Rhodamine 6G was used as the dye and permitted a tunable range of 560–620 nm. The laser was frequency stabilized to $\Delta\nu < 1$ MHz, and the wavelength was monitored by a

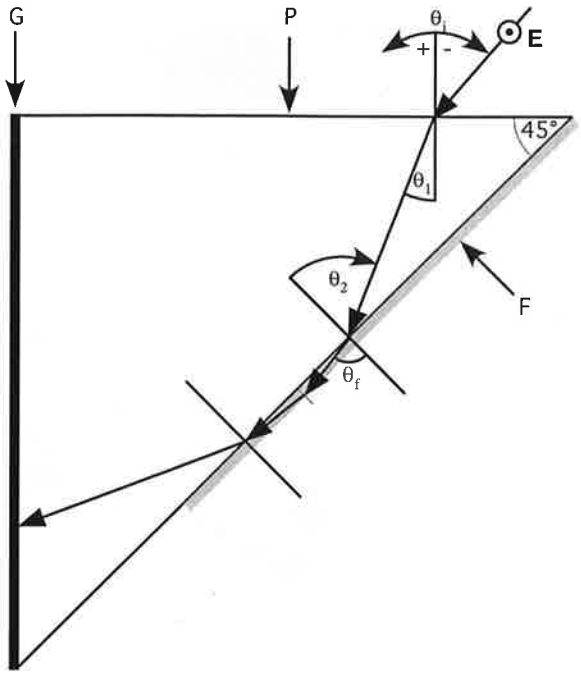

Fig. 1. Setup for holographic fabrication of infrared multilayer mirrors, showing the path of a ray through the prism–film assembly: F, film; P, 45° roof prism; G, black glass; **E**, electric field vector polarized perpendicular to the plane of incidence. Light is *s* polarized with respect to the prism face.

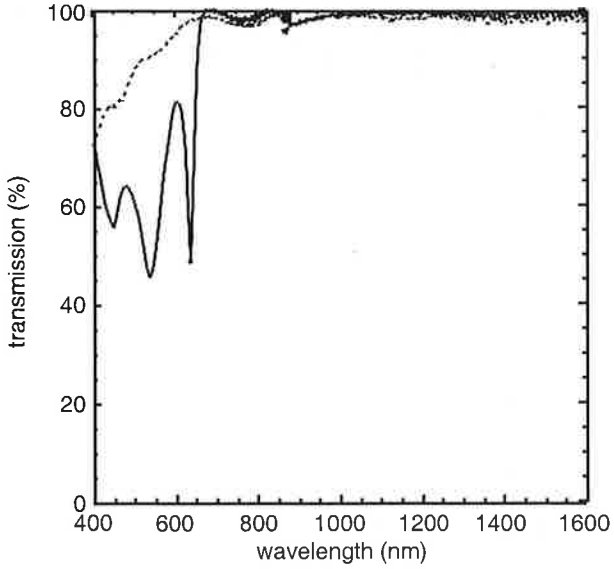

Fig. 2. Comparison of the transmission spectra through DuPont HRF-800X001-15 photopolymer film. Solid curve, before exposure; dashed curve, after polymerization.

Lasertechnics wavemeter with a resolution of 0.001 nm. The laser was tuned to $\lambda_0 = 590.0 \pm 0.1$ nm for all the exposures, and the beam was expanded, spatially filtered, and collimated. For all exposures, the power of the collimated beam was 1–2 mW/cm^2.

For these experiments we selected DuPont HRF-800X001-15 photopolymer film, which has a thickness of 15 μm. It has been determined that DuPont photopolymer has a shrinkage factor $S = 0.975 \pm 0.003$ and a preprocessed average index $n_f(632\text{ nm}) = 1.487 \pm 0.002$.[12] The DuPont HRF-800 × 001-15 photopolymer lies between two protective Mylar layers, one of which may be removed. We used an index-matching fluid of 1.67 to attach the Mylar–photopolymer sandwich to the prism. The thinner, removable layer of Mylar was attached to the prism.

To better understand the sensitivity of the DuPont photopolymer, we used a spectrophotometer to measure the transmission spectrum, before and after curing, over the range 400–1600 nm. These curves are shown in Fig. 2. As has been reported,[8] the photopolymer is absorptive (i.e., sensitive) to visible wavelengths; however, our curves show that it is essentially transparent (transmission greater than 95%) to infrared wavelengths of 1300–1600 nm. It is interesting to note that, over the visible spectrum, the photopolymer is most transparent (and thus least sensitive) to light near 590 nm, which is precisely the wavelength that we chose to use for our exposures. Although the lower sensitivity necessitates longer exposure times, it also means that the intensities of our interfering beams will be more nearly identical throughout the depth of the film, increasing the fringe contrast and better utilizing the available index modulation.

Exposures were made over a range of incident angles that varied from 0° to −10° (we used the sign convention shown in Fig. 1). Holograms were exposed until a fluence of 100 mJ/cm^2 within the film had been achieved. (This higher exposure energy was necessary because of the reduced film sensitivity at 590 nm.) In calculating the exposure times, which were of the order of 60 s, we took special care to account for Fresnel losses at the interfaces and the fall-off of power/area with the cosine of θ_f.

After exposure the thinner layer of Mylar was removed. A Kodak print roller was used to laminate the film, polymer side down, onto a float glass substrate, 1.7 mm thick. Following DuPont's instructions,[10] we cured the laminated plates, using broadband ultraviolet/white light, and then baked them for 2 h at 120 °C.

After cooling, the transmission spectra of the holograms were measured with a Perkin-Elmer spectrophotometer. Example spectra for four holograms are shown in Fig. 3.

One of our first interests was in characterizing the index dispersion of the DuPont HRF-800X001 photopolymer in the infrared range. Using our data and Eqs. (1)–(3), we calculated the average index of the photopolymer, n_f', as a function of replay wavelength λ. The results are plotted in Fig. 4. (The index modulation in the infrared, Δn, is described in Section 3 below.) We found no statistically significant variation in n_f' over the wavelength range 1300–1550 nm, implying that DuPont HRF-800X001 photopolymer has negligible index dispersion in the infrared range of interest. Disregarding data points beyond two standard deviations, we found the mean

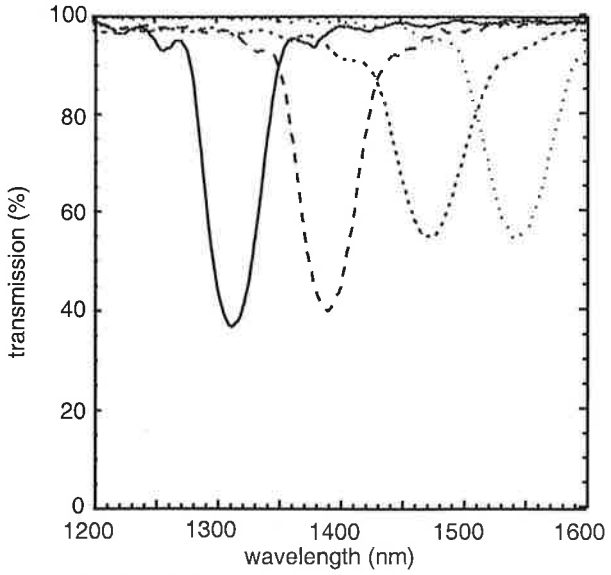

Fig. 3. Overlay of the transmission spectra of four holograms, showing reflection peaks at 1311, 1391, 1473, and 1541 nm.

value for n_f' to be 1.485 ± 0.005, as indicated by the dashed line in Fig. 4.

It became clear, over the course of our measurements, that one of the limiting factors in this experiment was the precision of the spectrophotometer. In most spectrophotometers (such as the Perkin-Elmer system used for these experiments) broadband radiation is filtered through a system of gratings to produce a beam of light with a wavelength that is tunable to a resolution of approximately 0.01 nm. This beam is then focused onto the surface of the test sample. The cone of the incident light can be as great as 10°. Such a beam is less than ideal for testing interference filters. There are two reasons

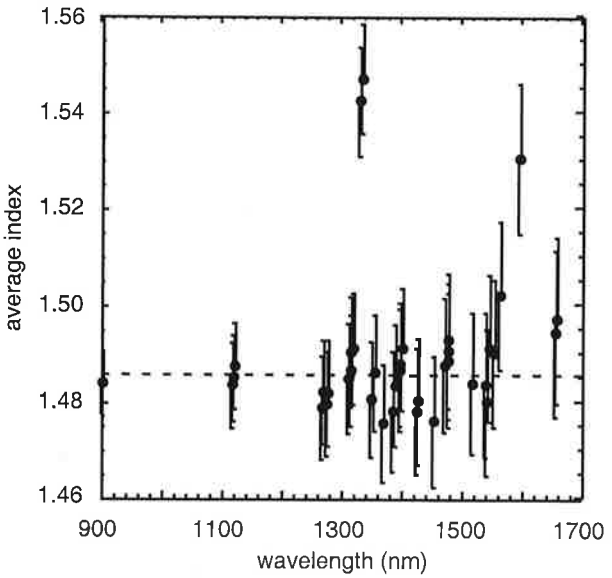

Fig. 4. Experimental data for the average index of refraction, n_f', of DuPont HRF-800X001 photopolymer after exposure and processing. Dashed line, mean value.

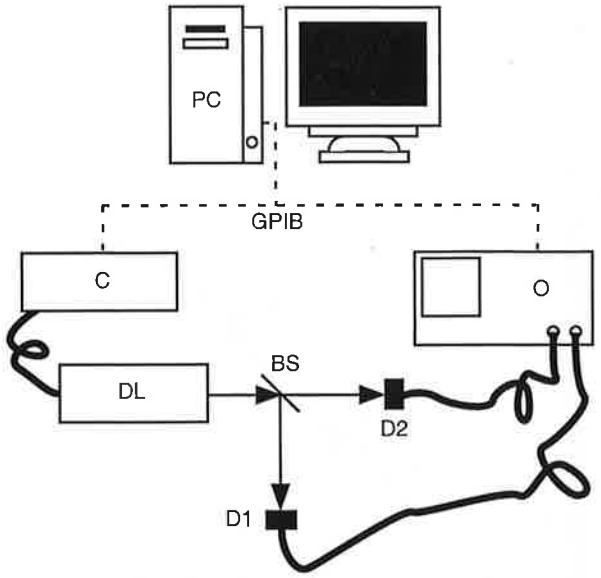

Fig. 5. Tunable infrared laser spectrophotometer system: C, controller for the diode laser; DL, tunable diode laser; BS, beam splitter; D1, D2, InGaAs photodetectors; O, digital oscilloscope; PC, digital computer with GPIB interface.

for this. First, because the test beam comes from a thermal source with limited coherence length, interference features may be missed if the filter is thicker than the coherence length of the test beam. Second, because the behavior of interference filters is, in general, highly angle dependent, illuminating an interference filter with a cone of light will cause the features of the reflection spectra to be broadened and slightly blueshifted. This broadening and shifting will obscure narrow features.

For these reasons we have developed a laser spectrophotometer system that features a coherent and collimated light source. This system is illustrated in Fig. 5. The light source is a tunable diode laser with a wavelength variable over the range 1469–1547 nm. The beam from the diode laser is split into two branches, a test arm and a reference arm. The intensity of the reference beam is measured by an InGaAs detector. The intensity of the test beam is measured by a second InGaAs detector after the beam first passes through the sample. The voltages from the two detectors are sent to a digital oscilloscope, which computes the ratio of the two signals. By recording this ratio as the laser wavelength is tuned, we trace the transmission through the sample as a function of wavelength. Finally, the transmission spectrum of the sample is normalized by the transmission spectrum of the test arm when the arm is empty. The system is calibrated with an acetylene absorption cell.[15]

3. Design Curves for Holographic Fabrication of Infrared Interference Filters

Having characterized the index of refraction, shrinkage, and sensitivity of the DuPont HRF-800X001 photopolymer, we were able to create design curves

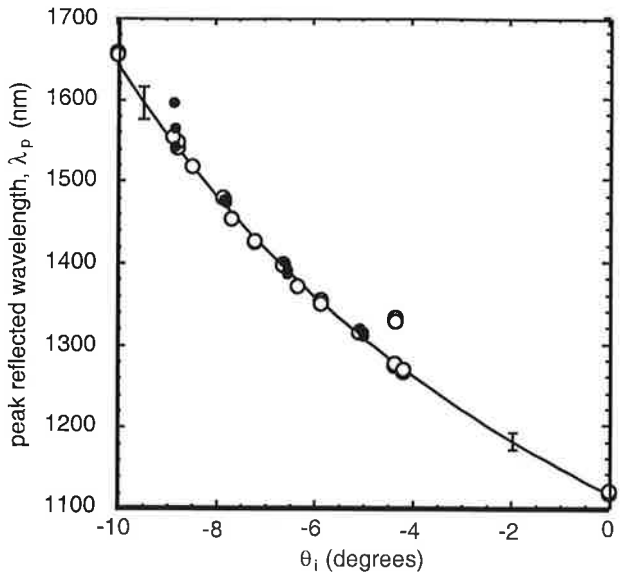

Fig. 6. Design curve relating exposure angle θ_i to peak reflected wavelength λ_p. Solid curve, plot of Eq. (4). The circles (filled and open) represent two sets of experimental data.

relating exposure angle θ_i to the resonant wavelength of the processed hologram, λ_p. The formula for this curve can be found by solution of Eqs. (1)–(3), with a reconstruction angle $\theta_f' = 0°$. The resulting relation is given by

$$\lambda = \lambda_0 S \frac{n_f'}{n_f}\left[1 - \frac{1}{2}\left(\frac{n_p}{n_f}\right)^2 + \frac{\sin\theta_i}{n_f^2} \times (n_p^2 - \sin^2\theta_i)^{1/2}\right]^{-1/2}. \quad (4)$$

A plot of this function is shown in Fig. 6. In evaluating this equation we used the average value of $n_f' = 1.485 \pm 0.005$, as described above. The plotted points represent the experimental data. The excellent agreement between the experimental data and the theoretical design curve demonstrates that our model is valid over the wavelength range indicated.

We then set out to construct design curves relating the efficiency and bandwidth of the filters to the thickness and index modulation of the film. In Subsection 3.A we explain the thin-film-decomposition technique in detail, and in Subsection 3.B we present the results of our calculations.

A. Thin-Film Decomposition

The central concept of thin-film decomposition is that an inhomogeneous multilayer film of arbitrary index profile $n(z)$ may be modeled as a stack of homogeneous layers. Within each layer the EM fields may be described as plane waves traveling through a material of constant index. By matching the boundary conditions between pairs of successive layers, one can ascertain the transmission and reflection properties of the film. One of the chief goals of this analysis is determination of the film transmission. These calculations are considerably streamlined by use of the chain-matrix formalism for multilayer films that was devised by Abeles.[22] As described in Section 1, the term "thin-film decomposition" was chosen in analogy to the nomenclature "thin grating decomposition."

In this paper we use the matrix notation found in Macleod's classic text, *Thin Film Optical Filters*.[23] Specifically, for a film layer of thickness d and index n upon a substrate with index n_s, the amplitudes of the electric and magnetic fields tangential to the air–film interface, a, and to the film–substrate interface, s, are related by the matrix equation

$$\begin{bmatrix} E_a \\ H_a \end{bmatrix} = \begin{bmatrix} \cos\delta & (i\sin\delta)/\eta \\ i\eta\sin\delta & \cos\delta \end{bmatrix}\begin{bmatrix} E_s \\ H_s \end{bmatrix}, \quad (5)$$

where δ is the phase thickness of the film and η is the optical admittance of the film. In general, δ and η are angle dependent, but for the special case of normal incidence they reduce to $\delta = 2\pi d/\lambda$, where λ is the wavelength of the incident light in vacuum and $\eta = n(\epsilon_0/\mu_0)^{1/2}$. Equation (5) is more useful when it is written in terms of indices of refraction rather than of electromagnetic fields. We can accomplish this transformation by noting that the substrate index, n_s, is given by the relation $n_s = (H_s/E_s)(\mu_0/\epsilon_0)^{1/2}$ and similarly by defining the effective index of the film–substrate composite as $n_a = (H_a/E_a)(\mu_0/\epsilon_0)^{1/2}$. Using these substitutions, we may write Eq. (5) as

$$\begin{bmatrix} B \\ C \end{bmatrix} = \begin{bmatrix} \cos\delta & (i\sin\delta)/n \\ in\sin\delta & \cos\delta \end{bmatrix}\begin{bmatrix} 1 \\ n_s \end{bmatrix}, \quad (6)$$

where $n_a = C/B$. The effective index of the film–substrate assembly, n_a, may then be used with the Fresnel relations to calculate the transmissivity and reflectivity of the film. It should be noted that, in general, n_a is complex and wavelength dependent. The matrix given in Eq. (6) is termed the characteristic matrix of the thin film and is denoted **M**. For a film consisting of more than one layer, one simply composes a characteristic matrix for each layer and then multiplies the matrices together to obtain a final matrix that is characteristic of the entire film.

For these calculations, we model the index within the film as a cosinusoidal variation given by the equation

$$n(z) = n_f' + \Delta n \cos\left(\frac{2\pi}{\Lambda} z\right), \quad (7)$$

where Δn represents the strength of the index modulation. In this case the index modulation is periodic, so the film can be divided into N identical cells (each one period thick) and a remainder. Once we have found the characteristic matrix for a single cell, we can find the characteristic matrix for the stack of N cells by self-multiplying the single cell matrix N times.

The first step in the decomposition process is to choose the thickness and the index for the homogeneous layers. Separate studies of the solution convergence were used to establish that $\Lambda/20$ is a

conservative choice for layer thickness and provides answers with accuracy surpassing the measurement capabilities of most spectrophotometers. We used the integrated average index of each slice of the inhomogeneous film as the index for the corresponding homogeneous layer. Once the index and the thickness of each layer have been determined, it is a simple matter to create the characteristic matrix for each layer by using Eq. (6). We find the characteristic matrices for the remainder and for a cell by multiplying the matrices of their constituent layers. As matrix multiplication is noncommutative, some care must be taken to multiply the matrices in the correct order; specifically, the matrix for the first illuminated layer is on the left, and all subsequent matrices follow on the right. To calculate the product of the identical characteristic matrices for the N cells, it is convenient to use an identity found in Born and Wolf's *Principles of Optics*.[24] Specifically, for a unimodular matrix $\mathbf{m}$, given by

$$\mathbf{m} = \begin{bmatrix} m_{11} & m_{12} \\ m_{21} & m_{22} \end{bmatrix}, \tag{8}$$

the Nth power of that matrix is

$$\mathbf{m}^N = \begin{bmatrix} m_{11}U_{N-1}(a) - U_{N-2}(a) & m_{12}U_{N-1}(a) \\ m_{21}U_{N-1}(a) & m_{22}U_{N-1}(a) - U_{N-2}(a) \end{bmatrix}, \tag{9}$$

where

$$a = \tfrac{1}{2}\,(m_{11} + m_{22}) \tag{10}$$

and U_N are the Chebyshev polynomials of the second kind:

$$U_N(a) = \frac{\sin[(N+1)\cos^{-1} a]}{(1-a)^{1/2}}. \tag{11}$$

By multiplying the characteristic matrix of the N cells by the characteristic matrix of the remainder, one ends up with a characteristic matrix that describes the entire film, denoted $\mathbf{M}_f$. Finally, one may find the effective index of the entire film–substrate assembly by plugging the characteristic matrix of the film, $\mathbf{M}_f$, into Eq. (6). The transmission through the film is given by the formula

$$T(\lambda) = \frac{4n_0\,\mathrm{Re}(n_s)}{(n_0B + C)(n_0B + C)^*}, \tag{12}$$

where n_0 is the index of the cover and the asterisk denotes the complex conjugate. For these calculations we assume that the cover and substrate indices are matched to the average index of the film (i.e., that $n_0 = n_s = n_f'$).

B. Design Curves for General Holographic Multilayers

As stated above, the purpose of carrying out these calculations has been to develop design curves to relate the efficiency and bandwidth of the holograms to the thickness and index modulation of the film. To this end, we used the thin-film-decomposition technique described above to compute the theoretical transmission spectra of a large ensemble of holograms. The index modulation, film thickness, and period were systematically varied in each of the calculations, and the spectra were evaluated to a precision of 1 nm over the range 1000–2000 nm. Afterward, the efficiencies and bandwidths of the spectra were measured, and the results analyzed.

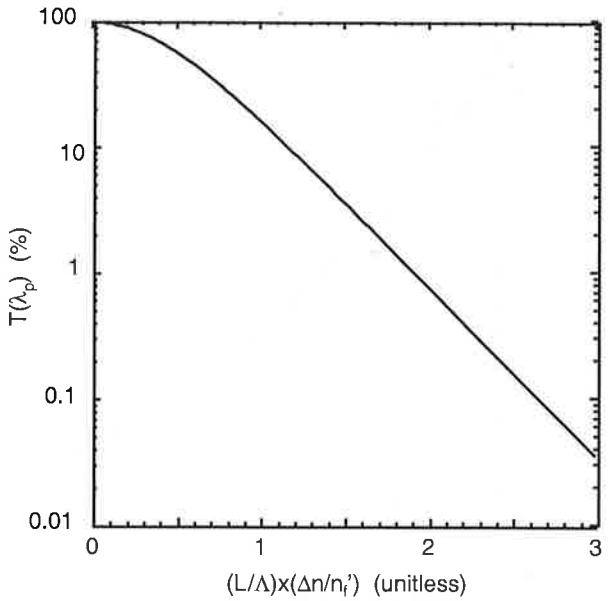

Fig. 7. Design curve plotting minimum transmission $T(\lambda_p)$ versus dimensionless parameter $(L/\Lambda) \times (\Delta n/n_f')$ for a cosinusoidal index variation. We calculated the curve by using thin-film decomposition.

Using the variable L to denote the thickness of the film, we found that, for holograms illuminated at optimal normal-incidence reconstruction wavelength λ_p, transmission efficiency $T(\lambda_p)$ decreased (i.e., reflection efficiency increased) in a smooth manner as a function of $(\Delta n/n_f') \times (L/\Lambda)$, as illustrated in Fig. 7. We observed that increasing either index modulation Δn or film thickness L has the same effect; that is, there can be a trade-off of index modulation for film thickness and vice versa.

We also created curves that revealed the interrelation between the FWHM bandwidth of the holographic multilayer, on the one hand, and the index modulation and film thickness, on the other, as shown in Fig. 8. For fixed thickness, bandwidth increases as index modulation increases. By contrast, for fixed index modulation, bandwidth decreases as thickness increases, seeming to approach an asymptotic limit dictated by the strength of the index modulation. These results demonstrate that film thickness and index modulation have different effects on the FWHM bandwidth of the hologram; that is, index modulation and film thickness cannot be traded for each other.

Using the design curve shown in Fig. 7, we deter-

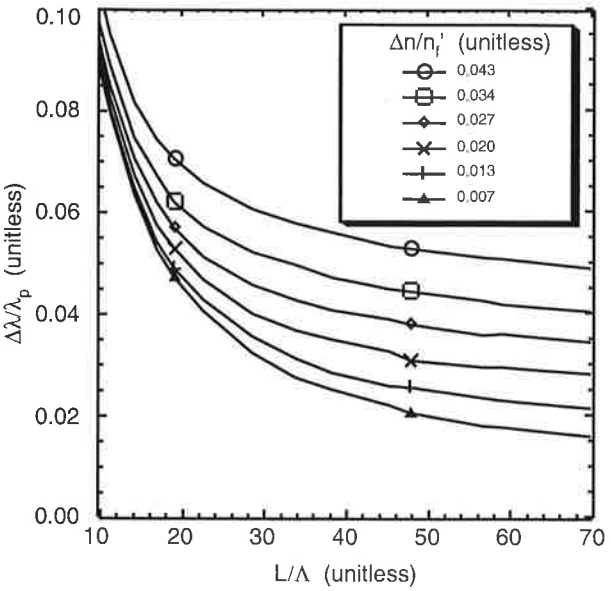

Fig. 8. Design curves for $\Delta\lambda/\lambda_p$ versus L/Λ, calculated by use of thin-film decomposition for a cosinusoidal index modulation and a range of index modulations characterized by $(\Delta n/n_f')$.

mined the size of the index modulation for the four example holograms whose transmission curves are shown in Fig. 3. The first hologram has a transmission minimum of 36.60% at 1311 nm; the second hologram has a transmission minimum of 39.57% at 1391 nm; the third hologram has a transmission minimum of 54.65% at 1473 nm; and the fourth hologram has a transmission minimum of 54.39% at 1541 nm. Using Fig. 7, we can see that these values correspond to values for $(\Delta n/n_f') \times (L/\Lambda)$ of $0.69\bar{8}$, $0.66\bar{6}$, $0.52\bar{7}$, and $0.52\bar{9}$, respectively. We know that the photopolymer has a final thickness (after shrinking) of $L = 14.625 \pm 0.045$ μm, and we can determine the period, Λ, by solving Eq. (2), given that $n_f' = 1.487 \pm 0.005$ and $\theta_f' = 0$ and that λ_p can be determined from the transmission spectrum of each hologram. Carrying out these calculations, we found the strength of the index modulation, Δn, for the four holograms to be 0.031, 0.032, 0.0265, and 0.028.

Conversely, the curves shown in Figs. 6–8 can be used in the design of a holographic filter. For example, if the desired replay wavelength, efficiency, and bandwidth are known, one can use Fig. 6 to determine the exposure angle and Figs. 7 and 8 to determine the proper thickness and index modulation for the hologram.

4. Summary

In this paper we have demonstrated a method for fabricating holographic interference filters for infrared applications by using a visible laser source and DuPont photopolymer film. The collimated laser illumination is coupled into the film at an oblique angle by use of a prism assembly, as illustrated in Fig. 1, and total internal reflection at the film–air interface creates the standing-wave interference pattern that is recorded within the film as index modulation.[2,3] By rotating the prism with respect to the incident beam, one can change the period of the final index modulation; thus the wavelength at which the hologram shows peak reflectivity at normal incidence will depend on the exposure angle. Figure 3 shows the transmission spectra for four such holograms, all recorded with the same exposure wavelength but each at a different exposure angle. With this exposure technique we created holograms with reflection peaks anywhere in the 1300–1600-nm range, by varying the exposure angle from 0° to −10°.

Using our experimental data, we determined that the index of refraction of the photopolymer in the near infrared is 1.485 ± 0.005. Combining this information with DuPont's published values for the index and shrinkage of the photopolymer at visible wavelengths,[12] we were able to generate a design curve that related the exposure angle to the peak reflection wavelength at normal incidence. The formula for this curve is given in Eq. (4), and the curve is traced in Fig. 6.

Finally, using thin-film decomposition, we have presented curves that relate the efficiency and bandwidth of the spectra to the thickness and index modulation of holograms with cosinusoidal index profiles as described in Eq. (7). These curves are shown in Figs. 7 and 8. Using these design curves, one may plan the exposure needed to create a holographic interference filter with a peak resonance at any desired wavelength, with any desired efficiency, and with any desired bandwidth. We stress that the thin-film-decomposition technique is valid for multilayer films of arbitrary index profile, not merely for periodic films.

We acknowledge the financial support of this project in part by the U.S. Army Research Office.

References

1. T. W. Stone and B. J. Thompson, eds., *Selected Papers on Holographic and Diffractive Lenses and Mirrors*, Vol. MS 34 of SPIE Milestones Series (SPIE Optical Engineering Press, Bellingham, Wash., 1991).
2. S. S. Duncan, J. A. McQuoid, and D. J. McCartney, "Holographic filters in dichromated gelatin position tuned over the near-infrared region," Opt. Eng. **24,** 781–785 (1985).
3. T. Stone, N. George, and B. D. Guenther, "Index variation and scattering in a holographic medium," in *Holographic Optics II: Principles and Applications*, G. M. Morris, ed., Proc. SPIE **1136,** 35–44 (1989).
4. R. Jacobsson, "Light reflection from films of continuously varying refractive index," in *Progress in Optics*, E. Wolf, ed. (North-Holland, Amsterdam, 1966), Vol. 5, Chap. 5, pp. 247–286.
5. D. H. Close, A. D. Jacobson, J. D. Margerum, R. G. Brault, and F. J. McClung, "Hologram recording on photopolymer materials," Appl. Phys. Lett. **14,** 159–160 (1969).
6. R. T. Ingwall and H. L. Fielding, "Hologram recording with a new photopolymer system," Opt. Eng. **24,** 808–811 (1985).
7. W. K. Smothers, T. J. Trout, A. M. Weber, and D. J. Mikish, "Hologram recording in DuPont's new photopolymer materials," in *Second International Conference on Holographic Systems, Components and Applications*, IEE Conf. Pub. **311,** 184–189 (1989).

8. J. L. Salter and M. F. Loeffler, "Comparison of dichromated gelatin and DuPont HRF-700 photopolymer as media for holographic notch filters," in *Computer and Optically Generated Holographic Optics*, I. Cindrich and S. H. Lee, eds., Proc. SPIE **1555,** 268–278 (1991).
9. L. T. Blair and L. Solymar, "Grating profiles in dichromated gelatin," Opt. Commun. **77,** 365–367 (1990).
10. T. J. Trout, W. J. Gambogi, and S. H. Stevenson, "Photopolymer materials for color holography," in *International Conference on Applications of Optical Holography*, T. Honda, ed., Proc. SPIE **2577,** 94–105 (1995).
11. K. W. Steijn, "Multicolor holographic recording in DuPont holographic recording film: determination of exposure conditions for color balance," in *Holographic Materials II*, T. J. Trout, ed., Proc. SPIE **2688,** 123–134 (1996).
12. S. H. Stevenson and K. W. Steijn, "A method for characterization of film thickness and refractive index in volume holographic materials," in *Holographic Materials*, T. J. Trout, ed., Proc. SPIE **2405,** 88–97 (1995).
13. H. J. Zhou, V. Morozov, and J. Neff, "Characterization of DuPont photopolymers in infrared light for free-space optical interconnects," Appl. Opt. **34,** 7457–7459 (1995).
14. A. Chen, Q. Gao, R. Fan, A. Harton, K. Wyatt, T. C. Felder, W. J. Gambogi, S. R. Mackara, K. W. Steijn, and T. J. Trout, "Enhanced reflective liquid crystal displays using DuPont holographic recording films," in *Holographic Materials IV*, T. J. Trout, ed., Proc. SPIE **3294,** 201–206 (1998).
15. K. Nakagawa, M. de Labachelerie, Y. Awaji, and M. Kourogi, "Accurate optical frequency atlas of the 1.5-μm bands of acetylene," J. Opt. Soc. Am. B **13,** 2708–2714 (1996).
16. M. G. Moharam and T. K. Gaylord, "Chain-matrix analysis of arbitrary-thickness dielectric reflection gratings," J. Opt. Soc. Am. **72,** 187–190 (1982).
17. X. Ning, "Analysis of multiplexed-reflection holographic gratings," J. Opt. Soc. Am. A **7,** 1436–1440 (1990).
18. R. Alferness, "Analysis of optical propagation in thick holographic gratings," Appl. Phys. **7,** 29–33 (1975).
19. R. Alferness, "Analysis of propagation at the second-order Bragg angle of a thick holographic grating," J. Opt. Soc. Am. **66,** 353–362 (1976).
20. T. W. Stone, "Holographic optical elements," Ph.D. dissertation (University of Rochester, Rochester, New York, 1986).
21. T. Stone and N. George, "Wavelength performance of holographic optical elements," Appl. Opt. **24,** 3797–3810 (1985).
22. P. F. Abeles, "Recherches sur la propagation des ondes électromagnétiques sinusoïdales dans le milieux stratifiés. Application aux couches minces," Ann. Phys. (Paris) **12,** 596–640, 706–784 (1950).
23. H. A. Macleod, *Thin-Film Optical Filters*, 2nd ed. (McGraw-Hill, New York, 1989).
24. M. Born and E. Wolf, *Principles of Optics: Electromagnetic Theory of Propagation, Interference and Diffraction of Light*, 7th ed. (Cambridge U. Press, Cambridge, 1999).

Extended Depth of Field With the Logarithmic Asphere

Wanli Chi and Nicholas George

Conventional camera lenses record pictures that are sharply focused at a specific distance set by the photographer. There is a certain range around this distance, known as the depth of field, for which the picture is fairly clear. Outside of this range, the picture is badly blurred. With smaller f/#, the depth of field is smaller.[1] Many investigators have sought to improve this situation, i.e., to obtain a greater depth of field at a given f/#. A noteworthy improvement is the cubic-phase mask reported by Dowski and Cathey, in which digital processing is used to improve a recorded picture that uses their novel lens and phase plate.[2]

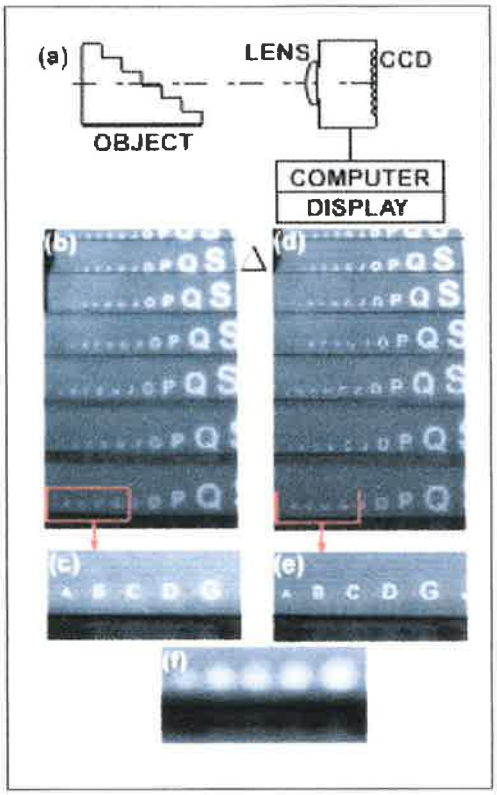

Figure 1. (a) Experimental setup for the integrated imaging and computer system; (b, c) experimental results using inverse-filter recovery; (d, e) maximum-entropy recovery; and (f) Nikon f/4 reference.

In our study of this basic problem, we sought a solution consisting of a circularly symmetric lens that has a radially varying focal length. This led us to a new class of lenses that we call "logarithmic aspheres."[3] At any range there is an annular ring that provides a sharp image while the remainder of the lens records a blur. Digital processing is then used to remove the blur. Figure 1 shows the setup with an object at 950 mm (Δ). Since the steps are 50 mm each, the closest step is at 700 mm. We see that excellent recovery is obtained using an image-plane form of the Weiner-Helstrom filter (b,c). Even better contrast and less ringing are obtained by use of maximum entropy processing (d,e). The depth of field is increased about tenfold. Impressively, too, the impulse response is theoretically diffraction limited. Moreover, one can simply insert a logarithmic phase plate in an existing camera lens and obtain the same improvement.

Two modern machines are employed in fabrication. One is the Model SX50 computer-controlled grinding machine manufactured by OptiPro Systems, Inc. The polishing and fine figuring is obtained using QED Technologies magnetorheological finishing machine. The lens is fabricated in an optical grade of quartz to an overall accuracy on the order of one-tenth wavelength.

Applications can be foreseen for imaging conditions where depth of field is an important issue; they include the single-use camera, the microscope, digital video and DVD pickup modules.

Acknowledgments

This research was supported in part by the Army Research Office.

References

1. R. Kingslake, *Optics in Photography*, SPIE Optical Engineering Press, Chapter 5.
2. E. R. Dowski and W. T. Cathey, Appl. Opt. **34**, 1859 (1995).
3. W. Chi and N. George, Opt. Lett. **26**, 875 (2001).

Wanli Chi and Nicholas George (ngeorge@troi.cc.rochester.edu) are with the Institute of Optics, University of Rochester, Rochester, New York.

Sampling, Demodulation and Phase Retrieval

Kedar Khare and Nicholas George

Phase retrieval is an important problem in optics. We have reported[1] an optimal and exact sampling procedure for phase measurement that is more efficient than the conventional Nyquist criterion. It is based on the Whittaker-Shannon theory but takes account of the carrier-frequency nature of fringe patterns. While it is clear from Shannon's work[2] that the space-bandwidth product controls the number of samples required, explicit formulas for efficient recovery of the envelope of a general FM/AM signal have not appeared in the literature. In our result we draw attention to direct coarse sampling of carrier-frequency signals. As an alternative to mixing, direct coarse sampling of both one- and two-dimensional carrier-frequency signals has many potential applications, e.g., in communications, holography, synthetic aperture radar and interferometry. The number of samples required is approximately reduced by the ratio $f_0/(2B_s)$, where f_0 is the carrier frequency and $2B_s$ is the bandwidth of the envelope.

Consider this sampling method for phase retrieval in the case of a two-beam hologram as illustrated below. An expanding spherical wave front was generated by slight axial offset of a beam expander and this was recorded with a plane reference beam incident at a small angle on a CCD detector. The interference pattern after subtracting the low frequency intensity terms (obtained by blocking one interfering beam at a time) is shown in Fig. 1(a). This pattern was sampled coarsely and interpolated according to our sampling formula. The resultant phase map is shown in Fig. 1(b). The fringe pattern has been sampled approximately once every two fringes rather than twice per fringe as expected from the Nyquist criterion. With our sampling procedure, we are also able to distinguish a convex wave front from a concave wave front.

The new sampling method described above provides a simple, exact and efficient alternative to existing phase retrieval techniques such as phase-shifting interferometry, adaptive optics, various iterative algorithms and holography.

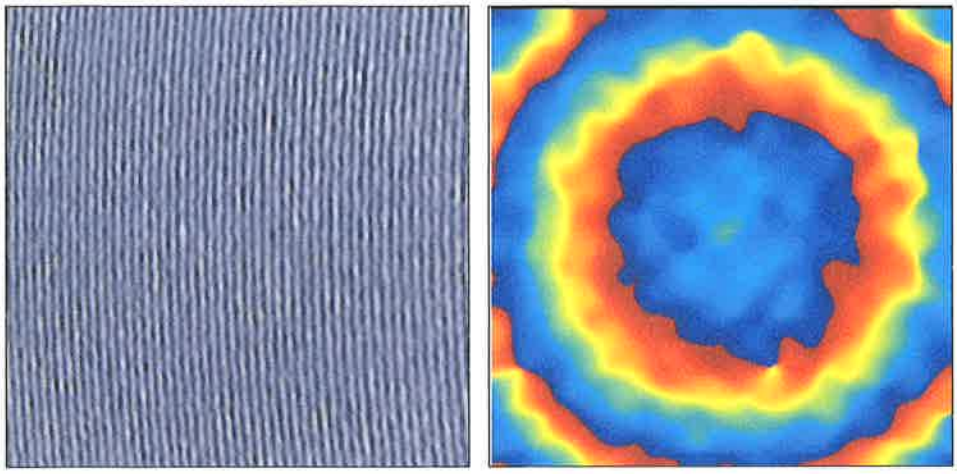

Figure 1. (a). Fringe pattern generated by interference of an expanding quadratic phase wave front with a plane reference beam at an angle. (b) Phase map obtained from the fringe pattern by use of our direct sampling formula.

References

1. K. Khare, N. George, Opt. Commun. **211**, 85-94 (2002).
2. C. E. Shannon, Communication in the presence of noise, Proc. IRE 37, 10 (1949).

Kedar Khare and Nicholas George (ngeorge@troi.cc.rochester.edu) are with the Institute of Optics, University of Rochester, Rochester, New York.

1004 OPTICS LETTERS / Vol. 28, No. 12 / June 15, 2003

Direct coarse sampling of electronic holograms

Kedar Khare and Nicholas George

The Institute of Optics, University of Rochester, Rochester, New York 14627

Received November 20, 2002

We describe a series of experiments in order to test a new sampling criterion for wavefront reconstruction from a carrier-frequency signal as obtained in electronic holography. Both a Fourier-transform configuration and a Fresnel-zone form of a digital holographic microscope are described. Direct coarse sampling of holograms with no phase-shifting elements can be used to obtain wavefront reconstruction, with the number of samples required reduced by the ratio $f_0/(2B_s)$, where f_0 is the carrier frequency and $2B_s$ is the signal bandwidth.

OCIS codes: 070.0070, 090.1760, 100.2650, 100.3010, 100.5070, 120.2650.

In electronic holography and interferometry it is often important to sample a fringe pattern. In a recent publication we showed theoretically that carrier-frequency fringe patterns can be efficiently coarsely sampled based on a modified form of the Whittaker–Shannon representation.[1] Herein we describe a series of experiments with which to test and verify these new expansions and to show that it is possible to reduce the number of samples required by approximately a ratio $f_0/(2B_s)$, where f_0 is the carrier frequency and $2B_s$ is the bandwidth of the complex envelope (signal).

Leith *et al.*[2,3] have successfully used electronic holography for time-gated and ensemble-averaged imaging through highly scattering media such as biological tissues.[2,3] Phase-shifting interferometry has also been used in optical metrology,[4] in three-dimensional imaging using wavelength diversity,[5] in three-dimensional data encryption,[6] and in color holography,[7] to name a few applications. The digital processing methods for reconstruction of holograms are typically either Fourier-transform based or employ phase-shifting techniques. In our approach we use direct coarse sampling of fringe patterns to obtain the complex envelope function. This is done in accordance with the fact that the information of interest in a hologram is contained in the complex envelope of the fringe pattern and not in the carrier. This approach to electronic holography does not require the use of Fourier transforms for the recovery of the complex field in the hologram plane; also, no phase-shifting elements are necessary.

We first state the sampling identity that we use later for the reconstruction of the complex field in the hologram plane.[1] In a two-beam holography setup, the object beam is approximately conical; the angular spectrum of waves at the hologram plane that subtends the object is centered about the normal. The reference beam is at an angle to the object beam and establishes the carrier frequency. The recorded hologram (apart from low-frequency intensity terms) may be described by a real-valued function:

$$g(x,y) = a(x,y)\exp(i2\pi f_0 x) + a^*(x,y)\exp(-i2\pi f_0 x). \tag{1}$$

Function $a(x,y)$ is the complex envelope of the fringe pattern, and f_0 denotes the carrier frequency, which is the reciprocal of the mean fringe period. Let the Fourier transform of envelope function $a(x,y)$ be nonzero only in a rectangular region of dimensions $2B_x \times 2B_y$ and be centered at the origin in the f_x–f_y plane. Then for $B_{x0} \geq B_x$ and $B_{y0} \geq B_y$ such that

$$\frac{f_0}{2B_{x0}} = N + \frac{1}{2}, \tag{2}$$

for a positive integer N,

$$g(x,y) = \sum_{m=-\infty}^{\infty}\sum_{n=-\infty}^{\infty} g\left(\frac{m}{4B_{x0}}, \frac{n}{2B_{y0}}\right) \times \operatorname{sinc}\left[2B_{x0}\left(x - \frac{m}{4B_{x0}}\right)\right] \operatorname{sinc}\left[2B_{y0}\left(y - \frac{n}{2B_{y0}}\right)\right] \times \cos\left[2\pi f_0\left(x - \frac{m}{4B_{x0}}\right)\right], \tag{3}$$

$$a(x,y) = \frac{1}{2}\sum_{m=-\infty}^{\infty}\sum_{n=-\infty}^{\infty} g\left(\frac{m}{4B_{x0}}, \frac{n}{2B_{y0}}\right) \times \operatorname{sinc}\left[2B_{x0}\left(x - \frac{m}{4B_{x0}}\right)\right] \operatorname{sinc}\left[2B_{y0}\left(y - \frac{n}{2B_{y0}}\right)\right] \times \exp\left(-i2\pi f_0 \frac{m}{4B_{x0}}\right). \tag{4}$$

For proofs of Eqs. (3) and (4) we refer the reader to Ref. 1.

Note that according to Eq. (2) the exponential term in Eq. (4) reduces to

$$\exp\left(-i2\pi f_0 \frac{m}{4B_{x0}}\right) = (-1)^{mN}(-i)^m, \tag{5}$$

so the alternate terms in each row of the sampling matrix contribute to the reconstruction of the real and the imaginary parts of $a(x,y)$, respectively. In Eqs. (3) and (4) the sampling rate is related to the bandwidth of envelope function $a(x,y)$ and not to carrier frequency f_0. The number of samples required is thus reduced significantly. We note that the

0146-9592/03/121004-03$15.00/0

Fourier-transform based processing or phase-shifting techniques commonly used in electronic holography are mathematically equivalent to the conventional mixing process in demodulation of carrier-frequency signals. In our sampling method this mixing step is replaced in principle by direct coarse sampling and interpolation. The sampling gain is obtained in the direction normal to the carrier fringes and approximately equals the ratio of the carrier frequency to the bandwidth of the envelope function.

The experimental setup consists of the Mach–Zehnder interferometer as shown in Fig. 1. For the hologram, the wave front from object O propagates to plane H and is subsequently imaged to the CCD array at C. Lens L (focal length, 20 cm) is optional, so one may use either a Fourier-transform configuration or a Fresnel-zone configuration. A suitable carrier frequency is introduced by a rotation of the mirror M_2 in the reference arm of the interferometer. The hologram in plane H is imaged onto a CCD detector in plane C by a telescopic imaging system with a magnification $f_2/f_1 = 5.5$. The sampling identity [Eq. (4)] requires a coarse sampling ratio; however, each sample must be sharp compared to the mean fringe period. In the experimental setup it is convenient to have a magnification system to make sure that the mean fringe period is approximately equal to 7 or 8 pixels on the CCD detection (pixel size, 20 μm square). A pixel value is then used as an individual sample, and the blurring caused by the integration of intensity over a pixel dimension is ignored. The magnification system introduces an unimportant scale factor between planes H and C that we omit in the further analysis. Complex object field $a(x, y)$ in the detector plane may be expressed in terms of object function $a_{\mathrm{obj}}(x', y')$ in plane O as

$$a(x,y) = \frac{i\exp(-i4\pi f/\lambda)}{\lambda f}\int_{-\infty}^{\infty}\int_{-\infty}^{\infty} dx'dy' a_{\mathrm{obj}}(x',y') \times \exp\left[i2\pi\left(\frac{xx'+yy'}{\lambda f}\right)\right] \quad (6)$$

when lens L is present and as

$$a(x,y) = \frac{i\exp(-i2\pi z/\lambda)}{\lambda z}\int_{-\infty}^{\infty}\int_{-\infty}^{\infty} dx'dy' a_{\mathrm{obj}}(x',y') \times \exp\left\{\frac{-i\pi}{\lambda z}[(x-x')^2+(y-y')^2]\right\} \quad (7)$$

when lens L is absent. In Eqs. (6) and (7), λ, f, and z denote the wavelength of the laser illumination, the focal length of lens L, and the distance between the object and the hologram plane, respectively. The intensity pattern recorded by the detector can be expressed as

$$I(x,y) = |a(x,y) + \exp(-i2\pi f_0 x)|^2 = 1 + |a(x,y)|^2 + a(x,y)\exp(i2\pi f_0 x) + a^*(x,y) \times \exp(-i2\pi f_0 x). \quad (8)$$

We measured the first two terms separately by blocking one arm of the interferometer. Then we substract them from $I(x, y)$ to obtain a carrier frequency signal as in Eq. (1). The sampling identity [Eq. (4)] is used for reconstruction of envelope function $a(x, y)$. Note that throughout the experiment one uses only a sparse array of pixel values as determined by the sampling identity [Eq. (4)].

We describe three experiments in wavefront recovery that use direct coarse sampling. In one we use a Fourier-transform configuration (Fig. 2) and in the second we use a Fresnel-zone configuration (Fig. 3). In the third we describe the performance of the recovery for undersampling and oversampling. In the experiment illustrated in Fig. 2, the three-pinhole object (500-μm-diameter pinholes, 2.5-mm

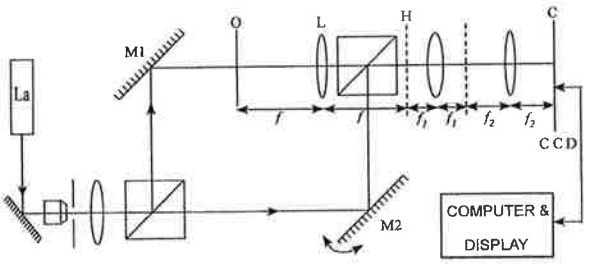

Fig. 1. Experimental setup: La, laser; M1, M2, mirrors; $f_2/f_1 = 5.5$; other abbreviations defined in text.

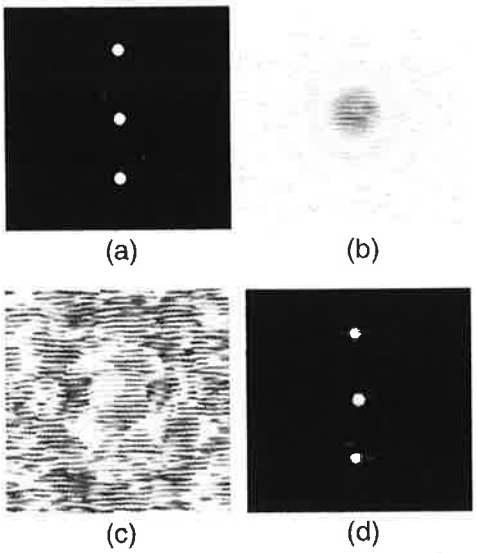

Fig. 2. Fourier-transform configuration: (a) object (three pinholes, 500-μm diameter), (b) amplitude (log scale) of the Fourier transform, (c) phase of the Fourier transform, (d) reconstruction of object by inverse Fourier transform.

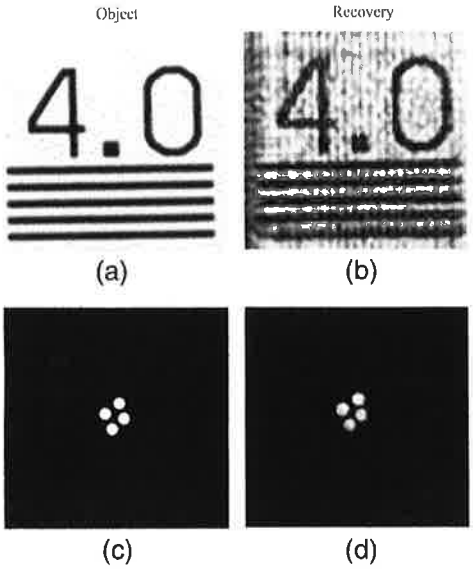

Fig. 3. Fresnel-zone configuration: (a) resolution chart, 4-line/mm object; (b) recovery; (c) four-pinhole object; (d) recovery by inverse Fresnel calculation.

center-to-center spacing) shown in Fig. 2(a) is used. Figures 2(b) and 2(c) show the recovered amplitude (in log scale) and phase of the Fourier transform of the object as calculated by the sampling formula. An inverse Fourier transform of the recovered complex field gives the reconstruction of the object as shown in Fig. 2(d). The illustration in Fig. 3 shows wave-front reconstruction in a lensless configuration. We remark that this configuration can be characterized as a digital holographic microscope. For objects, we used a part of a standard resolution chart as shown in Fig. 3(a) and four 500-μm-diameter pinholes arranged as shown in Fig. 3(c). The number 4.0 in Fig. 3(a) indicates a target with details of 4 lines pairs/mm. Holograms of these objects were sampled coarsely and interpolated to recover the field in the detector plane. An inverse Fresnel calculation was performed, and the recovered objects are shown in Figs. 3(b) and 3(d). A sampling gain of 3.5 over the conventional Nyquist rate was obtained in all the illustrations above. For a mean fringe period of 8 pixels, this sampling gain corresponds to looking at approximately every 15 pixel in a row of the recorded CCD image. As mentioned above, there is no sampling gain in the direction of the carrier fringes because the spectrum is centered at the zero frequency in the y direction. From the theory and experiments, it is clear that the direct sampling procedure described above provides an efficient compression algorithm for digital storage and transmission of holograms. We anticipate that this minimal sampling criterion will be widely used to compress digitally stored data.

As described above, when the spacing between samples is 15 pixels, set by Eq. (2), we have an excellent recovery. In the third experiment, for oversampling, we successively combined 14 separate reconstructions so we could see the quality of the recovery. We obtained the separate reconstructions by using pixels (1, 15, ...) for frame 1, then pixels (2, 16, ...) for frame 2, and so on. The quality was substantially unchanged from the results in Figs. 3(b) and 3(d). Presumably, in this experiment, if noise were added, the separate reconstructions would combine to give a better image quality. For undersampling using the same data, we found numerous artifacts in the recovery, e.g., for sampling at half the pixel spacing set by Eq. (2). Both of these results were as expected in accordance with the theory.

In summary, we have demonstrated a new sampling criterion that provides a simple, exact, and efficient alternative to the existing wavefront reconstruction techniques such as phase-shifting interferometry, adaptive optics, and holography.

This research was supported in part by the U.S. Army Research Office. N. George's e-mail address is ngeorge@troi.cc.rochester.edu.

References

1. K. Khare and N. George, Opt. Commun. **211,** 85 (2002).
2. E. Leith, H. Chen, Y. Chen, D. Dilworth, J. Lopez, R. Masri, J. Rudd, and J. Valdmanis, Proc. SPIE **1600,** 172 (1991).
3. E. Leith, P. Naulleau, and D. Dilworth, Opt. Lett. **21,** 1691 (1996).
4. M. Servin and M. Kujawinska, in *Handbook of Optical Engineering*, D. Malacara and B. J. Thompson, eds. (Marcel Dekker, New York, 2001).
5. J. C. Marron and T. J. Schulz, Opt. Lett. **17,** 285 (1992).
6. E. Tajahuerce and B. Javidi, Appl. Opt. **39,** 6595 (2000).
7. I. Yamaguchi, T. Matsumura, and J. Kato, Opt. Lett. **27,** 1108 (2002).

J. Opt. A: Pure Appl. Opt. **5** (2003) S157–S163 PII: S1464-4258(03)57412-8

Extended depth of field using a logarithmic asphere

Nicholas George and Wanli Chi

The Institute of Optics, University of Rochester, Rochester, NY 14627, USA

E-mail: ngeorge@troi.cc.rochester.edu

Received 5 December 2002, accepted for publication 27 February 2003
Published 22 August 2003
Online at stacks.iop.org/JOptA/5/S157

Abstract

Imaging systems are described which use a logarithmic asphere and image processing in order to increase the depth of field substantially beyond classical limits. A nonparaxial form of the diffraction theory integral for an impulse response is derived and evaluated in order to establish a precise expression for the transmission function of this asphere. This nonparaxial physical optics formulation provides results of fractional wavelength accuracy that enable one immediately to complete the design and fabrication of the optical system. Circularly symmetric aspherical lenses, either for single-lens cameras or blurring phase filters for use with commercial photographic lenses, have been fabricated using advanced grinding and finishing machines. Computer simulation studies are presented to show that a logarithmic asphere is capable of diffraction-limited performance over an extended depth of field. Experimental imaging results including digital processing by an inverse filter show a tenfold increase in the depth of field.

Keywords: Depth of field, imaging system, digital enhancement, lens, logarithmic asphere, nonparaxial diffraction

1. Introduction

Novel systems for extending the depth of field of imaging systems have been described in the literature [1–3]. The basic concept for these new systems is to extend the depth of field by computer processing of purposefully blurred images. If one is to find a single digital processing step that will work over a wide range of object distances, an integrated consideration of image acquisition and image processing is clearly necessary. It is agreed that the resolution and depth of field, two important features of an imaging system, cannot be improved arbitrarily over classical and well-understood limits by redesigning the imaging lens alone. Briefly, classical limitations state that the resolution is proportional to the numerical aperture of the lens and the depth of field is inversely proportional to the square of the numerical aperture [4]. In an earlier publication [3], we used Fermat's principle to derive a transmission function for a circularly symmetric asphere that will image a continuum of points along an optical axis to a single image point as the object distances range from s_1 to s_2 (α-design).

In this paper we provide a comprehensive theoretical foundation for this class of lenses which we call logarithmic aspheres. A precise formulation for the transmission function of this lens is obtained by writing the diffraction integrals for the linear optical system using exact distance expressions, say from the object plane to the input plane of the lens, and so on. Writing formulae for physical optics in this nonparaxial form enables the designer immediately to translate results into lens specifications that are of fractional wavelength accuracy. Also, in an appendix, we provide an expression for the transmission function of an 'ideal lens', i.e. one that images a single point-source object into a single diffraction-limited spot. This is interesting as an exercise in generalized Fourier optics; and it is directly helpful in separating our overall transmission function into a product of two terms: one for the blur function and another for the 'ideal' imaging. An important aspect of this separation is that it provides the transmission function for a blur filter which can be used in cascade with a commercial imaging lens.

In section 2.2 we use a stationary-phase evaluation of the integral for the impulse response of the lens. Recognizing that this is equivalent to an application of Fermat's principle, we obtain a differential equation for the transmission function of the asphere. After simplification, it is reduced to Bernoulli's

Table 1. Phase delays for the logarithmic asphere, $\Phi(\rho)$.

Ideal lens	$-\frac{2\pi}{\lambda}\left(\sqrt{s^2+\rho^2}+\sqrt{t^2+\rho^2}-s-t\right)+\Phi_F(0)$
α [3]	$-\left\{\frac{2\pi}{\lambda}\left(\sqrt{\rho^2+t^2}-t\right)+\frac{\pi}{\lambda}\frac{R^2}{s_2-s_1}\left[\ln\left\{2\frac{s_2-s_1}{R^2}\left[\sqrt{\rho^2+\left(s_1+\frac{s_2-s_1}{R^2}\rho^2\right)^2}+\left(s_1+\frac{s_2-s_1}{R^2}\rho^2\right)\right]+1\right\}-\ln\left(4\frac{s_2-s_1}{R^2}s_1+1\right)\right]\right\}+\Phi(0)$
α_m	$-\frac{2\pi}{\lambda}\left(\sqrt{t^2+\rho^2}-t\right)+\frac{1}{a_m A_m}\{\mathrm{li}(A_m t^2)-\mathrm{li}[A_m(t^2+\rho^2)]\}+\Phi(0)$
β	$-\frac{2\pi}{\lambda}\left(\sqrt{t^2+\rho^2}-t\right)+\frac{a_\beta(t^2+\rho^2)}{2}\ln\left[\frac{A_\beta}{e}(t^2+\rho^2)\right]-\frac{a_\beta t^2}{2}\ln\left[\frac{A_\beta}{e}t^2\right]+\Phi(0)$
γ	$-\frac{2\pi}{\lambda}\left(\sqrt{t^2+\rho^2}-t\right)-\frac{a_\gamma(t^2+\rho^2)}{2}\ln\left[\frac{A_\gamma}{e}(t^2+\rho^2)\right]+\frac{a_\gamma t^2}{2}\ln\left[\frac{A_\gamma}{e}t^2\right]+\Phi(0)$

$a_m=\frac{\lambda}{\pi}\frac{\sqrt{s_2^2+R^2}-s_1}{\ln(1+R^2/t^2)}$, $A_m=\frac{1}{t^2}\exp\left[\frac{s_1\ln(1+R^2/t^2)}{\sqrt{s_2^2+R^2}-s_1}\right]$, $\mathrm{li}(z)=\int_0^z\frac{\mathrm{d}u}{\ln u}$.

equation and we write three solutions, seen in table 1. In two of the solutions we assert the choice of a lens that will provide natural illumination, i.e. the image of a bright object point falls off inversely as the distance squared. We associate the intensity resulting from the stationary-phase evaluation as that which leads to the sharply focused object point. In section 3 we evaluate the intensity point spread functions precisely using a digital computer; and it is pointed out that the logarithmic asphere provides diffraction-limited images, i.e. an impulse response with the first zero somewhat inside that of the corresponding Airy disc. In section 4 we present comparative images using a Nikon lens and also our single-element logarithmic asphere. The images are of a picture of a tiger both in focus and at a displaced distance which is ten times the pixel-limited depth of field. These illustrations are in figures 8–10; and we see greatly improved imagery well outside of the conventional depth of field.

2. Diffraction theory for the asphere

In figure 1 we show a point source in the plane S imaged by the lens in plane I to plane II. From standard scalar diffraction theory, one can write the scalar amplitude $V_1(\rho,\phi)$ in plane I due to on-axis point source of amplitude V_0 as follows:

$$V_1(\rho,\phi)=V_0\frac{\exp\left(-\mathrm{i}\frac{2\pi}{\lambda}\sqrt{s^2+\rho^2}\right)}{\sqrt{s^2+\rho^2}}, \tag{1}$$

in which λ is the wavelength, s is the distance from S to I, and (ρ,ϕ) are transverse plane cylindrical coordinates in plane II.

For a lens with a phase delay $\Phi(\rho,\phi)$ using a harmonic time dependence $\exp(\mathrm{i}\omega t)$, we write a generalized transmission function for the lens, denoted by $T(\rho,\phi)$, as

$$T(\rho,\phi)=\exp[-\mathrm{i}\Phi(\rho,\phi)]. \tag{2}$$

The scalar field in plane II (ρ_2,ϕ_2) can be written from equations (1) and (2) in the following form:

$$V_2(\rho_2,\phi_2)=\int_0^R\rho\,\mathrm{d}\rho\int_0^{2\pi}\mathrm{d}\phi\frac{V_0}{r_{12}\sqrt{s^2+\rho^2}}\times\exp\left(-\mathrm{i}\left[\frac{2\pi}{\lambda}\left(\sqrt{s^2+\rho^2}+r_{12}\right)+\Phi(\rho,\phi)\right]\right), \tag{3}$$

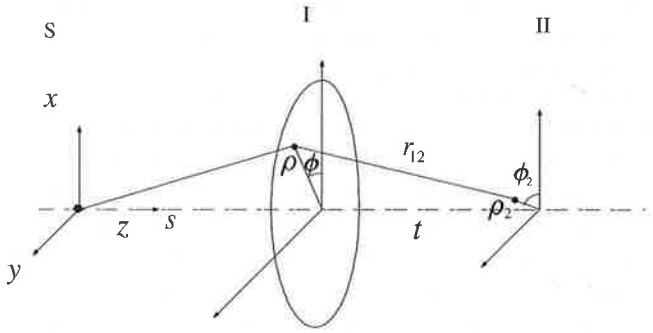

Figure 1. Sketch of nonparaxial diffraction theory.

in which the distance between planes I and II, r_{12}, is given by

$$r_{12}=[t^2+\rho^2+\rho_2^2-2\rho\rho_2\cos(\phi-\phi_2)]^{1/2}. \tag{4}$$

For the problem described herein, we confine our attention to circularly symmetric lenses. Two basic forms can be written from equations (3) and (4). First, for the circularly symmetric general case which is used in later computer calculations of the impulse responses, we write

$$V_2(\rho_2)=V_0\int_0^R\int_0^{2\pi}\mathrm{d}\phi\frac{\rho\,\mathrm{d}\rho}{\sqrt{s^2+\rho^2}}\times\exp\left(-\mathrm{i}\left[\frac{2\pi}{\lambda}\left(\sqrt{s^2+\rho^2}+r_{12}\right)+\Phi(\rho)\right]\right)\times\frac{\exp\left(-\mathrm{i}\frac{2\pi}{\lambda}r_{12}\right)}{r_{12}}. \tag{5}$$

For impulse response calculations with ρ_2 small, we can approximate r_{12} and integrate over ϕ in order to obtain the following useful expression:

$$V_2(\rho_2)=2\pi V_0\int_0^R\mathrm{d}\rho\frac{\rho}{\sqrt{t^2+\rho^2+\rho_2^2}\sqrt{s^2+\rho^2}}\times J_0\left(\frac{2\pi}{\lambda}\frac{\rho_2\rho}{\sqrt{t^2+\rho^2+\rho_2^2}}\right)\exp\left(-\mathrm{i}\left[\frac{2\pi}{\lambda}\left(\sqrt{s^2+\rho^2}+\sqrt{t^2+\rho^2+\rho_2^2}\right)+\Phi(\rho)\right]\right). \tag{6}$$

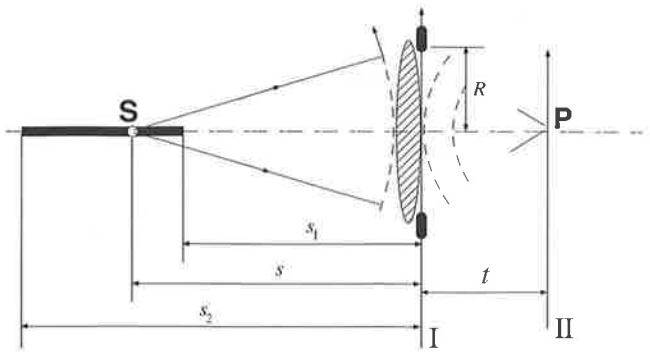

Figure 2. The notation for an extended depth of field lens.

2.1. Phase delay for a logarithmic asphere

Figure 2 shows the notation for the description of the lens transmission function $T(\rho)$ which will lead to an extended depth of field. The analysis involves computing the imaging of axial points s in the range from s_1 to s_2 in plane II at a distance t. From equation (6), we can write the on-axis intensity by taking the squared modulus of $V_2(0)$. Hence, the intensity $I(0; s)$ is written as:

$$I(0;s) = \left|2\pi \int_0^R \mathrm{d}\rho \frac{\rho}{\sqrt{s^2+\rho^2}\sqrt{t^2+\rho^2}} \times \exp\left(-\mathrm{i}\left[\frac{2\pi}{\lambda}\left(\sqrt{s^2+\rho^2}+\sqrt{t^2+\rho^2}\right)+\Phi(\rho)\right]\right)\right|^2, \quad (7)$$

in which ρ is the radial coordinate in the lens plane.

Equation (7) can be rewritten as

$$I(0;s) = \frac{4\pi^2}{s^2}\left|\int_0^R \frac{\rho}{\sqrt{t^2+\rho^2}} \times \exp\left(-\mathrm{i}\left[\Phi_P(\rho)+\frac{2\pi}{\lambda}\sqrt{s^2+\rho^2}\right]\right)\mathrm{d}\rho\right|^2, \quad (8)$$

in which we have defined $\Phi_P(\rho)$ by the following

$$\Phi_P(\rho) \triangleq \Phi(\rho) + \frac{2\pi}{\lambda}\sqrt{t^2+\rho^2}. \quad (9)$$

This keeps the exact non-paraxial phase term in the exponential. However, in the amplitude term we have made the approximation that $\sqrt{s^2+\rho^2}$ is approximated by s. Also in the camera application $s \gg R$, where R is the radius of the lens aperture.

The diffraction integral in equation (8) is evaluated by the method of stationary phase, i.e. we set the derivative of the entire phase term equal to zero. This yields the following identity for the stationary point r_0:

$$-\frac{\lambda}{2\pi}\Phi'_P(\rho_0) = \frac{\rho_0}{\sqrt{s^2+\rho_0^2}}, \quad (10)$$

in which Φ'_P denotes the derivative with respect to ρ. It is interesting to note that the stationary point expression in equation (10) is the same as the expression of Fermat's principle. In the following derivations, we use the stationary phase evaluation method to find the phase delay of the lens, but equally we can find out the correct relation of s as function of ρ_0, then solve equation (10) to derive the phase delay of the lens. While we omit the derivations using this method, we comment that the difference between the solutions of these two methods is small.

As is well known, the approximate value of equation (8) can be evaluated at the stationary point and the result is given by

$$I(0;s) \approx \frac{4\pi^2}{s^2}\frac{\lambda\rho_0^2}{\left|\frac{\lambda}{2\pi}\Phi''_P(\rho_0)+(s^2+\rho_0^2)^{-1/2}-\rho_0^2(s^2+\rho_0^2)^{-3/2}\right|} \times \frac{1}{t^2+\rho_0^2}, \quad (11)$$

in which Φ''_P denotes the second derivative of Φ_P.

Equations (10) and (11) are combined to yield the resulting form:

$$I(0;s) \approx \frac{4\pi^2}{s^2}\frac{2\pi\rho_0^2}{\left|\Phi''_P(\rho_0)-\Phi'_P(\rho_0)/\rho_0+\frac{\lambda^2}{4\pi^2}[\Phi'_P(\rho_0)]^3/\rho_0\right|} \times \frac{1}{t^2+\rho_0^2}. \quad (12)$$

In equation (12) we can independently specify the image brightness for an object point at various distances s. Clearly, the natural choice for this on-axis intensity is an inverse square dependence such that $I(0; s)s^2$ is a constant. For convenience, we define the constant (a) such that

$$I(0;s)s^2 = 4\pi^3/a. \quad (13)$$

Substitution of equation (13) into (12) gives us the basic differential equation for the phase function $\Phi_P(\rho_0, \phi)$ in equation (9), namely

$$(t^2+\rho_0^2)\left|\Phi''_P(\rho_0)-\Phi'_P(\rho_0)/\rho_0+\frac{\lambda^2}{4\pi^2}[\Phi'_P(\rho_0)]^3/\rho_0\right| = 2a\rho_0^2. \quad (14)$$

Since equation (14) is valid for object points s within the design range from s_1 to s_2 and since s and the stationary radius value ρ_0 are related by equation (10), we can rewrite equation (14) changing the notation ρ_0 to ρ for clarity in the solution of the differential equation. Additionally noting that the term

$$\left|\frac{\lambda^2}{4\pi^2}\frac{[\Phi'_P(\rho)]^3}{\rho}\right| \ll \left|\frac{\Phi'_P(\rho)}{\rho}\right|, \quad (15)$$

we can drop the third member of equation (14). Hence, by equation (14), we can write the following result for the phase function $\Phi_P(\rho)$, namely

$$|\Phi''_P(\rho)-\Phi'_P(\rho)/\rho| = \frac{2a\rho^2}{t^2+\rho^2}. \quad (16)$$

Since by equation (13) the term (a) is positive, these are two separate cases for equation (16). First, for case (i), assume that $\Phi''_P(\rho)-\Phi'_P(\rho)/\rho > 0$, and equation (16) becomes the Bernoulli equation, namely

$$\Phi''_P(\rho) - \frac{\Phi'_P(\rho)}{\rho} - \frac{2a\rho^2}{t^2+\rho^2} = 0. \quad (17)$$

The solution is readily written as

$$\Phi_P(\rho) = \frac{a(t^2+\rho^2)}{2}\ln\left[\frac{A}{e}(t^2+\rho^2)\right] \quad (18)$$

in which we have dropped an arbitrary constant and $e = 2.718\,28\ldots$. In order to evaluate the constant A, we substitute equation (18) into (10) and find the following result:

$$\frac{1}{\sqrt{s^2+\rho_0^2}} = -\frac{\lambda}{2\pi} a \ln[A(t^2+\rho_0^2)]. \tag{19}$$

In the design of the lens, we let the stationary point ρ_0 vary from 0 to R as the object distance varies from the near point s_1 to the outer point s_2, as in figure 2. Substitution of these values into equation (19) yields the following solutions for the constants a_β and A_β:

$$a_\beta = \frac{2\pi}{\lambda} \frac{\sqrt{s_2^2+R^2}/s_1 - 1}{\sqrt{s_2^2+R^2}\ln(1+R^2/t^2)} \tag{20}$$

$$A_\beta = \frac{1}{t^2}\exp\left[-\frac{\sqrt{s_2^2+R^2}}{\sqrt{s_2^2+R^2}-s_1}\ln(1+R^2/t^2)\right]. \tag{21}$$

For case (i) we denote this as the β-design. Therefore, in equations (20) and (21) we have used the notation a_β and A_β to distinguish this design from other cases. In the stationary phase evaluation of equation (8), the same phase terms are involved from the object point through the lens to the image as one uses in the application of Fermat's principle [3]. This equivalence of the stationary phase evaluation with Fermat's principle is reasonable since Fermat's principle can be derived from Maxwell's equations. Hence, it is clear that the stationary phase point ρ_0 (an annular ring at the lens) is the region of the lens that will make a sharp image for the corresponding object distance s. This physical description is also consistent with the definition of a local focal length for the lens that varies radially.

For case (ii) assume that $\Phi_P''(\rho) - \Phi_P'(\rho)/\rho < 0$. Using the same steps as before, one can immediately write the following results:

$$\Phi_P(\rho) = -\frac{a_\gamma(t^2+\rho^2)}{2}\ln\left[\frac{A_\gamma}{e}(t^2+\rho^2)\right] \tag{22}$$

where

$$a_\gamma = \frac{2\pi}{\lambda}\frac{1-\sqrt{s_1^2+R^2}/s_2}{\sqrt{s_1^2+R^2}\ln(1+R^2/t^2)} \tag{23}$$

$$A_\gamma = \frac{1}{t^2}\exp\left[\frac{\sqrt{s_1^2+R^2}}{s_2-\sqrt{s_1^2+R^2}}\ln(1+R^2/t^2)\right]. \tag{24}$$

Expressions (18), (20), (21) and expressions (22)–(24) together with equation (9) form two separate sets of solutions for the phase delay function of the lens for extended depth of field imaging. The phase delay of the lens is expressed as a logarithmic function, hence we call this lens a logarithmic asphere.

2.2. Logarithmic asphere designs

The main results of section 2.1 are summarized in table 1 and figure 3, in which case (i) is the β-design and case (ii) is the γ-design. The curves in figure 3 are obtained by plotting s versus ρ_0 from equation (19) using the appropriate values for the constants a and A. In the first publication on logarithmic aspheres, the design criterion was to keep the intensity $I(0; s)$ constant over the range from s_1 to s_2 [3], and this is shown as the curve labelled α in figure 3. In table 1, we show an α_m design which also provides a uniform intensity, but the design procedure follows that used in section 2.1 of this paper. While we omit the details of this derivation, it is noted that the differences are slight enough so that the curves cannot be distinguished at the scale of the plot. The lack of difference in α and α_m design curves implies that although the stationary phase method depends on the rapid oscillations of the integral away from the stationary point to justify the approximation, the result is nonetheless compatible with the Fermat's principle approach.

For an ideal lens that is designed to image an object point at s to an image point at t, as is shown in appendix, the phase function $\Phi_f(\rho)$ is given by

$$\Phi_F(\rho) = -\frac{2\pi}{\lambda}\left(\sqrt{s^2+\rho^2}+\sqrt{t^2+\rho^2}-s-t\right)+\Phi_F(0). \tag{25}$$

Equation (25) is particularly useful when it is necessary to fabricate a blur-like phase mask that is to be used in cascade with an available commercial imaging lens, as shown in figure 4. Denoting the blur-like phase mask by $\Phi_{\text{PHASE}}(\rho)$, we can write the following equation:

$$\Phi(\rho) = \Phi_F(\rho) + \Phi_{\text{PHASE}}(\rho) \tag{26}$$

in which $\Phi(\rho)$ is the total phase as summarized in table 1 for the α_m, β, γ designs. We illustrate the calculation of $\Phi_{\text{PHASE}}(\rho)$ for the β-design using equations (20), (21), (25), (26) and table 1. The result for the phase mask is given by

$$\Phi_{\text{PHASE}}(\rho) = \frac{2\pi}{\lambda}\sqrt{s^2+\rho^2} - \frac{\pi}{\lambda}\left[\frac{1}{s_1}+\frac{1-\ln(1+\rho^2/t^2)}{\ln(1+R^2/t^2)}\left(\frac{1}{s_1}-\frac{1}{\sqrt{s_2^2+R^2}}\right)\right] \times (t^2+\rho^2)+C, \tag{27}$$

in which

$$C = -\frac{2\pi}{\lambda}s+\frac{\pi}{\lambda}\left[\frac{1}{s_1}+\frac{1}{\ln(1+R^2/t^2)}\left(\frac{1}{s_1}-\frac{1}{\sqrt{s_2^2+R^2}}\right)\right] \times t^2+\Phi(0)-\Phi_F(0).$$

3. Computer simulations

3.1. Point spread function

The point spread function for an ideal diffraction-limited lens, as in table 1, is plotted in figure 5. Correspondingly, the curves for the impulse response of a β-logarithmic asphere are plotted in figure 5. It is important to notice that these curves are computed numerically from the following expression:

$$I(\rho_2; s) = |V_2(\rho_2)|^2, \tag{28}$$

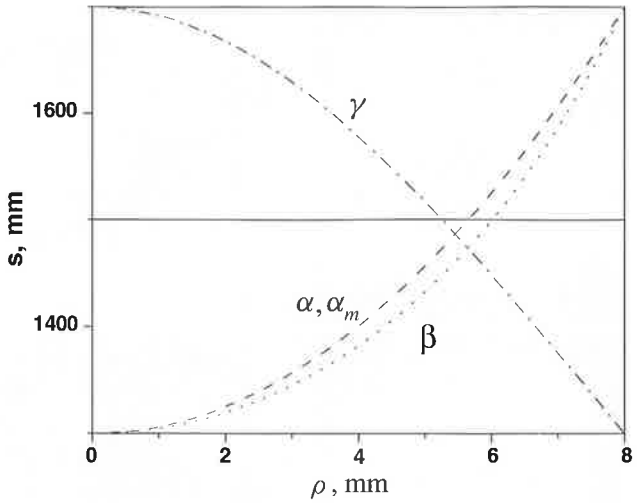

Figure 3. The plots of stationary points versus object distances. α lens in [3], β lens in case (i), γ lens in case (ii).

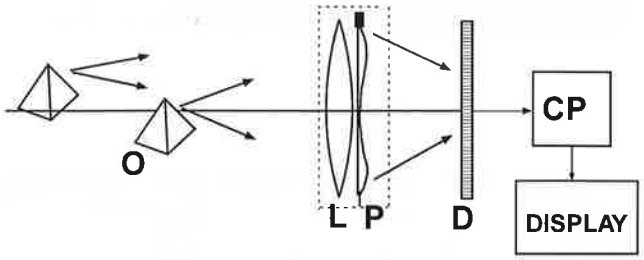

Figure 4. The experimental set-up for the integrated computational imaging system to extend the depth of field: O, object; L, lens; P, phase plate; D, detector; CP, computer processing.

using equation (5) for V_2 with the phase term $\Phi(\rho)$ from table 1. Also, this numerical evaluation is extremely accurate and the relative error in the numerical integration is of the order of 10^{-8}. It should be also emphasized that this calculation does not depend on the stationary phase discussion given in section 2.1. The radius of the aperture for both lenses is 8 mm. The ideal diffraction-limited lens has a focal length of 60 mm. For this lens with an object distance at 1500 mm (see figure 5), we find a sharp image at t of 62.5 mm with a first zero in the Airy disc at ρ_2 of 2.38 μm. When the object moves away from this position, one can see that the point spread function quickly becomes worse. Notice that the impulse responses at the diffraction limit distances ($\pm$8 mm) nearly overlap. For the β-design logarithmic asphere ($s_1 = 1300$ mm and $s_2 = 1700$ mm), the slope of the point spread functions is much more stable as the object distance varies. There are two interesting features in these plots. First, the point spread functions have their maximum value at the centre. This is not the case for the ideal diffraction-limited lens. Secondly, the first zeros of the point spread functions of the logarithmic asphere are even smaller than that of the ideal lens when the object is at a distance of 1500 mm. As a consequence of these features, we conclude that the stable shape of the impulse response leads to excellent image recovery. The diffraction-limited performance, as set by the first zero at $\rho_2 = 1.9$ μm, leads to a better resolution than that of the ideal lens of the same f-number.

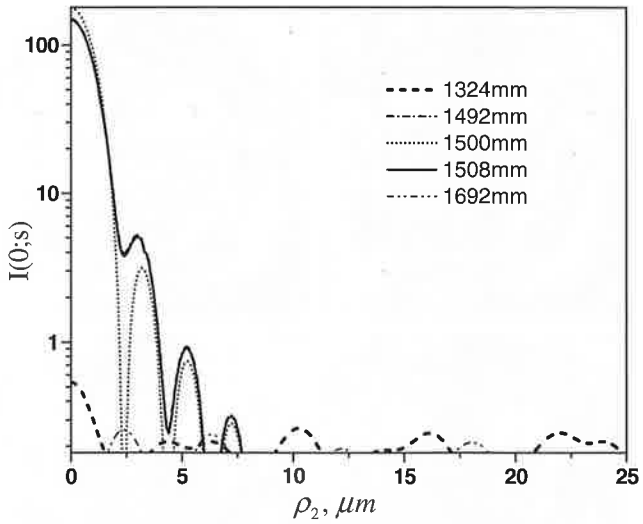

Figure 5. Curves for an ideal lens of the point spread function with an object point at various distances, s.

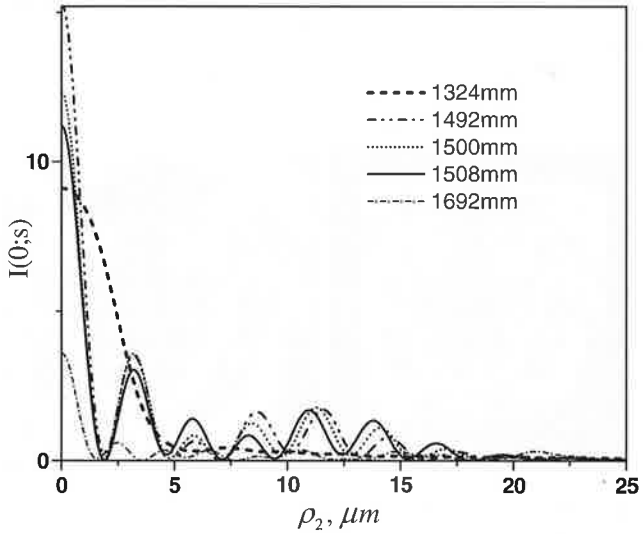

Figure 6. Curves of the point spread function of the β-design logarithmic asphere.

3.2. Computer simulation studies for the β-design logarithmic asphere

In this section we illustrate the performance of the β-design logarithmic asphere. In the simulation, an original photograph of a tiger is blurred by the calculated point spread function. First, for purposes of comparison, we show the photograph blurred using the ideal lens described in section 3.1. In figure 7, the upper left picture is sharply imaged at $s = 1500$ mm; and the upper right is badly blurred corresponding to a distance $s = 1430$ mm which is far beyond the diffraction-limited depth of field of $\pm$8 mm. Using a β-design with $s_1 = 1400$ mm and $s_2 = 1600$ mm, a radius of 8 mm and a $t = 62.5$ mm, we show the recovered images when $s = 1500$ mm (in focus) and the recovered image when $s = 1430$ mm. This last image is clearly of about the same quality as the in-focus image; and it is substantially better than that corresponding to the ideal, diffraction-limited lens. In the details of the simulation, we use a sampling interval corresponding to 0.2 μm in the ρ_2 dimension at plane II. This is much finer than the diffraction

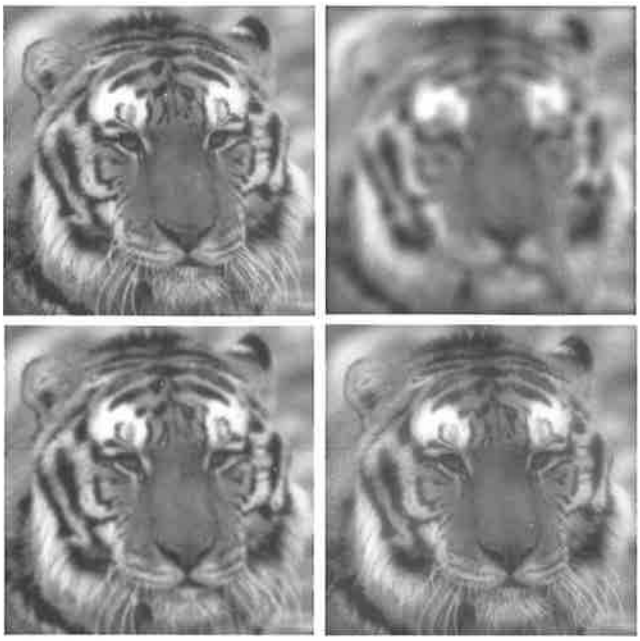

Figure 7. Computer simulation for β-design lens: upper left, ideal lens at 1500 mm; upper right, ideal lens at 1430 mm; lower left, log lens at 1500 mm; lower right, log lens at 1430 mm.

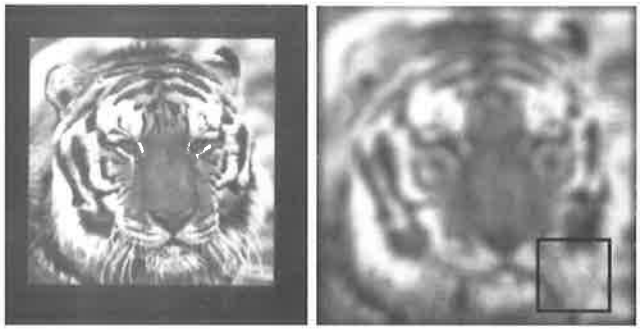

Figure 8. Nikon comparison photographs: left, in focus 950 mm; right, 700 mm.

limit imposed by the impulse response of the lens. In this computation the frame size is 3072 × 3072 pixels. This lets one clearly see the blur due to the lens.

4. Photographic experiments with the logarithmic asphere

A single-element type-α logarithmic asphere has been used in the complete set-up as shown in figure 4. This asphere was fabricated using an OptiPro model SX50 computer-controlled grinding machine and a QED magneto-rheological finisher as described in [3]. This lens was fabricated in an optical grade of quartz to an overall accuracy of the order of one-tenth of a wavelength. In the experiments, the CCD array has 576 × 384 pixels that are 23 μm × 23 μm. All experiments are conducted with an f-number of 4.

First, for the purposes of calibration, pictures are recorded of a tiger at a distance (in focus) of 950 mm using a high-quality Nikon Micro Nikkor 60 mm lens. Then the object is also recorded at a distance of 700 mm. The pixel-limited depth of field is 46 mm. As shown in figure 8 the blurred image is considerably degraded.

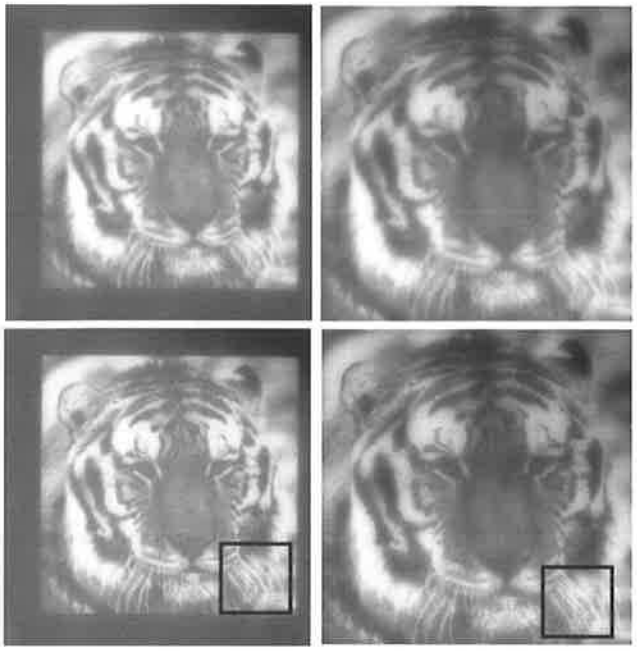

Figure 9. Photograph with logarithmic α-design asphere: upper left, in focus at 950 mm; upper right, at 700 mm; lower left, recovery at 950 mm; lower right, recovery at 700 mm.

Figure 10. Expanded view of whiskers: left, logarithmic asphere at 950 mm; right, logarithmic asphere at 700 mm; centre, Nikon at 700 mm.

Using the α-design lens, we recorded the photographs shown in figure 9. These show both the blurred images and the recovered images at distances of 950 and 700 mm respectively. One can readily observe that the recovered images are rather good even at the extended depth of field. In order to show the effectiveness of the recovery, figure 10 contains expanded views of the tiger's whiskers. While the whiskers are badly blurred in the photographs taken using the Nikon lens, one can clearly see them in detail with the photographs taken using the logarithmic asphere. This improvement in depth of field is 250 mm divided by 23 mm or approximately tenfold (10×).

For the image recovery, we used an inverse filter followed by a median filter [5]. A straightforward computation shows that the image plane based inverse filter is more than four times faster than a Fourier plane inverse filter. The matrix which we used in this image recovery is given by

$$\begin{bmatrix} 0 & -1 & 0 \\ -1 & 6 & -1 \\ 0 & -1 & 0 \end{bmatrix}.$$

5. Summary

A nonparaxial form of the diffraction theory integral for an impulse response is derived and evaluated numerically. Table 1

contains a summary of the phase terms $\Phi(\rho)$ for a series of different logarithmic aspheres as well as the phase delay $\Phi_F(\rho)$ for an ideal lens, described in the appendix. In equations (26) and (27), we describe how one can compute a blurring phase filter for use in cascade with a commercial imaging lens in order to obtain an extended depth of field. Precise calculations of the point spread functions are presented in figure 6 using equation (28). As an important result, these curves show that the log asphere is capable of diffraction-limited performance. For the β-design, computer simulations in figure 7 illustrate the extended depth of field compared with the ideal diffraction-limited asphere. This design provides a tenfold increase in the depth of field. In photographic experiments comparing the α-design with a high-quality Nikon lens at the same f-number, we show the extended depth of field for a complete system, as in figure 4, in a series of photographs. Figure 8 shows the Nikon system in focus and badly blurred at the extended depth of field. Figure 9 shows the logarithmic asphere at 950 and 700 mm. Figure 10 shows the expanded view of the whiskers clearly discernible at the extended depth of field.

Acknowledgment

This research was supported in part by the Army Research Office.

Appendix. Idealized lens

For the diffraction theory analysis, it is important to have an expression for the transmission function of an ideal lens that is valid in the nonparaxial regime. Let us define an ideal lens as one that images an object point at a distance s to a diffraction limited spot at a distance t, as shown in figure 2. Now we denote the transmission function for the ideal lens by $t_F(\rho)$, i.e. by

$$T_F(\rho) = \mathrm{e}^{-\mathrm{i}\Phi_F(\rho)}. \tag{A.1}$$

Clearly, equation (6) for the impulse response is valid where $\Phi_F(\rho)$ replaces $\Phi(\rho)$ in the exponential. We proceed to evaluate the integral setting $\rho_2 = 0$ and using the principle of stationary phase, or as we prefer by Fermat's principle. Letting P_{SOP} be defined by the expression

$$P_{SOP} = k(s^2 + \rho^2)^{1/2} + k(t^2 + \rho^2)^{1/2} + \Phi_F(\rho), \tag{A.2}$$

in which the wavenumber $k = 2\pi/\lambda$. Now we compute the derivative of P_{SOP} with respect to ρ and set it equal to zero. Then we integrate the expression from $\rho = 0$ to ρ. The result is of course the well-known first principle of optical design that the optical path length or phase retardation, P_{SOP}, in equation (A.2) is a constant. For the ideal lens, we find that the phase delay $\Phi_F(\rho)$ is given by the following important formula:

$$-\Phi_F(\rho) = k[(s^2+\rho^2)^{1/2} - s + (t^2+\rho^2)^{1/2} - t] - \Phi_F(0). \tag{A.3}$$

Substitution of equation (A.3) into (A.1) gives the desired nonparaxial form for the transmission function of the lens, namely:

$$T_F(\rho) = \exp\{\mathrm{i}k[(s^2 + \rho^2)^{1/2} - s + (t^2 + \rho^2)^{1/2} - t] - \mathrm{i}\Phi_F(0)\}. \tag{A.4}$$

While this form in equation (A.4) is valid in the nonparaxial regime, it is interesting as a check to make the usual Fresnel zone expansions of the quadratic forms in equation (A.4). This gives us the following well-known paraxial approximation for $\Phi_F(\rho)$, namely

$$-\Phi_F(\rho) \cong \frac{\pi}{\lambda}\left(\frac{1}{s} + \frac{1}{t}\right)\rho^2 - \Phi_F(0). \tag{A.5}$$

This is written with an implicit $\exp(\mathrm{i}\omega t)$ harmonic time dependence so that $T_F(\rho)$ is given by

$$T_F(\rho) \cong \exp\left\{\mathrm{i}\frac{\pi}{\lambda}\left(\frac{1}{s} + \frac{1}{t}\right)\rho^2 - \mathrm{i}\Phi_F(0)\right\}. \tag{A.6}$$

References

[1] Ojeda-Castaneda J and Berriel-Valdos L R 1990 Zone plate for arbitrarily high focal depth *Appl. Opt.* **29** 994–7
[2] Dowski E R Jr and Cathey W T 1995 Extended depth of field through wave-front coding *Appl. Opt.* **34** 1859–66
[3] Chi W and George N 2001 Electronic imaging using a logarithmic asphere *Opt. Lett.* **26** 875–7
[4] Smith W J 2000 *Modern Optical Engineering* 3rd edn (New York: McGraw-Hill) p 348 section 11.2
[5] Gonzalez R C and Woods R E 1993 *Digital Image Processing* 2nd edn (Reading, MA: Addison-Wesley) p 191 section 4.3.2

Fourier optical analysis of gradient-index array imaging

Xi Chen and Nicholas George

We present theory and experiments in which Fourier optics and the generalized Fresnel-zone integral form are used to characterize the imaging both of a single gradient-index rod and an array of nine rods. For the unity magnification SELFOC imager, we show that it has both internal and external Fourier transform planes. Careful treatment of the aperture function for off-axis points leads to a theoretical point-spread function that is in close agreement with experiments. Experiments are presented to illustrate the Fourier transform patterns as well as the imaging for single rods and for the entire array.

OCIS codes: 110.2760, 070.2580, 110.2990.

1. Introduction

Gradient-index (GRIN) arrays are widely used as imaging devices in copiers and printers. We present an analysis of these arrays based on Fourier optics for the purpose of contributing to a fuller understanding of the imaging, resolution, and information processing possibilities of these arrays. In the literature the treatment of the GRIN array has generally been based on geometrical optics or more specifically ray tracing in inhomogeneous media. Excellent treatments, including extensive references to the early history, are contained in the monographs by Buchdahl[1] and Marchand.[2] A computer method for the calculation of ray paths in GRIN rods is described by Montagnino.[3] An improved method for ray tracing in GRIN material that permits closed-form solutions is given by Marchand.[4] An efficient current method of ray tracing based on the standard numerical Runge–Kutta method is described by Sharma, *et al.*[5] Commercial optical software for numerical ray tracing in GRIN media is available for layout and optimization.[6]

For wave optics in an inhomogeneous, isotropic medium, Baues[7] derived integral equations based on solutions of the Helmholtz wave equation. In particular for a GRIN rod, a generalized Fresnel-zone integral is formulated in terms of the *ABCD* matrix for paraxial ray propagation. An independent comprehensive treatment of beam propagation connecting physical and geometrical optics has been published by Arnaud.[8–10] Based on the Hamiltonian theory of geometrical optics, he derived an extended Fresnel-zone form containing the *ABCD* matrix. These topics are also covered in the textbook *Lasers* by Seigman.[11] In a study of image transmission along a single GRIN rod, Yariv[12] compared the accuracy of an exact eigenfunction modal-dispersion analysis to an approximate paraxial Fresnel-zone form. K. Iga[13] also derived the transformation integral of the field by expanding the input field into eigenfunctions in the GRIN fiber. A comprehensive treatise on single-mode fiber and image transmission on a GRIN fiber has been published,[13–14] including experimental data on Fourier transforming and imaging. Important early treatment of paraxial imaging and Fourier transforming in a GRIN fiber was published by C. Gomez-Reino and E. Larrea,[15] followed by their analysis of the pupil function in GRIN material.[16] Further theoretical investigations of imaging and Fourier transforming in GRIN lenses is reported in a series of papers.[17–20] An extensive treatment of GRIN optics is provided in the recent monograph by Gomez-Reino *et al.*[21] As the applications of the GRIN arrays have become commonplace, many other factors of performance have been reported. Theoretical and experimental studies have shown that the off-axis irradiance from a single GRIN fiber follows an ellipsoidal distribution.[22–23]

We report theory and experiments in this paper to describe imaging with GRIN arrays in which a formulation based on Fourier optics is used. In Section 2 the single GRIN rod is analyzed with the general-

The authors are with The Institute of Optics, University of Rochester, 275 Hutchinson Road, Rochester, New York 14627-9000. N. George's e-mail address is ngeorge@troi.cc.rochester.edu.

Received 16 August 2002; revised manuscript received 12 March 2003.

0003-6935/03/224434-11$15.00/0

Table 1. Impulse Responses for the Grin Rod[a]

Fourier Transform Planes

Internal (vi):

$$h_{16}(x, y; x_1, y_1) = \frac{in_1\alpha}{\lambda \sin(\alpha d_6)} \exp[-ik(d_1 + n_1 d_6)] \exp\left[\frac{ikd_1(n_1\alpha)^2(x^2 + y^2)}{2\sin^2(\alpha d_6)}\right] \exp\left[\frac{ikn_1\alpha(x_1x + y_1y)}{\sin(\alpha d_6)}\right]$$

External (iv):

$$h_{14}(x, y; x_1, y_1) = \frac{in_1\alpha \sin(\alpha L)\exp[-ik(d_1 + n_1L + d_4)]}{\lambda} \times \exp\left\{\frac{ik[n_1^2\alpha^2 \sin^2(\alpha L)d_1 - n_1\alpha \sin(\alpha L)\cos(\alpha L)](x^2 + y^2)}{2}\right\}$$

$$\times \exp[ikn_1\alpha \sin(\alpha L)(x_1x + y_1y)]$$

Image Planes

Internal (vii):

$$h_{17}(x, y; x_1, y_1) = \frac{\exp[-ik(d_1 + n_1d_7)]}{\lambda^2 d_1^2 \cos(\alpha d_7)} \exp\left[\frac{-ik(x_1^2 + y_1^2)}{2d_1}\right] \exp\left[\frac{ik(x^2 + y^2)}{2d_1}\right] F^{-1}\{P(x_2, y_2)\}$$

External (v):

$$h_{15}(x, y; x_1, y_1) = \frac{\exp[-ik(d_1 + n_1L + d_2)]}{\lambda^2 M d_1^2} \exp\left[\frac{-ik(x_1^2 + y_1^2)}{2d_1}\right] \exp\left[\frac{ik\cos(\alpha L)(x^2 + y^2)}{2Md_1}\right] F^{-1}\{P(x_2, y_2)\}$$

$$|h_{15}(x, y; x_1, y_1)|^2 = \frac{|F^{-1}\{P(x_2, y_2)\}|^2}{\lambda^4 d_1^4 M^2}$$

[a]See Eq. (23) for M and Fig. 1 for plane designations.

ized Fresnel-zone theory referenced above. We carefully study the effective aperture to show an elliptical shape for off-axis object points. The point-spread functions (PSFs) for both internal and external Fourier transform and image planes are treated. The results are listed in Table 1. In Section 3, imaging by the full array of nine elements shown in Fig. 7 below is analyzed. With the earlier described off-axis pupil function, theoretical and experimental treatment is provided for the impulse response of the array. A statistical analysis is presented in which the optical path differences (OPDs) are used to establish the results for the array of nine fibers. Experimental results are presented of Fourier plane outputs, impulse responses, and imaging.

2. Fourier Optical Analysis

In this section we analyze the imaging of a single GRIN element using the methods of Fourier optics. This linear system, known as a GRIN rod, is shown in Fig. 1. First, we describe the important characteristics of one element of the widely used SELFOC LENS ARRAY (SLA) manufactured by the Nippon Sheet Glass Co., LTD.[24] Each single GRIN rod of the SLA has a refractive-index distribution represented by

$$n^2(r) = \begin{cases} n_1^2[1 - 2(r/R)^2\Delta] & r \le R \\ n_2^2 & r > R \end{cases}, \quad (1)$$

where Δ is given by

$$\Delta = \frac{n_1^2 - n_2^2}{2n_1^2}. \quad (2)$$

Second, from geometrical optics, one has the important *ABCD* matrix method for paraxial ray tracing through free space as well as through the GRIN medium.[11] Consider Fig. 1 with a ray height $x(z)$ and the ray-slope variable defined by $n(x)\mathrm{d}x(z)/\mathrm{d}z$ where $n(x)$ is the index of refraction at a height x from the optic axis. One can write the optical ray matrix between the input at $z = 0$ to an arbitrary z in the rod as follows:

$$\begin{bmatrix} x(z) \\ n\dfrac{\mathrm{d}x(z)}{\mathrm{d}z} \end{bmatrix} = \begin{bmatrix} A & B \\ C & D \end{bmatrix} \begin{bmatrix} x(0) \\ n(0)\dfrac{\mathrm{d}x(0)}{\mathrm{d}z} \end{bmatrix}. \quad (3)$$

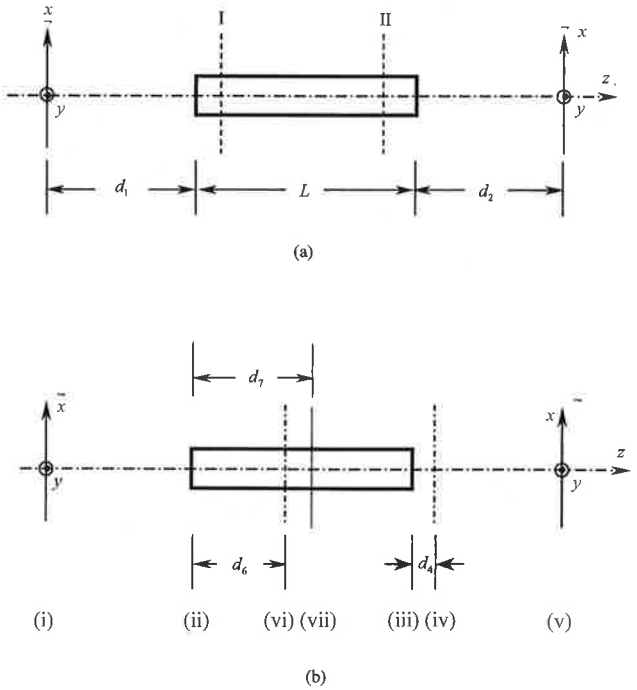

Fig. 1. Imaging setup for the GRIN rod with (i) an object plane and (v) an image plane: (a) basic dimensions and (b) the location of external and internal Fourier transform planes (iv), (vi) and imaging planes (v), (vii), respectively.

The ray matrix elements are given by[11]

$$\begin{bmatrix} A & B \\ C & D \end{bmatrix} = \begin{bmatrix} \cos(\alpha z) & \dfrac{\sin(\alpha z)}{n_1 \alpha} \\ -n_1 \alpha \sin(\alpha z) & \cos(\alpha z) \end{bmatrix}, \tag{4}$$

in which $\alpha = (2\Delta)^{1/2}/R$, the index gradient constant. The system is radially symmetric so a similar set of equations can be written for the y axis. These are omitted in the interest of brevity.

A. Physical Optics for the Gradient-Index Rod

A general treatment of propagation in an inhomogeneous isotropic media has been published by Baues,[7] including simplification to a generalized Fresnel-zone form. The generalized Fresnel-zone expression that is appropriate for analyzing the GRIN rod is given by[7,11]

$$V_2(x, y) = \frac{ik \exp(-ikL)}{2\pi B} \int_{-\infty}^{\infty} \int_{-\infty}^{\infty} \mathrm{d}x_0 \mathrm{d}y_0 V_1(x_0, y_0) \times \exp\left\{ -\frac{ik}{2B} [D(x^2 + y^2) - 2(x_0 x + y_0 y) + A({x_0}^2 + {y_0}^2)] \right\}. \tag{5}$$

Herein, we are using an $\exp(i\omega t)$ notation implicitly. This expression can be used to calculate the output scalar field $V_2(x, y)$ from the input scalar field $V_1(x, y)$, say, for any planes such as I to II in Fig. 1(a). Moreover for the GRIN rod, the elements A, B, C, D in Eq. (5) are given by Eqs. (1) to (4).

For the analysis of the linear optical system in Fig. 1, we would like to find both internal and external Fourier transform planes and image planes as has been asserted from the chain matrix analysis in Appendix A. Consider an input scalar amplitude of polarized electric field denoted by $V_1(x, y; \nu)$ at $z = 0$ when the temporal frequency ν is to be suppressed. To find the impulse response $h_{16}(x, y; x_0, y_0)$ from plane (i) to plane (vi), we use the following well-known form:

$$V_6(x, y) = \int_{-\infty}^{\infty} \int_{-\infty}^{\infty} \mathrm{d}x_0 \mathrm{d}y_0 V_1(x_0, y_0) h_{16}(x, y; x_0, y_0). \tag{6}$$

Taking an input scalar amplitude given by

$$V_1(x_0, y_0) = \delta(x_0 - x_1, y_0 - y_1), \tag{7}$$

corresponding to an input point source at (x_1, y_1), we can find the output at plane (vi) by combining Eqs. (5) to (7) and integrating over an idealized infinite aperture at plane (ii). The general result for h_{16} is given by

$$h_{16}(x, y; x_1, y_1) = \frac{ikd_0 \exp[-ik(d_1 + n_1 d_6)]}{2\pi d_1 B_6} \times \exp\left[\frac{-ik(D_6/B_6 - d_0/{B_6}^2)(x^2 + y^2)}{2} \right] \times \exp\left[\frac{-ik(1 - d_0/d_1)({x_1}^2 + {y_1}^2)}{2d_1} \right] \times \exp\left[\frac{ikd_0}{d_1 B_6} (x_1 x + y_1 y) \right], \tag{8}$$

in which the length d_0 is defined

$$\frac{1}{d_0} = \frac{1}{d_1} + \frac{A_6}{B_6}. \tag{9}$$

The matrix element B_6 is given by Eq. (4) as $\sin(\alpha d_6)/(n_1 \alpha)$. As yet, no assumptions have been made about the matrix elements A_6, B_6, C_6, D_6 for propagation in the GRIN rod from plane (i) to plane (vi). To find the location of an internal Fourier transform plane, we set the coefficient of the input quadratic term equal to zero, viz.,

$$\frac{ik}{2d_1} \left(\frac{d_0}{d_1} - 1 \right) = 0. \tag{10}$$

Substitution of Eq. (10) into Eq. (9) gives the condition

$$\frac{A_6}{B_6} = 0, \tag{11}$$

and by Eq. (4) we find the location of plane (vi) given by

$$\cos(\alpha d_6) = 0. \tag{12}$$

Hence, by substituting Eqs. (10) and (12) into (8), the final form for the impulse response to the internal Fourier transform plane (vi) is given by

$$h_{16}(x, y; x_1, y_1) = \frac{in_1 \alpha}{\lambda \sin(\alpha d_6)} \exp[-ik(d_1 + n_1 d_6)] \times \exp\left[\frac{ikd_1 (n_1 \alpha)^2 (x^2 + y^2)}{2 \sin^2(\alpha d_6)} \right] \times \exp\left[\frac{ikn_1 \alpha (x_1 x + y_1 y)}{\sin(\alpha d_6)} \right]. \tag{13}$$

We note that the location of the transform plane in Eq. (12) is consistent with the result based on geometrical optics in Eq. (A2).

From the coefficient of the $(x_1 x_6 + y_1 y_6)$ exponent, we deduce the scale of the Fourier transform f_x, f_y is given by

$$f_x = \frac{-n_1 \alpha x_6}{\lambda \sin(\alpha d_6)}, \qquad f_y = \frac{-n_1 \alpha y_6}{\lambda \sin(\alpha d_6)}. \tag{14}$$

Locating the external Fourier transform plane, (iv) in Fig. 1(b), requires that the procedure be analogous to that directly above. One starts with an input delta-function source at (x_1, y_1) in plane (i). Repeated applications of Eq. (5) for the propagation from (i) to (ii); (ii) to (iii); and (iii) to (iv) with integrations over idealized infinite apertures at (ii) and (iii) yield the following result. The amplitude impulse response, $h_{14}(x, y; x_1, y_1)$, is given by

$$h_{14}(x, y; x_1, y_1) = \frac{ikd_0q \exp[-ik(d_1 + n_1L + d_4)]}{2\pi d_1 B d_4} \times \exp\left[-ik\left(\frac{1}{2d_1} - \frac{q}{2d_1^2}\right)(x_1^2 + y_1^2)\right] \times \exp\left[\frac{ik}{2d_4}\left(\frac{d_0}{d_4} - 1 + \frac{qd_0^2}{B^2 d_4}\right)(x^2 + y^2)\right] \exp\left[\frac{ikd_0q}{d_1 B d_4}(x_1 x + y_1 y)\right], \tag{15}$$

in which we have defined d_0 as in Eq. (9), defined q as

$$\frac{1}{q} = \frac{1}{d_1} + \frac{A}{B} - \frac{d_4}{B(B + Dd_4)}, \tag{16}$$

and obtained the elements A, B, C, D from Eq. (4) for the entire rod of length L. Again, we found the position d_4 of the transform plane by zeroing out the quadratic exponent in $x_1^2 + y_1^2$. Hence, the distance d_4 is given by

$$d_4 = \frac{AB}{1 - AD} = \frac{-A}{C}, \tag{17}$$

$$d_4 = \frac{\cos(\alpha L)}{n_1 \alpha \sin(\alpha L)}, \tag{18}$$

in which

$$\alpha = \frac{(n_1^2 - n_2^2)^{1/2}}{n_1 R}. \tag{19}$$

Likewise, the Fourier transform scale f_x, f_y can be found from the coefficient of the linear terms in x_1, y_1. The scale of the transform is given by

$$f_x = \frac{-n_1 \alpha \sin(\alpha L)}{\lambda} x_4, \qquad f_y = \frac{-n_1 \alpha \sin(\alpha L)}{\lambda} y_4, \tag{20}$$

in which $k = 2\pi/\lambda$. For the transform plane in Eq. (20), we have added the subscript 4 for clarity.

B. Impulse Response for Imaging

Now, we consider the calculation of the amplitude impulse response and its intensity counterpart the incoherent PSF. For this calculation, we introduce an aperture function $P(x, y)$ at plane (ii), the front surface of the GRIN rod in Fig. 1. In Subsection 2.C we will relate this aperture function to the stop for the GRIN rod that we shall calculate using a nonparaxial, ray-trace computer program that is based on the Euler–Lagrange equations.[2,5]

For the positions of the imaging planes as calculated by the chain matrices, the external output image at plane (v) is given by Eq. (A8) and the internal image at plane (vii) is given by Eq. (A6), see Fig. 1. Proceeding as before to calculate the impulse response $h_{17}(x, y; x_1, y_1)$ and $h_{15}(x, y; x_1, y_1)$, we use an input delta function in plane (i) at (x_1, y_1), i.e., let $V_1(x_0, y_0)$ be given by

$$V_1(x_0, y_0) = \delta(x_0 - x_1, y_0 - y_1). \tag{21}$$

The blocking function $P(x, y)$ is inserted at plane (ii). The resulting expressions are shown in Table 1 for imaging impulse responses h_{17} and h_{15}, and their positions are verified with this physical optics calculation. The result for the overall imaging impulse response is given by

$$h_{15}(x, y; x_1, y_1) = \frac{\exp[-ik(d_1 + n_1L + d_2)]}{\lambda^2 M d_1^2} \times \exp\left[\frac{-ik(x_1^2 + y_1^2)}{2d_1}\right] \times \exp\left[\frac{ik\cos(\alpha L)(x^2 + y^2)}{2Md_1}\right] \times F^{-1}\{P(x_2, y_2)\}, \tag{22}$$

where the magnification M is defined by

$$M = \frac{1}{\cos(\alpha L) - n_1 \alpha d_1 \sin(\alpha L)}. \tag{23}$$

Also, the shape of the impulse response in Eq. (22) is controlled by the inverse transform, $F^{-1}\{P(x_2, y_2)\}$, which has been defined

$$F^{-1}\{P(x_2, y_2)\} = (\lambda d_1 M)^2 \int_{-\infty}^{\infty}\int_{-\infty}^{\infty} df_x df_y \times P(-\lambda d_1 M f_x, -\lambda d_1 M f_y) \times \exp[i2\pi f_x(x - Mx_1) + i2\pi f_y(y - My_1)], \tag{24}$$

in which the spatial-frequency variable f_x, f_y are defined by

$$f_x = -\frac{x_2}{\lambda d_1 M}, \qquad f_y = -\frac{y_2}{\lambda d_1 M}. \tag{25}$$

From Eqs. (22) to (25), we see that the impulse response on the image plane is proportional to the inverse Fourier transform of the aperture function. In Eq. (22), the quadratic-phase term shows that the GRIN imaging system is not shift invariant. As we know, the irradiance of the off-axis image for a single

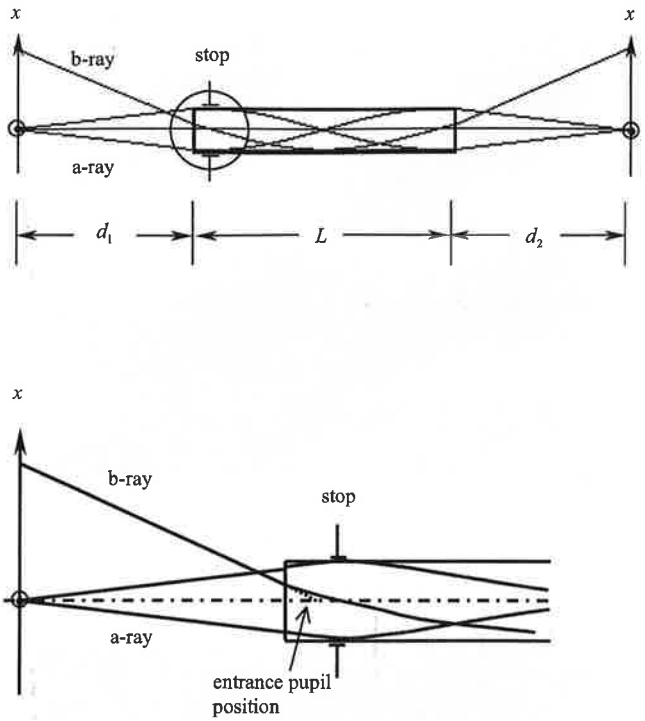

Fig. 2. Stop and entrance pupil position.

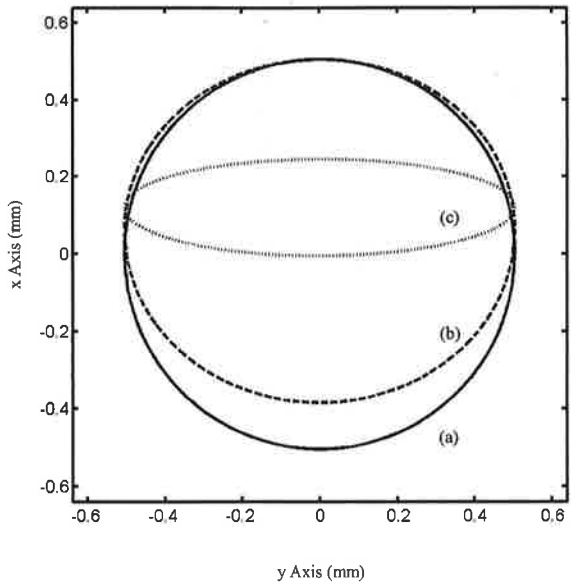

Fig. 3. Aperture functions $P(x_2, y_2)$ for SLA09-48 rod: (a) aperture function for on-axis object, (b) aperture function for off-axis object (1.045 mm, 0), (c) aperture function for object at (2.09 mm, 0).

GRIN rod falls off far more rapidly than the $\cos^4 \theta$ law.[22,23]

For incoherent illumination of the object, in general, one obtains the incoherent PSF by taking the absolute square value of h_{15} in Eq. (22), namely,

$$\hbar_{15}(x, y; x_1, y_1) = |h_{15}(x, y; x_1, y_1)|^2, \tag{26}$$

$$\hbar_{15}(x, y; x_1, y_1) = \frac{1}{\lambda^4 d_1^4 M^2} |F^{-1}\{P(x_2, y_2)\}|^2. \tag{27}$$

Interestingly from Eqs. (27) and (24), we see that the GRIN rod is ideally shift invariant with incoherent illumination. This basic result is used in computations below for the single rod and the entire array.

C. Aperture Function

To calculate the impulse response of the GRIN rod as in Eqs. (22) and (27), we need to determine the effective aperture function $P(x_2, y_2)$ at plane (ii). The aperture function defines the opening for rays passing through the system. We describe our calculation for this blocking function more fully below. The aperture stop position, shown in Fig. 2, is determined by the marginal ray (a-ray) originating at (0,0) in the object plane and remaining in the optical system as the limiting ray. The chief ray (b-ray) is shown passing through the center of the aperture stop from an extended position of the object.[25] The acceptance angle for each rod with 1:1 imaging is[26]

$$\theta = \tan^{-1} \frac{R|\sec(\alpha L/2)|}{d_1}. \tag{28}$$

For SLA09-48, the acceptance angle is computed to be $\theta = \pm 8.7°$. Rays outside this range do not propagate through the outlying rods and hence do not contribute to the image.

The stop position for 1:1 GRIN rod imaging (object and image planes coincide with primary planes) is at

$$z = \frac{\pi/2 - n\pi}{\alpha} + L/2,$$

where n is an integer. For SLA09-48 1:1 imaging, the stop position is at 1.39 mm away from the front surface of the rod, see Fig. 2. The intersection of the extended free space b-ray with the optical axis is the entrance pupil location. For SLA09-48, the entrance pupil is located at 0.87646 mm away from the front surface of the GRIN rod.

In the calculation of $P(x_2, y_2)$, it is important to consider an on-axis point source and consider separately off-axis points that are at the edge of the field of view. The aperture function is, of course, different for each of these points. Figure 3 shows the effective aperture functions for three points. For accuracy, these have been calculated with a software program for ray tracing that is based on the Euler–Lagrange equations and is valid for the nonparaxial case. For the on-axis point, $P(x_2, y_2)$ is circular and is unity for 0.96944 parts of the 1.045-mm diameter of the SLA09-48 rod that is used in our experiment. For the off-axis points at one and two diameters, we see that the effective aperture becomes elliptical in shape.

D. Single-Rod Performance

Table 1 contains a summary of the impulse responses for the single GRIN rod shown in Fig. 1. Using Fou-

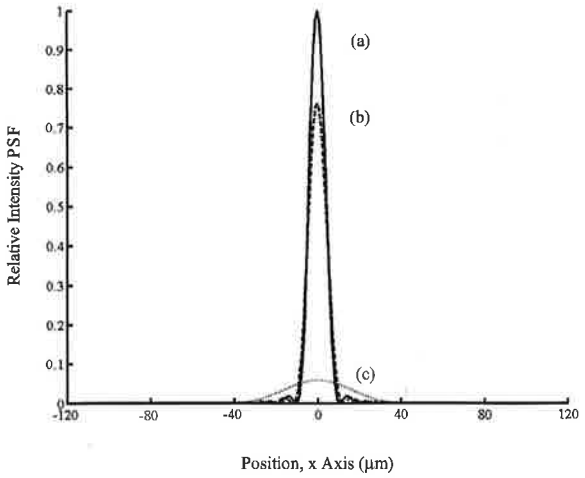

Fig. 4. Intensity PSFs for (a) an on-axis point source, (b) an object point at one diameter off axis, (c) an object point that is two diameters offset.

rier optics, we have derived positions of an internal Fourier transform plane as well as an imaging plane. An external Fourier plane and the final image plane are also identified. Figure 4 shows the intensity PSF, $|h_{15}|^2$, for an on-axis point source (4a) and for object points that are offset by one and two diameters [4(b) and 4(c), respectively]. The full-width, half-power points along the x axis are 9 μm [Fig. 4(a)] and 10 μm [Fig. 4(b)]. The increased width for the off-axis point is, of course, due to the vignetting shown by the somewhat narrower aperture function [Fig. 3(c)].

Experimentally, one can measure the cross section of the impulse response, $|h_{15}(x, 0)|^2$ by taking the derivative of the knife-edge image response function. Using this well-known method, we find that the single rod has a full-width, half-power dimension of 13.6 μm. We see the difference between the theory and the experimental result is small. The effect of aberrations is not included in the analysis.

To study the Fourier transform property of the GRIN rod, we used a setup with the SLA09-48 rod. The input object is a Ronchi ruling of 7.87 line pairs/mm in plane (i). This object is illuminated by a collimated helium–neon laser beam. The output pattern is observed in the external Fourier transform plane (iv) via an appropriate relay lens imaged onto a 582 × 782 pixel CCD, as shown in Fig. 5: along the f_x axis (upper) and along f_y (lower), as in Fig. 7 below. Using Eq. (20), one can compute the scale of the transform to find $f_x = 215.447x/\text{mm}^2$, where x is in units of millimeter. One can see more than 9 orders of diffraction corresponding to a spatial frequency of 70.8 line pairs/mm. These numbers are in excellent agreement with our measurements.

Figure 6 shows the image of a resolution chart labeled in line pairs per millimeter. For this experiment, we use a white-light source and record the image (v) with a relay lens and CCD. The orientation of the output plane is the same as in Fig. 5. At 18 line pairs/mm, one sees excellent resolution.

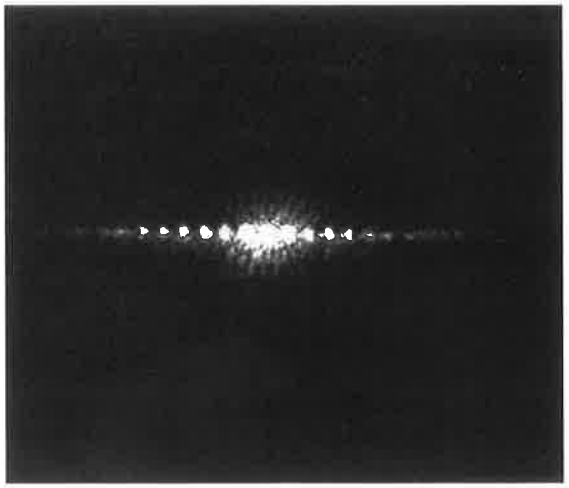

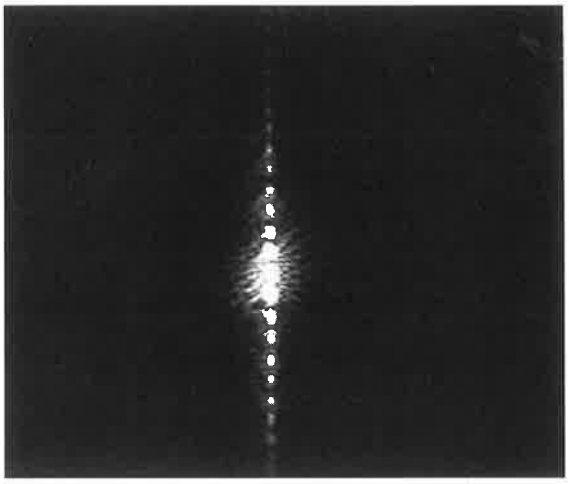

Fig. 5. Optical Fourier transform patterns at plane (iv) with Ronchi ruling of 7.87 line pairs/mm with pattern along x (upper) and pattern along y (lower).

3. Gradient-Index Array Performance

In this section we analyze the imaging of an array of GRIN rods. Typical of the commercial arrays is the SLA09-48 manufactured by the Nippon Sheet Glass Co. Ltd.[24] It is approximately 236.3 mm long, 4.8 mm wide, and with an optical lens length L of 20.36 ± 1.3 mm. This lens array has two rows of closely packed rods, as shown in the short section of Fig. 7. The rods have a diameter $2R$ = 1.045 mm with a parabolic index of refraction [see Eqs. (1) and (2)]. They are closely packed with a black silicone resin to provide stability and minimize crosstalk. There are 430 rods in all.

A. Fourier Transform Planes

For the array of Fig. 7, an infinite input plane wave is brought to a focus in plane (iv) in a pattern consisting of a series of tiny points centered on the axis of each

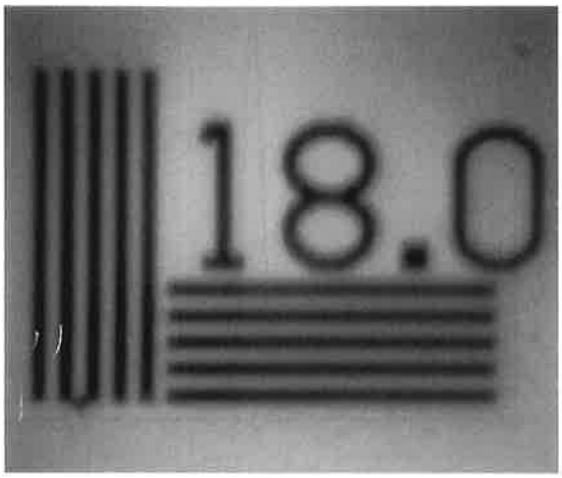

Fig. 6. Single rod imaging 18.0 line pairs/mm in white light.

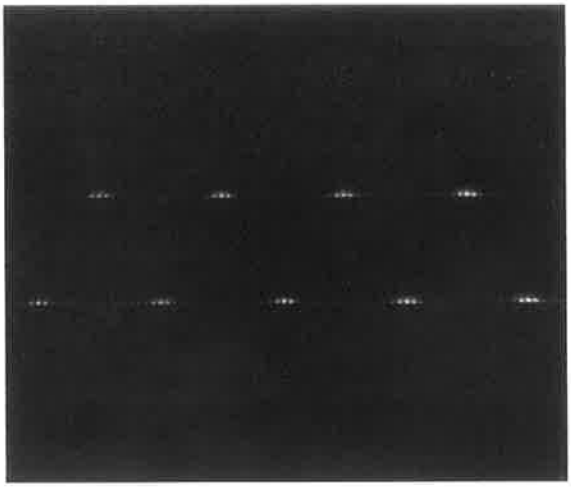

Fig. 8. Optical Fourier transform at plane (iv) for an extended object Ronchi ruling 11.8 line pairs/mm illuminated by an extended plane wave at 0.6328 μm.

rod. These mark the separate origins (f_x, f_y) of the Fourier transform plane for each rod. By means of an input object consisting of a Ronchi ruling of 11.8 line pairs/mm illuminated by a large-diameter, collimated helium–neon laser beam, the Fourier transform patterns are shown in Fig. 8.

B. Gradient-Index Array Imaging

With the object and the image distances $d_1 = d_2 = 13.8$ mm, the magnification is 1.000. As we have shown, the output in plane (v) is an erect image. With a typical object and incoherent illumination, there are nine rods contributing to the imaging of a single bright object point. Optical imaging and radiometric properties of arrays of GRIN rods are described in the literature.[26]

For a point source in plane (i) at $\delta(x - x_1)\delta(y - y_1)$,

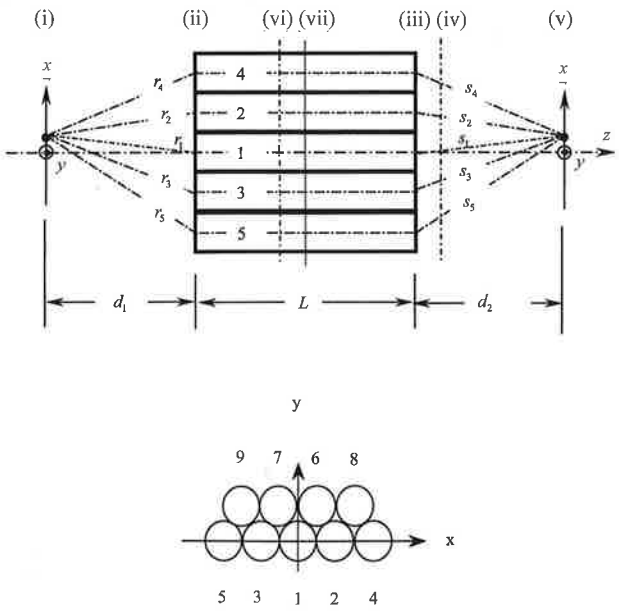

Fig. 7. Notation for the analysis of GRIN array imaging with an input source point (x_1, y_1) in plane (i) and an output position (x, y) in plane (v): side view (upper) and end view (lower).

consider the computation of the general amplitude impulse response for the nine elements of the array shown in Fig. 7. For the array, we denote the impulse response by $h_{15A}(x, y; x_1, y_1)$. For a linear system from Table 1, we can write this response in terms of the individual impulse responses, namely,

$$h_{15A}(x, y; x_1, y_1) = h_{15}^{(1)} + h_{15}^{(2)} + \ldots + h_{15}^{(9)}. \quad (29)$$

The superscript denotes the impulse response for that particular rod. Hence, for $h_{15}^{(4)}$ we can write the explicit form

$$h_{15}^{(4)} = \frac{\exp[-ik(d_1 + n_1 L_4 + d_2)]}{\lambda^2 M d_1^2} \times \exp\left\{\frac{-ik[(x_1 - 2D)^2 + y_1^2]}{2d_1}\right\} \times \exp\left\{\frac{ik\cos(\alpha L_4)[(x - 2D)^2 + y^2]}{2Md_1}\right\} \times F^{-1}\{P^{(4)}(x_2, y_2)\}, \quad (30)$$

in which the rod diameter $D = 2R$ and the optical length of the fourth rod is L_4. The impulse responses for each of the other rods follow directly from the form of Eq. (30).

For incoherent illumination, it is well known that the intensity-based impulse response is given by the absolute squared value of the corresponding amplitude impulse response.[27] Hence, for the case at hand by Eq. (29), one can write the following equation for $\hbar_{15A}$:

$$\hbar_{15A} = h_{15A} h_{15A}^*, \quad (31)$$

$$\hbar_{15A} = \sum_{m=1}^{9} |h_{15}^{(m)}|^2 + \sum_{m=1}^{9} \sum_{\substack{n=1 \\ m \neq n}}^{9} h_{15}^{(m)} h_{15}^{(n)*}. \quad (32)$$

As is shown in Appendix B, under the conditions that the OPDs are adequately large, e.g., because of r_m,

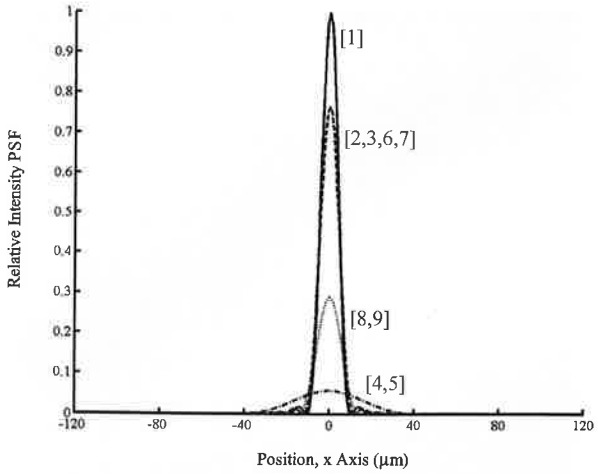

Fig. 9. Computed intensity PSFs for rods [1], [2,3,6,7], [8,9], [4,5].

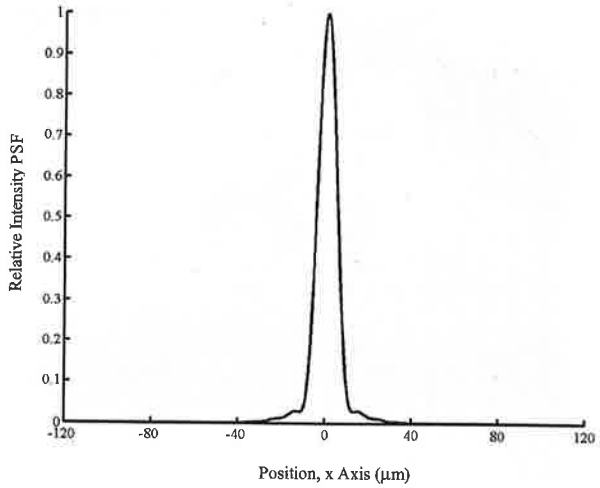

Fig. 10. Computed array intensity PSF along the x axis.

s_m, L_m, one can readily show that the double summation in Eq. (32) averaged over wavelength can be dropped. Hence, the impulse response for the GRIN array is given by

$$h_{15A}(x, y; x_1, y_1) = \sum_{m=1}^{9} |h_{15}^{(m)}|^2, \tag{33}$$

in which by Eq. (30), it follows that

$$|h_{15}^{(4)}|^2 = \frac{|F^{-1}\{P^{(4)}(x_2, y_2)\}|^2}{(\lambda d_1)^4 M^2}. \tag{34}$$

Figure 9 shows the x-axis plots for the individual incoherent impulse responses for the GRIN rods labeled. Figure 10 shows the overall impulse response from Eqs. (33) and (34).

Again using the derivative of the knife-edge image response, we have experimentally found the cross section of the intensity-based impulse response, $h_{15A}(x, 0)$. Figure 11(b) shows the impulse response of the array. Also, Fig. 11 shows the single-rod measurement that is described above in Subsection 2D. The half-power, full-width measured is approximately 28 μm for the array in comparison with our computed value of 10.7 μm. The major factor in this difference is attributed to alignment errors in the array. This difference has been established in separate measurements that are not elaborated further herein.

With illumination in white light and with the same setup as in Fig. 6, the imaging of the array is shown in Fig. 12. We see clearly that the overall resolution is excellent; the target object is at 18 line pairs/mm, and it is comparable with the result for the single rod, but of course with much brighter and more even illumination.

4. Summary

We have analyzed the GRIN array in detail using the linear systems formalism of Fourier optics. Starting with a review of the generalized Fresnel-zone formula in Eq. (5), we analyze the single rod and collect the main expressions in Table 1. New findings are the Fourier transform planes (vi) and (iv) shown together with the image planes (vii) and (v) in Fig. 1. These Fourier transform planes are located by means of a straightforward geometrical optics approach with the *ABCD* matrices in Appendix A as well as a Fourier optics approach leading to Eqs. (12) and (18). Corresponding transform-plane scaling is given by Eqs. (14) and (20). Experiments conducted to verify the transform-plane scaling are described in the text and are shown for a single rod in Fig. 5 and for an array in Fig. 8. Notice that the transform-plane centers for each rod remain distinct and separate even though there is a single input image as well as a single output image.

For the performance of a single rod, we present in Fig. 3 the effective apertures for off-axis points and in Fig. 4 the corresponding PSFs. From curves [4(c)], we can understand that points located two diameters off axis are not efficiently imaged.

For the GRIN array in Fig. 7, we find the general

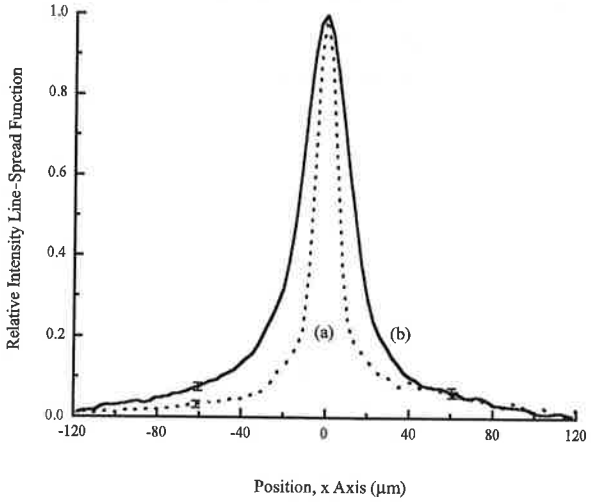

Fig. 11. Measured intensity line-spread function: (a) single rod and (b) GRIN array of nine rods.

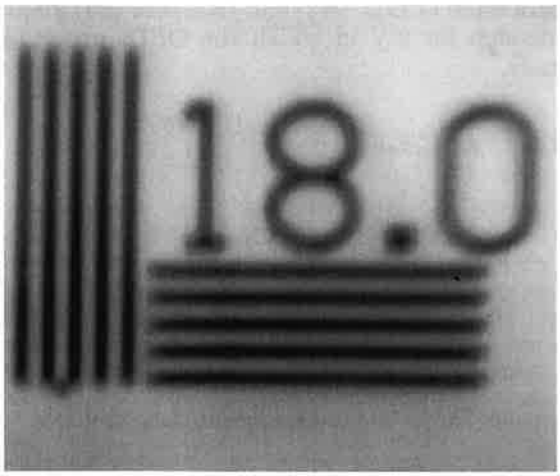

Fig. 12. GRIN array imaging 18 line pairs/mm in white light.

amplitude impulse response as given by Eqs. (29) and (30). For incoherent illumination Eqs. (33) and (34) are derived for the PSF based on an OPD analysis given in Appendix B. Theoretical PSF plots are given in Fig. 9 for each rod in the array and in Fig. 10 for the overall composite response. Good agreement with theory is shown by the Fig. 11(a) experimental result for the PSF of the single rod. The difference between the theory and the experimental result for the PSF of the array is attributed to alignment errors in the array.

The authors acknowledge helpful discussions with W. Chi, R. Herloski, W. Lama, R. Loce, R. Rolleston, and J. Taillie and the financial support in part by the U.S. Army Research Office.

Appendix A: Imaging and Fourier Transform Planes

For the GRIN rod shown in Fig. 1(a), one can find the position of an internal Fourier transform plane by using the chain matrix forms and setting the overall (11) element equal to zero. From the object plane to the plane located at $z = d_6$ inside the rod, a general form for the matrix C_{16} is readily computed to give the following value:

$$C_{16} = \begin{bmatrix} A_6 & A_6 d_1 + B_6 \\ C_6 & C_6 d_1 + D_6 \end{bmatrix}. \tag{A1}$$

Using Eq. (A1), one can find the position of the internal Fourier transform plane, d_6 in Fig. 1(b), by setting the (11) element equal to zero, i.e.,

$$A_6 = \cos(\alpha d_6) = 0. \tag{A2}$$

One can readily make a similar calculation to find the external Fourier transform plane at $z = L + d_4$, since the origin has been taken at the input face of the GRIN rod. Hence, from object plane to the external Fourier transform plane, the chain matrix C_{14} can be easily found to be

$$C_{14} = \begin{bmatrix} A_L + C_L d_4 & A_L d_1 + B_L + (C_L d_1 + D_L) d_4 \\ C_L & C_L d_1 + D_L \end{bmatrix}. \tag{A3}$$

The location of the external transform plane is found by setting the (11) element to zero, viz.,

$$A_L + C_L d_4 = \cos(\alpha L) - n_1 \alpha d_4 \sin(\alpha L) = 0. \tag{A4}$$

In the main body of the text, we show that Eqs. (A2) and (A4) are valid deductions based on physical optics. Also, one can readily show that the Fourier plane (vi) is imaged to the external Fourier plane (iv).

One can readily make a calculation of the position of the internal image plane located at $z = d_7$ by using the chain matrix forms and setting the overall (12) element equal to zero. From the object plane to the plane (vii) at $z = d_7$ inside the rod, the matrix C_{17} is expressed as the following value:

$$C_{17} = \begin{bmatrix} A_7 & A_7 d_1 + B_7 \\ C_7 & C_7 d_1 + D_7 \end{bmatrix}. \tag{A5}$$

Correspondingly, the position of the internal image plane, d_7 in Fig. 1(b), is given by

$$A_7 d_1 + B_7 = d_1 \cos(\alpha d_7) + \sin(\alpha d_7)/(n_1 \alpha) = 0. \tag{A6}$$

Similarly, one can find the position of the external image plane located at $z = L + d_2$ by setting the overall (12) element of the chain matrix equal to zero. From the object plane to the plane (v) at $z = L + d_2$, the matrix C_{15} is given by

$$C_{15} = \begin{bmatrix} A_L + C_L d_2 & A_L d_1 + B_L + (C_L d_1 + D_L) d_2 \\ C_L & C_L d_1 + D_L \end{bmatrix}. \tag{A7}$$

Hence, the position of the external image plane, d_2 in Fig. 1(a), is given by

$$\begin{aligned} A_L d_1 + B_L + (C_L d_1 + D_L) d_2 \\ = \cos(\alpha L) d_1 + \sin(\alpha L)/(n_1 \alpha) \\ + [-n_1 \alpha \sin(\alpha L) d_1 + \cos(\alpha L)] d_2 = 0. \end{aligned} \tag{A8}$$

Also, the internal image plane is imaged to the external image plane.

Finally, the magnification from object plane to the output, M, is given from Eq. (A7) as follows:

$$M = A_L + C_L d_2. \tag{A9}$$

Substitution of Eq. (A8) into (A9) yields the following result:

$$M = \frac{1}{C_L d_1 + D_L}. \tag{A10}$$

The C_L, D_L can be eliminated with Eq. (4). Thus, we arrive at a final expression for the magnification M in terms of the GRIN rod parameters, namely,

$$M = \frac{1}{\cos(\alpha L) - n_1 \alpha d_1 \sin(\alpha L)}. \tag{A11}$$

Note that Eq. (A11) agrees with the result derived from physical optics given by Eq. (23).

Appendix B: Intensity Impulse Response for the Array

Consider the calculation of the intensity impulse response, Eqs. (31) and (32) for the nine-element GRIN array shown in Fig. 7. As an overview, when the OPDs in a linear optical system exceed $\lambda/4$, one can no longer expect the intensity impulse responses to add coherently. Clearly the path-length differences between GRIN rods [1], [2,3], [4,5], [6,7], [8,9] are substantial in radians or wavelengths for the array dimensions given. So there are at least five independent elements with major phase terms acting to give validity to the incoherent superposition asserted in Eq. (33). Conceivably, one can obtain better resolution in the x direction by careful polishing of the array so as to minimize the OPD for the pairs grouped above, e.g., L_2 and L_3.

To understand the incoherent superposition quantitatively, we write $h_{15}^{(1)}(x, y; x_1, y_1)$ from Table 1 as follows:

$$h_{15}^{(1)}(x, y; x_1, y_1) = \frac{\exp[-ik(d_1 + n_1 L_1 + d_2)]}{\lambda^2 M d_1^{\,2}} \times \exp\left[\frac{-ik(x_1^{\,2} + y_1^{\,2})}{2d_1}\right] \times \exp\left[\frac{ik\,\cos(\alpha L_1)(x^2 + y^2)}{2Md_1}\right] \times F^{-1}\{P^{(1)}(x_2, y_2)\}. \tag{B1}$$

Now, we define the distances $r_1, r_2, \ldots, r_9$ as the distance from the input source point at (x_1, y_1) to the center point in plane (ii) of each respective rod. Also, correspondingly in the output, we define $s_1, s_2, \ldots, s_9$ as the Cartesian distance from the center point of the rod in plane (iii) to the output point (x, y) at which the intensity impulse response is being calculated. Also, one can recognize the Fresnel approximation for r_1 and s_1 in Eq. (B1), namely,

$$r_1 = d_1 + \frac{x_1^{\,2} + y_1^{\,2}}{2d_1}, \tag{B2}$$

$$s_1 = d_2 + \frac{x^2 + y^2}{2d_2}. \tag{B3}$$

Substitution of Eqs. (B2) and (B3) into (B1) yields an expression for $h_{15}^{(1)}$ in which the OPDs are evident, namely,

$$h_{15}^{(1)}(x, y; x_1, y_1) = \frac{\exp[-ik(r_1 + n_1 L_1 + s_1)]}{\lambda^2 M d_1^{\,2}} \times \exp\left(\frac{ik}{2}\left\{\left[\frac{1}{d_2} + \frac{\cos(\alpha L_1)}{Md_1}\right] \times (x^2 + y^2)\right\}\right) F^{-1}\{P^{(1)}(x_2, y_2)\}. \tag{B4}$$

Likewise, Eq. (30) can be rewritten as follows:

$$h_{15}^{(4)}(x, y; x_1, y_1) = \frac{\exp[-ik(r_4 + n_1 L_4 + s_4)]}{\lambda^2 M d_1^{\,2}} \times \exp\left\{\frac{ik}{2}\left[\frac{1}{d_2} + \frac{\cos(\alpha L_4)}{Md_1}\right] \times [(x - 2D)^2 + y^2]\right\} \times F^{-1}\{P^{(4)}(x_2, y_2)\}. \tag{B5}$$

It is interesting to note that the value of

$$\left[\frac{1}{d_2} + \frac{\cos(\alpha L_4)}{Md_1}\right]$$

is approximately 8.723×10^{-3}/mm for the array that we are analyzing.

In Eq. (32) for the intensity impulse response $h_{15A}(x, y; x_1, y_1; \nu)$, in which the individual terms $h_{15}^{(m)}(x, y; x_1, y_1; \nu)$ are given, for example, by Eqs. (B4) and (B5), it is clear that we are dealing with a generalized random walk. This situation is made more evident, if we write the general form of $h_{15}^{(m)}$ as

$$h_{15}^{(m)}(x, y; x_1, y_1; \nu) = p^{(m)} \exp[-ik(r_m + n_1 L_m + s_m)], \tag{B6}$$

in which

$$p^{(m)} = F^{-1}\{P^{(m)}(x_2, y_2)\} \times \exp\left\{\frac{ik}{2}\left[\frac{1}{d_2} + \frac{\cos(\alpha L_m)}{Md_1}\right][(x - \gamma_m D)^2 + (y - \varphi_m D)^2]\right\} \Big/ (\lambda^2 M d_1^{\,2}), \tag{B7}$$

and γ_m, φ_m are chosen in accord with the distances appropriate to the labeling in Fig. 7.

Now to show that we can drop the double sum terms in Eq. (32) and on the basis of the form of Eq. (B6), we will consider the following idealized sum for U that is defined as

$$U = \sum_{m=1}^{N} \sum_{n=1}^{N} \exp[ik(\rho_m - \rho_n)], \tag{B8}$$

in which ρ_m is defined as

$$\rho_m = r_m + n_1 L_m + s_m. \tag{B9}$$

One can rewrite this sum, as follows:

$$U = N + \sum_{m=1}^{N} \sum_{\substack{n=1 \\ m \neq n}}^{N} \exp[ik(\rho_m - \rho_n)]. \tag{B10}$$

This form of sum occurs in many fields of optics. For example, in the field of speckle, we find some useful forms.[28] It is interesting to calculate the expected value of this sum in Eq. (B10) and to compare the magnitude of the triangular sum ($m \neq n$) with the first term which is N. Taking the density function for the N heights ρ_m as $f(\rho)$ and forming the expected value $\langle U \rangle$, we readily find that

$$\langle U \rangle = N + N(N-1)F(k/2\pi)F^*(k/2\pi), \tag{B11}$$

in which the characteristic function $F(k/2\pi)$ is given by the following Fourier transform, i.e.,

$$F(k/2\pi) = \int_{-\infty}^{\infty} f(\rho)\exp(-ik\rho)d\rho. \tag{B12}$$

Taking the density function of heights to be uniform, we write

$$f(\rho) = \frac{1}{\Delta\rho}\,\mathrm{rect}\left(\frac{\rho - \rho_0}{\Delta\rho}\right), \tag{B13}$$

in which ρ_0 is the center distance and $\Delta\rho$ is the range of differences in path. From substitution of Eq. (B13) into Eq. (B12) and then into Eq. (B11), we find that the expected value for the intensity, $\langle U \rangle$, is given by

$$\langle U \rangle = N + N(N-1)(\lambda/\pi\Delta\rho)^2. \tag{B14}$$

For the GRIN array, the value of $\Delta\rho$ is 256 μm and $N = 9$. Thus, the ratio of the double sum to N in Eq. (B10) is given approximately as 3×10^{-6}, which is negligible.

An equally important aspect of the OPD calculation is to consider the wavelength decorrelation implicit in Eq. (B8) and hence also in Eq. (32). Drawing again from the theory of speckle, we can write the basic expression for decorrelation as

$$\frac{\lambda^2}{\Delta\lambda} = 2\pi\Delta\rho, \tag{B15}$$

where the OPD spans approximately 256 μm. From Eq. (B15), we calculate a wavelength decorrelation on the order of 1 Å. Hence, it is clear in the analysis of this system based on the assertions made in the proof that Eq. (33) is a valid representation for the intensity-based impulse response.

References

1. H. A. Buchdahl, *Optical Aberration Coefficients* (Dover, New York, 1968).
2. E. W. Marchand, *Gradient Index Optics* (Academic, New York, 1978).
3. L. Montagnino, "Ray tracing in inhomogeneous media," J. Opt. Soc. Am. **58,** 1667–1668 (1968).
4. E. W. Marchand, "Ray tracing in gradient-index media," J. Opt. Soc. Am. **60,** 1–7 (1970).
5. A. Sharma, D. Vizia Kumar, and A. K. Ghatak, "Tracing rays through graded-index media: a new method," Appl. Opt. **21,** 984–987 (1982).
6. Lambda Research Corporation, *OSLO Optics Reference Version 6.1* (Lambda Research Corporation, Littleton, Mass., 2001).
7. P. Baues, "Huygens' principle in inhomogeneous, isotropic media and a general integral equation applicable to optical resonators," Opto-Electronics **1,** 37–44 (1969).
8. J. A. Arnaud, "Nonorthogonal optical waveguides and resonators," Bell Syst. Tech. J. **48,** 2311–2348 (1970).
9. J. A. Arnaud, "Mode coupling in first-order optics," J. Opt. Soc. Am. **61,** 751–758 (1971).
10. J. A. Arnaud, "Hamiltonian theory of beam mode propagation," in *Progress in Optics* (North-Holland, Amsterdam, 1973), Vol. 11.
11. A. E. Siegman, *Lasers* (University Science Books, Sausalito, Calif., 1986).
12. A. Yariv, "On transmission and recovery of three-dimensional image information in optical waveguides," J. Opt. Soc. Am. **66,** 301–306 (1976).
13. K. Iga, "Theory for gradient-index imaging," Appl. Opt. **19,** 1039–1043 (1980).
14. K. Iga, Y. Kokubun, and M. Oikawa, *Fundamentals of Microoptics: Distributed-Index, Microlens, and Stacked Planar Optics* (Academic, Tokyo, 1984).
15. C. Gomez-Reino and E. Larrea, "Paraxial imaging and transforming in a medium with gradient-index: transmittance function," Appl. Opt. **21,** 4271–4275 (1982).
16. C. Gomez-Reino and E. Larrea, "Pupil effect in GRIN material," Appl. Opt. **22,** 970–973 (1983).
17. C. Gomez-Reino and J. Linares, "Paraxial Fourier transforming and imaging properties of a GRIN lens with revolution symmetry: GRIN lens law," Appl. Opt. **25,** 3418–3424 (1986).
18. C. Gomez-Reino, E. Acosta, and J. Linares, "Image and Fourier transform formation by GRIN lenses: pupil effect," J. Mod. Opt. **34,** 1501–1510 (1987).
19. E. Acosta, C. Gomez-Reino, and J. Linares, "Effective radius and numerical aperture of GRIN lenses with revolution symmetry," Appl. Opt. **26,** 2952–2955 (1987).
20. C. Gomez-Reino and J. Linares, "Optical path integrals in gradient-index media," J. Opt. Soc. Am. A **4,** 1337–1341 (1987).
21. C. Gomez-Reino, M. Victoria Perez, and C. Bao, *Gradient-Index Optics: Fundamentals and Applications* (Springer, New York, 2002).
22. K. Matsushita and M. Toyama, "Unevenness of illuminance caused by gradient-index fiber arrays," Appl. Opt. **19,** 1070–1075 (1980).
23. J. D. Rees and W. Lama, "Some radiometric properties of gradient-index fiber lenses," Appl. Opt. **19,** 1065–1069 (1980).
24. NSG America, Inc., *SELFOC Lens Array (SLA) Reference Book*, (NSG America, Inc., Somerset, N.J.).
25. W. J. Smith, *Modern Optical Engineering: The Design of Optical Systems*, (McGraw-Hill, New York, 1966).
26. W. Lama, "Optical properties of GRIN fiber lens array: dependence on fiber length," Appl. Opt. **21,** 2739–2746 (1982).
27. N. George and S. Wang, "Cosinusoidal transforms in white light," Appl. Opt. **23,** 787–797 (1984).
28. N. George and A. Jain, "Space and wavelength dependence of speckle intensity," Appl. Phys. **4,** 201–212 (1974).

INSTITUTE OF PHYSICS PUBLISHING JOURNAL OF PHYSICS A: MATHEMATICAL AND GENERAL

J. Phys. A: Math. Gen. **36** (2003) 10011–10021 PII: S0305-4470(03)62751-4

Sampling theory approach to prolate spheroidal wavefunctions

Kedar Khare and Nicholas George

The Institute of Optics, University of Rochester, Rochester, NY 14627, USA

E-mail: kedar@optics.rochester.edu and ngeorge@troi.cc.rochester.edu

Received 24 April 2003, in final form 1 August 2003
Published 17 September 2003
Online at stacks.iop.org/JPhysA/36/10011

Abstract

We use the Whittaker–Shannon sampling theorem to show that the eigenvalue problem for the sinc-kernel is equivalent to a discrete eigenvalue problem. The well-known eigenfunctions, namely, the prolate spheroidal wavefunctions, their corresponding eigenvalues and the orthogonality and completeness properties are determined without invoking the prolate spheroidal differential equation. This analysis based on the sampling theorem may be used for calculating the eigenvalues and eigenfunctions of bandlimited kernels in general as we illustrate with an additional example of the sinc^2-kernel.

PACS numbers: 02.30.Gp, 02.30.Nw, 02.30.Rz, 02.30.Zz, 02.60.Cb, 02.60.Ed

1. Introduction

Prolate spheroidal wavefunctions of order zero form a complete set of bandlimited functions that are orthogonal over a finite as well as infinite interval. They are eigenfunctions of the finite Fourier transform and also that of the sinc-kernel. The spheroidal wavefunctions are the solutions of the wave equation in spheroidal co-ordinate system [1, 2]. In a series of papers, Slepian *et al* [3–7] extensively investigated the properties of the prolate spheroidal functions and their relation to the uncertainty principle. These functions have found several applications, notably in the theory of laser resonators [8, 9]. Frieden [10] has reviewed the evaluation, design and extrapolation methods for optical signals using prolate functions. These functions also find important applications in the generalized information theory for inverse problems in signal processing [11].

The purpose of this paper is to present a novel approach, based on the Whittaker–Shannon sampling theorem, to the eigenvalue problem for the sinc-kernel. Our analysis also presents an insight into the fact that the number of significant eigenvalues for the sinc-kernel problem is of the order of the space-bandwidth product or the Shannon number of the system. As pointed out by the reviewers, the present work has some similarities with the recent publications of

0305-4470/03/3910011+11$30.00

Walter and Shen [12–14]. In their work, Walter and Shen have used the natural connection between the prolate spheroids and the sinc function to develop several new formulae that are further used to construct filter banks for digitized/sampled versions of bandlimited signals. Our goal in this paper is show that the eigenfunctions for the sinc-kernel, the corresponding eigenvalues and their orthogonality and completeness properties may be determined using the sampling theorem and some related identities, with no reference to the prolate spheroidal differential equation. We also wish to emphasize that the approach presented here is useful for treating the eigenvalue problems associated with general bandlimited kernels. To that effect, an additional illustration of our method for the sinc^2-kernel is provided.

The outline of the paper is as follows. In section 2, we briefly state the Whittaker–Shannon sampling theorem and some related identities, which will be found useful in later sections. The eigenvalue problem for the sinc-kernel is treated with our new sampling theorem based method in section 3. In section 4, we derive the orthogonality and completeness properties of the eigensolutions. Finally in sections 5 and 6, we present some numerical results obtained using the method described in earlier sections. The eigenvalues and eigenfunctions are computed for both the sinc- and the sinc^2-kernels.

2. Whittaker–Shannon sampling theorem

Consider a bandlimited function $g(x)$ in $L^2(-\infty, \infty)$ such that its Fourier transform $G(f)$ is non-zero only in the interval $[-B, B]$ in the frequency domain. Then the sampling theorem [15, 16] allows us to express $g(x)$ in terms of its equally spaced samples as follows:

$$g(x) = \sum_{m=-\infty}^{\infty} g\left(\frac{m}{2B}\right) \text{sinc}(2Bx - m) \tag{1}$$

where

$$\text{sinc}(x) = \frac{\sin \pi x}{\pi x}. \tag{2}$$

The sinc functions obey the following orthogonality relation:

$$\int_{-\infty}^{\infty} dx \, \text{sinc}(2Bx - m) \, \text{sinc}(2Bx - n) = \frac{1}{2B} \delta_{m,n} \tag{3}$$

where $\delta_{m,n}$ is the Kronecker delta which is zero for $m \neq n$ and equals 1 for $m = n$. As a special case of (1), we take $g(x)$ to be the bandlimited function $\text{sinc}[2B(x - x')]$ and write

$$\sum_{m=-\infty}^{\infty} \text{sinc}(2Bx - m) \, \text{sinc}(2Bx' - m) = \text{sinc}[2B(x - x')]. \tag{4}$$

The properties (3) and (4) show that the sinc functions centred at $m/(2B)$ for integral values of m form an orthogonal and complete set over $(-\infty, \infty)$ for the class of functions bandlimited to $[-B, B]$. Using (3), we find

$$g\left(\frac{m}{2B}\right) = 2B \int_{-\infty}^{\infty} dx \, g(x) \, \text{sinc}(2Bx - m) \tag{5}$$

and

$$\int_{-\infty}^{\infty} dx \, g^2(x) = \frac{1}{2B} \sum_{m=-\infty}^{\infty} g^2\left(\frac{m}{2B}\right). \tag{6}$$

All the above properties may be proved by straightforward calculations and we have stated them here since they will be needed in the following sections.

3. The eigenvalue problem for the sinc-kernel

Consider a one-dimensional imaging system, which passes all the spatial frequencies only in the range $[-B, B]$ with equal weight. When an object $O(x)$ in $[-L, L]$ is imaged using this system, the resultant field distribution $I(x)$ in the image plane is described by

$$\begin{aligned} I(x) &= \int_{-B}^{B} \mathrm{d}f\, \mathrm{e}^{\mathrm{i}2\pi f x} \int_{-L}^{L} \mathrm{d}x'\, \mathrm{e}^{-\mathrm{i}2\pi f x'} O(x') \\ &= 2B \int_{-L}^{L} \mathrm{d}x'\, \mathrm{sinc}[2B(x-x')] O(x'). \end{aligned} \tag{7}$$

The inversion problem of reconstructing $O(x)$ from $I(x)$ has been well studied in the literature in terms of the orthogonal set of eigenfunctions for the sinc-kernel [17]. These eigenfunctions happen to be the prolate spheroidal wavefunctions. The imaging situation described above, however, has no obvious connection with the prolate spheroidal differential equation satisfied by the eigenfunctions. In view of this, it is our aim in this paper to show that it is possible to arrive at the eigenfunctions of the sinc-kernel in an alternative way. The method presented below is direct (non-iterative) and is based on the sampling identities stated in section 2.

We start by considering the following problem:

$$\lambda_n \phi_n(x) = \int_{-L}^{L} \mathrm{d}x'\, \mathrm{sinc}[2B(x-x')] \phi_n(x'). \tag{8}$$

The above equation is a homogeneous Fredholm integral equation of the second kind with $\phi_n(x)$ and λ_n being the eigenfunctions and the associated eigenvalues, respectively. The kernel of the equation is symmetric and square integrable. The properties of eigenfunctions associated with symmetric kernels [18] will not be used for the purpose of the present section where we convert equation (8) to an equivalent discrete eigenvalue problem.

Using (4) we expand $\mathrm{sinc}[2B(x-x')]$ in (8) as a sampling series to get

$$\begin{aligned} \lambda_n \phi_n(x) &= \int_{-L}^{L} \mathrm{d}x' \sum_{m=-\infty}^{\infty} \mathrm{sinc}(2Bx-m)\, \mathrm{sinc}(2Bx'-m) \phi_n(x') \\ &= \sum_{m=-\infty}^{\infty} \lambda_n \phi_n\left(\frac{m}{2B}\right) \mathrm{sinc}(2Bx-m). \end{aligned} \tag{9}$$

The second step above follows from the integral equation (8). From (9), it is clear that the eigenfunctions $\phi_n(x)$ satisfy the sampling theorem (1) and hence are bandlimited to $[-B, B]$. Starting from:

$$\lambda_n \phi_n\left(\frac{m}{2B}\right) = \int_{-L}^{L} \mathrm{d}x'\, \mathrm{sinc}\left[2B\left(\frac{m}{2B}-x'\right)\right] \phi_n(x') \tag{10}$$

we now expand $\phi_n(x')$ as a sampling series to obtain

$$\begin{aligned} \lambda_n \phi_n\left(\frac{m}{2B}\right) &= \int_{-L}^{L} \mathrm{d}x'\, \mathrm{sinc}(2Bx'-m) \sum_{k=-\infty}^{\infty} \phi_n\left(\frac{k}{2B}\right) \mathrm{sinc}(2Bx'-k) \\ &= \sum_{k=-\infty}^{\infty} A_{mk} \phi_n\left(\frac{k}{2B}\right) \end{aligned} \tag{11}$$

where

$$A_{mk} = \int_{-L}^{L} \mathrm{d}x'\, \mathrm{sinc}(2Bx'-m)\, \mathrm{sinc}(2Bx'-k). \tag{12}$$

The integral equation (8) is thus equivalent to the discrete eigenvalue problem for the infinite matrix A. We point out that if we were to replace the sinc-kernel in (8) by a general bandlimited kernel $h(x - x')$ that may be expressed as a sampling series, the conclusion regarding the bandlimited nature of the eigenfunctions will still hold and it is also possible to formulate the discrete eigenvalue problem as in equations (10)–(12). Note that the eigenvalues of equation (8) are the same as that of the matrix A, and the elements of the corresponding discrete eigenvectors are the samples of the continuous eigenfunctions $\phi_n(x)$. The continuous eigenfunctions $\phi_n(x)$ can thus be determined from the discrete eigenvectors of A by using the sampling theorem as in (1). The knowledge of the fact that the solutions of (8) happen to be the prolate spheroidal functions is therefore not necessary for the computation of the eigenvalues and the eigenfunctions. Our study of the literature shows that the computation of prolate spheroids and their eigenvalues is performed using either asymptotic solutions of the prolate spheroidal differential equation [19–22] or Bouwkamp's method of Legendre series [23, 24]. Both these methods rely on the use of the prolate spheroidal differential equation. The sampling theory approach presented above thus provides an interesting alternative to the computation of prolate spheroids. From (12) we see that the matrix elements A_{mk} fall off to zero as the main lobes of the corresponding sinc-functions go beyond the range of integration $[-L, L]$, i.e. when $|m|, |k| > 2BL$. Clearly, only a square sub-matrix of A with the dimension of the order of the space-bandwidth product $(4BL)$ has elements with significant magnitude, so that, when calculating the eigenvalues by equating determinant$(A - \lambda I)$ to zero, it is clear that the number of significant eigenvalues for the sinc-kernel is at most of the order of $(4BL)$, the remaining eigenvalues being close to zero. This property has important implications in the solution of inverse problems (see, for example, [11]). Later in section 5 we will compare the trace of the matrix A with the sum of highest $c \sim (4BL)$ (Shannon number) calculated eigenvalues to illustrate this point. A much more quantitative analysis of the number of significant eigenvalues is presented in [5, 14].

4. Orthogonality and completeness properties of the eigenfunctions

The orthogonality and completeness properties of the prolate spheroids are well known and have been treated in detail before [3]. However, in the spirit of this paper we take a different route to proving them, once again by means of the sampling identities stated in section 2. We note that the proofs of orthogonality and completeness properties given below are specific to the sinc-kernel problem. For brevity, we denote the discrete eigenvectors of the matrix A by $u_n = \left[\ldots \phi_n\left(\frac{m}{2B}\right) \ldots\right]^T$, with T standing for the transpose of the row vector. The matrix A in (12) is real symmetric, so that its eigenvalues and eigenvectors must be real. Clearly, the eigenfunctions $\phi_n(x)$ obtained from the elements of u_n using the sampling theorem are also real. Note that the matrix A is also centrosymmetric with respect to the element A_{00}. It is known that the eigenvectors of symmetric centrosymmetric matrices are either symmetric or skew symmetric [25]. The corresponding continuous eigenfunctions $\phi_n(x)$ are therefore either even or odd. We assume the eigenfunctions $\phi_n(x)$ to be normalized to 1 over $(-\infty, \infty)$:

$$\int_{-\infty}^{\infty} \mathrm{d}x\, \phi_n^2(x) = 1 = \frac{1}{2B} \sum_{m=-\infty}^{\infty} \phi_n^2\left(\frac{m}{2B}\right). \tag{13}$$

The second equality above follows from (6) since $\phi_n(x)$ is bandlimited. The real symmetric nature of A assures that the matrix A may be factored in form $A = UA_dU^T$ such that A_d is a diagonal matrix with U obeying:

$$U^TU = 2B\,\hat{1} = UU^T. \tag{14}$$

The columns of U are formed by the eigenvectors u_n. The factor $2B$ above occurs due to the choice of normalization in (13). The non-degeneracy of eigenvalues for the sinc-kernel is known [3] and this fact along with the nature of A once again confirms (14). Equation (14) may be written explicitly in terms of the samples of eigenfunctions as follows:

$$\sum_{m=-\infty}^{\infty} \phi_n\left(\frac{m}{2B}\right)\phi_l\left(\frac{m}{2B}\right) = 2B\delta_{n,l} \tag{15}$$

and

$$\sum_{n=0}^{\infty} \phi_n\left(\frac{m}{2B}\right)\phi_n\left(\frac{k}{2B}\right) = 2B\delta_{m,k}. \tag{16}$$

Equations (15) and (16) above are simply the restatements of the first and the second equalities in (14), respectively. Walter and Shen have obtained equations (15) and (16) in their recent publications [12–14] using the well-known properties of prolate spheroids. Here, we have arrived at these relations independently as a consequence of the real symmetric nature of the matrix A defined in (12). We now proceed to prove the orthogonality and completeness properties of the eigensolutions.

4.1. Orthogonality and completeness over the bandlimited subspace of $L^2(-\infty, \infty)$

Using the sampling theorem (1) and the orthogonality condition (3), we can write

$$\begin{aligned}\int_{-\infty}^{\infty} \mathrm{d}x\, \phi_n(x)\phi_l(x) &= \sum_{m=-\infty}^{\infty}\sum_{k=-\infty}^{\infty} \phi_n\left(\frac{m}{2B}\right)\phi_l\left(\frac{k}{2B}\right)\frac{1}{2B}\delta_{m,k} \\ &= \frac{1}{2B}\sum_{m=-\infty}^{\infty} \phi_n\left(\frac{m}{2B}\right)\phi_l\left(\frac{m}{2B}\right) \\ &= \delta_{n,l}. \end{aligned} \tag{17}$$

The last step in (17) follows from (15). The orthogonality of the discrete eigenvectors is thus equivalent to the orthogonality of the continuous eigenfunctions over $(-\infty, \infty)$. Now consider

$$\sum_{n=0}^{\infty}\phi_n(x)\phi_n(x') = \sum_{m=-\infty}^{\infty}\sum_{k=-\infty}^{\infty}\left[\sum_{n=0}^{\infty}\phi_n\left(\frac{m}{2B}\right)\phi_n\left(\frac{k}{2B}\right)\right]\mathrm{sinc}(2Bx - m)\,\mathrm{sinc}(2Bx' - k). \tag{18}$$

The sum over index n is simplified by (16) and additionally using (4) we get

$$\sum_{n=0}^{\infty}\phi_n(x)\phi_n(x') = 2B\,\mathrm{sinc}[2B(x - x')]. \tag{19}$$

The above equation is just a restatement of the Mercer's theorem [18] with normalization of eigenfunctions as defined in (13). For an arbitrary function $g(x)$ that is bandlimited to $[-B, B]$, we therefore have

$$\int_{-\infty}^{\infty} \mathrm{d}x\, g(x)\sum_{n=0}^{\infty}\phi_n(x)\phi_n(x') = g(x'). \tag{20}$$

Thus, completeness of the eigensolutions over the class of functions in $L^2(-\infty, \infty)$ bandlimited to $[-B, B]$ is proved since an arbitrary bandlimited function $g(x)$ of this class may be represented as a linear combination of eigenfunctions $\phi_n(x)$.

4.2. Orthogonality and completeness over $L^2(-L, L)$

The dual orthogonality over infinite as well as finite intervals is a special property of the eigensolutions. It is well known that the eigenfunctions of a symmetric kernel associated with distinct eigenvalues are orthogonal over the range of integration $(-L, L)$. Nevertheless, we prove this property below using sampling identities. Consider:

$$\begin{aligned}\int_{-L}^{L} \mathrm{d}x\, \phi_n(x)\phi_l(x) &= \sum_{m=-\infty}^{\infty} \phi_n\left(\frac{m}{2B}\right) \int_{-L}^{L} \mathrm{d}x\, \mathrm{sinc}(2Bx - m)\phi_l(x) \\ &= \lambda_l \sum_{m=-\infty}^{\infty} \phi_n\left(\frac{m}{2B}\right) \phi_l\left(\frac{m}{2B}\right) \\ &= 2B\lambda_l \delta_{n,l}. \end{aligned} \tag{21}$$

To prove completeness over $L^2(-L, L)$ we start by writing equation (8) as

$$2B\lambda_n \phi_n(x) = \int_{-L}^{L} \mathrm{d}x'\, \phi_n(x') \int_{-B}^{B} \mathrm{d}f'\, \mathrm{e}^{\mathrm{i}2\pi f'(x-x')}. \tag{22}$$

Denoting the finite Fourier transform of $\phi_n(x)$ by

$$\Phi_n(f) = \int_{-L}^{L} \mathrm{d}x\, \phi_n(x)\, \mathrm{e}^{-\mathrm{i}2\pi f x} \tag{23}$$

and using (22), we see that the finite Fourier transform satisfies:

$$\frac{B}{L}\lambda_n \Phi_n(f) = \int_{-B}^{B} \mathrm{d}f'\, \Phi_n(f')\, \mathrm{sinc}[2L(f - f')]. \tag{24}$$

Equation (24) above is simply a scaled version of equation (8) and we thus conclude that

$$\Phi_n(f) = \int_{-L}^{L} \mathrm{d}x\, \phi_n(x)\, \mathrm{e}^{-\mathrm{i}2\pi f x} = \alpha_n \phi_n\left(\frac{Lf}{B}\right). \tag{25}$$

Here, α_n is a constant for the particular $\phi_n(x)$under consideration. The factor (L/B) in the argument of the last term above adjusts the scaling appropriately. It may be shown that $\alpha_n = i^n(2L\lambda_n)^{1/2}$, however, this value is of no consequence in what follows.

Using (25) and the identity (19), we observe that

$$\int_{-L}^{L} \mathrm{d}x\, \mathrm{e}^{-\mathrm{i}2\pi f x} \sum_{n=0}^{\infty} \frac{1}{\alpha_n} \phi_n(x)\phi_n\left(\frac{Lf'}{B}\right) = 2B\, \mathrm{sinc}[2L(f - f')]. \tag{26}$$

This result suggests the expansion:

$$\frac{L}{B} \sum_{n=0}^{\infty} \frac{1}{\alpha_n} \phi_n(x)\phi_n\left(\frac{Lf'}{B}\right) = \exp(\mathrm{i}2\pi f' x) \quad |x| < L. \tag{27}$$

This result has also been obtained in [24]. We now note that any function $p(x)$ in $L^2(-L, L)$ may be expressed as a Fourier expansion:

$$p(x) = \int_{-\infty}^{\infty} \mathrm{d}f\, P(f)\, \mathrm{e}^{\mathrm{i}2\pi f x} \tag{28}$$

and in view of (27) can thus be expressed as a linear combination of $\phi_n(x)$. The completeness in $L^2(-L, L)$ is thus proved. It is interesting to note that, the occurrence of the sinc-function as the kernel of the integral equation as well as the interpolation function in the sampling formula plays an important role in the orthogonality and completeness proofs above. This offers an explanation to the fact that among the functions bandlimited to $[-B, B]$, only the

Table 1. Ten largest eigenvalues for the sinc-kernel calculated using the sampling theorem based method for $c = 10$. The calculations are performed with the dimension N of the truncated matrix A taken equal to 51, 201 and 501, respectively. For maintaining consistency with the literature [19], values of $(2B\lambda_n)$are given in the table below.

n	$N = 51$	$N = 201$	$N = 501$
0	1.0000×10^{000}	1.0000×10^{000}	1.0000×10^{000}
1	1.0000×10^{000}	1.0000×10^{000}	1.0000×10^{000}[a]
2	9.9989×10^{-001}	9.9989×10^{-001}	9.9989×10^{-001}
3	9.9767×10^{-001}	9.9784×10^{-001}	9.9788×10^{-001}
4	9.7444×10^{-001}	9.7446×10^{-001}	9.7446×10^{-001}
5	8.1176×10^{-001}	8.2173×10^{-001}	8.2377×10^{-001}
6	4.4015×10^{-001}	4.4015×10^{-001}	4.4015×10^{-001}
7	1.0194×10^{-001}	1.0973×10^{-001}	1.1129×10^{-001}
8	1.4903×10^{-002}	1.4920×10^{-002}	1.4920×10^{-002}
9	1.1073×10^{-003}	1.2655×10^{-003}	1.2952×10^{-003}

[a] The eigenvalues corresponding to $n = 0, 1$ are not degenerate. Our calculations show that they differ in sixth significant digit. All the eigenvalues are less than one.

prolate spheroids enjoy the curious dual orthogonality property over finite as well as infinite intervals [3, 10]. We conclude this section by calculating the trace of the matrix A, which equals the total sum of its eigenvalues.

$$\mathrm{tr}(A) = \int_{-L}^{L} \mathrm{d}x \sum_{m=-\infty}^{\infty} \mathrm{sinc}^2(2Bx - m) = 2L. \tag{29}$$

We have used the special case $x = x'$ of the identity (4) for evaluation of the summation above.

5. Numerical computation of eigenfunctions and eigenvalues for the sinc-kernel

In this section, we illustrate the sampling theorem based method presented in section 3 for computation of the eigenfunctions. The Shannon number c in the literature on prolate spheroids [3] in our notation equals $2\pi BL$. We choose $L = 1$ and determine the eigenvalues and eigenfunctions for the special case $c = 10$. The reason for choosing this particular value of c is that, in the literature [1, 10, 21, 22], different asymptotic expansions are suggested for calculating the spheroidal functions depending on whether $c < 10$ or $c > 10$. Our method explained before is independent of the magnitude of c, apart from requiring the dimension of the truncated version of matrix A to be sufficiently larger than c. The matrix elements A_{mk} defined in (12) were first calculated by numerical integration using Gaussian quadrature (with the tolerance set to 10^{-10}) and the eigenvalue problem $Au_n = \lambda_n u_n$ was solved for a truncated version of the matrix A. The eigenvectors thus obtained were then interpolated with sinc-function according to the sampling theorem (1). We have calculated the first ten eigenvalues for truncated versions of matrix A with dimension $N = 51, 101, 151, 201, \ldots, 501$. In table 1, we show the ten largest eigenvalues for the cases $N = 51, 201, 501$, respectively. We observe that for $N = 151$ and beyond, the eigenvalues corresponding to the even orders have stabilized up to five significant digits and match with those obtained by Slepian and Sonneblick [19] using asymptotic expansions. The eigenvalues corresponding to the odd orders barring $n = 1$, on the other hand, have kept increasing progressively in third or fourth significant digit. For $N = 501$, the eigenvalues corresponding to orders $n = 3, 5, 7, 9$ match those in [19] up to

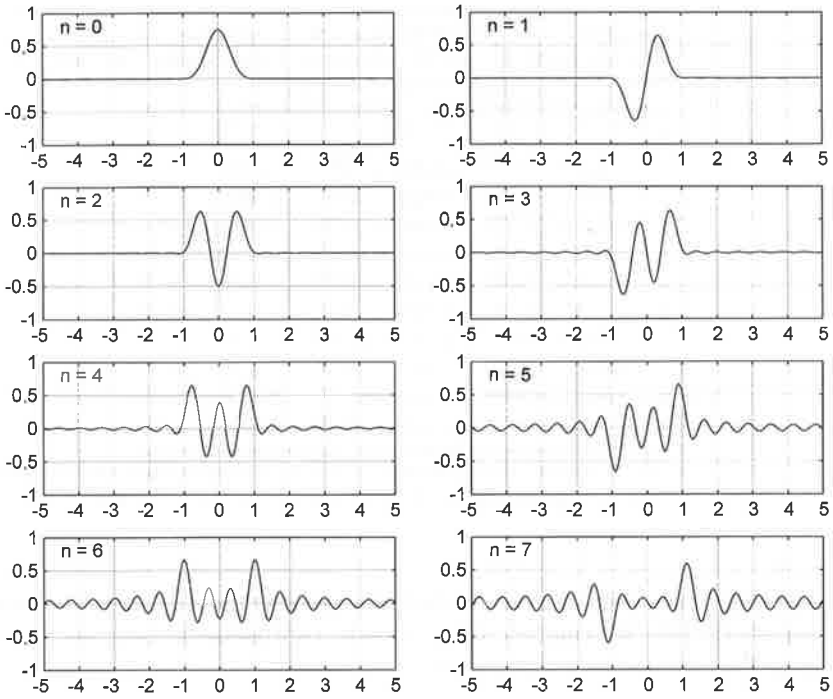

Figure 1. First eight eigenfunctions for the sinc-kernel calculated using the sampling theorem based method. The functions are even/odd for even/odd index n. The eigenfunction corresponding to index n has n zeros in the interval $[-1, 1]$.

4, 2, 2 and 2 significant digits, respectively. A further analysis is necessary for deciding the dimension of the matrix A for given accuracy requirements and the topic is beyond the scope of this paper. The sharp fall off in the eigenvalues beyond $n > 2c/\pi$ is evident. The sum of the first ten eigenvalues for all the cases $N = 51, \ldots, 501$, respectively is over 99% of the value of the trace as determined by equation (29). The first eight eigenfunctions calculated by interpolating the corresponding discrete eigenfunctions for the case $N = 501$ are shown in figure 1. As is well known, one sees that the functions $\phi_n(x)$ are even/odd for even/odd values of n. Also, $\phi_n(x)$ has n zeros in $[-1, 1]$.

6. Eigenvalue problem for the sinc^2-kernel

In this section we illustrate the general nature of our sampling theorem based method with an example of the eigenvalue problem for the sinc^2-kernel:

$$\mu_n \psi_n(x) = \int_{-L}^{L} \mathrm{d}x' \, \mathrm{sinc}^2[B(x - x')]\psi_n(x). \tag{30}$$

This problem has been studied before in the context of incoherent imaging systems [26 and references therein] using iterative methods to obtain an orthogonal set of eigenfunctions over $[-L, L]$ and approximate expressions for the eigenvalues have been presented. We believe that a direct method based on sampling theorem for general bandlimited kernels has not appeared in the literature. We have used B instead of $2B$ in the argument of sinc^2 in order to maintain the same bandwidth as in the sinc example. Following the analysis parallel to that presented

Table 2. Ten largest eigenvalues for the sinc^2-kernel calculated using the sampling theorem based method for $c = 10$. The calculations are performed with the dimension N of the truncated matrix A taken equal to 51, 201 and 501, respectively. Values of $(B\mu_n)$ are given in the table below.

n	$N = 51$	$N = 201$	$N = 501$
0	8.8802×10^{-001}	8.8802×10^{-001}	8.8802×10^{-001}
1	7.3441×10^{-001}	7.3441×10^{-001}	7.3441×10^{-001}
2	5.8579×10^{-001}	5.8579×10^{-001}	5.8579×10^{-001}
3	4.3822×10^{-001}	4.3822×10^{-001}	4.3822×10^{-001}
4	2.9652×10^{-001}	2.9652×10^{-001}	2.9652×10^{-001}
5	1.6363×10^{-001}	1.6363×10^{-001}	1.6363×10^{-001}
6	6.1095×10^{-002}	6.1097×10^{-002}	6.1097×10^{-002}
7	1.3420×10^{-002}	1.3426×10^{-002}	1.3426×10^{-002}
8	1.8151×10^{-003}	1.8132×10^{-003}	1.8132×10^{-003}
9	1.6746×10^{-003}	1.6846×10^{-003}	1.6848×10^{-003}

in equations (10)–(12), it is easy to see that for the solution of (30), one needs to solve the equivalent discrete eigenvalue problem for the infinite matrix A' with elements defined by

$$A'_{mk} = \int_{-L}^{L} \mathrm{d}x' \, \text{sinc}^2(Bx' - m/2) \, \text{sinc}(2Bx' - k). \tag{31}$$

The properties of the eigenfunctions $\psi_n(x)$will not be discussed here, as they have already appeared in literature [26] and also since the purpose of this example is simply to illustrate the application of the sampling theorem based method to kernels other than the sinc-kernel. We however note that, the eigenfunctions $\psi_n(x)$ do not enjoy the special properties of dual orthogonality, as is the case with prolate spheroids. To calculate the trace of matrix A', we write the sampling expansion for the sinc^2 function:

$$\text{sinc}^2[B(x - x')] = \sum_{m=-\infty}^{\infty} \text{sinc}^2(Bx' - m/2) \, \text{sinc}(2Bx - m). \tag{32}$$

Using the special case $x = x'$ of (32), we can write

$$\text{tr}(A') = \int_{-L}^{L} \mathrm{d}x \sum_{m=-\infty}^{\infty} \text{sinc}^2(Bx - m/2) \, \text{sinc}(2Bx - m) = 2L. \tag{33}$$

For numerical computations we have used the same values $L = 1, c = 2\pi BL = 10$ as in the previous section. The matrix elements as defined in (31) were once again computed using a Gaussian quadrature and the eigenvalue problem $A'w_n = \mu_n w_n$ was solved for the truncated versions of matrix A' having dimension $N = 51, 101, 151, \ldots, 501$. The ten largest eigenvalues for each of the three cases $N = 51, 201, 501$ are shown in table 2. We observe that for the cases $N = 301$ and beyond, all the ten eigenvalues have stabilized to five significant digits. The sum of the first ten eigenvalues for all the cases $N = 51, \ldots, 501$ is over 99% of the value of trace as determined by equation (33). The discrete eigenvectors w_n corresponding to the case $N = 501$ are interpolated using the sampling theorem (1) and the first eight continuous eigenfunctions are plotted in figure 2. The eigenfunctions are qualitatively similar to the sinc-kernel problem and the eigenvalues are seen to fall off almost linearly with the order index n.

All the computations in sections 5 and 6 were performed using standard routines available in the mathematical software MATLAB v. R12.

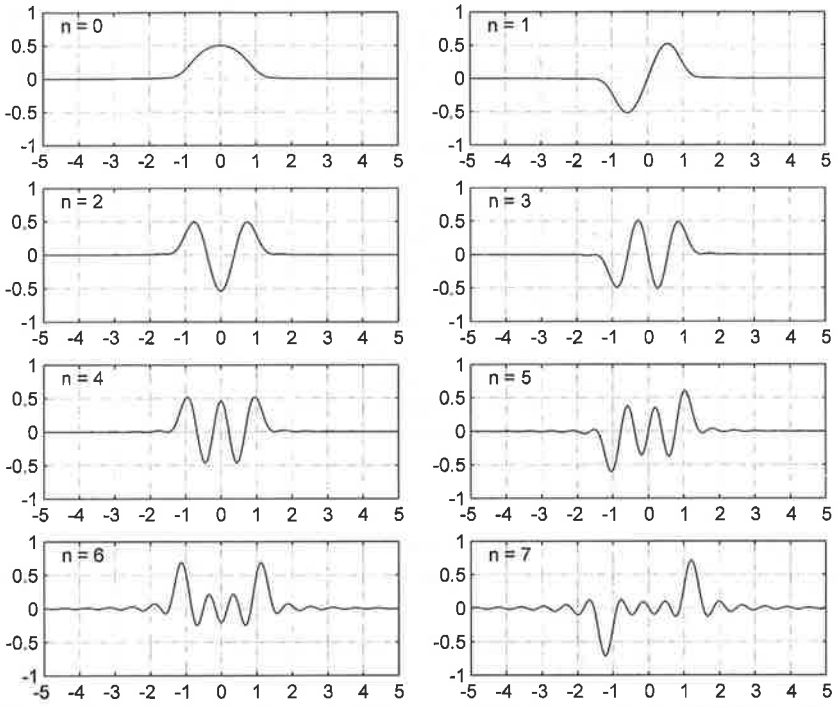

Figure 2. First eight eigenfunctions for the sinc^2-kernel calculated using the sampling theorem based method. The functions are even/odd for even/odd index n. The eigenfunction corresponding to index n has n zeros in the interval $[-1, 1]$.

7. Conclusion

In summary, we have treated the eigenvalue problem for the sinc-kernel with a novel approach, based on the Whittaker–Shannon sampling theorem. First, the eigenvalue problem (8) is converted to an equivalent discrete eigenvalue problem for the infinite matrix A defined in (12). It is shown that the eigenfunctions (prolate spheroidal wavefunctions) and the associated eigenvalues may be computed without any reference to the prolate spheroidal differential equation. The orthogonality and completeness properties of the eigenfunctions are also proved using sampling identities. It is pointed out that the appearance of the sinc-function as a kernel of the integral equation as well as the interpolation function in the sampling formula is important for the dual orthogonality of prolate spheroidal functions over finite as well as infinite intervals. The sampling theorem based method is illustrated with the computation of eigenfunctions and eigenvalues for the sinc-kernel with Shannon number $c = 10$. The method of calculating eigenfunctions and eigenvalues presented in this paper is applicable to general bandlimited kernels as illustrated by the sinc^2-kernel example.

Acknowledgments

This research was supported in part by the Army Research Office. The authors wish to thank the reviewers for their comments and for bringing to our attention the work of G G Walter and X A Shen.

References

[1] Flammer C 1957 *Spheroidal Wave Functions* (Stanford CA, University Press)
[2] Stratton J A, Morse P M, Chu L J, Little J D C and Corbato F J 1956 *Spheroidal Wave Functions* (New York: Wiley)
[3] Slepian D and Pollak H O 1961 Prolate spheroidal wave functions, Fourier analysis and uncertainty–I *Bell Syst. Tech. J.* **40** 43–63
[4] Landau H J and Pollak H O 1961 Prolate spheroidal wave functions, Fourier analysis and uncertainty—II *Bell Syst. Tech. J.* **40** 65–84
[5] Landau H J and Pollak H O 1962 Prolate spheroidal wave functions, Fourier analysis and uncertainty—III: the dimension of the space of essentially time- and band-limited signals *Bell Syst. Tech. J.* **41** 1295–336
[6] Slepian D 1964 Prolate spheroidal wave functions, Fourier analysis and uncertainty—IV: extensions to many dimensions; generalized prolate spheroidal functions *Bell Syst. Tech. J.* **43** 3009–57
[7] Slepian D 1978 Prolate spheroidal wave functions, Fourier analysis and uncertainty—V: the discrete case *Bell Syst. Tech. J.* **57** 1371–430
[8] Boyd G D and Gordon J P 1961 Confocal multimode resonator for millimetre through optical wavelength masers *Bell Syst. Tech. J.* **41** 489–508
[9] Boyd G D and Kogelnik H 1962 Generalized confocal resonator theory *Bell Syst. Tech. J.* **42** 1347–69
[10] Frieden B R 1971 Evaluation, design and extrapolation methods for optical signals, based on the use of prolate functions *Progress in Optics* vol 9 ed E Wolf (Amsterdam: North-Holland)
[11] Pike E R, McWhirter J G, Bertero M and de Mol C 1984 Generalized information theory for inverse problems in signal processing *Proc. IEE* **131** 660–7
[12] Walter G G and Shen X A 2003 Recovery of digitized signals using Slepian functions *ICASSP (IEEE)* vol VI pp 241–4
[13] Walter G G and Shen X A 2003 Sampling with prolate spheroidal functions *Am. Math. Soc.* Abstract 983 41–227
[14] Walter G G and Shen X A 2002 Sampling with prolate spheroidal wave functions *J. Sampling Theory Signal Image Process.* **2** 25–52
[15] Whittaker E T 1915 On the functions which are represented by the expansions of the interpolation theory *Proc. Roy. Soc. Edinburgh* **35** 181–94
[16] Shannon C E 1949 Communication in the presence of noise *Proc. IRE* **37** 10–21
[17] Bertero M, de Mol C and Viano G A 1979 The stability of inverse problems *Inverse Scattering Problems in Optics* ed H P Baltes (Berlin: Springer)
[18] Courant R and Hilbert D 1953 *Methods of Mathematical Physics* (New York: Interscience)
[19] Slepian D and Sonnenblick E 1965 Eigenvalues associated with prolate spheroidal wave functions of zero order *Bell. Syst. Tech. J.* **44** 1745–59
[20] Slepian D 1965 Some asymptotic expansions for prolate spheroidal wave functions *J. Math. Phys.* **44** 99–140
[21] Jen L and Hu C 1983 Spheroidal wave functions of large frequency parameters c = kf, the radiation fields of a metallic prolate spheroid excited by any circumferential slot *IEEE Trans. Antennas Propag.* **AP-31** 382–9
[22] Hu C 1986 Prolate spheroidal wave functions of large frequency parameters c = kf and their applications in electromagnetic theory *IEEE Trans. Antennas Propag.* **AP-34** 114–9
[23] Bouwkamp C J 1947 On spheroidal wave functions of order zero *J. Math. Phys.* **26** 79–92
[24] Xiao H, Rokhlin V and Yarvin N 2001 Prolate spheroidal wavefunctions, quadrature and interpolation *Inverse Probl.* **17** 805–38
[25] Cantoni A and Butler P 1976 Eigenvalues and eigenvectors of symmetric centrosymmetric matrices *Linear Algebr. Appl.* **13** 275–88
[26] Gori F and Palma C 1975 On the eigenvalues of the sinc^2 kernel *J. Phys. A: Math. Gen.* **8** 1709–19

Computational imaging with the logarithmic asphere: theory

Wanli Chi and Nicholas George

The Institute of Optics, University of Rochester, Rochester, New York 14627

Received May 29, 2003; revised manuscript received August 7, 2003; accepted August 12, 2003

A theory for an integrated system is described that combines a logarithmic aspheric imaging lens with maximum-entropy digital processing to extend the depth of field ten times over that of a conventional lens and to provide near-diffraction-limited resolution. Two types of logarithmic aspheres are derived that are circularly symmetric lenses with controlled continuous radial variation of focal length. The details of an iterative maximum-entropy algorithm are also presented. The properties of convergence and speed of the algorithm are greatly improved by introducing a metric parameter to adjust the weight of different pixel values of the recovered picture in each loop properly. © 2003 Optical Society of America

OCIS codes: 110.0110, 100.1830, 100.3010, 050.1940.

1. INTRODUCTION

In conventional photography, it is well known that objects are sharply in focus only over a limited distance known as the depth of field. The depth of field is inversely proportional to the square of the numerical aperture of the lens for diffraction-limited imaging. Prior research on extending the depth of field includes apodization by a weighted zone plate[1] and processing of the combination of slices of images from different object depths.[2] In the apodization method, the trade-off is decreased resolution and illumination for increased depth of field. With the multiple image slices, there is an increased complexity in the image-collection process. Alternatively, novel imaging systems have been described in the literature that purposefully blur the image with a phase mask at the aperture of the lens.[3–6] Thereafter, one uses digital processing of the internal image to extend the depth of field. These integrated computational imaging systems greatly alleviate the resolution, illumination, and image-gathering problems of earlier systems.

In this paper we describe an innovation in the class of lenses called logarithmic aspheres. Moreover, we describe a maximum-entropy algorithm that is specifically tailored to the depth-of-field configuration. Starting with nonparaxial scalar diffraction theory and with the constraint of circular symmetry in the lens design, we find the phase transmission of the lens that has radially varying focal length. At any object distance within the design range, there is always a circular annulus that contributes to sharp imaging, and the remainder of the lens causes blur. Digital processing of the intermediate blurred image caused by the logarithmic asphere will yield clear pictures with extended depth of field. The digital processing in this application is basically a deconvolution operation, which is a notoriously ill-defined problem. In optics, maximum-entropy methods were first described by Frieden,[7] and excellent results in image processing have been reported by Burch *et al.*[8]; several other authors have also made contributions in this field.[9–11] Our aim is to obtain a maximum-entropy algorithm that has excellent convergence and speed. We describe a new computational method carefully and fully.

2. LENS THEORY

A. Phase Delay of a Logarithmic Asphere

Consider the basic imaging lens setup in Fig. 1. The point source S, which is located at a distance s away from the lens at plane I, forms a blurred image at plane II at a distance t on the other side of the lens. Assume that the lens has a ring-type aperture, with radius from δR to R, where R is the radius of lens, and $0 \leqslant \delta R < R$. The center portion of the lens, meaning from axis to δR, is blocked by an opaque disk. Clearly, $\delta R = 0$ is the special case of full aperture.

The scalar electric field E_θ at the plane of the lens for a point source located at S can be expressed as

$$E_\theta = \frac{i}{\lambda_0}\frac{A}{\sqrt{\rho^2 + s^2}}\exp\left(-i\frac{2\pi}{\lambda_0}\sqrt{\rho^2 + s^2}\right), \qquad (1)$$

where $A\,\delta(x', y')$ is the electric field distribution at the object plane, λ_0 is the wavelength of light in vacuum, and $\exp(+i\omega t)$ dependence is used.

To facilitate fabrication of the lens, we choose a circularly symmetric phase function for the lens. From scalar diffraction theory, the point-spread function, i.e., the intensity of the image at plane II for the point source S, is given by

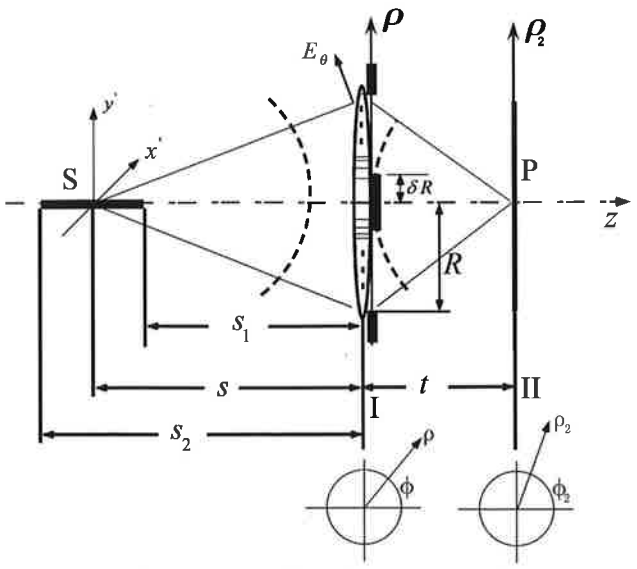

Fig. 1. Diagram of logarithmic asphere lens.

$$I(\rho_2;s) = \left| \int_{\delta R}^{R} \rho d\rho \int_0^{2\pi} d\phi \frac{i}{\lambda_0} \frac{A}{\sqrt{\rho^2 + s^2}} \frac{i}{\lambda_0} \times \frac{t}{[(\rho\cos\phi - \rho_2\cos\phi_2)^2 + (\rho\sin\phi - \rho_2\sin\phi_2)^2 + t^2]^{1/2}} \times \exp\left\{ -i\frac{2\pi}{\lambda_0}\sqrt{\rho^2 + s^2} - i\phi(\rho) - i\frac{2\pi}{\lambda_0}[(\rho\cos\phi - \rho_2\cos\phi_2)^2 + (\rho\sin\phi - \rho_2\sin\phi_2)^2 + t^2]^{1/2} \right\} \right|^2, \quad (2)$$

where (ρ,ϕ) and (ρ_2, ϕ_2) are the polar coordinates at planes I and II respectively, and $\phi(\rho)$ is the phase delay of the circular symmetric lens.

In Eq. (2), for the distance term we make the usual approximation for the amplitude term that $(\rho^2 + s^2)^{1/2} \approx s$. For the imaging lens, the point-spread function should be confined to a small region at plane II, so we can make the following approximation in the phase term:

$$(\rho\cos\phi - \rho_2\cos\phi_2)^2 + (\rho\sin\phi - \rho_2\sin\phi_2)^2 + t^2 \approx \rho^2 + t^2,$$

$$[(\rho\cos\phi - \rho_2\cos\phi_2)^2 + (\rho\sin\phi - \rho_2\sin\phi_2)^2 + t^2]^{1/2} \approx \sqrt{\rho^2 + t^2} - \frac{\rho\rho_2\cos(\phi - \phi_2)}{\sqrt{\rho^2 + t^2}}. \quad (3)$$

Substitution of expression (3) and integration over ϕ using a well-known Bessel function identity yield the following result for the point-spread function of the lens:

$$I(\rho_2;s) \approx \left| \int_{\delta R}^{R} \frac{2\pi A}{{\lambda_0}^2} \rho \frac{1}{s} \exp\left[-i\frac{2\pi}{\lambda_0}\sqrt{\rho^2 + s^2} - i\phi(\rho) - i\frac{2\pi}{\lambda_0}\sqrt{\rho^2 + t^2} \right] J_0\left(2\pi \frac{\rho\rho_2}{\lambda_0\sqrt{\rho^2 + t^2}} \right) d\rho \right|^2. \quad (4)$$

The on-axis intensity for this point-spread function can be found by setting $\rho_2 = 0$ in expression (4); i.e.,

$$I(\rho_2 = 0; s) = \frac{4\pi^2 t^2 A^2}{{\lambda_0}^4 s^2} \left| \int_{\delta R}^{R} \frac{\rho}{\sqrt{\rho^2 + t^2}} \exp\left[-i\frac{2\pi}{\lambda_0}\sqrt{\rho^2 + s^2} - i\phi(\rho) - i\frac{2\pi}{\lambda_0}\sqrt{\rho^2 + t^2} \right] d\rho \right|^2. \quad (5)$$

In the lens design the natural illumination is considered; i.e., the on-axis intensity is inversely proportional to the object distance squared. This naturally takes into account the drop in intensity that is due to farther object distances. So we need

$$I(\rho_2 = 0; s)s^2 = \frac{4\pi^2 t^2 A^2}{{\lambda_0}^4} \left| \int_{\delta R}^{R} \frac{\rho}{\sqrt{\rho^2 + t^2}} \exp\left[-i\frac{2\pi}{\lambda_0}\sqrt{\rho^2 + s^2} - i\phi(\rho) - i\frac{2\pi}{\lambda_0}\sqrt{\rho^2 + t^2} \right] d\rho \right|^2 \quad (6)$$

independent of s in order to obtain an extended depth of field.

To evaluate the integral in Eq. (6), we introduce a new function $\phi_P(\rho)$ related to the phase transmission of the lens, defined as follows:

$$\phi_P(\rho) \triangleq \phi(\rho) + \frac{2\pi}{\lambda_0}(\sqrt{\rho^2 + t^2} - t). \quad (7)$$

Now the problem becomes one of determining $\phi_P(\rho)$ such that

$$G \triangleq \left| \int_{\delta R}^{R} \frac{\rho}{\sqrt{\rho^2 + t^2}} \times \exp\left\{ -i\frac{2\pi}{\lambda_0}\left[\frac{\lambda_0}{2\pi}\phi_P(\rho) + \sqrt{\rho^2 + s^2} \right] \right\} d\rho^2 \quad (8)$$

is independent of s.

G can be evaluated by the method of stationary phase. Assume that there is only one stationary point ρ_0 that satisfies $\delta R \leq \rho_0 \leq R$. The stationary point ρ_0, by definition, satisfies

$$\frac{\lambda_0}{2\pi}\phi_P'(\rho_0) = -\rho_0/\sqrt{{\rho_0}^2 + s^2}. \quad (9)$$

The stationary-phase approximation result for G will be

$$G \approx \frac{{\lambda_0}{\rho_0}^2}{\left| \frac{\lambda_0}{2\pi}\phi_P''(\rho_0) + \frac{1}{\sqrt{{\rho_0}^2 + s^2}} - \frac{{\rho_0}^2}{({\rho_0}^2 + s^2)^{3/2}} \right|} \times \frac{1}{{\rho_0}^2 + t^2}. \quad (10)$$

Equations (9) and (10) are combined to eliminate the variable s, and the resulting form for G is given by

$$G = \frac{2\pi\rho_0^2}{\left|\phi_P''(\rho_0) - \frac{\phi_P'(\rho_0)}{\rho_0} + \frac{\lambda_0^2}{4\pi^2}\frac{[\phi_P'(\rho_0)]^3}{\rho_0}\right|}\frac{1}{\rho_0^2 + t^2}. \tag{11}$$

For this equation to be independent of s, which is a function of ρ_0 as expressed in Eq. (9), G must be independent of ρ_0. In other words, G must be a constant for all values ρ_0, $\delta R \leq \rho_0 \leq R$; i.e.,

$$(\rho^2 + t^2)\left|\phi_P''(\rho) - \frac{\phi_P'(\rho)}{\rho} + \frac{\lambda_0^2}{4\pi^2}\frac{[\phi_P'(\rho)]^3}{\rho}\right| = 2a\rho^2, \tag{12}$$

where a is a positive constant. Owing to the absolute value in Eq. (12), we consider two cases, (i) and (ii), leading to separate designs, as follows.

(i) When

$$\phi_P''(\rho) - \frac{\phi_P'(\rho)}{\rho} + \frac{\lambda_0^2}{4\pi^2}\frac{[\phi_P'(\rho)]^3}{\rho} \geq 0.$$

The solution of Eq. (12) is summarized below from Appendix A.1:

$$\begin{aligned}\phi_{P\beta}(\rho) = {} & a_\beta\frac{t^2 + \rho^2}{2}\{\ln[A_\beta(t^2 + \rho^2)] - 1\} \\ & + \frac{\lambda_0^2}{8\pi^2}\left\{\frac{1}{16}a_\beta^3(t^2 + \rho^2)^2[45 - 42\ln[A_\beta(t^2 \right. \\ & + \rho^2)] + 18\{\ln[A_\beta(t^2 + \rho^2)]\}^2 - 4\{\ln[A_\beta(t^2 \\ & \left. + \rho^2)]\}^3] - \frac{B_\beta\rho^2}{2}\right\} + \text{const.},\end{aligned} \tag{13}$$

where const. is an arbitrary constant phase delay determined by the center thickness of the lens. A_β and a_β are determined by letting

$$\begin{aligned} s = s_1 &\Rightarrow \rho_0 = \delta R, \\ s = s_2 &\Rightarrow \rho_0 = R, \end{aligned} \tag{14}$$

in Eq. (9) and substituting Eq. (14) into Eq. (13) without the perturbation-correction term. The result is the following:

$$\begin{aligned} a_\beta &= \frac{2\pi}{\lambda_0}\frac{1/\sqrt{\delta R^2 + s_1^2} - 1/\sqrt{R^2 + s_2^2}}{\ln\left(\frac{R^2 + t^2}{\delta R^2 + t^2}\right)}, \\ A_\beta &= \frac{1}{\delta R^2 + t^2}\exp\left[-\frac{\sqrt{R^2 + s_2^2}}{\sqrt{R^2 + s_2^2} - \sqrt{\delta R^2 + s_1^2}}\right. \\ &\quad \left.\times \ln\left(\frac{R^2 + t^2}{\delta R^2 + t^2}\right)\right]. \end{aligned} \tag{15}$$

Also, B_β is determined by assuming that the first-order correction should not change the slope of the ray at the edge of the lens; i.e.,

$$\phi_{P\beta}'(R) = \frac{\mathrm{d}}{\mathrm{d}\rho}\left(a_\beta\frac{t^2 + \rho^2}{2}\{\ln[A_\beta(t^2 + \rho^2)] - 1\}\right)_{\rho=R},$$

so we have

$$\begin{aligned} B_\beta = {} & -a_\beta^3(R^2 + t^2)(-6 + 6\ln[A_\beta(t^2 + \rho^2)] \\ & - 3\{\ln[A_\beta(t^2 + \rho^2)]\}^2 + \{\ln[A_\beta(t^2 + \rho^2)]\}^3). \end{aligned} \tag{16}$$

(ii) When

$$\phi_P''(\rho) - \frac{\phi_P'(\rho)}{\rho} + \frac{\lambda_0^2}{4\pi^2}\frac{[\phi_P'(\rho)]^3}{\rho} \leq 0,$$

similarly,

$$\begin{aligned}\phi_{P\gamma}(\rho) = {} & -a_\gamma\frac{t^2 + \rho^2}{2}\{\ln[A_\gamma(t^2 + \rho^2)] - 1\} \\ & + \frac{\lambda_0^2}{8\pi^2}\left\{\frac{1}{16}a_\gamma^3(t^2 + \rho^2)^2[-45 \right. \\ & + 42\ln[A_\gamma(t^2 + \rho^2)] - 18\{\ln[A_\gamma(t^2 + \rho^2)]\}^2 \\ & \left. + 4\{\ln[A_\gamma(t^2 + \rho^2)]\}^3] + \frac{B_\gamma\rho^2}{2}\right\} + \text{const.},\end{aligned} \tag{17}$$

where

$$\begin{aligned} a_\gamma &= \frac{2\pi}{\lambda_0}\frac{1/\sqrt{R^2 + s_1^2} - 1/\sqrt{\delta R^2 + s_2^2}}{\ln\left(\frac{R^2 + t^2}{\delta R^2 + t^2}\right)}, \\ A_\gamma &= \frac{1}{\delta R^2 + t^2}\exp\left[\frac{\sqrt{R^2 + s_1^2}}{\sqrt{\delta R^2 + s_2^2} - \sqrt{R^2 + s_1^2}}\right. \\ &\quad \left.\times \ln\left(\frac{R^2 + t^2}{\delta R^2 + t^2}\right)\right], \\ B_\gamma &= -a_\gamma^3(R^2 + t^2)(-6 + 6\ln[A_\gamma(t^2 + \rho^2)] \\ &\quad - 3\{\ln[A_\gamma(t^2 + \rho^2)]\}^2 \\ &\quad + \{\ln[A_\gamma(t^2 + \rho^2)]\}^3). \end{aligned} \tag{18}$$

In Eqs. (13) for $\phi_{P\beta}(\rho)$ and (17) for $\phi_{P\gamma}(\rho)$, the expressions include two terms: one main term and one from the perturbation-correction term. It is easy to verify that the correction term is negligible relative to the main term for reasonable $f/\#$. So, generally, each solution for the phase can be written without the correction term, as follows:

$$\phi_{P\beta}(\rho) = a_\beta\frac{t^2 + \rho^2}{2}\{\ln[A_\beta(t^2 + \rho^2)] - 1\} + \text{const.}, \tag{19}$$

where

$$\begin{aligned} a_\beta &= \frac{2\pi}{\lambda_0}\frac{1/\sqrt{\delta R^2 + s_1^2} - 1/\sqrt{R^2 + s_2^2}}{\ln\left(\frac{R^2 + t^2}{\delta R^2 + t^2}\right)}, \\ A_\beta &= \frac{1}{\delta R^2 + t^2}\exp\left[-\frac{\sqrt{R^2 + s_2^2}}{\sqrt{R^2 + s_2^2} - \sqrt{\delta R^2 + s_1^2}}\right. \\ &\quad \left.\times \ln\left(\frac{R^2 + t^2}{\delta R^2 + t^2}\right)\right], \end{aligned} \tag{20}$$

and

$$\phi_{P\gamma}(\rho) = -a_\gamma \frac{t^2 + \rho^2}{2}\{\ln[A_\gamma(t^2 + \rho^2)] - 1\} + \text{const.}, \tag{21}$$

$$s_{\beta,\gamma} = \left(\frac{4\pi^2}{\lambda^2 a_{\beta,\gamma}^{\ 2}}\{\ln[A_{\beta,\gamma}(t^2 + \rho^2)]\}^{-2} - \rho^2\right)^{1/2}. \tag{23}$$

For the β design obtained by substitution of Eq. (20) into Eq. (23), we find the following relation between the object distance and the stationary point:

$$s_\beta = \left\{\left[\frac{\sqrt{\delta R^2 + s_1^{\ 2}}\ln\left(\frac{t^2 + R^2}{t^2 + \delta R^2}\right)}{\left(\frac{\sqrt{\delta R^2 + s_1^{\ 2}}}{\sqrt{R^2 + s_2^{\ 2}}} - 1\right)\ln\left(\frac{t^2 + \rho^2}{t^2 + R^2}\right) + \frac{\sqrt{\delta R^2 + s_1^{\ 2}}}{\sqrt{R^2 + s_2^{\ 2}}}\ln\left(\frac{t^2 + R^2}{t^2 + \delta R^2}\right)}\right]^2 - \rho^2\right\}^{1/2}, \tag{24}$$

in which we have dropped the subscript zero from ρ_0.

Similarly, substitution of Eq. (22) into Eq. (23) yields the relation between object distance and stationary point for the γ-design lens:

$$s_\gamma = \left\{\left[\frac{\sqrt{\delta R^2 + s_2^{\ 2}}\ln\left(\frac{t^2 + R^2}{t^2 + \delta R^2}\right)}{\left(\frac{\sqrt{\delta R^2 + s_2^{\ 2}}}{\sqrt{R^2 + s_1^{\ 2}}} - 1\right)\ln\left(\frac{t^2 + \rho^2}{t^2 + R^2}\right) + \frac{\sqrt{\delta R^2 + s_2^{\ 2}}}{\sqrt{R^2 + s_1^{\ 2}}}\ln\left(\frac{t^2 + R^2}{t^2 + \delta R^2}\right)}\right]^2 - \rho^2\right\}^{1/2}. \tag{25}$$

where

$$a_\gamma = \frac{2\pi}{\lambda_0}\frac{1/\sqrt{R^2 + s_1^{\ 2}} - 1/\sqrt{\delta R^2 + s_2^{\ 2}}}{\ln\left(\frac{R^2 + t^2}{\delta R^2 + t^2}\right)},$$

$$A_\gamma = \frac{1}{\delta R^2 + t^2}\exp\left[\frac{\sqrt{R^2 + s_1^{\ 2}}}{\sqrt{\delta R^2 + s_2^{\ 2}} - \sqrt{R^2 + s_1^{\ 2}}} \times \ln\left(\frac{R^2 + t^2}{\delta R^2 + t^2}\right)\right]. \tag{22}$$

Equations (19)–(22) are the major results for the theory of the logarithmic lens. When combined with Eq. (8), they will yield the phase-delay function of the lens. Solution (19) is called the β design, and solution (21) is called the γ design. The lenses can be designed directly with the phase function described in this section, or they can also be realized by attaching the aberration part of the logarithmic asphere to the aperture of an existing conventional lens. The optical design, fabrication, and experiments with the logarithmic asphere will be reported in a later paper.

B. Best-Focus Ring and Point-Spread Function of the Logarithmic Asphere

It is of interest to consider the object distance as a function of the radius of the lens annulus that will form a sharp image of the object at image plane II. This ring makes the main contribution to the on-axis intensity of the point-spread function. In the stationary-phase evaluation of Eq. (6), we find the relationship between s and the corresponding annulus ring at ρ_0 given by Eq. (9).

Substitute Eq. (19) or (21) into Eq. (9) to find the following expression for the β, γ cases:

Equations (24) and (25) show the object distance as a function of the stationary-point position, or the best-focus ring of the lens for the β design and the γ design, respectively.

To compare the β and γ designs, we plot in Fig. 2 the curves of the object distance versus the position of the best-focus rings for the logarithmic aspheres. In the design, we choose $s_1 = 1400$ mm, $s_2 = 1615$ mm, $R = 8$ mm, and $\delta = 0$. As expected, for the β design the objects closer to the lens form sharp images by the center rings of the lens while objects farther away form sharp images by the edge rings. However, for the γ design, it is the converse. Also shown in Fig. 2 is the curve of β_0-type lens derived from ray optics and the energy argument detailed in Appendix A.2. This relation is very close to the

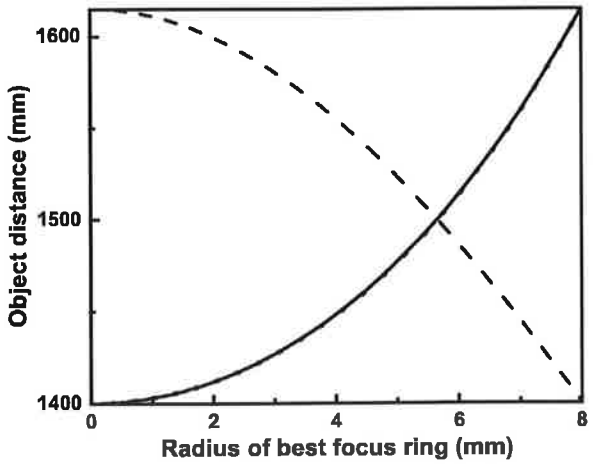

Fig. 2. Object distance versus radius of the best-focus ring for the logarithmic aspheres. Dash curve, γ design; solid curve, β design; dotted curve, β_0 design from ray optics. The $f/\#$ is 4, and the classical diffraction-limited depth of field is approximately ± 8 mm.

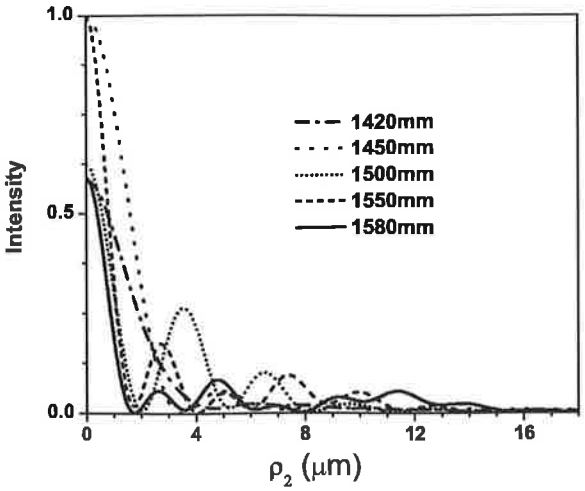

Fig. 3. Point-spread function of the β lens at various object distances. The designed depth-of-field range is the same as in Fig. 2, i.e., from 1400 to 1615 nm, and the wavelength of illumination is 0.5 μm.

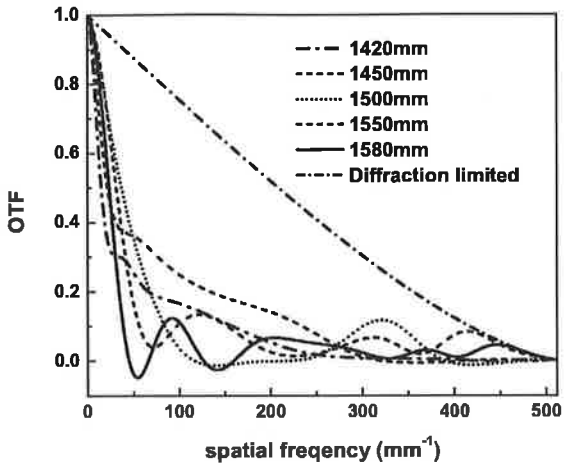

Fig. 4. OTFs of the lens corresponding to the point-spread functions shown in Fig. 3.

β design as described in this section, and the two β-type lenses have similar focus-ring correspondence with respect to the object distance. These curves uniquely determine the phase transmission of the lens from Eq. (9), which can be regarded as the statement of Fermat's principle, i.e., the derivative of total optical length from object to focus-ring ρ to image point is zero. Therefore we mention that the β-type lenses derived both from the evaluation of the diffraction integral and from ray optics yield similar phase transmission functions.

Figure 3 shows the point-spread functions of the β design lens for various object distances when the image is located at $t = 62.5$ mm and no stop is present, i.e., $\delta R = 0$. These curves, calculated numerically from Eq. (2), illustrate clearly the increase in depth of field of the logarithmic lens. This can be seen from two features of the point-spread function; first, the point-spread functions always have maximum intensities on axis, and second, the center of the point-spread function is comparable with the diffraction-limited spot size. One should notice that when the object is farther from the lens, the central lobe of the point-spread function becomes narrower. This is not the case for the γ-design curves, which are not shown here. For the γ-design lens, the width of the point-spread function is larger for farther object distances. Since also at farther distances the magnification of the image is smaller, both effects combine to make the γ design unfavorable for imaging at farther distances.

Another feature of the point-spread functions of the logarithmic asphere is the oscillation base, which results in reduced image contrast. Thus digital processing is a necessary step for extended depth-of-field imaging. Figure 4 shows the optical transfer functions (OTFs) of the lens that correspond to the point-spread functions in Fig. 3. For most of the object positions, the OTF has zero phase shift at the various spatial frequencies. At the extreme offset, $s = 1580$ mm, one sees some slight spurious resolution, i.e., a phase shift of π. Although linear digital-processing techniques are fairly successful, in Section 3 we describe a nonlinear maximum-entropy method to deal with the oscillation base of the point-spread functions for deblurring. This method gives superior results.

Since the β design is a better choice in most cases, it is of interest to consider the effect of apodization on the impulse response. For each apodization, we redesign the lens transmission function to start with the close-in point s at the edge of the stop. Figure 5 shows the point-spread functions for $\delta R = 0$, $0.3R$, and $0.6R$ of the β-design lenses at $s = 1420$ mm. The three curves correspond to full circular aperture and a center block with radius $0.3R$ and $0.6R$. The corresponding OTFs are shown in Fig. 6. These β-design lenses with center apodization are important for some telescope applications. The narrowing of the impulse responses for the close distance will lead to an improved depth of field when maximum-entropy processing is used. As expected, the center blocks result in a boost of high spatial frequencies, as shown in Fig. 6. It is important to note that besides the differences in apodization, the three designs in Figs. 5 and 6 have different phase transmission profiles.

As two important special cases, consider the β design for $\delta = 0$ and $\delta = 0$ with $s_2 = \infty$.

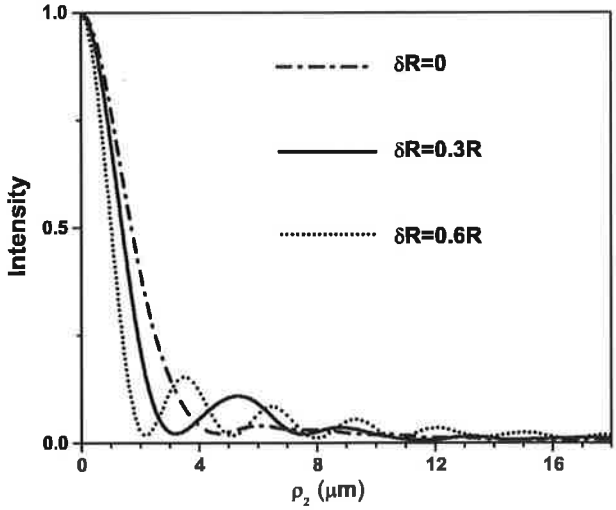

Fig. 5. Point-spread functions of the β lenses with different center block radii at an object distance of 1420 mm.

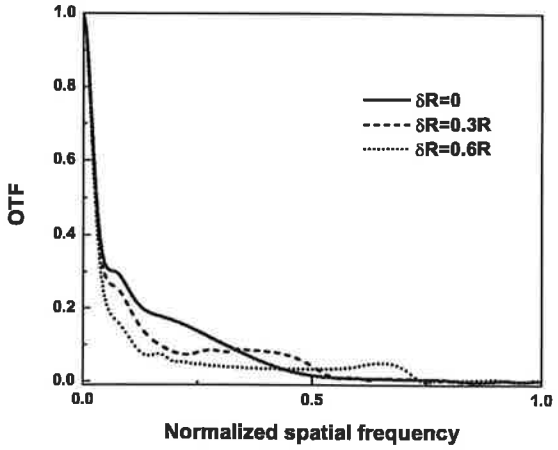

Fig. 6. OTFs corresponding to the point-spread functions shown in Fig. 5.

(i) $\delta R = 0$. The full aperture of lens is used. By Eq. (19),

$$\phi_{P\beta}(\rho) = a_\beta \frac{t^2 + \rho^2}{2}\{\ln[A_\beta(t^2 + \rho^2)] - 1\} + \text{const.}, \tag{26}$$

where

$$a_\beta = \frac{2\pi}{\lambda_0}\frac{1/s_1 - 1/\sqrt{R^2 + s_2^2}}{\ln(1 + R^2/t^2)},$$

$$A_\beta = \frac{1}{t^2}\exp\left[-\frac{\sqrt{R^2 + s_2^2}}{\sqrt{R^2 + s_2^2} - s_1}\ln(1 + R^2/t^2)\right]. \tag{27}$$

Also, by Eq. (24),

$$s = \left\{\left[\frac{s_1 \ln(1 + R^2/t^2)}{\left(\frac{s_1}{\sqrt{R^2 + s_2^2}} - 1\right)\ln\left(\frac{t^2 + \rho^2}{t^2 + R^2}\right) + \frac{s_1}{\sqrt{R^2 + s_2^2}}\ln(1 + R^2/t^2)}\right]^2 - \rho^2\right\}^{1/2}. \tag{28}$$

(ii) $\delta R = 0$ and $s_2 = \infty$. The full aperture of the lens is used, and the farthest object distance is infinity. Similarly,

$$\phi_{P\beta}(\rho) = a_\beta \frac{t^2 + \rho^2}{2}\{\ln[A_\beta(t^2 + \rho^2)] - 1\} + \text{const.}, \tag{29}$$

where

$$a_\beta = \frac{2\pi}{\lambda_0}\frac{1}{s_1 \ln(1 + R^2/t^2)},$$

$$A_\beta = \frac{1}{t^2 + R^2}, \tag{30}$$

or, explicitly,

$$\phi_{P\beta}(\rho) = \frac{\pi}{\lambda_0}\frac{t^2 + \rho^2}{s_1 \ln(1 + R^2/t^2)}\left[\ln\left(\frac{t^2 + \rho^2}{t^2 + R^2}\right) - 1\right] + \text{const.}, \tag{31}$$

and

$$s = s_1 \frac{\ln(1 + R^2/t^2)}{\ln\left(\frac{t^2 + R^2}{t^2 + \rho^2}\right)}. \tag{32}$$

Clearly, the phase function of this lens in Eq. (31) is still valid for the object at infinity. The point-spread functions of the lens still have similar central peaks, as shown in Fig. 3. For imaging an object at infinity, this design is an improvement over our earlier design in the literature.[5]

3. DIGITAL PROCESSING

A. Matrix Representation of a Linear Imaging System

Before image processing, a digital linear-system model must be established for a two-dimensional system. In a linear imaging system, the image $d(x, y)$ can be expressed as

$$d(x, y) = \int_{-\infty}^{\infty} f(\xi, \eta)h(x - \xi, y - \eta)\mathrm{d}\xi\mathrm{d}\eta + \theta(x, y), \tag{33}$$

where $f(x, y)$ is the object, $h(x, y)$ is the point-spread function of the lens, and $\theta(x, y)$ is the additive noise. In the digitized format for the two-dimensional object with size $A \times B$ and a point-spread function with size $C \times D$, the image will have size $M \times N$, where $M = A + C - 1$, $N = B + D - 1$. To form a linear-system model, we pad the object and the point-spread function with zeros to size $M \times N$; i.e.,

$$f(m, n) = \begin{cases} f(a, b) & 1 \le a \le A; \quad 1 \le b \le B \\ 0 & 1 + A \le m \le M; \quad 1 + B \le n \le N' \end{cases} \tag{34}$$

$$h(m, n) = \begin{cases} h(a, b) & 1 \le a \le C; \quad 1 \le b \le D \\ 0 & 1 + C \le m \le M; \quad 1 + D \le n \le N' \end{cases} \tag{35}$$

$$\theta(m, n) = \begin{cases} \theta(a, b) & 1 \le a \le C; \quad 1 \le b \le D \\ 0 & 1 + C \le m \le M; \quad 1 + D \le n \le N' \end{cases} \tag{36}$$

Using Eqs. (34)–(36), one can readily write the discrete equivalent of Eq. (33) to obtain

$$d(m, n) = \sum_{i=1}^{M} \sum_{j=1}^{N} f(i, j)h(m - i, n - j) + \theta(m, n). \tag{37}$$

To find a matrix representation, one can define f, d, and θ as MN-element column matrices representing the object, the image, and the noise, respectively, by reshaping the corresponding two-dimensional matrix row by row as follows:

$$\begin{aligned} f_{(m-1)N+n} &= f(m, n), \\ d_{(m-1)N+n} &= d(m, n), \\ \theta_{(m-1)N+n} &= \theta(m, n). \end{aligned} \tag{38}$$

Also, we define H as

$$H = \begin{bmatrix} H_1 & H_M & H_{M-1} & \cdots & H_2 \\ H_2 & H_1 & H_M & \cdots & H_3 \\ H_3 & H_2 & H_1 & \cdots & H_4 \\ \vdots & \cdots & \cdots & \cdots & \cdots \\ H_M & H_{M-1} & H_{M-2} & \cdots & H_1 \end{bmatrix}, \tag{39}$$

where

$$H_j \triangleq \begin{bmatrix} h(j, 1) & h(j, N) & \cdots & h(j, 2) \\ h(j, 2) & h(j, 1) & \cdots & h(j, 3) \\ \vdots & \cdots & \cdots & \cdots \\ h(j, N) & \cdots & \cdots & h(j, 1) \end{bmatrix}. \tag{40}$$

Then by Eqs. (38) and (39), the image model Eq. (37) can be written in matrix form as[12]

$$d = Hf + \theta. \tag{41}$$

B. Definition of the Maximum-Entropy Method

Assume that an image consists of photons in a number of pixel cells. For a known total number of photons W, we consider a distribution $\{f_i\}$, which means that the cells have photon number $f_1, f_2, \ldots f_i, \ldots f_n$ in this order. Then the possible number of ways that this image can be formed is given by

$$\Omega = W! \Big/ \prod_{i=1}^{n} f_i!, \tag{42}$$

where $W = \Sigma_{i=1}^{n} f_i$.

One can define the entropy as the natural logarithm of this number as follows:

$$S = \ln \Omega = \ln\left(W! \Big/ \prod_{i=1}^{n} f_i! \right) \approx W \ln W - \sum_{i=1}^{n} f_i \ln f_i. \tag{43}$$

This formula is considered to be the basic definition of the entropy of a specific image $\{f_i\}$. When the entropies of two images are compared, the assumption is made that the images have the same size and the same total photon number. With this assumption, some other definitions of entropy of an image could be, e.g.,

$$\begin{aligned} S_1 &= -\sum_{i=1}^{n} f_i \ln f_i, \\ S_2 &= -\sum_{i=1}^{n} p_i \ln p_i, \qquad p_i = f_i \Big/ \sum_{j=1}^{n} f_j, \\ S_3 &= -\sum_{i=1}^{n} \left(f_i \ln \frac{f_i}{\langle f \rangle} - 1 \right), \end{aligned} \tag{44}$$

$\langle f \rangle$ is the mean of the image.

It is easy to show that all these definitions are linearly related to one another. Also, f_i can be interpreted as the cell intensity instead of the photon number, because if one changes the f_i in the original entropy expression to intensity, a variable that is proportional to photon number, then the new expression of entropy is also linearly related to the original one.

Finally, the maximum-entropy problem in image recovery can stated as follows:

Assume that an object f is imaged to a CCD array by an imaging system with a point-spread function h. The noise θ is added with standard deviation σ. Mathematically, we can write

$$d = Hf + \theta. \tag{45}$$

As a useful constraint in the maximum-entropy method, we define the statistical measure C as follows[7]:

$$C = \sum_{i=1}^{n} \frac{1}{\sigma_i^2} \left(d_i - \sum_{k=1}^{n} H_{ik} f_k \right)^2. \tag{46}$$

Now the problem is to find an estimate of f that will maximize S_3, written from Eq. (44) as

$$S = -\sum_{i=1}^{n} \left(f_i \ln \frac{f_i}{\langle f \rangle} - 1 \right), \tag{47}$$

under the constraint of $C = C_{\text{aim}}$, where C_{aim} is the total number of pixels in the image.

The idea of maximum-entropy recovery is that when unknown noise is present in the blurred image, the final recovery can have many solutions that form a set all of which satisfy the noise statistical constraint $C = C_{\text{aim}}$. The maximum-entropy method picks the solution that has maximum probability in the sense expressed in Eq. (42). This maximum-entropy recovery not only has maximum probability but also has an internal mechanism to produce a smoother result. This mechanism is beneficial when noise is large, because the graininess of the final recovery resulting from the magnification of the noise will be smoothed out.

A diagram of the algorithm is shown in Fig. 7. In the measurement, an unknown object is convolved with the actual point-spread function, PSF, of the lens. Then noise is added in the process of imaging. In the recovery, we start with the initial estimate of the object and then calculate the image of this object by convolving with a single point-spread function. Then the difference between the measured blurred image and the calculated blurred image is calculated. If the difference is larger

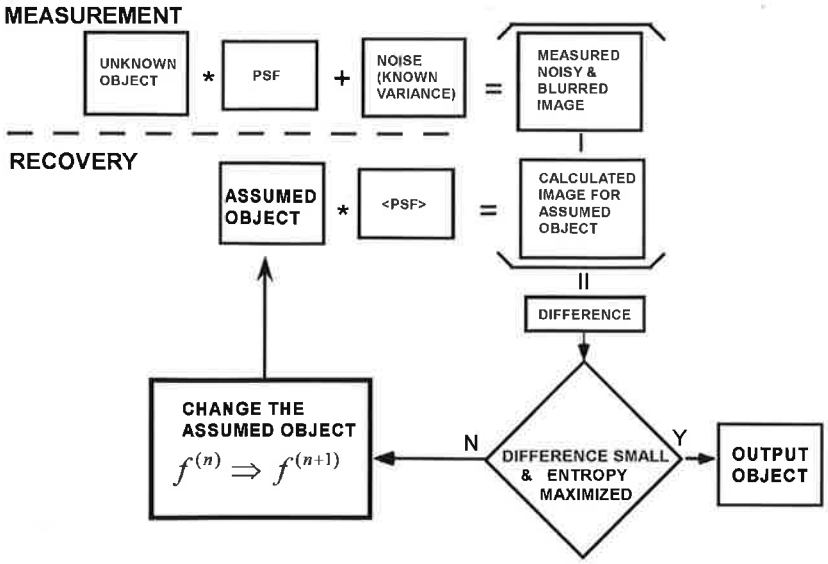

Fig. 7. Diagram of the maximum-entropy method. Above the dashed line is the measurement process; below the dashed line is the recovery iterative process described in Subsections 3.B and 3.C.

statistically than the noise in the experiment or the criterion of entropy maximization is not reached, a new estimation of the object is generated until both the noise constraint and the entropy-maximization criterion are met. How to estimate the next object from the earlier one is the essential part of the algorithm, which is described in detail below.

C. Description of the Algorithm

Two operators used in this section are defined in the following for convenience:

1. If f is a vector $f = \{f_i\}$, then $f^{\cdot\gamma}$ is a vector with its components defined as $(f^{\cdot\gamma})_i \triangleq \{ f_i{}^{\gamma}\}$.
2. If f and g are vectors of the same dimension, $f = \{f_i\}$ and $g = \{g_i\}$, then $f .\times g$ is a vector with its components defined as $(f .\times g)_i \triangleq \{f_i g_i\}$.

To find the solution of $\{f_k\}$, we use the Lagrange multiplier method. Define a new function

$$Q = S - \lambda C, \tag{48}$$

where λ is the Lagrange multiplier constant. Now the problem becomes that of maximizing Q under the constraint $C = C_{\text{aim}}$. Since Q is a function of n variables, where n is the number of pixels in the image, which is usually very large, an iterative numerical method has to be used to find the solution. In each iteration the standard way is first to determine the search directions in which the solution is estimated to lie and then to find the step length along these directions.

1. *Search Directions*

The choice of directional images is important in determining the convergence and speed of the algorithm. In the steepest-ascent method, the search direction for maximizing Q is ∇Q. But to adjust the weight of different pixel values f_i, we modify the direction to be

$$e_A = f^{\cdot\gamma} .\times \nabla Q. \tag{49}$$

In Eq. (49) we introduce a new metric parameter γ, which we show improves the speed of the maximum-entropy algorithm. For image deblurring in photography, the larger pixel values will have larger weight, so we choose $\gamma > 0$ to let the algorithm approach the desired larger pixel value faster. Generally γ is chosen from 0 to 1. Clearly, when $\gamma = 0$, e_A becomes the search direction for the steepest-ascent method. When $\gamma = 1$, e_A becomes the search direction used by Burch *et al.*[8]

At the maximum point Q, we have

$$\nabla Q = 0. \tag{50}$$

This implies that $\nabla Q \cdot \nabla Q$ needs to be minimized, too. So the next search direction should be $(1/2)\nabla(\nabla Q \cdot \nabla Q)$, or $\nabla\nabla Q \cdot \nabla Q$. Here $\nabla\nabla Q$ is the dyadic gradient whose component is defined as $(\nabla\nabla Q)_{ij} = \partial^2/(\partial f_i \partial f_j)Q$. Again, to emphasize the bigger pixel values, we modify the direction to be

$$e_B = f^{\cdot\gamma} .\times [\nabla\nabla Q \cdot (f^{\cdot\gamma} .\times \nabla Q)]. \tag{51}$$

Substitution of Eq. (48) into Eqs. (49) and (51) yields the following:

$$\begin{aligned} e_A &= f^{\cdot\gamma} .\times \nabla S - \lambda f^{\cdot\gamma} .\times \nabla C, \\ e_B &= \lambda^2 f^{\cdot\gamma} .\times [\nabla\nabla C \cdot (f^{\cdot\gamma} .\times \nabla C)] \\ &\quad - \lambda f^{\cdot\gamma} .\times [\nabla\nabla C \cdot (f^{\cdot\gamma} .\times \nabla S)] \\ &\quad + f^{\cdot\gamma} .\times [\nabla\nabla S \cdot (f^{\cdot\gamma} .\times \nabla S)] \\ &\quad - \lambda f^{\cdot\gamma} .\times [\nabla\nabla S \cdot (f^{\cdot\gamma} .\times \nabla C)]. \end{aligned} \tag{52}$$

Observing the above expression, we know that the two directions actually are linear combinations of many directions, which can be treated as separate search directions, viz.,

$$
\begin{aligned}
e_1 &= f^{\cdot\gamma} .\times \nabla S,\\
e_2 &= f^{\cdot\gamma} .\times \nabla C,\\
e_3 &= f^{\cdot\gamma} .\times [\nabla\nabla C \cdot (f^{\cdot\gamma} .\times \nabla C)],\\
e_4 &= f^{\cdot\gamma} .\times [\nabla\nabla C \cdot (f^{\cdot\gamma} .\times \nabla S)],\\
e_5 &= f^{\cdot\gamma} .\times [\nabla\nabla S \cdot (f^{\cdot\gamma} .\times \nabla S)],\\
e_6 &= f^{\cdot\gamma} .\times [\nabla\nabla S \cdot (f^{\cdot\gamma} .\times \nabla C)].
\end{aligned} \tag{53}
$$

From Eqs. (46) and (47), we have

$$
\begin{aligned}
(\nabla S)_i &= -\ln\frac{f_i}{\langle f\rangle},\\
(\nabla\nabla S)_{ij} &= -\frac{1}{f_i}\delta_{ij},
\end{aligned} \tag{54}
$$

$$
\begin{aligned}
(\nabla C)_i &= \sum_{k=1}^{n}\sum_{j=1}^{n}\frac{2}{\sigma_k{}^2}(H_{kj}f_j - d_k)H_{ki}\\
(\nabla\nabla C)_{ij} &= \sum_{k=1}^{n}\frac{2}{\sigma_k{}^2}H_{kj}H_{ki}.
\end{aligned} \tag{55}
$$

Substitution of Eqs. (54) and (55) into (53) yields the components of each search direction as follows:

$$
\begin{aligned}
(e_1)_i &= -f_i{}^{\gamma}\ln\frac{f_i}{\langle f\rangle},\\
(e_2)_i &= f_i{}^{\gamma}\sum_{k=1}^{n}\sum_{j=1}^{n}\frac{2}{\sigma_k{}^2}(H_{kj}f_j - d_k)H_{ki},\\
(e_3)_i &= f_i{}^{\gamma}\sum_{j=1}^{n}\sum_{k=1}^{n}\sum_{l=1}^{n}\sum_{m=1}^{n} f_m{}^{\gamma}\frac{4}{\sigma_k{}^2\sigma_l{}^2}\\
&\quad\times (H_{kj}f_j - d_k)H_{km}H_{li}H_{lm},\\
(e_4)_i &= -f_i{}^{\gamma}\sum_{j=1}^{n}\sum_{k=1}^{n} f_j{}^{\gamma}\frac{2}{\sigma_k{}^2}H_{ki}H_{kj}\ln\frac{f_j}{\langle f\rangle},\\
(e_5)_i &= f_i{}^{2\gamma-1}\ln\frac{f_i}{\langle f\rangle},\\
(e_6)_i &= -f_i{}^{2\gamma-1}\sum_{k=1}^{n}\sum_{j=1}^{n}\frac{2}{\sigma_k{}^2}(H_{kj}f_j - d_k)H_{ki}.
\end{aligned} \tag{56}
$$

In the algorithm we do not choose e_5 and e_6 as search directions, because when $\gamma = 0.5$, they decompose to e_1 and e_2, respectively; and also when $\gamma < 0.5$, for small pixel values they both involve dividing by small numbers, which can cause problems in numerical accuracy. So we choose e_1, e_2, e_3, e_4 as four search directions.

To simplify the algorithm, three search directions are enough for this problem; we can pick e_1, e_2, e_3, or we can pick e_1, e_2, $e_4 - \lambda e_3$ as another choice. The algorithm converges at about the same speed, although the latter choice is a little better. Here λ is a constant chosen by Eqs. (48) and (50); i.e., λ is given by

$$
\lambda = \left[\frac{\sum_{i=1}^{n} f_i{}^{\gamma}(\partial S/\partial f_i)^2}{\sum_{i=1}^{n} f_i{}^{\gamma}(\partial C/\partial f_i)^2}\right]^{1/2}. \tag{57}
$$

In either case three directions are just written as e_1, e_2, e_3 for simplicity. In the calculation of search directions, we notice that the directions e_2 and e_3 are basically the convolutions related to the real point-spread function h and object f, before $f(m, n)$ is shaped to one dimension. Care needs to be taken to make certain that there is no pixel shift or image-position shift after the convolution operation.

After three search directions are calculated for the current iteration (n), the job is to find an estimation of the object for the next iteration $f^{(n+1)}$, which is defined as

$$
f^{(n+1)} = f^{(n)} + \delta f, \tag{58}
$$

where δf is the change of image for the current iteration. It is defined as linear combinations of search directions, with their coefficients to be determined; i.e.,

$$
\delta f = x_1 e_1 + x_2 e_2 + x_3 e_3. \tag{59}
$$

2. Coefficients of Search Directions

Since S and C are functions of f that vary in a complicated way, we use a Taylor expansion to calculate their values as a function of the search directions. Retaining up to the quadratic terms, we write $\tilde{S}$ and $\tilde{C}$ as follows:

$$
\tilde{S} = S(f^{(n)}) + \nabla S \cdot \delta f + \tfrac{1}{2}\delta f \cdot \nabla\nabla S \cdot \delta f, \tag{60}
$$

$$
\tilde{C} = C(f^{(n)}) + \nabla C \cdot \delta f + \tfrac{1}{2}\delta f \cdot \nabla\nabla C \cdot \delta f. \tag{61}
$$

Substitution of Eq. (59) into Eqs. (60) and (61) yields the following expressions written in matrix form:

$$
\tilde{S} = S_0 + AX - \tfrac{1}{2}X^{\mathrm{T}}BX, \tag{62}
$$

$$
\tilde{C} = C_0 + MX + \tfrac{1}{2}X^{\mathrm{T}}NX. \tag{63}
$$

In Eqs. (62) and (63) the notation is defined as follows:

$$
\begin{aligned}
S_0 &= S(f^{(n)}),\\
C_0 &= C(f^{(n)}),\\
X &= [x_1 \quad x_2 \quad x_3]^{\mathrm{T}},\\
A &= [\nabla S \cdot e_1 \quad \nabla S \cdot e_2 \quad \nabla S \cdot e_3],\\
B &= -\begin{bmatrix} e_1\cdot\nabla\nabla S\cdot e_1 & e_1\cdot\nabla\nabla S\cdot e_2 & e_1\cdot\nabla\nabla S\cdot e_3\\ e_2\cdot\nabla\nabla S\cdot e_1 & e_2\cdot\nabla\nabla S\cdot e_2 & e_2\cdot\nabla\nabla S\cdot e_3\\ e_3\cdot\nabla\nabla S\cdot e_1 & e_3\cdot\nabla\nabla S\cdot e_2 & e_3\cdot\nabla\nabla S\cdot e_3\end{bmatrix},\\
M &= [\nabla C \cdot e_1 \quad \nabla C \cdot e_2 \quad \nabla C \cdot e_3],\\
N &= \begin{bmatrix} e_1\cdot\nabla\nabla C\cdot e_1 & e_1\cdot\nabla\nabla C\cdot e_2 & e_1\cdot\nabla\nabla C\cdot e_3\\ e_2\cdot\nabla\nabla C\cdot e_1 & e_2\cdot\nabla\nabla C\cdot e_2 & e_2\cdot\nabla\nabla C\cdot e_3\\ e_3\cdot\nabla\nabla C\cdot e_1 & e_3\cdot\nabla\nabla C\cdot e_2 & e_3\cdot\nabla\nabla C\cdot e_3\end{bmatrix}.
\end{aligned} \tag{64}
$$

$[\cdots]^{\mathrm{T}}$ denotes the transpose of the matrix. The matrices A, B, M, and N can be calculated from Eqs. (55) and (56).

Equations (62) and (63) can be simplified by introducing new variables to diagonalize B and N. First we find the rotation matrix R to diagonalize the matrix B; i.e.,

$$RBR^{\mathrm{T}} = \mathrm{diag}(\lambda_1, \lambda_2, \lambda_3), \tag{65}$$

where diag$(\cdots)$ denotes the diagonal matrix.

Define a new variable Y as follows:

$$Y = RX. \tag{66}$$

Substitution of Eqs. (66) and (65) into Eqs. (62) and (63) yields the following expressions:

$$\tilde{S} = S_0 + AR^{\mathrm{T}}Y - \tfrac{1}{2}Y^{\mathrm{T}}\mathrm{diag}(\lambda_1, \lambda_2, \lambda_3)Y, \tag{67}$$

$$\tilde{C} = C_0 + MR^{\mathrm{T}}Y + \tfrac{1}{2}Y^{\mathrm{T}}RNR^{\mathrm{T}}Y. \tag{68}$$

Some eigenvalues of B may be very small; we discuss this in the following two cases.

Case (i). Assume that none of $\lambda_1, \lambda_2, \lambda_3$ is small. We introduce Z such that

$$Z = \mathrm{diag}(\sqrt{\lambda_1}, \sqrt{\lambda_2}, \sqrt{\lambda_3})Y. \tag{69}$$

Substituting Eq. (69) into (67) and (68), we have

$$\tilde{S} = S_0 + AR^{\mathrm{T}}\mathrm{diag}\left(\frac{1}{\sqrt{\lambda_1}}, \frac{1}{\sqrt{\lambda_2}}, \frac{1}{\sqrt{\lambda_3}}\right)Z - \frac{1}{2}Z^{\mathrm{T}}Z, \tag{70}$$

$$\tilde{C} = C_0 + MR^{\mathrm{T}}\mathrm{diag}\left(\frac{1}{\sqrt{\lambda_1}}, \frac{1}{\sqrt{\lambda_2}}, \frac{1}{\sqrt{\lambda_3}}\right)Z + \frac{1}{2}Z^{\mathrm{T}}PZ, \tag{71}$$

where

$$P = \mathrm{diag}\left(\frac{1}{\sqrt{\lambda_1}}, \frac{1}{\sqrt{\lambda_2}}, \frac{1}{\sqrt{\lambda_3}}\right)RNR^{\mathrm{T}}\mathrm{diag}\left(\frac{1}{\sqrt{\lambda_1}}, \frac{1}{\sqrt{\lambda_2}}, \frac{1}{\sqrt{\lambda_3}}\right).$$

Introduce the second rotational matrix V to diagonalize P; i.e.,

$$VPV^{\mathrm{T}} = \mathrm{diag}(\mu_1, \mu_2, \mu_3), \tag{72}$$

and also define U as

$$U = VZ. \tag{73}$$

Then substitution of Eqs. (72) and (73) into Eqs. (70) and (71) yields the following expressions:

$$\tilde{S} = S_0 + AR^{\mathrm{T}}\mathrm{diag}\left(\frac{1}{\sqrt{\lambda_1}}, \frac{1}{\sqrt{\lambda_2}}, \frac{1}{\sqrt{\lambda_3}}\right)V^{\mathrm{T}}U - \frac{1}{2}U^{\mathrm{T}}U, \tag{74}$$

$$\tilde{C} = C_0 + MR^{\mathrm{T}}\mathrm{diag}\left(\frac{1}{\sqrt{\lambda_1}}, \frac{1}{\sqrt{\lambda_2}}, \frac{1}{\sqrt{\lambda_3}}\right)V^{\mathrm{T}}U + \frac{1}{2}U^{\mathrm{T}}\mathrm{diag}(\mu_1, \mu_2, \mu_3)U. \tag{75}$$

Combining Eqs. (66), (69), (73), we have the identity

$$X = R^{\mathrm{T}}\mathrm{diag}\left(\frac{1}{\sqrt{\lambda_1}}, \frac{1}{\sqrt{\lambda_2}}, \frac{1}{\sqrt{\lambda_3}}\right)V^{\mathrm{T}}U. \tag{76}$$

Case (ii). Assume λ_3 is small relative to λ_1, λ_2. In this case, we let $\lambda_3 \approx 0, y_3 = 0$ in Eq. (66) and also

$$\begin{bmatrix} z_1 \\ z_2 \\ z_3 = 0 \end{bmatrix} = \begin{bmatrix} \sqrt{\lambda_1} & 0 & 0 \\ 0 & \sqrt{\lambda_2} & 0 \\ 0 & 0 & 0 \end{bmatrix}\begin{bmatrix} y_1 \\ y_2 \\ y_3 = 0 \end{bmatrix}. \tag{77}$$

Then Eqs. (67) and (68) become

$$\tilde{S} = S_0 + AR^{\mathrm{T}}\mathrm{diag}\left(\frac{1}{\sqrt{\lambda_1}}, \frac{1}{\sqrt{\lambda_2}}, 0\right)Z - \frac{1}{2}Z^{\mathrm{T}}Z, \tag{78}$$

$$\tilde{C} = C_0 + MR^{\mathrm{T}}\mathrm{diag}\left(\frac{1}{\sqrt{\lambda_1}}, \frac{1}{\sqrt{\lambda_2}}, 0\right)Z + \frac{1}{2}Z^{\mathrm{T}}PZ, \tag{79}$$

where

$$P = \mathrm{diag}\left(\frac{1}{\sqrt{\lambda_1}}, \frac{1}{\sqrt{\lambda_2}}, 0\right)RNR^{\mathrm{T}}\mathrm{diag}\left(\frac{1}{\sqrt{\lambda_1}}, \frac{1}{\sqrt{\lambda_2}}, 0\right).$$

Introduce a second rotation matrix V, such that

$$VPV^{\mathrm{T}} = \begin{bmatrix} \mu_1 & 0 & 0 \\ 0 & \mu_2 & 0 \\ 0 & 0 & \mu_3 = 0 \end{bmatrix}, \tag{80}$$

where

$$V = \begin{bmatrix} \nu_{11} & \nu_{12} & 0 \\ \nu_{21} & \nu_{22} & 0 \\ 0 & 0 & 0 \end{bmatrix}.$$

Define a new variable U as

$$U = VZ, \tag{81}$$

then

$$\tilde{S} = S_0 + AR^{\mathrm{T}}\mathrm{diag}\left(\frac{1}{\sqrt{\lambda_1}}, \frac{1}{\sqrt{\lambda_2}}, 0\right)V^{\mathrm{T}}U - \frac{1}{2}U^{\mathrm{T}}U, \tag{82}$$

$$\tilde{C} = C_0 + MR^{\mathrm{T}}\mathrm{diag}\left(\frac{1}{\sqrt{\lambda_1}}, \frac{1}{\sqrt{\lambda_2}}, 0\right)V^{\mathrm{T}}U + \frac{1}{2}U^{\mathrm{T}}\mathrm{diag}(\mu_1, \mu_2, 0)U. \tag{83}$$

Combining Eqs. (66), (77) and (81), we have the identity

$$X = R^{\mathrm{T}}\mathrm{diag}\left(\frac{1}{\sqrt{\lambda_1}}, \frac{1}{\sqrt{\lambda_2}}, 0\right)V^{\mathrm{T}}U. \tag{84}$$

The other case, in which two values of $\lambda_1, \lambda_2, \lambda_3$ are small, can be treated in a similar way. In all cases we can write in general the following expressions of $\tilde{S}$ and $\tilde{C}$ with the quadratic matrices diagnolized:

$$\tilde{S} = S_0 + \sum s_i u_i - \frac{1}{2}\sum u_i^2, \tag{85}$$

$$\tilde{C} = C_0 + \sum c_i u_i + \frac{1}{2}\sum \mu_i u_i^2. \tag{86}$$

The relation between u_i and x_i ($i = 1, 2, 3$ or $i = 1, 2$ or $i = 1$) can be found in the identities Eqs. (76) or Eq. (84).

Now the maximum-entropy problem becomes one of maximizing $\tilde{S}$ in Eq. (85) under the constraint of $\tilde{C} = C_{\text{aim}}$ in Eq. (86).

$\tilde{C}$ in Eq. (86) has a minimum value of

$$\tilde{C}_{\min} = C_0 - \frac{1}{2}\sum \frac{c_i^2}{\mu_i}. \tag{87}$$

Clearly, $\tilde{C}_{\min}$ could be larger than C_{aim}. If this happens, then the maximization of S under the constraint of $\tilde{C} = C_{\text{aim}}$ will not have any solution. So we define a new constraint that can always be reached as follows:

$$\tilde{C} = \tilde{C}_0 \triangleq \max\left(C_0 - \frac{1}{3}\sum \frac{c_i^2}{\mu_i}, C_{\text{aim}}\right). \tag{88}$$

We use the Lagrange multiplier method to solve the maximization in Eq. (85) by introducing a new variable $\tilde{Q}$ as follows:

$$\tilde{Q} = \alpha\tilde{S} - \tilde{C}, \qquad \alpha > 0, \tag{89}$$

where $\alpha > 0$ guarantees that the solution found will maximize the entropy instead of minimizing it.

Substituting Eqs. (85) and (86) into Eq. (89), we find the values of u_i that maximize $\tilde{Q}$ as follows:

$$u_i = \frac{\alpha s_i - c_i}{\mu_i + \alpha}. \tag{90}$$

α is determined by solving the following equation, which is derived by substitution of Eq. (90) into Eq. (86) and by use of the constraint in Eq. (88):

$$C_0 + \sum c_i \frac{\alpha s_i - c_i}{\mu_i + \alpha} + \frac{1}{2}\sum \mu_i \left(\frac{\alpha s_i - c_i}{\mu_i + \alpha}\right)^2 = \tilde{C}_0, \qquad \alpha > 0. \tag{91}$$

After α is known, coefficients of x_1, x_2, x_3 are found by Eqs. (90) and (76) or Eq. (84), and the next assumed object for the next iteration can be calculated by Eqs. (58) and (59). At each iteration, one must reset the negative values in the assumed object to zero.

At each iteration, if the constraint of $C = C_{\text{aim}}$ is satisfied we also check to see whether the entropy is maximized by checking whether ∇Q is zero, or whether ∇S and ∇C are parallel by calculating the following value:

$$\text{test} = \frac{\nabla S \cdot \nabla C}{\sqrt{\nabla S \cdot \nabla S}\sqrt{\nabla C \cdot \nabla C}}. \tag{92}$$

The algorithm stops if $|\text{test}| < 0.1$.

There is a special case when coefficients of x_1, x_2, x_3 are too large such that the expressions in Eqs. (60) and (61) are not accurate. This is dealt with by Burch *et al.* by introduction of a distance penalty parameter.[8] However, we find that generally if the starting estimation of the object is a uniformly gray picture or a blurred picture, then this complexity can be avoided. Only when the starting image is random must we introduce the extra parameter in the algorithm in the first several loops only.

3. Convergence and Speed

To optimize the maximum-entropy algorithm, we have conducted an extended study of the effect of varying the parameter γ. Three different pictures of varying histograms are used: binary scene, zebra, and tiger. Each of these pictures has 256×256 pixels, with the maximum pixel value scaled to 255. Each picture is blurred by use of 15 normalized impulse responses, with the maximum blur consisting of a 5×5 matrix with 15 nonzero values and 10 zeros in the outer regions. Gaussian noise is added with a standard deviation σ ranging from 0.2 to 1.8 in nine steps. The metric parameter γ is given 21 values ranging from 0.0 to 1.0. Hence, in the computer simulations there are approximately 8,000 cases. Figure 8 shows the results in plots of the parameters $L\sigma/D$ versus γ, where L is the number of loops for the maximum-entropy calculation to converge, σ is the noise standard deviation, and D is the number of nonzero pixels in the blurring function. The starting images in the algorithm are uniformly gray pictures with pixel values equal to the mean of the blurred images. The rationale for using the parameter $L\sigma/D$ is explained as follows.

For the computer simulation, we find that the number of loops L for the maximum-entropy recovery is linearly proportional to the area of the point-spread function D or qualitatively proportional to the severity of the blur. The loop number is also approximately inversely proportional to the standard deviation of the noise σ.

For a wide variety of pictorial content, we see from Fig. 8 that the choice $\gamma = 0.4$ provides a much faster convergence than $\gamma = 1$. For the method of steepest ascent, $\gamma = 0$, the algorithm does converge, but it takes 173 times as many loops for a fixed σ/D than for the $\gamma = 0.4$ case (for the zebra). Another important feature that is not apparent from the curves is that when the metric γ is equal to or close to 1, there is a small chance that the algorithm will fail as a result of stagnation. From the experiment, the recommended value of the metric parameter is from 0.3 to 0.5. In summary, it is clear that the use of the metric parameter γ guarantees convergence and makes the algorithm converge much faster for a wide range of scenes.

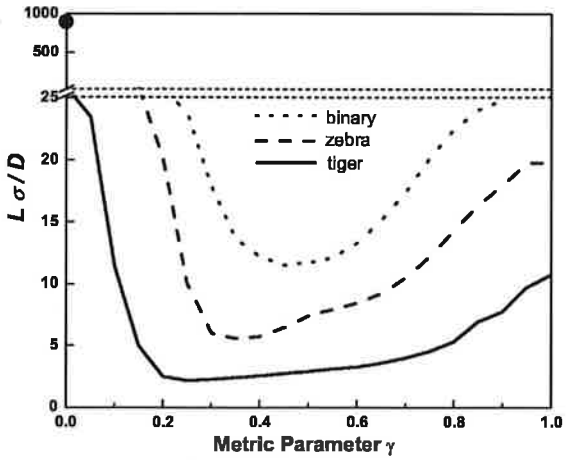

Fig. 8. Dependence of the algorithm loop number on the metric parameter γ. The big dot on the vertical axis is the value for the zebra image.

4. PERFORMANCE OF THE LOGARITHMIC-ASPHERE SYSTEM

In this section we describe computer simulations of the performance of the β-design logarithmic asphere shown in Fig. 3 and described in Section 2, used with the maximum-entropy algorithm described in Section 3, with the metric parameter $\gamma = 0.4$. To study the system resolution, first we consider the imaging of a two-point object, as in Fig. 9, separated by the diffraction limit. The images of the object blurred by the β-design logarithmic asphere are shown in Figs. 9(b)–9(d) for object distances $s = 1450$ mm, 1500 mm, and 1580 mm, respectively. Figures 9(e)–9(h) are the maximum-entropy recovery results for images in Figs. 9(a)–9(d) respectively. For comparison, we have shown the performance of an idealized perfect lens in Figs. 9(a) and 9(e). The reader will notice an excellent recovery due to the deconvolution inherent in the maximum-entropy algorithm. The standard deviation of the noise used in these recoveries is $\sigma = 1.5$. The point-spread function used for Figs. 9(b)–9(d) is the average point-spread function of the logarithmic asphere over the design range, and the point-spread function used for Fig. 9(a) is the actual diffraction blur of the ideal lens. In the maximum-entropy recovery, using any single member of the impulse responses shown in Fig. 3 will lead to near-perfect recovery at that distance. However, for extended depth of field, it is important to use the averaged point-spread function. Still, as seen in Figs. 9(b)–9(d), by the elimination of most of the oscillation rings and the narrowing of the blurs, one obtains nearly diffraction-limited resolution over the entire range.

In the second simulation, we use an object consisting of an image of zebras. Figure 10 shows (a) an image taken with a diffraction-limited lens with the object at $s = 1580$ mm and the best focus at $s = 1500$ mm; (b) the same object and distances with the β-design logarithmic asphere; and (c) the recovered image from (b) with use of the $\gamma = 0.4$ version of the maximum-entropy algorithm. The pixel size of the detector is negligible in this simulation. Notice that the blurred image in Fig. 10(a) is totally unrecognizable, whereas the image by the logarithmic lens is recognizable even before any image processing. The visibility of the low-contrast recognizable picture in Fig. 10(b) comes from the high on-axis value of the point-spread function of the β-design lens. When the object is located at 1500 mm, the best-focus position of a diffraction-limited lens, the depth of field of a diffraction-limited lens is approximately ± 8 mm.

In the maximum-entropy calculation, Fig. 7, the average point-spread function $\langle \mathrm{PSF} \rangle$ over the design range is used to obtain this recovery in Fig. 10(c). A short white line 20 μm in length in ρ_2 image space in Fig. 10(c) is drawn to shown the size of the image relative to the size of impulse response of the β-design logarithmic asphere in this simulation. The finest stripes in the zebra image have a width of ~ 1.2 μm. The contrast of the recovered image is increased, and the object at a distance $s = 1580$ mm is clearly resolved, although the OTF at this distance shows some unfavorable contrast inversion as in Fig. 4. Thus by applying the maximum-entropy method to the picture blurred by the logarithmic asphere, we have increased the depth of field approximately ten times relative to the diffraction-limited lens. In summary, we have described a circularly symmetric aspheric lens for extending the depth of field that is capable of nearly diffraction-limited resolution together with an improved algorithm that uses the maximum-entropy method.

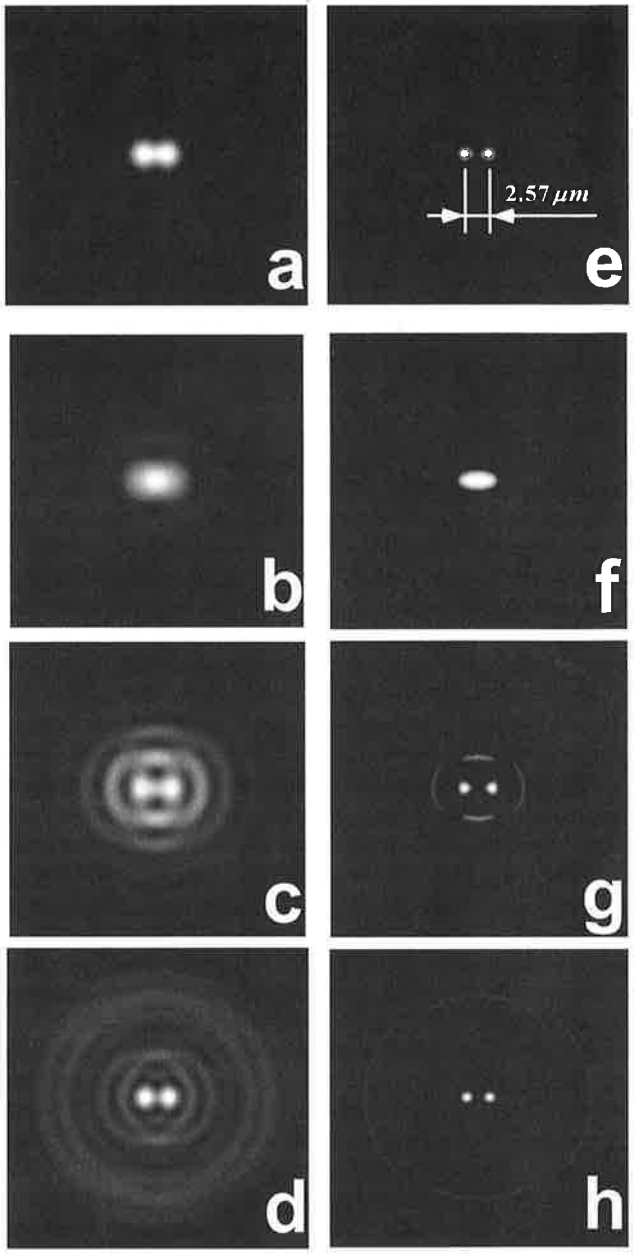

Fig. 9. Computer simulations of the resolution of a two-point object separated by the diffraction limit. (a) Blurred image by an idealized lens for the object at 1500 mm; (b), (c), and (d) blurred image by the logarithmic asphere for object at distances 1450, 1500, and 1580 mm, respectively; (e), (f), (g), and (h) maximum entropy recovery of images in (a), (b), (c), and (d), respectively.

APPENDIX A

1. Solution of the Differential Equation for $\phi_P(\rho)$

The transmission function for the lens, $\phi(\rho)$, is broken into two parts in Eq. (7), which introduces a partial phase

term $\phi_P(\rho)$. For case (i) the differential equation for $\phi_P(\rho)$ is obtained from Eq. (12):

$$(\rho^2 + t^2)\left\{\phi_P''(\rho) - \frac{\phi_P'(\rho)}{\rho} + \frac{\lambda_0^2}{4\pi^2}\frac{[\phi_P'(\rho)]^3}{\rho}\right\} = 2a_\beta\rho^2. \tag{A1}$$

For simplicity, write $\epsilon = \lambda^2/(8\pi^2)$, and then Eq. (A1) can be rewritten as

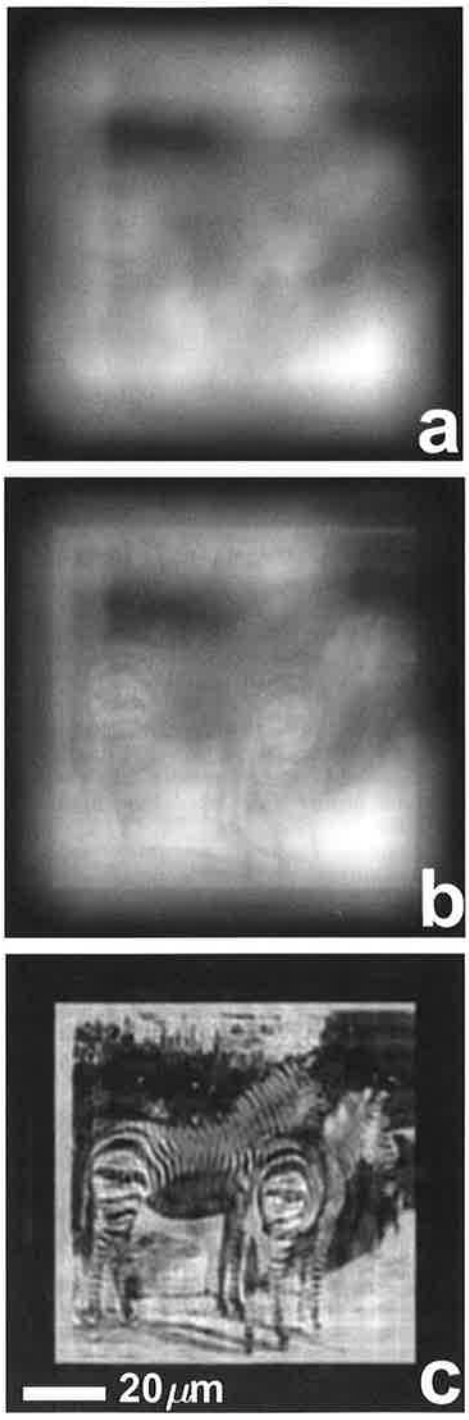

Fig. 10. Computer simulations of logarithmic asphere blur and recovery. (a) Image blurred by the diffraction-limited lens, (b) image blurred by the logarithmic asphere, (c) maximum-entropy recovery from (b).

$$(\rho^2 + t^2)\left\{\phi_P''(\rho) - \frac{\phi_P'(\rho)}{\rho} + 2\epsilon\frac{[\phi_P'(\rho)]^3}{\rho}\right\} = 2a_\beta\rho^2. \tag{A2}$$

Now let

$$\varphi(\rho) = \phi_P'(\rho); \tag{A3}$$

then Eq. (A2) is given by

$$(\rho^2 + t^2)\left\{\varphi'(\rho) - \frac{\varphi(\rho)}{\rho} + 2\epsilon\frac{[\varphi(\rho)]^3}{\rho}\right\} = 2a_\beta\rho^2. \tag{A4}$$

Clearly when $\epsilon = 0$, the above equation becomes the Bernoulli equation,

$$(\rho^2 + t^2)\left[\tilde{\phi}'(\rho) - \frac{\tilde{\phi}(\rho)}{\rho}\right] = 2a_\beta\rho^2. \tag{A5}$$

The exact solution of Eq. (A5) is

$$\tilde{\phi}(\rho) = a_\beta\rho\ln[A_\beta(t^2 + \rho^2)], \tag{A6}$$

where A_β is a constant.

We solve Eq. (A4) by a perturbation method. Assume that the solution of Eq. (A4) can be written in the form

$$\varphi(\rho) = \tilde{\phi}(\rho) + \epsilon\psi(\rho). \tag{A7}$$

Substitute Eqs. (A6) and (A7) into (A5), and collect the first-order term of ϵ. The result is also a Bernoulli equation,

$$\rho\psi' - \psi + 2\{a_\beta\ln[A_\beta(t^2 + \rho^2)]\}^3\rho^3 = 0, \tag{A8}$$

and its solution is given by

$$\psi = a_\beta^3\rho(t^2 + \rho^2)(6 - 6\ln[A_\beta(t^2 + \rho^2)] + 3\{\ln[A_\beta(t^2 + \rho^2)]\}^2 - \{\ln[A_\beta(t^2 + \rho^2)]\}^3) - B_\beta\rho, \tag{A9}$$

where B_β is a constant.

Combine Eqs. (A6), (A7), and (A9), and by use of Eq. (A3), we have the solution of Eq. (A2) as follows:

$$\phi_P(\rho) = a_\beta\frac{t^2 + \rho^2}{2}\{\ln[A_\beta(t^2 + \rho^2)] - 1\} + \epsilon\left[\frac{1}{16}a_\beta^3(t^2 + \rho^2)^2(45 - 42\ln[A_\beta(t^2 + \rho^2)] + 18\{\ln[A_\beta(t^2 + \rho^2)]\}^2 - 4\{\ln[A_\beta(t^2 + \rho^2)]\}^3) - \frac{B_\beta\rho^2}{2}\right] + \text{const.} \tag{A10}$$

2. Ray-Optics Theory for the β_0 Design

In the main text, on the basis of nonparaxial diffraction theory we derive an expression for the transmission function of the logarithmic asphere with the notation in Fig. 1. For the β-lens design it is of interest to present a ray-optics theory, as follows.

With reference to Fig. 1, the sharp image is obtained by the rays from point x_n refracted through the annular rings of radius r_n. First we separate the object range into N equal segments; the object distance for the nth segment is denoted z_n and can be written as

$$z_n = s_1 + (s_2 - s_1)n/N \tag{A11}$$

or, equivalently,

$$n = \frac{z_n - s_1}{s_2 - s_1}N. \tag{A12}$$

To provide the illumination that is consistent with intensity dropping naturally at larger object distances, the lens is separated into N rings with the area of the nth ring, a_n, inversely proportional to the object distance z_n squared, i.e., $(1/z_n)^2$. The rays from point S refracted by the nth ring of the lens converge to point P at the image plane. Hence, by Eq. (A11), one can show that

$$a_n = c[s_1 + (s_2 - s_1)n/N]^{-2}, \tag{A13}$$

where c is a constant.

From Eq. (A12), the total area within the nth ring is given by

$$\pi r_n^2 = c \sum_{n=1}^{[(x_n - s_1)/(s_2 - s_1)]N} [s_1 + (s_2 - s_1)n/N]^{-2}, \tag{A14}$$

and the total area of the lens is

$$\pi(R^2 - \delta R^2) = c\sum_{n=1}^{N} [s_1 + (s_2 - s_1)n/N]^{-2}. \tag{A15}$$

Combining Eqs. (A14) and (A15) to eliminate c, we have

$$r_n^2 = (R^2 - \delta R^2)\frac{\sum_{n=1}^{[(x_n - s_1)/(s_2 - s_1)]N} [s_1 + (s_2 - s_1)n/N]^{-2}}{\sum_{n=1}^{N} [s_1 + (s_2 - s_1)n/N]^{-2}}. \tag{A16}$$

Since the focal length varies continuously, we can obtain an integral form of Eq. (A16) by defining $\xi = n/N$. One can readily find the following form:

$$r_0^2 = (R^2 - \delta R^2)\frac{\int_0^{(s - s_1)/(s_2 - s_1)} [s_1 + (s_2 - s_1)\xi]^{-2} d\xi}{\int_0^1 [s_1 + (s_2 - s_1)\xi]^{-2} d\xi}. \tag{A17}$$

Integration of Eq. (A17) yields the final expression for the β_0 lens, as follows:

$$s = \frac{s_1 s_2(R^2 - \delta R^2)}{s_2(R^2 - \delta R^2) - (s_2 - s_1)r^2}, \qquad \delta R \leq r \leq R. \tag{A18}$$

Expression (A18) is the relation between object distance and the best focal ring of the lens if we want to make the on-axis point-spread function intensity decrease inversely proportional to the object distance squared. Note that in this ray-optics derivation, we did not consider the effect of inclination angles for rays from rings of different radius.

ACKNOWLEDGMENT

This research was supported in part by the U.S. Army Research Office.

Wanli Chi can be reached by email at chiw @optics.rochester.edu; Nicholas George can be reached by email at ngeorge@troi.cc.rochester.edu.

REFERENCES

1. J. Ojeda-Castaneda and L. R. Berriel-Valdos, "Zone plate for arbitrarily high focal depth," Appl. Opt. **29**, 994–997 (1990).
2. G. Hausler, "A method to increase the depth of focus by two step image processing," Opt. Commun. **6**, 38–42 (1972).
3. E. R. Dowski, Jr., and W. T. Cathey, "Extended depth of field through wave-front coding," Appl. Opt. **34**, 1859–1866 (1995).
4. J. van der Gracht, E. R. Dowski, Jr., W. T. Cathey, and J. P. Bowen, "Aspheric optical elements for extended depth of field imaging," in *Novel Optical Systems Design and Optimization*, J. M. Sasian ed., Proc. SPIE **2537**, 279–288 (1995).
5. W. Chi and N. George, "Electronic imaging using a logarithmic asphere," Opt. Lett. **26**, 875–877 (2001).
6. N. George and W. Chi, "Extended depth of field using the logarithmic asphere," J. Opt. A Pure Appl. Opt. **5**, S157–S163 (2003).
7. B. R. Frieden, "Restoring with maximum likelihood and maximum entropy," J. Opt. Soc. Am. **62**, 511–518 (1972).
8. S. F. Burch, S. F. Gull, and J. Skilling, "Image restoration by a powerful maximum entropy method," Comput. Vision Graph. Image Process. **23**, 113–128 (1983).
9. X. Zhuang, E. Østevold, and R. M. Haralick, "A differential equation approach to maximum entropy image reconstruction," IEEE Trans. Acoust. Speech Signal Process. **ASSP-35**, 208–218 (1987).
10. N. Wu, *The Maximum Entropy Method* (Springer-Verlag, Berlin, 1997), Chap. 3.
11. Henry Stark, *Image Recovery: Theory and Application* (Academic, Orlando, Fla., 1987), Chap. 5.
12. R. C. Gonzalez and R. E. Woods, *Digital Image Processing* (Addison-Wesley, Reading, Mass., 1992), Sect. 5.1.3.

Analysis of multitone holographic interference filters by use of a sparse Hill matrix method

Damon W. Diehl and Nicholas George

A theory is presented for the application of Hill's matrix method to the calculation of the reflection and transmission spectra of multitone holographic interference filters in which the permittivity is modulated by a sum of repeating functions of arbitrary period. Such filters are important because they may have two or more independent reflection bands. Guidelines are presented for accurately truncating the Hill matrix, and numerical methods are described for finding the exponential coefficient and the coefficients of the Floquet–Bloch waves within the filter. The latter calculation is performed by use of a computational technique known as inverse iteration. The Hill matrix for such problems is sparse, and thus, even though the matrix can be quite large, it may be efficiently stored and processed by a desktop computer. It is shown that the results of using Hill's matrix method are in close agreement with numerical calculations based on thin-film decomposition, a transfer-matrix technique. An important result of this research is the demonstration that Hill's matrix method may, in principle, be used to analyze any multiperiodic problem, so long as the periods are known to finite precision.

OCIS codes: 000.3860, 090.2890, 090.4220, 260.2110, 310.6860, 350.2460.

1. Introduction

Holographic mirrors (also known as pure-reflection holographic gratings) have wavelength selectivity properties and may be thought of as a class of interference filters. This notion of wavelength selectivity may be traced back to some of the earliest experimental work in interferometry.[1–3] For the history of reflection holography, the reader is directed to a publication of collected reprints.[4] Of particular interest are interference filters that reflect at multiple wavelength bands. Such filters have been fabricated by vacuum sputtering[5] and also through holographic processes.[6,7] A comprehensive overview of methods for analyzing reflection of light from films of continuously varying refractive index has been published in the treatise by Jacobsson.[8] Jacobsson discusses a transfer-matrix method in which an inhomogeneous film is modeled as a stack of thin homogeneous layers; that technique is referred to herein as thin-film decomposition. An analogous method for the analysis of volume gratings, called thin-grating decomposition, has been introduced by Alferness[9,10] and further developed by others.[11,12] Although dielectric gratings are not the subject of this paper, we include a few relevant citations that sample some of the key references in this extensive field.[13–19] More central to the topic are those publications that deal specifically with holographic mirrors.[20–22]

In the general study of waves in a periodic structure, one of the more important theoretical approaches depends on Hill's matrix method. This method of solution was discovered by the astronomer G. W. Hill in 1886 and used for the analysis of lunar perigee[23]; it was generalized to wave-propagation problems by Lord Rayleigh in the subsequent year.[24] Excellent treatments of Hill's equation, Floquet's theorem, and Hill's matrix method are presented by Whittaker and Watson[25] and by Magnus and Winkler.[26] Hill's matrix method has been applied to quantum mechanical oscillators by Biswas *et al.*[27] A comprehensive review of the work on electromagnetic waves in periodic structures, which mentions Hill's matrix method, has been published by Elachi.[28] Close agreement has been reported between Hill's matrix method and the extended coupled-waves analysis of Su and Gaylord.[29]

In this paper we demonstrate that Hill's matrix method may be used to analyze the normal-incidence reflection properties of multitone holographic interference filters, where multitone refers to an interference filter designed to reflect two or more wavelength

The authors are with The Institute of Optics, University of Rochester, 29 1/2 Sumner Park, Rochester, New York 14627-0186. D. W. Diehl's e-mail address is damon@optics.rochester.edu.

Received 6 June 2003; revised manuscript received 2 September 2003; accepted 2 September 2003.

0003-6935/04/010088-09$15.00/0

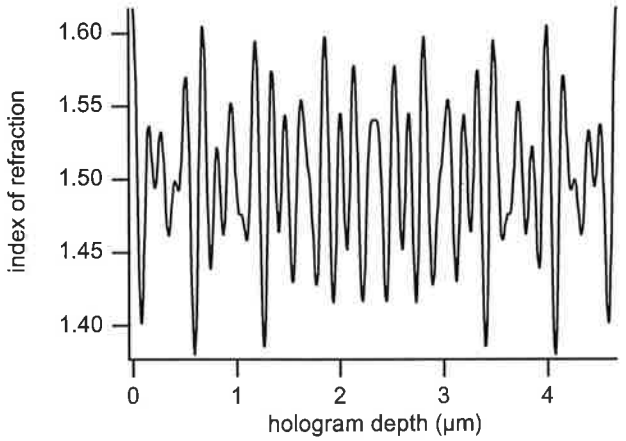

Fig. 1. Index of refraction versus hologram depth for one period of the example problem.

bands. The index profiles for such interference filters comprise the sum of repeating functions of arbitrary period and are generally quite complicated, as is illustrated by Fig. 1, which presents a portion of the index profile of an example three-tone filter, to be further studied in Section 3 below. Such filters were analyzed previously by thin-film decomposition and coupled-wave theory.[30]

In Section 2 it is established that Floquet's theorem may also be applied to a multitone problem, so long as a least common multiple (LCM) can be defined for the periods. In this case the differential equation may be transformed into an infinite system of homogeneous linear equations, which may be written in the form of an infinite matrix (the Hill matrix) multiplied by an infinite vector. This is analogous to an eigenvector problem. To find the solution, we present a procedure for determining the truncation size of the matrix, a numerical technique for finding the exponential coefficient (analogous to an eigenvalue), and a method of inverse iteration to determine the coefficients of the Floquet–Bloch waves within the film (analogous to an eigenvector).

In Section 3 we perform an example calculation, using Hill's matrix method to find the reflection spectrum of a three-tone holographic interference filter. In an independent method of solution, the result from Hill's matrix method is compared with the solution found by use of thin-film decomposition; good agreement is found.

2. Theory

Consider a lossless dielectric medium with a one-dimensional permittivity modulation described by the sum of two or more periodic functions of arbitrary period. This modulation may be described mathematically by the following formula:

$$\epsilon(z) = \sum_{l=1}^{N} f_l(z), \tag{1}$$

where $f_l(z) = f_l(z + \Lambda_l)$. We wish to calculate the reflection and transmission efficiencies for light incident upon this material at normal incidence, propagating in the $\hat{\mathbf{z}}$ direction with the electric field polarized in the $\hat{\mathbf{x}}$ direction. For these calculations it is assumed that the material is linear and isotropic and that the incident plane wave has a harmonic time dependence of $\exp(+i\omega t)$. The amplitude of the electric field, E_x, within the filter may then be described by use of the Helmholtz equation

$$\frac{\partial^2}{\partial z^2} E_x(z) + \frac{{k_0}^2}{\epsilon_0} \epsilon(z) E_x(z) = 0, \tag{2}$$

where ϵ_0 is the permittivity of free space and $k_0 = \omega/c = 2\pi/\lambda$. λ is the free-space wavelength of the incident light.

We wish to apply Floquet's theorem to this problem. Floquet's theorem states that, for any linear differential equation in which all the coefficients have period 2π, a basis for the solutions is $\exp(+\mu\xi)\phi(+\xi)$ and $\exp(-\mu\xi)\phi(-\xi)$, where μ is complex, ξ is a real, unitless variable, and $\phi(\xi)$ is a complex function with period 2π.[25] In this paper, μ is referred to as the exponential coefficient.

Floquet's theorem may be applied to Eq. (2) whenever $\epsilon(z)$ is periodic, so long as the change of variable $\xi = 2\pi z/\Lambda$ is made, where Λ is the period of $\epsilon(z)$. Equation (2) then takes the following form:

$$\left(\frac{2\pi}{\Lambda}\right)^2 \frac{\partial^2}{\partial \xi^2} E_x(\xi) + \frac{{k_0}^2}{\epsilon_0} \epsilon(\xi) E_x(\xi) = 0. \tag{3}$$

This prompts the question: "Under what circumstances will a permittivity profile, as described by Eq. (1), be periodic?" The answer is that the index profile is periodic if and only if there exists a LCM for the periods $\{\Lambda_1, \Lambda_2, \ldots, \Lambda_N\}$. The LCM is defined as the smallest number that is an integer multiple of all of the periods. The periods themselves need not be integers, however. For example, for the numbers 1.2, 1.5, and 2.1, the LCM is 42. A sufficient condition for the existence of the LCM for the set of periods is that each of the periods be known to finite precision. For this paper we assert that such is the case, allowing the use of Floquet's theorem.

Because $\epsilon(\xi)$ is periodic, it may be expanded in a Fourier series. Equation (3) may thus be written as

$$\frac{\partial^2}{\partial \xi^2} E_x(\xi) + \left[\sum_{m=-\infty}^{\infty} \theta_m \exp(im\xi)\right] E_x(\xi) = 0, \tag{4}$$

where a factor of $(\Lambda/2\pi)^2({k_0}^2/\epsilon_0)$ has been absorbed into the summation coefficients, θ_m. Defining ϵ_a to be the permittivity of the film in the limit of no modulation and using the relation $\epsilon = \epsilon_0 n^2$ yield a value of θ_0 given by the formula $\theta_0 = (\Lambda/2\pi)^2(k_0 n_a)^2$, where n_a is the index that corresponds to a permittivity of ϵ_a. Recall that k_0 is wavelength dependent and thus that the θ_m coefficients are also wavelength dependent.

Floquet's theorem assures us that Eq. (4) has a solution of the form

$$E_x(\xi) = \exp(\mu\xi)\phi(\xi) = \exp(\mu\xi)\sum_{l=-\infty}^{\infty} b_l \exp(il\xi), \tag{5}$$

where the periodic function $\phi(\xi)$ has been expanded in a Fourier series. Substituting Eq. (5) into Eq. (4) yields

$$\exp(\mu\xi)\sum_{l=-\infty}^{\infty}\left\{(\mu + il)^2 b_l \exp(il\xi) + \left[\sum_{m=-\infty}^{\infty}\theta_m \exp(im\xi)\right] b_l \exp(il\xi)\right\} = 0. \tag{6}$$

The b_l terms are the coefficients of the Floquet–Bloch waves within the filter. For Eq. (6) to be valid for all values of ξ, the summation over l must vanish; i.e.,

$$\sum_{l=-\infty}^{\infty}\left\{(\mu + il)^2 b_l \exp(il\xi) + \left[\sum_{m=-\infty}^{\infty}\theta_m \exp(im\xi)\right] b_l \exp(il\xi)\right\} = 0. \tag{7}$$

Collecting similar powers of $\exp(il\xi)$ yields

$$\sum_{l=-\infty}^{\infty}\exp(il\xi)\left[(\mu + il)^2 b_l + \sum_{m=-\infty}^{\infty}\theta_m b_{l-m}\right] = 0. \tag{8}$$

For Eq. (8) to vanish for all values of ξ, the coefficient of each $\exp(il\xi)$ term must vanish, i.e.,

$$\left[(\mu + il)^2 b_l + \sum_{m=-\infty}^{\infty}\theta_m b_{l-m}\right] = 0 \tag{9}$$

for every integer l.

Dividing by $(l^2 - \theta_0)$ yields the following recursion relation:

$$\frac{(i\mu - l)^2}{l^2 - \theta_0} b_l - \frac{\sum_{m=-\infty}^{\infty}\theta_m b_{l-m}}{l^2 - \theta_0} = 0 \tag{10}$$

for every integer l, which may be written in the form of an infinite matrix multiplied by an infinite vector:

$$\begin{bmatrix}
\ddots & \vdots & \vdots & \vdots & \vdots & \vdots & \iddots \\
\cdots & \dfrac{(i\mu+2)^2-\theta_0}{2^2-\theta_0} & \dfrac{-\theta_1}{2^2-\theta_0} & \dfrac{-\theta_2}{2^2-\theta_0} & \dfrac{-\theta_3}{2^2-\theta_0} & \dfrac{-\theta_4}{2^2-\theta_0} & \cdots \\
\cdots & \dfrac{-\theta_{-1}}{1^2-\theta_0} & \dfrac{(i\mu+1)^2-\theta_0}{1^2-\theta_0} & \dfrac{-\theta_1}{1^2-\theta_0} & \dfrac{-\theta_2}{1^2-\theta_0} & \dfrac{-\theta_3}{1^2-\theta_0} & \cdots \\
\cdots & \dfrac{-\theta_{-2}}{-\theta_0} & \dfrac{-\theta_{-1}}{-\theta_0} & \dfrac{(i\mu)^2-\theta_0}{-\theta_0} & \dfrac{-\theta_1}{-\theta_0} & \dfrac{-\theta_2}{-\theta_0} & \cdots \\
\cdots & \dfrac{-\theta_{-3}}{1^2-\theta_0} & \dfrac{-\theta_{-2}}{1^2-\theta_0} & \dfrac{-\theta_{-1}}{1^2-\theta_0} & \dfrac{(i\mu-1)^2-\theta_0}{1^2-\theta_0} & \dfrac{-\theta_1}{1^2-\theta_0} & \cdots \\
\cdots & \dfrac{-\theta_{-4}}{2^2-\theta_0} & \dfrac{-\theta_{-3}}{2^2-\theta_0} & \dfrac{-\theta_{-2}}{2^2-\theta_0} & \dfrac{-\theta_{-1}}{2^2-\theta_0} & \dfrac{(i\mu-2)^2-\theta_0}{2^2-\theta_0} & \cdots \\
\iddots & \vdots & \vdots & \vdots & \vdots & \vdots & \ddots
\end{bmatrix}
\begin{bmatrix} \vdots \\ b_{-2} \\ b_{-1} \\ b_0 \\ b_1 \\ b_2 \\ \vdots \end{bmatrix} = 0. \tag{11}$$

The division by $(l^2 - \theta_0)$ in Eq. (10) is necessary to guarantee the convergence of the determinant.[25] Unfortunately, this division introduces singularities into the problem whenever $l^2 - \theta_0 = 0$. Recall that $\theta_0 = (\Lambda/2\pi)^2(k_0 n_a)^2$. Solving for λ, we find that the Hill determinant blows up whenever $\lambda = \Lambda_{\mathrm{LCM}} n_a / l$ for any positive integer l. In solving the problem it is crucial to avoid these singular wavelengths.

The matrix relation in Eq. (11) represents a homogenous system of linear equations. Barring the trivial solution ($b_l = 0$ for every l), the equation can hold only if the determinant of the matrix is identically zero. This determinant is known as Hill's determinant[25] and is indicated by $\Delta(i\mu)$. The value of the exponential coefficient, μ, can be found by solution of the equation $\Delta(i\mu) = 0$. This is analogous to solving the eigenvalue problem $(\mathbf{A} - \mathbf{I}\lambda)\mathbf{v} = 0$, where $\mathbf{A}$ is a square matrix, $\mathbf{I}$ is the identity matrix, λ is an eigenvalue of $\mathbf{A}$, and $\mathbf{v}$ is the eigenvector of $\mathbf{A}$ that corresponds to λ. $(\mathbf{A} - \mathbf{I}\lambda)$ is a function of λ much as the Hill matrix is a function of μ.

Solving the formula $\Delta(i\mu) = 0$ for μ is a daunting undertaking. The task is simplified, however, by the following remarkable relationship:

$$\Delta(i\mu) = \Delta(0) - \frac{\sin^2(\pi i\mu)}{\sin^2(\pi\sqrt{\theta_0})} = 0, \tag{12}$$

where $\Delta(0)$ refers to the determinant of the infinite matrix in the limit $\mu \to 0$. A proof of this relationship is given by Whittaker and Watson.[25]

If the Hill matrix is truncated (as is generally nec-

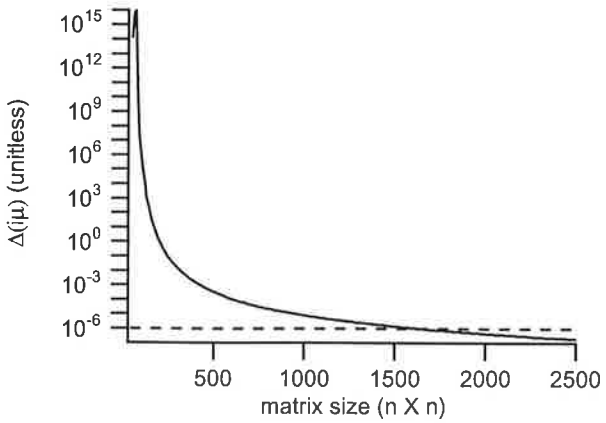

Fig. 2. Value of the Hill determinant, $\Delta(i\mu)$, as a function of matrix size. It can be seen that, as matrix size increases, the values of μ found by solution of Eq. (12) become better approximations of the root of the equation $\Delta(i\mu) = 0$. The dashed line shows that a matrix of 2497×2497 is sufficient to ensure that the Hill determinant is within 10^{-6} of 0. The test wavelength is 350 nm.

essary) the relation in Eq. (12) becomes an approximation. Specifically, a value of μ that makes one side of the equation vanish will not, in general, cause the other side to vanish. Thus a reasonable criterion for truncation is a matrix large enough that the value of μ found by solution of the right-hand side of Eq. (12) causes the Hill determinant on the left-hand side to vanish to within an accepted tolerance. For this paper, a tolerance of 10^{-6} has been chosen. In Fig. 2 the value of the Hill determinant is plotted versus matrix size for a three-tone example problem. The plot shows that, as matrix size increases, the value of μ found by solution of the right-hand side of Eq. (12) becomes a better approximation to the root of the equation $\Delta(i\mu) = 0$. This example is studied further in Section 3 below.

Equation (12) is a transcendental equation with an infinite number of solutions for μ. Each of the solutions is valid, and the solutions will yield identical results once boundary conditions are applied; however, it is most useful to choose the solution that reduces to the proper plane-wave solution in the limiting case of no index modulation. Specifically, when there is no index modulation, a plane-wave solution of the following form is expected:

$$E_x(z) = A \exp(ikz) + B \exp(-ikz), \qquad (13)$$

where $k = 2\pi n_a/\lambda$ and λ is the free-space wavelength. Comparing this solution to the form given by Floquet's theorem in Eq. (5) should make clear that Eq. (13) corresponds to the cases when all b_l vanish except for b_0 and when $\mu = \pm i\sqrt{\theta_0}$. In this limiting case, μ is strictly imaginary, and the traveling waves are unattenuated. It is expected that, when the θ_m coefficients are allowed to deviate from zero, μ will develop a small real component at certain resonant wavelengths; however, the imaginary component of μ will remain near the unperturbed value of $\pm i\sqrt{\theta_0}$. This knowledge may be used to pick an initial guess for the value of μ and then to apply Newton's method to search iteratively for the root in that region. Specifically, an initial guess of

$$\mu = \mathrm{Re}\left\{\frac{i}{\pi}\arcsin\left[\sqrt{\Delta(0)}\,\sin(\pi\sqrt{\theta_0})\right]\right\} + i\sqrt{\theta_0} \qquad (14)$$

works well.

It is worthwhile to consider under what circumstances the exponential coefficient μ has a real component, as the existence of a real component corresponds to the resonant wavelength bands of the hologram. Studying Eq. (14) reveals that μ has a real component whenever $\arcsin[\sqrt{\Delta(0)}\,\sin(\pi\sqrt{\theta_0})]$ has an imaginary component. It is therefore possible to find the location and width of the expected reflection bands of the film (i.e., the wavelengths for which μ has a real component) without finding the coefficients of the Floquet–Bloch waves or applying boundary conditions.

Once μ has been determined, the next step is to determine the values of the b_n coefficients. This is done by solution of the linear system of equations represented by the matrix relation in Eq. (11). As stated above, it is generally necessary to truncate the matrix to make the problem tractable. For a matrix truncated to a size of $(2m + 1)$ by $(2m + 1)$ (where m is a positive integer), the truncated matrix is denoted $[M_{2m+1}(i\mu)]$, and the system of linear equations becomes

$$[M_{2m+1}(i\mu)]\begin{bmatrix} b_{-m} \\ \vdots \\ b_{-1} \\ b_0 \\ b_1 \\ \vdots \\ b_m \end{bmatrix} = 0. \qquad (15)$$

Some subtlety is involved in finding the solution. Because μ has been determined to a finite precision by a numerical method, the Hill determinant $\Delta(i\mu)$ is equal to zero only within the precision limits of the calculation. Because the Hill determinant is not identically zero, standard methods of solving the linear system will result in the trivial solution $b_l = 0$ for every integer l in the range $\{-m, m\}$. To circumvent this obstacle, one may exploit the previously noted similarity between the Hill determinant and an eigenvalue problem. Calculation techniques have been developed for finding the eigenvector of a matrix, given an approximate eigenvalue. Of particular interest is the method of inverse iteration, which is credited to Wilkinson.[31,32] Inverse iteration generates a sequence of normalized vectors $\mathbf{v}_k$ from a given starting vector $\mathbf{v}_0$ by solving the following system of linear equations:

$$(\mathbf{A} - \hat{\lambda}\mathbf{I})\mathbf{v}_k = s_k\mathbf{v}_{k-1}, \qquad k \geq 1, \qquad (16)$$

where $\hat{\lambda}$ is an approximation to the eigenvalue λ and s_k is a positive number that is responsible for normalizing $\mathbf{v}_k$. To perform inverse iteration on the Hill matrix problem we replace $(\mathbf{A} - \hat{\lambda}\mathbf{I})$ in Eq. (16) by the truncated Hill matrix $[M_{2m+1}(i\mu)]$.

It has been demonstrated that a good choice for the initial vector $\mathbf{v}_0$ is a column vector consisting entirely of 1's. Frequently a single iteration yields an eigenvector that has an error less than the uncertainty of the eigenvalue. For an introduction to inverse iteration, the reader is directed to an excellent review paper by Ipsen.[33]

Once this system has been solved for all b_l, one can construct the solution by applying the boundary conditions. Consider a film of thickness L bounded on both sides by homogenous media with a cover index of n_c and a substrate index of n_s. If light with unit amplitude is incident upon the film in the $\hat{\mathbf{z}}$ direction, then the electric field within each of the regions will be of the following form:

$$E_x(z) = \begin{cases} (1)\exp(-ik_0 n_c z) + \rho\exp(+ik_0 n_c z) & z \le 0 \\ \exp\left(-\mu\dfrac{2\pi}{\Lambda}z\right)a^{(-)}\displaystyle\sum_{l=-m}^{m} b_l \exp\left(-il\dfrac{2\pi}{\Lambda}z\right) + \exp\left(+\mu\dfrac{2\pi}{\Lambda}z\right)a^{(+)}\sum_{l=-m}^{m} b_l \exp\left(+il\dfrac{2\pi}{\Lambda}z\right) & 0 \le z \le L, \\ \tau\exp[-ik_0 n_s(z-L)] & z \ge L \end{cases} \tag{17}$$

where ρ and τ are the amplitudes of the reflected and the transmitted waves, respectively, and $a^{(-)}$ and $a^{(+)}$ are the amplitudes for the two Floquet–Bloch solutions within the film. Because the tangential components of the electric and magnetic fields must be continuous across the interfaces at $z = 0$ and $z = L$, the boundary conditions can be expressed by the following four relations:

$$1 + \rho = a^{(-)}\sum_{l=-m}^{m} b_l + a^{(+)}\sum_{l=-m}^{m} b_l,$$

$$\tau = \exp\left(-\mu\frac{2\pi}{\Lambda}L\right)a^{(-)}\sum_{l=-m}^{m} b_l \times \exp\left(-il\frac{2\pi}{\Lambda}L\right) + \exp\left(+\mu\frac{2\pi}{\Lambda}L\right)a^{(+)} \times \sum_{l=-m}^{m} b_l \exp\left(+il\frac{2\pi}{\Lambda}L\right),$$

$$ik_0 n_c(-1 + \rho) = -a^{(-)}\frac{2\pi}{\Lambda}\sum_{l=-m}^{m} b_l(\mu + il) + a^{(+)}\frac{2\pi}{\Lambda}\sum_{l=-m}^{m} b_l(\mu + il),$$

$$-ik_0 n_s\tau = -a^{(-)}\exp\left(-\mu\frac{2\pi}{\Lambda}L\right)\frac{2\pi}{\Lambda}\sum_{l=-m}^{m} b_l(\mu + il)\exp\left(-il\frac{2\pi}{\Lambda}L\right) + a^{(+)}\exp\left(+\mu\frac{2\pi}{\Lambda}L\right)\frac{2\pi}{\Lambda} \times \sum_{l=-m}^{m} b_l(\mu + il)\exp\left(+il\frac{2\pi}{\Lambda}L\right). \tag{18}$$

This is a system of four linear equations and four unknowns, which can easily be solved for ρ, τ, $a^{(-)}$, and $a^{(+)}$.

3. Example Calculation with the Hill Matrix Method

Consider a three-tone holographic interference filter with a variation in permittivity described by the equation

$$\epsilon(z) = \epsilon_a + \sum_{j=1}^{3}\epsilon_j\cos\left(\frac{2\pi}{\Lambda_j}z\right) \tag{19}$$

and a thickness of $L = 25$ μm. We choose $\epsilon_a = 2.25\epsilon_0$ and $\epsilon_1 = \epsilon_2 = \epsilon_3 = 0.1216\epsilon_0$, where ϵ_0 is the permittivity of free space. We wish the filter to reflect the wavelengths $\lambda_1 = 400$ nm, $\lambda_2 = 500$ nm, and $\lambda_3 = 700$ nm when it is illuminated at normal incidence. We expect this to occur when $\Lambda_j = \lambda_j/(2n_a) = \lambda_j/(2\sqrt{\epsilon_a/\epsilon_0})$. Plugging in the appropriate values for λ_j and ϵ_a, we determine that the periods are given by $\Lambda_1 = 133.3300$ nm, $\Lambda_2 = 166.6625$ nm, and $\Lambda_3 = 233.3275$ nm. A plot of the index modulation corresponding to this choice of parameters is shown in Fig. 1. We calculate the reflection spectrum of this multitone holographic interference filter below, using Hill's matrix method and thin-film decomposition.

A. Hill's Matrix Method

A LCM exists for the three periods, and it has the value $\Lambda_{\mathrm{LCM}} = 4.66655$ μm. Expanding the permittivity in a Fourier expansion, we may determine the

θ_m terms from Eq. (4). Specifically, the values of θ_m are given by the following expression:

$$\theta_m = \left(\frac{\Lambda_{\mathrm{LCM}} k_0}{2\pi}\right)^2 \frac{1}{\epsilon_0} \begin{cases} \epsilon_a & m = 0 \\ \epsilon_3/2 & m = \pm 20 \\ \epsilon_2/2 & m = \pm 28 \\ \epsilon_1/2 & m = \pm 35 \\ 0 & \text{all other } m \end{cases} . \quad (20)$$

This is enough information to allow us to proceed with constructing the Hill matrix and calculating the Hill determinant. Note that $\theta_m = 0$ for all but seven values of m; thus the matrix comprises mostly zeros. This is known as a sparse matrix. One may greatly economize both computer memory and processing time by keeping track of only the nonzero elements of the matrix. For this reason we used the programming environment Matlab to handle the calculation of the Hill determinant, as it handles sparse matrices well.

As mentioned above, it is not feasible to calculate the determinant of an infinite matrix; therefore a first step toward a solution is truncating the Hill matrix. A reasonable requirement is to find a matrix size such that Eq. (12) is still valid to within an acceptable tolerance. Specifically, a matrix size is desired such that the value of μ found by solution of $\Delta(0) - \sin^2(\pi i\mu)/\sin^2(\pi\sqrt{\theta_0}) = 0$, yields a determinant as close to zero as desired, when μ is substituted into $\Delta(i\mu)$. For a tolerance of 10^{-6}, a matrix size of 2497×2497 is more than sufficient to meet this constraint at the test wavelength, 350 nm, as illustrated in Fig. 2.

Having truncated the matrix, we may solve the equation $\Delta(i\mu) = 0$ for μ by using Newton's method. This must be done for each wavelength to be tested. For this problem the spectrum is calculated over the range 350–750 nm, at a resolution of 0.01 nm. Over this interval singularities will occur near the following wavelengths: 368.412, 388.879, 411.754, 437.489, 466.655, 499.988, 538.448, 583.319, 636.348, and 699.983 nm. Test wavelengths that lie within 0.001 nm of one of these singularities will be skipped. Specifically, the reflection spectrum will not be calculated at 388.88 or 437.49 nm.

Figure 3 is a plot of Re(μ) versus free-space wavelength. Similarly, Fig. 4 is a plot of Im(μ) versus free-space wavelength. Notice that Re(μ) is identically zero except in the vicinity of 400, 500, and 700 nm. These nonzero regions define the reflection bands of the hologram. If finding the reflection bands were our only goal, then the calculation could be stopped here.

Having determined μ, we may use inverse iteration to calculate the 2497-element vector that describes the field structure within the hologram. This exercise must be repeated for every wavelength and the corresponding μ. The individual calculations take only a second or two, but the entire process (with nearly 40,000 wavelengths) takes several hours. However, a lower-resolution spectrum could be calculated in a matter of minutes.

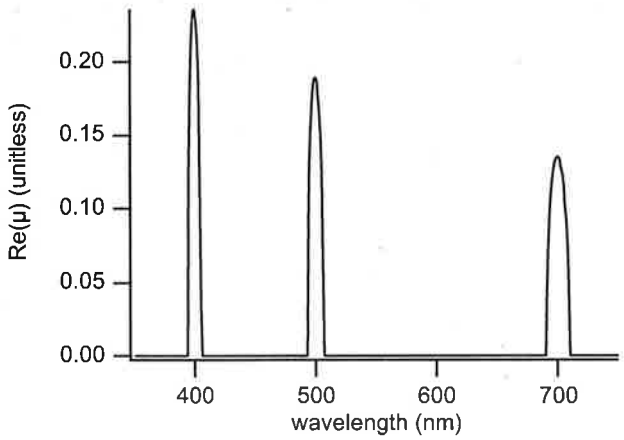

Fig. 3. Re(μ) versus free-space wavelength. The regions where Re(μ) > 0 correspond to the reflection bands of the hologram.

Once the field structure has been determined for each wavelength, the boundary conditions may be applied. These are set out in Eqs. (18). For this problem we have chosen to match the cover and the substrate to the average index of the filter by setting $n_c = n_s = n_a$. Solving for the four unknowns [ρ, τ, $a^{(+)}$, and $a^{(-)}$] is straightforward. Figure 5 is a plot of $R = |\rho|^2$ versus free-space wavelength, as calculated by Hill's matrix method.

B. Thin-Film Decomposition

The accuracy of the above calculation may be confirmed by separate calculations of the reflection spectrum by use of thin-film decomposition. In a previous publication[7] on the fabrication of holographic interference filters, the process of thin-film decomposition was explained in detail. In this sec-

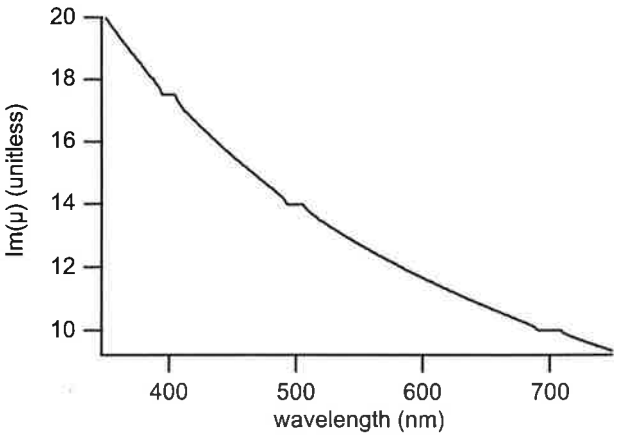

Fig. 4. Im(μ) versus free-space wavelength. The flat regions of the curve correspond to the wavelengths for which Re(μ) is nonzero.

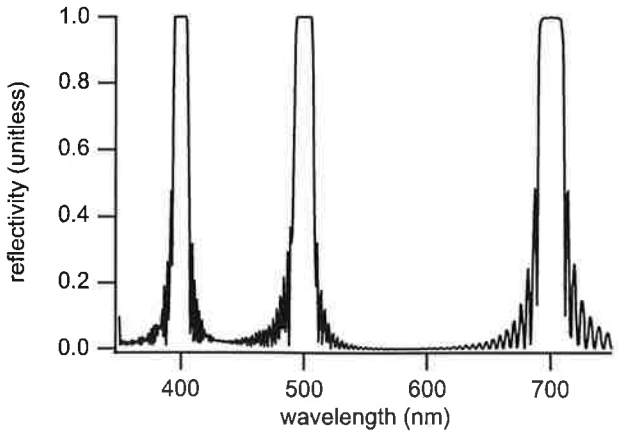

Fig. 5. Reflection spectrum of a three-tone holographic interference filter, as calculated by Hill's matrix technique.

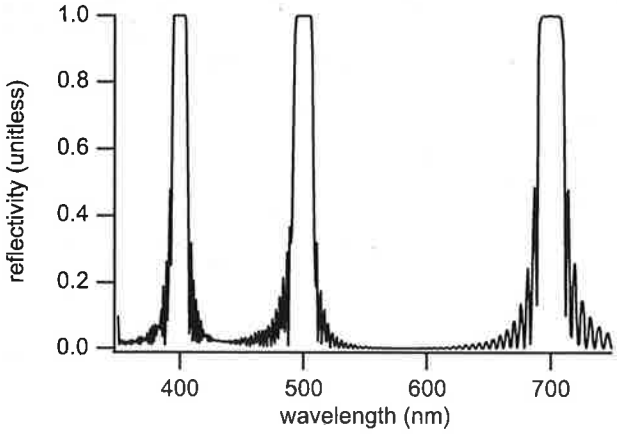

Fig. 6. Reflection spectrum of a three-tone holographic interference filter, as calculated by thin-film decomposition.

tion those results are briefly reviewed and applied to the current problem.

As was previously established,[8] an inhomogeneous stratified medium may be modeled as a stack of thin homogeneous layers. The wave equation can then be solved within each of these homogeneous regions, and one can calculate the reflection and transmission properties of the entire filter by matching the fields at the layer boundaries. The calculations can be expedited by use of matrix notation to characterize each layer. One can then calculate a characteristic matrix for the entire film by chain multiplying the characteristic matrices of each of the decomposition layers. In the research described here, the matrix formalism used by Macleod[34] was used.

It was previously established that, if each period of a holographic interference filter is decomposed into 300 layers, the reflectivity spectrum will be within 10^{-7} of the limiting solution.[35] For the three-tone problem being studied, the smallest period is 133.33 nm, and thus using a layer of 0.44-nm thickness will be more than sufficient to surpass the measurement limits of most spectrophotometers. After the film is decomposed into 56,251 layers, one may then apply transfer-matrix techniques to find the reflection spectrum of the stack of thin films. This spectrum is plotted in Fig. 6 and is clearly quite similar to that plotted in Fig. 5. To compare the two spectra quantitatively, one may calculate the difference between the two, as shown in Fig. 7. The two spectra differ by less than 0.01 (i.e., 1%) over the entire wavelength range.

4. Summary

In this paper a technique has been presented for calculation of the reflection and transmission spectra of multitone holographic interference filters in which the permittivity is modulated by a sum of repeating functions of arbitrary period, as shown in Eq. (1). So long as the component periods are known to finite precision, a least common multiple of the periods will exist, and the filter may be treated as periodic. Floquet's theorem may then be used to posit a solution to the Helmholtz equation. The trial solution is given by Eq. (5). With this trial solution, the Helmholtz equation may be transformed into a recursion relationship for the coefficients of the Floquet–Bloch waves within the material. This recursion relation, given by Eq. (10), may be written as an infinite matrix multiplied by an infinite vector, as shown in Eq. (11). Solving this system of equations is akin to solving an eigenvector problem. Specifically, the exponential coefficient, μ, may be thought of as an eigenvalue of the Hill matrix, and the vector that describes the Floquet-Bloch coefficients may be thought of as the corresponding eigenvector. Determining the exponential coefficient is greatly simplified through the use of the identity given by Eq. (12).

In general, the infinite Hill matrix must be truncated to a finite size. A criterion with which to de-

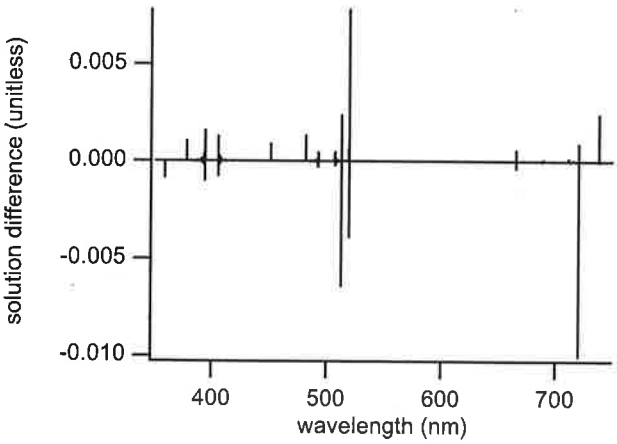

Fig. 7. Difference between the reflection spectra as calculated by Hill's matrix method and by thin-film decomposition. The result of subtracting the thin-film-decomposition spectrum from Hill's matrix method spectrum is shown.

termine how small the matrix may be, while it still yields the desired level of precision, must be found. The criterion presented in this paper is that the identity in Eq. (12) must hold to within a desired level of precision for the truncated matrix.

Equation (12) is a transcendental equation with an infinite number of solutions. Newton's method may be used to solve the equation for μ. Equation (14) is proposed as a good initial guess for μ, as it will converge properly in the limit of zero index modulation.

Once the matrix has been truncated and μ has been determined, the coefficients of the Floquet–Bloch waves within the material must be determined. This is a difficult problem to solve because the value for μ is an approximation, as it has been determined by a numerical method; this can force a trivial solution. We have shown, however, that a solution can be found by use of a technique called inverse iteration.

Given the coefficients of the Floquet–Bloch waves, one finds the solution for a given problem by matching boundary conditions. For a finite multitone structure bounded by semi-infinite homogenous media and illuminated at normal incidence, the appropriate boundary conditions are given by Eqs. (18).

As an example of this technique, a three-tone holographic interference filter was analyzed. Its permittivity is described by Eq. (19) and plotted in Fig. 1. It was determined that a matrix size of 2497×2497 was sufficient for the desired level of precision. The real and imaginary components of exponential coefficient μ are plotted in Figs. 3 and 4. The regions where μ takes on a real component correspond to the reflection bands of the filter. The reflection spectrum of the filter as calculated by Hill's matrix method is plotted in Fig. 5. Excellent agreement was found with the spectrum as calculated by thin-film decomposition, which is plotted in Fig. 6. It is believed that both methods converge to the same solution in their respective limits. The value of using Hill's matrix method is that it provides a closed-form solution for a rather complicated problem. Furthermore, for the example presented here, Hill's matrix method of solution takes ~30% less time than the thin-film decomposition solution; the two yield nearly identical spectra. However, it must be noted that thin-film decomposition is easier to apply to a broader class of problems, particularly when it cannot be argued that the modulation of the permittivity is periodic.

The authors thank Christopher J. Ditchman for helpful discussions regarding sparse matrices and Matlab. This research was supported in part by the U.S. Army Research Office.

References

1. O. Wiener, "Stehende Lichtwellen und die Schwingungrichtung polarisirten Lichtes," Ann. Phys. Chem. **40,** 203–243 (1890).
2. G. Lippmann, "Sur la théorie de la photographie des coulars simples et compusées par la méthode interférentielle," J. Phys. (Paris) **3,** 97–107 (1894).
3. P. Connes, "Silver salts and standing waves: the history of interference colour photography," J. Opt. (Paris) **18,** 147–166 (1987).
4. T. W. Stone and B. J. Thompson, eds., *Selected Papers on Holographic and Diffractive Lenses and Mirrors*, Vol. MS 34 of SPIE Milestones Series (SPIE Optical Engineering Press, Bellingham, Wash., 1991).
5. J. B. Adolph, R. W. Bertram, K. L. Yan, P. Zhou, and R. de Leon, "Design and fabrication of multi-line inhomogeneous rejection filters," in *Inhomogeneous and Quasi-Inhomogeneous Optical Coatings*, J. A. Dobrowolski and P. G. Verly, eds., Proc. SPIE **2046,** 141–146 (1993).
6. K. W. Steijn, "Multicolor holographic recording in DuPont holographic recording film: determination of exposure conditions for color balance," in *Holographic Materials II*, T. J. Trout, ed., Proc. SPIE **2688,** 123–134 (1996).
7. D. W. Diehl and N. George, "Holographic interference filters for infrared communications," Appl. Opt. **42,** 1203–1210 (2003).
8. R. Jacobsson, "Light reflection from films of continuously varying refractive index," in *Progress in Optics*, E. Wolf, ed. (North-Holland, Amsterdam, 1966), Vol. 5, Chap. 5, pp. 247–286.
9. R. Alferness, "Analysis of optical propagation in thick holographic gratings," Appl. Phys. **7,** 29–33 (1975).
10. R. Alferness, "Analysis of propagation at the second-order Bragg angle of a thick holographic grating," J. Opt. Soc. Am. **66,** 353–362 (1976).
11. T. W. Stone and N. George, "Wavelength performance of holographic optical elements," Appl. Opt. **24,** 3797–3810 (1985).
12. T. W. Stone, "Holographic optical elements," Ph.D. dissertation (University of Rochester, Rochester, N.Y., 1986).
13. C. V. Raman and N. S. N. Nath, "The diffraction of waves by high frequency sound waves. I, II," Proc. Ind. Acad. Sci. **2,** 406–420 (1935).
14. C. V. Raman and N. S. N. Nath, "The diffraction of waves by high frequency sound waves. III, IV," Proc. Ind. Acad. Sci. **3,** 75–84, 119–125 (1936).
15. H. Kogelnik, "Coupled wave theory for thick hologram gratings," Bell Syst. Tech. J. **48,** 2909–2947 (1969).
16. M. Chang and N. George, "Holographic dielectric grating: theory and practice," Appl. Opt. **9,** 713–719 (1970).
17. M. G. Moharam and T. K. Gaylord, "Rigorous coupled-wave analysis of planar-grating diffraction," J. Opt. Soc. Am. **71,** 811–818 (1981).
18. M. G. Moharam and T. K. Gaylord, "Planar dielectric grating diffraction theory," Appl. Phys. B **28,** 1–14 (1982).
19. P. St. J. Russell, "Optics of Floquet–Block waves in dielectric gratings," Appl. Phys. B **39,** 231–246 (1986).
20. M. G. Moharam and T. K. Gaylord, "Chain-matrix analysis of arbitrary-thickness dielectric reflection gratings," J. Opt. Soc. Am. **72,** 187–190 (1982).
21. Z. Zylberberg and E. Marom, "Rigorous coupled-wave analysis of pure reflection gratings," J. Opt. Soc. Am. **73,** 392–398 (1983).
22. M. G. Moharam and T. K. Gaylord, "Comments on analyses of reflection gratings," J. Opt. Soc. Am. **73,** 399–401 (1983).
23. G. W. Hill, "On the part of the motion of the lunar perigee which is a function of the mean motions of the Sun and Moon," Acta Math. **8,** 1–36 (1886).
24. Lord Rayleigh, "On the maintenance of vibrations by forces of double frequency, and on the propagation of waves through a medium endowed with a periodic structure," Phil. Mag. J. Sci. **24,** 145–159 (1887).
25. E. T. Whittaker and G. N. Watson, *A Course of Modern Anal-*

ysis, 4th ed. (Cambridge U. Press, Cambridge, 1927), Chap. 19, pp. 412–417.
26. W. Magnus and S. Winkler, "Hill's equation," in *Interscience Tracts in Pure and Applied Mathematics*, L. Bers, R. Courant,and J. J. Stoker, eds. (Wiley Interscience, New York, 1966), Vol. 20, Chap. 1, pp. 3–10.
27. S. N. Biswas, K. Datta, R. P. Saxena, P. K. Srivastava, and V. S. Varma, "The Hill determinant: an application to the anharmonic oscillator," Phys. Rev. D **4,** 3617–3620 (1971).
28. C. Elachi, "Waves in active and passive periodic structures: a review," Proc. IEEE **64,** 1666–1698 (1976).
29. D. L. Jaggard and C. Elachi, "Floquet and coupled-wave analysis of higher-order Bragg coupling in a periodic medium," J. Opt. Soc. Am. **66,** 674–682 (1976).
30. X. Ning, "Analysis of multiplexed-reflection holographic gratings," J. Opt. Soc. Am. A **7,** 1436–1440 (1990).
31. J. H. Wilkinson, "The calculation of eigenvectors of codiagonal matrices," Comput. J. **1,** 90–96 (1958).
32. J. H. Wilkinson, "Inverse iteration in theory and practice," in *Symposium Mathematica* (Instituto Nazionale de Alta Matematica, Rome, 1972), Vol. X, pp. 361–379.
33. I. C. F. Ipsen, "Computing an eigenvector with inverse iteration," Soc. Indust. Appl. Math. Rev. **39,** 254–291 (1997).
34. H. A. Macleod, *Thin-Film Optical Filters*, 2nd ed. (McGraw-Hill, New York, 1989).
35. P. Sharlandjiev and T. Mateeva, "Normal incidence holographic mirrors by the characteristic matrix method. Numerical examples," J. Opt. (Paris) **16,** 185–189 (1985).

Scanned-picture-beam holography for nonrigid objects

William W. Cook and Nicholas George

A technique is described for holographically recording nonrigid objects by scanning the picture beam in a small, bright spot across the object in a series of short exposures. The reference beam is incident across the entire recording medium during each exposure. This technique can freeze the motion of objects subject to ambient forcings, such as acoustic vibrations. Experiments are described in support of this method. Exposures are in the 1- to 10-ms range with 100 separate object regions. An analysis of certain factors affecting image quality, such as diffraction efficiency, is also presented. © 2004 Optical Society of America

OCIS codes: 090.2870, 090.2900, 090.4220, 110.2990, 110.4190, 110.6880.

1. Introduction

An axiom of pictorial holography is that the object and optical components must be as stable as possible during exposure. Object motion on the order of a wavelength during exposure can cause the image to be completely dark or to have prominent dark fringes.[1]

Although pulsed lasers can make holograms of rapidly moving objects, e.g., a bullet in flight,[2] continuous wave (cw) lasers have advantages, such as coherence properties, available wavelength number, continuous wavelength tuning (e.g., a dye laser), and ease of optical alignment.

Other researchers in holography have devised various scanned-beam techniques to record pictorial holograms.[3–6] Techniques demonstrated in the literature include scanning a small, bright reference beam over the film plate[3,4] and scanning a beam over the object and film together in a reflection holography method.[5]

In our experiment the picture beam is a small, bright spot that is scanned across an object is a series of short exposures. The light scattered from the small region of the object falls across the entire film plate. The reference beam also fills the film plate for each exposure. An identical reference beam is used for each exposure. The brightness of the illuminating spot allows each small region of the object to be recorded in an acceptably short exposure, thus freezing the object's motion. For a typical result one can reduce exposure time from ~10 s for the entire object to a series of 100 exposures, each of ~1 ms. A key feature of our technique is computer control of a shutter and a two-axis galvanometer to step the picture beam across the object. Although in this paper we concentrate on nonrigid objects, it is worthwhile to point out that this scanning method is also well suited for making holograms of fairly large objects that may be difficult to illuminate uniformly with one beam.

In Section 2 we derive expressions for the transmission functions of hologram film plates used to record an object in one exposure and in multiple exposures. In Section 3 the equations for transmission functions are used to derive an expression for the decrease in hologram fringe visibility when the object is recorded in multiple exposures. A computer simulation that compares our derivation with an experiment from the literature is presented. In Section 4 we describe laboratory implementation of scanned-picture-beam holography. In Section 5 pairs of holographic images are presented. For each pair, one hologram is made with a single exposure of a cw laser, and a second hologram is made with the scanned-beam method described here. The results show the superiority of the scanning method for a variety of everyday objects that are subject to small-amplitude ambient vibrations at acoustic or subacoustic frequencies. Section 6 addresses the possibility of interference between adjacent image regions of a scanned-beam hologram. Section 7 contains a summary.

The authors are with the University of Rochester, the Institute of Optics, River Campus Box 270186, Rochester, New York 14627-0186. W. W. Cook's e-mail address is wcook@optics.rochester.edu.

Received 13 June 2003; revised manuscript received 27 September 2003; accepted 5 November 2003.

0003-6935/04/081703-07$15.00/0

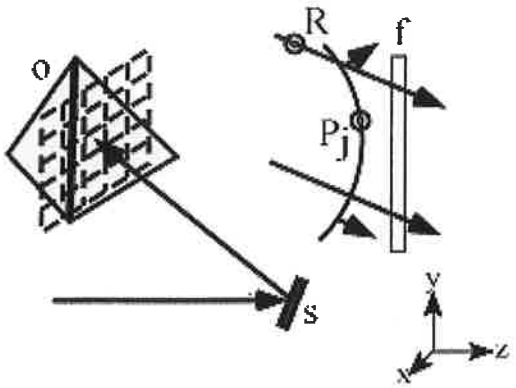

Fig. 1. Setup for scanned-picture-beam holography: o, object; s, scanner; P_j, picture beam from the jth object region; R, reference beam; f, hologram film plate.

2. Exposure Analysis for Scanned-Beam Holography

In this section we compare the transmission function of a developed hologram film plate used to record an object in one exposure with the transmission function of an identical film plate used to record the same object in multiple exposures. We choose the transmission function model to represent a grating-type hologram because it is convenient and because it can be applied to any number of recording media, e.g., film plates or sheets of photopolymer. This model does not attempt to account for thickness effects or for the underlying structure of the recording medium, such as the granular nature of developed film.

Central to this comparison of single-versus multiple-exposure pictorial holography is consideration of the object as being divided into N small regions. Figure 1 illustrates the recording of a pictorial hologram. A single electronically controlled shutter (not shown) is used to control the exposure time for both the reference beam and the picture beam. A typical exposure time is 1–10 ms, and a typical time between exposures is 30 ms, for a total exposure time on the order of 4 s. The reference beam illuminates the entire film plate. The picture beam is incident on some portion of the object. Light scatters from that portion of the object and is incident across the entire film plate.

We assume that all light incident on the film plate is polarized perpendicular to the plane of the paper. We neglect the small amount of cross-polarized light that may result from scattering by the object. It has been shown that diffuse objects typically cause a depolarization below 10%.[7] At a point (x, y) on the film plate, the electric field due to the reference beam is given by $\mathbf{x}|R(x, y)|\exp[i\phi(x, y)]$, where $\mathbf{x}$ is the unit vector along the x axis. The $\mathbf{x}$ component of the electric field due to the picture beam scattered from the jth region of the object is given by $\mathbf{x}|P_j(x, y)|\exp[i\theta_{P_j}(x, y)]$.

Given that the magnitude of the picture and reference beams are constant during an exposure of time T, the total energy density, $E_{\text{tot}}(x, y)$, deposited on the film at a point (x, y) during a single exposure is given by

$$E_{\text{tot}}(x, y) = T[P(x, y) + R(x, y)][P(x, y) + R(x, y)]^*, \quad (1)$$

where the asterisk denotes the complex conjugate value.

The transmission function of the developed film plate, $\Phi_s(x, y)$, will be proportional to $E_{\text{tot}}(x, y)$, assuming a linear recording. For convenience we set the proportionality constant to unity. Hence the transmission function of the film on which all N regions of the object are recorded simultaneously in one exposure is given by

$$\Phi_S(x, y) = T_S\left(\sum_j^N P_{S_j} + R_S\right)\left(\sum_j^N P_{S_j} + R_S\right)^*, \quad (2)$$

where the subscript s indicates a single exposure. The (x, y) dependence on the right-hand side (RHS) of Eq. (2) is omitted for clarity. Equation (2) indicates that we treat the electric field due to the picture beam incident at (x, y) on the recording medium as the sum of N separate, coherent fields, each scattered from a separate region of the object.

If we record the same object in a series of exposures, with each exposure recording one region, the transmission function is

$$\Phi_M(x, y) = \sum_j^N [T_{M_j}(P_{M_j} + R_M)(P_{M_j} + R_M)^*], \quad (3)$$

where the subscript m indicates multiple exposure.

Generally $|P_{M_j}| \neq |P_{S_j}|$ and $|R_M| \neq |R_S|$ because the beam intensities have to be adjusted differently for each type of hologram. Furthermore, because the optical path from laser to object is different from the single-exposure case to the multiple-exposure case, $\theta_{M_j}(x, y) \neq \theta_{S_j}(x, y)$. The reference beam path is the same for both types of holograms so that $\phi(x, y)$ is the same and does not require an s or m subscript.

If one carries out the multiplications in Eq. (2), the transmission function $\Phi_s(x, y)$ for the single-exposure case is given by

$$\Phi_S(x, y) = T_S\left\{\left(\sum_j^N |P_{S_j}|\right)^2 + |R_S|^2 + 2\sum_j^N [|P_{S_j}||R_S|\cos(\theta_{S_j} - \phi)]\right\}, \quad (4)$$

in which the third term on the RHS represents the interference between the reference beam and the single picture beam.

For the multiple-exposure case, one obtains $\Phi_M(x, y)$ as follows:

$$\Phi_M(x, y) = T_M\left\{\left(\sum_j^N |P_{M_j}|^2\right) + N|R_M|^2 + 2\sum_j^N [|P_{M_j}||R_M|\cos(\theta_{M_j} - \phi)]\right\}, \quad (5)$$

where now the third term on the RHS represents the interference between the reference beam and N separate picture beams. Equation (5) assumes that all the times T_{Mj} are equal.

We now develop our strategy for comparing single- and multiple-exposure holograms of the same object and relate this strategy to Eqs. (4) and (5).

The total energy deposited on the film plate is kept equal for each pair of holograms to keep the exposures on comparable portions of the exposure response curve of the film. We assert that the spatially varying portions of Eqs. (4) and (5) do not contribute to the average recorded intensity when it is averaged over many spatial periods. This includes the effects of interference between the fields scattered by different object regions in Eq. (4). In other words, when we expand the sum $(\Sigma_j^N |P_{S_j}|)^2$ from the RHS of Eq. (4), cross terms such as $|P_{S_1}||P_{S_2}|\cos(\theta_{S_1} - \theta_{S_2})$, when integrated over the area of the film plate, are negligible for calculations of the average energy deposited on the film. Thus we have

$$T_S\left[\left(\sum_j^N |P_{S_j}|^2\right) + |R_S|^2\right] = T_M\left[\left(\sum_j^N |P_{M_j}|^2\right) + N|R_M|^2\right]. \tag{6}$$

To make the recorded fringe visibility as high as possible and thus to maximize diffraction efficiency we make the intensity of the picture beam equal (or as near as possible) to that of the object beam during each exposure. These conditions give

$$\sum_j^N |P_{S_j}|^2 = |R_S|^2, \tag{7}$$

$$\sum_j^N |P_{M_j}|^2 = N|R_M|^2. \tag{8}$$

For Eq. (8) to hold we average the intensities of light scattered from various object regions and set the reference beam intensity equal to that average.

Using Eqs. (6)–(8) we can write

$$T_S|P_{S_j}|^2 = T_M|P_{M_j}|^2, \tag{9}$$

$$T_S|R_S|^2 = T_M N|R_M|^2. \tag{10}$$

To keep the amount of object movement during exposure acceptably small, we make T_M as short as possible. In subsequent calculations we will need the relation

$$T_S = CT_M, \tag{11}$$

where C is a constant. Usually $C \neq N$.

3. Theory for Multiple-Exposure Holography

In this section we use the transmission functions developed above to derive an equation for the fringe visibility of the hologram recorded when the picture beam is scanned in N exposures.

Referring to Eq. (4), the visibility of the fringe pattern due to the jth object region is given by

$$V_{S_j} = \left[\frac{2|P_{S_j}||R_S|}{\left(\sum_j^N |P_{S_j}|^2\right) + |R_S|^2}\right]T_S. \tag{12}$$

This expression can be considered valid as an average over a small region of the recording medium. Over this small region the effects of interference between the various P_{Sj}'s averages to a negligible number. We can write a similar expression for fringe visibility in the multiple-exposure case, V_{Mj}, by using Eq. (5).

Solving for the change in fringe visibility as a function of the number of exposures, we can use Eqs. (9)–(11) to write

$$\frac{V_{S_j}}{V_{M_j}} = \frac{T_S|P_{S_j}||R_S|}{T_M|P_{M_j}||R_M|} = \sqrt{N}. \tag{13}$$

The visibility of the jth fringe pattern—one of N patterns superimposed on the recording medium—decreases by $1/\sqrt{N}$ when each of the N separate object regions is recorded in a separate exposure.

The diffraction efficiency, η, of a hologram is inversely proportional to the number of exposures used to record the hologram:

$$\eta \propto 1/N, \tag{14}$$

where N is the number of exposures. Furthermore, for a given average exposure in an amplitude transmission medium,

$$V \propto \sqrt{\eta}, \tag{15}$$

where V is the fringe visibility of the recorded interference pattern.[8]

In the modeling of fringe visibility, there are several approximations that are customarily made. We assume grating-like patterns (i.e., simple plane-wave picture beams as well as minimal film thickness) so that the fringe pattern would be visible via a microscope. This model [e.g., resulting in Eq. (14)], has been found to agree well with theory.[8] In our computer simulation described below, we provide a test of Eq. (15) by using the above-described model.

In a technique taken from the literature,[9] the object is modeled as an array of point sources, which are distributed randomly over a 10 cm × 10 cm object plane normal to the optic axis and 20 cm from the film plate.

For a given number of point sources, the program calculates fringe patterns on the film plate for two sets of conditions: first, for all sources turned on at once and then for each source turned one at a time in sequence. The reference beam is a unit amplitude plane wave. The relative intensities are normalized in accordance with Eqs. (6)–(8) above, according to whether the sources are recorded simultaneously or sequentially. This normalization is calculated at the film-plate point closest to a given object point

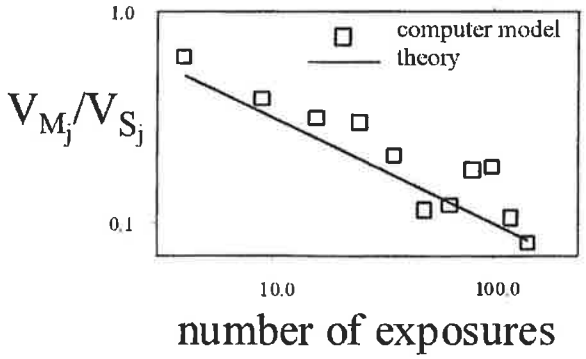

Fig. 2. Plot of ratio V_{M_j}/V_{S_j} versus the number of exposures.

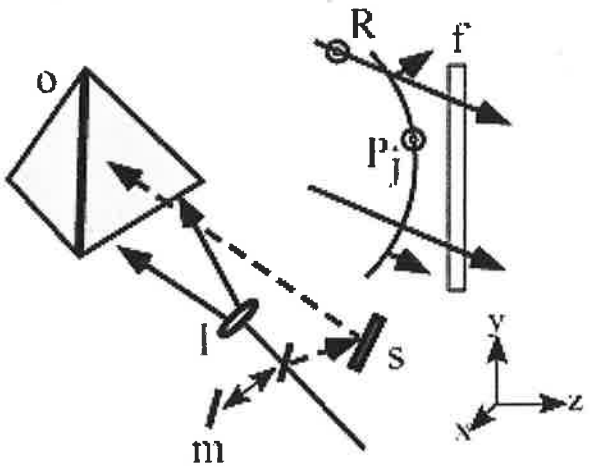

Fig. 3. Setup for recording an object with one exposure and then separately with multiple exposures by means of a scanned picture beam: o, object; s, scanner; m, mirror; l, lens; P_j, picture beam from the jth object region; R, reference beam; f, hologram film plate. The lens expands the picture beam to illuminate the entire object to produce a single-exposure hologram. Alternatively, the mirror moves into the beam path to select the scanner and to bypass the lens to make a multiple-exposure recording.

source, i.e., at the film plate with the same (x, y) coordinates as the object point source.

To measure V for the fringe pattern caused by light from a given point source, the maxima and minima are calculated for the pattern produced by that source alone as it interferes with the reference beam. Then the overall fringe pattern due to all object sources is sampled at these maxima and minima points. Each local maximum with an adjacent minimum is used to calculate a local value for V, and these local values are averaged over 50–100 adjacent quasiperiods.

To calculate one value for $V_{S_j}/V_{M_j}(N)$, both V_{Sj} and V_{Mj} are calculated for each of four small regions of the film plate, and the four measurements are averaged. The computer simulation shown in Fig. 2 agrees well with Eq. (15) and with the predictions from the literature.[8,9]

4. Experiments with Nonrigid Objects

This section addresses the laboratory implementation used to test the ideas presented in Sections 2 and 3. A two-axis galvanometric scanner is used to steer the beam across the object. An electronic shutter controls the exposure time. The scanner and shutter are controlled by a personal computer.

Before making a scanned hologram of a given object, we first make the best single-exposure hologram that the stability of the object allows. To ensure that our recording apparatus is in good order, we include stable reference objects in each hologram. Frequently the reference object, such as a bolt screwed into the top of the optical table, is clear in the image, whereas the nonstable object is dim or barely discernable to the eye.

The intended total energy density incident on the film plates owing to the picture and reference beams is in the range of 20–100 $\mu J/cm^2$, based on film characteristics. Before a hologram is recorded, each plate is exposed to one burst from a camera flash held approximately four m away. After completing the preflash and recording steps, we develop each film plate in the same manner. The advantage of using preflashing is that it standardizes the Hurter–Driffield curve from lot to lot, and it also linearizes the exposure curve, which is helpful with multiple exposures.[10]

Laser output power of ~1 W is sufficient to record objects with dimensions of ~10 cm × 10 cm at a distance of approximately 20 cm from the film plate. Our intent is to keep the exposure time in the 1–10-ms range to successfully record objects vibrating at frequencies of 1–100 Hz.

To implement the scanned-picture-beam idea in a way that can be fairly compared with a single-exposure hologram, we construct our recording apparatus so that the reference beam does not change while it is switching from one technique to the other. The picture beams for the two techniques are arranged so that they have as common an optical path as possible. In the single-exposure case, the picture beam is expanded and allowed to illuminate the entire object. Next, to make a scanned-picture-beam hologram, the picture beam is diverted away from the beam expanding lens via a mirror placed before the beam expander, toward a two-axis galvanometric scanner (see Fig. 3).

The two-axis scanner and an electronic shutter are controlled by a personal computer. The controlling software allows the user to input the following parameters: the coordinates of the four corners of the area to be scanned; the number of rows and columns in the raster pattern; and the delay time between the command for the scanner to step to the next position and that for the shutter to open for that exposure.

The program interpolates locations for each step. The scanned area can be of any quadrilateral shape within the range of motion of the scanner. The scanner-control electronics have a built-in coordinate system. A separate scanner-control program allows

the establishment of a reference between the scanner's coordinate system and the dimensions of each object. The shutter opening time is adjusted by the shutter controls. The delay before the shutter opens allows the scanner mirrors to settle.

The two-axis scanner is an effective polarization rotator. It is necessary to rotate the polarization of the picture beam before it reaches the scanner so that the beam comes out of the scanner in the desired polarization.

One useful implement is a variable beam splitter, a partial mirror on which the reflectivity varies in a controlled way. This device allows the ratio of *P*-to-*R* intensity to be adjusted without using neutral density filters and thus reducing laser power.

The results presented here are from amplitude-transmission holograms. Although we have bleached some of the film plates to produce phase-transmission holograms, the images seen here are all from unbleached plates.

5. Experimental Results

This section presents some examples of scanned-picture-beam holograms made with the apparatus described in Section 4.

Figure 4 illustrates one result. Figure 4(a) is a sketch of the object, a set of ground-glass vanes mounted in an aluminum frame that is bolted to the optical table. The two side vanes are secured at the top and the bottom. The middle vane (labeled OF) is secured at the bottom only. The middle vane is vibrated by a lever attached to a small loudspeaker. The loudspeaker is driven by a random signal with frequency components ranging from 0 to 10 Hz. The signal is generated on a personal computer, output via a digital-to-analog board, and amplified by a current amplifier to drive the vane. The laser used is an argon ion laser at $\lambda = 514$ nm with an output of $\sim$1 W. The film is Agfa 8E56. The laser is arranged to illuminate the ground-glass vanes from behind, as viewed here.

Figure 4(b) is a photograph of the image obtained from one exposure of 310 ms. The middle vane is almost completely obscured by fringes characteristic of an object that moves during holographic recording. Figure 4(c) shows the image obtained from 100 exposures of 1 ms each. The image of the middle vane is comparable with that of the outer vanes. Note the raster pattern of the illuminating spots.

Figure 5 shows a second result. Figure 5(a) is a photograph of the objects, two toys made of a ball-shaped mass of soft plastic flanges. These balls were allowed to rest on a rigid stage mounted on an optical table and unshielded from ambient forcings, such as air currents. Figure 5(b) shows an image produced by one exposure of 1.1 s. Note the image of the aluminum bolt in the foreground, which proves that a hologram was recorded. In Fig. 5(c) in which the objects are recorded by 100 exposures of 9 ms each, the plastic flanges are clearly imaged. The scanning technique illuminates a smaller solid angle than is typically the case for single-exposure holography. Therefore only a

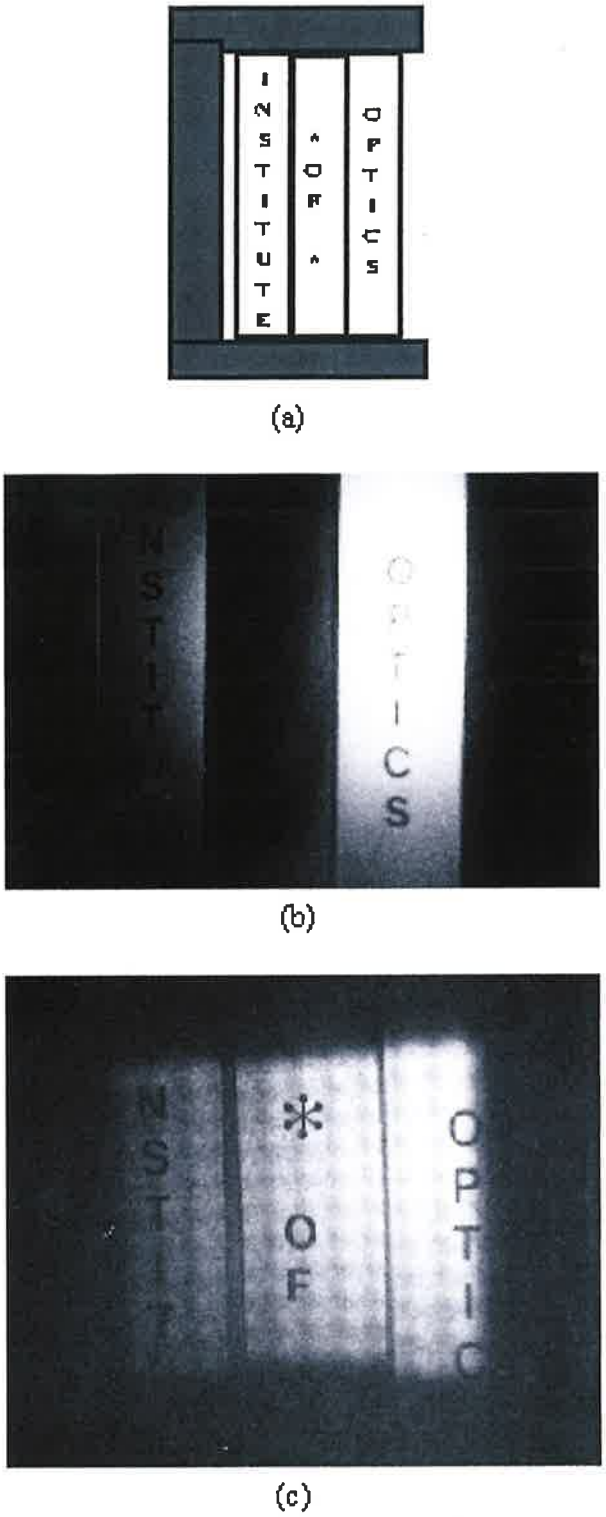

Fig. 4. Application of scanned-picture-beam holography. (a) Sketch of object with three ground-glass vanes in an aluminum frame. (b) Image from a hologram recorded in one exposure of 310 ms. The middle vane is driven during exposure by a small pusher motor. (c) Image from a hologram recorded in 100 exposures of 1 ms each. Middle-vane movement is identical to that of the single-exposure hologram.

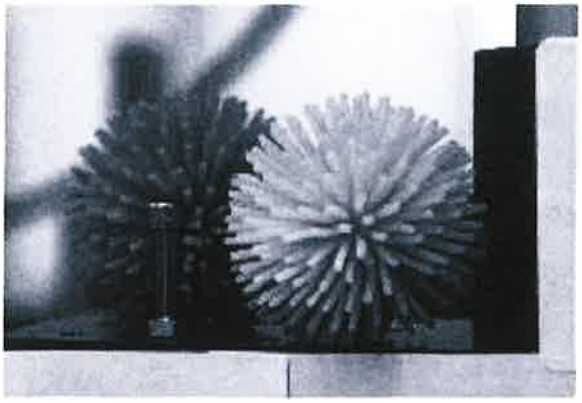

(a)

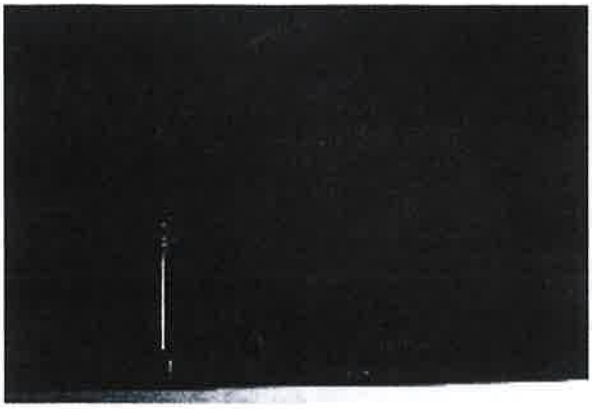

(b)

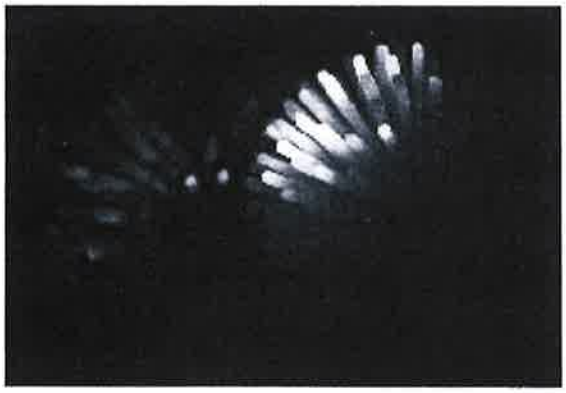

(c)

Fig. 5. Application of scanned-picture-beam holography. (a) Photograph of the objects, which are two small toy balls with plastic flanges. (b) Image from a hologram recorded with one exposure of 1.1 s. (c) Image from a hologram recorded with 100 exposures of 9 ms each.

portion of each ball is visible in the image because the rest of the object is in shadow.

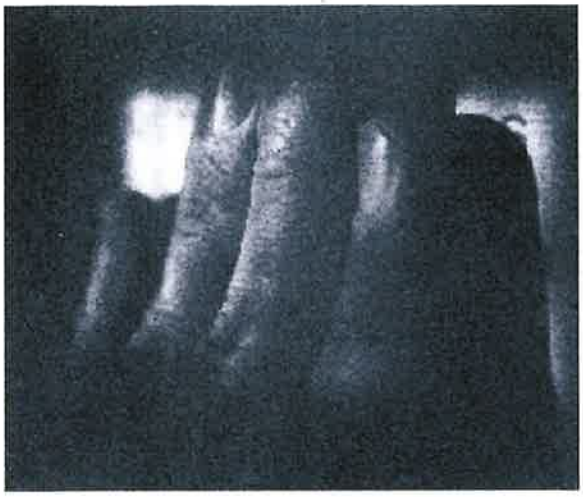

Fig. 6. Application of scanned-picture-beam holography showing an image of a live human hand recorded in 100 exposures of 2 ms each.

To produce the images in Fig. 5, a dye laser of $\lambda \sim 580$ nm and an output of ~500 mW is used with Agfa 8E75 film.

Figure 6 shows an image of a live human hand, a difficult subject to record holographically. The dye laser is used to make this hologram in 100 exposures of 2 ms each.

6. Discussion

Holographic interferometry uses multiple exposures of an object to measure small motions or deformations that occur between exposures. By contrast, the scanned-beam method is designed to eliminate the dark fringes that indicate object motion.

The image formed by a scanned-picture-beam hologram is an aggregate of N smaller images, each of one object region. Although the object regions are conceptually discrete and contiguous, in practice adjacent illuminated regions may overlap, especially when the illuminating spot has a Gaussian intensity profile with no distinct edge.

The area of overlap between adjacent illuminated object regions is recorded twice. The image of this region is then a superposition of two similar images, which can produce interference fringes localized at the image if the phase of the two images is not identical across the region of overlap. Fortunately, a practical recording apparatus produces fringes that are so small that the eye averages them to a constant value, as explained below.

During recording, each region of the object is illuminated by a narrow laser beam. The two beams that correspond to adjacent object regions are separated by an angle, θ, determined by the scanner step size and by the distance from the object to the scanner. In our experiments this angle was ~1°. If these beams are approximately plane waves, then the composite image of the two regions will be two plane waves separated by θ. For small θ the interference

fringes localized at the image will have a period, Λ, of $\Lambda = \lambda/\sin\theta$. In our experiments using $\lambda = 514$ nm, the fringes have a period of ~ 30 μm.

Because the fringes are formed by overlapping Gaussian amplitude wave fronts, the amplitude of the two beams is not equal over most of the overlap region. This amplitude difference contributes to low fringe visibility. None of our experiments produced fringes that are visible to the human eye. As a result of small fringe size and low fringe visibility in the overlap region, the eye averages the fringes to a value that approximates the incoherent sum of the overlapping intensities.

7. Summary

We have demonstrated the technique of scanned-picture-beam holography. This technique is superior to single-exposure holography for recording certain nonstable objects, particularly those that are subject to common ambient vibrations. It is also a useful method for making holograms of fairly large objects. The short exposure time made possible by a small, very bright picture beam keeps object motion acceptably small for objects that vibrate at acoustic or subacoustic frequencies with amplitudes of $\sim\lambda$ or larger.

We have used a two-dimensional transmission-function model of a hologram to derive expressions for the transmission function of holograms recorded in a single exposure [see Eq. (4)] and separately for the same object recorded with multiple exposures [see Eq. (5)]. We use Eqs. (4) and (5) to derive Eq. (13), showing that hologram fringe visibility decreases as $1/\sqrt{N}$, where N is the number of exposures used to record the hologram.

We also present a number of experimental results for the scanned-picture-beam method of holography. We show the superiority of the scanned-beam method for recording a vibrating glass vane [see Fig. (4)], a soft plastic toy [see Fig. (5)], and a human hand [see Fig. (6)].

We thank Don Schertler for programming the computer that controlled the shutter and the two-axis scanner in our experiments. This research was supported by the U.S. Army Research Office.

References

1. R. L. Powell and K. A. Stetson, "Interferometric vibration analysis by wave-front reconstruction," J. Opt. Soc. Am. **55,** 1593–1598 (1965).
2. R. E. Brooks, L. O. Heflinger, R. F. Wuerker, and R. A. Briones, "Holographic photography of high-speed phenomena with conventional and *Q*-switched ruby lasers," Appl. Phys. Lett. **7,** 92–94 (1965).
3. J. C. Palais, "Scanned beam holography," Appl. Opt. **9,** 709–711 (1970).
4. J. C. Palais and I. C. Vella, "Some aspects of scanned reference beam holography," Appl. Opt. **11,** 481–482 (1972).
5. T. Sh. Imedadze and Sh. D. Kakichashvili, "Scanning method of receiving high-effective reflective holograms on bichromate gelatine," in *Three Dimensional Holography: Science, Culture, Education*, T. H. Jeong and V. B. Markov, eds., Proc. SPIE **1238,** 439–441 (1989).
6. C. S. Vikram and H. Vardhan, "Recording linearity in multiple exposure holography," Nouv. Rev. Opt. Appl. **3,** 185–189 (1972).
7. N. George, A. Jain, and R. D. S. Melville, Jr., "Speckle, diffusers and depolarization," Appl. Phys. **6,** 65–70 (1975).
8. A. A. Friesem, A. Kozma, and G. F. Adams, "Recording parameters of spatially modulated coherent wave fronts," Appl. Opt. **6,** 851–856 (1967).
9. J. T. LaMacchia and C. J. Vincellete, "Comparisons of the diffraction efficiency of multiple exposure and single exposure holograms," Appl. Opt. **7,** 1857–1858 (1968).
10. M. Chang and N. George, "Holographic dielectric grating: theory and practice," Appl. Opt. **9,** 713–719 (1970).

Fractional finite Fourier transform

Kedar Khare and Nicholas George

The Institute of Optics, University of Rochester, Rochester, New York 14627

Received November 17, 2003; revised manuscript received February 19, 2004; accepted February 25, 2004

We show that a fractional version of the finite Fourier transform may be defined by using prolate spheroidal wave functions of order zero. The transform is linear and additive in its index and asymptotically goes over to Namias's definition of the fractional Fourier transform. As a special case of this definition, it is shown that the finite Fourier transform may be inverted by using information over a finite range of frequencies in Fourier space, the inversion being sensitive to noise. Numerical illustrations for both forward (fractional) and inverse finite transforms are provided. © 2004 Optical Society of America

OCIS codes: 070.2590, 200.3050, 000.3860.

1. INTRODUCTION

Fractional Fourier transform (FrFT) was introduced by Namias[1] in connection with certain problems in quantum mechanics. The transform also occurs naturally in the study of the quadratic gradient-index lenses.[2–4] The connection between the FrFT of a function and its Wigner distribution has been studied.[5] It is also known that Fresnel diffraction may be viewed as a FrFT operator.[6] Various optical implementations of the fractional-order Fourier transforms and operations such as convolution and filtering in fractional Fourier domains have been discussed.[7,8] Computational aspects of the FrFT have also been studied in detail.[9,10] A vast amount of literature dealing with various applications of the FrFT in optics and signal processing is now available.[11]

Our study shows that the literature on FrFT deals exclusively with fractionalization of the infinite Fourier transform [range of integration $(-\infty, \infty)$]. In practical measurements, however, the signals of interest are available only over a finite range. In view of this and the broad range of applications that the FrFT has found in optics and signal-processing literature in recent years,[11] an analytical definition of a fractional version of *finite* Fourier transform seems to be in order. In this paper we introduce such a definition, using the prolate spheroidal wave functions of order zero, and establish a connection between finite and infinite versions of the FrFT that has apparently been missing in the literature so far.

Throughout this paper we will write the finite Fourier transform of a function $g(x)$ in $\mathcal{L}^2(-L, L)$ as

$$F\{g(x)\} = \int_{-L}^{L} dx \exp(-i2\pi fx)g(x). \tag{1}$$

We perform the fractionalization of the above transform by using the fact that the prolate spheroidal functions described later in this paper are the eigenfunctions of this transform and also form a complete set of orthogonal functions in $\mathcal{L}^2(-L, L)$. In a recent investigation[12] we established an interesting connection between the prolate spheroidal wave functions and the Whittaker–Shannon sampling theorem[13] and presented a simple method for computation of prolate spheroidal wave functions and the corresponding eigenvalues. In this paper the prolate spheroidal functions obtained with our new method will be used for numerical computation of the fractional version of the finite Fourier transform in Eq. (1).

The outline of the paper is as follows. In Section 2 we briefly discuss the properties of the prolate spheroidal wave functions that are relevant for the fractionalization of the finite Fourier transform. The fractional finite Fourier transform (FFFT) is defined in Section 3, and the special case of inverse finite Fourier transform is discussed. In Section 4 we show that our definition of the FFFT asymptotically goes over to Namias's definition of the infinite FrFT. Finally, in Section 5 we provide numerical illustrations of our results in the previous sections.

2. PROLATE SPHEROIDAL WAVE FUNCTIONS OF ORDER ZERO

The prolate spheroidal functions are the solutions of the Helmholtz equation in a prolate spheroidal coordinate system.[14,15] The functions of interest to us in this paper are the angular prolate spheroids of order zero (solutions of the angular part of the Helmoltz equation in prolate spheroidal coordinates). These functions may be defined alternatively as the set of eigenfunctions satisfying the following homogeneous Fredholm integral equation of the second kind:[16]

$$\lambda_n \phi_n(x) = \int_{-L}^{L} dx' \, \mathrm{sinc}[2B(x - x')]\phi_n(x'). \tag{2}$$

Here $\phi_n(x)$ and λ_n denote the eigenfunctions and the associated eigenvalues, respectively, and

$$\mathrm{sinc}(x) = \frac{\sin \pi x}{\pi x}. \tag{3}$$

The eigenfunctions $\phi_n(x)$ for $n = 0, 1, 2,...$ are first, orthogonal over $(-\infty, \infty)$ as well as over $(-L, L)$,

$$\int_{-\infty}^{\infty} dx \, \phi_n(x)\phi_l(x) = \delta_{n,l}, \tag{4}$$

1084-7529/2004/071179-07$15.00

$$\int_{-\infty}^{\infty} dx\, \phi_n(x)\phi_l(x) = 2B\lambda_n \delta_{n,l}, \tag{5}$$

and second, complete for functions in $\mathcal{L}^2(-\infty, \infty)$ that are band limited to $(-B, B)$ and complete in $\mathcal{L}^2(-L, L)$. The eigenvalues λ_n are positive and ordered as $1 > 2B\lambda_0 > 2B\lambda_1 > 2B\lambda_2 > \cdots > 0$, the number of significant eigenvalues being approximately equal to the space–bandwidth product $4BL$. The corresponding eigenfunctions $\phi_n(x)$ have n zeros in $(-L, L)$ and a definite parity; i.e., $\phi_n(x) = (-1)^n \phi_n(-x)$. The functions $\phi_n(x)$ are also the eigenfunctions of the finite Fourier transform:

$$\int_{-L}^{L} dx \exp(-i2\pi fx)\phi_n(x) = i^{-n}(2L\lambda_n)^{1/2}\phi_n(Lf/B). \tag{6}$$

A short proof of this identity along with an explanation of a possible ambiguity in the sign of $i = \sqrt{-1}$ in the above equation is discussed in Appendix A. Two important identities that are relevant to the present paper are given below:

$$\exp(-i2\pi fx) = \frac{L}{B}\sum_{n=0}^{\infty} \frac{i^{-n}}{(2L\lambda_n)^{1/2}} \phi_n(x)\phi_n\left(\frac{Lf}{B}\right), \quad \text{for } |x| < L \tag{7}$$

and

$$\delta(x - x') = \frac{1}{2B}\sum_{n=0}^{\infty} \frac{1}{\lambda_n}\phi_n(x)\phi_n(x'), \quad \text{for } |x|, |x'| < L. \tag{8}$$

Identity (8) for the Dirac delta function can be easily derived from Eq. (7) and orthogonality condition (5). Relation (7) is well known;[17] for a short proof we refer the reader to our recent publication.[12] We are now in a position to define a fractional version of the finite Fourier transform defined in Eq. (1).

3. FRACTIONAL FINITE FOURIER TRANSFORM

We start by introducing two new variables for later convenience:

$$u = \sqrt{\frac{B}{L}}x, \qquad u' = \sqrt{\frac{L}{B}}f. \tag{9}$$

Equation (6) can be written in terms of the variables u and u' as follows:

$$\int_{-\sqrt{BL}}^{\sqrt{BL}} du \exp(-i2\pi uu')\phi_n\left(\sqrt{\frac{L}{B}}u\right) = i^{-n}(2B\lambda_n)^{1/2}\phi_n\left(\sqrt{\frac{L}{B}}u'\right). \tag{10}$$

The set of prolate spheroids $\phi_n(\sqrt{L/B}u)$ forms a complete orthogonal set in $\mathcal{L}^2(-\sqrt{BL}, \sqrt{BL})$, so that an arbitrary finite energy function $g(\sqrt{L/B}u)$ in $(-\sqrt{BL}, \sqrt{BL})$ may be expressed as a linear combination:

$$g\left(\sqrt{\frac{L}{B}}u\right) = \sum_{n=0}^{\infty} a_n \phi_n\left(\sqrt{\frac{L}{B}}u\right), \tag{11}$$

where

$$a_n = \sqrt{\frac{L}{B}}\frac{1}{2B\lambda_n}\int_{-\sqrt{BL}}^{\sqrt{BL}} du g\left(\sqrt{\frac{L}{B}}u\right)\phi_n\left(\sqrt{\frac{L}{B}}u\right). \tag{12}$$

From Eqs. (11) and (6) we can write the finite-Fourier-transform operation on $g(\sqrt{L/B}u)$ as

$$F\left\{g\left(\sqrt{\frac{L}{B}}u\right)\right\} = \sum_{n=0}^{\infty} a_n i^{-n}(2B\lambda_n)^{1/2}\phi_n\left(\sqrt{\frac{L}{B}}u'\right), \tag{13}$$

where a_n is defined in Eq. (12) and the range of integration is $(-\sqrt{BL}, \sqrt{BL})$.

We now introduce the FFFT operation. For real number α we define the fractional-order transform

$$F^{\alpha}\left\{g\left(\sqrt{\frac{L}{B}}u\right)\right\} = \int_{-\sqrt{BL}}^{\sqrt{BL}} du K(u, u';\alpha) g\left(\sqrt{\frac{L}{B}}u\right), \tag{14}$$

with the kernel $K(u, u';\alpha)$ given by

$$K(u, u';\alpha) = \sqrt{\frac{L}{B}}\sum_{n=0}^{\infty} i^{-n\alpha}(2B\lambda_n)^{\alpha/2-1} \times \phi_n\left(\sqrt{\frac{L}{B}}u\right)\phi_n\left(\sqrt{\frac{L}{B}}u'\right). \tag{15}$$

It is important to consider some special cases to show that this definition gives an appropriate fractional-order transform. For $\alpha = 0$ we have

$$K(u, u';0) = \sqrt{\frac{L}{B}}\sum_{n=0}^{\infty} \frac{1}{2B\lambda_n}\phi_n\left(\sqrt{\frac{L}{B}}u\right)\phi_n\left(\sqrt{\frac{L}{B}}u'\right) = \delta(u - u'), \quad \text{for } |u|, |u'| < \sqrt{BL}. \tag{16}$$

Here identity (8) was used. The transform of order zero thus keeps a function $g(\sqrt{L/B}u)$ unchanged:

$$\int_{-\sqrt{BL}}^{\sqrt{BL}} du g\left(\sqrt{\frac{L}{B}}u\right)K(u, u';0) = g\left(\sqrt{\frac{L}{B}}u'\right), \quad \text{for } |u'| < \sqrt{BL}. \tag{17}$$

For $\alpha = 1$ we may use identity (7) and write

$$K(u, u';1) = \exp(-i2\pi uu'), \tag{18}$$

so that we arrive at definition (1) of the finite Fourier transform. The FFFT operation [Eq. (14)] is clearly linear in nature. Next, consider a successive action of operations F^{α_1} and F^{α_2} for real numbers α_1 and α_2. The combined operation is described by the integral kernel

$$K'(u, u''; \alpha_1, \alpha_2) = \int_{-\sqrt{BL}}^{\sqrt{BL}} du' K(u, u'; \alpha_1) K(u', u''; \alpha_2) \tag{19}$$

The integral may be evaluated easily by using orthogonality property (5) of the prolate spheroidal functions, and we get

$$\begin{aligned} K'(u, u''; \alpha_1, \alpha_2) &= \sqrt{\frac{L}{B}} \sum_{n=0}^{\infty} i^{-n(\alpha_1+\alpha_2)} \\ &\quad \times (2B\lambda_n)^{(\alpha_1+\alpha_2)/2-1} \phi_n\left(\sqrt{\frac{L}{B}} u\right) \\ &\quad \times \phi_n\left(\sqrt{\frac{L}{B}} u''\right) \\ &= K(u, u''; \alpha_1 + \alpha_2). \end{aligned} \tag{20}$$

The FFFT operation is thus additive in its index. For convenience we will write the definition of the FFFT in terms of the coefficients a_n in Eq. (12):

$$F^{\alpha}\left\{g\left(\sqrt{\frac{L}{B}} u\right)\right\} = \sum_{n=0}^{\infty} a_n i^{-n\alpha} (2B\lambda_n)^{\alpha/2} \phi_n\left(\sqrt{\frac{L}{B}} u'\right). \tag{21}$$

We conclude this section by noting that the integral kernel

$$K(u, u'; -1) = \sqrt{\frac{L}{B}} \sum_{n=0}^{\infty} i^{n} (2B\lambda_n)^{-3/2} \phi_n\left(\sqrt{\frac{L}{B}} u\right) \phi_n\left(\sqrt{\frac{L}{B}} u'\right) \tag{22}$$

corresponds to the inverse finite Fourier transform F^{-1}. An important point here is that in this definition of the inverse transform, the range of integration is finite, viz., $(-\sqrt{BL}, \sqrt{BL})$. The knowledge of the finite Fourier transform of a function $g(\sqrt{L/B}u)$ over the range $u' : (-\sqrt{BL}, \sqrt{BL})$ is thus sufficient to recover the function, at least in principle.

Such an inversion may, however, pose practical difficulties imposed by the noise in the measurement of $F\{g(u)\}$ or the coefficients a_n. We note that in definition (21) with $\alpha = -1$, the coefficient a_n is divided by $(2B\lambda_n)^{1/2}$. We have already noted in Section 2 that the eigenvalues λ_n drop off very fast for $n > 4BL$. If such higher-order terms are included in the inverse recovery, we start dividing the noise on the corresponding coefficients a_n by small numbers, which may result in large unwanted oscillations. For a reasonable inverse recovery we must then truncate series (21), which amounts to a reduction in recovered information. We will illustrate this point with a numerical example in Section 5.

We would like to point out that the inversion of the finite transform as mentioned here is simply a manifestation of the extrapolation property of prolate spheroids.[16] Inverse scattering problems in optics require such an out-of-band extrapolation of Fourier space data[18] for achieving superresolution. The number of terms of series (21) with $\alpha = -1$ that allow a reasonable inversion in the presence of noise may be thought of as a quantitative measure of recoverable information in the inverse problem.

We conclude this section by noting that in the case of the forward transform of order 1, we multiply a_n by $(2B\lambda_n)^{1/2}$ so that there is no similar concern regarding division by small numbers.

4. ASYMPTOTIC LIMIT OF THE FRACTIONAL FINITE FOURIER TRANSFORM

In this section we study the behavior of the integral kernel $K(u, u'; \alpha)$ in the limit $L \to \infty$, $B \to \infty$ with the ratio $L/B \to 1$. In this limit, we may write $K(u, u'; \alpha)$ in Eq. (15) as

$$K_{\infty}(u, u'; \alpha) = \sum_{n=0}^{\infty} i^{-n\alpha} (2B\lambda_n)^{\alpha/2-1} \phi_n(u) \phi_n(u'). \tag{23}$$

The asymptotic expansions for the prolate spheroidal functions and their eigenvalues for large values of the parameter $c = 2\pi BL$ have been given by Slepian[19] and also quoted by Frieden.[17] The relevant asymptotic expansions are as follows. For large values of $c = 2\pi BL$ (typically ≥ 10) we have

$$\begin{aligned} \phi_n(u) &= \sqrt{\frac{2B\lambda_n}{LN_n}} \left[D_n\left(\sqrt{\frac{4\pi B}{L}} u\right) \right. \\ &\quad \left. + \sum_{j=1}^{\infty} (2c)^{-j} \sum_{k=-2j}^{2j} A_k^j D_{n+2k}\left(\sqrt{\frac{4\pi B}{L}} u\right) \right]. \end{aligned} \tag{24}$$

Here the functions $D_n(y)$ are defined as

$$D_n(y) = 2^{-n/2} \exp(-y^2/4) H_n(y/\sqrt{2}), \tag{25}$$

with $H_n(y)$ being the Hermite polynomial of order n. The constant N_n is for normalization and is given by

$$\begin{aligned} N_n &= \sqrt{\frac{1}{2BL}} n! \left[1 + \frac{1}{2^7 (4c^2)} \right. \\ &\quad \left. \times (n^4 + 2n^3 + 23n^2 + 12) \right]. \end{aligned} \tag{26}$$

The constants A_k^j are to be computed by an algorithm given by Slepian.[19] The eigenvalues λ_n are given by

$$\begin{aligned} 2B\lambda_n &= 1 - 4 \frac{\sqrt{\pi}}{n!} c^{n+1/2} \exp(-2c) \\ &\quad \times \left[1 - \frac{1}{32c} (6n^2 - 2n + 3) \right]. \end{aligned} \tag{27}$$

When these asymptotic expansions are used in Eq. (23), in the limit $c \to \infty$ with $L/B \to 1$, the integral kernel $K_{\infty}(u, u'; \alpha)$ reduces to

$$K_\infty(u, u'; \alpha) = \sqrt{2}\exp[-\pi(u^2 + u'^2)] \times \sum_{n=0}^{\infty} \frac{i^{-n\alpha}}{2^n n!} H_n(\sqrt{2\pi}u) H_n(\sqrt{2\pi}u'). \quad (28)$$

The integral kernel may be further simplified using the Mehler's formula for Hermite polynomials[20] to obtain

$$K_\infty(u, u'; \alpha) = \frac{\exp[-i(\frac{\pi}{4}\,\mathrm{sgn}(\sin\phi) - \frac{\phi}{2})]}{|\sin\phi|^{1/2}} \times \exp[i\pi(u^2\cot\phi - 2uu'\csc\phi + u'^2\cot\phi)], \quad (29)$$

where $\phi = \alpha\pi/2$ and sgn denotes the signum function. This in fact is the integral kernel in the definition of FrFT as proposed by Namias[1] (also see Ref. 3). Our definition of FFFT is thus consistent with the definition of infinite FrFT in the asymptotic limit. It is important to note that when $c \to \infty$, the eigenvalues have the property that $2B\lambda_n \to 1$ for all n. Inversion of infinite Fourier transform using information over all the frequency space therefore does not involve any divisions by small numbers as is the case with inversion of finite Fourier transform defined by using the kernel $K(u, u'; -1)$ in Eq. (22).

The quadratic phase factors in Eq. (29) allow one to cast the integral kernels for Fresnel diffraction, propagation through gradient-index media, etc., in the form of an infinite FrFT operator. The FFFT as defined by integral kernel (15), however, does not contain such quadratic phase factors. It therefore seems difficult to find optical implementations where the integral kernel $K(u, u';\alpha)$ may occur naturally. Thus, at present, the implementations of the FFFT seem to be limited to numerical ones.

5. NUMERICAL ILLUSTRATIONS

In this section we will provide two numerical illustrations of the finite transforms defined in Section 3. In the first illustration we will show the evolution of the (finite) Fourier transform of the triangle function $\Lambda(u)$ for orders $\alpha = 0.25, 0.5, 0.75, 1.0$. In the second illustration we will use the kernel $K(u, u'; -1)$ to get an approximate recovery of the $\Lambda(u)$ function from the values of the $\mathrm{sinc}^2(u')$ over $u' : (-1, 1)$. The computation of prolate spheroidal functions and their corresponding eigenvalues is important for these illustrations. In our recent publication[12] we have proposed a sampling-theorem-based method for this purpose. The important results of this investigation are summarized below.

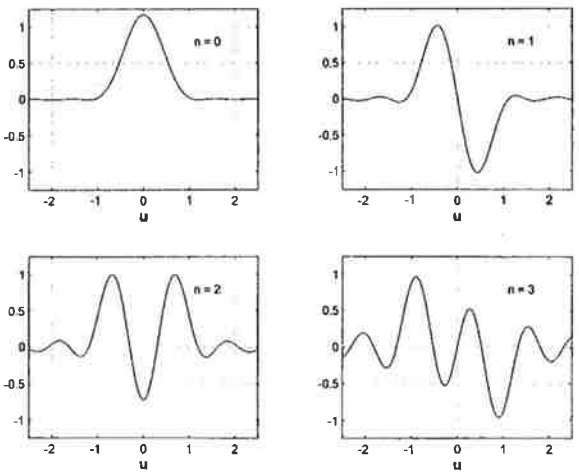

Fig. 1. First four prolate spheroidal functions of order zero calculated by using the sampling-theorem-based approach for the case $L = 1$ and $B = 1$.

Table 1. Ten Highest Eigenvalues of the Sinc Kernel for $L = 1$ and $B = 1$ Computed with the Sampling-Theorem-Based Approach

n	$2B\lambda_n$
0	9.9994×10^{-1}
1	9.9754×10^{-1}
2	9.5939×10^{-1}
3	7.2049×10^{-1}
4	2.7467×10^{-1}
5	4.2679×10^{-2}
6	3.4782×10^{-3}
7	1.8478×10^{-4}
8	7.4656×10^{-6}
9	2.2880×10^{-7}

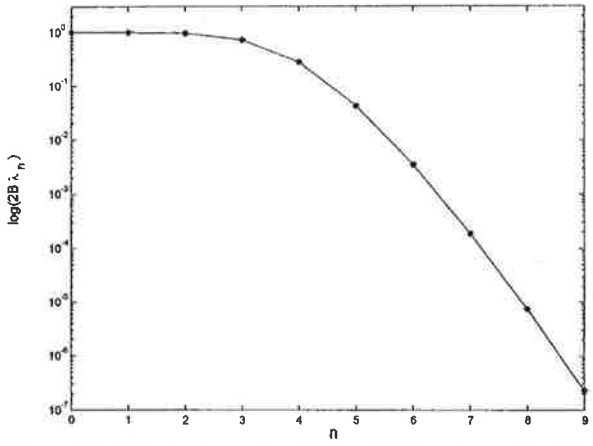

Fig. 2. Ten highest eigenvalues for the sinc kernel on a logarithmic scale. $L = 1$ and $B = 1$.

1. The eigenvalue problem (2) is equivalent to the eigenvalue problem for the infinite matrix A defined as

$$A_{mk} = \int_{-L}^{L} dx'\,\mathrm{sinc}(2Bx' - m)\mathrm{sinc}(2Bx' - k) \quad (30)$$

for integers $m, k = -\infty, \ldots, 0, \ldots, \infty$.

2. The discrete eigenvectors u_n of A are formed by the samples of the continuous eigenfunctions $\phi_n(x)$:

$$u_n = [\ldots\phi_n(m/2B)\ldots]^T, \quad (31)$$

with T denoting the transpose of the row vector.

For given values of L and B, one needs to compute the matrix A as defined in Eq. (30) by numerical integration.

Solving the eigenvalue problem $Au_n = \lambda_n u_n$ for the matrix A thus gives the eigenvalues λ_n, and the continuous eigenfunctions can be determined by sinc-interpolating the discrete eigenvectors according to the Whittaker–Shannon sampling theorem,[13] since the eigenfunctions $\phi_n(x)$ are band limited:

$$\phi_n(x) = \sum_{m=-\infty}^{\infty} \phi_n(m/2B)\mathrm{sinc}(2Bx - m). \qquad (32)$$

We believe that the method of computation of prolate spheroids and the corresponding eigenvalues as outlined above is conceptually much simpler than the method using asymptotic expansions that is available in literature.[19] For more details the reader is referred to Ref. 12 and references therein. Once the prolate spheroids and the corresponding eigenvalues have been computed, a truncated version of series (21) may be evaluated numerically.

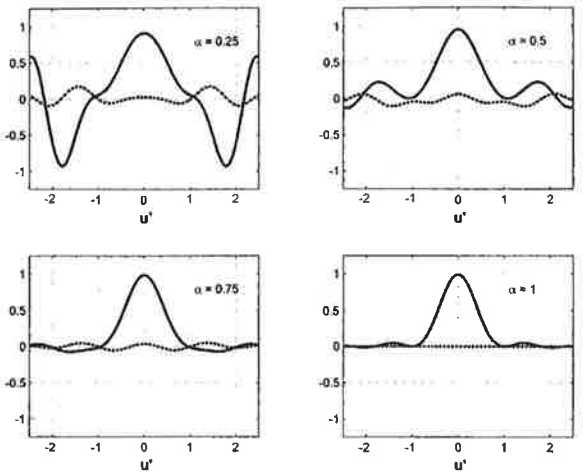

Fig. 3. Fractional finite Fourier transform of $\Lambda(u)$ corresponding to orders $\alpha = 0.25, 0.5, 0.75, 1.0$. The real and imaginary parts of the transform are shown by solid and dotted curves, respectively. The first ten prolate spheroids are used for computation.

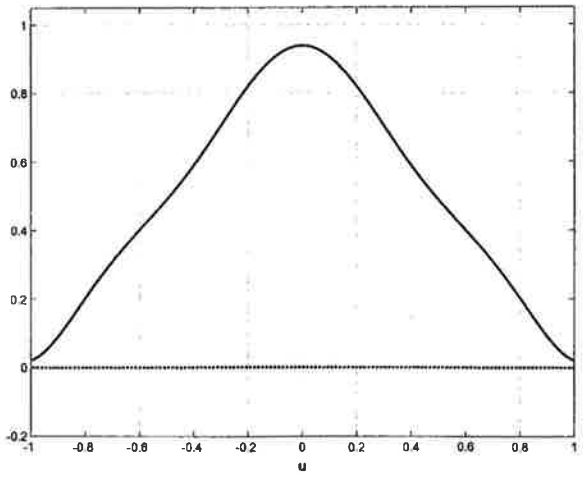

Fig. 4. Inverse finite Fourier transform of $\mathrm{sinc}^2(u')$ with use of Fourier space information over $u':(-1, 1)$. The real and imaginary parts of the transform are shown by solid and dotted curves, respectively. The first ten prolate spheroids are used for computation.

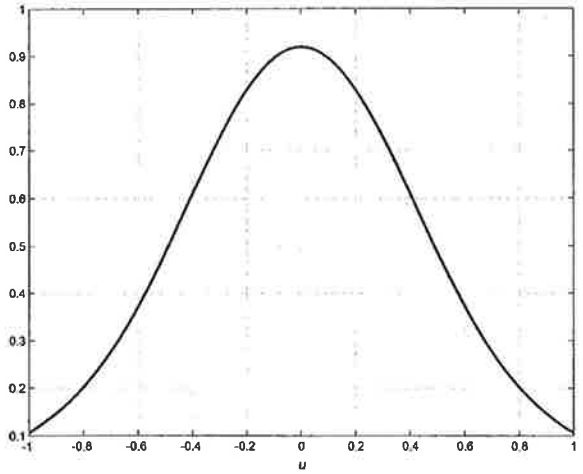

Fig. 5. Inverse finite Fourier transform of $\mathrm{sinc}^2(u')$ with use of Fourier space information over $u':(-1, 1)$. Tolerance in computation of a_n in Eq. (12) is set to 0.1. The series in Eq. (21) is truncated to $n = 5$. Only the real part of the recovery is shown.

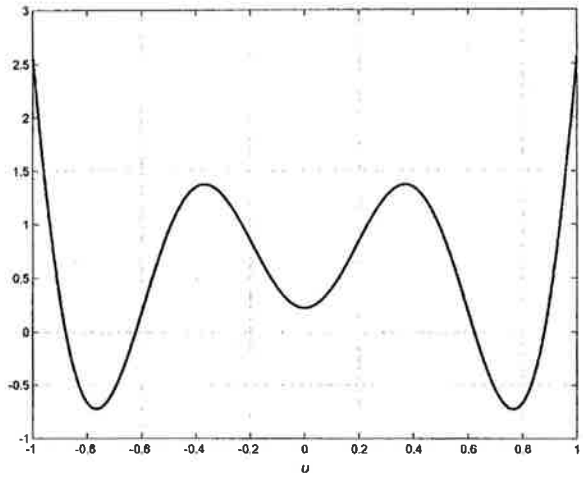

Fig. 6. Inverse finite Fourier transform of $\mathrm{sinc}^2(u')$ with use of Fourier space information over $u':(-1, 1)$. Tolerance in computation of a_n in Eq. (12) is set to 0.1. The series in Eq. (21) is truncated to $n = 6$. Only the real part of the recovery is shown.

For the purpose of illustration, we have used the first ten spheroidal functions corresponding to the numerical values $L = 1$ and $B = 1$. Figure 1 shows the plots of the first four eigenfunctions calculated with our method. The normalization is made according to Eq. (5). The ten highest eigenvalues are tabulated in Table 1 and are plotted in Fig. 2 on a logarithmic scale. The truncated form of A in Eq. (30) with dimension 101×101 is used for computation, each element being computed with an adaptive quadrature routine (with tolerance set to 10^{-10}). The test function

$$g(u) = \Lambda(u) = \begin{cases} 1 - |u|, & |u| \le 1 \\ 0, & \text{otherwise} \end{cases} \tag{33}$$

is used for illustration. The (finite) Fourier transform of $g(u)$ is equal to $\text{sinc}^2(u')$. The evolution of the transform from $\Lambda(u) \rightarrow \text{sinc}^2(u')$ is shown in four stages in Fig. 3, where the real and imaginary parts of the transform are plotted with solid and dotted curves, respectively. For order $\alpha = 1$ the agreement of the result with the $\text{sinc}^2(u')$ function is excellent. Figure 4 shows the recovery of the inverse transform of $\text{sinc}^2(u')$ with use of the information in the interval $u' : (-1, 1)$. The first ten prolate spheroidal functions are used for recovery, and the inverse kernel $K(u, u'; -1)$ is employed. The coefficients a_n for the forward and backward-transform illustrations above are once again determined by evaluating the integral in Eq. (12) by using an adaptive quadrature routine with tolerance set to 10^{-10}. All the computations were performed with the standard routines available in the mathematical software MATLAB version R12.

To study the effect of noise on inversion, we computed the coefficients a_n in the expansion of $\text{sinc}^2(u')$ with tolerance of 10^{-1}. From Table 1, we see that the eigenvalues $(2B\lambda_5)$ and beyond are less than 10^{-1}. The coefficients a_n known within an accuracy of 10^{-1} are divided by $(2B\lambda_n)^{1/2}$ according to Eq. (21) with $\alpha = -1$. Inclusion of terms corresponding $n \sim 5$ and beyond is thus expected to produce unwanted oscillations in the recovery. In Figs. 5 and 6 we show the inverse recovery by truncating series (21) to $n = 5$ and $n = 6$, respectively. The recovery corresponding to $n = 6$ is affected by noise. Depending on the accuracy in determining a_n, it is thus appropriate to omit the terms beyond $n = 5$ in this case. It is worth comparing the results of inverse recovery in Figs. 4 and 5 and noting that the presence of larger relative noise in the second case limits the recoverable information.

6. CONCLUSION

In summary, we have shown that the finite-Fourier-transform operation in Eq. (1) may be fractionalized by using the prolate spheroidal wave functions of order zero. The transform is shown to approach Namias's definition of the infinite fractional Fourier transform in the asymptotic limit. The linearity of the transform and the additive property of the index α of the transform are proved. It is pointed out that the inversion of the finite Fourier transform may be performed by using information over the finite region of Fourier space. Such inversion is sensitive to noise in the measurement of the finite Fourier transform. Prolate spheroidal functions and their eigenvalues are computed by using our new sampling-theorem-based approach[12] and further used for numerical illustrations of both forward and inverse transforms. Performance of inverse recovery in the presence of noise is also illustrated. For reasons explained in Section 4, at present we are not aware of experimental situations where the fractional finite Fourier transform defined here can occur naturally. The definition of inverse finite transform and the role of noise in inverse recovery are, however, important for inverse problems in optical imaging, where limited information in frequency space is available.

APPENDIX A

In this appendix we will give a short proof of Eq. (6). We start by writing the finite Fourier transform of $\phi_n(x)$ as

$$\Phi_n(f) = \int_{-L}^{L} dx \exp(-i2\pi fx)\phi_n(x). \tag{A1}$$

Next, we write integral equation (2) as

$$2B\lambda_n\phi_n(x) = \int_{-L}^{L} dx' \phi_n(x') \int_{-B}^{B} df' \exp[i2\pi f'(x - x')]$$

$$= \int_{-B}^{B} df' \exp(i2\pi f'x)\Phi_n(f'). \tag{A2}$$

Multiplication on both sides by $\exp(-i2\pi fx)$ followed by integration over $x : (-L, L)$ gives

$$\frac{B}{L}\lambda_n\Phi_n(f) = \int_{-B}^{B} df' \,\text{sinc}[2L(f - f')]\Phi_n(f'). \tag{A3}$$

This equation is simply a scaled version of Eq. (2), and we conclude that

$$\Phi_n(f) = \beta_n\phi_n\left(\frac{Lf}{B}\right). \tag{A4}$$

Here β_n is a constant possibly dependent on n, and the factor (L/B) in the argument on the right-hand side adjusts the scaling appropriately. To find the value of β_n, we take a finite Fourier transform of $\Phi_n(f)$:

$$\int_{-B}^{B} df \exp(-i2\pi fx')\Phi_n(f)$$

$$= 2B\int_{-L}^{L} dx \,\text{sinc}[2B(x + x')]\phi_n(x) = 2B\lambda_n\phi_n(-x'). \tag{A5}$$

Applying the same transformation to the right-hand side of Eq. (A4) gives

$$\beta_n\int_{-B}^{B} df \exp(-i2\pi fx')\phi_n\left(\frac{Lf}{B}\right) = \beta_n^2\frac{B}{L}\phi_n(x'). \tag{A6}$$

Using the parity relation $\phi_n(x') = (-1)^n\phi_n(-x')$ and equating the right-hand sides of Eqs. (A5) and (A6), we get

$$\beta_n = i^{-n}(2L\lambda_n)^{1/2}. \tag{A7}$$

This result combined with Eq. (A4) gives Eq. (6). There appears to be some ambiguity in the sign of $i = \sqrt{-1}$ in the above equation depending on how we write the parity relation. For instance, we could have written the parity relation as $\phi_n(-x') = (-1)^n\phi_n(x')$ instead, with the result that $\beta_n = i^n(2L\lambda_n)^{1/2}$. The former choice is made here so that we are consistent with the literature on fractional Fourier transforms.

ACKNOWLEDGMENTS

This research was supported in part by the U.S. Army Research Office.

Corresponding author Kedar Khare's e-mail address is kedar@optics.rochester.edu.

REFERENCES

1. V. Namias, "The fractional order Fourier transform and its applications to quantum mechanics," J. Inst. Math. Appl. **25**, 241–265 (1980).
2. H. M. Ozaktas and D. Mendlovic, "Fourier transforms of fractional order and their optical interpretation," Opt. Commun. **101**, 163–169 (1993).
3. D. Mendlovic and H. M. Ozaktas, "Fractional Fourier transforms and their optical implementation: I," J. Opt. Soc. Am. A **10**, 1875–1881 (1993).
4. H. M. Ozaktas and D. Mendlovic, "Fractional Fourier transforms and their optical implementation: II," J. Opt. Soc. Am. A **10**, 2522–2531 (1993).
5. A. W. Lohmann, "Image rotation, Wigner rotation, and the fractional Fourier transform," J. Opt. Soc. Am. A **10**, 2181–2186 (1993).
6. P. Pellat-Finet, "Fresnel diffraction and the fractional order Fourier transform," Opt. Lett. **19**, 1388–1390 (1994).
7. H. M. Ozaktas and D. Mendlovic, "Fractional Fourier optics," J. Opt. Soc. Am. A **12**, 743–751 (1995).
8. H. M. Ozaktas, B. Barshan, D. Mendlovic, and L. Onural, "Convolution, filtering, and multiplexing in fractional Fourier domains and their relation to chirp and wavelet transforms," J. Opt. Soc. Am. A **11**, 547–559 (1994).
9. C. Candan, M. A. Kutay, and H. M. Ozaktas, "The discrete fractional Fourier transform," IEEE Trans. Signal Process. **48**, 1329–1337 (2000).
10. S. Pei and J. Ding, "Simplified fractional Fourier transforms," J. Opt. Soc. Am. A **17**, 2355–2367 (2000).
11. H. M. Ozaktas, Z. Zalevsky, and M. A. Kutay, *The Fractional Fourier Transform with Applications in Optics and Signal Processing* (Wiley, Chichester, UK, 2001; this book contains a comprehensive list of publications on this subject.)
12. K. Khare and N. George, "Sampling theory approach to prolate spheroidal wave functions," J. Phys. A **36**, 10011–10021 (2003).
13. C. E. Shannon, "Communication in the presence of noise," Proc. IRE **37**, 10–21 (1949).
14. C. Flammer, *Spheroidal Wave Functions* (Stanford U. Press, Stanford, Calif., 1957).
15. J. A. Stratton, P. M. Morse, L. J. Chu, J. D. C. Little, and F. J. Corbato, *Spheroidal Wave Functions* (Wiley, New York, 1956).
16. D. Slepian and H. O. Pollak, "Prolate spheroidal wave functions, Fourier analysis and uncertainty—I," Bell Syst. Tech. J. **40**, 43–63 (1961).
17. B. R. Frieden, "Evaluation, design and extrapolation methods for optical signals, based on based on the use of prolate functions," in *Progress in Optics, Vol. IX*, E. Wolf ed. (Elsevier, New York, 1971), pp. 311–407.
18. M. Bertero and C. De Mol, "Super-resolution by data inversion," in *Progress in Optics*, *Vol. XXXVI* E. Wolf, ed. (Elsevier, New York, 1996), pp. 129–178.
19. D. Slepian, "Some asymptotic expansions for prolate spheroidal wave functions," J. Math. Phys. **44**, 99–140 (1965).
20. P. M. Morse and H. Feschbach, *Methods of Theoretical Physics* (McGraw-Hill, London, 1953), p. 781.

Available online at www.sciencedirect.com
SCIENCE DIRECT®
Optics Communications 245 (2005) 85–92
OPTICS COMMUNICATIONS
www.elsevier.com/locate/optcom

Integrated imaging with a centrally obscured logarithmic asphere

Wanli Chi *, Nicholas George [1]

Automatic Recognition and Control, Inc. Pittsford, NY 14534, USA

Received 14 May 2004; received in revised form 5 October 2004; accepted 5 October 2004

Abstract

We study an integrated computational imaging system which incorporates a centrally obscured logarithmic asphere lens and rapid maximum entropy processing. A careful study of imaging for a two-point object at various distances is presented to demonstrate diffraction limited resolution and a tenfold increase in the depth of field. Also the overall transfer function is defined and measured. This system is well suited to high-quality photography where one requires excellent resolution and good contrast with little or no artifacts.

PACS: 42.30.–d; 42.30.Va; 42.30.Wb
Keywords: Depth of field; Resolution; Logarithmic asphere; Central obscuration; Maximum entropy; Integrated computational imaging; OTF

1. Introduction

Extensive research efforts have been made to increase the depth of field while keeping a reasonable resolution. An early pioneering method for increasing the depth of field is reported by Hausler [1], who used motion of an object recorded on film in white light followed by processing in coherent illumination. Ojeda-Castaneda and Berriel-Valdos [2] have made the depth of field of an imaging system arbitrarily high by the apodization of an optics aperture which is similar to a weighted zone plate. A computer means for extending the depth of field was reported by Piepper and Korpel [3]. An important early contribution using an integrated computational imaging system to extend the depth of field was made by Poon and Motamedi [4], who blocked the center of the lens to eliminate zeros at small defocus and then used

* Corresponding author. Tel.: +1 5852756195; fax: +1 5854738722.
E-mail addresses: chiw@optics.rochester.edu (W. Chi), ngeorge@troi.cc.rochester.edu (N. George).
[1] Permanent address: The Institute of Optics, University of Rochester, 275 Hutchison Road, Rochester, NY 14627, USA

0030-4018/$ - see front matter © 2004 Elsevier B.V. All rights reserved.
doi:10.1016/j.optcom.2004.10.006

digital processing to correct the OTF distortion due to center obscuration. An outstanding advancement for extending the depth of field using an integrated computational imaging system was made by Cathey and co-workers [5–8]. They introduced a cubic phase mask or its modification to the aperture of the lens in order to obtain a defocus invariance magnitude transfer function of the optical system. A subsequent digital processing is used to correct the blurs. A new approach using a circularly symmetric lens called a logarithmic asphere and a rapidly converging maximum entropy processing has been described by us in a series of papers [9–11]. In this paper we present new results demonstrating that it is possible to attain diffraction limited performance over an extended range. In Fig. 4, we use a centrally obscured logarithmic lens to obtain this result. Computer simulations of the blur and the recovery are presented for two point sources separated by the Rayleigh limit. Excellent recovery is demonstrated for a wide range of object distances in Fig. 4. Also, we present overall OTF data including the digital processing in Fig. 8 and showing depth-of-field and OTF results far exceeding the classical limits.

2. Theory for the center obscured lens aperture

Consider an ideal imaging lens of focal length f and aperture radius R that is obscured from 0 to δR, as in Fig. 1, one can readily show that the impulse response for this lens is given by [10]:

$$I_0(\rho_2;s) \approx \left| \int_{\delta R}^{R} \frac{2\pi A}{\lambda_0^2} \rho \frac{1}{s} J_0\left(2\pi \frac{\rho\rho_2}{\lambda_0\sqrt{\rho^2+t^2}}\right) \mathrm{d}\rho \right|^2, \tag{1}$$

in which $I_0(\rho_2;s)$ is the output intensity at plane II in Fig. 1 at a radial coordinate value ρ_2 for a point source at a distance s. The distance s_0 corresponds to a sharp focus, i.e., $1/s_0 + 1/t = 1/f$. It is interesting to plot the intensity impulse response I_0 for a few values of δR from 0 to $0.5R$, as in Fig. 2. The center peak of the point spread function narrows down as the central obscuration is increased.

In addition to this narrowing of the impulse response, one can see that a central obscuration

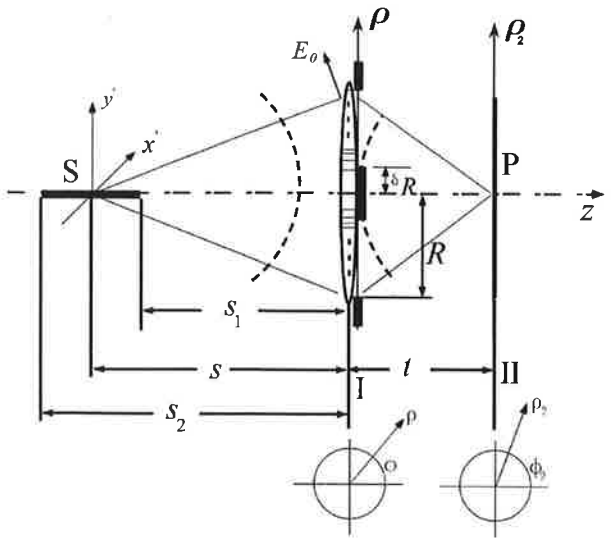

Fig. 1. The diagram of lens with center obscuration.

increases the depth of field by the following consideration of the OTF as defocus is introduced [4,12]. One can readily show that the defocus for an object point at s, offset from s_0, is given by $W_{20} = \frac{1}{2}(1/s - 1/s_0)R^2$, where R is the radius of the aperture. In calculation of the OTF for an apodization δR, it is immediately evident that the zeros and negative spatial frequency responses (contrast inversion) can be avoided for larger amounts of defocus with larger values for δR.

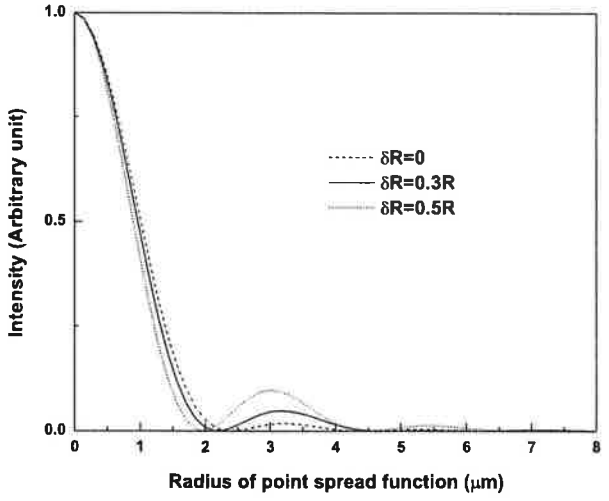

Fig. 2. The point spread functions of an ideal lens with different amount of central obscuration, plotted from Eq. (1).

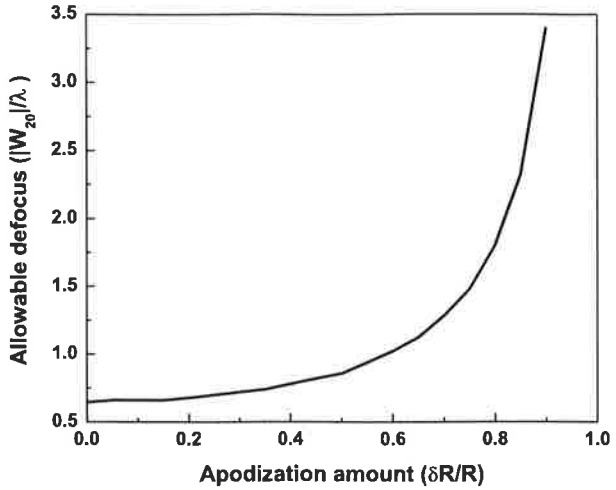

Fig. 3. The allowable defocus amount vs. central obscuration ratio for an ideal lens.

With the aid of a computer, we plot the OTFs at fixed δR for a range of offset distances s. We pick the largest $|s-s_0|$ at which there are no zeros in the OTF. This plot of the allowable defocus $|W_{20}|/\lambda$ vs. the apodization $\delta R/R$ is shown in Fig. 3. From this we observe that the larger defocus can be tolerated by increasing the central obscuration ratio $\delta R/R$. It is interesting, parenthetically, to compute the increased depth of field for an ideal lens (non-logarithmic asphere) when an apodization of $\delta R = 0.5R$ is used. From Fig. 3, we see that the depth of field which is proportional to $1/s-1/s_0 = 2W_{20}/R^2$ is given by 0.859 for a limited improvement of (0.859–0.644)/0.644, or only 33%.

In a previous publication, we developed a theory for the logarithmic asphere combined with maximum entropy recovery algorithm to extend the depth of field [10]. In this letter we describe an integrated imaging system that takes advantage of the properties of the circularly symmetric logarithmic lens, aperture obscuration and maximum entropy digital processing to extend the depth of field.

Now consider that the imaging lens in Fig. 1 is replaced by a logarithmic asphere and the central obscuration is retained. The logarithmic asphere is basically a multifocal length lens. Each annular ring of the lens has a different focal length. With a careful choice of the function of the object distances vs. the best focus rings, we can design the lens such that the on-axis intensity of the point spread function is inversely proportional to the object distance squared. This dropping of on-axis intensity of the impulse response is consistent with the decrease of the light collecting angle determined by this lens aperture. The lens so designed is called β-type logarithmic asphere. As we have shown in an earlier publication, Eq. (4) of [10], The point spread function of the β-type logarithmic asphere was approximated by the following diffraction integral:

$$I(\rho_2;s) \approx \left| \int_{\delta R}^{R} \frac{2\pi A}{\lambda_0^2} \rho \frac{1}{s} \exp\left[-\mathrm{i}\frac{2\pi}{\lambda_0}\sqrt{\rho^2+s^2} - \mathrm{i}\phi(\rho) - \mathrm{i}\frac{2\pi}{\lambda_0}\sqrt{\rho^2+t^2} \right] J_0\left(2\pi \frac{\rho\rho_2}{\lambda_0\sqrt{\rho^2+t^2}}\right) \mathrm{d}\rho \right|^2. \tag{2}$$

The stationary phase evaluation of the integral for β lens yields the following property:

$$I(\rho_2;s) \propto \frac{1}{s^2} J_0^2\left(2\pi \frac{\rho_2 \rho(s)}{\lambda_0\sqrt{\rho(s)^2+t^2}} \right). \tag{3}$$

where the expression of $\rho(s)$, the stationary point, can be obtained from Eq. (24) of [10], but it is not relevant here. Herein, for the logarithmic asphere derivation with central obscuration, the object point s_1 is sharply imaged at the edge $\rho = \delta R$ while the point s_2 is sharply imaged by the outer edge $\rho = R$ of the lens. For $\delta R \geqslant 0.3R$, we see that there is a considerable improvement in narrowing the impulse response of the logarithmic asphere at the close-in distance, e.g., Fig. 5 of [10]. From this figure and by Eq. (3), one can see that the center peak of the impulse response is approximately the width of first zero of the Bessel function of order zero, i.e., J_0. The consequence of this result is that when the object is close to the near point, if the whole aperture of lens is used, $\rho(s_1) \to 0$, then the width of the point spread function is large. Thus, the recovery for the close object distances is not satisfactory. In this letter we improve this performance by introducing the center obscuration to the logarithmic asphere, i.e., $\delta R \neq 0$. This center obscuration significantly narrows the center peak

of the point spread function for close distances. This provides a significant improvement on the point spread function for the β-lens at close object distances as is fully discussed below.

3. Performance of the obscured logarithmic asphere

In earlier experiments with the logarithmic lens, it has been found that the point spread function is invariant over a wide range of distances, thereby providing a tenfold increase in the depth-of-field. In this letter we demonstrate that the distance invariance is greatly improved by means of a central obscuration. In order to illustrate the diffraction limited performance of the integrated computational imaging system combining the center obscured logarithmic asphere and maximum entropy digital recovery, we show in Fig. 4 the images of a two-point object blurred by the ideal lens (left column) and the logarithmic asphere (center column) and its recovery (right column). In the design of the logarithmic asphere, we choose a close distance $s_1 = 1400$ mm, far distance $s_2 = 1615$ mm and the center distance $s_0 = 1500$ mm. The center obscuration $\delta R = 0.5R$. i.e., by area 25% of the aperture is not used. Clearly, This obscuration causes a 25% loss of light intensity, which needs to be considered in a final design trade-off. The distance of the two points is 2.57 μm, the minimum resolvable distance according to the Rayleigh criterion. In Fig. 4, the rows are for object distances 1450, 1492, 1500, 1508, and 1580 mm, respectively. The in-focus distance $s_0 = 1500$ mm with the conventional depth of field (for a full aperture $f/4.0$) ranging from 1492 to 1508 mm. In the recovery a single average impulse response over the design range is used for the five recoveries. The similarity of blur for the logarithmic asphere is clearly seen from the center column of the blurred images, all have two bright peaks at the center accompanied by low intensity oscillating rings. The center bright peaks also have similar sizes. The oscillating rings do not pose a problem since excellent recoveries are achieved for all five images. The two-point recovery (right column) shows excellent diffraction-limited resolution from 1450 to 1580 mm. At 1420 mm (not shown), the two points are still easily resolvable, but not as clearly as those in the figure. The improvement in the close-in distance is due to the narrower central peak of the point spread function for the close-in object. Also, importantly, there is less difference in the oscillating ring structure of the point spread function over the designed object range. These two factors lead to a point spread function that varies less with object distance, hence the average point spread function used in the digital processing provides a greatly improved output.

In the next simulation, we still use the same two-point object, but three logarithmic aspheres are used with center obscuration values of $\delta R = 0$, $0.3R$, $0.5R$, respectively. When the object is at a distance of $s = 1450$, or 50 mm closer than the best focus plane. we plot the recovered one dimensional pixel values in the two point direction in Fig. 5 along with the pixel values of the blurred image by an ideal lens. In the ideal lens curve, the full aperture of the lens is used. We observed a fully resolvable two point recovery with center obscuration of $\delta R = 0.5$. But when $\delta R = 0.3R$, the recovery points are barely resolvable; and when there is no central obscuration, the recovery points are unresolvable. These curves clearly shows the extra increase in performance for central obscuration. We emphasize that the increase in performance mainly comes from the similarities of the point spread functions over the design range instead of from the increase of the depth of field by central obscuration. Since we have seen from the earlier section that the increase in depth of field by central obscuration of aperture is very limited in our cases.

In Fig. 6, we repeat the curves as in Fig. 5 except that the object is at a distance of $s = 1500$ mm, the best focus position for the logarithmic aspheres and the ideal lens. Again, we see the advantage of the logarithmic asphere with central obscuration in both the resolving power and contrast.

For application to photography which is our interest, one would like to observe the performance of the obscured logarithmic asphere as shown by the pictures in Fig. 7. In this simulation, the tiger picture is at a distance of 1580 mm, the upper left is the recovered image for the logarithmic

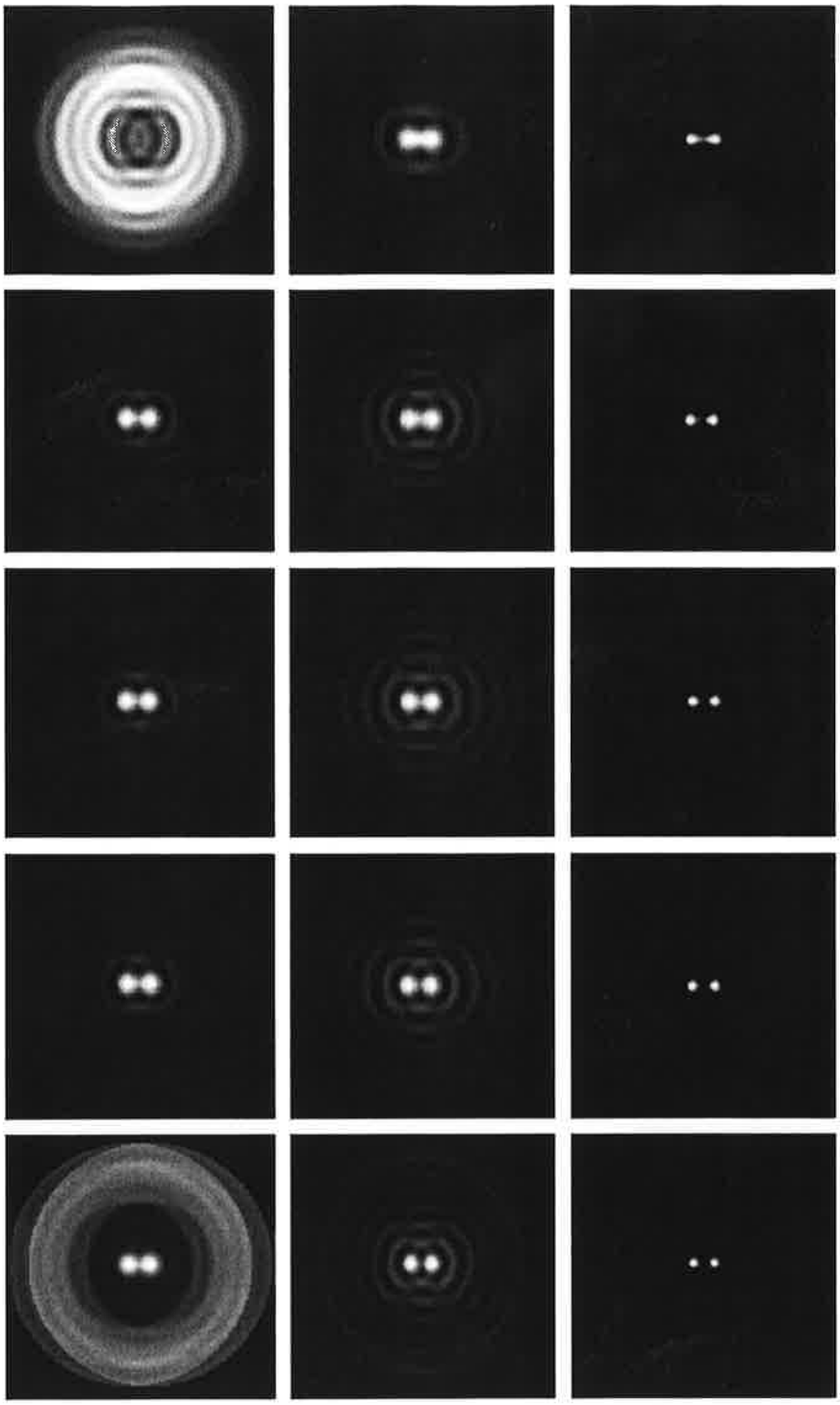

Fig. 4. Illustration of the performance of our integrated imaging system with a centrally obscured logarithmic asphere and maximum entropy image recovery. The first column shows the images by an ideal lens with central obscuration, the second column shows the blurred images by the log lens with center obscuration, the third column shows the maximum entropy recovery of images in the second column using an average point spread function. The rows from top to bottom correspond to the object distances at 1450, 1492, 1500, 1508, 1580 mm, respectively.

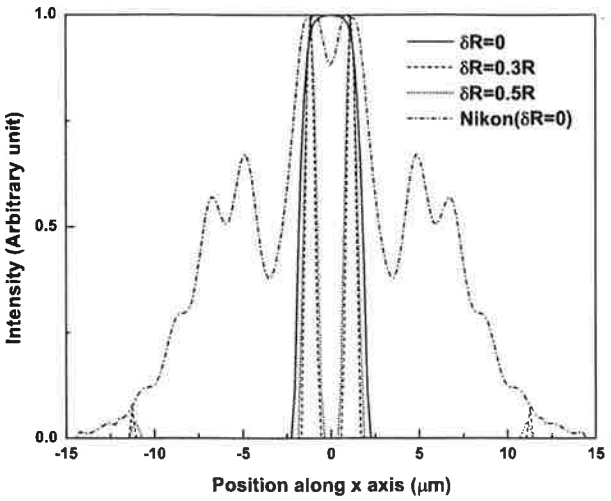

Fig. 5. The recovered data for a two point object at a distance of $s = 1450$ mm.

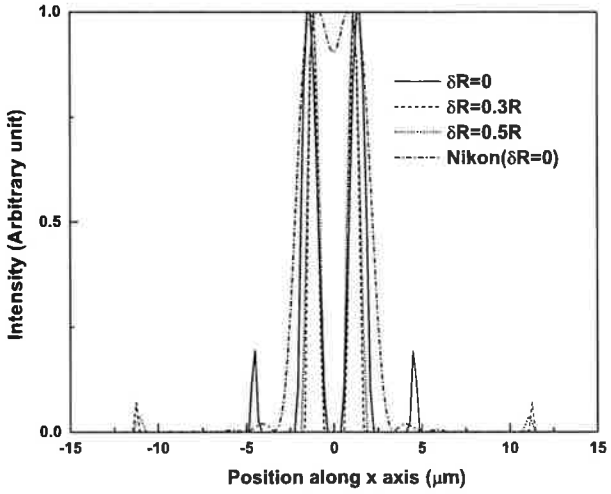

Fig. 6. The recovered data of a two point object at a distance of $s = 1500$ mm.

asphere without center obscuration. The lower left and lower right are the recovered images for the logarithmic asphere with central obscuration of $\delta R = 0.3R$, and $0.5R$, respectively. The upper right shows the image using the ideal lens with full aperture for comparison purpose. The logarithmic aspheres without and with obscuration are capable of extending the depth of field. While all the recoveries are fairly good, the recovered images for log aspheres with obscuration are better because there are less artifacts. The artifacts of the recovery appear since the average point spread function over the design range is used for all the recoveries. In inspecting these pictures, it is important to notice that the width of tiger whiskers in the simulation is about 0.7 μm, which is smaller than the diffraction limited spot size.

In further evaluation of the system performance, it is important to study the frequency response of the system. In intensity imaging systems, it is common to characterize their performance by the optical transfer function. Extending this notion to a computational imaging system, in principle, one can find the overall frequency response by dividing the spectrum of the recovered image by that for the input object. Hence, to find the overall frequency response, as in Fig. 8, we calculate the images of a point source at various object distances, and then apply the maximum entropy algorithm to these images to recover the point object, The recoveries can be considered as the combined impulse response of the integrated computational imaging system. The Fourier transform of the recoveries is plotted in Fig. 8. The curves are the combined transfer functions of the system over a range of object distances. One should note that the transfer function of the system is circularly symmetric and Fig. 8 shows its values along the radial direction over an extended depth of field. The relative spatial frequency 1.0 corresponds to the cutoff frequency of the diffraction limited lens for the same imaging settings. The amplitude of the overall transfer function of the new system is boosted up to diffraction limit over an extended object range. Also the phase of the overall transfer function is zero due to the circular symmetry of the impulse response. The diffraction limited performance for the integrated computational imaging system over an extended depth of field is clearly seen from these curves.

From Fig. 8, we see the excellent frequency domain response over the range from 1420 to 1580 mm. The diffraction limited depth of field for an ideal lens with the same settings is ±8 mm. So the depth of field of our system is 10 times that for a conventional ideal lens.

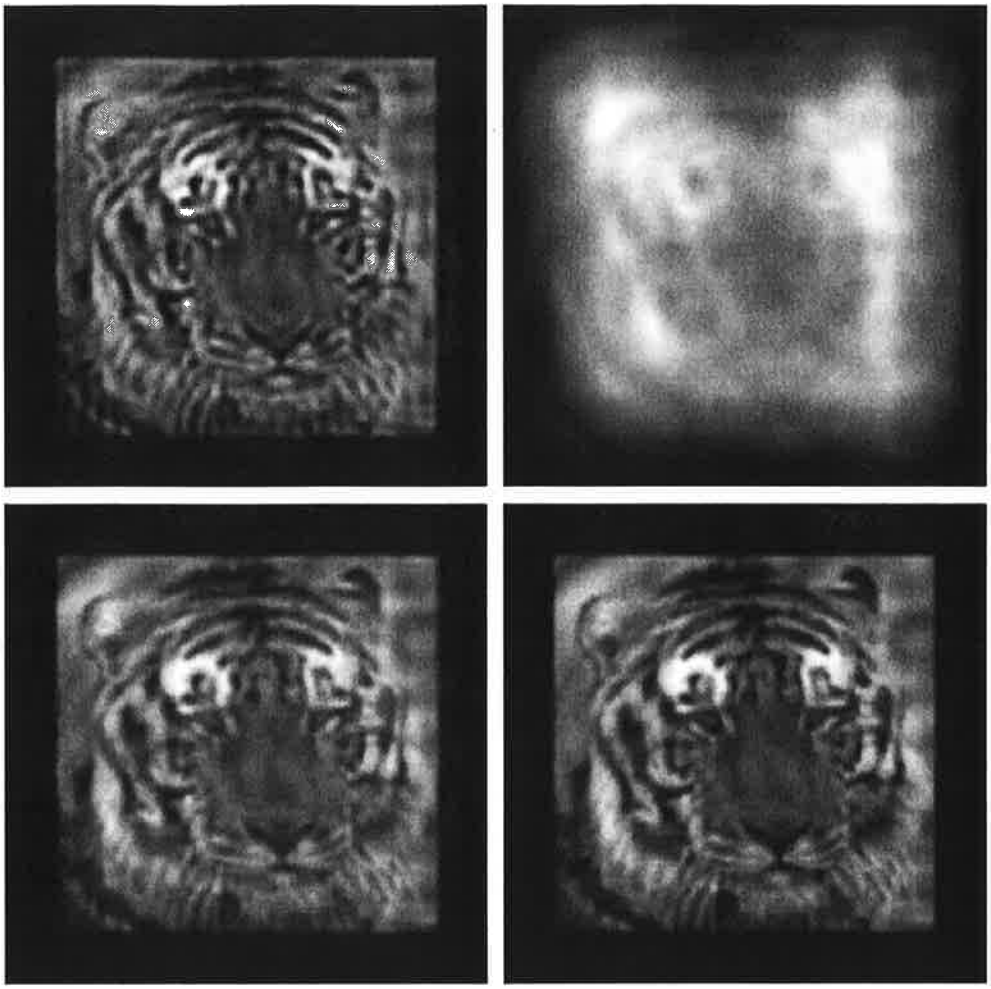

Fig. 7. The maximum entropy recovery of a tiger image blurred by logarithmic lenses with different central obscurations. Upper left: $\delta R = 0$; lower left: $\delta R = 0.3R$; lower right: $\delta R = 0.5R$; Upper right: image by ideal lens without central obscuration.

We maintain that in Fig. 8 the concept of overall transfer function is only an approximate index of the system performance because of the nonlinear digital processing involved. In other words, one can expect to find different overall transfer functions for various objects. Nonetheless, the transfer function shown in Fig. 8 is a good indication of performance of the integrated imaging system. In order to clarify this statement, we show in Fig. 9 the overall transfer function for objects at a distance of $s = 1580$ mm, where we use both a point and an edge object. The recoveries from the blur images by the log lens provide the overall point spread function and overall edge response function, respectively. From Fig. 9, we see that the overall transfer functions are similar for these two cases.

While the noise analysis of the integrated imaging system is not the scope of this communication, it is worthwhile to mention that there are two types of noise in the recovery. The first type is the additive noise contributed by the blurred picture. The second type is the convolution noise contributed by the difference between the point spread functions used for blur and recovery. The first type of noise can be minimized by reducing noise in the image detection process and designing the appropriate image deconvolution algorithm. The

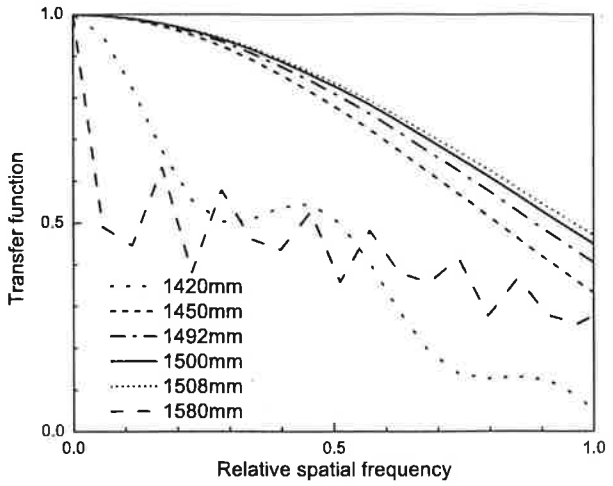

Fig. 8. The overall transfer function of the integrated imaging system for six object distances.

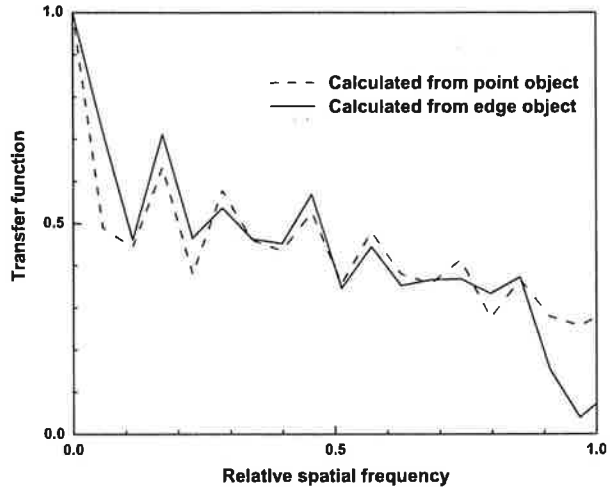

Fig. 9. The overall transfer function of the integrated imaging system at 1580 mm using point object and edge object.

second type of noise is the limiting factor for the depth of field extension because of the diffraction nature of light. The side peaks of the recoveries in Figs. 5 and 6 and the oscillation of the overall transfer function in Figs. 8 and 9 are the manifestation of the second type of convolution noise.

4. Conclusion

A computational imaging system that combines the advantages of the logarithmic asphere, center obscuration, and maximum entropy processing is studied by computer simulations. The improvement in the performance of the centrally obscured log asphere comes from the resulting similarities of the center peak and oscillation rings of the point spread functions over the designed depth of field, especially for the close-in distance. The performances of both the two points and the gray scale tiger imaging prove that the system with a centrally obscured log asphere excels in resolution and contrast. Measurements are also described for the determination of the overall transfer function, as shown in Figs. 8 and 9. By a study of various objects, we establish that the centrally-obscured logarithmic lens system provides a tenfold increase in the depth of field while maintaining diffraction limited resolution. Portions of this research [11] were was supported in part by the army research office.

References

[1] G. Hausler, Opt. Commun. 6 (1972) 38.
[2] J. Ojeda-Castaneda, L.R. Berriel-Valdos, Appl. Opt. 29 (1990) 994.
[3] R.J. Pieper, A. Korpel, Appl. Opt. 22 (1983) 1449.
[4] T. Poon, M. Motamedi, Appl. Opt. 26 (1987) 4612.
[5] E.R. Dowski Jr., W.T. Cathey, Appl. Opt. 34 (1995) 1859.
[6] J. van der Gracht, E.R. Dowski Jr., W.T. Cathey, J.P. Bowen, Proc. SPIE 2537 (1995) 279.
[7] S.S. Sherif, W.T. Cathey, E.R. Dowski Jr., Appl. Opt. 43 (2004) 2709.
[8] H.B. Wach, W.T. Cathey, E.R. Dowski, Appl. Opt. 37 (1998) 5359.
[9] W. Chi, N. George, Opt. Lett. 26 (2001) 875.
[10] W. Chi, N. George, J. Opt. Soc. Am. A 20 (2003) 2260.
[11] W. Chi, Computational imaging system for extended depth of field, PhD Thesis, University of Rochester, 2004.
[12] E.H. Linfoot, E. Wolf, Proc. Phys. Soc. London Ser. B 66 (1953) 145.

Sampling-theory approach to eigenwavefronts of imaging systems

Kedar Khare and Nicholas George

The Institute of Optics, University of Rochester, Rochester, New York 14627

Received June 4, 2004; revised manuscript received September 8, 2004; accepted September 21, 2004

We present a direct method based on the sampling theorem for computing eigenwavefronts associated with linear space-invariant imaging systems (including aberrated imaging systems). A potential application of the eigenwavefronts to inverse problems in imaging is discussed. A noise-dependent measure for the information-carrying capacity of an imaging system is also proposed. © 2005 Optical Society of America

OCIS codes: 110.2990, 100.3190, 070.6020.

1. INTRODUCTION

Linear space-invariant imaging systems are generically modeled by a 4F or cannonical optical processor as shown in Fig. 1. The input and output of this system are related by a convolution relation,

$$g_o(x) = \int_{-L}^{L} dx' p(x - x') g_i(x'), \tag{1}$$

where $p(x)$ is the impulse response of the system and is given by the Fourier transform of the aperture function[1] $P(f)$. The input function $g_i(x)$ is assumed to have a finite support $x:(-L, L)$. We also note that the aperture function $P(f)$ is expected to be of finite support, say, $f:(-B, B)$, for any practical system. The impulse response $p(x)$ is thus band limited and has a sampling expansion[2]:

$$p(x) = \sum_{m=-\infty}^{\infty} p\left(\frac{m}{2B}\right) \mathrm{sinc}(2Bx - m). \tag{2}$$

The purpose of this paper is to present a sampling-theorem-based procedure for treating the eigenvalue problem:

$$\mu_n \psi_n(x) = \int_{-L}^{L} dx' p(x - x') \psi_n(x'). \tag{3}$$

The aperture function $P(f)$ for a given system may be a general amplitude-phase-varying mask. The eigenfunctions $\psi_n(x)$ therefore represent complex wavefronts that pass through the imaging system unchanged apart from a constant multiplier. Henceforth we will refer to the eigenfunctions as the "eigenwavefronts" associated with the impulse response $p(x)$. Eigenfunction analysis of imaging systems and discussions of related topics such as degrees of freedom and resolving power have appeared in the optics literature.[3–6] A singular-value-based treatment of imaging is also well known.[7] However, we believe that a direct method based on the sampling theorem for computing the eigenvalues and eigenwavefronts of imaging systems as described here has not appeared in the literature. The outline of this paper is as follows. In Section 2 we start with our approach for treating Eq. (3) using the sampling theorem. The special case of sinc impulse response and prolate spheroids as the corresponding eigenwavefronts is also discussed briefly. In Section 3 we illustrate with two numerical examples the computation of eigenwavefronts for aberrated systems. In Section 4 we describe a potential application of the eigenwavefronts to inverse problems in imaging.

2. EIGENVALUE PROBLEM FOR A BAND-LIMITED IMPULSE RESPONSE

In this section we consider the eigenvalue problem in Eq. (3), which is a homogeneous Fredholm integral equation of the second kind with a band-limited kernel. We start by showing that $\psi_n(x)$s satisfy the sampling theorem. To show this, we write the impulse response in Eq. (3) as a sampling series to get

$$\begin{aligned}\mu_n \psi_n(x) &= \int_{-L}^{L} dx' \left[\sum_{m=-\infty}^{\infty} p\left(\frac{m}{2B} - x'\right) \right. \\ &\quad \left. \times \mathrm{sinc}(2Bx - m) \right] \psi_n(x') \\ &= \mu_n \sum_{m=-\infty}^{\infty} \psi_n\left(\frac{m}{2B}\right) \mathrm{sinc}(2Bx - m). \end{aligned} \tag{4}$$

Using this sampling expansion for $\psi_n(x')$ on the right-hand side of Eq. (3), we now write

$$\begin{aligned}\mu_n \psi_n\left(\frac{m}{2B}\right) &= \int_{-L}^{L} dx' p\left(\frac{m}{2B} - x'\right) \sum_{k=-\infty}^{\infty} \psi_n\left(\frac{k}{2B}\right) \\ &\quad \times \mathrm{sinc}(2Bx' - k) \\ &= \sum_{k=-\infty}^{\infty} A'_{mk} \psi_n\left(\frac{k}{2B}\right), \end{aligned} \tag{5}$$

where

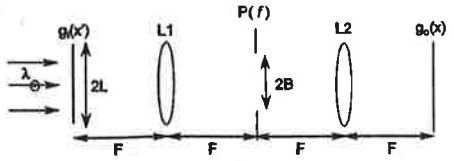

Fig. 1. Linear space-invariant imaging system.

$$A'_{mk} = \int_{-L}^{L} dx' p\left(\frac{m}{2B} - x'\right) \mathrm{sinc}(2Bx' - k). \quad (6)$$

From Eq. (5) we notice that the continuous eigenvalue problem in Eq. (3) is equivalent to a discrete eigenvalue problem for the matrix $\mathbf{A}'$ defined in Eq. (6). The discrete problem may be written as

$$\mathbf{A}'\mathbf{w}_n = \mu_n \mathbf{w}_n, \quad (7)$$

where the discrete eigenvectors of $\mathbf{A}'$ are given by

$$\mathbf{w}_n = \left[\ldots \psi_n\left(\frac{m}{2B}\right) \ldots\right]^{\mathrm{T}}, \quad (8)$$

where the superscript T denotes the transpose of the row vector. We observe that the discrete and continuous problems share the same eigenvalue spectrum and that the elements of the eigenvector $\mathbf{w}_n$ are the samples of the corresponding eigenwavefront spaced $\Delta x = 1/(2B)$ apart. The eigenwavefront $\psi_n(x)$ may thus be constructed by sinc-interpolating the discrete eigenvector $\mathbf{w}_n$ according to Eq. (4).

As a special case we take $p(x) = \mathrm{sinc}(2Bx)$ and denote the corresponding matrix by $\mathbf{A}$:

$$A_{mk} = \int_{-L}^{L} dx' \,\mathrm{sinc}(2Bx' - m)\mathrm{sinc}(2Bx' - k). \quad (9)$$

This case corresponds to an imaging system with a rect-function aperture given by $P(f) = \mathrm{rect}(f/2B)$. It is well known that the eigenwavefronts $\psi_n(x)$ in this case are the prolate spheroidal functions of order zero.[8,9] It is interesting to note that the matrix $\mathbf{A}'$ defined in Eq. (6) may be further simplified by expanding the impulse response in Eq. (6) as a sampling series with respect to the variable x':

$$A'_{mk} = \sum_{l=-\infty}^{\infty} p\left(\frac{m-l}{2B}\right) \int_{-L}^{L} dx' \times \mathrm{sinc}(2Bx' - l)\mathrm{sinc}(2Bx' - k) = \sum_{l=-\infty}^{\infty} p\left(\frac{m-l}{2B}\right) A_{lk}. \quad (10)$$

The matrix $\mathbf{A}'$ thus factorizes as

$$\mathbf{A}' = \mathbf{h}\mathbf{A}, \quad (11)$$

where the matrix $\mathbf{h}$ is defined as

$$h_{ml} = p\left(\frac{m-l}{2B}\right) \quad (12)$$

and the matrix $\mathbf{A}$ is as defined in Eq. (9). The above factorization of the matrix $\mathbf{A}'$ is convenient from a computational point of view. It is clear that the matrix $\mathbf{A}$ may be computed independently for given values of L and B and stored in computer memory. The matrix $\mathbf{h}$, on the other hand, may simply be formed by using the known samples of the impulse response $p(x)$. Thus for all systems with fixed values of L and B, the matrix $\mathbf{A}$ needs to be computed only once. This reduces computational effort in performing numerical integrations.

We conclude this section by remarking that the method for computing eigenwavefronts as proposed in this paper allows us to determine the samples of $\psi_n(x)$ beyond the range $x:(-L, L)$. This would not be possible if we were to solve the eigenvalue problem by approximating the integral on the right-hand side of Eq. (3) by some quadrature rule. The knowledge of $\psi_n(x)$ beyond $x:(-L, L)$ has important implications for inverse problems, as we shall see later in this paper.

3. EIGENWAVEFRONTS OF ABERRATED SYSTEMS: ILLUSTRATION

As an illustration, we now show computation of the eigenwavefronts and the corresponding eigenvalues for two aberrated imaging systems. Aberrations in imaging systems are often modeled by phase screens in the aperture $P(f)$ of the system. In the first example, we use a quadratic phase screen in the aperture to simulate a defocused system. For comparison, a second phase screen that has up to fifth-order terms is used in the second example.

We choose the numerical values $L = 2, B = 2$ and compute the eigenwavefronts for a 1λ defocused system. The aperture function for this case is given by

$$P_1(f) = \exp\left(i\frac{\pi}{2}f^2\right)\mathrm{rect}\left(\frac{f}{2B}\right). \quad (13)$$

The impulse response $p(x)$ is determined by Fourier transforming the above $P_1(f)$ numerically and is shown in Fig. 2. To compute the eigenwavefronts, the following procedure is used:

1. A 101 × 101 truncated version of the matrix $\mathbf{A}$ defined in Eq. (9) was computed. The numerical integrations were performed with the standard quadrature routine available in Matlab version 6. The size of the matrix

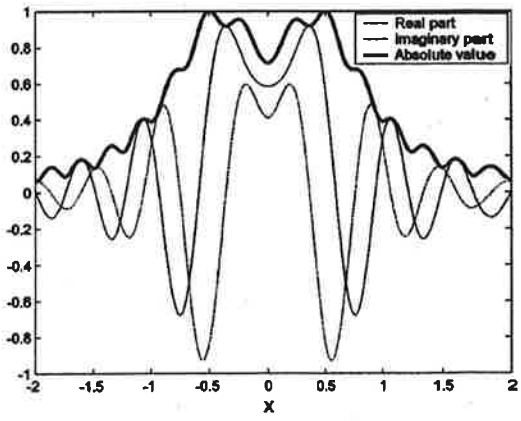

Fig. 2. Impulse response for a system with aperture function $P_1(f)$ in Eq. (13).

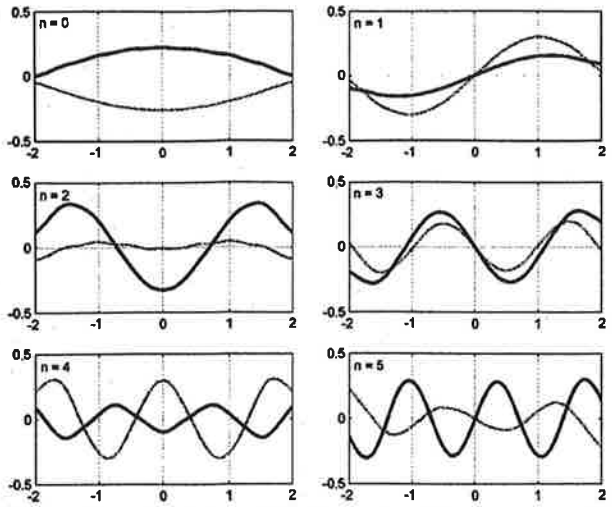

Fig. 3. First six eigenwavefronts corresponding to the impulse response in Fig. 2, with $L = 2, B = 2$. Solid and dotted curves show real and imaginary parts, respectively.

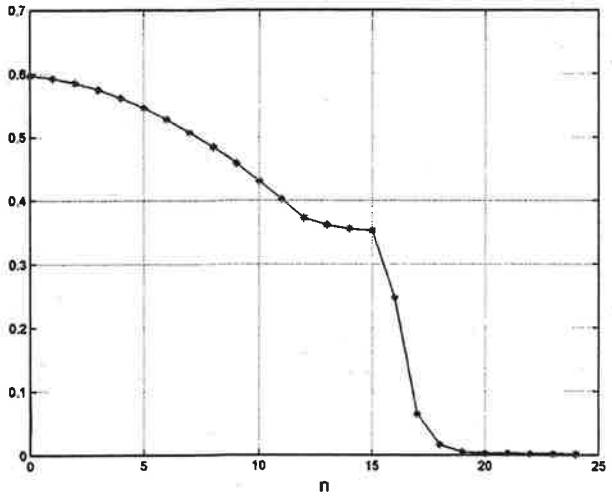

Fig. 4. Eigenvalues (absolute magnitude) corresponding to the impulse response in Fig. 2, with $L = 2, B = 2$.

is selected to be sufficiently larger than $(2B)(2L) = 4BL$ for reasons that will be clear later in the paper.

2. The matrix **h** defined in Eq. (12) was formed (101 × 101 truncated version) by using samples of the impulse response $p(x)$ shown in Fig. 2.

3. The matrix $\mathbf{A}'$ was computed as $\mathbf{A}' = \mathbf{hA}$.

4. The discrete eigenvalue problem as in Eq. (5) was solved to obtain the eigenvalues μ_n and the discrete eigenvectors $\mathbf{w}_n$. The discrete eigenvectors were then sinc-interpolated to obtain continuous eigenwavefronts.

The first six eigenwavefronts ordered according to the highest absolute eigenvalues for the case of the aperture function $P_1(f)$ in Eq. (13) are shown in Fig. 3, and the first 25 eigenvalues (absolute magnitude) are plotted in Fig. 4. Note that the eigenvalues decrease slowly in absolute magnitude for $n = 0$ to 15, and beyond $n > 15$ they fall off sharply. Clearly the eigenwavefronts $\psi_n(x)$ for $n > 15$ will pass from the input to the output of the system with a small multiplication factor. It is pleasing to note the consistency of this eigenvalue fall-off with the notion of space–bandwidth product of the system, which is given by $(2B)(2L) = 16$ in this example.

For the next example, we consider a system with the aperture function

$$P_2(f) = \exp\left[i\frac{\pi}{2}\left(f^2 + \frac{1}{2}f^3 + \frac{1}{2}f^4 + \frac{1}{4}f^5\right)\right]\mathrm{rect}\left(\frac{f}{2B}\right). \tag{14}$$

The higher-order terms in the phase function have been added to illustrate that the method for computing eigenwavefronts as proposed here is independent of any symmetry in aberrations with respect to the optic axis. The impulse response corresponding to this case is shown in Fig. 5. The first six eigenwavefronts are shown in Fig. 6, and the 25 highest-magnitude eigenvalues are plotted in Fig. 7. The same steps as outlined above in the first ex-

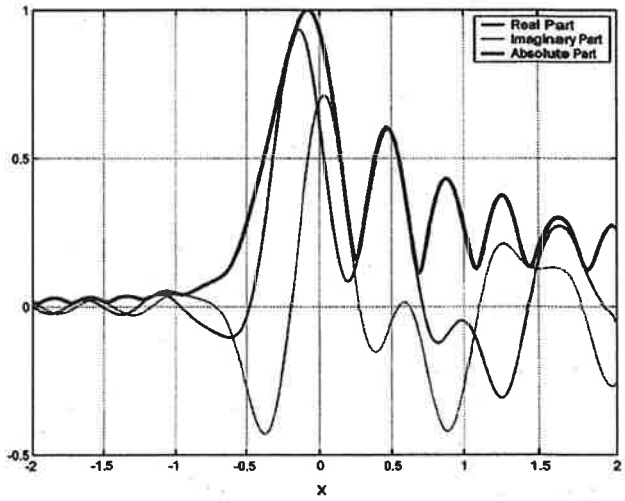

Fig. 5. Impulse response for a system with the aperture function $P_2(f)$ in Eq. (14).

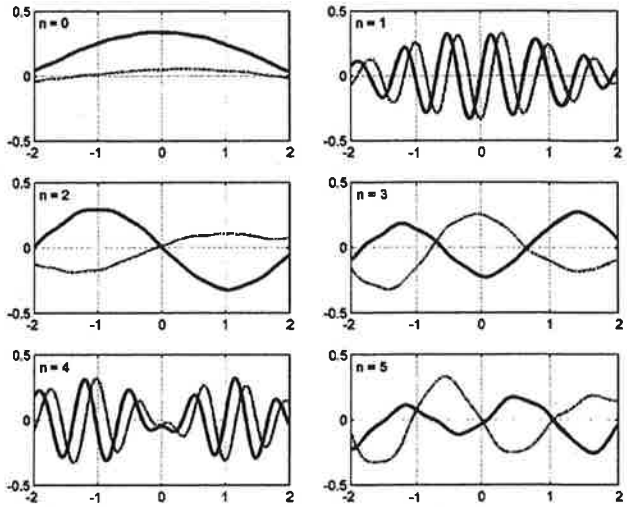

Fig. 6. First six eigenwavefronts corresponding to impulse response in Fig. 5, with $L = 2, B = 2$. Solid and dotted curves show real and imaginary parts, respectively.

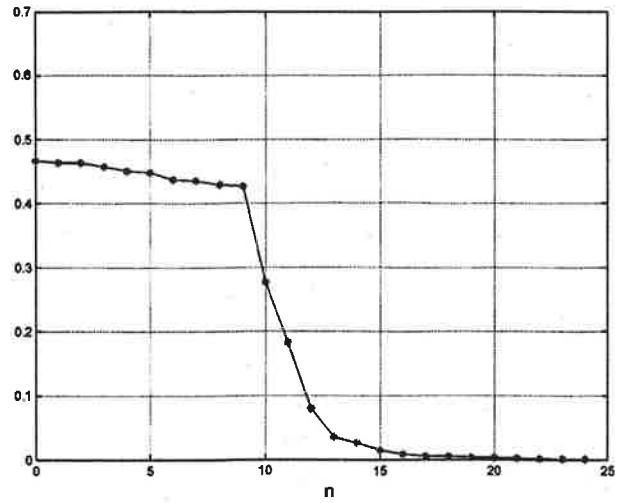

Fig. 7. Eigenvalues (absolute magnitude) corresponding to the impulse response in Fig. 5, with $L = 2$, $B = 2$.

ample were employed for this computation. The effect of increased aberrations on the eigenvalue spectrum is to reduce the magnitude of the highest eigenvalue. Also, the rate of fall-off in eigenvalues for $n = 0$ to 15 is faster than that in the first example (see Figs. 4 and 7). The eigenvalues for $n > 15$ are once again small in magnitude, as in the earlier case. The two examples above illustrate the general nature of our method for computation of eigenvalues and eigenwavefronts associated with band-limited impulse responses.

4. APPLICATION TO INVERSE PROBLEMS

In this section we consider a potential application of the eigenwavefronts to the inverse problem of estimating the input $g_i(x)$ from the measured output $g_o(x)$, which is generally ill-posed[10] in nature. Suppose we are able to represent the output $g_o(x)$ as a linear combination of the eigenwavefronts as

$$g_o(x) = \sum_n b_n \psi_n(x). \tag{15}$$

Then the input $g_i(x)$ may be estimated as

$$g_i(x) = \text{rect}\left(\frac{x}{2L}\right) \sum_n \frac{b_n}{\mu_n} \psi_n(x). \tag{16}$$

This solution is easily verified by substitution into Eq. (1). We note that the measured output $g_o(x)$ always contains some noise (which may not be possible to eliminate in principle) that corresponds to noise on the coefficients b_n. We have already noted that the eigenvalues of the system become very small in magnitude when the index n is much larger than $4BL$. If such higher-order terms are included in the inverse recovery in Eq. (16), we will start dividing the noise on b_n by small numbers. This may result in undesirable amplification of noise. We therefore need to truncate the series in Eq. (16) to a finite number of terms depending on the noise level. The number of allowable terms in Eq. (16) that result in a reasonable recovery may be considered a measure of the information-carrying capacity of the imaging system. Note that this measure is explicitly noise dependent, as opposed to the space–bandwidth $4BL$, which implicitly assumes that all the signals are known to a good accuracy. Regularization approaches[11] may be combined with the eigenfunction-based solution above to incorporate additional *a priori* information about the solution; however, discussion of this topic is beyond the scope of this paper.

We now apply the inversion procedure described above to the defocused system in the first example. We assume that the input to the system is a point source located at $x' = 0$, so that the output $g_o(x)$ is the impulse response shown in Fig. 2. Expansion of $g_o(x)$ as a linear combination as in Eq. (15) is not a trivial problem, since the eigenwavefronts are not orthogonal in general (the impulse response is non-Hermitian). To counter this difficulty we note that the output $g_o(x)$ in an ideal "no-noise" case must satisfy the sampling theorem as in Eq. (2). We may show this from Eq. (1) by following a similar reasoning in the case of $\psi_n(x)$ as in Eq. (4). We may then write Eq. (15) as

$$\sum_{m=-\infty}^{\infty} \left[\sum_n b_n \psi_n\left(\frac{m}{2B}\right) - g\left(\frac{m}{2B}\right) \right] \text{sinc}(2Bx - m) = 0. \tag{17}$$

Note that the sinc functions centered at integral multiples of $1/(2B)$ are linearly independent[12], so that, from Eq. (17) we must have

$$\sum_n b_n \psi_n\left(\frac{m}{2B}\right) = g_o\left(\frac{m}{2B}\right) \tag{18}$$

for all the values of m corresponding to the sample data points $g_o(m/2B)$. The samples of the eigenfunctions on the left-hand side of the above equation are known once the eigenvectors of the matrix $\mathbf{A}'$ have been computed. Thus one needs to solve a linear algebraic system of equations to determine the coefficients b_n, which may then be used to estimate the inverse solution as in Eq. (16). The effect of additive noise is to introduce fluctuations to the data samples on the right-hand side of Eq. (18) and consequently to alter the coefficients b_n. As we pointed out earlier, we are able to determine the eigenwavefronts beyond the range $x:(-L, L)$. This allows us to use the sample data points $g_o(m/2B)$ beyond this range for solution of the inverse problem. In this respect, the inversion procedure above is similar to the singular-value-decomposition method.[7]

In Fig. 8 we show the inverse solution estimated using the above procedure when a point-source input was assumed. We used 21 sample points in $x:[-2.5, 2.5]$ and correspondingly the first 21 eigenfunctions for inverse recovery. Notice the similarity of the inverse recovery to the $\text{sinc}(2Bx)$ function, which is the expected output in the absence of aberrations. The eigenfunctions have thus helped us in effectively nullifying the aberrations in the system. For the second example, with a fifth-order polynomial phase mask $P_2(f)$, we followed a similar procedure of inverse solution and obtained an excellent recovery almost identical to that depicted in Fig. 8.

We would like to point out that in the presence of noise in the measurement of the output $g_o(x)$, the inverse recoveries for the two cases are not expected to be identical.

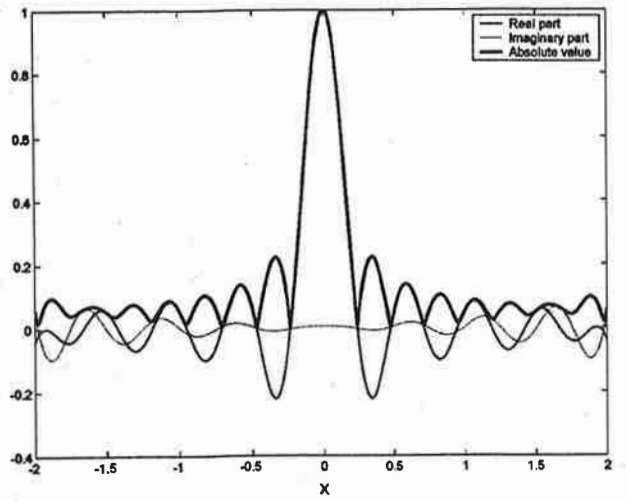

Fig. 8. Estimated inverse recovery for a point-source input. A system with the aperture function $P_1(f)$ is assumed, and correspondingly the eigenwavefronts in Fig. 3 are used for recovery.

The eigenvalues fall off faster in magnitude for the system with the aperture function $P_2(f)$ in Eq. (14). We may then expect that for a given noise level a reasonable inverse series solution for this case will contain fewer terms than when the aperture function is $P_1(f)$. In the presence of noise, one is thus able to recover less information from a system with higher aberrations.

We have performed some preliminary study[13] of the effect of additive noise on recovery, and the behavior of the inverse solutions is as expected from the above discussion of eigenvalue fall-off and noise levels. A detailed treatment of this topic and comparison of the inverse recoveries with those obtained by using other standard approaches (e.g., the Wiener filter) will be presented in a future publication.

5. CONCLUSION

In summary, we have presented a novel sampling-theorem-based procedure for treating the eigenvalue problems associated with band-limited integral kernels. The results were interpreted in the context of linear space-invariant imaging systems. The solution to the eigenvalue problem in Eq. (3) as presented here is quite general in nature and may find application to other problems where integral equations of the type of Eq. (1) occur, e.g., diffraction theory and Karhunen–Loeve expansions. A potential utility of the eigenwavefront method for image restoration problems was demonstrated with a numerical illustration, and a noise-dependent definition of the information-carrying capacity of an imaging system was also suggested with use of the eigenvalue spectrum.

ACKNOWLEDGMENTS

This research was supported in part by the U.S. Army Research Office and the Defense Advanced Research Projects Agency.

Kedar Khare's e-mail address is kedar@optics.rochester.edu.

REFERENCES AND NOTES

1. J. W. Goodman, *Introduction to Fourier Optics*, 2nd ed. (McGraw-Hill, New York, 1996).
2. C. E. Shannon, "Communication in the presence of noise," Proc. IRE **37**, 10–21 (1949).
3. C. K. Rushforth and R. W. Harris, "Restoration, resolution, and noise," J. Opt. Soc. Am. **58**, 539–545 (1968).
4. G. Toraldo Di Francia, "Degrees of freedom of an image," J. Opt. Soc. Am. **59**, 799–804 (1969).
5. F. Gori, "Integral equations for incoherent imagery," J. Opt. Soc. Am. **64**, 1237–1243 (1974).
6. M. Bendinelli, A. Consortini, L. Ronchi, and B. R. Frieden, "Degrees of freedom and eigenfunctions for the noisy image," J. Opt. Soc. Am. **64**, 1498–1502 (1974).
7. M. Bertero and E. R. Pike, "Resolution in diffraction-limited imaging: a singular value analysis," Opt. Acta **29**, 727–746 (1982).
8. D. Slepian and H. O. Pollak, "Prolate spheroidal wave functions, Fourier analysis and uncertainty—I," Bell Syst. Tech. J. **40**, 43–63 (1961).
9. K. Khare and N. George, "Sampling theory approach to prolate spheroidal wave-functions," J. Phys. A Math. Gen. **36**, 10011–10021 (2003).
10. A. N. Tikhonov and V. Y. Arsenin, *Solutions of Ill-Posed Problems* (Winston, Washington, D.C., 1977).
11. M. Bertero and P. Boccacci, *Introduction to Inverse Problems in Imaging* (Institute of Physics, London, 1998).
12. The linear independence follows from the fact that $\mathrm{sinc}(2Bx - m)$ and $\mathrm{sinc}(2Bx - k)$ are orthogonal over $(-\infty, \infty)$ for $m \neq k$.
13. K. Khare, "Mathematical topics in imaging: sampling theory and eigenfunction analysis of imaging systems," Ph.D. thesis (University of Rochester, Rochester, N.Y., 2004).

Light-emitting diode illumination design with a condensing sphere

Wanli Chi and Nicholas George

The Institute of Optics, University of Rochester, Rochester, New York 14627

Received October 28, 2005; revised February 8, 2006; accepted February 10, 2006; posted March 8, 2006 (Doc. ID 65618)

An illumination system is described that comprises a glass or plastic sphere, an embedded light-emitting diode (LED) source, and a reflecting or scattering mirror. The rays from the LED are either refracted in the forward direction or totally internally reflected by the sphere. The mirror breaks the total internal reflection and thus sends the rays in the forward direction. The illumination pattern and efficiency of the system are analyzed. This system is extremely compact and efficient and is a good starting point for a complex illumination system design. © 2006 Optical Society of America

OCIS codes: 220.2740, 080.2740, 150.2950, 230.3670, 080.0080.

1. INTRODUCTION

With the advancement of high-brightness light-emitting diodes (LEDs) and organic LED technologies,[1–7] LEDs have been increasingly used for numerous display and lighting applications ranging from traffic signal lighting, indoor/outdoor displays, automotive lighting, and imaging lighting as in machine vision applications. With the expanding use of the LED, there still exists a challenge to design a compact and efficient light collecting system. In current designs, a reflective cup at the bottom of the LED die and an epoxy dome lens are used in an indicator LED, but its light efficiency is low. In the design of high-power LEDs, the plastic dome lens is also generally used, but more emphasis is given to thermal management. While many aspects of LED illumination design need to be considered, including optical, thermal, electrical, and mechanical, in this paper we deal with the optical aspect. A device that we call a condensing sphere is proposed that has light collecting capability far exceeding a conventional lens or parabolic reflector. The extreme compactness of this novel condenser is another advantage.

Consider the system shown in Fig. 1 in which an LED (1) is embedded in a dielectric sphere (2) (or attached tightly to the sphere using index-matched material) to form the condenser optics; a small section of the sphere close to the LED may be roughened and then coated as a scattering mirror (3). Light emitted from the side or front surface of the LED is either refracted by the condensing sphere or totally internally reflected at the surface of the condensing sphere. As seen in Fig. 1, the rays represented by the dashed lines are refracted and exit the sphere in the desired forward direction. The rays represented by the solid lines are totally internally reflected at the surface of the sphere without loss of energy. If a perfect sphere is used, then these rays will be trapped inside the sphere. But with a section of scattering mirror on the surface of the condensing sphere, these trapped rays will be scattered in all directions, part of which are subsequently refracted outside the sphere in the desired direction. This process will continue until all the energy emitted by the LED is radiated outside of the sphere. Since the energy loss in this process is the small amount of partial reflection of rays at the right of the condensing sphere, e.g., the dashed ray F, this compact light collecting system is very efficient. This condensing sphere can be used widely, including in LED packaging and illumination design of packaged LEDs.

2. QUANTITATIVE ANALYSIS

A. Simplified Model

In order to study the basic properties of the angular illumination in this system, we use the first-order approximation, i.e., assume the LED is a point source located at the center of the scattering mirror inside the condensing sphere. We further assume the scattering mirror is circular; this will generate a circularly symmetric illumination pattern. The simplified model of Fig. 1 is shown in Fig. 2. The scattering mirror subtends a half-angle of α as shown. In the following we use this simplified model to study the light illumination pattern and the efficiency.

B. Angular Distribution of Illumination Pattern

First we consider the rays emitted by the LED that are directly refracted out of the condensing sphere. For a light ray emitted at the angle θ_1 shown in Fig. 2, the ray will refract to the far field with a direction denoted by the angle θ. Using Snell's law, one can compute the angle θ as

$$\theta = 2\theta_1 - \arcsin(n \sin \theta_1), \tag{1}$$

where n is the ratio of refractive index inside and outside the condensing sphere, and θ_1 must satisfy

$$\theta_1 \leq \theta_{1\max} = \arcsin(1/n) \tag{2}$$

to avoid total internal reflection so that the ray will refract at the surface of the sphere.

It is instructive to plot Eq. (1) for different refractive indices. In Fig. 3, we show the far-field angle θ versus the angle θ_1 of the corresponding ray inside the sphere for four different refractive indices: $n = 1.33, 1.5, (6\sqrt{3}-8)^{1/2}$,

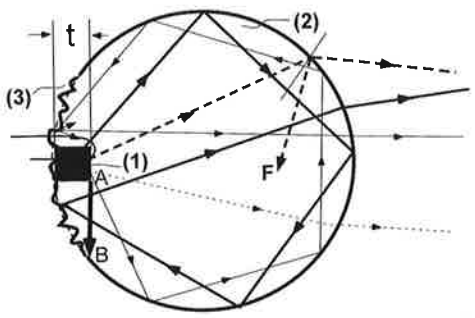

Fig. 1. Ray tracing diagram of a condensing sphere. (1) LED, (2) dielectric sphere, (3) scattering mirror.

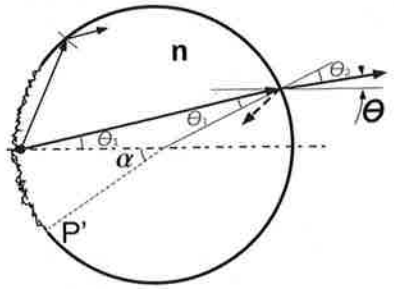

Fig. 2. Simplified model of Fig. 1.

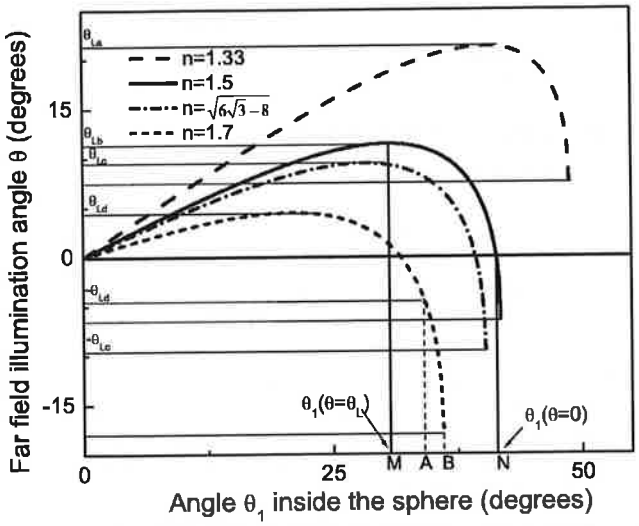

Fig. 3. Illumination angle θ versus the ray angle θ_1 inside the sphere (four difference cases).

and 1.7. Using Fig. 3, we explain how the maximum value of θ, denoted by θ_L, varies with the index of refraction as follows.

It is straightforward to compute the maximum angle of the illumination pattern for these directly refracted rays. We solve $\partial\theta/\partial\theta_1=0$ to find the angle θ_1, and then substitute it into Eq. (1). The result is

$$\theta_L = 2\arcsin\left(\frac{4-n^2}{3n^2}\right)^{1/2} - \arcsin\left(\frac{4-n^2}{3}\right)^{1/2}, \qquad (3)$$

where θ_L is the maximum angle of illumination pattern for rays from the LED that are directly refracted by the sphere.

It is interesting to point out that when $n>(6\sqrt{3}-8)^{1/2} \approx 1.547$, the rays from the LED with angle θ_1 very close to $\theta_{1\max}$ will be refracted by the sphere in a far-field direction outside the pattern defined by θ_L. An example is shown in the lower right of Fig. 3 where $n=1.7$. But the contributions from these are negligible compared with the total energy.

Next, we consider the rays that are totally internally reflected and scattered by the mirror. Let us consider the point P′ at the edge of the scattering mirror, i.e., at the angle α. A fraction of the scattered rays from point P′ are refracted by the sphere and radiated to the far field. By symmetry, the maximum angle of the far-field illumination pattern θ_S can be written as

$$\theta_S = \theta_L' + \alpha, \qquad (4)$$

where $\theta_L'=\theta_L$ as expressed in Eq. (3).

At this point, we can calculate the angular distribution pattern of the illumination field. This calculation is complicated and we use the nonsequential ray tracing function of the ZEMAX optics system design software[8] to provide quantitative results. Figure 4 shows the relative illumination intensity for the condensing sphere. In this example, the refractive index of the sphere is chosen to be 1.5. The scatter mirror extends a half angle of $\alpha=10°$ as shown in Fig. 2. The far-field intensity is calculated with an imaginary planar detector located at a distance of 10,000 mm to the right of the sphere with pixel size of 150 mm × 150 mm. Two cases are plotted: The dotted curve for the point source radiating 360° isotropically, and the solid curve is for the point source radiating to the right half-plane only, i.e., the radiation angle is 180°. The difference between far-field intensity distributions in Fig. 4 is small even for these two quite different radiation patterns of the point source. This implies that the far-field illumination pattern depends only slightly on the intensity distributions of the source. A second observation is that there are two regions in the illumination pattern, the center bright region with half angle θ_L and the extended taper region between θ_L and θ_S, where θ_L and θ_S are determined by Eqs. (3) and (4), where in this example $\theta_L=11.4°$ and $\theta_S=21.4°$. Equations (3) and (4) are thus sufficient for the initial choices of the refractive index and

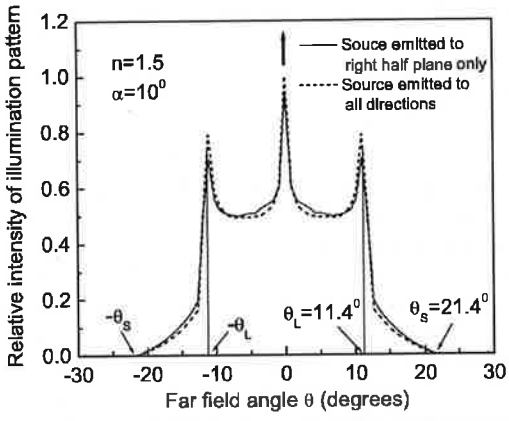

Fig. 4. Relative intensity versus angles of the far-field illumination pattern. The intensity (W/m^2) is calculated on a far-field plane perpendicular to the optical axis.

scattering mirror size in the illumination design.

It is interesting to note a circular ring peak and a center peak in the illumination pattern in this example. The main energy contribution to the peak of the circular ring is from the rays refracted from a narrow ring defined by $\theta_1(\theta=\theta_L)$ shown as point M in Fig. 3; the main contribution to the center peak is from the rays refracted from a narrow ring defined by $\theta_1(\theta=0)$ shown as point N in Fig. 3. For a simulation with $n=1.33$, in the illumination pattern (not shown) there still exists a circular ring peak, but there is no center peak. Care should be taken in the interpretation of the center peak intensity value in Fig. 4. The value is actually the average intensity over a region of 150 mm × 150 mm. The arrow at the top of Fig. 4 means the on-axis intensity value is much higher. The average axial intensity in a 1.5 mm × 1.5 mm region, calculated using ray optics, is over 20 times larger than that in the 150 mm × 150 mm region as shown in Fig. 4. The exact axial intensity is irrelevant for two reasons: (1) Diffraction is not taken into account in the simulation, and (2) the central peak decreases and even disappears when the ideal point source is replaced by a source with finite size, as will be shown in Subsection 2.D.

C. Light Collecting Efficiency

In our system the light loss mainly comes from the reflection (not total internal reflection) of the rays from the sphere surface, shown as the short-dashed ray in Fig. 2. We assume that the scattering mirror is small enough that these partially reflected rays cannot reach the mirror without significant loss of energy due to more partial reflections at the sphere surface. Also, we assume the rays are not polarized. From Fresnel reflection formulas, we find the energy transmission coefficient can be written as

$$T(\theta_1)=1-\frac{1}{2}\left[\left(\frac{n\cos\theta_1-\sqrt{1-n^2\sin^2\theta_1}}{n\cos\theta_1+\sqrt{1-n^2\sin^2\theta_1}}\right)^2+\left(\frac{\cos\theta_1-n\sqrt{1-n^2\sin^2\theta_1}}{\cos\theta_1+n\sqrt{1-n^2\sin^2\theta_1}}\right)^2\right]. \quad (5)$$

The theoretical light collecting efficiency can be expressed as

$$\eta=\frac{2\pi\int_0^{\theta_{1\max}}T(\theta_1)\sin\theta_1 d\theta_1}{2\pi\int_0^{\theta_{1\max}}\sin\theta_1 d\theta_1}. \quad (6)$$

The substitution of Eqs. (2) and (5) into Eq. (6) yields the efficiency of the condensing sphere. In this derivation of efficiency, we assume the rays refracted through the sphere region defined by $\theta_1<\theta_{1\max}$ are uniformly distributed over the sphere surface. In Fig. 5, the efficiency calculated from Eq. (6) is compared to the efficiency using the ZEMAX simulation. In the ZEMAX simulation, we assume the point source radiates to 360° isotropically, and the scattering mirror has a size defined by $\alpha=10°$. Since there is no absorption loss in the idealized condensing sphere, an imaginary large spherical detector array is placed around the sphere. The efficiency is calculated by finding the ratio of power in the illumination direction defined by $\theta<\theta_s$ and the total power on the detector array.

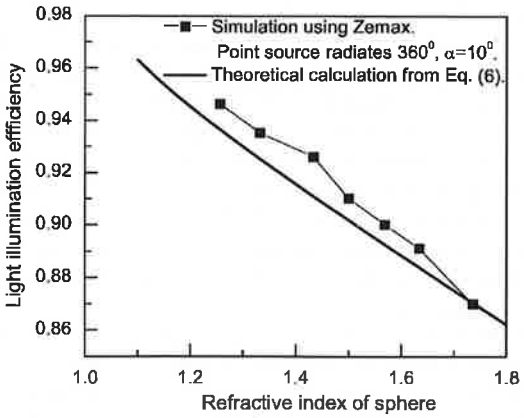

Fig. 5. Light collecting efficiency versus refractive index of sphere.

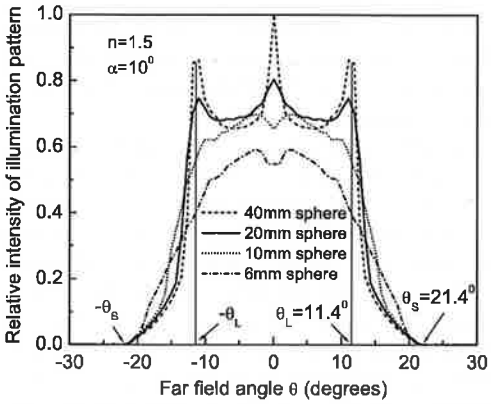

Fig. 6. Illumination pattern of condensing spheres with a finite-sized LED. The intensity (W/m^2) is calculated on a far-field plane perpendicular to the optical axis.

There are two reasons for slightly higher values from ZEMAX results: (i) The partially reflected rays that can be scattered by the scattering mirror and sent in the illumination direction are included in the ZEMAX simulation; (ii) in this example, the scattered rays immediately before refraction by the sphere are more likely to have a smaller θ_1, which means a higher transmission coefficient as shown by Eq. (5). But the small difference between the two curves in Fig. 5 implies that these two effects are not significant and we can use Eq. (6) to make a first-order estimation of the light collecting efficiency.

From the curves in Fig. 5, we see that the condensing sphere is capable of collecting most of the energy emitted by LED. For an index of refraction of 1.5, the central beam of radiation contains slightly more than 90% of the optical light emitted.

D. Example

In order to test the validity of our model, we use ray tracing software to calculate the performance of a realistic example. In this example shown as in Fig. 1, a cube-shaped LED die with a size of $t=0.3$ mm is embedded inside the edge of the sphere that has a refractive index of 1.5. The size of the scattering mirror is defined by $\alpha=10°$. The re-

fractive index and α are the same as those in Fig. 4 for easy comparison. Four different cases of spheres with diameters of 6, 10, 20, and 40 mm are calculated. 40% of light energy is emitted from the front surface and 15% from each of the four side surfaces. The light-emitting pattern is Lambertian for all five surfaces. Clearly for a condensing system it is important to effectively couple the 60% energy from the sides. While other designs have utilized the side emission, to our knowledge the method described herein is the most efficient with another advantage of compactness.

The intensity of the illumination pattern is calculated with an imaginary planar detector located at a distance of 10,000 mm away from the sphere. The pixel size of the detector is 150 mm × 150 mm. The results are shown in Fig. 6. Since the illumination patterns are rotationally symmetric, only radial data are plotted. The symmetry of the illumination pattern with a cubic die implies that condensing spheres with different die shapes, e.g. a cylindrical die, will generate similar far-field illumination patterns. More simulation studies show that the shape and radiation pattern of the LED die have little effect on the far-field illumination pattern.

These results fit well with our simplified model for the angular spread. The maximum angular spread of illumination pattern is very close to $\theta_S = 21.4°$, and the angle of central bright region is close to $\theta_L = 11.4°$ as calculated from our simplified model. Furthermore, the size of the LED die has a significant effect on the far-field pattern. As the diameter of the condensing sphere decreases, the intensity distribution deviates from the simplified model; we observe the difference in illumination patterns and the disappearance of the central and ring peaks for small spheres. More generally, in the geometrical optics domain, the far-field pattern depends on the size ratio between LED die and condensing sphere. Obviously, the ray reflection and refraction pattern will remain identical if a 6 mm condensing sphere with 0.3 mm die is changed to a smaller package of 3 mm sphere with 0.15 mm die; thus the far field also has the same intensity distributions.

The size ratio between LED die and sphere needs to satisfy a condition that the ray from the edge of the LED to the edge of the scattering mirror, denoted by AB in Fig. 1, must undergo total internal reflection. This sets the lower limit on the size of condensing sphere for this type of setup. In the above example of a 0.3 mm cubic die, $\alpha = 10°$, and $n = 1.5$, the diameter of the sphere can be as small as 6 mm. However, some other setups of condensing spheres do not have this size limitation; e.g., the die can be attached to the outside of the sphere. The study of different setups is beyond the scope of this paper.

The efficiency of the four different condensing spheres is also calculated with ZEMAX. The light collecting efficiencies for 6, 10, 20, and 40 mm spheres are 90.2, 90.7, 90.8, and 91.0%, respectively. The results are close to our simplified model, which has an efficiency of 91.13% from ZEMAX calculation and 90.09% from Eq. (6). We observe that the efficiency remains about the same for different sizes of condensing sphere, as long as the rays from the LED to the edge of the scattering mirror undergo total internal reflection.

3. CONCLUSION

We describe a compact and efficient light collecting system for LED sources. The analysis of the simplified model of our system shows the basic properties of this system. A typical efficiency is 90%. Many variations in this basic condenser system will be apparent to the reader. For example, two or more LEDs can be placed in the sphere to build a noncircularly symmetric illumination, an array of condensing spheres can be used for line illumination patterns, and so on. Moreover, we hope by a good understanding of the simple condensing sphere described in this paper, one can find a good starting point to design a highly efficient light collecting sphere which is also very compact.

ACKNOWLEDGMENTS

This research is supported in part by the Army Research Office, and the New York State Office of Science, Technology, and Academic Research (NYSTAR).

The e-mail addresses of the authors are chiw @optics.rochester.edu and ngeorge@troi.cc.rochester.edu.

REFERENCES

1. D. A. Steigerwald, J. C. Bhat, D. Collins, R. M. Fletcher, M. O. Holcomb, M. J. Ludowise, P. S. Martin, and S. L. Rudaz, "Illumination with solid state lighting technology," IEEE J. Sel. Top. Quantum Electron. **8**, 310–320 (2002).
2. K. Streubel, N. Linder, R. Wirth, and A. Jaeger, "High brightness AlGaInP light-emitting diodes," IEEE J. Sel. Top. Quantum Electron. **8**, 321–332 (2002).
3. C. Huh, K. Lee, E. Kang, and S. Park, "Improved light-output and electrical performance of InGaN-based light-emitting diode by microroughening of the p-GaN surface," J. Appl. Phys. **93**, 9383–9385 (2003).
4. A. R. Duggal, J. J. Shiang, C. M. Heller, and D. F. Foust, "Organic light-emitting devices for illumination quality white light," Appl. Phys. Lett. **80**, 3470–3472 (2002).
5. I. T. Ferguson, J. C. Carrano, T. Taguchi, and I. E. Ashdown, eds., *Fifth International Conference on Solid State Lighting*, Proc. SPIE **5941** (2005).
6. H. W. Yao, I. T. Ferguson, and E. F. Schubert, eds., *Light-Emitting Diodes: Research, Manufacturing, and Applications IV*, Proc. SPIE **3938** (2005).
7. Z. H. Kafafi, ed., *Organic Light-Emitting Materials and Devices*, Proc. SPIE **3148** (1997).
8. Zemax Development Corporation, http://www.zemax.com.

Polarization coded aperture

Wanli Chi, Kaiqin Chu and Nicholas George
The Institute of Optics, University of Rochester, Rochester NY 14627
chiw@optics.rochester.edu

Abstract: Two examples are presented to illustrate the advantages of polarization coded apertures, in which the incoming light will rotate its polarization at a portion of an aperture. In the first example the depth of field of a diffraction limited lens is increased without sacrificing the light throughput; in the second example the axial focal intensity of a pixelated Fresnel zone plate is increased by 100%. Both examples work for linearly polarized or unpolarized illumination.

OCIS codes: (110.1220) apertures; (260.5430) polarization; (999.9999) depth of field; (999.9999) Fresnel zone plate.

References and links

1. A. Ghosh, K. Murata and A. K. Chakraborty, "Frequency-response characteristics of a perfect lens masked by polarizing devices," J. Opt. Soc. Am. A **5,** 277–284 (1988).
2. D. R. Chowdhury, K. Bhattacharya, S. Sanyal and A. K. Chakraborty, "Performance of a polarization-masked lens aperture in the presence of spherical aberration," J. Opt. A: Pure and Applied Optics, **4,** 98–104 (2002).
3. A. Zlotnik, Z. Zalevsky and E. Marom, "Superresolution with nonorthogonal polarization coding," Appl. Opt. **44,** 3705–3715 (2005).
4. E. H. Linfoot and E. Wolf, "Diffraction images in systems with an annular aperture," Proc. Phys. Soc. B **66,** 145–149 (1953).
5. T-C Poon and M. Motamedi, "Optical digital incoherent image-processing for extended depth of field," Appl. Opt. **26,** 4612–4615 (1987).
6. J. Ojeda-Castaneda and L. R. Berriel Valdos, "Abitrarily high focal depth with finite aperture," Opt. Lett. **13,** 183–185 (1988).
7. E. R. Dowski, Jr. and W. T. Cathey, "Extended depth of field through wave-front coding," Appl. Opt. **34,** 1859–1866 (1995).
8. W. Chi and N. George, "Computational imaging with the logarithmic asphere: theory," J. Opt. Soc. Am. A **20,** 2260–2273 (2003).
9. P. Yeh and C. Gu, *Optics of Liquid Crystal Displays,* (John Wiley & Sons, Inc., New York, 1999). Chapter 9 and references therein.
10. T. D. Beynon, I. Kirk and T. R. Mathews, "Gabor zone plate with binary transmittance values," Opt. Lett. **17,** 544–546 (1992).
11. P. W. McOwan, M. S. Gordon and W. J. Hossack, "A switchable liquid crystal binary Gabor lens," Opt. Commun. **103,** 189–193 (1993).
12. R. E. English, Jr. and N. George, "Diffraction from a circular aperture: on axis field strength," Appl. Opt. **26,** 2360-2363 (1987).

1. Introduction

New imaging devices or better imaging properties can be obtained by utilizing the polarization of an electromagnetic (EM) wave [1]-[3]. In this paper we describe a novel polarization coding technique applied to the aperture of an imaging system. As the light passes through the aperture, the polarization of the incoming beam is rotated for a portion of the aperture while it is not rotated for the remaining portion. At the image plane the detector senses the two independent

#71216 - $15.00 USD
Received 22 May 2006; revised 20 June 2006; accepted 20 June 2006

orthogonal intensities of the polarized light. This polarization coded aperture system results in better imaging systems. In the first example, we show that the depth of field of a diffraction limited lens is improved. In the second example, we explain a pixelated Fresnel zone plate whose efficiency is doubled over that for conventional zone plate. Practical system implementation is made possible with current liquid crystal technology. This polarization coded aperture technique does not put any strict constraint on the polarization of illumination, since it works for either linear polarized or unpolarized illumination.

2. Extended depth of field

It is well known that the depth of field of a diffraction limited lens depends on its numerical aperture. The depth of field of a diffraction limited lens with clear aperture is proportional to the square of f-number. So for a diffraction limited lens with focal length f and clear circular aperture whose radius is R, the depth of field is inversely proportional to the area of the aperture. (The same statement is also held for ring aperture [4, 5], i.e., the depth of field for a ring aperture with radius from r to R is also inversely proportional to the area of the ring aperture.) Achieving the extended depth of field by reducing the aperture size is routinely done in photography. Also in the literature one uses various apodizations [4]-[6] e.g., a central obscuration, to extend the depth of field. The main disadvantage of the apodization method is that it decreases the light throughput and thus is not a good solution in low light level imaging applications. In this section, we introduce a type of polarization coding in the aperture of a diffraction limited lens to extend the depth of field. Consider a diffraction limited lens with a circular aperture shown in Fig. 1. The aperture with a radius of R is separated into two regions of equal area, the central circular region with a radius of r and the outer circular ring region with $R = \sqrt{2}r$. The polarization of the EM wave passing the outer ring region will be kept the same, and the polarization of the EM wave passing the central region will be rotated by 90^0. With the advancement in liquid crystal technology, there is no difficulty in realizing this type of aperture. Here we consider only the case with incoherent illumination.

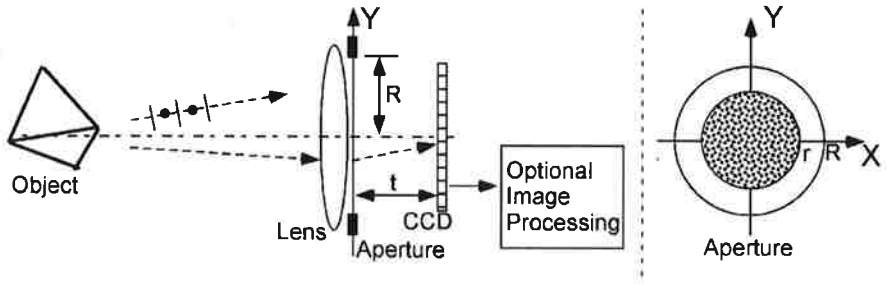

Fig. 1. The extended depth of field imaging setup with a polarization coded aperture.

When the incoming EM wave is polarized in Y direction, after passing the outer region of the aperture, the wave is still polarized in Y direction; but after passing the inner region of the aperture, the wave changes its polarization to the X direction. Since the CCD detects intensity proportional to $\mathbf{E} \cdot \mathbf{E}^*$, there is no interference between EM waves in orthogonal direction. The intensity point spread function (IPSF) of this imaging setup is obtained by the addition of two IPSFs of a diffraction limited lens, one with a circular aperture and another with a ring aperture shown shaded. This statement also holds for two other important cases: one where the EM wave is X-polarized and the other when the incoming light is unpolarized. Hence, in general one can write the intensity point spread function $I(\rho)$ for the Fig. 1 system as follows:

#71216 - $15.00 USD
Received 22 May 2006; revised 20 June 2006; accepted 20 June 2006

$$I(\rho)=\left|\int_0^r r'J_0(2\pi r'\frac{\rho}{\lambda t})\exp[i\frac{2\pi W}{\lambda}(\frac{r'}{R})^2]dr'\right|^2+\left|\int_r^R r'J_0(2\pi r'\frac{\rho}{\lambda t})\exp[i\frac{2\pi W}{\lambda}(\frac{r'}{R})^2]dr'\right|^2, \quad (1)$$

where a constant is dropped, ρ is the radial coordinate of the IPSF, λ is the wavelength of illumination, W is the defocus coefficient in the unit of number of wavelengths, and J_0 denotes the Bessel function of first type order zero. Since the principle works well for unpolarized light, no polarizer is needed to filter the incoming light.

The first term in Eq. (1) is the point spread function for central clear aperture with a radius of r; the second term is the point spread function for a ring aperture with radius from r to R. It is interesting to note that the constant phase delay introduced by the liquid crystal located at the central region of the aperture has no effect on the IPSF of the system. In Fig. 2 we show these intensity point spread functions. When $W=0$, It is observed that the IPSF for the ring aperture has a narrower central peak than that for full aperture and that the IPSF of the central aperture has a wider central peak. At the focused position the IPSF for the polarization coded aperture is the sum of IPSFs of central and ring apertures. In Fig. 2, we also plotted the IPSFs for a full aperture with defocus coefficient $W=0.5\lambda$. The axial intensity of this IPSF is about 40% of that for full aperture without defocus.

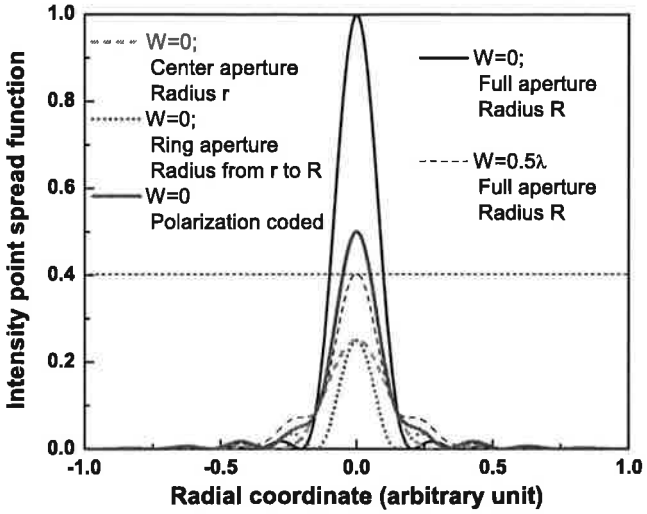

Fig. 2. The IPSFs of diffraction limited lens for central aperture; ring aperture and full aperture.

Since the depth of field is inversely proportional to the area of the aperture, so by separating the aperture into central clear aperture and outer ring aperture region with equal areas. We expected the depth of field is increased by a factor of 2 for central region and outer region respectively. Since the IPSFs of the two aperture regions are detected without amplitude interference, as explicit in Eq. (1), the depth of field of the polarization coded aperture system in Fig. 1 is also increased by a factor of 2. To qualitatively illustrate the increase in the depth of field, we show in Figs. 3 and 4 the IPSFs for a lens with polarization coded aperture and a lens

#71216 - $15.00 USD
Received 22 May 2006; revised 20 June 2006; accepted 20 June 2006

with conventional aperture, respectively. The defocus amounts in these two figures are set to be from $W = 0.5\lambda$ to 1.25λ. The intensities are normalized such that the axial intensity of the IPSF at the focused position for a full clear aperture with radius R is 1 (see Fig. 2). By comparing the size of IPSFs in Figs. 3 and 4 as the offset distance in location of object, as measured by defocus W, we see the substantial increase in the depth of field. Figures 5 and 6 show the Optical Transfer Functions (OTFs) corresponding to Figs. 3 and 4, respectively. We observe contrast inversions for a conventional aperture when defocus is 0.75λ, λ and 1.25λ; but there are no such contrast inversion for the polarization coded aperture and the OTFs are positive for all the spatial frequencies. This increase in depth of field can be easily understood since both cutdown the aperture (central region) and central aperture obscuration (outer region) induce the increase in depth of field.

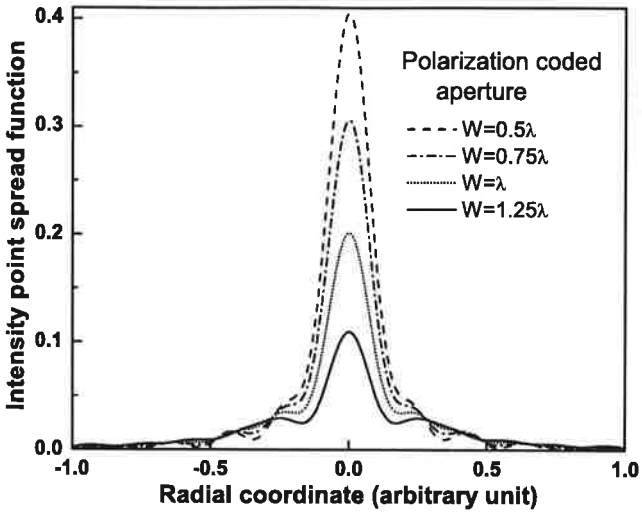

Fig. 3. The IPSFs of diffraction limited lens for a lens with polarization coded aperture.

When the incoming beam, e.g., from the off-axis object point, is obliquely incident to the central region of aperture, shown in Fig. 1, where the liquid crystal is present for polarization rotation, the rotation angle will be deviated from 90^0. This will affect the depth of field extension for large field of view. For a conventional liquid crystal aperture, a half field of view of 15^0 is anticipated. However, various techniques [9] have been developed to improve the wide angle performance of the liquid crystal devices, which extend the half angle performance to well over 50^0.

We expect this type of polarization coded aperture for extended depth of field to be extremely useful for low ambient light illumination since the optical throughput is the same as that for a big clear aperture with radius R. Another interesting feature of this design is that no aberration is introduced to the diffraction limited lens, so it is not necessary to deblur the detector image using digital processing techniques, which generally is required for the cubic phase mask method [7] and the logarithmic asphere method [8]. However, one still can choose to use the image processing to boost the high spatial frequency response, this is optional.

#71216 - $15.00 USD

Received 22 May 2006; revised 20 June 2006; accepted 20 June 2006

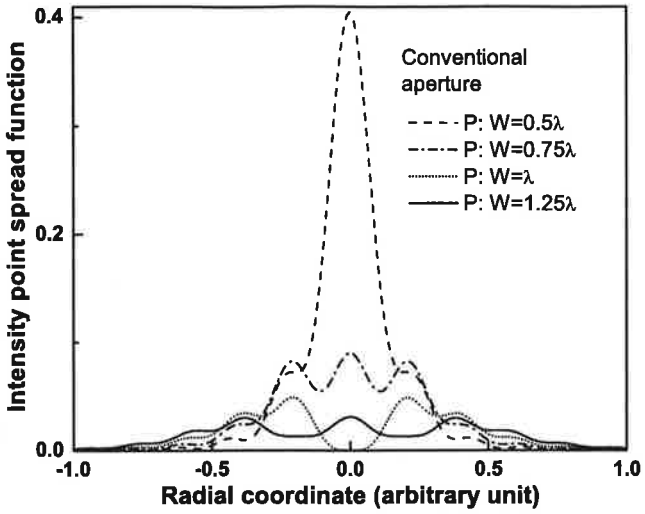

Fig. 4. The IPSFs of diffraction limited lens for a lens with conventional aperture.

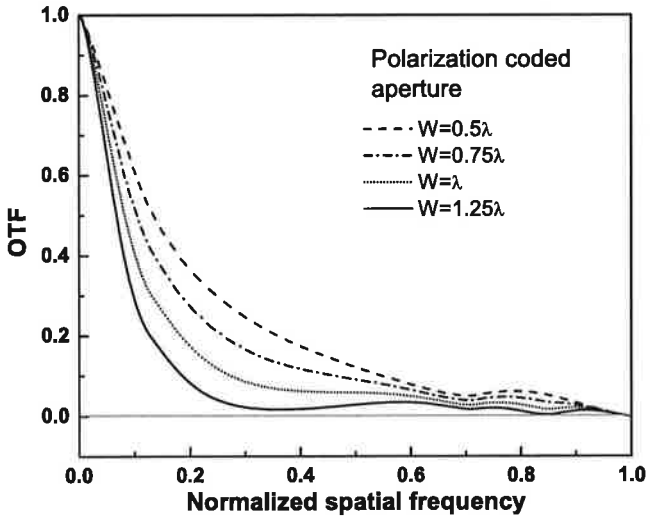

Fig. 5. The OTFs of diffraction limited lens for a lens with polarization coded aperture.

#71216 - $15.00 USD
Received 22 May 2006; revised 20 June 2006; accepted 20 June 2006

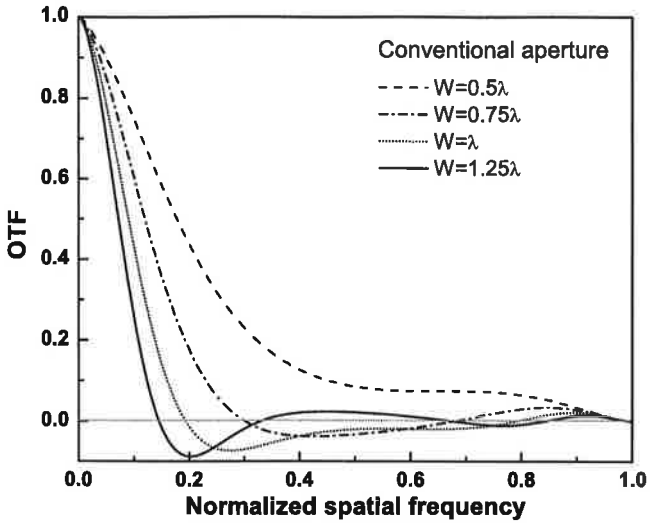

Fig. 6. The OTFs of diffraction limited lens for a lens with conventional circular aperture.

3. Pixelated Fresnel zone plate

Binary zone plates are diffractive elements with a binary transmission function. Common examples include the Fresnel zone plate, Beynon zone plate or binary Gabor zone plate [10, 11]. Generally, the total transmission of the binary zone plate is around 50%. i.e., half of incoming light energy is absorbed by the zone plate. Using the polarization coding idea, we impose a 90^0 polarization rotation for the zero transmission pixels of a zone plate. In this way the zone plate is effectively separated into two plates with orthogonal output polarizations. This yields an increase in the efficiency of the binary zone plate by 100%. In this section a pixelated Fresnel zone plate with a polarization coded aperture using a liquid crystal spatial light modulator (SLM) is described.

Consider the setup shown in Fig. 7. A plane wave is modulated by the SLM zone plate, which has a pixel size of a. The modulation takes two forms, the polarization of light is either rotated by 90^0 or not rotated by each pixel. After passing the SLM, the light is focused to point P, which is located at a distance f from the zone plate. The zone plate shown in Fig. 7 is called a pixelated zone plate since the smallest structure of the zone plate is the pixel size of the liquid crystal device.

To determine the optimum state of each pixel, we calculate the field contribution of each pixel to the axial point P. The axis field amplitude at focal point P, E_{mn}, from the contribution of pixel (x_m, y_n) is

$$E_{mn} = A \int_{y_n - a/2}^{y_n + a/2} \int_{x_m - a/2}^{x_m - a/2} \frac{f}{f^2 + x^2 + y^2} \exp(i \frac{2\pi}{\lambda} \sqrt{f^2 + x^2 + y^2}) dx dy, \qquad (2)$$

where A is a constant, λ is the wavelength of incoming plane wave. After evaluating this integral numerically, we can write the result in a form of $E_{mn} = |E_{mn}| \exp[i\phi_{mn}]$. Herein, We consider only the binary type plate. i.e., the polarization either changed by 90^0 or not changed and no amplitude or phase modulation is introduced. If the phase term ϕ_{mn} satisfies $-\pi/2 \leq \phi_{mn} < \pi/2$,

#71216 - $15.00 USD
Received 22 May 2006; revised 20 June 2006; accepted 20 June 2006

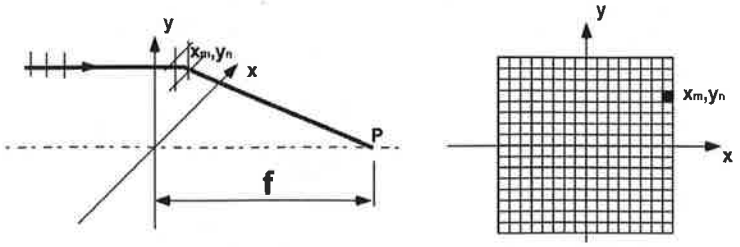

Fig. 7. The setup for pixelated zone plate. Left: setup; Right: pixelated zone plate

then we set the pixel (m,n) to be transmissive without rotation of polarization. Otherwise, if $-\pi \leq \phi_{mn} < -\pi/2$ or $\pi/2 \leq \phi < \pi$, we set the pixel be transmissive with a 90^0 rotation of the incoming wave polarization. Because EM waves with orthogonal polarizations do not interfere, the axial intensity at the focal point P can be written as following:

$$I_P = \left| \sum_{-\pi/2 \leq \phi_{mn} < \pi/2} E_{mn} \right|^2 + \left| \sum_{-\pi \leq \phi_{mn} < -\pi/2 \text{ or } \pi/2 \leq \phi_{mn} < \pi} E_{mn} \right|^2. \tag{3}$$

In Eq. (3) the first term is the axial intensity for a zone plate without polarization coding, and the second term is the axial intensity for another zone plate in which the pass and block pixels are complementary to the first plate. Theses two plates have approximately equal axial focal intensity independent of the fill factor of zone plates. Both terms in Eq. (3) change in the same manner if the fill factor of the zone zone plate is changed. so we have

$$I_P \simeq 2 \left| \sum_{-\pi/2 \leq \phi_{mn} < \pi/2} E_{mn} \right|^2. \tag{4}$$

i.e., the axial intensity of polarization coded binary zone plate is increased by 100% compared to the binary zone plate with 0 and 1 transmissions. This conclusion is valid independent of the liquid crystal zone plate fill factor.

Figure 8 shows one example of the pixelated Fresnel zone plate. In this example $f = 100mm$, $a = 15\mu m$ and $\lambda = 0.6\mu m$. The white pixel denotes that the EM field will keep its polarization after passing the plate and black pixel denotes that the EM field will rotate 90^0 after passing the plate. We note that the center region of the pixelated zone plate resembles a Fresnel zone plate. Due to the finite size of pixel sampling, the outer region deviates from the Fresnel zone plate. We call this plate the pixelated Fresnel zone plate with polarization coded aperture. Similar to the system described in Fig. 1, this pixelated Fresnel zone plate works for both linearly polarized and unpolarized light.

Figure 9 shows the computer simulation result of the axial intensities of the pixelated zone plates. The results of plates both with and without polarization coded aperture are shown. The polarization coded plate used in this simulation is shown in Fig. 8; and with the reference of Fig. 8, The pixelated zone plate without polarization coding has a transmission of 1 for white pixels and 0 for black pixels. It is clear in Fig. 9 that the axial intensity is increased by 100% for the polarization coded plate. Higher order focal points can be seen at positions of $f/3$, $f/5$, etc. Besides the doubling of the axial intensity for focal point P due to polarization coding of the zone plate aperture, an interesting effect of finite pixel size of SLM is that the axial intensity of higher order focal points is significantly lower than that of 1st order. (This is in contrast with the conventional Fresnel zone plate where the axial intensities of different order focal points

#71216 - $15.00 USD
Received 22 May 2006; revised 20 June 2006; accepted 20 June 2006

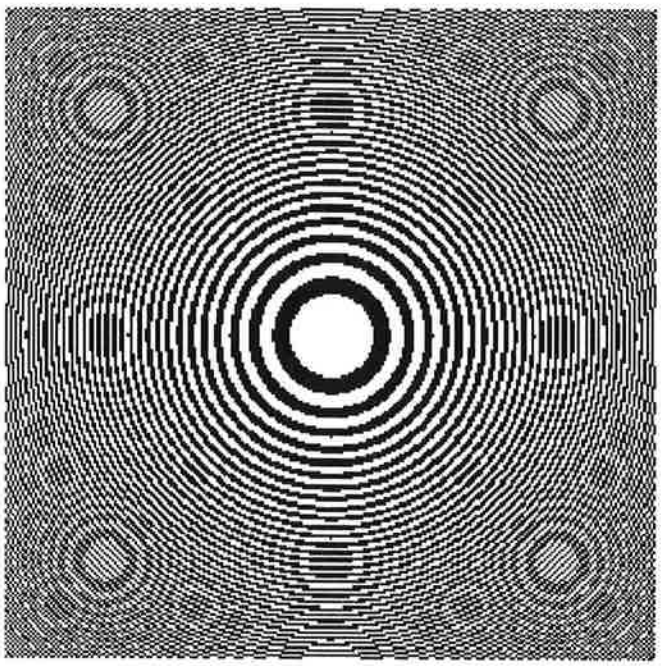

Fig. 8. A pixelated Fresnel zone plate. White pixel: no change in polarization; black pixel: polarization rotate 90^0.

are equal.) From Eq. (2), one can also calculate the polarization status of different orders. For example, if the input beam is linearly polarized, then the polarizations of the 1st order and zeroth order beam are orthogonal.

4. Conclusion

The polarization state at the aperture of an imaging system can be modified to yield a better imaging properties. Specifically in this paper, we describe a novel configuration where the polarization is rotated by 90^0 at a portion of aperture and kept the same for the rest of aperture. Since there is no interference between polarizations in orthogonal directions, this coded aperture is equivalent to the adding of two apertures. Since the principle works for both linear polarized and unpolarized light, no polarizer is required to filter the illumination light and there is no compromise of the light throughput. Using this polarized coded aperture concept, in the first example we show the extended depth of field imaging of a diffraction limited lens (by a factor of 2 without image processing) is achieved without sacrificing detector light intensity and is good for low light level imaging. The extended depth of field The optional image processing can also be done easily since there are no zero's and negatives in the OTF over a significant amount of defocus, as seen in Fig. 5. In the second example a pixelated Fresnel zone plate with polarization coding is illustrated which yields a 100% increase in diffraction efficiency. This research was supported in part by the Army Research Office.

5. Appendix:Axial intensity of Fresnel zone plate

Consider a Fresnel zone plate which has a focal length of f and $2N-1$ zones with the center first zone transmissive. The transmission function can be written as

#71216 - $15.00 USD
Received 22 May 2006; revised 20 June 2006; accepted 20 June 2006

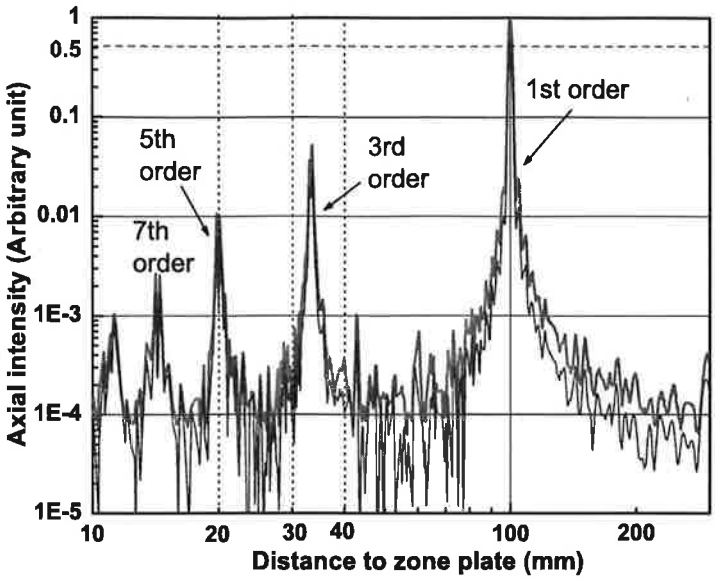

Fig. 9. Axial intensity of pixelated zone plates with and without polarization coded aperture. Thick red line: pixelated zone plate with polarization coded aperture as shown in Fig. 8; Thin blue line: pixelated zone plate without polarization coding.

$$t(r) = \sum_{n=1}^{2N-1} (-1)^{n+1} \mathrm{circ}(r/r_n), \tag{5}$$

where r is the radial coordinate of the zone plate and $r_n = \sqrt{n\lambda f}$.

For plane wave illumination with amplitude E_0, the axial field amplitude $E(z)$ at a distance of z can be written as

$$E(z) = \sum_{n=1}^{2N-1} (-1)^{n+1} E(z,n), \tag{6}$$

where $E(z,n)$ is the amplitude contribution for a circular aperture with radius r_n. $E(z,n)$ of Eq. (6) can be evaluated [12] exactly with the following result:

$$E(z,n) = E_0[\exp(i\frac{2\pi}{\lambda}z) - \frac{z}{\sqrt{z^2+r_n^2}}\exp(i\frac{2\pi}{\lambda}\sqrt{z^2+r_n^2})]. \tag{7}$$

Substitution of Eq. (7) into Eq. (6) and squaring gives the axial intensity of the zone plate at a distance z as follows:

$$I(z) = C\left|e^{i\frac{2\pi}{\lambda}z} + \sum_{n=1}^{2N-1}(-1)^n \frac{z}{\sqrt{z^2+n\lambda f}}\exp(i\frac{2\pi}{\lambda}\sqrt{z^2+n\lambda f})\right|^2, \tag{8}$$

where C is a constant.

#71216 - $15.00 USD
Received 22 May 2006; revised 20 June 2006; accepted 20 June 2006

*

Electronic Holography at Terrahertz and Infrared Frequencies

Nicholas George, Kedar Khare, and Wanli Chi
The Institute of Optics, University of Rochester

We describe a new holography system for recording holgrams that is practical from 1mm through 3μm wavelengths. These hitherto inaccessible bands of wavelength can now be recorded with excellent sensitivity and resolution using microbolometer arrays that have improved greatly in the past few years. These spectral bands are of usefulness for biomedical imaging as an alternative to x-rays in some situations, for astronomy, for industry and for night vision devices. In holography following Leith and Upatnieks, one records an interference pattern using a coherent source; and thereafter, reconstructs a wavefront which reproduces the phases and amplitudes of the original object waves. For our first experiments we will describe the verification of our assertion that one can truly record interference patterns. We use a simple Mach-Zehnder interferometer with laser illumination at 10.6μm. It is interesting that one can record the carrier frequency fringe of a hologram using a thermal detector even with a time constant of tens of milliseconds. For reconstructing the object wavefront in holography there are several well-known techniques. First, one needs to choose between an original illumination beam and a reversed beam. Then one can consider scaling the hologram to the visible band. Finally, with the hologram digitally recorded, one can use modern computer-generated visual displays. We will describe our experiments in which we use the efficient, direct sampling of the carrier frequency fringes [1,2]. Using well-known theories for the inverse scattering and the digital computer, one can calculate the field and the intensity back in the object space. Details of the phase unwrapping process will be described. This talk is dedicated to Professors Emmett N. Leith and Stephen A. Benton, eminent scholars and beloved colleagues.

---

[1] "Direct sampling and demodulation of carrier frequency signals," Opt. Comm. **211**, 85 (2002), K. Khare and N. George
[2] "Direct coarse sampling of electronic holograms," Opt. Lett. **28**, 1004 (2003), K. Khare and N. George.

---

* This is the text of a talk presented at the International Conference on Display Holography, Wales, UK, 2006.

Electronic Holography at Terrahertz and Infrared Frequencies

Nicholas George, Kedar Khare, and Wanli Chi
The Institute of Optics, University of Rochester

In this paper a novel means of holography is described that is practical from 1mm to 3μm wavelengths. This is a spectral band of increasing importance and usefulness, for night vision devices [1], for basic astronomy [2], and more recently for biomedical imaging as an alternative to x-rays in some situations. However, in this regime we have found little or no reports of holography. The reason for this is obvious; it is mostly due to the lack of a suitable recording medium that is comparable in usefulness to the familiar silver-bromide emulsion in the visible wavelengths. Also, another factor is the difficulty/expense of coherent sources of electromagnetic waves in this band.

For our experiments in holography, the recording configuration is shown in the Fig. 1. We are using a Mach-Zehnder interferometer so that we can obtain readily controllable beams at a small angle, i.e., below 5 degrees.

Generally, in the published literature there are many papers dealing with the imaging of objects. Both biomedical applications and baggage surveillance systems have been described. Basically, these are all attempts to provide safe alternatives to x-rays. Why would one want to have a hologram instead of a simple image? The basic reason is that the hologram records the full three-dimensional, volumetric scene in a planar sheet, i.e., the microbolometer array. In the reconstruction process, one can obtain the field or the intensity at any distance from the planar sheet. The hologram provides a recording that has no depth-of-field limitation of the type encountered in photography.

1. DETECTORS

Parenthetically, we remark that infrared detectors as well as microwave detectors are often classified as thermal detectors or photon detectors. The thermal detector consists of a detector material which absorbs the incident radiation thereby changing temperature and resistivity. The change is resistivity is sensed electrically. Typically such detectors are relatively slow, particularly with the associated electronics and a chopper amplifier. However, they can be extremely

sensitive. Since World War II, these detectors have been widely used, as bolometers, for the precise measurement of power at microwave frequencies. Recently there has been widespread use of microbolometer arrays. These uncooled arrays are capable of providing extremely good images at very low light levels [1-3]. They can be operated at video frame rates.

On the other hand, the photon detector can be described as a material that releases a hole-electron pair or an electron upon the absorption of a photon, as in a photodiode. This time constant is very much shorter than customary video rates. Included as photon detectors are the following "several photoeffects such as photoconductive, photovoltaic, photoelectromagnetic, Dember and photon drag" [3]. While the further details are not pertinent here, we remark that photomixing typically requires a comparatively short response time that is characteristic of the photon detector. For photomixing, the thermal detector has rarely been appropriate.

Interestingly, for recording the carrier frequency fringe pattern of a hologram, the thermal detector performs quite well, since a fraction of a second time constant is tolerable. We will describe comparative holographic recordings of three commercially available cameras at 10.6μm.

2. RECONSTRUCTING THE OBJECT WAVEFRONT

For reconstructing the object wavefront in holography, there are two well known techiques, dating back to the well-known research of E. N. Leith and J. Upatnieks. First, one simply uses the original wavelength used in the recording; and with a beam propagating in the direction of the original reference beam incident on the film plate, the original object wavefront is reconstructed. Alernatively, one can use a reversed reference beam and then the object's wavefront is reconstructed but now it is traveling toward the object. As is well-known, this reversal reference beam and the hologram give rise to the very useful pseudoscopic wavefront.

A second method that has been used at 10μm in the infrared is to record the hologram and then reduce the fringe pattern photographically. Thereafter, the

reduced fringe pattern is illuminated in the visible and an observer can see the object.

For the display of our holograms, we are using the direct sampling of the carrier frequency fringes as is customary in the field of digital holography. From this sampling, as is described in the literature [4,5], one can recover the phase and amplitude of the wavefront at the microbolometer array. Using well-known theories for inverse scattering and a digital computer, one can calculate the field and the intensity back in the object space. Often the calculation is approximated as an FFT. In the recording process it may be helpful to record two or three separate frames with a relative phase step in the reference beam, as is often done in phase unwrapping for automatic contouring.

3. EXPERIMENTAL PLAN AT ROCHESTER

For our first experiments, we have recorded holograms at 10.6μm in the infrared. For this we use a low power CO2 laser operating single mode at 10.6μm so as to provide carrier frequency fringes of high contrast. We show our first recordings of "holographic fringes", since they provide valuable information about the apparatus. They are particularly valuable in testing the resolution of the microbolometer arrays. Figures 2, 3, 4 show, respectively, a coarse fringe pattern, followed by the single beam with the other blocked and then a fine scale fringe pattern.

At the meeting it is planned to show both interference patterns and holograms for several objects. We will also show the computer display of the recovery as well. The objects being studied are listed: knife edge, expanding beam, converging beam, particulate sample.

4. SUMMARY

In this paper we describe a method of holography that is applicable throughout the electromagnetic spectrum from millimeter waves through to 3μm in the infrared. From 1 micron through the visible, probably a silicon based CCD is a preferable array. The read-out of carrier frequency patterns has already been demonstrated in the cited references [4,5]. These holograms provide 3D imagery as well as a safe substitute for x-ray images. Also follow-on research to

demonstrate that a stereo sequence is possible when the hologram platform is moving relative to the object would lead to a new form of synthetic aperture radar. This latter system would eliminate the need to make very large arrays of microbolometers. It is also interesting to consider recording stereo or holographic stereogram sequences using sparse microbolometer arrays. This technique would provide a superior angular perspective since that from a single array is relatively small.

References and Footnotes

[1] Uncooled Infrared Imaging Arrays and Sensors, P. W. Kruse and D. D. Skatrud, editors, Academic Press (1997).

[2] Submillimeter astronomy is an important international effort in which large telescopes and microbolometer arrays and photodectectors are both playing important roles. Extremely large mm wave telescopes are described in SPIE Int. Vol. 5382 (2004). Photodetector mixers are NbN-SIS (795 GHz), SiC, ErAs: GaAs, and so on. Hot electron bolometer mixers are described for THz frequencies by P. Forcardi and W. R. McGrath (JPL) in IEEE Antennas and Propagation, IEEE vol. 1 (2004), pp. 986-9. A large 42 kg, 62 crystal thermal detector array CUORICINO is being assembled in Italy for tests of "Dark Matter and Double Beta Decay". Multi-mode microbolometers for the 7 to 14 μm band with "color selectivity" are described by S. W. Han et al in Electronics Letters, vol. 40, Oct. 2004. The Planck ESO satellite (2007) will carry a bolometer array to provide very accurate images of the cosmic wave background fluctuations. Measurements are planned at 857 GHz, 350μm and also at 10.6μm, see P. Martin et al, 5th Int. Conf. On Space Optics (ICSO 2004). The Caltech Submillimeter Observatory has a SHARC II detector array of 384 elements for background limited images at 350 and 450μm, S. H. Moseley et al 10th Int. Workshop on Low Temperature Detectors (LTD-10), Genoa, Italy (2003).

[3] Infrared Detectors, A. Rogalski, Gordon and Breach Science Publishers (2000).

[4] "Direct sampling and demodulation of carrier frequency signals," Opt. Comm. **211**, 85 (2002), K. Khare and N. George

[5] "Direct coarse sampling of electronic holograms," Opt. Lett. **28**, 1004 (2003), K. Khare and N. George.

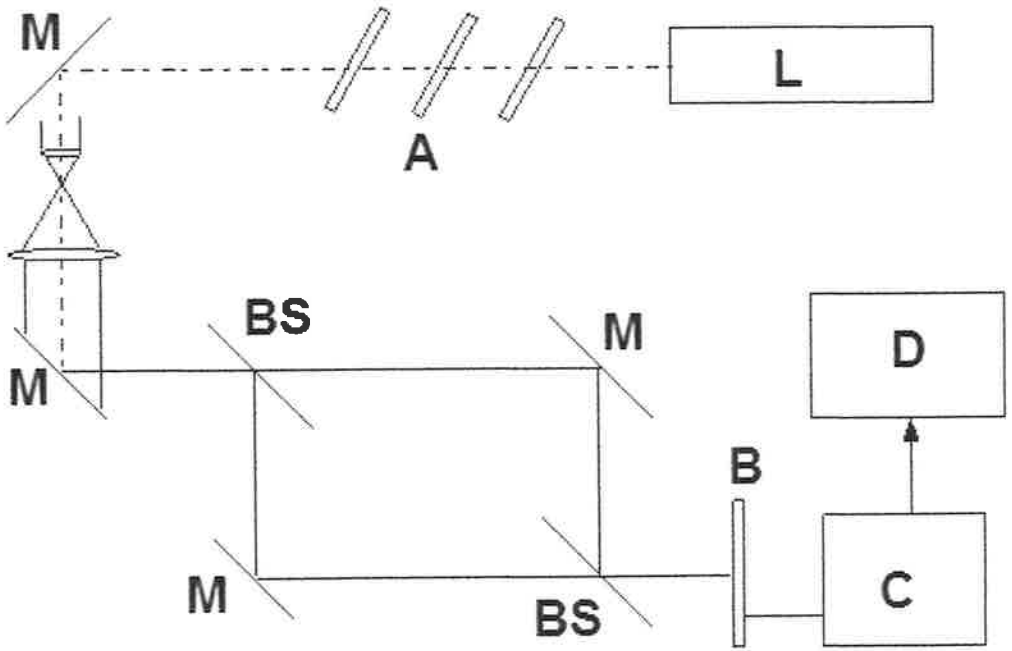

Fig. 1. Experimental setup for recording two-beam holograms at 10.6μm showing: (L) 10 watt CO2 laser; (A) attenuators; (M) mirror; (BS) beam splitter; (B) microbolometer camera Thermal-eye Model 2000B (320X240 pixels) or Indigo Omega Model 412 (164X128 pixels); (C) Computer; (D) display.

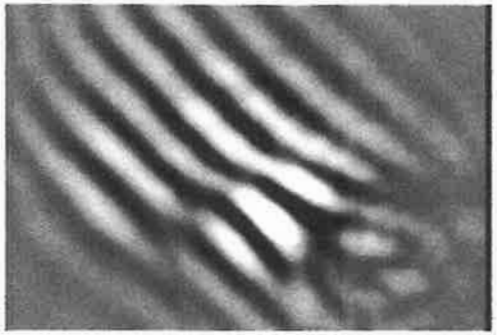

Fig. 2. Coarse-frequency fringes for two beam holographic system at 10.6μm, shown in Fig. 1.

Fig. 3. Recording with one beam of the Mach-Zehnder configuration blocked.

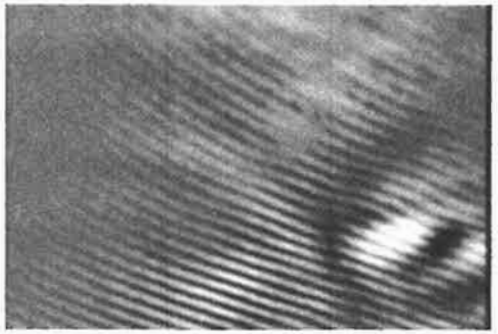

Fig. 4. Fine scale fringes with same setup as Fig. 2, 3.

ELECTRONIC HOLOGRAPHY AT TERAHERTZ AND INFRARED FREQUENCIES *

Nicholas George, Kedar Khare

In this unsolicited white paper, a novel means of holography is described that is practical from 1 mm through to 3 μmeter wavelengths. This is a spectral band of increasing importance and usefulness for night vision devices [1], for basic astronomy [2], and more recently for biomedical imaging as an alternative to x-rays. However, in this regime we have found little or no reports of holography. The reason for this is obvious; it is mostly due to the lack of a suitable recording medium that is comparable in usefulness to the familiar silver-bromide emulsion in the visible wavelengths. Also, another factor is the difficulty/expense of coherent sources of electromagnetic waves in this band.

1. RECORDING THE HOLOGRAM

In holography one records an interference pattern using a coherent source; and thereafter, reconstructs a wavefront which reproduces the phases and amplitudes of the original object wave scattered from the scene being recorded. Our approach in the recording is to use the microbolometer arrays that have improved greatly in the past several years. These are commercially available in sizes ranging from 4,000 to about 1 million pixels as shown in Fig. 2.1 of [3]. Very large arrays are now being produced for experiments in astronomy; and it is likely that these will be available commercially in the near future.

---

* "Long wavelength infrared holography using a microbolometer array," Invited Paper, OSA Annual Meeting, Rochester, NY, October 2006.

For our experiments in holography, the recording configuration is shown in the first figure attached. We are using reflecting optics so that we have a very broadband configuration.

Generally, in the published literature there are many papers dealing with the imaging of objects. Both biomedical applications and baggage surveillance systems have been described. Basically, these are all attempts to provide safe alternatives to x-rays. Why would one want to have a hologram instead of a simple image? The basic reason is that the hologram records the full three-dimensional, volumetric scene in a planar sheet, i.e., the microbolometer array. In the reconstruction process, one can obtain the field or the intensity at any distance from the planar sheet. The hologram provides a recording that has no depth-of-field limitation of the type encountered in photography.

1.1 Detectors

Parenthetically, we remark that infrared detectors as well as microwave detectors are often classified as thermal detectors or photon detectors. The thermal detector consists of a detector material which absorbs the incident radiation thereby changing temperature and resistivity. The change in resistivity is sensed electrically. Typically such detectors are relatively slow; however, they can be extremely sensitive. Since World War II, these detectors have been widely used, as bolometers, for the precise measurement of power at microwave frequencies. Recently there has been widespread use of microbolometer arrays. These uncooled arrays are capable of providing

extremely good images at very low light levels [1 - 3]. They can be operated at video frame rates.

On the other hand, the photon detector can be described as a material that releases a hole-electron pair or an electron upon the absorption of a photon, as in a photodiode. This time constant is very much shorter than customary video rates. Included as photon detectors are the following "several photoeffects such as photoconductive, photovoltaic, photoelectromagnetic, Dember and photon drag" [3]. While the further details are not pertinent here, we remark that photomixing typically requires a comparatively short response time that is characteristic of the photon detector. For photomixing, the thermal detector has rarely been appropriate.

Interestingly, for recording the carrier frequency fringe pattern of a hologram, the thermal detector performs quite well, since a fraction of a second time constant is tolerable.

2. RECONSTRUCTING THE OBJECT WAVEFRONT

For reconstructing the object wavefront in holography, there are two well-known techniques, dating back to the well-known research of E.N. Leith. First, one simply uses the original wavelength used in the recording; and with a beam propagating in the direction of the original reference beam incident on the film plate, the original object wavefront is reconstructed. Alternatively, one can use a reversed reference beam and then the object's wavefront is reconstructed but

now it is traveling toward the object. As is well-known, this reversal reference beam and the hologram give rise to the very useful pseudoscopic wavefront.

A second method that has been used at 10 μm in the infrared is to record the hologram and then to reduce the fringe pattern photographically. Thereafter, the reduced fringe pattern is illuminated in the visible and an observer can see the object.

For our experiments, it is planned to use the direct sampling of the carrier frequency fringes as has been reported by Khare and George [4, 5]. From this sampling, as is illustrated in the second figure attached, we have described and demonstrated that one can recover the phase and amplitude of the wavefront at the microbolometer array. Using well-known theories for inverse scattering and a digital computer, one can calculate the field and the intensity back in the object space. Often the calculation is approximated as an FFT. In the recording process it may be helpful to record two or three separate frames with a relative phase step in the reference beam, as is often done in phase unwrapping for automatic contouring.

3. EXPERIMENTAL PLAN AT ROCHESTER

For our first experiments, we plan to record and playback holograms recorded at 10 μm in the infrared. For this we will use a low power CO_2 laser operating single mode at 10.6 mu m so as to provide carrier frequency fringes of high contrast. From our earlier experiments, it is clear that the first stages will be achieved fairly directly. Mainly we need to provide an optical configuration that is

mostly reflector, as is shown by the Richey-Cretian configuration for the beam expander and picture beam. Of course we need to replace the he-ne laser with a CO_2 laser. The recording system will be a microbolometer array, replacing the CCD array. With these changes we will be able to record the first two-beam infrared hologram. The software for the reconstructions is already completed [4, 5].

For the second major phase of these experiments, we plan to record and playback holograms recorded in the terahertz band (2005-8). An appropriate source for this is shown in Figure 3, attached. It will also be advantageous to obtain a larger array than that presently being used in the infrared.

4. SUMMARY

In this memorandum, we describe a method of holography that is applicable throughout the electromagnetic spectrum from millimeter waves through to mu m or infrared. The read-out of carrier frequency fringe patterns has already been demonstrated in the cited references [4, 5] of Khare and George. These holograms would provide 3D imagery as well as a safe substitute for x-ray images. Also follow-on research to demonstrate that a stereo sequence is possible when the hologram platform is moving relative to the object would lead to a new form of synthetic aperture radar. This latter system would eliminate the need to make very large arrays of microbolometers. Laboratory experiments with sparse microbolometer arrays would provide important

information about the future possibilities of this novel imaging system. Many practical applications appear likely.

This research has been supported by the Physics Directorate of the Army Research Office.

References and Footnotes

[1] **Uncooled Infrared Imaging Arrays and Sensors**, P. W. Kruse and D.D. Skatrud, editors, Academic Press (1997).

[2] Submillimeter astronomy is an important international effort in which large telescopes and microbolometer arrays and photodetectors are both playing important roles. Extremely large mm wave telescopes are described in SPIE Int. vol. 5382 (2004). Photodetector mixers are NbN-SIS (795 GHz), SiC, ErAs: GaAs, and so on. Hot electron bolometer mixers are described for THz frequencies by P. Forcardi and W.R. McGrath (JPL) in *IEEE Antennas and Propagation*, IEEE vol. 1 (2004), pp. 986-9. A large 42 kg, 62 crystal thermal detector array CUORICINO is being assembled in Italy for tests of "Dark Matter and Double Beta Decay." Multi-mode microbolometers for the 7 to 14 μm band with "color selectivity" are described by S.W. Han et al in *Electronics Letters*, vol. 40, Oct. 2004. The Planck ESO satellite (2007) will carry a bolometer array to provide very acurage images of the cosmic wave background fluctuations. Measurements are planned at 857 GHz, 350 mu m and also at 10.6 mu m, see P. Martin et al, 5th Int. Conf. On Space Optics (ICSO 2004). The Caltech Submillimeter Observatory has a SHARC II detector array of 384 elements for background limited images at 350 and 450 mu m, S.H. Moseley et al 10th Int. Workshop on Low Temperature Detectors (LTD-10), Genoa, Italy (2003).

[3] **Infrared Detectors**, A. Rogalski, Gordon and Breach Science Publishers (2000).

[4] "Direct sampling and demodulation of carrier frequency signals," Opt. Comm. **211**, 85 (2002), K. Khare and N. George.

[5] "Direct coarse sampling of electronic holograms," Opt. Lett. **28**, 1004 (2003), K. Khare and N. George.

HOLOGRAPHY FROM MICROWAVES THROUGH INFRARED †

OBJECTIVE:

ELECTRONIC HOLOGRAPHY AT SUB-MM (TERAHERTZ) WAVELENGTHS AND AT 10 μm IN THE FAR INFRARED

BACKGROUND:

K. KHARE, N. GEORGE, OPT. COMM. 211, 85(2002)
DIRECT SAMPLING AND DEMODULATION OF CARRIER FREQUENCY SIGNALS

K. KHARE, N. GEORGE, OPT. LETT. 28, 1004(2003)
DIRECT COARSE SAMPLING OF ELECTRONIC HOLOGRAMS

EXPERIMENT:

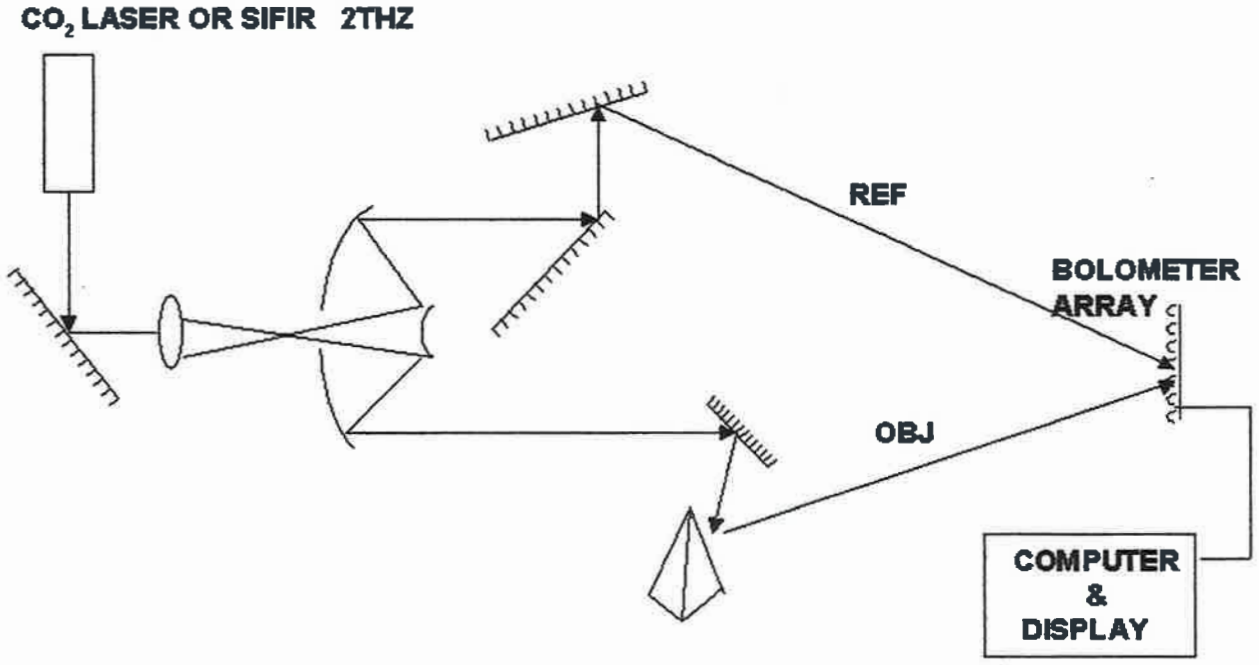

†RESEARCH SUPPORTED IN PART BY PHYSICS (R. HAMMOND), ARO.

SAMPLING THEORY FOR PHASE MEASUREMENT

HOLOGRAM

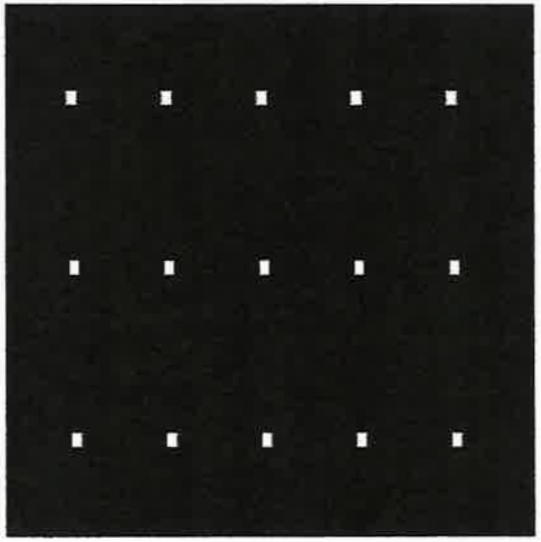

COARSE SAMPLING

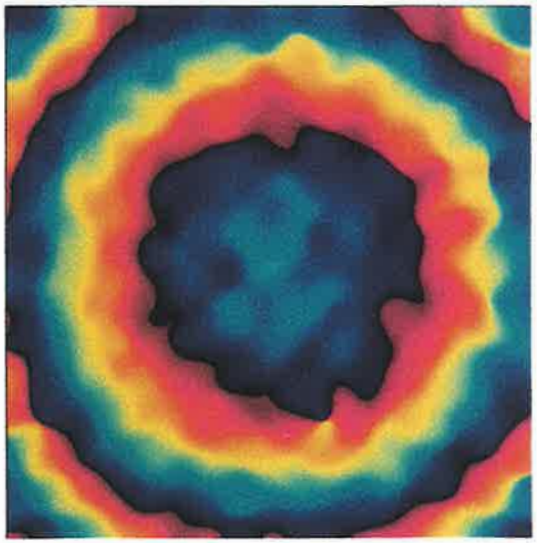

PHASE MAP

K. KHARE, N. GEORGE, "DIRECT SAMPLING AND DEMODULATION OF CARRIER FREQUENCY SIGNALS", OPT. COMM., 211, 85 (2002).

K. KHARE, N. GEORGE, "DIRECT COARSE SAMPLING OF ELECTRONIC HOLOGRAMS", OPT. LETT. 28, 1004 (2003).

SUB-MM IMAGING

- Stabilized Integrated FIR system
  SIFIR-50 (Coherent)

  Frequency ~2THz tunable
  Power ~100mw

- Applications:
  Replacement of X-rays (bone; teeth)
  Inspection for luggage
  Monitoring atmosphere conditions
  Others

- Novelty and Specialty of Electronic Group:
  Extended depth of field;
  Speckle;
  Automatic pattern recognization;
  IR imaging.

HOLOGRAPHY FROM MICROWAVES THROUGH INFRARED †

OBJECTIVE:

ELECTRONIC HOLOGRAPHY AT SUB-MM (TERAHERTZ) WAVELENGTHS AND AT 10 μm IN THE FAR INFRARED

BACKGROUND:

K. KHARE, N. GEORGE, OPT. COMM. 211, 85(2002) DIRECT SAMPLING AND DEMODULATION OF CARRIER FREQUENCY SIGNALS

K. KHARE, N. GEORGE, OPT. LETT. 28, 1004(2003) DIRECT COARSE SAMPLING OF ELECTRONIC HOLOGRAMS

EXPERIMENT:

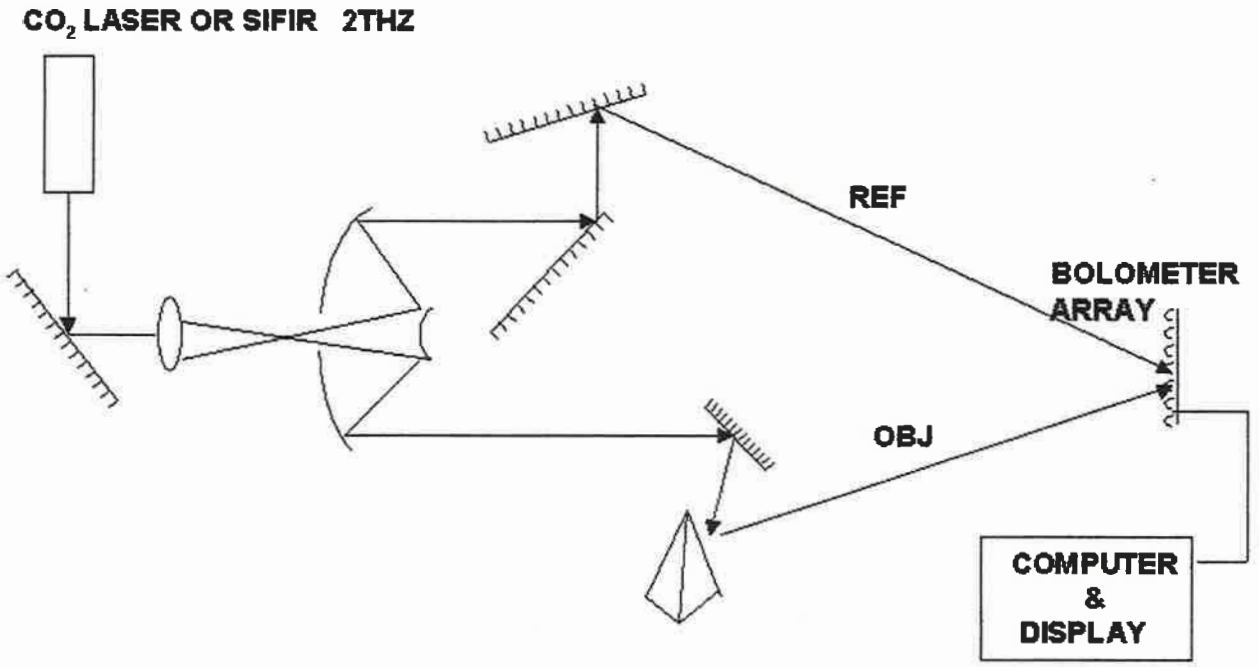

†RESEARCH SUPPORTED IN PART BY PHYSICS (R. HAMMOND), ARO.

SAMPLING THEORY FOR PHASE MEASUREMENT

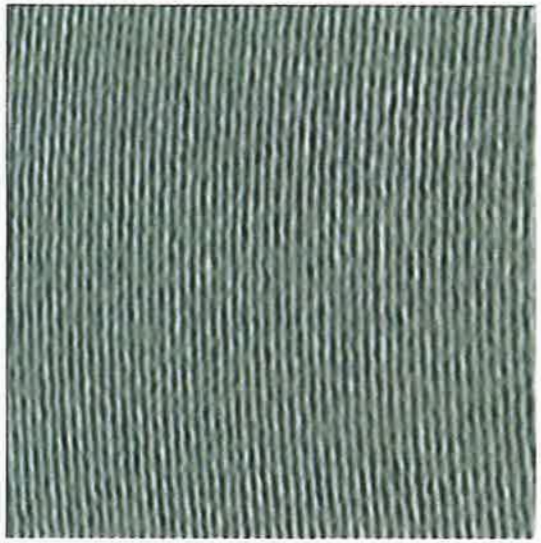

HOLOGRAM

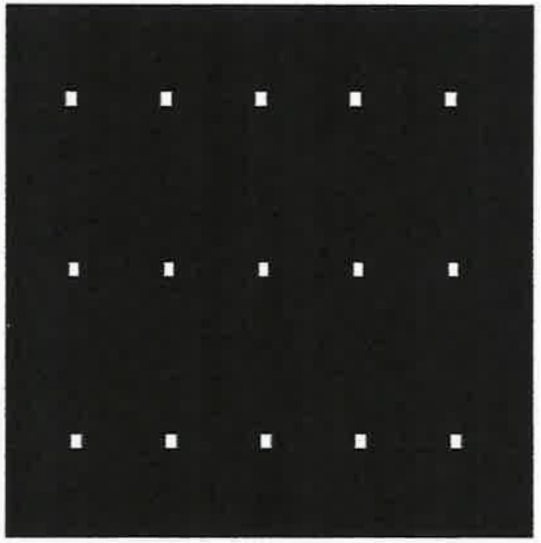

COARSE SAMPLING

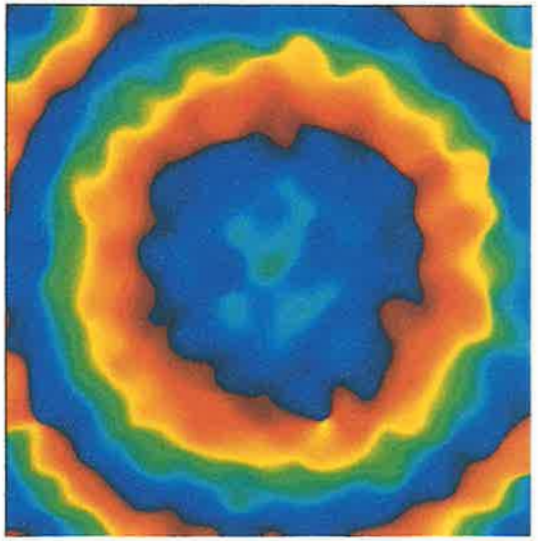

PHASE MAP

K. KHARE, N. GEORGE, "DIRECT SAMPLING AND DEMODULATION OF CARRIER FREQUENCY SIGNALS", OPT. COMM., 211, 85 (2002).

K. KHARE, N. GEORGE, "DIRECT COARSE SAMPLING OF ELECTRONIC HOLOGRAMS", OPT. LETT. 28, 1004 (2003).

SUB-MM IMAGING

- Stabilized Integrated FIR system
  SIFIR-50 (Coherent)

  Frequency ~2THz tunable
  Power ~100mw

- Applications:
  Replacement of X-rays (bone; teeth)
  Inspection for luggage
  Monitoring atmosphere conditions
  Others

- Novelty and Specialty of Electronic Group:
  Extended depth of field;
  Speckle;
  Automatic pattern recognization;
  IR imaging.

Available online at www.sciencedirect.com
ScienceDirect
Optics Communications 276 (2007) 1–7
OPTICS COMMUNICATIONS
www.elsevier.com/locate/optcom

Correlation function for speckle size in the right-half-space

Kaiqin Chu *, Nicholas George

The Institute of Optics, University of Rochester, Rochester, NY 14627, United States

Received 23 January 2007; received in revised form 16 March 2007; accepted 23 March 2007

Abstract

For radiation from a diffuser illuminated by a monochromatic plane wave, we calculate the field correlation using the Rayleigh–Sommerfeld–Smythe integral formula. This provides expressions of spatial correlation function valid at any point in the hemisphere. The non-paraxial formulas for the speckle sizes are new and the other results are consistent with the well-known solutions in the literature.

PACS: 42.25.Fx; 42.30.Kb; 42.30.Ms; 42.50.Ar; 42.68.Ay

Keywords: Spatial correlation; Speckle; Laser speckle; Longitudinal and transverse correlation functions

1. Introduction

In the literature one finds the correlation theory applied to the problem of determining the spatial size of speckle often with an emphasis on the Fresnel-zone region [1,2]. The three-dimensional structure or jelly-bean-like shape has been analyzed or measured by several authors [3–6]. Space and wavelength dependence of the speckle size [7] has been analyzed as well as experimental investigation of the statistics of optical fields in the near zone [8,9]. Many important applications of speckle have been made in optical metrology, particularly in the measurement of surface roughness and vibration [10,11].

In this paper we present a generalized analysis of the spatial correlation that is valid in the right-half-space. The calculation is based on a rigorous solution for the electromagnetic field in the right-half-space of a simple homogeneous medium [12]. From the spatial correlation function, we are able to obtain explicit expressions for speckle sizes not only in the Fresnel zone, but also in non-paraxial regions and regions well inside the Fresnel zone. In Section 2 we start with the exact Rayleigh–Sommerfeld–Smythe integral formula and in Sections 3 and 4 we derive the expressions for the field correlation function in regions where the propagation distance is much larger than the wavelength.

2. Theory and analysis of the spatial correlation function

Consider a phase type diffuser in the aperture Σ placed in the $z = 0$ plane and illuminated by $E_x(x', y', 0)$, an x-polarized monochromatic plane wave incident from the left as shown in Fig. 1.

For the harmonic time dependent case, $\exp(i\omega t)$, the electric field in the right-half-space can be found from a knowledge of the tangential electric field on the plane at $z = 0$, infinitesimally to the right of the diffuser. The original solution of this vector diffraction theory problem is due to Smythe [13] and is treated extensively elsewhere [12,14,15]. For our purposes, we prefer the explicit illustration of the existence theorem for the exact solution of Maxwell's equations given by the single expression of Smythe's formula. The electric field components E_x, E_y and E_z in the right-half-space can be written in terms of the tangential field components only [16], as follows:

* Corresponding author. Tel.: +1 585 275 6195; fax: +1 585 473 8722.
E-mail addresses: kaiqin@optics.rochester.edu (K. Chu), ngeorge@troi.cc.rochester.edu (N. George).

0030-4018/$ - see front matter © 2007 Elsevier B.V. All rights reserved.
doi:10.1016/j.optcom.2007.03.060

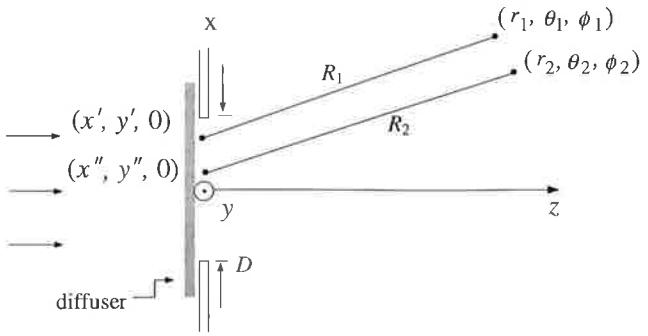

Fig. 1. Setup and coordinate system.

$$E_x(x,y,z) = \int\int_{\Sigma} E_x(x',y',0)\frac{e^{-ikR_1}}{2\pi R_1}\frac{z}{R_1}\left(ik+\frac{1}{R_1}\right)dx'\,dy', \quad (1)$$

$$E_y(x,y,z) = \int\int_{\Sigma} E_y(x',y',0)\frac{e^{-ikR_1}}{2\pi R_1}\frac{z}{R_1}\left(ik+\frac{1}{R_1}\right)dx'\,dy', \quad (2)$$

$$E_z(x,y,z) = \int\int_{\Sigma}\left(E_x(x',y',0)\frac{x'-x}{R_1}+E_y(x',y',0)\frac{y'-y}{R_1}\right) \times\frac{e^{-ikR_1}}{2\pi R_1}\left(ik+\frac{1}{R_1}\right)dx'\,dy'. \quad (3)$$

In these equations, R_1 is the distance between $(x',y',0)$ and (x,y,z) as shown in Fig. 1. The integration of Eqs. (1) and (3) is over the aperture $\sum$ and the integrands contain two terms: one is of order $\frac{1}{R_1}$ and will dominate in the Fresnel zone and the far field while the other of order $\frac{1}{R_1^2}$ will dominate in the near-field.

Also of course the magnetic field $\mathbf{H}(\mathbf{r})$ can be computed exactly from $\nabla\times\mathbf{E} = -i\omega\mu\mathbf{H}$. The exact solution of these integral equations can be approached by the methods of solving boundary value problems [17]. However, it is customary and useful in speckle problems to make an assertion of the tangential field distribution exiting the diffuser–aperture combination. In this case, one is ignoring the important aspect of the physical structure of the diffuser. This is an important problem, particularly for the nano-optics case where $z \leqslant \lambda$; however, it is not treated further in this paper.

For the speckle analysis of Fig. 1, we assert the value of $E_x(x,y,0)$ is given by a finite value within a circular aperture of diameter D and is zero outside. We assume that $E_y(x,y,0)$ is zero at $z=0$.

In the non-paraxial region, it is often more useful to have expressions for $E_\theta(r,\theta,\phi)$, $E_\phi(r,\theta,\phi)$ and $E_r(r,\theta,\phi)$ in spherical coordinates. Following the derivation of Eqs. (1) and (3), one can alternatively write the following exact expressions:

$$E_\theta(r,\theta,\phi) = \int\int_{\Sigma} E_x(x',y',0)\frac{e^{-ikR_1}}{2\pi R_1}\left(ik+\frac{1}{R_1}\right) \times\frac{r\cos\phi - x'\sin\theta}{R_1}dx'\,dy'; \quad (4)$$

$$E_\phi(r,\theta,\phi) = \int\int_{\Sigma} E_x(x',y',0)\frac{e^{-ikR_1}}{2\pi R_1}\left(ik+\frac{1}{R_1}\right) \times\frac{r\cos\theta\sin\phi}{R_1}dx'\,dy'; \quad (5)$$

$$E_r(r,\theta,\phi) = \int\int_{\Sigma} E_x(x',y',0)\frac{e^{-ikR_1}}{2\pi R_1}\left(ik+\frac{1}{R_1}\right) \times\frac{x'\cos\theta}{R_1}dx'\,dy'. \quad (6)$$

In the calculation of spatial correlation from the electric field described by Eqs. (4)–(6), it is often interesting to consider the perpendicular component of the electric field $E_\perp$ which is defined as

$$E_\perp(r,\theta,\phi) = \sqrt{E_\theta^2+E_\phi^2}. \quad (7)$$

Consequently, $E_\perp \perp \hat{\mathbf{r}}$, where $\hat{\mathbf{r}}$ is the radial unit vector in spherical coordinates.

In the study of speckle size it is well known that the thin rough diffuser generates an exiting signal that is described as a zero-mean complex Gaussian random process that is circular. General treatments of the moment expansions for this type of Gaussian random process are reported in the literature [2,18–20]. Here it is important to understand that the speckle size in intensity is characterized by a study of the spatial correlation function in energy density of the electric field, namely,

$$R_{U_1U_2}(r_1,\theta_1,\phi_1;r_2,\theta_2,\phi_2) = \langle U_1(r_1,\theta_1,\phi_1)U_2^*(r_2,\theta_2,\phi_2)\rangle = \langle E_{1\perp}E_{1\perp}^*E_{2\perp}E_{2\perp}^*\rangle, \quad (8)$$

where $E_{i\perp}$, $i=1,2$ is the perpendicular electric field defined in Eq. (7) in the position of (r_i,θ_i,ϕ_i) in the right half space.

According to Reed's moment theorem and assuming the electric field possesses circular Gaussian statistics, one can simplify the expansion of Eq. (8) as

$$\begin{aligned} R_{U_1U_2}&(r_1,\theta_1,\phi_1;r_2,\theta_2,\phi_2) \\ &= \langle|E_{1\perp}|^2\rangle\langle|E_{2\perp}|^2\rangle + |\langle E_{1\perp}E_{2\perp}\rangle|^2 + |\langle E_{1\perp}E_{2\perp}^*\rangle|^2 \\ &\quad - 2|\langle E_{1\perp}\rangle\langle E_{2\perp}\rangle|^2 \\ &= \langle|E_{1\perp}|^2\rangle\langle|E_{2\perp}|^2\rangle + |\langle E_{1\perp}E_{2\perp}^*\rangle|^2 - |\langle E_{1\perp}\rangle\langle E_{2\perp}\rangle|^2. \end{aligned} \quad (9)$$

From a consideration of $R_{U_1U_2}$, it is clear that the spatial dependence of this correlation function depends strongly on the mixed terms contained in the amplitude of second order moment J_A defined by

$$J_A(r_1,\theta_1,\phi_1;r_2,\theta_2,\phi_2) = \langle E_{1\perp}E_{2\perp}^*\rangle = \langle E_\perp(r_1,\theta_1,\phi_1)E_\perp^*(r_2,\theta_2,\phi_2)\rangle. \quad (10)$$

The size of the speckle is determined by the fall-off of this correlation function in terms of the difference $|\vec{\mathbf{r}_1}-\vec{\mathbf{r}_2}|$. For specific cases of interest in Section 3, we calculate the correlation functions in xz-plane in terms of the angular difference $\Delta\theta=\theta_2-\theta_1$ as well as the radial difference $\Delta r = r_2 - r_1$. Similarly in Section 4, the appropriate correlation functions are calculated in the yz-plane. From those results, the transverse speckle size and the longitudinal speckle size are readily derived in order to illustrate the well-known jelly-bean-like shape of a speckle. The formulas are summarized in Table 1.

Table 1
Speckle sizes in the right-half space of the aperture

Positions	Speckle		
	Transverse size $d_\perp$	Longitudinal size $d_\parallel$	
Nonparaxial region (including far field, fresnel zone)	$1.22\frac{r}{D\cos\theta}\lambda$	Farfield	∞
		Fresnal zone and closer	$\frac{1}{1+\cos^2\theta}\left(\frac{4r}{D}\right)^2\lambda$
Paraxial region $\sqrt{1+\left(\frac{D}{2z}\right)^2} \leqslant 2\left(\frac{z}{\lambda}\right)^{2/3}$	$1.22\sqrt{1+\left(\frac{D}{2z}\right)^2}\frac{z}{D}\lambda$	$\left(1-\sqrt{1+\left(\frac{D}{2z}\right)^2}\right)^{-1}\lambda$	

3. Correlation function and speckle size in the xz-plane where $z \gg \lambda$

When $z \gg \lambda$, $|ik| \gg |\frac{1}{R_1}|$ so that the $\frac{1}{R_1^2}$ near-field term can be neglected in Eqs. (4)–(6). First we will consider the spatial correlation function in the xz-plane where $\phi = 0$ and $E_\perp(r,\theta,0) = E_\theta$. The correlation function $J_A(r_1,\theta_1,0;r_2,\theta_2,0)$ is formed using Eq. (4) and neglecting the near-field terms which yields:

$$J_A(r_1,\theta_1,0;r_2,\theta_2,0) = \int\int_\Sigma\int\int_\Sigma \langle E_x(x',y',0)E_x^*(x'',y'',0)\rangle \times \frac{e^{-ik(R_1-R_2)}}{\lambda^2 R_1 R_2}\frac{(r_1 - x'\sin\theta_1)}{R_1} \times \frac{(r_2 - x''\sin\theta_2)}{R_2}\,dx'\,dy'\,dx''\,dy''. \tag{11}$$

In the evaluation of this integral it is greatly simplified if one assumes a white-noise diffuser in the input aperture [21]. There are important physical limitations implicit in this assumption of a delta-function for the correlation length. Since the correlation still builds rapidly longitudinally (see the text of Eq. (31)), it can be thought of as arising from a conventional frosted glass with transverse variations or correlation on the scale of a few μm. With a spread of ±60° from a white noise diffuser, the effective correlation length builds from Angstrom-like dimensions to 10λ in a Δz in the order of 10λ. What is lost in this model is the capability to work back to determine the actual height profile of some diffuser. In the nano-optics regime where scales of roughness on the order of nano-meters are to be ascertained, it might be useful to consider also the actual height profiles. Herein, we do not consider this case further.

The correlation function for $\langle E_x(x',y',0)E_x^*(x'',y'',0)\rangle$ can then be written as follows:

$$\langle E_x(x',y',0)E_x^*(x'',y'',0)\rangle = C\delta(x'-x'',y'-y''), \tag{12}$$

in which $C = |E_0|^2\Delta A$. E_0 is the exiting electric field amplitude and ΔA is the correlation area of the diffuser. For simplicity we set $C = 1$.

Substitution of Eq. (12) into Eq. (11) and integration over x'', y'' yields the correlation function in the form of

$$J_A(r_1,\theta_1,0;r_2,\theta_2,0) = \int\int_\Sigma \frac{e^{ik(R_2-R_1)}}{\lambda^2 R_1^2 R_2^2}(r_1 - \rho'\sin\theta_1\cos\varphi') \times (r_2 - \rho'\sin\theta_2\cos\varphi')\rho'\,d\rho'\,d\phi'. \tag{13}$$

The most common simplification of $e^{ik(R_2-R_1)}$ is taking the Fresnel approximations of both e^{ikR_2} and e^{ikR_1}. However this approximation limits the results to the paraxial region in the Fresnel zone of the aperture. In this letter, we take $e^{ik(R_2-R_1)}$ as one function and Taylor expand it into terms of $\frac{\|R_2-R_1\|}{\|r_2+r_1\|}$ provided the separation distance between $(r_1,\theta_1,0)$ and $(r_2,\theta_2,0)$ is small compared to the propagation distances r_1 and r_2.

3.1. Correlation function in the transverse direction and the transverse speckle size

In the transverse direction where the angular separation is $\Delta\theta$ and $r_1 = r_2 = r$; $\theta_1 = \theta - \Delta\theta/2$, $\theta_2 = \theta + \Delta\theta/2$, we can write the correlation coefficient as:

$$J_A\left(r,\theta-\frac{\Delta\theta}{2},0;r,\theta+\frac{\Delta\theta}{2},0\right) \sim \int\int_\Sigma\left(\frac{1-\frac{\rho'}{r}\sin\theta\cos\varphi'}{1+\left(\frac{\rho'}{r}\right)^2-2\frac{\rho'}{r}\sin\theta\cos\varphi'}\right)^2 \times e^{-ik\frac{\rho'\cos\varphi'\cos\theta\Delta\theta}{\sqrt{1+\left(\frac{\rho'}{r}\right)^2-2\frac{\rho'}{r}\sin\theta\cos\varphi'}}}\rho'\,d\rho'\,d\phi'. \tag{14}$$

Direct integration of Eq. (14) is non-trivial. However, both the amplitude part and the phase part inside the integrand contain terms of ρ'/r so that one can expand them into sums of ρ'/r terms:

$$\left(\frac{1-\frac{\rho'}{r}\sin\theta\cos\phi'}{1+\left(\frac{\rho'}{r}\right)^2-2\frac{\rho'}{r}\sin\theta\cos\phi'}\right)^2 = 1+2\sin\theta\cos\phi'\frac{\rho'}{r}+\cdots \tag{15}$$

$$\frac{\frac{\rho'}{r}\cos\phi'}{\sqrt{1+\left(\frac{\rho'}{r}\right)^2-2\frac{\rho'}{r}\sin\theta\cos\phi'}} = \frac{\rho'}{r}\cos\phi'+\left(\frac{\rho'}{r}\cos\phi'\right)^2\sin\theta+\cdots \tag{16}$$

provided that $\rho'/r < 1$. Thus in regions where $\rho'_{\max} \ll r$, the field correlation function in Eq. (14) becomes:

$$J_A \sim \int\int_\Sigma e^{-ik\rho'\cos\phi'\cos\theta\Delta\theta}\rho'\,d\rho'\,d\phi' \sim \frac{J_1(a)}{a}, \tag{17}$$

in which

$$a = kD\cos\theta\Delta\theta/2, \tag{18}$$

a is the normalized separation distance between the two field points $(r,\theta-\Delta\theta/2,0)$ and $(r,\theta+\Delta\theta/2,0)$, $D = \rho'_{\max}$ is the diameter of the aperture. J_1 is the Bessel function of the first order. Eq. (17) tells us that the correlation function in this region is a Fourier transform of the shape of

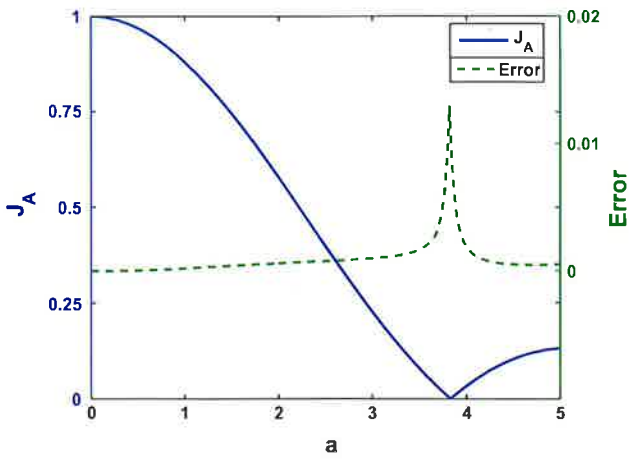

Fig. 2. Numerical calculation of Eq. (14) for $J_A(a)$ vs. a together with expanded error plot using the approximate result in Eq. (17) when $\frac{r}{D}=4$, $\theta=\frac{\pi}{6}$.

the diffuser. Fig. 2 is a plot of field correlation using Eq. (14) and it agrees within 1% to the approximation result of Eq. (17) when $r/D=4$ and $\theta=\pi/6$. The approximate formula in Eq. (17) gives good results when $r/D\geqslant 4$ and $\theta\leqslant\pi/4$.

It is interesting to notice that the expression of Eq. (17) is valid in regions where the far field assumption is not valid. Actually the result is still valid well inside the Fresnel zone region. For example, the Fresnel zone criteria requires $z\gg 10$ mm when the diameter of the aperture is 1 mm and the wavelength is 0.5 μm, the far field approximation requires $z\gg 1000$ mm. Fig. 2 shows that the approximation of Eq. (17) is valid even when $r=4$ mm. Further, Eq. (17) is also valid in the non-paraxial region as we can see from Fig. 2.

For the correlation as in Eq. (17), we find its first local minimum at $a\approx 3.83$. The transverse speckle size $d_\perp=r\Delta\theta$ and can be written as:

$$d_\perp=r\frac{2a}{kD\cos\theta}=1.22\frac{r}{D\cos\theta}\lambda. \tag{19}$$

In the special case of $\theta=0$, i.e., on-axis, we substitute $\theta=0$ into Eq. (14) and obtain the spatial correlation function in the form of

$$J_A\left(z-\frac{\Delta z}{2},0,0;z+\frac{\Delta z}{2},0,0\right)$$
$$\sim\int\int_\Sigma\left(\frac{1}{1+\left(\frac{\rho'}{z}\right)^2}\right)^2 e^{ikz\Delta\theta\frac{\frac{\rho'}{z}\cos\varphi'}{\sqrt{1+\left(\frac{\rho'}{z}\right)^2}}}\rho'\,d\rho'\,d\varphi'$$
$$\sim\frac{J_1(\alpha)}{\alpha}, \tag{20}$$

in which

$$\alpha=kr\Delta\theta\frac{D}{2z}\frac{1}{\sqrt{1+\left(\frac{D}{2z}\right)^2}}. \tag{21}$$

For this paraxial case,the speckle size can be derived from the first local minimum of Eq. (20) and accordingly the result is given as follows:

$$d_\perp^0\approx 1.22\sqrt{1+\left(\frac{D}{2z}\right)^2}\frac{z}{D}\lambda. \tag{22}$$

Eqs. (20) and (22) hold as $\sqrt{1+(\frac{D}{2z})^2}\ll 2(\frac{z}{\lambda})^{2/3}$. For example, when the diameter of the aperture is 1 mm and the wavelength is 0.5 μm, the approximation of Eq. (20) requires that $z\gg 0.4$ mm. Note that the Fresnel approximation requires $z\gg 10$ mm, it is remarkable that the spatial correlation function as in Eq. (20) and the speckle size as in Eq. (22) can be applied in regions well inside the Fresnel zone.

If $z>D$, the on-axis transverse speckle size can be approximated from Eq. (22) as: $d_\perp^0\approx 1.22\frac{z}{D}\lambda$. Comparing results of the non-paraxial case in Eq. (19) and the paraxial case in Eq. (22), we find that generally the speckle size is on the order of the beam spread width caused by the diffraction from an aperture illuminated by a plane wave travelling down the observing direction. The relative aperture size in the observing direction becomes $D\cos\theta$. Hence the dependence on the viewing angle θ in Eq. (19) for the non-paraxial speckle size.

3.2. Correlation function in the radial direction and the longitudinal speckle size

Next we derive expressions for the spatial correlation in the radial direction where $r_1=r-\Delta r/2$, $r_2=r+\Delta r/2$ and $\theta_1=\theta_2=\theta$. By expanding Eq. (13) in terms of $\Delta r/r$, we can write the spatial correlation as:

$$J_A\left(r-\frac{\Delta r}{2},\theta,0;r+\frac{\Delta r}{2},\theta,0\right)$$
$$\sim\int\int_\Sigma\left(\frac{1-\frac{\rho'}{r}\sin\theta\cos\varphi'}{1+\left(\frac{\rho'}{r}\right)^2-2\frac{\rho'}{r}\sin\theta\cos\varphi'}\right)^2$$
$$\times e^{-ik\frac{\left(1-\frac{\rho'}{r}\cos\varphi'\sin\theta\right)\Delta r}{\sqrt{1+\left(\frac{\rho'}{r}\right)^2-2\frac{\rho'}{r}\sin\theta\cos\varphi'}}}\rho'\,d\rho'\,d\varphi'. \tag{23}$$

Depending on how far the observing points are away from the diffuser, we can approximate the phase part of the integrand of Eq. (23) by Taylor expansion:

$$\frac{1-\frac{\rho'}{r}\sin\theta\cos\phi'}{\sqrt{1+\left(\frac{\rho'}{r}\right)^2-2\frac{\rho'}{r}\sin\theta\cos\phi'}}$$
$$=1+\frac{\sin^2\theta\cos^2\phi'-1}{2}\left(\frac{\rho'}{r}\right)^2+\cdots. \tag{24}$$

For the amplitude part of the integrand of Eq. (23), it can be treated same as Eq. (15).

So in the far field, the correlation function in Eq. (23) becomes

$$J_A\left(r-\frac{\Delta r}{2},\theta,0;r+\frac{\Delta r}{2},\theta,0\right)\sim\int\int_\Sigma e^{-ikr\Delta r}\rho'\,d\rho'\,d\varphi'. \tag{25}$$

We observe that the amplitude of the correlation is a constant in terms of the spatial separation distance Δr. This means that the longitudinal speckle size is infinity in the far field. From this, it is also clear that in the far zone, the speckle pattern is angularly invariant; It spreads out with the increasing radial distance but the speckle content does not vary.

In the Fresnel region, we take the second order term $(\frac{\rho'}{r})^2$ into account and Eq. (23) becomes

$$\begin{aligned} &J_A\left(r-\frac{\Delta r}{2},\theta,0;r+\frac{\Delta r}{2},\theta,0\right)\\ &\sim\int\int_\Sigma\left(1+2\sin\theta\cos\varphi'\frac{\rho'}{r}\right)e^{ik\Delta r\left(1+\frac{\sin^2\theta\cos^2\varphi'-1}{2}(\frac{\rho'}{r})^2\right)}\rho'\,d\rho'\,d\varphi'\\ &\sim\int_0^1 e^{-i\beta\xi}J_0\left(\frac{\sin^2\theta}{1+\cos^2\theta}\beta\xi\right)d\xi, \end{aligned} \tag{26}$$

in which

$$\beta=k\Delta r(1+\cos^2\theta)\left(\frac{D}{4r}\right)^2. \tag{27}$$

From Eq. (26), we can find its first local minimum occurs when $\beta\approx 2\pi$. So the longitudinal speckle size can be derived from Eq. (27) and is expressed as

$$d_\parallel=\Delta r=\frac{\beta}{k(1+\cos^2\theta)(D/4r)^2}=\frac{1}{1+\cos^2\theta}\left(\frac{4r}{D}\right)^2\lambda. \tag{28}$$

In the special case of on-axis longitudinal correlation where $\theta_1=\theta_2=0$ and $r_1=z-\Delta z/2$, $r_2=z+\Delta z/2$, Eq. (23) takes the form of

$$\begin{aligned} &J_A\left(z-\frac{\Delta z}{2},0,0;z+\frac{\Delta z}{2},0,0\right)\\ &\sim\int\int_\Sigma\frac{1}{(1+(\frac{\rho'}{z})^2)^2}e^{\frac{ik\Delta z}{\sqrt{1+(\frac{\rho'}{z})^2}}}\rho'\,d\rho'\,d\varphi'\\ &\sim\frac{1}{ik\Delta z}\left[\left(1-\frac{1}{ik\Delta z}\right)e^{ik\Delta z}-\left(\frac{1}{\sqrt{1+(\frac{D}{2z})^2}}-\frac{1}{ik\Delta z}\right)e^{\frac{ik\Delta z}{\sqrt{1+(\frac{D}{2z})^2}}}\right]. \end{aligned} \tag{29}$$

For this paraxial case, the speckle size is obtained from the fall-off of Eq. (29) and can be written as:

$$d_\parallel^0=\frac{\lambda}{1-\frac{1}{\sqrt{1+(\frac{D}{2z})^2}}}. \tag{30}$$

From Eq. (30) we see that when $\frac{D}{2z}\ll 1$, $d_\parallel^0=8\left(\frac{z}{D}\right)^2\lambda$. Both Eqs. (28) and (30) are consistent with each other in that all of them are proportional to $\left(\frac{r}{D}\right)^2\lambda$.

A simple interpretation of the dependence of the speckle size on $\left(\frac{r}{D}\right)^2\lambda$ can be made by considering the propagation of the field from one speckle. If the transverse beam width due to propagation is bigger than one transverse speckle size $d_\perp$, other speckles will start to affect the field and the longitudinal correlation of the field will decrease. The allowable propagation distance between a speckle and the field behind it should satisfy the following criteria:

$$d_\parallel\bullet\frac{\lambda}{d_\perp}\sim d_\perp. \tag{31}$$

The criteria specified by Eq. (31) implicitly requires that the longitudinal length should be on the order of $(\frac{r}{D})^2\lambda$ since $d_\perp$ is proportional to $\frac{r}{D}$.

4. Correlation function and speckle size in the *yz*-plane where $z\gg\lambda$

In the *yz*-plane where $\phi=\pi/2$, the perpendicular electric field $E_\perp$ can be formed by substituting $\phi=\pi/2$ into Eqs. (4), (5) and using Eq. (7) which yields:

$$E_\perp=ik\int\int_\Sigma E_x(x',y',0)\frac{e^{-ikR_1}}{2\pi R_1}\frac{\sqrt{r^2\cos^2\theta+x'^2\sin^2\theta}}{R_1}\,dx'\,dy', \tag{32}$$

where the near-field term is neglected.

Again with the white-noise diffuser assumption [21], we can write the correlation function as follows:

$$\begin{aligned} &J_A\left(r_1,\theta_1,\frac{\pi}{2};r_2,\theta_2,\frac{\pi}{2}\right)\\ &=\int\int_\Sigma\frac{e^{ik(R_2-R_1)}}{\lambda^2R_1^2R_2^2}\sqrt{r_1^2\cos^2\theta_1+\rho'2\cos^2\varphi'\sin^2\theta_1}\\ &\quad\times\sqrt{r_2^2\cos^2\theta_2+\rho'2\cos^2\varphi'\sin^2\theta_2}\rho'\,d\rho'\,d\varphi'. \end{aligned} \tag{33}$$

4.1. Correlation function in the transverse direction and the transverse speckle size

With the same approximation method for calculation of the correlation function in the *xz*-plane, we can find that in the transverse direction where $r_1=r_2=r$ and $\theta_1=\theta-\Delta\theta/2$, $\theta_2=\theta+\Delta\theta/2$, the field correlation is formed using Eq. (33) and can be written as

$$\begin{aligned} &J_A\left(r,\theta-\frac{\Delta\theta}{2},\frac{\pi}{2};r,\theta+\frac{\Delta\theta}{2},\frac{\pi}{2}\right)\\ &\sim\int\int_\Sigma\left(\frac{\sqrt{\cos^2\theta+\left(\frac{\rho'\cos\varphi'\sin\theta}{r}\right)^2}}{1+\left(\frac{\rho'}{r}\right)^2-2\frac{\rho'}{r}\sin\theta\cos\varphi'}\right)^2\\ &\quad\times e^{-ik\frac{\rho'\cos\theta\Delta\theta/2\sin\varphi'}{\sqrt{1+\left(\frac{\rho'}{r}\right)^2-2\frac{\rho'}{r}\sin\theta\cos\varphi'}}}\rho'\,d\rho'\,d\varphi'. \end{aligned} \tag{34}$$

When $\rho'/r<1$, the phase part of the integrand inside Eq. (34) can be approximated using Eq. (16) and the amplitude part of the integrand inside Eq. (34) can be approximated as:

$$\frac{\sqrt{\cos^2\theta+(\frac{\rho'\cos\varphi'\sin\theta}{r})^2}}{1+\left(\frac{\rho'}{r}\right)^2-2(\frac{\rho'}{r}\sin\theta\cos\varphi'}\Big)^2 = \cos^2\theta\left(1+4\sin\theta\sin\varphi'\frac{\rho'}{r}+\cdots\right). \tag{35}$$

So in the far field Eq. (34) can be simplified to:

$$J_A\left(r,\theta-\frac{\Delta\theta}{2},\frac{\pi}{2};r,\theta+\frac{\Delta\theta}{2},\frac{\pi}{2}\right)\sim\cos^2\theta\frac{J_1(a)}{a}, \tag{36}$$

where a is defined in Eq. (18). Comparing Eq. (36) with Eq. (17) we see that their amplitudes will fall off at the same speed in terms of $\Delta\theta$ and thus we will have the same transverse speckle size as expressed in Eq. (19).

For the special case $\theta=0$, the field correlation in the transverse direction is obtained by substituting $\theta=0$ into Eq. (34) which yields:

$$J_A\left(z,-\frac{\Delta\theta}{2},\frac{\pi}{2};z,+\frac{\Delta\theta}{2},\frac{\pi}{2}\right) \sim\int\int_\Sigma\left(\frac{1}{1+\left(\frac{\rho'}{z}\right)^2}\right)^2 e^{\frac{ikz\Delta\theta\frac{\rho'}{r}\cos\varphi'}{\sqrt{1+\left(\frac{\rho'}{z}\right)^2}}}\rho'\,d\rho'\,d\varphi'\sim\frac{J_1(\alpha)}{\alpha}, \tag{37}$$

where α is defined in Eq. (21). Again, Eq. (37) is the same as Eq. (20). Thus the transverse speckle size in the paraxial region of the yz-plane will be the same as that of the xz-plane and it can be expressed as Eq. (22).

4.2. Correlation function in the radial direction and the longitudinal speckle size

For the correlation function in the radial direction where $r_1=r-\Delta r/2$, $r_2=r+\Delta r/2$ and $\theta_1=\theta_2=\theta$, the field correlation can be formed from Eq. (33) and can be written as

$$J_A\left(r-\frac{\Delta r}{2},\theta,\frac{\pi}{2};r+\frac{\Delta r}{2},\theta,\frac{\pi}{2}\right) \sim\int\int_\Sigma\frac{\cos^2\theta-\frac{\rho'}{r}\sin\theta\sin\varphi'}{(1+\left(\frac{\rho'}{r}\right)^2-2\frac{\rho'}{r}\sin\theta\cos\varphi')^2} \times e^{\frac{-ik\left(1-\frac{\rho'}{r}\sin\varphi'\sin\theta\right)\Delta r}{\sqrt{1+\left(\frac{\rho'}{r}\right)^2-2\frac{\rho'}{r}\sin\theta\cos\varphi'}}}\rho'\,d\rho'\,d\varphi'. \tag{38}$$

We see that the integrand in Eq. (38) is a function of ρ'/r and when $\rho'\leqslant r$, its amplitude term can be written in the form of Taylor Expansion:

$$\frac{\cos^2\theta-\frac{\rho'}{r}\sin\theta\sin\varphi'}{(1+\left(\frac{\rho'}{r}\right)^2-2\frac{\rho'}{r}\sin\theta\cos\varphi')^2} = \cos^2\theta\left(1+4\sin\theta\cos\varphi'\frac{\rho'}{r}+\cdots\right). \tag{39}$$

The phase term of the integrand in Eq. (38) can be written as Eq. (24). So in the far field, the field correlation is:

$$J_A\sim\cos^2\theta\int\int_\Sigma e^{-ikr\Delta r}\rho'\,d\rho'\,d\varphi', \tag{40}$$

which resembles Eq. (25) in the xz-plane except the coefficient. This also means that the speckle size will be inifinity by the same argument in Section 3.2.

In the Fresnel Zone, one takes the second term of ρ'/r into account and obtains the field correlation defined in Eq. (38) as follows:

$$\begin{aligned}J_A&\left(r-\frac{\Delta r}{2},\theta,\frac{\pi}{2};r+\frac{\Delta r}{2},\theta,\frac{\pi}{2}\right)\\ &\sim\cos^2\theta\int\int_\Sigma\left(1+4\sin\theta\sin\varphi'\frac{\rho'}{r}\right)\\ &\quad\times e^{-ik\frac{\sin^2\theta\sin^2\varphi'-1}{2}(\frac{\rho'}{r})^2\Delta r}\rho'\,d\rho'\,d\varphi'\\ &\sim\cos^2\theta\int_0^1 e^{-i\beta\xi}J_0\left(\frac{\sin^2\theta}{1+\cos^2\theta}\beta\xi\right)d\xi,\end{aligned} \tag{41}$$

where β is defined in Eq. (27). Comparing Eqs. (41) and (26), we see that the correlation functions in the longitudinal direction of the xz-plane and the yz-plane are the same except the coefficients and they will fall off at the same speed in terms of Δr. This means that we will have the same longitudinal speckle size in the yz-plane as that in the xz-plane which is described by Eq. (28).

For the special case when $\theta_1=\theta_2=0$; $r_1=z-\Delta z$, $r_2=z+\Delta z$, the spatial correlation in the longitudinal direction is formed by substituting $\theta=0$ into Eq. (38) which yields:

$$J_A\left(z-\frac{\Delta z}{2},0,\frac{\pi}{2};z+\frac{\Delta z}{2},0,\frac{\pi}{2}\right) \sim\cos^2\theta\int\int_\Sigma\frac{1}{(1+(\frac{\rho'}{z})^2)^2}e^{\frac{ik\Delta z}{\sqrt{1+\left(\frac{\rho'}{z}\right)^2}}}\rho'\,d\rho'\,d\varphi'. \tag{42}$$

Eq. (42) resembles Eq. (29) except the coefficient and we will have the same longitudinal speckle size as described by Eq. (30) in the yz-plane.

From the results in this section and the previous section, we find that the speckle sizes are the same for both the xz- and yz-planes. This means that the speckle actually is a spheroid. Of course for apertures of different shape than circular, one will find other cross-sectional shapes for the speckle. For spatial correlations and speckle sizes in planes other than the xz-plane and the yz-plane, they should have the same dependence on $|r_1-r_2|$ and $|\theta_1-\theta_2|$. We omit the discussions in those planes for the sake of brevity.

5. Conclusion

In summary, we have calculated the spatial correlation functions from the exact Rayleigh–Sommerfeld–Smythe integral formula and derived the speckle sizes for various regions. The speckle sizes are summarized in Table 1. The non-paraxial formulas are new and the other results are consistent with the well-known solutions in the literature [1–7].

Acknowledgement

This research was supported by the US Army Research Office.

References

[1] Lester I. Goldfisher, Autocorrelation function and power spectral density of laser-produced speckle patterns, JOSA 55 (1965) 247.
[2] J.W. Goodman, in: J.C. Dainty (Ed.), Laser Speckle and Related Phenomena, Springer-Verlag, Heidelberg, Berlin, 1984.
[3] Nicholas George, Optics News (1976) 4.
[4] C.E. Halford, W.L. Gamble, Nicholas George, Opt. Eng. 26 (12) (1987) 263.
[5] Ludger Leushacke, Manfred Kirchner, J. Opt. Soc. Am. A 7 (5) (1990) 27.
[6] Q.B. Li, F.P. Chiang, Appl. Opt. 31 (29) (1992) 287.
[7] Nicholas George, Atul Jain, Appl. Phys. 4 (1974) 201.
[8] Adeal Apostol, Aristide Dogariu, Opt. Lett. 29 (3) (2004) 235.
[9] M. Giglio, M. Carpineti, A. Vailati, Phy. Rev. Lett. 85 (2) (2000) 1416.
[10] Robert K. Erf, Speckle Metrology, Academic Press, 1978.
[11] H.J. Tiziani, OPTIK 112 (9) (2001) 70.
[12] W.R. Smythe, Static and Dynamic Electricity, third ed., revised., Summ-Hemisphere, New York, 1989, p. 478.
[13] W.R. Smythe, Phys. Rev. 72 (1947) 1066.
[14] C.J. Bouwkamp, Rep. Prog. Phys. 17 (1954) 35.
[15] John David Jackson, Classical Electrodynamics, third ed., Wiley, 1999, Chap. 10.7.
[16] R. Edward English Jr., Nicholas George, Appl. Opt. 26 (12) (1987) 2360.
[17] Fritz E. Borgnis, Charles H. Papas, Randwertprobleme der Mikrowellenphysik, Springer-Verlag, German, 1955.
[18] L. Mandel, in: E. Wolf (Ed.), Progress in Optics II, North-Holland, Amersterdan, 1963, p. 181.
[19] I.S. Reed, On a moment theorem for complex Gaussian process, IRE Trans. Inf. Theory IT-8, (1962) 194.
[20] L.G. Shirley, Laser speckle from thin and cascaded diffusers, Appendix A, Ph.D. thesis, University of Rochester, 1988, p. 162.
[21] Nicholas George, SPIE 556 (1985) 8.

Infrared holography using a microbolometer array

Nicholas George,[1] Kedar Khare,[1,2] and Wanli Chi[1,*]

[1]The Institute of Optics, University of Rochester, Rochester, New York 14627, USA
[2]Currently with GE Global Research, Niskayuna, New York 12309, USA

*Corresponding author: chiw@optics.rochester.edu

Received 26 April 2007; revised 14 July 2007; accepted 20 July 2007;
posted 25 July 2007 (Doc. ID 82479); published 4 September 2007

We describe a series of experiments to demonstrate holography at far-infrared wavelengths using an uncooled microbolometer array. Simple interference patterns and Fresnel zone holograms are recorded with a 10 W cw CO_2 laser illumination in a Mach–Zehnder interferometer setup. A sparse-sampling method is used to sample the hologram at a rate dependent on the bandwidth of the object wavefront rather than the carrier frequency. The samples are then used to reconstruct the complex object wavefront in the hologram plane, which is Fresnel backpropagated for image reconstruction. Uncooled microbolometer arrays are most commonly used in passive mode to image the thermal–blackbody radiation. Their technology has matured to include the wavelength range of far-infrared to submillimeter radiation. The use of microbolometers with active illumination for holography, as described in this paper, suggests their interesting future applications. © 2007 Optical Society of America

OCIS codes: 090.0090, 100.2650, 100.3010, 100.5070, 260.3160.

1. Introduction

The pioneering research by Emmett Leith and Juris Upatnieks in optical wavefront reconstruction in the 1960s [1] has been the foundation for significant developments in many disciplines of science and engineering. In this paper we describe what we believe to be a novel electronic hologram that is based on these concepts. Typically, in an off-axis holography setup, the reference beam is introduced at an angle to the object wavefront and provides a central carrier frequency in the recorded interference pattern. The formation of a hologram and its replay is then analogous to modulation and demodulation of information in AM–FM communication. The replay of a hologram may be performed by physically reilluminating the recorded film plate with the conjugate reference beam. In the past 10–15 years, with the availability of charge-coupled detector arrays, electronic or digital holography in the visible range has also gained popularity [2–6]. In this case, the replay or image reconstruction is performed through digital processing of the recorded hologram to mimic the physical reconstruction.

0003-6935/08/04000A7-6$15.00/0

Early in the field of holography, considerable effort was expended to increase the range of holography beyond the visible wavelengths. Although efforts were made to record holograms at 10.6 μm, they were not successful due to the lack of a suitable recording medium, such as silver bromide or dichromatic gelatin in the visible. In a comprehensive review of media for holography at 10.6 μm by Beaulieu and Lessard [7], more than 12 separate recording materials are described, including photochromic film, gelatin film, wax film, and photoresist. In an early work by Chivian *et al.* [8], successful recordings at 10.6 μm were obtained using a thermochromic material, cuprous mercuric iodide, to record an on-axis interference pattern, and later a two-step photographic process was used to view the reconstruction using a He–Ne laser. Another important early media study is the infrared holography experiments with thermal bleaching of organic photochromic films also in a two-step process [9]. Related rough surface interferometry at 10.6 μm has been studied (1) to test IR transmitting materials, (2) for optical metrology of aspheres, and (3) to study rough surfaces [10]. In this research the detector is a pyroelectric videcon that is compatible with a conventional TV format. All in all, it is safe to say that no entirely satisfactory recording medium had been developed for long-wave infrared radiation. It does

appear that the microbolometer array may be the answer due to its excellent sensitivity and its compatibility with digital electronics.

In this paper we demonstrate what we believe to be a novel method for holography in the infrared using a microbolometer array as the recording medium with object illumination provided by a carbon dioxide laser operating at a 10.6 μm wavelength. This thermal detector array shows great promise for extending the practical waveband of holography from 1 μm well into the far-infrared or even into the submillimeter band of wavelengths. One can obtain high-quality holographic recordings at video rates of 30 frames/s using reference beam levels of milliwatts per centimeter squared and other power levels that are reminiscent of common practice either with a helium–neon or an argon-ion laser. The uncooled infrared imaging arrays at 10.6 μm are described in the literature [11] and a few commercial cameras are available, such as the Thermal-Eye 2000B that we used in our experiments [12]. To our knowledge, the only earlier publication on the recording of digital holograms at 10.6 μm is the report by Allaria *et al.* [13], in which a pyroelectric detector is used as an IR sensor.

We describe a two-beam hologram in which we use a Mach–Zehnder interferometer, a 10 W cw CO_2 laser, and a sensitive uncooled microbolometer array for recording electronic holograms. We also describe what we believe to be a novel algorithm for the direct sampling of carrier-frequency signals that is particularly simple and efficient. Following a description of the sampling algorithm, we present a series of experiments: interference fringes between two plane waves to show the high quality of the hologram, expanding a spherical picture wave and a plane wave, and a hologram recording of a transmissive object with the letters EL. An oral presentation of portions of this work on electronic holograms was made recently in a session dedicated to the memory of Professor Emmett N. Leith, a great scientist and beloved colleague [14,15]. Similarly, this first publication is dedicated to him.

2. Sparse-Sampling of Electronic Holograms

In a two-beam holography setup, the object beam is approximately conical with the angular spectrum of waves being centered on the normal to the hologram plane. The reference beam is at an angle and establishes the carrier frequency. The recorded hologram (apart from low-frequency intensity terms) may be described by a real-valued function:

$$g(x, y) = E_o(x, y)\exp(i2\pi f_o x) + E_o^*(x, y)\exp(-i2\pi f_o x). \quad (1)$$

The function $E_o(x, y)$ is the complex envelope of the fringe pattern and f_o denotes the carrier frequency or the mean fringe period, which is typically much larger than the effective bandwidth of the envelope function. Sampling of electronic holograms is an important issue for their digital storage, processing, and transmittal over communication channels (e.g., television). The highest frequency content in the function $g(x, y)$ is determined by the carrier frequency f_o. It is clear that with the knowledge of the carrier frequency (from the experimental setup), the unknown information in the object function has a highest frequency much smaller than the carrier. It is then valuable to seek a sampling criterion in which the sampling rate is related to the bandwidth of the object function $E_o(x, y)$ rather than the carrier frequency f_o. We have studied sparse-sampling formulae for direct sampling and demodulation of electronic holograms [16,17]. As is explained below the sparse sampling of the original recording enables one to eliminate the carrier frequency without the conventional demodulation, thereby saving much computation fast Fourier transforms. Moreover, in Subsection 3.C, we describe a method for improving the signal-to-noise ratio by the addition of four frames resulting from the sparse sampling.

Let the Fourier transform of the envelope function $E_o(x, y)$ be effectively band limited to a rectangular region of dimensions $2B_x \times 2B_y$ and centered on the origin in $f_x - f_y$ or spatial-frequency plane. Then for $B_{xo} \geq B_x$ and $B_{yo} \geq B_y$ such that

$$\frac{f_o}{2B_{xo}} = N + \frac{1}{2}, \quad (2)$$

for a positive integer N, we may write the following sampling expansions:

$$g(x, y) = \sum_{m=-\infty}^{\infty}\sum_{n=-\infty}^{\infty} g\left(\frac{m}{4B_{xo}}, \frac{n}{2B_{yo}}\right)\mathrm{sinc}\left[2B_{xo}\left(x - \frac{m}{4B_{xo}}\right)\right] \times \mathrm{sinc}\left[2B_{yo}\left(y - \frac{n}{2B_{yo}}\right)\right]\cos\left[2\pi f_o\left(x - \frac{m}{4B_{xo}}\right)\right], \quad (3)$$

$$E_o(x, y) = \frac{1}{2}\sum_{m=-\infty}^{\infty}\sum_{n=-\infty}^{\infty} g\left(\frac{m}{4B_{xo}}, \frac{n}{2B_{yo}}\right)\mathrm{sinc}\left[2B_{xo}\left(x - \frac{m}{4B_{xo}}\right)\right] \times \mathrm{sinc}\left[2B_{yo}\left(y - \frac{n}{4B_{yo}}\right)\right]\exp\left(-i2\pi f_o \frac{m}{4B_{xo}}\right). \quad (4)$$

For the proofs of the above results we refer the reader to [12,13], and in the following paragraphs we highlight some interesting features of the sampling formulae. The half-integer condition in Eq. (2) above is necessary for the nonoverlap of frequency bands in the Fourier domain in the sampling and interpolation process. It is important to observe that the sampling intervals in the above formulae are dependent on the bandwidth of the object function $E_o(x, y)$. The sampling gain is obtained in the direction normal to the carrier fringes and approximately equals the ratio of the carrier frequency to the bandwidth of the envelope function. Further, according to Eq. (2), the exponential term in Eq. (4) reduces to

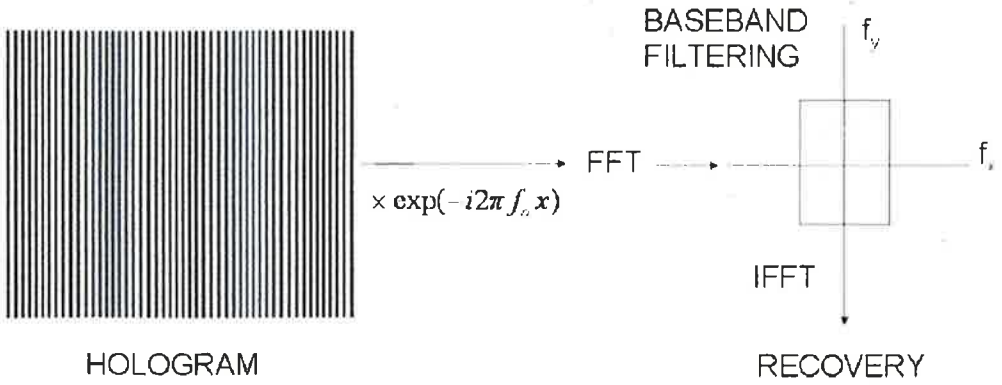

Fig. 1. Schematic diagram showing Fourier-transform-based processing of electronic holograms. FFT, fast Fourier transform; IFFT, inverse fast Fourier transform.

$$\exp\left(-i2\pi f_o \frac{m}{4B_{xo}}\right) = (-1)^{mN}(-i)^m, \qquad (5)$$

so that the alternate samples in each row of the sampling matrix contribute to the reconstruction of the real and the imaginary parts of $E_o(x, y)$, respectively.

The digital processing methods commonly used for digital processing of electronic holograms are either Fourier transform based or use a phase-shifting interferometry approach. The Fourier-transform-based approach is shown schematically in Fig. 1. The recorded hologram is multiplied by an exponential function representing the conjugate reference beam, followed by Fourier space baseband filtering to obtain the information about the complex object wavefront at the hologram plane. In the phase-shifting method, the phase of the reference beam is stepped in a predetermined manner and typically four or five interference patterns are used to obtain both the amplitude and phase information about the object wavefront at the hologram plane. We note that the Fourier-transform-based processing or phase-shifting techniques commonly used in electronic holography are mathematically equivalent to the conventional mixing process in demodulation of carrier-frequency signals. In our sparse-sampling method, this mixing step is replaced in principle by direct sampling and interpolation incorporating the knowledge of the carrier frequency without requiring any Fourier transformation operations. We also mention that if the carrier-frequency used in the sampling formulae differs from the actual carrier frequency by a small amount Δf_o, the reconstructions will show an overall beat pattern at Δf_o, which may be used to correct the error in f_o.

3. Experiments

A. Basic Setup for Recording

Consider the setup shown in Fig. 2, we use a Mach–Zehnder interferometer to record the off-axis hologram. A single-mode CO_2 laser (MPB Communications, Montreal, Quebec, Canada, Model GN-502) emits lights at 10.6 μm. The beam size is 3.6 mm and the output power is 10 W, which is sufficient for our hologram recording. The infrared beam is attenuated and directed to a beam expander that consists of two positive lenses with focal lengths of 25 and 125 mm. Two mirrors and two 50/50 beam splitters are used to form a Mach–Zehnder interferometer. With the Mach–Zehnder interferometer, we obtain the picture wave in the lower arm and the reference beam coming in as a plane wave at an angle that can be easily adjusted by tilting the mirror in the reference arm.

To facilitate the alignment, ZnSe material, which is transmissive to red light, is used for the lenses and beam splitters. A He–Ne laser beam is introduced by a flip mirror. Before the alignment, the adjustment is made to make sure that the He–Ne beam and the CO_2 beam are collinear. This is accomplished by checking the beam position near the laser and 5 m away. Thereafter, the alignment of the system using the He–Ne laser beam should be accurate enough for later fine adjustment when the camera is placed at the hologram plane. Although the setup is on a floating table, we typically do not float the table since the long-wave infrared system is not nearly so sensitive to vibration as a visible holography system.

The object used in this experiment is an opaque brass shim that has letters of 1 mm linewidth cut in by a milling machine, i.e., the letters inscribed are EL (7 mm across), standing for Emmett Leith. The microbolometer array (Thermal-Eye 2000B) is located

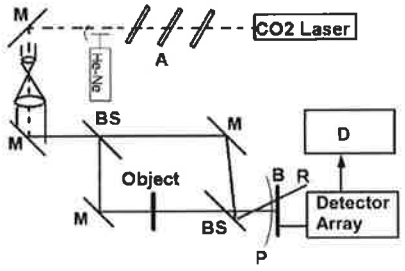

Fig. 2. Setup for infrared digital holography: A, attenuator; m, mirror; BS, beam splitter; P, picture wavefront; R, reference beam; D, display.

570 mm away from the object to record the intensity of the interference between the object and reference beams, which is offset by 1.6 deg. The array is an uncooled detector with a pixel size of 50 μm and an array size of 320 × 240. It is sensitive to a wavelength range of 7 to 14 μm. A battery-type dc power supply is used to avoid noise due to fluctuations of power supply. The interference image is collected by a computer via a PLEXTOR video frame grabber (PX-M402U).

B. Recording Fringe Patterns and Gratings

In the first experiment, we simply record the interference patterns of two plane waves with different angles. The purpose of this experiment is to show that microbolometer arrays are capable of recording fringe patterns of high quality at 10.6 μm and to check the smallest fringe separation the array is capable of recording. Figure 3 shows the results of two different angular separations of plane wave interference. Figure 3(a) shows the fringe pattern with a period of 2 mm, which corresponds to 0.3 deg separation between two plane waves. Figure 3(b) is the interference pattern with a period of 0.6 mm and a two-beam angle of 1 deg. Although it is clear that the fringe pattern with a period of 0.6 mm can be faithfully recorded as shown in Fig. 3(b), we emphasize that still finer fringes are possible. The pixel size of the microbolometer array is 50 μm. This implies that the finest fringe period can reach up to 0.1 mm, although some moiré pattern will be present in such fine fringes.

In the second simple illustration we show an interference pattern recorded using a plane beam and a diverging beam (Fig. 4). The diverging beam was generated by inserting a slightly defocused beam expander in the object arm of the interferometer. We could observe a linear motion of the zero-order fringe as the defocus in the beam expander changed sign—i.e., divergent to convergent beam. We include this example as a tutorial since it illustrates in a simple case the basis of the two-beam hologram. One can see clearly how the phase of a wave is recorded and the distinction between an expanding and a converging beam recorded by intensity.

Fig. 4. Interference of an expanding wave and a plane wave.

C. Experiment with a Transmissive Object

In this experiment, an opaque brass shim with the letters EL is placed in the lower arm of the interferometer. The optical path length from the object to the detector plane is $R = 570$ mm. The angular separation between the two beams is 1.6 deg, which yields a fringe period of 0.375 mm.

From the data given, the diffraction-limited resolution at the hologram itself is approximately $\lambda R/L$ where $R = 570$ mm and the detector's aperture $L = 15$ mm. This diffraction limit is of the order of 0.5 mm. The linewidth of the letters EL is 1.0 mm. To recover the object from the recorded intensity pattern, three images are taken. Figures 5(a) and 5(b) are the pattern with the object beam and reference beam, respectively. Figure 5(c) shows the hologram pattern recorded on the microbolometer array.

The hologram intensity recorded at the detector plane can be written as

$$I_d = |E_o + \exp(-i2\pi f_o x)|^2. \tag{6}$$

In the recovery process, we first subtract the intensities of both the reference and object beams from the interference intensity to obtain the carrier-frequency signal $E_0 \exp(i2\pi f_0 x) + E_0^* \exp(-i2\pi f_0 x)$. The direct-sampling method as in Eq. (4) is used to determine

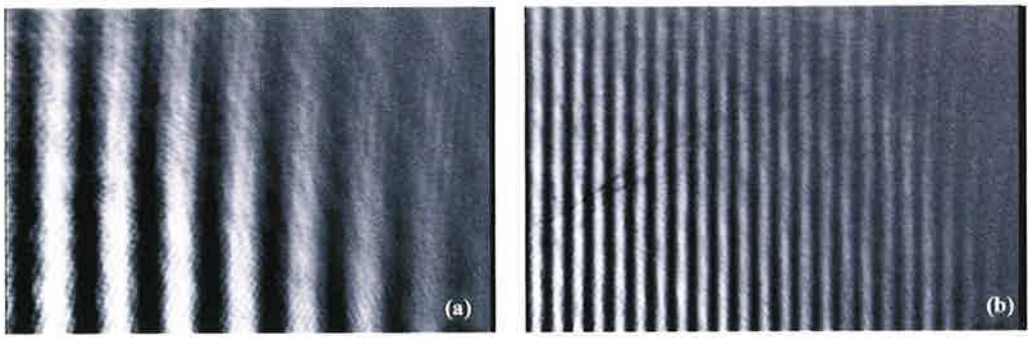

Fig. 3. Two-beam interference pattern recorded on a microbolometer array: (a) two-beam angle 0.3 deg; (b) two-beam angle 1 deg.

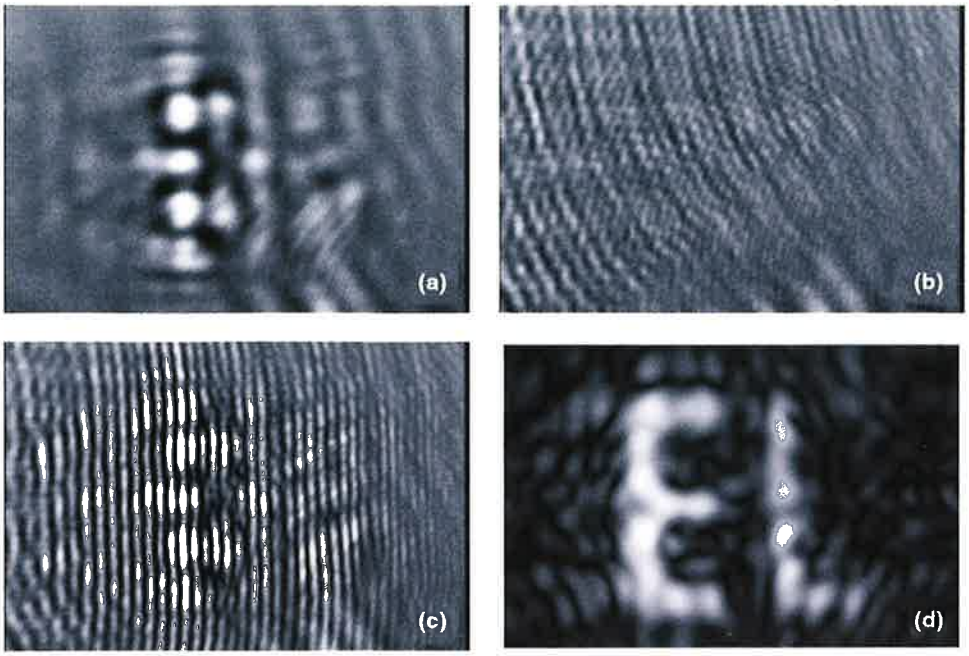

Fig. 5. Experimental recovery of a hologram of a transmissive object: (a) recorded diffraction pattern with only the object arm, (b) recorded plane wave pattern with only the reference arm, (c) recorded off-axis hologram, (d) recovery at the sparse-sampling interval.

the object field $E_o(x, y)$ at the detector plane. Note that in the process of subtracting the intensity terms we only need to consider the sparse array of samples as in Eq. (4).

A Fresnel backpropagation is then applied to recover the object field according to

$$E_{obj}(x, y) = \frac{-i \exp(i2\pi z/\lambda)}{\lambda z} \int_{-\infty}^{\infty} \int_{-\infty}^{\infty} dx' dy' E_o(x', y') \times \exp\left\{\frac{i\pi}{\lambda z}[(x - x')^2 + (y - y')^2]\right\}. \quad (7)$$

The calculation above is further simplified if we use the sampling formula (4) for $E_o(x, y)$, so that only one operation of Fresnel backprojection for a product of sinc functions is required. The contributions from various terms in the summation may then be added with appropriate phase shifts. The recovery of the object after sampling and Fresnel backpropagation is shown in Fig. 5(d).

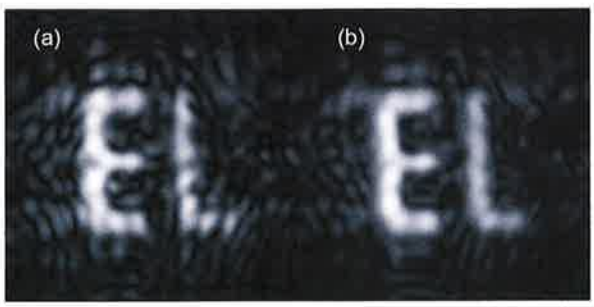

Fig. 6. Image recovery using (a) one set of sparse samples and (b) averaging recoveries from four independent sample sets.

A total number of 40 fringes was observed in the particular setup across the field of view. In this example we have obtained a sampling gain of ~3 over the conventional usage of the Nyquist sampling interval. This gain will be higher for finer fringes since the object beam bandwidth remains the same for the same object. The sampling array used for the reconstruction consists of a sparse array of pixels. We may use data from more detector pixels as follows. For example, the first reconstruction may be performed by using pixel numbers 1, $(M + 1)$, $(2M + 1)$, $(3M + 1), \ldots,$ etc. in a pixel row; the second reconstruction may be performed using another set of pixels 2, $(M + 2)$, $(2M + 2), \ldots,$ etc. in a pixel row and so on. Here M is an integer closest to the sampling interval $(1/4B_{xo})$ along the x axis. Note that each set of samples above contains all the information needed to reconstruct the image. Figure 6(b) below shows the average of four independently reconstructed images. One of the individual reconstructions is shown in Fig. 6(a) for comparison. The specklelike noise is seen to decrease due to this averaging to obtain an excellent image recovery.

4. Summary

We have described a novel method for holography in the far-infrared wavelength regime using a microbolometer array. Active illumination from a 10.6 μm CO_2 laser was used to record a hologram with an angle between the object and reference beams equal to ~1.6 deg. The setup is less sensitive

to vibrations as compared with that at visible wavelengths. A sparse-sampling method is used to reconstruct the complex object field in the hologram plane and image reconstruction is achieved by Fresnel backpropagation to the object plane. Several important features of the sparse-sampling method are discussed. Two important advantages of this novel signal recovery method are that (1) the picture signal is recovered directly without demodulation and (2) the signal-to-noise ratio is improved by later superposition of individual frames, thereby using all the data. The microbolometer arrays are an ideal choice for recording far-infrared holograms and also appear to be an attractive choice for holography at even longer (submillimeter) wavelengths.

This research was sponsored in part by the U.S. Army Research Office.

References

1. E. N. Leith and J. Upatnieks, "Reconstructed wavefronts and communication theory," J. Opt. Soc. Am. **52,** 1123–1130 (1962).
2. U. Schnars and W. Jueptner, *Digital Holography: Digital Hologram Recording, Numerical Reconstruction, and Related Techniques* (Springer-Verlag, 2007).
3. L. Yaroslavsky, *Digital Holography and Digital Image Processing: Principles, Methods, Algorithms* (Kluwer Academic, 2003).
4. E. Leith, H. Chen, Y. Chen, D. Dilworth, J. Lopez, R. Masri, J. Rudd, and J. Valdmanis, "Imaging through tissues with electronic holography and femtosecond pulses," Proc. SPIE **1600,** 172–177 (1991).
5. E. Tajahuerce and B. Javidi, "Encrypting three-dimensional information with digital holography," Appl. Opt. **39,** 6595–6601 (2000).
6. I. Yamaguchi, T. Matsumura, and J. Kato, "Phase-shifting color digital holography," Opt. Lett. **27,** 1108–1110 (2002).
7. R. M. Beaulieu and R. A. Lessard, "Review of recording media for holography at 10.6 microns," Proc. SPIE **3011,** 298–305 (1997).
8. J. S. Chivian, R. N. Claytor, and D. D. Eden, "Infrared holography at 10.6 μm," Appl. Phys. Lett. **15,** 123–125 (1969).
9. T. Izawa and M. Kamiyama, "Infrared holography with organic photochromic films," Appl. Phys. Lett. **15,** 201–201 (1969).
10. O. Kwon, J. C. Wyant, and C. R. Hayslett, "Rough surface interferometry at 10.6 μm," Appl. Opt. **19,** 1862–1869 (1980).
11. P. W. Kruse and D. D. Skatrud, *Uncooled Infrared Imaging Arrays and Systems* (Academic, 1997), Vol. 47.
12. Thermal-Eye, Model 2000B, barium strontium titanate (320 × 240 pixel array), L3 Communications Infrared Products, Dallas, Tex, USA.
13. E. Allaria, S. Brugioni, S. D. Nicolas, P. Ferraro, S. Grilli, and R. Meucci, "Digital holography at 10.6 μm," Opt. Commun. **215,** 257–262 (2003).
14. N. George, K. Khare, and W. Chi, "Electronic holography at terahertz and infrared frequencies," in *Proceedings of the Seventh International Symposium on Display Holography,* H. I. Bjelkhagen, ed. (River Valley, 2006), pp. 117–119.
15. N. George, K. Khare, and W. Chi, "Long-wave infrared holography using a microbolometer array," presented at the Annual Meeting of the Optical Society of America, Rochester, New York, 8–12 October 2006.
16. K. Khare and N. George, "Direct sampling and demodulation of carrier-frequency signals," Opt. Commun. **211,** 85–94 (2002).
17. K. Khare and N. George, "Direct coarse sampling of electronic holograms," Opt. Lett. **28,** 1004–1006 (2003).

Speckle in the 4F optical system

Nien-An Chang* and Nicholas George

The Institute of Optics, University of Rochester, Rochester, New York 14627, USA

*Corresponding author: nachang@optics.rochester.edu

Received 23 April 2007; revised 24 July 2007; accepted 1 August 2007;
posted 8 August 2007 (Doc. ID 82242); published 18 September 2007

We provide a comprehensive analysis of the space and wavelength dependence of speckle generated by a thin diffuser and imaged by a 4F optical system. The use of this space-invariant system is shown to lead to the well-known features of speckle patterns in an analytically simple and elegant manner, thereby providing a clear insight into speckle in an optical configuration that includes the Fresnel zone, the optical Fourier transform plane, and the image plane. In our analysis we assume a white-noise diffuser. The spatial variation mainly depends on the imaging system, whereas the wavelength dependence is related to diffuser heights. Motion dynamics of speckle are also included.

OCIS codes: 030.6140, 110.6150.

1. Introduction

The statistics of speckle have been investigated by many researchers. One of the earliest studies was made by Lord Rayleigh, who established the mathematical basis for the analysis of statistics of the problem of random walk [1]. The modern treatment of speckle is covered extensively in the published literature and in textbooks [2–5]. We include some relevant references about the space and wavelength dependence of speckle [6–13]. Cheng *et al.* [13] use image-speckle contrast to obtain the lateral-correlation length and roughness, and they accomplish this by changing the size of the filtering aperture and fitting the theoretical formula for speckle contrast to the experimental data. Earlier analytical work on the space and wavelength dependence of speckle can be found in the literature [7–9]. In a free-space geometry Leushacke and Kirchner [11] and Li and Chiang [12] have written important literature. These analyses are accurate in the Fresnel zone region and therefore they provide precise results. However, the appearance of quadratic phase terms make the derivations difficult and lengthy.

In this paper we describe the space and wavelength dependence of speckle in a 4F optical system. One of our major objectives is to establish the basic features of speckle patterns by the choice of an optical system that can be analyzed without undue simplifying assumptions or deductions that would not be well known to nonexperts in the field. In this context the usefulness of the 4F optical system appears to offer an elegant configuration for one to study speckle effects. In Fourier optics this optical system is particularly advantageous for a consideration of imaging and processing since the cumbersome quadratic exponential factors generally associated with Fresnel zone propagation largely cancel out. Hence, it is an ideal configuration, as well, for a careful treatment of speckle in an optical system. For the space dependence of speckle, we particularly focus on results concerning the decorrelation of speckle patterns along the optical axis.

The 4F optical system is composed of an input plane, two lenses of focal length F, an aperture, and an output image plane (see Fig. 1). We use a thin diffuser, also known as a phase-type diffuser, as the object that is imaged by the 4F optical system. The space and wavelength dependence of speckle is examined by using the cross-spectral density function $\langle w(x_1, y_1, z_1; \nu_1) w^*(x_2, y_2, z_2; \nu_2)\rangle$, where w is the energy density in the electric field; x, y, and z are spatial coordinates in a Cartesian coordinate system; and ν is the frequency. The energy density $w(x, y, z; \nu)$ is given by $w = \mathbf{E} \cdot \mathbf{E}^*$, which, for the linearly polarized electric field E_y, reduces simply to $w = E_y E_y^*$, where herein we assume harmonic time dependence given by $\exp[i\omega t]$. In Subsection 2.A we describe the fea-

0003-6935/08/0400A13-8$15.00/0

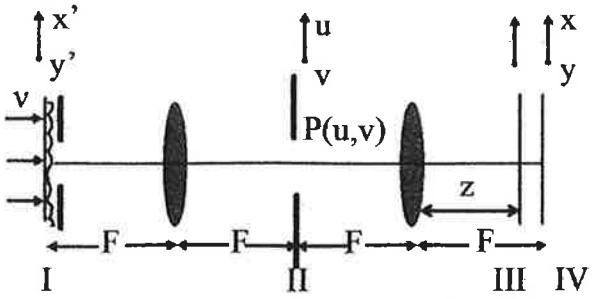

Fig. 1. 4F optical system. Object is imaged onto the output plane by two lenses with focal length F and an aperture with diameter D.

tures of speckle generated through a 4F optical system with a rectangular aperture. The spatial offset along the optical axis needed to decorrelate the speckle patterns is found to be the depth of field of the system [14] and is in good agreement with previous studies [11,12]. In Subsection 2.B the motion dynamics of speckle at any plane are discussed. We describe the dynamics of speckle patterns, created by the illumination of a fixed wavelength on a thin diffuser, in four zones shown in Fig. 5 below. The result shows that when the object is moved upward, the speckle pattern moves upward in zone I and downward in zones II, III, and IV. The statistics of speckle dynamics produced by a moving diffuse object were also extensively investigated by Asakura and co-workers [15–18]. The speckle dynamics mentioned above are categorized as the objective motion of the speckle. Speckle motion observed by human eyes, on the other hand, depends on whether the observer is nearsighted or farsighted, and Sinclair explained this interesting phenomena in terms of aberration theory, including a proposal for diagnosis [19]. This type of motion on an internal inaccessible moving screen is not considered further in the study of the motion dynamics of speckle in this paper.

2. Space and Wavelength Dependence of Speckle

Suppose a monochromatic plane-polarized field with frequency ν is normally incident on a thin diffuser as in Fig. 1. It is assumed that the incident field experiences only phase change and essentially remains plane polarized. Thus in the analysis only a single component of the tangential electric field is considered. In brief review of the analysis for the 4F optical processor, we summarize the computation from plane I to II (the Fourier transform) and then from plane II to IV to obtain the image in Appendix A.1–2. In Appendix A.3, we derive an expression for $E_{y3}(x, y, z; \nu)$ at plane III, which is an axial distance z away from the second lens. This output scalar electric field $E_{y3}(x, y, z; \nu)$ is given by

$$E_{y3}(x, y, z; \nu) = \frac{-\nu^2 e^{ik(3F+z)}}{c^2F^2}\int_{-\infty}^{\infty}\int_{-\infty}^{\infty}\int_{-\infty}^{\infty}\int_{-\infty}^{\infty} du\,dv\,dx'\,dy' \times e^{-i2\pi\eta h(x',y')}P(u, v) \times e^{\frac{i\pi\nu(z-F)(u^2+v^2)}{cF^2}+\frac{i2\pi\nu(xx'+yy')u+(yx'+xy')v]}{cF}}, \quad (1)$$

where c is the speed of light, $\exp[-i2\pi\eta h(x', y')]$ is the expression for a phase-type diffuser at the input plane, $h(x', y')$ is the roughness of the diffuser, $\eta = (n - 1)\nu/c$ is the normalized frequency variable, and n is the refractive index of the diffuser. The space and wavelength dependence of the speckle is calculated using the cross-spectral density function

$$\langle w(x_1, y_1, z_1; \nu_1)w^*(x_2, y_2, z_2; \nu_2)\rangle = \langle E_y(x_1, y_1, z_1; \nu_1)E_y^*(x_1, y_1, z_1; \nu_1) \times E_y(x_2, y_2, z_2; \nu_2)E_y^*(x_2, y_2, z_2; \nu_2)\rangle. \quad (2)$$

With the assumption of Gaussian statistics for the output electric field, the expectation value of the product of four normal, stationary, random variables can be expanded as follows [20]:

$$\langle w(x_1, y_1, z_1; \nu_1)w^*(x_2, y_2, z_2; \nu_2)\rangle = \langle w(x_1, y_1, z_1; \nu_1)\rangle\langle w(x_2, y_2, z_2; \nu_2)\rangle + |\langle E_y(x_1, y_1, z_1; \nu_1)E_y^*(x_2, y_2, z_2; \nu_2)\rangle|^2. \quad (3)$$

In this section we calculate the second-order moment for the Eq. (3) cross-correlation function $\langle E_y(x_1, y_1, z_1; \nu_1)E_y^*(x_2, y_2, z_2; \nu_2)\rangle$. From this we can obtain speckle size as a function of space and wavelength parameters. The correlation function of the output electric field is given by

$$\langle E_{y3}(x_1, y_1, z_1; \nu_1)E_{y3}^*(x_2, y_2, z_2; \nu_2)\rangle = \int_{-\infty}^{\infty}\cdots\int_{-\infty}^{\infty} du\,du'\,dv\,dv'\,dx'\,dx''\,dy'\,dy'' \times \langle e^{-i2\pi[\eta_1 h(x',y') - \eta_2 h(x'',y'')]}\rangle \times H(x_1, y_1, z_1; u, v; x', y'; \nu_1) \times H^*(x_2, y_2, z_2; u', v'; x'', y''; \nu_2), \quad (4)$$

where $H(x, y, z; u, v; x', y'; \nu)$ is written as

$$H(x, y, z; u, v; x', y'; \nu) = \frac{\nu^2}{c^2F^2}P(u, v)e^{\frac{i\pi\nu(z-F)(u^2+v^2)}{cF^2}+\frac{i2\pi\nu[(x+x')u+(y+y')v]}{cF}}. \quad (5)$$

We assume that the input random process is spatially stationary, hence depending only on the coordinate difference $(x' - x'', y' - y'')$. Then it is convenient to adopt R_g as the correlation function for the input random process,

$$R_g(x' - x'', y' - y''; \eta_1, \eta_2) = \langle\exp\{-i2\pi[\eta_1 h(x', y') - \eta_2 h(x'', y'')]\}\rangle. \quad (6)$$

We also assume a white-noise diffuser, an idealized phase-type diffuser with short spatial correlation lengths. This type of diffuser yields a simplified result that provides clear insight into speckle sizes. A detailed description of the correlation function, R_g, for a

white-noise diffuser is given in [9] and is written as

$$R_g(x'-x'', y'-y''; \eta_1, \eta_2) = A(\eta_1, \eta_2)\delta(x'-x'', y'-y'') \times e^{-\frac{[2\pi(\eta_1-\eta_2)\sigma]^2}{2}}, \quad (7)$$

assuming $h(x', y')$ and $h(x'', y'')$ have zero means and equal rms values σ. The constant A is

$$A(\eta_1, \eta_2) = \frac{2\pi l_0^2}{\alpha^2}[1 - e^{-\alpha}(1+\alpha)], \quad (8)$$

where l_0 is the correlation length and $\alpha = (2\pi\sigma)^2\eta_1\eta_2$. Integrating over dx'' and dy'', we can then write Eq. (4) as

$$\begin{aligned}\langle E_{y3}(x_1, y_1, z_1; \nu_1)E_{y3}^*(x_2, y_2, z_2; \nu_2)\rangle &= Ae^{-\frac{[2\pi(\eta_1-\eta_2)\sigma]^2}{2}}\int_{-\infty}^{\infty}\cdots\int_{-\infty}^{\infty} du\,du'\,dv\,dv'\,dx'\,dy' \\ &\times H(x_1, y_1, z_1; u, v; x', y'; \nu_1) \\ &\times H^*(x_2, y_2, z_2; u', v'; x', y'; \nu_2). \end{aligned} \quad (9)$$

We calculate the integration by inserting Eq. (5) into Eq. (9), and the calculation is detailed in Appendix B. We have the following result:

$$\begin{aligned}\langle E_{y3}(x_1, y_1, z_1; \nu_1)E_{y3}^*(x_2, y_2, z_2; \nu_2)\rangle &= \frac{A\nu_0^2 e^{-\frac{[2\pi(\eta_1-\eta_2)\sigma]^2}{2}}}{c^2F^2}\int_{-\infty}^{\infty}\int_{-\infty}^{\infty} du'\,dv'P(u', v') \\ &\times e^{\frac{i2\pi\nu_0}{cF}[(x_1-x_2)u'+(y_1-y_2)v']}e^{\frac{i\pi\nu_0(z_1-z_2)}{cF^2}(u'^2+v'^2)}, \end{aligned} \quad (10)$$

where ν_0 is the mean of ν_1 and ν_2. Note that now the wavelength variation is separated from the space variation. The concept of speckle sizes is illustrated in Fig. 2. The speckle size along the plane perpendicular to the optical axis is called $d_\perp$, and the speckle size along the optical axis is called $d_\parallel$. The speckle sizes are interpreted as the variation needed to decorrelate the cross-correlation function, i.e., when the value reaches the first minimum.

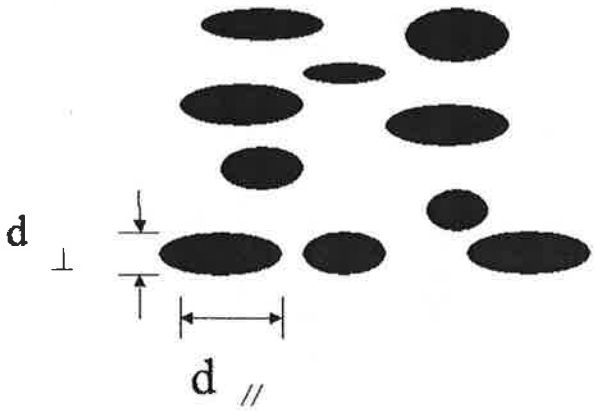

Fig. 2. Speckle sizes in two dimensions.

For $d_\perp$, $d_\perp$ is obtained by setting $z_1 = z_2 = z$, i.e.,

$$\begin{aligned}\langle E_{y3}(x_1, y_1, z_1; \nu_1)E_{y3}^*(x_1+\Delta x, y_1+\Delta y, z; \nu_2)\rangle &= \frac{A\nu_0^2 e^{-\frac{[2\pi(\eta_1-\eta_2)\sigma]^2}{2}}}{c^2F^2}\int_{-\infty}^{\infty}\int_{-\infty}^{\infty} du'\,dv'P(u', v') \\ &\times e^{\frac{i2\pi\nu_0}{cF}[\Delta x u'+\Delta y v']}, \end{aligned} \quad (11)$$

where $\Delta x = x_1 - x_2$ and $\Delta y = y_1 - y_2$.

For $d_\parallel$, $d_\parallel$ is obtained by setting $x_1 = x_2 = x$ and $y_1 = y_2 = y$, i.e.,

$$\begin{aligned}\langle E_{y3}(x, y, z_1; \nu_1)E_{y3}^*(x, y, z_2; \nu_2)\rangle &= \frac{A\nu_0^2 e^{-\frac{[2\pi(\eta_1-\eta_2)\sigma]^2}{2}}}{c^2F^2} \\ &\times \int_{-\infty}^{\infty}\int_{-\infty}^{\infty} du'\,dv'P(u', v')e^{\frac{i\pi\nu_0\Delta z}{cF^2}(u'^2+v'^2)}, \end{aligned} \quad (12)$$

where $\Delta z = z_1 - z_2$.

A. Square Aperture

For a square aperture, the aperture function $P(u', v') = \mathrm{rect}(u'/D)\mathrm{rect}(v'/D)$. Equation (11) becomes

$$\langle E_{y3}(x_1, y_1, z; \nu_1)E_{y3}^*(x_1+\Delta x, y_1+\Delta y, z; \nu_2)\rangle = \frac{A\nu_0^2D^2e^{-\frac{[2\pi(\eta_1-\eta_2)\sigma]^2}{2}}}{c^2F^2}\mathrm{sinc}\left(\frac{D\nu_0\Delta x}{cF}\right)\mathrm{sinc}\left(\frac{D\nu_0\Delta y}{cF}\right). \quad (13)$$

The speckle sizes along the x and y axes are defined as the interval for the absolute value of the cross-correlation function to reach the first minimum, i.e., $d_\perp = \Delta x = \Delta y = cF/\nu_0 D$, which is the size of an airy disk.

Equation (12) becomes

$$\langle E_{y3}(x, y, z_1; \nu_1)E_{y3}^*(x, y, z_2; \nu_2)\rangle = \frac{A\nu_0^2D^2e^{-\frac{[2\pi(\eta_1-\eta_2)\sigma]^2}{2}}}{c^2F^2}\left[\frac{C(t)}{t} + i\frac{S(t)}{t}\right]^2, \quad (14)$$

where $t = \sqrt{D^2\nu_0|\Delta z|/2cF^2}$ and C and S are the Fresnel integral of cosine and sine, respectively, and are defined in the literature [21] as follows:

$$C(\xi) = \int_0^\xi \cos\left(\frac{\pi t^2}{2}\right)dt, \quad (15)$$

$$S(\xi) = \int_0^\xi \sin\left(\frac{\pi t^2}{2}\right)dt. \quad (16)$$

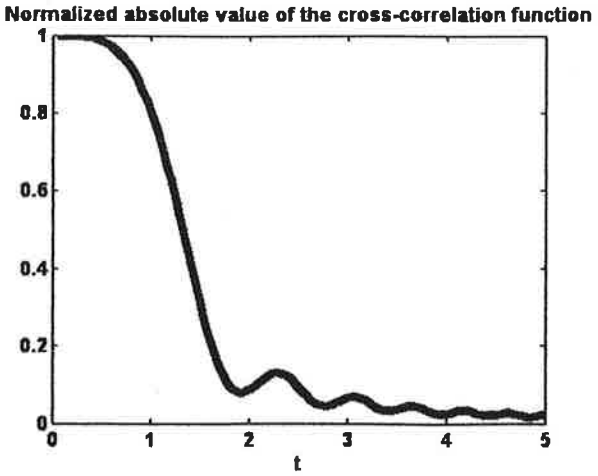

Fig. 3. Normalized absolute value of the cross-correlation function versus t using a square aperture.

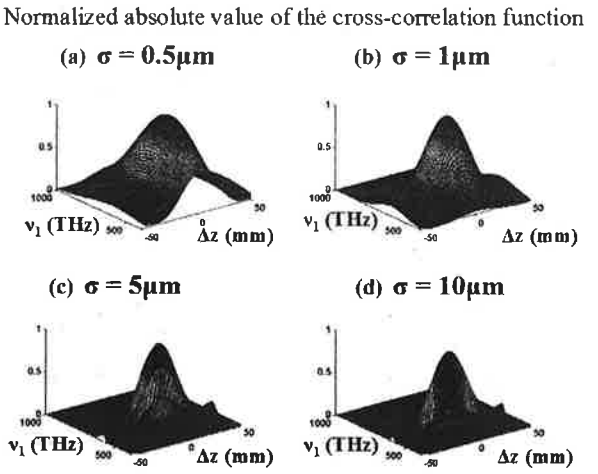

Fig. 4. Normalized cross-spectral density function versus Δz and λ_2 using a square aperture with varying diffuser roughness.

The first minimum of the absolute value of the cross-correlation function is located at $t \approx 2$ (see Fig. 3). The speckle size along the z axis $d_\parallel$ is given by

$$d_\parallel \approx \frac{8cF^2}{\nu_0 D^2}, \tag{17}$$

which is the depth of field of the system [14]. If speckle patterns recorded at ν_1 and ν_2 are cross correlated, the correlation function will sharply drop within a spectral interval, which defines the wavelength spacing for decorrelation. For wavelength dependence of speckle, i.e., $z_1 = z_2 = z$,

$$\langle E_{y3}(x, y, z; \nu_1) E_{y3}^*(x, y, z; \nu_2)\rangle = \frac{A\nu_0^2 e^{-\frac{[2\pi(\eta_1-\eta_2)\sigma]^2}{2}}}{c^2F^2}. \tag{18}$$

Using the definition for η and considering the speckle to be decorrelated when the exponential decreases to $\exp(-1)$, we find that the wavelength interval required to decorrelate the speckle is given by

$$\Delta\nu = \frac{\sqrt{2}c}{\sigma(n-1)}. \tag{19}$$

As seen in Fig. 4, the temporal frequency interval is seen to decrease sharply as the rms roughness σ increases. The spatial variation is insensitive to σ as predicted by Eq. (17). Values of aperture diameter $D = 1$ mm, focal length $F = 100$ mm, and $\lambda_1 = 0.5$ μm are used.

B. Motion Dynamics of Speckle at Any Plane

1. *Motion Dynamics of Speckle in Zone I*

In the analysis of motion dynamics of speckle at any plane, we assume Fresnel zone approximation (paraxial approximation) and one-dimensional analysis, i.e., the output speckle intensity w_1 at zone I in Fig. 5 is given by [22]

$$w_1(x_1, z_1; \lambda) = |E_{y1}(x_1, z_1; \lambda)|^2 = \frac{1}{\lambda^2 F z_1}\left|\int_{-\infty}^{\infty}\int_{-\infty}^{\infty} dx' d\xi_1 E_0(x')P(x') \times e^{\frac{i\pi x'^2}{\lambda F}+\frac{i\pi\xi_1^2}{\pi z_1}-\frac{i2\pi}{\lambda}\left(\frac{x'}{F}+\frac{x_1}{z_1}\right)\xi_1}\right|^2, \tag{20}$$

where $E_0(x')$ is the scalar electric field coming out of the diffuser and $P(x) = \mathrm{rect}(x'/D_1)$ is the aperture function right next to the diffuser. By integrating over $d\xi_1$, we have

$$w_1(x_1, z_1; \lambda) = \frac{1}{\lambda F}\left|\int_{-\infty}^{\infty} dx' E_0(x')P(x') e^{\frac{i\pi(F-z_1)x'^2}{\lambda F^2}-\frac{i2\pi x_1 x'}{\lambda F}}\right|^2. \tag{21}$$

By moving the object (diffuser and aperture) up by the amount of a, i.e., $E_0(x')P_1(x')$ is now $E_0(x' - a)P_1(x' - a)$, the speckle pattern becomes

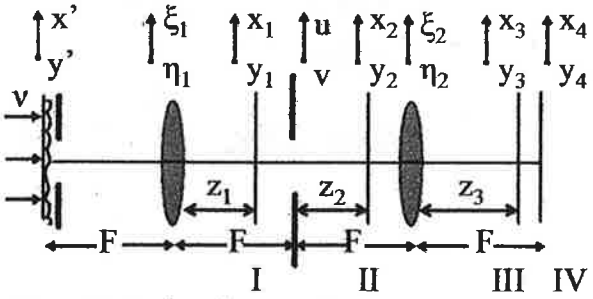

Fig. 5. Motion dynamics of speckle in zones I, II, III, and IV.

$$w_1'(x_1, z_1; \lambda) = \frac{1}{\lambda F}\left|\int_{-\infty}^{\infty} dx' E_0(x'-a)P_1(x'-a) \times e^{\frac{i\pi(F-z_1)x'^2}{\lambda F^2} - \frac{i2\pi x_1 x'}{\lambda F}}\right|^2. \quad (22)$$

Introducing a new variable $x'' = x' - a$, Eq. (22) is given by

$$w_1'(x_1, z_1; \lambda) = \frac{1}{\lambda F}\left|\int_{-\infty}^{\infty} dx'' E_0(x'')P_1(x'') \times e^{\frac{i\pi(F-z_1)x''^2}{\lambda F^2} - \frac{i2\pi}{\lambda}\left[x_1 - \left(1-\frac{z_1}{F}\right)a\right]x''}\right|^2. \quad (23)$$

By comparing $w_1'(x_1, z_1; \lambda)$ and $w_1(x_1, z_1; \lambda)$, we have

$$w_1'(x_1, z_1; \lambda) = w_1\left(x_1 - \left(1-\frac{z_1}{F}\right)a; \lambda\right). \quad (24)$$

The speckle pattern in zone I in Fig. 5 from shifting the diffuser upward by the amount of a is shifted upward by the amount of $(1 - z_1/F)a$. We observe the same result in our experimental setup. In the geometrical optics point of view, one can trace rays from an infinite conjugate through the first lens and obtain an upright pattern in zone I. The pattern moves in the same direction as the object and has a magnification of $(1 - z_1/F)$. Another interesting observation is when we move the CCD to the transform plane (the aperture) the speckle pattern twinkles instead of translating. As the light scatters from the diffuser, each point of the speckle pattern results from the sum of the phases from the whole area of the diffuser, which can be modeled as a random walk. The speckle pattern decorrelates when we move the diffuser by the distance of half the diffuser size.

2. Motion Dynamics of Speckle in Zone II

The output speckle intensity in zone II in Fig. 5 is given by [22]

$$w_2(x_2, z_2; \lambda) = |E_{y2}(x_2, z_2; \lambda)|^2 = \frac{1}{\lambda z_2}\left|\int_{-\infty}^{\infty} du E_2(u)P_2(u)e^{\frac{i\pi}{\lambda z_2}(x_2-u)^2}\right|^2, \quad (25)$$

where $E_2(u)$ and $P_2(u)$ are the scalar electric field and the aperture function located halfway between the two lenses, respectively. $E_2(u)$ is written as

$$E_2(u) = \sqrt{\frac{-i}{\lambda F}}\int_{-\infty}^{\infty} dx' E_0(x')P_1(x')e^{-\frac{i2\pi x' u}{\lambda F}}. \quad (26)$$

Assume $P_2(u) = \mathrm{rect}(u/D_2)$, then Eq. (25) becomes

$$w_2(x_2, z_2; \lambda) = \frac{1}{\lambda^2 F z_2}\left|\int_{-\infty}^{\infty}\int_{-\infty}^{\infty} dx' du E_0(x')P_1(x') \times \mathrm{rect}\left(\frac{u}{D_2}\right)e^{\frac{i\pi}{\lambda z_2}u^2 - \frac{i2\pi}{\lambda}\left(\frac{x'}{F}+\frac{x_2}{z_2}\right)u}\right|^2. \quad (27)$$

Integrating over du we have

$$w_2(x_2, z_2; \lambda) = \frac{1}{2\lambda F}\left|\int_{-\infty}^{\infty} dx' E_0(x')P_1(x')e^{\frac{i\pi z_2 x'^2}{\lambda F^2} - \frac{i2\pi x' x_2}{\lambda F}} \times \left\{C\left[\frac{D_2 - 2\left(x_2 + \frac{z_2 x'}{F}\right)}{\sqrt{2\lambda z_2}}\right] + C\left[\frac{D_2 + 2\left(x_2 + \frac{z_2 x'}{F}\right)}{\sqrt{2\lambda z_2}}\right] + iS\left[\frac{D_2 - 2\left(x_2 + \frac{z_2 x'}{F}\right)}{\sqrt{2\lambda z_2}}\right] + iS\left[\frac{D_2 + 2\left(x_2 + \frac{z_2 x'}{F}\right)}{\sqrt{2\lambda z_2}}\right]\right\}\right|^2. \quad (28)$$

By moving the object (diffuser and aperture) up by the amount of a, i.e., $E_0(x' - a)P_1(x' - a) = E_0(x'')P_1(x'')$, the speckle pattern becomes

$$w_2'(x_2, z_2; \lambda) = \frac{1}{2\lambda F}\left|\int_{-\infty}^{\infty} dx'' E_0(x'')P_1(x'') \times e^{\frac{i\pi z_2 x''^2}{\lambda F^2} - \frac{i2\pi x''\left(x_2 + \frac{z_2 a}{F}\right)}{\lambda F}} \times \left\{C\left[\frac{D_2 - 2\left(\left(x_2 + \frac{z_2 a}{F}\right) + \frac{z_2 x''}{F}\right)}{\sqrt{2\lambda z_2}}\right] + C\left[\frac{D_2 + 2\left(\left(x_2 + \frac{z_2 a}{F}\right) + \frac{z_2 x''}{F}\right)}{\sqrt{2\lambda z_2}}\right] + iS\left[\frac{D_2 - 2\left(\left(x_2 + \frac{z_2 a}{F}\right) + \frac{z_2 x''}{F}\right)}{\sqrt{2\lambda z_2}}\right] + iS\left[\frac{D_2 + 2\left(\left(x_2 + \frac{z_2 a}{F}\right) + \frac{z_2 x''}{F}\right)}{\sqrt{2\lambda z_2}}\right]\right\}\right|^2. \quad (29)$$

By comparing $w_2'(x_2, z_2; \lambda)$ and $w_2(x_2, z_2; \lambda)$, we have

$$w_2'(x_2, z_2; \lambda) = w_2\left(x_2 + \frac{z_2 a}{F}; \lambda\right). \quad (30)$$

The speckle pattern in zone II in Fig. 5 from shifting the object upward by the amount of a is shifted downward by the amount of $z_2 a/F$. We observe the same

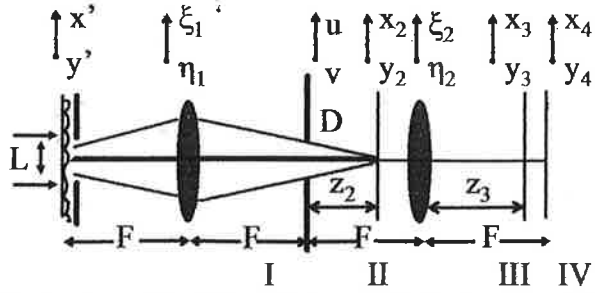

Fig. 6. Area of the diffuser that is contributing to one on-axis point.

result in our experimental setup. In the geometrical optics point of view, one can trace rays from an infinite conjugate through the first lens and the aperture and obtain a reversed image in zone II. The pattern moves in the opposite direction as the object and has a magnification of z_2/F. As we move the CCD slowly away from the transform plane to the second lens, we observe the translation and the twinkling effect of the speckle pattern. Also it takes less shifting of the diffuser to decorrelate the speckle pattern as we move the CCD closer to the second lens. From a simple geometry calculation, the area of the diffuser that is contributing to a certain point at a distance z_2 from the transform plane in Fig. 6 is found to be $L = FD/z_2$, where D is the aperture size. The speckle pattern decorrelates when the diffuser is moved by half the size, i.e., $FD/2z_2$.

3. *Motion Dynamics of Speckle in Zone III*

The output speckle intensity in zone III in Fig. 5 is given by [22]

$$w_3(x_3, z_3; \lambda) = |E_{y3}(x_3, z_3; \lambda)|^2 = \frac{-1}{\lambda F}\left|\int_{-\infty}^{\infty} du E_2(u) P_2(u) e^{\frac{i\pi}{\lambda F}\left(1-\frac{z_3}{F}\right)u^2 - \frac{i2\pi x_3 u}{\lambda F}}\right|^2. \tag{31}$$

Inserting Eq. (32) into Eq. (31) and integrating over du we have

$$w_3(x_3, z_3; \lambda) = \frac{-F}{2(F-z_3)}\left|\int_{-\infty}^{\infty} dx' E_0(x') P_1(x') \times e^{-\frac{i\pi}{\lambda(F-z_3)}x'^2 - \frac{i2\pi x_3 x'}{\lambda(F-z_3)}} \times \left\{C\left[\sqrt{\frac{F-z_3}{2\lambda F^2}}\left(D_2 - \frac{2F(x'+x_3)}{F-z_3}\right)\right] + C\left[\sqrt{\frac{F-z_3}{2\lambda F^2}}\left(D_2 + \frac{2F(x'+x_3)}{F-z_3}\right)\right] + iS\left[\sqrt{\frac{F-z_3}{2\lambda F^2}}\left(D_2 - \frac{2F(x'+x_3)}{F-z_3}\right)\right] + iS\left[\sqrt{\frac{F-z_3}{2\lambda F^2}}\left(D_2 + \frac{2F(x'+x_3)}{F-z_3}\right)\right]\right\}\right|^2. \tag{32}$$

By moving the object (diffuser and aperture) up by the amount of a, i.e., $E_0(x'-a)P_1(x'-a) = E_0(x'')P_1(x'')$, the speckle pattern becomes

$$w_3'(x_3, z_3; \lambda) = \frac{-F}{2(F-z_3)}\left|\int_{-\infty}^{\infty} dx'' E_0(x'') P_1(x'') \times e^{-\frac{i\pi}{\lambda(F-z_3)}x''^2 - \frac{i2\pi(x_3+a)x''}{\lambda(F-z_3)}} \times \left\{C\left[\sqrt{\frac{F-z_3}{2\lambda F^2}}\left(D_2 - \frac{2F(x''+(x_3+a))}{F-z_3}\right)\right] + C\left[\sqrt{\frac{F-z_3}{2\lambda F^2}}\left(D_2 + \frac{2F(x''+(x_3+a))}{F-z_3}\right)\right] + iS\left[\sqrt{\frac{F-z_3}{2\lambda F^2}}\left(D_2 - \frac{2F(x''+(x_3+a))}{F-z_3}\right)\right] + iS\left[\sqrt{\frac{F-z_3}{2\lambda F^2}}\left(D_2 + \frac{2F(x''+(x_3+a))}{F-z_3}\right)\right]\right\}\right|^2. \tag{33}$$

By comparing $w_3'(x_3, z_3; \lambda)$ and $w_3(x_3, z_3; \lambda)$, we have

$$w_3'(x_3, z_3; \lambda) = w_3(x_3 + a; \lambda). \tag{34}$$

The speckle pattern in zone III in Fig. 5 from shifting the object upward by the amount of a is shifted downward by the amount of a. We observe the same result in our experimental setup. In the geometrical optics point of view, one can trace rays from an infinite conjugate through the lens system and obtain a reversed image in zone III. The pattern moves in the opposite direction as the object and has a magnification of 1. We observe only the translation of speckle. The area of the diffuser that is contributing each point of the speckle pattern is about the size of a resolution cell.

4. *Motion Dynamics of Speckle in Zone IV*

The output speckle intensity in zone IV (imaged plane) in Fig. 5 can be obtained from Eq. (31) by taking $z_3 = F$:

$$w_4(x_4, F; \lambda) = \frac{-D_2^2}{\lambda F}\left|\int_{-\infty}^{\infty} dx' E_0(x') P_1(x') \times \operatorname{sinc}\left[\frac{D_2(x'+x_4)}{\lambda F}\right]\right|^2. \tag{35}$$

By moving the object (diffuser and aperture) up by the amount of a, i.e., $E_0(x'-a)P_1(x'-a) = E_0(x'')P_1(x'')$, the speckle pattern becomes

$$w_4'(x_4, F; \lambda) = \frac{-D_2^2}{\lambda F}\left|\int_{-\infty}^{\infty} dx'' E_0(x'') P_1(x'') \times \operatorname{sinc}\left[\frac{D_2(x''+(x_4+a))}{\lambda F}\right]\right|^2. \tag{36}$$

By comparing $w_4'(x_4, z_4; \lambda)$ and $w_4(x_4, z_4; \lambda)$, we have

$$w_4'(x_4, z_4; \lambda) = w_4(x_4 + a; \lambda). \tag{37}$$

The speckle pattern in zone IV in Fig. 5 from shifting the object upward by the amount of a is shifted downward by the amount of a. We observe the same result in our experimental setup. In the geometrical optics point of view, one can trace rays from an infinite conjugate through the lens system to the image plane and obtain a reversed image in zone IV. The pattern moves in the opposite direction as the object and has a magnification of 1. We observe only the translation of speckle. The area of the diffuser that is contributing each point of the speckle pattern is approximately the size of a resolution cell.

3. Conclusion

The objectives of this paper are to demonstrate that by use of the 4F optical configuration one can deliver precise results that are accurate to the limits of the Fresnel zone configuration. The cumbersome quadratic phase terms that appear in other lens configurations drop out in the beginning, thus making the 4F optical system an ideal testbed for the study and demonstration of most aspects of speckle, as is set forth in this paper. The spatial distance along the x (y) axis needed to decorrelate the speckle patterns is the size of an airy disk and the spatial distance along the optical axis needed to decorrelate the speckle patterns is approximately the depth of field of the system. The simple forms involved in the 4F optical system also provide clear insight into the motion dynamics of speckles. By moving the diffuser, the speckle pattern remains partially correlated except shifted by some amount. Of course, in the image plane the speckle moves, but it retains a high degree of correlation providing a measure of the space invariance of the 4F imaging system. If the diffuser is moved up by the amount of a, the speckle pattern in zone I is shifted up by the amount of $[1 - (z_1/F)]a$, shifted down by z_2a/F in zone II, and shifted down by a in zones III and IV. We also observe the twinkling phenomenon of the speckle pattern at the transform plane and zone II.

Appendix A: Analysis for the 4F Optical System

1. Optical Fourier Transform Configuration

With monochromatic illumination and for an arbitrary input imaged by a single lens with focal length F, from plane I to plane II in Fig. 1, we can write an expression for the scalar electric field component in plane II, $E_{y2}(u, v; \nu)$, in terms of the input at plane I, $E_{y1}(x', y'; \nu)$. The output field is the two-dimensional Fourier transform of the input field,

$$E_{y2}(u, v; \nu) = \frac{i\nu e^{-ik2F}}{cF}\int_{-\infty}^{\infty}\int_{-\infty}^{\infty} dx'dy' E_{y1}(x', y'; \nu) \times e^{\frac{i2\pi\nu(ux'+vy')}{cF}}, \quad \text{(A.1.1)}$$

where the wavenumber $k = 2\pi\nu/c$, where c is the speed of light. The two lens systems in cascade can be treated using this result as the basic building block.

2. Complete 4F Optical System

Consider a 4F optical system composed of two Fourier-transform lens systems as in Fig. 1. Using the results for a single Fourier section, the scalar component in plane IV, $E_{y4}(x, y; \nu)$, is written as

$$E_{y4}(x, y; \nu) = \frac{i\nu e^{-ik2F}}{cF}\int_{-\infty}^{\infty}\int_{-\infty}^{\infty} dudvP(u, v)E_{y2}(u, v; \nu) \times e^{\frac{i2\pi\nu(ux+vy)}{cF}}. \quad \text{(A.2.1)}$$

Inserting Eq. (A.1.1) into Eq. (A.2.1), we have

$$E_{y4}(x, y; \nu) = \frac{-\nu^2 e^{ik4F}}{c^2F^2}\int_{-\infty}^{\infty}\int_{-\infty}^{\infty}\int_{-\infty}^{\infty}\int_{-\infty}^{\infty} dudvdx'dy' \times E_{y1}(x', y'; \nu)P(u, v)e^{\frac{i2\pi\nu[u(x+x')+v(y+y')]}{cF}}. \quad \text{(A.2.2)}$$

In this paper, we also discuss the space dependence along the optical axis. In other words, we need to express the output electric field at planes other than the image plane as well. The analysis is included in the next subsection.

3. Complete 4F Optical System

The output field at plane III, which is z distance away from the second lens, is given by

$$E_{y3}(x, y; \nu) = \frac{i\nu e^{-ik(F+z)}}{cF}\int_{-\infty}^{\infty}\int_{-\infty}^{\infty} dudvP(u, v) \times E_{y2}(u, v; \nu)e^{\frac{i\nu\pi(z-F)}{cF^2}(u^2+v^2)+\frac{i2\pi\nu(ux+vy)}{cF}}. \quad \text{(A.3.1)}$$

Inserting Eq. (A.1.1) into Eq. (A.3.1), we have

$$E_{y3}(x, y; \nu) = \frac{-\nu^2 e^{ik(3F+z)}}{c^2F^2}\int_{-\infty}^{\infty}\int_{-\infty}^{\infty}\int_{-\infty}^{\infty}\int_{-\infty}^{\infty} dudvdx'dy' \times E_{y1}(x', y'; \nu)P(u, v) \times e^{\frac{i\nu\pi(z-F)}{cF^2}(u^2+v^2)+\frac{i2\pi\nu[u(x+x')+v(y+y')]}{cF}}. \quad \text{(A.3.2)}$$

Comparing the expression for the output electric field at plane III to IV, the expression has an extra square term besides the Fourier transform term, which is introduced by the z distance departure from the image plane. In the text, Eq. (1) follows directly from Eq. (A.3.1) above.

Appendix B: Calculation of the Cross-Correlation Function, Eq. (9)

In Appendix B we present the details for the calculation of the second-order moment of the scalar electric field amplitudes, including both spatial and

temporal frequency offsets. In the text, the resulting Eq. (9) is found from Eq. (A.3.1) by forming the second moment, namely,

$$\langle E_{y3}(x_1, y_1, z_1; \nu_1) E_{y3}^*(x_2, y_2, z_2; \nu_2)\rangle = \frac{A\nu_1^2\nu_2^2 e^{-\frac{[2\pi(\eta_1-\eta_2)\sigma]^2}{2}}}{c^4F^4} \int_{-\infty}^{\infty}\cdots\int_{-\infty}^{\infty} du\,du'\,dv\,dv'\,dx'\,dy' \times P(u, v)P^*(u', v') e^{\frac{i2\pi x'}{cF}[u\nu_1-u'\nu_2]+\frac{i2\pi y'}{cF}[v\nu_1-v'\nu_2]} \times e^{\frac{i2\pi}{cF}[x_1u\nu_1-x_2u\nu_2]+\frac{i2\pi}{cF}[y_1v\nu_1-y_2v'\nu_2]} \times e^{\frac{i\pi\nu_1(z_1-F)(u^2+v^2)}{cF^2}-\frac{i\pi\nu_2(z_2-F)(u'^2+v'^2)}{cF^2}}, \quad (B.1)$$

in which Eqs. (5)–(8) are used, leading to Eq. (9).

Now we can integrate Eq. (B.1) with respect to the object plane (x', y'). This integration results in a delta function, $\delta(u\nu_1/cF - u'\nu_2/cF, v\nu_1/cF - v'\nu_2/cF)$. After integrating over du and dv, Eq. (B.1) becomes

$$\langle E_{y3}(x_1, y_1, z_1; \nu_1) E_{y3}^*(x_2, y_2, z_2; \nu_2)\rangle = \frac{A\nu_2^2 e^{-\frac{[2\pi(\eta_1-\eta_2)\sigma]^2}{2}}}{c^2F^2} \int_{-\infty}^{\infty}\int_{-\infty}^{\infty} du'\,dv' P\left(\frac{\nu_2 u'}{\nu_1}, \frac{\nu_2 v'}{\nu_1}\right) \times P^*(u', v') e^{\frac{i2\pi\nu_2}{cF}[(x_1-x_2)u'+(y_1-y_2)v']} \times e^{\frac{i\pi\nu_2(u'^2+v'^2)}{cF^2}\left[\frac{\nu_2}{\nu_1}(z_1-F)-(z_2-F)\right]}. \quad (B.2)$$

For a typical thin diffuser, the required frequency tuning is of the order of 10 μm for the visible illumination. Thus $\nu_2/\nu_1 = (\nu_0 + \delta\nu/2)/(\nu_0 - \delta\nu/2) \approx 1$ and $\nu_2 = \nu_0 + \delta\nu/2 \approx \nu_0$, where ν_0 and $\delta\nu$ are the mean and the difference of ν_1 and ν_2, respectively. Using the fact that $P(u', v')$ is a real-number function, we have

$$\langle E_{y3}(x_1, y_1, z_1; \nu_1) E_{y3}^*(x_2, y_2, z_2; \nu_2)\rangle = \frac{A\nu_0^2 e^{-\frac{[2\pi(\eta_1-\eta_2)\sigma]^2}{2}}}{c^2F^2} \int_{-\infty}^{\infty}\int_{-\infty}^{\infty} du'\,dv' P(u', v') \times e^{\frac{i2\pi\nu_0}{cF}[(x_1-x_2)u'+(y_1-y_2)v']} e^{\frac{i\pi\nu_0(z_1-z_2)}{cF^2}(u'^2+v'^2)}. \quad (B.3)$$

This result is given in the main text as Eq. (10).

The authors acknowledge the support of this research by the Army Research Office, and Nien-An Chang is partially supported by a fellowship from the Rosalind and Milton Chang Foundation.

References

1. Lord Rayleigh, "On the resultant of a large number of vibrations of the same pitch and of arbitrary phase," Phil. Mag. **10,** 73–78 (1880).
2. R. K. Erf, *Speckle Metrology* (Academic, 1979).
3. J. C. Dainty, *Laser Speckle and Related Phenomena* (Springer-Verlag, 1984).
4. J. W. Goodman, *Speckle Phenomena in Optics* (Roberts and Company, 2006).
5. M. Franon, *Laser Speckle and Applications in Optics* (Academic, 1979).
6. B. Eliason and F. M. Mottier, "Determination of the granular radiance distribution of diffuser and its use for vibration analysis," J. Opt. Soc. Am. **61,** 559–565 (1971).
7. N. George and A. Jain, "Space and wavelength dependence of speckle intensity," Appl. Phys. **4,** 201–212 (1974).
8. N. George, A. Jain, and R. D. S. Melville, "Experiments on the space and wavelength dependence of speckle intensity," Appl. Phys. **7,** 157–169 (1975).
9. N. George, "Speckle at various planes in an optical system," Opt. Eng. **25,** 754–764 (1986).
10. H. Kadono, T. Asakura, and N. Takai, "Roughness and correlation-length measurements of rough-surface object using the speckle contrast in the diffraction field," Optik **80,** 115–120 (1988).
11. L. Leushacke and M. Kirchner, "Three-dimensional correlation coefficient of speckle intensity for rectangular and circular apertures," J. Opt. Soc. Am. A **7,** 827–832 (1990).
12. Q. B. Li and F. P. Chiang, "Three-dimensional dimension of laser speckle," Appl. Opt. **31,** 6287–6291 (1992).
13. C. Cheng, C. Liu, N. Zhang, T. Jia, R. Li, and Z. Xu, "Absolute measurement of roughness and lateral-correlation length of random surfaces by use of the simplified model of image-speckle contrast," Appl. Opt. **41,** 4148–4156 (2002).
14. R. Kingslake, *Optics in Photography* (SPIE Press, 1992).
15. N. Takai, T. Iwai, and T. Asakura, "Correlation distance of dynamic speckles," Appl. Opt. **22,** 170–177 (1983).
16. T. Asakura and N. Takai, "Dynamic laser speckles and their application to velocity measurements of the diffuser object," Appl. Opt. **25,** 179–194 (1981).
17. T. Okamoto and T. Asakura, "Effects of imaging properties on dynamic speckles produced by a set of moving phase screens," Waves Random Media **2,** 49–65 (1992).
18. T. Nakamura and T. Asakura, "Cross-correlation function of dynamic speckles from rotating cylindrical objects," Optik **108,** 13–19 (1998).
19. D. C. Sinclair, "Demonstration of chromatic aberration in the eye using coherent light," J. Opt. Soc. Am. **55,** 575–576 (1965).
20. I. S. Reed, "On a moment theorem for complex Gaussian processes," IRE Trans. Inf. Theor. **IT-8,** 194–195 (1962).
21. M. Abramowitz and I. A. Stegun, *Handbook of Mathematical Functions: With Formulas, Graphs, and Mathematical Tables* (Dover, 1965).
22. J. W. Goodman, *Introduction to Fourier Optics* (McGraw-Hill, 1996).

Resolution analysis of a gradient-index rod and a gradient-index lens array

Xi Chen and Nicholas George*

The Institute of Optics, University of Rochester, Rochester, New York 14627, USA

*Corresponding author: ngeorge@troi.cc.rochester.edu

Received 23 July 2008; revised 4 September 2008; accepted 8 October 2008; posted 10 October 2008 (Doc. ID 99319); published 14 November 2008

The physical optics analysis of a gradient-index (GRIN) rod and a GRIN lens array with aberrations is presented. We investigated the optical path length and aberration of a GRIN rod without definition of the stop plane. We also defined an effective aberration transmission function to include aberrations into physical optics analysis. Our theoretical results of impulse responses agree excellently with experiments. For a single GRIN rod, we obtained a theoretical value of 10.3 μm and an experimental value of 10.4 μm for the full width at half-maximum of the intensity point-spread function. For a GRIN array, the theoretical value of 19.2 μm and the experimental measurement of 19.9 μm agree to within 4%. This physical optics methodology with aberrations included can be applied to optical design software. The resolution difference in xerographic process for test material along the "parallel-to-perpendicular" directions is observed. It agrees with the theoretical result for the intensity impulse response of the GRIN array calculated with a second-order correction.

OCIS codes: 110.2760, 080.5692, 080.1010, 110.2990.

1. Introduction

A gradient-index (GRIN) rod is a cylinder with a square-law refractive index and two planar end surfaces. The rod has a radial symmetry in the index of refraction, which is the highest on-axis. It is commonly used as an objective lens or a relay lens for endoscopes. Its small size, weight, and advantage of Petzval correction make it a powerful imaging device. Moreover, GRIN lens arrays made of several hundred aligned GRIN rods are widely used as imagers for copiers and printers.

The image quality of a GRIN rod system has been studied extensively using geometric optics [1–7]. Aberration coefficients of a symmetrical imaging system were obtained by use of Buchdahl's theory and by solving the meridional and skew ray equations, respectively [1–6]. Also, aberration formulas for a single GRIN rod were derived based on the ray path solutions [8]. Different numerical techniques have been used to solve the Euler–Lagrange equations to realize ray-tracing algorithms in GRIN media [9–13], among which the Sharma method has been applied in commercial optical software [14,15]. Apart from the geometric optics techniques, physical optics was also applied to analyze paraxial imaging and Fourier transformation by a single GRIN rod and GRIN array lenses [16–20]. Guided modes inside GRIN media were derived to find the maximum length of GRIN fiber for coherent imaging and communication [16]. The guided modes were also used to obtain the diffraction pattern under the Fresnel-zone approximation and to study the focusing spot size [17,18]. In addition, the variation of the degree of coherence of the intensity at the image plane was studied when the object is incoherently illuminated [19]. A summary of the paraxial imaging and Fourier transforming by the GRIN medium was published in a book by Gomez-Reino *et al.* [20] and in a thesis by Chen [21]. In our previous paper we described the physical optics analysis of the GRIN rod and the GRIN lens array [22]. This, of course, provides insight as to the resolution. However, none of the earlier analyses have treated the subject of aberrations using methods of physical optics. Aberrations

0003-6935/08/336190-12$15.00/0

evaluation is essential for GRIN-media-based imaging since the aberrations severely degrade the resolution. It is important to develop a theory for the physical optics analysis of a GRIN rod with careful treatment of aberrations and also to include considerations of optical path difference (OPD) for GRIN fibers in the array.

In this paper we extend our previous study [22] to develop a physical optics analysis of both a GRIN rod and GRIN array lenses with the consideration of aberrations and OPD. Our paper consists of seven sections and three appendices. In Section 2 we calculate the optical path length (OPL) for rays through the GRIN rod, where the ray-intercept curves are compared with the results in the commercial optical design software reports. Also, the aberration on the output plane 3 of the rod is calculated. In Section 3 we provide the definition of the effective aberration transmission function of a GRIN rod. The physical understanding of the connection between the transmission function and the aberration is described. In Section 4 we derive the physical optics formulas of a single GRIN rod for nonparaxial imaging. In Sections 5 and 6 we present the physical optics analyses and the associated experimental results for a single GRIN rod and a GRIN array in the presence of aberrations. We also compare them with those obtained with the paraxial imaging assumption. In Section 7 we provide our conclusions about the resolution analysis. The details of this study of GRIN array resolution, in both theory and experiment, are described in Appendices A, B, and C. The well-known difference of GRIN array resolution for "parallel-to-perpendicular" textual material is explained in detail.

2. Calculation of the Optical Path Length and Aberration

In this section we present the ray-tracing algorithm based on the exact solution to the Euler–Lagrange equation and the OPL calculation. Also, based on the OPL calculation, we compute the aberration on the output plane 3 of the rod (see Fig. 1). This calculation of aberration on plane 3 instead of the exit pupil plane is beneficial for our physical optics analysis, which is described in Section 4.

A. Ray Tracing and Optical Path Length Calculation

The single GRIN rod imaging system is shown in Fig. 1. The GRIN rod has a radius size of R. The refractive index of the GRIN rod is defined as

$$n^2(r) = n_1^2(1-\alpha^2 r^2), \qquad r \le R, \tag{1}$$

where n_1 is the on-axis refractive index, α is the gradient constant, and R is the radius of the GRIN rod. The rays' trace in an inhomogeneous medium is governed by the Euler–Lagrange equation [7]. The derivation of this equation from the Helmholtz wave equation can be found in [23]. The Euler equation in vector form is written as

$$\vec{\nabla} n = \frac{\mathrm{d}}{\mathrm{d}s}\left(n\frac{\mathrm{d}\vec{r}}{\mathrm{d}s}\right), \tag{2}$$

where n is the refractive index at $\vec{r}$, $\vec{r}$ is the ray's position in the medium, and $\mathrm{d}s$ is the infinitesimal distance over the ray path. This vector equation can be rewritten as three scalar equations for the coordinates of a ray, respectively. The exact solution of the scalar equations for the rays with coordinates (x,y,z) in a GRIN rod is given by

$$\begin{aligned} x(z) &= \cos\left(\frac{n_1\alpha z}{\sqrt{n_1^2 - n_1^2\alpha^2(x^2(0)+y^2(0)) - (1-\gamma_0^2)}}\right)x(0) + \frac{1}{n_1\alpha}\sin\left(\frac{n_1\alpha z}{\sqrt{n_1^2 - n_1^2\alpha^2(x^2(0)+y^2(0)) - (1-\gamma_0^2)}}\right)\alpha_0, \\ y(z) &= \cos\left(\frac{n_1\alpha z}{\sqrt{n_1^2 - n_1^2\alpha^2(x^2(0)+y^2(0)) - (1-\gamma_0^2)}}\right)y(0) + \frac{1}{n_1\alpha}\sin\left(\frac{n_1\alpha z}{\sqrt{n_1^2 - n_1^2\alpha^2(x^2(0)+y^2(0)) - (1-\gamma_0^2)}}\right)\beta_0, \end{aligned} \tag{3a}$$

$$\begin{aligned} n\frac{\mathrm{d}x(z)}{\mathrm{d}s} &= -n_1\alpha\sin\left(\frac{n_1\alpha z}{\sqrt{n_1^2 - n_1^2\alpha^2(x^2(0)+y^2(0)) - (1-\gamma_0^2)}}\right)x(0) + \alpha_0\cos\left(\frac{n_1\alpha z}{\sqrt{n_1^2 - n_1^2\alpha^2(x^2(0)+y^2(0)) - (1-\gamma_0^2)}}\right), \\ n\frac{\mathrm{d}y(z)}{\mathrm{d}s} &= -n_1\alpha\sin\left(\frac{n_1\alpha z}{\sqrt{n_1^2 - n_1^2\alpha^2(x^2(0)+y^2(0)) - (1-\gamma_0^2)}}\right)y(0) + \beta_0\cos\left(\frac{n_1\alpha z}{\sqrt{n_1^2 - n_1^2\alpha^2(x^2(0)+y^2(0)) - (1-\gamma_0^2)}}\right), \end{aligned} \tag{3b}$$

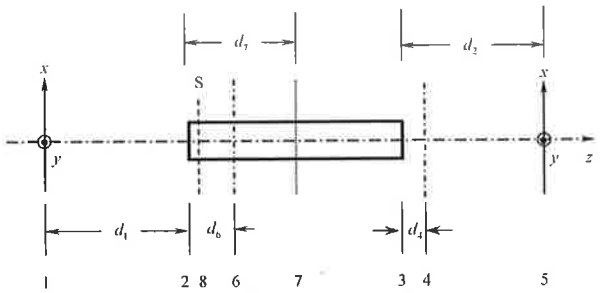

Fig. 1. Imaging setup for the GRIN rod with two end surfaces 2 and 3, an object plane 1, external and internal Fourier transform planes 4 and 6, external and internal image planes 5 and 7. Plane 8 is the stop plane (S). The definition of the Fourier transform planes 4 and 6 are discussed in [22].

where $(x(0),y(0),0)$ is the coordinate of the input ray on plane 2 located at $z=0$, $(\alpha_0,\beta_0,\gamma_0)$ are the cosines of incident angles with respect to the axes x, y, and z for the input ray in the air, ds is the infinitesimal distance over the ray path, $dx(z)/ds$ is the cosine of the ray's angle with respect to the x axis, and α is the gradient constant of the rod. Equations (3a) and (3b) are the exact solution of the Euler–Lagrange equation for rays in a GRIN medium. It can be simplified for a paraxial approximation with small input ray heights $x(0)$ and $y(0)$ and input ray angle with respect to the optical axis. The paraxial approximation of Eq. (3) for x and $n(dx/ds)$ is written as

$$x(z)=\cos(\alpha z)x(0)+\sin(\alpha z)\frac{\alpha_0}{n_1\alpha},$$
$$n\frac{dx(z)}{ds}=-n_1\alpha\sin(\alpha z)x(0)+\cos(\alpha z)\alpha_0. \quad (4)$$

We can write a similar equation for y and $n(dy/ds)$. From Eq. (4) we obtain the matrix equation for the GRIN rod which is written as

$$\begin{bmatrix}AB\\CD\end{bmatrix}=\begin{bmatrix}\cos(\alpha L) & \frac{\sin(\alpha L)}{n_1\alpha}\\ -n_1\alpha\sin(\alpha L) & \cos(\alpha L)\end{bmatrix}, \quad (5)$$

where L is the length of the GRIN rod. The matrix in Eq. (5) connects the input optical ray at $z=0$ with height $x(0)$ and the ray-slope variable defined by $(n(x)dx(z)/dz)|_{z=0}$ to the output optical ray at an arbitrary z in the rod as follows:

$$\begin{bmatrix}x(z)\\ n\frac{dx(z)}{dz}\end{bmatrix}=\begin{bmatrix}A & B\\ C & D\end{bmatrix}\begin{bmatrix}x(0)\\ n(0)\frac{dx(0)}{dz}\end{bmatrix}, \quad (6)$$

where matrix elements A, B, C, and D are functions of z. We also obtain the following equation:

$$ds=\frac{n dz}{\sqrt{n_1^2-n_1^2\alpha^2(x_0^2+y_0^2)-(1-\gamma_0^2)}}, \quad (7)$$

where ds is the infinitesimal distance over the ray path, and dz is the projection of ds along the z axis.

To illustrate how rays propagate in the GRIN rod and form images, we present rays in the GRIN rod in Fig. 2. They are traced by the use of Eq. (3) with $d_1=13.782\,\text{mm}$, $n_1=1.608$, gradient constant $\alpha=0.1783\,\text{mm}^{-1}$, GRIN rod length of $L=20.4\,\text{mm}$, and rod radius size of $R=0.5225\,\text{mm}$. These parameter values are used for calculation and illustration in this paper. Rays 0 to 5 form an internal image of the axial object. The other trapped rays form an image of the object at $(2R,0)$ on the input plane 1. The rays with nonzero slopes at the boundary of the GRIN rod, where the refractive index has the same value as the refractive index of the cladding, cannot be trapped in the GRIN rod. These rays propagating in the cladding are absorbed by the black silicone cladding.

The OPL from point A to point B is defined as $\text{OPL}=\int_A^B n(r)ds$. Inserting Eq. (7) into this definition, the OPL of rays in a GRIN rod can be obtained by the following equation:

$$\text{OPL}=\frac{\int_{z_0}^{z} n^2(r(z))dz}{\sqrt{n_1^2-n_1^2\alpha^2(x_0^2+y_0^2)-(1-\gamma_0^2)}}. \quad (8)$$

This equation is used to calculate the OPL for rays in a GRIN rod.

Numerically, OPL is obtained by the following procedure. First we calculate the Gaussian image plane position d_2 and magnification power M, which can be derived from Eq. (5). Also, d_2 and M are expressed in Eqs. (27) and (28) in Section 4. Second we trace the rays that go through the evenly spaced grids on plane 2 by the use of Eq. (3). Finally we use Eq. (8), which can be integrated by trapezoidal numerical integration [24], to find the OPL through the GRIN rod.

We notice that the definition of a stop on either plane 2 or 3 is required in commercial software [15] to find the central reference ray. The central reference ray is defined as the ray passing through the center of the defined stop. The central reference ray is used to obtain the paraxial image location and other first-order optical parameters in commercial

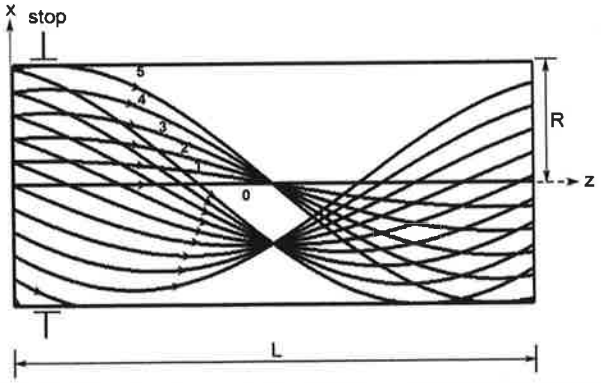

Fig. 2. Rays form images in the GRIN rod: rays 0 to 5 from an on-axis object form an on-axis image. Other rays from the object at $(2R,0)$ form an off-axis image.

software. However, such a requirement could lead to missing the central reference ray, because in a GRIN rod imaging system, the stop may not be located at any end surface of the GRIN rod. For example, if the stop is defined on plane 2, the central reference ray incident from an off-axis object point at $(4R, 0)$, and passing through the center of plane 2 cannot propagate through the GRIN rod. Missing the central reference ray would cause a problem when the software is used to calculate its location for further calculation of aberrations. To solve this problem, we determine the Gaussian image position from the results of first-order optics instead of using the central reference ray. The first-order optics parameters could be derived with Eq. (5). The location for the stop is shown in Fig. 2. This approach will result in a simple and accurate calculation of aberration.

A common graphic representation for aberration defects used in optical design is the ray-intercept curve. Usually the ray-intercept curve plots the image space displacement as a function of the object space fractional coordinates at the stop aperture. The image space displacement is defined as the difference between the intersection of the ray on the image plane and the Gaussian image point (x_5, y_5). The stop aperture is not defined in our system because of the reason discussed previously. To illustrate the aberration defects, we plot the image space displacement as a function of the rays' coordinates on plane 2. The rays' traces are calculated using Eq. (3) and the same parameters used for calculating the rays' position in Fig. 2. Figures 3(a) and 3(b) show the ray-intercept curves for an on-axis object point and an off-axis object point at $(2R, 0)$, respectively. Both object points locate along the x axis. The ray fans are originated from the object and cross the 201 sampling grids along the x axis of plane 2. These ray fans are the so-called meridional or tangential ray fans. For comparison, we also plot in light gray the OSLO plots. We define the stop on plane 2 in OSLO software. Clearly the two plots [Fig. 3(a)] coincide with each other for the axial object, as does the paraxial image point with the central reference ray's intersection for an axial object on the image plane, indicating a corresponding accuracy within our result and in the OSLO result. The central reference ray defined by OSLO crosses the center of plane 2. However, the two plots in Fig. 3(b) are not the same, although quite close, for the two-radius off-axis object. The difference is caused by the difference between the location of the first-order image point and the off-axis object's central reference ray's intersection point on the image plane. Clearly our calculation of aberration has an advantage, because no definition of stop plane is required.

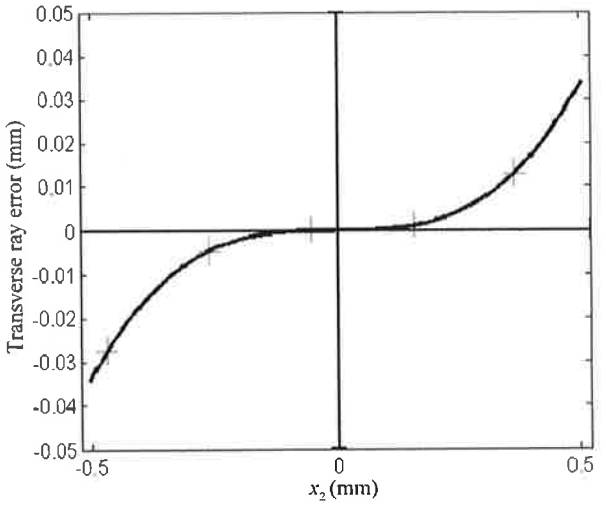

(a)

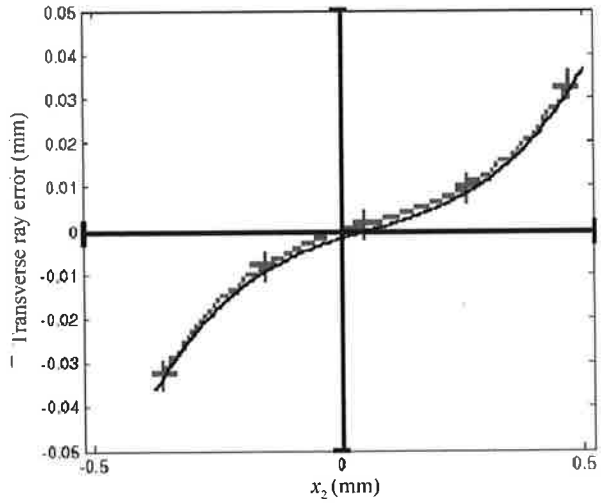

(b)

Fig. 3. Ray-intercept curves, transverse ray error ε_x versus x_2, for (a) an on-axis object and (b) an off-axis object at $(2R, 0)$.

B. Aberration

The wave aberration Ω is defined as the OPL of a ray measured from its intersection point $\bar{Q}$ on the Gaussian reference sphere to its location Q on the equal phase wavefront (Fig. 4). The Gaussian reference sphere centers at P'^*, which is the paraxial image point [25]. The true ray intersects with the paraxial image plane at P'. We notice that the wave aberration Ω is usually referred to the exit pupil plane instead of plane 3 in Fig. 4. Here we would like to know the amount of wave aberration on plane 3 of a GRIN rod for an axial object point. Mathematically the wave aberration Ω is written as

$$\begin{aligned}\Omega &= \bar{Q}Q = \mathrm{OPL}(PQ) - \mathrm{OPL}(P\bar{Q}) \\ &= \mathrm{OPL}(PQ) - \mathrm{OPL}(PA) - \mathrm{OPL}(A\bar{Q}),\end{aligned} \tag{9}$$

where $\mathrm{OPL}(PQ)$ stands for the OPL from point P to point Q, and point A is the intersection point of the ray on plane 3. The sign of Ω is defined as $\Omega > 0$ when the equal phase wavefront is ahead of the Gaussian

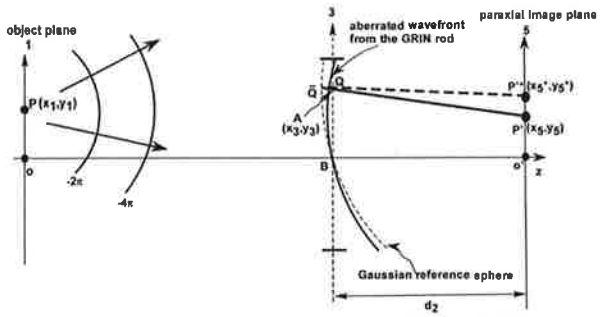

Fig. 4. Wave aberration on plane 3 of a GRIN rod. We use $e^{i\omega t}$ notation here.

reference sphere. We can approximately express $\mathrm{OPL}(A\bar{Q})$ as

$$\begin{aligned}\mathrm{OPL}(A\bar{Q}) &\cong \mathrm{OPL}(AP'^{*}) - \mathrm{OPL}(\bar{Q}P'^{*}) \\ &= \sqrt{d_2^2 + (x_3 - x_5^*)^2 + (y_3 - y_5^*)^2} \\ &\quad - \sqrt{d_2^2 + x_5^{*2} + y_5^{*2}}, \end{aligned} \tag{10}$$

where (x_3, y_3) is the coordinate of the intersection point A on plane 3, (x_5^*, y_5^*) is the coordinate of P'^*, and d_2 is the distance between plane 3 and the paraxial image plane 5. For an axial object point, (x_5^*, y_5^*) is (0, 0). We combine Eqs. (9) and (10) and obtain

$$\begin{aligned}\Omega = \bar{Q}Q &= \mathrm{OPL}(PQ) - \mathrm{OPL}(PA) \\ &\quad - \sqrt{d_2^2 + (x_3 - x_5^*)^2 + (y_3 - y_5^*)^2} \\ &\quad + \sqrt{d_2^2 + x_5^{*2} + y_5^{*2}} = \mathrm{OPL}(PBP'^{*}) - \mathrm{OPL}(PA) \\ &\quad - \sqrt{d_2^2 + (x_3 - x_5^*)^2 + (y_3 - y_5^*)^2}, \end{aligned} \tag{11}$$

where $\mathrm{OPL}(PBP'^{*})$ is the total OPL for the ray, from the object point to the paraxial image point, passing through point B, which is the intersection point of the optical axis with plane 3. If plane 3 is the exit pupil plane, then $\mathrm{OPL}(PBP'^{*})$ is the total OPL for the chief ray. Chief ray is defined as the ray passing through the center of the stop aperture. We notice that $\mathrm{OPL}(PBP'^{*}) - \sqrt{d_2^2 + (x_3 - x_5^*)^2 + (y_3 - y_5^*)^2}$ is the OPL, from the object point to its intersection point on plane 3 of the ideal ray. The ideal ray is defined as the ray in a perfect lens that forms the equal phase wavefront centered at the paraxial image point. Both the true ray and its counterpart ideal ray originate from the object point P at (x_1, y_1) and intersect on plane 3 at point A with coordinate (x_3, y_3). Let $\mathrm{OPL}_{\mathrm{ideal}} = \mathrm{OPL}(PBP'^{*}) - \sqrt{d_2^2 + (x_3 - x_5^*)^2 + (y_3 - y_5^*)^2}$, then we have Eq. (11) rewritten as

$$\Omega = \mathrm{OPL}_{\mathrm{ideal}} - \mathrm{OPL}(PA). \tag{12}$$

We define

$$\delta_0 = \mathrm{OPL}(PA) - \mathrm{OPL}_{\mathrm{ideal}} = -\Omega. \tag{13}$$

The positive value of Ω or negative value of δ_0 corresponds to an equal phase wavefront ahead of the Gaussian reference sphere. As an example, a positive lens always has the equal phase wavefront more bent than the Gaussian reference sphere for an axial object point. This is the so-called under-corrected spherical aberration [26]. Because the ray passing through the center of plane 3 for a GRIN rod may not be able to propagate through the GRIN rod for an off-axial object point, we make a little modification on Eq. (13). We define δ as the OPD between the true ray's OPL from the object point P and the ray's intersection point A with plane 3 and its counterpart ideal ray's OPL between point P and point A. Mathematically δ is expressed as

$$\begin{aligned}\delta &= \mathrm{OPL}(PA) - [(d_1 + n_1 * L + d_2) \\ &\quad - \sqrt{d_2^2 + (x_3 - x_5^*)^2 + (y_3 - y_5^*)^2}], \end{aligned} \tag{14}$$

where $(d_1 + n_1 * L + d_2)$ is the total OPL for the axial object point. Therefore δ can be written in terms of the wave aberration Ω as

$$\delta = -\Omega + \Delta l = \delta_0 + \Delta l, \tag{15}$$

where Δl is the difference between the total OPL of the chief ray and the axial total OPL $(d_1 + n_1 * L + d_2)$; δ_0 is defined in Eq. (13). From Eq. (15) we can calculate the wave aberration Ω from δ. Therefore δ will be used in the definition of the effective aberration transmission function in Section 3. Clearly δ is a function of $(x_3, y_3; x_1, y_1)$. We rewrite Eq. (14) as

$$\begin{aligned}\delta(x_3, y_3; x_1, y_1) &= \mathrm{OPL}(x_3, y_3; x_1, y_1) \\ &\quad + \sqrt{d_2^2 + (x_3 - x_5^*)^2 + (y_3 - y_5^*)^2} \\ &\quad - (d_1 + n * L + d_2), \end{aligned} \tag{16}$$

where $\mathrm{OPL}(x_3, y_3; x_1, y_1)$ can be obtained by the OPL calculation from the object point (x_1, y_1) to its intersection point (x_3, y_3) on plane 3 as described in Subsection 2.A. The Gaussian image point (x_5^*, y_5^*) is obtained by the first-order optics result.

Figures 5(a) and 5(b) show the cross sections of OPD, $\delta(x_3, y_3; x_1, y_1)$, along the x axis on plane 3 for an axial object and an off-axis object at $(2R, 0)$, respectively. The GRIN rod analyzed here has $n_1 = 1.608$ and $\alpha = 0.1783\,\mathrm{mm}^{-1}$ as in Eq. (1). OPD is plotted as a function of the tangential ray fan's coordinates x_3 on plane 3. The largest OPD could be obtained by finding the largest difference between δ, shown in Fig. 5, for different rays. The largest OPDs are 0.30 and 0.39 μm for the axial object and the two-radius off-axis object, respectively. The polynomial expansion of $\delta(x_3, 0; 0, 0)$ for the axial object can be written as

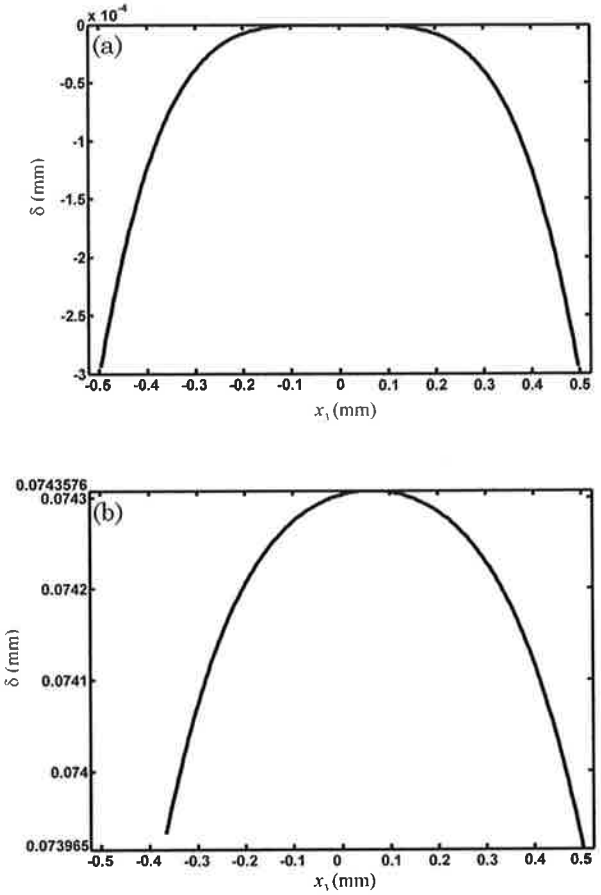

Fig. 5. Cross sections of OPD, $\delta(x_3,0;x_1,y_1)$, along the x axis on plane 3 for (a) an axial object and (b) an off-axis object at $(2R,0)$.

$$\delta(x_3,0;0,0) = -0.0048\rho^4 - 0.0002\rho^6 - 0.0002\rho^8 - 0.0002\rho^{10}, \quad |\rho| \le 0.4964\,(\text{mm}), \tag{17}$$

where $\rho = \sqrt{x_3^2 + y_3^2}$. The ρ^4 term coefficient gives us the third-order spherical aberration OPD of $0.291\,\mu$m, which equals 0.5λ for wavelength λ of $0.57\,\mu$m. The coefficients of higher-order terms in Eq. (17) correspond to the fifth-order and higher-order spherical aberration coefficients.

The positive value of wave aberration Ω or negative value of δ for an axial object point at larger ρ indicates that this GRIN rod (SLA09-48A) with 1:1 imaging has under-corrected spherical aberration as shown in Fig. 5. However, a GRIN rod with a positive power does not always have under-corrected spherical aberration.

3. Effective Aberration Transmission Function

To include aberrations induced by refraction and propagation in a GRIN rod in our physical optics analysis presented in Section 4, we include aberrations into the effective aberration transmission function $T_3(x_3,y_3;x_1,y_1)$. In this paper we use the notation of $e^{i\omega t}$ implicitly as shown by the wavefront phases in Fig. 4.

In the physical optics picture, the phase delay of a ray propagating in the GRIN rod, from the object plane to plane 3, can be written as $e^{i\omega t - ik\mathrm{OPL}(x_3,y_3;x_1,y_1)}$. By the use of Eqs. (13) and (15), we obtain the phase delay of a ray as $e^{-ik[\mathrm{OPL}_{\mathrm{ideal}}(x_3,y_3;x_1,y_1)+\delta(x_3,y_3;x_1,y_1)]}$, where a constant phase term $e^{ik\Delta l}$ is dropped.

We define the effective aberration transmission function $T_3(x_3,y_3;x_1,y_1)$ for the GRIN rod as

$$T_3(x_3,y_3;x_1,y_1) = P_{3\mathrm{aperture}}(x_3,y_3;x_1,y_1) \times e^{-ik\delta(x_3,y_3;x_1,y_1)}, \tag{18}$$

where $P_{3\mathrm{aperture}}(x_3,y_3;x_1,y_1)$ is the aperture function on plane 3, which defines the opening for rays passing through the system, and $\delta(x_3,y_3;x_1,y_1)$ is the OPD between the true ray's OPL and the OPL of the ideal ray. $\delta(x_3,y_3;x_1,y_1)$ can be calculated using Eq. (16). The calculation of $P_{3\mathrm{aperture}}(x_3,y_3;x_1,y_1)$ can be obtained in [22]. From Eq. (18), one can see that the effective aberration transmission function is the transmission function for only aberrations with a limited aperture $P_{3\mathrm{aperture}}(x_3,y_3;x_1,y_1)$. The calculation of $T_3(x_3,y_3;x_1,y_1)$ will be used to calculate the point-spread function (PSF) in Section 4.

4. Physical Optics Analysis of a Single Gradient-Index Rod

Here we present the physical optics formalism for a GRIN system including aberrations. We apply the generalized Fresnel-zone integral to wave propagation through a GRIN medium. The Fresnel-zone integral expression is given by [27–29]

$$V_2(x,y) = \frac{ik\exp(-ikL)}{2\pi B}\int_{-\infty}^{\infty}\int_{-\infty}^{\infty} dx_0 dy_0 V_1(x_0,y_0) \times \exp\left\{-\frac{ik}{2B}[D(x^2+y^2) - 2(x_0x + y_0y) + A(x_0^2+y_0^2)]\right\}, \tag{19}$$

where $V_1(x_0,y_0)$ and $V_2(x,y)$ are input and output scalar amplitudes of polarized electric fields, respectively. A, B, C, and D are the elements of the $\begin{pmatrix} AB \\ CD \end{pmatrix}$ matrix describing the first-order geometric optics of the system between planes 1 and 2.

To find the impulse response $h_{15}(x_5,y_5;x_0,y_0)$ from plane 1 to plane 5, we use the following well-known form for a space-variant imaging system:

$$V_5(x_5,y_5) = \int_{-\infty}^{\infty}\int_{-\infty}^{\infty} dx_0 dy_0 V_1(x_0,y_0) h_{15}(x_5,y_5;x_0,y_0). \tag{20}$$

Taking an input scalar amplitude given by

$$V_1(x_0,y_0) = \delta(x_0 - x_1, y_0 - y_1), \tag{21}$$

corresponding to an input point source at (x_1,y_1), we can find the output at plane 5 by combining Eqs. (19)–(21), integrating over an idealized infinite aperture at plane 2, and using the identity of $\int_{-\infty}^{\infty} du e^{-(ik/2F)[u-(r+x)]^2} = (1-i)(\frac{\pi F}{k})^{1/2}$. The general result for h_{15} is given by

$$h_{15}(x_5,y_5;x_1,y_1) = \frac{-l\exp[-ik(d_1+n_1L+d_2)]}{\lambda^2 d_1 B d_2} \int\int dx_3 dy_3 \exp\left[\frac{-ik}{2d_1}\left(1-\frac{l}{d_1}\right)(x_1^2+y_1^2)\right]$$
$$\times \exp\left[\frac{-ik}{2d_2}(x_5^2+y_5^2)\right] \exp\left[\frac{-ik\left(\frac{D}{B}+\frac{1}{d_2}-\frac{l}{B^2}\right)}{2}(x_3^2+y_3^2)\right] \exp\left[-ik\left(\frac{x_5}{d_2}-\frac{lx_1}{d_1 B}\right)x_3\right.$$
$$\left. - ik\left(\frac{y_5}{d_2}-\frac{ly_1}{d_1 B}\right)y_3\right] T_3(x_3,y_3;x_1,y_1), \tag{22}$$

in which λ is the wavelength, k is the wavenumber, d_1 and d_2 are the object distance and image distance, respectively, as shown in Fig. 1, and $T_3(x_3,y_3;x_1,y_1)$ is the effective aberration transmission function. We defined l as

$$l = \frac{Bd_1}{Ad_1 + B}. \tag{23}$$

The matrix elements A, B, C, and D are given by Eq. (5). To find the location of the external image plane, we set the coefficient of the quadratic term of (x_3^2,y_3^2) equal to zeros, viz.,

$$\frac{D}{B} + \frac{1}{d_2} - \frac{l}{B^2} = 0. \tag{24}$$

Substitution of Eq. (23) into Eq. (24) gives the location of the image plane

$$d_2 = -\frac{Ad_1 + B}{Cd_1 + D}. \tag{25}$$

Also, it is known that the zeros of the linear phase terms of x_3 and y_3 correspond to the central maximum of the intensity PSF in general, thus we can obtain the central position of the image spot. From the central position of the image spot, we obtain the magnification power M as

$$M = \frac{x_5}{x_1} = \frac{y_5}{y_1} = \frac{-1}{Cd_1 + D}. \tag{26}$$

Substituting Eq. (5) into Eqs. (25) and (26), we can obtain

$$d_2 = -M\left[\cos(\alpha L)d_1 + \frac{\sin(\alpha L)}{n_1\alpha}\right], \tag{27}$$

$$M = \frac{1}{\cos(\alpha L) - n_1\alpha d_1 \sin(\alpha L)}. \tag{28}$$

Hence, by substituting Eqs. (23)–(28) into Eq. (22), the final form of the impulse response on the image plane 5 is given by

$$h_{15}(x_5,y_5;x_1,y_1) = \frac{M\exp[-ik(d_1+n_1L+d_2)]}{\lambda^2 d_2^2}$$
$$\times \exp\left[\frac{ik\cos(\alpha L)M(x_1^2+y_1^2)}{2d_2}\right]$$
$$\times \exp\left[\frac{-ik(x^2+y^2)}{2d_2}\right] F^{-1}\{T_3(x_3,y_3;x_1,y_1)\}. \tag{29}$$

In Eq. (29), $F^{-1}\{T_3(x_3,y_3;x_1,y_1)\}$ is the inverse Fourier transform of the effective aberration transmission function $T_3(x_3,y_3;x_1,y_1)$ and is defined as

$$F^{-1}\{T_3(x_3,y_3;x_1,y_1)\} = (\lambda d_2)^2 \int_{-\infty}^{\infty}\int_{-\infty}^{\infty} df_x df_y$$
$$T_3(\lambda d_2 f_x, \lambda d_2 f_y; x_1, y_1)$$
$$\times \exp[i2\pi f_x(x - Mx_1) + i2\pi f_y(y - My_1)], \tag{30}$$

where $f_x = x_3/\lambda d_2$ and $f_y = y_3/\lambda d_2$. Equation (29) shows that the impulse response is proportional to the inverse Fourier transform of the effective aberration transmission function $T_3(x_3,y_3;x_1,y_1)$ with aberrations included.

5. Resolution Analysis of a Single Gradient-Index Rod

Here we analyze the intensity PSF for a single GRIN rod and compare it with the theoretical PSF without considering aberrations and the experimental results. The intensity PSF can be obtained by the use of Eqs. (27)–(30). Figure 6 shows the intensity PSFs for different object points. The full-width at

half-maximum (FWHM) are 10.3, 11.4, and 28.5 μm for the on-axis [Fig. 6(a)], one-radius off-axis [Fig. 6(b)], and two-radius off-axis [Fig. 6(c)] objects, respectively. As described in [22], the FWHMs of the intensity PSFs are 9.0 and 10.0 μm for the axial and two-radius off-axis objects, respectively, without considering aberrations. Clearly our results counting in aberrations differ greatly from those obtained for ideal ones without considering aberrations. Moreover, such aberrations severely degrade the resolution of the GRIN rod, especially for off-axis object points.

We carried out the experiment to compare the measured PSF with our theoretical calculation. We measured the image of a 5 μm pinhole, which is an axial object, through a single GRIN rod and a Newport objective. The illumination source is an incoherent white light source. The GRIN rod is one of the SLA09-48A array's rods. It has $n_1 = 1.608$ and $\alpha = 0.1783\,\mathrm{mm}^{-1}$. The image of the pinhole magnified by the objective is imaged onto a CCD with the pixel size of 8.3 μm × 8.3 μm. The schematic setup is shown in Fig. 7. The best resolution we obtained is a FWHM of 11.5 μm for the intensity PSF. To obtain a more accurate result of the PSF, we measured the intensity PSF of the objective separately, using the same 5 μm pinhole as the object. The objective's FWHM is 2.7 μm × 3.1 μm. We denote the intensity PSF of the system on the CCD plane (Fig. 7) as $I_{\mathrm{total}}(x_6/M, y_6/M)$, where (x_6, y_6) are the coordinates of the CCD plane, and M is the objective's magnification power. The objective's intensity PSF and the GRIN rod's intensity PSF are denoted as $I_{\mathrm{objective}}(x_6/M, y_6/M)$ and $I_{\mathrm{rod}}(x_5, y_5)$, respectively, where (x_5, y_5) are the coordinates of the GRIN rod's image plane. We can write the relationship between them by the following explicit form

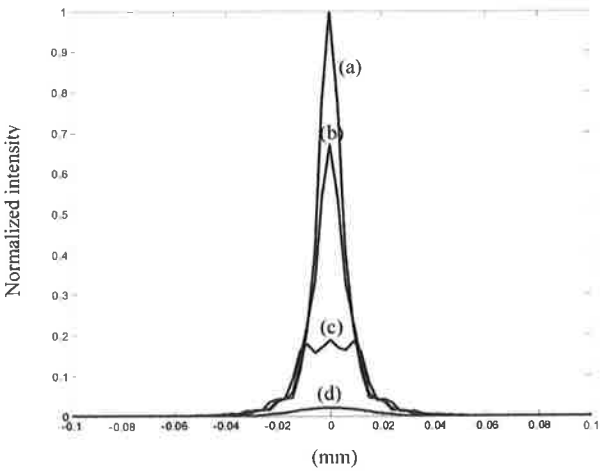

Fig. 6. Cross section along the x axis of the intensity PSFs for different object points: (a) an on-axis object; (b) an off-axis object at $(R, 0)$; (c) an off-axis object at $(2R, 0)$; and (d) an off-axis object at $(4R, 0)$.

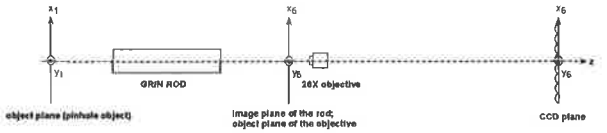

Fig. 7. Single rod's PSF measurement setup.

$$I_{\mathrm{total}}\left(\frac{x_6}{M}, \frac{y_6}{M}\right) = \int_{-\infty}^{\infty}\int_{-\infty}^{\infty} I_{\mathrm{objective}}\left(\frac{x_6}{M} - x_5, \frac{y_6}{M} - y_5\right) \times I_{\mathrm{rod}}(x_5, y_5)\,\mathrm{d}x_5\,\mathrm{d}y_5, \tag{31}$$

in which M is the magnification power of the objective. From Eq. (31) we can obtain the PSF of the GRIN rod, $I_{\mathrm{rod}}(x_5, y_5)$, by deconvolution between I_{total} and $I_{\mathrm{objective}}$. $I_{\mathrm{rod}}(x_5, y_5)$ is shown in Fig. 8. The FWHM of I_{rod} is 10.2 μm × 10.6 μm along the x and y axes, respectively. The average FWHM is 10.4 μm. This number agrees with our theoretical result, 10.3 μm, within 1% for the axial object's intensity PSF.

Comparing our theoretical and experimental results in the presence of aberrations with those obtained without considering aberrations, we can conclude that the aberrations of a single GRIN rod imaging system significantly affect the imaging quality, especially for off-axis objects. Hence it is clear that aberrations must be included to obtain accurate values for resolution.

6. Analysis of Gradient-Index Array Resolution

Here we investigate the resolution of a two-row GRIN array imaging system (GRIN array: SLA09-48 made by Nippon Sheet Glass Corp.). One object point is typically imaged by nine adjacent GRIN rods, as shown in Fig. 9. With an incoherent illumination, the intensity PSF $\mathcal{R}_{15A}$ for the array is approximated

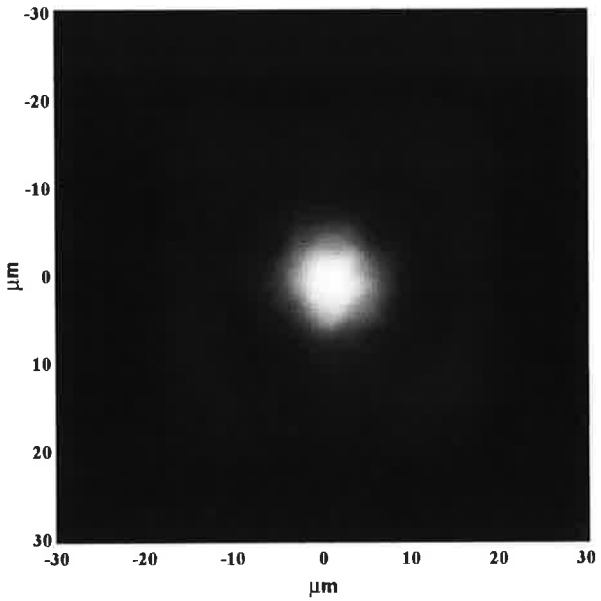

Fig. 8. Intensity PSF of the GRIN rod, $I_{\mathrm{rod}}(x_5, y_5)$.

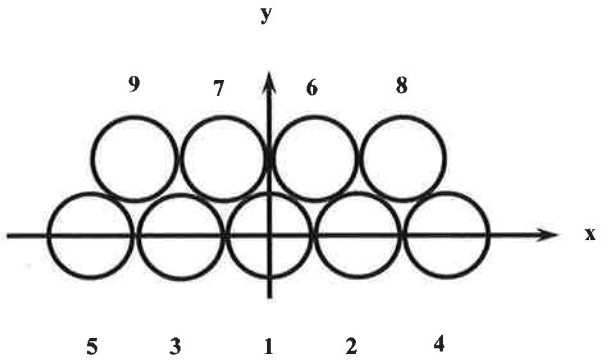

Fig. 9. GRIN rods contributing to the imaging of the object at the center of rod 1 in a two-row GRIN array.

as the essential sum of the intensity PSF of each GRIN rod [22]:

$$\mathcal{h}_{15A}(x_5,y_5;x_1,y_1)=\sum_{m=1}^{9}|h_{15}^{(m)}|^2, \tag{32}$$

in which subscripts 1 and 5 denote plane 1 to plane 5, subscript A stands for array, and the superscript denotes the impulse response for that particular mth rod. Hence, for $|h_{15}^{(m)}|^2$, we can write the following explicit form based on Eq. (29):

$$|h_{15}^{(m)}|^2=\frac{M^2|F^{-1}\{T_3^{(m)}(x_3,y_3;x_1,y_1)\}|^2}{(\lambda d_2)^4}. \tag{33}$$

More comprehensive study of the intensity PSF $\mathcal{h}_{15A}$ is described in Appendix A. From Eqs. (32) and (33), we calculate each rod's intensity PSF with aberrations considered and obtain the total intensity PSF for the array. The FWHMs of GRIN array's intensity PSFs for six different object points are listed in Table 1. Table 1 shows that the location of the object points does not play an important role as it does for a single GRIN rod. The size variations of the PSFs are within 2 μm, which is approximately 10% of the average FWHM. This is due to the periodicity of the array and the incoherent sum of images by adjacent rods. As a result, we can treat the GRIN array imaging system as an isoplanatic system. It was shown that, without considering aberrations, the FWHM of the intensity PSF is 10.7 μm for a GRIN array [22]. Clearly the aberrations dramatically degrade the resolution of a GRIN array. To accurately analyze the resolution of the GRIN array, we must include the aberrations into our physical optics formalism. Experimentally we measured the image of a 5 μm pinhole and calculated the intensity PSF by deconvolution between the image and the 5 μm pinhole object as we did for a single GRIN rod. For the well-aligned "best" arrays, our measurement of 19.9 μm for the FWHM of the array's intensity PSF along the x-axis cross section is in excellent agreement with our theoretical prediction of 19.2 μm for an axial object point as shown in Table 1. Here the "best" arrays means the three positions of the GRIN array that have the smallest FWHM for intensity PSF. The average value of the FWHM for these three intensity PSFs is 19.9 μm along the x axis and 18.4 μm along the y axis. The large degradation of resolution is mainly due to the aberrations of adjacent GRIN rods. Also, it is noted that we have not included misalignment in our theory, and this degrades resolution too.

7. Conclusion

In this paper we have extended the physical optics treatment of the GRIN rod and GRIN array systems with aberrations included into the analysis. To include the aberrations, we have investigated the OPL for a GRIN rod. The OPD between the true wavefront and the ideal wavefront on plane 3 are shown in Fig. 5. Unlike the commercial software that requires the definition of the stop position, we define the effective aberration transmission function $T_3(x_3,y_3;x_1,y_1)$ on plane 3 of a GRIN rod. This methodology provides a more accurate result for calculation of aberrations and corresponding impulse response. As defined by Eq. (18), the effective aberration transmission function $T_3(x_3,y_3;x_1,y_1)$ includes the aberrations by the calculation of the OPD, δ, which is defined in Eq. (16).

The main result of the physical optics analysis is the impulse response function, h_{15}, as derived in Eq. (29), which includes the aberrations. Our theoretical result for the PSF of a single GRIN rod is shown in Fig. 6. The corresponding experimental result is shown in Fig. 8. We obtained a theoretical value of 10.3 μm and an experimental value of 10.4 μm for an axial object's FWHM of the intensity PSF. For the single GRIN rod, the theory and experimental result agree within 1%. For a GRIN array, the theoretical results of PSFs' FWHMs for six different object points are shown in Table 1. The theoretical value of 19.2 μm agrees well with experimental measurement of 19.9 μm for FWHM along the x-axis cross section of the array's intensity PSF. In Table 2, comparison is made between the theory without aberrations included, theory including aberrations, and experimental data. Our physical optics analysis, with aberrations included, provides a powerful tool for the resolution analysis of GRIN imaging systems. This formalism could be valuable for commercial optical

Table 1. Gradient-Index Array Intensity Point-Spread Functions' Full-Width at Half-Maximum for Different Object Points

Object Location (x,y) (unit of R, radius of one rod)	(0,0)	(1,0)	(0,1)	(0,−1)	$(0,\sqrt{3})$	$(0,1+\sqrt{3})$
FWHM (μm)	(19.2,19.1)	(18.1,18.0)	(18.3,18.1)	(22.9,23.1)	(18.9,18)	(20.7,21.2)

Table 2. Comparison between the Full-Width at Half-Maximum of Intensity Point-Spread Functions

	Theory without Aberrations Included (μm)	Theory with Aberrations Included (μm)	Experiment (μm)
GRIN rod	9.0	10.3	10.4
GRIN array	10.7	19.2	19.9

design software to provide a better evaluation of the image quality for GRIN imaging systems.

For a white light source and spatially incoherent illumination, we have assumed that the intensity impulse response of the GRIN array is the incoherent sum of the intensity impulse responses of the GRIN rods, contributing to imaging as given in Eq. (32). In Appendix A we prove that this assumption is valid only if the difference between the OPL of each GRIN rod is roughly larger than 5 μm. In Eq. (A3) we provide a second order correction to the intensity impulse response of the array by including the cross-interfering terms of the amplitude impulse responses of the pairing rods with the same OPL. In Appendix B we study the resolution difference in the zerographic process comparing "parallel-to-perpendicular" textual material. As shown in Fig. 10, the intensity PSF of the array is narrower along the x axis than the y axis. This tells us that the resolution along the "parallel" (x axis) direction should be better than the "perpendicular" (y axis) direction. This theoretical result agrees with the experimental result of the resolution bars image as shown in Fig. 11.

This research was supported in part by the Army Research Office.

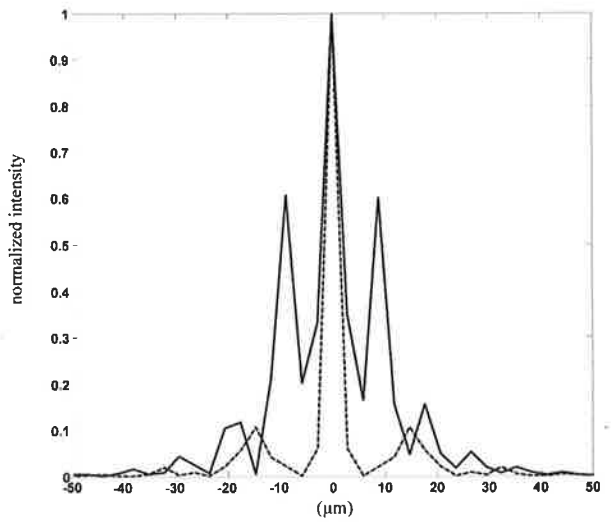

Fig. 10. Cross sections of the intensity PSF of the GRIN array along the x axis (dotted curve) and the y axis (solid curve) by coherently summing the amplitude PSFs of the five central GRIN rods [see Eq. (A2)]. This theory includes effects of aberration and OPD but not misalignment.

Fig. 11. Two-row SELFOC array imaging 18 line pairs/mm resolution target in white light.

Appendix A: Combination of Amplitude Impulse Responses including Substantial Differences in Optical Path Lengths

For incoherent illumination, it is well-known that the intensity-based impulse response is given by the absolute squared value of the corresponding amplitude impulse response. Hence we can write the following equation for the intensity impulse response $\mathcal{h}_{15A}$:

$$\mathcal{h}_{15A} = \left|\sum_{m=1}^{9} h_{15}^{(m)}\right|^2 = \sum_{m=1}^{9} |h_{15}^{(m)}|^2 + \sum_{m=1}^{9} \sum_{\substack{n=1 \\ n \neq m}}^{9} h_{15}^{(m)} h_{15}^{(n)*}. \tag{A1}$$

Considering a white light illumination source, we can derive that the condition for decorrelation between the cross terms in Eq. (A1) as the following form [21]:

$$|\rho^{(m)} - \rho^{(n)}| = \frac{\lambda_1 \lambda_2}{\lambda_2 - \lambda_1}, \tag{A2}$$

in which $|\rho^{(m)} - \rho^{(n)}|$ is the OPD between rods (m) and (n), and λ_1 and λ_2 are the wavelengths for the white light source spectrum range. For example, we assume three color channels in the range of 0.40 and 0.65 μm, then $|\rho^{(m)} - \rho^{(n)}|$ is 5 μm. As long as the smallest OPD between different rods is larger than 5 μm, the approximation made for Eq. (32) by ignoring the cross-interfering terms between different rods is valid. For an object point located at the center of rod 1, the OPL difference between rod 1 and rod 3 is over 71 μm, which can be seen from Fig. 5 by comparing the OPLs for an axial object and an off-axis object at $(2R, 0)$. Clearly there are no interfering terms between rod 1 and any other rods. The OPLs through

rods 2, 3, 6, and 7 for the object at the center of rod 1 are the same due to the symmetric arrangement of these rods in a two-row SELFOC array [30]. Similarly, the OPLs between rods 8 and 9 are the same. The optical path lengths between rods 4 and 5 are the same. In Eq. (32) we ignore this fact that the pairing of these teams can have a second-order correction to the impulse response. This more complicated analysis could be made following the steps here.

Because of the severe vignetting of rods 4, 5, 8, and 9, we could only consider rods 1, 2, 3, 6, and 7 into the analysis. The intensity impulse response $\hbar_{15A}$ of the array could be written as the following form:

$$\begin{aligned}\hbar_{15A} = {} & |h_{15}^{(1)}|^2 + |h_{15}^{(2)}|^2 + |h_{15}^{(3)}|^2 + |h_{15}^{(6)}|^2 + |h_{15}^{(7)}|^2 + h_{15}^{(2)}h_{15}^{(3)*} + h_{15}^{(2)*}h_{15}^{(3)} \\ & + h_{15}^{(2)}h_{15}^{(6)*} + h_{15}^{(2)*}h_{15}^{(6)} + h_{15}^{(2)}h_{15}^{(7)*} + h_{15}^{(2)*}h_{15}^{(7)} + h_{15}^{(3)}h_{15}^{(6)*} + h_{15}^{(3)*}h_{15}^{(6)} \\ & + h_{15}^{(3)}h_{15}^{(7)*} + h_{15}^{(3)*}h_{15}^{(7)} + h_{15}^{(6)}h_{15}^{(7)*} + h_{15}^{(6)*}h_{15}^{(7)},\end{aligned} \tag{A3}$$

where the amplitude impulse response $h_{15}^{(m)}$ for the mth rod could be calculated using Eqs. (29) and (30).

Appendix B: Theoretical Study of Resolution in the Xerographic Process Comparing "Parallel-to-Perpendicular" Textual Material

From the computer results of five amplitude impulse responses of rods 1, 2, 3, 6, and 7 with OPL in the phase terms, we could calculate the intensity impulse response $\hbar_{15A}$ of the array using Eq. (A3). The cross section of $\hbar_{15A}$ along the x axis (array direction) is shown in Fig. 10 as the dotted curve. The cross section of $\hbar_{15A}$ along the y axis is shown in Fig. 10 as the solid curve. The zero intensity PSF occurs at $\pm 5.8\,\mu$m along the x axis and occurs at $\pm 14.8\,\mu$m along the y axis. This computer result tells us that the resolution in the zerographic process along the "parallel" (x axis) direction should be better than the resolution along the "perpendicular" (y axis) direction. In Appendix C, we will show the experimental results of the resolution bars along both directions.

The other way to physically understand the resolution of the array is considering the four rods (rods 2, 3, 6, and 7) in the array as one lens, because the chief rays of these four rods have the same OPL. These lenses have different aperture size along the x axis and the y axis. Let the aperture size be $L_x \times L_y$. $L_x = 6R$ and $L_y = (2+\sqrt{3})R$, where R is the radius of one GRIN rod. We know that the first zero of the PSF occurs at $\lambda d_2/L_x = 2.4\,\mu$m along the x axis and occurs at $\lambda d_2/L_y = 3.9\,\mu$m along the y axis. This simplified model also tells us that the resolution along the "parallel" direction is better than the resolution along the "perpendicular" direction.

Appendix C: Experimental Data for Resolution of Xerographic Two-Row SELFOC Lens Array

We copied several sheets of IEEE Std 167A-1987 Facsimile Test Chart using commercial copier machines. We find that the resolution bars perpendicular to the x axis (array direction) are imaged more sharply than the resolution bars parallel to the x axis. To show this phenomenon more clearly, we record the image of 18 line pairs/mm resolution bars imaged by the SELFOC09-48A array onto a CCD. The image is shown in Fig. 11. We clearly see that the overall resolution is excellent. Also, we see the perpendicular bars are imaged more sharply than the horizontal bars. This difference indicates the resolution along the "parallel" (x axis) direction is better than the resolution along the "perpendicular" (y axis) direction for a GRIN array.

References

1. P. J. Sands, "Third-order aberrations of inhomogeneous lenses," J. Opt. Soc. Am. **60**, 1436–1443 (1970).
2. P. J. Sands, "Inhomogeneous lenses, III. Paraxial optics," J. Opt. Soc. Am. **61**, 879–885 (1971).
3. D. T. Moore and P. J. Sands, "Third-order aberrations of inhomogeneous lenses with cylindrical index distributions," J. Opt. Soc. Am. **61**, 1195–1201 (1971).
4. W. Streifer and K. B. Paxton, "Analytical solution of ray equations in cylindrically inhomogeneous guiding media. 1: Meridional rays," Appl. Opt. **10**, 769–775 (1971).
5. K. B. Paxton and W. Streifer, "Analytic solution of ray equations in cylindrically inhomogeneous guiding media. Part 2: skew rays," Appl. Opt. **10**, 1164–1171 (1971).
6. K. B. Paxton and W. Streifer, "Aberrations and design of graded-index (GRIN) rods used as image relays," Appl. Opt. **10**, 2090–2096 (1971).
7. E. W. Marchand, *Gradient Index Optics* (Academic, 1978).
8. E. W. Marchand, "Third-order aberrations of the photographic Wood lens," J. Opt. Soc. Am. **66**, 1326–1330 (1976).
9. L. Montagnino, "Ray tracing in inhomogeneous media," J. Opt. Soc. Am. **58**, 1667–1668 (1968).
10. E. W. Marchand, "Ray tracing in gradient-index media," J. Opt. Soc. Am. **60**, 1–7 (1970).
11. D. T. Moore, "Ray tracing in gradient-index media," J. Opt. Soc. Am. **65**, 451–455 (1975).
12. A. Sharma, D. Vizia Kumar, and A. K. Ghatak, "Tracing rays through graded-index media: a new method," Appl. Opt. **21**, 984–987 (1982).
13. A. Sharma, "Computing optical path length in gradient index media: a fast and accurate method," Appl. Opt. **24**, 4367–4370 (1985).

14. M. P. Rimmer, "Ray tracing in inhomogeneous media," *Optical System Design, Analysis, and Production Conference, SPIE*, Geneva, Switzerland, April 1983, Vol. 399.
15. Lambda Research Corporation, *OSLO Optics Reference Release 6.1* (Lambda Research Corporation, 2001).
16. A. Yariv, "On transmission and recovery of three-dimensional image information in optical waveguides," J. Opt. Soc. Am. **66**, 301–306 (1976).
17. K. Iga, "Theory for gradient-index imaging," Appl. Opt. **19**, 1039–1043 (1980).
18. K. Iga, Y. Kokubun, and M. Oikawa, *Fundamentals of Microoptics: Distributed-Index, Microlens, and Stacked Planar Optics* (Academic, 1984).
19. G. P. Agrawal, "Imaging characteristics of square law media," Nouv. Rev. Opt. **7**, 299–303 (1976).
20. C. Gomez-Reino, M. V. Perez, and C. Bao, *Gradient-Index Optics: Fundamentals and Applications* (Springer, 2002).
21. X. Chen, "Gradient-index fiber array for imaging," Ph.D. dissertation (University of Rochester, 2006).
22. X. Chen and N. George, "Fourier optical analysis of gradient-index array imaging," Appl. Opt. **42**, 4434–4444 (2003).
23. J. D. Jackson, *Classical Electrodynamics*, 3rd ed. (Wiley, 1998), pp. 380–381.
24. S. D. Conte and C. de Boor, *Elementary Numerical Analysis*, 3rd ed. (McGraw-Hill, 1980), Chap. 7.
25. R. H. Longhurst, *Geometrical and Physical Optics* (Longman's, Green and Company, Ltd., 1957).
26. W. J. Smith, *Modern Optical Engineering: The Design of Optical Systems* (McGraw-Hill, 1966).
27. P. Baues, "Huygens' principle in inhomogeneous, isotropic media and a general integral equation applicable to optical resonators," Opto-electronics **1**, 37–44 (1969).
28. J. A. Arnaud, "Hamiltonian theory of beam mode propagation," in *Progress in Optics* (North-Holland, 1973), Vol. 11.
29. A. E. Seigman, *Lasers* (University Science Books, 1986).
30. J. D. Rees and W. Lama, "Some radiometric properties of gradient-index fiber lenses," Appl. Opt. **19**, 1065–1069 (1980).

Optics Optimization in High-Resolution Imaging Module with Extended Depth of Field

Xi Chen*[a], Dmitry Bakin[a], Changmeng Liu[a], Nicholas George[b]
[a]Aptina Imaging, 3080 North 1st Street, San Jose, CA, USA 95134-5134
[b]The Institute of Optics, University of Rochester, Rochester, New York, USA 14627

ABSTRACT

The standard imaging lens for a high resolution sensor was modified to achieve the extended depth of field (EDoF) from 300 mm to infinity. In the module the raw sensor outputs are digitally processed to obtain high contrast images. The overall module is considered as an integrated computational imaging system (ICIS). The simulation results for illustrative designs with different amount of spherical aberrations are provided and compared. Based on the results of simulations we introduced the limiting value of the PSF Strehl ratio as the integral threshold criteria to be used during EDoF lens optimization. A four-element standard lens was modified within the design constraints to achieve the EDoF performance. Two EDoF designs created with different design methods are presented. The imaging modules were compared in terms of Strehl ratios, limiting resolution, modulation frequencies at 50% contrast, and SNR. The output images were simulated for EDoF modules, passed through the image processing pipeline, and compared against the images obtained with the standard lens module.

Keywords: extended depth of field, lens optimization, image processing, integrated computational imaging system

1. INTRODUCTION

Today the overall quality of an image from a digital camera or a mobile phone camera is determined by the combined performance of optics, imaging sensor and digital image processing. The intensive development of the CMOS imaging technology, allowed creating high-resolution imaging module having pixel size as small as 1.75μm and less. When the pixel size of a sensor is getting smaller, the lens has to have larger relative aperture to maintain and improve the SNR of the system. One of the important characteristics of the camera, which affects the image quality, is its Depth-of-field (DOF). In mobile phone cameras the DOF can be limited due to use of fast lens and small pixels. There have been a number of publications addressing work on extending DOF in camera systems. Prior research includes such diverse approaches as apodization by a weighted zone plate[1], depth estimation[2-5], light field photograhpy[6], phase masks with digital processing[7-11]. The weighted zone plate method allowed achieving a high Strehl ratio over large defocus region. In this method the resolution could be further improved after applying digital image processing. Various depth estimation methods are based on estimating high-order statistics (HOS) in an image, on edge detection and blur measurement, on using multiple cameras to acquire images of a scene or on processing multiple defocused images. The depth estimation method based on single image provides limited depth resolution. Also the accuracy of depth map could be affected by scene contents. Use of multiple cameras or multiple defocused images would require more resources. In the method based of light field photography the depth extension is achieved by inserting a microlens array between main lens and sensor. Each microlens in the array produces an image of the exit pupil of the lens camera onto a unique area of the sensor. The camera then extracts information about both horizontal and vertical parallax, which improves the reliability of the depth estimates. The drawback of this camera is low overall resolution.

There have been several approaches to achieving extended depth of field using phase masks in combination with digital processing. In such integrated computational imaging system, the optical transfer function (OTF) or point spread function (PSF) is purposely blurred to become more invariant with object distance. The blurred images are then digitally recovered using the invariant PSF. There is no light loss due to decreased aperture. Among these approaches, the logarithmic asphere[8, 10, 11] has circularly symmetry. The design of the logarithmic asphere is based on the Fermat's Principle which provides more invariant PSF. The logarithmic asphere profile could be expressed in terms of spherical aberration which is easy to test.

*xchen@aptina.com; phone 1 408 660 2662; www.aptina.com

Novel Optical Systems Design and Optimization XI, edited by R. John Koshel, G. Groot Gregory, James D. Moore Jr., David H. Krevor, Proc. of SPIE Vol. 7061, 706103 · © 2008 SPIE
CCC code: 0277-786X/08/$18 · doi: 10.1117/12.795970

In this paper, we study how different optical design optimization methods affect EDoF performance of CMOS camera when accounting for demosaicing and focus recovery (FR) post-processing. The overall image quality is characterized against critical parameters of the optical system, such as spherical aberration, shape of PSF, and Strehl ratio. Two optical design optimization methods for extending depth of field of ICIS are presented. The performance is compared against that of a standard imaging module. A series of lenses were designed to introduce different amount of spherical aberrations. Their performances are compared in terms of Strehl ratio, resolution before and after FR algorithm, MTF50 before and after FR, SNR before and after FR. Thresholds on Strehl ratios for imaging modules with 1.75μm pixel are defined based on results of camera scene modeling (CSM) simulations. Further, we explore how modification of a standard imaging lens for a specific 1.75μm 3 mega-pixel sensor extends the depth-of-field. Two EDoF designs are presented and compared with the standard imaging module. The first EDoF lens is designed with logarithmic asphere EDoF technology. The basic idea of logarithmic asphere is reviewed. The second EDoF lens is developed based on optimization for achieving uniform PSFs over full field and range of object distances.

2. BASIC REQUIREMENTS TO PSF SHAPE AND STREHL RATIO

We used invariant PSF method to design lenses with EDoF properties over predefined range of object distances. The on-axis PSF invariance was achieved by applying logarithmic asphere algorithm[8, 10, 11]. A series of lenses were generated with the amount of spherical aberrations ranging from 0 to 6.824λ. The corresponding Strehl ratio was in the range from 1 to 0.1. All lenses have had the same first-order optics parameters values, such as F-number of 2.4, effective focal length of 3.79 mm and half diagonal field of view of 30.5°. The PSF profile of each lens was used to generate simulated image of a scene. The final image output accounted for optics, sensor response, and image processing. The simulated results represent a real Bayer image output from the CMOS sensor with simulated camera noises added. This raw Bayer image was demosaiced to generate the bitmap and further processed for FR and basic color pipeline. The digitally recovered image is then evaluated for MTF, and SNR. The recovered image characteristics were measured for a series of lenses with 3 mega-pixel 1.75μm pixel sensor with and without FR algorithm. The two representative PSFs for lenses with different amount of 3rd-order spherical aberrations and defocus and with Strehl ratio of 0.1 and 1 are shown in Figs. 1. No other aberrations were introduced into the designs.

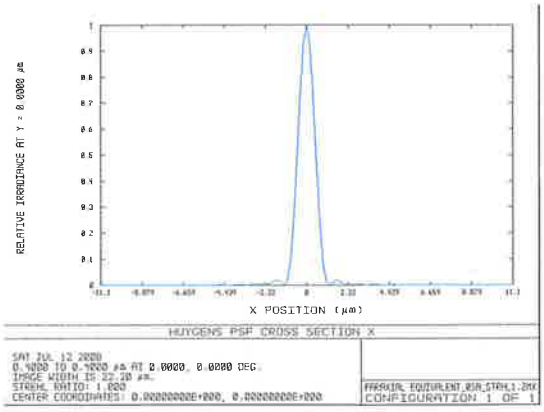

Fig. 1(a) The PSF for an ideal diffraction- limited lens without aberrations; the Strehl ratio is 1.

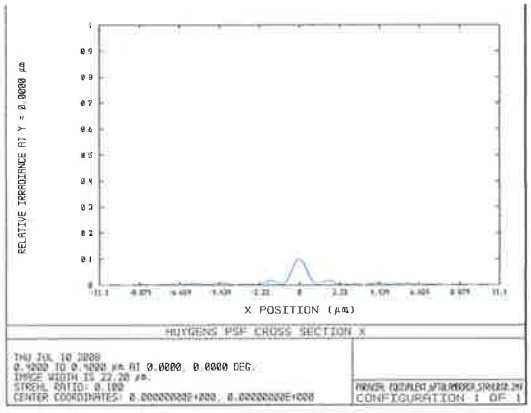

Fig. 1(b) The PSF for a lens with 6.824λ spherical aberration and compensated defocus; the Strehl ratio is 0.1.

The reference image produced with an ideal diffraction-limited lens (Strehl ratio of 1) (shown in Fig. 1 (a)) was simulated for 1.75μm 3 mega-pixel sensor. It is shown in Fig. 2(a). The central part of the image was cropped on Fig. 2(b) to show details. The finest resolution bars in the upper left corner in Fig. 2(b) are smeared out due to aliasing which is limited by sensor's pixel size. We measure the MTF of this image using Imatest software. SNR is measured for the third darkest gray patch in Fig. 2(b). From Fig. 2(b), we see that the finest resolution bar in the left upper corner is smeared out due to aliasing. We notice that the red and blue channels of images in Figs. 2 have degraded after demosaicing. Demosaicing procedure causes loss in image quality even when the diffraction-limited optics was used.

Fig. 2(a) The reference image simulated with an ideal lens. The lens has no aberrations; Strehl ratio of 1. The sensor has 3 million pixels, size 1.75μm.

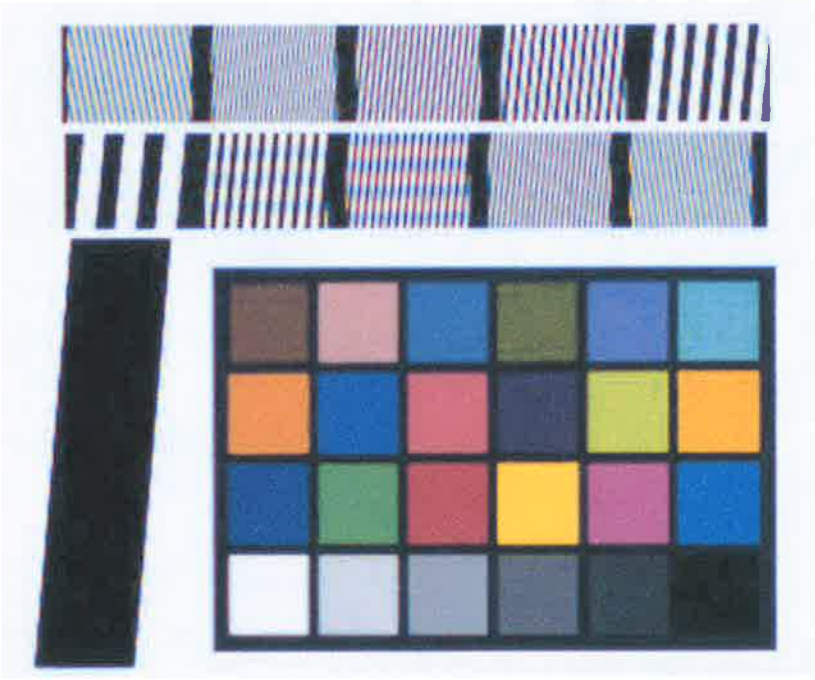

Fig. 2(b) The cropped central part of the simulated image after demosaicing as shown in Fig. 2(a).

Additional Bayer images for a 1.75μm 3mega-pixel CMOS sensor were simulated using the lens PSFs with different amount of spherical aberrations. These images were further processed with the FR and color pipeline algorithms. In the FR algorithm the simulated PSFs were applied to restore the details of original scene. The modulation frequencies at 50% MTF (MTF50) along with the SNR values for demosaiced images before and after FR algorithm are presented in Table I. MTF50 was measured using Imatest software.

From Table I it follows that the FR processing does improve the image contrast. The MTF50 is improved after FR processing. But the cut-off frequency for a lens could not be improved by image restoration. When OTF has zeros at frequencies less then Nyquist, the cut-off resolution is limited by optics instead of pixel. As the result, the FR processing did not raise the cut-off frequencies of blurred images. FR amplified noise was depending on lens Strehl

ratio. The perfect lens with Strehl ratio of 1 has the best image quality. After considering cut-off resolution, image contrast, and SNR of the processed image, we choose the Strehl ratio of 0.3 as the limiting threshold for EDoF design with 1.75 μm CMOS sensor.

Table I. Comparison of modulation frequencies at 50% MTF (MTF50) and the SNR values for 1.75μm, 3 mega-pixel CMOS sensor imaging modules with various amounts of spherical aberrations

Amount of spherical aberration (λ)	Strehl ratio	Frequency for 50% MTF (cys/mm)		SNR	
		Before FR	After FR	Before FR	After FR
0	1	101	-	30.1	-
1.93	0.5	81	91	28.5	27.3
2.53	0.3	86	89	28.5	26.3
2.70	0.25	66	89	30.1	26.3
2.90	0.2	66	90	28.1	23.3
6.82	0.1	32	54	27.0	19.3

3. OPTICAL DESIGN OPTIMIZATION FOR EDOF LENS

Further, we explore several optics optimization methods to be applied for designing high-resolution EDoF imaging module. We've used the standard imaging lens as the starting design, and converted it into an EDoF lens. Two examples of extended depth-of-field imaging lens are presented here. The first one is done with logarithmic asphere technology. The second design is done with off-axis field optimization based on logarithmic asphere design. The focus recovery algorithm allows achieving the best recovery of a scene image when the PSF stays constant over range of object distances and the full field. For restoring high resolution images the Strehl ratio of invariant PSF's should stay above the threshold value as was described in section 2.

3.1 Standard imaging lens module

The first-order optics parameters for the standard lens are listed here: half field of view of 30.5°; F-number of 2.8; maximum chief ray angle (CRA) is 28.4°; geometrical distortion of 1.7% (barrel); axial color is 3μm for spectrum range from 0.43μm to 0.65μm; lateral color is 0.4μm. This lens was designed for a 1.75μm, 3 mega-pixel CMOS sensor. The layout of this lens is shown in Fig. 3. The stop is located on the rear surface of the first lens element. This lens has 0.36λ of spherical aberration. All surfaces are standard or aspheric surfaces. We plotted the PSFs for object at 10meters, 65cm and 30cm in Figs. 4. Both PSFs' shape and Strehl ratio strongly vary with object distances. This variation in PSF leads to unrecoverable blurred images for out-of-focus objects.

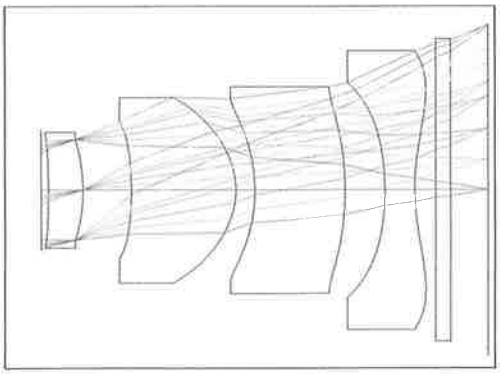

Fig. 3 The layout of the standard imaging lens.

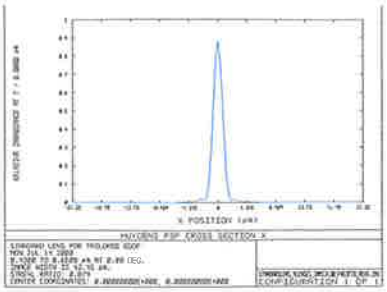

Fig. 4(a) On-axis PSF for a standard lens with object at 10meters. Strehl ratio is 0.879.

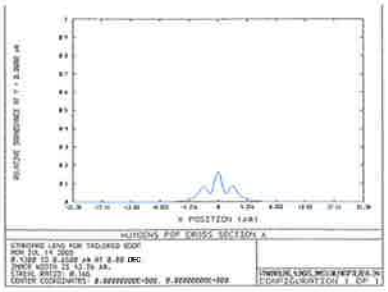

Fig. 4(b) On-axis PSF for a standard lens with object at 65cm. Strehl ratio is 0.165.

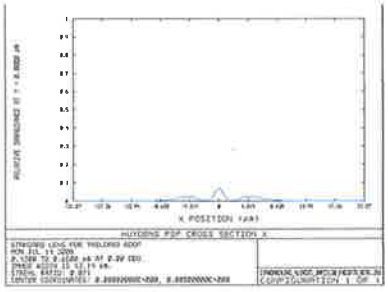

Fig. 4(c) On-axis PSF for a standard lens with object at 30cm. Strehl ratio is 0.071.

The plot of on-axis PSF Strehl ratio vs. object distance for this lens is shown in Fig. 5. The x-axis is object distance from 250mm to 10meters. The y-axis is the PSF Strehl ratio for an axial object. It is seen that the Strehl ratio drops below 0.3 when an object distance is less then 770mm.

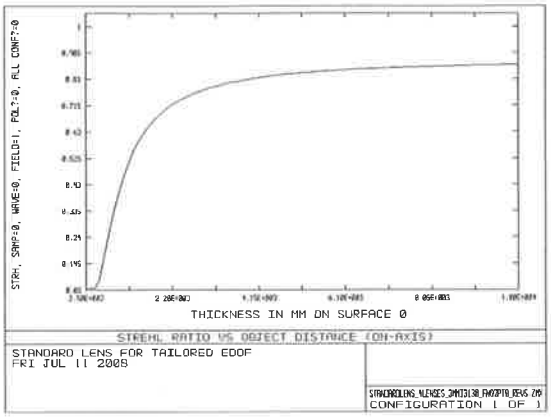

Fig. 5 The axial PSF Strehl ratio vs. object distance (from 250mm to 10meters) for a standard imaging lens.

The simulated images for scene objects positioned at 10meters, 65cm and 30cm are shown in Figs. 6(a), (b) and (c). They are cropped from the whole field images. When object gets closer (shown in Figs. 6(b) and (c)), the second finest resolution bar is not resolvable anymore. The poor image quality at 65cm and 30cm is within our expectation from PSFs in Figs. 4(b) and 4(c). The Strehl ratio, spatial frequency for 50% MTF, and SNR for objects at 10meters, 65cm and 30cm are summarized in Table II. The SNR for object at 30cm is very high due to defocus blurring.

Table II. Performance of a standard imaging module with 1.75μm sensor.

Object distance	Strehl Ratio (at 40% field height)	MTF50 Frequency (cys/mm)	SNR
10meters	0.82	103	29.6
650mm	0.20	71	30.1
300mm	0.06	42	54.5

Fig. 6(a)

Fig. 6(b)

Fig. 6(c)

Fig. 6(a) 100% cropped simulated image for a standard lens imaging module with object at 10meters; Fig. 6(b) simulated image for a standard lens with object at 65cm; Fig. 6(c) simulated image for a standard lens with object at 30cm. The detector is a 1.75μm, 3mega-pixel CMOS sensor.

3.2 Logarithmic asphere EDoF design method

The logarithmic asphere EDoF technology[8, 10, 11] purposely blurs the point spread function so that PSF is invariant with object distance. The logarithmic asphere lens has circularly symmetry with controlled continuous radial variation of focal length. Each radial ring has one specific local focal length which provides a sharp focus of a specific object distance on the detector plane. Therefore the images for objects within EDoF range are always sharply focused by one specific ring of the lens and defocused by the other rings. The phase delay function $\phi_\beta(\rho)$ of a logarithmic asphere EDoF lens is given by[10]

$$\phi_\beta(\rho)=\alpha_\beta\frac{t^2+\rho^2}{2}\{\ln[A_\beta(t^2+\rho^2)]-1\}+\frac{\lambda_0^2}{8\pi^2}\{\frac{1}{16}\alpha_\beta^3(t^2+\rho^2)^2[45-42\ln[A_\beta(t^2+\rho^2)]+\ldots$$
$$18\{\ln[A_\beta(t^2+\rho^2)]\}^2-4\{\ln[A_\beta(t^2+\rho^2)]\}^3]-\frac{B_\beta\rho^2}{2}\}-\frac{2\pi}{\lambda_0}(\sqrt{t^2+\rho^2}-t)+const., \quad (1)$$

Where t is the detector location; α_β and A_β are calculated with pre-determined EDoF range. $\phi_\beta(\rho)$ is the sum of the phase transmission of an ideal diffraction-limited lens and the phase delay of the phase plate which provides EDoF. If we expand the phase delay function of the phase plate into polynomial of ρ^2, it turns out the main terms are ρ^4 and ρ^6 which represent the 3rd-order and 5th-order spherical aberrations. With first-order optics parameters and pre-determined EDoF range for object distance and Eq. (1), we could calculate the phase delay function of a logarithmic asphere phase plate and convert it into surface profile. Before we calculate the phase delay function of the logarithmic asphere phase plate, we specify which surface in the standard imaging lens to be modified. We know from the aberration theory that modification on the stop surface does not change other third-order off-axis aberrations such as coma, astigmatism, and Petzval curvature. Therefore we determine to modify the surface which is the closest to the stop. We modify the rear surface of the first lens element, which is the stop surface as shown in Fig. 3, by minor change of the aspheric coefficients for ρ^4, ρ^6 and ρ^8. The logarithmic asphere EDoF lens has the same first-order optics parameters as the standard lens described in section 3.1. The geometric distortion is 1.7% (barrel). The axial color is

3μm for spectrum from 0.43μm to 0.65μm. The lateral color is 0.35μm. This minor modification introduces -2.31λ of spherical aberrations to the standard imaging lens. Therefore the logarithmic asphere EDoF lens has -1.95λ of spherical aberrations. The on-axis PSFs for objects at 10meters, 65cm and 30cm are shown in Figs. 7. The Strehl ratios are 0.303, 0.570 and 0.191 for 10meters, 65cm and 30cm, respectively. Comparing Figs. 7 with Figs. 4, we see that as the object distance changes, the logarithmic asphere EDoF lens has more consistent PSFs than the standard lens.

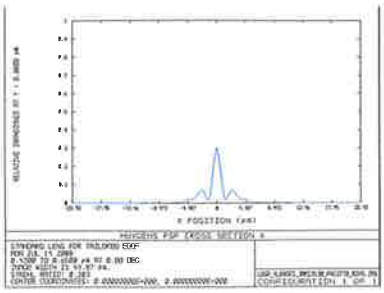

Fig. 7(a) On-axis PSF for logarithmic sphere EDoF lens with object at 10meters. Strehl ratio is 0.303.

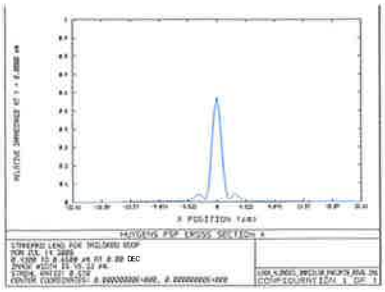

Fig. 7(b) On-axis PSF for logarithmic sphere EDoF lens with object at 65cm. Strehl ratio is 0.570.

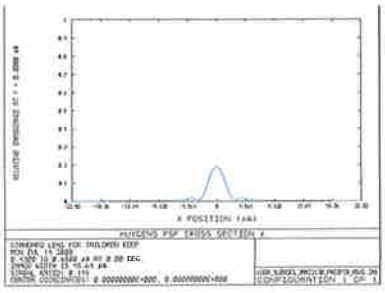

Fig. 7(c) On-axis PSF for logarithmic sphere EDoF lens with object at 30cm. Strehl ratio is 0.191.

We simulated logarithmic asphere EDoF module images and applied the FR algorithm with the PSF at 65cm for objects at 10meters, 65cm and 30cm. The cropped images are shown in Figs. 8. The second finest resolution bars on all three images could be resolved. The image contrast on Fig. 8(b) is the best among the three images. The image quality parameters are summarized in Table III for objects at 10meters, 65cm and 30cm. For extended depth-of field range of 300mm to infinity, there is no big loss in resolution. The contrast of images at 65cm and 10meters are comparable to the contrast of a standard lens at best-focus distance. SNR are lower than standard lens due to the noise amplification by digital processing.

Fig. 8(a)

Fig. 8(b)

Fig. 8(c)

Fig. 8(a) cropped simulated images for the logarithmic asphere EDoF lens at object distance 10meters; Fig. 8(b) simulated image for object at 65cm; Fig. 8(c) simulated image for object at 30cm. The detector is a 1.75μm, 3mega-pixel CMOS sensor.

Table III. Performance of a logarithmic asphere EDoF imaging module with 1.75μm sensor.

Object distance	Strehl Ratio (at 40% field height)	MTF50 Frequency (cys/mm)	SNR
10meters	0.27	100	21.8
650mm	0.45	102	22.0
300mm	0.23	61	21.9

3.3 Optimization off-axis field performance in EDoF design

To further improve the off-axis field performance, we optimized the logarithmic asphere EDoF lens to obtain more uniform point spread function over the entire field and over the range of object distances. We allowed the aspheric coefficients, radius of curvatures and thickness of lenses to vary. The first-order optics parameters are constrained to be the same as before. Geometrical distortion is 1.4% (barrel). The axial color is 4μm for spectrum range of 0.43μm to 0.65μm. The lateral color is 0.7μm. The maximum CRA is 29°. The amount of spherical aberration which is the combination of 3rd-order, 5th-order and 7th-order spherical aberrations is -0.7λ. The lens layout is shown in Fig. 9. The axial PSFs at 10meters, 65cm and 30cm are shown in Figs. 10. The variation in PSF is much less than the standard imaging lens. The Strehl ratios vary from 0.259 to 0.385 for object distances from 30cm to infinity. The PSFs maintain more uniform shape in comparison to the standard imaging lens.

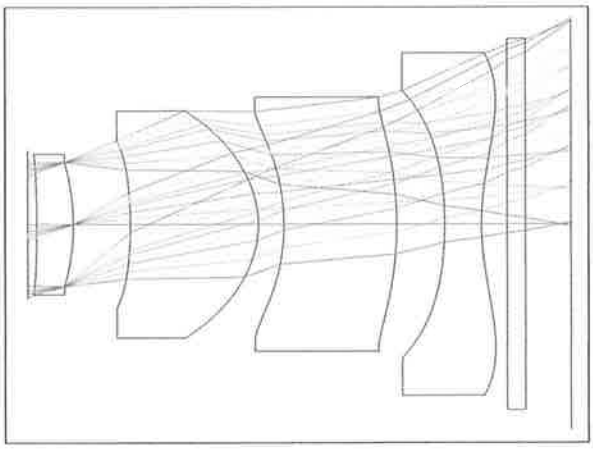

Fig. 9 The lens layout for the optimized off-axis performance EDoF lens.

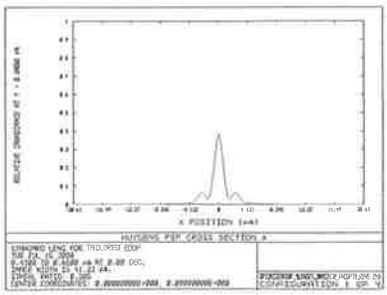

Fig. 10(a) On-axis PSF for optimized off-axis performance EDoF lens with object at 10meters. Strehl ratio is 0.385.

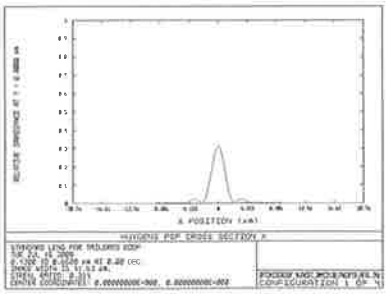

Fig. 10(b) On-axis PSF for optimized off-axis performance EDoF lens with object at 65cm. Strehl ratio is 0.314.

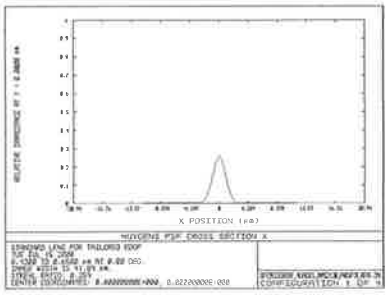

Fig. 10(c) On-axis PSF for optimized off-axis performance EDoF lens with object at 65cm. Strehl ratio is 0.259.

The gradual improvements in the EDoF extension performance could be observed on Figs.11(a-c), comparing the through-focus MTF plots prepared for the standard lens, the logarithmic asphere lens, and the lens with optimized off-axis performance.

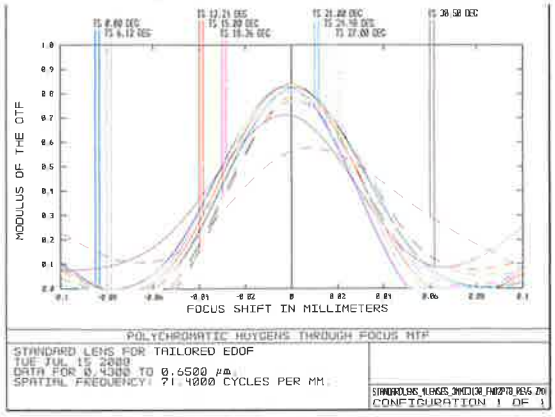

Fig. 11(a) Huygens through-focus MTF at Ny/4 (71.4cys/mm) for the standard imaging lens.

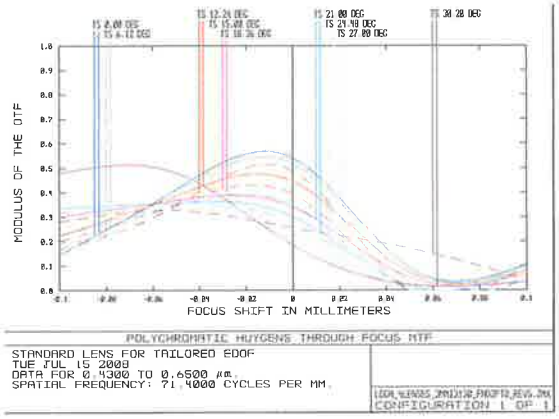

Fig. 11(b) Huygens through-focus MTF at Ny/4 (71.4cys/mm) for the logarithmic asphere EDoF lens.

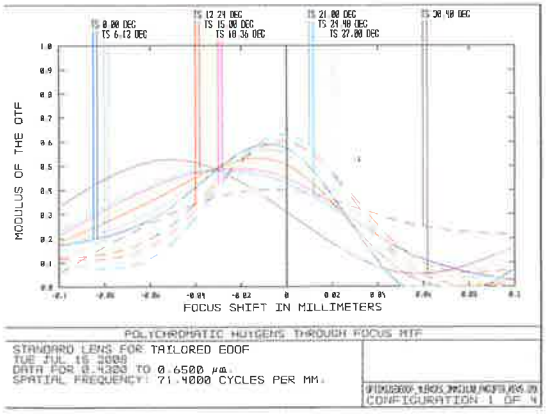

Fig. 11 (c) Huygens through-focus MTF at Ny/4 (71.4cys/mm) for the EDoF lens with optimized off-axis performance.

The simulated image for the optimized lens in a 1.75μm, 3mega-pixel CMOS sensor module was processed through focus recovery algorithm. The cropped part of the recovered image corresponding to 60% to 80% field heights is compared with those for the ideal lens module and for the logarithmic asphere EDoF lens module in Fig. 12(c). The object scene selected for simulation was the same scene as simulated in Fig. 2 (a). The object distance is equal to 10 meters.

Fig. 12(a) 100% cropped left corner in the simulated image for an ideal diffraction-limited lens.

Fig. 12(b) 100% cropped left corner in the recovered image for the logarithmic asphere EDoF lens.

Fig. 12(c) 100% cropped left corner in the recovered image for the optimized off-axis performance EDoF lens.

The observation of images shown on Figs. 12(a-c) confirms that the ideal lens produced the best image quality. The off-axis field performance of the improved off-axis EDoF lens is better than logarithmic asphere EDoF lens in terms of resolution and contrast. The improved EDoF lens has the resolution and contrast comparable with the perfect lens, while at the same time it produced more artifacts and noise. A better off-axis performance requires less variant PSF over field or slowly varying PSF over field with PSF Strehl ratio to be above the 0.3 threshold level for good SNR. The comparison of simulated images between the EDoF modules having lenses optimized with different design approaches provides guidance on improving the lens design optimization procedures for better off-axis performance.

To compare the performance of the improved off-axis EDoF lens against that of the standard lens, we analyzed the 100% cropped parts of images simulated for the standard lens, described earlier in section 3.1. The Figs. 13(a), (b) and (c) are prepared for objects at 10meters, 65cm and 30cm, respectively. The imaging module has a 1.75μm, 3mega-pixel CMOS sensor. In the images prepared for the standard lens imaging module we can see the how the resolution and contrast get lost as the object moved closer to the lens. For comparison the images of the improved off-axis performance EDoF lens are shown in Figs. 14. The sensor is the same as the one for the standard lens imaging module. When comparing images on Figs. 13 and 14, it is visible that the image quality at 10meters is about the same for both modules. The image of the EDoF module is getting slightly better than that of the standard lens module when object is at 65cm. The image of the EDoF module is becoming superior to that for the standard lens module when object is at 30cm. The EDoF imaging module extends the depth-of-field to 30cm or closer which gives 2x extension factor then that of the standard lens module.

Fig. 13(a) standard lens with object at 10meters.

Fig. 13(b) standard lens with object at 65cm.

Fig. 13(c) standard lens with object at 30cm.

Fig. 14(a) EDoF lens with improved off-axis performance at 10meters.

Fig. 14(b) EDoF lens with improved off-axis performance at 65cm.

Fig. 14(c) EDoF lens with improved off-axis performance at 30cm.

4. CONCLUSION

It was demonstrated that the optical design for the high-resolution EDoF camera can be optimized from a standard lens by introducing the proper amount of the spherical aberrations into optical elements, and simultaneously controlling the uniformity of the Point Spread Function over the required range of object distances and over the full field. The Strehl Ratio value of the PSF can be used as the one universal integral parameter for lens optimization. The image resolution

and the overall quality are strongly affected by size and shape of a point spread function and Strehl Ratio. From the analysis of the performance of the EDoF imaging module with 1.75μm 3 mega-pixel CMOS sensor, we concluded that during optimization the lens PSF Strehl ratio should be kept above the 0.3 threshold value. We've designed two EDoF lenses – one based on logarithmic asphere algorithm, and the other based on off-axis performance optimization. The performances of both EDoF imaging modules were compared against that of a standard imaging module. The optimized EDoF imaging modules allowed extending the depth-of-field to 30cm. As shown in Figs. 13 and 14, the images at object distances 10meters, 65cm and 30cm taken with the EDoF imaging module look as good as the best-focused image taken with the standard lens imaging module. An EDoF extension factor in the range of 2 to 3 was achieved.

5. ACKNOWLEDGEMENT

We are very thankful to our colleagues Dr. Brian Keelan, Dr. Dan Delescue and Dr. Junqing Chen for their suggestions and supports. We are also very thankful to Dr. Wanli Chi at the Institute of Optics, University of Rochester for his great ideas and suggestions.

REFERENCES

[1] Jorge Ojeda-Castaneda and Berriel-Valdos, L. R., "Zone plate for arbitrarily high focal depth," Appl. Opt. 29, 994-997 (1990).

[2] Ko, J., Kim, M. and Kim, C., "2d-to-3d stereoscopic conversion: Depth-map estimation in a 2d single-view image," in Proc. SPIE Applications of Digital Image Processing XXIX, (2007).

[3] Bae, S. and Durand, F., "Defocus magnification," Computer Graphics Forum 26, 571-579 (2007).

[4] Marr, D. and Poggio, T., "A computational theory of human stereo vision," Proc. Royal Soc. London Ser. B 204, 301-328 (1979).

[5] Grossmann, P., "Depth from focus," Pattern Recogn. Lett. 5, 63-69 (1987).

[6] Ng, R., Levoy, M., Bredif, M., Duval, G., Horowitz, M., Hanrahan, P., "Light field photography with a hand-held plenoptic camera," Stanford Tech Report CTSR 2005-02, 1-11.

[7] Dowski, E. R. and Cathey, W. T., "Extended depth of field through wave-front coding," Appl. Opt. 34, 1859-1866 (1995).

[8] Chi, W. and George, N., "Electronic imaging using a logarithmic asphere," Opt. Lett. 26, 875-877 (2001).

[9] Ben-Eliezer, E., Marom, E., Konforti, N., and Zalevsky Z., "Radial mask for imaging systems that exhibit high resolution and extended depths of field," Appl. Opt. 45, 2001-2013 (2001).

[10] Chi, W. and George, N., "Computational imaging with the logarithmic asphere: theory," J. Opt. Soc. Am. A 20, 2260-2273 (2003).

[11] George, N. and Chi, W., "extended depth of field using a multi-focal length lens with a controlled range of spherical aberration and a centrally obscured aperture," US Patent 7,336,430, B2.

Extending the depth of field through unbalanced optical path difference

Kaiqin Chu,* Nicholas George, and Wanli Chi

Institute of Optics, University of Rochester, Rochester, New York 14627, USA

*Corresponding author: kaiqin@optics.rochester.edu

Received 3 September 2008; accepted 28 October 2008;
posted 13 November 2008 (Doc. ID 100724); published 19 December 2008

We describe a simple method to extend the depth of field of a conventional camera by inserting a transparent annular ring in front of the pupil of the lens. The insertion of the ring creates an unbalanced optical path difference across the lens aperture, which partitions the pupil and leads to an extended depth of field. This system is analyzed by diffraction and random process theory. Experiments are reported that are in good agreement with the theory. © 2008 Optical Society of America

OCIS codes: 030.0030, 100.0100, 110.0110, 120.0120, 130.0130, 220.0220.

1. Introduction

In an earlier paper [1], we described a polarization coding configuration to achieve extended depth of field in an imaging system where a polarization rotation device is placed in the pupil plane of the imaging system. The light coming from the center region of the pupil has its polarization rotated 90° while the light coming from the outer region of the pupil has its polarization unchanged. Because of their orthogonal polarizations, the light diffracted by the central and outer regions of the pupil should be added by terms of intensities when they meet at the detector. In this sense, the pupil is partitioned into a disk and an annular ring by those orthogonal polarizations. In this paper we will describe an imaging system where we partition the pupil into separate annular rings with "decoupling" caused by selected unbalance in the optical paths for the imaging of an axial point, as is explained below. This method of partitioning depends on a concept of spatial coherence and it is important at the outset to have a clear explanation of the notion of optical path difference (OPD), which is one of the fundamental principles of optical system design. "The Rayleigh criterion, or limit, allows not more than one-quarter wavelength of OPD over the wave front with respect to a reference sphere about a selected image point in order that the image may be 'sensibly' perfect" [2]. In explaining OPD, Cornady [3,4] describes the statement of the Rayleigh quarter-wavelength limit as "arising from the true genius of this great Physicist who generalized from a small number of test cases." From today's modern viewpoint of imaging and coherence, the Rayleigh limit on OPD [5] is an interferometric criterion that has been greatly clarified by holography [6].

It is well known that the depth of field of a lens is greatly increased by using a smaller aperture and, moreover, that an obscured annular aperture is also effective [7]. Earlier work on extended depth-of-field improvements with an obscured aperture are found in the literature [8]. Herein we consider the analysis of the point-spread function for a lens that has been annularly partitioned by providing purposefully unbalanced paths, as shown in Fig. 1. From Fourier optics it is well known that one can write an amplitude-based point-spread function (APSF) h_{12} for the imaging system shown in Fig. 1. From this, one derives the intensity point-spread function (PSF) as $|h_{12}|^2$ [9]. Moreover, we show that with adequate unbalance in optical paths, the overall PSF is obtained by the sum $\sum_{m=1}^{M} |h_{12}^{(m)}|^2$, where $h_{12}^{(m)}$ is the APSF of each annular segment of the aperture and M is the total number of annular regions. Thus, the partition of the lens aperture by unbalanced OPD will lead to a relatively invariant PSF with respect to defocus and the depth of field is extended.

0003-6935/08/366895-09$15.00/0

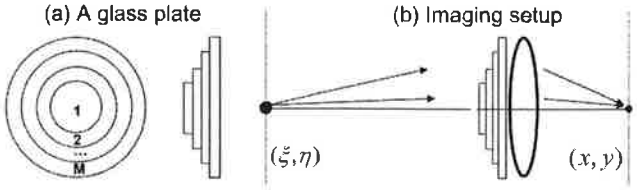

Fig. 1. Proposed imaging system to extend depth of field: (a) the inserted plate; (b) the modified imaging system.

To our knowledge, our approach is the first to utilize the concept of unbalanced OPD for imaging, particulary for extending the depth of field. The image formation process of our system involves aperture diffraction and random processes. In this paper we give a mathematical description of the principle of pupil partitioning by unbalanced OPD (Section 2). The unbalanced OPD is created through insertion of thin glass plates with selected thickness. The effect of the thickness of the plates is discussed in Section 3. Then we proceed to derive the PSF of the partitioned lens (Section 4) and study its properties (Section 5). The imaging performance is tested through computer simulations (Section 6) and laboratory experiments (Section 7). The conclusion is given in Section 8.

2. Pupil Partitioning by Unbalanced OPD Purposefully Created through Insertion of Thin Glass Plates

Consider a conventional imaging system as shown in Fig. 2, in which planes I and II are not necessarily conjugate planes of each other; i.e., $\frac{1}{z_1}+\frac{1}{z_2}-\frac{1}{f}$ can be arbitrary. The amplitude impulse response can be written as [9]

$$h_{12}(x,y,\xi,\eta;\nu)=\frac{-\exp\left[-ik\left(z_1+z_2+\frac{\xi^2+\eta^2}{2z_1}+\frac{x^2+y^2}{2z_2}\right)\right]\nu^2}{c^2z_1z_2}\times\iint_{\Sigma}P(u,v)\times\exp\left[-ik\frac{u^2+v^2}{2}\left(\frac{1}{z_1}+\frac{1}{z_2}-\frac{1}{f}\right)\right]\times\exp\left\{ik\left[\left(\frac{\xi}{z_1}+\frac{x}{z_2}\right)u+\left(\frac{\eta}{z_1}+\frac{y}{z_2}\right)v\right]\right\}\times du\,dv,$$

where the integration is over the pupil of the lens Σ and $P(u,v)$ is the amplitude transmission function of the pupil. In this paper all integrations are assumed to be from $-\infty$ to ∞ unless specified otherwise. Under spatially incoherent and broadband illumination, the output intensity can be written as [10]

$$I(x,y)=\iiint S(\xi,\eta;\nu)|o(\xi,\eta)|^2|h_{12}(x,y,\xi,\eta;\nu)|^2d\xi d\eta d\nu, \quad (1)$$

where $S(\xi,\eta;\nu)$ is the spectrum of the illumination source. $o(\xi,\eta)$ is the amplitude transmission function of the object. Thus, the intensity PSF of a conventional imaging system under broadband illumination is

$$|h_{12}(x,y,\xi,\eta)|^2=\int S(\nu)|h_{12}(x,y,\xi,\eta;\nu)|^2d\nu. \quad (2)$$

The spatial variation of the illumination is ignored here since it would only introduce a scaling factor to the PSF. When we break the pupil of the lens into two regions, Σ_1 and Σ_2, as shown in the right side of Fig. 2, the lens transmission can be rewritten as

$$P(u,v)=\begin{cases}P_1(u,v), & (u,v)\in\Sigma_1;\\ P_2(u,v), & (u,v)\in\Sigma_2.\end{cases} \quad (3)$$

The total diffraction at the image plane should be the coherent sum of the diffractions from Σ_1 and Σ_2. Thus, the total PSF can be written as

$$|h_{12}(x,y,\xi,\eta)|^2=\int S(\nu)|h_{12}^{(1)}(x,y,\xi,\eta;\nu)+h_{12}^{(2)}(x,y,\xi,\eta;\nu)|^2d\nu, \quad (4)$$

where

$$h_{12}^{(1)}(x,y,\xi,\eta;v)=\frac{-\exp\left[-ik\left(z_1+z_2+\frac{\xi^2+\eta^2}{2z_1}+\frac{x^2+y^2}{2z_2}\right)\right]\nu^2}{c^2z_1z_2}\times\iint_{\Sigma_1}P_1(u,v)\times\exp\left[-ik\frac{u^2+v^2}{2}\left(\frac{1}{z_1}+\frac{1}{z_2}-\frac{1}{f}\right)\right]\times\exp\left\{ik\left[\left(\frac{\xi}{z_1}+\frac{x}{z_2}\right)u+\left(\frac{\eta}{z_1}+\frac{y}{z_2}\right)v\right]\right\}\times du\,dv,$$

$$h_{12}^{(2)}(x,y,\xi,\eta;v)=\frac{-\exp\left[-ik\left(z_1+z_2+\frac{\xi^2+\eta^2}{2z_1}+\frac{x^2+y^2}{2z_2}\right)\right]\nu^2}{c^2z_1z_2}\times\iint_{\Sigma_2}P_2(u,v)\times\exp\left[-ik\frac{u^2+v^2}{2}\left(\frac{1}{z_1}+\frac{1}{z_2}-\frac{1}{f}\right)\right]\times\exp\left\{ik\left[\left(\frac{\xi}{z_1}+\frac{x}{z_2}\right)u+\left(\frac{\eta}{z_1}+\frac{y}{z_2}\right)v\right]\right\}\times du\,dv,$$

are the APSF of lenses with pupil Σ_1 and Σ_2, respectively.

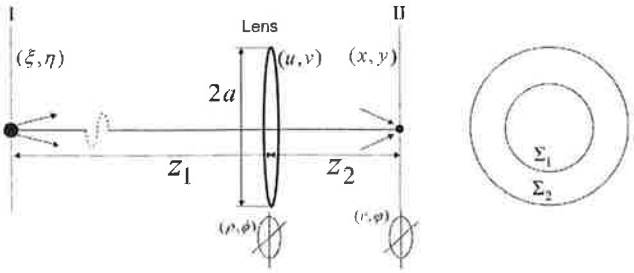

Fig. 2. Conventional imaging system.

When a thin plate of thickness

$$d = \begin{cases} d_1, & (u,v) \in \Sigma_1 \\ d_2, & (u,v) \in \Sigma_2 \end{cases} \tag{5}$$

is inserted in front of the pupil plane, as shown in Fig. 2, the transmission function for the glass plate can be derived by considering the optical path length (OPL) of light when passing through the plate. Figure 3 is an enlarged view of the glass plate. The first surface of the plate is in plane (1) and the last surface is in plane (3). When light passes the plate through region Σ_1, the physical path (represented by AB in Fig. 3) equals d_1 and the OPL between plane (3) is nd_1. For light passing the plate through region Σ_2, it will first pass through an air slab of thickness $d_1 - d_2$ and then pass through the glass slab of thickness d_2 (represented by CDE in Fig. 3). Thus, the OPL in region Σ_2 is $d_1 - d_2 + nd_2$. The transmission function from plane (1) to plane (3) can be written as

$$t_{\text{plate}}(u,v) = \begin{cases} \exp(-iknd_1), & (u,v) \in \Sigma_1 \\ \exp[-ik(d_1 - d_2 + nd_2)], & (u,v) \in \Sigma_2 \end{cases}. \tag{6}$$

The total pupil function when the glass plate is considered can be written as

$$P^{(p)}(u,v) = \begin{cases} P_1(u,v)\exp(-iknd_1), & (u,v) \in \Sigma_1; \\ P_2(u,v)\exp[-ik(d_1 - d_2 + nd_2)], & (u,v) \in \Sigma_2, \end{cases} \tag{7}$$

where the superscript (p) stands for a lens with the plate inserted. The amplitude response of the individual region can be found directly by plugging Eq. (7) into Eq. (5). The total amplitude response of the pupil with the plate can be written as

$$\begin{aligned} h_{12}^{(p)}(x,y,\xi,\eta;\nu) &= h_{12}^{(1)}(x,y,\xi,\eta;\nu)\exp(-iknd_1) \\ &\quad + h_{12}^{(2)}(x,y,\xi,\eta;\nu) \\ &\quad \times \exp[-ik(d_1 - d_2 + nd_2)]. \end{aligned} \tag{8}$$

The defocus and higher-order aberrations caused by the plate are ignored for now and will be discussed in Section 3. The PSF of the system under broadband illumination can be written as

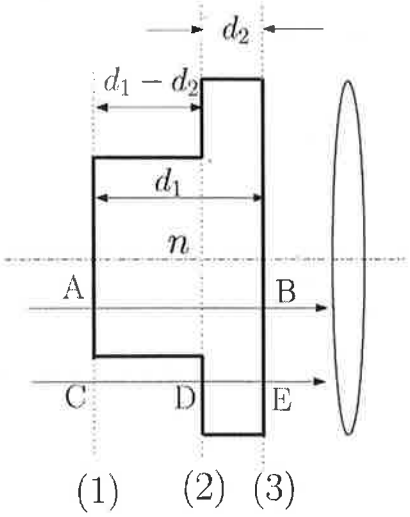

Fig. 3. Phase plate model for derivation of the transmission function of the glass plate.

$$\begin{aligned} |h_{12}^{(p)}(x,y,\xi,\eta)|^2 &= \int S(\nu)|h_{12}^{(1)}(x,y,\xi,\eta;\nu) \\ &\quad \times \exp(-iknd_1) + h_{12}^{(2)}(x,y,\xi,\eta;\nu) \\ &\quad \times \exp[-ik(d_1 - d_2 + nd_2)]|^2 \mathrm{d}\nu \\ &= |h_{12}^{(1)}(x,y,\xi,\eta)|^2 + |h_{12}^{(2)}(x,y,\xi,\eta)|^2 \\ &\quad + \text{cross term}, \end{aligned} \tag{9}$$

where

$$\begin{aligned} |h_{12}^{(1)}(x,y,\xi,\eta)|^2 &= \int S(\nu)|h_{12}^{(1)}(x,y,\xi,\eta;\nu)|^2 \mathrm{d}\nu, \\ |h_{12}^{(2)}(x,y,\xi,\eta)|^2 &= \int S(\nu)|h_{12}^{(2)}(x,y,\xi,\eta;\nu)|^2 \mathrm{d}\nu, \end{aligned} \tag{10}$$

are the PSF of lenses with apertures Σ_1 and Σ_2, respectively. The cross term in Eq. (9) can be written as

$$\begin{aligned} \text{cross term} = 2\mathrm{Re}\Big\{ \int S(\nu)\exp[-ik(n-1)(d_1 - d_2)] \\ \times h_{12}^{(1)}(x,y,\xi,\eta;\nu)h_{12}^{(2)*}(x,y,\xi,\eta;\nu)\mathrm{d}\nu \Big\}. \end{aligned} \tag{11}$$

For a color-corrected imaging system, the OPD between regions Σ_1 and Σ_2 before the insertion of the plate is caused by the inherent aberrations. It should be less than a quarter of the center wavelength according to Rayleigh [5], i.e., $h_{12}^{(1)}(x,y,\xi,\eta;\nu)$ $h_{12}^{(2)*}(x,y,\xi,\eta;\nu)$ is a slow-varying function of the frequency. After the insertion of the plate, especially when $|d_1 - d_2|$ is on the order of tens of wavelength or more, the OPD between regions Σ_1 and Σ_2 is dominated by the difference of the optical thickness of the plate ($|(n-1)(d_1 - d_2)|$). $\exp(-ik(n-1)(d_1 - d_2))$ oscillates rapidly with respect to the frequency. Thus $h_{12}^{(1)}(x,y,\xi,\eta;\nu)h_{12}^{(2)*}(x,y,\xi,\eta;\nu)$ can be taken out of

the integration in Eq. (11), i.e.,

$$\text{cross term} = 2\text{Re}\left\{h_{12}^{(1)}(x,y,\xi,\eta;\nu_0)h_{12}^{(2)*}(x,y,\xi,\eta;\nu_0) \times \int S(\nu)\exp[-ik(n-1)(d_1-d_2)]\mathrm{d}\nu\right\}, \quad (12)$$

where ν_0 is the center frequency of the spectrum of the source. The integration in Eq. (12) is the temporal transform of the source spectrum $S(\nu)$ and can be written in the form of the autocorrelation function of the source $R(\tau)$, i.e.,

$$\int S(\nu)\exp[-ik(n-1)(d_1-d_2)]\mathrm{d}\nu = R(\tau), \quad \tau = \left|\frac{(n-1)(d_1-d_2)}{c}\right|. \quad (13)$$

For a source with coherence time τ_c, Eq. (13) will be zero when $\tau \geq \tau_c$. Thus, when $\tau > \tau_c$, the cross term of Eq. (9) approaches zero, and we can rewrite Eq. (9) as

$$|h_{12}^{(p)}(x,y,\xi,\eta)|^2 = |h_{12}^{(1)}(x,y,\xi,\eta)|^2 + |h_{12}^{(2)}(x,y,\xi,\eta)|^2 \times |(n-1)(d_1-d_2)| \geq c\tau_c = l_c, \quad (14)$$

where l_c is the coherence length of the source. Equation (14) means that when the OPD between Σ_1 and Σ_2 is larger than the coherence length of the source, light passing through Σ_1 and Σ_2 are independent of each other and their intensities superpose incoherently at the detector plane to form the final image. $h_{12}^{(1)}(x,y,\xi,\eta;\nu)h_{12}^{(2)*}(x,y,\xi,\eta;\nu)$ disappears from the total PSF. The pupil is thus partitioned into two uncorrelated regions Σ_1 and Σ_2.

Obviously, the above analysis can be extended to the case of M steps of partition of the pupil where $M > 2$.

3. Effects of the Thicknesses of the Inserted Plates

When the inserted plate is not thin, the OPD between the two regions will still be able to decorrelate the diffractions from the two regions as long as the condition specified in Eq. (14) is satisfied. However, the defocus induced by the plate should be taken into account during the calculation of the PSF, which can be written as [11,12]

$$\Phi_{\text{defocus}}(u,v) = -k\frac{(n-1)d}{n}\frac{u^2+v^2}{2z_1^2}, \quad (15)$$

where n and d are the refractive index and thickness of the plate, respectively. Since the thickness in regions Σ_1 and Σ_2 are different, the defocus will be different in the two regions. They can be included in the transmission function of the pupil, i.e.,

$$P_1^{(d)}(u,v) = P_1(u,v) \times \exp\left[-ik\left(nd_1 + \frac{(n-1)d_1}{n}\frac{u^2+v^2}{2z_1^2}\right)\right], \quad (u,v) \in \Sigma_1;$$

$$P_2^{(d)}(u,v) = P_2(u,v) \times \exp\left[-ik\left(d_1 - d_2 + nd_2 + \frac{(n-1)d_2}{n}\frac{u^2+v^2}{2z_1^2}\right)\right], \quad (u,v) \in \Sigma_1, \quad (16)$$

where the superscript (d) indicates that the defocus induced by the plate has been included. Replacing $P_1(u,v)$ and $P_2(u,v)$ in Eq. (5) with $P_1^{(d)}(u,v)$ and $P_2^{(d)}(u,v)$, defined as in Eq. (16), and then using Eq. (14), we can find the PSF when the pupil is partitioned through the insertion of thick plates.

4. Example of a Circularly Symmetric Imaging Lens with Pupil Partitioned

When a diffraction-limited lens is under spatially incoherent illumination, the image is the convolution between the geometric prediction of the object and its intensity PSF [9], i.e.,

$$I(x,y) = \int S(\nu)\iint |o_g(\tilde{\xi},\tilde{\eta})|^2 p(x-\tilde{\xi},y-\tilde{\eta},;\nu)\mathrm{d}\tilde{\xi}\mathrm{d}\tilde{\eta}\mathrm{d}\nu = \iint |o_g(\tilde{\xi},\tilde{\eta})|^2 p(x-\tilde{\xi},y-\tilde{\eta})\mathrm{d}\tilde{\xi}\mathrm{d}\tilde{\eta}, \quad (17)$$

where $\tilde{\xi} = -\frac{z_2}{z_1}\xi$, $\tilde{\eta} = -\frac{z_2}{z1}\eta$,

$$o_g(\tilde{\xi},\tilde{\eta}) = o\left(-\frac{z_2}{z_1}\xi, -\frac{z_2}{z_1}\eta\right) \quad (18)$$

is the geometric prediction of the object, and

$$p(x-\tilde{\xi},y-\tilde{\eta};\nu) = p\left(x+\frac{z_2}{z_1}\xi, y\frac{z_2}{z_1}\eta;\nu\right) = |h_{12}(x,y,\xi,\eta;\nu)|^2 \quad (19)$$

is the space-invariant version of the PSF when the illumination is monochromatic. The intensity PSF under broadband illumination can be derived by integrating Eq. (19) over the spectrum of the source and the result is

$$p(x-\tilde{\xi},y-\tilde{\eta}) = \int S(\nu)|h_{12}(x,y,\xi,\eta;\nu)|^2 \mathrm{d}\nu$$
$$= \int \frac{4\pi^2 S(\nu)\nu^4}{c^4 z_1^2 z_2^2} \left| \iint_{\Sigma} P(u,v) \times \exp\left[-ik\frac{u^2+v^2}{2}\left(\frac{1}{z_1}+\frac{1}{z_2}-\frac{1}{f}\right)\right] \times \exp\left\{ik\left[\left(\frac{\xi}{z_1}+\frac{x}{z_2}\right)u+\left(\frac{\eta}{z_1}+\frac{y}{z_2}\right)v\right]\right\} \times \mathrm{d}u\mathrm{d}v\right|^2 \mathrm{d}\nu.$$

When the lens is circularly symmetric and the radius of its aperture is a, we can simplify the PSF further as

$$p(r) = \int \frac{4\pi^2 S(\nu)\nu^4}{c^4 z_1^2 z_2^2} \left| \int_0^a \exp\left[-ik\frac{\rho^2}{2}\left(\frac{1}{z_1}+\frac{1}{z_2}-\frac{1}{f}\right)\right] \times J_0\left(\frac{kr\rho}{z_2}\right)\rho\mathrm{d}\rho\right|^2 \mathrm{d}\nu, \tag{20}$$

where $r=\sqrt{x^2+y^2}$, $\rho=\sqrt{u^2+v^2}$, and J_0 is the zeroth-order Bessel function.

By inserting in front of the aperture of the lens a plate with refractive index n and whose thickness can be described as

$$d = \begin{cases} d_1, & 0 \le \rho \le \varepsilon a; \\ d_2, & \varepsilon a < \rho \le a, \end{cases} \tag{21}$$

unbalanced OPD is created as described in Section 2. When $|(n-1)(d_1-d_2)| \ge l_c$, the pupil is partitioned into two regions according to Eq. (14). The PSF of each region should be written as

$$p^{(1)}(r) = \int \frac{4\pi^2 S(\nu)\nu^4}{c^4 z_1^2 z_2^2} \times \left| \int_0^{\varepsilon a} \exp\left[-ik\frac{\rho^2}{2}\left(\frac{1}{z_1}+\frac{1}{z_2}-\frac{1}{f}+\frac{n-1}{n}\frac{d_1}{z_1^2}\right)\right] \times J_0\left(\frac{kr\rho}{z_2}\right)\rho\mathrm{d}\rho\right|^2 \mathrm{d}\nu,$$
$$p^{(2)}(r) = \int \frac{4\pi^2 S(\nu)\nu^4}{c^4 z_1^2 z_2^2} \times \left| \int_0^{\varepsilon a} \exp\left[-ik\frac{\rho^2}{2}\left(\frac{1}{z_1}+\frac{1}{z_2}-\frac{1}{f}+\frac{n-1}{n}\frac{d_2}{z_1^2}\right)\right] \times J_0\left(\frac{kr\rho}{z_2}\right)\rho\mathrm{d}\rho\right|^2 \mathrm{d}\nu. \tag{22}$$

Here the defocus induced by the plate is included in the calculation. The total intensity PSF of the partitioned lens is

$$p^{(p)}(r) = p^{(1)}(r) + p^{(2)}(r). \tag{23}$$

When the lens contains aberrations, the aberration term $\Phi(\rho,\phi)$ can be included in the transmission function of the pupil [9]. Then we use Eq. (10) to find the PSFs for regions Σ_1 and Σ_2 as

$$p^{(1a)}(r) = \int \frac{S(\nu)\nu^4}{c^4 z_1^2 z_2^2} \times \left| \int_0^{2\pi}\int_0^{\varepsilon a} \exp\left[-ik\frac{\rho^2}{2}\left(\frac{1}{z_1}+\frac{1}{z_2}-\frac{1}{f}+\frac{n-1}{n}\frac{d_1}{z_1^2}\right) + \Phi(\rho,\phi)\right] J_0\left(\frac{kr\rho}{z_2}\right)\rho\mathrm{d}\rho\mathrm{d}\phi\right|^2 \mathrm{d}\nu,$$
$$p^{(2a)}(r) = \int \frac{S(\nu)\nu^4}{c^4 z_1^2 z_2^2} \times \left| \int_0^{2\pi}\int_{\varepsilon a}^{a} \exp\left[-ik\frac{\rho^2}{2}\left(\frac{1}{z_1}+\frac{1}{z_2}-\frac{1}{f}+\frac{n-1}{n}\frac{d_2}{z_1^2}\right) + \Phi(\rho,\phi)\right] J_0\left(\frac{kr\rho}{z_2}\right)\rho\mathrm{d}\rho\mathrm{d}\phi\right|^2 \mathrm{d}\nu, \tag{24}$$

where the added subscript (a) indicates that aberrations are included. The total PSF for a lens with aberrations and its pupil partitioned can be written as

$$p^{(pa)}(r) = p^{(1a)}(r) + p^{(2a)}(r). \tag{25}$$

Extension to an M-step partitioned lens is trivial and is not included here ($M > 2$) for the sake of brevity.

5. Properties of the Point Spread Function for an Annularly Partitioned Lens

In this section we will use the formulas (Eqs. (22)–(25)) to calculate the PSF and to study the evolution of the peak intensity and full width at half-maximum (FWHM) of the central lobe of the PSF over defocus. The integrals in Eqs. (22) and (24) can be evaluated by the Gauss-quadrature formulas [14], which have been widely used for calculation of PSFs of a circular imaging system [15–17]. The results of the calculations are shown in Figs. 4 and 5 for a perfect lens case and in Fig. 6 for a lens with aberrations. During the calculation, the focal length of the lens is assumed to be 60 mm and the diameter of the pupil of the lens is 21.43 mm, which means that the lens is operating at f-number 2.8. The distance between the lens and the image plane z_2 is assumed to be 65.44 mm, i.e., the lens focuses at 722 mm in object space. The source spectrum is assumed to be Gaussian with center frequency ν_0 and variance $\Delta\nu$, which corresponds to a green LED with linewidth of 40 nm. Thus, the coherence length of the source is about 7 μm. The reason to choose a colored source instead of white light is that,

for a color CCD or a CMOS camera, usually one detector element sees only one of the colors (for example, red, green, and blue for RGB sensor arrays). The effective source for that particular detector element is either red or green or blue. The inserted plate can be as simple as a ring where $d_1 = 0$. Here we take the thickness of the ring d_2 to be 1 mm and refractive index $n = 1.5$. The OPD between regions Σ_1 and Σ_2 is about 0.5 mm, which is much larger than the coherence length of the source (7 μm). Thus, the pupil is partitioned into a circular disk and an annular ring. The partition ratio is chosen to be $\varepsilon = \frac{\sqrt{2}}{2}$ so that the areas of regions Σ_1 and Σ_2 are equal to each other.

Figure 4 plots three examples of the PSF with different amounts of defocus. (a) is the case of the unpartitioned lens and (b) is the case of the partitioned lens. Comparing (a) and (b) of Fig. 4, we see that the shape of the PSF of a lens with its pupil partitioned changes much slower than that of the unpartitioned lens. To study how the intensity PSFs (IPSF) change with defocus, the peak intensity is normalized with respect to its value at focus position and plotted in Fig. 5(a). The FWHM of the mainlobe of the IPSFs is plotted in Fig. 5(b). We see that the peak intensity for the partitioned lens decreases at about half the

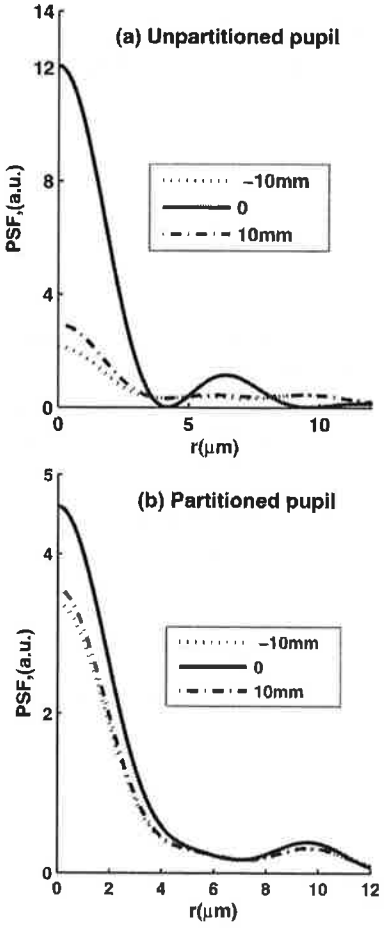

Fig. 4. PSF examples of a perfect lens for three object distances: (a) unpartitioned pupil, (b) partitioned pupil with unbalanced OPD, Eq. (23).

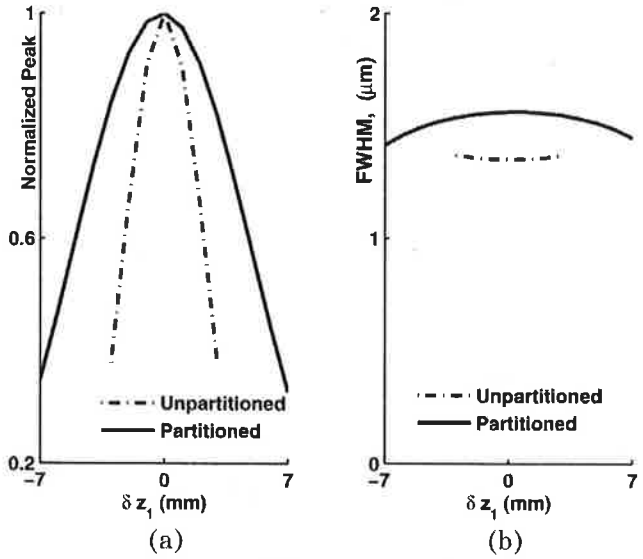

Fig. 5. (a) Peak and (b) FWHM of the central lobe of PSF of a lens before the partition (dashed curve) and after the partition (solid curve).

speed of the unpartitioned lens. Within the range of object distance of interest in this paper, the FWHM for the partitioned lens remains around 1.5 μm and at around 1.3 μm for the unpartitioned lens. Taking both the peak and FWHM into account, we can say that the two-step partitioning of the pupil extends the depth of field by a factor of 2:1, approximately.

When the lens has aberrations, Eqs. (24) and (25) are used for the calculation of IPSFs and the results are shown in Fig. 6. These plots show that, even for a lens with aberrations, the partitioning of the pupil by insertion of a glass ring can extend the depth of field as well.

6. Numerical Testing of the Proposed System

In the simulation, we use a standard resolution target (as shown in Fig. 7) as the object. The parameters of the lens are the same as specified in Section 5. The images of the object at focus position as well as at positions away from the focus in either directions are simulated using Eq. (17) with Gaussian noise added. The travelling range of the object is (−2 cm, 2 cm) with respect to the focus position for the unpartitioned lens and (−4 cm, 4 cm) for the partitioned lens. From Fig. 8, we can see that the speed of blurring of the partitioned lens due to defocus is slower even though the in-focus image is less sharp when compared to those of the unpartitioned lens. This drawback can be overcome by digital processing, for example, by the inverse filter [18] or the maximum entropy method [19,20]. Here we will use the maximum entropy method since it will introduce less spurious structures in the recovered images, especially for sharp-edged objects (for details about the algorithm of maximum entropy method, see [20]). Note the object is blurred differently by the imaging system depending on the object distances. The corresponding PSF should be used for a true deconvolu-

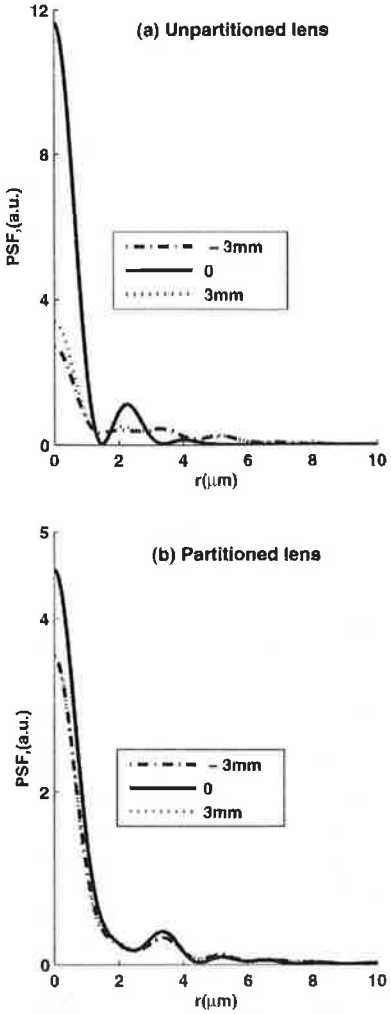

Fig. 6. PSF examples of an aberrated lens (a) without or (b) with partition, $W_{040} = 0.55$, $W_{060} = 0.15$.

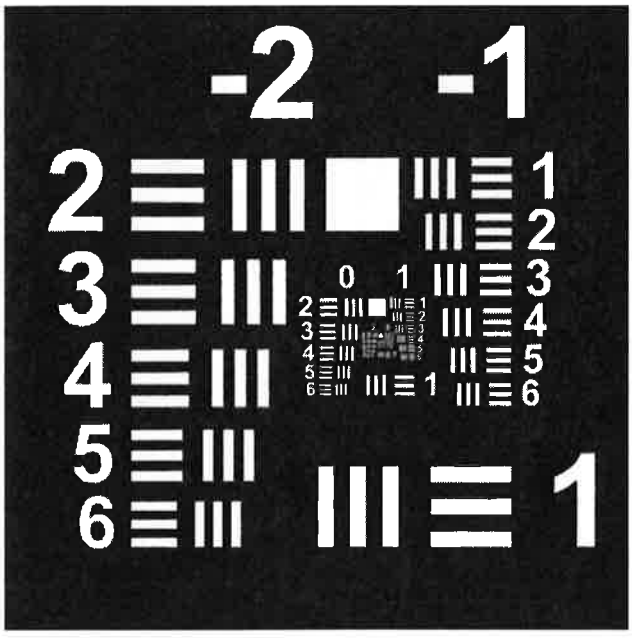

Fig. 7. Original object.

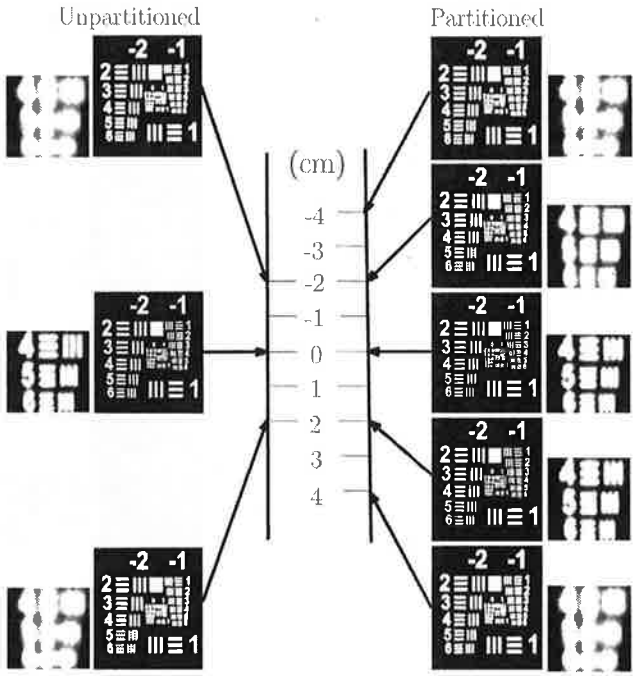

Fig. 8. Blurred images when the object shown in Fig. 7 is moved along the optical axis and the lens is focused at the "0" position. A segment of the image is digitally magnified and placed next to the image.

tion. In practice, however, the object distance is unknown. So we will use the average PSF (averaged over the distances travelled by the object during the capture of the image) to process all the images. The results of the recovery are shown in Fig. 9. The success of digital processing depends mostly on the degree of the similarity between the used PSF and the true PSF. For the unpartitioned lens, the success lasts from −1.5 to 1.5 cm. Beyond this range, the PSF used in the processing deviates away from the true PSF too much for the deconvolution to succeed, as we can see from Fig. 9. For the partitioned lens, the success range of digital processing is from −4 to 4 cm. From Fig. 9, we see that the reconstructed images from the partitioned lens are as sharp as those from the unpartitioned lens and it remains sharp over a range twice of that of the unpartitioned lens.

7. Laboratory Testing of the Proposed System

Ideally, the annular ring should be inserted right in the pupil plane of a camera lens. However, for most commercially available camera lenses, the pupil is not accessible. Thus, we will place the ring in front of the lens, which is equivalent to partition the lens in the pupil plane for on-axis imaging. A ring is fabricated by drilling a hole of diameter 4.49 mm in a UV photographic filter. The filter itself is about 2 mm thick and its refractive index is about 1.5. The effective thickness is about 1 mm and is much larger than the coherence length of the illumination, which in our case is about 7 μm. The lens is a micro-Nikon lens of focal length 60 mm operating

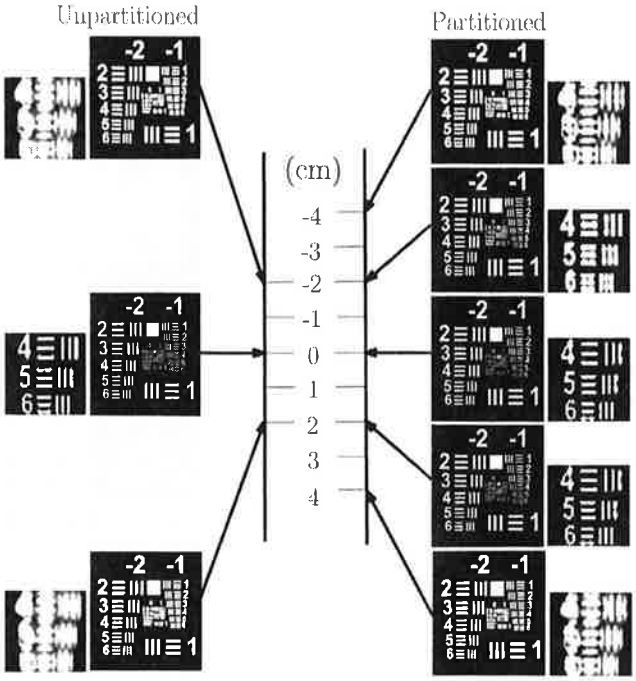

Fig. 9. Recovery from images shown in Fig. 8.

at f-number 8. During the measurement of the PSF, we place a 40× objective behind the lens to relay the images of the PSF onto a Sony XCD-SX910 sensor array whose pixel size is 4.65 μm. A green LED (from LED Supply, part L1-0-G5TH15-1) is used to illuminate a 10 μm pinhole that is placed upstream to the Nikon lens and is about 722 mm away from the lens. The images of the PSF are taken when the lens, with or without the ring inserted, and the downstream elements are held fixed while the pinhole and the illuminating LED are moved together along the optical axis with a step size of 5 mm. From the captured images shown in Fig. 10, we see that the PSF of the lens alone changes dramatically over distances of (−2 cm, 3 cm) while the PSF of the lens with the ring inserted remains relatively unchanged over the same distances.

The width of the PSF for the lens with the ring, however, is larger, which means that the image contrast will be lower. With digital processing, the image contrast can be boosted. To investigate the final imaging performance of the partitioned lens with digital processing, we conducted a resolution test where a two-point object is used. The object is composed of two circular dots with diameters of 20 μm and separated by 100 μm. The captured images are shown in Fig. 11. We see that the images of the two dots taken in the focused position barely touch each other and they remain recognizable over the distances (−1.5 cm, 1.5 cm) by visible inspection. When the UV-filter ring is inserted, the object remains recognizable from −3 to 5 cm, as shown in Fig. 11. The contrast, however, is lower compared to those of the unpartitioned lens. Then we use the maximum entropy method [8,20] to deconvolve all the images with the average PSF. The reconstructed images are shown in Fig. 12. The success of digital processing happens when two crisply sharp points are reconstructed. For the unpartitioned lens, the success of the image processing lasts from −1 to 1 cm, and from −3 to 5 cm for the partitioned lens. Note that, for those successfully recovered images, the contrast for each is as high as the other. This means that the digital processing can boost up the contrast of the images taken by the partitioned lens and the

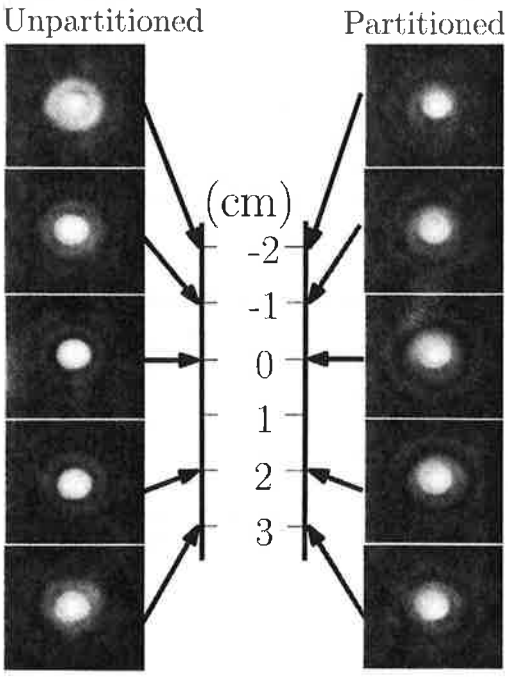

Fig. 10. PSF measured over different object positions.

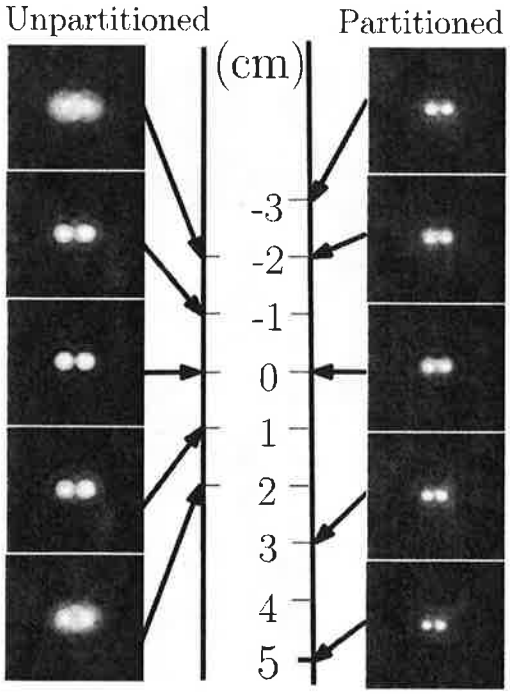

Fig. 11. Blurry images before digital processing.

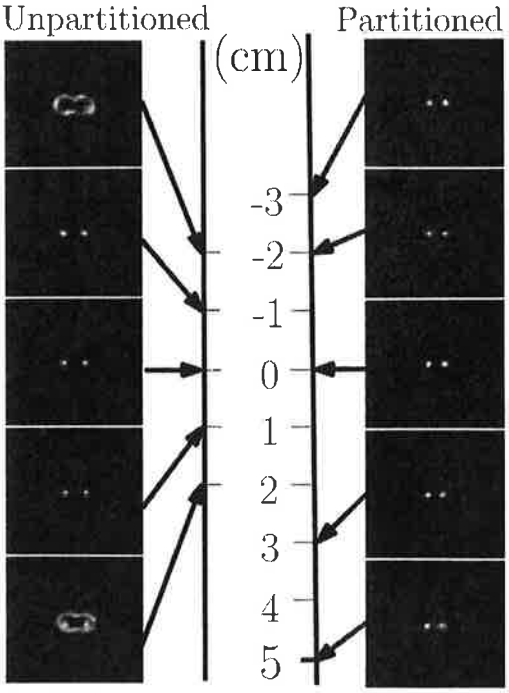

Fig. 12. Recovery from images shown in Fig. 11.

overall resolution of the system is not lost due to partitioning. From the experimental results shown in Fig. 10–12, we conclude that the experiments have shown that the depth of field of a partitioned lens is twice of that of the unpartitioned lens. Further, the contrast of the image is as good as the unpartitioned lens after digital processing.

8. Summary

In Figs. 1 and 2, a simple method is shown for increasing the depth of field of an integrated camera and computer system. We review the concept of OPD and use modern coherence theory to explain quantitatively the enhanced depth of field that can be achieved. Figure 4(b) shows the relative invariance of the PSF with distances for object positions along the optical axis. Final images are shown for the perfect unmodified lens compared to the modified lens in Fig. 9. Maximum entropy processing is used in this computer simulation. In experiments using a 60 mm micro-Nikon lens, comparative two-point recovered images are shown in Fig. 12 for the unmodified lens and for the partitioned lens. We can describe quantitatively the improvement in depth of field by a calculation of the ratio (close-in distance–focal distance) for the partitioned lens to (close-in distance–focal distance) for the unpartitioned lens. The improvement is 5 times in our two-point test experiment. The depth of field can be further improved by increasing the number of annular rings.

This research is funded in part by the United States Army Research Office (USARO) and Aptina Imaging, Inc.

References

1. W. Chi, K. Chu, and N. George, "Polarization coded aperture," Opt. Express **14**, 6634–6642 (2006).
2. W. J. Smith, *Modern Optical Engineering*, 3rd ed. (SPIE Press), p. 355.
3. A. E. Conrady, *Applied Optics and Optical Design, Part I* (Dover, 1957), pp. 136.
4. A. E. Conrady, *Applied Optics and Optical Design, Part II* (Dover, 1960), pp. 585.
5. Lord Rayleigh, "On the accuracy of focus necessary for sensibly perfect definition," in *Scientific Papers* (Cambridge U. Press, 1899), Vol. 1, pp. 430–432.
6. E. N. Leith and G. J. Swanson, "Optical processing techniques in incoherent light," Proc. SPIE **388**, 38 (1983).
7. E. H. Linfoot and E. Wolf, "Diffraction images in systems with an annular aperture," Proc. Phys. Soc. B **66**, 145–149 (1957).
8. W. Chi and N. George, "Integrated imaging with a centrally obscured logarithmic asphere," Opt. Commun. **245**, 85–92 (2005).
9. J. W. Goodman, *Introduction to Fourier Optics*, 2nd ed. (McGraw-Hill, 1996).
10. L. Mandel and E. Wolf, *Optical Coherence and Quantum Optics* (Cambridge U. Press, 1995).
11. W. J. Smith, *Modern Optical Engineering*, 3rd ed. (SPIE Press), p. 100.
12. J. Braat, "Analytical expressions for the wave-front aberration coefficients of a tilted plane-parallel plate," Appl. Opt. **36**, 8459–8467 (1997).
13. M. Born and E. Wolf, *Principles of Optics*, 7th ed. (Cambridge U. Press, 1995).
14. P. J. Davis and I. Polonsky, "Numerical interpolation, differentiation, and integration," in *Handbook of Mathematical Functions with Formulas, Graphs, and Mathematical Tables*, 9th ed., M. Abramowitz and I. A. Stegun, eds. (Dover, 1972), pp. 887–888.
15. R. Barakat, "Total illumination in a diffraction image containing spherical aberration," J. Opt. Soc. Am. **51**, 152–157 (1961).
16. R. Barakat and M. V. Morello, "Computation of the total illuminance (encircled energy) of an optical system from the design data for rotationally symmetric aberrations," J. Opt. Soc. Am. **54**, 235–240 (1964).
17. V. N. Mahajan, "Aberrated point spread functions for rotationally symmetric aberrations," Appl. Opt. **22**, 3035–3041 (1983).
18. C. W. Helstrom, "Image restoration by the method of least squares," J. Opt. Soc. Am. **57**, 297–303 (1967).
19. B. R. Frieden, "Restoring with maximum likelihood and maximum entropy," J. Opt. Soc. Am. **62**, 511–518 (1972).
20. W. Chi and N. George, "Computational imaging with the logarithmic asphere: theory," J. Opt. Soc. Am. A **20**, 2260–2273 (2003).

Sensor modulation transfer function measurement using band-limited laser speckle

Xi Chen,[1*] Nicholas George,[2] Gennadiy Agranov,[1] Changmeng Liu[1] and Bob Gravelle[1]

[1]*Aptina Imaging, 3080 N. First Street, San Jose, CA, 95124, USA*
[2]*The Institute of Optics, University of Rochester, Rochester, NY, 14627, USA*
[*]*Corresponding author: xchen@aptina.com*

Abstract: A new methodology for image sensor modulation transfer function measurement using band-limited laser speckle is presented. We use a circular opal milk glass diffuser illuminated by a 5mW He-Ne laser and a linear polarizer to generate band-limited speckle on the sensor. The power spectral density cut-off frequency of the speckle is chosen to be twice that of the sensor Nyquist frequency by placing the sensor at the specific Z location along the optical axis. For the speckle input, we calculate the power spectral density at the sensor using the Rayleigh-Sommerfeld integral and then measure the output power spectral density for the speckle pattern captured by the sensor. With these data, the two-dimensional image sensor modulation transfer function (MTF) is calculated.

OCIS codes: (130.6010) Sensors; (030.6140) Speckle; (120.0120) Instrumentation, measurement, and metrology

References and links

1. D. N. Sitter, Jr., J. S. Goddard, and R. K. Ferrell, "Method for the measurement of the modulation transfer function of sampled imaging systems from bar-target patterns," Appl. Opt. **34**, 746-751 (1995).
2. M. Estribeau and P. Magnan, "Fast MTF measurement of CMOS imagers using ISO 12233 slanted edge methodology," Proc. SPIE **5251**, 243-251 (2004).
3. B. T. Teipen and D. L. MacFarlane, "Liquid-crystal-display projector-based modulation transfer function measurements of charge-coupled-device video camera systems," Appl. Opt. **39**, 515-525 (2000).
4. J. E. Greivenkamp and A. E. Lowman, "Modulation transfer function measurement of sparse-array sensors using a self-calibrating fringe pattern," Appl. Opt. **33**, 5029-5036 (1994).
5. M. Sensiper, G. D. Boreman, A. D. Ducharme, and D. R. Snyder, "Modulation transfer function testing of detector arrays using narrow-band laser speckle," Opt. Eng. **32**, 395-400 (1993).
6. S. K. Park, R. Schowengerdt, and M. Kaczynski, "Modulation-transfer-function analysis for sampled image systems," Appl. Opt. **23**, 2572-2582 (1984).
7. N. George, A. Jain, and R. D. S. Melville Jr., "Speckle, diffusers, and depolarization," Appl. Phys. **6**, 65-70 (1975).
8. N. George, A. Jain, and R. D. S. Melville Jr., "Experiments on the space and wavelength dependence of speckle," Appl. Phys. **7**, 157-169 (1975).
9. N. George, "Speckle at various planes in an optical system," Opt. Eng. **25**, 754-764 (1986).
10. P. Z. Peebles, Jr., *Probability, random variables, and random signal principles*, 3rd Ed. (McGraw-Hill, Inc., New York, 1993).
11. A. Papoulis, "Generalized sampling expansion," *IEEE* Trans. Circuits Syst. **24**, 652-654 (1977).

1. Introduction

CMOS image sensors are widely used on digital imaging devices. The modulation transfer function (MTF) of the image sensors is an important characteristic to evaluate the overall imaging system quality. The image sensor MTF reflects the spatial frequency response of the sensor. It is determined by the spatial structure and optical and electrical cross-talk of the pixels.

There have been several techniques widely used for measuring sensor MTF. For example, the sensor MTF is measured with bar targets [1], slanted edge technique [2], random targets [3], self-calibrating fringe pattern [4], and laser speckle modulated with a double-slit aperture

#102216 - $15.00 USD Received 30 Sep 2008; revised 10 Nov 2008; accepted 14 Nov 2008; published 20 Nov 2008

[5]. Among these methods, the slanted edge method is commonly applied in industry. A super resolution scan can be created with a slanted edge [2], which solves the sample-scene phase problem [6]. The random targets method also solves the sample-scene phase problem. However using either a slanted edge or random targets requires a high quality lens to image the targets or patterns on the sensor. This need for a high quality lens greatly limits the application to image sensors with pixel size less than 2.0μm. The laser speckle modulated with a double-slit aperture provides MTF value at one single frequency for each single measurement as well. Also, only one dimensional MTF data depending on the direction of slit apertures is measured.

In this paper we present a new method for image sensor MTF measurements using band-limited laser speckle. The setup is simpler compared to other methods and it is particularly well-suited when the pixels are small. There are no lenses or slit apertures used in the setup. The advantage inherent in the use of a speckle pattern for this input is that it contains an excellent range of spatial frequencies from low to very high values. The limiting spatial frequency on the high side is given approximately by $\frac{D}{\lambda Z}$ in the setup of Fig. 1. The two-dimensional sensor MTF data are obtained with each measurement. The method is applicable to sensors with small pixels. In Section 2, we present the theory we used to obtain the sensor MTF using band-limited laser speckle. The way to generate and calculate the speckle pattern and power spectral density is described. In Section 3, the experimental results for a 6.0μm monochrome CMOS sensor and a 2.2μm monochrome CMOS sensor are presented. The calculated input power spectral density is also compared with the measured data. The measured sensor MTF using our band-limited laser speckle method is compared with the data obtained using the standard slanted edge technique. The two methods provide results in excellent agreement, which indicates applicability of our developed methodology to characterization of modern CMOS image sensors with small pixel size.

2. Theory of measuring sensor MTF using band-limited laser speckle

Here we describe our methodology of measuring sensor MTF using laser speckle generated by a circular opal milk glass diffuser and a linear polarizer. The speckle theory involved in this method is explained. The power spectral density (PSD) of the speckle pattern on the sensor plane is calculated. The aliasing artifact involved in the sensor MTF measurement is described. The method to avoid aliasing artifact is also presented.

2.1. Speckle theory for sensor MTF measurement

We consider the linearly polarized speckle patterns. In our experimental setup, it is necessary to use a linear polarizer after the opal milk glass (OMG) diffuser in order to obtain a linearly polarized laser speckle pattern. The intensity of the speckle at the input to the sensor plane is a random process $I(x,y)$ with coordinates (x,y) at the sensor plane. The output signal from the sensor is denoted as $S(x,y)$. If the response of the sensor is linear and the system is shift-invariant, then the output signal $S(x,y)$ can be expressed as:

$$S(x,y) = \iint I(x_1,y_1)h(x-x_1,y-y_1)dx_1dy_1, \tag{1}$$

where h is the impulse response for the image sensor. As explained in [6], the sensor array is not a spatially shift-invariant system. The response is dependent on the relative location of the point source and pixel center. By using the slanted edge or random targets or laser speckle, the sample-scene phases are averaged. With the averaging of the sample-scene phases and the use of speckle pattern, the sensor array becomes spatially shift-invariant as described by Eq. (1).

It is well-known that the ensemble-averaged autocorrelation function of the output signal for a spatially shift-invariant linear system is related to the ensemble-averaged autocorrelation function of the input random signal as:

#102216 - $15.00 USD Received 30 Sep 2008; revised 10 Nov 2008; accepted 14 Nov 2008; published 20 Nov 2008

$$R_S(\Delta x,\Delta y) = R_I(\Delta x,\Delta y) * h(\Delta x,\Delta y) * h^*(-\Delta x,-\Delta y), \quad (2)$$

where $R_s(\Delta x,\Delta y)$ is the ensemble-averaged autocorrelation function of the captured speckle intensity pattern; $R_I(\Delta x,\Delta y)$ is the ensemble-averaged autocorrelation function of the input speckle intensity pattern; h is the impulse response function of the image sensor. We Fourier transform Eq. (2), then we obtain

$$PSD_S(f_x,f_y) = PSD_I(f_x,f_y)MTF^2, \quad (3)$$

where $PSD_S(f_x,f_y)$ is the power spectral density (PSD) of the speckle intensity captured by the CMOS sensor; $PSD_I(f_x,f_y)$ is the PSD of the input speckle intensity on the sensor plane; MTF is the modulation transfer function for the sensor. Eq. (3) is consistent with the published literature [5]. To measure this sensor MTF, we need to measure the $PSD_s(f_x,f_y)$ of the speckle pattern captured by CMOS sensor and calculate the input $PSD_I(f_x,f_y)$ of the speckle on the sensor plane.

One way to obtain the PSD of the input speckle on the sensor plane is to calculate the scalar electric field on the sensor plane. The experimental setup is shown in Fig. 1. The OMG diffuser has a diameter of D=25mm at the input aperture plane. The distance between this aperture plane and the sensor plane is Z. A 5mW He-Ne laser is used for illumination. The collimated laser light illuminates the OMG diffuser. A linear polarizer is placed behind the OMG diffuser so that only a scalar electric field is considered here. In the following paragraphs we describe the diffuser and the calculation of the intensity $I(x,y)$ received at the CMOS detector.

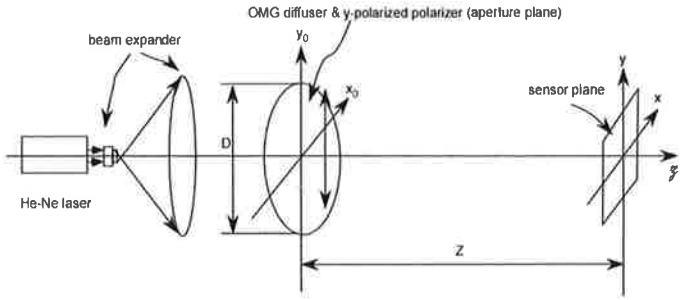

Fig. 1. Experimental setup

For creating a fully developed speckle pattern at the CMOS detector, it is well-known that one needs to use a volume-type of thick diffuser so that no specular beam is present. Opal milk glass (300 to 700 μm thickness) is an ideal choice for this, since from electron microscope studies it is known to consist of tiny (0.1 μm) spheres of higher index material created by thermally cycling glass around the annealing temperature. The output radiation for an input laser beam is fully depolarized with electric field spatial fluctuations in the exiting plane approaching the theoretical limit of $\lambda/2$, see [7]. Alternatively, one can use an integrating sphere instead of OMG since the 100 or so bounces produces a fine source for speckle experiments. However, we have found that the stability to mechanical vibrations of the OMG provides a superior result.

#102216 - $15.00 USD Received 30 Sep 2008; revised 10 Nov 2008; accepted 14 Nov 2008; published 20 Nov 2008

Interesting too, while the field variations at the output of a 25mm OMG may be on the order of 10^9 in numerical calculations of a fully developed speckle pattern, one can obtain excellent results taking only 10^4 random points, as we described below [8].

We first generate the scalar electric field $E_0(x_0, y_0)$ on the aperture plane. For visible light or laser light, the OMG is like an ideal black body. The output radiation is completely unpolarized and fully speckled. Therefore, the phase of the linearly polarized electric field along the y-axis, $E_0(x_0, y_0)$, on the aperture plane is a uniformly distributed random variable. Let us assume the electric field $E_0(x_0, y_0)$ as:

$$E_0(x_0, y_0) = A(x_0, y_0) * e^{-i\theta(x_0, y_0)}, \tag{4}$$

where $A(x_0, y_0)$ is the amplitude of the electric field. $A(x_0, y_0)$ is a Gaussian function of (x_0, y_0) measured with a power meter. It is expressed as

$$A(x_0, y_0) = e^{-\frac{\ln 5}{2(D/2)^2}(x_0^2 + y_0^2)}, \tag{5}$$

where $A(x_0, y_0)$ is normalized at the center of the diffuser; $D = 25mm$ which is the diameter size of the OMG diffuser. With the power meter, we measure the laser illumination intensity at the edge of the OMG diffuser is one fifth of that at the center of the diffuser. Phase $\theta(x_0, y_0)$ is a random variable with probability density function of

$$P_\theta(\theta) = \begin{cases} \dfrac{1}{10\pi} & 0 \le \theta < 10\pi \\ 0 & otherwise. \end{cases} \tag{6}$$

With the random field on the aperture plane given by Eqs. (4) to (6), we can calculate the scalar electric field $E_y(x, y)$ on the sensor plane which is located at Z away from the aperture plane. We calculate the scalar electric field on the sensor plane using the Rayleigh-Sommerfeld integral which is the exact solution to Maxwell equation with the evanescent waves neglected, as shown below:

$$E_y(x, y, Z) = \frac{iz}{\lambda} \int_{-\infty}^{\infty} \int_{-\infty}^{\infty} dx_0 dy_0 E_0(x_0, y_0, 0) \frac{e^{-i\frac{2\pi}{\lambda}\sqrt{Z^2 + (x-x_0)^2 + (y-y_0)^2}}}{Z^2 + (x-x_0)^2 + (y-y_0)^2}, \tag{7}$$

where $E_y(x, y, Z)$ is the scalar electric field on the sensor plane, Z is the distance between the aperture plane at $z = 0$ and sensor plane at $z = Z$ and λ is the illumination laser light wavelength. With Eqs. (4) to (7), we calculate the speckle intensity pattern $I(x, y, Z)$ which is the absolute square of $E_y(x, y, Z)$. The laser illumination intensity on the diffuser has to be measured accurately for an accurate calculation of $E_y(x, y, Z)$. The reason that we numerically calculate PSD of the input speckle pattern on the sensor instead of treating $PSD_I(f_x, f_y)$ as the auto-correlation function of the amplitude of the scalar electric filed on the aperture plane is the Fresnel-zone approximation of Eq. (7) is not valid anymore when Z is comparable with the diffuser size and sensor size. As a part of the numerical simulation of the delta function sources on the opal milk glass, we also include a random position of this

#102216 - $15.00 USD Received 30 Sep 2008; revised 10 Nov 2008; accepted 14 Nov 2008; published 20 Nov 2008

grid by means of uniformly distributed random points (x_0, y_0). The integration of Eq. (7) is replaced by summing the kernel of the integral over the aperture plane numerically. To calculate $E_y(x, y, Z)$ accurately, we sample the aperture plane at $z = 0$ with 100 by 100 random points. While the actual number of independent delta-like sources at the exit plane of the diffuser may be on the order of 10^9, we show by direct computer studies that results of about 1% accuracy can be attained using this sampling of 100 by 100 points.

The calculated speckle pattern with $\lambda = 0.6328\mu m$, $D = 25mm$, $Z = 87mm$ is shown in Fig. 2.

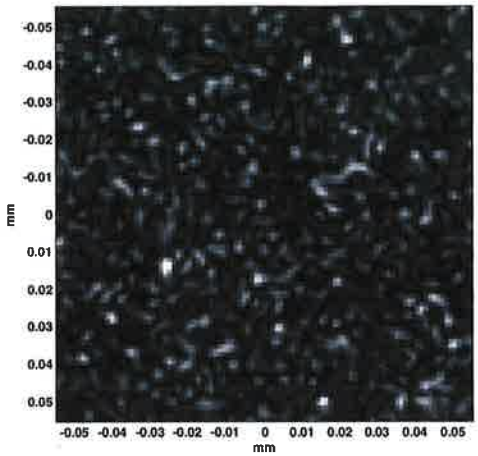

Fig. 2. The input speckle pattern calculated for sensor located at $Z = 87mm$ away from the aperture plane.

The transverse coherence length d_t of the speckle is 2.2μm. d_t is interpreted as the variation needed to decorrelate the auto-correlation function of the speckle. It is known [9] that the transverse speckle size d_t is given by

$$d_t = \frac{\lambda}{D} Z. \tag{8}$$

The size of the speckle d_t is chosen as the pixel size of the sensor by positioning the sensor with the right distance Z from the OMG diffuser. To measure the MTF of the sensor with pixel size of P, we locate the sensor at $z = Z$ which is given by

$$Z = \frac{P}{\lambda} D. \tag{9}$$

Hence, we obtain $Z = 87mm$ for pixel size of 2.2μm. With this choice of Z, the speckle has a PSD that is high enough at the Nyquist frequency of the sensor and becomes 0 at double the Nyquist frequency. This can be seen in Fig. 3.

We calculate the $PSD(f_x, f_y)$ of the speckle from the definition of PSD [10] which is given by

#102216 - $15.00 USD Received 30 Sep 2008; revised 10 Nov 2008; accepted 14 Nov 2008; published 20 Nov 2008

$$PSD(f_x, f_y) = \lim_{X,Y\to\infty} \frac{E\left\langle \left| u_{XY}(f_x, f_y) \right|^2 \right\rangle}{XY}, \tag{10}$$

where X,Y are the overall size of the speckle pattern along the x and y axes, respectively. X,Y should be much larger than the average size of the speckle. For example, we choose $X = Y = 111\mu m$ for speckle of 2.2μm size as shown in Fig. 2. In Eq. (10), $E\langle \bullet \rangle$ stands for the operation of ensemble average over independent samples. To obtain an accurate PSD, we ensemble average 150 independent samples. In Eq. (10), $u_{XY}(f_x, f_y)$ is the Fourier transform of the zero-mean speckle intensity, $I(x,y) - \overline{I(x,y)}$. $\overline{I(x,y)}$ is the mean value of the speckle intensity $I(x,y)$ over the spatial range X,Y. By calculating the Fourier transform of the zero-mean speckle intensity instead of the speckle intensity $I(x,y)$, we exclude the δ-function at the DC component of the PSD. As an example, we show PSD of the calculated 2.2μm size speckle in Fig. 3. The δ-function at zero frequency of the PSD is excluded to calculate the sensor MTF. The solid curve is the calculated PSD plot with ensemble averaging over 150 independent samples. The dashed curve is the polynomial fitting of the calculated PSD curve. The x-axis is the spatial frequency in units of the Nyquist frequency of 2.2μm pixel. We use Ny to stand for the Nyquist frequency. Here Ny=227.3cys/mm for a 2.2μm pixel size sensor.

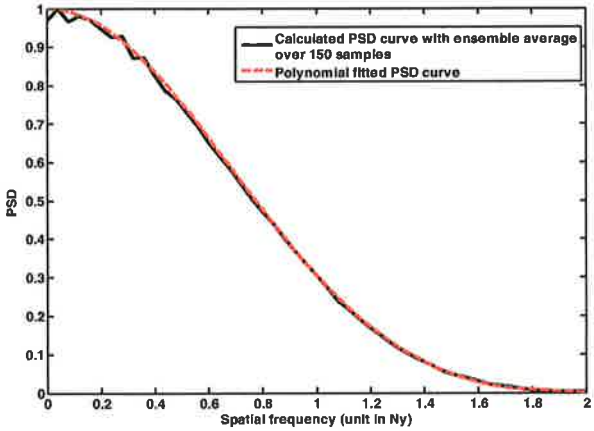

Fig. 3. The PSD of the speckle pattern shown in Fig. 2. The δ-function at zero frequency of the speckle PSD is excluded. The solid curve in black is the calculated PSD plot with ensemble averaging over 150 independent samples. The dashed curve in red is the polynomial fitting of the PSD curve. The x-axis is the spatial frequency in units of the Nyquist frequency. We use Ny to stand for the Nyquist frequency. Here Ny=227.3cys/mm for the 2.2μm pixel size. It is clear that the PSD is much higher than 0 at the Nyquist frequency of the sensor. The cut-off frequency of the PSD is 2Ny.

2.2 Avoid aliasing in the sensor MTF measurement

To maintain high signal at the Nyquist frequency of the sensor, the input PSD for the speckle has a cut-off frequency at 2Ny as shown in Fig. 3. The higher cut-off frequency than Ny causes aliasing artifacts in the PSD of the measured speckle pattern on the sensor. From Eq. (3), we see that the aliasing in $PSD_S(f_x, f_y)$ causes inaccurate measurement of sensor MTF.

To avoid aliasing artifacts in the measurement, we sub-sample the speckle pattern on the sensor with half pixel size so that the sub-sampled speckle image has Nyquist frequency of 2Ny. The sub-sampling is done by recording the speckle pattern on the sensor at a zero

#102216 - $15.00 USD Received 30 Sep 2008; revised 10 Nov 2008; accepted 14 Nov 2008; published 20 Nov 2008

shifting location, then shifting the sensor by a half-pixel along the x-axis location, shifting the sensor by a half-pixel along the y-axis location and shifting the sensor by half-pixels along both the x- and the y-axes location. We then obtain the half-pixel sampled speckle image by combining these four images using the Generalized Sampling Theorem [11]. The $PSD_S(f_x,f_y)$ of the half-pixel sampled speckle image has a Nyquist frequency of 2Ny. There are no aliasing artifacts on it. Figs. 4 show the concept of our anti-aliasing method. Mathematically, the anti-aliasing by sub-sample is achieved by the following procedure:

$$I_b(x,y)=\sum_{i=0}^{1}{}'\sum_{j=0}^{1}{}'[h(x,y)\otimes I(x,y)\sum_{n=-\infty}^{\infty}{}'\sum_{m=-\infty}^{\infty}{}'\delta(\frac{x-mP-r_i}{P})\delta(\frac{y-nP-s_j}{P})], \quad (11)$$

where I_b is the captured speckle pattern, h is the impulse response function of the image sensor, I is the input speckle pattern on the sensor, P is the pixel size of the sensor and r_i, s_j are the sub-sample shift movements along the x- and y-axes, respectively. $\otimes$ stands for the convolution operator. The Fourier transform of Eq. (11) is expressed in Eq. (12) as:

$$\chi_b(f_x,f_y)=\sum_{i=0}^{1}\sum_{j=0}^{1}[H(f_x,f_y)\bullet\sum_{n=-\infty}^{\infty}\sum_{m=-\infty}^{\infty}\chi(f_x-\frac{m}{P},f_y-\frac{n}{P})e^{-i2\pi(\frac{mr_i}{P}+\frac{ns_j}{P})}], \quad (12)$$

where χ_b is the Fourier transform of I_b, H is the Fourier transform of h, and χ is the Fourier transform of I. From Eq. (12), we can see that the Fourier transform of the detected laser speckle pattern consists of the non-aliased term for $m=0$, $n=0$ and higher order terms when $m\neq 0$ or $n\neq 0$. To avoid aliasing, we choose r_i and s_j as $r_0=0$, $r_1=0.5P$, $s_0=0$ and $s_1=0.5P$ for the four sub-sample recording positions. With this choice, the $m=0,n=\pm 1$ term, $m=\pm 1,n=0$ term and $m=\pm 1,n=\pm 1$ term are all zero in Eq. (12). The even higher orders are not considered because the laser speckle pattern has limited bandwidth of 2Ny.

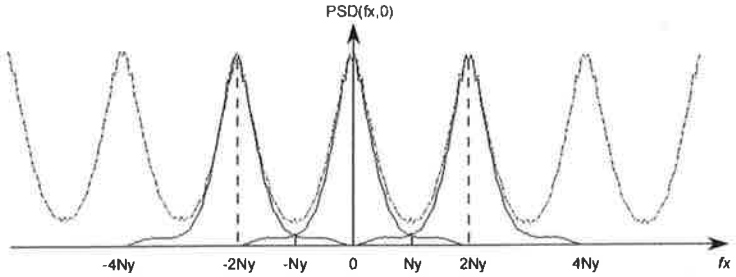

Fig. 4. (a) The cross-section of the measured speckle $PSD_s(f_x,0)$ shown in dash curve is aliased due to the sensor Nyquist frequency (Ny) is lower than the speckle PSD cut-off frequency which is twice the Nyquist frequency. The solid curves are the $PSD(f_x,0)$ without aliasing. The repeating of the unaliased PSD with a period of 2Ny is due to the discrete sampling of $1/(2Ny)$ by the sensor in the space domain.

#102216 - $15.00 USD Received 30 Sep 2008; revised 10 Nov 2008; accepted 14 Nov 2008; published 20 Nov 2008

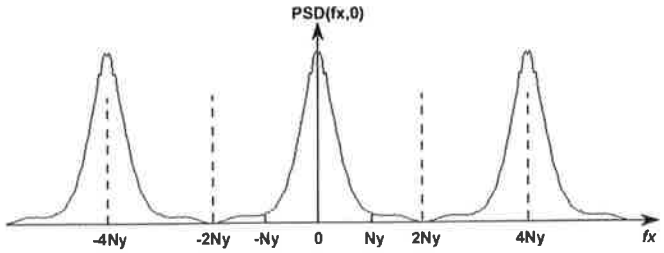

Fig. 4. (b) The cross-section of the sub-sampled speckle PSD. There is no aliasing artifacts because the sub-sampling has sampling size corresponding to twice the Nyquist frequency of the sensor.

The inaccuracy of the sub-sample shift movements r_1 and s_1 could lead to non-zero higher order terms in Eq. (12) and therefore the error in sensor MTF. Let us define the deviation of r_1 and s_1 from half pixel as Δ_x and Δ_y. Δ_x and Δ_y are in the range of (-0.5P, 0.5P). We require each aliased term such as $m=1,n=0$ be less than five percentages of the non-aliased term to guarantee less than five percentages error in sensor MTF measurement. This requirement could be written as Eq. (13) for $m=1,n=0$ term.

$$\left|2-2e^{-i2\pi\frac{\Delta_x}{P}}\right| \le 0.05. \tag{13}$$

To obtain five percentages error in the measurement, $\Delta_x,\Delta_y \le 4*10^{-3}P$. For a 2.2$\mu$m pixel-sized sensor, the translational stage for the sub-sample movement needs a resolution of 8.75nm. This number is on the same order of magnitude as the sensor pixel alignment tolerance which is a few nanometers. This requirement on the sub-sample shift movement can be met with commercial ultra-precision motor stages which have 1nm resolution.

3. Experimental results

We present the MTF measurement of Aptina's monochrome CMOS sensor MI350 with 6.0μm pixel size in Section 3.1. We investigate the applicability of the developed technique to measure MTF of the monochrome image sensor to avoid effects of color filters on sensor MTF measurements. The applicability of the developed methodology to color image sensors will be considered in the future. The speckle method is compared with the slanted edge method. The data from two methods are within excellent agreement. The results for another Aptina's monochrome CMOS sensor MI5100 with 2.2μm pixel size are described in Section 3.2.

3.1 On-axis MTF measurement for a monochrome CMOS sensor with 6.0μm pixels

Using Eq. (9) and a pixel size of $P=6.0\mu m$, we locate the sensor at $Z=237mm$ away from the 25mm OMG diffuser. Image sensor works in the linear mode of operation. Integration time is adjusted to provide the signal from the brightest part of the speckle pattern close to the linear full well capacity. All digital correction circuitries are disabled. The speckle pattern is recorded in a raw image data format. To measure the on-axis sensor MTF, the OMG diffuser and the image sensor are both placed perpendicular to the optical axis which is determined by the collimated He-Ne laser light. To obtain the PSD of the speckle on the sensor, we ensemble average over speckle patterns generated with 25 OMG diffusers. For each OMG diffuser, we record speckle patterns at 4 locations- no sensor shift, sensor shifted by 3.0μm along the x-axis with a linear piezoelectric transducer (PZT), sensor shifted by 3.0μm along

#102216 - $15.00 USD Received 30 Sep 2008; revised 10 Nov 2008; accepted 14 Nov 2008; published 20 Nov 2008

the y-axis and sensor shifted by 3.0μm along both the x- and the y-axes. The x-axis is along the row direction of the sensor. The y-axis is along the column direction of the sensor. At each location, multiple frames are recorded and then averaged to eliminate temporal noise of the sensor. As explained in Section 2, we obtain the PSD of the speckle on the sensor, $PSD_S(f_x, f_y)$, from the half pixel sub-sampled speckle patterns on the sensor. The cross-sections of $PSD_S(f_x, f_y)$ along the x- and the y-axes are shown in Figs. 5. The spatial frequency range is from 0 to 2Ny of the sensor. The side lobes in Fig. 5(b) may be due to the limited accuracy of movement along the y-axis of the PZT. The gravity of the PZT stage, sensor and other mechanical mounts may cause the shift of the sensor along the y-axis is not 3μm. This inaccurate shift causes error in the PSD.

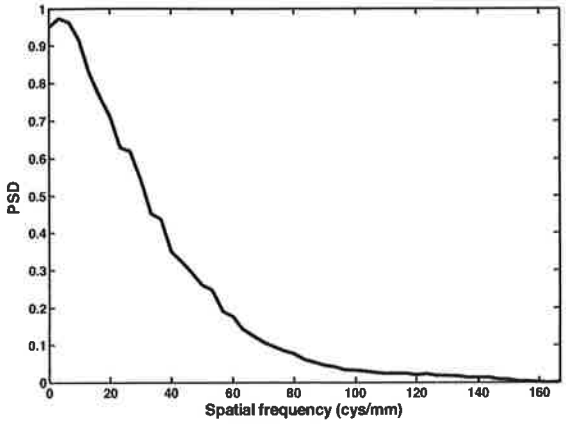

Fig. 5. (a) The x-axis cross-section of the measured PSD the speckle pattern on the 6.0μm pixel size CMOS sensor. The spatial frequency range is from 0 to 2Ny.

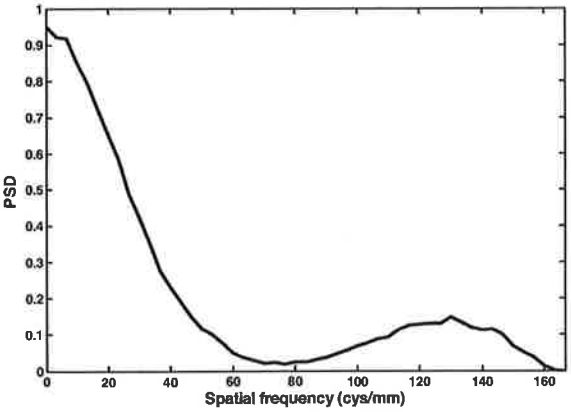

Fig. 5. (b) The y-axis cross-section of the measured PSD of the speckle pattern on the 6.0μm pixel size CMOS sensor. The x-axis in the plot is the spatial frequency. The range is from 0 to 2Ny.

The input power spectral density $PSD_I(f_x, f_y)$ is calculated as described in Section 2. The calculated cross-section of $PSD_I(f_x, f_y)$ is shown in Fig. 6 as the dashed black curve.

#102216 - $15.00 USD Received 30 Sep 2008; revised 10 Nov 2008; accepted 14 Nov 2008; published 20 Nov 2008

To testify the accuracy of the theoretical calculation of $PSD_I(f_x, f_y)$, we measure the speckle pattern with a 2.2μm pixel size monochrome CMOS sensor. The measured power spectral density $PSD_s(f_x, f_y)$ including the 2.2μm pixel size MTF and the PSD of 6μm-size speckle pattern is plotted in Fig. 6 as the black solid curve. The loss of smoothness in the measured power spectral density curve is due to the limited number of ensemble average. The curve will be smooth if we do ensemble average over more diffusers. To take the 2.2μm pixel-size monochrome CMOS sensor MTF into account, the product of the theoretical calculation of $PSD_I(f_x, f_y)$ and the square of 2.2 μm sensor MTF is plotted as the red dotted curve in Fig. 6. The measurement of 2.2 μm sensor MTF is described in Section 3.2 and the data are shown in Fig. 9. Comparing the three curves in Fig. 6, we can conclude that the theoretical calculation of the input PSD of the speckle on the sensor plane, $PSD_I(f_x, f_y)$, is very accurate.

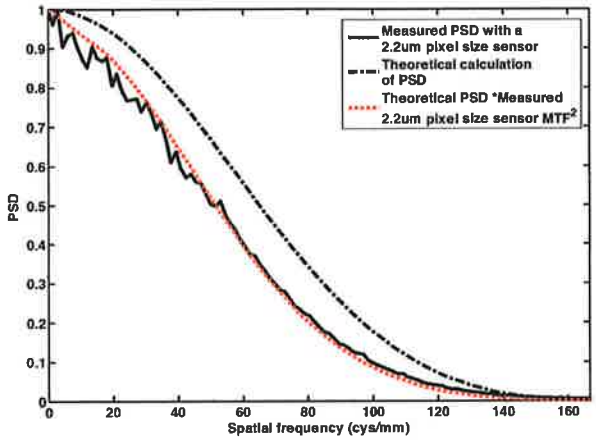

Fig. 6. The comparison between the theory and measurement of the input power spectral density, $PSD_I(f_x, f_y)$. The average speckle size is 6μm. The theoretical calculation is shown in black dashed curve. The measured data is shown in black solid curve. The measured $PSD_I(f_x, f_y)$ data is captured with a 2.2μm sensor. The product of the theoretical calculation of $PSD_I(f_x, f_y)$ and the square of 2.2μm sensor MTF is shown as the dotted red curve. The theoretical calculation and experimental data agree with each other very well.

Using Eq. (3) with calculated input $PSD_I(f_x, f_y)$ and the measured $PSD_S(f_x, f_y)$ data for a 6.0μm CMOS sensor, we obtain the MTF data for the 6.0μm monochrome CMOS sensor. The measured sensor MTF along the x-axis is shown in Fig. 7 as the dotted blue curve. The polynomial fitting of it is shown in Fig. 7 as the solid red curve. As a comparison, the measured MTF along the x-axis using the slanted edge technique is shown in Fig. 7 as the dash-dot green curve. To obtain the MTF data using the slanted edge technique, the ISO12233 target is imaged by a diffraction-limited lens with F# of 9.0 onto the CMOS sensor. A red color filter is used for illumination. The lens F# is chosen to match the equivalent F# of Z/D in the speckle setup. The lens MTF is measured by the Fisba interferometer. The lens and sensor overall MTF is estimated using the Imatest software from the slanted edge image. We obtain the sensor MTF using the slanted edge technique by dividing the overall MTF with the diffraction-limited lens MTF. From Fig. 7, we can see that the laser speckle method and the ISO12233 slanted edge technique provide very similar sensor MTF results. The

#102216 - $15.00 USD Received 30 Sep 2008; revised 10 Nov 2008; accepted 14 Nov 2008; published 20 Nov 2008

agreement between the two measurements proves the accuracy of the laser speckle method for MTF measurement of a sensor.

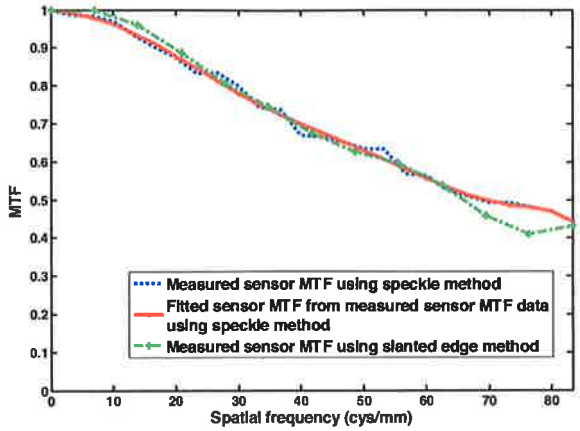

Fig. 7. The 6.0μm monochrome CMOS sensor MTFs along the x-axis. The dotted blue curve is the measured sensor MTF using laser speckle method; the solid red curve is the polynomial fitting of the measured sensor MTF data using speckle method; the dash-dot green curve is the measured sensor MTF using the slanted edge method. The range of the spatial frequency is from 0 to the Nyquist frequency of the 6.0μm sensor.

3.2 On-axis MTF measurement for a monochrome CMOS sensor with 2.2μm pixels

With the development of CMOS technology, the pixel size has shrunk dramatically. With small pixel size less than 2μm, the slanted edge technique is limited by the lens quality. Due to the fact that laser speckle method does not require using a lens, we consider this approach as a very promising technique for measuring the MTF of modern CMOS image sensors with small and super small pixels. In this section, we describe the experimental results for measuring MTF of Aptina's MI5100 monochrome image sensor with 2.2μm pixel size. To obtain the input PSD of the speckle with cut-off frequency at twice the Nyquist frequency of the sensor, the sensor is placed at $Z = 87mm$ away from the OMG diffuser. The same procedures for a 6.0μm sensor MTF measurement are repeated. The input power spectral density $PSD_I(f_x, f_y)$ is calculated and shown in Fig. 3. The measured $PSD_S(f_x, f_y)$ along the x-axis is shown in Fig. 8.

#102216 - $15.00 USD Received 30 Sep 2008; revised 10 Nov 2008; accepted 14 Nov 2008; published 20 Nov 2008

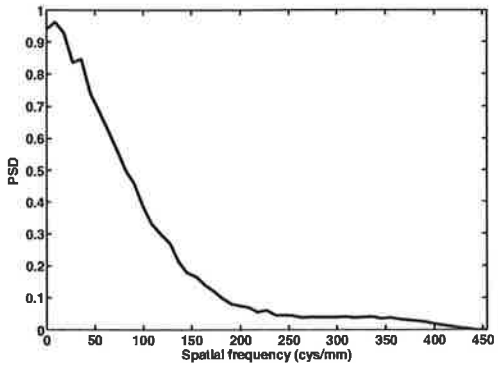

Fig. 8. The measured power spectral density, $PSD_S(f_x, f_y)$, cross-section along the x-axis for a 2.2μm pixel size monochrome CMOS sensor. The range of the spatial frequency is from 0 to twice the Nyquist frequency.

Using Eq. (3), we could derive the MTF for the sensor. The cross-section of the MTF along the row direction is shown in Fig. 9. As a comparison, the MTF of the sensor is measured using the slanted edge technique with a lens of F# 3.5. These two techniques provide very close results as shown in Fig. 9. This proves the applicability of measuring small pixel sensors with band-limited speckle pattern.

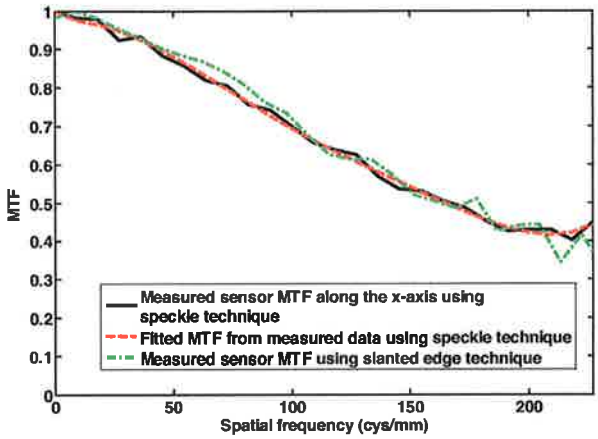

Fig. 9. The cross-section of MTF along the x-axis for a 2.2μm pixel-size monochrome CMOS sensor. The black solid curve is the measured sensor MTF using laser speckle technique. The red dash curve is the polynomial fitting of the measured MTF using speckle technique. The green dash-dot curve is the measured sensor MTF using the slanted edge technique with a F#3.5 lens. The range of the spatial frequency is from 0 to the Nyquist frequency of a 2.2μm sensor .

4. Conclusions

For high-performance integrated optical and digital imaging systems, it is essential to have the capability for measuring the response of the sub-systems and the overall system. In this paper we describe a new method for measuring the MTF, hence the performance of the CMOS detector. We show quantitatively that this metrology system for the MTF is accurate and presents results in agreement with MTF measurements using the standard ISO 12233 slanted edge technique. Importantly, we assert that this novel speckle method is particularly

#102216 - $15.00 USD Received 30 Sep 2008; revised 10 Nov 2008; accepted 14 Nov 2008; published 20 Nov 2008

advantageous for sensors even with pixel size down to 1μm. Moreover, the speckle method can be used to measure the MTF of the sensor alone since it does not require the use of a high-quality lens nor the fabrication of special test masks.

To measure sensor MTF at high spatial frequencies around the Nyquist frequency of the sensor, we place the sensor at Z away from the diffuser. Z is defined by Eq. (9). For the speckle, we present how to calculate the input power spectral density $PSD_i(f_x, f_y)$ using the Rayleigh Sommerfeld integral. To testify the accuracy of our calculation, we measure the PSD of 6μm-size speckle by a 2.2μm pixel-size sensor. The theoretical calculation and measurement data are presented in Fig. 6. They agree with each other very well.

Two monochrome CMOS sensors are measured. To avoid aliasing artifacts due to the insufficient sampling of the speckle patterns by the sensors, we sub-sample the speckle patterns by shifting the sensors with half pixel size steps. The anti-aliasing concept is shown in Figs. 4. The error due to inaccurate sub-sample shift movements is discussed. The requirement on sub-sample shift accuracy for five percentages error or less is provided in Eq. (13). The MTF data for a 6.0μm pixel sensor are shown in Fig. 7 compared with the MTF data measured by the ISO12233 slanted edge method. The two results are in excellent agreement. The MTF data for a 2.2μm pixel sensor are shown in Fig. 9. The results obtained with the speckle technique and the slanted edge technique are very close. This agreement proves the accuracy of our laser speckle technique. As a next step we are planning to extend this new MTF measurement technique on color sensors and sensors with shifted μlenses used in mobile applications.

Acknowledgments

We acknowledge Dr. Wanli Chi at the Institute of Optics, University of Rochester for his helpful discussions and suggestions. We acknowledge our colleagues Doug Fettig, Ian Clark, Sergey Velichko, Feng Li, Dmitry Bakin, Donna Cao, Elaine Jin, Igor Karasev, and Stephen Beveridge for their support.

#102216 - $15.00 USD Received 30 Sep 2008; revised 10 Nov 2008; accepted 14 Nov 2008; published 20 Nov 2008

Optics Communications 282 (2009) 2110–2117

Contents lists available at ScienceDirect

Optics Communications

journal homepage: www.elsevier.com/locate/optcom

Phase-coded aperture for optical imaging

Wanli Chi *, Nicholas George

The Institute of Optics, University of Rochester, Rochester, NY 14627, USA

ARTICLE INFO

Article history:
Received 19 August 2008
Received in revised form 20 January 2009
Accepted 12 February 2009

PACS:
42.30.–d
42.30.Va
42.30.Rx
42.30.Wb

Keywords:
Coded aperture system
Phase retrieval
Optical diffraction
Integrated computational imaging

ABSTRACT

For the optical spectrum region, we describe a novel phase-coded aperture imaging system that can be used in a computational imaging camera. The optical design includes a phase-only screen followed by a detector array. A specific diffraction pattern forms at the detector array when the wavefront from a point source object passes through the phase screen. Since diffraction effects cannot be ignored in the optical regime, an iterative phase retrieval method is used to calculate the phase coded screen. Correlation type processing can be applied for the image recovery. Computer simulation results are presented to illustrate the excellent imaging performance of this camera.

1. Introduction

Coded aperture imaging systems [1–5] are widely used in X-ray and gamma-ray astronomical imaging. The system can be considered as a multiple pinhole camera, where instead of a single-pinhole aperture, it uses a complicated transmission pattern as an aperture. Subsequent image processing can reveal the object with a much better signal to noise ratio than with a single-pinhole camera. Research has been reported to find a suitable aperture pattern, including for example, the early Fresnel zones [1], the improved scattered random pinholes [2], and later magnificent patterns based on a cyclic difference set, e.g., the uniformly redundant array [3]. Hundreds of papers are included in a website resource [5] with regular update.

With emphasis on the optical regime, related development for a variety of coded aperture systems can be found in numerous articles in two Proceedings of SPIE [6,7]. Of particular interest in these two volumes are a keynote paper by Keith Lewis [8] and an invited paper by Tim Clark and Esko Jaska [9].

In the optical region we believe that there are many virtues which deserve to be considered for a camera that uses a correlation system, especially with the advancement of increased computer power for the digital processing. In the optical regime due to large diffraction effects at these much longer wavelengths, the direct use of the X-ray/gamma-ray coded aperture (scattered pinholes, uniformly redundant array, etc.) does not work. Consideration of this deleterious diffraction effect is illustrated in Appendix A.

In this paper, we describe such a novel phase-coded aperture for incoherent optical imaging. The main difference between X-ray/gamma-ray and visible/infrared imaging is that in optical imaging the diffraction effect cannot be ignored. Referring to Fig. 1, we explore our novel imaging setup where the X-ray coded aperture is replaced by a phase-only screen and its diffraction pattern at the image plane is a coded pattern. A phase retrieval approach is applied to calculate the phase-only screen which is used to generate the image plane coded pattern. In the paper, we explain how our phase-coded mask is an excellent solution for the correlation process at the detector and it provides an ideal lossless mask.

The novel features of our camera include that it is a lossless sensitive system, that it can be ultra-thin, and that it is capable of multi-wavelength imaging with a monochromatic detector array. The paper is organized as follows: In Section 2 we describe the theory of the coded aperture camera in the optical region when diffraction effects are considered. The simulation result of our system is shown in Section 3. In Section 4 we discuss the details of the system design and illustrate its performance on a noisy image or a gray scale object. Section 5 is the discussion and summary.

* Corresponding author.
E-mail address: chiw@optics.rochester.edu (W. Chi).

0030-4018/$ - see front matter © 2009 Elsevier B.V. All rights reserved.
doi:10.1016/j.optcom.2009.02.031

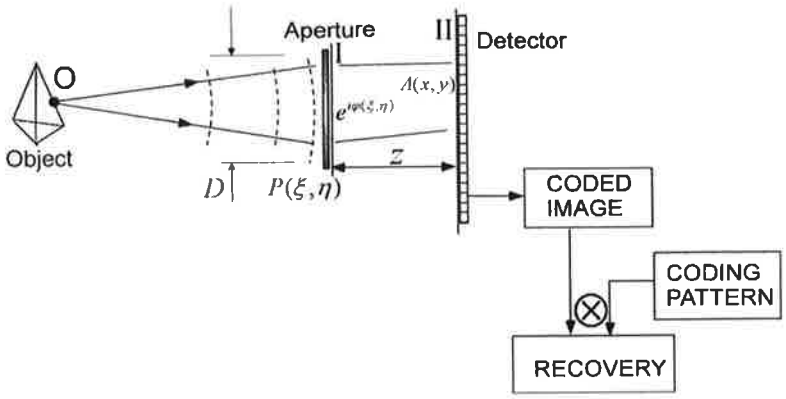

Fig. 1. The diagram of coded aperture system in the optical region. Symbols are defined as follows. $P(\xi,\eta)$, electric field amplitude transmission of the phase screen; $e^{i\varphi(\xi,\eta)}$, the electric field at plane I immediately after the phase screen for a point object O; $A(x,y)$, the intensity pattern at detector plane II for a point object O; z, the distance between plane I and plane II; D, the size of aperture of phase screen.

2. Basic principle

Coded aperture imaging systems are usually designed for X-ray and gamma-ray imaging where diffraction effects are negligible. In the optical region, one needs to consider the effect of diffraction. We illustrate the basic layout of the phase-coded aperture imaging system in Fig. 1; the object is incoherently illuminated. A phase-only aperture with a transmission function of $P(\xi,\eta)$ is used to modulate the incoming wavefront from the object. For a point object at O, the phase aperture can form a specific intensity pattern or a coded pattern, $A(x,y)$, on a detector array (plane II). Subsequent image processing of the coded image leads to recovery of the object. While the system shown in Fig. 1 has the simplest optical set-up with a phase-only aperture and the detector array, one can modify it to other forms, for example, an achromatic Fourier transform [10,11] can be incorporated into the optical setup to improve the wide optical spectrum band performance. Clearly, there are three basic topics in the design: finding an appropriate pattern for the point spread function, $A(x,y)$; finding the aperture function $P(\xi,\eta)$ that can generate the corresponding pattern $A(x,y)$; finding the recovered object by image processing.

In an optical system clearly $A(x,y)$ should be as close to a uniformly redundant array as typically used in an X-ray camera, and $P(\xi,\eta)$ is a transmission function required to form this array. While in the X-ray camera, there is little difference between the aperture pattern $P(\xi,\eta)$ and detector pattern $A(x,y)$; on the other hand, diffraction effects in the optical regime leads to marked difference between $P(\xi,\eta)$ and $A(x,y)$. An important novel aspect in the paper is to calculate $P(\xi,\eta)$ from the desired $A(x,y)$. In this section we briefly describe the basic principles; one can refer to Section 4 for the details of these design problems. We emphasize the first problem is in finding the pattern $A(x,y)$ which is important in the conceptual understanding of the camera.

Since $A(x,y)$ is an intensity pattern formed by diffraction from a finite aperture of $P(\xi,\eta)$, $A(x,y)$ must be real, non-negative, and bandlimited. After $A(x,y)$ is determined, one can use a standard phase retrieval algorithm [12,13] to calculate the aperture function $P(\xi,\eta)$. Let $t(x,y)$ be the binary function for the uniformly redundant array in coded aperture imaging [3]. As shown in Fig. 2, this pattern has sharp edges and thus is not band-limited. Even though the idealized binary edges are not realizable when diffraction is taken into account, we seek a solution for $A(x,y)$ that is realizable, as follows.

As is detailed in Section 4, we generate this realizable pattern of $A(x,y)$ by convolving $t(x,y)$ with a non-negative bandlimited blocking function $b(x,y)$ as shown in the following equation:

$$A(x,y) = \int\int t(\xi,\eta)b(x-\xi,y-\eta)d\xi d\eta \triangleq t(x,y) * b(x,y), \tag{1}$$

where $*$ is the convolution operation. This convolution operation is a key for the realizability of the imaging system. Only when $A(x,y)$ is bandlimited with appropriate bandwidth does the solution of phase screen function $P(\xi,\eta)$ in Fig. 1 exist.

Considering an imaging application as in Fig. 1, for an object $O(x,y)$, the image $I(x,y)$ of a noise free system can be written as,

$$I(x,y) = \int\int A(x-x',y-y')O(x',y')dx'dy' \triangleq A(x,y) * O(x,y). \tag{2}$$

In the recovery we calculate the estimate of object, $\hat{O}(x,y)$, as correlation of $I(x,y)$ and $t_R(x,y)$, i.e.,

$$\hat{O}(x,y) = \int\int t_R(x',y')I(x'-x,y'-y)dx'dy' \triangleq I(x,y) \otimes t_R(x,y), \tag{3}$$

where $\otimes$ is the correlation operation and

$$t_R(x,y) = \int\int [\{t(x-x',y-y') - \bar{t}]\mathrm{comb}(x'/D_x,y'/D_y)dx'dy', \tag{4}$$

in which D_x and D_y are the size of the uniformly redundant array $t(x,y)$ in x and y directions, respectively; and

$$\bar{t} = \frac{1}{D_xD_y}\int_{-D_x/2}^{D_x/2}\int_{-D_y/2}^{D_y/2} t(x,y)dxdy \tag{5}$$

is the average of function $t(x,y)$; and

$$\mathrm{comb}(x,y) = \sum_{i,j}\delta(x-i,y-j), \tag{6}$$

is a comb function.

Combining Eqs. (1)–(4) yields the result of $\hat{O}(x,y)$ as follows:

$$\hat{O}(x,y) = t(x,y) \otimes [t(x,y) - \bar{t}] * \mathrm{comb}(x/D_x,y/D_y) * b(x,y) * O(x,y), \tag{7}$$

where the sequence of convolution and correlation operations is from left to right.

The uniformly redundant array, $t(x,y)$ as shown in Fig. 2, has the following correlation property:

$$t(x,y) \otimes [t(x,y) - \bar{t}] * \mathrm{comb}(x/D_x,y/D_y) = C\mathrm{comb}(x/D_x,y/D_y) * [\Lambda(x/\Delta_x)\Lambda(y/\Delta_y)], \tag{8}$$

where C is a constant, and $\Lambda(x) = \max(1-|x|,0)$ is a triangle function; as shown in Fig. 2, Δ_x and Δ_y are the smallest feature size of the

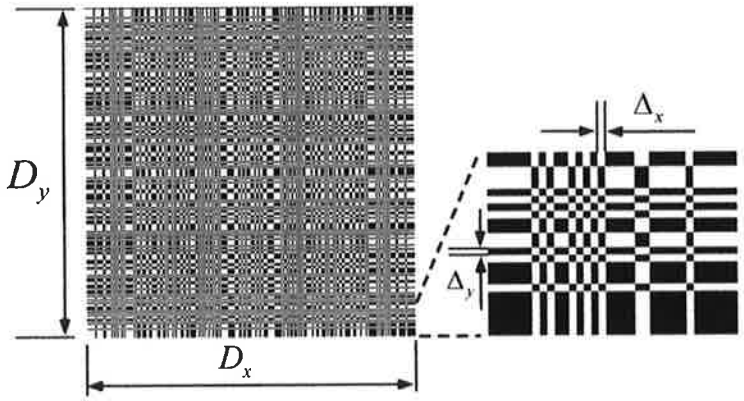

Fig. 2. An example of uniform redundant array used in coded aperture imaging system.

array in x and y directions, respectively. Plotting Eq. (8), one can readily see an ideal correlation function with no background variations or "artifacts". This type of cyclic correlation is described in detail in the literature [3] and represents a considerable advancement over the random array of pinholes due to Dicke [2].

Substitute Eqs. (8) into (7), we have the estimate of object $\widehat{O}(x,y)$ in the following:

$$\widehat{O}(x,y) = \mathrm{Ccomb}(x/D_x, y/D_y) * [\Lambda(x/\Delta_x)\Lambda(y/\Delta_y)] * b(x,y) * O(x,y). \tag{9}$$

Eq. (9) shows the recovered object and its shifted versions. If the field of view is constrained in the following form:

$$-D_x/2 \leqslant x < D_x/2 \quad \& \quad -D_y/2 \leqslant y < D_y/2, \tag{10}$$

then there is no overlap in shifted versions of object, we can recover the object $\widehat{O}_1(x,y)$ as,

$$\widehat{O}_1(x,y) = C[\Lambda(x/\Delta_x)\Lambda(y/\Delta_y)] * b(x,y) * O(x,y). \tag{11}$$

We note that the field of view constraint in Eq. (10) is in image space, i.e., x and y in Eq. (10) are the Cartesian coordinates at the detector plane.

From Eq. (11), the point spread function of the coded aperture system in the optical region, $p(x,y)$, can be written in the following:

$$p(x,y) = [\Lambda(x/\Delta_x)\Lambda(y/\Delta_y)] * b(x,y),$$

$$p(x,y) = \int\int [\Lambda(x'/\Delta_x)\Lambda(y'/\Delta_y)] b(x-x', y-y')dx'dy'. \tag{12}$$

This point spread function combines both the optical imaging and the correlation type digital processing.

From Eq. (12), the correlation type digital processing yields an image blurred by two parts: The smallest feature size of the uniformly redundant array $t(x,y)$ and the bandlimited function $b(x,y)$. It is important to note that in the detection process, the object information with spatial frequencies higher than the bandlimit of $b(x,y)$ is lost due to diffraction by the phase screen $P(x,y)$ of a finite size. Without extra object constraint, it is unwise to remove this blur function $b(x,y)$. This is true even for an imaging system with a diffraction limited lens, in which case $b(x,y)$ is an Airy disk for a circular aperture [14].

3. Simulation results

In Fig. 3a, we show a realizable pattern $A(x,y)$ at the detector plane. It is the image of the uniformly redundant array $t(x,y)$ shown in Fig. 2 by a diffraction limited square aperture lens and

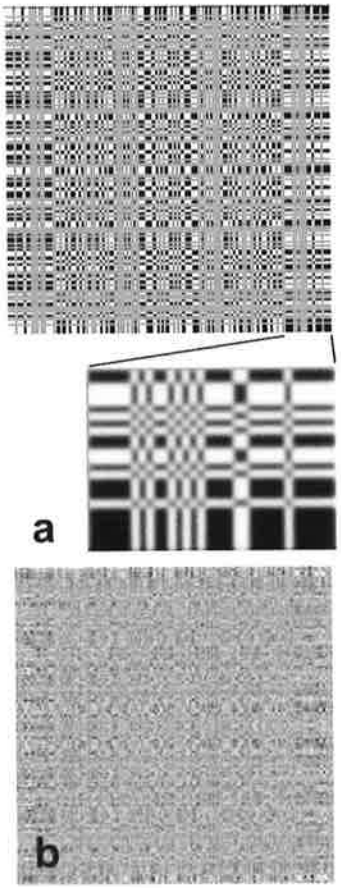

Fig. 3. The pattern of intensity point spread function $A(x,y)$ at plane II in Fig. 1 and the corresponding phase screen $P(x,y)$ at plane I that can generate such pattern. (a) A digitally constructed pattern from uniformly redundant array shown in Fig. 2 using Eq. (1); and (b) the phase screen to generate the pattern in a calculated using phase retrieval algorithm.

is generated digitally from Eq. (1). A section of the pattern $A(x,y)$ is magnified to see the detailed features of such a pattern. The edge is blurred compared to that of the uniformly redundant array in Fig. 2. Fig. 3b is the corresponding phase function that can generate such a pattern for an axial point source at infinity. the phase values from $-\pi$ to π are shown from dark to bright. In this simulation we

use the following parameters. Both the sizes of the pattern $A(x,y)$ and phase screen $P(x,y)$ are 2 mm × 2 mm and the distance between phase screen and detector is $z = 5$ mm. The wavelength of illumination is $\lambda = 4$ μm. The imaging results are shown in Fig. 4. Upper image of Fig. 4 is the object used in simulation; middle image of Fig. 4 is the decoded image using the correlation method described in Section 2; lower image of Fig. 4 is the image by a diffraction limited lens with the same square aperture. We observe the excellent imaging results for the coded aperture system as shown in middle image of Fig. 4. Also, we see the image of the coded aperture system is a little more blurry than that of the diffraction limited lens, this is because the point spread function of such a system, as in Eq. (12), is wider than that of the diffraction limited system. Some extra digital deconvolution can be applied to the middle image in Fig. 4 to remove the effect of triangle blur function in Eq. (12) and recover a diffraction limited result. This extra blur is not a significant disadvantage of the optical region coded aperture imaging system.

One virtue of our system is its simplicity. The optical subsystem includes only a phase screen followed by a detector array, while the conventional diffraction limited lens is hard to design and fabricate, especially in ultra-thin format. Our system works both in the visible and infrared optical region. The simplicity of our infrared system is clearly an advantage compared to a conventional infrared imaging systems.

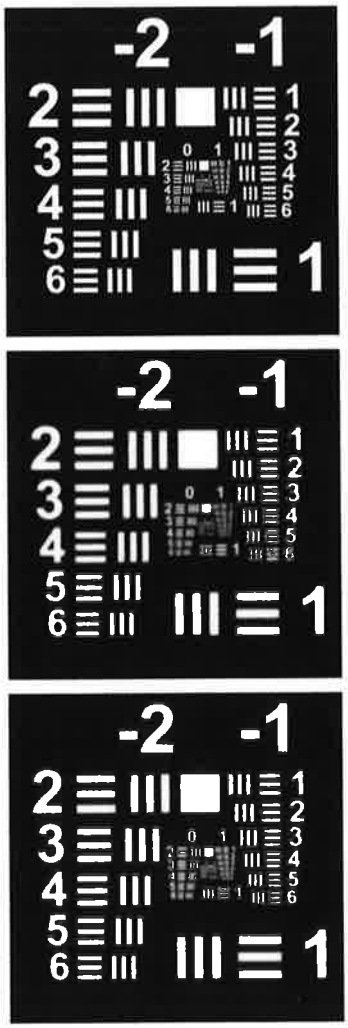

Fig. 4. Imaging results of coded aperture system in optical region. Upper: object; middle: recovered image from coded aperture system; lower: image by diffraction limited lens.

4. Detailed considerations of system design

The important thing in the system design is to find an appropriate intensity pattern $A(x,y)$ which is generated by some phase screen for a point source object. In this section we explain in detail how to find $A(x,y)$, i.e., Eq. (1) in Section 2 is explained in detail. We also discuss briefly the phase retrieval algorithm to determine the aperture function $P(\xi,\eta)$ and to complete the image recovery.

4.1. Finding intensity pattern $A(x,y)$

In order to find the intensity point spread function $A(x,y)$ (See Fig. 1) from Eq. (1), we need to define functions $b(x,y)$ and $t(x,y)$.

4.1.1. Define function $b(x,y)$

To define the bandlimited function $b(x,y)$, we emphasize that the function $A(x,y)$ is bandlimited. We need to know the cutoff frequency of the function $A(x,y)$ in order to define $b(x,y)$. As a side note, any signal with finite duration is not bandlimited. But thinking in this way would not help in any way with our system design problem. So in this paper we do not consider bandlimit in such a strict sense.

Refer to Fig. 1, we only consider y component of the electric field. the incoming field from a point source passes the phase screen. Assuming implicit $\exp(+i\omega t)$ dependence, at plane I immediately after the phase screen, one can write the electric field as,

$$E_i(\xi,\eta) = \exp[i\varphi(\xi,\eta)]. \tag{13}$$

Using Rayleigh–Sommerfeld diffraction theory, we can calculate the field at plane II with a distance of z from plane I in the following:

$$E_0(x,y,z) = \int\int \exp[i\varphi(\xi,\eta)]\frac{\exp(-ikR)}{2\pi R}\left(ik+\frac{1}{R}\right)\frac{z}{R}d\xi d\eta, \tag{14}$$

where $R = [z^2 + (x-\xi)^2 + (y-\eta)^2]^{\frac{1}{2}}$.

The spatial spectrum $\widetilde{E}_0(f_x,f_y)$ of the electric field at plane II is defined as,

$$\widetilde{E}_0(f_x,f_y) = \int\int E_0(x,y,z)\exp[-i2\pi(f_x x + f_y y)]dxdy, \tag{15}$$

where f_x and f_y denote the variables in the spatial frequency domain. Substitute Eqs. (14) into (15), one can find out

$$\widetilde{E}_0(f_x,f_y) = \widetilde{E}_i(f_x,f_y)\exp\left[-ikz\sqrt{1-\lambda^2(f_x^2+f_y^2)}\right], \tag{16}$$

where $\widetilde{E}_i(f_x,f_y)$ is the spatial spectrum of the electric field at plane I defined in the following:

$$\widetilde{E}_0(f_x,f_y) = \int\int E_0(x,y,z)\exp[-i2\pi(f_x x + f_y y)]dxdy. \tag{17}$$

Eq. (16) is the exact solution of Maxwell Equation for y component of electric field spatial spectrum transfer. The field spatial spectrum is determined by two terms: The spatial spectrum of field at plane I and the transfer function as shown in second term of Eq. (16). When the distance between screen (plane I) and detector (plane II) is much larger than the wavelength of illumination λ, then the second term of Eq. (16) is subject to the exponential decay for $|f_x^2 + f_y^2| > 1/\lambda^2$. So we can say the cutoff frequency in the second term is $1/\lambda$.

In principle, the phase screen can be made as fine as possible and there is no cutoff frequency for the first term of Eq. (16). But

in an actual system, the diffraction pattern at the detector plane (plane II in Fig. 1) has to be finite size so that it can be fully collected by the detector. So The cutoff frequency of the first term in Eq. (16) is determined by the optical configurations.

In a thin configuration, i.e., the distance z between planes I and II in Fig. 1 is smaller than aperture size D, It is generally the second term of Eq. (16) that will determine the cutoff frequency of electric field $E_0(x,y)$ at plane II of Fig. 1. In a thick configuration, $z > D$, we can estimate the diffraction limited resolution size δ at the detector plane in the following well known formula,

$$\delta \approx \lambda z/D. \tag{18}$$

Thus the cutoff frequency of $E_0(x,y)$ for thick configuration can be approximated as,

$$f_{\max} \approx 1/\delta \approx D/(\lambda z). \tag{19}$$

From the above analysis we find the cutoff frequency f_{Emax} of electric field $E_0(x,y)$ is the following:

$$f_{Emax} \approx \min[1/\lambda, D/(\lambda z)]. \tag{20}$$

After the cutoff frequency of $E_0(x,y)$ is determined, we can find out the cutoff frequency of intensity pattern $A(x,y)$ at plane II of Fig. 1. $A(x,y)$ can be written as,

$$A(x,y) = |E_0(x,y,z)|^2. \tag{21}$$

From Fourier transform theory, we have the spatial spectrum of the intensity pattern $A(x,y)$ can be written as autocorrelation of in the following form:

$$\widetilde{A}(f_x,f_y) = \int\int \widetilde{E}_0(f'_x,f'_y)\widetilde{E}_0(f'_x - f_x, f'_y - f_y)df'_x df'_y. \tag{22}$$

Clearly, the cutoff spatial frequency f_{Amax} of intensity pattern $A(x,y)$ is twice that of electric field $E_0(x,y,z)$, or,

$$f_{Amax} \approx \min[2/\lambda, 2D/(\lambda z)]. \tag{23}$$

In an actual electronic imaging system, there is one more factor in the design of intensity pattern $A(x,y)$. The detector array can only sample the pattern in finite intervals. To avoid an aliasing effect, $A(x,y)$ needs to be bandlimited up to the Nyquist frequency. Assume the distance between neighbor pixels of the detector is Δ, then the highest spatial frequency of $A(x,y)$ set by the detector sampling is $1/(2\Delta)$.

A simple way to find a nonnegative bandlimited signal $A(x,y)$ is to convolve a not bandlimited signal with a nonnegative bandlimited function $b(x,y)$. $b(x,y)$ must have upper spatial frequency equal to the cutoff frequency of the pattern $A(x,y)$, which is the lesser value of $f_{A\max}$ as in Eq. (23) and $1/(2\Delta)$. As one example, $b(x,y)$ can be an intensity point spread function of a diffraction limited lens with an appropriate size finite aperture, the cutoff frequency is determined by the aperture size of the lens as is well known in Fourier optics [14].

4.1.2. Define function $t(x,y)$

In mathematics and X-ray imaging applications, it is well known that the uniformly redundant array has a perfect correlation property, as shown in Eq. (8). That is, the correlation in Eq. (8) does not have background variations which can introduce extra noise in the recovered image even with noise free detection process. This is an important criterion in the choice of $t(x,y)$. Any pattern with such correlation property as shown in Eq. (8) would work in the system design. In this paper, we use uniformly redundant array as a starting point. The definition of the uniformly redundant array in a matrix format, t_{ij} with a size of $r \times s$, is as follows, [3]:

$$t_{ij} = \begin{cases} 0 & \text{if } i = 0, \\ 1 & \text{if } j = 0 \ \ \& \ \ i \neq 0, \\ 1 & \text{if } C(r,i)C(s,j) = 1, \\ 0 & \text{otherwise}, \end{cases} \tag{24}$$

where t and s are two prime numbers, $r - s = 2$, and

$$C(r,i) = \begin{cases} 1 & \text{if there exists an integer } n, 1 \leqslant n < r, \\ & \text{such that } i = n^2 \cdot \mathrm{mod}(r) \\ -1 & \text{otherwise}. \end{cases} \tag{25}$$

In the system design, we need to choose two parameters in the uniformly redundant array, the feature size of the array Δ_x, Δ_y and the total array size D_x and D_y.

From Eq. (12), one can see that in order to have the best resolution of the system, one need to make Δ_x and Δ_y as small as possible. But another limiting factor is that $A(x,y)$, as calculated in Eq. (1), need to have good contrast. From Eq. (1), the contrast of $A(x,y)$ is larger for larger feature size of the uniformly redundant array. By considering both Eqs. (1) and (12), one can set Δ_x and Δ_y be about the same as the feature size of $b(x,y)$. or mathematically,

$$2\Delta_x f_{x\mathrm{Max}} \approx 1 \ \& \ 2\Delta_y f_{y\mathrm{Max}} \approx 1, \tag{26}$$

where $f_{x\mathrm{Max}}$ and $f_{y\mathrm{Max}}$ are the largest spatial frequency of $b(x,y)$ in x and y directions, respectively.

The total size D_x and D_y of the array $t(x,y)$ can be determined from the field of view constraint in Eq. (10). For a detector with a size of $X \times Y$, Eq. (10) needs to be true for any point (x,y) at detector ($|x| < X/2$ and $|y| < Y/2$). This implies that D_x and D_y need to satisfy the following:

$$D_x \geqslant X/2 \quad \& \quad D_y \geqslant Y/2. \tag{27}$$

4.2. Calculate phase screen $P(\xi,\eta)$

After intensity pattern $A(x,y)$ is known, the next step in the system design is to calculate an aperture with a transmission function of $P(\xi,\eta)$ that can be used to generate the specific intensity pattern $A(x,y)$. A phase type aperture is preferred in many applications. This is basically a phase retrieval problem with a diagram shown in Fig. 5. It is an iterative phase calculation method. We start with an electric field with a amplitude of $E(x,y) = \sqrt{A(x,y)}$; then a free space back propagation is used to calculate the aperture function at plane I of Fig. 1. We denote this aperture function as $|P(\xi,\eta)|\exp[i\phi(\xi,\eta)]$. In order to find a phase screen, we set the aperture constraint, i.e., change $|P(\xi,\eta)|$ to 1. Then a free space propagation is applied to find out the electric field at detector plane II as shown in Fig. 1. We denote the thus found electric field as $F(x,y)\exp[i\psi(x,y)]$. Afterwards, the detector plane intensity constraint is applied, i.e., change $F(x,y)$ to $\sqrt{A(x,y)}$. Next, we performance a free space back propagation again, and the process is repeated. Using this iterative approach, we eventually can calculate a phase-only screen that will generate the required intensity pattern $A(x,y)$.

In this algorithm we emphasize that free space propagation and back propagation can be easily calculated exactly in the spatial frequency domain using Eq. (16). So this calculation is good in nonparaxial case when, for example, the distance between the screen and detector planes are smaller than the aperture size of the screen (thin camera configuration).

While phase retrieval algorithms in the above description are generally known in the literature, we note that in our system design some extra data constraint [15] can be used in the phase retrieval algorithm to improve the performance of the coded aperture system. As one example, in order to have an extremely

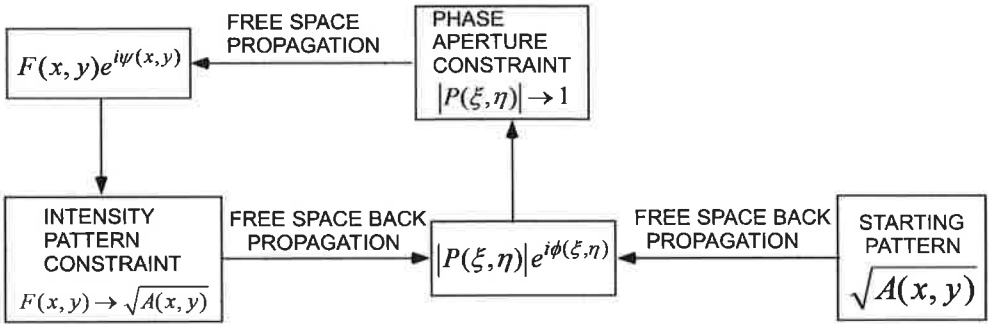

Fig. 5. A phase retrieval diagram to find out a phase type aperture function $P(\xi,\eta)$ from image plane intensity pattern $A(x,y)$.

wide field of view, we need to calculate a phase screen which can generate a similar intensity pattern for both an on-axis object point and an off-axis point source. Similar extra data constraints can be used to design a system with large depth of field or to reduce the sensitivity of intensity pattern dependence on parameter z, the distance between phase screen and detector plane. These issues are outside of the scope of this paper, which only presents a novel coded aperture imaging system.

4.3. Image recovery

The image recovery in the optical region coded aperture system is similar to that in X-ray imaging as proposed by Dicke [2]. There is a rich literature [5] in this area. Besides the simple correlation type processing described in Section 2, other methods include photon tagging, linear filter, maximum entropy, iterative removal of sources.

While it is important to study image quality for different recovery methods under the noisy detection conditions, it is beyond the scope of this paper to present such results. However, we simply show an image recovery using the correlation type processing as described in Section 2. Fig. 6 is the recovery similar to that shown in the middle image of Fig. 4 except that in Fig. 6 a Gaussian noise is added to the intermediate coded image. The standard deviation of the Gaussian noise is one percent that of the signal value of the intermediate image. In this system as shown in Fig. 1, the detector linear size is twice that of the pattern size $A(x,y)$ (See Eq. 10), the dark and bright structure of the object is not seen in the intermediate image. The intermediate image is bright at the center and it tapers to dark at the edge of the detector. The noise added to the intermediate image has a standard deviation which is one percent of the intermediate image. So the noise added to the center is much larger than the noise added to the edge of the intermediate image. An acceptable recovery is achieved using a simple correlation type processing.

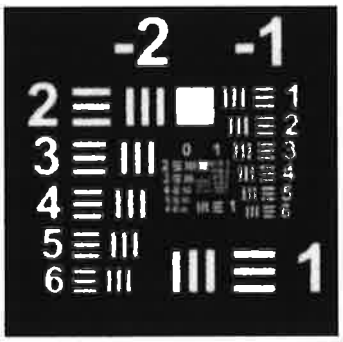

Fig. 6. Image recovery of a coded aperture system with 1% of gaussian noise in the intermediate image. A simple correction type processing as explained in Section 2 is used.

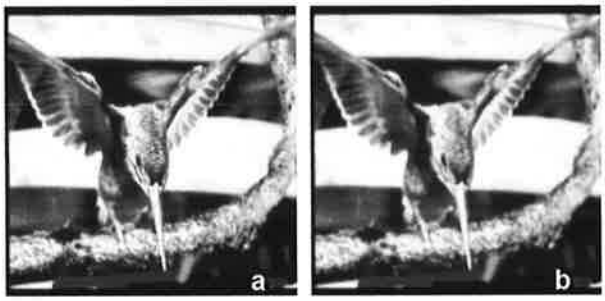

Fig. 7. Simulated imaging results of coded aperture system in optical region with gray scale object. (a) Diffraction limited image; and (b) recovered image using coded aperture system.

In order to illustrate the effectiveness of the novel camera system with an image that displays gray scale, Fig. 7 shows the simulated imaging results using the object of a hummingbird. Fig. 7a shows the diffraction limited image taken with diffraction limited lens with same aperture size as that of the phase coded aperture system, i.e., 2 mm × 2 mm aperture. The recovered image using the phase-coded aperture system is shown in Fig. 7b. No noise is included in the intermediate image for coded aperture system. A careful comparison of the high frequency detail and variable contrast shown excellent image quality. Even small contrast variation on the upper rail of the wooden fence is clearly observed in the image. Although not shown in figures, good image recovery results are also obtained with 1% noise added to the intermediate image at the detector plane.

5. Discussions and summary

A coded aperture imaging system suitable for the optical regime has been proposed, analyzed and demonstrated. The aperture pattern of a uniformly redundant array is changed to a bandlimited pattern and used as the point spread function of the optical subsystem. The intermediate image is coded by this complicated point spread function, and a correlation type of processing is used to decode the image and recover the object. In the camera design, one needs to pay attention to the field of view constraint as explained in Section 2.

An important feature of this coded aperture system is that it can be used for multi-wavelength imaging with a monochromatic detector array. This is useful especially in the infrared region where most of the detector arrays only measure the total intensity over

the whole wavelength range. To realize the multi-wavelength application, basically for a point source at different wavelengths λ_a, λ_b and so on, the phase screen will generate different intensity patterns $A(x,y;\lambda_a), A(x,y;\lambda_b)$ on the detector. The intermediate image is the supposition of images over all spectral ranges. The pattern of $A(x,y;\lambda_m)$ is used for recovery of object at wavelength λ_m by applying the same correlation method outlined in Section 2. A discussion of this multi-wavelength imaging capability is in the Appendix B.

In the design of such a system, the big challenge is the low contrast of the intermediate coded image; especially for multi-wavelength applications, one needs to balance the number of wavelengths and contrast. While not explained in this paper, an interesting alternative configuration by incorporating an achromatic Fourier transform [10,11] into the optical system will help in intermediate image contrast for wide spectral multi-wavelength application. A detailed study of color imaging will be published at a later time.

This camera has numerous other interesting features. One feature is that it produces high quality images for binary objects and also for those with extended gray scale. The computer simulation shows excellent recovery with a simple correlation type of image processing, see Fig. 4. With ever increasing computer power and advances in configurations of detector arrays, we believe this type of camera system has great potential for application in futuristic smart cameras.

Acknowledgements

This research was supported in part by Micron Inc., and the US Army Research Office.

Appendix A. X-ray system is inoperative in the optical imaging

In the optical coded aperture system described in Fig. 1, it is important to understand that simply using the same uniformly redundant array that is useful in the X-ray system as an amplitude mask is not appropriate for the optical regime. For the X-ray camera, one places the uniformly redundant array $t(x,y)$ in Fig. 2 and Eq. (24) at plane I in Fig. 1. For the camera design in Section 3, we use $\lambda = 4$ μm, $\Delta = 8$ μm and $z = 5$ mm. Clearly, for the infrared camera to be operative, the detail of the correlation mask features in Fig. 2 needs to be preserved at plane II in Fig. 1. The diffraction spread S is computed approximately as follows, [14]:

$$S = \frac{\lambda}{\Delta} z. \tag{A.1}$$

For the values cited, we find a diffraction spread S by about 2.5 mm. This large smear of 2.5 mm compared to the needed resolution in detail of 8 μm is absolutely prohibitive. Hence, it is clear that the mask of uniformly redundant array cannot be located at plane I of Fig. 1 for optical imaging.

In our novel adaptation of the X-ray camera to the optical wavelengths, as shown in Fig. 3, we devise a lossless phase mask $P(\xi,\eta)$ placed in plane I in Fig. 1 that acts effectively to provide an intensity point spread function $A(x,y)$ at plane II in Fig. 1. One sees this by comparing Fig. 3a to Fig. 2. Hence, in this appendix, we have shown the limitation imposed by the effect of diffraction. Also in this paper we have shown that the use of phase retrieval methods presents a very useful result for the camera design.

Appendix B. Basic concept of multi-wavelength imaging

In this appendix we explain the concept of multi-wavelength imaging capability of our phase-coded aperture imaging system. We stress that the multi-wavelength imaging can be accomplished with a monochromatic detector array. Only the basic ideas are illustrated herein. Referring to Fig. B.1, we assume the object consists of three sources $O_a(x,y), O_b(x,y)$, and $O_c(x,y)$ radiating at wavelength of λ_a, λ_b, and λ_c, respectively. The image at the detector can be written as,

$$I(x,y) = A_a * O_a + A_b * O_b + A_c * O_c, \tag{B.1}$$

where $A_a(x,y), A_b(x,y)$ and $A_b(x,y)$ are the intensity distribution at detector plane for axial point source of wavelength λ_a, λ_b, and λ_c, respectively. In order to recover the object at a wavelength of λ_a, one calculates the following correlation function,

$$\widehat{O}_a(x,y) = A_{aR} \otimes I, \tag{B.2}$$

where

$$A_{aR}(x,y) = \int\int [A_a(x',y') - \overline{A}_a] comb(x/L_{ax}, y/L_{ay}) dx' dy', \tag{B.3}$$

and L_{ax} and L_{ay} are the size of $A_a(x,y)$ in x and y directions, respectively.

The substitution of Eqs. (B.1) into (B.2) yields,

$$\widehat{O}_a(x,y) = O_a * (A_a \otimes A_{aR}) + O_b * (A_b \otimes A_{aR}) + O_c * (A_c \otimes A_{aR}). \tag{B.4}$$

From Section 2, we note that the first term in Eq. (B.4) contains the recovered object at wavelength λ_a. A proper design of the aperture phase plate will ensure that coded patterns A_a and A_b, A_c are uncorrelated, i.e., $A_b \otimes A_{aR} \approx 0$ and $A_c \otimes A_{aR} \approx 0$ so that in Eq. (B.4) there is no contributions in the second and third terms in the recovery of object at wavelength λ_a. This can be fulfilled by controlling the thickness variations of the phase plate at the aperture

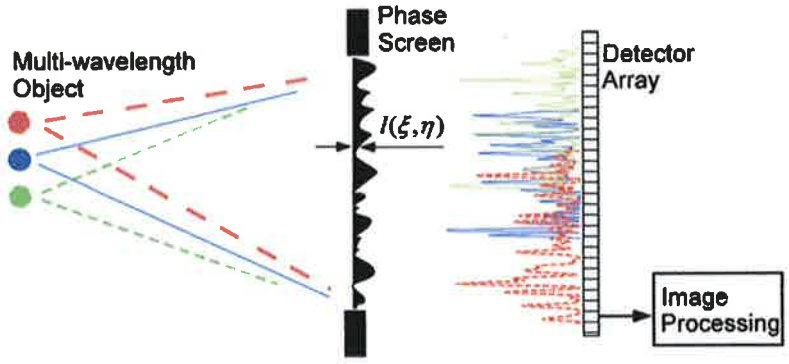

Fig. B.1. A schematic illustration to show the concept of multi-wavelength imaging.

plane [16]. Refer to Fig. B.1, we can write the transmission of the phase plate as

$$P(\xi,\eta;\lambda) = \exp[i2\pi(n-1)l(\xi,\eta)/\lambda], \tag{B.5}$$

where n is refractive index of the plate of thickness $l(\xi,\eta)$. Generally, if the phase delay functions for two wavelengths are different, then their diffraction patterns would be uncorrelated for the two wavelengths. The analysis [16] shows that if the standard deviation of plate thickness, $l(\xi,\eta)$, satisfies

$$\sigma_l \geqslant \frac{\lambda_a\lambda_b}{2\pi(n-1)|\lambda_a-\lambda_b|}, \tag{B.6}$$

then we have $A_b \otimes A_{aR} \approx 0$ in Eq. (20). In this phase-coded aperture camera, it is important to point out that the lossless phase mask provides an excellent resolution since the Bayer color filter is no longer needed and color crosstalk between neighboring pixels can be eliminated or controlled. The details and fine points about color crosstalk between different wavelengths in this system are to be treated in a later paper.

References

[1] L. Mertz, N.O. Young, in: K.J. Habell (Ed.), Proceedings, International Conference on Optical Instruments and Techniques, Chapman & Hall, London, 1961, p. 305.
[2] R.H. Dicke, Astrophys. J. 153 (1968) L101.
[3] E.E. Fenimore, T.M. Cannon, Appl. Opt. 17 (1978) 337.
[4] A. Busboom, H.D. Schotten, H. Elders-Boll, J. Opt. Soc. Am. A 14 (1997) 1058.
[5] <http://astrophysics.gsfc.nasa.gov/cai/>.
[6] David P. Casasent, Timothy Clark (Ed.), Proc. SPIE 6714, 2007.
[7] David P. Casasent, Stanley Rogers (Ed.), Proc. SPIE 7096, 2008.
[8] Keith Lewis, Proc. SPIE 6714 (2007) 671402.
[9] Tim Clark, Esko Jaska, Proc. SPIE 6714 (2007) 671403.
[10] N. George, S. Wang, Appl. Opt. 23 (1984) 787.
[11] J. Lancis, P. Andres, W.D. Furlan, A. Pons, Opt. Lett. 19 (1994) 402.
[12] J.R. Fienup, Opt. Lett. 3 (1978) 27.
[13] R. Rolleston, N. George, Appl. Opt. 25 (1986) 178.
[14] J.W. Goodman, Introduction to Fourier Optics, McGraw-Hill, 1996.
[15] R.G. Paxman, T.J. Schulz, J.R. Fienup, J. Opt. Soc. Am. A 9 (1992) 1072.
[16] N. George, A. Jain, Appl. Phys. A: Mater. Sci. Process. 4 (1974) 201.

Incoherently combining logarithmic aspheric lenses for extended depth of field

Kaiqin Chu,* Nicholas George, and Wanli Chi

The Institute of Optics, University of Rochester, Rochester, New York 14627, USA

*Corresponding author: kaiqin@optics.rochester.edu

Received 25 June 2009; revised 1 September 2009; accepted 1 September 2009; posted 2 September 2009 (Doc. ID 113343); published 22 September 2009

We describe a method for combining concentric logarithmic aspheric lenses in order to obtain an extended depth of field. Substantial improvement in extending the depth of field is obtained by carefully controlling the optical path difference among the concentric lenses so that their outputs combine incoherently. The system is analyzed through diffraction theory and the point spread function is shown to be highly invariant over a long range of object distances. After testing the image performance on a three-dimensional scene, we found that the incoherently combined logarithmic aspheres can provide a high-quality image over an axial distance corresponding to a defocus of $\pm 14(\lambda/4)$. Studies of the images of two-point objects are presented to illustrate the resolution of these lenses. © 2009 Optical Society of America

OCIS codes: 110.5220, 220.1000, 260.1960, 100.1830, 350.4600, 030.1670.

1. Introduction

For a conventional imaging system or in photography, the captured image is usually the convolution of the point spread function (PSF, also known as the impulse response) of the lens with the object. Within the depth of field, the PSF should be invariant for consistent imaging performance. Since the PSF is the diffraction pattern of the pupil of the system, many scientists have attempted to modify the pupil of the imaging system by inserting a phase mask in the aperture plane so that the diffraction pattern of the modified aperture changes little or less with defocus. Example include the cubic phase mask [1], the logarithmic asphere [2,3], and those developed more recently [4,5]. Each phase mask is optimized over a certain range of object distances. This range decreases with increasing numerical aperture. Thus, for a large-aperture lens, there is still a need to extend the depth of field beyond the capacity of a single phase mask. In this paper we suggest a method to incoherently combine concentric phase masks so that each mask is responsible for only a portion of the focus range. It is then possible to achieve a substantially longer focus range while maintaining high-quality imaging for large-aperture lenses. The key to the combination is that each element should be independent of the others so that their PSFs can be summed incoherently. A coherently summed PSF from those elements will behave exactly like that from one phase mask and may fail to give the desired depth of field.

There are two ways to combine phase masks incoherently. One is through the use of a polarization-coded aperture, where individual zones of the aperture transmit orthogonally polarized light. Thus, light transmitted by each zone should be added incoherently at the detector array [6]. Another method is through unbalanced optical path difference (OPD). Through insertion of a thin glass plate or ring in the lens aperture, enough OPD can be created between the center disk and the outer annulus of the aperture that these two regions become uncorrelated to each other and act independently in the formation of the image [7]. Combining these two regions through unbalanced OPD leads to an extended depth of field while maintaining the resolution of the whole lens aperture. In principle, this combining method can be applied to any pupil or phase mask as long as the system is illuminated by a broadband source.

0003-6935/09/285371-09$15.00/0

The image performance of a single logarithmic asphere has been carefully studied in the literature [8–10]. In this paper we will show that by incoherently combining outputs from two logarithmic aspheres, the shape of the PSF can be further stabilized with respect to defocus, i.e., the depth of field can be further extended. For an example we will show that, for the incoherently combined logarithmic aspheric lens with f-number 2.8, the depth of field can be extended to be 14-fold of that for a diffraction-limited lens.

The paper is organized as follows. First, we give a brief description of the logarithmic asphere lens with the aim to list the essential formulas for later use. Then, in Section 3, we combine two aspheres through unbalanced OPD by inserting a thin glass plate in the aperture plane. The PSF of the combined lens is derived and shown to be highly invariant over a very long range of object distances. In Section 4 we give a brief introduction of the image processing algorithm. The image performance of the combined lens is tested on a three-dimensional (3D) scene with sharp-edged objects and on a two-point object (Section 5). A summary of the reported work is given in Section 6.

2. Brief Description of a Logarithmic Aspheric Lens

A series of logarithmic aspheric lenses were proposed by Chi and George to extend the depth of field [3]. The analysis of this paper is on a β-type design but equally applies to other designs. As shown in Fig. 1, a logarithmic aspheric lens with a circular aperture of radius R is designed to focus between s_1 and s_2, with the image plane located at t. The phase profile of the lens can be written as

$$\Phi_{\log}(\rho; s_1, s_2) = -k\left\{\sqrt{t^2+\rho^2} - t + \frac{a(t^2+\rho^2)}{2}\ln\left[\frac{A(t^2+\rho^2)}{e}\right] - \frac{at^2}{2}\ln\left[\frac{At^2}{e}\right]\right\} + \Phi(0), \quad (1)$$

where $\rho \le R$, $\Phi(0)$ is a constant and

$$a = \frac{\frac{1}{s_1} - \frac{1}{\sqrt{R^2+s_2^2}}}{\ln\frac{R^2+t^2}{t^2}}, \quad (2)$$

$$A = \frac{1}{t^2}\exp\left[-\frac{\sqrt{s_2^2+R^2}}{\sqrt{R^2+s_2^2}-s_1}\ln\left(\frac{R^2+t^2}{t^2}\right)\right]. \quad (3)$$

The dependence of the phase profile on the design parameters (s_1, s_2) can be seen from the dependence of a and A on those design parameters, as shown in Eqs. (2) and (3). We can define a position s_0 between s_1 and s_2 that satisfies

$$\frac{1}{s_1} + \frac{1}{s_2} = \frac{2}{s_0} \quad (4)$$

as the nominal focus position. Distances Δs_{near} and Δs_{far}, defined as

$$\Delta s_{\text{near}} = s_0 - s_1, \quad (5)$$

$$\Delta s_{\text{far}} = s_2 - s_0, \quad (6)$$

will be the near and far portion of the depth of field, respectively. In this paper we are mostly concerned with the near portion of the depth of field, Δs_{near}, because, when the object is moved away from the focus plane, the defocus increases faster for the case of moving toward the imaging lens than for the case of moving away from the imaging lens.

The image performance and depth of field of such lenses are decided by the PSFs. Considering a point source in the object plane and following the standard scalar diffraction theory, we can write the nonparaxial form of the PSF of a lens with phase profile Φ as follows [8]:

$$\mathrm{PSF}(\rho_2, s; \nu) = \left| \int_0^R \frac{e^{-i\left[k\left(\sqrt{s^2+\rho^2}+\sqrt{t^2+\rho^2+\rho_2^2}\right)+\Phi(\rho)\right]}}{k^2\sqrt{t^2+\rho^2+\rho_2^2}\sqrt{s^2+\rho^2}} \times J_0\left(\frac{k\rho_2\rho}{\sqrt{t^2+\rho^2+\rho_2^2}}\right)\rho \mathrm{d}\rho \right|^2, \quad (7)$$

where $\nu = ck/2\pi$, ρ_2 is the radial coordinate in the image plane, and s is the object distance. The phase profile of the lens Φ can be substituted with $\Phi_{\log}$, shown in Eq. (1). In this paper we are interested in lenses with large numerical apertures.

Figures 2 and 3 show the PSFs for a diffraction-limited lens and a single logarithmic asphere with various amounts of defocus. Both lenses have the same f-number of 2.8 and are designed to focus at $s_0 = 1514\,\text{mm}$. The design parameters for the logarithmic asphere are $s_1 = 1154\,\text{mm}$ and $s_2 = 2200\,\text{mm}$. The defocus amount will be about -24λ

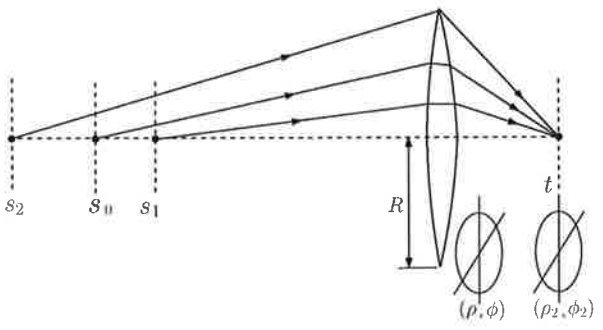

Fig. 1. Logarithmic lens designed to focus between (s_1, s_2).

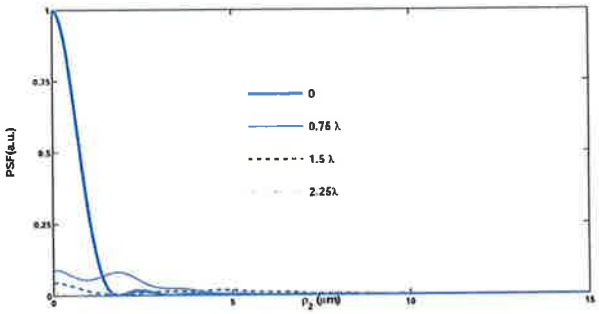

Fig. 2. PSFs from a diffraction-limited lens with various defocus amounts.

for objects at the s_1 plane and 24λ for objects at the s_2 plane. The detector array is placed at 62.5 mm away from the lens aperture, i.e., $t = 62.5$ mm. Thus, the nominal focal length of the lens is 60 mm (calculated from the lens law, $1/f = 1/s_0 + 1/t$). The radius of the lens aperture is 10.7 mm. The center wavelength of the illumination source is $0.5\,\mu$m. Clearly we can see that different amounts of defocus will lead to different shapes of the PSF. However, the difference is much smaller in the logarithmic asphere case than in the diffraction-limited lens case. In the following, we will show that the difference in PSFs with different amounts of defocus can be even smaller by incoherently combining two logarithmic aspheres. Other than extended depth of field, another benefit of the highly invariant PSFs is that the distance variance of the imaging system due to defocus can be ignored and linear image processing algorithms can be used for image deconvolutions, as we will show in Sections 4 and 5.

3. Incoherently Combine Two Concentric Logarithmic Lenses

As we have demonstrated in earlier work [7], we can insert a glass plate in the lens aperture purposefully to create OPD between annular segments of the aperture. With enough OPD, these two segments can be considered as independent imaging lenses. The diffractions from these two segments are combined incoherently to form the captured image. In combining two logarithmic aspheres together with this method, we can design each asphere with its own focal range. This gives us an opportunity to extend the depth of field by having the two logarithmic lenses focusing on two different portions of the object space. We choose the inner segment to have design parameters s_{11} and s_{12}, while the design parameters for the outer segment are chosen to be s_{21} and s_{22}, as shown in Fig. 4. The total focus range for the combined logarithmic lens is somewhere between (s_{11}, s_{22}). Each asphere is designed to have same aperture area, i.e., the radius of the inner lens is $R/\sqrt{2}$ and the inner and outer radii of the outer lens are $R/\sqrt{2}$ and R, respectively. The phase profile for each of logarithmic aspheres can be written as

$$\Phi_{\log}^{(i)}(\rho; s_{i1}, s_{i2}) = -k\left\{(\sqrt{t^2+\rho^2} - t) + \frac{a_i(t^2+\rho^2)}{2}\ln\left[\frac{A_i(t^2+\rho^2)}{e}\right] - \frac{a_i t^2}{2}\ln\left(\frac{A_i t^2}{e}\right)\right\} + \Phi_i(0), \tag{8}$$

where $i = 1, 2$. $\Phi_{\log}^{(1)}$ and $\Phi_{\log}^{(2)}$ are the phase profile for the inner and outer logarithmic aspheres, respectively. The parameters a_1, A_1, a_2, and A_2 can be written as

$$a_1 = \frac{\frac{1}{s_{11}} - \frac{1}{\sqrt{R^2/2+s_{12}^2}}}{\ln\frac{R^2/2+t^2}{t^2}}, \tag{9}$$

$$A_1 = \frac{1}{t^2}\exp\left[-\frac{\sqrt{s_{12}^2+R^2/2}}{\sqrt{R^2/2+s_{12}^2}-s_{11}}\ln\left(\frac{R^2/2+t^2}{t^2}\right)\right], \tag{10}$$

$$a_2 = \frac{\frac{1}{\sqrt{R^2/2+s_{21}^2}} - \frac{1}{\sqrt{R^2+s_{22}^2}}}{\ln\frac{R^2+t^2}{\delta R^2+t^2}}, \tag{11}$$

$$A_2 = \frac{1}{R^2/2+t^2}\exp\left[-\frac{\sqrt{s_{22}^2+R^2}}{\sqrt{R^2+s_{22}^2}-\sqrt{R^2/2+s_{21}^2}} \times \ln\left(\frac{R^2+t^2}{R^2/2+t^2}\right)\right]. \tag{12}$$

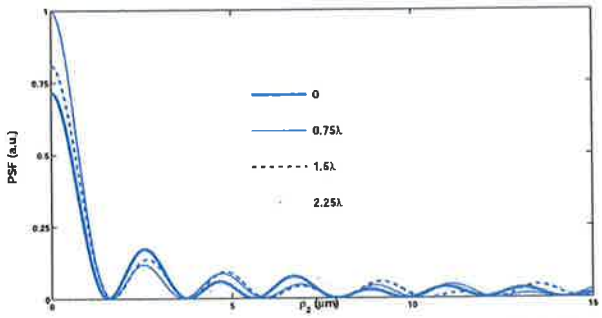

Fig. 3. PSFs from a single logarithmic aspheric lens with various defocus amounts.

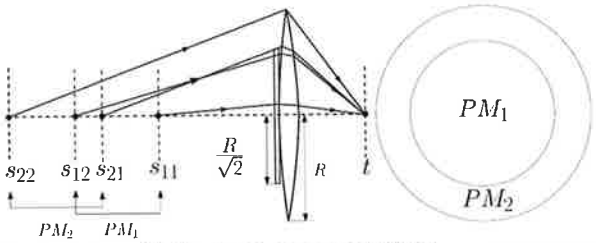

Fig. 4. Lens with the inner phase mask (PM_1) focusing between (s_{11}, s_{12}) and outer phase mask (PM_2) focusing at (s_{21}, s_{22}). The thin glass plate in the pupil plane will create enough OPD to uncorrelate these two phase masks.

With a thin glass disk whose radius is the same as that of the inner logarithmic lens inserted in the pupil plane, as shown in Fig. 4, an OPD is created between the inner and outer lenses. With enough thickness, the OPD between these two lenses can be larger than the coherence length of the illumination source. Then these two lenses will be uncorrelated to each other and their PSFs will add up in terms of intensity after an ensemble average [7]. The whole lens is then composed of two concentric logarithmic aspheres and these two aspheres are combined incoherently. The total PSF of the combined lens can be written in the form of an intensity sum, i.e.,

$$\mathrm{PSF}_{\mathrm{whole}}(\rho_2, s) = \int S(\nu)\{\mathrm{PSF}_1(\rho_2, s; \nu) + \mathrm{PSF}_2(\rho_2, s; \nu)\}\mathrm{d}\nu, \tag{13}$$

where $S(\nu)$ is the spectrum of the source and

$$\mathrm{PSF}_1(\rho_2, s; \nu) = \left| \int_0^{R/\sqrt{2}} \mathrm{d}\rho \frac{\rho e^{-i\left[k\left(\sqrt{s^2+\rho^2}+\sqrt{t^2+\rho^2+\rho_2^2}\right)+\Phi_{\log}^{(1)}+\frac{(n-1)d}{n}\frac{\rho^2}{2s^2}\right]}}{k^2\sqrt{t^2+\rho^2+\rho_2^2}\sqrt{s^2+\rho^2}} \times J_0\left(\frac{k\rho_2\rho}{\sqrt{t^2+\rho^2+\rho_2^2}}\right)\right|^2, \tag{14}$$

$$\mathrm{PSF}_2(\rho_2, s; \nu) = \left| \int_{R/\sqrt{2}}^{R} \mathrm{d}\rho \frac{\rho e^{-i\left[k\left(\sqrt{s^2+\rho^2}+\sqrt{t^2+\rho^2+\rho_2^2}\right)+\Phi_{\log}^{(2)}\right]}}{k^2\sqrt{t^2+\rho^2+\rho_2^2}\sqrt{s^2+\rho^2}} \times J_0\left(\frac{k\rho_2\rho}{\sqrt{t^2+\rho^2+\rho_2^2}}\right)\right|^2 \tag{15}$$

are the PSFs of the inner and outer logarithmic aspheres, respectively. n and d are the refractive index and thickness of the inserted glass plate, respectively. In this paper we assume that the system is color corrected and the defocus introduced by the glass plate [the last phase term in Eq. (14)] is included in the PSF of the inside lens. If a glass ring is inserted, then the defocus should be added to the PSF instead.

During the numerical calculation of the PSFs of the combined logarithmic aspheres, the parameters for the inner phase mask are $s_{11} = 1154\,\mathrm{mm}$ and $s_{12} = 1593\,\mathrm{mm}$, and $s_{21} = 1435\,\mathrm{mm}$ and $s_{22} = 2200\,\mathrm{mm}$ for the outer phase mask. The pair of the outer parameters are (1154 mm, 2200 mm) and are the same design parameters of the single logarithmic asphere discussed in Section 2. Clearly the PSF depends not only on the outer parameters s_{11}, s_{22}, but also on the inner parameters s_{12}, s_{21}. The choices of the inner parameters of s_{12} and s_{21} are results of the optimization where a stable and high Strehl ratio are achieved over the longest object distances. The freedom to have two extra parameters s_{12}, s_{21} comes from the fact that two logarithmic lenses are used in the configuration of the proposed lens system.

Figure 5(a) shows the PSFs from the incoherently combined logarithmic aspheres for the same series of defocus amounts shown in Figs. 2 and 3. Comparing Figs. 2 and 3 and Fig. 5(a), we see that, by combining two logarithmic lens incoherently, we are able to stabilize the shapes of the PSFs over these values of defocus. From Fig. 5(b) we see that the PSF with 4λ defocus stays essentially the same as the in-focus PSF. This will lead to stable image performance over defocus and, thus, the combined lens has an extended depth of field compared to a single logarithmic asphere with the same design parameters and aperture size and, obviously, to a diffraction-limited lens with the same aperture size.

As for the thickness of the glass plate inserted, it should be able to generate enough OPD between these two logarithmic lenses so that these two lenses become uncorrelated and are combined incoherently. If the plate is of glass material, a thickness of 7 μm is enough [7]. This plate can be inserted in the entrance pupil of the imaging lens, where its purpose to create enough OPD is still fulfilled. The advantage gained by this is that the incident angle on the plate is usually small as the objects are typically far from

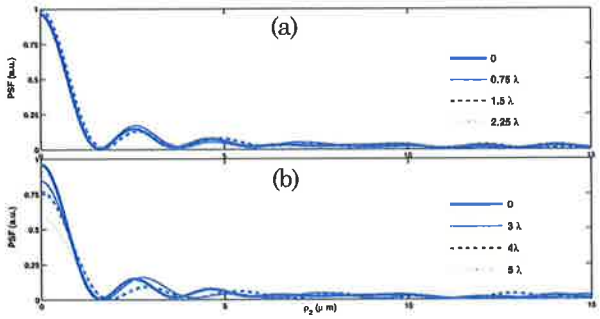

Fig. 5. PSFs from the incoherently combined logarithmic aspheres with various defocus amounts. (a) PSFs of the lens with the same defocus values as in Figs. 2 and 3 (b) PSFs of the lens with even larger defocus.

the lens in photography. Because the plate is so thin and the incident angle is small, traveling through the plate will change the propagation path so little that the change can be neglected. Thus, the defocus introduced because of the insertion of the plate can be neglected. Furthermore, with the plate being so thin, its effect on off-axis performance is also negligible. As to the off-axis performance of the single logarithmic aspheric lens itself, work has been done to achieve consistent image performance for both on-axis and off-axis object positions [10]. The interested reader can refer to this paper for details.

4. Image Formation of a Three-Dimensional Scene and Digital Image Processing

For a 3D scene, objects may be distributed anywhere in the scene. Different objects are not necessarily blurred in the same way. So in the sensor array, the image is formed according to the following equation:

$$I(x,y) = \sum_m O_m(x,y,s_m) * \mathrm{PSF}(x,y,s_m) + n(x,y), \tag{16}$$

where O_m is the mth object located a distance of s_m from the lens and $*$ stands for the convolution operation. The noise $n(x,y)$ is assumed to be additive and Gaussian. The system is distance variant in this sense. The narrower the depth of field, the more severe the space variance of the image formation. This imposes a major hurdle for the post-image processing where the knowledge of the object position is not readily available. There are several schemes of image reconstruction for general space-variant systems [11–13]. However, they rely on prior knowledge of how the PSF varies in the scene. For general imaging applications or photography, objects could be anywhere within the 3D scene. It becomes impossible to have the prior knowledge of the corresponding PSFs for individual objects.

The optical design proposed in this paper helps to make the system less distance variant so that an averaged PSF (averaging over the depth of field) can be an approximation of the true PSF at each object location. If the image processing algorithm can constrain the solution space so that the object can be reconstructed with an approximate PSF, we can perform deconvolutions on the whole scene with one PSF, and the image processing will be substantially sped up. An important implication of the work in this paper is the ability to use a fast, linear reconstruction algorithm to deblur images collected by the combined logarithmic lenses due to the high degree of defocus invariance in the combined lenses' joint PSF. In this paper, we will use a total-variation-based algorithm where both the total variation and the fidelity term are simultaneously minimized, as shown in Eq. (17):

$$\min_{\hat{O}} \iint \sqrt{\left(\frac{\partial \hat{O}}{\partial x}\right)^2 + \left(\frac{\partial \hat{O}}{\partial y}\right)^2}\,dxdy + \frac{\mu}{2}\iint |\hat{O} * \mathrm{PSF} - I|^2 dxdy, \tag{17}$$

where $\hat{O}$ is the estimate of the 3D scene and μ is the weight of the fidelity term. This algorithm was first proposed by Rudin *et al.* [14] for denoising and now is implemented to perform both image deblurring and denoising [15–19]. Minimization of the total variation itself is not a linear operation, and the algorithm can be slow and expensive in terms of computation capacity. Several methods have been proposed to speed up the optimization [15–18]. Recently, Wang *et al.* proposed an alternating minimization method that is, to our knowledge, the fastest. In essence the algorithm has been linearized so that the minimizer can be found through the use of the fast Fourier transform algorithm [19].

The total-variation-based algorithm itself is not designed to perform distance-variant image recovery. However, by modifying the algorithm slightly, the performance on a space-variant scene can be quite good, as we will show later in this paper. In order to understand how the modified algorithm can handle the inexactness of the PSF, we will list the essential steps of the original algorithm and explain what we modify to handle the inexact PSF. For details of the original algorithm, the interested reader can refer to the original paper [19]. First, a new variable $W = [w_1, w_2]$ is introduced to approximate $\frac{\partial \hat{O}}{\partial x}, \frac{\partial \hat{O}}{\partial y}$. We can write an approximate form of Eq. (17) as

$$\min_{W,\hat{O}} \iint \sqrt{w_1^2 + w_2^2}\,dxdy + \frac{\beta}{2}\iint \left[\left(w_1 - \frac{\partial \hat{O}}{\partial x}\right)^2 + \left(w_2 - \frac{\partial \hat{O}}{\partial y}\right)^2\right] dxdy + \frac{\mu}{2}\iint |\hat{O} * \mathrm{PSF} - I|^2 dxdy. \tag{18}$$

Note that W is not defined as

$$\left[\frac{\partial \hat{O}}{\partial x}, \frac{\partial \hat{O}}{\partial y}\right],$$

but it will gradually approach the derivative of the object function during the optimization of Eq. (18) for large β values. In this sense, Eq. (18) is equivalent to Eq. (17) when $\beta \to \infty$.

The optimization of Eq. (18) can be found through optimizing two subproblems, defined as follows.

1. For a fixed $\hat{O}$, find the minimizer W for the following problem:

$$\min_{W} \iint \sqrt{w_1^2 + w_2^2}\,dxdy + \frac{\beta}{2}\iint \left[\left(w_1 - \frac{\partial \hat{O}}{\partial x}\right)^2 + \left(w_2 - \frac{\partial \hat{O}}{\partial y}\right)^2\right] dxdy. \quad (19)$$

2. For a fixed W, find the minimizer $\hat{O}$ for

$$\min_{\hat{O}} \frac{\beta}{2}\iint \left[\left(w_1 - \frac{\partial \hat{O}}{\partial x}\right)^2 + \left(w_2 - \frac{\partial \hat{O}}{\partial y}\right)^2\right] dxdy + \frac{\mu}{2}\iint |\hat{O} * \mathrm{PSF} - I|^2 dxdy. \quad (20)$$

Both Eqs. (19) and (20) have analytical solutions [19]. So the algorithm to find the minimizer of Eq. (18) becomes alternately minimizing Eqs. (19) and (20) with respect to W and $\hat{O}$. The algorithm stops when both W and $\hat{O}$ have converged, which means that more alternating minimization would not change the value of either W and $\hat{O}$. Then we can increase β in Eq. (18) and find a new pair of W, $\hat{O}$ through the procedure described above. The sequence generated by this procedure is proved to converge and the convergence rate has been shown to be q linear [19].

In our application of the algorithm, we will use an average PSF, defined as

$$\overline{\mathrm{PSF}}(\rho_2) = \overline{\mathrm{PSF}(\rho_2, s)}, \qquad s \in (s_1, s_2), \quad (21)$$

to replace the PSF in Eqs. (17) and (18). Notice the original cost function in Eq. (17) contains a fidelity term with weight μ. The smaller μ is, the more tolerant the optimization will be of an inexact PSF. During the optimization, we will relax the requirement on the fidelity by decreasing μ gradually, so that, at the beginning of the optimization, we emphasize fitting our estimated image to the measurement, and the algorithm behaves like an inverse filter. The estimate of the object through inverse filtering in general will be noisy and have spurious structures. Then we gradually increase the relative weight of the total variation by increasing β to smooth the estimates. With this procedure, we are able to get satisfactory reconstructions using the average PSF (as we will show in Section 5). A diagram of the modified algorithm is shown in Fig. 6.

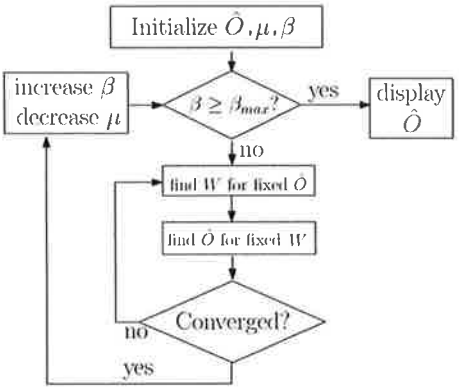

Fig. 6. Diagram of the total-variation-based algorithm.

5. Imaging Performance of the Incoherently Combined Logarithmic Aspheres

A. Imaging a Three-Dimensional Scene

In the image simulation of a 3D scene, we use three sharp-edged objects to represent objects far from the lens, in the focus plane, and close to the lens (for example, a semicircle, a square, and a triangle, as shown in Fig. 7). The detector array sees the whole scene as a two-dimensional picture with all range information lost, as shown in Fig. 8. By studying how edges from the far object, the in-focus object, and the near object spread, we can objectively evaluate the image performance. During the image simulation, we blur each object according to its position. All the blurred images from different objects are summed up and then additive noise is added to form the final blurry and noisy image according to Eq. (16). The noise-to-signal ratio is 0.01 in this paper. This is a typical value for an 8 bit detector array.

For the diffraction-limited lens with an f-number of 2.8 and focused at 1514 mm, when objects are moved away from the focus position by ±5 mm, the defocus amount is about a quarter wavelength and, according to Rayleigh, the lens is still considered to be focusing at these objects [20]. With more defocus, i.e., the objects are moved farther away from the focus plane, the objects are considered to be out of focus and the images of these objects will be quite blurry. Figure 9 shows the images taken by the diffraction-limited lens when the far object and near object are ±5, ±10, and ±15 mm away from the focus position. The edge spread functions for those positions are plotted in Fig. 9(d). The Rayleigh limit is marked and will be used as a threshold. Images with a shallower edge compared to this threshold will be considered as out of focus.

Images taken by the combined logarithmic aspheres when the far object and the near object are ±10, ±40, and ±70 mm away from the focus plane are shown as examples in Fig. 10. The edge spread functions in the positions are also shown in Fig. 10(d). We notice that, although these objects are severely blurred, they are all blurred similarly. The modified total-variation-based image

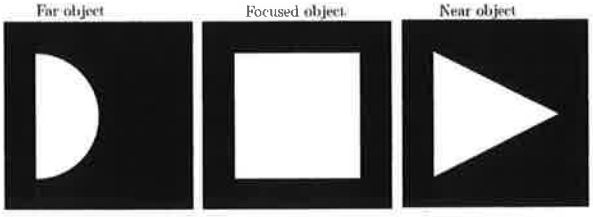

Fig. 7. Three sharp-edged objects.

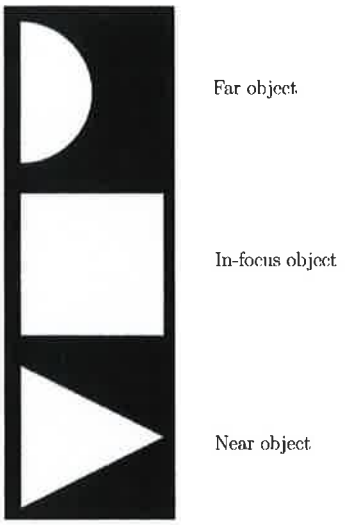

Fig. 8. Scene seen by the detector array.

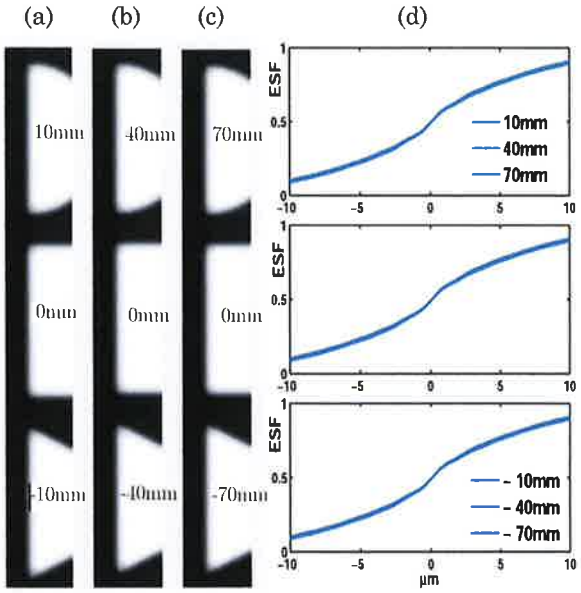

Fig. 10. Images taken with the incoherently combined logarithmic aspheres. (a) Object position, (10, 0, −10) mm; (b) object position, (40, 0, −40) mm; (c) object position: (70, 0, −70) mm; and (d) edge spread functions for these positions.

reconstruction algorithm described in Section 4 is applied to these blurry and noisy images, with results shown in Fig. 11. We see that the edges of these reconstructed images are all crisp and they are either steeper or as steep as the Rayleigh limit. This means that the final images in those positions can be considered to be perfectly imaged by the combined logarithmic aspheric lens. Beyond the range (−70 mm, 70 mm), the reconstructed images are not satisfactory and the corresponding edges are shallower than the Rayleigh limit. In the digital processing, we have used $\beta_0 = 2$, $\beta_{\max} = 2^{22}$, and $\mu = 0.05$. The rate of increase in β is 2 and the rate of decrease in μ is 1.4. The particular choices listed here are not critical to the reconstruction and, in general, follow the recommendations listed in Ref. [19]. The computation time is about 1 min for an image size of 2000 × 2000 pixels on a laptop computer with an Intel Core 2 at 2.00 GHz processor for an image size of 2000 × 2000 pixles. Based on these figures, we conclude that the depth of field for the incoherently combined

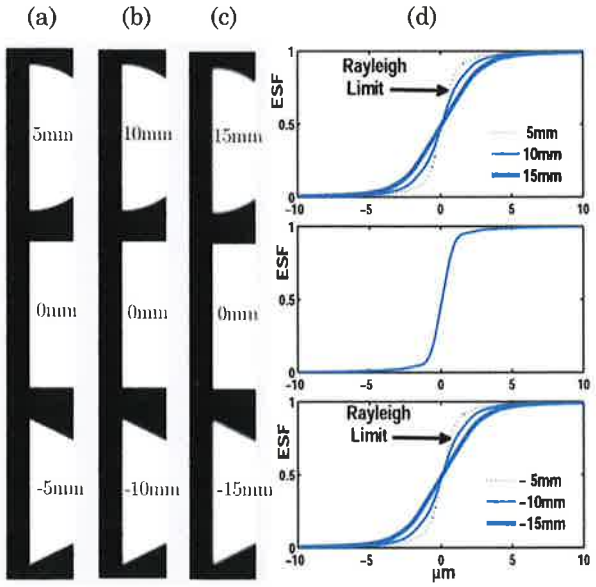

Fig. 9. Images taken with the diffraction-limited lens. (a) Object position, (5, 0, 5) mm; (b) object position, (10, 0, −10) mm; (c) object position, (15, 0, −15) mm; and (d) edge spread functions for those positions.

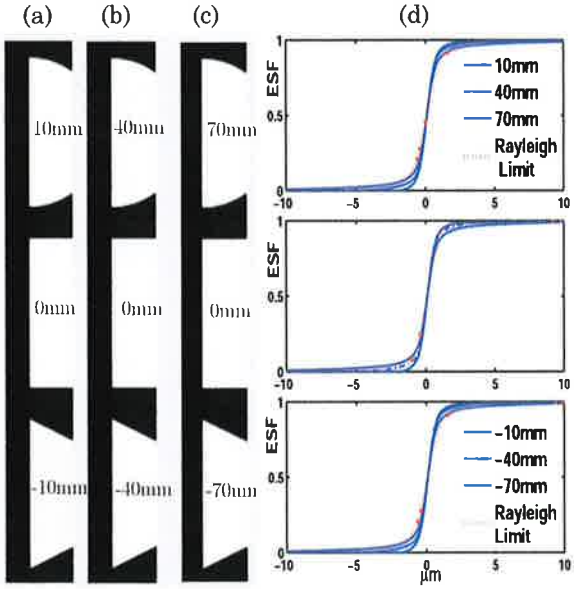

Fig. 11. Reconstruction from the images shown in Fig. 10. (a) Object position, (10, 0, −10) mm; (b) object position, (40, 0, −40) mm; (c) object position, (70, 0, −70) mm; and (d) edge spread functions for these positions.

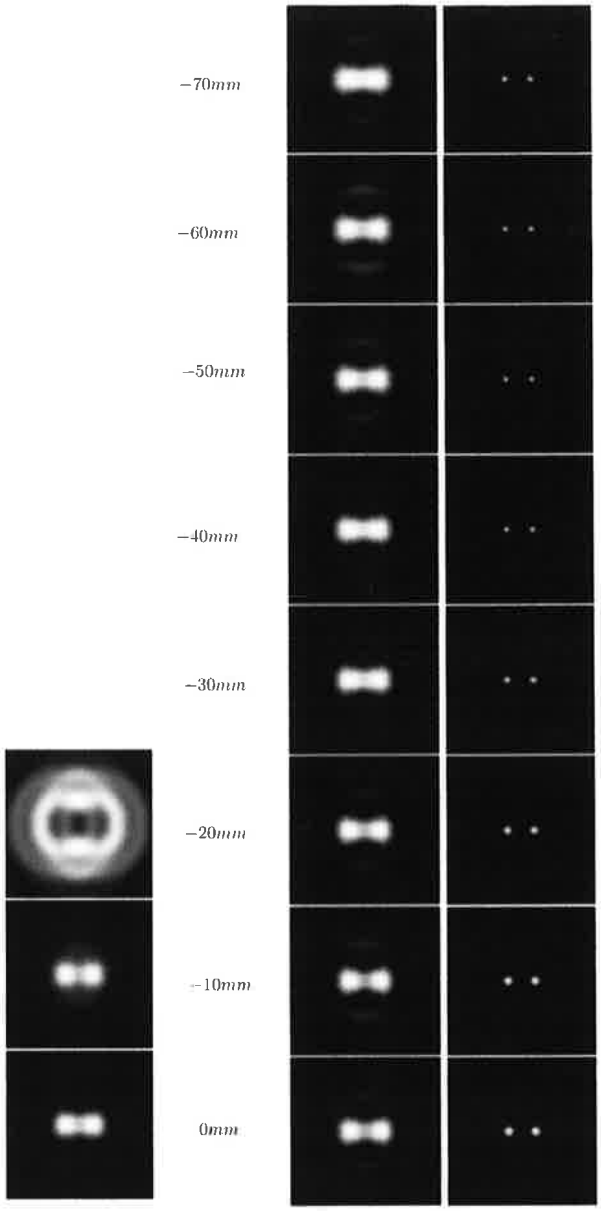

Fig. 12. Lateral resolution study with a two-point object at various object distances from the focus plane, as labeled. (a) Images from a diffraction-limited lens (images beyond −20 mm are too blurry to show here). (b) Blurry images taken by the incoherently combined logarithmic aspheres and the reconstructed images.

logarithmic aspheres is (−70 mm, 70 mm). Hence, we see that this integrated lens and digital processing system provides essentially diffraction-limited quality. For the depth of field, the range of performance corresponds to a defocus of about ±14 times $\lambda/4$.

B. Resolution

A separate criteria by Rayleigh relates to the resolution of a two-point object [21]. As is well known, the resolvable separation in the image space is given by the following formula:

$$d = 1.22\lambda f/\sharp. \tag{22}$$

According to Eq. (22), the resolution should be 1.7 μm when the f-number is 2.8 and the nominal wavelength of the illumination source is 0.5 μm. In the simulation experiment, we have two points separated by 1.7 μm in the image plane. The blurry images are simulated for objects within the depth of field found in Subsection 5.A, allowing us to apply the modified total-variation-based algorithm as described in Section 4 to process the blurry images of the two points. During the reconstruction, only one PSF is used for all positions considered. Figure 12 shows the blurry images taken by a diffraction-limited lens and the incoherently combined logarithmic lens. The similarity among the blurry images with different object distances from the combined lens is evident in Fig. 12. The reconstructed images are also shown in Fig. 12. We see that these two points are well resolved for all the object distances we have considered in Subsection 5.A. Thus we conclude that the resolutions within the depth of field of the combined logarithmic aspheric lens is the same as the original diffraction-limited lens. Of course, when the noise increases, we might expect some resolution loss. In this paper, we have chosen a typical noise level for an 8 bit detector. The total-variation-based algorithm was suggested initially for denoising. It would be interesting to analyze the signal-to-noise performance of the proposed system with this algorithm, but that is beyond the scope of this paper.

6. Summary

In this paper we studied a combination of logarithmic aspheres with unbalanced optical paths to show that superior extension of depth of field can be obtained. In Section 2 we briefly reviewed the performance of the logarithmic asphere. In Section 3 we presented a useful design of the combined logarithmic aspheres for an f-number of 2.8 with a 60 mm focal length. Figure 5 shows the superior performance for this incoherently combined logarithmic asphere. We saw excellent invariance or stability of the PSF for a defocus range of 4λ. In computer simulation studies, we showed that this integrated lens and digital processing system provides essentially diffraction-limited quality. For the depth of field, the range of performance corresponds to a defocus of about 14 times $\lambda/4$.

This research is funded in part by the United States Army Research Office (USARO) and Aptina Imaging, Inc.

References

1. E. R. Dowski Jr. and W. T. Cathey, "Extended depth of field through wave-front coding," Appl. Opt. **34**, 1859–1865 (1995).
2. W. Chi and N. George, "Electronic imaging using a logarithmic asphere," Opt. Lett. **26**, 875–877 (2001).
3. W. Chi and N. George, "Computational imaging with the logarithmic asphere: theory," J. Opt. Soc. Am. A **20**, 2260–2273 (2003).

4. J. Ojeda-Castaneda, J. E. A. Landgrave, and H. M. Escamilla, "Annular phase-only mask for high focal depth," Opt. Lett. **30**, 1647–1649 (2005).
5. E. Ben-Eliezer, E. Marom, N. Konforti, and Zeev Zalevsky, "Radial mask for imaging systems that exhibit high resolution and extended depths of field," Appl. Opt. **45**, 2001–2013 (2006).
6. W. Chi, K. Chu, and N. George, "Polarization coded aperture," Opt. Express **14**, 6634–6642 (2006).
7. K. Chu, N. George, and W. Chi, "Extending the depth of field through unbalanced OPD," Appl. Opt. **47**, 6895–6903 (2008).
8. N. George and W. Chi, "Extended depth of field using a logarithmic asphere," J. Opt. A Pure Appl. Opt. **5**, S157 (2003).
9. W. Chi and N. George, "Integrated imaging with a centrally obscured logarithmic asphere," Opt. Commun. **245**, 85–92 (2005).
10. X. Chen, D. Bakin, C. Liu, and N. George, "Optics optimization in high-resolution imaging module with extended depth of field," Proc. SPIE **7061**, 1–12 (2008).
11. H. J. Trussel and B. R. Hunt, "Image restoration of space variant blurs by sectioned methods," in *Proceedings of IEEE International Conference on Acoustics, Speech, and Signal Processing* (IEEE, 1978), Vol. 3, pp. 196–198.
12. J. G. Nagy and D. P. O'Leary, "Restoring images degraded by spatially variant blur," SIAM J. Sci. Comput. **19**, 1063–1082 (1998).
13. T. P. Costello and W. B. Mikhael, "Efficient restoration of known space-variant blurs from physical optics by sectioning with modified Wiener filtering," Digital Signal Process. **13**, 1–22 (2003).
14. L. Rudin, S. Osher, and E. Fatemi, "Nonlinear total variation based noise removal algorithms," Phys. D **60**, 259–268 (1992).
15. C. R. Vogel and M. E. Oman, "Iterative methods for total variation denoising," SIAM J. Sci. Comput. **17**, 227–238 (1996).
16. A. Chambolle and P. L. Lions, "Image recovery via total variation minimization and related problems," Numer. Math. **76**, 167–188 (1997).
17. T. F. Chan, G. H. Golub, and P. Mulet, "A nonlinear primal-dual method for total variation-based image restoration," SIAM J. Sci. Comput. **20**, 1964–1977 (1999).
18. D. Goldforb and W. Yin, "Second-order cone programming methods for total variation-based image restoration," SIAM J. Sci. Comput. **27**, 622–645 (2005).
19. Yilun Wang, Junfeng Yang, Wotao Yin, and Yin Zhang, "A new alternating minimization algorithm for total variation image reconstruction," Tech. Rep. TR07-10 (Rice University, Department of Computational and Applied Mathematics, 2007).
20. Lord Rayleigh, "On the accuracy of focus necessary for sensibly perfect definition," in *Scientific Papers* (Cambridge U. Press, 1899), Vol. 1, pp. 430–432.
21. W. J. Smith, *Modern Optical Engineering*, 3rd ed. (McGraw-Hill, 2001).

US 20100002310A1

(19) **United States**

(12) **Patent Application Publication**

(10) **Pub. No.: US 2010/0002310 A1**

(43) **Pub. Date: Jan. 7, 2010**

George et al.

(54) **EXTENDED DEPTH-OF-FIELD LENSES AND METHODS FOR THEIR DESIGN, OPTIMIZATION AND MANUFACTURING**

(75) Inventors: **Nicholas George**, Pittsford, NY (US); **Xi Chen**, San Jose, CA (US)

Correspondence Address:
Kramer Levin Naftalis & Frankel LLP
1177 Avenue of the Americas
New York, NY 10036 (US)

(73) Assignee: **MICRON TECHNOLOGY, INC.**, Boise, ID (US)

(21) Appl. No.: **12/167,741**

(22) Filed: **Jul. 3, 2008**

Publication Classification

(51) **Int. Cl.**
G02B 13/18 (2006.01)
B29D 11/00 (2006.01)
G06F 17/10 (2006.01)

(52) **U.S. Cl.** **359/715**; 264/1.1; 703/2

(57) **ABSTRACT**

For rotationally symmetric aspheric lenses, one can establish lens design and layout based upon the phase delay function $\exp[-i\phi(\rho)]$. An embodiment of the invention is a method for calculating a corresponding variation in focal length denoted by $f(\rho)$. According to an aspect, one can also assert a shape for the focal length $f(\rho)$ and thereafter calculate a phase delay function in order to synthesize a novel lens. New EDoF lens designs are obtained by selection of an inner and outer focal length connected by a simple curve that can be approximate by a polynomial. From the selected $f(\rho)$, one can synthesize a finished EDoF lens design and fabricate the lens. Another aspect of this invention is directed to a method to tailor prior-art EDoF lenses so that their performance over some range is improved.

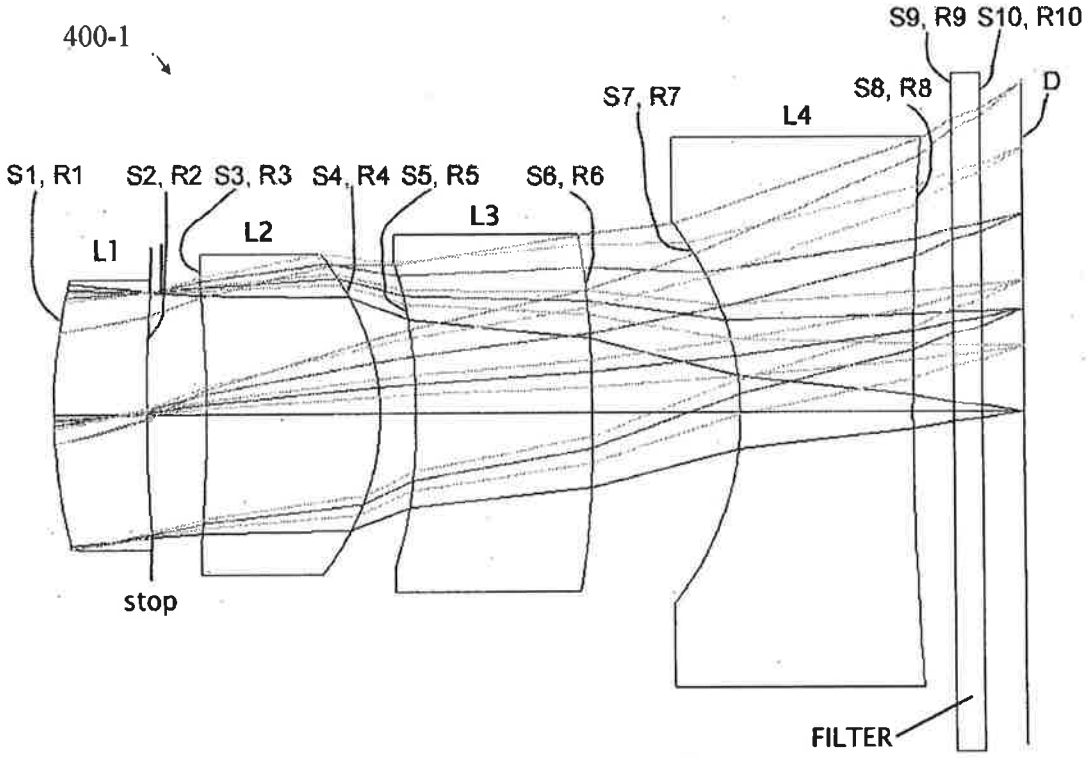

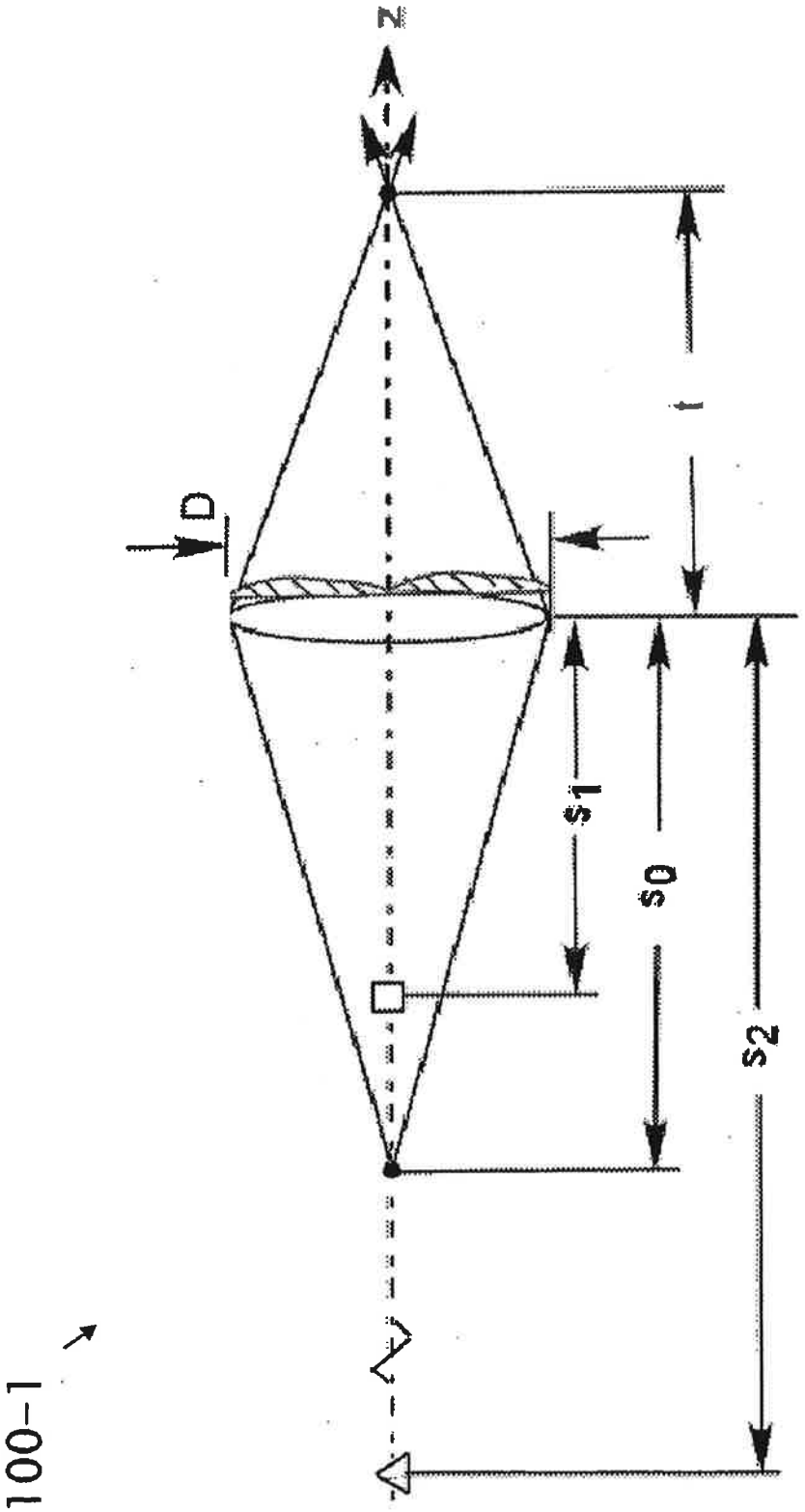

Fig. 1

Table 1-2

Strehl Ratios at Different Object Distances

Object Distance (mm)	100	150	204	250	300	650	900	infinity
Log asphere β design	0.001	0.005	0.014	0.039	0.045	0.261	0.416	0.291
Tailored parabolic EDoF design	0.003	0.019	0.067	0.087	0.227	0.338	0.338	0.291

Table 2-2

FWHM of PSFs at Different Object Distances

Object Distance (mm)	100	150	204	250	300	650	900	infinity
Log Asphere β Design (um)	>38.32	14.966	6.258	3.224	4.84	2.448	1.876	1.39
Tailored parabolic EDoF design (um)	12.492	2.676	2.652	3.706	2.202	1.6632	1.4524	1.3928

Fig. 2

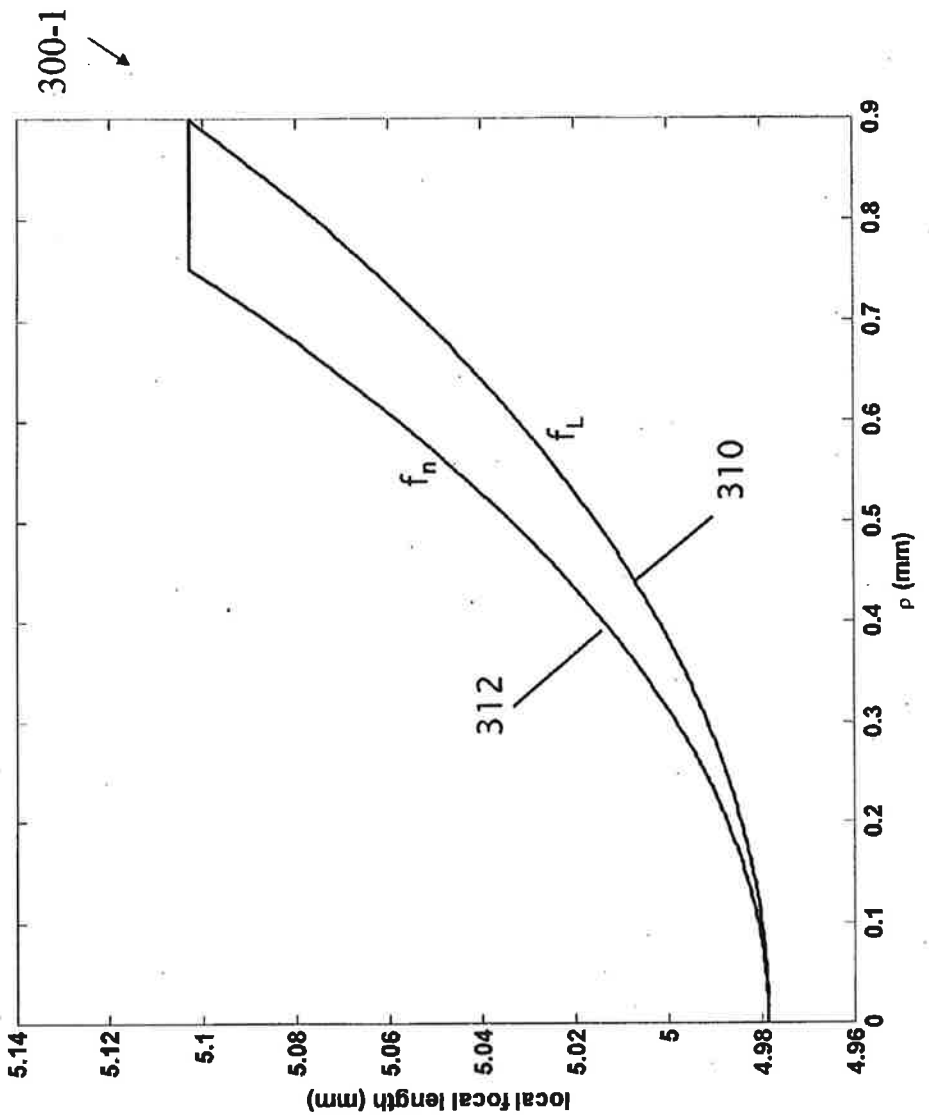
300-1
local focal length (mm)
5.14
5.12
5.1
5.08
5.06
5.04
5.02
5
4.98
4.96
0
0.1
0.2
0.3
0.4
0.5
0.6
0.7
0.8
0.9
ρ (mm)
f_n
f_L
310
312

Fig. 3

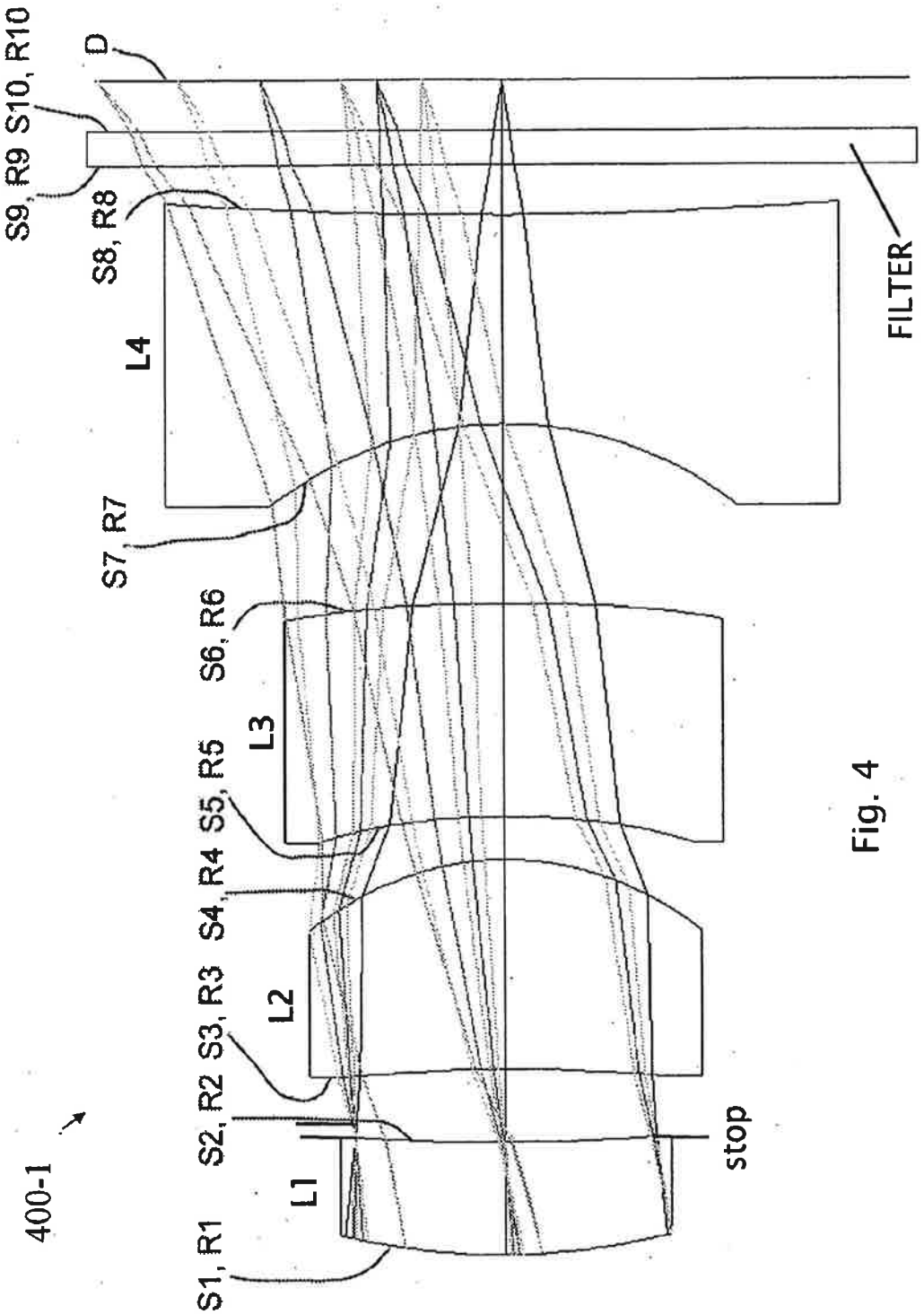
400-1
S1, R1
S2, R2
S3, R3
S4, R4
S5, R5
S6, R6
S7, R7
S8, R8
S9, R9
S10, R10
D
L1
L2
L3
L4
stop
FILTER

Fig. 4

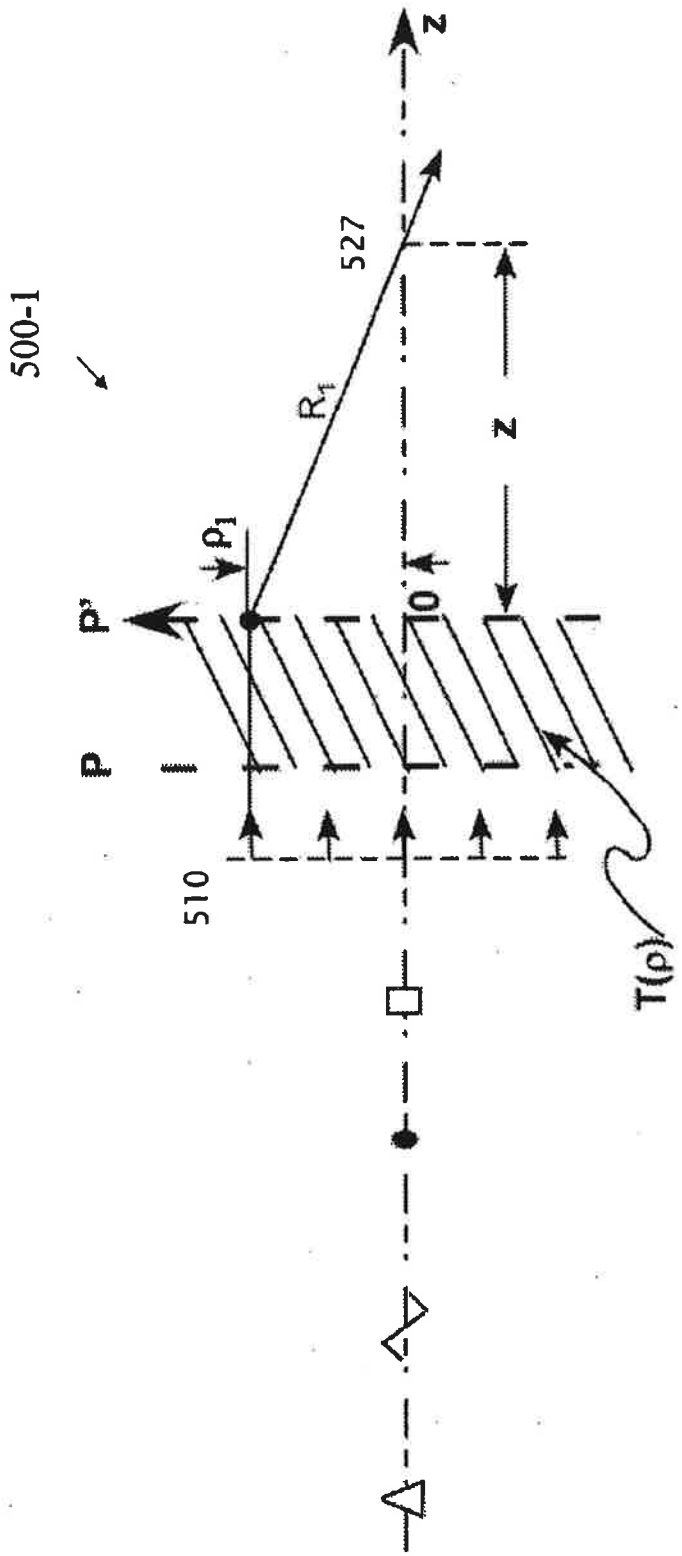

Fig. 5

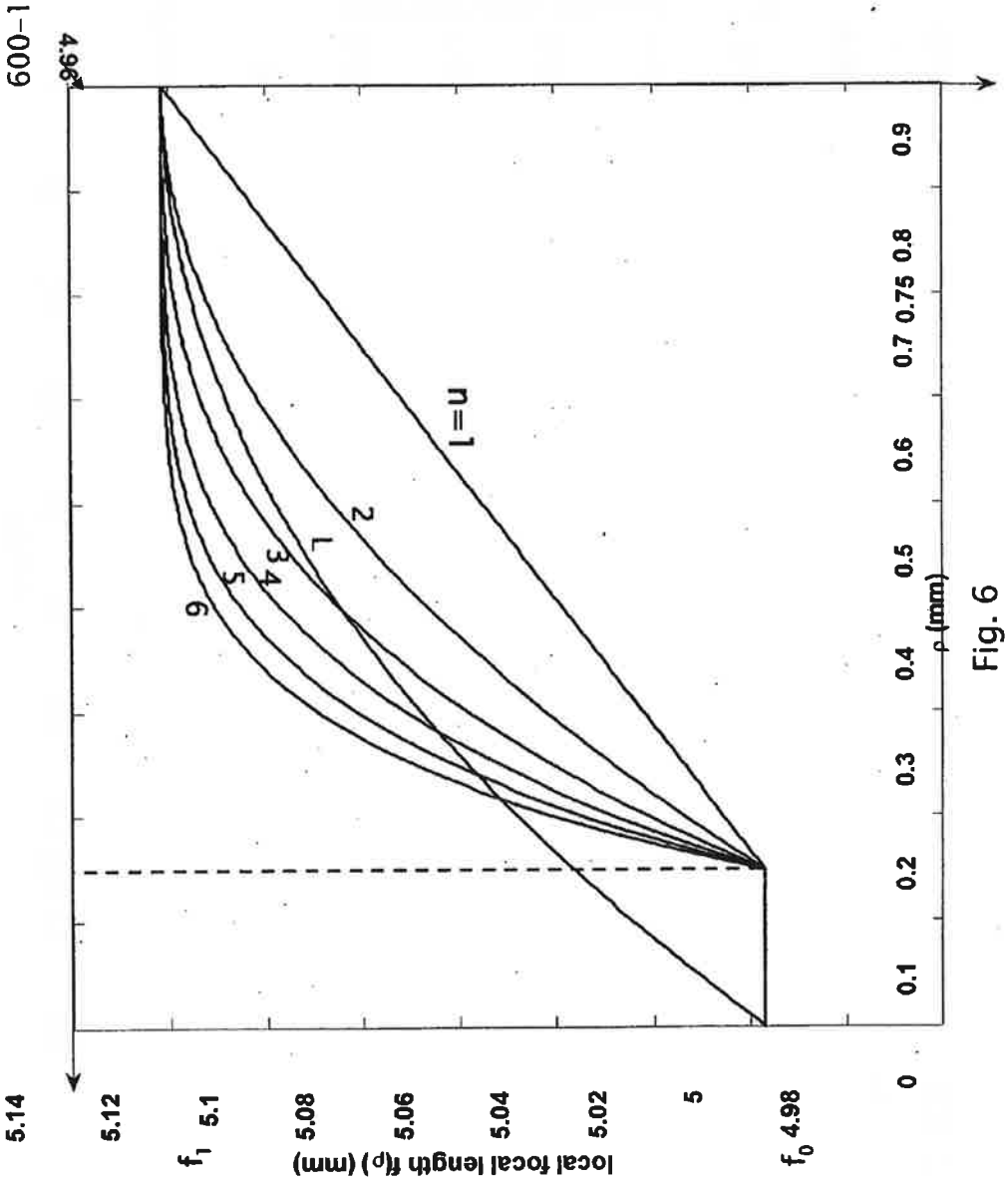
600-1
4.96
n=1
2
L
3
4
5
6
0
0.1
0.2
0.3
0.4
0.5
0.6
0.7
0.75
0.8
0.9
ρ (mm)
5.14
5.12
5.1
5.08
5.06
5.04
5.02
5
4.98
f1
f0
local focal length f(ρ) (mm)

Fig. 6

700-1

Table 1-7

Strehl Ratios at Different Object Distances

Object Distance (mm)	100	150	204	250	300	650	900	infinity
Strehl ratio for n=2 design	0.003	0.019	0.067	0.087	0.227	0.338	0.338	0.291
Strehl ratio for n=3 design	0.004	0.020	0.082	0.147	0.275	0.218	0.230	0.294
Strehl ratio for n=4 design	0.003	0.018	0.094	0.167	0.297	0.146	0.171	0.294

FIG. 7

800-1

Table 1-8

FWHM of PSFs at Different Object Distances

Object Distance (mm)	100	150	204	250	300	650	900	infinity
FWHM of PSF for n=2 design (μm)	12.492	2.676	2.652	3.706	2.202	1.6632	1.4524	1.3928
FWHM of PSF for n=3 design (μm)	8.318	3.012	2.872	2.86	2.148	1.4972	1.3638	1.3942
FWHM of PSF for n=4 design (μm)	18.842	3.208	2.774	2.734	2.096	1.4808	1.3484	1.392

FIG. 8

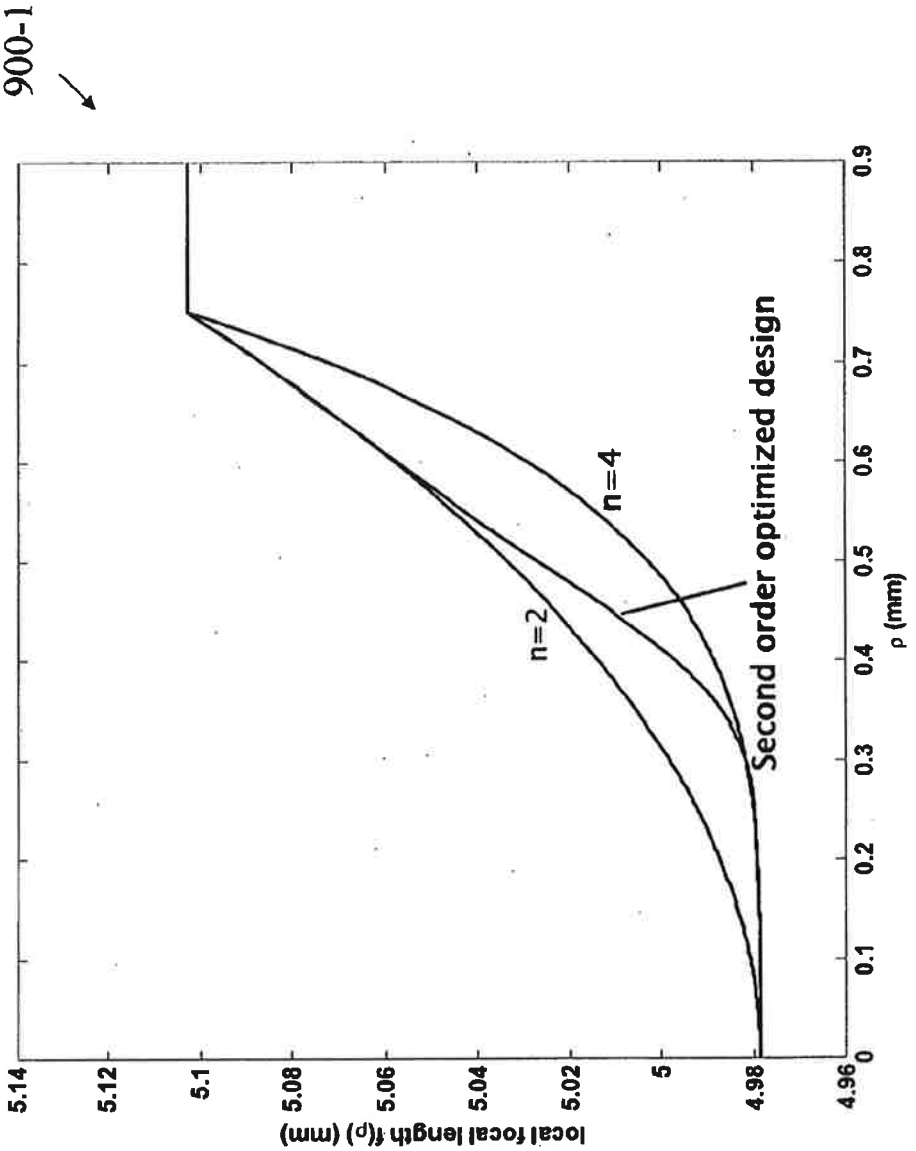
900-1
local focal length f(ρ) (mm)
5.14
5.12
5.1
5.08
5.06
5.04
5.02
5
4.98
4.96
0
0.1
0.2
0.3
0.4
0.5
0.6
0.7
0.8
0.9
ρ (mm)
n=2
n=4
Second order optimized design

FIG. 9

Table 1-10

Strehl Ratios at Different Object Distances

Object Distance (mm)	100	150	204	250	300	650	900	infinity
Strehl ratio for n=2 design	0.003	0.019	0.067	0.087	0.227	0.338	0.338	0.291
Strehl ratio for n=4 design	0.003	0.018	0.094	0.167	0.297	0.146	0.171	0.294
Strehl ratio for second order optimized design	0.005	0.027	0.091	0.143	0.253	0.233	0.275	0.293

Table 2-10

FWHM of PSFs at Different Object Distances

Object Distance (mm)	100	150	204	250	300	650	900	infinity
FWHM of PSF for n=2 design (μm)	12.492	2.676	2.652	3.706	2.202	1.6632	1.4524	1.3928
FWHM of PSF for n=4 design (μm)	18.842	3.208	2.774	2.734	2.096	1.4808	1.3484	1.392
FWHM of PSF for second order optimized design	7.266	3.02	2.902	2.844	2.108	1.510	1.3890	1.4242

FIG. 10

Surface	Curvature Radius (mm)	Distance (mm)	Conic	Index of Refraction (d line)	Abbe Number
*s1	R1: 3.344	0.649	2.00	N1: 1.603001	ν1: 65.44
*s2	R2: 14.526 Aperture Stop	0.417	-2.00		
*s3	R3: -11.386	1.200	-2.00	N2: 1.528554	ν2: 76.98
*s4	R4: -1.591	0.249	-1.72		
*s5	R5: -4.611	1.214	-2.00	N3: 1.846663	ν3: 23.83
*s6	R6: -13.893	1.028	1.00		
s7	R7: -2.037	1.195		N4: 1.516800	ν4: 64.17
s8	R8: 24.599	0.280			
s9	R9: ∞	0.200		N5: 1.516330	ν5: 64.14
s10	R10: ∞	0.286			

* Even aspheric surfaces

FIG. 11(a)

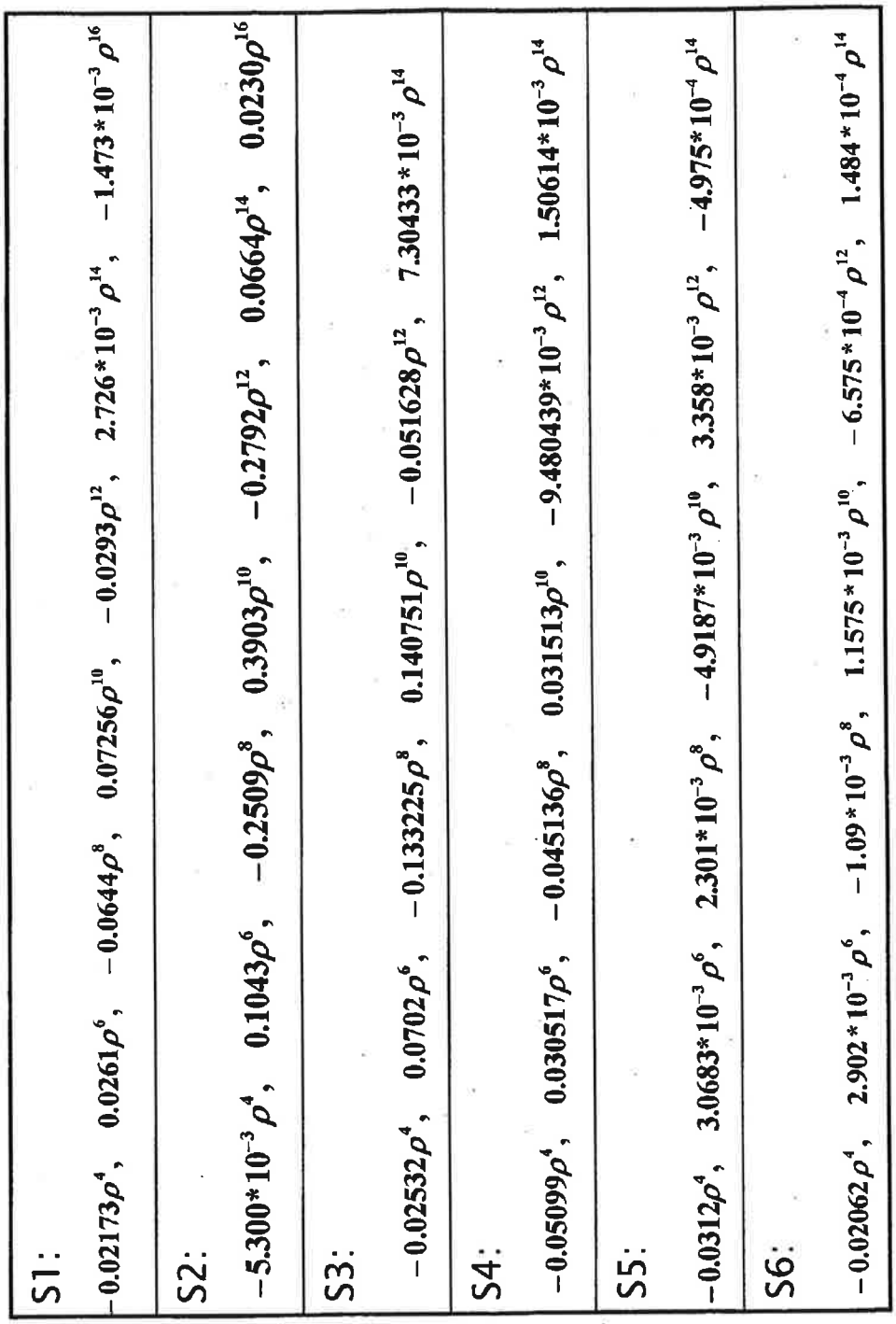
S1:
$-0.02173\rho^4$, $0.0261\rho^6$, $-0.0644\rho^8$, $0.07256\rho^{10}$, $-0.0293\rho^{12}$, $2.726*10^{-3}\rho^{14}$, $-1.473*10^{-3}\rho^{16}$
S2:
$-5.300*10^{-3}\rho^4$, $0.1043\rho^6$, $-0.2509\rho^8$, $0.3903\rho^{10}$, $-0.2792\rho^{12}$, $0.0664\rho^{14}$, $0.0230\rho^{16}$
S3:
$-0.02532\rho^4$, $0.0702\rho^6$, $-0.133225\rho^8$, $0.140751\rho^{10}$, $-0.051628\rho^{12}$, $7.30433*10^{-3}\rho^{14}$
S4:
$-0.05099\rho^4$, $0.030517\rho^6$, $-0.045136\rho^8$, $0.031513\rho^{10}$, $-9.480439*10^{-3}\rho^{12}$, $1.50614*10^{-3}\rho^{14}$
S5:
$-0.0312\rho^4$, $3.0683*10^{-3}\rho^6$, $2.301*10^{-3}\rho^8$, $-4.9187*10^{-3}\rho^{10}$, $3.358*10^{-3}\rho^{12}$, $-4.975*10^{-4}\rho^{14}$
S6:
$-0.02062\rho^4$, $2.902*10^{-3}\rho^6$, $-1.09*10^{-3}\rho^8$, $1.1575*10^{-3}\rho^{10}$, $-6.575*10^{-4}\rho^{12}$, $1.484*10^{-4}\rho^{14}$

FIG. 11(b)

Table 1-12

Strehl Ratios at Different Object Distances for On-Axis Objects

Object Distance (mm)	100	150	204	250	300	650	900	infinity
Standard lens	0.002	0.003	0.004	0.013	0.009	0.067	0.299	0.837
Logarithmic asphere β design based on standard lens	0.002	0.007	0.023	0.036	0.077	0.266	0.377	0.290
Tailored parabolic EDoF based on standard lens	0.003	0.017	0.071	0.148	0.238	0.258	0.293	0.296

Table 2-12

FWHM of PSFs at Different Object Distances for On-Axis Objects

Object Distance (mm)	100	150	204	250	300	650	900	infinity
Standard lens (um)	>43.42	>42.16	34.32	19.96	21.46	6.372	1.7738	1.6162
Logarithmic asphere β design based on standard lens (um)	32.76	6.948	4.582	4.74	3.612	2.352	1.8628	1.342
Tailored parabolic EDoF based on standard lens (um)	15.410	5.864	3.492	2.76	2.218	1.622	1.4666	1.4104

FIG. 12

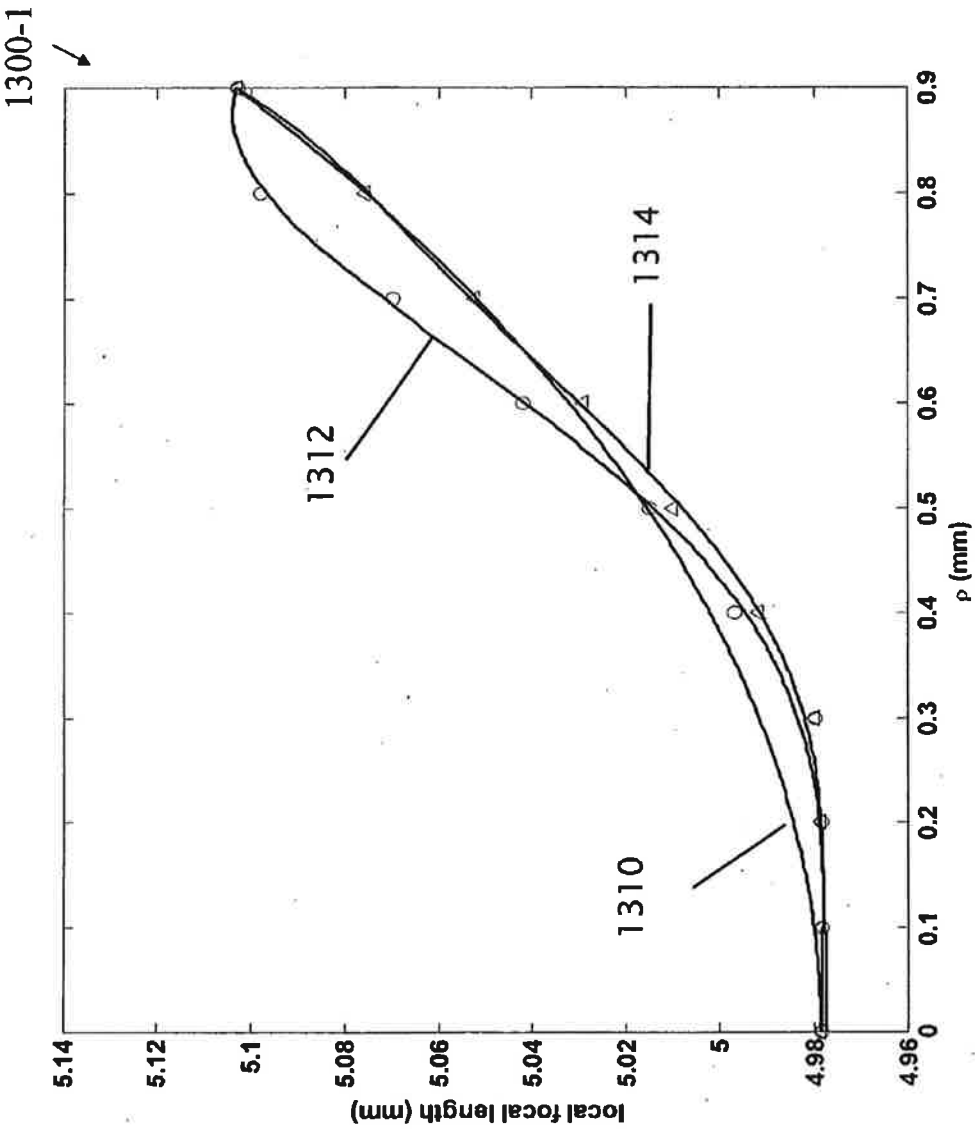
1300-1
1312
1314
1310
local focal length (mm)
ρ (mm)
5.14
5.12
5.1
5.08
5.06
5.04
5.02
5
4.98
4.96
0
0.1
0.2
0.3
0.4
0.5
0.6
0.7
0.8
0.9

Fig. 13

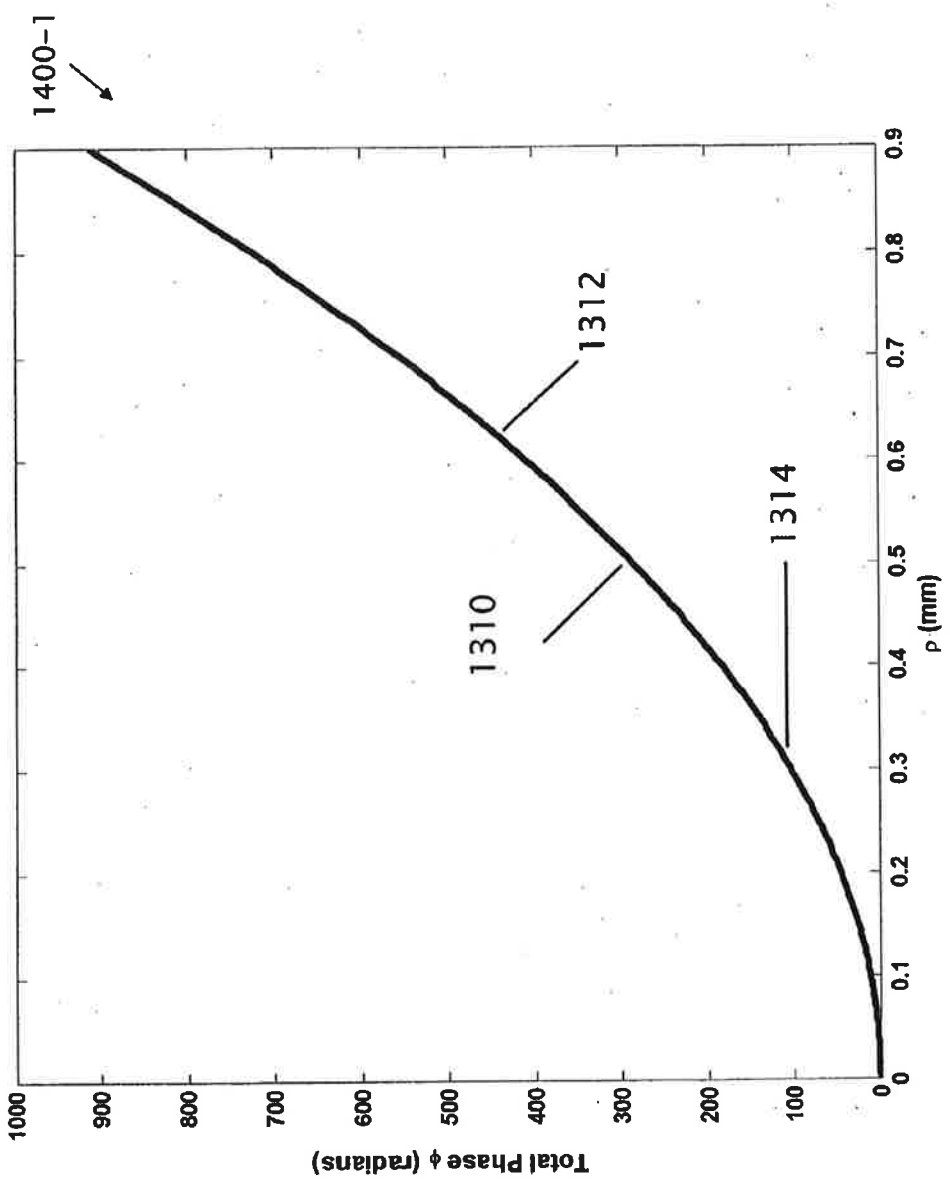
1400-1
1312
1314
1310
Total Phase ϕ (radians)
ρ (mm)
0
100
200
300
400
500
600
700
800
900
1000
0.1
0.2
0.3
0.4
0.5
0.6
0.7
0.8
0.9

FIG. 14

Table 1-15

Strehl Ratios at Different Object Distances

Object Distance (mm)	100	150	204	250	300	650	900	infinity
Log Asphere β Design	0.001	0.005	0.014	0.039	0.045	0.261	0.416	0.291
Log Asphere β Design Tailored I	0.002	0.008	0.044	0.069	0.150	0.214	0.258	0.292
Log Asphere β Design Tailored II	0.001	0.005	0.015	0.048	0.051	0.231	0.340	0.292

Table 2-15

FWHM of PSFs at Different Object Distances

Object Distance (mm)	100	150	204	250	300	650	900	infinity
Log Asphere β Design (um)	>38.32	14.966	6.258	3.224	4.84	2.448	1.876	1.39
Log Asphere β Design Tailored I (um)	22.52	11.126	3.436	3.772	2.726	2.046	1.629	1.338
Log Asphere β Design Tailored II (um)	35.58	15.028	6.202	2.938	4.544	2.52	1.971	1.344

FIG. 15

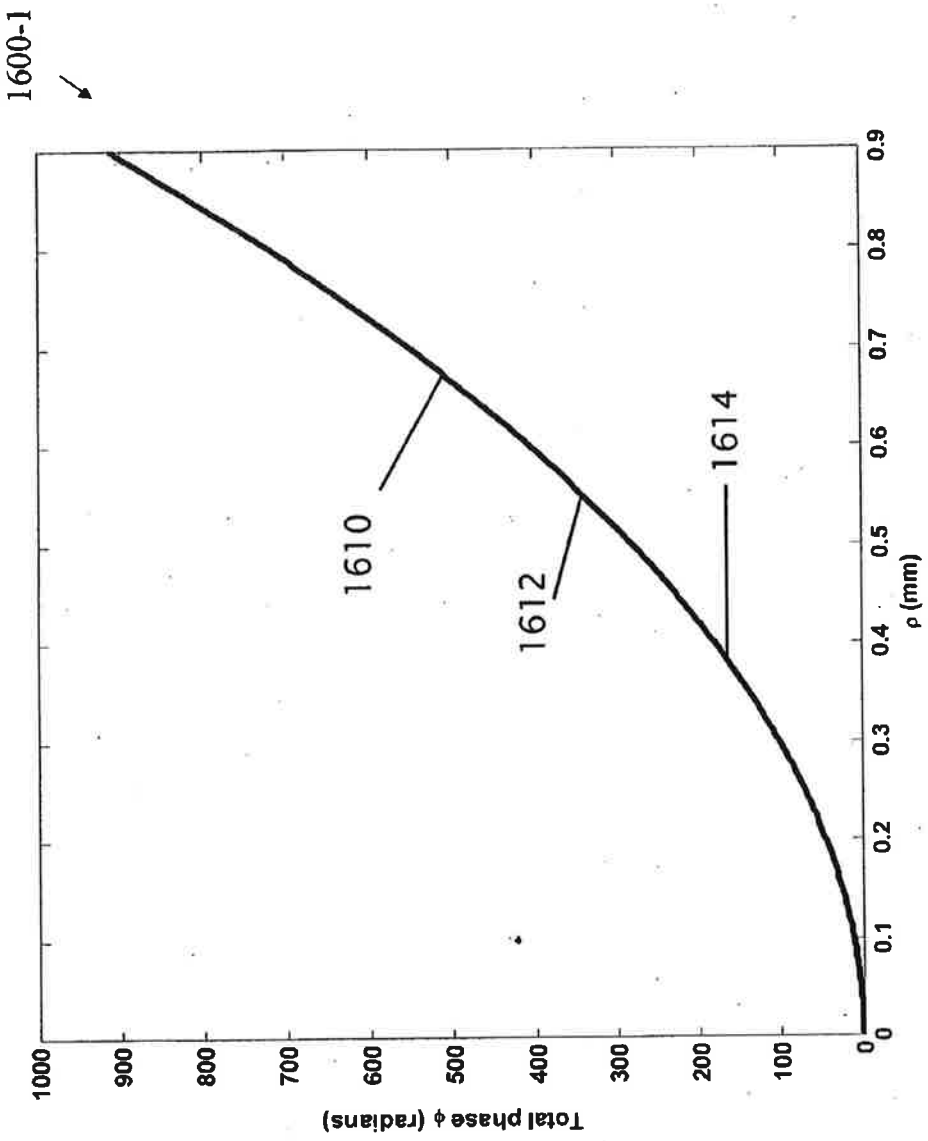
1600-1
1610
1612
1614
Total phase ϕ (radians)
ρ (mm)
0
100
200
300
400
500
600
700
800
900
1000
0.1
0.2
0.3
0.4
0.5
0.6
0.7
0.8
0.9

FIG. 16

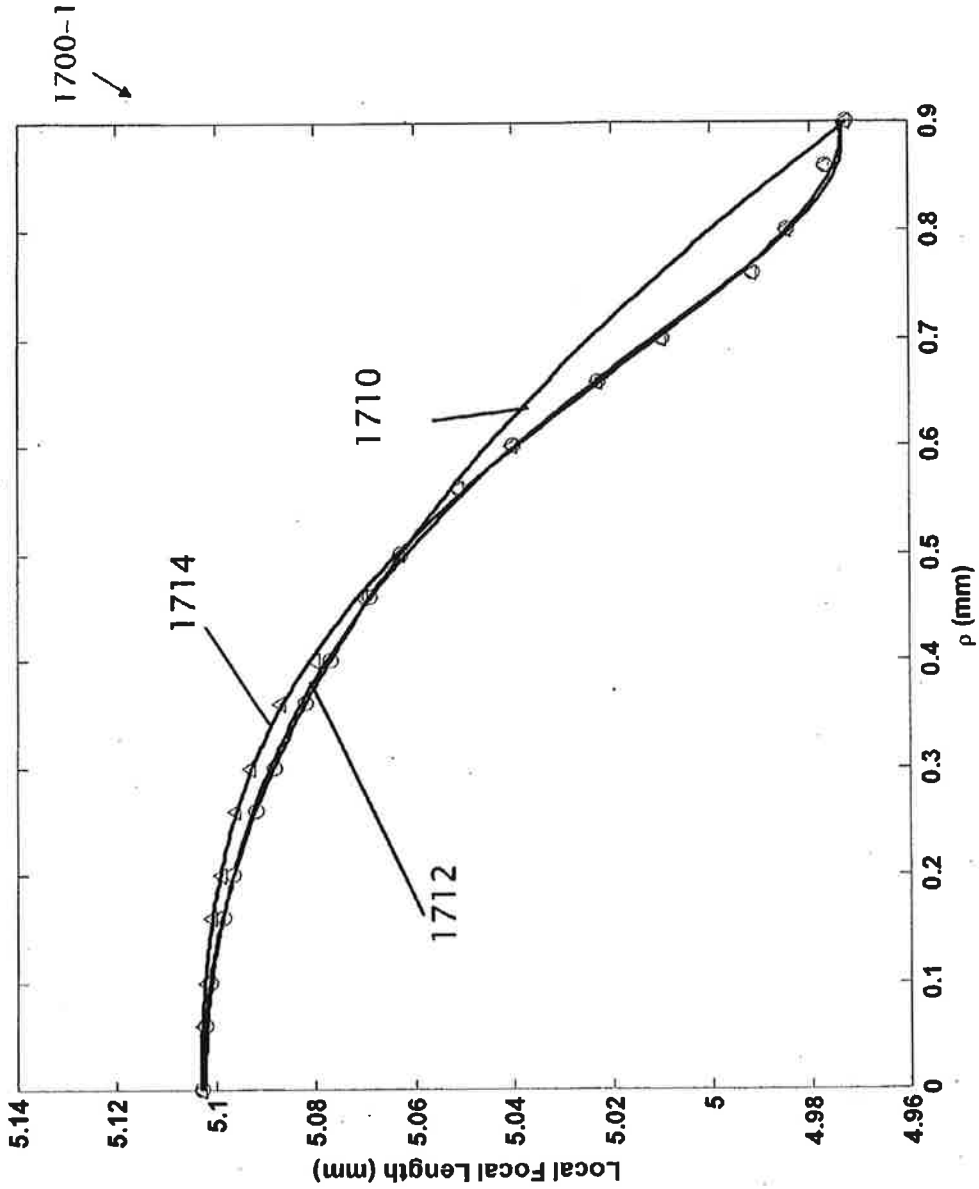
1700-1
1710
1714
1712
Local Focal Length (mm)
5.14
5.12
5.1
5.08
5.06
5.04
5.02
5
4.98
4.96
ρ (mm)
0
0.1
0.2
0.3
0.4
0.5
0.6
0.7
0.8
0.9

FIG. 17

Table 1-18

Strehl Ratios at Different Object Distances

Object Distance (mm)	100	150	204	250	300	650	900	infinity
Log Asphere γ Design	0.002	0.006	0.009	0.040	0.036	0.237	0.363	0.290
Log Asphere γ Design Tailored I	0.001	0.006	0.015	0.024	0.056	0.258	0.244	0.290
Log Asphere γ Design Tailored II	0.001	0.004	0.013	0.010	0.052	0.269	0.266	0.281

Table 2-18

FWHM of PSFs at Different Object Distances

Object Distance (mm)	100	150	204	250	300	650	900	infinity
Log Asphere γ Design (um)	1.533	31.96	28.04	1.340	14.428	1.241	1.383	2.266
Log Asphere γ Design Tailored I (um)	>36.334	34.4	27.4	1.257	1.253	1.283	1.239	1.849
Log Asphere γ Design Tailored II (um)	>36.314	>35.7	29.44	25.78	1.315	1.365	1.300	1.540

FIG. 18

EXTENDED DEPTH-OF-FIELD LENSES AND METHODS FOR THEIR DESIGN, OPTIMIZATION AND MANUFACTURING

TECHNICAL FIELD

[0001] Embodiments of the invention are generally related to the field of imaging and optical lens design, optimization and manufacturing. More particularly, embodiments of the invention are directed to aspheric (including multi-focal) and extended depth-of-field (EDOF) lenses (including phase masks); tailored aspheric and extended depth-of-field lenses (T-EDoF); and methods pertaining to the design, optimization, and manufacture of aspheric and extended depth-of-field lenses (including T-EDoF).

DESCRIPTION OF RELATED ART

[0002] Lenses used in conventional digital and 35 mm photography cameras can have zoom and focus features that are manual or automated. Generally, these cameras have a limited depth-of-field. With reference to FIG. **1**, the classical depth-of-field can be expressed as

$$s_2 - s_1 \cong \frac{4\lambda s_0^2}{D^2},$$

where s_0, s_1, s_2 are, respectively, the object focus point, the inner object distance and the outer object distance where blur is just evident to an observer; D is the diameter of the aperture, and λ is the average visible wavelength taken as λ=0.55 μm (micron meters).

[0003] Cameras have become commonplace via their incorporation into various devices such as mobile (cell) telephones. Today's cell phone-picture-takers want to take pictures of their friends' faces in the backdrop of distant views and everything in-between, and get sharp, clear results that they can view and send around the world. Current extended depth-of-field cameras limit this ability.

[0004] It is well known to purposefully blur an image, record that image, and sometime later with additional processing extend the depth-of-field. Integrated computing and imaging technology has made various improvements in the depth-of-field that can be obtained with a lens focused at a field point s_0. These improvements can also be used by cameras that have automatic focus and/or zoom features. One factor that can assist in successfully extending the depth-of-field is maintaining a substantially uniform (i.e., z-axis variant) point-spread-function (PSF) along the optical axis. This allows image processing, e.g., inverse filtering or maximum entropy processing, which both depend on a knowledge of the blurred point-spread-function, to be most effective.

[0005] The operation of any lens, n, can be expressed quantitatively by its amplitude transmission function $T_n(\rho)$, defined by

$$T_n(\rho) = \frac{U_{out}(\rho)}{U_{in}(\rho)} = e^{-i\phi_n(\rho)}. \quad (1)$$

in which the scalar electric field out is denoted by $U_{out}(\rho)$ and the input scalar electric field is $U_{in}(\rho)$. The function $\phi(\rho)$ is called the phase delay (measured in radians) for the lens. The amplitude transmission function can contain a detailed description of lens performance in terms of wavefronts of the propagating light. A given phase delay function $\phi(\rho)$ can establish a lens description in terms that an optical designer can use and from which the lens can then be fabricated.

[0006] The making (i.e., design and, if desired, manufacturing) of an aspheric lens can be a relatively complicated and expensive endeavor. The basis of current technology is timely set forth in the seminal article by D. J. Bajuk, *Computer Controlled Generation of Rotationally Symmetric Aspheric Surfaces*, Opt. Engr. 15 No. 5, 401 (1976). Typically, the design of an asphere is based on deriving a sag height departure from a reference sphere. A skilled optical designer can use knowledge about the sag height to determine the lens transmission function as set forth in Eq. (1) above. Fourier optics techniques provide the mathematical tools for lens system design and layout. Commercially available software has been developed to readily facilitate aspheric lens system design and layout. Making the asphere is greatly facilitated by computer-controlled machinery and, in certain circumstances, by skilled hand labor.

[0007] In view of the foregoing, it may be advantageous to have a simplified and less costly approach for designing aspheric lenses and those having extended depth of field (EDoF). It may also be advantageous to be able to simply and efficiently optimize the performance of existing aspheric EDoF lenses/systems.

BRIEF DESCRIPTION OF DRAWINGS

[0008] FIG. **1** schematically shows an idealized diffraction-limited lens of focal length F and diameter 2R with an object point at s_0 imaged to a detector at t, and a depth of field from inner s_1 to outer s_2.

[0009] FIG. **2** shows a tabular comparison of a tailored parabolic EDoF lens according to an embodiment of the invention with a prior art EDoF logarithmic asphere in terms of Strehl ratio and the full-width half maximum of the Point Spread Function (PSF), versus object distance.

[0010] FIG. **3** shows a comparative graph of curves of local focal length as a function of lens radius for a tailored parabolic EDoF lens according to an embodiment of the invention and a prior art EDoF logarithmic asphere.

[0011] FIG. **4** shows a detailed optical design configuration for a tailored parabolic EDoF lens according to an embodiment of the invention.

[0012] FIG. **5** schematically shows a notation for a lens having a phase delay $\phi(\rho)$ and focal length $f(\rho)$, illustrating a point of stationary phase at ρ_1.

[0013] FIG. **6** shows a comparative graph of n^{th}-order polynomial curves representing a family of EDoF aspheric lenses according to certain aspects of an embodiment of the invention and a prior art EDoF β-logarithmic aspheric lens.

[0014] FIG. **7** shows a comparative table of Strehl ratios for the n=2, 3, 4 lenses represented by the curves in FIG. **6**.

[0015] FIG. **8** shows a comparative table of PSF-FWHM values for the n=2, 3, 4 lenses represented by the curves in FIG. **6**.

[0016] FIG. **9** shows a graph of curves of focal length versus lens radius for n=2, 4 tailored EDoF designs and a hyper-optimized EDoF design according to certain aspects of an embodiment of the invention.

[0017] FIG. **10** shows a tabular comparison of the tailored parabolic (n=2) EDoF lens, the polynomial tailored (n=4) EDoF lens, and the hyper-optimized tailored EDoF lens, from

FIG. **9**, according to certain aspects of an embodiment of the present invention with regard to Strehl ratio and the full-width half maximum of the PSF, versus object distance.

[0018] FIGS. **11**(*a*), **11**(*b*) show actual lens data for the lens design illustrated in FIG. **4**.

[0019] FIG. **12** shows tabular comparisons of Strehl ratio and FWHM of PSF vs. object distance between a diffraction limited actual lens, a prior art EDoF β-Logarithmic asphere actual lens, and the tailored parabolic EDoF actual lens as shown in FIG. **4**.

[0020] FIG. **13** shows a graph of curves of focal length versus lens radius for a prior art EDoF β-Logarithmic asphere and two optimization designs according to certain aspects of an embodiment of the invention.

[0021] FIG. **14** shows a graph of total phase delay $\phi(\rho)$ vs. lens radius of three overlaid curves of the prior art EDoF β-Logarithmic asphere and the two embodied optimization designs depicted in FIG. **13**.

[0022] FIG. **15** shows tabular comparisons of Strehl ratio and FWHM of PSF vs. object distance of the β-Logarithmic asphere and the two optimization designs depicted in FIG. **13**.

[0023] FIG. **16** shows a graph of total phase delay $\phi(\rho)$ vs. lens radius of three overlaid curves for a prior art EDoF γ-Logarithmic asphere and two optimization designs according to certain aspects of an embodiment of the invention.

[0024] FIG. **17** shows a graph of curves of focal length versus lens radius for a prior art EDoF γ-Logarithmic asphere and two optimization designs according to certain aspects of an embodiment of the invention.

[0025] FIG. **18** shows tabular comparisons of Strehl ratio and FWHM of PSF vs. object distance of the prior art EDoF γ-Logarithmic asphere and the two embodied optimization designs depicted in FIG. **17**.

DETAILED DESCRIPTION

[0026] Ray optics is an alternate (to physical optics) useful way of describing the operation of a lens in terms of, e.g., its f/#, focal length, f, and diameter, D, which are readily measurable quantities. It would be advantageous to directly associate the description of an EDoF lens in terms of the phase delay for the lens with the ray optics parameters. More particularly, since the intermediate image blur and the EDoF can be controlled by the radial variation of the focal length $f(\rho)$, the ability to associate this ray optics parameter with the conventional Fourier optics tools used by lens designers would be useful.

[0027] Further benefits and advantages may be realized by providing new classes of z-axis rotationally or circularly symmetric lenses that can capture a purposefully blurred image as described by a known point spread function and provide an improved output scene after image processing.

[0028] The potential benefits and advantages of extending practical lens design for circularly/rotationally symmetric aspheric lenses based upon a knowledge of the phase delay function $\exp[-i\phi(\rho)]$ include, without limitation, the capability to: directly calculate a corresponding variation in focal length denoted by $f(\rho)$; provide a shape for the focal length $f(\rho)$ and thereafter directly calculate a phase delay function in order to conventionally synthesize a lens; specify improved performance EDoF lens designs simply by selection of an inner and outer focal length connected by a simple curve that can be approximated by a polynomial; tailor the prior-art EDoF lenses so that their performance over a specified range can be improved; and use basic physical notions and/or geometric optics to choose an $f(\rho)$ and directly determine the corresponding phase delay $\phi(\rho)$ to design the lens and fabricate it as desired.

[0029] An embodiment of the invention is a method for directly determining a focal length $f(\rho)$ of a rotationally symmetric, aspheric lens as a function of lens radius ρ from a known phase delay function $\phi(\rho)$. The phrase 'directly determining' as used herein means that one can simply mathematically determine expressions for $f(\rho)$ and $\phi(\rho)$ from respective, corresponding known expressions for $\phi(\rho)$ and $f(\rho)$, and vice-versa.

[0030] Based on Maxwell's equations and, in particular, the Rayleigh-Sommerfeld-Smythe integral form, the following new formula can be used to express the radially varying focal length of a lens $f(\rho)$ in terms of its phase delay $\phi(\rho)$, as follows:

Given the function $\phi(\rho)$,

$$f(\rho)=\left[\left(\frac{k\rho}{\phi'(\rho)}\right)^2-\rho^2\right]^{1/2}. \tag{2}$$

Alternatively, given the focal length $f(\rho)$,

$$\phi'(\rho)=\frac{-k\rho}{[f^2(\rho)+\rho^2]^{1/2}}. \tag{3}$$

In these equations $\phi'(\rho)=d\phi(\rho)/d\rho$ is the first derivative of the phase delay function. Equation (3) is simply another form obtained from Eq. (2). The phase delay $\phi(\rho)$ can then be obtained by:

$$\phi(\rho)=\int_0^{\rho}\phi'(\rho_1)d\rho_1=\int_0^{\rho}\frac{-k\rho}{[f^2(\rho_1)+\rho_1^2]^{1/2}}d\rho_1, \tag{4}$$

where ρ_1 is the variable of integration running from 0 to ρ. Since integration provides a smoothing operation, $f(\rho)$ is not required to have a high degree of precision, thus Eq. (4) can give a stable functional solution for the phase delay function $\phi(\rho)$ of the EDoF lens in accordance with an embodiment of the invention.

[0031] The description of an aspheric lens is given by its transmission function, $T(\rho)$, as follows:

$$T(\rho)=e^{-i\phi(\rho)}, \tag{5}$$

in which circular/rotational symmetry is assumed. Based on the phase delay function $\phi(\rho)$, a formula can be derived to directly express the local focal length $f(\rho)$ as a function of the lens radius. The phase term $\phi(\rho)$ in the amplitude transmission function can be expressed as a power series, e.g., given by:

$$\phi(\rho)=-\frac{2\pi}{\lambda_0}\{\alpha_0+\alpha_2\rho^2+\alpha_3\rho^3+\alpha_4\rho^4+\alpha_5\rho^5+\alpha_6\rho^6+\dots\}, \tag{6}$$

in which the α's are known. Moreover, the quadratic term gives the paraxial focal length as follows:

$$e^{i\frac{2\pi}{\lambda_0}\alpha_2\rho^2} = e^{i\frac{\pi}{\lambda_0 F_0}\rho^2}, \tag{7}$$

in which harmonic time dependence $\exp(i\omega_0 t)$ is implicitly assumed. Hence by Eq. (3), the overall paraxial focal length, F_0, is given as

$$F_0 = \frac{1}{2\alpha_2}. \tag{8}$$

[0032] According to an embodiment of the invention, an expression for the radial value of the focal length f(ρ) is determined by a local rate of change of φ(ρ). For electromagnetic radiation (light) **510** coming through the aperture shown as a principal plane P of the schematic EDoF lens **512** in FIG. **5**, the exact solution of Maxwell's equations for a transverse scalar component of the electric field determined by the Rayleigh-Sommerfeld-Smythe solution can be written as:

$$E_y(x, y, z) = \int_{-\infty}^{\infty}\int dx'dy' E_y(x', y', 0)\frac{e^{-ikR_1}}{2\pi R_1}\frac{z}{R_1}\left(ik + \frac{1}{R_1}\right), \tag{9}$$

where the exiting field $E_y(x', y', 0) = T(\rho)\cdot 1$ for a plane wave input. In Eq. (9) and elsewhere, an $\exp(+i\omega t)$ harmonic time dependence notation is used.

[0033] For a rotationally symmetric lens, and making standard approximations to eliminate amplitude variations, Eq. (9) can be re-written as follows:

$$E_y(0, 0, z) = A\int d\rho' e^{-ik\Phi(\rho')-ikR_1}, \tag{10}$$

where

$$A = \frac{z}{R_1}\left(ik + \frac{1}{R_1}\right)\Big/(2\pi R_1)$$

where has been assumed constant and taken out of the integral as a standard approximation.

[0034] Eq. (10) will give rise to a peak value at some axial point z when $E_y(0,0,z)$ takes on a peak value. This represents an axial ray crossing as shown at **527** in FIG. **5** coming from a radial point ρ_1. This ray can be found from the principle of stationary phase applied to find an approximate integration of Eq. (10). For the phase term in the integral of Eq. (10) given by

$$\phi(\rho')+kR_1=\phi(\rho')+k[\rho^2+z^2]^{1/2}, \tag{11}$$

the point of stationary phase is found by setting the derivative with respect to ρ' equal to zero. This stationary point in the integral over ρ' is denoted as ρ_1. Then,

$$\phi'(\rho_1) + \frac{k\rho_1}{[f^2(\rho_1)+\rho_1^2]^{1/2}} = 0, \tag{12}$$

in which the axial crossing point at z (**527** in FIG. **5**) is replaced by $f(\rho_1)$, the result sought. Now, selecting f(ρ) for an asphere to be fabricated, the lens can have a phase delay function φ(ρ) given by the integration of Eq. (12), namely:

$$\phi(\rho) = \int_0^{\rho}\phi'(\rho_1)d\rho_1$$
$$\phi(\rho) = \int_0^{\rho}\frac{-k\rho}{[f^2(\rho_1)+\rho_1^2]^{1/2}}d\rho_1, \tag{13}$$

as set forth above.

[0035] According to another embodiment, via Eq. (12) an assumed or known form for the phase delay of the lens can be used to directly find the value of the radial focal length for the asphere, namely:

$$f(\rho) = \pm\left[\left(\frac{k\rho}{\phi'(\rho)}\right)^2 - \rho^2\right]^{1/2}. \tag{14}$$

[0036] This formula can be used to analyze an arbitrary asphere given φ'(ρ). The expression for φ'(ρ) can be differentiated and used to calculate f(ρ). Typically, the proper choice of sign will be physically obvious.

[0037] Another embodiment of the invention is a method of 'tailoring' the design of a previously designed EDoF lens. The term 'tailoring' as used herein includes modifying the prior design of an EDoF lens to obtain improved EDoF performance.

[0038] An example of the current embodiment is illustrated and discussed in connection with FIG. **1**. An EDoF lens **100-1** having parameters applicable for use in a cell-phone or a miniature digital camera, for example, is specified to operate from s_1=204.5 mm to s_2=∞, with D (2R) equal to 1.8 mm and f/# equal to 2.8. An EDoF β-logarithmic asphere can be designed using techniques known in the art. From this design, one skilled in the art can obtain the phase delay function of the logarithmic asphere denoted here by $\phi_L(\rho)$, where the subscript L refers to the logarithmic asphere lens. Using Eq. (2), $f_L(\rho)$ vs. ρ can be calculated as shown by curve **310** in FIG. **3**.

[0039] The tailored EDoF design according to the instant embodiment is obtained by drawing the $f_n(\rho)$ curve **312** in FIG. **3**, where the subscript n refers to a 'new' (tailored) parabolic lens. It can be seen that the tailored parabolic lens has the same range of focal lengths, from 4.979 mm to 5.103 mm, as the β-logarithmic asphere lens. Moreover, a simple quadratic curve or parabolic shape is used but with a flat, fixed focal length from $0.75<\rho\leqq 0.9$. The parabolic EDoF design can be summarized with the following equations:

$$f(\rho) = \begin{cases} 4.979 + 0.22\rho^2, & 0 \le \rho < 0.75 \text{ mm} \\ 5.103 & 0.75 < \rho \le 0.9 \text{ mm} \end{cases} \tag{15}$$

$$\phi(\rho)=1146.4\rho^2-28.04\rho^4-24.52\rho^6+24.03\rho^8. \tag{16}$$

This result illustrates the design of the new, tailored EDoF lens according to an embodiment of the invention.

[0040] FIG. **2** present a tabular comparison of performance data for the tailored parabolic EDoF lens and the prior-art

EDoF βP-logarithmic asphere with regard to Strehl ratio and the full-width half maximum of the Point Spread Function (PSF) versus object distance in mm. As shown in FIG. **2**, the Strehl ratio for the tailored parabolic design is higher at all object distances except 900 mm than that for the β-logarithmic asphere. The Strehl ratio is an indicator of image quality particularly at lower light levels. Moreover, the PSF for the tailored parabolic design indicates better performance than for the prior art lens at all distances even as close as 100 mm. Also, with regard to the full-width half maximum of the PSF criterion, the tailored parabolic design outperforms the prior art lens at all distances from 100 mm to infinity except at 250 mm. Thus, the tailored parabolic lens has better EDoF characteristics than the prior art β-logarithmic lens when the overall specifications are identical. Furthermore, the tailored parabolic EDoF lens can provide good performance over a larger axial distance than specified in the design goals.

[0041] The T_n (ρ), f/#, D, and f_n (ρ) values can be used to prepare an optical layout for this tailored lens. FIG. **4** shows the detailed lens layout **400-1** for the design of the tailored EDoF lens described by curve **312** in FIG. **3** for f_n (ρ) vs. ρ and the performance data tabulated in FIG. **2**.

[0042] It is further noted that the results of the method embodiment disclosed herein above verify the stability of the embodied EDoF design process to small deviations in the shape of the f(ρ) vs. ρ curve. In the process of integrating Eq. (3) to find φ(ρ), stable solutions for the form of the transmission function T(ρ)=exp[−iφ((ρ)] can be obtained.

[0043] In regard to this embodiment and others to be presented below, it is important to recognize that various optimizations can be made. These optimizations can be used to determine a best solution φ((ρ) starting with basic overall specifications for the EDoF lens, optimization criteria, and a starting form for a family of focal lengths f(ρ).

[0044] Another embodiment of the invention is directed to a method for designing a rotationally symmetric, aspheric EDoF lens from the specification of its focal length versus radius, f(ρ), rather than by its phase delay function φ(ρ). There are various advantages associated with such a method including, but not limited to: the relative ease in generating a specific range of focal lengths based on simple geometrical optics equations relating to the desired range of operation; the ability to modify a specific lens design to meet a new requirement, e.g., improve an existing lens to work better close-in so that it can record business cards, inventory labels, and the like; and, the capability to improve an existing lens so that the image quality at larger distances or elsewhere is enhanced; i.e., in sum, tailoring the EDoF lens.

[0045] Various embodiments of the invention use three criteria when tailoring an existing EDoF lens such as: 1) Strehl ratio—a larger Strehl ratio indicates better image quality; 2) PSF width invariance—the invariance of the width of the point spread function along the optical axis can provide a fairly accurate measure of the performance of the digital processing to remove the purposeful blur caused by the EDoF lens; and 3) PSF narrowness—the narrowness of the FWHM of the PSF can provide a fairly accurate measure of the resolution of the optical system.

[0046] In one embodiment, a camera system that incorporates an EDoF lens provides imagery from an inner distance s_1=204.5 mm to an outer distance s_2 equal to infinity. The lens is specified to have f/2.8 and a diameter D equal to 1.8 mm. A curve of f(ρ) versus ρ for a prior art logarithmic asphere is shown as the L curve in the graph **600-1** in FIG. **6**. FIG. **6** further shows a family of n^{th}-degree polynomial-based curves (n=1 to 6) that represent a family of aspherical EDoF lenses according to various embodiments of the invention. The focal length of these n^{th}-degree polynomial lenses is described by the following equation:

$$f(\rho)=a+b\rho^n, \tag{17}$$

where the constants a, b can be expressed in terms of the smallest focal length f_0 and the largest focal length f_1. The resultant family of n^{th}-degree polynomial aspheric lenses can be described by:

$$f(\rho) = f_0 + \frac{f_1 - f_0}{\rho_1^n}\rho^n, \tag{18}$$

where n ranges from 1 to 6, including non-integer values.

[0047] A reasonable set of values for the focal lengths can be calculated from the specifications using simple geometric optical formulas. For the lens specification:

$$s_1=204.5 \text{ mm}, s_2=\infty f/2.8, D=1.8 \text{ mm}, \tag{19}$$

the focal length is determined as f=5.040 mm. For the inner focus distance s_1, the EDoF equations can be obtained by extending the classical Rayleigh criterion with an improvement factor M, as follows:

$$\frac{1}{s_0} - \frac{1}{s_2} = \frac{M2\lambda}{D^2}, \tag{20}$$

$$\frac{1}{s_1} - \frac{1}{s_0} = \frac{M2\lambda}{D^2}, \tag{21}$$

where FIG. **1** shows the inner and outer distances s_1, s_2, respectively. Letting $s_2=\infty$ and eliminating s_0, gives the basic result for s_1:

$$\frac{1}{s_1} = \frac{M4\lambda}{D^2} \tag{22}$$

For an inner distance s_1=204.5 mm; D=1.8 mm, and λ=0.55 μm, Eq. (22) gives a predicted improvement factor for EDoF of M=7.2. Optimization can provide values for M up to 10 to 12.

[0048] At this point, the detector distance t is determined to be 5.103 mm as shown in FIG. **1**. The calculated smaller focal length value f_0 in Eq. (18) equals 4.979 mm. The calculated larger focal length value f_1 in Eq. (18) equals 5.103 mm. Using these values and the description connecting f(ρ) and φ((ρ) set forth above, a curve φ((ρ) for each value of n can be calculated, as further illustrated below.

[0049] It will be appreciated that the simple polynomial designs can be readily further optimized. The procedure can also be facilitated using digital computers and standard optimization methods. Careful study of the value of the slope φ'(ρ) at the distances where further tailoring is suggested can be used in the optimization process, for example.

[0050] As shown above and with reference to Tables 1-2, 2-2 in FIG. **2**, an n=2, parabolic shape of f(ρ) vs. ρ provided excellent EDoF response. Similarly, the Tables 1-7 and 1-8 of FIGS. **7** and **8**, respectively, show comparative performance of the tailored EDoF designs for n=2, 3, 4 for Strehl ratios and

PSF-FWHM at different object distances. The designs follow the process detailed above. These results indicate that adequate EDoF performance is obtained for the simple polynomial cases n=2, 3, 4, which, in general, are better than the prior art logarithmic asphere lens at close distances.

[0051] An embodiment of the invention is directed to a method for 'hyper-optimizing' an EDoF lens design; i.e., performing a second-order-, or hyper-optimization on the 'tailored' designs as described above. For the second-order or hyper-optimization, a more complicated polynomial approximation can be used to further tailor the previous designs. According to one aspect, the Strehl ratio can be maximized using the data in Table 1-7 of FIG. **7**. As shown therein, the Strehl ratio for n=4 is superior out to 300 mm, while the n=2 values are better for axial distances above 650 mm. Thus, with reference to the graph **900-1** in FIG. **9**, a new curve **920** for f(ρ) can be drawn following the n=4 curve out to ρ=0.3 mm and then smoothly joined with the n=2 curve at ρ=0.6 mm and above. The polynomial for f(ρ) of curve **920** is given by:

$$f(\rho) = 2073.27\rho^{10} - 7606.74\rho^{9} + 11632.56\rho^{8} - 9568.84\rho^{7} + 4563.12\rho^{6} + \ldots - 1272.79\rho^{5} + 201.77\rho^{4} - 16.69\rho^{3} + 0.60\rho^{2} - 0.0055\rho + 4.9786. \quad (23)$$

By Eq. (13), the phase delay for the second-order tailoring is given from Eq. (23) as follows:

$$\phi(\rho)=35.862\rho^{8}-38.728\rho^{6}-26.883\rho^{4}+1149.6\rho^{2}. \quad (24)$$

[0052] The Tables 1-10, 2-10 in FIG. **10** show that the Strehl ratio is improved compared to the n=2 case for objects closer than 300 mm and is better than the n=4 case for object distances from 650 mm to infinity. The PSF is generally uniform and narrow for object distances from 204 mm to infinity.

[0053] With further reference to FIG. **4**, the design layout **410** of the tailored parabolic EDoF lens described by the function ϕ(ρ) of Eq. 16 is illustrated. Such a design could be completed by an optical system designer using the popular ZEMAX® or CODE V® optical system design programs.

[0054] The tailored parabolic lens system **410** as shown in FIG. **4** includes four elements and one IR filter. A stop is located at the rear surface of the first lens element. The lens system has f/#=2.8, entrance pupil diameter D=1.8 mm, and effective focal length f=5.04 mm. The field of view is 46 degrees. This tailored parabolic EDoF lens has a small amount of axial color, 2.5 μm for spectrum from 0.466 μm to 0.620 μm, and low (0.875%) distortion. The detailed lens data are shown in FIGS. **11**(*a*) and **11**(*b*). The comparisons between the Strehl ratio and FWHM of the PSF for a standard diffraction limited actual lens with four elements and one IR filter, a corresponding prior art EDoF β-logarithmic asphere lens, and a corresponding tailored parabolic EDoF lens are shown in the Tables 1-12, 2-12 in FIG. **12**. The actual standard diffraction limited lens focuses at a 2500 mm object distance. The Strehl ratio is as high as 0.98. FIG. **12** shows that the depth-of-field of the standard lens is small. The Strehl ratio drops very fast versus object distance. The β-logarithmic asphere lens extends the depth-of-field to a range of 204.5 mm to infinity. The tailored parabolic EDoF lens according to an embodiment of the invention has increased performance in comparison to the logarithmic asphere lens in terms of the FWHM of the PSF over most of the range of 100 mm to infinity. The tailored parabolic EDoF lens also has increased performance over the logarithmic asphere lens in terms of the Strehl ratio everywhere from 100 mm to infinity except at 900 mm, but even there the difference is minor. It should be noted that the performance of the prior discussed embodiments for lenses is very close to the earlier theoretical calculations.

[0055] According to one aspect of an embodiment, a method is directed to tailoring a prior art EDoF logarithmic asphere having a centrally obscured aperture. The illustrative method includes the following steps:

[0056] 1. Designing a diffraction-limited (or perfect) lens, $\phi_P(\rho)$, with the proper f/# and diameter D;

[0057] 2. Computing the total phase delay for the logarithmic lens $\phi_L(\rho)$ (including the prior art Log-asphere β or Log-asphere γ designs);

[0058] 3. Computing a phase mask $\phi_E(\rho)$ sufficient to provide EDoF, such that $\phi_L(\rho)=\phi_P(\rho)+\phi_E(\rho)$;

[0059] 4. Using the $\phi_L(\rho)$ and Eq. (2) above, calculating the corresponding f(ρ) for the logarithmic asphere, as well as the FWHM of the PSF and the PSF vs. distance along the optical axis;

[0060] 5. Modifying f(ρ) to tailor the response. In doing this, it can also be advantageous to decrease the slope of f(ρ) corresponding to values of ρ for which the image needs to be improved. This may be effective since it increases the energy passing through the selected ρ for which that portion of the object is sharply focused;

[0061] 6. Modifying f(ρ) to tailor the response using optimization methods and iterative calculations that are based on the criteria set forth above; and

[0062] 7. Using the result in Eq's. (5), (6) to determine the tailored lens function $\phi_T(\rho)$.

[0063] The following example will further illustrate this process. The overall lens specifications remain as: D=1.8 mm, f/2.8, s_1=204.5 mm, and s_2=infinity. Following steps 1-3 outlined immediately above, a person skilled in the art can determine

$$\phi_{Logasphere\beta}(\rho)=1147.3\rho^{2}-28.2554\rho^{4}+0.4303\rho^{6}-0.0089\rho^{8}\text{(radians)}. \quad (25)$$

Using Eq. (25) in Eq. (2), one can determine the focal length f(ρ) vs. ρ for this lens, shown as curve **1310** in FIG. **13**. Following step 5 as described herein above, curves **1312** (tailored I) and **1314** (tailored II) represent two possible tailored versions for the improved aspheric lens. It is anticipated that both of these design can provide increased close-in performance. From Eq. (13) for finding the phase delay from the focal length, the total phase delay functions can be calculated for the two new lens designs. The resulting equations are as follows:

$$\phi_{TailoredI}(\rho)=1148.1\rho^{2}-17.5938\rho^{4}-40.9461\rho^{6}+30.2619\rho^{8}\text{(radians)} \quad (26)$$

$$\phi_{TailoredII}(\rho)=1148.7\rho^{2}-22.0359\rho^{4}-19.4152\rho^{6}+14.0623\rho^{8}\text{(radians)}. \quad (27)$$

These new curves for phase delay are also plotted in graph 1400-1 of FIG. **14**, however it is difficult to see the departures on the scale of the curves given. This result does illustrate, however, that it is hardly possible or practical to tailor the designs of these aspheres by simply resketching on the plots of total phase delay. But, since the three lenses are specified by the total phase delays as given in Eqs. (25), (26), (27), it is possible to both compute their performance and/or design

their lens layout. The Tables 1-15, 2-15 in FIG. **15** show comparative performance results in terms of the Strehl ratio and the PSF-FWHM for the three designs. Object distances from 100 mm to infinity are shown, although the design specification is for an inside distance of 204.5 mm.

[0064] Recalling that a higher Strehl ratio indicates better image quality, the Tables show that both of the tailored lenses are as good or improved over the prior art log asphere from 100 mm to 650 mm. Only at 900 mm does the log lens show better performance; however, the Strehl ratios of 0.258 and 0.340 are sufficient for restoration by digital processing.

[0065] For the full-width-half-maximum of the point spread function, uniformity as well as thinness both indicate improved performance. Performance of all three designs is good above 204 mm; however, the tailored design I shows a larger improvement than the others.

[0066] In another embodiment, a method is directed to tailoring a prior art (Log-Asphere γ) lens design. The three equations for the overall lens phase delays are given by

$$\phi_{Logasphere}(\rho)=1119.4\rho^2+6.7614\rho^4-0.0178\rho^6-0.000569\rho^8(\text{radians}) \quad (28)$$

$$\phi_{Tailored I}(\rho)=1120.1\rho^2-1.7961\rho^4+25.8703\rho^6-17.4082\rho^8(\text{radians}) \quad (29)$$

$$\phi_{Tailored II}(\rho)=1119.4\rho^2-2.1516\rho^4+30.1008\rho^6-21.1628\rho^8(\text{radians}). \quad (30)$$

The phase delays for the y design and tailored versions I & II are shown by the overlaid curves in FIG. **16**. Respective curves **1710**, **1712**, **1714** of the radially varying focal lengths f(ρ) vs. ρ are shown in FIG. **17**. The Tables 1-18, 2-18 of comparative performance are shown in FIG. **18**.

[0067] From FIG. **17** for the focal lengths, the tailoring I curve **1712** with low slope at short focal lengths is chosen to improve the close-in performance with the tailoring II curve **1714** to improve the region around 900 mm. Overall the tailoring I curve provides the most benefit for a particular lens design.

[0068] It will be apparent to those skilled in the art that various modifications and variations can be made to the present invention without departing from the spirit and scope of the invention. Thus it is intended that the present invention cover the modifications and variations of this invention provided they come within the scope of the appended claims and their equivalents.

We claim:

1. A method for making an aspheric lens, comprising:

a) selecting a radially varying focal length value f(ρ) for the lens; and

determining a corresponding radially varying phase delay function φ(ρ).

2. The method of claim **1**, further comprising fabricating the lens.

3. The method of claim **1**, further comprising modifying a performance metric of the lens as a function of f(ρ).

4. The method of claim **3**, further comprising modifying a Strehl ratio of the lens.

5. The method of claim **3**, further comprising modifying a Point Spread Function of the lens.

6. The method of claim **1**, further comprising modifying a depth-of-field value of the lens as a function of f(ρ).

7. The method of claim **1**, further comprising determining an extended depth-of-field of the lens by selecting an inner object distance s_1 and an outer object distance s_2.

8. The method of claim **1**, further comprising determining a polynomial representation of f(ρ) and obtaining a curve of f versus ρ over a desired range of ρ.

9. The method of claim **8**, further comprising modifying a portion of the curve to provide improved lens performance over a desired object distance sub-range and determining a corresponding modified polynomial representation of f(ρ).

10. The method of claim **1**, comprising making a rotationally symmetric, aspheric lens having an extended depth of field.

11. The method of claim **1**, wherein step (a) further comprises relating f(ρ) and φ(ρ) via the expression

$$\varphi(\rho)=\int_0^{\rho}\frac{-k\rho}{[f^2(\rho_1)+\rho_1^2]^{1/2}}d\rho_1,$$

where ρ_1 is the variable of integration running from zero to ρ.

12. The method of claim **9**, further comprising modifying a portion of the curve to provide improved lens performance over a desired object distance sub-range and determining a corresponding modified polynomial representation of $f(\rho)_{mod}$.

13. The method of claim **12**, further comprising determining a modified phase delay function $\phi(\rho)_{mod}$ of the lens from the modified focal length $f(\rho)_{mod}$.

14. The method of claim **13**, wherein

$$\varphi(\rho)_{mod}=\int_0^{\rho}\frac{-k\rho}{[f^2(\rho_1)_{mod}+\rho_1^2]^{1/2}}d\rho_1,$$

where ρ_1 is the variable of integration running from zero to ρ.

15. A method for optimizing the design of a rotationally symmetric, aspheric, extended depth of field (EDOF) lens specified by a known phase delay function $\phi_L(\rho)$, where ρ is the lens radius, comprising:

determining a value of the radially-varying focal length $f_L(\rho)$ of the lens from the known phase delay function $\phi_L(\rho)$, wherein said lens has a given range of focal lengths over the range of ρ;

determining a new value of a radially-varying focal length $f_{new}(\rho)$ of the lens that is different than $f_L(\rho)$, wherein $f_{new}(\rho)$ incorporates the given range of focal lengths over a range of ρ_{new}, where ρ_{new} is less than ρ; and

determining a new value of a phase delay function $\phi_{new}(\rho_{new})$.

16. The method of claim **15**, wherein the value of $f_{new}(\rho)$ is constant over a range between about $0.8\rho \leqq \rho_{new} < \rho$.

17. The method of claim **15**, further comprising expressing $f_{new}(\rho)$ as a curve that can be approximated by an n^{th}-order polynomial, where $1 \leqq n \leqq 6$ including non-integer values.

18. The method of claim **17**, wherein the curve is a parabola.

19. The method of claim **17**, further comprising hyper-optimizing the optimized design, comprising:

generating a plurality of curves based on at least two different values of n;

determining a value of a lens performance metric over a desired range of object distances for each of the curves;

selecting the values of the lens performance metrics for two of the curves;

selecting a better range of performance metric values for a corresponding range of object distances over a radial portion ρ_1 of a first one of the two curves and selecting a better range of performance metric values for a corresponding range of different object distances over a radial portion ρ_2 of a second one of the two curves;

generating a new curve $f_{new\text{-}hyper}(\rho)$ that includes the radial portions of the first and the second curves and, which, smoothly connects the first curve at ρ_1 to the second curve at ρ_2;

determining a polynomial expression for the new, hyper-optimized function $f_{new\text{-}hyper}(\rho)$; and

directly determining a hyper-optimized phase delay function $\phi_{hyper}(\rho)$ as a function of the lens radius ρ.

20. The method of claim **19**, wherein

$$\varphi_{hyper}(\rho) = \int_0^{\rho} \frac{-k\rho}{[f_{new\text{-}hyper}(\rho_1) + \rho_1^2]^{1/2}} d\rho_1,$$

where ρ_1 is the variable of integration running from zero to ρ.

21. A method for designing an aspheric lens that includes a diffraction limited lens and a phase mask, having an extended depth of field (EDoF), comprising:

determining a phase delay function $_P(\rho)$ of the diffraction limited lens, where ρ is the lens radius;

determining a total phase delay function $\phi_L(\rho)$ of the EDoF lens;

determining a phase delay function $\phi_E(\rho)$ of the phase mask to provide a desired EDoF, where $\phi_L(\rho)=\phi_O(\rho)+\phi_E(\rho)$;

determining a radially-varying focal length function $f_L(\rho)$ of the EDoF lens from the function $\phi_L(\rho)$;

determining a value of a lens performance metric for the EDoF lens;

modifying $f_L(\rho)$ so as to tailor the design to improve the performance metric; and

determining a tailored phase delay function $\phi_T(\rho)$.

22. The method of claim **21**, further comprising recalculating the value of the lens performance metric for the tailored EDoF lens.

23. The method of claim **22**, further comprising modifying the tailored $f(\rho)$ value to further tailor the lens performance.

24. The method of claim **23**, further comprising recalculating the value of the lens performance metric for the furthered tailored EDoF lens.

25. The method of claim **21**, wherein determining $f_L(\rho)$ comprises determining a polynomial representation of $f_L(\rho)$ and obtaining a curve of f_L versus ρ for a desired range of ρ.

26. The method of claim **25**, further comprising modifying a portion of the curve to provide improved lens performance over a desired object distance sub-range and determining a corresponding modified polynomial representation of $f_L(\rho)$.

27. The method of claim **26**, further comprising determining a modified phase delay function $\phi_L(\rho)$ of the lens from the modified focal length $f_L(\rho)$.

28. The method of claim **25**, wherein the step of modifying $f_L(\rho)$ so as to tailor the design to improve the performance metric comprises decreasing the slope of the curve of $f_L(\rho)$ corresponding to values of ρ over which improved performance is desired.

29. A rotationally symmetric, aspheric lens system having an extended depth of field, comprising:

a first lens L1 including a front surface S1 having a radius of curvature R1 and a rear surface S2 having a radius of curvature R2;

a second lens L2 including a front surface S3 having a radius of curvature R3 and a rear surface S4 having a radius of curvature R4;

a third lens L3 including a front surface S5 having a radius of curvature R5 and a rear surface S6 having a radius of curvature R6; and

a fourth lens L4 including a front surface S7 having a radius of curvature R7 and a rear surface S8 having a radius of curvature R8,

disposed along an optical axis, wherein the lens system has the following parameter values:

Surface	Curvature Radius (mm)	Thickness (mm)	Conic	Index of Refraction (d line)	Abbe Number
S1	R1: 3.344	0.649	2.00	N1: 1.603001	v1: 65.44
S2	R2: 14.526	0.417	−2.00		
S3	R3: −11.386	1.200	−2.00	N2: 1.528554	v2: 76.98
S4	R4: −1.591	0.249	−1.72		
S5	R5: −4.611	1.214	−2.00	N3: 1.846663	v3: 23.83
S6	R6: −13.893	1.028	1.00		
S7	R7: −2.037	1.195		N4: 1.516800	v4: 64.17
S8	R8: 24.599	0.280			

where the Thickness parameter represents a length along the optical axis from a lens system component surface to the next sequential lens system component surface.

30. The lens system of claim **29**, further comprising a stop located at S2.

31. A rotationally symmetric, aspheric EDoF imaging system, comprising the lens system of claim **30**, further comprising;

a filter having a front surface S9 and a rear surface S10 disposed adjacent S8; and

a detector D disposed adjacent S10

wherein:

Surface	Curvature Radius (mm)	Distance (mm)	Conic	Index of Refraction (d line)	Abbe Number
S9	R9: ∞	0.200		N5: 1.516330	v5: 64.14
S10	R10: ∞	0.286			

32. The imaging system of claim **31**, further comprising a stop located at S2.

* * * * *

Wavelength decorrelation of speckle in propagation through a thick diffuser

Nien-An Chang,[1,2] Nicholas George,[1,3] and Wanli Chi[1]

[1]*The Institute of Optics, University of Rochester, Rochester, New York 14627, USA*
[2]*E-mail: nachang@optics.rochester.edu*
[3]*E-mail: ngeorge@optics.rochester.edu*

Received July 7, 2010; revised November 17, 2010; accepted November 24, 2010; posted December 9, 2010 (Doc. ID 131311); published January 28, 2011

We present a careful theoretical analysis for the wavelength decorrelation of speckle intensity that occurs when plane-polarized laser illumination is propagated through an optical system consisting of a thick diffuser in cascade with the space-invariant 4 F imaging system and a CCD monitoring configuration. Based on Maxwell's equations for propagation into the right half-space, our formulation for a scalar component of the electric field is accurate well inside of the Fresnel zone and in the nonparaxial regime as well. The diffuser is described as an artificial dielectric consisting of tiny dielectric spheres embedded in a host medium and randomly spaced. We model the thick diffusers using a thin multilayer decomposition, and we write computer software describing the output speckle pattern amplitude which results from the propagation of an input plane wave. This model provides a good description for opal milk glass (OMG), and we illustrate the usefulness of this software by two applications. First, for a series of OMG diffusers of varying thickness, we present curves for the wavelength decorrelation of speckle that are found to be in good agreement with earlier experiments by George *et al.* [Appl. Phys. **7**, 157 (1975)]. Also, these results are used to compute internal parameters of these diffusers. Second, using these values, we present some first-order statistics of the intensity for this diffuser series and show that they are in accord with the published literature.

OCIS codes: 030.6140, 290.5825, 290.7050.

1. INTRODUCTION

Speckle has been an active field in optics since the first observations of reflected light from laboratory walls of the newly discovered red laser line at 632.8 nm from the helium–neon laser (1962). While review of the extensive literature resulting from these investigations is beyond the scope of this paper, it is worthwhile to mention authoritative texts covering this field: one by Dainty [1] and another by Goodman [2]. Also, for a number of years speckle was found to be mainly a troublesome source of noise, say in holography and microscopy. Thereafter, scientists began to find practical systems applications using "speckle concepts." An early collection of these is described in [3].

In this paper, we present a theory for the wavelength decorrelation of speckle in a thick diffuser. Our goal is to provide an accurate model based on electromagnetic theory for a diffuser that is composed of tiny, spherical particles in a host medium. As the light propagates through the diffuser, each particle scatters a portion of the incident radiation. In our theory, since the particles are tiny, care is taken to allow for accuracy in the wide angle of the scattering (nonparaxial) as well as the close proximity of the nearby particles (near-field). The details of this model are described in Section 2. Section 3 contains the propagation theory based upon Fourier optics that is written by us using the exact solution of Maxwell's equations for propagation into the right half-space, known as the Rayleigh–Sommerfeld–Smythe form [4]. While there will be backscatter comparable to the forward scatter, we neglect its contribution to a secondary forward scatter based on a numerical estimate, which we omit in the interest of brevity. Hence, we limit our solution to the "dilute" thick diffuser.

Theory for speckle in a thick diffuser is important for two main reasons. First is that it gives insight concerning the possibility of determining internal quantities relative to a complex turbid medium. Second is that it will lead to better-controlled diffusers for other experiments in image science. In this paper, to test the theory, we limit our investigation to the use of a series of six diffusers made from commercial flashed opal milk glass (OMG) with thicknesses ranging from 25 μm to 500 μm. These diffusers are ideal, and they have been used in a wide variety of applications. Their space and wavelength dependence of speckle has been carefully measured and published in an earlier, independent paper [5] and a thesis by Melville [6]. The usefulness of a series of varying thickness is readily apparent in the two illustrative applications presented in this paper: wavelength decorrelation and first-order intensity probability density functions.

Theory for the wavelength decorrelation of speckle proceeds by considering the thick diffuser as a cascade of thin diffusers, as shown in Figs. 1 and 2. With the advent of modern digital computing methods, three important successes have served to guide us. First is the research on thick holographic gratings, called thin-grating decomposition by Alferness [7] and others [8]. Second is the analysis of holographic multilayers consisting of thin slabs of varying index [9]. Third are the numerous programs written to simulate atmospheric turbulence, e.g., Wave Train [10]. We term our analysis: thin-diffuser decomposition.

For the sake of completeness, we also mention the research on the space and wavelength dependence of speckle including cascades of two or more diffusers [11–15], although these papers considered mostly a thin diffuser model appropriate

Table 1. Summary of the Features from the Theoretical Intensity Correlation Curves of a Series of Opal Glass Diffusers

Thickness (μm)	Number of Screens	Measured Transmission, Specular	Contrast Ratio C_r	$R_w(\infty)$,	Decorrelation Wavelength Interval (angstrom)
25	25	9.98×10^{-2}	0.33	—	—
50	49	1.3×10^{-2}	0.43	—	—
100	90	4.39×10^{-5}	0.77	0.8 ± 0.02	15.8
200	196	8.35×10^{-6}	0.98	0.58 ± 0.02	6.18
300	305	5.3×10^{-6}	0.996	0.55 ± 0.02	3.45
500	525	4.59×10^{-6}	1	0.51 ± 0.013	2.44

for frosted or ground glass. Interesting research on wavelength dependence of speckle to find object shape is also reported in the published literature [16].

Section 4 contains a summary and an extract of suitable forms from the exact results for scatter by a dielectric sphere using the well-known Lorenz–Mie theory together with a separate treatment for the direct or specular beam. Interesting means for calculation of the cross-polarized speckle pattern are obvious from this but are not included herein. Hence, we neglect the buildup of this cross-polarized beam that becomes important for the thicker OMG; and as an approximation, we also neglect the small fraction of this beam that is returned to contribute to the original polarization. This accuracy of our simulation is decreased for OMG diffusers that are thicker than 400 μm.

Section 5 includes a full description of our experimental apparatus. As shown in Fig. 9, this 4 F optical metrology system consists of a OMG diffuser as an input object illuminated by the plane-polarized input from a tunable dye laser. The imaged speckle pattern at the output of the 4 F optical system is recorded with a high-quality CCD camera and computer system. The terminology "4F imaging system" is used to describe this space-invariant imager consisting of two lenses each of focal length F with spacing between input object and output object planes of four focal lengths [17].

Section 6 provides a step-by-step procedure on establishing the internal features of diffusers. The initial parameters are finely adjusted to the final values, and a listing of properties of opal glass diffusers are given in Tables 1 and 2. The information in this section provides an outline, enabling one to estimate the characteristics of the OMG diffuser.

As a second illustrative application of the computer software and our monitoring apparatus in Section 7, we include the first-order statistics of speckle intensity from the dye laser experiment on opal glasses as a comparison to our simulation result. We also include a comparison to the Rician distribution, which is the known density for a constant phasor added to a random phasor sum. A summary is given in Section 8.

2. STATEMENT OF PROBLEM

In this paper, we apply modern digital computing methods to the task of analyzing a dilute thick diffuser. We consider this optical system to be a cascade of thin layers each with randomly distributed particles, followed by a thin free-space region as shown in Fig. 1. Suppose a thick diffuser with N particles is sliced into M screens; each screen has N/M particles randomly positioned throughout the whole screen. The scattering effect from each particle is described by the Lorenz–Mie theory, and a summary of the scattering theory is provided in Appendix A. The cascade system can be implemented in Matlab. A cascade model along with the monitor system is shown in Fig. 2. The monitor system is composed of a space-invariant 4 F imager and a CCD detector at the image plane. A polarization analyzer (A) is placed as the input object (IP-A). Each screen contains a random distribution of particles where the particle locations for each screen are represented by $t_m(x, y)$. And the propagation between each screen is expressed by an impulse response, $p_m(x, y)$. Fig. 2(a) shows the image space operations as a cascade of an input field product with the thin screen followed by a convolution with the impulse responses for propagation through the free space between each screen. However, the actual calculation proceeds using FFT routines as shown in Fig. 2(b) so that only products are used in image space for the propagation through the thin screen, $t_m(x, y)$, and in transform space with a product that involves $P_m(f_x, f_y)$, the Fourier transform of the impulse response $p_m(x, y)$.

In this paper, we emphasize the wavelength dependence of speckle generated by a dilute thick diffuser. The space and wavelength characteristics of speckle can be found in the literature, and a simple method to analyze the speckle features is given in the paper by Chang and George [17]. The reasons for the emphasis on the wavelength dependence of speckle are as follows: the space dependence of speckle, also referred to as speckle size, is determined by the F number of the optical system, while the wavelength dependence of speckle reveals the interior information of a diffuser. The wavelength dependence of speckle is expressed by the intensity variation at a given position as the wavelength of illumination changes. From the wavelength dependence of the appropriate intensity-based correlation function, one finds the wavelength interval for decorrelation. This is roughly the wavelength variation needed for a bright speckle to become dark. An $\exp(i\omega t)$ harmonic time dependence is used throughout this paper.

3. THEORY FOR PROPAGATION IN ONE CELL OF THE DIFFUSER

In order to illustrate the theory, we take out one part of the cascade and analyze the scalar field at the $(m + 1)$th screen, a

Table 2. Basic Flashed Opal Glass Properties

Number Density ($1/\mu m^3$)	Medium Index	n_r	Particle Diameter (μm)
0.95	1.5	1.009 ± 0.0004	0.4

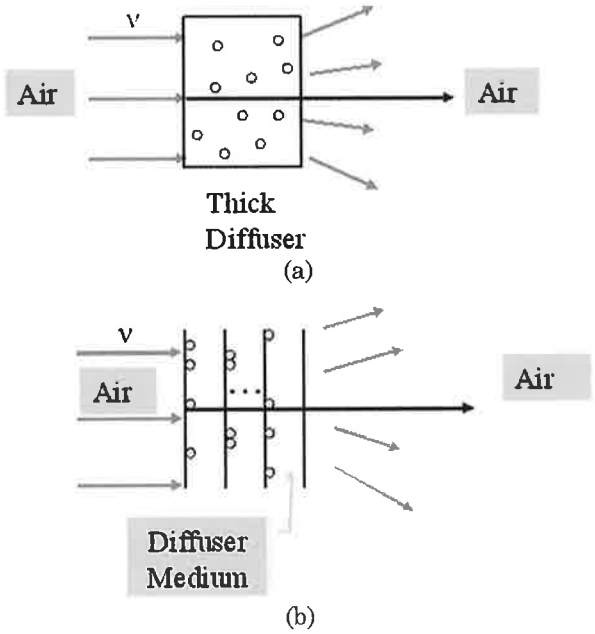

Fig. 1. (a) Decomposition of a thick diffuser with spherical particles as shown into (b) a cascade of thin screens with a small free-space region in between.

distance away from the mth screen as shown in Fig. 3(a). The scalar field $E_{y,m+1}(x_{m+1}, y_{m+1})$ at the $(m+1)$th plane is written as a convolution of the incident field $E_{y,m}$ with the propagator. This exact solution of Maxwell's equations for propagation into the right half-space is given by the well-known Rayleigh–Sommerfeld–Smythe integral as follows [4]:

$$E_{y,m+1}(x_{m+1}, y_{m+1}; z_{m+1}) = \int_{-\infty}^{\infty}\int_{-\infty}^{\infty} \mathrm{d}x_m \mathrm{d}y_m E_{y,m}(x_m, y_m; z_m) \times \frac{\exp(-ikR)}{2\pi R}\frac{d_m}{R}\left(ik + \frac{1}{R}\right), \quad (1)$$

where $k = \frac{2\pi}{\lambda}$, λ is the illumination wavelength, $R = R_{m,m+1} = [(x_{m+1} - x_m)^2 + (y_{m+1} - y_m)^2 + d^2]^{1/2}$, and d is the distance between the two screens. $E_{x,m+1}$ is given analogously. Since Eq. (1) is exact, it includes all near-field and propagation terms and it is accurate at wide angles.

From the form of Eq. (1) as a perfect convolution, one can identify what is appropriately called the impulse response for propagation of the scalar electric field component $E_{y,m}$. As is well known, taking the spatial Fourier transform of this space-invariant impulse response with respect to the transverse coordinates (x, y) gives the transfer function which one recognizes is the angular spectrum representation, as shown in Fig. 3(b). More details are included on this in the literature [4], and the typical contour integrals are included in Budden [18] and Clemmow [19]. Our calculation is accurate nonparaxially since we use angular spectrum representation as shown in Fig. 3(b), i.e.,

$$V_{y,m+1}(f_x, f_y; z_{m+1}) = V_{y,m}(f_x, f_y; z_m) \times \exp\left(ikd\sqrt{1 \quad (\lambda f_x)^2 \quad (\lambda f_y)^2}\right), \quad (2)$$

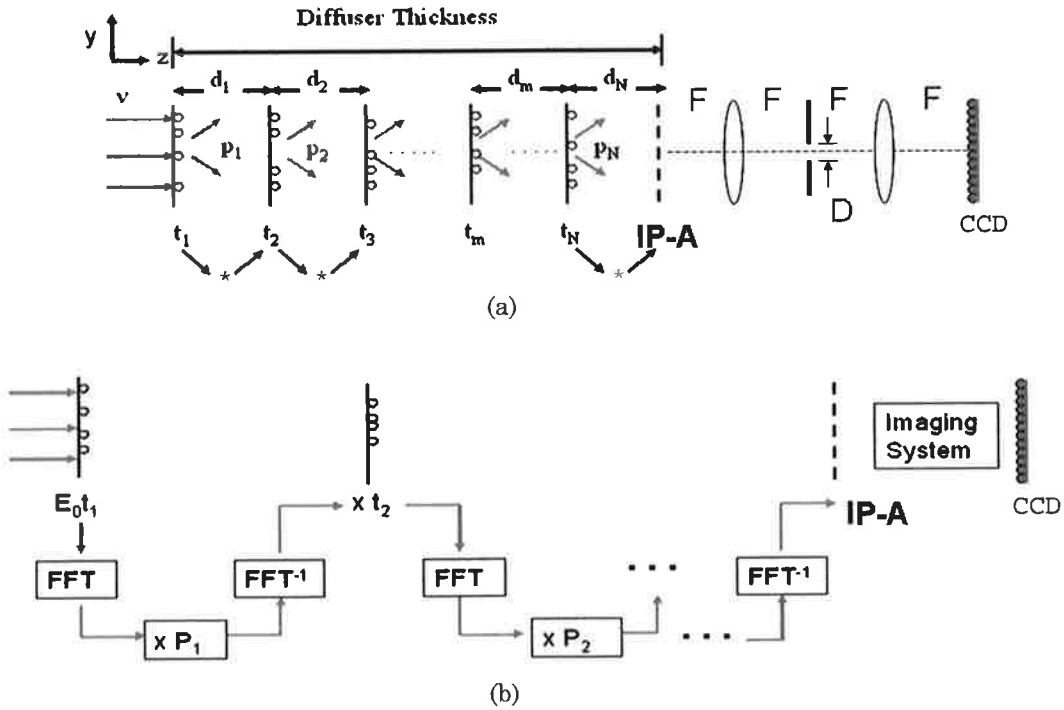

Fig. 2. Plane-polarized optical wave is normally incident on the cascade-model thick diffuser and the output is imaged onto the CCD by a 4 F imager. A polarization analyzer (A) is located as the input object (IP-A). Propagation through the cascades can be computed in the amplitude plane as shown in (a). However, the actual calculation routines are based on switching between the amplitude and Fourier plane as shown in (b) to allow an all-products operation. t_i is the binary maps of particle locations at each screen, which is explained in Fig. 8, and P_i is the transfer function of propagating and scattering of the field.

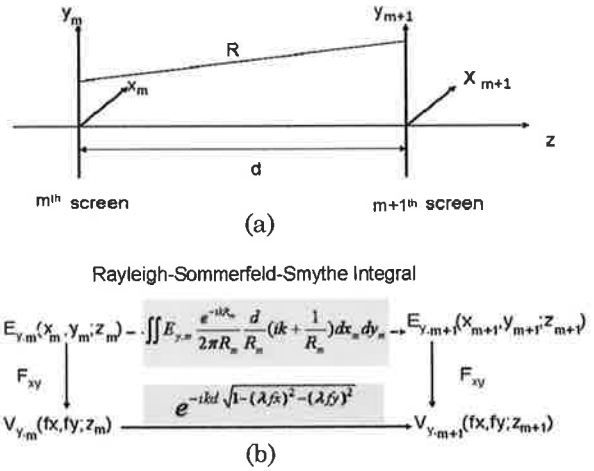

Fig. 3. (a) Section out of a cascade model where light propagates from the mth screen to the $(m+1)$th screen. The corresponding operation in space and Fourier domain is illustrated in (b), where a convolution expressed as a Rayleigh–Sommerfeld–Smythe integral equation in the space domain has a simpler counterpart in the Fourier domain.

where $V_{y,m+1}$ and $V_{y,m}$ are the Fourier transforms of $E_{y,m+1}$ and $E_{y,m}$ respectively. By comparing the two outputs at amplitude and Fourier plane, we find the following relation:

$$\mathfrak{F}_{xy}\left[\frac{\exp(-ikR)}{2\pi R}\frac{d}{R}\left(ik+\frac{1}{R}\right)\right] = \exp\left(-ikd\sqrt{1-(\lambda f_x)^2-(\lambda f_y)^2}\right), \quad \text{for } 1-(\lambda f_x)^2-(\lambda f_y)^2 \geq 0.$$
$$= \exp\left(-kd\sqrt{(\lambda f_x)^2+(\lambda f_y)^2-1}\right), \quad \text{for } 1-(\lambda f_x)^2-(\lambda f_y)^2 < 0, \tag{3}$$

where $\mathfrak{F}$ stands for the Fourier transform operation, and f_x and f_y denote the spatial frequencies along x and y directions, respectively. Note that the discussion above explains the optical propagation through a free-space region. Scattering from particles is described separately in Section 4.

4. SCATTERING FROM SPHERES

Scattering from spheres has been investigated and carefully described by van de Hulst [20] and Kerker [21]. In the general case in which one needs to treat large spheres, our basic computer method is generally applicable. For this reason, we have included a summary of the Lorenz–Mie theory results for a sphere of arbitrary radius in Appendix A. With larger and larger spheres, one simply includes more terms. However, in the body of this paper, we will consider only the small spheres, i.e., spheres whose size is smaller than a wavelength. In this case, the general theory reduces to the Rayleigh theory for scattering by small particles.

It needs to be emphasized that the application of Eqs. (1)–(3) is being made in an approximate manner, since all of the conditions for their validity are not being rigorously met. In Fig. 4, the scattering field at a distance, r, away from the sphere is calculated to be Eq. (A7) in Appendix A. The incident wave travels along the positive z axis with electric vector polarized along the y axis. The particle has its center at the origin. The dipole moment is excited along y axis. The scattering angle, ψ, is measured from the dipole direction to the scattering direction, whereas θ is measured from the scattering direction to the z axis and ϕ is the angle between the projected field onto the x–y plane and the y axis. The scattered field is written as

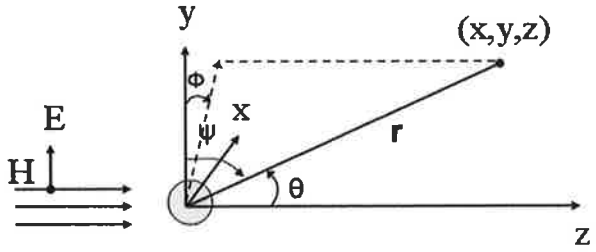

Fig. 4. Scattering from a small sphere, and the coordinates are illustrated. Relative index ratio $n_r = m_1/m_2$, in which indices m_1 and m_2 are for sphere and medium, respectively.

$$\mathbf{E}_\psi = E_\phi\hat{\phi} + E_\theta\hat{\theta} = k_2^2 a^3 \frac{n_r^2-1}{n_r^2+2} E_{\text{inc}} \frac{\exp(-ik_2 r)}{r}\sin\psi\hat{\psi}, \tag{4}$$

where k_2 is the wavenumber in the host medium, n_r is the relative index of the sphere, a is the sphere radius, E_{inc} is the incident field on the sphere, ψ is the angle measured from the scattering direction to the y axis (dipole radiation direction), and $\sin\psi = (x^2+z^2)^{1/2}/r$.

A. Scattering: Particle to Particle

Suppose there are two particles located a distance, d, apart and an incident wave illuminates the first particle at $(x_1, y_1, 0)$ as shown in Fig. 5; the scattered wave at the second particle, located at (x_2, y_2, d) is expressed as

$$\mathbf{E}_\psi = k^2 a^3 \frac{n_r^2-1}{n_r^2+2} E_{\text{inc},1} \frac{\exp(-ikr)}{r}\sin\psi\hat{\psi}, \tag{5}$$

where $r = [(x_2-x_1)^2+(y_2-y_1)^2+d^2]^{1/2}$, $\sin\psi = ((x_2-x_1)^2+d^2)^{1/2}/r$, and $\hat{\psi}$ is the unit vector. A dipole at the second particle is induced at an angle as in Figs. 5 and 6(a). Herein, we assume a simpler geometry by using only the y component of the incident field on the second particle as shown in Fig. 6(b). We drop the nontangential remaining component of the induced dipole. Hence, the result is given by

$$E_{\text{inc},2}\hat{y} = E_\psi \sin\psi\hat{y} = k^2 a^3 \frac{n_r^2-1}{n_r^2+2} E_{\text{inc},1} \frac{((x_2-x_1)^2+d^2)\exp(-ikr)}{r^3}\hat{y}. \tag{6}$$

We can then calculate the scattered field toward the next screen by extending Eq. (6) to include many particles on each screen.

Suppose there are N_m particles located on the mth screen at random positions as shown in Fig. 7, (x'_1, y'_1, d), (x'_2, y'_2, d), (x'_3, y'_3, d), …, (x'_{N_m}, y'_{N_m}, d). The scattered field at a fixed point on the $(m+1)$th screen is written as

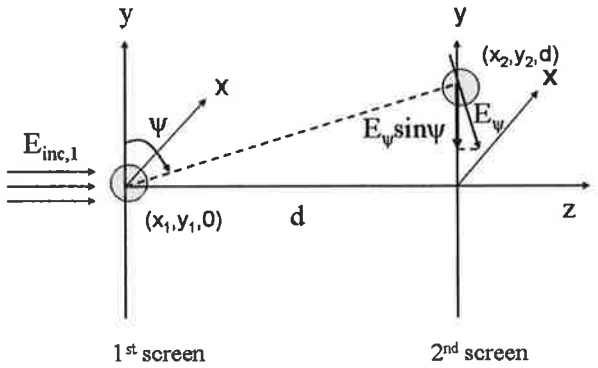

Fig. 5. Two particles are located a distance, d, apart. An incident wave illuminates the first particle at $(x_1, y_1, 0)$, and the scattered wave subsequently illuminates the second particle, located at (x_2, y_2, d).

$$E_{y,m+1,s}(x,y) = k^2a^3\frac{n_r^2-1}{n_r^2+2}\left\{\frac{[(x-x_1')^2+d^2]\exp(-ikr_1)}{r_1^3}E_{\text{inc},m}(x_1',y_1') + \frac{[(x-z_2')^2+d^2]\exp(-ikr_2)}{r_2^3}E_{\text{inc},m}(z_2',y_2') + \cdots + \frac{[(x-x_{N_m}')^2+d^2]\exp(-ikr_{N_m})}{r_{N_m}^3}E_{\text{inc},m}(x_{N_m}',y_{N_m})\right\}, \quad (7)$$

where $r_j = [(x-x_j')^2+(y-y_j')^2+d^2]^{1/2}$. Equation (7) can also be expressed in a convolution form as

$$E_{y,m+1,S}(x,y) = k^2a^3\frac{n_r^2-1}{n_r^2+2}\int_{-\infty}^{\infty}\int_{-\infty}^{\infty}\left[\sum_{j=1}^{N_m}\delta(x'-x_j',y'-y_j')\right]E_{\text{inc},m}(x',y') \times\frac{[(x-x')^2+d^2]\exp\left(-ik\sqrt{(x-x')^2+(y-y')^2+d^2}\right)}{\sqrt{(x-x')^2+(y-y')^2+d^2}^3}\,dx'dy', \quad (8)$$

which can be easily calculated in the Fourier transform domain using a computer. The sum of all delta terms $\sum_{j=1}^{N_m}\delta(x'-x_j',y'-y_j')$ represents a two-dimensional location map of the N_m particles, where ones represent position occupied by a particle and zeros represent unoccupied positions as shown in Fig. 8. Equation (8) represents the scattering field from a thin screen with many particles. In Section 4.B, Eq. (8) will be combined with the direct beam to generate the final output.

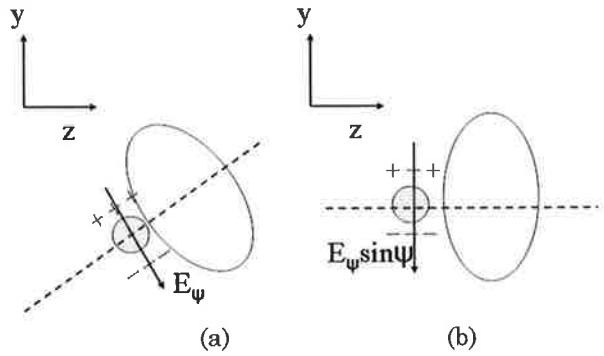

Fig. 6. Incident field at the second particle (a) showing the dipole moment induced at an angle ψ. In order to simplify the calculation, we only use the y component of the electric field to keep the dipole radiation symmetrical as shown in (b).

B. Combination of Direct Beam and Scattering Field

At the $(m+1)$th screen, the incident field $E_{\text{inc},(m+1)}$ is calculated as the combination of the direct beam and the scattering field. The scattered field is derived from Eq. (8), and the direct beam is generated from the free-space propagation, Eq. (1). Now that we have the expressions for the direct beam and the scattered field, we can readily add them up, i.e.,

$$\begin{aligned}E_{\text{inc},m+1}(x,y) &= E_{y,m+1,D}(x,y) + E_{y,m+1,S}(x,y)\\ &= \int_{-\infty}^{\infty}\int_{-\infty}^{\infty}dx'dy'E_{\text{inc},m}(x',y')\\ &\quad\times\frac{d\exp(-ik[(x-x')^2+(y-y')^2+d^2]^{1/2})}{(x-x')^2+(y-y')^2+d^2}\\ &\quad\times\left(ik+\frac{1}{\sqrt{(x-x')^2+(y-y')^2+d^2}}\right)\\ &\quad+k^2a^3\frac{n_r^2-1}{n_r^2+2}\times\int_{-\infty}^{\infty}\int_{-\infty}^{\infty}\sum_{j=1}^{N_m}\delta_m(x'-x_j',y'-y_j')E_{\text{inc},m}(x',y')\\ &\quad\times\frac{[(x-x')^2+d^2]\exp\left(-ik\sqrt{(x-x')^2+(y-y')^2+d^2}\right)}{\sqrt{(x-x')^2+(y-y')^2+d^2}^3}dx'dy'.\end{aligned} \quad (9)$$

Equation (9) is computed in the Fourier domain as a product, i.e.,

$$\begin{aligned}V_{\text{inc},m+1}(f_x,f_y) &= k^2a^3\frac{n_r^2-1}{n_r^2+2}V_{\text{rev},m}\mathfrak{F}_{xy}\left[\frac{(x^2+d^2)\exp(-ik\sqrt{x^2+y^2+d^2})}{\sqrt{x^2+y^2+d^2}^3}\right]\\ &\quad+V_{\text{inc},m}(f_x,f_y)\exp\left(-ikd\sqrt{1-(\lambda f_x)^2-(\lambda f_y)^2}\right),\end{aligned} \quad (10)$$

where $V_{\text{inc},m} = \mathfrak{F}_{xy}[E_{\text{inc},m}(x,y)]$ is the Fourier transform of the incident beam, and $V_{\text{rev},m} = \mathfrak{F}_{xy}[\sum_{j=1}^{N}\delta_m(x-x_j',y-y_j')E_{\text{inc},m}(x,y)]$ is the Fourier transform of the incident beam through the two-dimensional particle position map of the mth screen. Equation (10) is key, as the output of the $(m+1)$th screen will be subsequently fed as the input to the next screen.

5. SPECKLE METROLOGY USING THE SPACE-INVARIANT 4 F IMAGING SYSTEM [17]

In the last section, Eq. (9) provides an expression for the scalar electric field component at the output face of a diffuser that is to be coupled into the space-invariant 4 F imaging system, as shown in Fig. 2. This imaging system has been developed especially for speckle measurements, and it possesses many significant refinements over our earlier metrology system. A major refinement is the use of a CCD detector that is coupled to a computer system so that extensive data collection and processing is facilitated. This system has been reported in the literature [17].

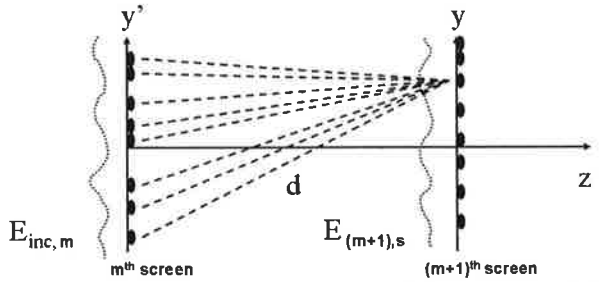

Fig. 7. Scattering field at a fixed point on the $(m+1)$th screen is the sum of scattered fields from all particles on the mth screen.

In this paper, for clarity, Fig. 9 shows the setup more completely including the source details as well as the data collection. It consists of a Coherent Innova 70 tunable dye laser Model No. 599 (TL), polarizer (P) set to pass E_y, OMG, analyzer (A), lenses of $F = 200$ mm, variable aperture (D) (typically 1 mm), Atmel Camelia 4M B/W CCD with 14 μm pixel size, digital computer (DC), and display. The polarizer ensures a plane-polarized light source while the analyzer placed at the output face of the diffuser is to block any cross-polarized term from the scattering process in the OMG diffusers, especially for 300 μm or 500 μm diffusers. Illumination wavelength from the dye laser is calibrated by a Coherent WaveMaster Model No. 33-2650 (W). Automatic power input controller is not shown. Power is measured using an Ophir Orion PD 300 power meter, basic reading to approximately 10 pW. In the 4 F system, the aperture D is used to control the speckle size in the output image. Typically, as explained in Section 6, we set D so that the speckle array is 20×20 speckles. This gives us spatially independent samples since the total signal at any pixel in the image plane is only collecting light from a circle on the OMG diffuser as set by hh^* for the 4 F system. Full explanation of this sampling procedure is given in [17,22].

6. WAVELENGTH DECORRELATION OF SPECKLE OMG

As an important test of the theory and software described in the previous sections, we compute the wavelength decorrelation of laser light by propagation through a series of OMG diffusers; see Fig. 2. As referenced earlier in the literature [5,6], there is much interesting data about these diffusers. Let us briefly mention that the specular transmission values as a function of thickness were carefully measured. Also the Rician density characteristic of a large phasor with several random speckle contributors was described and measured for this series of diffusers, together with earlier references.

Herein, since it is most relevant to our studies, we repeated the measurement of the transmission of a specular or direct term for the transmission; see Table 1. This gives one the con-

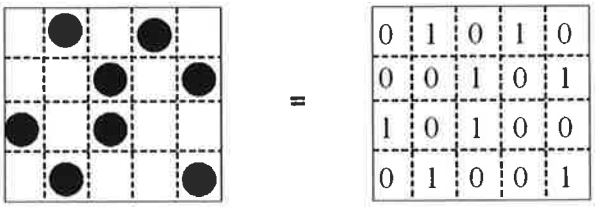

Fig. 8. This figure shows the numerical representation of the random particle positions.

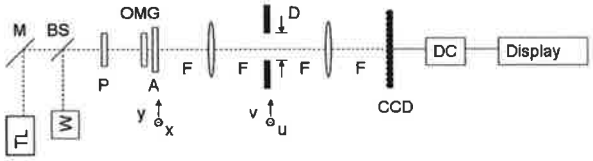

Fig. 9. 4 F optical metrology system is shown. It consists of a Coherent Innova 70 tunable dye laser Model No. 599 (TL), polarizer (P) set to pass E_y, OMG, analyzer (A), lenses of $F = 200$ mm, variable aperture (D) (typically 1 mm), Atmel Camelia 4 M B/W CCD with 14 μm pixel size, digital computer (DC), and display. Illumination wavelength from the dye laser is calibrated by Coherent WaveMaster Model No. 33-2650 (W). Automatic power input adjustment is not shown. M, mirror. BS, beam splitter. F, focal length.

trast ratio C_R defined as the ratio of the standard deviation of intensity σ to the mean $\bar{w}_x$, i.e., $C_R = \sigma/\bar{w}_x$. From the literature [2,5], the first-order probability density for Rician statistics, $P(w_x)$ is given by

$$P(w_x) = \frac{1}{\bar{w}_x(1-\sqrt{1-C_R^2})} \exp\left[\frac{-(w_x+\bar{w}_x\sqrt{1-C_R^2})}{\bar{w}_x(1-\sqrt{1-C_R^2})}\right] \times I_0\left[\frac{2(w_x\bar{w}_x\sqrt{1-C_R^2})^{1/2}}{\bar{w}_x(1-\sqrt{1-C_R^2})}\right], \tag{11}$$

where $\bar{w}_x$ is the mean intensity for plane-polarized speckle. The function I_0 is the modified Bessel's function of order zero.

For our calculations, we can fix the diameter of the spheres in the opal-glass diffusers at 0.4 μm from reviewing the electron micrographs (SEM) by Melville [6]. This leaves us with the relative index n_r, which is the ratio of the index of the spheres to that of the host medium, as a parameter to vary. Also another parameter to vary is the number density of scattering sphere per unit volume, N_d.

As an interesting consideration in the computations, we found that it is important to maintain a degree of homogeneity and randomness in the diffuser. The particles are randomized in the (x, y) plane. We also introduce a phase irregularity in the screen spacing, along the z axis. This eliminates any type of array factor or crystalline resonances. Hence, for a diffuser with thickness L, width D, and number of particles N, the mean free path L_m is written as

$$L_m = \sqrt[3]{\frac{D^2 L}{N}}. \tag{12}$$

The number of screens $M = L/L_m$ has an expression of

$$M \sim \left(\frac{L^2 N}{D^2}\right)^{\frac{1}{3}}. \tag{13}$$

The typical screen spacing in this paper is around 1 μm. The conditions for the Fresnel zone approximation, commonly used for describing the free-space propagation, are not met with the close spacing and wide scattering angles from each small particle. However, our theory has been written so that it accurately describes the complicated phenomena when the observation point is very close to the object and at wide angles.

A. Computer Study: Propagation through a Dilute Thick Diffuser

Two-dimensional maps of particle positions are generated as ones and zeros at random positions. These maps are saved for later evaluation at each different wavelength. A plane wave serves as the incident illumination on the first screen. The output field from Eq. (9) is calculated as it becomes the input to the next screen, and by looping the sequence M times to represent propagation through M screens, we have the scalar electric field coming out of a thick diffuser. This field is then imaged by the 4 F optical system to create an intensity (speckled) pattern at the image plane. This process is repeated at different wavelengths, and the imaged speckled patterns are used to evaluate the wavelength decorrelation of speckle [12].

The wavelength decorrelation of speckle is examined by using the intensity correlation function $\langle w(x,y;\lambda)w(x,y;\lambda+\Delta\lambda)\rangle$ where w is the intensity of a speckled pattern and λ is the illumination wavelength. $w(x,y;\lambda)$ is given by $w=\mathbf{E}\cdot\mathbf{E}^*$, which reduces to $w=E_yE_y^*$ for a linearly polarized electric field E_y.

The bracket $\langle\rangle$ denotes an ensemble average [23]. In our 4 F optical metrology apparatus with space-invariant imaging, we sample the output pattern from tiny pixel detectors that are spaced by two or more speckle diameters [17]. This gives us an excellent approximation to the use of physically, completely independent diffusers. Here we focus on the wavelength decorrelation of speckle; the intensity correlation function, $R_w(x,y;\lambda,x,y;\lambda+\Delta\lambda)$, is written as

$$R_w(x,y,\lambda;x,y,\lambda+\Delta\lambda)=\int_{\lambda}^{\lambda+\Delta\lambda}w(\lambda')w^*(\lambda'-\Delta\lambda)\mathrm{d}\lambda'. \quad (14)$$

The intensity correlation function is calculated by shifting $w(\lambda)$ along the wavelength axis and summing over the overlapping values to the unshifted one. However, when calculating the correlation function from a random process with a limited length, the intensity correlation has a triangular shape due to the zero padding when shifting the random process. In order to eliminate this, the method called cyclic autocorrelation is implemented. In this method, one calculates the correlation function so that when the random process is shifted, the values not overlapping with the unshifted one are padded with the values over the bound of the unshifted one. In this paper, intensity values from nine pixels, which are evenly spread and located at least two speckles apart, are generally used. One intensity correlation function is generated with the cyclic autocorrelation of the intensities on any one pixel. Nine intensity correlation functions are averaged to obtain a final curve with an associated error bar.

B. Wavelength Decorrelation for the OMG Diffusers

As explained in Section 6, the relative index of refraction, n_r, and the number of scattering spheres per unit volume, N_d, are used to fit the wavelength decorrelation curves. We describe the iterative calculation as follows. Starting with $n_r=1.05$ and $N_d=2$ per $\mu\mathrm{m}^3$, we calculate trial autocorrelations for a wavelength range from 578 nm to 580.4 nm in steps of 0.01 nm. Since the thickness controls the amount of the specular transmission, the $R_w(\infty)$ is lower as the thickness increases; see Fig. 10.

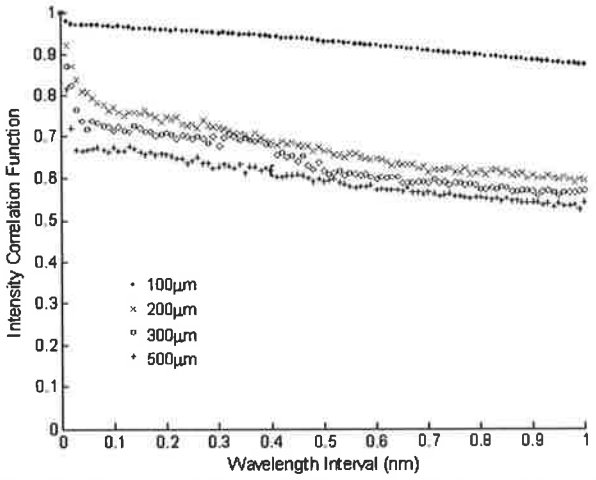

Fig. 10. Computer simulation for the wavelength decorrelation of speckle, Eq. (13), for four thicknesses of OMG. Wavelength interval $\Delta\lambda$ starts at $\lambda=578.0$ nm.

Figure 10 shows the final computer simulation for the wavelength decorrelation of the output intensity of the four principal diffusers. Figure 11 shows the sensitivity of the correlation curves to changes in n_r from 1.009 by ±0.0004. While our experimental laser apparatus can only be tuned in 0.1 nm steps, the computer simulation is run at an expanded resolution of 0.01 nm in order to provide a better look at the autocorrelation for small wavelength offsets. Table 1 summarizes our results for the diffuser set resulting from the computer simulation, and Table 2 summarizes the diffuser parameters which we have established for our opal glass.

7. FIRST-ORDER STATISTICS OF INTENSITY FOR THE OMG DIFFUSERS

In this section, as a further test of our computer simulation, we present a study of the first-order statistics of intensity for the OMG diffusers. Now that the OMG parameters have been established by the correlation studies, as summarized in Tables 1 and 2 and Figs. 10–13, this is a relatively straightforward task.

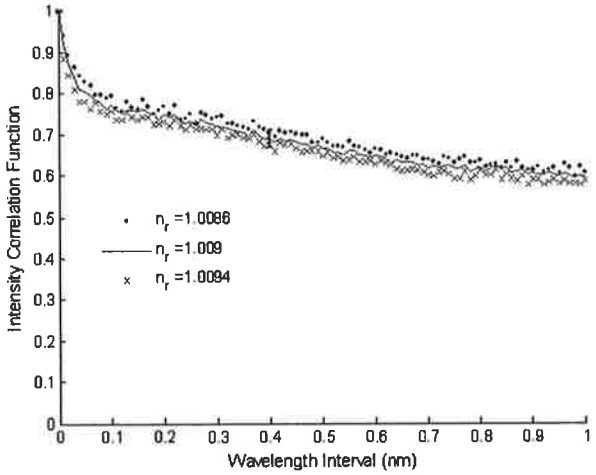

Fig. 11. Computer simulation for the wavelength decorrelation as in Fig. 9 to show the variation with relative index n_r for the 200 μm OMG.

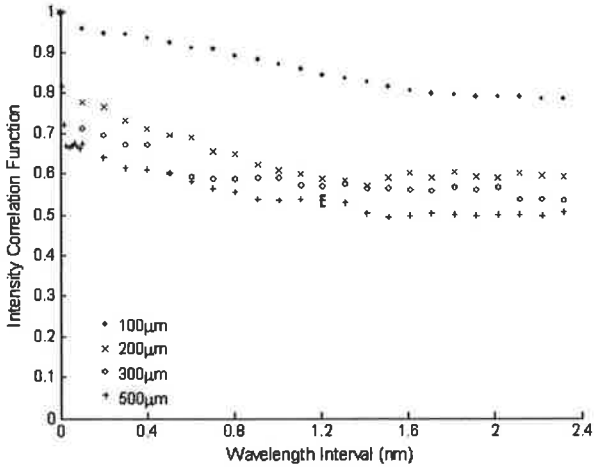

Fig. 12. Computer simulation for wavelength decorrelation versus $\Delta\lambda$ for four thicknesses.

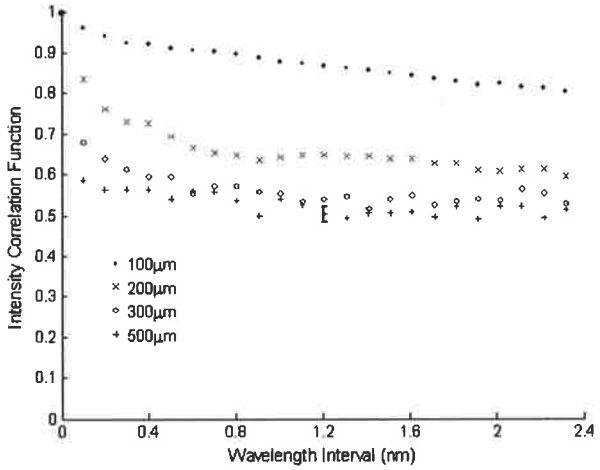

Fig. 13. Actual laser-OMG wavelength decorrelation versus $\Delta\lambda$ to compare to Fig. 11.

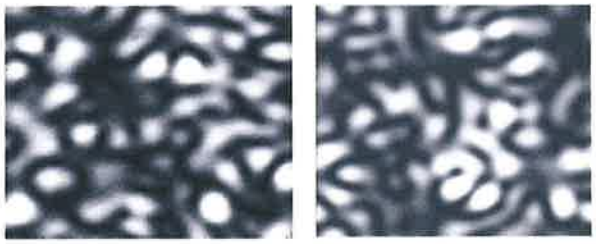

Fig. 14. Speckle patterns: (a) actual laser 200 μm OMG diffuser and (b) computer simulation.

OMG diffusers are well-suited for quantitative speckle experiments due to their homogeneity and the controllable specular transmission. On the other hand, ordinary frosty glass is quite variable and has a specular transmission of a few percent that can be troublesome if it is not expected.

Figure 14(a) shows the actual laser intensity in the image plane of the 4 F system in Fig. 9 with a 1 mm aperture and a 200 mm focal length. A 200 μm OMG diffuser is used, and the speckle is plane-polarized. The corresponding computer simulation is shown in Fig. 14(b). Intensity autocorrelations in the $(x–y)$ image plane establish the well-known speckle size. Separately looking at 10 different simulations with a few laser speckle patterns, one cannot separate or distinguish them.

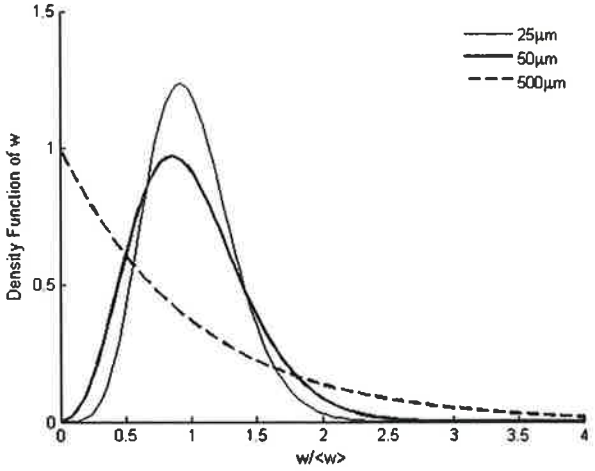

Fig. 15. First-order Rician density for three OMG diffusers [2,5].

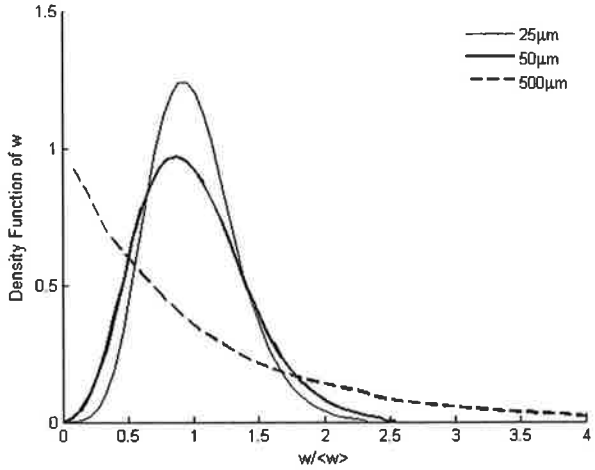

Fig. 16. First-order density of speckle intensity using computer simulation.

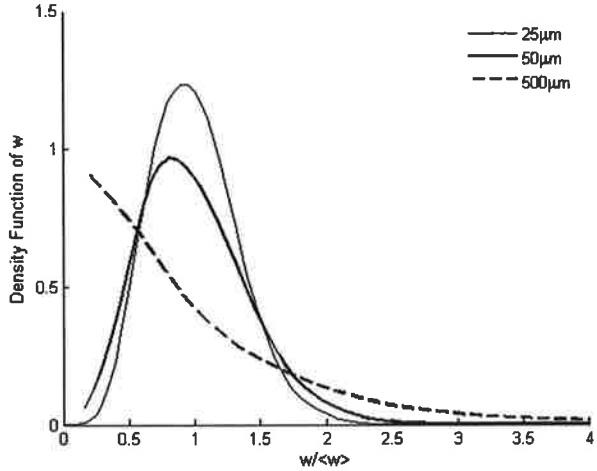

Fig. 17. First-order density of speckle intensity using actual laser OMG for comparison to Fig. 15.

Figure 15 is a plot of the Rician density in Eq. (11) for C_R corresponding to three separate OMG diffusers. These curves are seen to be in close agreement with our Fig. 16 computer simulations and our Fig. 17 laser-OMG diffuser experiments, as well.

8. SUMMARY

Based on Maxwell's equations for propagation into the right half-space, an approximate theory is presented for the wavelength decorrelation of speckle as a monochromatic plane wave propagates through a thick diffuser. Sections 2–4 contain a statement of the problem and the basic theoretical approach including illustrations of the thin-diffuser decomposition in Figs. 2–4. Our theory is limited to a scalar component of the electric field, as explained herein, and the experiments include a polarization analyzer at the output of the imager; see IP-A in Fig. 2. Further details about the depolarized speckle pattern are given in the literature [5,6,22] and are to be the subject of a second paper. In this paper, two major equations are utilized to describe the propagation phenomena in a cascade system. One is Eq. (1), the Rayleigh–Sommerfeld–Smythe integral, which is an exact solution to the Maxwell's equations. It includes both the near-field and the propagation terms. The second exact equation is Eq. (2) for the angular spectrum representation. Hence, the theory is valid nonparaxially.

We also use the Lorenz–Mie scattering theory, see Appendix A. As described in Sections 3 and 4, these concepts are combined to result in Eqs. (9) and (10) for the forthcoming computer calculation. In Section 6, we study the wavelength decorrelation of speckle in OMG. Our computer simulation of the propagating through OMG followed by optical metrology in the space-invariant 4 F system is seen to be in excellent agreement with actual laser experiments. Details of the experiment setup can be found in Section 5. The internal features of an opal glass are derived from the procedure described in Section 6 and summarized in Tables 1 and 2. For flashed opal glass, a new result for the relative index of the spherical scatterers is found to be $n_r = 1.009$. In Section 7 we describe the first-order statistics of the speckle intensity in OMG diffusers of different thicknesses. These results provide a second test of the optical metrology system as well as the computer simulation. They are in excellent agreement with the Rician density.

APPENDIX A: SCATTERING FROM A SPHERE

This section gives a brief overview of the scattering theory from Kerker [21]. Herein, we assume harmonic time dependence by $\exp(i\omega t)$. A dielectric sphere with a refractive index of m_1 and a radius, a, smaller than a wavelength is illuminated by an electromagnetic field in a medium with an index of m_2 as in Fig. 4. We know from Lorenz–Mie theory that the Hertz–Debye potentials are solutions of the homogeneous wave equation which can be solved by the method of separation of the variables. By using the boundary conditions that the tangential components of $\mathbf{E}$ and $\mathbf{H}$ be continuous across the spherical surface $r = a$, one can obtain the expression of the scattered wave,

$$r\pi_1^s = -\frac{1}{k_2^2}\sum_{n=1}^{\infty} i^{n-1}\frac{2n+1}{n(n+1)}a_n\zeta_n(k_2 r)P_n^{(1)}(\cos\theta)\cos(\phi), \tag{A1}$$

$$r\pi_2^s = -\frac{1}{k_2^2}\sum_{n=1}^{\infty} i^{n-1}\frac{2n+1}{n(n+1)}b_n\zeta_n(k_2 r)P_n^{(1)}(\cos\theta)\sin(\phi), \tag{A2}$$

where θ is measured from the scattering direction to the z axis, ϕ is the angle between the projected field onto the x–y plane and the y axis, ζ_n is the Hankel function, $P_n^{(1)}$ is the Legendre function of the first kind, $k_2 = m_2 k_0$, m_2 is the refractive index of the medium, $k_0 = 2\pi/\lambda_0$ is the propagation constant in free space, λ_0 is the wavelength *in vacuo*, and $r = (x^2 + y^2 + z^2)^{1/2}$. The coefficients a_n and b_n are given by

$$a_n = \frac{S_n(\alpha)S_n'(\beta) - n_r S_n(\beta)S_n'(\alpha)}{\zeta_n(\alpha)S_n'(\beta) - n_r S_n(\beta)\zeta_n'(\alpha)}, \tag{A3}$$

$$b_n = \frac{n_r S_n(\alpha)S_n'(\beta) - S_n(\beta)S_n'(\alpha)}{n_r\zeta_n(\alpha)S_n'(\beta) - S_n(\beta)\zeta_n'(\alpha)}, \tag{A4}$$

where S_n is the Ricatti–Bessel function, $\alpha = 2\pi m_2 a/\lambda_0$, a is the sphere radius, $\beta = n_r\alpha$, and $n_r = m_1/m_2$ is the refractive index of the particle relative to that of the medium. The addition of a prime to the Ricatti–Bessel functions denotes differentiation with respect to their arguments.

When α and n_r are sufficiently small, the term containing a_1 becomes the leading term in the expressions for the amplitude functions. Consider the scattered field at distances sufficiently far from the particles so that $k_2 r \gg n$, where n is the order of the Ricatti–Bessel function and $n = 1$ for small α and n_r; the radial components E_r and H_r fall off quickly so that they may be neglected, and the final result, with $P_n^{(1)}(\cos\theta) = \sin(\theta)$, becomes

$$E_\phi = k_2^2 a^3\frac{n_r^2 - 1}{n_r^2 + 2}E_{\text{inc}}\frac{\exp(-ik_2 r)}{r}\sin\phi, \tag{A5}$$

$$E_\theta = k_2^2 a^3\frac{n_r^2 - 1}{n_r^2 + 2}E_{\text{inc}}\frac{\exp(-ik_2 r)}{r}\cos\theta\cos\phi, \tag{A6}$$

where E_{inc} is the incident field on the sphere, $r = (x^2 + y^2 + z^2)^{(1/2)}$. These two fields can be represented with one expression, i.e.,

$$\mathbf{E}_\psi = E_\phi\hat{\phi} + E_\theta\hat{\theta} = k_2^2 a^3\frac{n_r^2 - 1}{n_r^2 + 2}E_{\text{inc}}\frac{\exp(-ik_2 r)}{r}\sin\psi\hat{\psi}, \tag{A7}$$

where ψ is the angle measured from the scattering direction to the dipole radiation direction. This result is given in the main text as Eq. (3).

ACKNOWLEDGMENTS

The authors acknowledge helpful discussions with Nicholas Bigelow, Richard Hammond, Richard D. S. Melville, Stojan Radic, and Robert C. Waag. The research is supported in part by the U.S. Army Research Office (Physics Division).

REFERENCES

1. J. C. Dainty, *Laser Speckle and Related Phenomena* (Springer-Verlag, 1984).
2. J. W. Goodman, *Speckle Phenomena in Optics* (Roberts, 2007).
3. N. George and D. C. Sinclair, eds., feature issue "Speckle in Optics," J. Opt. Soc. Am. **66**(11), (1976).
4. N. George, "Lensless electronic imaging," Opt. Commun. **133**, 22–26 (1997).
5. N. George, A. Jain, and R. D. S. Melville Jr., "Experiments on the space and wavelength dependence of speckle," Appl. Phys. **7**, 157–169 (1975).
6. R. D. S. Melville, "The thick diffuser," Ph.D. thesis (California Institute of Technology, 1975).
7. R. Alferness, "Analysis of optical propagation in thick holographic gratings," Appl. Phys. **7**, 29–33 (1975).
8. T. Stone and N. George, "Wavelength performance of holographic optical elements," Appl. Opt. **24**, 3797–3810 (1985).
9. D. W. Diehl and N. George, "Holographic interference filters for infrared communications," Appl. Opt. **42**, 1203–1210 (2003).
10. Wave Train Software, MZA Associates Corp., http://www.mza.com.
11. J. W. Goodman, "Statistical properties of laser sparkle patterns," Tech. Rep. T. R. 2303-1 (Stanford Electronics Laboratories, 1963).
12. N. George and A. Jain, "Space and wavelength dependence of speckle intensity," Appl. Phys. **4**, 201–212 (1974).
13. L. G. Shirley and N. George, "Speckle from a cascade of two thin diffusers," J. Opt. Soc. Am. A **6**, 765–781 (1989).
14. D. L. Fried, "Laser eye safety: the implications of ordinary speckle statistics and of speckled-speckle statistics," J. Opt. Soc. Am. **71**, 914–916 (1981).
15. D. J. Shertler and N. George, "Uniform scattering patterns from grating diffuser cascades for display applications," Appl. Opt. **38**, 291–303 (1999).
16. L. G. Shirley and P. A. Lo, "Bispectral analysis of the wavelength dependence of speckle: remote sensing of object shape," J. Opt. Soc. Am. A **11**, 1025–1046 (1994).
17. N. Chang and N. George, "Speckle in the 4 F optical system," Appl. Opt. **47**, A13–A20 (2008).
18. K. G. Budden, *The Wave-Guide Mode Theory of Wave Propagation* (Logos, 1961).
19. P. C. Clemmow, *The Plane Wave Spectrum Representation of Electromagnetic Fields* (Pergamon, 1966).
20. H. C. van de Hulst, *Light Scattering by Small Particles* (Dover, 1981).
21. M. Kerker, *The Scattering of Light and Other Electromagnetic Radiation* (Academic, 1969).
22. N. Chang, "Speckle in a thick diffuser," Ph.D. thesis (University of Rochester, 2009).
23. A. Papoulis and S. U. Pillai, *Probability, Random Variables and Stochastic Processes with Errata Sheet*, 4th ed. (McGraw-Hill, 2002).

Optical imaging with phase-coded aperture

Wanli Chi and Nicholas George
The Institute of Optics, University of Rochester, Rochester, NY, 14627
chiw@optics.rochester.edu

Abstract: Experimental results are shown for an integrated computational imaging system with a phase-coded aperture. A spatial light modulator works as a phase screen that diffracts light from a point object into a uniformly redundant array. Excellent imaging results are achieved after correlation processing. The system has the same depth of field as a diffraction-limited lens. Potential applications are discussed.

OCIS codes: (110.0110) Imaging systems; (110.7348) Wavefront encoding; (110.1758) Computational imaging; (100.0100) Image processing.

References and links

1. W. Chi and N. George, "Phase-coded aperture for optical imaging," Opt. Commun. **282,** 2110-2117 (2009).
2. R.H. Dicke, "Scatter-hole cameras for X-rays and Gamma rays," Astrophys. J. **153,** L101 (1968).
3. E.E. Fenimore and T.M. Cannon, "Coded aperture imaging with uniformly redundant array," Appl. Opt. **17,** 337-347 (1978).
4. R.G. Simpson and H.H. Barrett, "Coded aperture imaging," in *Imaging in Diagnositc Medicine*, S. Nudel-man, (Ed.) (Plenum, New York, 1980).
5. F.R. Fienup, "Phase retrieval algorithms: a comparison," Appl. Opt. **21,** 2758-2769 (1982).
6. J.C. Dainty and F.R. Fienup, "Phase retrieval and image reconstruction for astronomy," in *Image Recovery: Theory and Application*, H. Stark, (Ed.) (Academic, Florida, 1987).
7. *Adaptive Coded Aperture Imaging and Non-imaging Sensors*, D.P. Casasent and T. Clark (Ed.), Proc. SPIE **6714** (2007).
8. *Adaptive Coded Aperture Imaging and Non-imaging Sensors II*, D.P. Casasent and S. Rogers (Ed.), Proc. SPIE **7096** (2008).

1. Introduction

The advances in computer speed and image processing make possible optical imaging without conventional lenses. In this paper we report experimental studies of a previously described incoherent imaging system without focusing lens [?]. In our approach the optical coded aperture imager consists of a phase plate followed by a detector array, as shown in Fig. ??. It represents a novel extension of the X-ray coded aperture system [?, ?, ?] to optical wavelengths, where we have applied phase retrieval concepts [?, ?] to design the phase plate whose diffraction pattern is a bandlimited uniformly redundant array (bl-URA). By this design means, we find a point spread function of the optical part that is a bandlimited uniformly redundant array. Thereafter, a correlation processing is applied to image on the detector to recover the object. In Sec. ?? a general theory of linear integrated imaging is presented. Sections ?? and ?? contains descriptions of the experimental setup and results of the optical coded aperture system. Section ?? includes conclusion and potential applications of this new imager.

2. Linear system theory on integrated imaging

Consider a shift-invariant linear optical imaging system, the image $i(x,y)$ can be expressed as a function of object $o(x,y)$ and point spread function (PSF) $h(x,y)$ in the following convolution form,

$$i(x,y) = \int o(\xi,\eta)h(x-\xi,y-\eta)d\xi d\eta. \tag{1}$$

Herein, we would like to assert that Eq. (??) can be considered as a general form for optical imaging where $h(x,y)$ can be any realizable function. More specifically, $h(x,y)$ need not be delta-like function for sharp imaging, as is seen below.

Assume there exists a linear shift invariant operator $L\{\bullet\}$ which, when applied to $h(x,y)$, yields the following result,

$$L\{h(x,y)\} = f_\delta(x,y) + g(x,y), \tag{2}$$

where $f_\delta(x,y)$ is a Dirac delta-like function, e.g., Airy disk function, it is spatially separated from function $g(x,y)$. Then we can add after the optical system a linear digital processing system by applying the optical image to the linear operator $L\{\bullet\}$, the result is

$$L\{i(x,y)\} = \int o(\xi,\eta)f_\delta(x-\xi,y-\eta)d\xi d\eta + \int o(\xi,\eta)g(x-\xi,y-\eta)d\xi d\eta. \tag{3}$$

The first term in Eq. (??) is a recovered sharp image, and $f_\delta(x,y)$ is the PSF of the overall system including both optics and image processing.

In the design process of an integrated imaging system, an important step is to find function $h(x,y)$ which i) is realizable with optical system and ii) can transform to a delta-like function under some linear operators. In application, the optical system generally has further constraints on optical material, size, number of elements etc. so the function must be further required to be realizable with optical system satisfying these constraints.

The linear operator $L\{\bullet\}$ can take many forms. For example, it can be identity operator, differential operator, correlation operator.

The simplest example of integrated imaging is a diffraction limited lens with full circular aperture, where $h(x,y)$ is a delta-like Airy disk, and $L\{\bullet\}$ is an identity operator. Another example is an integrated system where the image is blurred by lens aberrations and a subsequent linear deconvolution algorithm is applied to the intermediate image to yield a sharp picture.

In an earlier paper [?] we presented one more example to expand linear imaging system design possibilities, in which $h(x,y)$ is a bl-URA, and linear operator $L\{\bullet\}$ is a correlation operator. The main purpose of this article is to present experimental results of such system we call phase coded aperture imaging system.

Briefly, the phase coded aperture optical imager consists of a phase plate followed by a detector array. For a point source, the diffraction pattern caused by the phase plate is the PSF of the optical system. It is a bl-URA calculated in the following,

$$h(x,y) = t(x,y) * b(x,y), \tag{4}$$

where * means convolution, $t(x,y)$ is a uniformly redundant array (URA) and $b(x,y)$ is a bandlimited function. A phase retrieval method is used to calculate the phase function that yields such a bl-URA. Linear operator is defined as

$$L\{h(x,y)\} = h(x,y) \otimes t_R(x,y), \tag{5}$$

where $\otimes$ is a correlation operator, $t_R(x,y)$ is a repeated URA with mean removed, i.e.,

$$t_R(x,y) = \int [t(x-\xi, y-\eta) - \bar{t}]\mathrm{comb}(\xi/D_x, \eta/D_y)d\xi d\eta, \tag{6}$$

in which D_x , D_y are the sizes of URA in X and Y directions, respectively; and $\bar{t}$ is the mean value of URA $t(x,y)$.

Combining Eqs. (??)-(??) yields the following result,

$$L\{h(x,y)\} = C\mathrm{comb}(x/D_x, y/D_y) * \Lambda(x/\Delta_x, y/\Delta_y) * b(x,y), \tag{7}$$

where $\Lambda(\bullet)$ is a triangle function; and Δ_x, Δ_y are the pixel size of URA in X and Y directions, respectively. Eq. (??) consists of an array of delta-like functions as

$$f_\delta(x,y) = \Lambda(x/\Delta_x, y/\Delta_y) * b(x,y). \tag{8}$$

So by correlating $i(x,y)$ with $t_R(x,y)$, we can recover a sharp image with overall PSF of the including image processing by linear operator $L\{\bullet\}$ as $f_\delta(x,y)$ shown in Eq. (??).

3. Experimental setup

The experimental setup is shown in Fig. ??. The object is illuminated by spatially incoherent light with a single wavelength of 633nm. (This is realized by a He-Ne beam passing through a rotating diffuser). The incoming beam passes a beam splitter and then is reflected by a spatial light modulator phase screen (Holoeye HEO1080P). The phase profile of the reflected beam is modified by an extra phase delay from 0 to 2π, as shown in Fig. 1, where black means 0 and white means 2π. This phase modulated wave is then reflected by the beam splitter and received by a detector array. The phase profile is calculated using Fresnel domain phase retrieval method. Parameters of the setup are the following. the spatial modulator has a pixel size of $8\mu m$ and fill factor of 85% ; the detector array has a pixel size of $13\mu m$ and pixel number of 1024×1024; the distance between object plane and phase screen is $1275mm$; the equivalent free space distance between phase screen and detector array is $204.4mm$; and the square aperture in front of phase screen has a dimension of $5.5mm \times 5.5mm$.

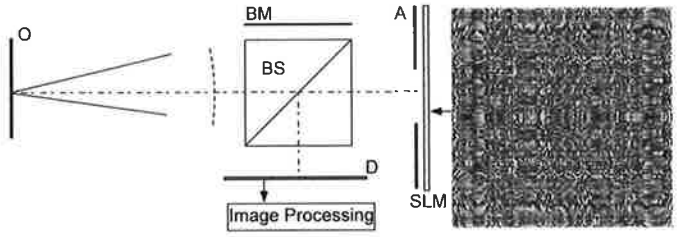

Fig. 1. The experimental setup for the coded aperture imaging system. O: Object; BS: Beam Splitter; A: Aperture; SLM: Spatial light modulator; D: Detector array; BM: Blackened metal plate.

4. Experimental results

The linear operator processing steps are illustrated in Fig. ??. A point source located at a distance of $1275mm$ is imaged by the coded aperture system shown in Fig. ??. The intermediate image is cross correlated with a repeated URA and the central portion of the correlation picture is the recovery of the point source image. We mention that the recovered image is half the size

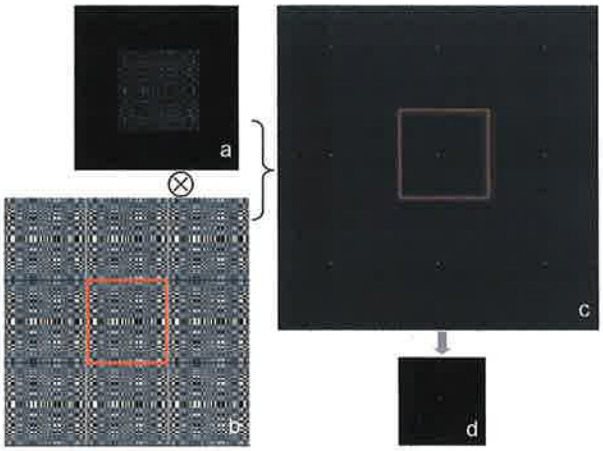

Fig. 2. Illustration of the correlation image processing using a point object located at a distance of 1275*mm*. (a) the intermediate image or bl-URA at the detector, D in Fig. ??, (also refer to Fig. ??a); (b) the repeated URA pattern; (c) the result of image cross-correlation between (a) and (b); (d) recovery or the center section of (c).

of the intermediate image. This constrains the maximum size of an object (field of view) that can be faithfully imaged. The recovered point is the overall point spread function of the coded aperture imaging system including optics and digital processing.

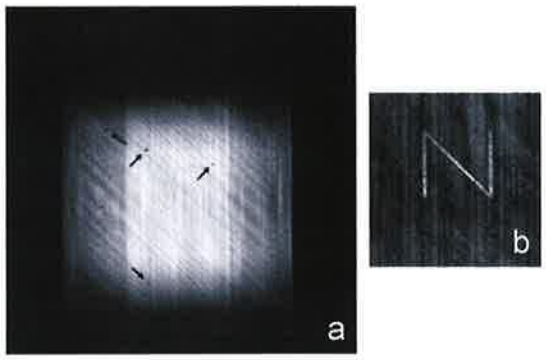

Fig. 3. Experimental result with a letter object located at a distance of 1275*mm*. (a) intermediate image (the arrows indicate regions where CCD pixel response is low. All of these are not labeled); (b) image recovery result by correlation processing. The linear size of recovery is about half the size of the intermediate image.

Fig. ?? shows the imaging results for a letter object located at a distance of 1275*mm*. The intermediate image in Fig. ??a is processed linearly using the same correlation method, and the recovery result is shown in Fig. ??b. In Fig. ??a we observe a general feature of the intermediate image for an extended object. The intermediate image has an overall envelop shape that is bright in the center and intensity slowly drops to zero at the edge. There are also small scale intensity variations which reflect the details of object. In Fig. ??a one can see regions of the CCD where

detector response is low. This causes a big intensity drop (specks in image, some indicated with arrow) compared to the envelop. Despite this, a good recovery is still achieved as shown in Fig. ??b. In image recovery, one can simply change these low values to bigger ones such that the envelop of the intermediate image is smooth. The exact value of these small regions has little effect on the recovery result.

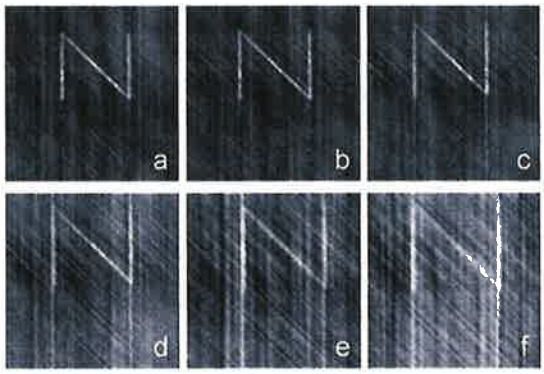

Fig. 4. Image recovery result for the object located at different distances. The same URA pattern as shown in Fig. ?? is used for correlation processing. The object is located at a distance of (a) 1275*mm*; (b) 1225*mm*; (c) 1175*mm*; (d) 1100*mm*; (e) 1050*mm*; (f) 1000*mm*. The corresponding defocus amounts are 0, $\lambda/4$, $\lambda/2$, λ, 1.3λ and 1.6λ, respectively.

Figure ?? shows the recovery result when the object distance is changed over a range from 1275*mm* to 1000*mm*. This corresponds to defocus amounts up to 1.6λ. In the recovery the same repeated URA pattern is used for correlation processing of all the intermediate images at different distances. The depth of field of the coded aperture system is similar to that of a diffraction limited lens. i.e., the images within $\pm\lambda/4$ defocus are considered good quality. However, the defocused image quality degradation takes a different form as compared with that for a conventional diffraction limited lens. For a coded aperture system, if there exists large defocus, then one observes the repetition of objects over the whole scene. The intensity of these repetitions increases as the defocus amount is larger.

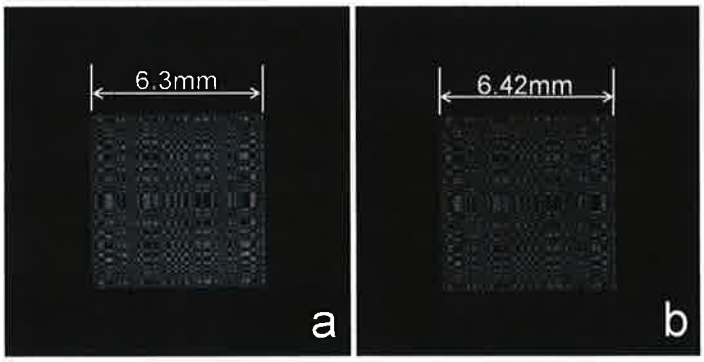

Fig. 5. The intermediate images for a point object located at (a) 1275*mm* and (b) 1100*mm*.

In order to understand the cause of artifacts due to different object distances, we showed in Fig. ?? the point spread functions of the optical system for two object distances: 1275*mm* and 1100mm. The distance of 1100mm corresponds to a defocus of λ . Two differences are noticed: (i) the fine details of the point spread function are different; (ii) the full sizes of the point spread functions are different. The size of the PSF for a focused distance is 6.3*mm*, while the size of the defocused PSF is 6.42*mm*. (The sizes of PSFs are found by correlating the PSFs with repeated URA of different scales. The size of the URA which yields the best recovered point object is considered as the size of the PSF of the optical system.)

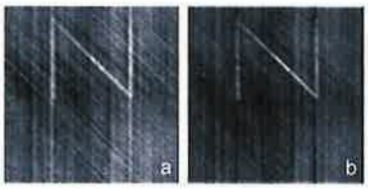

Fig. 6. Image recovery result for object located at 1100mm using repeated URA pattern of different scales. The size of URA array is (a) 6.3*mm*, (b) 6.42*mm*.

A much better recovery can be obtained for a defocused object if a correct size URA is used in recovery. This is shown in Fig. ??, where the URA with size of 6.42*mm* is used to recover the object located at the defocused distance of 1100*mm*. We see a significant improvement of image quality.

5. Concluding remarks

In literature there are many efforts to extend X-ray coded aperture system to optical imaging [?, ?]. In a approach based on linear system theory, we have described an integrated computational imaging system in two parts: the optical system followed by a linear operator. The linear operator transforms PSF of the optical system into a delta-like function, Eq. (??). For the illustration of the coded aperture in Eq. (??), the linear operator is a correlation operation. In correlation processing it is important to set the size of URA the same as that of the PSF of the optical imager. Experimental results are presented that prove the imaging capability of this coded aperture system. Good imaging is obtained using a CCD with non-uniform pixel response. The depth of field of the coded aperture system is the same as that of diffraction limited lens. i.e., $\pm\lambda/4$ defocus is acceptable.

For objects closer than the focused plane, the PSF array of coded aperture system is larger. While not shown in the paper, the PSF size is smaller if the object is farther away from the plane of focus. So one can distinguish the sign of defocus for a coded aperture system. Furthermore, the defocus amount can be found accurately by correlating the intermediate image (point or extended) with repeated URA of different scales. So besides the imaging application, the coded aperture system can be used in a ranging application.

Since there is no focusing element in the system, a bright laser beam in the object space will not form a point at the detector plane, instead light is diffracted over a large area of the detector. This provides damage protection for the detector. Unlike infrared imaging with lenses, there is no light reflected back to the object field for this coded aperture system; hence, this makes it useful in some applications.

This research is supported in part by the Army Research Office.

US 20110085051A1

(19) **United States**

(12) **Patent Application Publication**

(10) **Pub. No.: US 2011/0085051 A1**

(43) **Pub. Date: Apr. 14, 2011**

Chi et al.

(54) **OPTICAL ELEMENT, DEVICE, METHOD, AND APPLICATIONS**

(75) Inventors: **Wanli Chi**, Rochester, NY (US); **Nicholas George**, Pittsford, NY (US)

(73) Assignee: **UNIVERSITY OF ROCHESTER**, Rochester, NY (US)

(21) Appl. No.: **12/898,060**

(22) Filed: **Oct. 5, 2010**

Related U.S. Application Data

(60) Provisional application No. 61/250,224, filed on Oct. 9, 2009.

Publication Classification

(51) **Int. Cl.**
H04N 5/228 (2006.01)
G02F 1/35 (2006.01)

(52) **U.S. Cl.** **348/222.1**; 359/326; 348/E05.031

(57) **ABSTRACT**

A novel phase-coded aperture, associated imaging system, and design method is disclosed. The optical imaging system includes a coded-aperture followed optically by a detector array and includes an image processor. A diffraction pattern in the form of a band-limited uniformly redundant array is formed on the detector array when focusable radiation from a point source in object space is modulation by the transmission function of the coded-aperture. Since diffraction effects cannot be ignored in the optical regime, an iterative phase retrieval method is used to calculate the phase-coded aperture transmission function. Correlation type processing can be applied for the image recovery.

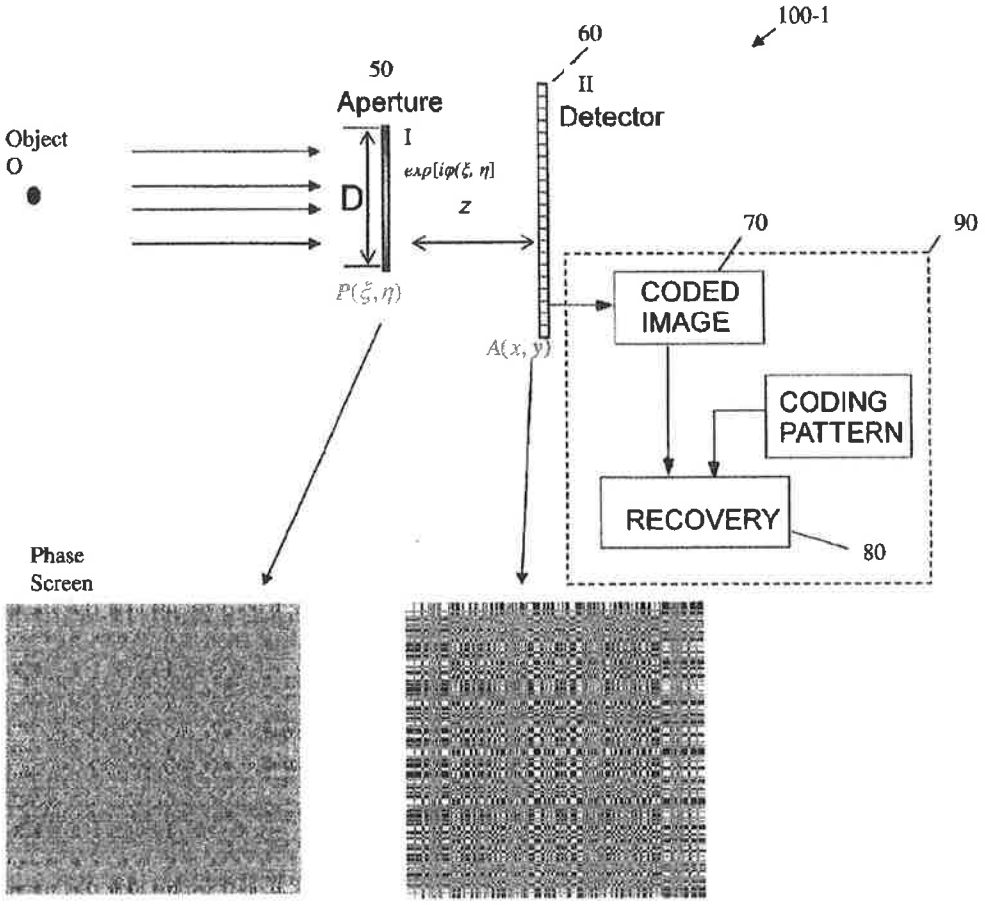

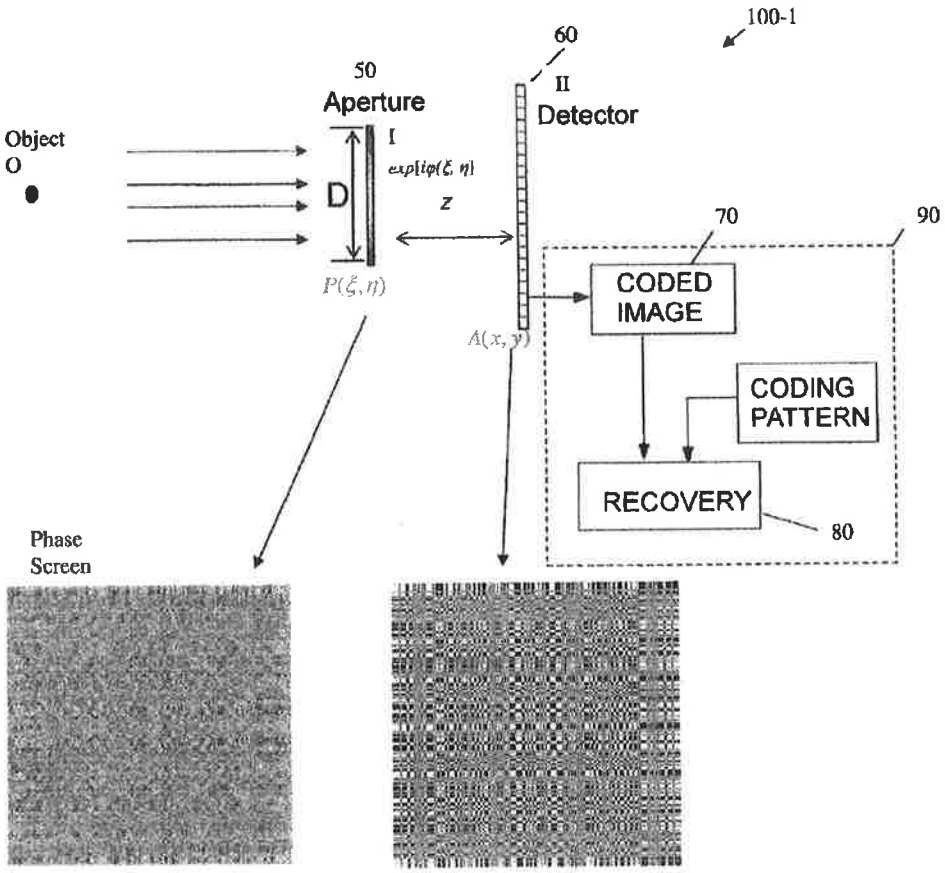
100-1
60
II
Detector
50
Aperture
I
Object
O
D
$\exp[i\varphi(\xi,\eta)]$
z
$P(\xi,\eta)$
$A(x,y)$
70
90
CODED IMAGE
CODING PATTERN
RECOVERY
80
Phase Screen

FIG. 1A

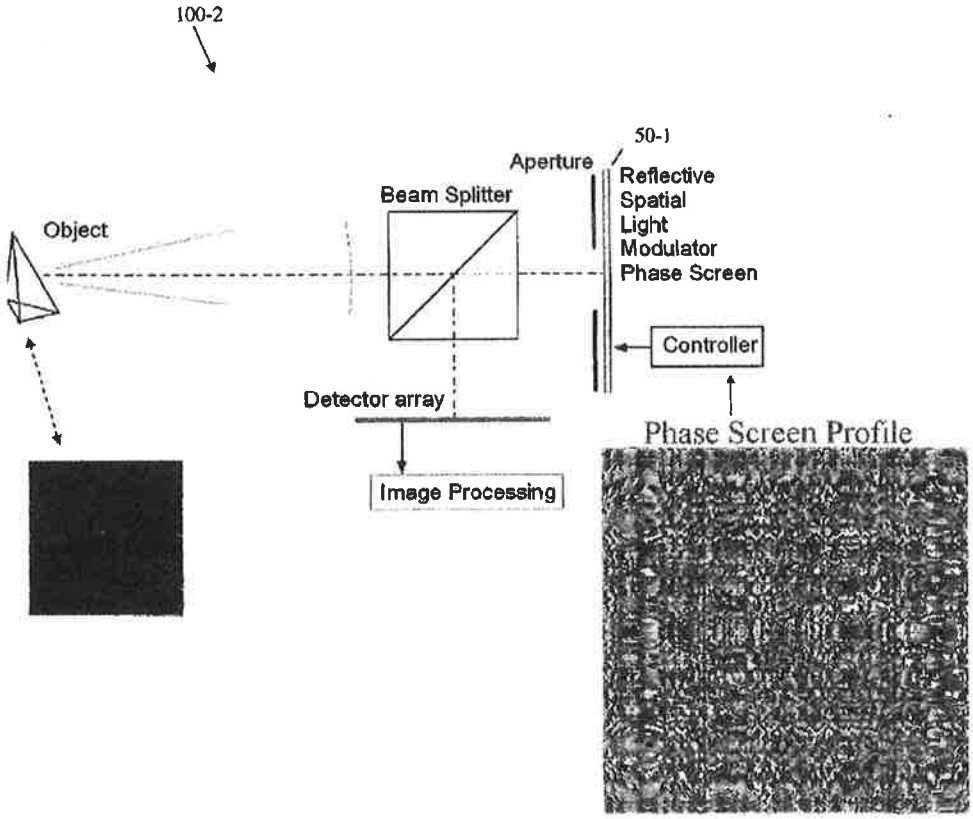
100-2
50-1
Aperture
Reflective
Spatial
Light
Modulator
Phase Screen
Beam Splitter
Object
Controller
Detector array
Phase Screen Profile
Image Processing

FIG. 1B

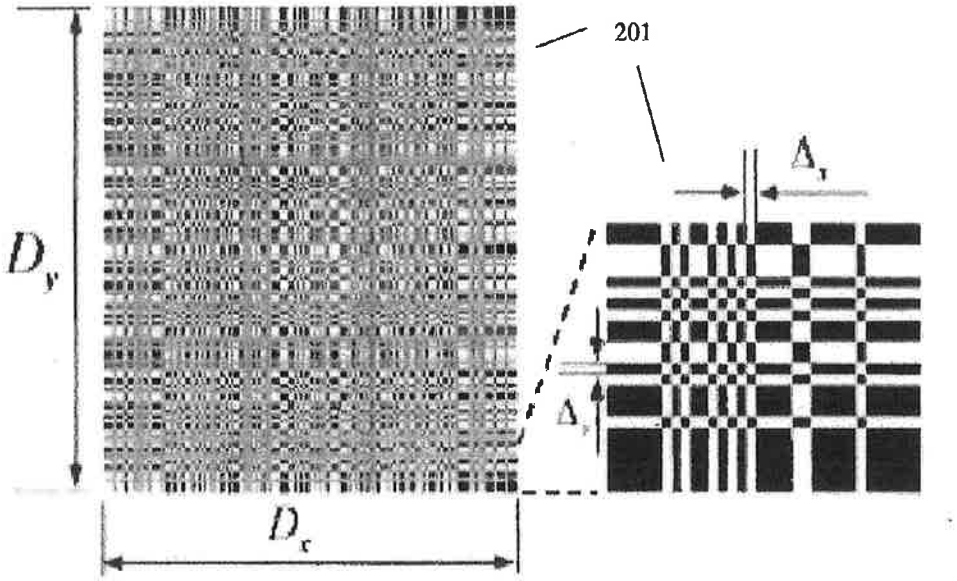

FIG. 2

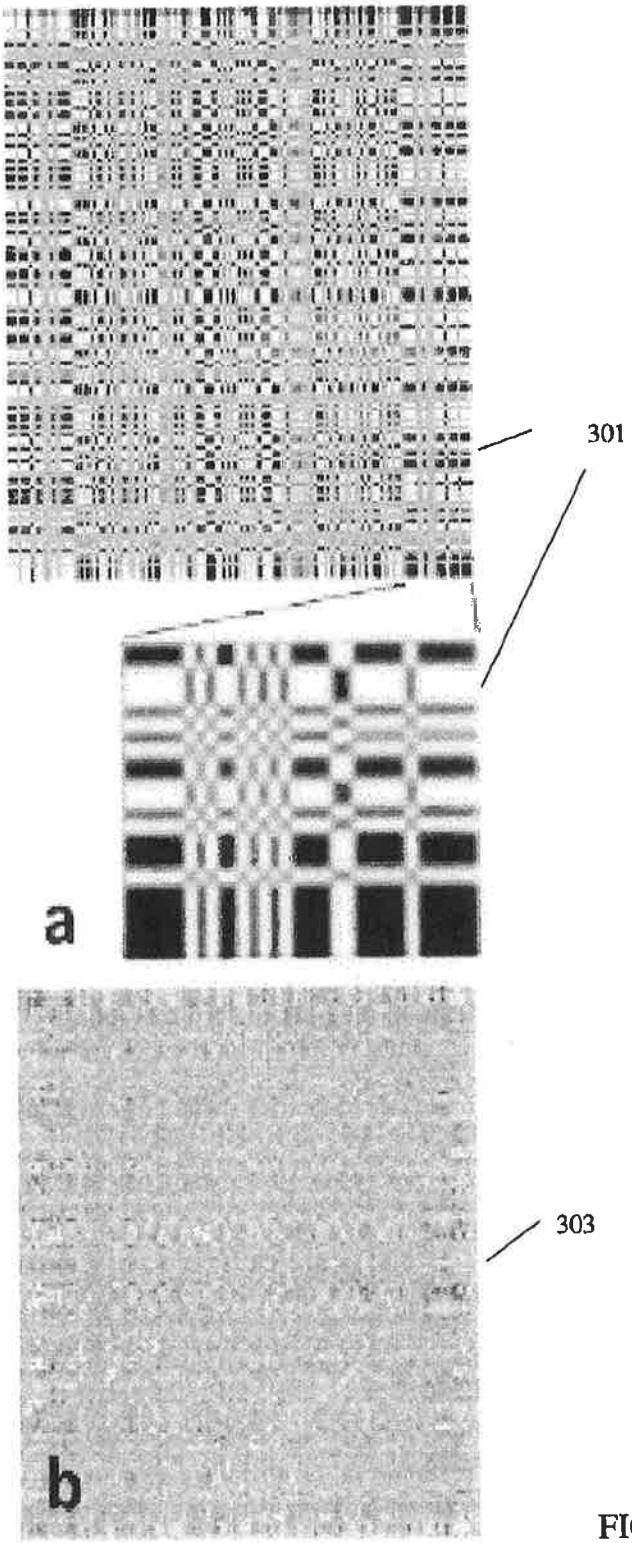

FIG. 3

(a)

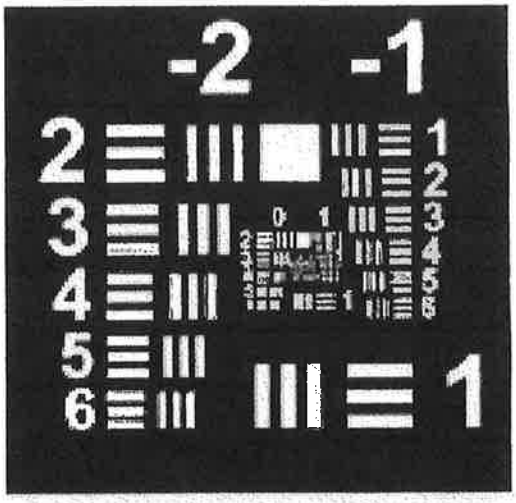

(b)

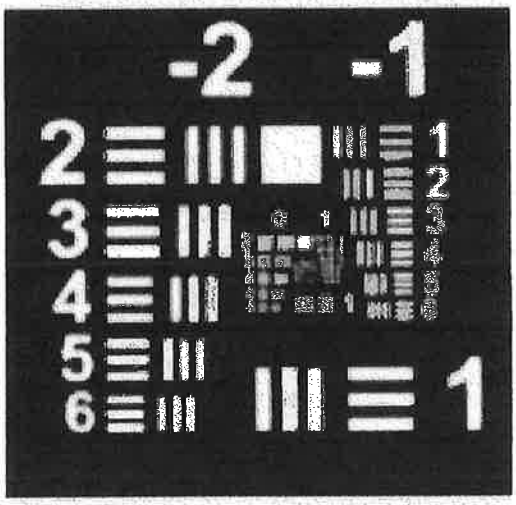

(c)

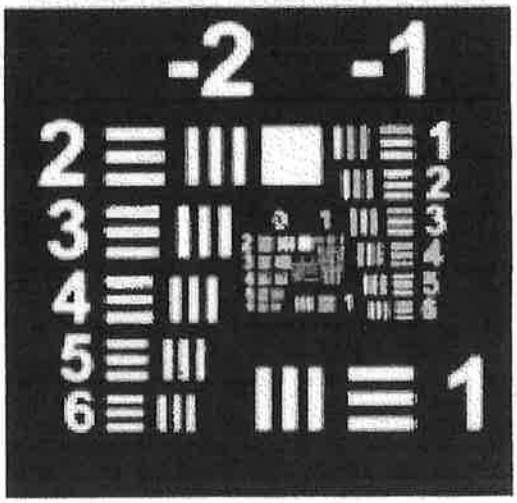

FIG. 4

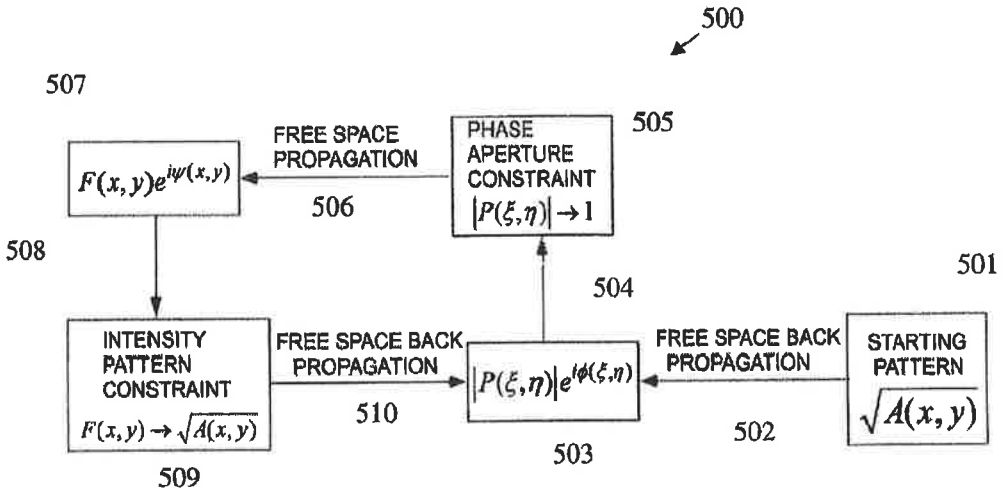
500
507
$F(x,y)e^{i\psi(x,y)}$
FREE SPACE PROPAGATION
506
PHASE APERTURE CONSTRAINT
$|P(\xi,\eta)| \rightarrow 1$
505
508
504
501
INTENSITY PATTERN CONSTRAINT
$F(x,y) \rightarrow \sqrt{A(x,y)}$
509
FREE SPACE BACK PROPAGATION
510
$|P(\xi,\eta)|e^{i\phi(\xi,\eta)}$
503
FREE SPACE BACK PROPAGATION
502
STARTING PATTERN
$\sqrt{A(x,y)}$

FIG. 5

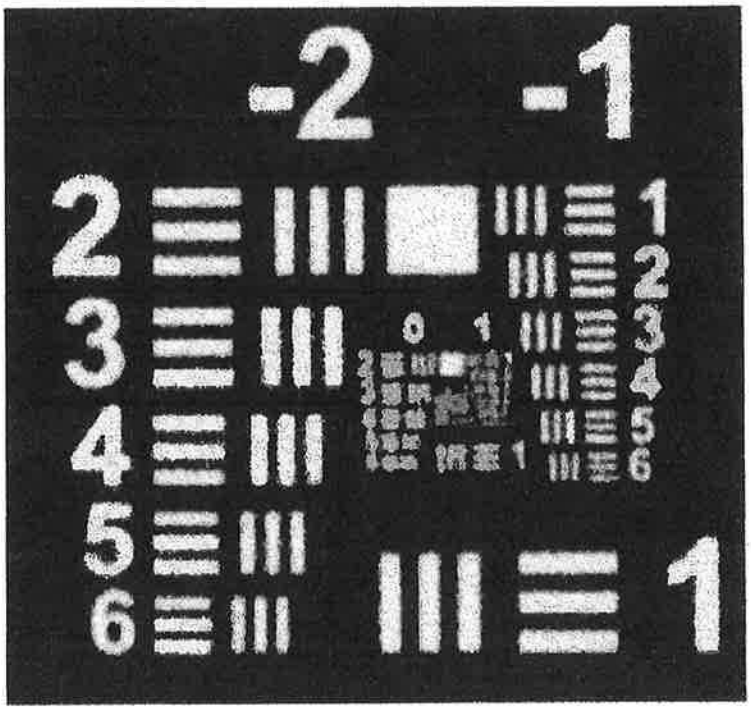

FIG. 6

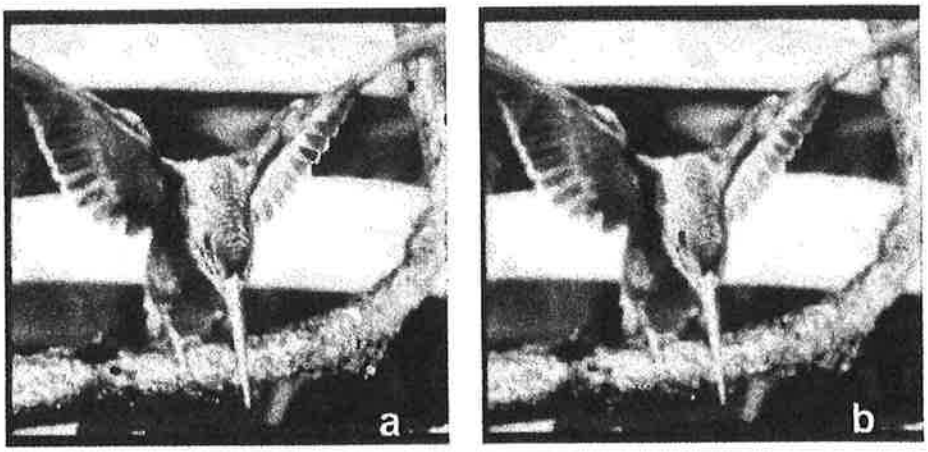

FIG. 7

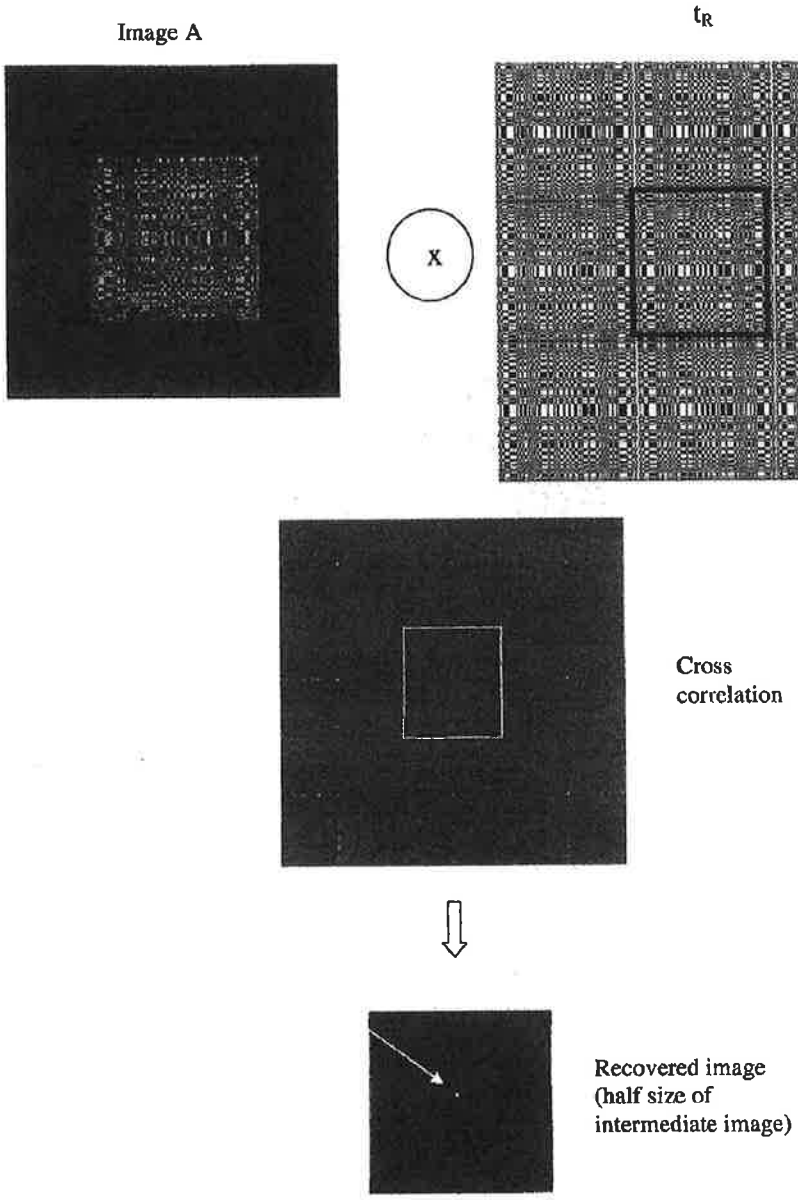
Image A
t_R
X
Cross correlation
Recovered image (half size of intermediate image)

FIG. 8

OPTICAL ELEMENT, DEVICE, METHOD, AND APPLICATIONS

CROSS-REFERENCE TO RELATED APPLICATIONS

[0001] This application claims priority to U.S. provisional Patent Application Ser. No. 61/250,224 filed on Oct. 9, 2009, the content of which is incorporated herein by reference in its entirety.

FEDERALLY SPONSORED RESEARCH

[0002] This invention was made with government support from the U.S. Army Research Office under contract number W911NF-09-1-0425. The government has rights in this invention.

BACKGROUND OF THE INVENTION

[0003] 1. Field of the Invention

[0004] Embodiments of the present invention relate generally to coded aperture optics, systems, and methods operable with and pertaining to focusable radiation and, more particularly, to an optical element for generating a band-limited uniformly redundant array (bl-URA) from light within a spectrum of focusable radiation, an optical imaging device incorporating the optical element, and a method for determining a transmission function $P(\xi, \eta)$ for an optical element that will generate a desired intensity pattern A(x,y) on a detector from light within a spectrum of focusable radiation from a point on an object.

[0005] 2. Technical Background

[0006] Conventional refractive and reflective optical components (e.g., lenses, mirrors) are not useful for imaging nonfocusable radiation such as, e.g., γ-rays and X-rays. The comparatively shorter wavelengths simply do not refract in the more suitable manner of comparatively longer wavelengths in, e.g., the visible spectrum. However, a simple pinhole camera can be used as an imaging device for γ-rays and X-rays because diffraction effects are minimal, in contrast to those effects in the UV to sub-millimeter and, particularly the visible, regime, which cannot be ignored.

[0007] The concept of using a coded aperture to image nonfocusable radiation was first introduced by L. Mertz and N. Young, Proc. Conf. Optical Instruments and Techniques, London 1961, p. 305 and later implemented with random arrays by R. H. Dicke, Astrophys. J. 153, L 101 (1968) and J. G. Ables, Proc. Astron. Soc. Aust. 4, 172 (1968); see also U.S. Pat. No. 3,700,895). In the formulation by Dicke and Ables, the opening of a single pinhole camera was replaced by many randomly arranged pinholes collectively known as the aperture. Each point of a self-luminous object projected a shadow of the aperture on a recorded image plane (picture). Subsequent correlation processing of the picture yielded a reconstructed image that resembled the original self-luminous objects.

[0008] Uniformly redundant arrays (URAs) used for coded aperture imaging were first disclosed by Edward E. Fenimore et al. in U.S. Pat. No. 4,209,780 as well as in Applied Optics, 17, p. 337, Feb. 1, 1980, Applied Optics, 17, p. 3562, Nov. 16, 1978, Applied Optics, 18, p. 945, Apr. 1, 1979, and in Los Alamos Scientific Laboratory Mini-Review, LASL-78-102, January 1979. U.S. Pat. Nos. 4,360,797 and 4,389,633 disclose further information about coded aperture imaging.

[0009] A variety of coded aperture systems pertaining to the optical regime are reported in David P. Casasent, Timothy Clark (Ed.), Proc. SPIE 6714 (2007); David P. Casasent, Stanley Rogers (Ed.), Proc. SPIE 7096 (2008); Keith Lewis, Proc. SPIE 6714 (2007) 671402; and Tim Clark, Esko Jaska, Proc. SPIE 6714 (2007) 671403.

[0010] The inventors have recognized the many benefits and advantages realizable by a coded aperture optics operable over the focusable radiation spectrum.

SUMMARY

[0011] An embodiment of the invention is an optical element for generating a band-limited uniformly redundant array (bl-URA) from light within a spectrum of focusable radiation. The embodiment includes an optical element characterized by a light transmission function, $P(\xi, \eta)$, such that light within the spectrum of focusable radiation incident on the optical element from a point location in an object space of the optical element is optically transformed by $P(\xi, \eta)$ into a band-limited uniformly redundant array (bl-URA), A(x,y), in an image space of the optical element. The optical element may consist of only a single optical element. The optical element may have a surface region that is at least partially transmissive for the light within the spectrum of focusable radiation. The optical element may have a surface region that is at least partially reflective for the light within the spectrum of focusable radiation. The optical element may be an amplitude-only aperture. The optical element may be a phase-only aperture. The optical element may be a combination amplitude/phase aperture. The optical element may consist of a single refractive optical component. The optical element may consist of a plurality of refractive optical components. The optical element may comprise a refractive optical component and a phase aperture. The optical element may be a programmable spatial light modulator. According to the embodiment, A(x,y) is a real, non-negative, band-limited, uniformly redundant array (bl-URA). The spectrum of focusable radiation is in a range from ultraviolet to sub-millimeter wavelengths. The spectrum of focusable radiation may be in a range from visible to infrared wavelengths.

[0012] An embodiment of the invention is an optical imaging device. The optical imaging device includes an optical element characterized by a light transmission function, $P(\xi, \eta)$, such that light within the spectrum of focusable radiation incident on the optical element from a point location in an object space of the optical element is optically transformed by $P(\xi, \eta)$ into a band-limited uniformly redundant array (bl-URA), A(x,y), in an image space of the optical element; a detector disposed in the image space such that the bl-URA is formed on the detector; and an image processor adapted to recover an image of an object from the detected bl-URA. According to the embodiment, A(x,y) is a real, non-negative, band-limited, uniformly redundant array (bl-URA).

[0013] An embodiment of the invention is a method for determining a transmission function $P(\xi, \eta)$ for an optical element that will generate a desired intensity pattern A(x,y) on a detector from light within a spectrum of focusable radiation from a point on an object. The method includes the steps of: determining a real, non-negative, band-limited uniformly redundant array, A(x,y), that will be generated on a detector by an optical element characterized by a transmission function $P(\xi, \eta)$, from light within the spectrum of focusable radiation from a point on the object; defining an electric field having an amplitude $E(x,y)=[A(x,y)]^{1/2}$; calculating the

transmission function $P(\xi, \eta)$ in a plane immediately adjacent a known position of the optical element by performing a free space back propagation, and denoting the transmission function $|P(\xi, \eta)|\exp[i\phi(\xi,\eta)]$; determining an electric field at a known detector plane location by performing a free space propagation, and denoting this electric field $F(x,y)\exp[i\psi(x, y)]$;

[0014] applying a detector plane intensity constraint by setting $F(x,y)\rightarrow[A(x,y)]^{1/2}$; performing another free space back propagation; and calculating the optical element transmission function $P(\xi, \eta)$ that will generate the desired intensity pattern A(x,y). According to an illustrative aspect in which the optical element is a phase-only element, the method includes the further steps of: setting an aperture constraint such that $|P(\xi, \eta)|$ is set to 1, after the step of calculating the transmission function $P(\xi, \eta)$; and repeating the steps of: calculating the transmission function $P(\xi, \eta)$ in a plane immediately adjacent a known position of the optical element by performing a free space back propagation, and denoting the transmission function $|P(\xi, \eta)|\exp[i\phi(\xi,\eta)]$; determining an electric field at a known detector plane location by performing a free space propagation, and denoting this electric field $F(x,y)\exp[i\psi(x,y)]$; applying a detector plane intensity constraint by setting $F(x,y)\rightarrow[A(x,y)]^{1/2}$; and performing another free space back propagation. According to another illustrative aspect in which the optical element is an amplitude-only element, the method includes the further steps of: setting an aperture constraint by setting $\phi(\xi, \eta)$ to 0, after the step of calculating the transmission function $P(\xi, \eta)$; and repeating the steps of: calculating the transmission function $P(\xi, \eta)$ in a plane immediately adjacent a known position of the optical element by performing a free space back propagation, and denoting the transmission function $|P(\xi, \eta)|\exp[i\phi(\xi,\eta)]$; determining an electric field at a known detector plane location by performing a free space propagation, and denoting this electric field $F(x,y)\exp[i\psi(x,y)]$; applying a detector plane intensity constraint by setting $F(x,y)\rightarrow[A(x, y)]^{1/2}$; and performing another free space back propagation.

[0015] Additional features and advantages of the invention will be set forth in the detailed description which follows, and in part will be readily apparent to those skilled in the art from that description or recognized by practicing the invention as described herein, including the detailed description which follows, the claims, as well as the appended drawings.

[0016] It is to be understood that both the foregoing general description and the following detailed description are merely exemplary of the invention, and are intended to provide an overview or framework for understanding the nature and character of the invention as it is claimed. The accompanying drawings are included to provide a further understanding of the invention, and are incorporated in and constitute a part of this specification. The drawings illustrate various embodiments of the invention, and together with the description serve to explain the principles and operation of the invention.

BRIEF DESCRIPTION OF THE DRAWINGS

[0017] FIG. **1A** shows a schematic diagram of a coded aperture imaging system in which the optical element is a transmission-type phase-only coded aperture, according to a non-limiting, illustrative embodiment of the invention; FIG. **1B** shows a schematic diagram of a coded aperture imaging system in which the optical element is a reflective spatial light modulator phase screen, according to an alternative, illustrative aspect of the invention;

[0018] FIG. **2** shows an exemplary uniformly redundant array (URA) as known in the art of X-ray imaging;

[0019] FIGS. **3**(*a, b*) show a digitally constructed point spread function (PSF) from the URA of FIG. **2** and the phase screen used to generate the PSF, respectively, according to an illustrative embodiment of the invention;

[0020] FIGS. **4**(*a,b,c*) show the imaging results of a coded aperture camera according to an illustrative aspect of he invention, specifically (a) the object; (b) the recovered image according to an illustrative aspect of the invention; and (c) a comparative image from a diffraction limited lens;

[0021] FIG. **5** is a flow chart diagram illustrating the steps of a phase-only screen design method according to a non-limiting, exemplary embodiment of the invention;

[0022] FIG. **6** shows a coded aperture system recovered image according to an illustrative aspect of the invention;

[0023] FIG. **7** shows simulated imaging results of a coded aperture system in the optical regime with a grey scale object; specifically, (a) a diffraction limited image and (b) a recovered image using a coded aperture system according to an exemplary aspect of the invention; and

[0024] FIG. **8** shows a point source object and image recovery using the system illustrated in FIG. **1B**, according to an illustrative embodiment of the invention.

DETAILED DESCRIPTION OF EMBODIMENTS OF THE INVENTION

[0025] Reference will now be made in detail to the present exemplary embodiments of the invention, non-limiting examples of which are illustrated in the accompanying drawings. Wherever possible, the same reference numbers will be used throughout the drawings to refer to the same or like parts.

[0026] As used herein, the term "focusable" radiation or light when used in conjunction with the embodied optical element for generating a band-limited uniformly redundant array (bl-URA), means electromagnetic radiation spanning the UV through IR spectrum, which can be focused by a refractive or a reflective optical component, unlike gamma (γ)- or X-rays, which are referred to in the art as nonfocusable radiation. The term "focusable" radiation or light, when used in conjunction with the embodied optical imaging device, additionally refers to wavelengths for which diffraction effects are no longer negligible, as understood in the art.

[0027] The exemplary optical element and imaging device embodiments described in detail below will be discussed, for convenience, substantially in terms of a transmission-type phase-only coded aperture optical element and imaging device using same. However, a person skilled in the art would appreciate that reflection-based elements and systems as well as amplitude-only and combination amplitude/phase optical elements, all of which operate under the same basic principles as the transmission-type phase-only coded aperture optical element and imaging device, are merely alternative aspects and are covered as if fully and expressly set forth herein. That is, in the optical element embodiment, all of the various aspects referred to immediately above will be characterized by a light function, $P(\xi, \eta)$, such that light within the spectrum of focusable radiation incident on the optical element from a point location in an object space of the optical element is optically transformed by $P(\xi, \eta)$ into a band-limited uniformly redundant array (bl-URA), A(x,y), in an image space of the optical element. Thus the term 'light transmission function' represented by $P(\xi, \eta)$ is used herein without limitation to a 'transmission-type' coded-aperture optical ele-

ment, imaging device, and method, but is equally applicable to reflection-based aspects as well.

[0028] FIG. **1**A schematically illustrates a transmission-type phase-coded optical imaging system **100-1** and includes an optical phase-only screen **50**, also referred to herein as a phase-coded aperture optical element. An object having an object point O is shown in FIG. **1**A since the system **100** is an 'imaging' system; however, the object O is not part of the embodied invention per se.

[0029] Focusable light from a point O in the object (i.e., the object is incoherently illuminated) on an object side (i.e., to the left of the phase-only aperture **50**) of the system is incident on the aperture. The phase-only aperture **50** has an aperture D and a transmission function $P(\xi, \eta)$ that defines the electric field amplitude transmission of the phase-only screen. The electric field at plane I immediately after the phase-only screen for the point object O is represented by $\exp[i\phi(\xi, \eta)]$. The incoming wavefront from the object point O is modulated by the transmission function $P(\xi, \eta)$ of the coded-aperture **50** and forms a specific coded intensity pattern A(x, y) (i.e., a coded image **70**; a point spread function (PSF)) on a detector array **60** located at plane II, which is disposed a distance z from plane I. Subsequent image processing of the coded image **70** using iterative phase retrieval methods to perform correlation-type image processing via an image processor **90** (both described in further detail below) leads to recovery **80** of the object.

[0030] The exemplary optical imaging device **100-1** illustrated in FIG. **1**A can operate as a computational imaging camera. Such a camera essentially consisting only of a coded aperture, a detector array, and an image processor provides a lossless sensitive apparatus that includes, but is not limited to, the following attributes over a traditional camera: lighter weight, ultra-thin device; high resolution with pixel size below the current color cross-talk limit defined by conventional color filters; potential multi-spectral imaging capability in a single CMOS detector; wide dynamic range; wide field of view; potential extended depth of field. These attributes provide benefits and advantages for, but not limited to, the following applications: satellite camera; computational imaging solutions that provide object attributes (e.g., velocity, range) in addition to an image of an object; improved IR imaging solutions that reduce or eliminate the need to thermally compensate IR lens materials; mechanically simple microscopes and telescopes; and ultra-compact consumer cameras.

[0031] There are three basic problems associated with and solved by the instant invention: finding an appropriate intensity pattern for the point spread function A(x, y); finding the coded-aperture transmission function $P(\xi, \eta)$ that will generate the corresponding pattern A(x, y) when focusable radiation from a point location in object space is incident on the coded-aperture; and, finding the recovered object by image processing.

[0032] According to the embodied invention, the intensity pattern A(x, y) formed on the detector should be similar (but novel as described below) to a uniformly redundant array (URA) as is typically used in an X-ray camera (which is not band-limited), and $P(\xi, \eta)$ will be the transmission function that forms this URA when focusable radiation from a point location in object space is incident on the coded-aperture having such a transmission function. While in the X-ray camera, there is little difference between the aperture transmission pattern $P(\xi, \eta)$ and the detector pattern A(x, y), in the optical regime diffraction effects lead to a marked difference between $P(\xi, \eta)$ and A(x, y). Thus according to a method embodiment described in greater detail below, $P(\xi, \eta)$ for focusable radiation will be calculated from the desired A(x, y).

[0033] Since A(x, y) is an intensity pattern formed by diffraction from a finite aperture, D, of $P(\xi, \eta)$, A(x, y) must be real, non-negative, and band-limited. Once A(x, y) is determined, a standard phase retrieval algorithm such as reported by J. R. Fienup, Opt. Lett. 3 (1978) 27 or, by R. Rolleston, N. George, Appl. Opt. 25 (1986) 178 may be used to calculate the coded-aperture transmission function $P(\xi, \eta)$. To begin, let t(x, y) be the binary function for the URA in coded-aperture imaging as described, e.g., by E. E. Fenimore, T. M. Cannon, Appl. Opt. 17 (1978) 337. As shown in the inset in FIG. **2**, this pattern has sharp edges and thus is not band-limited. Even though the idealized binary edges are not realizable when diffraction is taken into account, a solution is sought for A(x, y) that is realizable, as follows:

[0034] t(x, y) is convolved with a non-negative, band-limited blocking function b(x, y) according to

$$A(x,y)=\iint t(\xi,\eta)b(x-\xi,y-\eta)d\xi d\eta \triangleq t(x,y)*b(x,y), \quad (1)$$

where * is the convolution operation. For focusable radiation, A(x,y) must be band-limited with appropriate bandwidth to provide an operable solution for the phase screen transmission function $P(\xi, \eta)$.

[0035] For the imaging application as shown in FIG. **1**A, for an object O(x, y), the image I(x, y) in a noise-free system can be written as

$$I(x,y)=\iint A(x-x',y-y')O(x',y')dx'dy' \triangleq A(x,y)*O(x,y), \quad (2)$$

[0036] In the coded image recovery, the estimated object $\hat{O}$ is calculated as the correlation of I(x,y) and $t_R(x, y)$ as:

$$\hat{O}(x,y)=\iint t_R(x',y')I(x-x',y-y')dx'dy' \triangleq I(x,y)\star t_R(x,y), \quad (3)$$

where $\star$ is the correlation operator and

$$t_R(x,y)=\iint[t(x-x',y-y')-t_{avg}]\mathrm{comb}(x'/D_x,y'/D_y)dx'dy', \quad (4)$$

in which D_x and D_y are the size of the URA t(x,y) in x and y directions, respectively; and

$$t_{avg}=[D_x,D_y]^{-1}\int_{-Dx/2}^{Dx/2}\int_{-Dy/2}^{Dy/2}t(x,y)dxdy \quad (5)$$

is the average of the function t(x,y); and

$$\mathrm{comb}(x,y)=\Sigma_{ij}\,\delta(x-i,y-j), \quad (6)$$

is a comb function.

[0037] Combining Esq. (1)-(4) yields the result of $\hat{O}(x, y)$ as follows:

$$\hat{O}(x,y)=t(x,y)\star[t(x,y)-t_{avg}]*\mathrm{comb}(x'D_x,y'/D_y)*b(x,y)*O(x,y), \quad (7)$$

where the sequence of convolution and correlation operations is from left to right.

[0038] The URA t(x,y) as shown in FIG. **2** has the following correlation property:

$$t(x,y)\star[t(x,y)-t_{avg}]*\mathrm{comb}(x'/D_x,y'/D_y)=C\mathrm{comb}(x/D_x,y/D_y)*[\Lambda(x/\Delta_x)\Lambda(y/\Delta_y)], \quad (8)$$

where C is a constant, and $\Lambda(x)=\max(1-|x|, 0)$ is a triangle function; as shown in FIG. **2**, Δ_x and Δ_y are the smallest feature size of the array in x and y directions, respectively. Plotting Eq. (8), one obtains an ideal correlation function with no background variations or "artifacts". This type of cyclic correlation is described in detail in E. E. Fenimore, T. M. Cannon, Appl. Opt. 17 (1978) 337 and represents a considerable

advancement over the random array of pinholes reported in R. H. Dicke, Astrophys. J. 153 (1968) L101.

[0039] Substituting Eqs. (8) into (7) provides the estimate of object O(x, y) as:

$$\check{O}(x,y)=C\mathrm{comb}(x/D_x, y/D_y)*[\Lambda(x/\Delta_x)\Lambda(y/\Delta_y)])*b(x,y)*O(x,y). \quad (9)$$

[0040] Eq. (9) shows the recovered object and its shifted versions. If the field of view is constrained in the following form:

$$-D_x/2\leq D_x/2 \text{ and } -D_y/2\leq D_y/2. \quad (10)$$

then there is no overlap in shifted versions of the object and the object $O_t(x, y)$ can be recovered as

$$\check{O}_t(x,y)=C[\Lambda(x/\Delta_x)\Lambda(y/\Delta_y)]*b(x,y)*O(x,y). \quad (11)$$

The field of view constraint in Eq. (10) is in image space, i.e., x and y in Eq. 10 are the Cartesian coordinates at the detector plane II.

[0041] From Eq. (11), the PSF of the coded aperture system **100-1** in the optical region p(x, y) can be written as:

$$\rho(x,y)=[\Lambda(x/\Delta_x)\Lambda(y/\Delta_y)]*b(x,y),$$

$$\rho(x,y)=\iint[\Lambda(x'/\Delta_x)\Lambda(y'/\Delta_y)]b(x-x',y-y')dx'dy'. \quad (12)$$

This point spread function combines both the optical imaging and the correlation type digital processing.

[0042] From Eq. (12), the correlation type digital processing yields an image blurred by two parts: the smallest feature size of the uniformly redundant array t(x, y) and the band-limited function b(x, y). In the detection process, the object information with spatial frequencies higher than the band limit of b(x, y) is lost due to diffraction by the phase screen P(x, y) of a finite size. Without extra object constraint, it is beneficial to not remove this blur function b(x, y), even for an imaging system with a diffraction limited lens, in which case b(x, y) is an Airy disk for a circular aperture.

Detailed System Design

[0043] The following description explains in detail how to determine A(x, y) for focusable radiation according to an embodiment of the invention. To determine A(x, y), the functions b(x, y) and t(x, y) must be defined.

Defining b(x, y)

[0044] For the band-limited function A(x, y), it is advantageous to know the cutoff frequency. Here we note that any signal with finite duration is not considered to be band-limited for the purpose of the instant invention; however, we consider band-limited as used herein as follows.

[0045] With reference again to FIG. **1**A, we consider only the y-component of the electric field. The incoming field from a point source O is incident on and passes the phase screen **50**. Assuming implicit $\exp(+i\omega t)$ dependence at plane I immediately after the phase screen, one can write the electric field as

$$E_t(\xi,\eta)=\exp[i\phi(\xi,\eta)]. \quad (13)$$

[0046] Using Rayleigh-Sommerfield diffraction theory, one can calculate the field at plane II at a distance z from plane I as follows:

$$E_0(x,y,z)=\iint\exp[i\phi(\xi,\eta)](e^{-ikR}/2\pi R)(ik+1/R)(z/R)d\xi d\eta, \quad (14)$$

where $R=[z^2+(x-\xi)^2+(y-\eta)^2]^{1/2}$.

[0047] The spatial spectrum $E_0(f_x, f_y)$ of the electric field at plane II is defined as

$$\check{E}_0(f_x,f_y)=\iint E_0(x,y,z)\exp[-i2\pi(f_x x+f_y y)]dxdy, \quad (15)$$

where f_x and f_y denote the variables in the spatial frequency domain. Substituting Eqs. (14) into (15),

$$\check{E}_0(f_x,f_y)=\check{E}_t(f_x,f_y)\exp[-ikz(1-\lambda^2(f_x^2+f_y^2))^{1/2}], \quad (16)$$

where $E_t(f_x, f_y)$ is the spatial spectrum of the electric field at plane I defined as follows:

$$\check{E}_0(f_x,f_y)=\iint E_0(x,y,z)\exp[-i2\pi(f_x x+f_y y)]dxdy. \quad (17)$$

[0048] Eq. (16) is the exact solution of Maxwell's Equations for the y component of the electric field spatial spectrum transfer. The field spatial spectrum is determined by two terms: the spatial spectrum of the field at plane I and the transfer function as shown in the second term of Eq. (16). When the distance between the phase-only screen **50** (plane I) and the detector **60** (plane II) is much larger than the wavelength of illumination k, then the second term of Eq. (16) is subject to the exponential decay for $|f_x^2+f_y^2|\geqq 1/\lambda^2$. As such, the cutoff frequency in the second term is $1/\lambda$.

[0049] In principle, the phase screen **50** can be made as fine as possible and there is no cutoff frequency for the first term of Eq. (16). But in an actual system, the diffraction pattern at the detector plane (plane II in FIG. **1**A) has to be a finite size so that it can be fully collected by the detector. Thus the cutoff frequency of the first term in Eq. (16) is determined by the optical configurations. In an exemplary aspect, the Cartesian (x, y) dimensions of the URA intensity pattern A(x, y) on the detector **60** are, respectively, half that of the detector dimensions X, Y.

[0050] In a thin imaging device configuration, i.e., the distance z between planes I and II in FIG. **1**A is smaller than the coded-aperture size D, it is generally the second term of Eq. (16) that will determine the cutoff frequency of the electric field $E_0(x, y)$ at plane II of FIG. **1**A. In a thick configuration, z>D, the diffraction limited resolution size δ at the detector plane (II) can be estimated by the well known formula:

$$\delta=\lambda z/D. \quad (18)$$

[0051] Thus the cutoff frequency of $E_0(x, y)$ for a thick configuration can be approximated as

$$f_{max}\approx 1/\delta\approx D/\lambda z. \quad (19)$$

[0052] From the above analysis, the cutoff frequency f_{Emax} of the electric field $E_0(x, y)$ is

$$f_{Emax}\approx\min[1/\lambda, D/\lambda z]. \quad (20)$$

[0053] After the cutoff frequency of $E_0(x, y)$ is determined, the cutoff frequency of the intensity pattern A(x, y) at plane II of FIG. **1**A can be written as:

$$A(x,y)=|E_0(x,y,z)|^2. \quad (21)$$

[0054] From Fourier transform theory, the spatial spectrum of the intensity pattern A(x, y) can be written as an autocorrelation as:

$$\check{A}_0(f_x,f_y)=\iint\check{E}_0(f'_x,f'_y)\check{E}_0(f'_x-f_x,f'_y-f_y)df'_x df'_y \quad (22)$$

[0055] Clearly, the cutoff spatial frequency f_{Amax} of the intensity pattern A(x, y) is twice that of the electric field $E_0(x,y,z)$, or,

$$f_{Amax}\approx\min[2/\lambda, 2D/\lambda z]. \quad (23)$$

[0056] In an actual electronic imaging system, there is one more factor that should be considered in the design of the band-limited intensity pattern A(x, y). The detector array can only sample the pattern in finite intervals. To avoid an aliasing effect, A(x, y) needs to be band-limited up to the Nyquist frequency. Assuming the distance between neighboring pixels of the detector is Δ, then the highest spatial frequency of A(x, y) set by the detector sampling is 1/2Δ.

[0057] One way to find a nonnegative, band-limited signal A(x, y) is to convolve a not band-limited signal with a nonnegative band-limited function b(x, y). b(x, y) must have an upper spatial frequency equal to the cutoff frequency of the pattern A(x, y), which is the lesser value of f_{Amax} as in Eq. (23) and 1/2Δ. As one example, b(x, y) can be an intensity point spread function of a diffraction limited lens with an appropriate size finite aperture; the cutoff frequency is then determined by the aperture size of the lens as is well known in Fourier optics.

Defining t(x, y)

[0058] In mathematics and X-ray imaging applications, it is well known that the uniformly redundant array has a perfect correlation property, as shown in Eq. (8). That is, the correlation in Eq. (8) does not have background variations that can introduce extra noise in the recovered image even with a noise free detection process. This is an important criterion in the choice of t(x, y). Any pattern with such correlation property as shown in Eq. (8) will work in the system design. In a nonlimiting, illustrative aspect, we use a uniformly redundant array as a starting point. A uniformly redundant array is a two dimensional binary array whose cyclic autocorrelation has constant side lobes. One example of the URA in a matrix format, t_{ij} with a size of r×s, is known as follows:

$$t_{ij} = \begin{cases} 0 & \text{if } i = 0, \\ 1 & \text{if } j = 0 \ \& \ i \neq 0, \\ 1 & \text{if } C(r, i)C(s, j) = 1, \\ 0 & \text{otherwise,} \end{cases} \tag{24}$$

where t and s are two prime numbers, r−s=2, and

$$C(r, i) = \begin{cases} 1 & \text{if there exists an integer } n, \ 1 \leq n < r, \\ & \text{such that } i = n^2 \cdot \text{mod}(r) \\ -1 & \text{otherwise.} \end{cases} \tag{25}$$

We note that all the cyclic shifted versions of t_{ij} above are also URAs because their cyclic autocorrelation functions have constant sidelobes.

[0059] In the instant system design, we choose two parameters in the URA, the feature size of the array Δ_x, Δ_y and the total array size D_x and D_y.

[0060] Eq. (12) shows that in order to have the best resolution of the system, Δ_x and Δ_y should be as small as possible. However, another limiting factor is that A(x, y), as calculated in Eq. (1), should have good contrast. From Eq. (1), the contrast of A(x, y) is larger for larger feature size of the uniformly redundant array. By considering both Eqs. (1) and (12), one can set Δ_x and Δ_y to be about the same as the feature size of b(x, y); or mathematically,

$$2\Delta_x f_{xMax} \approx 1 \text{ and } 2\Delta_y f_{yMax} \approx 1, \tag{26}$$

where f_{xMax} and f_{yMax} are the largest spatial frequency of b(x, y) in the x and y directions, respectively.

[0061] The total size D_x and D_y of the array t(x, y) can be determined from the field of view constraint in Eq. (10). For a detector with a size of X×Y, Eq. (10) needs to be true for any point (x,y) at detector (|x|<X/2 and |y|<Y/2). This implies that D_x and D_y need to satisfy the following:

$$D_x \geq X/2 \text{ and } D_y \geq Y/2. \tag{27}$$

Calculating the Phase-Only Screen Transmission Function P(ξ, η)

[0062] After the band-limited intensity pattern A(x, y) is known, the next step in the system design is to calculate an aperture with a transmission function of P(ξ, η) that can be used to generate the specific intensity pattern A(x, y). Although a phase-only type aperture may be preferred in many applications, a phase retrieval process **500** as shown in FIG. **5** can be used for a phase-only type aperture, an amplitude-only type aperture, or a combination amplitude/phase-type aperture, which can be either of a transmission-type or a reflection-type. The calculation method involves an iterative phase calculation.

[0063] In FIG. **5**, the process **500** starts at step **501** with an electric field having an amplitude of $E(x, y)=[A(x, y)]^{1/2}$. At step **502** a free space back propagation is used to calculate the aperture function at plane I of FIG. **1**A. We denote this aperture function as $|P(\xi, \eta)|\exp[i\phi(\xi, \eta)]$ at step **503**. In order to find a desired phase-only screen, according to an illustrative aspect, we set the aperture constraint, i.e., change $|P(\xi, \eta)|$ to 1, at step **505**. At step **506**, a free space propagation is applied to find the electric field at detector plane II as shown in FIG. **1**A, at step **507**. We denote the thus found electric field as $F(x, y)\exp[i\psi(x, y)]$. The detector plane intensity constraint is then applied at step **509**, i.e., change $F(x, y)$ to $[\Lambda(x, y)]^{1/2}$. At step **510**, we perform another free space back propagation, and the process is repeated. Using this iterative approach, we eventually can calculate a phase-only screen P(ξ, η) that will generate the required intensity pattern A(x, y).

[0064] In this algorithm, the free space propagation and back propagation can be simply calculated exactly in the spatial frequency domain using Eq. (16). Therefore this calculation is good in non-paraxial case when, for example, the distance between the screen and detector planes are smaller than the aperture size of the screen (i.e., thin camera configuration).

[0065] According to an alternative illustrative aspect, the process **500** can be carried out for an amplitude-only coded-aperture by simply setting the aperture constraint differently, i.e., setting $\phi(\xi, \eta)$ to 0 in step **503**, then performing the steps as recited above. According to a further alternative, illustrative aspect in which a combination amplitude/phase aperture is used, only a single iteration is necessary to determine the appropriate transmission function. Thus regardless of the type of phase screen being designed and used, the same rationale controls; i.e., design a coded-aperture system, with or without lens, whose diffraction pattern is a band-limited URA. In this regard, a single or multiple refractive element(s) (e.g., lens(es)) or a combination of lens(es) plus phase mask could be utilized for P(ξ, η) to generate the required intensity pattern A(x, y) for focusable radiation. For example, an optional negative lens with a 1 mm aperture in combination with a phase plate could be used for a 5 mm detector system.

Alternatively, an optional positive lens may be used in combination with a phase plate if the size of aperture is larger than half the size of detector.

[0066] While phase retrieval algorithms in the above description are generally known in the literature, we note that in our system design some extra data constraints as reported in R. G. Paxman, T. J. Schulz, J. R. Fienup, J. Opt. Soc. Am. A 9 (1992) 1072 may be used in the phase retrieval algorithm to improve the performance of the coded aperture system. As one example, in order to have an extremely wide field of view, we calculate a phase-only screen that can generate a similar intensity pattern for both an on-axis object point and an off-axis point source. Similar extra data constraints may be used to design a system with large depth of field or to reduce the sensitivity of intensity pattern dependence on parameter z, the distance between the phase screen and the detector plane.

Simulation Results

[0067] In FIG. **3***a*, we show a realizable band-limited intensity pattern $\Lambda(x, y)$ **301** at the detector plane (II; not shown). It is the image of the known uniformly redundant array $t(x, y)$ **201** shown in FIG. **2** by a diffraction limited square aperture lens (not shown) and is generated digitally from Eq. (1). A section of the pattern $\Lambda(x, y)$ **301** is magnified to see the detailed features of such a pattern. The edge is blurred compared to that of the uniformly redundant array **201** in FIG. **2**. FIG. **3***b* shows the corresponding phase function **303** that can generate such a pattern (**301**) for focusable light from an axial point source at infinity. The phase values from $-\pi$ to π are shown from dark to bright. In this simulation we use the following parameters: Both the sizes of the pattern $\Lambda(x, y)$ **301** and phase screen $P(x, y)$ **303** are 2 mm×2 mm, and the distance between the phase screen and the detector is z=5 mm The wavelength of illumination is λ=4 μm.

[0068] The imaging results are shown in FIGS. **4**(*a-c*). FIG. **4***a* shows the object used in simulation; FIG. **4***b* shows the decoded image using the correlation method described herein above; FIG. **4***c* shows a comparative image formed by a diffraction limited lens with the same square aperture. One can observe the excellent imaging results for the coded aperture system as shown in FIG. **4***b*. The image of the coded aperture system is a little more blurry than that of the diffraction limited lens because the point spread function of such a system, as in Eq. (12), is wider than that of the diffraction limited system. Some extra digital deconvolution can be applied to the image in FIG. **4***b* to remove the effect of the triangle blur function in Eq. (12) and recover a diffraction limited result. This extra blur is not a significant disadvantage of the optical region coded aperture imaging system.

[0069] Advantageously, embodiments of the systems described herein can be extraordinarily simple. In an illustrative system aspect **100-1** as shown in FIG. **1**A, the optical subsystem includes only a phase-only screen **50** followed by a detector array **60** (and image processor **90**), while a conventional diffraction limited lens is comparatively difficult to design and fabricate, especially in an ultra-thin format comparable to the instant coded-aperture system. The embodied system works both in the visible and infrared optical region. The simplicity of the embodied infrared system is clearly an advantage compared to conventional infrared imaging systems.

Image Recovery

[0070] In addition to the correlation-type processing described with respect to FIG. **5**, above, alternative known methods may include photon tagging, linear filtering, maximum entropy, and iterative removal of sources.

[0071] FIG. **6** shows an image **601** recovered using the correlation type processing as described hereinabove and is similar to that shown in the FIG. **4***b*, except that in FIG. **6** a Gaussian noise is added to the intermediate coded image. The standard deviation of the Gaussian noise is one percent (1%) of that of the signal value of the intermediate image. In the system as shown in FIG. **1**A, the detector linear size is twice that of the pattern size $A(x, y)$ (See Eq. 10); the dark and bright structure of the object is not seen in the intermediate image. The intermediate image is bright at the center and it tapers to dark at the edge of the detector. The noise added to the intermediate image has a standard deviation that is one percent of the intermediate image, so the noise added to the center is much larger than the noise added to the edge of the intermediate image.

[0072] In order to illustrate the effectiveness of the instant novel camera system with an image that displays gray scale, FIG. **7** shows the simulated imaging results using the object of a hummingbird. FIG. **7***a* shows the diffraction limited image taken with a diffraction limited lens with the same aperture size as that of the embodied phase-coded aperture system, i.e., 2 mm×2 mm aperture. The recovered image using the phase-coded aperture system is shown in FIG. **7***b*. No noise is included in the intermediate image for the coded-aperture system. A careful comparison of the high frequency detail and variable contrast shows excellent image quality. Even small contrast variations in the upper rail of the wooden fence are clearly observed in the image. Although not shown in the figures, good image recovery results were also obtained with 1% noise added to the intermediate image at the detector plane.

[0073] A phase-only coded-aperture and associated system are illustrative embodiments of the invention. As mentioned above, in alternative illustrative aspects, the coded-aperture may be an amplitude-only optical element or a combination amplitude/phase optical element, and respective, alternative illustrative systems may incorporate same. For example, FIG. **1**B shows an alternative illustrative coded-aperture imaging system **100-2** in which the coded-aperture **50-1** is a programmable reflective-type liquid crystal, such as the Holoeye HEO 1080P programmable spatial light modulator. Each pixel of the modulator can be programmed to phase change over a range of 2π and thus can be used as a reflective phase plate. In the experimental setup shown in FIG. **1**B, each pixel of the spatial light modulator was 8 μm; the fill factor was 85%; and a $0\text{-}2\pi$ phase modulation was at λ=0.633 μm. Detector pixels were 13 μm. The object was located 1275 mm from the phase screen and the phase screen to detector separation was 204.4 mm The aperture was 5.5 mm×5.5 mm.

[0074] FIG. **8** shows a point source image and recovery using the experimental system setup **100-2** shown in FIG. **1**B and the phase retrieval method **500** illustrated in FIG. **5**.

[0075] Fabrication of transmission-type or reflection-type coded-aperture optical elements as embodied herein can be made using photolithographic processes well known in the semiconductor art. Once a master is made via photolithography, quantities of coded-aperture optical elements can be made by well known molding processes. Transmission-type elements may be made using dielectric materials such as glass and plastic, for example. Reflection-type elements can be made from a variety of metals or other materials that can be reflection coated.

[0076] All references, including publications, patent applications, and patents cited herein are hereby incorporated by reference in their entireties to the same extent as if each reference were individually and specifically indicated to be incorporated by reference and were set forth in its entirety herein.

[0077] The use of the terms "a" and "an" and "the" and similar referents in the context of describing the invention (especially in the context of the following claims) are to be construed to cover both the singular and the plural, unless otherwise indicated herein or clearly contradicted by context. The terms "comprising," "having," "including," and "containing" are to be construed as open-ended terms (i.e., meaning "including, but not limited to,") unless otherwise noted. The term "connected" is to be construed as partly or wholly contained within, attached to, or joined together, even if there is something intervening.

[0078] The recitation of ranges of values herein are merely intended to serve as a shorthand method of referring individually to each separate value falling within the range, unless otherwise indicated herein, and each separate value is incorporated into the specification as if it were individually recited herein.

[0079] All methods described herein can be performed in any suitable order unless otherwise indicated herein or otherwise clearly contradicted by context. The use of any and all examples, or exemplary language (e.g., "such as") provided herein, is intended merely to better illuminate embodiments of the invention and does not impose a limitation on the scope of the invention unless otherwise claimed.

[0080] No language in the specification should be construed as indicating any non-claimed element as essential to the practice of the invention.

[0081] It will be apparent to those skilled in the art that various modifications and variations can be made to the present invention without departing from the spirit and scope of the invention. There is no intention to limit the invention to the specific form or forms disclosed, but on the contrary, the intention is to cover all modifications, alternative constructions, and equivalents falling within the spirit and scope of the invention, as defined in the appended claims. Thus, it is intended that the present invention cover the modifications and variations of this invention provided they come within the scope of the appended claims and their equivalents.

We claim:

1. An optical element for generating a band-limited uniformly redundant array (bl-URA) from light within a spectrum of focusable radiation, comprising:

an optical element characterized by a light transmission function, $P(\xi, \eta)$, such that light within the spectrum of focusable radiation incident on the optical element from a point location in an object space of the optical element is optically transformed by $P(\xi, \eta)$ into a band-limited uniformly redundant array (bl-URA), A(x,y), in an image space of the optical element.

2. The optical element of claim **1**, wherein the optical element consists of a single optical element.

3. The optical element of claim **1**, wherein the optical element has a surface region that is at least partially transmissive for the light within the spectrum of focusable radiation.

4. The optical element of claim **1**, wherein the optical element has a surface region that is at least partially reflective for the light within the spectrum of focusable radiation.

5. The optical element of claim **1**, wherein the optical element is an amplitude-only aperture.

6. The optical element of claim **1**, wherein the optical element is a phase-only aperture.

7. The optical element of claim **1**, wherein the optical element is a combination amplitude/phase aperture.

8. The optical element of claim **1**, wherein the optical element consists of a refractive optical component.

9. The optical element of claim **1**, wherein the optical element consists of a plurality of refractive optical components.

10. The optical element of claim **1**, wherein the optical element comprises a refractive optical component and a phase aperture.

11. The optical element of claim **1**, wherein the optical element is a programmable spatial light modulator.

12. The optical element of claim **1**, wherein the optical element has Cartesian x,y surface dimensions equal to or greater than one millimeter, respectively.

13. The optical element of claim **1**, wherein A(x,y) is a real, non-negative, band-limited, uniformly redundant array (bl-URA).

14. The optical element of claim **1**, wherein the spectrum of focusable radiation is in a range from ultraviolet to submillimeter wavelengths.

15. The optical element of claim **14**, wherein the spectrum of focusable radiation is in a range from visible to infrared wavelengths.

16. An optical imaging device, consisting of:

an optical element characterized by a light transmission function, $P(\xi, \eta)$, such that light within the spectrum of focusable radiation incident on the optical element from a point location in an object space of the optical element is optically transformed by $P(\xi, \eta)$ into a band-limited uniformly redundant array (bl-URA), A(x,y), in an image space of the optical element;

a detector disposed in the image space such that the bl-URA is formed on the detector; and

an image processor adapted to recover an image of an object from the detected bl-URA.

17. The optical imaging device of claim **16**, wherein A(x,y) is a real, non-negative, intensity pattern and the optical element characterized by $P(\xi, \eta)$ has a finite aperture size.

18. The optical imaging device of claim **16**, wherein A(x,y) is a convolution of a binary function t(x,y) for uniformly redundant array with a non-negative, bandlimited blocking function b(x,y), as follows:

$$A(x,y)=\iint t(\xi,\eta)b(x-\xi,y-\eta)d\xi d\eta \triangleq t(x,y)*b(x,y),$$

where * is the convolution operation.

19. The optical imaging device of claim **18**, wherein A(x,y) is a point spread function p(x,y) described by:

$$p(x,y)=[\Lambda(x/\Delta_x)\Lambda(y/\Delta_y)]*b(x,y),$$

$$p(x,y)=\iint[\Lambda(x'/\Delta_x)\Lambda(y'/\Delta_y)]b(x-x',y-y')dx'dy',$$

where $\Lambda(x)=\max(1-|x|,0)$ is a triangle function and Δ_x and Δ_y are the smallest feature size of the bl-URA in x and y directions, respectively, at the detector.

20. The optical imaging device of claim **18**, wherein the bandlimited blocking function b(x,y) is an Airy disc for a circular aperture.

21. The optical imaging device of claim **20**, wherein the bl-URA has a cut-off frequency as follows:

$$2\Delta_x f_{xMax}\approx 1 \text{ and } 2\Delta_y f_{yMax}\approx 1,$$

where f_{xMax}, f_{yMax} are the largest spatial frequency of b(x,y) in x and y directions, respectively, at the detector.

22. The optical imaging device of claim **16**, wherein A(x,y) at the detector has an x-dimension and a y-dimension that are equal to or less than a total size X/2 and Y/2, respectively, where the detector has a size of X×Y.

23. The optical imaging device of claim **16**, wherein the object is a continuous object.

24. The optical imaging device of claim **17**, wherein the optical element and the detector are separated by a distance, z, that is less than the finite aperture size of the optical element.

25. The optical imaging device of claim **16**, wherein the device is a computational imaging camera.

26. A method for determining a transmission function P(ξ, η) for an optical element that will generate a desired intensity pattern A(x,y) on a detector from light within a spectrum of focusable radiation from a point on an object, comprising:

a) determining a real, non-negative, band-limited uniformly redundant array, A(x,y), that will be generated on a detector by an optical element characterized by a transmission function P(ξ, η), from light within the spectrum of focusable radiation from a point on the object;

b) defining an electric field having an amplitude $E(x,y)=[A(x,y)]^{1/2}$;

c) calculating the transmission function P(ξ, η) in a plane immediately adjacent a known position of the optical element by performing a free space back propagation, and denoting the transmission function $|P(\xi, \eta)|\exp[i\phi(\xi,\eta)]$;

d) determining an electric field at a known detector plane location by performing a free space propagation, and denoting this electric field $F(x,y)\exp[i\psi(x,y)[$;

e) applying a detector plane intensity constraint by setting $F(x,y)\rightarrow[A(x,y)]^{1/2}$;

f) performing another free space back propagation; and

g) calculating the optical element transmission function P(ξ, η) that will generate the desired intensity pattern A(x,y).

27. The method of claim **26**, further comprising:

c1) after step (c), setting an aperture constraint such that $|P(\xi,\eta)|$ is set to 1, wherein the optical element is a phase-only element; and

h) repeating steps (c-f).

28. The method of claim **26**, further comprising:

c1) in step (c), setting $\phi(\xi, \eta)$ to 0, wherein the optical element is an amplitude-only element; and

h) repeating steps (c-f).

* * * * *

Illustrative EDOF topics in Fourier optics

Nicholas George, Xi Chen, and Wanli Chi
The Institute of Optics, University of Rochester, Rochester, NY 14627

ABSTRACT

In this talk we present a series of illustrative topics in Fourier Optics that are proving valuable in the design of EDOF camera systems. They are at the level of final examination problems that have been made solvable by a student or professor having studied from one of Joseph W. Goodman's books—our tribute for his 75th year. As time permits, four illustrative topics are 1) Electromagnetic waves and Fourier optics; 2) The perfect lens; 3) Connection between phase delay and radially varying focal length in an asphere and 4) tailored EDOF designs.

Keywords: Fourier optics, electromagnetic waves, extended depth of field, perfect lens, symmetric asphere, lens phase delay, digital camera

1. INTRODUCTION

Since 1968 one of us has taught classes every year at Rochester's Institute of Optics and earlier at the California Institute of Technology using one or another of Professor Joseph W. Goodman's splendid books. This effort includes principal thesis supervision of 51 doctoral scholars as well as lectures to several hundred graduate students. Since most research topics can be conveniently grouped into a few distinct problems, it seemed natural in searching to fill 15 to 20 minutes to describe separate illustrative problems that were enhanced by reading of the Goodman Books.

So as there are many teachers and professors in the audience, my talk is structured like a problem set, in Fourier optics of course. We are always looking for interesting illustrative problems that add color and life to a subject and that leave the student with an experience that he will continue to think about from time to time in his/her future. So here is my Goodman Problem Set, written to expand the subject and to illustrate certain important system issues in the design of extended depth of field cameras. Each topic is reasonable to solve, but not painfully obvious I hope, and just right for a graduate student who is studying Fourier optics, electromagnetic waves, speckle, or lenses.

2. ELECTROMAGNETIC WAVES AND FOURIER OPTICS

One of the central topics in Fourier optics is how to write linear system equations for a cascade of lenses [1]. Typically, there is an input plane (0) with a transparency $T_O(x_O,y_O)$ followed by transmission in free space (0 to 1), ... , (4 to 5) with lenses of transmission function T_1, ... , T_4, as shown in Fig. 1. The input scene, T_O, is illuminated by a monochromatic, polarized laser tone and the output is recorded at plane (5) using a fine-scaled CMOS detector. In Fig. (1) as the light propagates along the optic axis, i.e., along z, we will see that the propagation problem consists of **products** with the idealized transmission functions followed by **convolutions** to describe the free-space propagation. Thereafter, in the design of the complete digital camera system, one needs to extend the system equations from the output of the CMOS detector to the final output display, including the digital image processing.

As we explain in Sec. 2.1 below, the input E_{XO} (x,y;v) is the scalar electric field component in a HTD or temporal Fourier transform signal representation. Also, E_{X5} (x_5, y_5; v) is the corresponding temporal transform output.

Tribute to Joseph W. Goodman, edited by H. John Caulfield, Henri H. Arsenault, Proc. of SPIE Vol. 8122, 812204 · © 2011 SPIE · CCC code: 0277-786X/11/$18 · doi: 10.1117/12.895960

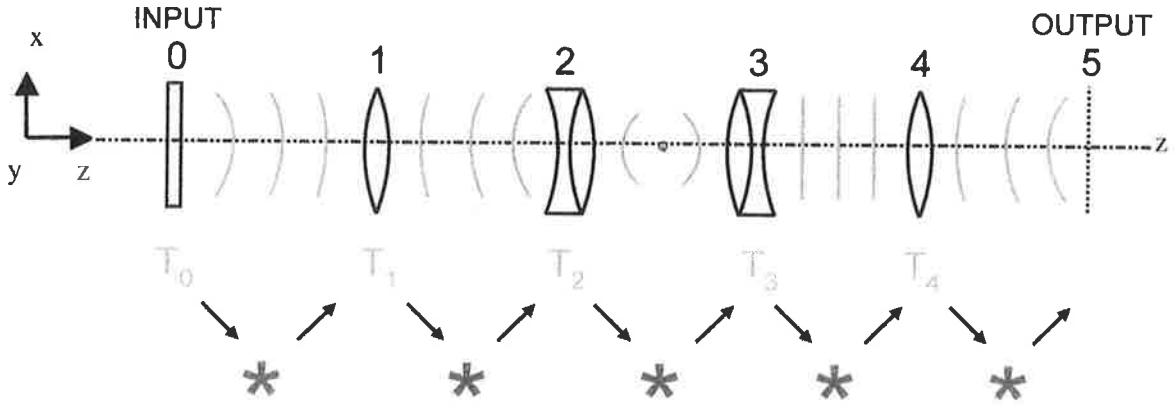

CALCULATION OF OUTPUT WAVES

TRANSMISSION THROUGH LENS... PRODUCT

FREE SPACE PROPAGATION... CONVOLUTION

Fig. 1 Fourier Physical Optics--Summary

In order to understand the calculation of the propagation in the free-space regions between the transmission functions, it is helpful briefly to provide a review of the basic equations of Maxwell and summary charts of the main results in Tables 2.1 to 2.3 below. Then, when we present solutions of the scalar wave equation, you will understand that the scalar variable is the transverse electric field vector.

2.1 Summary sheet of Maxwell's equations—The cheat sheet [2-4]

Consider the real-valued, time-dependent electric field $\mathcal{E}(\mathbf{r},t)$ and the magnetic field $\mathcal{H}(\mathbf{r},t)$ in a simple free-space dielectric as from (0 to 1) or (1 to 2) and so on in Fig. 1. Signal representations are summarized in Fig. 2.

Table 2.1 Time dependent real-valued functions

1.	$\nabla \times \mathcal{E}(\mathbf{r},t) = -\dfrac{\partial \mathcal{B}(\mathbf{r},t)}{\partial t}$
2.	$\nabla \times \mathcal{H}(\mathbf{r},t) = \mathcal{J}(\mathbf{r},t) + \dfrac{\partial \mathcal{D}(\mathbf{r},t)}{\partial t}$
3.	$\nabla \cdot \mathcal{D}(\mathbf{r},t) = \rho(\mathbf{r},t)$
4.	$\nabla \cdot \mathcal{B}(\mathbf{r},t) = 0$
5.	$\nabla \cdot \mathcal{J}(\mathbf{r},t) = -\dfrac{\partial}{\partial t}\rho(\mathbf{r},t)$
6.	$\nabla \times \nabla \times \mathcal{E}(\mathbf{r},t) + \mu\varepsilon \dfrac{\partial^2}{\partial t^2}\mathcal{E}(\mathbf{r},t) = -\mu \dfrac{\partial}{\partial t}\mathcal{J}(\mathbf{r},t)$

Table 2.2 Temporal Fourier Transform or HTD $e^{i\omega t}$ [2-4]

1.	$\nabla \times \mathbf{E}(\mathbf{r};\nu) = -i\omega\mu\mathbf{H}(\mathbf{r};\nu)$
2.	$\nabla \times \mathbf{H}(\mathbf{r};\nu) = \mathbf{J}(\mathbf{r};\nu) + i\omega\varepsilon\mathbf{E}(\mathbf{r};\nu)$
3.	$\nabla \times \nabla \times \mathbf{E}(\mathbf{r};\nu) - \omega^2\mu\varepsilon\mathbf{E}(\mathbf{r};\nu) = -i\omega\mu\mathbf{J}(\mathbf{r};\nu)$
4.	$\left(\nabla^2 + k^2\right)E_x(x,y,z) = 0$

Table 2.3 Exact solutions of Maxwell's equation for propagation into the right-half-space. The Rayleigh, Sommerfeld, Smythe form [5-8]

1.	$E_x(x,y,z) = \int_{-\infty}^{\infty}\int dx'dy' E_x(x',y',0)\dfrac{e^{-ikR_1}}{2\pi R_1}\left(ik + \dfrac{1}{R_1}\right)\dfrac{z}{R_1}$
2.	$E_y(x,y,z) = \int_{-\infty}^{\infty}\int dx'dy' E_y(x',y',0)\dfrac{e^{-ikR_1}}{2\pi R_1}\left(ik + \dfrac{1}{R_1}\right)\dfrac{z}{R_1}$
3.	$E_z(x,y,z) = \int_{-\infty}^{\infty}\int dx'dy' \left\{E_x(x',y',0)\dfrac{x'-x}{R_1} + E_y(x',y',0)\dfrac{y'-y}{R_1}\right\}\dfrac{e^{-ikR_1}}{2\pi R_1}\left(ik + \dfrac{1}{R_1}\right)$

[N. George 2001]

Table 2.1 contains the time dependent basic Maxwell's equations (1-4); Eq. (5) is the continuity equation expressing conservation of charge; and Eq. (6) is the wave-equation for the electric field vector $\mathcal{E}(\mathbf{r},t)$ derived from taking $\nabla \times \nabla \times \mathcal{E}$ in Eq. (1) of Table 2.1, substituting $\mathcal{B} = \mu\mathcal{H}$ and $\mathcal{D} = \varepsilon\mathcal{E}$ in a simple dielectric medium [2-4].

Table 2.2 follows by simply making the steady-state, harmonic time dependence assertion in which $g_1(\mathbf{r},t)$ is replaced by $g_2(\mathbf{r})\exp(i\omega t)$ for all functions in Table 2.1 [2-4]. We note, too, that in more complex problems, when input spectra are involved as in Statistical Optics, it is common instead to take a temporal Fourier transform. Formally or notationally, the same equations are obtained. Hence, the temporal Fourier transform case in Table 2.2 uses the following notation:

$$\mathbf{E}(\mathbf{r};\nu) = \int_{-\infty}^{\infty} \mathcal{E}(\mathbf{r},t)e^{-i2\pi\nu t}dt \tag{1}$$

and

$$\mathcal{E}(\mathbf{r};t) = \int_{-\infty}^{\infty} \mathbf{E}(\mathbf{r},\nu)e^{i2\pi\nu t}d\nu \quad , \tag{2}$$

where $k = 2\pi/\lambda = \omega/c = 2\pi\nu/c$.

In Fig. 2 we show the signal representations being used in Tables 2.1 to 2.3 in more detail than is necessary for the paper at hand. However, we wanted to show the more general usage including angular spectrum as well as statistical optics in order to explain our preference for the $\exp(+i\omega t)$ in the HTD representation and its consistency with our Fourier transform notation. Herein, we take the spatial Fourier transform with the **conventional** $\exp[-i2\pi(f_x x + f_y y)]$ notation and the temporal transform with the $\exp[-i2\pi\nu t]$. It is a simple exercise to show that the equations in Tables 2.2 – 2.3 are equivalent provided one uses the HTD with $\exp(+i\omega t)$.

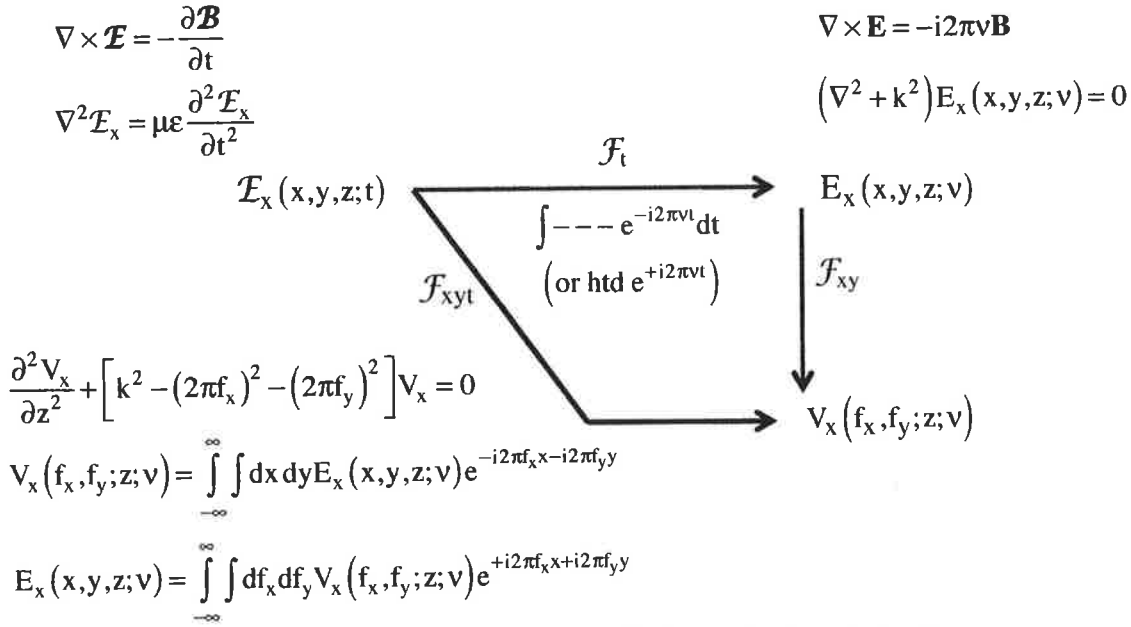

Fig. 2 Signal Representations in Electromagnetic Waves and Fourier Optics

Table 2.3 has exact solutions of Maxwell's equations for propagation into the right-half-space of a simple dielectric medium when $z \geq 0$. The basic result is derived in many texts with slightly different ways of stating the specific conditions of the problem [1, 5-8, ...].

One common, practical problem statement is to place a perfectly conducting, infinitesimally thin conducting sheet at $z = 0$. For vector diffraction theory problems, a careful hole or aperture is cut into the sheet and it is illuminated by a monochromatic source. The agreed-upon final solution is given by use of formulae in the table, known by some as the Rayleigh-Sommerfeld solution, and by others as the Rayleigh-Sommerfeld-Smythe solution. The problem of radiation into the right-half-space has several important and distinct steps going back over more than 100 years; hence, "it has many fathers." Goodman does a nice job of describing this long history [1], and we can seek his comments at the meeting.

Why Smythe? While Sommerfeld appears to have been first or at least early to recognize that in the HTD case either the tangential electric field or the tangential magnetic field on a closed boundary surrounding a source-free region was necessary and sufficient to obtain a complete solution for $\mathbf{E}(\mathbf{r};\nu)$ and $\mathbf{H}(\mathbf{r};\nu)$ in and on the boundary, Smythe was at least early to write the existence theorem explicitly in his text [5]. Also he was first to write the complete exact solution for the right-half-space problem in a vector form in his famous Phys. Rev. (1947) paper [6]. The Smythe expression is given by the following (HTD):

$$\mathbf{E}(\mathbf{r};\nu) = \frac{1}{2\pi}\nabla \times \int_{z'=0} \hat{z}' \times \mathbf{E}(\mathbf{r}') \frac{e^{-ikR_1}}{R_1} dx'dy' \tag{3}$$

in which the free space Green's function G is given by

$$G(\mathbf{r},\mathbf{r}') = \frac{e^{-ikR_1}}{4\pi R_1}, \tag{4}$$

and $\mathbf{E}(\mathbf{r}')$ at $(x',y',0)$ is the final field in an aperture.

It is a challenging, stimulating problem to find E_X, E_Y, E_Z given in Table 2.3 from the vector form [7].

There are many fascinating aspects to the result in Table 2.3 as follows:

1. If you supply $E_X(x', y',0)$ and set $E_Y(x',y',0) = 0$, there will not be any cross-polarization as light is propagated into a simple medium (linear, isotropic in constant μ, ε).

2. If you supply E_X and E_Y on the boundary then you can calculate **E**, **H** everywhere in the RHS, including on the boundary. In Table 2.3 Eqs. (1-3) are a set of exact integral equations.

3. You can assert any tangential **E** on the boundary (including outward waves only as $z \rightarrow \infty$) and find the solutions. These are exact integral equations and you need not use Kirchhoff's aperture assumption nor otherwise describe an opening in the $z = 0$ plane.

4. For near-field optics, the integral equation forms of Maxwell's equations are still exact solutions.

5. Another exact, useful and readily proven result for the RHS is given by [7]:

$$E_{x,y}(x,y,z) = -\frac{\partial}{\partial z}\int_{-\infty}^{\infty}\int dx'dy' E_{x,y}(x',y',0)\frac{e^{-ikR_1}}{2\pi R_1}. \tag{5}$$

2.2 Illustrative convolution form

Now that the lengthy prologue about electromagnetic waves is finished we can return to Fig. 1.

For any free space region in Fig. 1, asserting that $E_Y(x',y',0;v) = 0$ and the input is $E_X(x',y',0;v)$, by Table 2.3, one can write:

$$E_x(x,y,z) = \iint_{z'=0} E_x(x',y',0)e\frac{-ikR_1}{2\pi R_1}\left(ik+\frac{1}{R_1}\right)\frac{z}{R_1}dx'dy' \tag{6}$$

in which

$$R_1 = \left[(x-x')^2+(y-y')^2+z^2\right]^{1/2} \tag{7}$$

We see that the impulse response of each section in free space forms a perfect convolution with the transverse plane input coordinates. This comment is precise for all angles given by z/R_1 from 0 to $\pm\,\pi/2$.

Both the approximate far-zone and the Fresnel zone expansions present problems at large angles and close in insofar as the convolution form/expansion. However, with PC computing the exact impulse-response form can be used; so one is not limited to the dreaded paraxial approximations that so limit the application of physical optics to optical system design.

For us today, using Maxwell's equations and the formulae presented on the previous pages, we can see that a diffraction pattern is made up by the superposition of radiation from differential elements given by

$$E_x(x',y',0)dx'dy' \tag{8}$$

These give rise to "secondary waves" which are traveling in the right-half-space with a very weak angular dependence given by the term z/R_1. The superposition weighting is given in amplitude and phase by the term:

$$p(x-x',y-y') = \frac{e^{-ikR_1}}{2\pi R_1}\left(ik+\frac{1}{R_1}\right)\frac{z}{R_1} \tag{9}$$

Dropping the offset or convolution form, of course, gives us the impulse response [8] for propagation into the RHS:

$$p(x,y) = \frac{e^{-ikr}}{2\pi r}\left(ik+\frac{1}{r}\right)\frac{z}{r} \tag{10}$$

Hence, from Maxwell's equation in Eqs. (6-10) we have found a rigorous statement of Huygens' principle stated more than three hundred years ago in the description of the propagation of a wavefront.

3. THE PERFECT LENS [12]

3.1 Statement of the illustrative problem

Now we turn our attention to the definition of the lens transmission function. We assert that one would like to have a more abstract definition for an ideal lens—a definition not encumbered by paraxial matters nor details of glass index nor curvatures. To be more explicit, for Fourier Physical Optics, we seek a transmission function, $T(\rho)$ or $T_C(x,y)$, that is valid for all F/#.

3.2 Definition of a transmission function

Consider a circularly symmetric lens that has a uniform phase delay $\Phi(\rho)$ where the radial coordinate in the transverse plane is given by $\rho = [x^2 + y^2]^{1/2}$. Now the transmission function $T(\rho)$ is (partially) defined as follows:

$$T(\rho) = e^{-i\Phi(\rho)} = \frac{\text{Scalar transform transverse electric field exiting}}{\text{Scalar transform transverse electric field entering}} \quad (11)$$

An ideal lens is one that converts the expanding output wave from a point source into a plane wave. But these can be deduced from our EM theory, as follows. Now consider this case of a point source at a distance F from the input plane (I) of the lens. Hence, as with an electric dipole or a tiny pinhole, the electric field component at z = F is given by:

$$E_x(\rho) = \hat{x}\frac{Ae^{-ikr}}{2\pi r}\left(ik + \frac{1}{r}\right)\frac{z}{r}, \quad (12)$$

where A is an arbitrary constant with exp(iωt) suppressed. Also $r^2 = F^2 + \rho^2$ and neglecting apodization and (near field) distance terms, we have the idealized amplitude transmission function, T_1, given by

$$T_1(\rho) = \frac{1}{e^{-ikr}} \quad (13)$$

Now from Eq. (16) we can obtain the first form for the transmission function T(ρ) for a thin lens by setting the phase shift to zero at ρ = 0; the result is as follows:

$$T(\rho) = e^{ik\left[\left(F^2+\rho^2\right)^{1/2} - F\right]} \quad (14)$$

It is informative to expand this transmission function in a power series in terms of (ρ/F). The result is given by

$$T(\rho) = e^{ikF\left[\frac{1}{2}\left(\frac{\rho}{F}\right)^2 - \frac{1}{8}\left(\frac{\rho}{F}\right)^4 + \frac{1}{16}\left(\frac{\rho}{F}\right)^6 - \frac{5}{128}\left(\frac{\rho}{F}\right)^8 + \cdots\right]} \quad (15)$$

This lens gives diffraction-limited performance at all F/#. Also, we see that the first term corresponds to the paraxial focal length of Fourier optics when one is using the Fresnel zone forms. In this case one finds

$$T_{pa}(\rho) = e^{i\frac{\pi\rho^2}{\lambda F}} \quad (16)$$

Note we are using a HTD corresponding to exp(iωt).

Following the same procedure for a lens which turns a point source at s_1 into a diffraction-limited object image at s'_1, we find the lens description T_b as follows:

$$T_b(\rho) = \frac{e^{ik\left[\left(s_1'^2+\rho^2\right)^{1/2} - s_1'\right]}}{e^{-ik\left[\left(s_1^2+\rho^2\right)^{1/2} - s_1\right]}} \quad (17)$$

$$T_b(\rho) = e^{ik\left[\left(s_1'^2+\rho^2\right)^{1/2} - s_1' + \left(s_1^2+\rho^2\right)^{1/2} - s_1\right]} \quad (18)$$

Again, we can expand this exponent using [G & R: 1.112] to yield:

$$T_b(\rho)=e^{ik\left(s_1'\left[\frac{1}{2}\left(\frac{\rho}{s_1'}\right)^2-\frac{1}{8}\left(\frac{\rho}{s_1'}\right)^4+\frac{1}{16}\left(\frac{\rho}{s_1'}\right)^6-\frac{5}{128}\left(\frac{\rho}{s_1'}\right)^8+\cdots\right]+s_1\left[\frac{1}{2}\left(\frac{\rho}{s_1}\right)^2-\frac{1}{8}\left(\frac{\rho}{s_1}\right)^4+\frac{1}{16}\left(\frac{\rho}{s_1}\right)^6-\frac{5}{128}\left(\frac{\rho}{s_1}\right)^8+\cdots\right]\right)} \tag{19}$$

In the form above we see that the paraxial imaging gives us an overall focal length F in which

$$\frac{1}{F}=\frac{1}{s_1}+\frac{1}{s_1'} \tag{20}$$

as one would expect. Hence, Eqs. (15) and (19) provide us with basic abstract definitions for the amplitude transmission function of diffraction-limited lenses of arbitrary diameter.

4. THEORY FOR THE RADIALLY SYMMETRIC ASPHERE [12]

4.1 Statement of the Problem

As a practical restriction for production reasons in the design of lenses for extended depth of field (EDOF), we have restricted ourselves to lenses that are radially symmetric [9-12]. While the designs themselves are beyond the scope of this paper, herein we would like to extend the discussion of Sec. 3 to describe a more general radially symmetric asphere in which the focal length is varying with the radius..

Consider a radially symmetric asphere described by the phase delay function $\phi(\rho)$ with a corresponding amplitude transmission function $T(\rho)$ which are related by

$$T(\rho)=e^{-i\Phi(\rho)} \tag{21}$$

Now as a basic design tool it is important to establish a corresponding focal length $f(\rho)$ for this asphere.

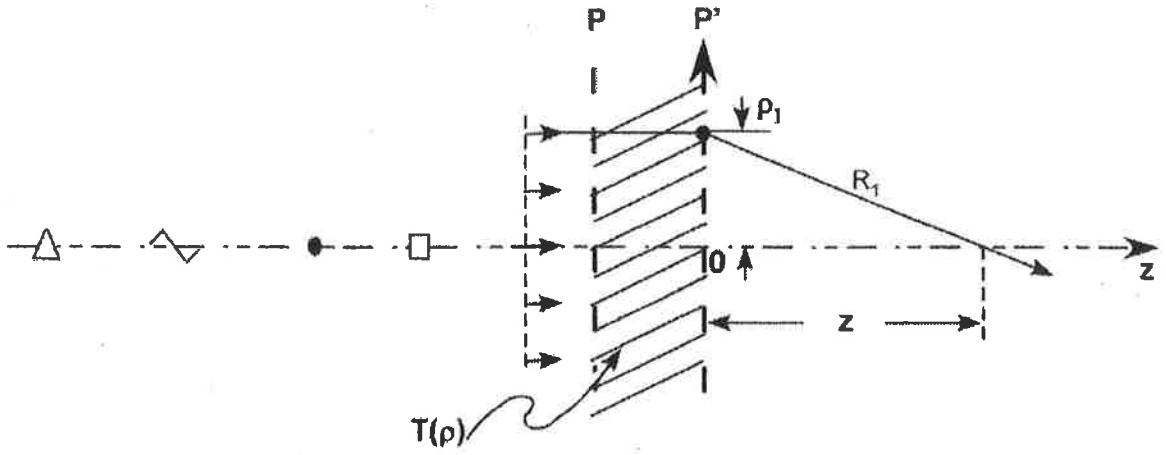

Fig. 3 Notation for lens phase delay (ρ) with focal length $f(\rho)$. The point of stationary phase is at ρ_1. In the object space distance from plane P to □ is s_1; to • is s_0; and to Δ is s_2 as in Eq. (28).

4.2 Connection between wavefront $\phi(\rho)$ and focal length $f(\rho)$

As a basic point of definition for $f(\rho)$, we assume an incident plane-polarized plane wave in Fig. 3 and by Eq. (11), the exiting field will be given by $\exp(-i\phi(\rho))$ at plane P′. Hence from Table 2.3 one can write the exact solution of Maxwell's equation for the transverse scalar component $E_X(x,y,z)$ in the RHS as

$$E_x(x,y,z) = \iint_{z=0} dx'dy' e^{-i\phi(\rho')-ikR_1} \frac{1}{2\pi R_1}\left(ik+\frac{1}{R_1}\right)\frac{z}{R_1}, \qquad (22)$$

in which other terms are defined in Sec. 2.

Now for the camera lens the incident plane wave will give a converging cone of rays. And at (ρ_1) we show a ray heading mostly to cross the optic axis at z. With a radially varying focal length, it is clear that rays will cross at larger values of z from larger radii than (ρ_1) provided that we have so designed the lens. Hence, one can find the peak in the integral in Eq. (22) for any fixed z from the principle of stationary phase, as follows.

For the phase term $[\phi(\rho') + kR_1]$ in Eq. (22), we compute the derivative with respect to ρ' and set it to zero, giving us the result

$$\phi'(\rho_1) + \frac{k\rho_1}{\left[f^2(\rho_1)+\rho_1^2\right]^{1/2}} = 0, \qquad (23)$$

in which we have replaced the crossing point z by $f(\rho_1)$.

This is the fundamental result that we have been seeking. Hence, one sees that if we have a knowledge of $f(\rho)$ for some asphere that we wish to fabricate, the lens will have a phase delay function $\phi(\rho)$ given by the integration $\phi'(\rho_1)$ in Eq. (23), namely

$$\phi(\rho) = \int_0^\rho \phi'(\rho_1)d\rho_1$$

$$\phi(\rho) = \int_0^\rho \frac{-k\rho_1}{\left[f^2(\rho_1)+(\rho_1^2)\right]^{1/2}}d\rho_1 \qquad (24)$$

As is well-known in mathematics, an integration provides a smoothing operation. And as we have found in practice, the knowledge of $f(\rho)$ does not have to be too precise and Eq. (27) will still give a stable functional solution for the phase delay function $\phi(\rho)$ of the EDOF lens.

Conversely by Eq. (23), one can use an assumed or known form for the phase delay of the lens and find the value of the radial focal length for the asphere, namely

$$f(\rho) = \pm\left[\left(\frac{k\rho}{\phi'(\rho)}\right)^2 - \rho^2\right]^{1/2}. \qquad (25)$$

Again, this is an extremely helpful formula from which to analyze an arbitrary asphere, given its $\phi'(\rho)$. We take a derivative and calculate $f(\rho)$. Typically, the proper choice of sign is obvious physically.

It is interesting to write a separate explicit form of Eq. (23) as follows. In Eq. (26) we show a physically instructive "right triangle expression," *viz.*

$$\rho^2 + f^2(\rho) = \left[\frac{k\rho}{\phi'(\rho)}\right]^2 \tag{26}$$

Finally as an instructive illustration to check our algebra, we ask: "What would the form be of the phase delay $\Phi(\rho)$ if the $f(\rho) = F$ is **constant**?" After substitution of the **constant** F value into Eq. (24), one can integrate the expression directly to yield the result:

$$T(\rho) = e^{-i\Phi(\rho)}$$

$$T(\rho) = e^{ik\left[\left(\rho^2+F^2\right)^{1/2} - F\right]} \tag{27}$$

We see that Eqs. (14) and (27) are in agreement, providing a nice consistency result on our algebra.

5. EDOF LENSES & FOURIER OPTICS

5.1 Introduction

In the closing section of this paper, we present practical computations for the extended-depth-of-field using the various forms of Eqs. (23, 25, 26). First we provide a brief background discussion of small digital camera systems developed using the logarithmic asphere lens and its derivatives [8-12]. The material described herein is contained in publications as referenced and no unpublished corporate data are included. The basic logarithmic asphere lens is a form of a radially varying focal length [9-12] and the method of tailoring aspheres is described in [12]. Corporations involved in supporting portions of these projects are the University of Rochester; GG&C/MRDC; and Micron Aptina.

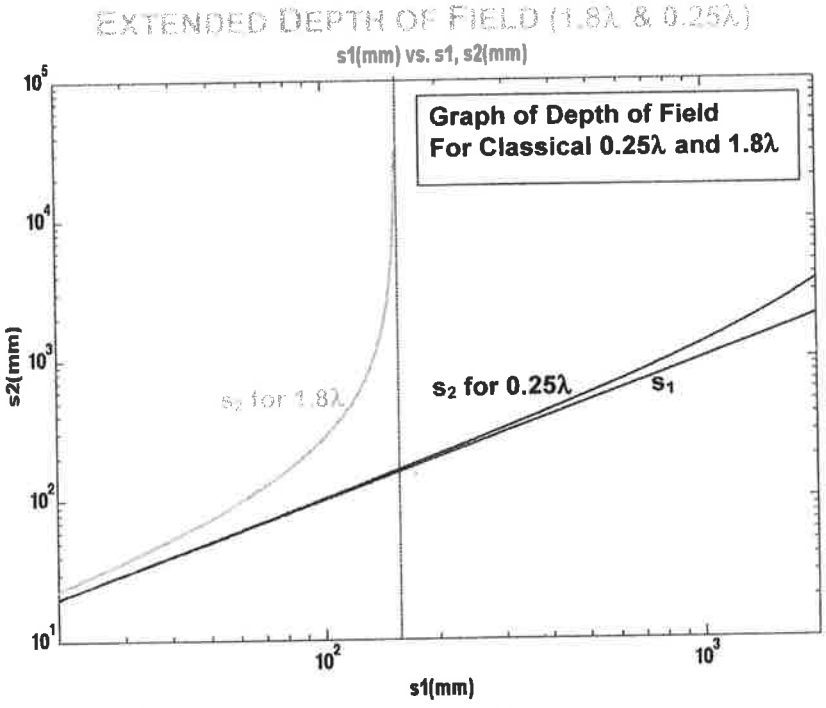

Fig. 4 Extended depth of field (1.8λ & 0.25λ)

5.2 Depth of field and the M-improvement factor [12]

Consider a basic digital camera built around the compound, extended-depth-of-field lens shown in Fig. 3 where the object space is to the left of the cross hatched PP′ principal planes. The CMOS detector is located at a position z = t to the right of P′, "since light travels from left to right at The Institute of Optics." Distances are measured from the symbol to the plane P, as follows in Eq. (28):

$$\begin{aligned} \Delta \quad & \text{outside depth of field} = s_2 \\ \bullet \quad & \text{lens focus set for} \quad = s_o \\ \square \quad & \text{inside depth of field} = s_1 \end{aligned} \tag{28}$$

For a conventional single focus lens which is diffraction limited, the "Rayleigh limit" on defocus is that the difference in distance between the axial ray and the edge ray to the reference sphere can be λ/4. For our method of digital image processing, we find that defocus of Mλ/4 is tolerable where M can range from 5 to 10. Excellent results for image quality are represented when M = 7.2. Let us summarize the well-known depth-of-field equations with the improvement factor M, as follows:

$$\frac{1}{s_o} - \frac{1}{s_2} = \frac{M2\lambda}{D^2} \tag{29}$$

$$\frac{1}{s_1} - \frac{1}{s_o} = \frac{M2\lambda}{D^2} \tag{30}$$

For the overall system, it is interesting to sum Eqs. (29) and (30) to yield

$$\frac{1}{s_1} - \frac{1}{s_2} = \frac{M4\lambda}{D^2} \tag{31}$$

If one sets $s_2 = \infty$, the inside imaging is of high quality at

$$\frac{1}{s_1} = \frac{M4\lambda}{D^2} \tag{32}$$

This spectacular prediction for focus is best studied graphically as shown in Fig. 4. The plot is logarithmic showing s_2 *vs* s_1 for M = 8 and for the Rayleigh case with M = 1.

When the EDOF lens is focused using Eq. (32), a high-quality image is obtained for distances from roughly 150 mm to ∞ without focusing. When the original imaging lens is set for the same inside dimension, it has extremely poor depth of field, as seen in the distance s_1 to s_2 when M = 1 in Fig. 4.

5.3 EDOF logarithmic asphere

The logarithmic asphere is one of the more successful approaches to EDOF, since it provides a considerable improvement factor with M ranging from 5 to 12 as described first in [9]. Also since it is symmetrical in ρ, it is readily produced using modern manufacturing methods.

For the initial logarithmic lens design, we list the following lens specifications: [f/# = 2.8, D = 1.8 mm, f = 5.040mm, s_1 = 204.5 mm, s_2 = ∞]. For a design λ = 0.55 μm, choice M = 7.2, Eq. (32) gives us the improvement factor over the Rayleigh limit of M = 7.2 which is fine. Following the β-design by Eq. (7) in [9], one can calculate φ(ρ) for the log-lens that is plotted in Fig. 5 where we see φ(ρ) *vs.* (ρ). We also provide a power series expansion that is needed to specify the manufacture of the EDOF lens. By Eq. (25) and using φ′(ρ), we calculate the radially varying focal length for the asphere as shown in Fig. 6 varying from 4.979 mm to 5.103 mm as ρ goes from 0 to 0.90 mm respectively.

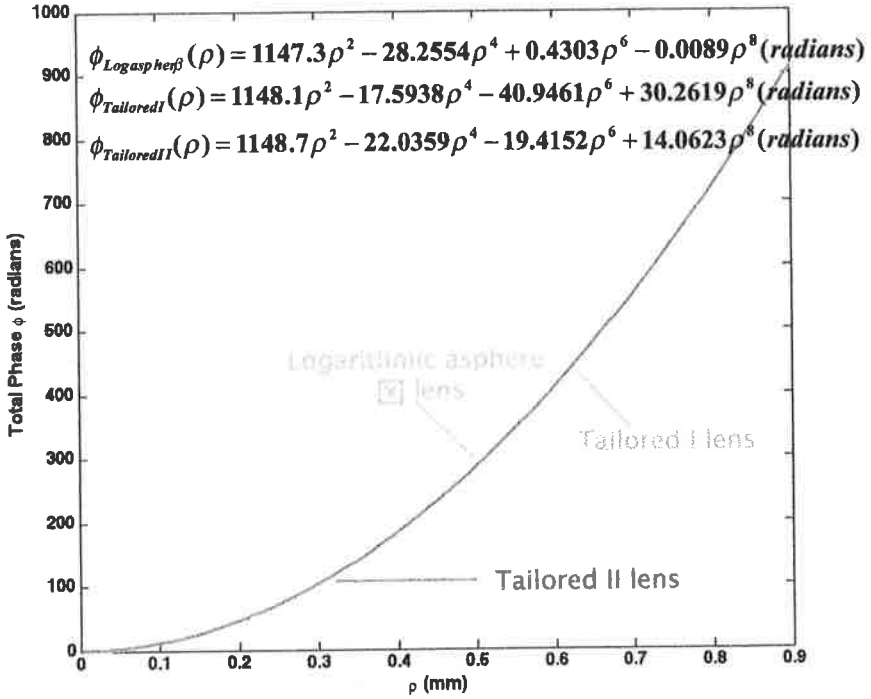

Fig. 5 Total phase delays $\phi(\rho)$ for log asphere β design and its tailored versions I & II.

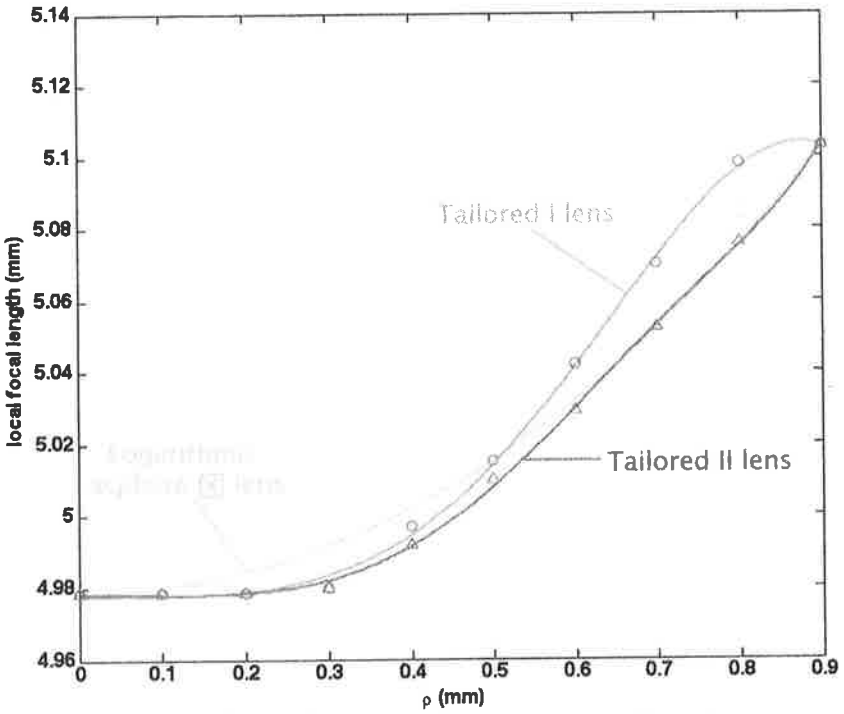

Fig. 6 Focal length $f(\rho)$ vs. ρ for log asphere β design and its tailored versions I & II.

Table of Strehl Ratios at Different Object Distances

Object Distance (mm)	100	150	204	250	300	650	900	infinity
Log Asphere ☒ Design	0.001	0.005	0.014	0.039	0.045	0.261	0.416	0.291
Log Asphere ☒ Design Tailored I	0.002	0.008	0.044	0.069	0.150	0.214	0.258	0.292
Log Asphere ☒ Design Tailored II	0.001	0.005	0.015	0.048	0.051	0.231	0.340	0.292

Table of FWHM of PSFs at Different Object Distances

Object Distance (mm)	100	150	204	250	300	650	900	infinity
Log Asphere ☒ Design (um)	>38.32	14.966	6.258	3.224	4.84	2.448	1.876	1.39
Log Asphere ☒ Design Tailored I (um)	22.52	11.126	3.436	3.772	2.726	2.046	1.629	1.338
Log Asphere ☒ Design Tailored II (um)	35.58	15.028	6.202	2.938	4.544	2.52	1.971	1.344

Table 5.1 Image quality features for extended depth of field (EDOF)

In order to assess this design, we calculate the point spread function at several points in the object space and also the Strehl ratio, Table 5.1. Looking at the line labeled Log Asphere β Design, one sees that performance is poor at s = 100 mm, picking up nicely between 150 mm and 200 mm. Excellent Strehl ratio and fairly constant point spread function denoted by full width half maximum (FWHM) are obtained out to infinity.

Now we are ready to consider the tailoring process, as set forth in [12]. We have found that the Strehl ratio and the FWHM are both good features on which to evaluate overall good image quality. From Table 5.1 if one wishes to improve the lens, say for close-in performance, then simply keeping the focal length small for a larger portion of the lens provides this desired response.

The tailored I lens is designed by placing a few (0) on a Fig. 6 plot of $f(\rho)$ *vs.* ρ. An alternate tailored II lens design is established with the triangular (Δ). With MATLAB one readily converts these choices into the curves shown in Fig. 6. Equation (24) provides the two new designs for the manufacturer's specification: ϕ_1, ϕ_2 as plotted in Fig. 5.

With this illustration one clearly sees the advantage in tailoring EDOF response by means of studying the performance of the lens with a direct comparison to $f(\rho)$ *vs.* ρ calculations.

As one sees in Table 5.1 both of the tailored designs perform much better at the close-in object distances with the tailoring. This feature is important if one wishes to record data records using a cell-phone type of camera.

The excellent depth of field for the lens shown in Fig. 6 can be seen in the Fig. 7 photograph "Ducks in a Row." This color photograph shows excellent image quality over a range from a few inches to twenty feet where the standard eye chart is seen.

Fig. 7. EDOF performance is shown in the photograph "Ducks in a Row" by Nicholas George and Xi Chen.

SUMMARY

In the first part of this paper we describe the application of Fourier optics to lens cascades or compound lenses when the F/# is small. For circularly symmetric lens systems, we explain how to apply Fourier optics in this general case when the propagation is not paraxial. From rigorous EM theory, as summarized in Table 2.3, it is shown that the well-known scalar Helmholtz wave equation for the tangential electric field, Eq. (6), is applicable provided one uses the appropriate impulse response. While the calculation typically requires a laptop PC or MAC, it is straightforward and exact provided that the designer also uses a lens transmission formula that is not paraxially limited. In Sec. 4 we describe transmission functions suitable for radially symmetric aspheres and in Sec. 5 we provide EDOF illustrations where these have proven to be useful both in the logarithmic asphere and in tailored EDOF lenses.

This research was supported in part by the Physics Division of the Army Research Office.

REFERENCES

[1] Goodman, J.W., [Introduction to Fourier Optics], Mc Graw-Hill, New York, 1st Edition (1968) & 3rd Edition (2004).
[2] Papas, C.H., [Theory of Electromagnetic Wave Propagation], Mc Graw-Hill, New York (1965).
[3] Balanis, C.A., [Advanced Engineering Electromagnetics], John Wiley & Sons, New York (1989)
[4] Kong, J.A., [Electromagnetic Wave Theory], EMW Publishing, Cambridge (2008).
[5] Smythe, W.R., [Static and Dynamic Electricity], 3rd Edition, Revised Printing, Taylor & Francis (1989).
[6] Smythe, W.R., "The Double Current Sheet in Diffraction," Phys. Rev. **72**, 1066 (1947).
[7] English, R.E., Jr., and George, N., "Diffraction from a circular aperture: on-axis field strength," Appl Opt. **26** (12), 2360-2363 (1987).
[8] George, N., "Lensless electronic imaging], Opt. Comm. **133**, 22-26 (1997).
[9] Chi, W and George, N., "Electronic imaging using a logarithmic asphere," Opt. Lett. **26**, 375-377 (2001).
[10] George, N., and Chi, W., "Extended Depth of Field Using a Multi-Focal Length Lens With a Controlled Range of Spherical Aberration and a Centrally Obscured Aperture," U.S. Patent 7,336,430 B2 (2008).
[11] Chi, W., and George, N., "Computational imaging with the logarithmic asphere: theory," J. Opt. Soc. Am. A **20**, 2260-2273 (2003).
[12] George, N., and Chen, X., "Extended Depth-of-Field Lenses and Methods for Their Design, Optimization and Manufacturing, U.S. Patent Application Publication US2010/0002310 A1 (2010).

Remotely measuring a thin dielectric coating on a metallic cylinder

Nicholas George[1] and Paul Zavattero[1,*]

[1]*Institute of Optics, University of Rochester, Rochester, New York 14627, USA*
**zavatter@optics.rochester.edu*

Abstract: A laser optical metrology system is described that remotely measures at high rate the presence and thickness of a thin-film lubricant on metallic cylinders with diameters on the order of 0.5 mm. Applications include remote measurement of hypodermic needle dielectric coating thickness in a clean room environment. High accuracy computer simulation of the electric field scattered from a coated cylinder by an incident laser beam is demonstrated using the condition numbers of the matrices defined by the boundary value matching equations derived from the eigenfunction expansion of the exact solution to Maxwell's equations. Dielectric coatings from 1 μm to 50 μm are seen to be readily observed and accurately measured using a remotely placed CMOS array. Distinctive signatures are shown for film thicknesses in the range from 0 to 10 μm, and an appropriate location for CMOS detector placement is determined from the scattering patterns.

OCIS codes: (120.4630) Optical inspection; (240.0310) Thin films; (260.1960) Diffraction theory; (260.2110) Electromagnetic optics; (290.5825) Scattering theory; (290.5820) Scattering measurements; (050.1755) Computational electromagnetic methods; (070.5010) Pattern recognition.

References and links

1. C. A. Balanis, *Advanced Engineering Electromagnetics* (J. Wiley & Sons, 1989).
2. J. A. Kong, *Electromagnetic Wave Theory* (EMW Publishing, 2008).
3. J. J. Bowmann, T. B. A. Senior, and P. L. E. Uslenghi, *Electromagnetic and Acoustic Scattering by Simple Shapes* (North Holland, 1969).
4. M. Kerker, *The Scattering of Light and Other Electromagnetic Radiation* (Academic, 1969).
5. *Handbook of Ellipsometry*, H.G. Tompkins and E.A. Irene, Eds. (William Andrew, 2005).
6. G. James, *Geometrical Theory of Diffraction for Electromagnetic Waves* (Peregrinus, 2003).
7. V. Borovikov and B. Kinber, *Geometrical Theory of Diffraction* (Institute of Electrical Engineers, 1994).
8. G. Strang, *Linear Algebra and its Applications* (Thompson Brooks/Cole, 2006).

1. Introduction

In this paper we consider a monochromatic plane wave incident normally on a metallic cylinder that has a thin dielectric coating. The TMz incident wave is linearly polarized along the z-axis of the coated cylinder, as shown in Fig. 1, where the incident electric and magnetic fields are denoted by $E_z^{inc}\mathbf{z}$ and $\mathbf{H}^{inc}$. The scattered electric field wave $\mathbf{E}_z^{scat}$ emanates at all angles $0 \le |\phi| \le \pi$. For this scattering configuration the exact solution of Maxwell's equations is well known [1–4]. There is considerable literature for various practical situations, mainly in the microwave regime. However, our interest is motivated by the need for accurate and rapid metrology of various fluids used as lubricants and coating deposition on hypodermic needles and other medical devices. Typically, for these applications the product $2\pi a / \lambda$ of incident laser radiation wavenumber and cylinder radius (a) spans a range from 3×10^3 to 1×10^6 radians.

Since many medical devices such as hypodermic needles are manufactured in a clean room environment, it is desirable to have a remote sensing means both for checking the

#154692 - $15.00 USD Received 15 Sep 2011; revised 26 Oct 2011; accepted 25 Nov 2011; published 14 Dec 2011

presence or absence of the thin lubricant and also to measure its thickness, $T = b - a$, typically $4\mu m$ or so. While not directly applicable to the clean room requirement, it is interesting to try using a laboratory microscope in inspecting for a thin micron-like film on a curved surface. Even using a modern microscope, one finds that imaging this thin film is quite difficult. Ellipsometry is the well-known measurement method for measuring the thickness of thin films on flat surfaces and sophisticated precise instruments using polarimetry are commercially available [5]. To our knowledge none of these instruments will rapidly measure the thin film on the curved surface at optical wavelengths with the small radius (0.225 mm) that we are considering. The authors stress the applicability and compatibility of the novel Fig. 1 apparatus to high-rate production of coated needles or wires, since neither polarization optics nor microscopic objectives are required in the optical train.

In this research our major goal is to demonstrate from exact theory and careful computer simulation that the remote sensing approach shown in Fig. 1 is adequate and practical for determining the presence of a thin film coating on a cylinder, and for estimating its thickness. Section 2 presents a brief review of the theory. In Section 3 a new error analysis of the eigenfunction expansion is developed showing that a direct calculation of the eigenfunction series for $\mathbf{E}_z^{scatt}$ is feasible without recourse to the Watson transformation or the geometrical theory of optics [6,7]. Features of the simulated scattered electric field are discussed in Section 4 to show that it is practical, with a CMOS detector, to sense remotely enough of the scattered radiation to obtain the desired results on the presence of a thin film coating and its thickness in the μm range.

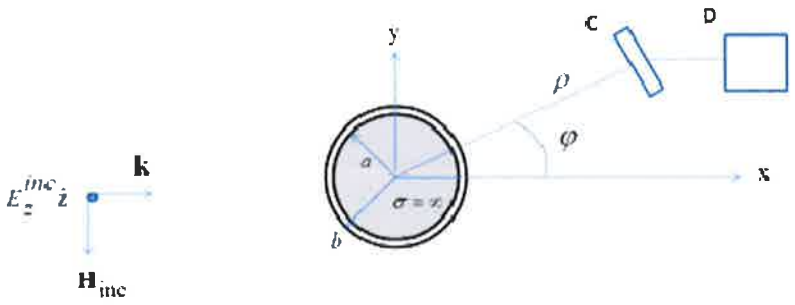

Fig. 1. Optical metrology system schematic: C = detector array, D = computer

2. Electromagnetic theory for the scattered field

In order to determine an appropriate scattering angle for placement of the detector array in the metrology configuration shown in Fig. 1, it is necessary to evaluate accurately the scattered field at very high frequencies over π steradians. The results presented in this paper show that it is feasible to compute the scattered field where needed by truncating its eigenfunction expansion infinite series to a finite sum, in contrast to previous authors using other methods [6,7]. The development of the eigenfunction expansion is summarized below.

The advantage to using a computationally feasible implementation of the eigenfunction expansion is that the electric field can then be computed simply and accurately at any point in the radiation field.

The incident plane wave electric field with wavenumber k_0 shown in Fig. 1 takes the form

$$\mathbf{E}^{inc} = E_0 e^{-ik_0 x}\hat{\mathbf{z}} = E_0 e^{-ik_0 \rho\cos\phi}\hat{\mathbf{z}}, \tag{1}$$

#154692 - $15.00 USD Received 15 Sep 2011; revised 26 Oct 2011; accepted 25 Nov 2011; published 14 Dec 2011

in which the harmonic time dependence $\exp(i\omega_0 t)$ is suppressed, and where $\hat{\mathbf{z}}$ is the unit vector along the cylinder axis. Equation (1) can be rewritten using a well-known Fourier series representation [1–3] in the form given in Eq. (2):

$$\mathbf{E}^{inc} = E_0\left(\sum_{-\infty}^{\infty} i^{-m} J_m(k_0\rho)e^{im\phi}\right)\hat{\mathbf{z}}. \tag{2}$$

The scattered electric field has the form of outgoing waves [1–3], and therefore can be written as a superposition of Hankel functions of the second kind:

$$\mathbf{E}^{scatt} = E_0\left(\sum_{-\infty}^{\infty} A_m H_m^{(2)}(k_0\rho)e^{im\phi}\right)\hat{\mathbf{z}}. \tag{3}$$

Inside the dielectric coating, the electric field can be written as a sum of Bessel functions of the first and second kind:

$$\mathbf{E}^{diel} = E_0\left(\sum_{-\infty}^{\infty}\left(B_m J_m(k_1\rho) + C_m Y_m(k_1\rho)\right)e^{im\phi}\right)\hat{\mathbf{z}}, \tag{4}$$

where k_1 depends on the ratio n_1 / n_0 of the dielectric and scattering media indices of refraction:

$$k_1 = \frac{n_1}{n_0}k_0. \tag{5}$$

The tangential component of the electric field vanishes at the surface of the conducting cylinder at $\rho = a$, and the tangential components of both the electric field and the magnetic field are continuous at the surface of the dielectric at $\rho = b$. These conditions result, for each m, in three independent linear equations in the coefficients A_m, B_m, and C_m. The requirement that the tangential electric field vanish at the surface of the conducting cylinder means that the coefficients C_m can be eliminated setting Eq. (4) to 0 at $\rho = a$:

$$C_m = -\frac{J_m(k_1 a)}{Y_m(k_1 a)}B_m. \tag{6}$$

The linear equations for A_m and B_m resulting from the requirement for continuity of the tangential component of the magnetic field $\mathbf{H}$ at the dielectric boundary $\rho = b$ is obtained from Faraday's law

$$\mathbf{H} = -\frac{1}{i\omega\mu}\nabla\times\mathbf{E} \tag{7}$$

applied at $\rho = b$ to the electric fields $\mathbf{E}^{scatt}$ and $\mathbf{E}^{diel}$ defined in Eqs. (3) and (4). In this problem the electric fields involved are everywhere parallel to the z-axis, so the magnetic field $\mathbf{H}$ has only radial and azimuthal components H_ρ and H_ϕ. The tangential component of the magnetic field at the surface of the dielectric at $\rho = b$ is the azimuthal component H_ϕ, which in this case is given by

$$H_\phi = \frac{1}{i\omega\mu}\frac{\partial E_z}{\partial\rho}. \tag{8}$$

A second linear equation for A_m and B_m is obtained by equating the tangential dielectric field in Eq. (3) at the surface of the dielectric boundary $\rho = b$ to the total tangential electric

#154692 - $15.00 USD Received 15 Sep 2011; revised 26 Oct 2011; accepted 25 Nov 2011; published 14 Dec 2011

field formed from the sum of Eqs. (2) and (3). The linear equations for A_m and B_m take the form

$$\Lambda_m \begin{bmatrix} A_m \\ B_m \end{bmatrix} = \begin{bmatrix} i^{-m} J_m(k_0 b) \\ i^{-m} J'_m(k_0 b) \end{bmatrix} \tag{9}$$

where

$$\Lambda_m = \begin{bmatrix} -H_m^{(2)}(k_0 b) & -\left[J_m(k_1 b) - \dfrac{J_m(k_1 a)}{Y_m(k_1 a)} Y_m(k_1 b) \right] \\ H_m^{(2)'}(k_0 b) & \dfrac{k_1}{k_0}\left[J'_m(k_1 b) - \dfrac{J_m(k_1 a)}{Y_m(k_1 a)} Y'_m(k_1 b) \right] \end{bmatrix} \tag{10}$$

A formal solution to Eq. (9) for A_m can be written in terms of the determinant of the 2 x 2 matrix Λ_m and its entries using Cramer's rule, as follows:

$$A_m = \frac{i^{-m}}{\det \Lambda_m}\left[\Lambda_m^{22} J_m(k_0 b) - \Lambda_m^{12} J'_m(k_0 b) \right]. \tag{11}$$

The accuracy of values for A_m computed using Eq. (11) depends on Λ_m being well-conditioned [8]. If Λ_m is ill-conditioned, the relative accuracy of computed values for A_m will be overly sensitive to roundoff errors, as discussed in more detail below.

3. Numerical analysis and computational accuracy

In order to generate satisfactory values for $\mathbf{E}^{scatt}$ using a truncated eigenfunction expansion,

$$\mathbf{E}_{est}^{scatt} = E_0 \left(\sum_{-M}^{M} A_m H_m^{(2)}(k_0 \rho) e^{im\phi} \right) \hat{\mathbf{z}}, \tag{12}$$

two requirements must be met. First, the coefficients A_m used in Eq. (12) must be numerically accurate. Second, the value of M chosen for Eq. (12) must be large enough so that the terms omitted from the exact eigenfunction expansion in Eq. (3) are negligible.

For a given value of m, the reliability of the computed eigenfunction expansion coefficient A_m depends on the sensitivity of its computed value to computer roundoff errors. The condition number c_m [8] of the matrix Λ_m bounds the effect of roundoff errors on computed values of the expansion coefficients A_m as follows. Let

$$\Lambda_m x_m = y_m, \tag{13}$$

where x_m and y_m represent numerically exact values as follows:

$$x_m = \begin{bmatrix} A_m \\ B_m \end{bmatrix}, \quad y_m = \begin{bmatrix} i^{-m} J_m(k_0 b) \\ i^{-m} J'_m(k_0 b) \end{bmatrix}. \tag{14}$$

Roundoff errors present in the computed values for the Bessel function $J_m(k_0 b)$ and its derivative $J'_m(k_0 b)$ in the right-hand side of Eq. (9) can be viewed as introducing a perturbation δy_m to the exact value of y_m defined by Eq. (13). This perturbation causes the computed value of x_m to contain an error term δx_m to which the perturbed version of Eq. (13) applies:

#154692 - $15.00 USD Received 15 Sep 2011; revised 26 Oct 2011; accepted 25 Nov 2011; published 14 Dec 2011

$$\Lambda_m(x_m + \delta x_m) = y_m + \delta y_m. \tag{15}$$

The condition number c_m bounds the relative error in the computed solution due to roundoff errors as follows:

$$\frac{|\delta x_m|}{|x_m|} \le c_m \frac{|\delta y_m|}{|y_m|}. \tag{16}$$

A similar expression bounds the effect of roundoff errors in Λ_m on errors on the computed solution in terms of the condition number c_m . Equation (16) shows that if the condition number c_m is too large, a slight variation in the value of y_m caused by roundoff errors can cause unacceptably large errors in the computed value for x_m .

To provide an example, suppose that 16-digit double precision accuracy is employed and the computed values for the Bessel function $J_m(k_0 b)$ and its derivative $J'_m(k_0 b)$ in Eq. (11) are accurate to one part in 10^{-16}. If the condition number of the matrix Λ_m is 10^{10}, then the resulting relative error in A_m is less than 0.0001%.

Figure 2 gives a plot of the condition number c_m of the matrix Λ_m defined in Eq. (10) as a function of m for the case where the inner cylinder radius a is 0.225 mm and the dielectric coating thickness T is 10 microns. For this geometry, $k_0 b \approx 3025$. Figure 2 shows that Λ_m is well-conditioned when $m < k_0 b$ but becomes ill-conditioned when $m \ge 3200$. This gives an absolute limit on the number of terms M that can be included in the finite sum approximation to the eigenfunction expansion in Eq. (12).

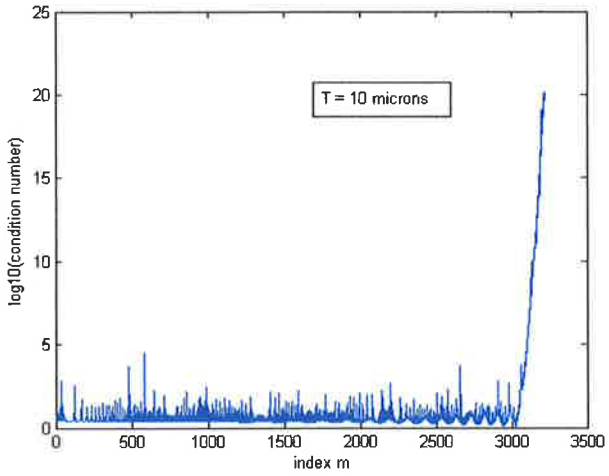

Fig. 2. Logarithm of condition number c_m of Λ_m

Truncating the eigenfunction expansion infinite sum at a finite value causes the computed value $\mathbf{E}_{est}^{scatt}$ to differ from the exact value $\mathbf{E}^{scatt}$ by an amount that depends on the values of the Fourier coefficients $A_m H_m^{(2)}(k_0 \rho)$ for $m > M$. Figure 3 shows a plot of the logarithm of $\left|A_m H_m^{(2)}(k_0 \rho)\right|$ when the inner cylinder radius a is 0.225 mm and the dielectric coating thickness T is 10 microns.

#154692 - $15.00 USD Received 15 Sep 2011; revised 26 Oct 2011; accepted 25 Nov 2011; published 14 Dec 2011

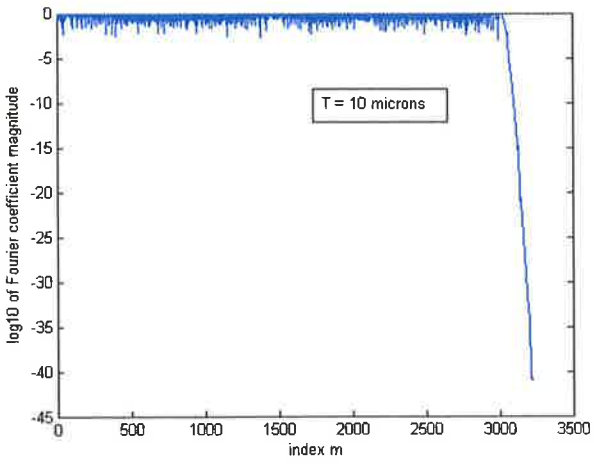

Fig. 3. logarithm of Fourier coefficient magnitude $\left|A_m H_m^{(2)}(k_0\rho)\right|$

Figure 3 shows that the Fourier coefficient magnitudes are generally comparable in magnitude for $m < k_0 b$ but then decrease exponentially very rapidly. When the matrix Λ_m becomes ill-conditioned at approximately $m \approx 3200$, values of $\left|A_m H_m^{(2)}(k_0\rho)\right|$ are seen to be physically negligible, and decrease monotonically at an approximately exponential rate.

The Fourier coefficient magnitudes become physically negligible for values of m well below the threshold value of 3200 where the invertibility of Λ_m becomes problematic.

In the case considered here, use of the cylindrical coordinate frame enables use of the Fast Fourier Transform (FFT) to evaluate the computed scattered field. This extends application of the method to cases where a very large number of Fourier coefficients must be determined. The applicability of the FFT is apparent if Eq. (4) for the approximate scattered field $\mathbf{E}_{est}^{scatt}$ is evaluated at scattering angles $\phi_l = l\dfrac{2\pi}{2M}$, for $-2M \le l \le 2M$, so that

$$\mathbf{E}_{est}^{scatt}(\phi_l) = E_0\left(\sum_{-M}^{M} A_m H_m^{(2)}(k_0\rho)e^{iml(2\pi/2M)}\right)\hat{\mathbf{z}}.$$

It is apparent that the sequence of values $\mathbf{E}_{est}^{scatt}(\phi_l)$ is determined by the FFT of the sequence $\left\{A_n H_m^{(2)}(k_0\rho)\right\}$ of length $2M$.

The approach outlined above can be offered as a candidate for consideration for solving other scattering problems in which boundary value conditions give rise to a set of linear equations for the eigenfunction expansion coefficients. The procedure is to evaluate the condition number of the matrix associated with the boundary value matching linear equation set, and simultaneously monitor the value of the eigenfunction expansion coefficients. This is done successively for each eigenfunction coefficient until all remaining coefficients are negligible. If an excessive number of terms are required, or if the matrices to be inverted become ill-conditioned before the associated expansion coefficients are negligible, then another method must be considered. The advantage to the present method is that it gives a uniformly accurate expansion of the scattered field everywhere, without requiring additional error analyses.

#154692 - $15.00 USD Received 15 Sep 2011; revised 26 Oct 2011; accepted 25 Nov 2011; published 14 Dec 2011

4. Preliminary design for optical metrology system & discussions

We describe the optical metrology for measuring the thin lubricant coating on a polished metallic cylinder, as shown in Fig. 1. Since our theory and calculations are based on exact solutions of Maxwell's equations, it will be clear and convincing that it is relatively simple and effective first to detect the presence or absence of said thin dielectric coating and secondly to measure the thickness in the range from 1 μm to 100 μm. The incident plane-polarized laser beam can be obtained from a low power He-Ne laser (10 mw) or from a medium power Argon laser (1 to 10 w). From prior studies of hypodermic needles, it is known that a 4 mm circular spot is effective to model the infinite laser beam (unless one wishes to study the variation of film thickness along the length of the needle). The scattered beam is measured in power by the CCD or CMOS detector array by recording a signal proportional to the energy density in the electric field, i.e., to $\left|\mathbf{E}^{\text{scatt}}\right|^2$.

From well-known ranging calculations, one can readily show that placing a CMOS detector array at distances ρ ranging from 30 mm to 200 mm will permit one to record the scatter pattern with adequate angular resolution. To illustrate these choices below, we study features in the scattered radiation at a fixed radius of 100 mm and consider a detector array of 10 mm to 14 mm with twelve million pixels. Also we assume a laser power on the order of one watt at wavelength λ equal to 488 nm in a spot size of 4 mm diameter. Summarizing, we normalize the following curves to an incident TMz electric field with amplitude E_z^{inc} of 25×10^3 v/m that is consistent with the above-stated values. There is no trouble with signal level in this system relativeto typical CMOS detector noise characteristics.

4.1 Plane wave scattering by conducting circular cylinder with dielectric coating for $0 \le \phi \le \pi$

Using Eq. (12) we plot curves in Figs. 4-6 for scattering from a metallic cylinder with radius a at 0.225 mm with dielectric coating thicknesses T of 0 μm, 4 μm and 10 μm respectively, over a range of scattering angles φ from 0 to π. The normally incident TMz polarized plane wave travels in the (+ x) direction. Figures 4-6 show values for $\left|\mathbf{E}^{scatt}\right|^2$, with all curves normalized to the incident electric field amplitude of 25 x 10^3 V/m that corresponds approximately to a laser power level of 1 watt in a uniform beam diameter of 4 mm. There is much signature material at various angles and these data clearly show an ease of classification and measurement for the determination of thickness. The curves also show much hidden detail so that finer resolution is needed in the curves as is given below.

#154692 - $15.00 USD Received 15 Sep 2011; revised 26 Oct 2011; accepted 25 Nov 2011; published 14 Dec 2011

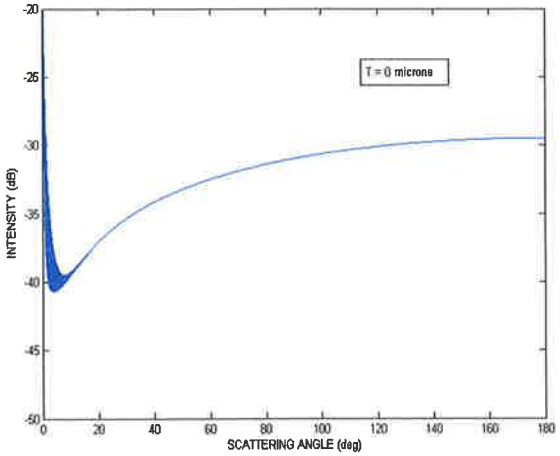

Fig. 4. Normalized scattered field intensity $\left|E^{scatt}\right|^2$, dielectric thickness = 0

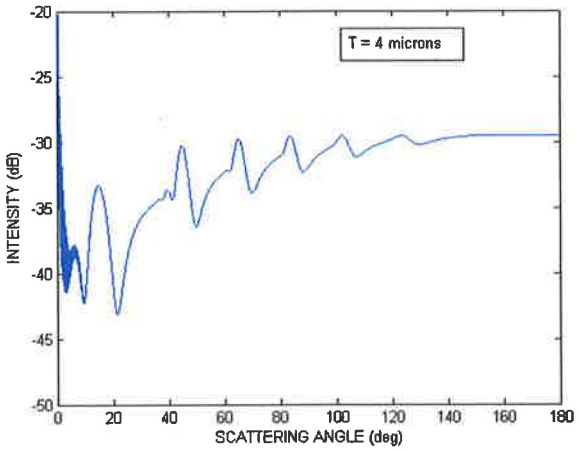

Fig. 5. Normalized scattered field intensity $\left|E^{scatt}\right|^2$, dielectric thickness = 4 microns

#154692 - $15.00 USD Received 15 Sep 2011; revised 26 Oct 2011; accepted 25 Nov 2011; published 14 Dec 2011

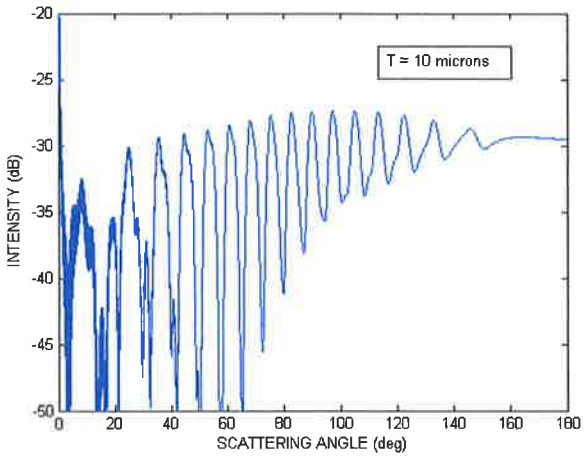

Fig. 6. Normalized scattered field intensity $\left|\mathbf{E}^{\text{scatt}}\right|^2$, dielectric thickness = 10 microns

4.2 Backscattering for the TMz incident polarization

While not central to our optical metrology system, the backscattering of radiation shows an interesting resonance for a thickness in the neighborhood of one micron with a dielectric coating index of refraction $n_0 = 1.5$. Figure 7 shows backscattered energy density for a 20 degree range in the backscatter region. We plot $\left|\mathbf{E}^{\text{scatt}}\right|^2$ normalized to 25 x 10^3 V/m incident electric field for a thin one-micron dielectric film. It has a multiple frequency-modulated (FM) spectrum. Detailed consideration is beyond the scope of this paper.

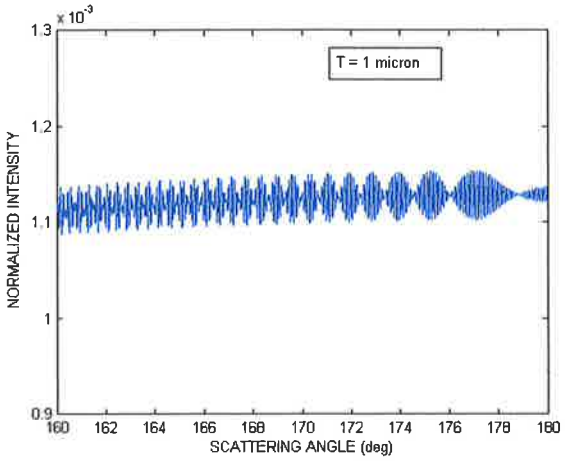

Fig. 7. Backscattered energy intensity $\left|\mathbf{E}^{\text{scatt}}\right|^2$, dielectric thickness = 1 micron

#154692 - $15.00 USD Received 15 Sep 2011; revised 26 Oct 2011; accepted 25 Nov 2011; published 14 Dec 2011

4.3 Forward scattering for the TMz incident polarization

There are two aspects to the measurement at hand. For a complete "fingerprint" of the thickness, recording scattered intensity over a large range of scattering angle at fine resolution is certainly the most conservative procedure. However, if the primary interest is in dielectric coating thickness determination, equivalent results can be obtained with less data storage and simpler software analysis if the data is appropriately sampled, as described in this section.

First, we plot the energy density curves for a limited twenty-degree range, i.e., $0 \le \varphi \le \pi / 9$. Figures 8 and 9 show scattered field energy density curves for dielectric coating thicknesses T at 0 μm thickness and 4 μm, respectively. We plot these on a linear y-axis scale in order that one can see the small amplitude differences. Again, the complex frequency of the oscillations is apparent. Clearly, the high frequency term is similar in both scatterers and a quick calculation shows one that the spatial frequency is determined by the angular scattering width of $\lambda / 2b$ radians. This radian frequency changes by a small percentage as the film thickness T increases, as one can verify by close study of the figures.

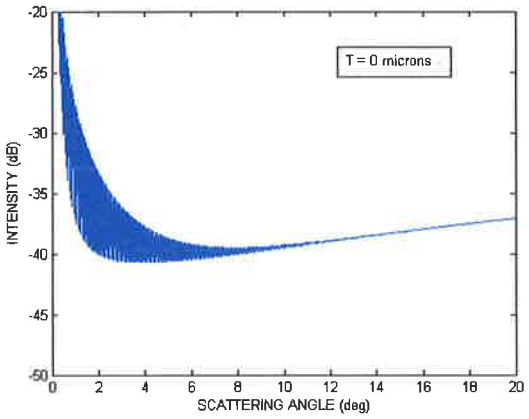

Fig. 8. Scattered energy density, dielectric thickness = 0 microns

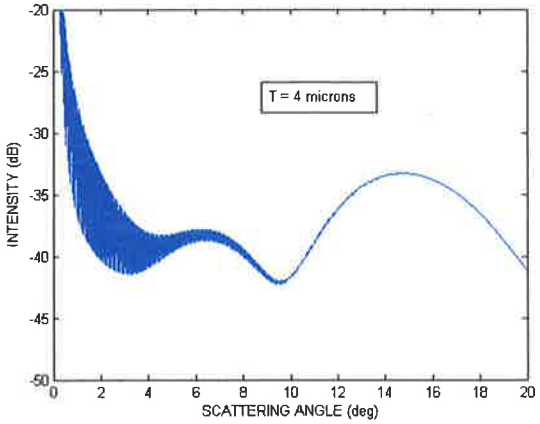

Fig. 9. Scattered energy density, dielectric thickness = 4 microns

#154692 - $15.00 USD Received 15 Sep 2011; revised 26 Oct 2011; accepted 25 Nov 2011; published 14 Dec 2011

Moreover, the low-frequency modulation term apparent when the 4 μm coating is in place is a clear feature of the dielectric coating, and it provides an accurate way for measurement of the thickness, T.

To study this in further detail, it is helpful to spread out the plots in ϕ even further, as shown in Figs. 10 through 12 which are for dielectric thicknesses of 0, 4, and 8 microns respectively.

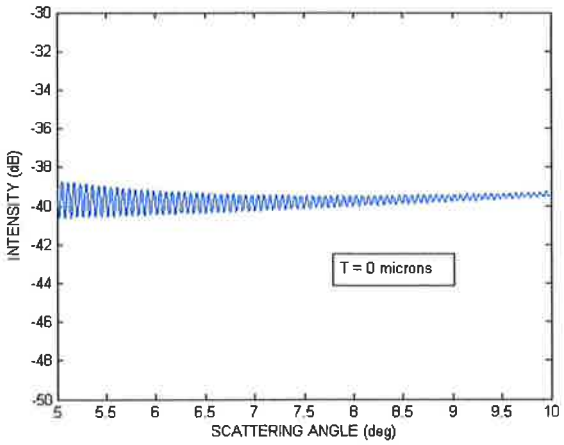

Fig. 10. Scattered energy density, dielectric thickness = 0

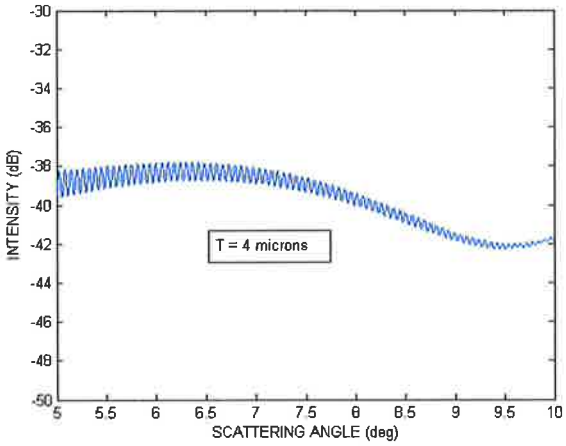

Fig. 11. Scattered energy density, dielectric thickness = 4 microns

#154692 - $15.00 USD Received 15 Sep 2011; revised 26 Oct 2011; accepted 25 Nov 2011; published 14 Dec 2011

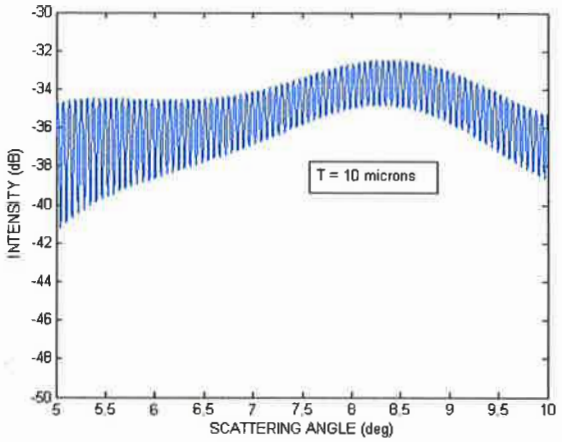

Fig. 12. Scattered energy density, dielectric thickness = 4 microns

Two classes of algorithms are immediately evident from these exact theoretical curves: in one the carrier frequency variation *vs.* thickness is read out and in the other the lower modulation frequency can be monitored. The details of these algorithms are beyond the scope of this paper

5. Summary

A laser optical metrology system is shown to be effective for the rapid and remote determination of the presence or absence as well as the thickness of a thin dielectric coating on a hypodermic cylinder. In the approach presented, a TMz polarized plane wave is incident on the dielectric coated cylinder oriented along the z-axis, and analysis of the scattering pattern is used to determine the thickness of a thin dielectric coating. Exact solutions for the scattered wave are given with the eigenvalue expansion coefficients written explicitly for the scattered field $\mathbf{E}^{scatt}$. Computational accuracy of the resulting values is analyzed using a new application of the condition numbers of the matrices representing the boundary value matching equations. Clear signatures in the scattered electric field are seen for various thicknesses of the thin dielectric film over the range of scattering angles from 0 to 180 degrees. Neither direct forward scattering nor back-scattering are ideal choices for the problem at hand. The scattered field is used to show that placement of a CMOS detector in the range of scattering angles from 5 to 10 degrees is well-suited for the metrology of the thin dielectric film. Scattered field characteristics suitable for use for pattern recognition determination of thickness include amplitude, carrier frequency, and low-frequency modulation. It is interesting to see that the modern desktop computer provides the means for applications of the calculation of exact solutions of Maxwell's equations to the optical scientist who need not be a specialist in electromagnetic waves.

Acknowledgment

This research is supported by the Physics Division of the U.S. Army Research Office.

#154692 - $15.00 USD Received 15 Sep 2011; revised 26 Oct 2011; accepted 25 Nov 2011; published 14 Dec 2011

US008107156B2

(12) **United States Patent**
George et al.

(10) **Patent No.: US 8,107,156 B2**
(45) **Date of Patent: Jan. 31, 2012**

(54) **DIGITAL BINARY MEMS WAVEFRONT CONTROL**

(75) Inventors: **Nicholas George**, Pittsford, NY (US); **Kedar Khare**, Rochester, NY (US)

(73) Assignee: **University of Rochester**, Rochester, NY (US)

(*) Notice: Subject to any disclaimer, the term of this patent is extended or adjusted under 35 U.S.C. 154(b) by 398 days.

(21) Appl. No.: **12/304,025**

(22) PCT Filed: **Jun. 28, 2006**

(86) PCT No.: **PCT/US2006/025254**

§ 371 (c)(1),
(2), (4) Date: **Dec. 9, 2008**

(87) PCT Pub. No.: **WO2008/002314**

PCT Pub. Date: **Jan. 3, 2008**

(65) **Prior Publication Data**

US 2010/0245976 A1 Sep. 30, 2010

(51) **Int. Cl.**
G02B 26/00 (2006.01)

(52) **U.S. Cl.** **359/290**; 359/291

(58) **Field of Classification Search** 359/290, 359/291

See application file for complete search history.

(56) **References Cited**

U.S. PATENT DOCUMENTS

4,786,124	A	11/1988	Stone et al.	
5,624,437	A	4/1997	Freeman et al.	
6,220,707	B1	4/2001	Bille	
6,394,999	B1	5/2002	Williams et al.	
6,413,251	B1	7/2002	Williams	
6,529,311	B1	3/2003	Bifano et al.	
2002/0190922	A1*	12/2002	Tsao	345/32
2005/0088738	A1	4/2005	Islam et al.	
2006/0092497	A1	5/2006	Duncan	

OTHER PUBLICATIONS

James Jones; Patent Cooperation Treaty PCT International Search Report; Jul. 21, 2008; 5 pp.
James Jones; Patent Cooperation Treaty PCT Written Opinion of the International Searching Authority; Jul. 21, 2008; 6 pp.
Giles et al.; Setting up a liquid crystal phase screen to simulate atmospheric turbulence; Processing of SPIE; vol. 4124; 2000 SPIE; 89-97.

(Continued)

Primary Examiner — Ricky Mack
Assistant Examiner — James Jones
(74) *Attorney, Agent, or Firm* — William Greener; Bond, Schoeneck & King, PLLC

(57) **ABSTRACT**

Embodiments of the invention are directed to a new type of phase screen, i.e., an opto-electronic device that can convert a distorted incoming optical wavefront into a plane wave or, conversely, transform a plane wave into a prescribed varying output wavefront. The basic concept involves novel binary all-digital MEMS interferometer configurations that can be used to create controlled and arbitrary optical wavefront using only 0,1 amplitude changes followed by differential propagation distances to convert these amplitude variations into controllable and/or continuous phase variations. Clustered pixel notions, such as Floyd-Steinberg, Stucki or other algorithms useful in digital half-tone printing, are simultaneously employed to create controllable grey-level variations as well as continuous phase variations. Desired grey-levels can be obtained wherein each pixel is formed by, e.g., a 3×3 or 5×5 cluster of mirrors. Both the filling-in of the outputs of the binary mirror (0,1) and the grey-levels are accomplished simply by spatial averaging over a short propagation distance.

14 Claims, 10 Drawing Sheets

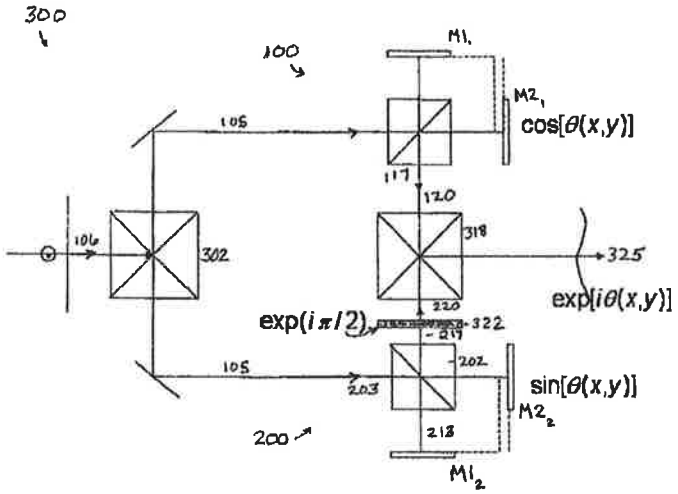

OTHER PUBLICATIONS

Bifano et al.; Micromachined Deformable Mirrors for Dynamic Wavefront Control; Proceedings of SPIE; vol. 5553; SPIE, Bellingham, WA, 2004; 1-16.

Serati et al.; Advances in liquid crystal based devices for wavefront control and beamsteering; 13 pp.

Perreault et al.; High-Resolution Wavefront Control Using Micromirror Arrays; Solid-State Sensor, Actuator and Microsystems Workshop, Hilton Head Island, South Carolina, Jun. 6-10, 2004; 83-86.

Doble et al.; The Application of MEMS Technology for Adaptive Optics in Vision Science; IEEE Journal of Selected Topics in Quantum Electronics, vol. 10, No. 3 May/Jun. 2004; 629-635.

Krulevitch et al.; MOEMS spatial light modulator development at the Center for Adaptive Optics; Proceedings of SPIE; vol. 4983; 2003 SPIE; 227-234.

Perreault et al.; Adaptive optic correction using microelectromechanical deformable mirrors; Optical Engineering, vol. 41, No. 3, 561-566; Mar. 2002; Society of Photo-Optical Instrumentation Engineers.

Mali et al.; Development of microlectromechanical deformable mirrors for phase modulation of light; Optical Engineering vol. 36, No. 2, 542-548; Feb. 1997; Society of Photo-Optical Instrumentation Engineers.

* cited by examiner

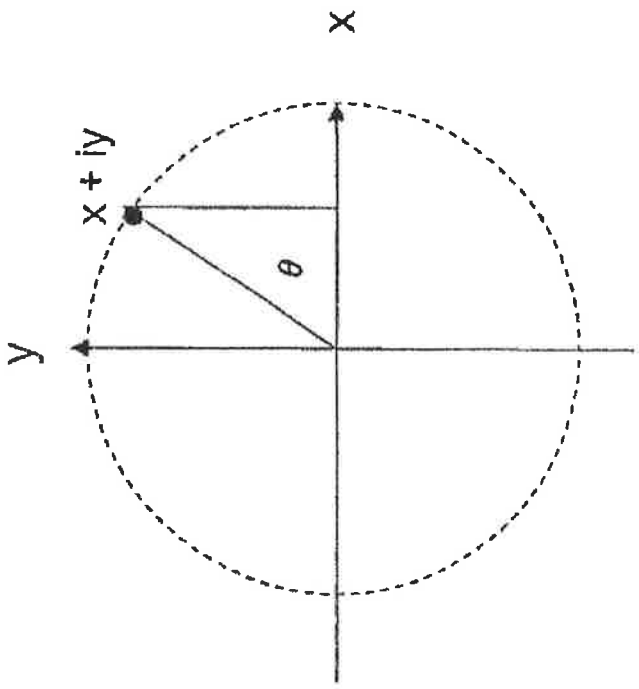

FIG. 1

FIG. 2A

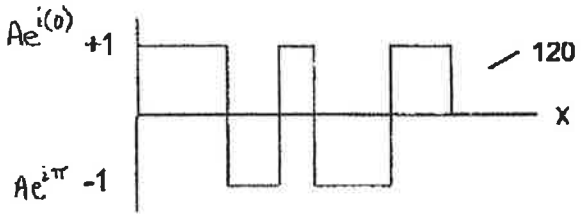

FIG. 2B

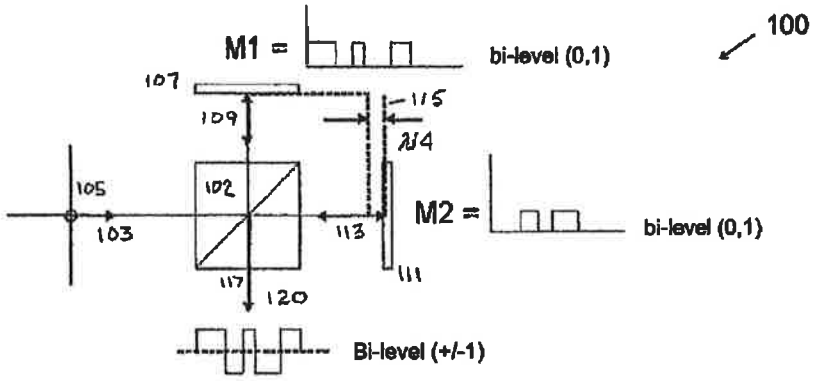

FIG. 2C

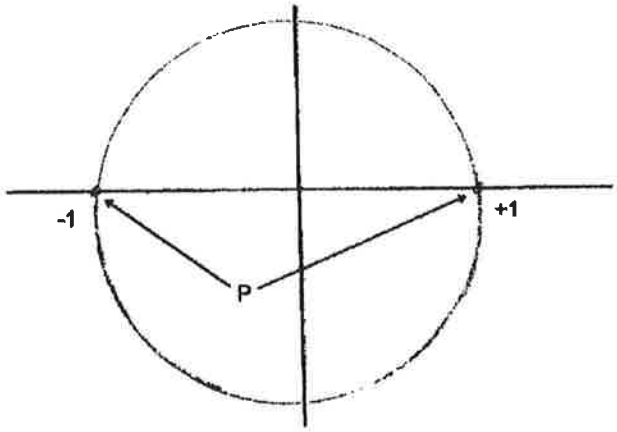

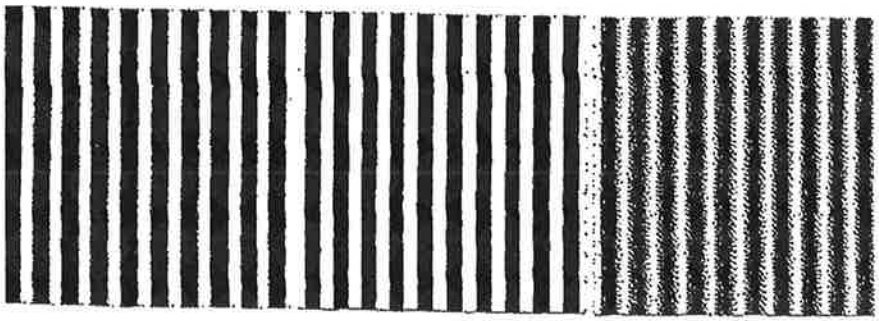

FIG. 3(a) FIG. 3(b) FIG. 3(c)

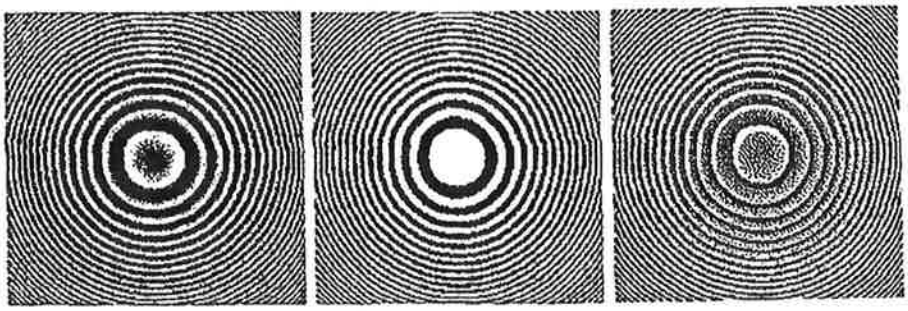

FIG. 6(a) FIG. 6(b) FIG. 6(c)

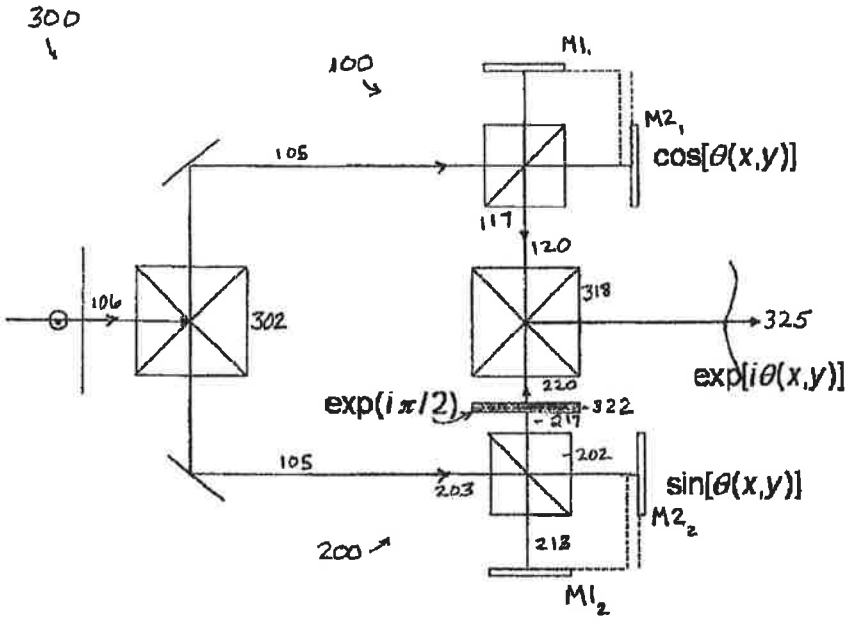

FIG. 4A

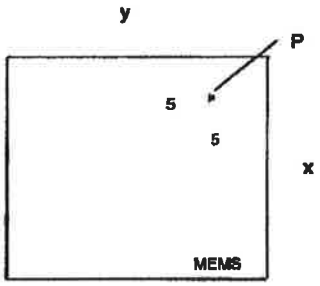

FIG. 4B

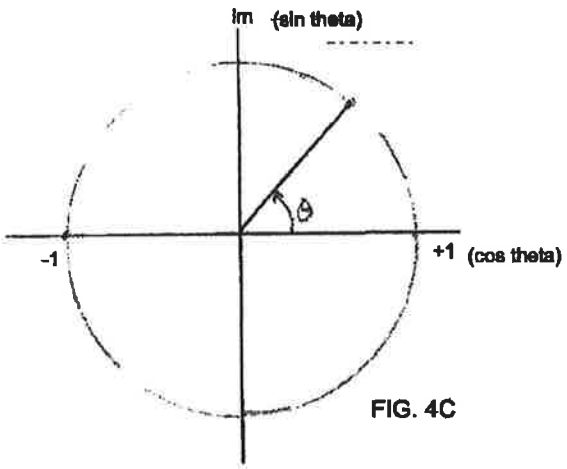

FIG. 4C

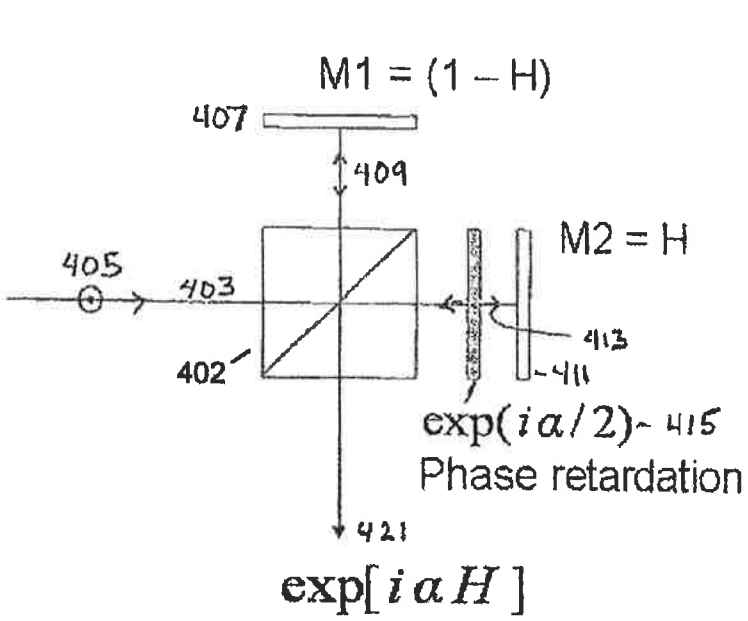
400
M1 = (1 – H)
407
409
M2 = H
405
403
413
402
411
exp(iα/2)- 415
Phase retardation
421
exp[iαH]

FIG. 5

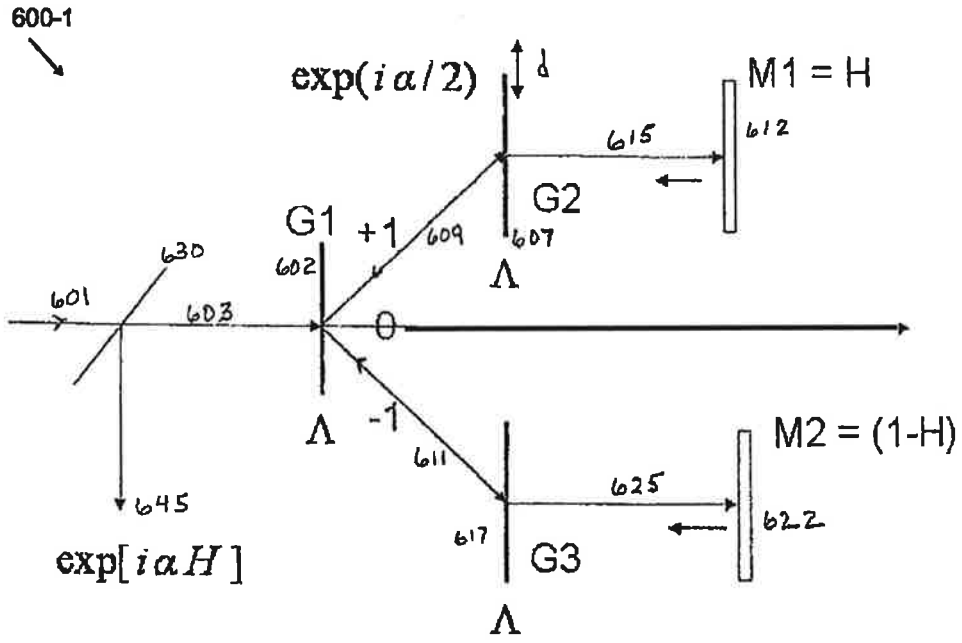
600-1
exp(iα/2)
d
M1 = H
615
612
G2
G1
+1
609
607
602
630
601
603
0
Λ
Λ
-1
611
M2 = (1-H)
625
622
617
G3
645
exp[iαH]
Λ

FIG. 7A

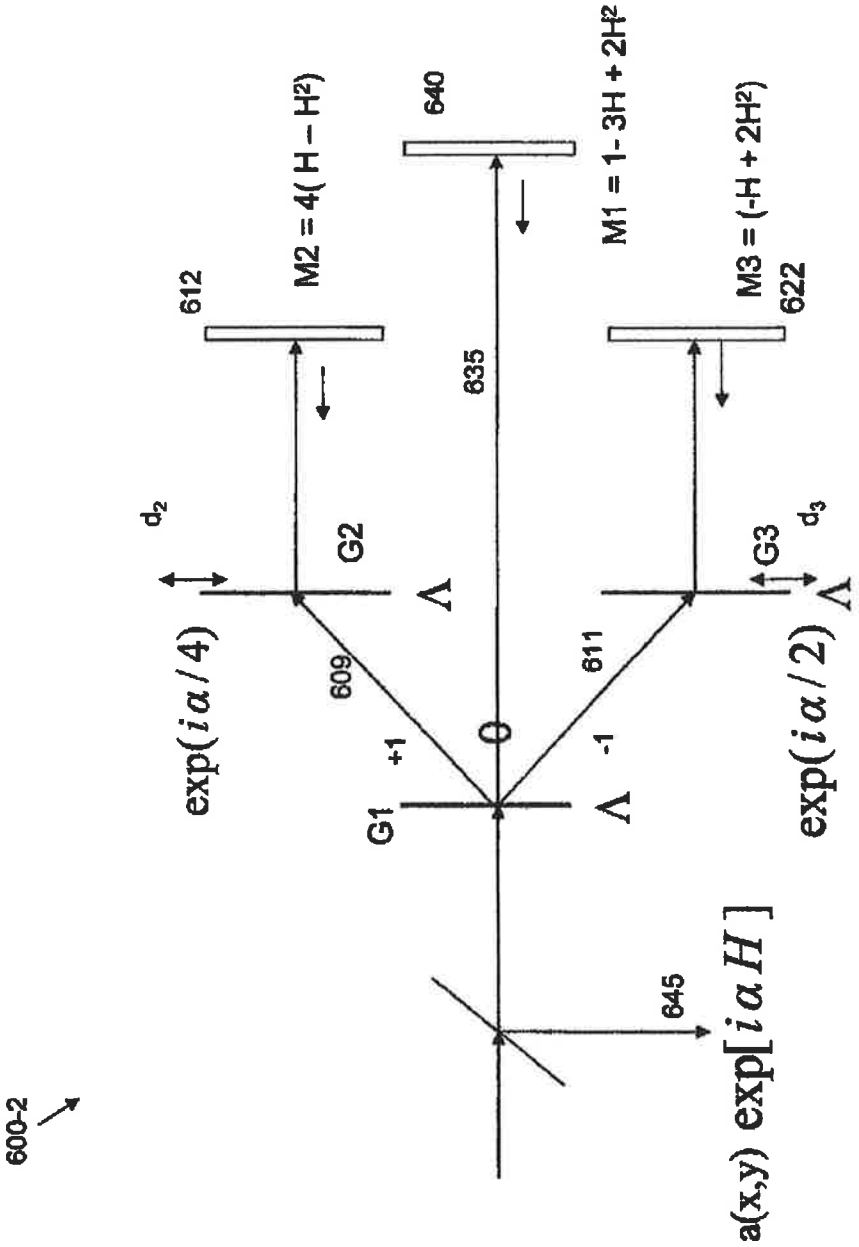
600-2
a(x,y) exp[ia H]
645
640
M1 = 1- 3H + 2H²
M2 = 4(H – H²)
M3 = (-H + 2H²)
612
622
635
d2
d3
G2
G3
G1
+1
0
-1
609
611
exp(ia/4)
exp(ia/2)

Fig. 7B

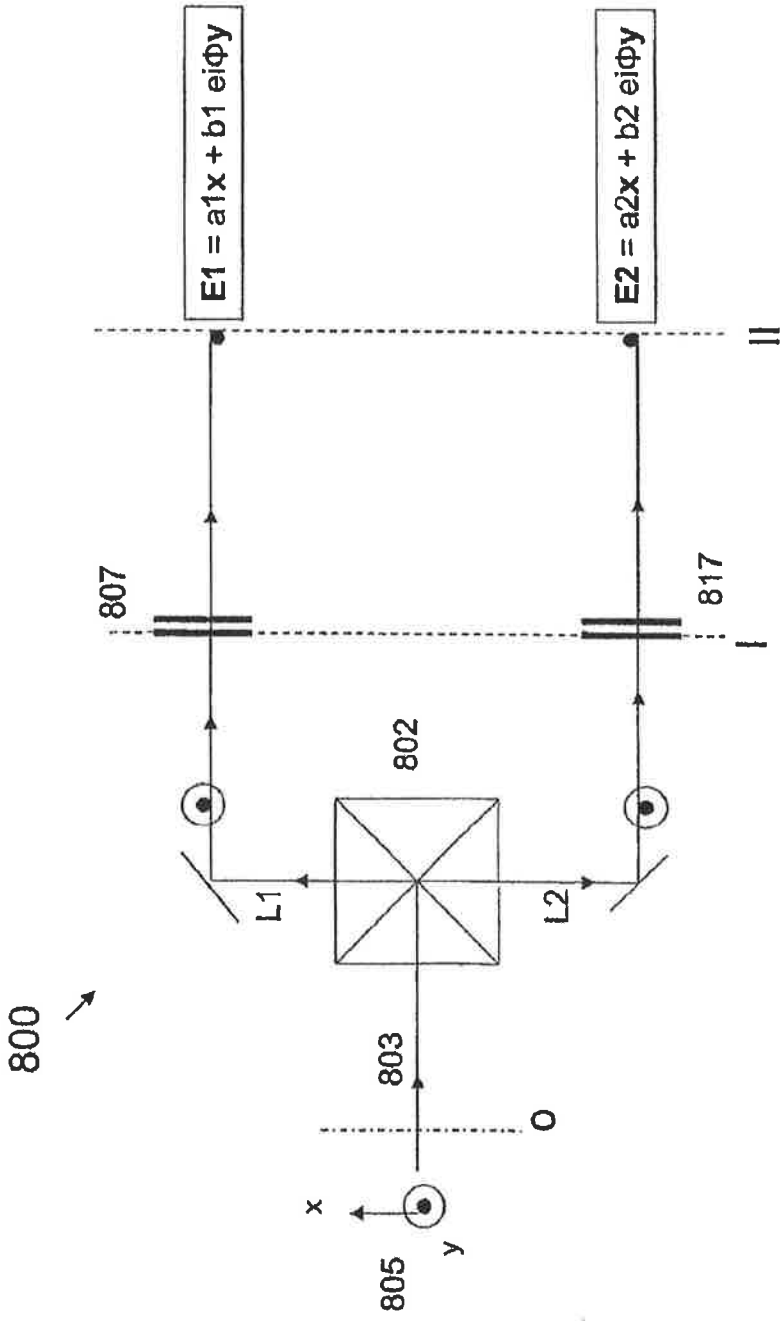
E1 = a1x + b1 eiφy
E2 = a2x + b2 eiφy
II
I
807
817
802
L1
L2
800
803
O
x
y
805

FIG. 8

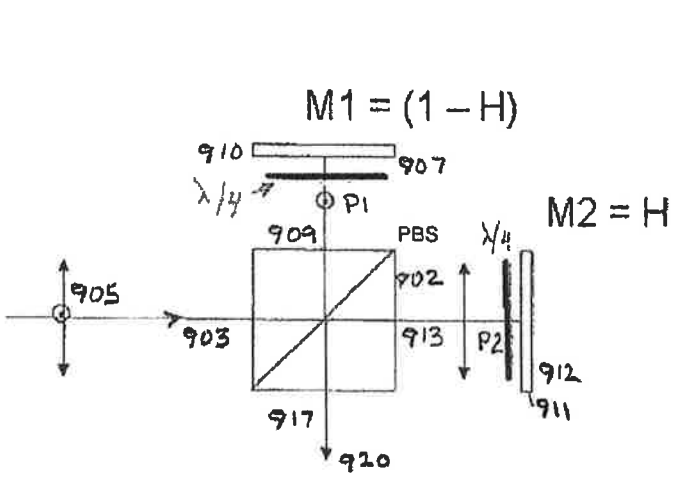
900
M1 = (1 – H)
910
907
λ/4
P1
M2 = H
909
PBS
λ/4
905
902
903
913
P2
912
911
917
920

FIG. 9A

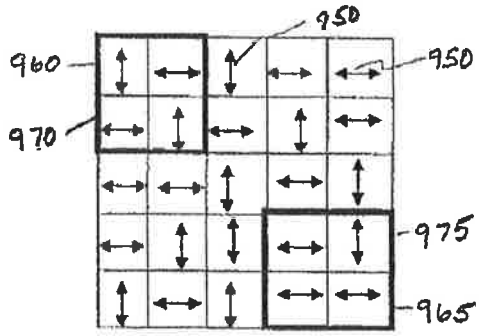
950
960
950
970
975
965

FIG. 9B

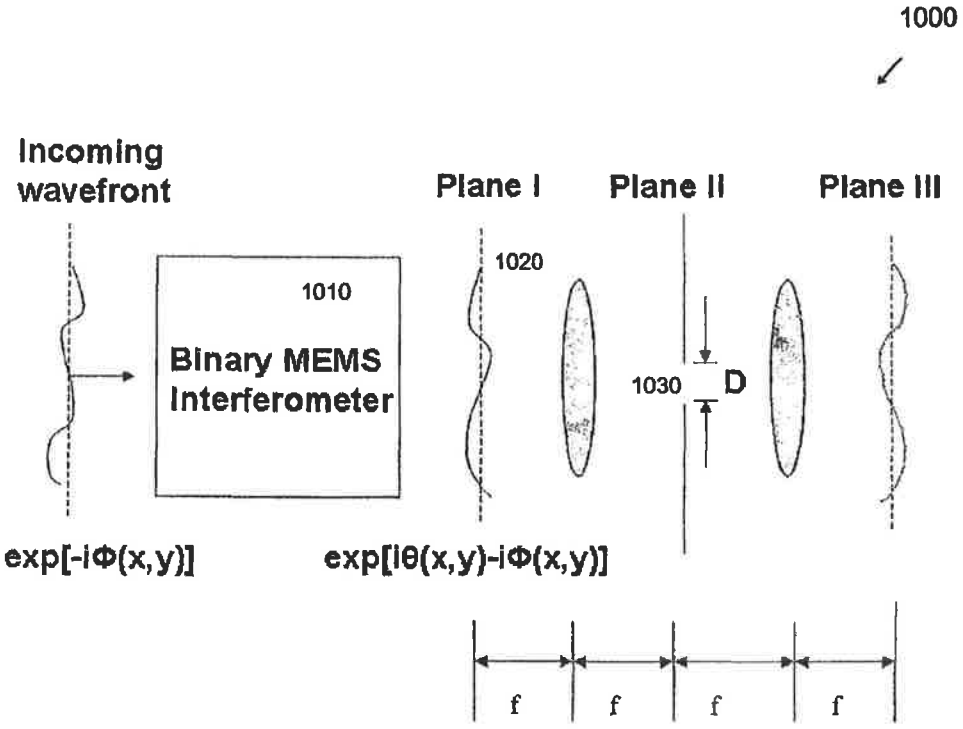
1000
Incoming wavefront
1010
Binary MEMS Interferometer
Plane I
Plane II
Plane III
1020
1030
D
exp[-iΦ(x,y)]
exp[iθ(x,y)-iΦ(x,y)]
f
f
f
f

FIG. 10

DIGITAL BINARY MEMS WAVEFRONT CONTROL

FEDERALLY SPONSORED RESEARCH

This invention was made with U.S. Government Support under Contract Number DAAD 19-03-1-0185 (44430-PH), awarded by the US Army Research Office. The Federal Government has certain rights in the invention.

RELATED APPLICATIONS

This application is a national stage filing of PCT/US2006/025254 filed on 28 Jun. 2006 and claims priority thereto.

BACKGROUND OF THE INVENTION

1. Field of the Invention

Embodiments of the invention are most generally related to the field of optical modulation and opto-electronic imaging. More particularly, embodiments of the invention are directed to novel apparatus and methods that effect phase and absolute value of the amplitude, hereinafter amplitude, control over an optical wavefront, and to applications directed to atmospheric sensing, optical metrology, astronomical and ophthalmic imaging, adaptive optics and interferometry.

2. Description of Related Art

In optical interferometry one often needs to generate a particular function form for the variation of amplitude over a given transverse plane starting, for example, from a uniform plane wave. As a specific instance in optical metrology, one generates the family of Zernike polynomials using modern optical interferometers with special masks incorporated. These specified wavefronts are used to test the accuracy of a particular optical surface being fabricated. In addition there are other instances when a distorted wavefront needs to be corrected so as to provide a plane wave output or a converging wave of specific radius of curvature for the equiphase of the propagating wave. For instance, when an optical signal travels from point A to point B, the quality of the received signal is less than that of the transmitted signal. This degradation is due to variation in the uniformity of the medium (index of refraction) that the light propagates through in going from point A to point B. Common examples include the light from a star that is distorted by atmospheric turbulence; poor vision due to defects in the optics of the eye; and, noisy communication caused by a non-uniform index of refraction over the signal path.

Viewed simply, a point source of light such as a star, for example, radiates spherical wavefronts of light in all directions. A wavefront is the locus of points having the same phase i.e., have the same path length from the source. To a distant viewer on earth, the wavefront of the light traveling along the viewer's line of sight is in the form of a flat, uniform plane of light; i.e., a plane wavefront. However, when the index of refraction of the propagation medium changes, the path lengths are no longer equal or normal to the propagating plane wavefront. Instead, the wavefront is distorted or aberrated. Thus the phase of the wavefront is no longer uniform over the spatial extent of the wavefront.

Wavefront sensors are now commonly used to measure higher-order aberrations of a wavefront propagated through an optical system. A Shack-Hartmann sensor is often the principal component of modern ophthalmic wavefront measuring devices. Several other types of wavefront sensors are also commercially popular. Once a distorted wavefront is measured and quantified, it may be desirable to compensate

the wavefront; i.e., to bring it back to its non-aberrated state. Deformable minors, referred to as adaptive or active optics (AO) depending upon their application, are well known in the art. An adaptive optics imaging system, for example, is designed to correct for phase distortions in the optical wavefront in near real time to obtain improved image quality. Adaptive optical imaging originated as a tool for improving the performance of ground-based large telescopes for astronomical imaging through atmospheric turbulence. Another application is the correction of atmospheric turbulence over horizontal propagation paths. Adaptive imaging techniques have also been applied to wavefront control of large astronomical telescopes by using high power lasers and guide stars to generate perturbed wavefronts for correction of the astronomical image. Adaptive optics and wavefront control are also commonly used in laser fusion to correct for minute phase perturbations as the laser beam propagates through various lenses of the system. The typical components used in a present day adaptive system are listed in Table 1.

TABLE 1

Wavefront Sensors	Wavefront Correctors
Shack-Hartmann Sensor	Continuous membrane mirrors with PZT
Curvature sensor	Segmented mirrors with PZT
Shearing interferometer	Bimorph Mirrors
Smartt interferometer	MEM micro-mirrors
Pyramid sensor	Liquid Crystal SLMs

Conventional designs for wavefront correctors include segmented mirror devices with each mirror segment having tip/tilt and piston controls, and continuous membrane (analog) devices with a number of actuators on their back side for deforming the mirror surface. Bimorph mirror technology uses two piezoelectric wafers bonded together with an array of electrodes. The outer surface of one of the mirror acts as a mirror. These devices are most suitably used with a curvature sensor configuration. More recent technologies used for phase screens, as they are sometimes called, include liquid crystal spatial light modulators (SLMs) and analog-type MEMS based micro-mirrors. Spatial light modulation is used, for example, in the fields of optical information processing, projection displays, video and graphics monitors, televisions, astronomy and electrophotographic printing. There, optical beams are deflected by mirror arrays where it is desired to be able to individually phase adjust the reflected light from each mirror. Often, the phase screen in an AO telescope is the single most troublesome component in the system. Typically, the phase screen is an LCD used in transmission mode with a voltage applied in an x-y coordinate system, pixel by pixel. It can also take the form of multiple PZT actuators used to push or deform a smooth mirror membrane into an aberration compensating surface shape.

Cost is an important factor in choosing an appropriate deformable mirror technology for a given application. Piezo-activated (PZT) deformable mirrors can cost over $1000 per actuator, thus a large mirror array can be extremely expensive. MEMS devices are typically manufactured using fabrication methods developed in the semiconductor industry. Comparatively, MEMS technology offers a low-cost attractive alternative. There are generally two types of micro-mirror arrays: (1) Devices with piston and tip/tilt controls for micro-mirrors; and (2) simple ON/OFF type binary micro-mirror arrays. The state-of-the-art devices of the first type have ~1000 micro-mirrors each about 300 microns on a side, and each having an ~2 micron piston stroke motion and ~7 kHz frame rate. The ON/OFF type (i.e., digital binary MEMS) devices on the

other hand have close to a million mirror elements, each being ~17 micron on a side. Digital binary MEMS mirror technology has been developed over the last two decades. Arrays consisting of ~10^6 mirrors that impart binary (1,0) amplitude modulation to the incident wavefront at ~10 kHz frame rates are now available commercially at low cost. They have found widespread application, for example, in projection display systems. In recent years other applications of these arrays have evolved, e.g. in generation of (1,0) mask patterns in lithography, for implementing a moving aperture in a confocal microscope, for obtaining multiplexing Hadamard type mask patterns in spectroscopy applications, etc. The ability to provide only (1,0) type amplitude modulation has thus far been treated as a limitation that has prevented their use in adaptive systems for phase correction. A new way of wavefront phase coding is required that will permit the use of binary mirror arrays for wavefront phase modulation.

It is possible to generate selected wavefronts using deformable MEMS mirrors or LCD spatial light modulators. There are, however, certain disadvantages associated with their use. These devices typically cannot work over a broad range of wavelengths from the visible to long wavelength infra-red. As mentioned above, the cost for a 1000×1000 actuator assembly is prohibitive. MEMS devices currently used in adaptive optics setups do not offer as high resolution as may be desired for a particular application. The control of a large mirror array is complex and a large MEMS array can be susceptible to backlash errors. Half-toned characterization of phase front, as will be described below and used in conjunction with embodiments of the instant invention, would require high computational loading using the aforementioned deformable mirror devices.

In view of the challenges and disadvantages associated with wavefront phase control using deformable mirrors and/or LCD SLMs, the inventors have recognized that significant benefits may be realized by the various embodiments and aspects of the invention described in detail below and as defined in the appended claims. As mentioned above, a new way of wavefront phase coding is required that will permit the use of digital binary mirror arrays for wavefront phase modulation. The ability to generate an arbitrary wavefront using only binary (ON/OFF) micro-mirror arrays combined with digital half-toning methods and differential propagation distances has several advantages over deformable analog MEMS mirrors or LC spatial light modulators. The benefits and advantages include, but are not limited to, the ability to generate arbitrary wavefronts using only binary (ON/OFF) micro-mirror arrays combined with digital half-toning methods; broadband performance over the wavelength range from the visible to LWIR; an effective frame size of ~200×200 to 300×300 pixels using digital half-toning algorithms over, e.g., 3×3 or 5×5 mirror blocks at a fraction of the cost for comparable MEMS performance; resolution that far exceeds analog MEMS device capability; simpler operation; less susceptibility to backlash errors; lower computational load, easy system calibration; all digital architecture; environmental robustness and stability, and others that will be recognized by persons skilled in the art.

As used herein, the term 'analog' refers to a continuous membrane mirror surface that may be deformed by a number of actuators coupled to the rear surface of the membrane, or, to a MEMS device where the individual mirrors can be stepped over multiple positions instead of simple binary 0,1. In contrast, a 'digital' binary MEMS mirror, as that term will be used in conjunction with various embodiments and aspects of the invention described herein, will refer to a MEMS mirror array in which each individual mirror segment can only be in an "ON" position (referred herein below as having a 1 value and oriented to retro-reflect incident light) or an "OFF" position (referred to herein below as having a 0 value and tilt-oriented to reflect incident light away from the intended optical path).

FIG. 1 shows what is known as an Argand diagram, which is used to illustrate the geometric representation of a complex number as simply a point in the complex plane. An Argand diagram is a plot of complex numbers as points z=x+iy in the complex plane using the x-axis as the real axis and the y-axis as the imaginary axis, where $z=(abs)z\ e^{i\theta}$. In the figure, the radius of dashed circle represents the complex modulus (abs)z of z and the angle θ represents its complex argument or what can be called the phase. The phase, θ, corresponds to the counterclockwise angle from the positive real axis, i.e., the value of θ such that x=(abs)z(cos θ) and y=(abs)z(sin θ). Since a wavefront may be described by Euler's equation $e^{i\theta(x,y)}=\cos\theta+i\sin\theta$, in conjunction with various embodiments of the invention described herein below, the notation of the Argand diagram may be useful to the reader in illustrating various aspects of the invention.

The advantages and benefits provided by the teachings disclosed herein and the embodiments of the invention disclosed and claimed will become more apparent to persons skilled in the art in view of the following description and drawings.

SUMMARY OF THE INVENTION

Most generally, embodiments of the invention are directed to a new type of phase screen, i.e., an opto-electronic device that can convert a distorted incoming optical wavefront into a plane wave or, conversely, transform a plane wave into a prescribed varying output wavefront. The basic concept involves novel binary all-digital MEMS configurations that can be used to create an arbitrary optical wavefront using only 0,1 amplitude changes followed by differential propagation distances to convert these amplitude variations into controllable and/or continuous phase variations. As used herein, the term 'arbitrary' wavefront refers to a pixel phase value that can be represented anywhere in the complex plane described by an associated Argand diagram, rather than just on the unit value circle boundary or on some other restricted portion of the complex plane. Clustered pixel notions, such as Floyd-Steinberg, Stucki or other algorithms useful in digital half-tone printing, are simultaneously employed to create controllable grey-level variations as well as continuous phase variations. Desired grey-levels can be obtained wherein each pixel is formed by a cluster of 3×3 mirrors or 5×5 mirrors, for example. Both the filling-in of the outputs of the binary mirror (0,1) and the grey-levels are accomplished simply by short propagation.

According to an embodiment of the invention, an optical control component includes a first component beam divider/combiner disposed along a first component input optical path of an incident optical wavefront; a first component binary MEMS device $M1_1$ comprising an $(n_{x,y}\times m_{x,y})_{M1}$ mirror array disposed optically downstream of the first component beam divider/combiner along an M1 optical path having a total optical path length $L1_1$ (i.e., L1 is a double-pass distance); a first component binary MEMS device $M2_1$ comprising an $(n_{x,y}\times m_{x,y})_{M2}$ mirror array disposed optically downstream of the first component beam divider/combiner along an $M2_1$ optical path different than the $M1_1$ optical path having a total optical path length $L2_1$; and phase retarder means for making $L1_1$ different than $L2_1$, wherein at least an $M1_1$ mirror sub array $(X\times Y)_{M1}$ is in an ON/OFF state and a complementary at

least an $M2_1$ mirror sub array $(X\times Y)_{M2}$ is in an OFF/ON state, further wherein an output wavefront propagating along a first component output optical wavefront path has a controlled modulation.

Another embodiment of the invention is directed to an optical control device comprising a first optical control component as described immediately above; a second optical control component including a second component beam divider/combiner disposed along a second component input optical path of an input optical wavefront; a second component binary MEMS device $M1_2$ comprising an $(n_{x,y}, m_{x,y})_{M1}$ mirror array disposed optically downstream of the second beam divider/combiner component along an $M1_2$ optical path having a total optical path length $L1_2$; a second component binary MEMS device $M2_2$ comprising an $(n_{x,y}, m_{x,y})_{M2}$ mirror array disposed optically downstream of the second beam divider/combiner component along an $M2_2$ optical path different than the $M1_2$ optical path having a total optical path length $L2_2$; and phase retarder means for making $L1_2$ different than $L2_2$, wherein at least an $M1_2$ mirror sub array $(X\times Y)_{M1}$ is in an ON/OFF state and a complementary at least an $M2_2$ mirror sub array $(X\times Y)_{M2}$ is in an OFF/ON state, further wherein an output wavefront propagating along a second component output optical wavefront path has a controlled modulation; an input beam divider disposed optically intermediate an incoming wavefront and the first and second optical control components, wherein the output optical wavefront from the input beam divider is the input optical wavefront to the first and second optical control components; an output beam combiner disposed to optically combine the respective first and second component modulated output wavefronts; and phase shifting means for providing a controlled phase difference between the first and second component phase modulated output wavefronts, wherein a resultant output wavefront has a phase that is different than the input optical wavefront phase by an amount $\theta(x,y)$.

An alternative embodiment of the invention is directed to an optical control device that uses a two-level half-toning algorithm to generate a controlled wavefront. The device comprises a diffractive, input wavefront divider/combiner (G) disposed along an optical axis of the input wavefront; a first component diffractive wavefront divider/combiner (G1) disposed to optically intercept one of a positive and a negative n^{th}-order output beam from the input wavefront divider/combiner; a first component binary MEMS device M1 comprising an $(n_{x,y}, m_{x,y})_{M1}$ mirror array disposed optically downstream of the first beam divider/combiner component along an M1 optical path, wherein at least an M1 mirror sub array $(X\times Y)_{M1}$ is in a selected ON/OFF state that provides a half-tone phase value H, where $0\leqq H\leqq 1$; a second component diffractive wavefront divider/combiner (G2) disposed to optically intercept either a complementary negative or positive n^{th}-order output beam from the input wavefront divider/combiner; a second component binary MEMS device M2 comprising an $(n_{x,y}, m_{x,y})_{M2}$ mirror array disposed optically downstream of the second beam divider/combiner component along an M2 optical path, wherein a complementary M2 mirror sub array $(X\times Y)_{M2}$ is in a selected complementary OFF/ON state that provides a half-tone phase value $(1-H)$, where $0\leqq(1-H)\leqq 1$; and at least one optical component that in-couples the input wavefront and out-couples an output wavefront having a controlled phase that is different than the input wavefront phase. According to an aspect, the diffractive wavefront divider/combiner, the first component diffractive wavefront divider/combiner and the second component diffractive wavefront divider/combiner are diffraction gratings each having a grating period Λ.

Another embodiment of the invention is directed to an optical control device comprising a polarizing beam divider/combiner disposed along a component input optical path of an incident optical wavefront, providing one polarization state $P1_1$ and another polarization state $P2_1$; a quarter wave plate which on two passes will cause the exiting P1 to rotate by 90 degrees so as to pass through the polarizer beam divider/combiner; a first binary MEMS device $M1_1$ comprising an $(n_{x,y}, m_{x,y})_{M1}$ mirror array disposed optically downstream of the polarizing beam divider/combiner along an $M1_1$ optical path of P1, wherein at least an M1 mirror sub array $(X\times Y)_{M1}$ is in a selected ON/OFF state that provides a half-tone phase value $(1-H)$, where $0\leqq(1-H)\leqq 1$; a second quarter wave plate; and a second binary MEMS device M2 comprising an $(n_{x,y}, m_{x,y})_{M2}$ mirror array disposed optically downstream of the polarizing beam divider/combiner along an M2 optical path of P2, wherein an M2 mirror sub array $(X\times Y)_{M2}$ is in a selected complementary OFF/ON state that provides a half-tone phase value H, where $0\leqq H\leqq 1$, further wherein an output wavefront propagating along an output optical wavefront path has a polarization coded phase profile over a transverse cross section of the output wavefront.

According to a related embodiment, a grating-based interferometer device uses a novel three-level half-toning algorithm to generate an arbitrary wavefront having controlled amplitude and phase. In this embodiment, a third MEMS component is disposed so as to intercept the zero-order diffracted beam. The wavefront can be expressed as the sum of polynomials in H(x,y) having appropriate phase. When relative phase delays are introduced between each of the three beams, they can be combined to produce an arbitrary wavefront having an absolute amplitude and phase expressed as $a(x,y)\exp[i\theta(x,y)]$.

Another embodiment of the invention is directed to an optical control device, comprising a beam divider/combiner disposed along an input optical path of an incident optical wavefront; a first binary MEMS device M1 comprising an $(n_{x,y}, m_{x,y})_{M1}$ mirror array disposed optically downstream of the first component beam divider/combiner along an M1 optical path providing an $M1_{out}$ wavefront, wherein at least an M1 mirror sub array $(X\times Y)_{M1}$ is in an ON/OFF state that provides a half-tone phase value expressed as $1-H(x,y)$, wherein H(x,y) represents a two-level value equal to 0 or 1; a second binary MEMS device M2 comprising an $(n_{x,y}, m_{x,y})_{M2}$ mirror array disposed optically downstream of the beam divider/combiner along an M2 optical path providing an $M2_{out}$ wavefront, wherein a complementary M2 mirror sub array $(X\times Y)_{M2}$ is in an OFF/ON state that provides a half-tone phase value expressed as H(x,y); and phase retarder means for providing a controlled phase difference between the $M1_{out}$ wavefront and the $M2_{out}$ wavefront, further wherein a resultant output wavefront obtained from the interference of the $M1_{out}$ wavefront and the $M2_{out}$ wavefront is different than the input optical wavefront by an amount $\alpha H(x,y)$ where $-\pi\leqq\alpha\leqq\pi$. According to an aspect, the device effects a wavefront coding on the input wavefront expressed as $e^{i\alpha H(x,y)}=(1-H)+e^{i\alpha}H$, wherein $1-H(x,y)$ is the half-tone phase coding provided by the ON/OFF state of M1, H is the half-tone phase coding provided by the OFF/ON state of M2, and $e^{i\alpha}$ represents the relative phase term between $M1_{out}$ and $M2_{out}$.

According to an aspect of the above described embodiments, a telecentric telescope may be disposed in the output wavefront plane to shift the output plane further downstream. The size of the telescope aperture can be used to control the size (X×Y) of the mirror sub-array over which the spatial averaging is performed in order to realize the half-toning effects.

Another embodiment of the invention is directed to a method for controlling an optical wavefront WF, comprising the steps of providing a first controllable binary MEMS device $M1_1$ comprising an $(n_{x,y}, m_{x,y})_{M1}$ mirror array, wherein each mirror can be set only to a binary ON/OFF position, and a second controllable binary MEMS device $M2_1$ comprising an $(n_{x,y}, m_{x,y})_{M2}$ mirror array, wherein each mirror can be set only to a binary ON/OFF position; providing an incident optical wavefront WF_{1i}; splitting the incident optical wavefront into $WF1_1$ along a first optical path $L1_1$ to $M1_1$ and into $WF2_1$ along a second optical path $L2_1$ to $M2_1$; modulating $WF1_1$ reflected from $M1_1$ by setting at least one M1 mirror sub array $(X_{x,y}\times Y_{x,y})_{M1}$<array $(n_{x,y}\times m_{x,y})_{M1}$ to an ON position and modulating $WF2_1$ reflected from $M2_1$ by setting a complementary at least one mirror sub array $(X_{x,y}\times Y_{x,y})_{M2}$<array $(n_{x,y}\times m_{x,y})_{M2}$ to an OFF position; providing an optical path length difference $\Delta L1L2$ in a range $0<\Delta L1L2\leqq(2n+1)\lambda/2$, where n=0, 1, 3, . . . , so as to provide a phase shift $\leqq\pi$; and obtaining a desired output optical wavefront WF_{1o} by optically combining reflected $WF1_1$ and reflected $WF2_1$. According to an aspect, modulating a phase profile of the wavefront by setting the at least one mirror sub array $(X_{x,y}\times Y_{x,y})$ to a selected ON/OFF position comprises providing an averaged grey-scale pixel value over the sub array. An aspect further includes employing a half-toning algorithm, wherein a single grey-scale pixel is represented by a spatially averaged dot pattern over the X×Y mirror sub array. As will be appreciated, the mirror sub array is equivalent to a mirror cluster that is used to define a pixel, as is known in the field of digital imaging.

In various aspects of the above mentioned embodiments, the at least some of the mirror array is one or more cluster arrays X×Y (<n×m), wherein each mirror cluster array X×Y represents a pixel and is characterized by at least a two-level phase half-toning approximation. In particular aspects, X=Y and n=m.

These and other objects, advantages and benefits provided by embodiments of the invention will now be set forth in detail with reference to the detailed description and the drawing figures and as defined in the appended claims.

BRIEF DESCRIPTION OF THE DRAWINGS

FIG. **1** shows a general Argand diagram, which is used to illustrate the geometric representation of a complex number as simply a point in the complex plane, provided as an aid in understanding the invention;

FIGS. **2***a*, **2***b* and **2***c*, respectively, illustrate a square wave pattern used to modulate an input wavefront; an optical control component according to an embodiment of the invention; and an Argand diagram representation of the interferometric output from the optical control component;

FIGS. **3***a*, **3***b* and **3***c* show alternating dark/bright bar patterns illustrating half-toning in conjunction with the component in FIG. **2***b*. FIG. **3***a* illustrates a cosine function; FIG. **3***b* shows a hard-thresholding version of FIG. **3***a*; and FIG. **3***c* shows a half-toned version of FIG. **3***a* obtained using the known Stucki algorithm;

FIG. **4***a* shows an interferometer-based optical control device for generating an arbitrary wavefront a(x,y)exp[iθ(x,y)] according to an embodiment of the invention;

FIG. **4***b* schematically illustrates a pixel point P(x,y) in an exemplary 5×5 mirror sub array of the MEMS device of FIG. **4***a*;

FIG. **4***c* shows an Argand diagram representation of point P(x,y) of FIG. **4***b*;

FIG. **5** shows an interferometer-based optical control device for generating a selected wavefront exp[iθ(x,y)] according to another embodiment of the invention;

FIGS. **6***a*-**6***c* show alternating dark/bright ring patterns illustrating half-toning in conjunction with the device in FIG. **5**. FIG. **6***a* illustrates a continuous quadratic phase function; FIG. **6***b* shows a hard-thresholding version of FIG. **6***a*; and FIG. **6***c* shows a half-toned version of FIG. **6***a* obtained using the known Stucki algorithm;

FIG. **7**A shows a diffraction-interferometer-based optical control device that uses a two-level algorithm for generating a wavefront exp[iθ(x,y)] according to another embodiment of the invention;

FIG. **7**B shows a diffraction-interferometer-based optical control device that uses a three level algorithm for generating an arbitrary wavefront a(x,y)exp[iθ(x,y)] according to another embodiment of the invention;

FIG. **8** is a schematic system diagram used to illustrate the concept of polarization controlled wavefront phase coding;

FIGS. **9***a* and **9***b* illustrate an exemplary polarization-interference-based optical control device for generating an arbitrary wavefront, and the polarization states in different pixel blocks at an output screen of the device, respectively, according to another embodiment of the invention; and

FIG. **10** schematically shows a telecentric telescope according to an aspect of the invention.

DETAILED DESCRIPTION OF A PREFERRED EMBODIMENT OF THE INVENTION

As used herein, the term 'digital binary MEMS' refers to a micro-electromechanical mirror array system that is subject only to binary (i.e., ON/OFF or 1,0) control by tilting each mirror facet to a retro-reflecting (1) position for incident light (ON position) or to an off-axis (0; tilted or OFF) reflecting position for the incident light.

The term 'amplitude' as used herein will be recognized by those skilled in the art as referring to a complex number with a real part and an imaginary part or, equivalently, with an absolute value amplitude and a phase angle, as is a well-known signal representation in the solutions of Maxwell's equations in a harmonic time-dependent formalism.

According to a first illustrative embodiment and with reference to FIGS. **2***a*-**2***c* and **3***a*-**3***c*, we disclose a novel approach to wavefront generation using binary amplitude modulation of an input plane wave. The basic problem of wavefront generation is to achieve a wavefront described by exp[iθ(x,y)], when the function θ(x,y) is specified. Using the relation

$$\exp[i\theta(x,y)]=\cos[\theta(x,y)]+e^{i\pi/2}\sin[\theta(x,y)], \quad (1)$$

we require a way to represent cos [θ(x,y)] and sin [θ(x,y)], which can then be added interferometrically with the appropriate relative phase term of $e^{i\pi/2}$ to generate the desired wavefront. The cosine and sine can take values in the range of [−1, 1].

A first embodiment according to the invention illustrates the generation of square-wave functions **120** that can take on bi-level values (+1, −1) using binary mirror (digital binary MEMS) devices. FIG. **2***a* shows a square-wave pattern **120** that may be used to modulate an input wavefront **105** (FIG. **2***b*). The square-wave function can take only two values: (+1), i.e., $e^{i\theta}$ corresponding to a phase of θ=0 and (−1), i.e., $e^{i\theta}$ corresponding to a phase of θ=π radians. FIG. **2***b* shows a first interferometrically-based optical control component **100** for obtaining the square-wave modulation **120** of the input plane wave **105**. The input wavefront **105** is split into two equal

(non-complex) amplitude parts by a first component beam divider/combiner **102** that is disposed along a first component optical path **103** of the incident wavefront. The reflected split wavefront is incident on a first component digital binary MEMS device $M1_1$. $M1_1$ comprises a mirror array **107** denoted by $(n_{x,y} \times m_{x,y})_{M1}$. The $M1_1$ optical path **109** from the beam splitter surface to $M1_1$ and back to the beam splitter surface (i.e., double pass) has an optical path length $L1_1$. The transmitted split wavefront is incident on a first component digital binary MEMS device $M2_1$. $M2_1$ comprises a mirror array **111** denoted by $(n_{x,y} \times m_{x,y})_{M2}$. In an exemplary aspect, n=m. The $M2_1$ optical path **113** from the beam splitter surface to $M2_1$ and back to the beam splitter surface has an optical path length $L2_1$. Phase retarder means **115**, in the form of a phase plate, differential optical path length or other known phase altering component or technique for producing a differential optical path $\Delta L1L2$ equal to $\lambda/2$ ($\lambda/4$ per pass) is also shown. In the MEMS array $M1_1$, a sub array X×Y (≤n×m) of mirrors corresponding to a (+1) value (θ=0) of the square-wave are ON, whereas in the MEMS array $M2_1$, a complementary sub array of mirrors X×Y corresponding to a (−1) value (θ=π) of the square wave are ON. In an exemplary aspect, X×Y. A phase difference of r radians between the two reflected wavefront components is introduced using an extra optical path difference $\Delta L1L2$ equal to $\lambda/2$ in the $M2_1$ optical path, which is achieved as shown in FIG. **2***b* by translating $M2_1$ by $\lambda/4$ relative to $M1_1$. However, in order to generate either cosine or sine functions as discussed above, one must be able to represent grey-scale values in terms of two levels: (+1) and (−1). This can be achieved by averaging over the sub arrays of the two levels (+1) and (−1) using a half-toning technique as described below.

Half-toning algorithms are widely used in printing devices where it is required to represent grey-scale pictures using only two levels; i.e., a black dot or a blank white space. According to the embodiment, a single grey-scale pixel in a half-toned picture consists of a dot pattern over an exemplary block (X×Y) of 3×3 or 5×5 mirrors. The grey-scale is achieved using spatial averaging over this block. Both the filling-in of the outputs of the binary mirror (0,1) and the grey-levels are accomplished simply by light propagation. The diffraction spreading distance λR/w equal to 2w, in order to have a spreading into e.g., 9 mirror segments (3×3) is easily computed, where λ is the wavelength, R is the distance and w is the pixel size. For w=10 μm and λ=0.5 μm, R=400 μm. This distance is sufficiently small so that the filling-in of the wavefront is not a problem in a practical device. When a half-toned pattern is printed on a paper and viewed by an observer, the spatial averaging is performed by the human eye. The eye, however, cannot resolve the fine dot pattern, so the printed image appears to have several levels between the black dot and the white blank.

FIGS. **3***a*-**3***c* show alternating bar pattern illustrations of half-toning for a cosine function between two levels (+1) and (−1). The optical control component **100** in FIG. **2***b* functions as an interferometer for generating a wavefront with two phase levels. The component **100** MEMS arrays $M1_1$, $M2_1$ can be controlled so that the mirror sub arrays with levels (+1) and (−1) are arranged according to a selected half-toning algorithm. FIG. **3***a* shows a cosine function. FIG. **3***b* shows a hard-thresholded version of the cosine function; i.e., the non-negative pixels in FIG. **3***a* are assigned a value of (+1), whereas the negative pixels are assigned a value of (−1). It can be seen that the grey-scale is completely lost in this simple thresholding operation. FIG. **3***c* shows a half-toned version of the cosine function using the well known Stucki half-toning algorithm. The grey-scale effect is now achieved by using spatial averaging over a block of 10 pixels implying that 11 grey-levels (**0-10**) are achievable in a spatial-averaged sense. The white and black pixels in FIG. **3***c* represent values of (+1) and (−1) respectively. The half-toning concept can thus be used for generating the sine and cosine functions for an arbitrary wavefront. The inventors are not aware of the prior use of the half-toning concept in the context of wavefront generation as further described below.

Using the optical control component **100** shown in FIG. **2***b*, one can obtain a half-toned version of the sine or cosine functions required for wavefront generation. The (+1) and (−1) mirror sub arrays (pixels) in the half-toned pattern are turned ON in MEMS arrays $M1_1$ and $M2_1$, respectively. The value (−1) is achieved from the path difference of $\lambda/2$ in the two arms of the component. Spatial averaging over pixel blocks is achieved simply by propagating the light over a very short distance. For a given θ(x,y), it is thus possible to generate cos [θ(x,y)] and sin [θ(x,y)] by using a control component **100** as shown in FIG. **2***b*.

FIG. **4***a* shows an interferometer-based optical control device **300**. The device **300** comprises two identical components **100** (**200**) as shown in FIG. **2***b* for generating a wavefront described by exp[iθ(x,y)]. An incoming wavefront **106** is split into two output optical wavefronts **105** by an input beam divider **302** (e.g., an X-cube). The two output optical wavefronts **105** are the input optical wavefronts to the device components **100**, **200**. One arm of the device **300** consists of a first optical control component **100** as described above. Control component **100** provides an output **120** in the form cos [θ(x,y)]. A second aim of device **300** consists of a second optical control component **200** that is essentially identical to component **100**. Component **200** includes a second component beam divider/combiner **202** disposed along a second component input optical path **203** of an input optical wavefront **105**. A second component digital binary MEMS device $M1_2$ comprising an n×m mirror array **207** denoted by $(n_{x,y}, m_{x,y})_{M1}$ is disposed optically downstream of the second beam divider/combiner component **202** along an $M1_2$ optical path **213** having a total optical path length $L1_2$. A second component digital binary MEMS device $M2_2$ comprising an n×m mirror array **211** denoted by $(n_{x,y}, m_{x,y})_{M2}$ is disposed optically downstream of the second beam divider/combiner component **202** along an $M2_2$ optical path **214** having a total optical path length $L2_2$ that is different than the $M1_2$ optical path **213**. Phase retarder means **215** are employed to make $L1_2$ different than $L2_2$. At least some sub array (X×Y) of the mirror array **207** is in an ON/OFF state and a complementary at least some similar sub array of the mirror array **211** is in an OFF/ON state. As such, component **200** functions similarly to component **100** but produces an output **220** in the form sin [θ(x,y)]. An output beam combiner **318** is disposed in output optical paths **117**, **217** to optically combine the respective cos [θ(x,y)] and sin [θ(x,y)] modulated outputs. Phase shifting means **322** disposed between beam splitter **202** and output beam combiner **318** provides a phase difference equal to $\pi/2$. The resultant output wavefront **325** expressed as $e^{i\theta(x,y)}$ thus has a different phase than the input optical wavefront by an amount θ(x,y).

FIG. **4***b* illustrates a pixel P(x,y) in an exemplary 5×5 mirror sub array (X×Y) of a MEMS component of FIG. **4***a*. At point P(x,y), the complex amplitude at point P has the form $e^{i\theta(x,y)}$ consisting of a real number (amplitude) part (cos θ) and an imaginary (phase) part i(sin θ) making up the complex amplitude value. FIG. **4***c* is an Argand diagram representation of the complex amplitude at P(x,y) where the circumference of the circle is the locus of amplitudes and phase at position P. In the example, the real amplitude value is one.

The interferometer device **300** illustrated in FIG. **4**(*a*) may also be used to generate a complex optical wavefront having a varying absolute value of amplitude denoted by a(x,y). More precisely, the use of half-toning concepts on the sub-assemblies **100**, **200** allows one to use component **100** for the generation of a(x,y)cos θ(x,y) and, similarly, component **200** for the generation of a(x,y)sin θ(x,y), where $0 \leqq a(x,y) \leqq 1$. An output function g(x,y) can thus be obtained by combining the two outputs as follows:

$$g(x,y)=a(x,y)\exp[i\theta(x,y)]=a(x,y)[\cos\theta(x,y)+i\sin\theta(x,y)].$$

Hence, the wavefront generation device can be used to generate an optical wavefront of arbitrary absolute value amplitude and phase.

Another embodiment of the invention is directed to a device and associated method for more advanced wavefront coding, benefiting from a simplification of hardware used in the embodiment described above through the employment of a more sophisticated algorithm. According to this embodiment, one may again generate a phase function $\theta(x,y)$, $0 \leqq \theta(x,y) \leqq \alpha$, for a constant angle α, using only binary (0,1) type amplitude modulation. Thus we intend to generate an output wavefront expressed as $e^{i\theta(x,y)}$. As a first step, we convert θ(x,y) to a binary picture H(x,y), which is a two-dimensional array with either zeros or ones. Therefore, we let $\theta(x,y) \approx \alpha H(x,y)$ so that $e^{i\theta(x,y)}$ can be expressed as $e^{i\alpha H(x,y)}$. The exponential can be expressed in the well-known form as:

$$e^{i\alpha H(x,y)}=1+i\alpha H+[(i\alpha)^2/2!]H^2+\ldots \quad (2)$$

For H(x,y) values limited to (0,1), $H^N=H$; thus (3)

$$e^{i\alpha H(x,y)} = [1-(\alpha^2/2!)H+(\alpha^4/4!)H-\ldots]+ iH[\alpha-(\alpha^3/3!)+(\alpha^5/5!)-\ldots] \quad (4)$$

$$= (1-H)+H[1-(\alpha^2/2!)+(\alpha^4/4!)-\ldots]+ iH[\alpha-(\alpha^3/3!)+(\alpha^5/5!)-\ldots] \quad (5)$$

$$= (1-H)+H[\cos\alpha+i\sin\alpha] \quad (6)$$

$$= (1-H)+H\exp(i\alpha) \quad (7)$$

The novel algorithm leading to equation (7) may be realized in a two-beam interferometer device. Table II shows the values taken by the two terms in right hand side of equation (7) for the two values (0,1) taken by H.

TABLE II

	(1-H)	H exp(iα)
H = 0	1	0
H = 1	0	exp(iα)

Thus if H=0, then $e^{i\alpha H}=1$ and the corresponding pixel phase is zero; and if H=1, then $e^{i\alpha H}=e^{i\alpha}$ and the corresponding pixel phase is α, where H represents a half-tone phase value obtained by turning a $MEMS_1$ sub array X×Y ON, and (1−H) represents the complement of H obtained by turning a $MEMS_2$ sub array X×Y OFF. By propagation or low-pass filtering, as is well-known to an optical engineer, one obtains an output that is an average over a block of m×m pixels. It is thus possible to obtain m^2 (e.g., 3×3 or 5×5) levels of phase between 0 to α.

The results of the novel two-level algorithm presented above may be realized by the optical control device **400** illustrated in FIG. **5**. The device **400** comprises a beam divider/combiner **402** disposed along an input optical path **403** of an incident optical wavefront **405**. Incident wavefront **405** may be a plane wave expressed as $e^{i\theta(x,y)}$ or an aberrated wavefront expressed as $e^{-i\phi(x,y)}$. A first digital binary MEMS device M1 comprises an n×m mirror array $(n_{x,y}, m_{x,y})_{M1}$ **407** disposed optically downstream of the first component beam divider/combiner along an M1 optical path **409**. At least some sub array $(X \times Y)_{M1}$ of the mirror array is programmed to be in an ON/OFF state that provides a half-tone phase value expressed as 1−H(x,y), wherein H(x,y) represents a two-level value equal to 0 or 1 as described above. A second digital binary MEMS device M2 has an n×m mirror array $(n_{x,y}, m_{x,y})_{M2}$ **411** disposed optically downstream of the beam divider/combiner along an M2 optical path **413**. A complementary mirror sub array $(X \times Y)_{M2}$ is programmed to be in an OFF/ON state that provides a half-tone phase value expressed as H(x,y) as shown in FIG. **5**. Phase retarder means **415** are provided to obtain a controlled phase difference between the $M1_{out}$ wavefront and the $M2_{out}$ wavefront of α/2. A resultant output wavefront **421** expressed as $e^{i\alpha H}$ is obtained from the interference of the $M1_{out}$ wavefront (1−H) and the $M2_{out}$ wavefront (H). The wavefront **421** thus has a phase difference from the input optical wavefront **405** by an amount αH(x,y) (equal to θ(x,y)), where $-\pi \leqq \alpha \leqq \pi$. If the input wave is an aberrated wavefront expressed as $e^{-i\phi(x,y)}$ as referred to above, then the output wavefront from device **400** will be expressed as $e^{i[\theta(x,y)-\phi(x,y)]}$. The device operation changes the phase between the optical input and optical output by θ(x,y) radians.

An exemplary illustration is shown in FIG. **6***a*-**6***c* when H is a quadratic function (x^2+y^2) and the wavefront expression is $\exp[i\alpha(x^2+y^2)]$. FIG. **6***a* shows the profile of a continuous quadratic phase function. FIG. **6***b* shows the phase profile obtained by hard-thresholding of the FIG. **6***a* profile at a level between 0 to 2π. FIG. **6***c* shows the half-toned version of the FIG. **6***a* profile using the Stucki algorithm. In the figure, a white dot denotes phase=0; a black dot denotes phase=π radians. Grayscale effect is achieved in the half-toned FIG. **6***c* by means of spatial averaging.

FIG. **7**A illustrates an embodiment of a wavefront control device **600-1** that uses a two-level half-toning algorithm for controlled wavefront generation. Apart from adaptive optics applications, the inventors have recognized a need for a spatial phase modulation that is independent of wavelength. Potential applications may include various defense-based and space-borne interferometer systems. For example, one may need a phase front of θ(x,y) in the blue wavelengths (λ_1) and thereafter wish to generate the same phase θ(x,y) in the red portion (λ_2) of the spectrum. An interferometer-based optical control device **600-1** that supports this capability uses a modified form of an achromatic phase-shifting interferometer. In this regard, the disclosure of U.S. Pat. No. 4,786,124 is herein incorporated by reference in its entirety to the fullest allowable extent. Device **600-1** includes a diffractive, input wavefront divider/combiner **602** denoted by G1 disposed along an optical axis **603** of an input wavefront **601**. A first component diffractive wavefront divider/combiner **607** denoted by G2 is disposed to optically intercept a positive **609** (or a negative **611**) n^{th}-order output beam from the input wavefront divider/combiner **602**. In an exemplary aspect, a first-order diffractive beam from G1 is incident on G2 (and as described below, a negative first-order diffractive beam from G1 is incident on G3). A first component digital binary MEMS device **612** denoted by M1 is disposed optically downstream of the first beam divider/combiner component along an M1 optical path **615** providing an optical path length (double pass) of L2. M1 comprises an n×m mirror array $(n_{x,y}, m_{x,y})_{M1}$ **613** (not

shown). The mirror array includes a mirror sub array (X×Y<n×m) that is in a selected ON/OFF state to provide a two-level half-tone phase value H(x,y), where 0≦H≦1. According to an illustrative aspect, H(x,y) has the values (0,1). A second component diffractive wavefront divider/combiner **617** denoted by G3 is disposed to optically intercept the negative first-order output beam **611** from the input wavefront divider/combiner **602**. A second component digital binary MEMS device **622** denoted by M2 is disposed optically downstream of the second beam divider/combiner component along an M2 optical path **625** providing an optical path length (double pass) of L3. M2 comprises an n×m mirror array $(n_{x,y}, m_{x,y})_{M2}$ **623** (not shown). The mirror array includes a mirror sub array (X×Y <n×m) that is in a selected complementary OFF/ON state that provides a two-level half-tone phase value (1−H(x,y)), where 0≦(1−H)≦1 (e.g., H=0, 1). Optical component **630** is provided to in-couple the input wavefront **601** and out-couple the resultant output wavefront **645**. In a particular aspect, G1, G2 and G3 are diffraction gratings each having a grating period A. G2 is displaced transversely a distances d relative to G3, where 0<d<Λ, to provide a phase shift α/2 between the two arms of the device. For achromatic operation, L2 is equal to L3. The device **600-1** provides a resultant output wavefront **645** expressed as $e^{i\alpha H_{(x,y)}}$ with a controlled phase αH(x,y) that is different than the input wavefront phase. The device **600-1** and operation thereof may have further potential application for phase correction in sparse-aperture telescope systems.

FIG. **7B** illustrates another embodiment of a wavefront control device **600-2**, similar to control device **600-1**, that uses a three-level half-toning algorithm for controlled, arbitrary wavefront generation. The inventors recognize the need for a wavefront control device that can generate an arbitrary wavefront a(x,y) exp[iθ(x,y)]. A wavefront control device **600-2** as illustrated in FIG. **7B** is based on a novel algorithm that provides a three-level interferometric binary structure derived as follows. It is possible to write identities for expressing phase in terms of amplitude modulation when more than two levels are used to obtain θ(x,y) values spanning the whole complex plane. For example, for a three-level algorithm in which each pixel in H(x,y) can take three values, e.g., (0, ½, 1), the wavefront can be represented as follow:

It is thus possible to express phase as a sum of polynomials in H(x,y) with appropriate phase. Table III shows the values taken by the three terms on the right hand side of equation (8) for the three values (0, ½, 1) taken by H.

TABLE III

	$1 - 3H + 2H^2$	$4[H - H^2]\exp(i\alpha/2)$	$[-H + 2H^2]\exp(i\alpha)$
H = 0	1	0	0
H = ½	0	$\exp(i\alpha/2)$	0
H = 1	0	0	$\exp(i\alpha)$

This algorithm can be embodied by the grating-based interferometer device **600-2** illustrated in FIG. **7A**. The device will be capable of generating an arbitrary wavefront a(x,y) exp[iθ(x,y)] using all-digital binary MEMS as disclosed herein. As shown, the input beam **601** is split by grating **602** (denoted by G1) into three beams: a zero-order beam **635** and $\pm 1^{st}$-order beams **609**, **611**. The three beams **635**, **611** and **609** have respective two-way or total phase delays of 0, α/2 and α. As illustrated, the path lengths of the three beams have been made balanced or of equal length. The reflected beams from the new MEMS **640** (denoted now by M1) and MEMS **612** (M2) and **622** (M3) are combined at grating **602** (G1) and directed by the beam splitter **630** to provide an arbitrary wavefront a(x,y) exp[iθ(x,y)]. As described herein, appropriate half-toning techniques are used to generate the required absolute amplitude a(x,y).

Another embodiment of the invention directed to a polarization-based optical control device and method will now be described in relation to FIGS. **8**, **9***a* and **9***b*. The current embodiment allows output wavefront phase control through polarization modulation of the incoming wavefront. An explanation of the meaning of phase difference between two beams in incoming wavefront. An explanation of the meaning of phase difference between two beams in different states of polarization will aid in illustrating the exemplary embodiment presented below.

With reference to the illustrative system **800** in FIG. **8**, consider an incoming plane polarized beam **805** having polarization axes x, y as shown split in two parts L1, L2 by a beam-splitter **802**. The two beams L1, L2 pass through respective birefringent media **807**, **817** (e.g., a series of quarter or half-wave plates) having some relative orientation difference, which are located in plane I. The two beams acquire distinct states of elliptical polarization expressed as $E_1=a_1x+b_1e^{i\Phi 1}y$ and $E_2=a_2x+b_2e^{i\Phi 2}y$ at observation plane II. It can be assumed that the two beams gain the same phase due solely to their propagation. However, the two beams have a relative phase difference between them from the change in polarization state. A simple criterion for the phase difference between two beams in two different polarization states is as follows: if the two beams in distinct polarization states described by vectors E_1 and E_2 are interfered, the resultant intensity is given by:

$$I_{12}=|E_1|^2+|E_2|^2+2|E_1||E_2|\cos\phi_{12} \quad (8)$$

The phase between the two polarization states is ϕ_{12} as seen from the cross-term. According to the instant embodiment, half-toning algorithms can be employed to generate variable polarization states across the transverse cross section of the wavefront.

An exemplary case is illustrated with reference to optical control device **900** in FIG. **9***a*. An incident plane wave P(x,y) **905** polarized at 45^0 is split into two polarization states P1, P2 by a polarizing beam splitter **902** disposed along optical axis **903**. A first digital binary MEMS device **910** denoted by M1 is disposed optically downstream of the polarizing beam splitter **902** along an M1 optical path **909**. M1 comprises an n×m mirror array $(n_{x,y}, m_{x,y})_{M1}$ **907** in which a phase value represented as (1−H), where 0≦(1−H)≦1. A second digital binary MEMS device **912** denoted by M2 is disposed optically downstream of the polarizing beam splitter **902** along an M2 optical path **913**. M2 comprises an n×m mirror array $(n_{x,y}, m_{x,y})_{M2}$ **911**, in which a complementary mirror sub array X×Y(<n×m) is in a selected complementary OFF/ON state that provides P2 with a half-tone phase value H, where 0≦H≦1. The reflected wavefronts P1, P2, each having passed twice through a quarter wave plate so as to couple efficiently through the beam combiner/divider, are optically combined by the polarizing beam splitter **902** to produce a resultant output wavefront **920** propagating along an output optical wavefront path **917**.

FIG. **9***b* illustrates the polarization states **950** in two representative individual pixel blocks **960**, **965** corresponding to two illustrative 2×2 mirror sub arrays **970**, **975**. The two orthogonal polarization states x, y will not exhibit any interference as the corresponding cross-term in equation (7) would be zero. However, averaging over the pixel blocks **960**, **965** gives rise to a gray-scale in polarization state. For example, block **960** can be characterized by $E_1=2x+2y$; block

965 can be characterized by E_2=3x+1y. Pixels in the averaged or low-pass filtered wavefront thus have a polarization state in between two orthogonal states used for half-toning. In FIG. 9*b*, the two pixel blocks can thus acquire a phase difference ϕ_{12} as given in equation (8), which can be used for phase correction in adaptive imaging applications. While a simple illustration of two orthogonally polarized components without any additional phase terms has been presented, a person skilled in the art will appreciate that more general realizations involving two elliptical polarization levels for half-toning are also possible. Moreover, a person skilled in the art will recognize that this embodiment, which has been described for the generation of the wavefront exp[iθ(x,y)], may be employed to generate an arbitrary wavefront a(x,y)exp[iθ(x, y)] by appropriate algorithmic control of the half-toning process as described above.

The embodiments described above disclose various digital binary MEMS mirror array configurations for phase front coding. The device and method embodiments have current and prospective widespread applicability to various adaptive optical systems, including, for example, those used in defense related atmospheric compensation and in laser fusion.

FIG. **10** depicts the use of a telecentric telescope **1000** with an illustrative digital binary MEMS device **1010** according to an embodiment of the invention. As shown in the figure, an output wavefront **1020** is generated in plane I by the device **1010**. If desired, the output plane can be optically shifted downstream to plane III. This may be achieved by inserting the telecentric telescope **1000** between planes I and III as shown. The size D of the aperture **1030** in plane II controls the size (X×Y) of the mirror sub-array over which the spatial averaging is performed in order to realize the desired half-toning effects described above.

Having thus described the various embodiments of the invention, it will be apparent to those skilled in the art that the foregoing detailed disclosure is presented by way of example only and thus is not limiting. Various alterations, improvements and modifications recognized by those skilled in the art, though not expressly stated herein, may be made and are intended to be within the spirit and scope of the claimed invention. Additionally, the recited order of processing elements or sequences, or the use of numbers, letters, or other designations, is not intended to limit the claimed processes to any order except as may be specified in the claims. Accordingly, embodiments of the invention are limited only by the following claims and equivalents thereto.

REFERENCES

The subject matter disclosed in the following citations is herein incorporated by reference in their entireties to the fullest extent allowed by applicable laws and rules.

D. Dudley, W. Duncan, J. Slaughter, "Emerging digital micromirror device (DMD) applications", SPIE 4985, 14 (2003).

H. W. Babcock, "The possibility of compensating astronomical sensing", Publ. Astron. Soc. Pac. 65, 229 (1953).

F. Roddier, "Effects of atmospheric turbulence in optical astronomy", *Progress in Optics*, E. Wolf (Ed.), vol. 19, 281 (1981).

R. K. Tyson, *Principles of Adaptive Optics*, (Academic press) (1998).

M. C. Roggemann and B. M. Welsh, *Imaging through the atmosphere*, (CRC press) (1996).

M. C. Roggemann, B. M. Welsh, R. Q. Fugate, "Improving the resolution of ground based telescopes", Rev. Mod. Phys. 69, 437 (1997).

F. Roddier (Ed.), *Adaptive optics in astronomy*, (Cambridge Univ. Press), (1998).

T. Weyrauch, M. A. Vorontsov, "Atmospheric compensation with a speckle beacon in strong scintillation conditions: directed energy and laser communication applications", Appl. Opt, 44, 6388 (2005).

M. A. Vorontsov, M. Yu, "Compensation of distant phase-distorting layers" Part I & II, J. Opt. Soc. Am. A 21, 1645, 1659 (2004).

M. A. Vorontsov, E. W. Justh, L. A. Beresnev, "Adaptive optics with advanced phase-contrast techniques", Part I & II, J. Opt. Soc. Am. A 18, 1289, 1300 (2001).

Doble, N., Yoon, G. Y., Chen, L., Bierden, P., Singer, B., Olivier, S., Williams, D. R., "Use of a microelectromechanical mirror for adaptive optics in the human eye", Optics Letters 27, 1537 (2002).

Roorda, A, Williams, D. R. (2000) "Adaptive Optics and Retinal Imaging", OSA Trends in Optics and Photonics Vol. 35, Vision Science and its Applications, Vasudevan Lakshminarayanan, Ed. (Optical Society of America, Washington, D.C.) 151-162.

D. T. Gavel, E. L. Gates, C. E. Max, S. S. Oliver, B. Bauman, D. Pennington, B. Macintosh, J. Patience, C. Brown, P. Danforth, R. Hurd, S. Severson, J. Lloyd, "Recent science and engineering results with the laser guide star adaptive optics system at Lick observatory", Proc. SPIE 4839, 354 (2003).

Laboratory for Laser Energetics, Annual Report 2005, DOE/SF/19460-646,

Inertial Fusion Program and National Laser Users' Facility Program, January 2006.

C. E. Max, Adaptive Optics course material, <www.ucolick.org/~max/298C>

E. N. Ribak, "Deformable mirrors", in *Adaptive Optics for Astronomy*, D. Alloin and J. M. Mariotti, (Ed.), Kluwer, Boston (1994).

T. Bifano, R. K. Mali, J. Dorton, J. Perreault, N. Vandelli, M. Horenstein, D. Castanon, "Continuous membrane surface micromachined silicon deformable mirrors", Opt. Engg. 36, 1354 (1997).

W. D. Cowan, M. K. Lee, B. M. Welsh, V. M. Bright, M. C. Roggemann, "Surface micromachined segmented mirrors for adaptive optics", IEEE Journal of Selected Topics in Quantum Electronics 5, 90 (1999).

Weyrauch, T., Vorontsov, M. A., Bifano, T. G., Giles, M. K., "Adaptive Optics Systems with Micromachined Mirror Array and Stochastic Gradient Descent Controller". Proc. SPIE 4124, High-Resolution Wavefront Control: Methods, Devices, and Applications., August 2000.

J. A. Perreault, T. G. Bifano, B. M. Levine, M. N. Horenstein, "Adaptive optic correction using micromechanical deformable mirrors", Opt. Eng. 41, 561 (2002).

R. Ulichney, *Digital Halftoning*, MIT Press (1988).

N. George and T. Stone, Opt. Comm. 67, 185 (1988).

N. George and S. Radic, "Photomixing of achromatically frequency-modulated incoherent light", Opt. Lett, 18, 1038 (1993).

S. Pancharatnam, "Generalized theory of interference and its applications", Proc. Indian Acad. Sci. A44, 261 (1956).

R. Bhandari, "Polarization of light and topological phases", Phys. Rep. 182, 1 (1997).

Z. Bomzon, G. Biener, V. Kleiner, E. Hasman, "Space-variant Pancharatnam-Berry phase elements with computer generated sub-wavelength gratings", Opt. Lett. 27, 1141 (2002).

F. S. Roux, "Geometric phase lens", J. Opt. Soc. Am. A 23, 476 (2006).

K. Khare and N. George, "Direct coarse-sampling of electronic holograms", Opt. Lett. 28, 1004 (2003).

K. Khare and N. George, "Sampling theory approach to prolate spheroidal wave functions", J. Phys. A: Math. & General 36, 10011 (2003).

K. Khare and N. George, "Fractional finite Fourier transform", J. Opt. Soc. Am.: A 21, 1179 (2004).

K. Khare and N. George, "Sampling theory approach to eigenwavefronts of imaging systems", J. Opt. Soc. Am.: A 22, 434 (2005).

K. Khare, "Bandpass sampling and bandpass analogues of prolate spheroidal functions", Signal Processing, (2006), (accepted in press).

K. Khare, "Sampling theorem, bandlimited integral kernels and inverse problems", to be submitted to Inverse Problems.

We claim:

1. An optical control component, comprising:

a first component beam divider/combiner disposed along a first component input optical path of an incident optical wavefront;

a first component binary MEMS device $M1_1$ comprising an $(n_{x,y}\times m_{x,y})_{M1}$ mirror array disposed optically downstream of the first component beam divider/combiner along an M1 optical path having a total optical path length $L1_1$;

a first component binary MEMS device $M2_1$ comprising an $(n_{x,y}\times m_{x,y})_{M2}$ mirror array disposed optically downstream of the first component beam divider/combiner along an $M2_1$ optical path different than the $M1_1$ optical path having a total optical path length $L2_1$; and

phase retarder means for making $L1_1$ different than $L2_1$,

wherein an at least one $M1_1$ sub array $(X\times Y)_{M1}$ is in an ON/OFF state and a complementary an at least one $M2_1$ sub array $(X\times Y)_{M2}$ is in an OFF/ON state, further wherein an output wavefront propagating along a first component output optical wavefront path has a controlled modulation, wherein $L1_1$ is different than $L2_1$ by an amount $\Delta_1 L1L2$, where $0<\Delta_1 L1L2\leqq(2n+1)\lambda/2$, where n=0, 1, 3, . . . , so as to provide a phase shift $\leqq\pi$ radians.

2. An optical control component, comprising:

a first component beam divider/combiner disposed along a first component input optical path of an incident optical wavefront;

a first component binary MEMS device $M1_1$ comprising an $(n_{x,y}\times m_{x,y})_{M1}$ mirror array disposed optically downstream of the first component beam divider/combiner along an M1 optical path having a total optical path length $L1_1$;

a first component binary MEMS device $M2_1$ comprising an $(n_{x,y}\times m_{x,y})_{M2}$ mirror array disposed optically downstream of the first component beam divider/combiner along an $M2_1$ optical path different than the $M1_1$ optical path having a total optical path length $L2_1$; and

phase retarder means for making $L1_1$ different than $L2_1$,

wherein an at least one $M1_1$ sub array $(X\times Y)_{M1}$ is in an ON/OFF state and a complementary an at least one $M2_1$ sub array $(X\times Y)_{M2}$ is in an OFF/ON state, further wherein an output wavefront propagating along a first component output optical wavefront path has a controlled modulation, wherein X=Y and n=m.

3. An optical control component, comprising:

a first component beam divider/combiner disposed along a first component input optical path of an incident optical wavefront;

a first component binary MEMS device $M1_1$ comprising an $(n_{x,y}\times m_{x,y})_{M1}$ mirror array disposed optically downstream of the first component beam divider/combiner along an M1 optical path having a total optical path length $L1_1$;

a first component binary MEMS device $M2_1$ comprising an $(n_{x,y}\times m_{x,y})_{M2}$ mirror array disposed optically downstream of the first component beam divider/combiner along an $M2_1$ optical path different than the $M1_1$ optical path having a total optical path length $L2_1$; and

phase retarder means for making $L1_1$ different than $L2_1$,

wherein an at least one $M1_1$ sub array $(X\times Y)_{M1}$ is in an ON/OFF state and a complementary an at least one $M2_1$ sub array $(X\times Y)_{M2}$ is in an OFF/ON state, further wherein an output wavefront propagating along a first component output optical wavefront path has a controlled modulation, wherein $M1_1$ sub array $(X\times Y)_{M1}$ in an ON/OFF state and the complementary M2 sub array $(X\times Y)_{M2}$ in the OFF/ON state are each one or more cluster arrays $X\times Y<n\times m$, further wherein each cluster array X×Y is characterized by at least a two level half-toning phase approximation.

4. An optical control device, comprising:

a first optical control component further comprising:

a first component beam divider/combiner disposed along a first component input optical path of an incident optical wavefront;

a first component binary MEMS device $M1_1$ comprising an $(n_{x,y}\times m_{x,y})_{M1}$ mirror array disposed optically downstream of the first component beam divider/combiner component along an M1 optical path having a total optical path length $L1_1$;

a first component binary MEMS device $M2_1$ comprising an $(n_{x,y}\times m_{x,y})_{M2}$ mirror array disposed optically downstream of the first component beam divider/combiner along an $M2_1$ optical path different than the $M1_1$ optical path having a total optical path length $L2_1$; and

phase retarder means for making $L1_1$ different than $L2_1$,

wherein an at least one $M1_1$ sub array $(X\times Y)_{M1}$ is in an ON/OFF state and a complementary an at least one $M2_1$ sub array $(X\times Y)_{M2}$ is in an OFF/ON state, further wherein an output wavefront propagating along a first component output optical wavefront path has a controlled modulation;

a second optical control component, comprising:

a second component beam divider/combiner disposed along a second component input optical path of an input optical wavefront;

a second component binary MEMS device $M1_2$ comprising an $(n_{x,y}\times m_{x,y})_{M1}$ mirror array disposed optically downstream of the second beam divider/combiner component along an $M1_2$ optical path having a total optical path length $L1_2$;

a second component binary MEMS device $M2_2$ comprising an $(n_{x,y}\times m_{x,y})_{M2}$ mirror array disposed optically downstream of the second beam divider/combiner component along an $M2_2$ optical path different than the $M1_2$ optical path having a total optical path length $L2_2$; and

phase retarder means for making $L1_2$ different than $L2_2$,

wherein an at least one $M1_2$ sub array $(X\times Y)_{M2}$ is in an ON/OFF state and a complementary an at least one $M2_2$ sub array $(X\times Y)_{M2}$ is in an OFF/ON state, further wherein an output wavefront propagating along a second component output optical wavefront path has a controlled modulation;

an input beam divider disposed optically intermediate an incoming wavefront and the first and second optical control components, wherein the output optical wave-

front from the input beam divider is the input optical wavefront to the first and second optical control components;

an output beam combiner disposed to optically combine the respective first and second component modulated output wavefronts; and

phase shifting means for providing a controlled phase difference between the first and second component phase modulated output wavefronts,

wherein a resultant output wavefront has a different phase than the input optical wavefront by an amount $\theta(x,y)$.

5. The device of claim **4**, wherein $L1_2$ is different than $L2_2$ by an amount $\Delta_2 L1L2$ where $0<\Delta_2 L1L2\leqq(2n+1)\lambda/2$, where n=0, 1, 3, . . . , so as to provide a phase shift $\leqq\pi$ radians.

6. The device of claim **4**, wherein X=Y and n=m.

7. The device of claim **4**, wherein the $M1_2$ sub array $(X\times Y)_{M1}$ in an ON/OFF state and the complementary $M2_2$ sub array $(X\times Y)_{M2}$ in the OFF/ON state are each one or more cluster arrays $X\times Y<n\times m$, further wherein each cluster array X×Y is characterized by at least a two level half-toning phase approximation.

8. The device of claim **4**, wherein the device is a phase screen.

9. The device of claim **4**, further comprising an optical telescope disposed optically downstream of the output wavefront of the device.

10. The device of claim **9**, wherein the telescope is a telecentric configuration that has an aperture that controls the mirror sub array size.

11. A method for controlling an optical wavefront WF, comprising:

providing a first controllable binary MEMS device $M1_1$ comprising an $(n_{x,y}\times m_{x,y})_{M1}$ mirror array, wherein each mirror can be set only to a binary ON/OFF position, and a second controllable binary MEMS device $M2_1$ comprising an $(n_{x,y}\times m_{x,y})_{M2}$ mirror array, wherein each mirror can be set only to a binary ON/OFF position;

providing an incident optical wavefront WF_{1i};

splitting the incident optical wavefront into $WF1_1$ along a first optical path $L1_1$ to $M1_1$ and into $WF2_1$ along a second optical path $L2_1$ to $M2_1$;

modulating $WF1_1$ reflected from $M1_1$ by setting at least one sub-array $(X_{x,y}\times Y_{x,y})_{M1}$ to an ON position and modulating $WF2_1$ reflected from $M2_1$ by setting a complementary at least one sub-array $(X_{x,y}\times Y_{x,y})_{M2}$ to an OFF position;

providing an optical path length difference $\Delta L1L2$ in a range $0<\Delta L1L2\leqq(2n+1)\lambda/2$, where n=0, 1, 3, . . . , so as to provide a phase shift $\leqq\pi$ radians; and

obtaining a desired output optical wavefront WF_{1o} by optically combining reflected wavefront $WF1_1$ and reflected wavefront $WF2_1$.

12. The method of claim **11**, wherein modulating a phase profile of the wavefront by setting the at least one sub-array $(X_{x,y}\times Y_{x,y})$ to a selected ON/OFF position comprises providing a grey-scale pixel value over the sub-array.

13. The method of claim **12**, comprising employing a half-toning algorithm, wherein a single grey-scale pixel is represented by a spatially averaged dot pattern over the X×Y mirror array.

14. A method for changing a wavefront by a desired amount described by $\exp[i\theta(x,y)]$ when $\theta(x,y)$ is specified, comprising:

generating a cosine modulated output wavefront WF_{1out} expressed as $\cos[\theta(x,y)]$ according to the method of claim **12**;

generating a sine modulated output wavefront WF_{2out} expressed as $\sin[\theta(x,y)]$according to the method of claim **12**;

providing a $\pi/2$ phase shift to the sine modulated output wavefront WF_{2out}; and

optically adding the cosine modulated output wavefront WF_{1out} and the phase shifted, sine modulated output wavefront WF_{2out}.

* * * * *

FOURIER OPTICS

NICHOLAS GEORGE
THE INSTITUTE OF OPTICS

DECEMBER 2012

ngeoge@optics.rochester.edu
Hajim College of Engineering & Applied Sciences
University of Rochester
Rochester, New York 14627

Fourier optics

Nicholas George, University of Rochester
Prof. Nicholas George accepted the invitation on 31 May 2010

Fourier optics is the field of physics that encompasses the study of light at visible wavelengths but including infrared and ultraviolet portions of the electromagnetic spectrum as well. Based upon Maxwell's equations for the electromagnetic field and using modern transform mathematics, principally Fourier transform theory in the solutions, Fourier Optics is particularly well-suited to the study of cascades of lenses and phase masks as are widely used in optical instruments ranging from microscopes to telescopes, i.e., linear optical systems. Fourier Optics also incorporates the advances in communication theory in the treatment of coherency topics to permit a rich, full analysis of optical systems that use various sources of illumination ranging from incoherent or white light to modulated laser beams. For Physical Optics, systems study of the point-spread-function and the optical transfer function can be described in a rigorous fashion. General transmission functions for lenses can be formulated and optical-system design that is valid in the non-paraxial regime is now practical. Fourier Optics places the analyses of linear optical systems on a rigorous theoretical foundation enabling one to calculate resolution, imaging and other interference phenomena in a careful and accurate fashion.--Nicholas George, Optics, Rochester 2010.

Sponsored by: Antoine Moreau, Blaise Pascal University, Clermont-Ferrand, France

Category: Optics

FOURIER OPTICS

NICHOLAS GEORGE
JOSEPH C. WILSON PROFESSOR OF ELECTRONIC IMAGING
PROFESSOR OF OPTICS
THE INSTITUTE OF OPTICS

Contents

List of Figures

1 Introduction to electromagnetic waves and Fourier optics

The foundations of the subject of Fourier Optics rest on Maxwell's equations, the early studies of interference and interferometry, coherence, and imaging. Important advances in the mathematics of transform theory leading to communication theory from 1900 to the present greatly aided our understanding of these phenomena; the general notion of signal representations such as HTD $\exp(i\omega t)$ herein, and the Fourier transform for optics, and the Laplace transform for electronic circuits. Professor P. M. Duffieux authored "L'integral de Fourier et ses applications à l'optique", Masson Editeur, Paris, 1970 with first editions going back to the early forties. "It represents the first book-length treatment of what is now called Fourier optics" [1]. At the (1970) meeting of the International Symposium on the applications of Holography (ICO) in Besçancon, at a Medal awarding address, Dr. Duffieux told a charming story of how a mathematics professor and colleague had told him about the Fourier transform when PMD showed him some integral forms he had derived in study of the earlier work of Ernst Abbe.

Interestingly the technological advances in monochromatic sources in electronics, particularly radio and microwave from 1900 to 1950 lead to greatly enhanced theoretical studies and many now-classic textbooks, appeared using HTD of amplitudes.

In optics intensity based considerations were more commonly employed. A notable exception is the brilliant advances in coherence theory leading to phase contrast microscopy. However, in Optics this situation changes dramatically with the invention and development of holography and nearly monochromatic lasers. The theoretical treatment and understanding of these novel devices were greatly aided by the appearance of now classic textbooks on Fourier Optics [2, 3].

This article contains a modern complete theoretical treatment of Fourier Optics based on Maxwell's equations and current signal representations, as devised from the subject of communication theory.

1.1 Maxwell's equations in real-valued form

The basic equations of electromagnetic theory are briefly reviewed for a simple linear medium so that the signal representation herein can be carefully explained. In this first section, we describe the time-varying real-valued electric field vector $\mathcal{E}(\mathbf{r},t)$ and the time-varying magnetic field vector $\mathcal{H}(\mathbf{r},t)$ in Eq. (1) Faraday's Law and Eq. (2) the generalized Ampere's circuit law including Maxwell's electric displacement term. Undergraduate level derivation of these first six differential equations of electrodynamics and their application across the electromagnetic spectrum appear in many texts, e.g., [4] Griffiths. This article is written using the SI/mks system of units. The time-dependent real-valued functions are related as given in Eqs. (1) through (6):

$$\nabla \times \mathcal{E}(\mathbf{r},t) = -\frac{\partial \mathcal{B}(\mathbf{r},t)}{\partial t} \tag{1}$$

$$\nabla \times \mathcal{H}(\mathbf{r},t) = \mathcal{J}(\mathbf{r},t) + \frac{\partial \mathcal{D}(\mathbf{r},t)}{\partial t} \tag{2}$$

$$\nabla \bullet \mathcal{D}(\mathbf{r},t) = \rho(\mathbf{r},t) \tag{3}$$

$$\nabla \bullet \mathcal{B}(\mathbf{r},t) = 0 \tag{4}$$

$$\nabla \bullet \mathcal{J}(\mathbf{r},t) = -\frac{\partial}{\partial t}\rho(\mathbf{r},t) \tag{5}$$

$$\nabla \times \nabla \times \mathcal{E}(\mathbf{r},t) + \mu\varepsilon \frac{\partial^2}{\partial t^2}\mathcal{E}(\mathbf{r},t) = -\mu \frac{\partial}{\partial t}\mathcal{J}(\mathbf{r},t) \tag{6}$$

The field vectors are written in boldface type and the common symbols are used for divergence ($\nabla\bullet$) and curl ($\nabla\times$). Restricting the media to simple dielectrics, the constitutive parameters for permittivity ε and permeability μ also give us

$$\mathcal{B} = \mu\mathcal{H} \tag{7}$$

and

$$\mathcal{D} = \varepsilon\mathcal{E} \tag{8}$$

An exact solution of Maxwell's equations is obtained when one has $\mathcal{E}(\mathbf{r},t)$ and $\mathcal{H}(\mathbf{r},t)$ that satisfy Eqs. (1) and (2). Other paths to exact solutions are to obtain $\mathcal{E}(\mathbf{r},t)$ from Eq. (6) and then use Eqs. (1) and (7) to find $\mathcal{H}(\mathbf{r},t)$. Finally, one can introduce any of a variety of vector potentials that have been developed for particular cases.

1.2 Fourier analysis in three dimensions

Consider a scalar function $g(x,y,t)$ with two transverse spatial coordinates and one temporal coordinate. Now define the Fourier transform $G(f_x,f_y;\nu)$ by the following equation:

$$G(f_x,f_y;\nu)=\iiint_{-\infty}^{\infty} g(x,y,t)e^{-i2\pi(f_x x+f_y y+\nu t)}dxdydt \tag{9}$$

It is a straightforward exercise to show that the inversion expression is given by Eq. (10):

$$g(x,y,t)=\iiint_{-\infty}^{\infty} G(f_x,f_y;\nu)e^{i2\pi(f_x x+f_y y+\nu t)}df_x df_y d\nu \tag{10}$$

This notation and sign convention is used throughout this paper. It is particularly convenient since the sign of the exponents in the transform kernel are all negative while those of the inversion are all positive.

1.3 Maxwell's differential equations in temporal transform form

In Sec. 1.2, the notation for Fourier analysis in three dimension has been presented in order to place in evidence the sign convention to be used. Now, however, we use the obvious form for the temporal transform alone, since we wish to compare the resultng equations to "standard" HTD expressions.

Important integral solutions of Maxwell's equations are readily obtained using temporal Fourier transform forms of Eqs. (1) (2) and (6) with the corresponding results in Eqs. (11) , (12) and (13) , (14) directly below:

$$\nabla\times\mathbf{E}(\mathbf{r};\nu)=-i\omega\mu\mathbf{H}(\mathbf{r};\nu) \tag{11}$$

$$\nabla\times\mathbf{H}(\mathbf{r};\nu)=\mathbf{J}(\mathbf{r};\nu)+i\omega\varepsilon\mathbf{H}(\mathbf{r};\nu) \tag{12}$$

$$\nabla\times\nabla\times\mathbf{E}(\mathbf{r};\nu)-\omega^2\mu\varepsilon\mathbf{E}(\mathbf{r};\nu)=-i\omega\mu\mathbf{J}(\mathbf{r};\nu) \tag{13}$$

$$(\nabla^2+k^2)\mathbf{E}(x,y,z)=0 \tag{14}$$

Equation (14) is valid in a source free region.

Now these temporal transform equations are exact and rigorous for optical sources which are transient. Since temporal frequency ν is a variable, solving the above equations gives us a new path to solving problems in which there are broadband sources or multi-tone spectra.

$$\nabla \times \mathcal{E} = -\frac{\partial \mathcal{B}(\mathbf{r},t)}{\partial t} \qquad \nabla \times \mathbf{E} = -i2\pi\nu\mathbf{B}$$

$$\nabla^2 \mathcal{E}_x = \mu\varepsilon \frac{\partial^2 \mathcal{E}_x}{\partial t^2} \qquad (\nabla^2 + k^2)E_x(x,y,z;\nu) = 0$$

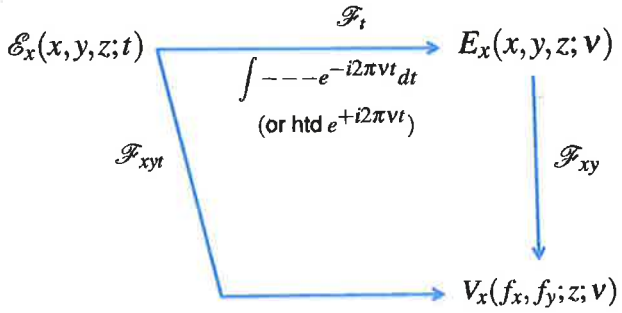

$$\frac{\partial^2 V_x}{\partial z^2} + [k^2 - (2\pi f_x)^2 - (2\pi f_y)^2]V_x = 0$$

$$V_x(f_x,f_y;z;\nu) = \int\int_{-\infty}^{\infty} dxdy\, E_x(x,y,z;\nu)e^{-i2\pi f_x x - i2\pi f_y y}$$

$$E_x(x,y,z;\nu) = \int\int_{-\infty}^{\infty} df_x df_y\, V_x(f_x,f_y;z;\nu)e^{+i2\pi f_x x + i2\pi f_y y}$$

Figure 1: Signal representations in Electromagnetic Waves and Fourier Optics

In order to place emphasis on the significance of the result to be inferred from Eqs. (11) through (14), let us observe that Eqs. (11) and (12) are simply and precisely the harmonic-time-dependence differential equations for an electromagnetic wave. The reader is cautioned , however, that our Eq. (9) notation is consistent with an exp($i\omega t$) as in ref. [6].

In Fig. 1 we show the signal representations being used in Sections 1.1 and 1.2 in more detail than is necessary for the paper at hand. However, we wanted to show the more general usage including angular spectrum as well as statistical optics in order to explain our preference for the exp($+i\omega t$)

in the HTD representation and its consistency with our Fourier transform notation.

2 Propagation into the right-half-space

Maxwell's equations give us the means to obtain exact solutions of many optics problems. Both the Hertzian electric dipole and the magnetic dipole are significant and important and covered in many textbooks [5] - [7]. In optics, diffraction theory topics such as propagation through screens, slits, and various apertures were studied extensively for several hundred years. Also lens trains formed by a cascade of lenses along an optical axis is a common configuration, as in Sec. 5.

2.1 Rayleigh-Sommerfeld-Smythe solution

Consider a monochromatic electromagnetic wave traveling along the optic z-axis and incident on an aperture as in Fig. 2. This is a classic problem in the propagation of waves since the time of Francesco Grimaldi and Christiaan Huygens.

We assume there are sources of radiation only in the region $z < 0$ and that we have knowledge of the "field" in the aperture. The radiation propagates into the right-half-space which is a simple source-free region. Viewed with today's understanding, as will be shown, if one views this as a boundary-value problem, there will be an exact integral form of the radiation at $z > 0$ for $\mathcal{E}(\mathbf{r},t)$ and $\mathcal{H}(\mathbf{r},t)$ that converges to the given tangential electric field $\hat{z} \bullet \mathcal{E}(\mathbf{r},t)$. As is illustrated by the solution, the tangential input electric field at $z = 0$ is the necessary and sufficient input specification, as recognized first by Sommerfeld for the HTD case.

Now to obtain the desired solution for radiation in the right-half-space one starts with Eq. (14) rewritten for each Cartesian component, viz.,

$$\nabla^2 E_x(x,y,z) + k^2 E_x = 0 \tag{15}$$

$$\nabla^2 E_y(x,y,z) + k^2 E_y = 0 \tag{16}$$

$$\nabla^2 E_z(x,y,z) + k^2 E_z = 0 \tag{17}$$

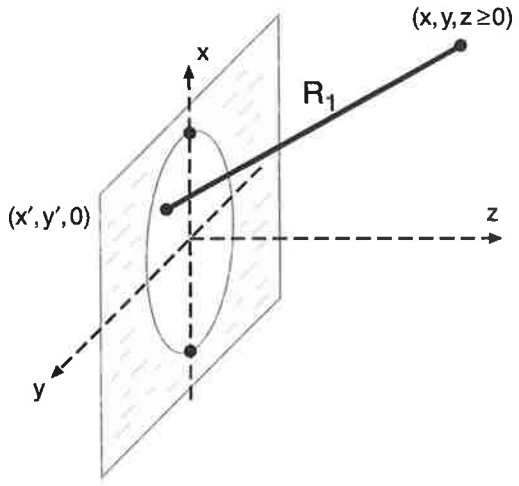

Figure 2: Radiation into the right-half-space from a circular aperture in the $z = 0$ plane

Now consider the use of a Green's function solution using either Eq. (15) or (16), as follows. We write

$$G_s(\nabla^2 + k^2)E_x = 0 \tag{18}$$

$$E_x(\nabla^2 + k^2)G_s = -\delta(\mathbf{r} - \mathbf{r}')E_x \tag{19}$$

where $\mathbf{r}'$ is at $(x_1, y_1, z_1 \geq 0)$ in the right-half-space, as shown in Fig. 3 and the vector operations are at the point $\mathbf{r}(x, y, z)$. Moreover, the Green's function $G_s(x, y, z; x_1, y_1, z_1)$ has a singularity at $\mathbf{r}'$. Forming the difference of Eqs. (18) and (19) and integration over the right-half-volume and using Green's second identity yield the following intermediate result:

$$E_x(x_1, y_1, z_1) = \iint_{RHS} (G_s \nabla E_x - E_x \nabla G_s) \bullet \hat{\mathbf{n}}_{out} dA \tag{20}$$

Sommerfeld broke this integration in Eq. (20) into parts asserting that the integral over the hemisphere in the far zone goes to zero for a finite

aperture source (see Eq. (22) below).

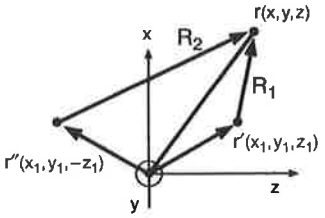

Figure 3: Notation in the calculation for Sommerfeld's Green's function with a δ-function at point $r'(x_1,y_1,z_1)$ in the right-half-space.

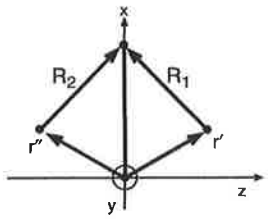

Figure 4: Sommerfeld's Green's function in Eq. (23) and integration over the $z=0$ plane.

The integration over the plane at $z=0$ has two members by a proper choice of the Green's function G_s, one can zero out the first member of the integration over the $z=0$ plane, regardless of the non-zero value of ∇E_x there. Hence by Eq. (18), the scalar component E_x for $z \geq 0$ is given by

$$E_x(x_1,y_1,z_1 \geq 0) = \iint_{z=0} E_x \nabla G_s \bullet \hat{\mathbf{z}}\ dxdy \tag{21}$$

Moreover summarizing, one has the Sommerfeld radiation condition that the term $S \to 0$ where S is given by

$$S = \iint_{R_1 \to \infty} (G_s \nabla E_x - E_x \nabla G_s) \bullet \hat{\mathbf{r}}\ dA \to 0. \tag{22}$$

Also, the appropriate choice for $G_s(x,y,0;x_1,y_1,z_1)$ is given by

$$G_s = \frac{e^{-ikR_1}}{4\pi R_1} - \frac{e^{-ikR_2}}{4\pi R_2} \tag{23}$$

in which

$$R_1 = [(x-x_1)^2 + (y-y_1)^2 + (z-z_1)^2]^{1/2} \tag{24}$$

and

$$R_2 = [(x-x_1)^2 + (y-y_1)^2 + (z+z_1)^2]^{1/2}. \tag{25}$$

In Figs. 3 and 4, one sees that placing r'' as the image point of r' in the z-plane establishes that $G_s(x,y,0;x_1,y_1,z_1)=0$ in the $z=0$ place as required to drop out the term in the integral regardless of the value of ∇E_x.

Thus, the Green's function choice by Sommerfeld in Eq. (23) is the key to finding an exact solution for E_x in the right-half-space.

A straightforward algebraic calculation on $G_s(x,y,z;x_1,y_1,z_1)$ for

$$\nabla G_s \bullet \hat{\mathbf{z}} = \left.\frac{\partial G_s}{\partial z}\right|_{z=0} \tag{26}$$

leads to the important result:

$$\left.\frac{\partial G_s}{\partial z}\right|_{z=0} = \frac{e^{-ikR_1}}{2\pi R_1}(ik+\frac{1}{R_1})\frac{z_1}{R_1}. \tag{27}$$

Substitution of Eq. (27) into Eq. (21) yields the desired result for the interior scalar electric field component, namely

$$E_x(x_1,y_1,z_1\geq 0) = \iint_{-\infty}^{\infty} dxdy\, E_x(x,y,0)\frac{e^{-ikR_1}}{2\pi R_1}(ik+\frac{1}{R_1})\frac{z_1}{R_1} \tag{28}$$

in which the distance R_1 is given exactly by Eq. (24).

Now, typical of Green's function solutions, we make a change in coordinates in Eq. (28) in order to have the aperture point labeled $(x',y',0)$ and the interior RHP point (x,y,z) as in Fig. 2. The result of this relabeling in coordinates leads to the desired final form for

$$E_x(x,y,z\geq 0) = \iint_{\substack{-\infty \\ z=0}}^{\infty} dx'dy' E_x(x',y',0)\frac{e^{-ikR_1}}{2\pi R_1}(ik+\frac{1}{R_1})\frac{z}{R_1} \tag{29}$$

and of course now R_1 in Eq. (29) becomes

$$R_1 = [(x-x')^2+(y-y')^2+(z-0)^2]^{1/2}. \tag{30}$$

One can complete this derivation by stating that this result can also be written for $E_y(x,y,z\geq 0)$. Now using $\nabla \bullet \mathbf{E}(x,y,z;\nu)=0$, we can find an expression for E_z that stresses its dependence on E_x and E_y. We omit the details of this calculation until later in Eq. (35) since there is much more to write about these results using an independent approach in Sec. 2.2 below.

2.2 Impulse response for propagation into the RHS

In linear optical systems a topic of central interest is to derive an exact impulse response for propagation into the right-half-space (RHS). In Sec. 2.1 Eq. (29) is presented as a rigorous solution of Maxwell's equation for this impluse response. It is applicable over the entire range that Maxwell's equations holds from near field optics to telescopes. Hence, in this article it seemed worthwhile to develop an independent derivation of Eq. (29) and related material.

Again consider the setup and notation in Figs. 2 for radiation into the RHS. Smythe was at least early to write out a detailed existence theorem for electromagnetic waves in a closed source-free region, and he stressed the necessary and sufficient need for either the tangential electric field or the tangential magnetic field, although he did not explicitly cover a region such as the RHS [8]. Also Smythe was first to write the complete exact solution for the right-half-space problem in an entirely vector form in his famous Phys. Rev. (1947) paper [9]. The vector result for the internal field is given in Fourier optics or HTD form as follows:

$$\mathbf{E}(\mathbf{r};v) = \frac{1}{2\pi}\nabla \times \iint_{z'=0} \hat{z}' \times \mathbf{E}(\mathbf{r}')\frac{e^{-ikR_1}}{R_1}\, dx'dy' \tag{31}$$

in which the free-space Green's function G is appropriate as follows:

$$G(\mathbf{r},\mathbf{r}') = \frac{e^{-ikR_1}}{4\pi R_1}, \tag{32}$$

and $\mathbf{E}(\mathbf{r}')$ at $(x',y',0)$ is the final field in the aperture.

Let me describe some illuminating illustrative exercises for the dedicated reader. Derive the equations below in Eq. (33) to (35) for the components.

To verify that this result in Eq. (31) is an exact solution for Maxwell's equations, one needs to verify that the vector $\mathbf{E}(\mathbf{r};v)$ is a solution of the vector wave equation (13) or (14).

It is fascinating to see the impulse responses for propagation into the RHS for a simple medium. There is no "mixing" of the x and y polarizations. Moreover, both the E_x and E_y are seen to contribute to the E_z component. This illustrates very nicely the existence theorem for this situation

and Maxwell's equations. For the RHS problem, one can supply any reasonable functions for the tangential components E_x and E_y (necessary and sufficient) but any more will likely lead to inconsistent results.

2.3 Summary of impulse response

2.3.1 The Right-Half-Space

Here are the exact solutions of Maxwell's equations for propagation in the right-half-space.

The Rayleigh-Sommerfeld-Smythe formulas:

$$E_x(x,y,z) = \iint_{-\infty}^{\infty} dx'dy' E_x(x',y',0) \frac{e^{-ikR_1}}{2\pi R_1}(ik + \frac{1}{R_1})\frac{z}{R_1} \tag{33}$$

$$E_y(x,y,z) = \iint_{-\infty}^{\infty} dx'dy' E_y(x',y',0) \frac{e^{-ikR_1}}{2\pi R_1}(ik + \frac{1}{R_1})\frac{z}{R_1} \tag{34}$$

$$E_z(x,y,z) = \iint_{-\infty}^{\infty} dx'dy' \{E_x(x',y',0)\frac{x'-x}{R_1} + E_y(x',y',0)\frac{y'-y}{R_1}\}\frac{e^{-ikR_1}}{2\pi R_1}(ik + \frac{1}{R_1}) \tag{35}$$

Another exact, useful and readily proven result for the RHS is given by [10]:

$$E_{x,y}(x,y,z) = -\frac{\partial}{\partial z}\iint_{-\infty}^{\infty} dx'dy' E_{x,y}(x',y',0)\frac{e^{-ikR_1}}{2\pi R_1} \tag{36}$$

They are valid for $z \geq 0$, and R_1 is given by Eq. (30), Fig. 2.

Many scientists have contributed to an understanding of interference patterns arising as light propagates, e.g., from two pinholes, through an open aperture, or from an array of coherent sources. Huygens' principle stated more than three hundred years ago in the description of the propagation of a wavefront is among the earliest major contributions. His asserions are in accord with the theory which we have presented.

For us, today, using Maxwell's equations and the formula presented on the previous page, we can see that a diffraction pattern is made up by the

superposition of radiation from differential elements given by

$$dx'dy'E_x(x',y',0).$$

These give rise to "secondary waves" which are traveling in the right-half-space with a very weak angular dependents given by the term z/R_1. The superposition weighting is given precisely in amplitude and phase by the term:

$$\frac{e^{-ikR_1}}{2\pi R_1}(ik+\frac{1}{R_1})\frac{z}{R_1}$$

All of the physical details of interference patterns are contained in these formulas for the radiation in the right-half-space resulting from a given aperture distribution.

2.3.2 The full 4π-steradian space

In the classic text on electromagnetic wave by Papas [5], there is an excellent treatment of radiation from monochromatic sources in unbounded regions, i.e., 4π steradians. He describes two methods of solution: vector potentials and the dyadic Green's function. While our emphasis for optics is on the right-half-space topic, it is important to mention this basic result for the impulse response for the 4π-steradian or full-space case.

For the same simple medium with constitutive parameters μ, ε, one has the same group of Maxwell's equations as our Eqs. (11), (12).

The magnetic vector potential $\mathbf{A}$ is defined by

$$\mathbf{B} = \nabla \times \mathbf{A}. \tag{37}$$

Hence, by Eq.Eq. (11), one can write the $\mathbf{E}$ field as

$$\mathbf{E} = -i\omega\mathbf{A} - \nabla\phi. \tag{38}$$

With the choice of the Lorenz gauge relating $\mathbf{A}$ and ϕ, namely that

$$\nabla \bullet \mathbf{A} + i\omega\varepsilon\mu\phi = 0 \tag{39}$$

one can write a wave equation as follows:
for the vector potential $\mathbf{A}(\mathbf{r};\nu)$:

$$\nabla^2\mathbf{A}+k^2\mathbf{A}=-\mu\mathbf{J}. \tag{40}$$

Presenting a Green's function solution, Papas derives the integral equation solution for the radiation into free space, 4π-steradians:

$$\mathbf{A}(\mathbf{r})=\iiint_{-\infty}^{\infty} dx'dy'dz'J(\mathbf{r}')\frac{e^{-ik\mathbf{R}_1}}{4\pi R_1} \tag{41}$$

Equation (41) is the basis equation for radiation of electromagnetic waves into free space in a spherical configuration. It is particularly useful for radiation of current sources as given by $\mathbf{J}(\mathbf{r}',v)$ where the R_1 is given by

$$R_1=[(x-x')^2+(y-y')^2+(z-z')^2]^{1/2} \tag{42}$$

It is important to understand these two distinct radiation problems. They are often confused. First, one has the scalar electric field components propagating into the right-half-space expressed in terms of source-terms in the plane at $z=0$. The solutions are given in Eqs. (33) to (36).

Secondly, in the radiation into 4π-space, we have the vector potential $\mathbf{A}(\mathbf{r};v)$ resulting from source currents $\mathbf{J}(\mathbf{r}';v)$, and the resulting impulse response given by the free-space Green's function in Eq. (41).

3 Optical diffraction illustrations

The theory of Fourier Physical Optics as presented in the earlier sections of this article is based on Maxwell's equations. The precision possible with rigorous or exact solutions of electromagnetic theory is discussed in some detail in Jackson [11]. This enormous range includes wavelength or frequency from fractional cycles per second to ultraviolet and of course DC. It includes power range from $10^{-}20$ watts to many megawatts. It also includes subpulse propagation as well as $\mu\mu$sec transients. Many new fields

are developing in optics such as computational imaging that are permitting the solution of many boundary value problems, and near-field optics problems that were considered inaccessible until rather recently.

3.1 The circular aperture

For a first illustration, it is helpful to start with an important problem in which a theoretical approach leads to interesting results [10]. Consider a perfectly conducting, infinitesimally thin conducting plane sheet containing a circular aperture of radius (a) placed in the (x,y) plane at $z = 0$, as shown in Fig. 5. It is illuminated by a plane-polarized monochromatic plane wave with wave number $k = 2\pi/\lambda$ where $\lambda \ll a$ so boundary effects can be ignored. Clearly, Eq. (33) or (36) can be used. Let us restrict our solution to the optic axis z so that we gain an understanding of the different zones shown. Hence, for a fixed amplitude E_o of the scalar component of electric field, by Eq. (36), one can write the field along the optical axis $E_x(0,0,z;v)$ as

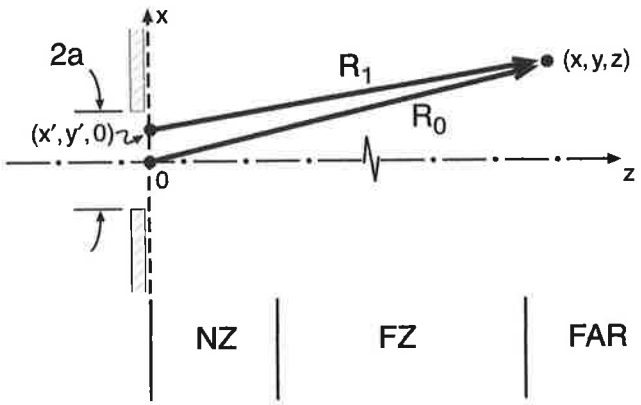

Figure 5: Uniformly illuminated circular aperture of radius (a) is calculated on axis to provide clear picture of (NZ) near field, (FZ) Fresnel zone and the FAR-zone. [10]

$$E_x(0,0,z\geq 0) = -\frac{\partial}{\partial z}\iint_A dx'dy' E_x(x',y',0)\frac{e^{-ikR_1}}{2\pi R_1}, \tag{43}$$

in which the illumination is given in polar coordinates, viz.

$$E_x(x',y',0) = E_o circ(\rho/a), \quad \rho = [x'^2+y'^2]^{1/2} \tag{44}$$

and the distance R_1 given in polar form is

$$R_1 = [\rho^2+z^2]^{1/2}. \tag{45}$$

Equation (43) is rewritten to yield:

$$E_x(0,0,z\geq 0) = -E_o\frac{\partial}{\partial z}\int_0^a \frac{e^{-ik(\rho^2+z^2)^{1/2}}}{(\rho^2+z^2)^{1/2}} 2\pi\rho d\rho. \tag{46}$$

This can be integrated exactly to yield the result:

$$E_x(0,0,z\geq 0) = E_o\{e^{-ikz} - \frac{z}{d}e^{-ikd}\} \tag{47}$$

where

$$d = \sqrt{a^2+z^2}. \tag{48}$$

First as expected, when $z\to 0$, the radiation field at the aperture reduces to the input E_o. As described in Sec. 2.2, this result is consistent with the existence theorem for Maxwell's equations, Eqs. (1) through (4), extended to the right-half-space and adding Sommerfeld radiation condition, given by Eq. (22). We see that specification of HTD together with the tangential electric field at the input plane $z=0$.

By Eq. (34) one sees that $E_y(x,y,z\geq 0)$ is identically zero as expected. And of course, one can calculate E_z by Eq. (35) clearly dependent on the non-zero tangential electric field, E_x, input.

In order to study the z-dependence of E_x further, it is interesting to think of the calculation as in the HTD signal representation. By Eqs. (47) and (48), one can insert the time dependence simply as follows:

$$E_x(0,0,z;t) = E_o\{e^{-ikz} - \frac{z}{\sqrt{z^2+a^2}}e^{-ik\sqrt{z^2+a^2}}\}e^{+i2\pi\nu t}. \tag{49}$$

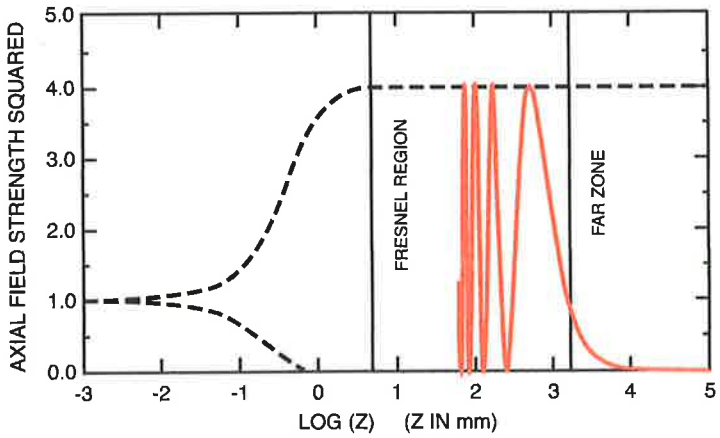

Figure 6: Axial field strength squared $w(z)$ vs $log(z)$ for uniformly illuminated circular aperture, as in Eq. (51) The dashed lines are the envelope of $w(z)$. The actual value of $w(z)$ is plotted in red in the Fresnel zone for the first few cycles, but it is too fine scalar to plot accurately.

In order to monitor the optical field along the optical axis, one can use a single photodiode or a CMOS detector array. Hence, in our illustrative study, we will use energy density in the E_x electric field. Hence, we define w as follows

$$w(z) = |E_x(0,0,z:t)|^2. \tag{50}$$

Hence combining Eq. (47) and (48) with some algebra yields the following form:

$$w(z) = |E_o|^2\{1 + \frac{z^2}{z^2+a^2} - 2\frac{z}{\sqrt{z^2+a^2}}\cos k[\sqrt{z^2+a^2} - z]\} \tag{51}$$

in which $k = 2\pi/\lambda$.

No approximations have been made in deriving Eq. (51) for the squared electric field component E_x from the initial solution in Eq. (47). Hence, it is

useful as an illustration, and it is plotted in Fig. 6.

The plot shows Eq. (51) for $w(z)$ vs. z in mm. The aperture diameter $2a$ = 1 mm and the optical wavelength λ = 0.5 μm. The envelope for $w(z)$ is plotted as the dashed lines since the amplitude variations in the optical field are tiny compared to the z-axis mm scale.

This theoretical problem provides a lovely illustration of the main radiation zones that are so important in diffraction problems. Here we would like to point out that the far-zone or Fraunhofer zone start at roughly 1 meter for the one-millimeter aperture. And in this region, the electric field falls off as $1/z$ while the intensity falls off as $1/z^2$.

Coming in closer, one sees the natural occurrence of another zone called the Fresnel zone, treated in Sec. 3.3 below. Looking at the scale in Fig. 6, the Fresnel zone comes to an end at about 6 mm. If one goes in closer, the calculations become very difficult to carry out in closed form if one goes off-axis. However, they are nicely handled with modern digital computers and computational imaging.

From Eqs. (33) and (35) as well as the discussion of Eq. (38) for the impulse response of the right-half-space, it is appropriate to discuss the new field of computational optics. Viewing the main equations for the right-half-space, we have emphasized the notion that the interior that the interior fields in a closed volume with no internal sources can be calculated from a knowledge, say, of the tangential component of the electric field (necessary and sufficient). From the illustration of the simple circular aperture, Fig. 6, one clearly sees the field $E_x(0,0,z)$ converges to the input tangential field, E_o. This is generally true for all of the RHP forms.

For near-field optics it is interesting to take note of the two members of the amplitude impulse response:

$$p(x,y;x',y';\nu) = \frac{e^{-ikR_1}}{2\pi R_1}(ik+\frac{1}{R_1})\frac{z}{R_1} \tag{52}$$

It is important to notice that the $1/R_1$ term will be dominant in the overall integration whenever

$$\begin{aligned} |(1/R_1)/(ik)| &\gg 1 \\ kR_1 &\ll 1 \\ R_1 &\ll \lambda/8. \end{aligned} \tag{53}$$

In the illustration of the circular aperture, of course both terms are included in the calculation. An advanced and comprehensive treatment of the theory of diffraction is provided by Born and Wolf [12].

3.2 The far-zone

Now starting with a more general aperture shape in the $z = 0$ plane of Fig. 2, we consider that an x-plane polarized scalar electric field $E_x(x',y',0;\nu)$ is used as the illustration. Hence, we seek an approximate, more integrable form of the exact Eq. (33) that is repeated as Eq. (54), i.e.,

$$E_x(x,y,z:\nu) = \iint_{-\infty}^{\infty} dx'dy' E_x(x',y',0)\frac{e^{-ikR_1}}{2\pi R_1}(ik+\frac{1}{R_1})\frac{z}{R_1} \tag{54}$$

The far-zone, also known as the Fraunhofer region, is characterized by large values of R_1. Mainly in this treatment, we would like carefully to point out the conventional theoretical assumptions in the integration of Eq. (33) or (54) in the far-zone region.

In the far-zone calculation, however, the situation is vastly different relative to accuracy for $exp(-ikR_1)$. The phase term needs to be accurate to the order of $\pm\pi/8$ no matter how large R_o is. For example, if you are making measurements at 10 m with an optical wavelength of 0.5 μm, the kR_o is the order of $4\pi \times 10^7$ radians; and the tolerance error in R_1 is fractionally well below one part in 10^7.

Hence, in the far-zone, Eq. (54) can be approximated by

$$E_x(x,y,z;\nu) = \frac{ik}{2\pi R_o}\left(\frac{z}{R_o}\right)\iint_{-\infty}^{\infty} dx'dy' E_x(x',y',0)e^{-ikR_1} \tag{55}$$

For the illustration problem, consider an open rectangular aperture that is L_x by L_y length in the conducting metallic sheet at $z = 0$. We take $L_{x,y} > \lambda$ so that we can study the patterns from slits to large square apertures. Using the notation in Fig. 5, we already understand that the distance $R_o \gg \lambda$ so only the ik member in Eq. (54) remains for the far-zone.

Moreover, amplitude terms that are approximated in this integration will cause errors in percentage that are roughly that of the approximation. Hence if a five-percent accuracy solution is sought, then amplitude terms need only be accurate to five-percent.

For the R_1 in the phase term $(-ikR_1)$, we write

$$R_1^2 = [(x-x')^2 + (y-y')^2 + (z-0)^2]^{1/2} \tag{56}$$

Since the far-zone term is often used for telescopes, it is useful to have the expansion valid for large angles θ where

$$\frac{z}{R_o} = \cos\theta \tag{57}$$

is recognized as the spherical angle coordinate.

Hence, one factors out $R_o = (x^2+y^2+z^2)^{1/2}$ in the expansion of Eq. (56). For the Fraunhofer zone, the resulting expression for the distance R_1 is approximated by the following:

$$R_1 \cong R_o - \frac{xx'+yy'}{R_o}, \tag{58}$$

$$R_o \gg \frac{2x'^2}{\lambda} \quad \text{all cases of coordinates,} \tag{59}$$

$$E_{x,y}(x,y,z) = \frac{ie^{-ikR_o}}{\lambda R_o}\left(\frac{z}{R_o}\right)\iint_{-\infty}^{\infty} dx'dy'E_{x,y}(x',y',0)e^{i2\pi\left[\left(\frac{x}{\lambda R_o}\right)x' + \left(\frac{y}{\lambda R_o}\right)y'\right]} \tag{60}$$

In Eq. (60) the integration is only over the aperture and this is included as a blocking function in the scalar input field $E_{x,y}(x',y',0)$. It is customary in Fourier optics to write the limits of integration as running over $\pm\infty$. Hence in a cascaded system in which there are many integrals running from $\pm\infty$, and this is to emphasize that the order of integration can be interchanged. This is a key factor in many calculations.

Noting that the exponent in Eq. (60) is of the form of a Fourier transform in which the spatial frequency variables are (f_x, f_y), one can rewrite Eq. (60) in the following form:

$$E_{x,y}(x,y,z) = \frac{ie^{-ikR_o}}{\lambda R_o}\left(\frac{z}{R_o}\right)\iint_{-\infty}^{\infty} dx'dy'E_{x,y}(x',y',0)e^{-i2\pi[f_x x' + f_y y']}, \tag{61}$$

in which the spatial frequency variables (f_x, f_y) are defined by

$$f_x = -\frac{x}{\lambda R_o} \quad \text{and} \qquad f_y = -\frac{y}{\lambda R_o}. \tag{62}$$

It is interesting to use Eq. (59) to estimate the axial distance for which the above calculation is valid. Assume that the rectangle in the $z = 0$ plane is on the order of 1 mm and that $\lambda = 0.5\mu$m. Then, Eq. (59) gives $R_o > 4$m as the starting point for the far-zone. This is nicely in accord with our discussion in connection with the Fig. 6 curve showing somewhat over 1 meter for the circular aperture.

Moreover, we also clearly see the $1/R_o$ fall off of the electric field corresponding to an inverse R^2 power.

Moreover, the error in the phase term involved in the exponent can be shown to be a maximum at the $\theta = 0$ angle, decreasing as the angle increases. So factoring out the R_o in the derivation of Eq. (60) is imperative so that Eq. (58) is good at all angles in the right-half-space; i.e., it is not paraxially limited.

3.2.1 The rectangular aperture

For the rectangular aperture L_x by L_y in length Eq. (60) can be integrated directly to yield the following far-zone radiation pattern:

$$E_x(x,y,z) = \frac{ie^{-ikR_o}}{\lambda R_o}\left(\frac{z}{R_o}\right) L_x L_y \frac{\sin\left(\frac{\pi x L_x}{\lambda R_o}\right)}{\left(\frac{\pi x L_x}{\lambda R_o}\right)} \frac{\sin\left(\frac{\pi y L_y}{\lambda R_o}\right)}{\left(\frac{\pi y L_y}{\lambda R_o}\right)}. \tag{63}$$

Or in Fourier optics notation, one has

$$E_x(x,y,z) = \frac{ie^{-ikR_o}}{\lambda R_o}\left(\frac{z}{R_o}\right) L_x L_y \mathrm{sinc}(f_x x)\mathrm{sinc}(f_y y). \tag{64}$$

3.3 The Fresnel zone

In Sec. 3.1 the illustration of the axial field behavior in the right-half-space using a circular aperture showed us that there is a near zone, followed by

a Fresnel zone, and then at larger distances the far-zone. In Sec. 3.2 for the far-zone, we illustrated the theory and a careful calculation that was demonstrated to be good in the right-half-space when the overall range distance $R_o \gg 2x^2/\lambda$. Numerically, we estimated that for small millimeter apertures, one can calculate accurate patterns when $R_o \gtrsim 4$ m. We asserted that the calculation is excellent at all angles. This calculation is an easy extension of the material presented.

However, one very important calculation in Fourier optics is to treat lenses, either a single lens or a cascade of lenses. In this Sec. 3.3 we describe the Fresnel-zone calculation. It is very important since it can be used to handle lens cascades where the spacing is generally much smaller than in the far-zone. As shown for the circular aperture, Figs. 5 and 6, hopefully we are dealing with several millimeters rather than meters.

For the Fresnel zone, the theory proceeds as in Sec. 3.2. First for Eq. (33), we need to establish an expansion for the phase term. Using the notation as in Fig. 5, the exact expression for the distance R_1 is given by

$$R_1 = [(x-x')^2 + (y-y')^2 + (z-0)^2]^{1/2}. \tag{65}$$

Factoring z and using the binomial expansion gives the following form:

$$R_1 \cong z + \frac{(x-x')^2 + (y-y')^2}{2z}. \tag{66}$$

Factoring with removal of z and leaving (x,y) in the series limits one to a paraxial solution. It is better, however, with regard to axial distance, i.e., valid much closer-in. The limitation on primed coordinates (all cases) is characterized by the following:

$$z^3 \gtrsim \frac{(x-x')^4}{2\lambda}. \tag{67}$$

For a 1 mm aperture, this gives an axial distance $z \approx 10$ mm when $\lambda = 0.5\mu$m. For the Fresnel zone case, Eq. (33) can rewritten as

$$E_x(x,y,z;\nu) = \frac{iz}{\lambda R_o^2}\iint_{-\infty}^{\infty} dx'dy' E_x(x',y',0)e^{-ikR_1}, \tag{68}$$

$$E_x(x,y,z;\nu) = \frac{ie^{-ikz}}{\lambda z}\iint_{-\infty}^{\infty} dx'dy' E_x(x',y',0)e^{-\frac{i\pi}{\lambda z}[(x-x')^2+(y-y')^2]}. \tag{69}$$

In many instances of lens design using modern digital computers, one can use Eq. (68) with the exact exponential. However, Eq. (69) is the standard form for a Fresnel calculation. The reader is left to use Eq. (67) to predict the starting point for the Fresnel zone region comparing this estimate to the exact values of the axial field strength as in Fig. 6 from Eq. (51).

4 Transmission function theory for lenses

4.1 Review of simple lens models [2]

Most of the theory relative to the right-half-space topic is concerned with how wavefronts propagate in this region. However, one of the central problems in Fourier optics is to analyze a cascade of lenses that have been placed along an optical axis, say, for the formation of an image or to describe a compound lens. It is important to develop an understanding of the operation of lenses and an analytical theory that is useful for wavefronts. Clearly, too, there is a considerable theory about the design and performance of lenses, since they date back to our earliest history. We are careful in the following material to use sign conventions and language that is consistent with usage in the field of geometric optics, i.e., first-order or Gaussian optics. Our simple cases are to have light traveling from left to right in the positive z-axis direction. Convergent lenses have a positive focal length f. A glass lens with index of refraction n and two positive radii is shown in Fig. 7.

A simple thin lens of glass with index of refraction n will have a focal length f given by

$$\frac{1}{f} = (n-1)\left(\frac{1}{R_1} - \frac{1}{R_2}\right), \tag{70}$$

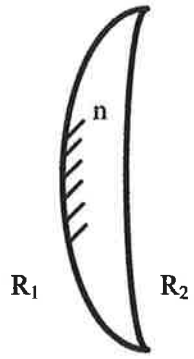

Figure 7: Convergent lens with R_1, R_2 positive and a positive focal length as in Eq. (70)

where R_1 and R_2 are radii of spherical end segments, and the lens is used in air.

Also a point source at s_1 in front of the lens will be imaged at a distance s_1' given by the lensmaker's equation:

$$\frac{1}{s}+\frac{1}{s_1'}=\frac{1}{f}. \tag{71}$$

Now in order to bring wavefronts into the picture, as shown in red in Fig. 8, consider a plane wave entering the lens which is thicker at the optic axis than at its edges. For a lens that has a spherical segment, the exiting wavefronts will bend forward as shown. Now the phase delay of the plane wave between planes **I** and **II** can be calculated approximately by summing $\sum kl$ in a straight ray through the plano-convex structure shown having positive radius R_1 at plane **I** and an infinite radius at the plane **II** exit.

Now defining the amplitude transmission function, $T_{12}(\rho)$, as follows:

$$T_{12}(\rho)=\frac{\text{Scalar electric field exiting (II)}}{\text{Scalar electric field entering (I)}} \tag{72}$$

or

$$T_{12}(\rho)=e^{-i\Phi_1}, \tag{73}$$

we can sum the phase delays:

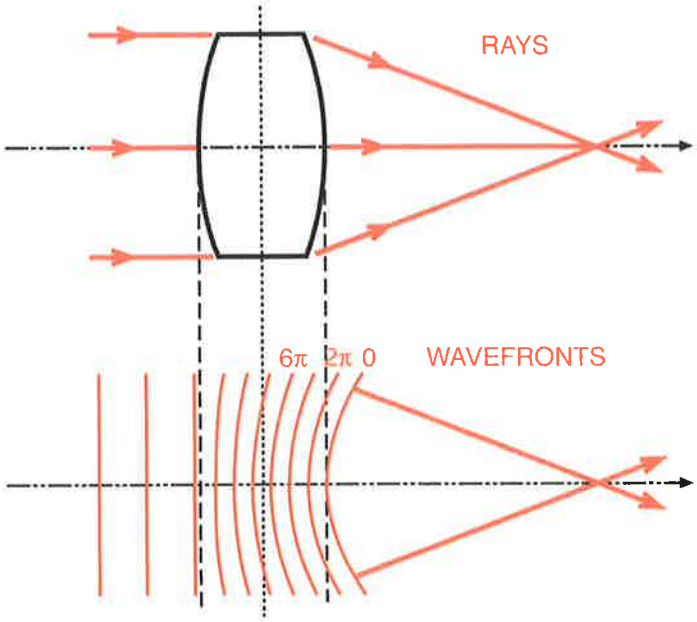

Figure 8: Positive lens with rays (upper) and wavefronts (lower).
The converging wavefronts are labelled with phase corresponding to HTD of exp($i\omega t$) dependence

$$\Phi_1(\rho) = k_o \sum n l_n \tag{74}$$

in which n is the glass index of refraction and $k_o = 2\pi/\lambda_o$, where λ_o is the free space wavelength.

Assuming a spherical R_1 (which can be refined in the next section), one can write the departure δ as is well-known:

$$\delta = R_1 - \sqrt{R_1^2 - \rho^2} \tag{75}$$

Then the phase delay $\Phi(\rho)$ is given by

$$\Phi_1(\rho) = k_o \delta + n k_o h(\rho). \tag{76}$$

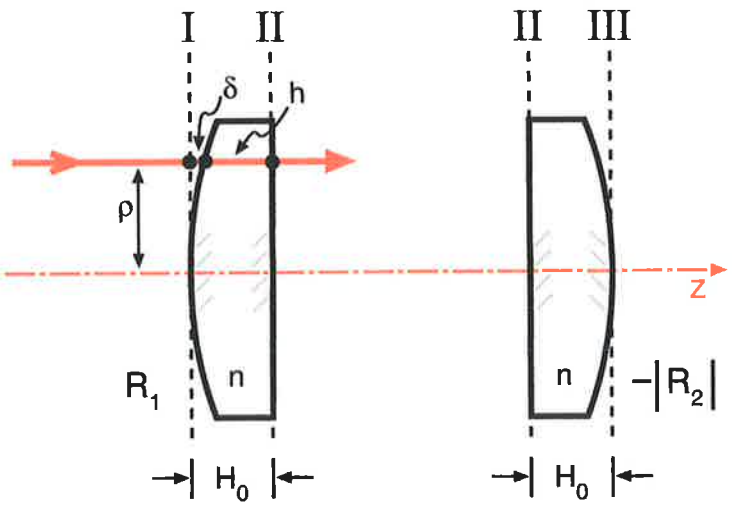

Figure 9: Notation for plano-convex lens with central thickness H_o. Calculation of phase delay at red ray δ in air and h(ρ) in glass.

Combining Eq. (75) and (76) assuming $\rho/R_1 \ll 1$ yields the approximate form:

$$\Phi_1(\rho) = -k_o(n-1)\frac{\rho^2}{2R_1} + nk_oH_o \tag{77}$$

in which H_o is the thickness of the lens at $\rho = 0$.

In Fig. 9 we form a double-convex lens by placing the two lens elements together. Now in forming the overall transmission function, it is asserted that this is simply the product of the two transmission functions. The details follow.

For the second lens, let us be careful with signs, i.e.,

$$\Phi_2 = -k_o(n-1)\frac{\rho^2}{-2|R_2|} + nk_oH_o. \tag{78}$$

And since R_2 itself is negative. we rewrite Eq. (78) as follows:

$$\Phi_2 = -k_o(n-1)\frac{\rho^2}{2R_2} + nk_oH_o. \tag{79}$$

Hence, by the defining expression in Eq. (72), we form the product of the transmission functions corresponding to Eqs. (77) and (79). Moreover, the thin lens approximation is to set $H_o = 0$. Hence, the sum of Eqs. (77) and (79) yields the thin lens approximation for the plase delay. The corresponding transmission function for the double-convex lens is given by substitution of Eqs. (77) and eqrefeq79 with $H_o = 0$ into Eq. (73). Thus, the derivation yields the transmission function as follows:

$$T(\rho) = e^{ik_o\frac{(n-1)}{2}\rho^2(\frac{1}{R_1} - \frac{1}{R_2})} \tag{80}$$

With the positive lens one needs to have a positive focal length. From Eq. (80) and comparing to Eq. (70), clearly one has

$$\begin{aligned} \frac{1}{f} &= (n-1)(\frac{1}{R_1} - \frac{1}{R_2}) \quad \text{and} \\ T(\rho) &= e^{+\frac{ik_o\rho^2}{2f}}. \end{aligned} \tag{81}$$

Lets look at the sign in Eq. (81). It tells us that the phase of the "forward-curved" wave in the output is bent forward as is clear from Fig. 8. This sign for the transmission function is in accord with an $exp(i\omega t)$ notation.

4.2 Generalized transmission function for aspheres

The transmission model for a lens as given in Sec. 4.1 is based on a mixture of ray and wave optics. It has the advantage of building a good physical understanding of the performance of a lens, but it does not give much insight into what would constitute an ideal shape for a lens nor on what would lead to a lens of idealized performance. For Fourier optics one needs a more abstract definition of a lens that is based on diffraction theory. This formulation also should not be based on the assertion of simple spherical surfaces. With today's knowledge we understand that some aspherical surface is needed if one is planning excellent performance.

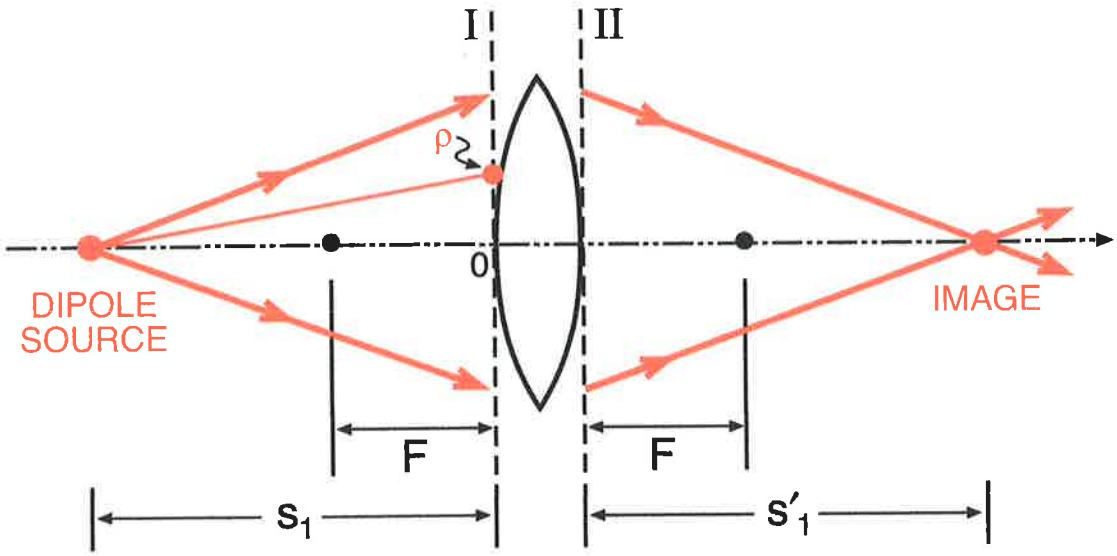

Figure 10: Transmission function for imaging the point source with an asphere, see Eqs. (82) to (85)

For the Fourier optics model, we prefer to start with a result or foundation based on Maxwell's equations. So assume a monochromatic plane-polarized light from a laser of wavelength λ. From Eq. (33) for a delta function input point source at a distance s_1 from the lens in Fig. 10, one can immediately write the expanding wavefront at plane I, $E_x(\rho)$ given by $\exp(-ik\sqrt{s_1^2-\rho^2})$ where apodization is dropped.

Now a few example and some reflection leads one to an answer of the following question. What exiting wavefront will lead to a point source at a distance s_1' from plane II? Of course it will likely be blurred by diffraction.

The answer is that the exiting wavefront from plane II needs to have a wavefront given by $\exp(ik\sqrt{s_1'^2+\rho^2})$. Again we have neglected the possibility of using apodization.

The transmission function for a lossless aspheric lens $T(\rho)$ is then defined with a phase delay or sag factor $\Phi(\rho)$, as follows:

$$T(\rho) = \frac{\text{Scalar electric field exiting plane II}}{\text{Scalar electric field entering plane I}} \tag{82}$$

$$T(\rho) = e^{-i\Phi} \tag{83}$$

$$T(\rho) = \frac{e^{+ik[(s_1'^2+\rho^2)^{1/2}-s_1']}}{e^{-ik[(s_1^2+\rho^2)^{1/2}-s_1]}}, \tag{84}$$

in which the radius $\rho = \sqrt{x^2+y^2}$ in the transverse plane as in Fig. 10. We have made the lens thin by introducing the subtraction terms s_1' and s_1, in the numerator and denominator, respectively. The transmission of Eq. (84) is expanded in terms powers of $(\rho/s_1')^{2m}$ and $(\rho/s_1)^{2m}$ using G & R: 1.112 to yield

$$T_b(\rho) = e^{ik\left(s_1'\left[\frac{1}{2}\left(\frac{\rho}{s_1'}\right)^2 - \frac{1}{8}\left(\frac{\rho}{s_1'}\right)^4 + \frac{1}{16}\left(\frac{\rho}{s_1'}\right)^6 - \frac{5}{128}\left(\frac{\rho}{s_1'}\right)^8 + \cdots\right] + \right.}$$
$$\left. + s_1\left[\frac{1}{2}\left(\frac{\rho}{s_1}\right)^2 - \frac{1}{8}\left(\frac{\rho}{s_1}\right)^4 + \frac{1}{16}\left(\frac{\rho}{s_1}\right)^6 - \frac{5}{128}\left(\frac{\rho}{s_1}\right)^8 + \cdots\right]\right) \tag{85}$$

Eq. (85) is a complete specification for an asphere in a power series expansion. While a complete discussion of this transmission function is beyond the scope of this article, more details can found in the literature [13]. Detailed aberration theory references are also cited [12, 14, 15].

4.3 Illustrative design of the tailored asphere

In optical system design it is commonplace to design aspheric lenses using modern digital computer software. Large apertures are readily handled. Moreover, a lens specification in terms of phase delay as the $\phi(\rho)$ in Eq. (82) to (85) is readily manufactured. This specification based on Fourier optics and wavefronts makes an important connection of Fourier optics to geometric optics or optical system design.

Axicons are lens elements having the property of transforming a point source of light into an axial segment, i.e., increasing the depth of field. In

such an application one typically has a range of focal lengths to accommodate, call it $f(\rho)$. If one proposes to create a lens design with a radially symmetric aspheric lens, it is necessary to establish an appropriate phase delay $\Phi(\rho)$ and a corresponding transmission function, $T_a(\rho)$ for the lens maker.

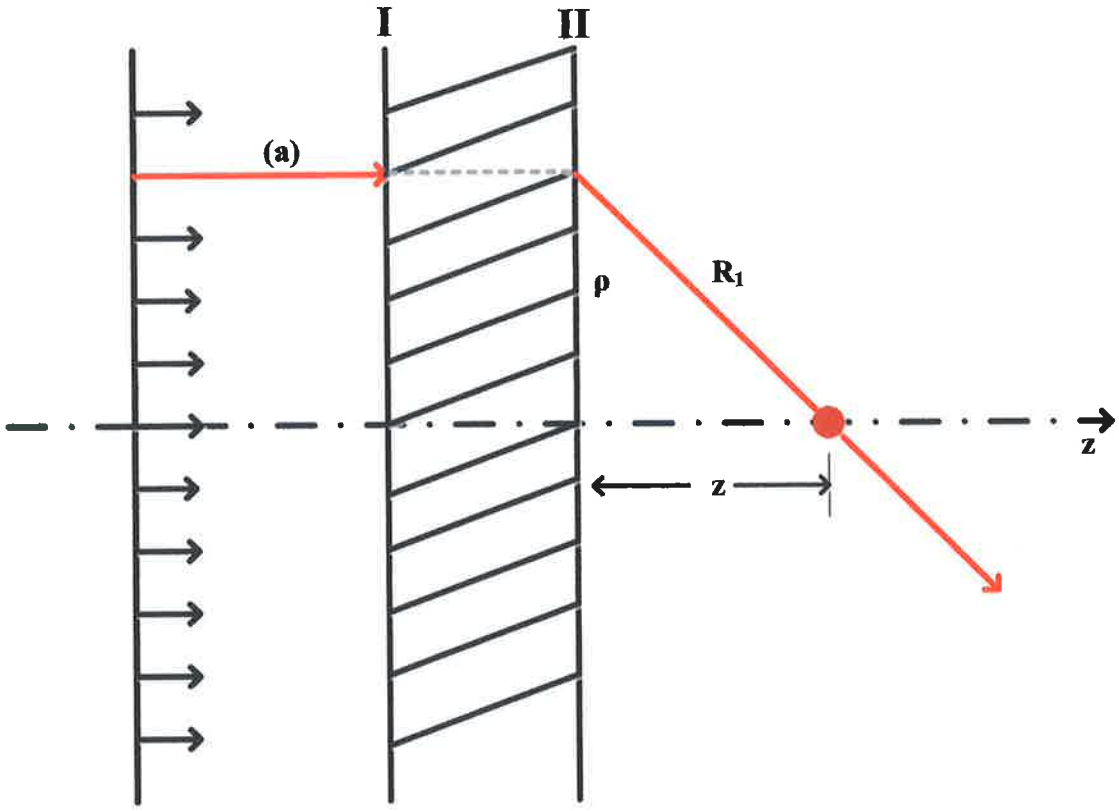

Figure 11: Aspheric lens $\Phi(\rho)$ between planes **I** - **II** with plane wave incident. Ray (a) has an effective focal length shown as z.

In the following paragraphs of this section, we describe the design of an asphere given a desired radial variation in focal length using Fourier optics wavefront notions. More specifically, we wish to establish the relationship between $\phi(\rho)$ and the corresponding radially varying focal length $f(\rho)$, as

in Fig. 11. This is a basic question.

Consider the asphere is between planes **I, II**. A plane polarized plane wave in incident. Rays at different heights are refracted to the optical axis crossing at different values z for each ray. Clearly the problem is ideally suited to our Rayleigh-Sommerfeld-Smythe formulation.

Choosing Eq. (33) and recognizing that the phase term $\exp(-ikR_1)$ is controlling, we write the reduced form for the axial field, E_x:

$$E_x(0,0,z;\nu) = ik \int_{II} E_x(\rho,z;\nu)\frac{e^{-ikR_1}}{R_1^2} z\rho d\rho \tag{86}$$

in which $R_1 = (\rho^2+z^2)^{1/2}$. Clearly the exiting E_x is given by

$$\begin{aligned} E_x(\rho,z:\nu) &= T(\rho)E_o \quad or \\ E_x(\rho,z:\nu) &= E_o e^{-i\phi(\rho)} \end{aligned} \tag{87}$$

Substitution of Eq. (87) into Eq. (86) yields the following integration:

$$E_x(0,0,z;\nu) = ikE_o \int_{II} \frac{e^{-i(\phi(\rho)+kR_1)}}{R_1^2} z\rho d\rho \tag{88}$$

Stationary phase is used to evaluate this integration and to find the $z = f(\rho)$ for the ray (a) in Fig. 9. Hence, one has

$$\frac{d\phi(\rho)}{d\rho} + \frac{k\rho}{(\rho^2+z^2)^{1/2}} = 0. \tag{89}$$

Substitution of $z = f(\rho)$ into Eq. (89) gives a basic result:

$$\frac{d\phi(\rho)}{d\rho} = \frac{-k\rho}{(\rho^2+f^2)^{1/2}}. \tag{90}$$

Clearly, if one is given a specification for the focal length of the lens, Eq. (90) is readily integrated, say numerically, to find the $\phi(\rho)$ as required.

When one wishes to find the focal length $f(\rho)$ given the slope in the phase delay, $\phi'(\rho)$, Eq. (90) is readily rewritten, as follows:

$$f(\rho) = \pm\left[\left(\frac{k\rho}{\phi'(\rho)}\right)^2 - \rho^2\right]^{1/2} \tag{91}$$

As a practical point about this synthesis procedure, it is remarked that physically one can in general develop a specification $f(\rho)$ and then compute $\phi(\rho)$ for the lens design. Tailoring the design by directly adjusting $\phi(\rho)$ is not practical since the total phase is very large, say 1000 radians, and the tailoring needed is small [13].

4.4 The paraxial approximation for a lens transmission function

In Sec. 4.2 the ideal transmission function is defined by Eq. (82) and (84). Then, neglecting possible apodization means, we describe an ideal lens by the transmission function, Eq. (85) using the Maxwell based results for propagation into the right-half-space. It is particularly important to take note of the fact there is no paraxial limit in any of this.

A simple binomial expansion in terms of $(\rho/s)^2$ is known to converge when this term is less than unity. Thus, in high quality diffraction-limited design, it is not unusual to go out to the tenth power of (ρ/s). Practical examples of combining modern lens design software with Fourier optics techniques occur in the literature [13].

For an introduction to Fourier optics, it is typical to base the deductions mainly on illustrations drawn from far-zone and Fresnel thinking. Hence, herein, we would like to make this connection as well.

Clearly as ρ/s_1 and rho/s_1' become small, Eq. (85) can be approximated by retaining only the first members. Hence, the paraxial form for the transmission function is given by

$$T_p(\rho) = e^{i\frac{k}{2}\rho^2(\frac{1}{s_1}-\frac{1}{s_1'})} \tag{92}$$

Equation (92) provides a nice confirmation of the signs seen in Eqs. (80) and (81).

5 Cascade of lenses & impulse response

The cascade of lenses shown in Fig. 12 is one of the central topics in Fourier optics. For definiteness in this linear system, consider four simple thin lenses (1 to 4) with an input transparency (0) illuminated by a

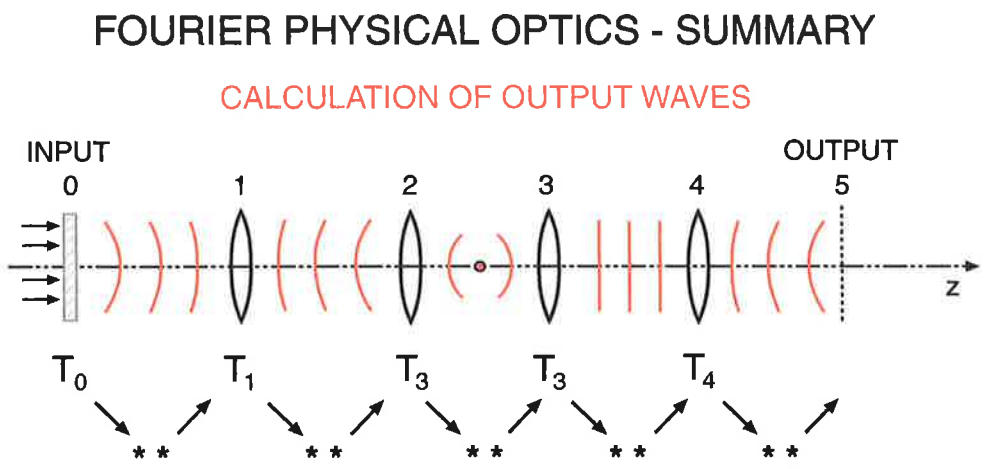

Figure 12: Cascade of 4 lenses for imaging input to plane 5. This is a central topic in Fourier optics to compute the impulse response p_{05} for the cascade

monochromatic plane wave with its electric field along the x-axis. Propagation of light in the open spaces 0 to 1, 1 to 2, ... and 4 to 5 can by analyzed by repeated applications of the Sec. 3.3 Fresnel zone means or by Eq. (33) the exact expression. The double asterisks stand for the two-dimensional convolutions over the transverse planes. And of course the transmissions through each lens are treated by products using $T_1(\rho)$, $T_2(\rho)$ and so on, as described in Sec. 4.

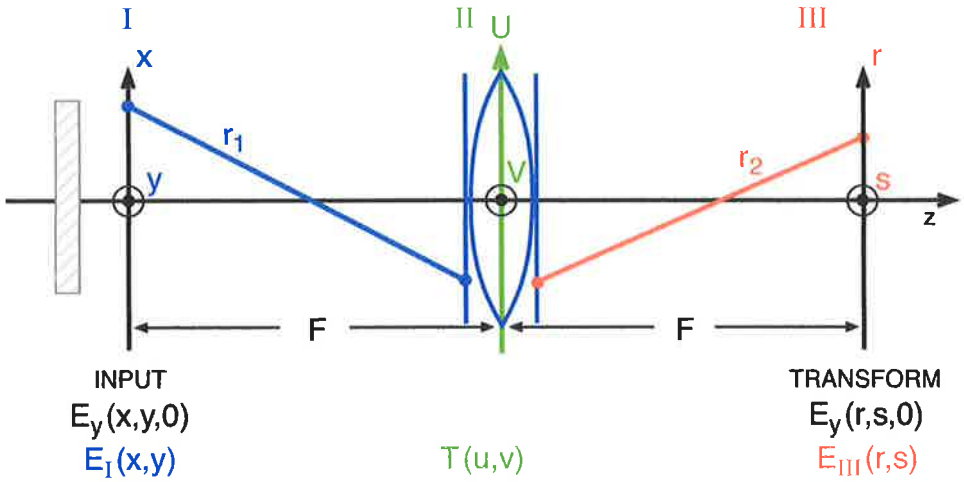

Figure 13: The optical Fourier transform configuration.
From two Fresnel zone calculations, one finds an ideal Fourier transform in plane **III** for the input $E_I(x,y)$.

6 The optical Fourier transform

Consider the configuration with an illuminated picture in plane **I** (x,y), a lens of focal length F in plane **II** (u,v), and an output plane **III** (r,s) as shown in Fig. 13. The Fresnel zone calculation is given in detail with a color code corresponding to the figure. The reader is invited to fill in the missing details in this computation after a careful study of the color code in Fig. 13 compared with Eqs. (93) through (97). Equation (96) is a major result.

For the Fresnel zone calculation:

$$E_{II} = e^{\frac{ik(u^2+v^2)}{2F}} \frac{ike^{-ikF}}{2\pi F} \underbrace{\iint_{-\infty}^{\infty} dxdy\, E_I(x,y) e^{-\frac{ik}{2F}[(u-x)^2+(v-y)^2]}}_{I} \tag{93}$$

$$E_{III} = \frac{ike^{-ikF}}{2\pi F} \iint_{-\infty,II}^{\infty} du dv \, E_{II}(u,v) e^{-\frac{ik}{2F}[(u-r)^2+(v-s)^2]} \tag{94}$$

$$\text{Integrate using } \int_{-\infty}^{\infty} du e^{-\frac{ik}{2F}[u-(r+x)]^2} = (1-i)\left(\frac{\pi F}{k}\right)^{1/2} \tag{95}$$

$$E_{III} = \frac{ie^{-i\frac{2\pi 2F}{\lambda}}}{\lambda F} \iint_{-\infty,I}^{\infty} dx dy E_I(x,y) e^{i2\pi\frac{1}{F\lambda}[rx+sy]} \tag{96}$$

$$\text{in which } f_x = \frac{-r}{F\lambda} \text{ and } f_y = \frac{-s}{F\lambda}. \tag{97}$$

7 The optical transform hybrid processor

As shown in Fig. 13 and Sec. 6, the F to F spacing provides an ideal Fourier transform in amplitude of the scalar electric field, E_x in Eq. (96). There is a phase delay due to the propagation distance (2F). This configuration has a singular position in Fourier optics, since it enables, the study and visualization of the optical Fourier transform of various complicated objects.

In learning Fourier transform theory, the function $g(x,y)$ and its associated pair $G(f_x,f_y)$ are studied, but there is no "alignment" described between axes x,y with those in transform space, i.e., with f_x,f_y. Mathematically, this is a correct point of view, since the function space (x,y) and the Fourier space (f_x,f_y) are not in the same domains.

However practice develops some handy points of view; and in optical transform configurations, the x,y plane is generally parallel to the f_x,f_y plane; and the respective axes are collinear, i.e., x with f_x and y with f_y. The handy rules of thumb which we use on patterns in function space in order to describe their corresponding patterns in transform space are summarized in Fig. 14. These rules have proven very helpful in the development of diffraction pattern sampling. Several optical-transform-hybrid processors have been developed using a front-end lens and some form

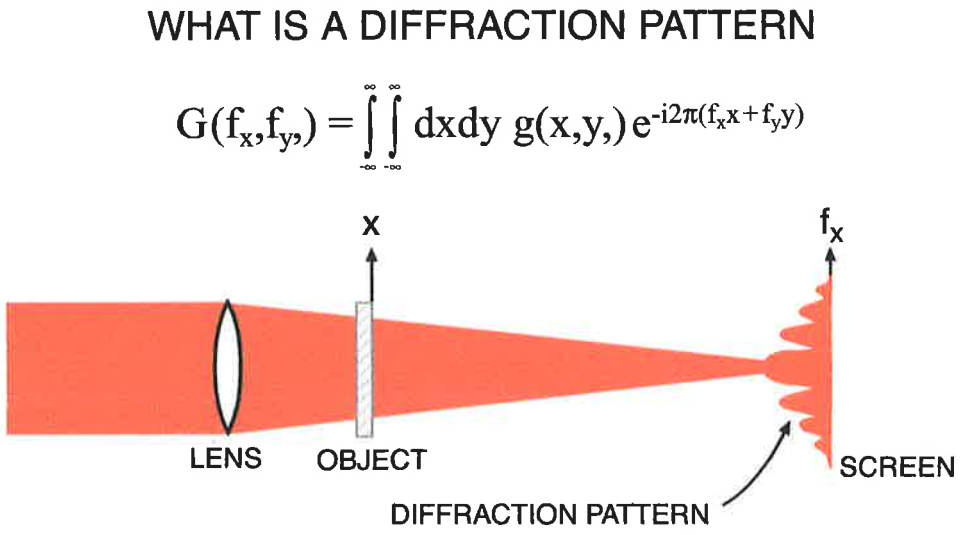

Figure 14: The basis of diffraction-pattern-sampling for pattern recognition in optical-electronic processors is summarized in 4 rules

of photodetector array placed in the back focal plane. Commonly used are the linear photodiode array, the CCD, the CMOS, and the ring-wedge detectors [16, 17].

One more practical point to mention is that photodetectors are sensitive to the energy density in the electric field, i.e., proportional to $\mathbf{E} \bullet \mathbf{E}^*$. This includes vision, film cameras, and the digital cameras. So in Eq. (96) of Sec. 6, the $|E_{III}|^2$ is reading the Fourier transform squared. The practical laboratory point is that in an optical setup with a laser illumination if you find one position where there is a broad spot of illumination followed by another position where the illumination narrows to a tiny point, you have found excellent positions for an object transparency and its optical Fourier

transform intensity, respectively. There are scale factors involved, and you might make up a problem set to find them. They have been purposely omitted in the equation of Fig. 14. In practice the object is slid along the optical axis and the transform pattern recorded at the detector becomes smaller as the distance decreases.

7.1 The ring-wedge photodetector [16]

For sampling the Fourier transform intensity, an interesting hybrid processor uses a photodiode array that is divided into two 180° portions. In one portion, there are 32 pie-shaped wedges; and on the other half, there are 32 annular rings. These choices were based on providing as fine a sampling as is necessary for pattern recognition of very fine grained photographs or for particulate analysis.

With particulate analysis the quantitative study did not progress very well using lasers due to the difficulties with speckle. As the understanding of speckle progressed, it became clear that the annular detector rings are ideally suited for averaging out the variations caused by speckle and excellent for measuring histogram-like patterns even with complicated mixtures of size distributions.

In pattern recognition it is an interesting question to wonder why would one use a Fourier transform base of data rather than the original object's pixel data. There is probably no simple answer; but clearly system-wise, one method of approach may be vastly simpler. Also if one can get data down early in the system, as from one-million pixels to thirty-two, that is likely to be advantageous [17].

In Fig. 15, the three illustrations on this page show (left) the optical transform of a sharp hypodermic needle, (middle) a hypodermic needle with a defective tip, and (right) the optical transform to the defective needle. Commercially, this sensitivity of the transform pattern to edge and tip defects is used as the basis for production testing of dosposable hypodermic needles. The commercial system can make operator-independent quality assessment at the rate of one inspection per millisecond. Moreover, the testing is non-destructive and it can be done in a clean-room.

Related literature appears on diffraction pattern sampling in white light [18] and the ring-wedge detector and neural networks [19], particulate sizing [20] and image quality [21].

Figure 15: Rapid, millisecond testing of quality of sharpness of hypodermic needles (2.5 billion needles per year) is accomplished with the ring-sedge optical transform
hybrid: (left) excellent quality; poor needle; poor transform.

8 Canonical optical processor - the 4F system

In Fourier optics, the Fourier optical transform configuration is a cornerstone of the subject both as a theoretical achievement and a practical system that is application relevant. Equally central to Fourier optics is the cascade of two Fourier transform configurations. As shown in Fig. 16, at the close of this section, we have used a focal length F_1 for the first lens, then a stop and filter transparency $P(u,v)$ at plane **II** followed by a second lens of focal length of focal length F_2 and an output plane **III**(r,s). Separate labeling of the transverse coordinates has been used for clarity.

Clearly for a two lens cascade, we can analyze it for the output at plane **III**. With just a circular stop in plane **II**, we need first to recognize that the output plane **III** is an image plane of **I**. And the image is inverted and magnified in the ratio of $-F_2/F_1$.

Study of this system is useful in the explanation of imaging and diffraction limitations in imaging simply by considering rect or circ function apertures for the transmission function $P(u,v)$. This system is shown at the end of this section in Fig. 16, together with final equations resulting from the derivation of the following paragraphs. Also, the fundamental concepts of

optical information processing can be learned by considering the various filtering operations that are possible with appropriate choices of the mask $P(u,v)$.

Using the results of the calculation for a single Fourier-section in Sec. 6, we can immediately write an expression for the scalar component in plane **III**, $E_3(r,s)$, in terms of the input at plane **I**: $E_1(x,y)$ and the transmission mask $P(u,v)$. The notation for the transverse plane coordinates is **I** (x,y), **II** (u,v), and **III** (r,s). These coordinates are chosen with different symbols so that the integrals over planes **I** and **II** can be regrouped, as shown, without confusion.

With monochromatic illumination and for an arbitrary input [both incorporated in the function $E_1(x,y)$], we see that the output $E_3(r,s)$ is obtained by completing a convolution-like integration of $E_1(x,y)$ with an impulse-response kernel. To make this linear system form more evident, we define the impulse response $p(r+F_2x/F_1, s+F_2y/F_1)$ by Eqs. (98) and (99), as follows:

$$p(r+\frac{F_2}{F_1}x, s+\frac{F_2}{F_1}y) = \frac{e^{-i\frac{4\pi}{\lambda}(F_1+F_2)}}{F_1/F_2} \iint_{-\infty}^{\infty} df_r df_s\, P(u,v) e^{-i2\pi[f_r(r+\frac{F_2}{F_1}x)+f_s(s+\frac{F_2}{F_1}y)]} \tag{98}$$

in which the spatial frequency variable f_r, f_s are

$$f_r = \frac{-u}{F_2\lambda} \quad \text{and} \quad f_s = \frac{-v}{F_2\lambda} \tag{99}$$

The output $E_3(r,s)$ is given in terms of the impulse response $p(r,s)$ as follows in Eq. (100):

$$E_3(r,s) = \iint_{-\infty}^{\infty} dxdy\, p(r+\frac{F_2}{F_1}x, s+\frac{F_2}{F_1}y)\, E_1(x,y). \tag{100}$$

In this manner we derived the important linear system result which expresses the output of the lens-filter-lens cascade in the convolution-like form of the input $E_1(x,y)$ with the impulse response $p(r,s)$. Moreover, we have obtained an explicit formula for the function $p(r,s)$ in terms of the lens-filter configuration.

Impulse Response: The following illustrative example serves to clarify the language impulse-response. Consider the canonical processor to be illuminated by a delta-like pinpoint of light at the position $x = x_o$, $y = y_o$. What is the output in plane **III**? From the general result, substitution of $E_1(x,y) = \delta(x-x_o, y-y_o)$ and integration yield the result shown in Eq. (101), viz.,

$$E_{3\delta}(r,s) = p(r+\frac{F_2}{F_1}x_o, s+\frac{F_2}{F_1}y_o) \tag{101}$$

The system is said to be space-invariant.

Spatial-Frequency Scaling: For simple pupil-like masks in plane **II**, the canonical processor will form an image in plane **III** of an object in plane **I** with a magnification of $(-F_2/F_1)$. In the derivation above, frequency scaling is with respect to the output plane **III**.

In general, however, spatial frequency scaling can be done either with respect to output plane coordinates using Eq. (102):

$$f_r = \frac{-u}{F_2\lambda} \quad and; \quad f_s = \frac{-v}{F_2\lambda} \tag{102}$$

or with respect to input plane coordinates using Eq. (103):

$$f_x = \frac{-u}{F_1\lambda} \quad and; \quad f_y = \frac{-v}{F_1\lambda} \tag{103}$$

From Eq. (100) to (103) we write the output scalar electric field in terms of the input. This result is accurate to the Fresnel zone accuracy with all phase terms retained in Eqs, (104) and (105). With all phase terms retained, as before:

$$E_3(r,s) = \frac{-e^{-i\frac{4\pi}{\lambda}(F_1+F_2)}}{\lambda^2 F_1 F_2} \iint_{-\infty}^{\infty} dxdy\, E_1(x,y) \bullet$$
$$\bullet \iint_{-\infty}^{\infty} dudv\, P(u,v) e^{i2\pi\left[\frac{u}{\lambda F_2}(r+\frac{F_2}{F_1}x)+\frac{v}{\lambda F_2}(s+\frac{F_2}{F_1}y)\right]} \tag{104}$$

CANONICAL OPTICAL PROCESSOR

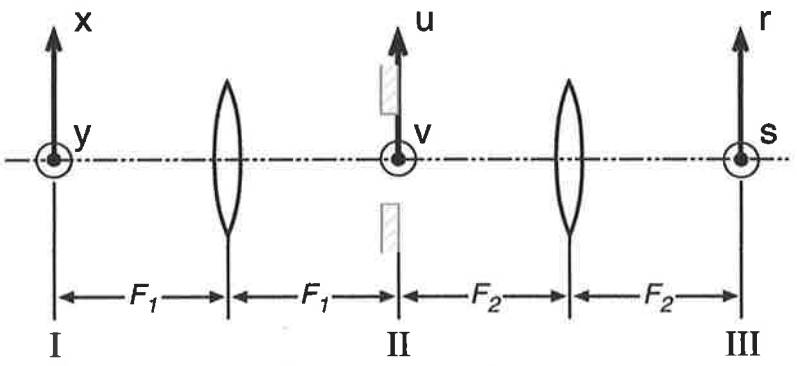

I. OBJECT PLANE	$E_1(x,y;v)$
II. TRANSFORM PLANE	$P(u,v;v)$
III. IMAGE PLANE	$E_3(r,s;v)$

Figure 16: The 4-F optical processing provides both an idealized space-invariant image as well as a perfect optical Fourier transform. It is useful both in theoretical calculations and in laboratory.

or

$$E_3(r,s) = \iint_{-\infty}^{\infty} dxdy\, E_1(x,y)\Big\{\frac{-e^{-i\frac{4\pi}{\lambda}(F_1+F_2)}}{F_1/F_2}\cdot \cdot \iint_{-\infty}^{\infty} d(\frac{u}{\lambda F_2})d(\frac{v}{\lambda F_2})\, P(u,v)e^{i2\pi[\frac{u}{\lambda F_2}(r+\frac{F_2}{F_1}x)+\frac{v}{\lambda F_2}(s+\frac{F_2}{F_1}y)]}\Big\} \tag{105}$$

From Eqs. (100) to (103) we write the output scalar electric field in terms

of the input. This result is accurate to the Fresnel zone accuracy with all phase terms retained in Eqs. (104) and (105).

9 Summary

The article on Fourier optics and electromagnetic waves provides a readable, concise, and rigorous treatment that will be clear and understandable without particular experience or background. There are 8 separate sections starting with a discussion of Maxwell's equations in real-valued time dependent form. Then in Sec. 1.2, the standard notation of the Fourier transform and its inversion is defined. The signal representation is explained and summarized in Fig. 1.

Section 2 treats the central problem of propagation into the right-half-space. The rigorous explanation of the integral expression goes by the name Rayleigh-Sommerfeld-Smythe. The addition of the Smythe name is mine (N. George) because his rigorous theory has clarified what is often confusing in the optics literatures. The basic equations are summarized in Eq. (33) to (36).

To make the material readable and interesting for the theorist who is not experienced with Optics, we are very careful with the choice of the first illustrative problem. In Sec. 3.1, it is the exact calculation of the radiation along the optical axis [10] from a circular aperture. As an exact calculation, it serves as an excellent choice for the student to really think about, There is little or no jargon as well.

Then, in Sec. 2 the far-zone is treated using the far-zone approximation that is not paraxially limited. Section 3.3 has the standard Fresnel zone coverage. Section 4 contains a thorough discussion of lenses from the wavefront point of view. This is Sec. 4.2. Fairly recent thinking about aspheres is presented together with an explanation of how to go from wavefront delay ϕ to focal length f in Eq. (90). Whenever possible the Fourier optics or wavefront presentation is made without paraxial approximations. It does seem that future applications with the use of digital computers will greatly expand the practicality of optical system design using Fourier optics.

In the later sections of the article, we describe some important illustrations of Fourier optics. This includes the ideal F to F optical Fourier transform and then the 4F canonical processor. If you see errors or mistakes, my apologies, please send me an email: ngeorge@optics.rochester.edu.

References

[1] Duffieux, P.M., *The Fourier Transform and Its Applications to Optics.* (English translation: Second edition) Masson, Editeur, Paris (1970)

[2] Goodman, J.W., *Introduction to Fourier Optics.* McGraw-Hill, New York, 1st Edition (1968) & 3rd Edition (2004)

[3] Papoulis, A., *Systems and Transforms with Applications in Optics.* McGraw-Hill, New York (1968)

[4] Griffiths, D.J., *Introduction to Electrodynamics.* Second Edition, Prentice Hall, New Jersey (1989)

[5] Papas, C.H., *Theory of Electromagnetic Wave Propagation.* McGraw-Hill, New York (1965)

[6] Balanis, C.A., *Advanced Engineering Electromagnetics.* John Wiley & Sons, New York (1989)

[7] Kong, J.A., *Electromagnetic Wave Theory.* EMW Publishing, Cambridge (2008)

[8] Smythe, W.R., *Static and Dynamic Electricity.* 3rd Edition, Revised Printing, Taylor & Francis (1989)

[9] Smythe, W.R., *The Double Current Sheet in Diffraction.* Phys. Rev. 72, 1066 (1947)

[10] English, R.E., Jr., and George, N., *Diffraction from a circular aperture: on-axis field strength.* Appl. Opt. **26** (12), 2360-2363 (1987)

[11] Jackson, J.D., *Classical Electrodynamics.* Third Edition, John Wiley & Sons, New York (1999)

[12] Born, M., and Wolf, E. *Principle of Optics.* Pergamon Press, New York (1959)

[13] George, N., and Chen, X., *Extended Depth-of-Field Lenses and Methods for Their Design, Optimization and Manufacturing.* U.S. Patent Application Publication US2010/0002310 A1 (2010)

[14] Kidger, M.J., *Fundamental of Optical Design*. SPIE Press Monograph, PM 92 (2001)

[15] Welford, W.T., *Aberrations of the Symmetrical Optical System*. Academic Press (1974)

[16] George, Nicholas; J.T. Thomasson, *Photodetector Light Pattern Detector*. U.S. Pat. No. 3,689,772 (1972)

[17] George, Nicholas; Niels Jensen; J.T. Thomasson, *Diffraction Pattern Sampling for Real-Time Pattern Recognition*. J. Opt. Soc. Am.; 1380A (1972)

[18] Wang, Shen-ge; N. George, *Fresnel zone transforms in spatially incoherent illumination*. Appl. Opt, **24**, pp. 842-850 (1985)

[19] N. George; Wang, Shen-ge; and D.L. Venable, *Pattern recognition using the ring-wedge detector and neural network software*. SPIE 1134 (1989)

[20] Coston, S.D; N. George; *Particle size inversion*. Appl. Opt. **30**, pp. 4786-4794 (1991)

[21] Bertanger, D.M.; N. George, *All digital ring-sedge detector applied to automatic image quality assessment*. Appl. Opt. **39**, pp. 4080-4097 (2000)

Deductive derivation of the displacement term in Maxwell's equations

Songfeng Han and Nicholas George*

The Institute of Optics, University of Rochester, Rochester, New York 14623, USA
**Corresponding author: ngeorge@optics.rochester.edu*

Received May 8, 2013; revised July 6, 2013; accepted July 12, 2013;
posted July 18, 2013 (Doc. ID 190160); published 0 MONTH 0000

A new objective derivation is presented for the occurrence of the displacement term in Maxwell's $\nabla \times \mathbf{H}(\mathbf{r}, t)$ equation. Starting with an integral form of Ampere's generalized experimental circuit law for the force between differential current elements and vector analysis, we establish the "electric current term" proportional to $\partial \mathbf{D}/\partial t$ that is causing important contributions to the magnetic induction. This displacement term also enables the important wave equation forms for **E** and **H**. These results are in precise accord with Maxwell's notion of "true current" and the present form of Maxwell's equations. Moreover, it is obtained by straightforward analysis without recourse either to arguments about symmetry that in fact Maxwell himself did not use or to philosophical assertions.

OCIS codes: (260.2110) Electromagnetic optics; (030.0030) Coherence and statistical optics; (350.0350) Other areas of optics; (070.0070) Fourier optics and signal processing; (110.2960) Image analysis; (200.0200) Optics in computing.

http://dx.doi.org/10.1364/JOSAA.99.099999

1. INTRODUCTION

In this paper we present a deductive derivation of the displacement current term in Maxwell's equation for $\nabla \times \mathbf{H}$ but without invoking a symmetry argument nor other assertions. Our derivation starts with Ampere's generalized experimental circuit law for the force between differential current elements, which is today's commonly used approach that introduces the square-law dependence for the magnetic induction **B**; and it places in evidence the vector direction of the forces [1]. Sections 2 and 3 contain the detail of our new deductive derivation. However, let the present authors emphasize that the displacement current term has a completely accepted basis as a significant factor in Maxwell's equations and a long history dating back to several major treatises by Maxwell during the period from 1855 to 1864 [2–6].

Before turning to our derivation in Sections 2 and 3, let us review briefly the rich history involved in the development of classical electromagnetic theory and also establish by a careful search that our derivation is new and based upon simple, straightforward theoretical analysis. Our review below is divided into three periods: (A) The Maxwell Period; (B) Electro-magnetic Waves (1880–1914); (C) TV, Microwaves, Optics (1914–2013).

A. The Maxwell Period

In general terms as we make this review, we seek to see how close the early theory is to today's representation; but this review is not in any sense a careful study of the detailed history of electromagnetic theory. Hopefully, in this regard, the reader will find our references are adequate and helpful.

Electromagnetic theory was established during the nineteenth century by the cumulative efforts of many great scientists of the period. The most significant contributions were made by James Clerk Maxwell, who conceived the theoretical foundations, now known as Maxwell's equations. Several publications covering his achievements are still important and worth careful study today [2–6].

In this study the authors of this paper found it helpful to read some of the scholarly authoritative articles on this early period in addition to current textbooks. An excellent starting point is the treatise by Whittaker that is a book of 470 pages covering "from the age of Descartes to the close of the nineteenth century" [7]. This text has detailed explanations of Maxwell's concepts, physics, and mathematics. Being published in 1910, it has a relatively current or modern notation. This we found helpful in learning to read Maxwell's important theories of the electromagnetic field in their original form, as referenced above. Whittaker devotes an entire chapter 8 of 39 pages to Maxwell's contributions.

For further scholarly, authoritative articles on this early period, two important current articles by Bork are cited: "Maxwell, displacement current, and symmetry" (1963, [8]) and "Maxwell and the electromagnetic wave equation" (1967, [9]). From these one learns that Maxwell's important theories of the electro-magnetic field can be read in their original form.

Maxwell introduced displacement current using "objective reasoning" based on an ether theory. He also used concepts of dielectric theory but also extended these in his reasoning to include the vacuum case. Moreover, and importantly, he did not use "symmetry between $\nabla \times \mathbf{E}$ and Faraday's law to argue for the displacement term. This argument or assertion for "mathematical symmetry and beauty" came later by Oliver Heaviside.

In the second article, Bork goes much more deeply into Maxwell's 1865 paper in the *Philosophical Transactions*

of the Royal Society, which is Maxwell's first full-blown treatment of electromagnetic theory [4]. Bork presents "three charts in his discussion of Maxwell's derivations of the wave equations from the basic equations of electromagnetic theory" [9].

What one clearly sees is Maxwell's many equations and is his assertion that the total current, $\mathbf{J}_t$, is the actual conduction current, $\mathbf{J}$, summed with the displacement current, i.e.,

$$\mathbf{J}_t = \mathbf{J} + \frac{\partial \mathbf{D}}{\partial t}. \tag{1}$$

Again, Bork points out that symmetry in the waves between electric and magnetic fields is not mentioned by Maxwell, while there is "a symmetry imposed later by Heaviside and Hertz."

In 1972, Chen-To Tai published an important scholarly article "On the presentation of Maxwell's theory" [10]. Using the same major references by Maxwell, but missing Bork's paper, Tai points out that JCM prefers integral forms rather than differential equations. Tai has also provided an elegant recapitulation of Maxwell's original works. Maxwell's memoir consists of seven parts, viz.,

I. Introductory
II. On Electromagnetic Induction
III. General Equations of the Electromagnetic Field
IV. Mechanical Actions in the Field
V. Theory of Condensers
VI. Electromagnetic Theory of Light
VII. Calculations of the Coefficients of Electromagnetic Induction.

Equation (1) above appears in part III denoted by the letter [A], and it was the first equation in the memoir denoted by letters. Maxwell stated that $\mathbf{J}_t$ is "the true electric flow due to the variation of electric displacement as well as to true conduction."

It is interesting to read Maxwell's original writing in the listing cited. One can readily see that he wrote the continuity equation as well as verifying the $\nabla \times \mathbf{H}$ in the quaternion form—it is written as a series of partial derivations [4].

In our research, considering how electrostatics and magneto-statics led to Maxwell's Equations, it is important to study how and when time dependence was incorporated. With their experiments in 1831, Faraday and his co-workers of the period introduced $\partial \mathbf{B}/\partial t$. Before Maxwell introduced the "true current" concept of $\partial \mathbf{D}/\partial t$, as described above, apparently the notion of conservation of charge was also well-known. In fact the equation of continuity was known to Maxwell, as we still write it today, as follows:

$$\nabla \cdot \mathbf{J}(\mathbf{r}, t) + \frac{\partial \rho(\mathbf{r}, t)}{\partial t} = 0, \tag{2}$$

in which $\mathbf{J}(\mathbf{r}, t)$ is the current/area and $\rho(\mathbf{r}, t)$ is the charge per unit volume.

This notion of charge conservation is due to Benjamin Franklin (1747), although we have not found who was first to write this theorem explicitly in the form of Eq. (2). Equation (2) is clearly found in Maxwell's writings.

In closing this section of review, we quote Tai directly about Maxwell. Tai states: "In the history of science James Clerk Maxwell (1831–1879) is a brilliant star. His theory of electromagnetism was enumerated in 1864 and it comprised all previously known results, both experimental and theoretical, on electricity and magnetism. It further predicted the existence of electromagnetic waves that were later confirmed by Hertz. Maxwell's theory was used by Einstein as the ladder to formulate the Theory of Relativity, a scientific revolution that consolidated the foundation of mechanics previously constructed by Newton and paved the way to the atomic age." [10]

B. Electromagnetic Waves (1880–1914)

Since magnetostatics and electrostatics developed quite independently over all of history until the 1800s, it is clearly a fascinating topic to study who knew what and when. Clearly the scope of the present paper is much more limited. From today's physics we are seeking to explain displacement current in the simplest and clearest way possible. As is certainly well known, the inclusion of the displacement current and Maxwell's work in general led to a revolutionary advancement in science and technology by joining the fields of magnetics and electricity.

Once Maxwell added the displacement current to the field equations, it was clear that propagation of these waves was possible. This led to many important contributions by many scientists, as set forth in a text by Hunt [11] and in a series of review papers [12–14].

In the book *The Maxwellians*, Hunt describes the effort of about a dozen major scientists and engineers who extended the work on Maxwell's theories in a great variety of ways including the connections of electromagnetism with optics and light. Heaviside, who later made significant contributions on electromagnetics and in mathematics, said that it took him literally years to master concepts of displacement current and electromagnetic waves. Poynting, of course, studied the energy transport aspects of the wave motion. Also, Poynting studied the flow of energy in a capacitor discharged rapidly by a conductor, shedding some light on the notion of displacement current.

Heinrich Hertz conducted a series of experiments initially with laboratory Leyden jars and spark gaps. Transmission and reception of electromagnetic waves were clearly demonstrated (1888). He and others in the same period showed a variety of important early phenomena demonstrating effects analyzed using Maxwell's theories. Much of his apparatus is housed in the Deutsches Museum in Munich [14]. Hertz was a gifted theorist and experimentalist who died quite young (1857–1894).

C. TV, Microwaves, Optics (1914–2013)

For our present day search, we surveyed several generations of important textbooks in order to learn their approach to the derivation of Maxwell's equations. Typically for each period, we studied both beginning or undergraduate textbooks and advanced or graduate treatises. The results of this study are reported below in two stages: 1.C.1 includes a tangential report on the subject of relativity and electromagnetic theory that is of great scientific and pedagogical interest, and while not directly in the scope of the present paper, it seemed to merit brief mention; and 1.C.2 contains a report that we have not found any alternative deductive derivation for including displacement current in the curl **B** equation.

1. Derivation of Maxwell's Equations Using Relativity and Coulomb's Force Law

During our search for a deductive derivation for the displacement current term in Maxwell's equations, we found a much more sweeping derivation had been published for the entire group of Maxwell's equations using only Coulomb's force law for charged particles and Einstein's Special Theory of Relativity [15]. Using one frame with charges at rest and another in uniform motion, L. Page has published this marvelous result. Elliott has studied and extended these concepts in papers and a textbook that is in current use in courses at the University of California, Los Angeles [16,17].

2. Alternative Displacement Current Derivations

In our literature search for these displacement current derivations, we found that initially the advanced texts had carefully explained derivations, but these have moved into the undergraduate books. And several of the current graduate texts start their first chapter with a careful statement of the overall equations but with virtually no proof at all. None of the numerous texts we surveyed had the new derivation that the authors in the present paper are reporting in Sections 2 and 3 below. Also none of the authors in our survey used a modern configuration theoretically to explain Maxwell's result. Perhaps one could argue that countless modern communication systems make this obvious. But we are thinking of simple systems with biconical antennas or the like that can be treated exactly theoretically, including calculations of power with the Poynting vector. This is an interesting direction for research, but it is in a different direction than this present paper.

In current textbooks there has not been much difference in the derivations of the displacement current terms from that of Maxwell, except for the introduction of vector analysis. Maxwell clearly described a "true current" and he used the equation of continuity.

Briefly, Jackson explains carefully how the relation $\nabla \cdot (\mathbf{J} + \partial \mathbf{D}/\partial t) = 0$ can fix the problem in the static Ampere's law for $\nabla \times \mathbf{H}$. Also a similar but more detailed explanation is given under the heading "How Maxwell Fixed Ampere's Law" [18].

For introductory course textbooks, there is similar analysis of how to fix Ampere's law together with practical illustrations of the charging of condensers as well as moving sheets of electrons to create a magnetic field [19,20].

2. THEORY FOR THE DISPLACEMENT CURRENT TERM

A. Magnetostatics Prior to the Displacement Term

Consider Fig. 1 showing two separate currents I_1 and I_2 in wires, respectively Eqs. (1) and (2). For the differential elements $d\mathbf{l}_1$ and $d\mathbf{l}_2$ an experimental observation is the differential force $\delta \mathbf{f}_{1\,\mathrm{on}\,2}$ between them. Integration of the force of wire (1) on (2) gives the total force. As described in the literature [1], this resulted from experimental research by Biot and Savart (1820) and Ampere (1820–1825). The differential force $\delta \mathbf{f}_{1\,\mathrm{on}\,2}$ is given by

$$\delta \mathbf{f}_{1\,\mathrm{on}\,2} = \frac{\mu_0}{4\pi} I_2 d\mathbf{l}_2 \times \frac{I_1 d\mathbf{l}_1 \times \hat{\mathbf{r}}_{12}}{R_{12}^2}, \tag{3}$$

in which

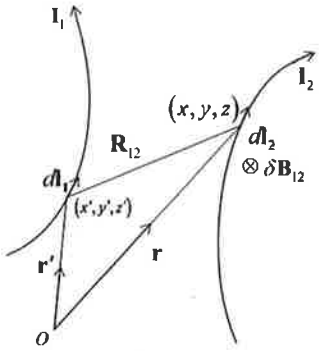

Fig. 1. Notation for magnetic induction $\delta \mathbf{B}_{12}$ caused by differential current element $\mathbf{I}_1 d\mathbf{l}_1$ at $d\mathbf{l}_2(x, y, z)$. F1:1 F1:2

$$\mathbf{R}_{12} = \mathbf{r} - \mathbf{r}'. \tag{4}$$

The unit vector between elements $d\mathbf{l}_1$ and $d\mathbf{l}_2$ is denoted by $\hat{\mathbf{r}}_{12}$. Currents I_1 and I_2 with directions $d\mathbf{l}_1$ and $d\mathbf{l}_2$, respectively, are shown, while μ_0 is permeability (henry/meter).

Equation (3) provides the following definition for the magnetic induction $\mathbf{B}(\mathbf{r})$ due to current $I_1(\mathbf{r}')$ by integration over $I_1 d\mathbf{l}_1$ as given by Eq. (5):

$$\mathbf{B}(\mathbf{r}) = \frac{\mu_0}{4\pi} \int_1 \frac{I_1 d\mathbf{l}_1 \times \hat{\mathbf{r}}_{12}}{R_{12}^2}. \tag{5}$$

Rewriting Eq. (5) with current per unit area $\mathbf{J}(\mathbf{r}')$ and dV' for the differential volume at $\mathbf{r}'$ gives the following form for the magnetic induction $\mathbf{B}(\mathbf{r})$. This expression is the integral form for Ampere's law or the Biot–Savart law:

$$\mathbf{B}(\mathbf{r}) = \frac{\mu_0}{4\pi} \int_V \frac{\mathbf{J}(\mathbf{r}') \times \hat{\mathbf{r}}_{12}}{R^2} dV'. \tag{6}$$

Likewise, from Eq. (3) one can write the differential force of the magnetic induction at $\mathbf{r}$ as follows:

$$\delta \mathbf{F}_2(\mathbf{r}) = I_2 d\mathbf{l}_2 \times \mathbf{B}(\mathbf{r}) \tag{7}$$

or

$$\delta \mathbf{F}_2(\mathbf{r}) = \mathbf{J}(\mathbf{r}) dV \times \mathbf{B}(\mathbf{r}). \tag{8}$$

For this formulation of magnetic induction, the notation is shown in Fig. 2. This formulation is consistent with that in two excellent current texts on electromagnetic theory [1,18].

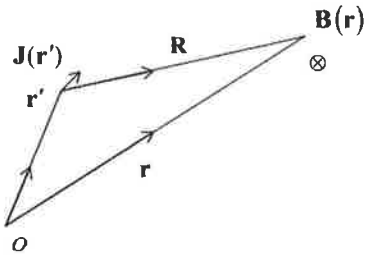

Fig. 2. Notation for magnetic field induction $\mathbf{B}(\mathbf{r})$ as in Eq. (16). F2:1

B. Electromagnetic Field Equations Prior to Displacement Current

The equation of charge conservation known also as the equation of continuity was known to Maxwell as we still write it today, repeating Eq. (2) as follows:

$$\nabla \cdot \mathbf{J}(\mathbf{r},t) + \frac{\partial \rho(\mathbf{r},t)}{\partial t} = 0, \tag{9}$$

in which $\rho(\mathbf{r},t)$ is the electric charge density in coulomb/m^3 and the other symbols are as previously defined. We assume a simple medium with scalar μ, ε, σ, where σ is the ohmic conductivity. At this point, let us summarize the field equations

$$\text{Ampere's Law} \qquad \nabla \times \mathbf{H} = \mathbf{J} \tag{10}$$

$$\text{Faraday's Law} \qquad \nabla \times \mathbf{E} = -\frac{\partial \mathbf{B}}{\partial t} \tag{11}$$

$$\text{Gauss' Law} \qquad \nabla \cdot \mathbf{D} = \rho \tag{12}$$

$$\text{Magnetic Induction} \qquad \nabla \cdot \mathbf{B} = 0. \tag{13}$$

Let us review the troublesome inconsistency between Eqs. (9) and (10). From taking the divergence of Eq. (10), one concludes the following:

$$0 = \nabla \cdot (\nabla \times \mathbf{H}) = \nabla \cdot \mathbf{J}. \tag{14}$$

The finding of $\nabla \cdot \mathbf{J} = 0$ is the historically troublesome inconsistency with Eq. (9) since $\partial\rho/\partial t$ is not always zero. Presumably, one can remedy this by a modification of Eq. (10) as is clearly necessary.

In Section 2, we have summarized the known equations of electrostatics and magnetostatics around 1860 but using today's notations. If one wishes to extend these equations to include transient phenomena, it is observed that there is time dependence already in Eq. (11) that entered due to the experimental findings of Faraday. Also for time dependence, one can observe that Eq. (9) is likely to be important since it is the appropriate equation in which to incorporate transient or temporal dependence of sources, say as can be described by $\rho(\mathbf{r},t)$ and $\mathbf{J}(\mathbf{r},t)$. These matters are treated below in Section 3.

3. PRESENTATION OF THE NEW DERIVATION

Following the lead of our current references, we note that from the Biot–Savart relation for $\mathbf{B}(\mathbf{r})$ in Eq. (6) one can readily compute or verify Eq. (13) for $\nabla \cdot \mathbf{B}$.

Computing $\nabla \cdot \mathbf{B}$ from the integral form in Eq. (6), one immediately finds the Eq. (13) result, namely that

$$\nabla \cdot \mathbf{B}(\mathbf{r}) = 0. \tag{15}$$

Both [1 and 18] are in accord on this and for brevity we omit the details.

The computation for $\nabla \times \mathbf{B}(\mathbf{r})$ is more pertinent and more central to our research. Let us outline the computation presented in the remaining paragraphs of this section of our paper. Using Eq. (6) to compute $\nabla \times \mathbf{B}(\mathbf{r})$, we expand this into two main integrals. By expansion, the first term member is seen to be Ampere's law. Expansion of the second term is more involved and it has been evaluated using two differing derivations in Sections 3.A and 3.B below. We were pleased to find that both approaches yielded the same answer for the displacement current term. In both methods we use the Eq. (9) charge conservation equation and only deductive reasoning, i.e., purely mathematical.

In our derivations, having started with the experimental force equation originally established by Biot and Savart and separately by Ampere [1], we proceed in the following to find an integral expression for the $\nabla \times \mathbf{B}(\mathbf{r})$ using Eq. (6) and the notation shown in Fig. 2 where the field point is given by unprimed coordinates $\mathbf{r}(x,y,z)$ and the source point is given in primed coordinates $\mathbf{r}'(x',y',z')$. In the calculation of $\nabla \times \mathbf{B}(\mathbf{r})$, clearly the ∇ operates on the $\mathbf{r}$ and not on the $\mathbf{r}'$; and therefore, in the vector expansion of the integrand, only two of the four terms are nonzero. So nothing is dropped in this calculation and the precise result for the $\nabla \times \mathbf{B}(\mathbf{r})$ is given by Eq. (16):

$$\nabla \times \mathbf{B}(\mathbf{r}) = \frac{\mu_0}{4\pi}\int_V \left[\mathbf{J}(\mathbf{r}')\left(\nabla \cdot \frac{\hat{\mathbf{r}}_{12}}{R^2}\right) - \left((\mathbf{J}(\mathbf{r}') \cdot \nabla)\frac{\hat{\mathbf{r}}_{12}}{R^2}\right)\right] dV'. \tag{16}$$

In the published literature, one finds this equation in Section 5.3 of the discussion of magnetostatics in [18].

At this point in our derivation, since we know from Eq. (16) that the first member will (likely) provide the conduction current, it is reasonable to anticipate that the second member may be the displacement current.

Evaluation of the first term in Eq. (16) is obtained in the following form:

$$\frac{\mu_0}{4\pi}\int_V \left[\mathbf{J}(\mathbf{r}')\left(\nabla \cdot \frac{\hat{\mathbf{r}}_{12}}{R^2}\right)\right] dV' = \mu_0 \mathbf{J}(\mathbf{r}), \tag{17}$$

by using the well-known vector relation

$$\nabla \cdot \left(\frac{\hat{\mathbf{r}}_{12}}{R^2}\right) = 4\pi\delta(\mathbf{r}-\mathbf{r}'). \tag{18}$$

In Eq. (17) we recognize Ampere's law for the evaluation of the first member of Eq. (16).

In the evaluation of the second member of Eq. (16), one makes the derivative interchange from $\mathbf{r}$ to $\mathbf{r}'$ often used in analysis with Green's function, i.e., as follows:

$$-(\mathbf{J}(\mathbf{r}') \cdot \nabla)\frac{\hat{\mathbf{r}}_{12}}{R^2} = (\mathbf{J}(\mathbf{r}') \cdot \nabla')\frac{\hat{\mathbf{r}}_{12}}{R^2}, \tag{19}$$

including the customary change in sign.

Hence, the second member in Eq. (16) takes the following form given in Eq. (20):

$$-\frac{\mu_0}{4\pi}\int_V (\mathbf{J}(\mathbf{r}') \cdot \nabla)\frac{\hat{\mathbf{r}}_{12}}{R^2} dV' = \frac{\mu_0}{4\pi}\int_V (\mathbf{J}(\mathbf{r}') \cdot \nabla')\frac{\hat{\mathbf{r}}_{12}}{R^2} dV'. \tag{20}$$

For the evaluation of Eq. (20), we analyze it in a component form. The x-component of Eq. (20) can be written as follows:

$$\frac{\mu_0}{4\pi}\int_V (\mathbf{J}(\mathbf{r}')\cdot\nabla')\frac{x-x'}{R^3}\mathrm{d}V' = \frac{\mu_0}{4\pi}\int_V \nabla'\cdot\left(\frac{x-x'}{R^3}\mathbf{J}(\mathbf{r}')\right)\mathrm{d}V' - \frac{\mu_0}{4\pi}\int_V \frac{x-x'}{R^3}\nabla'\cdot\mathbf{J}(\mathbf{r}')\mathrm{d}V'. \quad (21)$$

In the evaluation of the first of the two integrals in Eq. (21), we use Gauss's Theorem to obtain the surface integral and we let the surface expand to a region where the surface currents are zero. Hence, the value of the first integral in Eq. (21) is zero, namely:

$$\frac{\mu_0}{4\pi}\int_V \nabla'\cdot\left(\frac{x-x'}{R^3}\mathbf{J}(\mathbf{r}')\right)\mathrm{d}V' = \frac{\mu_0}{4\pi}\oint_s \frac{x-x'}{R^3}\mathbf{J}(\mathbf{r}')\cdot\mathrm{d}\mathbf{S} = 0. \quad (22)$$

For the second integral in Eq. (21), we use Eq. (9), the conservation of charge, to obtain the form

$$-\frac{\mu_0}{4\pi}\int_V (\nabla'\cdot\mathbf{J}(\mathbf{r}'))\frac{x-x'}{R^3}\mathrm{d}V' = \frac{\mu_0}{4\pi}\frac{\partial}{\partial t}\int_V \rho(\mathbf{r}')\frac{x-x'}{R^3}\mathrm{d}V'. \quad (23)$$

Equation (23) is substituted into Eq. (21) to form the following evaluation of the x component:

$$\frac{\mu_0}{4\pi}\int_V (\mathbf{J}(\mathbf{r}')\cdot\nabla')\frac{x-x'}{R^2}\mathrm{d}V' = \frac{\mu_0}{4\pi}\frac{\partial}{\partial t}\int_V \rho(\mathbf{r}')\frac{x-x'}{R^3}\mathrm{d}V'. \quad (24)$$

Hence, by combining Eqs. (17) and (24) for substitution into Eq. (16), we find the central result, i.e., the basic new form for $\nabla\times\mathbf{B}(\mathbf{r},t)$ in Eq. (25), as follows:

$$\nabla\times\mathbf{B}(\mathbf{r},t) = \mu_0\mathbf{J}(\mathbf{r},t) + \frac{\mu_0}{4\pi}\frac{\partial}{\partial t}\int_V \rho(\mathbf{r}',t)\frac{\hat{\mathbf{r}}_{12}}{R^2}\mathrm{d}V'. \quad (25)$$

Equation (25) is evaluated in two separate ways in Sections 3.A and 3.B below.

A. Derivation Using an Integral Expression for the Electric Field

In the first evaluation of Eq. (25), we use the electrostatic form for the electric field vector that is derived from Coulomb's force law for electric charges. The resulting formula for $\mathbf{E}(\mathbf{r},t)$ is given in integral form by Eq. (26), viz.,

$$\mathbf{E}(\mathbf{r},t) = \frac{1}{4\pi\epsilon_0}\int_V \rho(\mathbf{r}',t)\frac{\hat{r}_{12}}{R^2}\mathrm{d}V', \quad (26)$$

where time dependence is included in the $\rho(\mathbf{r}',t)$ term.

Taking the time derivative of Eq. (26) and substitution into Eq. (25) yield the following desired end result:

$$\nabla\times\mathbf{B}(\mathbf{r},t) = \mu_0\mathbf{J}(\mathbf{r},t) + \mu_0\frac{\partial\mathbf{D}(\mathbf{r},t)}{\partial t}. \quad (27)$$

In Eq. (27) we see that the displacement current appears in the $\nabla\times\mathbf{B}(\mathbf{r},t)$ formula completing this derivation.

B. Derivation Using Gauss s Law

In this section we present an alternative derivation for the displacement current term using Eq. (12) Gauss's Law substituted in the second member term in Eq. (25). This evaluation below leads directly to our final result, verifying Eq. (27).

We present this alternative derivation since we felt that some might question the validity of using the Eq. (26) integral form for the electric field based on the statics derivation that uses Coulomb's force law, particularly if one had studied Table 15-1 in Feynman [19] that lists our Eq. (26) for vector $\mathbf{E}(\mathbf{r})$ as true only for statics. Our alternative derivation starts with Eq. (12) that is listed as "True Always".

Substitution of Eq. (12) into Eq. (25) yields the following expression for $\nabla\times\mathbf{B}(\mathbf{r},t)$:

$$\times\mathbf{B}(\mathbf{r},t) = \mu_0\mathbf{J}(\mathbf{r},t) + \frac{\mu_0}{4\pi}\frac{\partial}{\partial t}\int_V \cdot\mathbf{D}(\mathbf{r}',t)\frac{\hat{r}_{12}}{R^2}\mathrm{d}V', \quad (28)$$

in which the primes trace to $(\mathbf{r}',t)$. The second member on the right side of Eq. (28) is expanded to yield the following:

$$\frac{\mu_0}{4\pi}\frac{\partial}{\partial t}\int_V [\nabla'\cdot\mathbf{D}(\mathbf{r}',t)]\mathbf{G}(\mathbf{r}-\mathbf{r}')\mathrm{d}V' = \frac{\mu_0}{4\pi}\frac{\partial}{\partial t}\int_V \nabla'\cdot[\mathbf{D}(\mathbf{r}',t)\mathbf{G}(\mathbf{r}-\mathbf{r}')]\mathrm{d}V' + -\frac{\mu_0}{4\pi}\frac{\partial}{\partial t}\int_V \mathbf{D}(\mathbf{r}',t)[\nabla'\cdot\mathbf{G}(\mathbf{r}-\mathbf{r}')]\mathrm{d}V'. \quad (29)$$

The Green's function $\mathbf{G}(\mathbf{r}-\mathbf{r}')$ is given by

$$\mathbf{G}(\mathbf{r}-\mathbf{r}') = \frac{\hat{r}_{12}}{R^2} \quad (30)$$

and following the vector algebra in [1] yields

$$\nabla'\cdot\mathbf{G}(\mathbf{r}-\mathbf{r}') = -4\pi\delta(\mathbf{r}-\mathbf{r}'). \quad (31)$$

In the evaluation of Eq. (29), we show that the first member on the right-hand side is zero, as follows. By Gauss's theorem, the volume integral is converted to a surface integral and the product of this integral falls off as $1/R^3$ so that this term is zero.

For the second member, one proceeds as follows. Substitution of Eq. (31) onto Eq. (29) and evaluation of the integration yields the following result for the second member of Eq. (29):

$$-\frac{\mu_0}{4\pi}\frac{\partial}{\partial t}\int_V \mathbf{D}(\mathbf{r}',t)[\nabla'\cdot\mathbf{G}(\mathbf{r}-\mathbf{r}')]\mathrm{d}V' = \mu_0\frac{\partial}{\partial t}\mathbf{D}(\mathbf{r},t). \quad (32)$$

For Eq. (29) the evaluation is obtained by substitution of Eqs. (30) and (32), yielding

$$\frac{\mu_0}{4\pi}\frac{\partial}{\partial t}\int_V [\nabla'\cdot\mathbf{D}(\mathbf{r}',t)]\frac{\hat{r}_{12}}{R^2}\mathrm{d}V' = \mu_0\frac{\partial}{\partial t}\mathbf{D}(\mathbf{r},t). \quad (33)$$

Finally, substitution of Eq. (33) into Eq. (28) yields Maxwell's $\nabla\times\mathbf{B}(\mathbf{r},t)$ formula:

$$\nabla\times\mathbf{B}(\mathbf{r},t) = \mu_0\mathbf{J}(\mathbf{r},t) + \mu_0\frac{\partial\mathbf{D}(\mathbf{r},t)}{\partial t}. \quad (34)$$

Hence, identical formulas are obtained with both derivations in Sections 3.A and 3.B. This completes the derivation.

4. SUMMARY

In the published literature on Maxwell's equations, the $\nabla \times \mathbf{H}(\mathbf{r}, t)$ equation called variously generalized Ampere's circuit law or Ampere's law with Maxwell's correction had been derived from magnetostatics and electrostatics with two major arguments. Currently, one approach is to argue "symmetry": Magnetic fields generate electric fields (as in Faraday's law); hence, it is reasonable that electric fields should generate magnetic fields and the displacement current term added to the $\nabla \times \mathbf{H}$ does this. Added to this assertion is the important fact that the continuity equation establishes the needed correction to conduction current. Together these factors make a credible argument.

The authors of this paper made a careful literature search in order to see if the literature contains a newer and more deductive derivation since Maxwell's time. We felt it should be easy to devise something physical and more modern than "charging capacitors" to complete the story of displacement current. This study is reported in Sections 1, 2. Interestingly, while the reading is a little difficult and the theory is lacking today's vector calculus, Maxwell certainly had most or nearly all of the topics correct: continuity equation, true current including $\partial \mathbf{D}/\partial t$ and unfortunately ether. Moreover, he did not argue for "symmetry."

What the authors did derive for this paper is a new deductive derivation for the $\partial \mathbf{D}/\partial t$ term in the $\nabla \times \mathbf{H}(\mathbf{r}, t)$ formula. Aided by the modern vector algebra, we describe a straightforward derivation for $\nabla \times \mathbf{H}$ in Secs. 3.A and 3.B. Nothing is dropped starting from Eq. (6) for magnetostatic $\mathbf{B}(\mathbf{r})$ and the equations known by Maxwell: Eqs. (9) to (13). No assertions are made. The results are Eqs. (27) and (34) using two analyses in 3.A and 3.B, respectively.

ACKNOWLEDGMENTS

This research is supported in part by Dr. Richard Hammond, Physics Division, U.S. Army Research Office.

REFERENCES

1. J. D. Jackson, *Classical Electrodynamics* (Wiley, 1999).
2. J. C. Maxwell, *Treatise on Electricity and Magnetism* (Clarendon, 1873).
3. J. C. Maxwell, *Treatise on Electricity and Magnetism* (Clarendon, 1881).
4. J. C. Maxwell, *The Scientific Papers of James Clerk Maxwell* (Cambridge University, 1890, Repr. Dover, 1952).
5. J. C. Maxwell, *Treatise on Electricity and Magnetism* (Clarendon, 1892, Repr. Dover, 1954).
6. J. C. Maxwell and J. Fleeming, "On the elementary relations between electrical measurements," BA Report 130–163 (1863).
7. E. T. Whittaker, *History of the Theories of Aether and Electricity*, 1st ed. (Longmans Green and Company, 1910).
8. A. M. Bork, "Maxwell, displacement current and symmetry," Am. J. Phys. **31**, 854–859 (1963).
9. A. M. Bork, "Maxwell and the electromagnetic wave equation," Am. J. Phys. **35**, 844–849 (1967).
10. C.-T. Tai, "On the presentation of Maxwell's theory," IEEE **60**, 936–945 (1972).
11. B. J. Hunt, *The Maxwellians* (Cornell University, 1991).
12. T. K. Sarkar, M. Salazar-Palma, and D. L. Sengupta, "Who was James Clerk Maxwell and what was and is his electromagnetic theory," IEEE Antennas Propag. Mag. **51**, 97–116 (2009).
13. A. J. Schwab, "Maxwell, Hertz and German radio-wave history," IEEE **86**, 1312–1318 (1998).
14. J. H. Bryant, "The first century of microwaves—1886 to 1984," IEEE Trans. Microwave Theory Tech. **36**, 830–858 (1988).
15. L. Page, "A derivation of the fundamental relations of electrodynamics from those of electrostatics," Am. J. Sci. **s4-34**, 57–68 (1912).
16. R. S. Elliott, "Relativity and electricity," IEEE Spectrum 140–152 (1966).
17. R. S. Elliott, *Electromagnetics: History, Theory, and Applications*, Electromagnetic Wave Series (IEEE, 1993).
18. D. J. Griffiths, *Introduction to Electrodynamics* (Prentice Hall, 1999).
19. R. P. Feynman, R. B. Leighton and M. L. Sands, *The Feynman Lectures on Physics*, Vol. **2** (Addison-Wesley, 1963).
20. S. Liao, P. Dourmashkin, and J. Belcher, *Introduction to Electricity and Magnetism* (Pearson, 2004).

Queries

1. AU: In the sentence beginning, "Moreover, and importantly" there's a closing quoation mark missing. Where would you like that to go?

2. AU: Please check for the two operator signs "+" and "-" in Eq. (29) for correctness.

3. AU: Please check publisher and year for refs. [4, 5].

4. AU: Please check whether the ref. [6] is report type?

5. AU: Please check the journal title for refs. [10, 12, 13] is correct?

6. A check of online databases revealed a possible error in this reference. The volume has been changed from '34' to 's4-34'. Please confirm this is correct.

7. AU: Please provide volume number for [16].

Deductive derivation of the displacement term in Maxwell's Equations

Songfeng Han[1] and Nicholas George[1]

[1]The Institute of Optics, University of Rochester, Rochester, New York 14623, USA

We present a new deductive derivation of the displacement current term in Maxwell's equation for $\nabla \times \mathbf{B}$ but without invoking a symmetry argument nor other assertions.

1. THEORY FOR THE DISPLACEMENT CURRENT TERM

The integral form for Ampere's Law or the Biot- Savart Law is

$$\mathbf{B}(\mathbf{r}) = \frac{\mu_0}{4\pi}\int_V \frac{\mathbf{J}(\mathbf{r}')\times\hat{\mathbf{r}}_{12}}{\mathrm{R}^2}dV'. \qquad (1)$$

This resulted from experimental research by Biot and Savart (1820) and Ampere (1820-1825). The equation of charge conservation known also as the equation of continuity was known to Maxwell as we still write it today as follows:

$$\nabla\cdot\mathbf{J}(\mathbf{r},t)+\frac{\partial\rho(\mathbf{r},t)}{\partial t} = 0. \qquad (2)$$

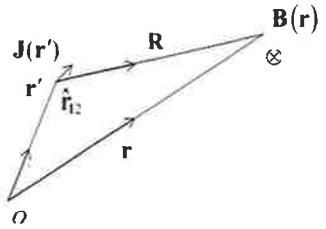

Fig. 1 Notation for magnetic field induction as in Eq. (1).

An important aspect of our novel derivation is to recognize that time-dependent fluctuations of $\rho(\mathbf{r},t)$ and $\mathbf{J}(\mathbf{r},t)$, as is in Eq. (2), would be the key to incorporation of time into the static equations. This point was missed in two major texts on EM theory in which Eq. (3) was erroneously evaluated.

2. PRESENTATION OF THE NEW DERIVATION

In our derivations, having started with the experimental force equation originally established by Biot and Savart and separately by Ampere, we proceed to find an integral expression for $\nabla \times \mathbf{B}$ using Eq. (1) and the notation shown in Fig. 1 where the field point is given by unprimed coordinates r(x,y,z) and the source point is given in primed coordinates r'(x',y',z').

$$\nabla\times\mathbf{B}(\mathbf{r},t)=\frac{\mu_0}{4\pi}\int_V\left[\mathbf{J}(\mathbf{r}',t)\left(\nabla\frac{\hat{\mathbf{r}}_{12}}{\mathrm{R}^2}\right)-\left(\left(\mathbf{J}(\mathbf{r}',t)\,\nabla\right)\frac{\hat{\mathbf{r}}_{12}}{\mathrm{R}^2}\right)\right]dV'. \qquad (3)$$

The first member will provide the conduction current, the second member is more involved. Careful calculation gives the x-component of the second term as follows:

$$\frac{\mu_0}{4\pi}\int_V\left(\mathbf{J}(\mathbf{r}')\,\nabla'\right)\frac{x-x'}{\mathrm{R}^3}dV'=\frac{\mu_0}{4\pi}\int_V\nabla'\left(\frac{x-x'}{\mathrm{R}^3}\mathbf{J}(\mathbf{r}')\right)dV'-\frac{\mu_0}{4\pi}\int_V\frac{x-x'}{\mathrm{R}^3}\nabla'\cdot\mathbf{J}(\mathbf{r}')dV' \qquad (4)$$

Using the equation of continuity and the proper choice for the integral volume yields the following result:

$$\nabla\times\mathbf{B}(\mathbf{r},t)=\mu_0\mathbf{J}(\mathbf{r},t)+\frac{\mu_0}{4\pi}\frac{\partial}{\partial t}\int_V\rho(\mathbf{r}',t)\frac{\hat{\mathbf{r}}_{12}}{\mathrm{R}^2}dV' \qquad (5)$$

Substitution of Gauss' Law into the equation and evaluation of the result yield

$$\nabla\times\mathbf{B}(\mathbf{r},t)=\mu_0\mathbf{J}(\mathbf{r},t)+\mu_0\frac{\partial\mathbf{D}(\mathbf{r},t)}{\partial t} \qquad (6)$$

3. Conclusion

What the authors did present for this paper is both Eq. (5) and the new deductive derivation for the $\frac{\partial \mathbf{D}}{\partial t}$ term in the $\nabla \times \mathbf{H}(\mathbf{r},t)$ formula. Aided by the modern vector algebra, we describe a straightforward derivation . Nothing is dropped starting from Eq. (1) for magnetostatic s and the equations known by Maxwell. No assertions are made. The results are Eqs. (5)-(6).

Our research leads to the following modification and enlargement of a well-known Table 15-1 in Feynman's lectures Vol. II

Electrostatics $\nabla\times\mathbf{E}(\mathbf{r}) = 0$ $\mathbf{E}(\mathbf{r}) = \frac{1}{4\pi\varepsilon_0}\int_{V'}\frac{\rho(\mathbf{r}')\hat{\mathbf{r}}_{12}}{R^2}dV'$ Magnetostatics $\nabla\times\mathbf{B}(\mathbf{r}) = 0$ $\mathbf{B}(\mathbf{r}) = \frac{\mu_0}{4\pi}\int_{V'}\frac{\mathbf{J}(\mathbf{r}')\times\hat{\mathbf{r}}_{12}}{R^2}dV'$
Electromagnetic Field (Lorenz Gauge) Maxwell's Equations $\nabla\times\mathbf{E}(\mathbf{r},t) = -\frac{\partial\mathbf{B}(\mathbf{r},t)}{\partial t}$ $\qquad$ $\nabla\cdot\mathbf{E}(\mathbf{r},t) = \frac{\rho(\mathbf{r},t)}{\varepsilon_0}$ $\nabla\times\mathbf{B}(\mathbf{r},t) = \mu_0\mathbf{J}(\mathbf{r},t) + \mu_0\varepsilon_0\frac{\partial\mathbf{E}(\mathbf{r},t)}{\partial t}$ $\qquad$ $\nabla\cdot\mathbf{B}(\mathbf{r},t) = 0$ Equation of Continuity $\nabla\cdot\mathbf{J}(\mathbf{r},t) + \frac{\partial\rho(\mathbf{r},t)}{\partial t} = 0$ EM Theory Form of Biot-Savart Law $\mathbf{B}(\mathbf{r};\nu) = \frac{\mu_0}{4\pi}\int_{V'}\left(\nabla\frac{e^{-ikR}}{R}\right)\times\mathbf{J}(\mathbf{r};\nu)dV'$ Papas: Theory of Electromagnetic Wave Propagation, Eq. (2.37), HTD Form $\mathbf{B}(\mathbf{r};t) = \frac{\mu_0}{4\pi}\int_{V'}\left\{[\mathbf{J}(\mathbf{r}',t')]_{ret}\frac{\hat{\mathbf{r}}_{12}}{\mathrm{R}^2}+\left[\frac{\partial\mathbf{J}(\mathbf{r}',t')}{\partial t'}\right]_{ret}\times\frac{\hat{\mathbf{r}}_{12}}{cR}\right\}dV'$ Jefimenko: Electricity and Magnetism, Eq. (15-7.6), EM Theory Formula for the Electric Field Vector $\mathbf{E}(\mathbf{r};\nu) = -i\omega\mu_0\int_{V'}\left[\left(\mathbf{u}+\frac{1}{k^2}\nabla\nabla\right)\frac{e^{-ikR}}{R}\right]\cdot\mathbf{J}(\mathbf{r}';\nu)dV'$ Papas: Eq. (2.36) $\mathbf{E}(\mathbf{r};t) = \frac{1}{4\pi\varepsilon_0}\int_{V'}\left\{\frac{\hat{\mathbf{r}}_{12}}{\mathrm{R}^2}[\rho(\mathbf{r}',t')]_{ret}+\frac{\hat{\mathbf{r}}_{12}}{cR}\left[\frac{\partial\rho(\mathbf{r}',t')}{\partial t'}\right]_{ret}-\frac{1}{c^2R}\left[\frac{\partial\mathbf{J}(\mathbf{r}',t')}{\partial t'}\right]_{ret}\right\}dV'$ Jefimenko: Eq. (15-7.5) ** $[\,]_{ret}$ represent substitution $t' \to t - \frac{R}{c}$.

Table 1. (Upper) Equations for the static field and (lower) for the Electromagnetic Field for augmented Table 15-1 in Feynman lectures vol. II. The time retardation brackets $[\,]_{ret}$ represent substitution $t' \to t - \frac{R}{c}$.

This research is supported in part by Dr. Richard Hammond, Physics Division, U.S. Army Research Office.

[1] J. D. Jackson, *Classical Electrodynamics* (Wiley, 1999).
[2] D. J. Griffith, *Introduction to Electrodynamics* (Prentice Hall, 1999).
[3] R. P. Feynman, R. B. Leighton and M. L. Sands, *The Feynman Lectures on Physics*, Vol. 2 (Addison-Wesley, 1963).
[4] T. Biswas, "Displacement current – a direct derivation," Am. J. Phys. **56**, 373-374 (1988).
[5] D. J. Griffiths, and M. A. Heald, "Timedependent generalizations of the Biot-Savart and Coulomb laws," Am. J. Phys. 59, 111-117 (1991).
[6] O. D. Jefimenko, *Electricity and Magnetism* (Second Edition, Electret Scientific Company, 1989)
[7] C. H. Papas, *Theory of Electromagnetic Wave Propagation* (McGraw-Hill, 1965).

408

US008634126B2

(12) **United States Patent**
George et al.

(10) **Patent No.: US 8,634,126 B2**
(45) **Date of Patent: *Jan. 21, 2014**

(54) **DIGITAL BINARY MEMS WAVEFRONT CONTROL**

(71) Applicant: **University of Rochester**, Rochester, NY (US)

(72) Inventors: **Nicholas George**, Pittsfore, NY (US); **Kedar Khare**, New Delhi (IN)

(73) Assignee: **University of Rochester**, Rochester, NY (US)

(*) Notice: Subject to any disclaimer, the term of this patent is extended or adjusted under 35 U.S.C. 154(b) by 0 days.

This patent is subject to a terminal disclaimer.

(21) Appl. No.: **13/662,928**

(22) Filed: **Oct. 29, 2012**

(65) **Prior Publication Data**

US 2013/0063804 A1 Mar. 14, 2013

Related U.S. Application Data

(63) Continuation of application No. 12/304,025, filed as application No. PCT/US2006/025254 on Jun. 28, 2006, now Pat. No. 8,107,156.

(51) **Int. Cl.**
G02B 26/00 (2006.01)

(52) **U.S. Cl.**
USPC **359/290**; 359/291

(58) **Field of Classification Search**
USPC 359/290, 291
See application file for complete search history.

(56) **References Cited**

U.S. PATENT DOCUMENTS

2005/0088738 A1 * 4/2005 Islam et al. 359/484

* cited by examiner

Primary Examiner — James Jones
(74) *Attorney, Agent, or Firm* — William Greener; Bond, Schoeneck & King, PLLC

(57) **ABSTRACT**

Embodiments of the invention are directed to a new type of phase screen, i.e., an opto-electronic device that can convert a distorted incoming optical wavefront into a plane wave or, conversely, transform a plane wave into a prescribed varying output wavefront. The basic concept involves novel binary all-digital MEMS interferometer configurations that can be used to create controlled and arbitrary optical wavefront using only 0,1 amplitude changes followed by differential propagation distances to convert these amplitude variations into controllable and/or continuous phase variations. Clustered pixel notions, such as Floyd-Steinberg, Stucki or other algorithms useful in digital half-tone printing, are simultaneously employed to create controllable grey-level variations as well as continuous phase variations. Desired grey-levels can be obtained wherein each pixel is formed by, e.g., a 3×3 or 5×5 cluster of mirrors. Both the filling-in of the outputs of the binary mirror (0,1) and the grey-levels are accomplished simply by spatial averaging over a short propagation distance.

4 Claims, 10 Drawing Sheets

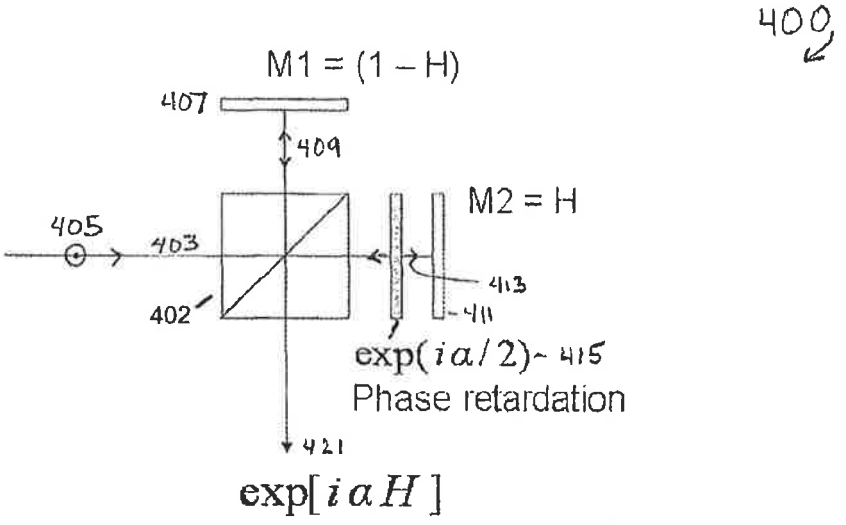

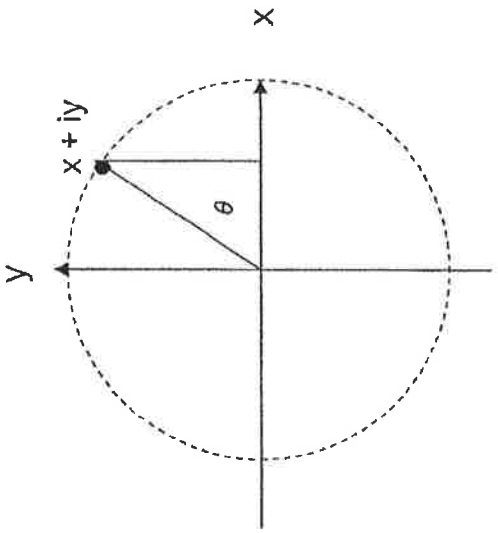

FIG. 1

FIG. 2A

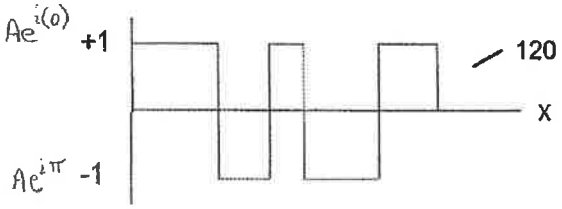

FIG. 2B

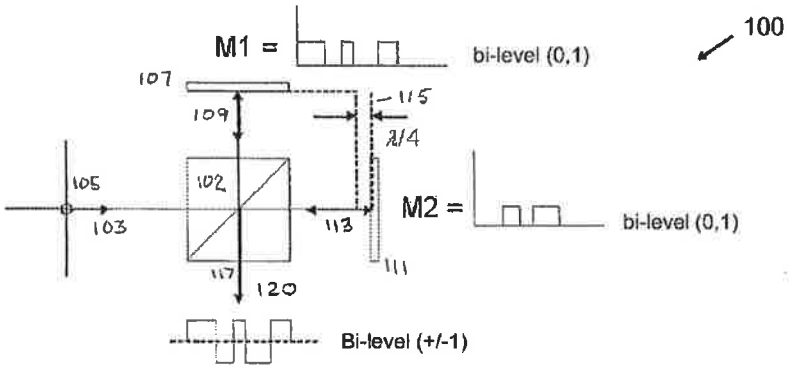

FIG. 2C

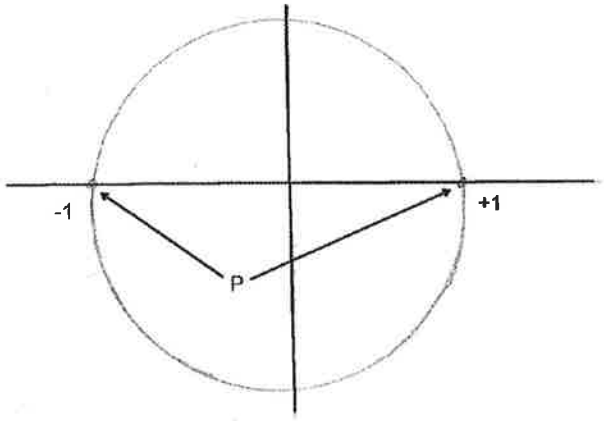

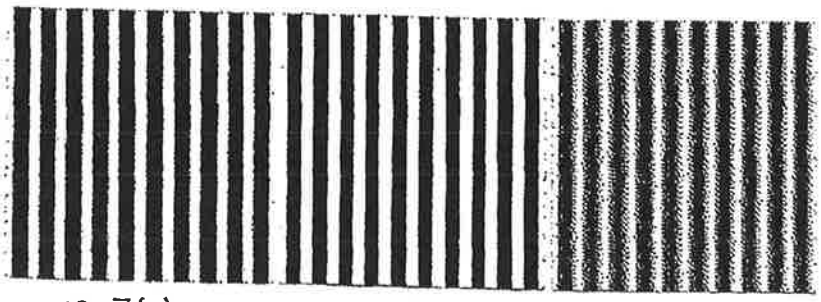

FIG. 3(a) FIG. 3(b) FIG. 3(c)

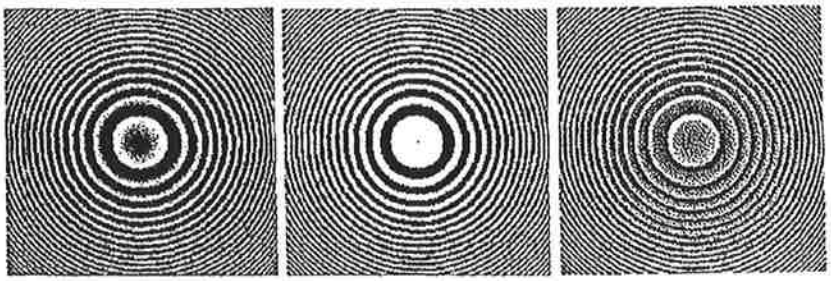

FIG. 6(a) FIG. 6(b) FIG. 6(c)

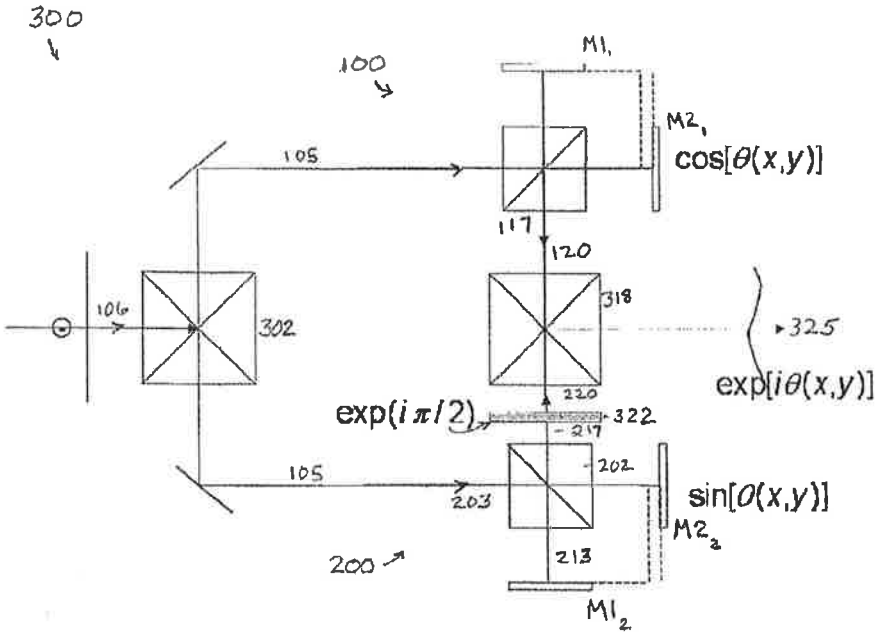

FIG. 4A

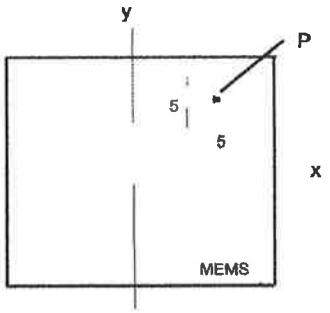

FIG. 4B

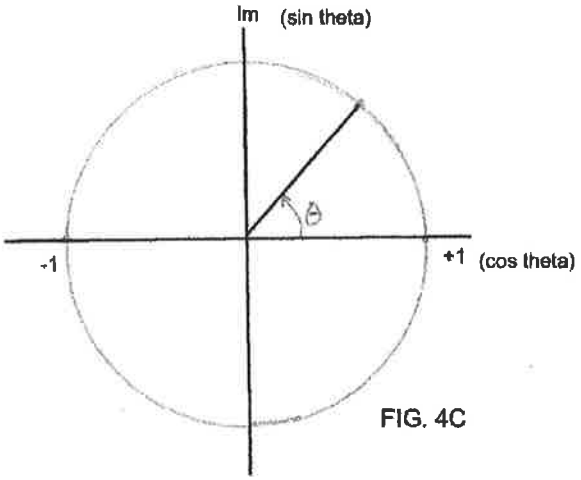

FIG. 4C

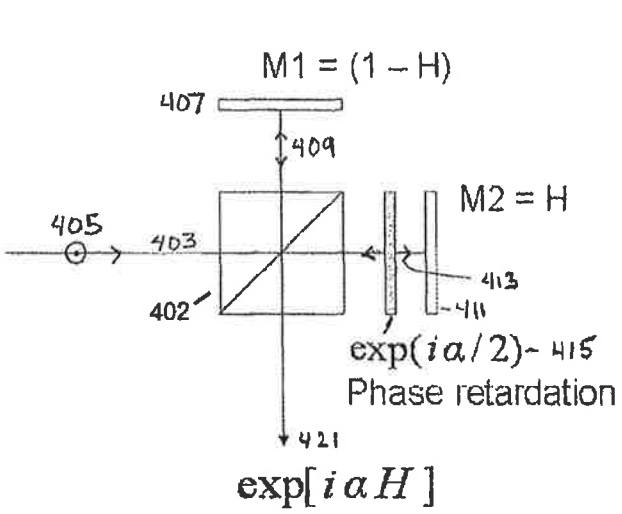
400
M1 = (1 – H)
407
409
M2 = H
405
403
413
411
402
exp(iα/2)- 415
Phase retardation
421
exp[iαH]

FIG. 5

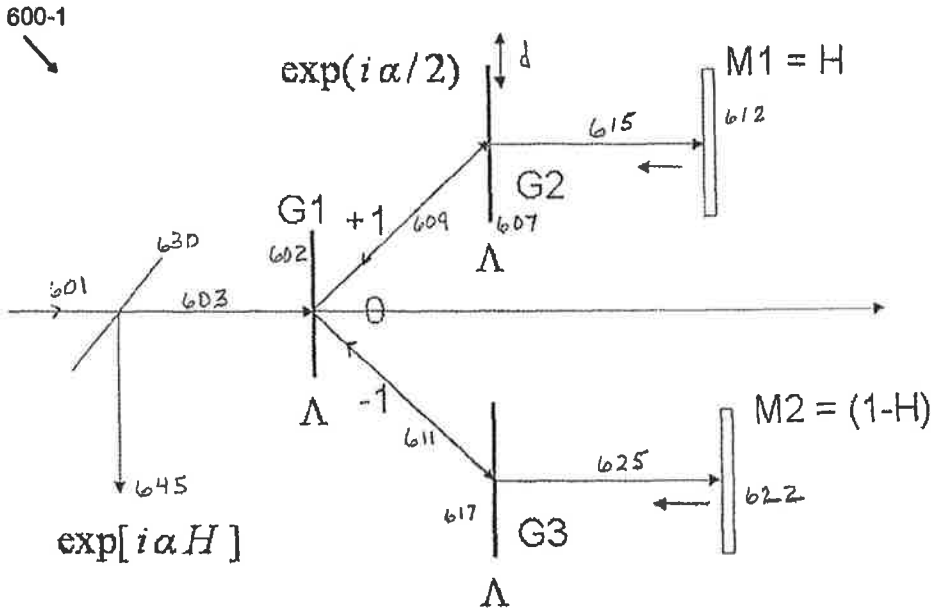
600-1
exp(iα/2)
d
M1 = H
615
612
G2
G1
+1
609
607
602
630
601
603
0
Λ
-1
611
M2 = (1-H)
625
622
617
G3
645
exp[iαH]
Λ
Λ

FIG. 7A

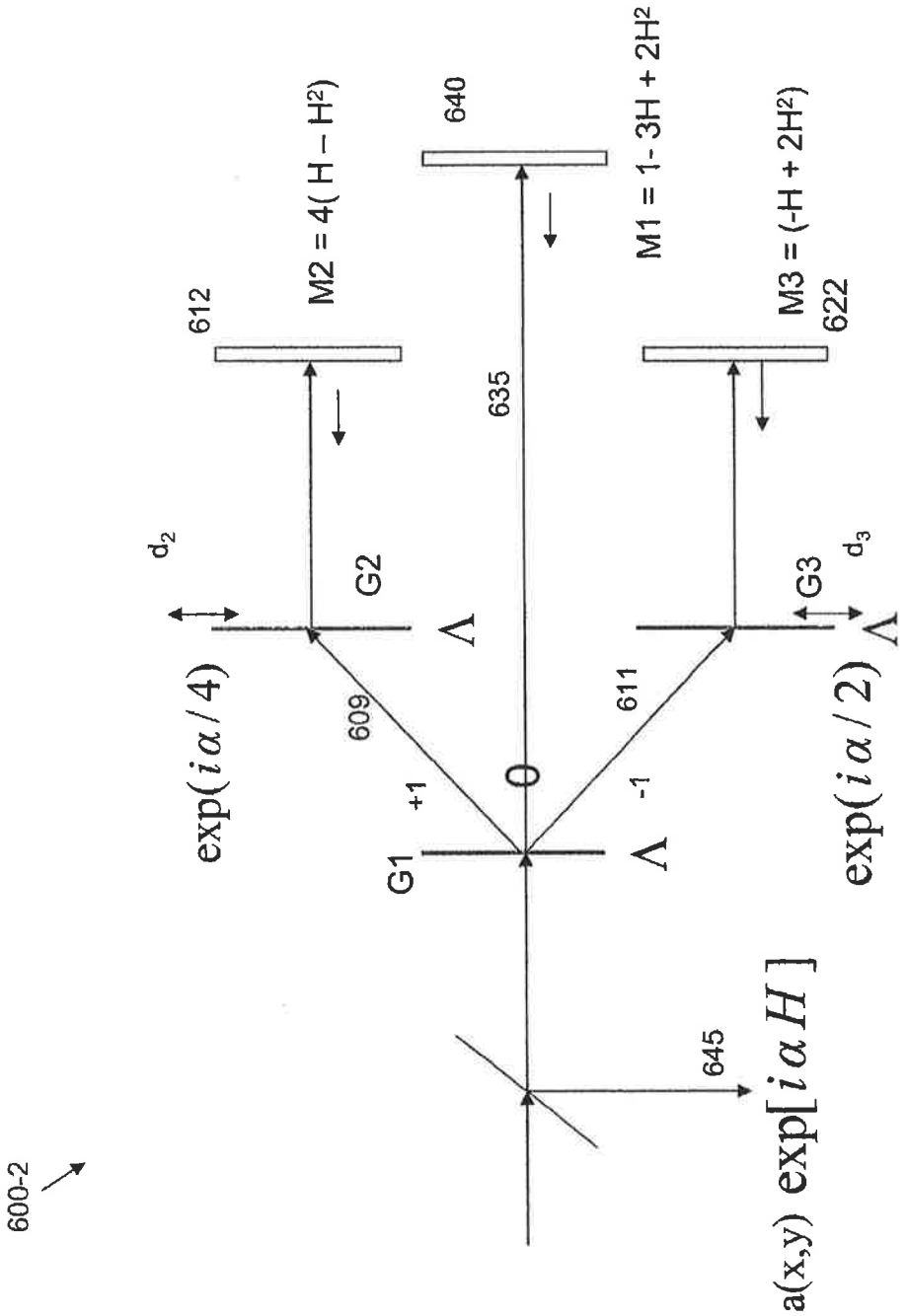
600-2
a(x,y) exp[i α H]
645
640
635
612
M2 = 4(H – H²)
622
M1 = 1- 3H + 2H²
M3 = (-H + 2H²)
d2
G2
d3
G3
G1
609
611
+1
-1
0
exp(i α / 4)
exp(i α / 2)

Fig. 7B

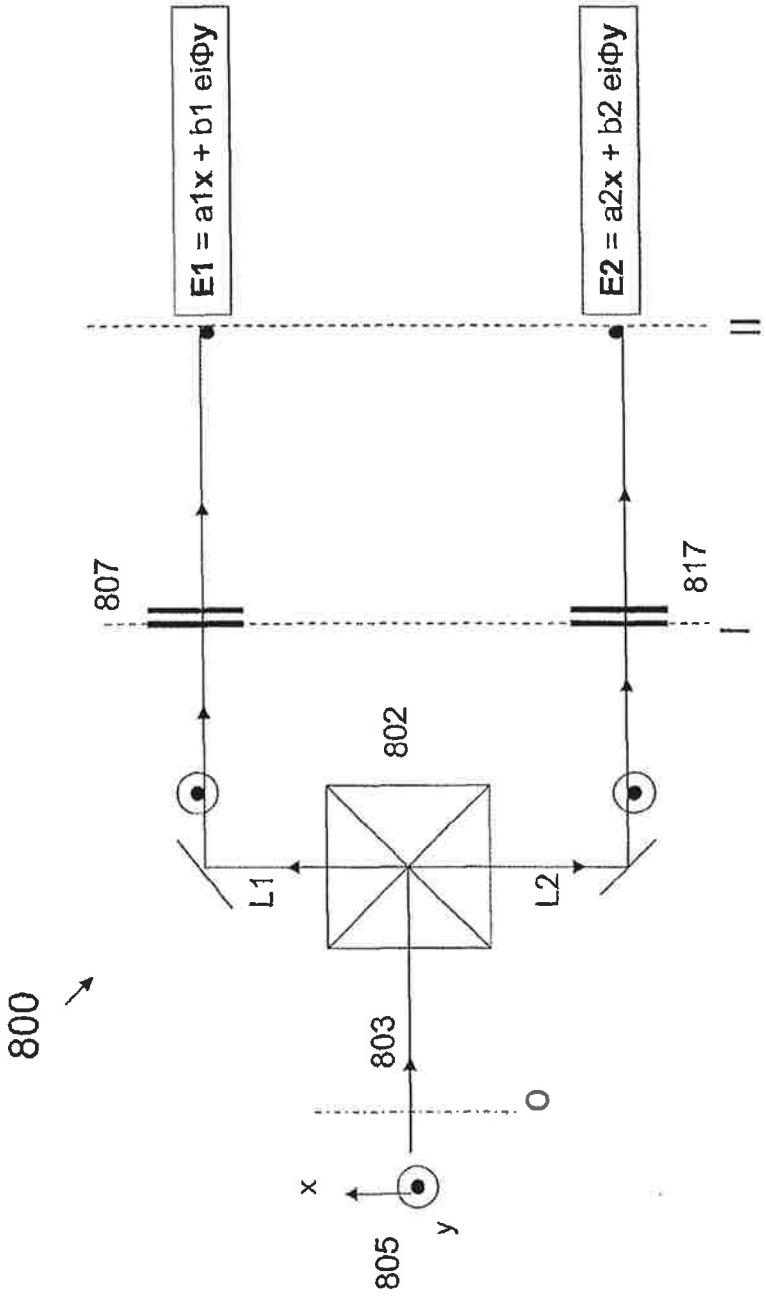
E1 = a1x + b1 eiφy
E2 = a2x + b2 eiφy
II
I
807
817
802
L1
L2
800
803
O
x
y
805

FIG. 8

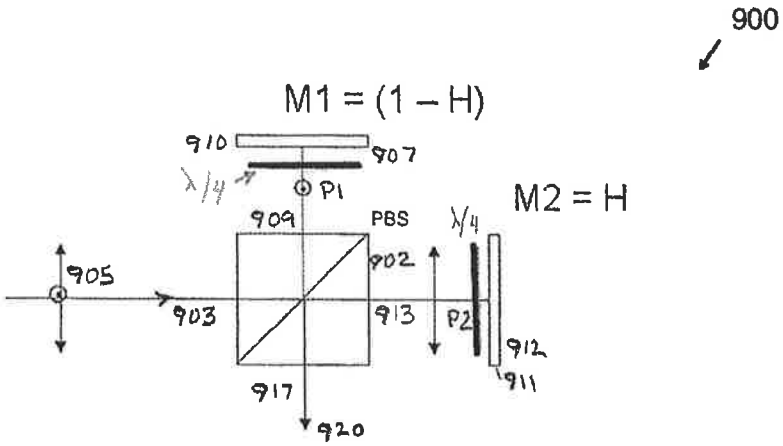
900
M1 = (1 – H)
910
907
λ/4
P1
M2 = H
909
PBS
λ/4
905
902
903
913
P2
912
911
917
920

FIG. 9A

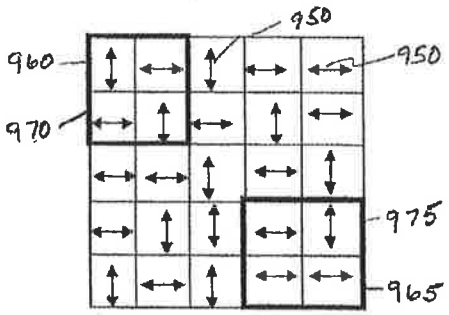
950
960
950
970
975
965

FIG. 9B

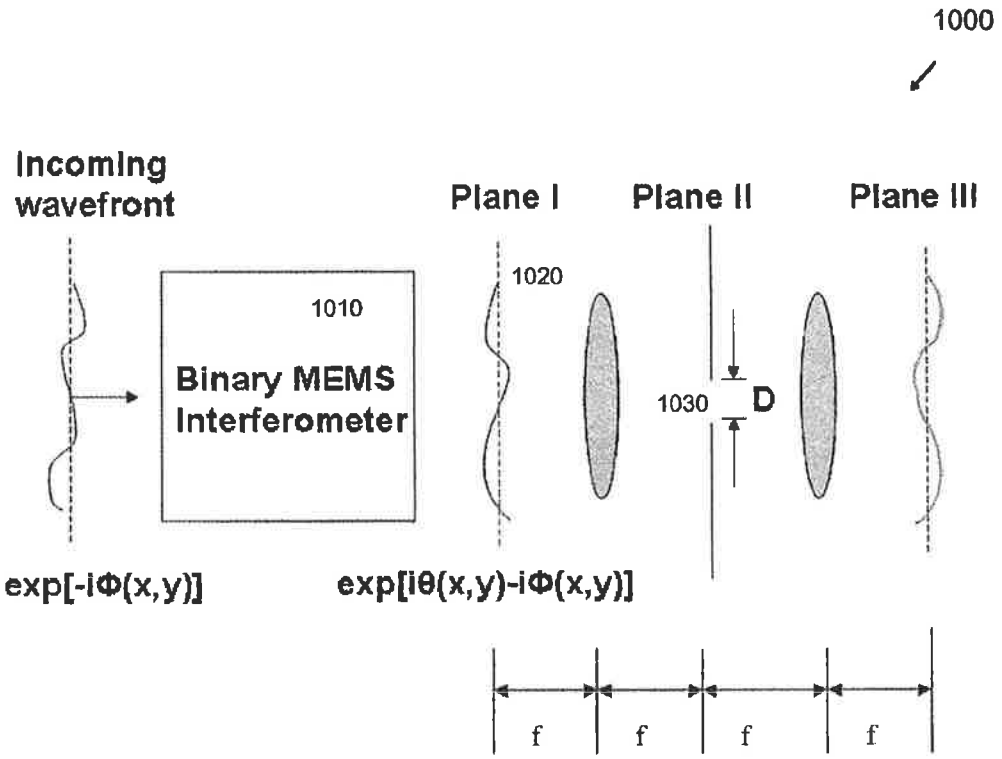
1000
Incoming wavefront
Plane I
Plane II
Plane III
1010
Binary MEMS Interferometer
1020
1030
D
exp[-iΦ(x,y)]
exp[iθ(x,y)-iΦ(x,y)]
f
f
f
f

FIG. 10

DIGITAL BINARY MEMS WAVEFRONT CONTROL

RELATED APPLICATIONS

This application is a continuation of, and claims the full line of priority to U.S. application Ser. No. 12/304,025 filed on Dec. 9, 2008, which itself is a US national stage filing of PCT/US2006/025254 filed on 28 Jun. 2006, the subject matter of which are incorporated herein by reference in their entireties.

FEDERALLY SPONSORED RESEARCH

This invention was made with U.S. Government Support under Contract Number DAAD 19-03-1-0185 (44430-PH), awarded by the US Army Research Office. The Federal Government has certain rights in the invention.

BACKGROUND OF THE INVENTION

1. Field of the Invention

Embodiments of the invention are most generally related to the field of optical modulation and opto-electronic imaging. More particularly, embodiments of the invention are directed to novel apparatus and methods that effect phase and absolute value of the amplitude, hereinafter amplitude, control over an optical wavefront, and to applications directed to atmospheric sensing, optical metrology, astronomical and ophthalmic imaging, adaptive optics and interferometry.

2. Description of Related Art

In optical interferometry one often needs to generate a particular function form for the variation of amplitude over a given transverse plane starting, for example, from a uniform plane wave. As a specific instance in optical metrology, one generates the family of Zernike polynomials using modern optical interferometers with special masks incorporated. These specified wavefronts are used to test the accuracy of a particular optical surface being fabricated. In addition there are other instances when a distorted wavefront needs to be corrected so as to provide a plane wave output or a converging wave of specific radius of curvature for the equiphase of the propagating wave. For instance, when an optical signal travels from point A to point B, the quality of the received signal is less than that of the transmitted signal. This degradation is due to variation in the uniformity of the medium (index of refraction) that the light propagates through in going from point A to point B. Common examples include the light from a star that is distorted by atmospheric turbulence; poor vision due to defects in the optics of the eye; and, noisy communication caused by a non-uniform index of refraction over the signal path.

Viewed simply, a point source of light such as a star, for example, radiates spherical wavefronts of light in all directions. A wavefront is the locus of points having the same phase i.e., have the same path length from the source. To a distant viewer on earth, the wavefront of the light traveling along the viewer's line of sight is in the form of a flat, uniform plane of light; i.e., a plane wavefront. However, when the index of refraction of the propagation medium changes, the path lengths are no longer equal or normal to the propagating plane wavefront. Instead, the wavefront is distorted or aberrated. Thus the phase of the wavefront is no longer uniform over the spatial extent of the wavefront.

Wavefront sensors are now commonly used to measure higher-order aberrations of a wavefront propagated through an optical system. A Shack-Hartmann sensor is often the

principal component of modern ophthalmic wavefront measuring devices. Several other types of wavefront sensors are also commercially popular. Once a distorted wavefront is measured and quantified, it may be desirable to compensate the wavefront; i.e., to bring it back to its non-aberrated state. Deformable mirrors, referred to as adaptive or active optics (AO) depending upon their application, are well known in the art. An adaptive optics imaging system, for example, is designed to correct for phase distortions in the optical wavefront in near real time to obtain improved image quality. Adaptive optical imaging originated as a tool for improving the performance of ground-based large telescopes for astronomical imaging through atmospheric turbulence. Another application is the correction of atmospheric turbulence over horizontal propagation paths. Adaptive imaging techniques have also been applied to wavefront control of large astronomical telescopes by using high power lasers and guide stars to generate perturbed wavefronts for correction of the astronomical image. Adaptive optics and wavefront control are also commonly used in laser fusion to correct for minute phase perturbations as the laser beam propagates through various lenses of the system. The typical components used in a present day adaptive system are listed in Table 1.

TABLE 1

Wavefront Sensors	Wavefront Correctors
Shack-Hartmann Sensor	Continuous membrane mirrors with PZT
Curvature sensor	Segmented mirrors with PZT
Shearing interferometer	Bimorph Mirrors
Smartt interferometer	MEM micro-mirrors
Pyramid sensor	Liquid Crystal SLMs

Conventional designs for wavefront correctors include segmented mirror devices with each mirror segment having tip/tilt and piston controls, and continuous membrane (analog) devices with a number of actuators on their back side for deforming the mirror surface. Bimorph mirror technology uses two piezoelectric wafers bonded together with an array of electrodes. The outer surface of one of the mirror acts as a mirror. These devices are most suitably used with a curvature sensor configuration. More recent technologies used for phase screens, as they are sometimes called, include liquid crystal spatial light modulators (SLMs) and analog-type MEMS based micro-mirrors. Spatial light modulation is used, for example, in the fields of optical information processing, projection displays, video and graphics monitors, televisions, astronomy and electrophotographic printing. There, optical beams are deflected by mirror arrays where it is desired to be able to individually phase adjust the reflected light from each mirror. Often, the phase screen in an AO telescope is the single most troublesome component in the system. Typically, the phase screen is an LCD used in transmission mode with a voltage applied in an x-y coordinate system, pixel by pixel. It can also take the form of multiple PZT actuators used to push or deform a smooth mirror membrane into an aberration compensating surface shape.

Cost is an important factor in choosing an appropriate deformable mirror technology for a given application. Piezo-activated (PZT) deformable mirrors can cost over $1000 per actuator, thus a large mirror array can be extremely expensive. MEMS devices are typically manufactured using fabrication methods developed in the semiconductor industry. Comparatively, MEMS technology offers a low-cost attractive alternative. There are generally two types of micro-mirror arrays: (1) Devices with piston and tip/tilt controls for micro-mirrors; and (2) simple ON/OFF type binary micro-mirror arrays. The

state-of-the-art devices of the first type have ~1000 micro-mirrors each about 300 microns on a side, and each having an ~2 micron piston stroke motion and ~7 kHz frame rate. The ON/OFF type (i.e., digital binary MEMS) devices on the other hand have close to a million mirror elements, each being ~17 micron on a side. Digital binary MEMS mirror technology has been developed over the last two decades. Arrays consisting of ~10^6 mirrors that impart binary (1,0) amplitude modulation to the incident wavefront at ~10 kHz frame rates are now available commercially at low cost. They have found widespread application, for example, in projection display systems. In recent years other applications of these arrays have evolved, e.g. in generation of (1,0) mask patterns in lithography, for implementing a moving aperture in a confocal microscope, for obtaining multiplexing Hadamard type mask patterns in spectroscopy applications, etc. The ability to provide only (1,0) type amplitude modulation has thus far been treated as a limitation that has prevented their use in adaptive systems for phase correction. A new way of wavefront phase coding is required that will permit the use of binary mirror arrays for wavefront phase modulation.

It is possible to generate selected wavefronts using deformable MEMS mirrors or LCD spatial light modulators. There are, however, certain disadvantages associated with their use. These devices typically cannot work over a broad range of wavelengths from the visible to long wavelength infra-red. As mentioned above, the cost for a 1000×1000 actuator assembly is prohibitive. MEMS devices currently used in adaptive optics setups do not offer as high resolution as may be desired for a particular application. The control of a large mirror array is complex and a large MEMS array can be susceptible to backlash errors. Half-toned characterization of phase front, as will be described below and used in conjunction with embodiments of the instant invention, would require high computational loading using the aforementioned deformable mirror devices.

In view of the challenges and disadvantages associated with wavefront phase control using deformable mirrors and/or LCD SLMs, the inventors have recognized that significant benefits may be realized by the various embodiments and aspects of the invention described in detail below and as defined in the appended claims. As mentioned above, a new way of wavefront phase coding is required that will permit the use of digital binary mirror arrays for wavefront phase modulation. The ability to generate an arbitrary wavefront using only binary (ON/OFF) micro-mirror arrays combined with digital half-toning methods and differential propagation distances has several advantages over deformable analog MEMS mirrors or LC spatial light modulators. The benefits and advantages include, but are not limited to, the ability to generate arbitrary wavefronts using only binary (ON/OFF) micro-mirror arrays combined with digital half-toning methods; broadband performance over the wavelength range from the visible to LWIR; an effective frame size of ~200×200 to 300×300 pixels using digital half-toning algorithms over, e.g., 3×3 or 5×5 mirror blocks at a fraction of the cost for comparable MEMS performance; resolution that far exceeds analog MEMS device capability; simpler operation; less susceptibility to backlash errors; lower computational load, easy system calibration; all digital architecture; environmental robustness and stability, and others that will be recognized by persons skilled in the art.

As used herein, the term 'analog' refers to a continuous membrane mirror surface that may be deformed by a number of actuators coupled to the rear surface of the membrane, or, to a MEMS device where the individual mirrors can be stepped over multiple positions instead of simple binary 0,1. In contrast, a 'digital' binary MEMS mirror, as that term will be used in conjunction with various embodiments and aspects of the invention described herein, will refer to a MEMS mirror array in which each individual mirror segment can only be in an "ON" position (referred herein below as having a 1 value and oriented to retro-reflect incident light) or an "OFF" position (referred to herein below as having a 0 value and tilt-oriented to reflect incident light away from the intended optical path).

FIG. **1** shows what is known as an Argand diagram, which is used to illustrate the geometric representation of a complex number as simply a point in the complex plane. An Argand diagram is a plot of complex numbers as points z=x+iy in the complex plane using the x-axis as the real axis and the y-axis as the imaginary axis, where $z=(abs)z\, e^{i\theta}$. In the figure, the radius of dashed circle represents the complex modulus (abs)z of z and the angle θ represents its complex argument or what can be called the phase. The phase, θ, corresponds to the counterclockwise angle from the positive real axis, i.e., the value of θ such that x=(abs)z (cos θ) and y=(abs)z (sin θ). Since a wavefront may be described by Euler's equation $e^{i\,\theta(x,y)}=\cos\theta+i\sin\theta$, in conjunction with various embodiments of the invention described herein below, the notation of the Argand diagram may be useful to the reader in illustrating various aspects of the invention.

The advantages and benefits provided by the teachings disclosed herein and the embodiments of the invention disclosed and claimed will become more apparent to persons skilled in the art in view of the following description and drawings.

SUMMARY OF THE INVENTION

Most generally, embodiments of the invention are directed to a new type of phase screen, i.e., an opto-electronic device that can convert a distorted incoming optical wavefront into a plane wave or, conversely, transform a plane wave into a prescribed varying output wavefront. The basic concept involves novel binary all-digital MEMS configurations that can be used to create an arbitrary optical wavefront using only 0,1 amplitude changes followed by differential propagation distances to convert these amplitude variations into controllable and/or continuous phase variations. As used herein, the term 'arbitrary' wavefront refers to a pixel phase value that can be represented anywhere in the complex plane described by an associated Argand diagram, rather than just on the unit value circle boundary or on some other restricted portion of the complex plane. Clustered pixel notions, such as Floyd-Steinberg, Stucki or other algorithms useful in digital half-tone printing, are simultaneously employed to create controllable grey-level variations as well as continuous phase variations. Desired grey-levels can be obtained wherein each pixel is formed by a cluster of 3×3 mirrors or 5×5 mirrors, for example. Both the filling-in of the outputs of the binary mirror (0,1) and the grey-levels are accomplished simply by short propagation.

According to an embodiment of the invention, an optical control component includes a first component beam divider/combiner disposed along a first component input optical path of an incident optical wavefront; a first component binary MEMS device $M1_1$ comprising an $(n_{x,y}\times m_{x,y})_{M1}$ mirror array disposed optically downstream of the first component beam divider/combiner along an M1 optical path having a total optical path length $L1_1$ (i.e., L1 is a double-pass distance); a first component binary MEMS device $M2_1$ comprising an $(n_{x,y}\times m_{x,y})_{M2}$ mirror array disposed optically downstream of the first component beam divider/combiner along an $M2_1$

optical path different than the $M1_1$ optical path having a total optical path length $L2_1$; and phase retarder means for making $L1_1$ different than $L2_1$, wherein at least an $M1_1$ mirror sub array $(X\times Y)_{M1}$ is in an ON/OFF state and a complementary at least an $M2_1$ mirror sub array $(X\times Y)_{M2}$ is in an OFF/ON state, further wherein an output wavefront propagating along a first component output optical wavefront path has a controlled modulation.

Another embodiment of the invention is directed to an optical control device comprising a first optical control component as described immediately above; a second optical control component including a second component beam divider/combiner disposed along a second component input optical path of an input optical wavefront; a second component binary MEMS device $M1_2$ comprising an $(n_{x,y}, m_{x,y})_{M1}$ mirror array disposed optically downstream of the second beam divider/combiner component along an $M1_2$ optical path having a total optical path length $L1_2$; a second component binary MEMS device $M2_2$ comprising an $(n_{x,y}, m_{x,y})_{M2}$ mirror array disposed optically downstream of the second beam divider/combiner component along an $M2_2$ optical path different than the $M1_2$ optical path having a total optical path length $L2_2$; and phase retarder means for making $L1_2$ different than $L2_2$, wherein at least an $M1_2$ mirror sub array $(X\times Y)_{M1}$ is in an ON/OFF state and a complementary at least an $M2_2$ mirror sub array $(X\times Y)_{M2}$ is in an OFF/ON state, further wherein an output wavefront propagating along a second component output optical wavefront path has a controlled modulation; an input beam divider disposed optically intermediate an incoming wavefront and the first and second optical control components, wherein the output optical wavefront from the input beam divider is the input optical wavefront to the first and second optical control components; an output beam combiner disposed to optically combine the respective first and second component modulated output wavefronts; and phase shifting means for providing a controlled phase difference between the first and second component phase modulated output wavefronts, wherein a resultant output wavefront has a phase that is different than the input optical wavefront phase by an amount $\theta(x,y)$.

An alternative embodiment of the invention is directed to an optical control device that uses a two-level half-toning algorithm to generate a controlled wavefront. The device comprises a diffractive, input wavefront divider/combiner (G) disposed along an optical axis of the input wavefront; a first component diffractive wavefront divider/combiner (G1) disposed to optically intercept one of a positive and a negative n^{th}-order output beam from the input wavefront divider/combiner; a first component binary MEMS device M1 comprising an $(n_{x,y}, m_{x,y})_{M1}$ mirror array disposed optically downstream of the first beam divider/combiner component along an M1 optical path, wherein at least an M1 mirror sub array $(X\times Y)_{M1}$ is in a selected ON/OFF state that provides a half-tone phase value H, where $0\le H\le 1$; a second component diffractive wavefront divider/combiner (G2) disposed to optically intercept either a complementary negative or positive n^{th}-order output beam from the input wavefront divider/combiner; a second component binary MEMS device M2 comprising an $(n_{x,y}, m_{x,y})_{M2}$ mirror array disposed optically downstream of the second beam divider/combiner component along an M2 optical path, wherein a complementary M2 mirror sub array $(X\times Y)_{M2}$ is in a selected complementary OFF/ON state that provides a half-tone phase value $(1-H)$, where $0\le(1-H)\le 1$; and at least one optical component that in-couples the input wavefront and out-couples an output wavefront having a controlled phase that is different than the input wavefront phase. According to an aspect, the diffractive wavefront divider/combiner, the first component diffractive wavefront divider/combiner and the second component diffractive wavefront divider/combiner are diffraction gratings each having a grating period Λ.

Another embodiment of the invention is directed to an optical control device comprising a polarizing beam divider/combiner disposed along a component input optical path of an incident optical wavefront, providing one polarization state $P1_1$ and another polarization state $P2_1$; a quarter wave plate which on two passes will cause the exiting P1 to rotate by 90 degrees so as to pass through the polarizer beam divider/combiner; a first binary MEMS device $M1_1$ comprising an $(n_{x,y}, m_{x,y})_{M1}$ mirror array disposed optically downstream of the polarizing beam divider/combiner along an $M1_1$ optical path of P1, wherein at least an M1 mirror sub array $(X\times Y)_{M1}$ is in a selected ON/OFF state that provides a half-tone phase value $(1-H)$, where $0\le(1-H)\le 1$; a second quarter wave plate; and a second binary MEMS device M2 comprising an $(n_{x,y}, m_{x,y})_{M2}$ mirror array disposed optically downstream of the polarizing beam divider/combiner along an M2 optical path of P2, wherein an M2 mirror sub array $(X\times Y)_{M2}$ is in a selected complementary OFF/ON state that provides a half-tone phase value H, where $0\le H\le 1$, further wherein an output wavefront propagating along an output optical wavefront path has a polarization coded phase profile over a transverse cross section of the output wavefront.

According to a related embodiment, a grating-based interferometer device uses a novel three-level half-toning algorithm to generate an arbitrary wavefront having controlled amplitude and phase. In this embodiment, a third MEMS component is disposed so as to intercept the zero-order diffracted beam. The wavefront can be expressed as the sum of polynomials in H(x,y) having appropriate phase. When relative phase delays are introduced between each of the three beams, they can be combined to produce an arbitrary wavefront having an absolute amplitude and phase expressed as $a(x,y)\exp[i\theta(x,y)]$.

Another embodiment of the invention is directed to an optical control device, comprising a beam divider/combiner disposed along an input optical path of an incident optical wavefront; a first binary MEMS device M1 comprising an $(n_{x,y}, m_{x,y})_{M1}$ mirror array disposed optically downstream of the first component beam divider/combiner along an M1 optical path providing an $M1_{out}$ wavefront, wherein at least an M1 mirror sub array $(X\times Y)_{M1}$ is in an ON/OFF state that provides a half-tone phase value expressed as $1-H(x,y)$, wherein H(x,y) represents a two-level value equal to 0 or 1; a second binary MEMS device M2 comprising an $(n_{x,y}, m_{x,y})_{M2}$ mirror array disposed optically downstream of the beam divider/combiner along an M2 optical path providing an $M2_{out}$ wavefront, wherein a complementary M2 mirror sub array $(X\times Y)_{M2}$ is in an OFF/ON state that provides a half-tone phase value expressed as H(x,y); and phase retarder means for providing a controlled phase difference between the $M1_{out}$ wavefront and the $M2_{out}$ wavefront, further wherein a resultant output wavefront obtained from the interference of the $M1_{out}$ wavefront and the $M2_{out}$ wavefront is different than the input optical wavefront by an amount $\alpha H(x,y)$ where $-\pi\le\alpha\le\pi$. According to an aspect, the device effects a wavefront coding on the input wavefront expressed as $e^{i\alpha H(x,y)}=(1-H)+e^{i\alpha}H$, wherein $1-H(x,y)$ is the half-tone phase coding provided by the ON/OFF state of M1, H is the half-tone phase coding provided by the OFF/ON state of M2, and $e^{i\alpha}$ represents the relative phase term between $M1_{out}$ and $M2_{out}$.

According to an aspect of the above described embodiments, a telecentric telescope may be disposed in the output wavefront plane to shift the output plane further downstream.

The size of the telescope aperture can be used to control the size (X×Y) of the mirror sub-array over which the spatial averaging is performed in order to realize the half-toning effects.

Another embodiment of the invention is directed to a method for controlling an optical wavefront WF, comprising the steps of providing a first controllable binary MEMS device **M1** comprising an $(n_{x,y}, m_{x,y})_{M1}$ mirror array, wherein each mirror can be set only to a binary ON/OFF position, and a second controllable binary MEMS device $M2_1$ comprising an $(n_{x,y}, m_{x,y})_{M2}$ mirror array, wherein each mirror can be set only to a binary ON/OFF position; providing an incident optical wavefront WF_{1i}; splitting the incident optical wavefront into $WF1_1$ along a first optical path $L1_1$ to $M1_1$ and into $WF2_1$ along a second optical path $L2_1$ to $M2_1$; modulating $WF1_1$ reflected from $M1_1$ by setting at least one M1 mirror sub array $(X_{x,y}\times Y_{x,y})_{M1}$<array $(n_{x,y}\times m_{x,y})_{M1}$ to an ON position and modulating $WF2_1$ reflected from $M2_1$ by setting a complementary at least one mirror sub array $(X_{x,y}\times Y_{x,y})_{M2}$<array $(n_{x,y}\times m_{x,y})_{M2}$ to an OFF position; providing an optical path length difference $\Delta L1L2$ in a range $0<\Delta L1L2\leq(2n+1)\lambda/2$, where n=0, 1, 3, . . . , so as to provide a phase shift≤π; and obtaining a desired output optical wavefront WF_{1o} by optically combining reflected $WF1_1$ and reflected $WF2_1$. According to an aspect, modulating a phase profile of the wavefront by setting the at least one mirror sub array $(X_{x,y}\times Y_{x,y})$ to a selected ON/OFF position comprises providing an averaged grey-scale pixel value over the sub array. An aspect further includes employing a half-toning algorithm, wherein a single grey-scale pixel is represented by a spatially averaged dot pattern over the X×Y mirror sub array. As will be appreciated, the mirror sub array is equivalent to a mirror cluster that is used to define a pixel, as is known in the field of digital imaging.

In various aspects of the above mentioned embodiments, the at least some of the mirror array is one or more cluster arrays X×Y (<n×m), wherein each mirror cluster array X×Y represents a pixel and is characterized by at least a two-level phase half-toning approximation. In particular aspects, X=Y and n=m.

These and other objects, advantages and benefits provided by embodiments of the invention will now be set forth in detail with reference to the detailed description and the drawing figures and as defined in the appended claims.

BRIEF DESCRIPTION OF THE DRAWINGS

FIG. **1** shows a general Argand diagram, which is used to illustrate the geometric representation of a complex number as simply a point in the complex plane, provided as an aid in understanding the invention;

FIGS. **2***a*, **2***b* and **2***c*, respectively, illustrate a square wave pattern used to modulate an input wavefront; an optical control component according to an embodiment of the invention; and an Argand diagram representation of the interferometric output from the optical control component;

FIGS. **3***a*, **3***b* and **3***c* show alternating dark/bright bar patterns illustrating half-toning in conjunction with the component in FIG. **2***b*. FIG. **3***a* illustrates a cosine function; FIG. **3***b* shows a hard-thresholding version of FIG. **3***a*; and FIG. **3***c* shows a half-toned version of FIG. **3***a* obtained using the known Stucki algorithm;

FIG. **4***a* shows an interferometer-based optical control device for generating an arbitrary wavefront a(x,y)exp[iθ(x,y)] according to an embodiment of the invention;

FIG. **4***b* schematically illustrates a pixel point P(x,y) in an exemplary 5×5 mirror sub array of the MEMS device of FIG. **4***a*;

FIG. **4***c* shows an Argand diagram representation of point P(x,y) of FIG. **4***b*;

FIG. **5** shows an interferometer-based optical control device for generating a selected wavefront exp[iθ(x,y)] according to another embodiment of the invention;

FIGS. **6***a*-**6***c* show alternating dark/bright ring patterns illustrating half-toning in conjunction with the device in FIG. **5**. FIG. **6***a* illustrates a continuous quadratic phase function; FIG. **6***b* shows a hard-thresholding version of FIG. **6***a*; and FIG. **6***c* shows a half-toned version of FIG. **6***a* obtained using the known Stucki algorithm;

FIG. **7**A shows a diffraction-interferometer-based optical control device that uses a two-level algorithm for generating a wavefront exp[iθ(x,y)] according to another embodiment of the invention;

FIG. **7**B shows a diffraction-interferometer-based optical control device that uses a three level algorithm for generating an arbitrary wavefront a(x,y)exp[iθ(x,y)] according to another embodiment of the invention;

FIG. **8** is a schematic system diagram used to illustrate the concept of polarization controlled wavefront phase coding;

FIGS. **9***a* and **9***b* illustrate an exemplary polarization-interference-based optical control device for generating an arbitrary wavefront, and the polarization states in different pixel blocks at an output screen of the device, respectively, according to another embodiment of the invention; and

FIG. **10** schematically shows a telecentric telescope according to an aspect of the invention.

DETAILED DESCRIPTION OF A PREFERRED EMBODIMENT OF THE INVENTION

As used herein, the term 'digital binary MEMS' refers to a micro-electromechanical mirror array system that is subject only to binary (i.e., ON/OFF or 1,0) control by tilting each mirror facet to a retro-reflecting (1) position for incident light (ON position) or to an off-axis (0; tilted or OFF) reflecting position for the incident light.

The term 'amplitude' as used herein will be recognized by those skilled in the art as referring to a complex number with a real part and an imaginary part or, equivalently, with an absolute value amplitude and a phase angle, as is a well-known signal representation in the solutions of Maxwell's equations in a harmonic time-dependent formalism.

According to a first illustrative embodiment and with reference to FIGS. **2***a*-**2***c* and **3***a*-**3***c*, we disclose a novel approach to wavefront generation using binary amplitude modulation of an input plane wave. The basic problem of wavefront generation is to achieve a wavefront described by exp[iθ(x,y)], when the function θ(x,y) is specified. Using the relation

$$\exp[i\theta(x,y)]=\cos[\theta(x,y)]+e^{i\pi/2}\sin[\theta(x,y)], \quad (1)$$

we require a way to represent cos [θ(x,y)] and sin [θ(x,y)], which can then be added interferometrically with the appropriate relative phase term of $e^{i\,\pi/2}$ to generate the desired wavefront. The cosine and sine can take values in the range of [−1, 1].

A first embodiment according to the invention illustrates the generation of square-wave functions **120** that can take on bi-level values (+1,−1) using binary mirror (digital binary MEMS) devices. FIG. **2***a* shows a square-wave pattern **120** that may be used to modulate an input wavefront **105** (FIG. **2***b*). The square-wave function can take only two values: (+1),

i.e., e^{a} corresponding to a phase of θ=0 and (−1), i.e., $e^{i\theta}$ corresponding to a phase of θ=π radians. FIG. **2***b* shows a first interferometrically-based optical control component **100** for obtaining the square-wave modulation **120** of the input plane wave **105**. The input wavefront **105** is split into two equal (non-complex) amplitude parts by a first component beam divider/combiner **102** that is disposed along a first component optical path **103** of the incident wavefront. The reflected split wavefront is incident on a first component digital binary MEMS device $M1_1$. $M1_1$ comprises a mirror array **107** denoted by $(n_{x,y}\times m_{x,y})_{M1}$. The $M1_1$ optical path **109** from the beam splitter surface to $M1_1$ and back to the beam splitter surface (i.e., double pass) has an optical path length $L1_1$. The transmitted split wavefront is incident on a first component digital binary MEMS device $M2_1$. $M2_1$ comprises a mirror array **111** denoted by $(n_{x,y}\times m_{x,y})_{M2}$. In an exemplary aspect, n=m. The $M2_1$ optical path **113** from the beam splitter surface to $M2_1$ and back to the beam splitter surface has an optical path length $L2_1$. Phase retarder means **115**, in the form of a phase plate, differential optical path length or other known phase altering component or technique for producing a differential optical path ΔL1L2 equal to λ/2 (λ/4 per pass) is also shown. In the MEMS array $M1_1$, a sub array X×Y (≤n×m) of mirrors corresponding to a (+1) value (θ=0) of the square-wave are ON, whereas in the MEMS array $M2_1$, a complementary sub array of mirrors X×Y corresponding to a (−1) value (θ=π) of the square wave are ON. In an exemplary aspect, X=Y. A phase difference of π radians between the two reflected wavefront components is introduced using an extra optical path difference ΔL1L2 equal to λ/2 in the $M2_1$ optical path, which is achieved as shown in FIG. **2***b* by translating $M2_1$ by λ/4 relative to $M1_1$. However, in order to generate either cosine or sine functions as discussed above, one must be able to represent grey-scale values in terms of two levels: (+1) and (−1). This can be achieved by averaging over the sub arrays of the two levels (+1) and (−1) using a half-toning technique as described below.

Half-toning algorithms are widely used in printing devices where it is required to represent grey-scale pictures using only two levels; i.e., a black dot or a blank white space. According to the embodiment, a single grey-scale pixel in a half-toned picture consists of a dot pattern over an exemplary block (X×Y) of 3×3 or 5×5 mirrors. The grey-scale is achieved using spatial averaging over this block. Both the filling-in of the outputs of the binary mirror (0,1) and the grey-levels are accomplished simply by light propagation. The diffraction spreading distance λR/w equal to 2w, in order to have a spreading into e.g., 9 mirror segments (3×3) is easily computed, where λ is the wavelength, R is the distance and w is the pixel size. For w=10 μm and λ=0.5 μm, R=400 μm. This distance is sufficiently small so that the filling-in of the wavefront is not a problem in a practical device. When a half-toned pattern is printed on a paper and viewed by an observer, the spatial averaging is performed by the human eye. The eye, however, cannot resolve the fine dot pattern, so the printed image appears to have several levels between the black dot and the white blank.

FIGS. **3***a*-**3***c* show alternating bar pattern illustrations of half-toning for a cosine function between two levels (+1) and (−1). The optical control component **100** in FIG. **2***b* functions as an interferometer for generating a wavefront with two phase levels. The component **100** MEMS arrays $M1_1$, $M2_1$ can be controlled so that the mirror sub arrays with levels (+1) and (−1) are arranged according to a selected half-toning algorithm. FIG. **3***a* shows a cosine function. FIG. **3***b* shows a hard-thresholded version of the cosine function; i.e., the non-negative pixels in FIG. **3***a* are assigned a value of (+1), whereas the negative pixels are assigned a value of (−1). It can be seen that the grey-scale is completely lost in this simple thresholding operation. FIG. **3***c* shows a half-toned version of the cosine function using the well known Stucki half-toning algorithm. The grey-scale effect is now achieved by using spatial averaging over a block of 10 pixels implying that 11 grey-levels (0-10) are achievable in a spatial-averaged sense. The white and black pixels in FIG. **3***c* represent values of (+1) and (−1) respectively. The half-toning concept can thus be used for generating the sine and cosine functions for an arbitrary wavefront. The inventors are not aware of the prior use of the half-toning concept in the context of wavefront generation as further described below.

Using the optical control component **100** shown in FIG. **2***b*, one can obtain a half-toned version of the sine or cosine functions required for wavefront generation. The (+1) and (−1) mirror sub arrays (pixels) in the half-toned pattern are turned ON in MEMS arrays $M1_1$ and $M2_1$, respectively. The value (−1) is achieved from the path difference of λ/2 in the two arms of the component. Spatial averaging over pixel blocks is achieved simply by propagating the light over a very short distance. For a given θ(x,y), it is thus possible to generate cos [θ(x,y)] and sin [θ(x,y)] by using a control component **100** as shown in FIG. **2***b*.

FIG. **4***a* shows an interferometer-based optical control device **300**. The device **300** comprises two identical components **100** (**200**) as shown in FIG. **2***b* for generating a wavefront described by exp[iθ(x,y)]. An incoming wavefront **106** is split into two output optical wavefronts **105** by an input beam divider **302** (e.g., an X-cube). The two output optical wavefronts **105** are the input optical wavefronts to the device components **100**, **200**. One arm of the device **300** consists of a first optical control component **100** as described above. Control component **100** provides an output **120** in the form cos [θ(x,y)]. A second arm of device **300** consists of a second optical control component **200** that is essentially identical to component **100**. Component **200** includes a second component beam divider/combiner **202** disposed along a second component input optical path **203** of an input optical wavefront **105**. A second component digital binary MEMS device $M1_2$ comprising an n×m mirror array **207** denoted by $(n_{x,y}, m_{x,y})_{M1}$ is disposed optically downstream of the second beam divider/combiner component **202** along an $M1_2$ optical path **213** having a total optical path length $L1_2$. A second component digital binary MEMS device $M2_2$ comprising an n×m mirror array **211** denoted by $(n_{x,y}, m_{x,y})_{M2}$ is disposed optically downstream of the second beam divider/combiner component **202** along an $M2_2$ optical path **214** having a total optical path length $L2_2$ that is different than the $M1_2$ optical path **213**. Phase retarder means **215** are employed to make $L1_2$ different than $L2_2$. At least some sub array (X×Y) of the mirror array **207** is in an ON/OFF state and a complementary at least some similar sub array of the mirror array **211** is in an OFF/ON state. As such, component **200** functions similarly to component **100** but produces an output **220** in the form sin [θ(x,y)]. An output beam combiner **318** is disposed in output optical paths **117**, **217** to optically combine the respective cos [θ(x,y)] and sin [θ(x,y)] modulated outputs. Phase shifting means **322** disposed between beam splitter **202** and output beam combiner **318** provides a phase difference equal to π/2. The resultant output wavefront **325** expressed as $e^{i\theta(x,y)}$ thus has a different phase than the input optical wavefront by an amount θ(x,y).

FIG. **4***b* illustrates a pixel P(x,y) in an exemplary 5×5 mirror sub array (X×Y) of a MEMS component of FIG. **4***a*. At point P(x,y), the complex amplitude at point P has the form $e^{i\theta(x,y)}$ consisting of a real number (amplitude) part (cos θ) and

an imaginary (phase) part i(sin θ) making up the complex amplitude value. FIG. **4***c* is an Argand diagram representation of the complex amplitude at P(x,y) where the circumference of the circle is the locus of amplitudes and phase at position P. In the example, the real amplitude value is one.

The interferometer device **300** illustrated in FIG. **4**(*a*) may also be used to generate a complex optical wavefront having a varying absolute value of amplitude denoted by a(x,y). More precisely, the use of half-toning concepts on the sub-assemblies **100**, **200** allows one to use component **100** for the generation of a(x,y)cos θ(x,y) and, similarly, component **200** for the generation of a(x,y)sin θ(x,y), where $0 \le a(x,y) \le 1$. An output function g(x,y) can thus be obtained by combining the two outputs as follows:

$$g(x,y)=a(x,y)\exp[i\theta(x,y)]=a(x,y)[\cos\theta(x,y)+i\sin\theta(x,y)].$$

Hence, the wavefront generation device can be used to generate an optical wavefront of arbitrary absolute value amplitude and phase.

Another embodiment of the invention is directed to a device and associated method for more advanced wavefront coding, benefiting from a simplification of hardware used in the embodiment described above through the employment of a more sophisticated algorithm. According to this embodiment, one may again generate a phase function $\theta(x,y)$, $0 \le \theta(x,y) \le \alpha$, for a constant angle α, using only binary (0,1) type amplitude modulation. Thus we intend to generate an output wavefront expressed as $e^{i\theta(x,y)}$. As a first step, we convert θ(x,y) to a binary picture H(x,y), which is a two-dimensional array with either zeros or ones. Therefore, we let $\theta(x,y)=\alpha H(x,y)$ so that $e^{i\theta(x,y)}$ can be expressed as $e^{i\alpha H(x,y)}$. The exponential can be expressed in the well-known form as:

$$e^{i\alpha H(x,y)}=1+i\alpha H+[(i\alpha)^2 2!]H^2+\ldots \quad (2)$$

For $H(x,y)$ values limited to (0,1), $H^N=H$; thus (3)

$$e^{i\alpha H(x,y)} = [1-(\alpha^2/2!)H+(\alpha^4/4!)H-\ldots]+ \quad (4)$$

$$iH[\alpha-(\alpha^3/3!)+(\alpha^5/5!)-\ldots]$$

$$=(1-H)+H[1-(\alpha^2/2!)+(\alpha^4/4!)-\ldots]+ \quad (5)$$

$$iH[\alpha-(\alpha^3/3!)+(\alpha^5/5!)-\ldots]$$

$$=(1-H)+H[\cos\alpha+i\sin\alpha] \quad (6)$$

$$=(1-H)+H\exp(i\alpha) \quad (7)$$

The novel algorithm leading to equation (7) may be realized in a two-beam interferometer device. Table II shows the values taken by the two terms in right hand side of equation (7) for the two values (0,1) taken by H.

TABLE II

	(1-H)	H exp(iα)
H = 0	1	0
H = 1	0	exp(iα)

Thus if H=0, then $e^{i\alpha H}=1$ and the corresponding pixel phase is zero; and if H=1, then $e^{i\alpha H}=e^{i\alpha}$ and the corresponding pixel phase is α, where H represents a half-tone phase value obtained by turning a $MEMS_1$ sub array X×Y ON, and (1−H) represents the complement of H obtained by turning a $MEMS_2$ sub array X×Y OFF. By propagation or low-pass filtering, as is well-known to an optical engineer, one obtains an output that is an average over a block of m×m pixels. It is thus possible to obtain m^2 (e.g., 3×3 or 5×5) levels of phase between 0 to α.

The results of the novel two-level algorithm presented above may be realized by the optical control device **400** illustrated in FIG. **5**. The device **400** comprises a beam divider/combiner **402** disposed along an input optical path **403** of an incident optical wavefront **405**. Incident wavefront **405** may be a plane wave expressed as $e^{i\theta(x,y)}$ or an aberrated wavefront expressed as $e^{-i\Phi(x,y)}$. A first digital binary MEMS device M1 comprises an n×m mirror array $(n_{x,y}, m_{x,y})_{M1}$ **407** disposed optically downstream of the first component beam divider/combiner along an M1 optical path **409**. At least some sub array $(X\times Y)_{M1}$ of the mirror array is programmed to be in an ON/OFF state that provides a half-tone phase value expressed as 1−H(x,y), wherein H(x,y) represents a two-level value equal to 0 or 1 as described above. A second digital binary MEMS device M2 has an n×m mirror array $(n_{x,y}, m_{x,y})_{M2}$ **411** disposed optically downstream of the beam divider/combiner along an M2 optical path **413**. A complementary mirror sub array $(X\times Y)_{M2}$ is programmed to be in an OFF/ON state that provides a half-tone phase value expressed as H(x,y) as shown in FIG. **5**. Phase retarder means **415** are provided to obtain a controlled phase difference between the $M1_{out}$ wavefront and the $M2_{out}$ wavefront of α/2. A resultant output wavefront **421** expressed as $e^{i\alpha H}$ obtained from the interference of the $M1_{out}$ wavefront (1−H) and the $M2_{out}$ wavefront (H). The wavefront **421** thus has a phase difference from the input optical wavefront **405** by an amount αH(x,y) (equal to θ(x,y)), where $-\pi \le \alpha \le \pi$. If the input wave is an aberrated wavefront expressed as $e^{-\Phi(x,y)}$ as referred to above, then the output wavefront from device **400** will be expressed as $e^{i[\theta(x,y)-\Phi(x,y)]}$. The device operation changes the phase between the optical input and optical output by θ(x,y) radians.

An exemplary illustration is shown in FIG. **6***a*-**6***c* when H is a quadratic function (x^2+y^2) and the wavefront expression is $\exp[i\alpha(x^2+y^2)]$. FIG. **6***a* shows the profile of a continuous quadratic phase function. FIG. **6***b* shows the phase profile obtained by hard-thresholding of the FIG. **6***a* profile at a level between 0 to 2π. FIG. **6***c* shows the half-toned version of the FIG. **6***a* profile using the Stucki algorithm. In the figure, a white dot denotes phase=0; a black dot denotes phase=π radians. Grayscale effect is achieved in the half-toned FIG. **6***c* by means of spatial averaging.

FIG. **7**A illustrates an embodiment of a wavefront control device **600-1** that uses a two-level half-toning algorithm for controlled wavefront generation. Apart from adaptive optics applications, the inventors have recognized a need for a spatial phase modulation that is independent of wavelength. Potential applications may include various defense-based and space-borne interferometer systems. For example, one may need a phase front of θ(x,y) in the blue wavelengths (λ_1) and thereafter wish to generate the same phase θ(x,y) in the red portion (λ_2) of the spectrum. An interferometer-based optical control device **600-1** that supports this capability uses a modified form of an achromatic phase-shifting interferometer. In this regard, the disclosure of U.S. Pat. No. 4,786,124 is herein incorporated by reference in its entirety to the fullest allowable extent. Device **600-1** includes a diffractive, input wavefront divider/combiner **602** denoted by G1 disposed along an optical axis **603** of an input wavefront **601**. A first component diffractive wavefront divider/combiner **607** denoted by G2 is disposed to optically intercept a positive **609** (or a negative **611**) n^{th}-order output beam from the input wavefront divider/combiner **602**. In an exemplary aspect, a first-order diffractive beam from G1 is incident on G2 (and as described below, a negative first-order diffractive beam from G1 is incident on

G3). A first component digital binary MEMS device **612** denoted by M1 is disposed optically downstream of the first beam divider/combiner component along an M1 optical path **615** providing an optical path length (double pass) of L2. M1 comprises an n×m mirror array $(n_{x,y}, m_{x,y})_{M1}$ **613** (not shown). The mirror array includes a mirror sub array (X×Y<n×m) that is in a selected ON/OFF state to provide a two-level half-tone phase value H(x,y), where 0≤H≤1. According to an illustrative aspect, H(x,y) has the values (0,1). A second component diffractive wavefront divider/combiner **617** denoted by G3 is disposed to optically intercept the negative first-order output beam **611** from the input wavefront divider/combiner **602**. A second component digital binary MEMS device **622** denoted by M2 is disposed optically downstream of the second beam divider/combiner component along an M2 optical path **625** providing an optical path length (double pass) of L3. M2 comprises an n×m mirror array $(n_{x,y}, m_{x,y})_{M2}$ **623** (not shown). The mirror array includes a mirror sub array (X×Y<n×m) that is in a selected complementary OFF/ON state that provides a two-level half-tone phase value (1−H(x,y)), where 0≤(1−H)≤1 (e.g., H=0,1). Optical component **630** is provided to in-couple the input wavefront **601** and out-couple the resultant output wavefront **645**. In a particular aspect, G1, G2 and G3 are diffraction gratings each having a grating period Λ. G2 is displaced transversely a distances d relative to G3, where 0≤d<Λ, to provide a phase shift a/2 between the two arms of the device. For achromatic operation, L2 is equal to L3. The device **600-1** provides a resultant output wavefront **645** expressed as $e^{i\alpha H(x,y)}$ with a controlled phase αH(x,y) that is different than the input wavefront phase. The device **600-1** and operation thereof may have further potential application for phase correction in sparse-aperture telescope systems.

FIG. **7B** illustrates another embodiment of a wavefront control device **600-2**, similar to control device **600-1**, that uses a three-level half-toning algorithm for controlled, arbitrary wavefront generation. The inventors recognize the need for a wavefront control device that can generate an arbitrary wavefront a(x,y) exp[iθ(x,y)]. A wavefront control device **600-2** as illustrated in FIG. **7B** is based on a novel algorithm that provides a three-level interferometric binary structure derived as follows. It is possible to write identities for expressing phase in terms of amplitude modulation when more than two levels are used to obtain θ(x,y) values spanning the whole complex plane. For example, for a three-level algorithm in which each pixel in H(x,y) can take three values, e.g., (0, ½, 1), the wavefront can be represented as follow:

$$\exp[i\alpha H(x,y)]=[1-3H+2H^2]+4[H-H^2]\exp(i\alpha/2)+[-H+2H^2]\exp(i\alpha). \quad (8)$$

It is thus possible to express phase as a sum of polynomials in H(x,y) with appropriate phase. Table III shows the values taken by the three terms on the right hand side of equation (8) for the three values (0, ½, 1) taken by H.

TABLE III

	$1 - 3H + 2H^2$	$4[H - H^2]\exp(i\alpha/2)$	$[-H + H^2]\exp(i\alpha)$
H = 0	1	0	0
H = 1/2	0	exp(iα/2)	0
H = 1	0	0	exp(iα)

This algorithm can be embodied by the grating-based interferometer device **600-2** illustrated in FIG. **7A**. The device will be capable of generating an arbitrary wavefront a(x,y) exp[iθ(x,y)] using all-digital binary MEMS as disclosed herein. As shown, the input beam **601** is split by grating **602** (denoted by G1) into three beams: a zero-order beam **635** and ±1st-order beams **609**, **611**. The three beams **635**, **611** and **609** have respective two-way or total phase delays of 0, α/2 and α. As illustrated, the path lengths of the three beams have been made balanced or of equal length. The reflected beams from the new MEMS **640** (denoted now by M1) and MEMS **612** (M2) and **622** (M3) are combined at grating **602** (G1) and directed by the beam splitter **630** to provide an arbitrary wavefront a(x,y) exp[iθ(x,y)]. As described herein, appropriate half-toning techniques are used to generate the required absolute amplitude a(x,y).

Another embodiment of the invention directed to a polarization-based optical control device and method will now be described in relation to FIGS. **8**, **9***a* and **9***b*. The current embodiment allows output wavefront phase control through polarization modulation of the incoming wavefront. An explanation of the meaning of phase difference between two beams in different states of polarization will aid in illustrating the exemplary embodiment presented below.

With reference to the illustrative system **800** in FIG. **8**, consider an incoming plane polarized beam **805** having polarization axes x, y as shown split in two parts L1, L2 by a beam-splitter **802**. The two beams L1, L2 pass through respective birefringent media **807**, **817** (e.g., a series of quarter or half-wave plates) having some relative orientation difference, which are located in plane I. The two beams acquire distinct states of elliptical polarization expressed as $E_1=a_1x+b_1e^{i\Phi 1}y$ and $E_2=a_2x+b_2e^{i\Phi 2}y$ at observation plane II. It can be assumed that the two beams gain the same phase due solely to their propagation. However, the two beams have a relative phase difference between them from the change in polarization state. A simple criterion for the phase difference between two beams in two different polarization states is as follows: if the two beams in distinct polarization states described by vectors E_1 and E_2 are interfered, the resultant intensity is given by:

$$I_{12}=|E_1|^2+|E_2|^2+2|E_1||E_2|\cos\phi_{12} \quad (8)$$

The phase between the two polarization states is ϕ_{12} as seen from the cross-term. According to the instant embodiment, half-toning algorithms can be employed to generate variable polarization states across the transverse cross section of the wavefront.

An exemplary case is illustrated with reference to optical control device **900** in FIG. **9***a*. An incident plane wave P(x,y) **905** polarized at 45° is split into two polarization states P1, P2 by a polarizing beam splitter **902** disposed along optical axis **903**. A first digital binary MEMS device **910** denoted by M1 is disposed optically downstream of the polarizing beam splitter **902** along an M1 optical path **909**. M1 comprises an n×m mirror array $(n_{x,y}, m_{x,y})_{M1}$ **907** in which a mirror sub array X×Y (<n×m) is in a selected ON/OFF state that provides P1 with a half-tone phase value represented as (1−H), where 0≤(1−H)≤1. A second digital binary MEMS device **912** denoted by M2 is disposed optically downstream of the polarizing beam splitter **902** along an M2 optical path **913**. M2 comprises an n×m mirror array $(n_{x,y}, m_{x,y})_{M2}$ **911**, in which a complementary mirror sub array X×Y (<n×m) is in a selected complementary OFF/ON state that provides P2 with a half-tone phase value H, where 0≤H≤1. The reflected wavefronts P1, P2, each having passed twice through a quarter wave plate so as to couple efficiently through the beam combiner/divider, are optically combined by the polarizing beam splitter **902** to produce a resultant output wavefront **920** propagating along an output optical wavefront path **917**.

FIG. **9***b* illustrates the polarization states **950** in two representative individual pixel blocks **960**, **965** corresponding to

two illustrative 2×2 mirror sub arrays **970**, **975**. The two orthogonal polarization states x, y will not exhibit any interference as the corresponding cross-term in equation (7) would be zero. However, averaging over the pixel blocks **960**, **965** gives rise to a gray-scale in polarization state. For example, block **960** can be characterized by $E_1=2x+2y$; block **965** can be characterized by $E_2=3x+1y$. Pixels in the averaged or low-pass filtered wavefront thus have a polarization state in between two orthogonal states used for half-toning. In FIG. **9***b*, the two pixel blocks can thus acquire a phase difference ϕ_{12} as given in equation (8), which can be used for phase correction in adaptive imaging applications. While a simple illustration of two orthogonally polarized components without any additional phase terms has been presented, a person skilled in the art will appreciate that more general realizations involving two elliptical polarization levels for half-toning are also possible. Moreover, a person skilled in the art will recognize that this embodiment, which has been described for the generation of the wavefront $\exp[i\theta(x,y)]$, may be employed to generate an arbitrary wavefront $a(x,y)\exp[i\theta(x,y)]$ by appropriate algorithmic control of the half-toning process as described above.

The embodiments described above disclose various digital binary MEMS mirror array configurations for phase front coding. The device and method embodiments have current and prospective widespread applicability to various adaptive optical systems, including, for example, those used in defense related atmospheric compensation and in laser fusion.

FIG. **10** depicts the use of a telecentric telescope **1000** with an illustrative digital binary MEMS device **1010** according to an embodiment of the invention. As shown in the figure, an output wavefront **1020** is generated in plane I by the device **1010**. If desired, the output plane can be optically shifted downstream to plane III. This may be achieved by inserting the telecentric telescope **1000** between planes I and III as shown. The size D of the aperture **1030** in plane II controls the size (X×Y) of the mirror sub-array over which the spatial averaging is performed in order to realize the desired half-toning effects described above.

Having thus described the various embodiments of the invention, it will be apparent to those skilled in the art that the foregoing detailed disclosure is presented by way of example only and thus is not limiting. Various alterations, improvements and modifications recognized by those skilled in the art, though not expressly stated herein, may be made and are intended to be within the spirit and scope of the claimed invention. Additionally, the recited order of processing elements or sequences, or the use of numbers, letters, or other designations, is not intended to limit the claimed processes to any order except as may be specified in the claims. Accordingly, embodiments of the invention are limited only by the following claims and equivalents thereto.

REFERENCES

The subject matter disclosed in the following citations is herein incorporated by reference in their entireties to the fullest extent allowed by applicable laws and rules.

D. Dudley, W. Duncan, J. Slaughter, "Emerging digital micromirror device (DMD) applications", SPIE 4985, 14 (2003).

H. W. Babcock, "The possibility of compensating astronomical sensing", Publ. Astron. Soc. Pac. 65, 229 (1953).

F. Roddier, "Effects of atmospheric turbulence in optical astronomy", *Progress in Optics*, E. Wolf (Ed.), vol. 19, 281 (1981).

R. K. Tyson, *Principles of Adaptive Optics*, (Academic press) (1998).

M. C. Roggemann and B. M. Welsh, *Imaging through the atmosphere*, (CRC press) (1996).

M. C. Roggemann, B. M. Welsh, R. Q. Fugate, "Improving the resolution of ground based telescopes", Rev. Mod. Phys. 69, 437 (1997).

F. Roddier (Ed.), *Adaptive optics in astronomy*, (Cambridge Univ. Press), (1998).

T. Weyrauch, M. A. Vorontsov, "Atmospheric compensation with a speckle beacon in strong scintillation conditions: directed energy and laser communication applications", Appl. Opt. 44, 6388 (2005).

M. A. Vorontsov, M. Yu, "Compensation of distant phase-distorting layers" Part I & II, J. Opt. Soc. Am. A 21, 1645, 1659 (2004).

M. A. Vorontsov, E. W. Justh, L. A. Beresnev, "Adaptive optics with advanced phase-contrast techniques", Part I & II, J. Opt. Soc. Am. A 18, 1289, 1300 (2001).

Doble, N., Yoon, G. Y., Chen, L., Bierden, P., Singer, B., Olivier, S., Williams, D. R., "Use of a microelectromechanical mirror for adaptive optics in the human eye", Optics Letters 27, 1537 (2002).

Roorda, A. Williams, D. R. (2000) "Adaptive Optics and Retinal Imaging", OSA Trends in Optics and Photonics Vol. 35, Vision Science and its Applications, Vasudevan Lakshminarayanan, Ed. (Optical Society of America, Washington, D.C.) 151-162.

D. T. Gavel, E. L. Gates, C. E. Max, S. S. Oliver, B. Bauman, D. Pennington, B. Macintosh, J. Patience, C. Brown, P. Danforth, R. Hurd, S. Severson, J. Lloyd, "Recent science and engineering results with the laser guide star adaptive optics system at Lick observatory", Proc. SPIE 4839, 354 (2003).

Laboratory for Laser Energetics, Annual Report 2005, DOE/SF/19460-646,

Inertial Fusion Program and National Laser Users' Facility Program, January 2006.

C. E. Max, Adaptive Optics course material, <www.ucolick.org/~max/298C>

E. N. Ribak, "Deformable mirrors", in *Adaptive Optics for Astronomy*, D. Alloin and J. M. Mariotti, (Ed.), Kluwer, Boston (1994).

T. Bifano, R. K. Mali, J. Dorton, J. Perreault, N. Vandelli, M. Horenstein, D. Castanon, "Continuous membrane surface micromachined silicon deformable mirrors", Opt. Engg. 36, 1354 (1997).

W. D. Cowan, M. K. Lee, B. M. Welsh, V. M. Bright, M. C. Roggemann, "Surface micromachined segmented mirrors for adaptive optics", IEEE Journal of Selected Topics in Quantum Electronics 5, 90 (1999).

Weyrauch, T., Vorontsov, M. A., Bifano, T. G., Giles, M. K., "Adaptive Optics Systems with Micromachined Mirror Array and Stochastic Gradient Descent Controller". Proc. SPIE 4124, High-Resolution Wavefront Control: Methods, Devices, and Applications., August 2000.

J. A. Perreault, T. G. Bifano, B. M. Levine, M. N. Horenstein, "Adaptive optic correction using micromechanical deformable mirrors", Opt. Eng. 41, 561 (2002).

R. Ulichney, *Digital Halftoning*, MIT Press (1988).

N. George and T. Stone, Opt. Comm. 67, 185 (1988).

N. George and S. Radic, "Photomixing of achromatically frequency-modulated incoherent light", Opt. Lett. 18, 1038 (1993).

S. Pancharatnam, "Generalized theory of interference and its applications", Proc. Indian Acad. Sci. A44, 261 (1956).

R. Bhandari, "Polarization of light and topological phases", Phys. Rep. 182, 1 (1997).

Z. Bomzon, G. Biener, V. Kleiner, E. Hasman, "Space-variant Pancharatnam-Berry phase elements with computer generated sub-wavelength gratings", Opt. Lett. 27, 1141 (2002).

F. S. Roux, "Geometric phase lens", J. Opt. Soc. Am. A 23, 476 (2006).

K. Khare and N. George, "Direct coarse-sampling of electronic holograms", Opt. Lett. 28, 1004 (2003).

K. Khare and N. George, "Sampling theory approach to prolate spheroidal wave functions", J. Phys. A: Math. & General 36, 10011 (2003).

K. Khare and N. George, "Fractional finite Fourier transform", J. Opt. Soc. Am.: A 21, 1179 (2004).

K. Khare and N. George, "Sampling theory approach to eigenwavefronts of imaging systems", J. Opt. Soc. Am.: A 22, 434 (2005).

K. Khare, "Bandpass sampling and bandpass analogues of prolate spheroidal functions", Signal Processing, (2006), (accepted in press).

K. Khare, "Sampling theorem, bandlimited integral kernels and inverse problems", to be submitted to Inverse Problems.

We claim:

1. An optical control component, comprising:

a first component beam divider/combiner disposed along a first component input optical path of an incident optical wavefront;

a first component binary MEMS device $M1_1$ comprising an $(n_{x,y} \times m_{x,y})_{M1}$ mirror array disposed optically downstream of the first component beam divider/combiner along an M1 optical path having a total optical path length $L1_1$;

a first component binary MEMS device $M2_1$ comprising an $(n_{x,y} \times m_{x,y})_{M2}$ minor array disposed optically downstream of the first component beam divider/combiner along an $M2_1$ optical path different than the $M1_1$ optical path having a total optical path length $L2_1$; and

phase retarder means for making $L1_1$ different than $L2_1$, wherein an at least one $M1_1$ sub array $(XxY)_{M2}$ is in an ON/OFF state and a complementary an at least one $M2_1$ sub array $(XxY)_{M2}$ is in an OFF/ON state, further wherein an output wavefront propagating along a first component output optical wavefront path has a controlled modulation.

2. The component of claim **1**, wherein $L1_1$ is different than $L2_1$ by an amount $\Delta_1 L1L2$, where $0 < \Delta_1 L1L2 \leq (2n+1)\lambda/2$, where $n=0, 1, 3, \ldots$, so as to provide a phase shift $\leq \pi$ radians.

3. The component of claim **1**, wherein X=Y and n=m.

4. The component of claim **1**, wherein the M1 sub array $(XxY)_{M1}$ in an ON/OFF state and the complementary M2 sub array $(XxY)_{M2}$ in the OFF/ON state are each one or more cluster arrays XxY <nxm, further wherein each cluster array XxY is characterized by at least a two level half-toning phase approximation.

* * * * *

INDEX

TABLE OF CONTENTS FOR VOLUMES I THROUGH V

CHRONOLOGICAL LISTING OF TITLES

VOLUME I: DIFFRACTION THEORY & ELECTRONIC IMAGING SYSTEMS

"Spectral Coincidences Between Emission Lines of the CO Laser and Absorption Lines of Nitrogen Oxides," IEEE J. Quantum Electronics **6**, Dec. (1970), R.T. Menzies, Nicholas George, and M.L. Bhaumik. 1

"Use of CO Laser Lines to Detect Oxides of Nitrogen in the Atmosphere," J. Opt. Soc. Am. **60**, 1550A (1970), R.T. Menzies and Nicholas George. 1

"Intensity-Induced Changes in Optical Polarization in Glasses," Phys. Rev. B. Jan 15, 1972, Adelbert Owyoung, R.W. Hellwarth, and Nicholas George. 1

"Origin of the Nonlinear Refractive Index of Liquid CCl_4," Phys. Rev. A **4**, 2342 (1971), R.W. Hellwarth, Adelbert Owyoung, and Nicholas George 1

"The Space Bandwidth Product of Multichannel Coherent Processors," J. Opt. Soc. Am. **62**, 1366A (1972), R.B. MacAnally and Nicholas George. 1

"Detection of Mode-Locked Laser Signals," Optics Communications **5**, 407 (1972), R.J. D'Orazio and Nicholas George. 1

"Diffraction of Laguerre Gaussian Beams by an Aperture," J. Opt. Soc. Am. **62**, 1119 (1972), A.C. Livanos and Nicholas George. 1

"Matched-Filter Detection of Mode-Locked Laser Signals," Applied Optics **12**, 2367 (1973), R.J. D'Orazio and Nicholas George. 1

"Matched Filter Detection of Mode-Locked Laser Signals," in **Space Optics** edited by B.J. Thompson and R.R. Shannon, ICO IX Conference Proc. (National Academy of Sciences, Washington, D.C., 1974), 461-475. 1

"Edge Diffraction of a Convergent Wave," Applied Optics **14**, 608 (1975), A.C. Livanos and Nicholas George. 1

"A Profile: The Teaching of Optics by the Faculty of The Institute of Optics," IEEE Trans. on Education, May 1980, Nicholas George and Karin Strand. 1

"Image reconstruction from partial Fresnel zone information," Appl. Opt. **25**, pp. 178-183, 1986, Robert Rolleston and Nicholas George. 1

"Polarization and Wavelength Effects on the Scattering From Dielectric Cylinders," Appl. Opt. **24**, pp. 4141-4145, 1985, M.A.G. Abushagur and Nicholas George. 1

"Stationary phase approximations in Fresnel zone magnitude-only reconstructions," JOSA A **4**, pp. 148-153, 1987, Robert Rolleston and Nicholas George. 1

"Diffraction from a small square aperture: approximate aperture fields," JOSA A **5**, pp. 192-199, 1988 R. Edward English,Jr. and Nicholas George. 1

"Diffraction from a circular aperture: on-axis field strength," Appl. Opt. **26**, pp. 2360-2366, 1987, R. Edward English, Jr. and Nicholas George. 1

"Diffraction patterns in the shadows of disks and obstacles," Appl. Opt. **27**, pp. 1581-1587, 1988, R. Edward English, Jr. and Nicholas George. 1

"Comparison of wavelength scanning and pulse echo systems in remote sensing," Opt. Comm. **77**, pp. 91-98, 1990, Donald J. Schertler and Nicholas George. 1

"Beam splitter cube for white-light interferometry," Opt. Eng. **31**, pp. 2191-2196, 1992, Keith B. Farr and Nicholas George. 1

"Photomixing of achromatically frequency-modulated incoherent light," Opt. Lett. **18**, pp. 1038-1040, 1993, Nicholas George and Stojan Radic. 1, 2

"A case study: Dual-use technologies and University Research Initiatives," Army RD & A Bull. **PB 70-93-6**, pp. 19-23, 1993, Nicholas George, B.D. Guenther, and Vincent Piarulli. 1

"Novel centering method for overlapping correction in halftoning," IS&T's 47th Annual Conference/ICPS 1994, pp. 483-486, 1994, Shen-ge Wang, Keith T. Knox, and Nicholas George. 1

"Controlled blurring in image processing," IS&T's 47th Annual Conference/ICPS 1994, pp. 534-535, 1994, Brian J. Stossel and Nicholas George. 1

"Ultrafast pulse propagation in periodic optical media: a generalized finite-difference time-domain approach," Opt. Lett. **19**, pp. 1064-1066, 1994, Stojan Radic and Nicholas George. 1

"Holographic contouring using tunable lasers," Opt. Lett. **19**, pp. 1879-1881, 1994, Nicholas George and Wenjun Li. 1, 2

"$\lambda/4$-shifted nonlinear periodic structure: theory of low-intensity switching," International Symposium on Guided-Wave Optoelectronics, Weber Research Institute, 26-28 October, 1994, New York, New York, Stojan Radic, Nicholas George, and Govind P. Agrawal. 1

"Optical switching in $\lambda/4$-shifted nonlinear periodic structures," Opt. Lett. **19**, pp. 1789-1791, 1994, Stojan Radic, Nicholas George, and Govind P. Agrawal. 1

"Nonlinear DFB phase-shifted structure: all-optical, low-intensity switching device," LEOS '94 7th Annual Meeting, Conference Proceedings **2**, pp. 61-62, 1994, Boston, Stojan Radic, Nicholas George, and Govind P. Agrawal. 1

"Analysis of nonuniform nonlinear distributed feedback structures: generalized transfer matrix method," J. Quantum Electron. **31**, pp. 1326-1336, 1995, Stojan Radic, Nicholas George, and Govind P. Agrawal. 1

"Generalized distributed feedback design: amplification, filtering, and switching," in *Physics and Simulation of Optoelectronic Devices III,* Proc. SPIE **2399**, pp. 37-48, 1995, Stojan Radic, Nicholas George, and Govind P. Agrawal. 1

"Theory of low-threshold optical switching in nonlinear, phase-shifted, periodic structures," J. Opt. Soc. Am. B **12**, pp. 671-680, 1995, Stojan Radic, Nicholas George, and Govind P. Agrawal. 1

"Low-threshold optical switching in non-uniform nonlinear distributed feedback structures," Optics & Photonics News **6**, pp. 18-19 1995, Stojan Radic, Nicholas George, and Govind Agrawal. 1

"Multiple point impulse responses: controlled blurring and recovery," Opt. Comm. **121**, pp. 156-165, 1995, Bryan J. Stossel and Nicholas George. *Erratum*, Opt. Comm. **122**, p. 212, 1996. 1

"Lensless electronic imaging, "Opt. Comm. **133**, pp. 22-26,1997, Nicholas George. 1

"Theory for the propagation of short electromagnetic pulses," Opt. Comm. **133**, pp. 1-6, 1997, Nicholas George and Stojan Radic. 1

"The Center for Electronic Imaging Systems: Imaging in the Information Age," Proc. International Conference on Engineering Education, Rio de Janeiro, 1998, C.N. George and Nicholas George. 1

"Electronic imaging using a logarithmic asphere," Opt. Lett. **26**, pp. 875-877, 2001, Wanli Chi and Nicholas George. 1

"Direct sampling and demodulation of carrier-frequency signals," Opt. Comm., 2002, Kedar Khare and Nicholas George. 1

VOLUME II: HOLOGRAPHY

"Index variation and scattering in a holographic medium," Proc. Soc. Photo-Opt. Instr. Eng., **1136**, 1989, Thomas Stone, Nicholas George, and B.D. Guenther. 2

"Photomixing of achromatically frequency-modulated incoherent light," Opt. Lett. **18**, pp. 1038-1040, 1993, Nicholas George and Stojan Radic. 1, 2

"Holographic contouring using tunable lasers," Opt. Lett. **19**, pp. 1879-1881, 1994, Nicholas George and Wenjun Li. 1, 2

"Uniform scattering patterns from grating-diffuser cascades for display applications," Appl. Opt. **38**, pp. 291-303, 1999, D.J. Schertler and Nicholas George. 2, 3

VOLUME III: SPECKLE & STATISTICAL OPTICS

TITLE	SECTION
"Spatial Distribution of Thermal Radiation at Microwave Frequencies," California Institute of Technology, Ph.D. dissertation (1959), Nicholas George.	1, 3
"Radiation Patterns of a Noise-Excited Thin Slot," IRE-PGMTT **8**, 116 (1960), Nicholas George.	1, 3
"Speckle in Microscopy," Optics Communications **6**, 253 (1972), Nicholas George and Atul Jain.	3
"Speckle Reduction Using Multiple Tones of Illumination," Applied Optics **12**, 1202 (1973), Nicholas George and Atul Jain, and abstract in J. Opt. Soc. Am. **62**, 1356A (1972).	3
"The Wavelength Diversity of Speckle," SPIE Jour. Dev. in Laser Technology **17**, 150 (1973), Nicholas George and Atul Jain.	3
"Space and Wavelength Dependence of Speckle Intensity," Applied Physics **4**, 201 (1974), Nicholas George and Atul Jain.	3
"Speckle, Diffusers, and Depolarization," Applied Physics **6**, 65 (1975), Nicholas George, Atul Jain, and R.D.S. Melville.	3
"Experiments on the Space and Wavelength Dependence of Speckle," Applied Physics—Invited Paper **7**, 157 (1975), Nicholas George, Atul Jain, and R.D.S. Melville.	3
"Speckle From a Cascade of Two Diffusers," Optics Communications **15**, 71 (1975), Nicholas George and Atul Jain.	3
"Speckle," Optics News **14**, January 1976, Nicholas George.	3
"The Wavelength Sensitivity of Back-Scattering," Optics Communications **16**, 328 (1976), Nicholas George.	3
"Remote sensing of large roughened spheres," Optica Acta **23**, 367 (1976), Nicholas George, A.C. Livanos, J.A. Roth, and C.H. Papas.	3
"Speckle Noise and Object Contrast," article in **Image Analysis and Evaluation** edited by R. Shaw, SPSE Conference Proc. (SPSE, Washington, D.C. 1977), 202, B.D. Guenther, Nicholas George, C.R. Christensen, J.S. Bennett.	3
"Scattering by Glass Microballoons," J. Opt. Soc. Am. **66**, 1135A (1976), Nicholas George.	3

"Topical issue on speckle," J. Opt. Soc. Am. **66**, 1316 (1976), Nicholas George and Douglas C. Sinclair. 3

"Speckle Noise in Displays," J. Opt. Soc. Am. **66**, 1282 (1976), Nicholas George, C.R. Christensen, J.S. Bennett, B.D. Guenther. 3

"Speckle from Rough Moving Objects," J. Opt. Soc. Am. **66**, 1182 (1976), Nicholas George. 3

"Laser Propagation Experiments Using a Controlled Turbulent Gaseous Mixture," J. Opt. Soc. Am. **67**, 1375A (1977), and **69**, 1435A (1979) Nicholas George and Lambertus Hesselink. 3

"Object Detectability in Speckle Noise," Conference on Lasers, 1978, pp. 637-645, C.R. Christensen, B.D. Guenther, J.S. Bennett, Anil Jain, Nicholas George, Adam Kozma. 3

"Diffraction by serrated apertures," J. Opt. Soc. Am. **70**, 6-17 (1980), Nicholas George and G.M. Morris. 3

"Matched filtering using band limited illumination," Opt. Lett. **5**, pp. 202-204 (1980), G.M. Morris and Nicholas George. 3, 4

"Space and wavelength dependence of a dispersion-compensated matched filter," Appl. Opt. **19**, pp. 3843-3850 (1980), G.M. Morris and Nicholas George. 3, 4

"Frequency-plane filtering with an achromatic optical transform," Opt. Lett. **5**, pp. 446-448 (1980), G.M. Morris and Nicholas George. 3, 4

"Optical matched filtering in noncoherent illumination," invited paper in **Current Trends in Optics**, ed. by F.T. Arecchi and F.R. Aussenegg, Taylor and Francis, London, 1981, Nicholas George and G.M. Morris. 3, 4

"Matched filtering in white light illumination," Proc. of SPIE, **388**, 11-22, 1983, Nicholas George and G.M. Morris. 3, 4

"Cosinusoidal transforms in white light," Appl. Opt. **23**, 700-710, 1984, Nicholas George and Shen-ge Wang. 3, 4

"Fresnel zone transforms in spatially incoherent illumination," Appl. Opt. **24**, pp. 842-850, 1985, Shen-ge Wang and Nicholas George. 3, 4

"About speckle," SPIE Proceedings of International Speckle Conference, Vol. 556, pp. 8-27, San Diego, 1985, Nicholas George, reprinted as "Speckle at various planes in an optical system," Opt. Eng. **25**, pp. 754-764, 1986. 3

"Diffuser transmission functions and far-zone speckle patterns," SPIE Proceedings of International Speckle Conference, Vol. 556, pp. 63-69, San Diego 1985, Lyle Shirley and Nicholas George. 3

"Speckle at various planes in an optical system," Opt. Eng. **25**, 754-764, 3

1986, Nicholas George.

"Wide-angle diffuser transmission functions and far-zone speckle," JOSA A **4**, pp. 734-745, 1987, Lyle G. Shirley and Nicholas George. 3

"Diffraction analysis of rough reflective surfaces," Appl. Opt. **26**, pp. 2364-2375, 1987, Karen Allardyce and Nicholas George. 3

"Diffuser radiation patterns over a large dynamic range," Appl Opt.**27**, pp. 1850-1861, 1988, Lyle G. Shirley and Nicholas George. 3

"Speckle from a cascade of two thin diffusers," JOSA A **6**, pp. 765-781 (1989), Lyle G. Shirley and Nicholas George. 3

"Radiated spectrum from two partially correlated dipoles," JOSA A **6**, pp. 1150-1155 (1989), Avshalom Gamliel and Nicholas George. 3

"Features in the optical transform of serrated apertures and discs," J. Opt. Soc. Am. A **6**, pp.1815-1826, 1989, Madeleine Beal and Nicholas George. 3

"Correlation Theory of Electromagnetic Radiation Using Multipole Expansions," in **Recent Advances in Electromagnetic Theory**, (Springer-Verlag, Berlin, 1990), pp. 144-182, Nicholas George and Avshalom Gamliel. 3

"Particle sizing by inversion of the optical transform pattern," Appl. Opt. **30**, pp. 4786-4794, 1991, Scott D. Coston and Nicholas George. 3

"Recovery of particle size distributions by inversion of the optical transform intensity," Opt. Lett. **16**, pp. 1918-1920, 1991, Scott D. Coston and Nicholas George. 3

"Speckle observation of pulsed laser-induced dynamics in a guest-host smectic A liquid crystal system," Liq. Crystals **12**, pp. 689-696, 1992, M.J. Guardalben and Nicholas George. 3

"Backscattering cross section of a tilted, roughened disc," J. Opt. Soc. Am. A, **9**, pp. 2056-2066, 1992, Donald J. Schertler and Nicholas George. 3

"Roughness determination by speckle-wavelength decorrelation," Opt. Lett., **18**, pp. 391-393, 1993, Donald J. Schertler and Nicholas George. 3

"The backscattering cross section of a roughened sphere," J. Opt. Soc. Am. A **11**, pp. 2286-2297, 1994, Donald J. Schertler and Nicholas George. 3

"Uniform scattering patterns from grating-diffuser cascades for display applications," Appl. Opt. **38**, pp. 291-303, 1999, D.J. Schertler and Nicholas George. 2, 3

VOLUME IV: AUTOMATIC OBJECT RECOGNITION

TITLE	SECTION
"Diffraction Pattern Sampling for Real-Time Pattern Recognition," J. Opt. Soc. Am. **62**, 1380A (1972), Nicholas George, J.T. Thomasson, and Niels Jensen.	4
"Diffraction Pattern Sampling for Recognition and Metrology," Proceedings of the Technical Program, SPIE Electro-Optical Systems Division Conference, 494-503 (Industrial and Scientific Conference Management, Chicago, 1975), Nicholas George and H.L. Kasdan.	4
"Measuring Tiny Gaps Using Diffraction Pattern Sampling," Proc. of 1976 International Optical Computing Conference, Capri, Nicholas George and H.L. Kasdan.	4
"Linewidth Measurement by Diffraction Pattern Analysis," Proc. of the Technical Program, SPIE Electro-Optical Systems Division Conference, **80**, 54, H.L. Kasdan and Nicholas George.	4
"Measurement of Optical Fiber Diameter Using the Fast Fourier Transform," Appl. Opt. **19**, pp. 2031-2033 (1980), M.A.G. Abushagur and Nicholas George.	4
"Matched filtering using band limited illumination," Opt. Lett. **5**, pp. 202-204 (1980), G.M. Morris and Nicholas George.	3, 4
"Space and wavelength dependence of a dispersion-compensated matched filter," Appl. Opt. **19**, pp. 3843-3850 (1980), G.M. Morris and Nicholas George.	3, 4
"Frequency-plane filtering with an achromatic optical transform," Opt. Lett. **5**, pp. 446-448 (1980), G.M. Morris and Nicholas George.	3, 4
"Optical matched filtering in noncoherent illumination," invited paper in **Current Trends in Optics**, ed. by F.T. Arecchi and F.R. Aussenegg, Taylor and Francis, London, 1981, Nicholas George and G.M. Morris.	3, 4
"Matched filtering in white light illumination," Proc. of SPIE, **388**, 11-22, 1983, Nicholas George and G.M. Morris.	3, 4
"Cosinusoidal transforms in white light," Appl. Opt. **23**, 700-710, 1984, Nicholas George and Shen-ge Wang.	3, 4
"Fresnel zone transforms in spatially incoherent illumination," Appl. Opt. **24**, pp. 842-850, 1985, Shen-ge Wang and Nicholas George.	3, 4
"Sine-cosine cascade correlator with real-valued filters," Opt. Lett. **12**, pp. 383-385, 1987, Shen-ge Wang and Nicholas George.	4

"Pattern recognition using the ring-wedge detector and neural-network software," Proc. Soc. Photo-Opt. Instr. Eng., **1134**, 1989, Nicholas George, Shen-ge Wang, and D.L. Venable. 4

"Recognition of threaded objects by spatial spectrum analysis," Appl. Opt. **30**, pp. 1379-1387, 1991, B.J. Stossel and Nicholas George. 4

"Neural networks applied to diffraction pattern sampling," Appl. Opt. **33**, pp. 3127-3134, 1994, Nicholas George and Shen-ge Wang. 4

"Automatic image quality assessment," IS&T's 47th Annual Conference ICPS 1994, pp. 436-438, 1994, David M. Berfanger and Nicholas George. 4

"Infrared target simulation and recognition," 1994 IEEE Dual Use Technologies and Applications Conference, 23-26 May 1994, SUNY Institute of Technology, Utica/Rome, New York, Andreas E. Savakis and Nicholas George. 4

"Prototype of a flexible image recognition system," 1994 IEEE Dual Use Technologies and Applications Conference, 23-26 May 1994, SUNY Institute of Technology, Utica/Rome, New York, Alexander D. Mirzaoff and Nicholas George. 4

"All-digital ring-wedge detector applied to fingerprint recognition," Appl. Opt. **38**, pp. 357-369, 1999, D.M. Berfanger and Nicholas George. 4

"All-digital ring-wedge detector applied to automatic image quality assessment," Appl. Opt. **39**, pp. 4080-4097, 2000 D.M. Berfanger and Nicholas George. 4

VOLUME V: PUBLICATIONS 2000-2014

TITLE

"All digital ring-wedge detector applied to automatic image quality assessment," Appl. Opt. **39**, pp. 4080-4097, 2000, D.M. Berfanger and Nicholas George.

"Electronic imaging using the logarithmic asphere," Opt. Lett. **26**, No. 12, pp. 875-877, 2001, Wanli Chi and Nicholas George.

"Direct sampling and demodulation of carrier-frequency signals," Opt. Comm. **211**, pp. 85-94, 2002, Kedar Khare and Nicholas George.

"Holographic interference filters for infrared communications," Appl. Opt. **42**, No. 7, pp. 1203-1210, 2002, Damon W. Diehl and Nicholas George.

"Extended depth of field with the logarithmic asphere," Opt. & Photonics News, Dec. 2002, Wanli Chi and Nicholas George.

"Sampling, demodulation and phase retrieval," Opt. & Photonics News, Dec. 2002, Kedar Khare and Nicholas George.

"Direct coarse sampling of electronic holograms," Opt. Lett. **28**, No. 12, pp. 1004-1006, 2003, Kedar Khare and Nicholas George.

"Extended depth of field using the logarithmic asphere," J. Optics A, **5**, pp. S157-S163, Special Issue: Optics for the Quality of Life, 2003, Nicholas George and Wanli Chi.

"Fourier optical analysis of gradient-index array imaging," Appl. Opt., **42**, No. 22, pp. 4434-4444, 2003, Xi Chen and Nicholas George.

"Sampling theory approach to prolate spheroidal wave functions, " Journal of Physics A, **36**, pp. 10011-10021, September 2003, Kedar Khare and Nicholas George.

"Computational imaging with the logarithmic asphere: theory," JOSA A, **20** No. 12, pp. 2260 – 2273, 2003, Wanli Chi and Nicholas George.

"Analysis of multitone holographic interference filters using a sparse Hill's matrix method," Appl. Opt. **43**, pp. 88 – 98, 2004, Damon W. Diehl and Nicholas George.

"Scanned-picture-beam holography for nonrigid objects," Appl. Opt. **43**, pp. 1703-1709, 2004, William W. Cook and Nicholas George.

"Fractional finite Fourier transform," J. Opt. Soc. Am. A **21**, pp. 1179-1185, 2004, K. Khare and Nicholas George.

"Integrated imaging with a centrally obscured logarithmic asphere," Opt. Comm. **245**, pp. 85-92, 2005, Wanli Chi and Nicholas George.

"Sampling theory approach to eigenwavefronts of imaging systems," J. Opt. Soc. Am. A **22**, p. 434, 2005, K. Khare and Nicholas George.

"Light-emitting diode illumination design with a condensing sphere," J. Opt. Soc. Am. A, **23**, No. 9, pp. 2295-2298, 2006, Wanli Chi and Nicholas George.

"Polarization coded aperture," Optics Express **14**, p. 6634, 2006, Wanli Chi, Kaiqin Chu, and Nicholas George.

"Electronic holography at terahertz and infrared frequencies," Proceedings of the International Conference on Display Holography, Wales, 2006, Nicholas George, Kedar Khare, and Wanli Chi.

"Long wavelength infrared holography using a microbolometer array," Invited Paper, OSA Annual Meeting, Rochester, NY, October 2006, Nicholas George, K. Khare and Wanli Chi.

"Correlation function for speckle size in the right-half-space," Opt. Commun. **276**, pp. 1-7, 2007, Kaiqin Chu and Nicholas George.

"Infrared holography using a microbolometer array," Appl. Opt. **47** No. 4, pp. A7 – A12, 2008, Nicholas George, Kedar Khare and Wanli Chi.

"Speckle in the 4F optical system," Appl. Opt. **47**, No.4, pp. A13 – A20, 2008, Nien-An Chang and Nicholas George.

"Resolution analysis of a gradient-index rod and a gradient-index lens array," Appl. Opt., November 2008, Xi Chen and Nicholas George.

"Optics Optimization in High-Resolution Imaging Module with Extended Depth of Field," Proceedings SPIE, **7061**, pp. 1-12, 2008, Xi Chen, Dmitry Bakin, Changmeng Lieu, Nicholas George.

"Extending the depth of field through unbalanced optical path difference," Appl. Opt. **47**, No. 36, pp. 6895-6903, 2008, Kaiqin Chu, Nicholas George and Wanli Chi.

"Sensor modulation transfer function measurement using band-limited laser speckle," Opt. Express, **16**, No. 24, 2008, Xi Chen, Nicholas George, Gennadiy Agranov, Changmeng Liu and Bob Gravelle.

"Phase-Coded aperture for optical imaging," Opt. Comm. **282**, pp. 2110-2117, 2009, Wanli Chi and Nicholas George.

"Incoherently combining logarithmic aspheric lenses for extended depth of field," Appl. Opt. **48**, pp. 5371-5379, 2009, Kaiqin Chu, Nicholas George and Wanli Chi.

"Extended depth-of-field lenses and methods for their design, optimization and manufacturing, U.S. Patent Application Publication US 2010/0002310 Al, Jan. 7, 2010, Nicholas George and Xi Chen.

"Wavelength decorrelation of speckle in propagation through a thick diffuser," J. Opt. Soc. Am. A **28**, No. 2, Feb. 2011, Nien-an Chang, Nicholas George, and Wanli Chi.

"Optical imaging with phase-coded aperture," Optics Express **19**, Issue 5, 4294-4300, 2011, Wanli Chi and Nicholas George.

"Optical Element, Device, Method, and Applications," U.S. Patent Publication US 2011/0085051 A1, 2011, Wanli Chi and Nicholas George.

"Illustrative EDOF topics in Fourier optics," Invited Talk, SPIE Annual Meeting, Tribute to Joseph W. Goodman 75th Year, August 2011, Nicholas George, Xi Chen, and Wanli Chi.

"Remotely measuring a thin dielectric coating on a metallic cylinder," Opt. Express **19**, Issue 27, 26684-26695, December 2011, Nicholas George and Paul Zavattero.

"Digital Binary MEMS Wavefront Control," U.S. Patent No. 8,107,156 B2, 2012, Nicholas George and Kedar Khare.

"Fourier Optics," © 2012, published as a monograph written in an advanced style and presently posted as freeware on UR web. Further publishing on this and related topics is underway.

"Deductive derivation of the displacement term in Maxwell's equations," September 2013, unpublished manuscript with supplementary poster/talk, Songfeng Han and Nicholas George.

"Digital Binary MEMS Wavefront Control," U.S. Patent No. 8,634,126 B2, 2014, Nicholas George and Kedar Khare.

CHRONOLOGICAL LISTING OF TITLES

"Holography and Stereoscopy: The Holographic Stereogram," Phot. Science Engin. **13**, 342 (1969), Nicholas George and J.T. McCrickerd. 2

"Axial Magnetic Field Effects on a Saturated He-Ne Laser Amplifier," IEEE J. Quantum Electronics **6**, 117 (1970), R.T.Menzies, Andrew Dienes, and Nicholas George. 1

"Holographic Dielectric Grating: Theory and Practice," Appl. Opt. **9**, 713 (1970), Milton Chang and Nicholas George; and Summary in J. Quantum Electronics **5**, 333 (1969). 2

"Nonlinear Refraction Indices of CS_2-CCl_4 Mixtures," Opto Electronics **1**, No. 4, 213 (1970), R.W. Hellwarth and Nicholas George. 1

"Spectral Coincidences Between Emission Lines of the CO Laser and Absorption Lines of Nitrogen Oxides," IEEE J. Quantum Electronics **6**, Dec. (1970), R.T. Menzies, Nicholas George, and M.L. Bhaumik. 1

"Use of CO Laser Lines to Detect Oxides of Nitrogen in the Atmosphere," J. Opt. Soc. Am. **60**, 1550A (1970), R.T. Menzies and Nicholas George. 1

"Full-View Holograms," Optics Communications **1**, 457 (1970), Nicholas George. 2

"Experiments with Full-View Holographic Stereograms," J. Opt. Soc. Am. **60**, 1554A (1970), Nicholas George. 2

"Intensity-Induced Changes in Optical Polarization in Glasses," Phys. Rev. B. Jan 15, 1972, Adelbert Owyoung, R.W. Hellwarth, and Nicholas George. 1

"Origin of the Nonlinear Refractive Index of Liquid CCl_4," Phys. Rev. A **4**, 2342 (1971), R.W. Hellwarth, Adelbert Owyoung, and Nicholas George. 1

"Diffraction Pattern Sampling for Real-Time Pattern Recognition," J. Opt. Soc. Am. **62**, 1380A (1972), Nicholas George, J.T. Thomasson, and Niels Jensen. 4

"The Space Bandwidth Product of Multichannel Coherent Processors," J. Opt. Soc. Am. **62**, 1366A (1972), R.B. MacAnally and Nicholas George. 1

"Speckle in Microscopy," Optics Communications **6**, 253 (1972), Nicholas George and Atul Jain. 3

"Detection of Mode-Locked Laser Signals," Optics Communications **5**, 407 (1972), R.J. D'Orazio and Nicholas George. 1

"Diffraction of Laguerre Gaussian Beams by an Aperture," J. Opt. Soc. Am. **62**, 1119 (1972), A.C. Livanos and Nicholas George. 1

"Matched-Filter Detection of Mode-Locked Laser Signals," Applied Optics **12**, 2367 (1973), R.J. D'Orazio and Nicholas George. 1

"Speckle Reduction Using Multiple Tones of Illumination," Applied Optics **12**, 1202 (1973), Nicholas George and Atul Jain, and abstract in J. Opt. Soc. Am. **62**, 1356A (1972). 3

"The Wavelength Diversity of Speckle," SPIE Jour. Dev. in Laser Technology **17**, 150 (1973), Nicholas George and Atul Jain. 3

"Matched Filter Detection of Mode-Locked Laser Signals," in **Space Optics** edited by B.J. Thompson and R.R. Shannon, ICO IX Conference Proc. (National Academy of Sciences, Washington, D.C., 1974), 461-475. 1

"Space and Wavelength Dependence of Speckle Intensity," Applied Physics **4**, 201 (1974), Nicholas George and Atul Jain. 3

"Speckle, Diffusers, and Depolarization," Applied Physics **6**, 65 (1975), Nicholas George, Atul Jain, and R.D.S. Melville. 3

"Experiments on the Space and Wavelength Dependence of Speckle," Applied Physics—Invited Paper **7**, 157 (1975), Nicholas George, Atul Jain, and R.D.S. Melville. 3

"Speckle From a Cascade of Two Diffusers," Optics Communications **15**, 71 (1975), Nicholas George and Atul Jain. 3

"Edge Diffraction of a Convergent Wave," Applied Optics **14**, 608 (1975), A.C. Livanos and Nicholas George. 1

"Speckle," Optics News **14**, January 1976, Nicholas George. 3

"The Wavelength Sensitivity of Back-Scattering," Optics Communications **16**, 328 (1976), Nicholas George. 3

"Diffraction Pattern Sampling for Recognition and Metrology," Proceedings of the Technical Program, SPIE Electro-Optical Systems Division Conference, 494-503 (Industrial and Scientific Conference Management, Chicago, 1975), Nicholas George and H.L. Kasdan. 4

"Measuring Tiny Gaps Using Diffraction Pattern Sampling," Proc. of 1976 International Optical Computing Conference, Capri, Nicholas George and H.L. Kasdan. 4

"Linewidth Measurement by Diffraction Pattern Analysis," Proc. of the Technical Program, SPIE Electro-Optical Systems Division Conference, **80**, 54, H.L. Kasdan and Nicholas George. 4

"Remote sensing of large roughened spheres," Optica Acta **23**, 367 (1976), Nicholas George, A.C. Livanos, J.A. Roth, and C.H. Papas. 3

"Speckle Noise and Object Contrast," article in **Image Analysis and Evaluation** edited by R. Shaw, SPSE Conference Proc. (SPSE, Washington, D.C. 1977), 202, B.D. Guenther, Nicholas George, C.R. Christensen, J.S. Bennett. 3

"Scattering by Glass Microballoons," J. Opt. Soc. Am. **66**, 1135A (1976), Nicholas George. 3

"Topical issue on speckle," J. Opt. Soc. Am. **66**, 1316 (1976), Nicholas George and Douglas C. Sinclair. 3

"Speckle Noise in Displays," J. Opt. Soc. Am. **66**, 1282 (1976), Nicholas George, C.R. Christensen, J.S. Bennett, B.D. Guenther. 3

"Speckle from Rough Moving Objects," J. Opt. Soc. Am. **66**, 1182 (1976), Nicholas George. 3

"Laser Propagation Experiments Using a Controlled Turbulent Gaseous Mixture," J. Opt. Soc. Am. **67**, 1375A (1977), and **69**, 1435A (1979) Nicholas George and Lambertus Hesselink. 3

"Object Detectability in Speckle Noise," Conference on Lasers, 1978, pp. 637-645, C.R. Christensen, B.D. Guenther, J.S. Bennett, Anil Jain, Nicholas George, Adam Kozma. 3

"Diffraction by serrated apertures," J. Opt. Soc. Am. **70**, 6-17 (1980), Nicholas George and G.M. Morris. 3

"Measurement of Optical Fiber Diameter Using the Fast Fourier Transform," Appl. Opt. **19**, pp. 2031-2033 (1980), M.A.G. Abushagur and Nicholas George. 4

"Matched filtering using band limited illumination," Opt. Lett. **5**, pp. 202-204 (1980), G.M. Morris and Nicholas George. 3, 4

"A Profile: The Teaching of Optics by the Faculty of The Institute of Optics," IEEE Trans. on Education, May 1980, Nicholas George and Karin Strand. 1

"Space and wavelength dependence of a dispersion-compensated matched filter," Appl. Opt. **19**, pp. 3843-3850 (1980), G.M. Morris and Nicholas George. 3, 4

"Frequency-plane filtering with an achromatic optical transform," Opt. Lett. **5**, pp. 446-448 (1980), G.M. Morris and Nicholas George. 3, 4

"Optical matched filtering in noncoherent illumination," invited paper in **Current Trends in Optics**, ed. by F.T. Arecchi and F.R. Aussenegg, Taylor and Francis, London, 1981, Nicholas George and G.M. Morris. 3, 4

"Bandwidth of holographic optical elements," Opt. Lett. **7**, 445-447 (1982), Thomas Stone and Nicholas George. 2

"Matched filtering in white light illumination," Proc. of SPIE, **388**, 11-22, 1983, Nicholas George and G.M. Morris. 3, 4

"Cosinusoidal transforms in white light," Appl. Opt. **23**, 700-710, 1984, Nicholas George and Shen-ge Wang. 3, 4

"Fresnel zone transforms in spatially incoherent illumination," Appl. Opt. **24**, pp. 842-850, 1985, Shen-ge Wang and Nicholas George. 3, 4

"About speckle," SPIE Proceedings of International Speckle Conference, Vol. 556, pp. 8-27, San Diego, 1985, Nicholas George, reprinted as "Speckle at various planes in an optical system," Opt. Eng. **25**, pp. 754-764, 1986. 3

"Diffuser transmission functions and far-zone speckle patterns," SPIE Proceedings of International Speckle Conference, Vol. 556, pp. 63-69, San Diego 1985, Lyle Shirley and Nicholas George. 3

"Wavelength performance of holographic optical elements," Appl. Opt. **24**, pp. 3797-3810, 1985, Thomas Stone and Nicholas George. 2

"Image reconstruction from partial Fresnel zone information," Appl. Opt. **25**, pp. 178-183, 1986, Robert Rolleston and Nicholas George. 1

"Polarization and Wavelength Effects on the Scattering From Dielectric Cylinders," Appl. Opt. **24**, pp. 4141-4145, 1985, M.A.G. Abushagur and Nicholas George. 1

"Speckle at various planes in an optical system," Opt. Eng. **25**, 754-764, 1986, Nicholas George. 3

"Stationary phase approximations in Fresnel zone magnitude-only reconstructions," JOSA A **4**, pp. 148-153, 1987, Robert Rolleston and Nicholas George. 1

"Wide-angle diffuser transmission functions and far-zone speckle," JOSA A **4**, pp. 734-745, 1987, Lyle G. Shirley and Nicholas George. 3

"Diffraction analysis of rough reflective surfaces," Appl. Opt. **26**, pp. 2364-2375, 1987, Karen Allardyce and Nicholas George. 3

"Diffraction from a small square aperture: approximate aperture fields," JOSA A **5**, pp. 192-199, 1988 R. Edward English,Jr. and Nicholas George. 1

"Diffraction from a circular aperture: on-axis field strength," Appl. Opt. **26**, pp. 2360-2366, 1987, R. Edward English, Jr. and Nicholas George. 1

"Sine-cosine cascade correlator with real-valued filters," Opt. Lett. **12**, pp. 383-385, 1987, Shen-ge Wang and Nicholas George. 4

"Diffuser radiation patterns over a large dynamic range," Appl Opt.**27**, pp. 1850-1861, 1988, Lyle G. Shirley and Nicholas George. 3

"Diffraction patterns in the shadows of disks and obstacles," Appl. Opt. **27**, pp. 1581-1587, 1988, R. Edward English, Jr. and Nicholas George. 1

"Hybrid diffractive-refractive lenses and achromats," Appl. Opt. **27**, pp. 2960-2971, 1988, Thomas Stone and Nicholas George. 2

"Achromatized holographic phase shifter and modulator," Opt. Comm. **67**, pp. 185-191, 1988, Nicholas George and Thomas Stone. 2

"White light interferometry with an achromatic phase shifter," Proc. SPIE, **883**, pp. 196-202, 1988, Nicholas George and Thomas Stone. 2

"Speckle from a cascade of two thin diffusers," JOSA A **6**, pp. 765-781 (1989), Lyle G. Shirley and Nicholas George. 3

"Radiated spectrum from two partially correlated dipoles," JOSA A **6**, pp. 1150-1155 (1989), Avshalom Gamliel and Nicholas George. 3

"Features in the optical transform of serrated apertures and discs," J. Opt. Soc. Am. A **6**, pp.1815-1826, 1989, Madeleine Beal and Nicholas George. 3

"Holography" in **Ullman's Encyclopedia of Industrial Chemistry,** 5th Edition, VCH Publishers, Weinheim, 1989, Nicholas George and Thomas Stone. 2

"Pattern recognition using the ring-wedge detector and neural-network software," Proc. Soc. Photo-Opt. Instr. Eng., **1134**, 1989, Nicholas George, Shen-ge Wang, and D.L. Venable. 4

"Index variation and scattering in a holographic medium," Proc. Soc. Photo-Opt. Instr. Eng., **1136**, 1989, Thomas Stone, Nicholas George, and B.D. Guenther. 2

"Correlation Theory of Electromagnetic Radiation Using Multipole Expansions," in **Recent Advances in Electromagnetic Theory**, (Springer-Verlag, Berlin, 1990), pp. 144-182, Nicholas George and Avshalom Gamliel. 3

"Comparison of wavelength scanning and pulse echo systems in remote sensing," Opt. Comm. **77**, pp. 91-98, 1990, Donald J. Schertler and Nicholas George. 1

"Recognition of threaded objects by spatial spectrum analysis," Appl. Opt. **30**, pp. 1379-1387, 1991, B.J. Stossel and Nicholas George. 4

"Particle sizing by inversion of the optical transform pattern," Appl. Opt. **30**, pp. 4786-4794, 1991, Scott D. Coston and Nicholas George. 3

"Recovery of particle size distributions by inversion of the optical transform intensity," Opt. Lett. **16**, pp. 1918-1920, 1991, Scott D. Coston and Nicholas George. 3

"Speckle observation of pulsed laser-induced dynamics in a guest-host smectic A liquid crystal system," Liq. Crystals **12**, pp. 689-696, 1992, M.J. Guardalben and Nicholas George. 3

"Backscattering cross section of a tilted, roughened disc," J. Opt. Soc. Am. A, **9**, pp. 2056-2066, 1992, Donald J. Schertler and Nicholas George. 3

"Beam splitter cube for white-light interferometry," Opt. Eng. **31**, pp. 2191-2196, 1992, Keith B. Farr and Nicholas George. 1

"Roughness determination by speckle-wavelength decorrelation," Opt. Lett., **18**, pp. 391-393, 1993, Donald J. Schertler and Nicholas George. 3

"Photomixing of achromatically frequency-modulated incoherent light," Opt. Lett. **18**, pp. 1038-1040, 1993, Nicholas George and Stojan Radic. 1, 2

"Novel centering method for overlapping correction in halftoning," IS&T's 47th Annual Conference/ICPS 1994, pp. 483-486, 1994, Shen-ge Wang, Keith T. Knox, and Nicholas George. 1

"A case study: Dual-use technologies and University Research Initiatives," Army RD & A Bull. **PB 70-93-6**, pp. 19-23, 1993, Nicholas George, B.D. Guenther, and Vincent Piarulli. 1

"Neural networks applied to diffraction pattern sampling," Appl. Opt. **33**, pp. 3127-3134, 1994, Nicholas George and Shen-ge Wang. 4

"Automatic image quality assessment," IS&T's 47th Annual Conference ICPS 1994, pp. 436-438, 1994, David M. Berfanger and Nicholas George. 4

"Controlled blurring in image processing," IS&T's 47th Annual Conference/ICPS 1994, pp. 534-535, 1994, Brian J. Stossel and Nicholas George. 1

"The backscattering cross section of a roughened sphere," J. Opt. Soc. Am. A **11**, pp. 2286-2297, 1994, Donald J. Schertler and Nicholas George. 3

"Infrared target simulation and recognition," 1994 IEEE Dual Use Technologies and Applications Conference, 23-26 May 1994, SUNY Institute of Technology, Utica/Rome, New York, Andreas E. Savakis and Nicholas George. 4

"Prototype of a flexible image recognition system," 1994 IEEE Dual Use Technologies and Applications Conference, 23-26 May 1994, SUNY Institute of Technology, Utica/Rome, New York, Alexander D. Mirzaoff and Nicholas George. 4

"Ultrafast pulse propagation in periodic optical media: a generalized finite-difference time-domain approach," Opt. Lett. **19**, pp. 1064-1066, 1994, Stojan Radic and Nicholas George. 1

"Holographic contouring using tunable lasers," Opt. Lett. **19**, pp. 1879-1881, 1994, Nicholas George and Wenjun Li. 1, 2

"$\lambda/4$-shifted nonlinear periodic structure: theory of low-intensity switching," International Symposium on Guided-Wave Optoelectronics, Weber Research Institute, 26-28 October, 1994, New York, New York, Stojan Radic, Nicholas George, and Govind P. Agrawal. 1

"Optical switching in λ/4-shifted nonlinear periodic structures," Opt. Lett. **19**, pp. 1789-1791, 1994, Stojan Radic, Nicholas George, and Govind P. Agrawal. 1

"Nonlinear DFB phase-shifted structure: all-optical, low-intensity switching device," LEOS '94 7th Annual Meeting, Conference Proceedings **2**, pp. 61-62, 1994, Boston, Stojan Radic, Nicholas George, and Govind P. Agrawal. 1

"Analysis of nonuniform nonlinear distributed feedback structures: generalized transfer matrix method," J. Quantum Electron. **31**, pp. 1326-1336, 1995, Stojan Radic, Nicholas George, and Govind P. Agrawal. 1

"Generalized distributed feedback design: amplification, filtering, and switching," in *Physics and Simulation of Optoelectronic Devices III,* Proc. SPIE **2399**, pp. 37-48, 1995, Stojan Radic, Nicholas George, and Govind P. Agrawal. 1

"Theory of low-threshold optical switching in nonlinear, phase-shifted, periodic structures," J. Opt. Soc. Am. B **12**, pp. 671-680, 1995, Stojan Radic, Nicholas George, and Govind P. Agrawal. 1

"Low-threshold optical switching in non-uniform nonlinear distributed feedback structures," Optics & Photonics News **6**, pp. 18-19 1995, Stojan Radic, Nicholas George, and Govind Agrawal. 1

"Multiple point impulse responses: controlled blurring and recovery," Opt. Comm. **121**, pp. 156-165, 1995, Bryan J. Stossel and Nicholas George. *Erratum*, Opt. Comm. **122**, p. 212, 1996. 1

"Lensless electronic imaging, "Opt. Comm. **133**, pp. 22-26,1997, Nicholas George. 1

"Theory for the propagation of short electromagnetic pulses," Opt. Comm. **133**, pp. 1-6, 1997, Nicholas George and Stojan Radic. 1

"The Center for Electronic Imaging Systems: Imaging in the Information Age," Proc. International Conference on Engineering Education, Rio de Janeiro, 1998, C.N. George and Nicholas George. 1

"Uniform scattering patterns from grating-diffuser cascades for display applications," Appl. Opt. **38**, pp. 291-303, 1999, D.J. Schertler and Nicholas George. 2, 3

"All-digital ring-wedge detector applied to fingerprint recognition," Appl. Opt. **38**, pp. 357-369, 1999, D.M. Berfanger and Nicholas George. 4

"All-digital ring-wedge detector applied to automatic image quality assessment," Appl. Opt. **39**, pp. 4080-4097, 2000 D.M. Berfanger and Nicholas George. 4, 5

"Electronic imaging using a logarithmic asphere," Opt. Lett. **26**, pp. 875-877, 2001, Wanli Chi and Nicholas George. 1, 5

"Direct sampling and demodulation of carrier-frequency signals," Opt. Comm., 2002, Kedar Khare and Nicholas George. 1,5

"Holographic interference filters for infrared communications," Appl. Opt. **42**, No. 7, pp. 1203-1210, 2002, Damon W. Diehl and Nicholas George. 5

"Extended depth of field with the logarithmic asphere," Opt. & Photonics News, Dec. 2002, Wanli Chi and Nicholas George. 5

"Sampling, demodulation and phase retrieval," Opt. & Photonics News, Dec. 2002, Kedar Khare and Nicholas George. 5

"Direct coarse sampling of electronic holograms," Opt. Lett. **28**, No. 12, pp. 1004-1006, 2003, Kedar Khare and Nicholas George. 5

"Extended depth of field using the logarithmic asphere," J. Optics A, **5**, pp. S157-S163, Special Issue: Optics for the Quality of Life, 2003, Nicholas George and Wanli Chi. 5

"Fourier optical analysis of gradient-index array imaging," Appl. Opt., **42**, No. 22, pp. 4434-4444, 2003, Xi Chen and Nicholas George. 5

"Sampling theory approach to prolate spheroidal wave functions," Journal of Physics A, **36**, pp. 10011-10021, September 2003, Kedar Khare and Nicholas George. 5

"Computational imaging with the logarithmic asphere: theory," JOSA A, **20** No. 12, pp. 2260 – 2273, 2003, Wanli Chi and Nicholas George. 5

"Analysis of multitone holographic interference filters using a sparse Hill's matrix method," Appl. Opt. **43**, pp. 88 – 98, 2004, Damon W. Diehl and Nicholas George. 5

"Scanned-picture-beam holography for nonrigid objects," Appl. Opt. **43**, pp. 1703-1709, 2004, William W. Cook and Nicholas George. 5

"Fractional finite Fourier transform," J. Opt. Soc. Am. A **21**, pp. 1179-1185, 2004, K. Khare and Nicholas George. 5

"Integrated imaging with a centrally obscured logarithmic asphere," Opt. Comm. **245**, pp. 85-92, 2005, Wanli Chi and Nicholas George. 5

"Sampling theory approach to eigenwavefronts of imaging systems," J. Opt. Soc. Am. A **22**, p. 434, 2005, K. Khare and Nicholas George. 5

"Light-emitting diode illumination design with a condensing sphere," J. Opt. Soc. Am. A, **23**, No. 9, pp. 2295-2298, 2006, Wanli Chi and Nicholas George. 5

"Polarization coded aperture," Optics Express **14**, p. 6634, 2006, Wanli Chi, Kaiqin Chu, and Nicholas George. 5

"Electronic holography at terahertz and infrared frequencies," Proceedings of the International Conference on Display Holography, Wales, 2006, Nicholas George, Kedar Khare, and Wanli Chi. 5

"Long wavelength infrared holography using a microbolometer array," Invited Paper, OSA Annual Meeting, Rochester, NY, October 2006, Nicholas George, K. Khare and Wanli Chi. 5

"Correlation function for speckle size in the right-half-space," Opt. Commun. **276**, pp. 1-7, 2007, Kaiqin Chu and Nicholas George. 5

"Infrared holography using a microbolometer array," Appl. Opt. **47** No. 4, pp. A7 – A12, 2008, Nicholas George, Kedar Khare and Wanli Chi. 5

"Speckle in the 4F optical system," Appl. Opt. **47**, No.4, pp. A13 – A20, 2008, Nien-An Chang and Nicholas George. 5

"Resolution analysis of a gradient-index rod and a gradient-index lens array," Appl. Opt., November 2008, Xi Chen and Nicholas George. 5

"Optics Optimization in High-Resolution Imaging Module with Extended Depth of Field," Proceedings SPIE, **7061**, pp. 1-12, 2008, Xi Chen, Dmitry Bakin, Changmeng Lieu, Nicholas George. 5

"Extending the depth of field through unbalanced optical path difference," Appl. Opt. **47**, No. 36, pp. 6895-6903, 2008, Kaiqin Chu, Nicholas George and Wanli Chi. 5

"Sensor modulation transfer function measurement using band-limited laser speckle," Opt. Express, **16**, No. 24, 2008, Xi Chen, Nicholas George, Gennadiy Agranov, Changmeng Liu and Bob Gravelle. 5

"Phase-Coded aperture for optical imaging," Opt. Comm. **282**, pp. 2110-2117, 2009, Wanli Chi and Nicholas George. 5

Appl. Opt. **48**, pp. 5371-5379, 2009, Kaiqin Chu, Nicholas George and Wanli Chi. 5

"Extended depth-of-field lenses and methods for their design, optimization and manufacturing, U.S. Patent Application Publication US 2010/0002310 Al, Jan. 7, 2010, Nicholas George and Xi Chen. 5

"Wavelength decorrelation of speckle in propagation through a thick diffuser," J. Opt. Soc. Am. A **28**, No. 2, Feb. 2011, Nien-an Chang, Nicholas George, and Wanli Chi. 5

"Optical imaging with phase-coded aperture," Optics Express **19**, Issue 5, 4294-4300, 2011, Wanli Chi and Nicholas George. 5

"Optical Element, Device, Method, and Applications," U.S. Patent Publication US 2011/0085051 A1, 2011, Wanli Chi and Nicholas George. 5

"Illustrative EDOF topics in Fourier optics," Invited Talk, SPIE Annual Meeting, Tribute to Joseph W. Goodman 75th Year, August 2011, Nicholas George, Xi Chen, and Wanli Chi. 5

"Remotely measuring a thin dielectric coating on a metallic cylinder," Opt. Express **19**, Issue 27, 26684-26695, December 2011, Nicholas George and Paul Zavattero. 5

"Digital Binary MEMS Wavefront Control," U.S. Patent No. 8,107,156 B2, 2012, Nicholas George and Kedar Khare. 5

"Fourier Optics," © 2012, published as a monograph written in an advanced style and presently posted as freeware on UR web. Further publishing on this and related topics is underway. 5

"Deductive derivation of the displacement term in Maxwell's equations," September 2013, unpublished manuscript with supplementary poster/talk, Songfeng Han and Nicholas George. 5

"Digital Binary MEMS Wavefront Control," U.S. Patent No. 8,634,126 B2, 2014, Nicholas George and Kedar Khare.